GSI Scientific Report 2015

GSI Report 2016-1

DOI:10.15120/GR-2016-1

ISSN: 0174-0814
and GSI Report 2016-1

Publisher: GSI Helmholtzzentrum für Schwerionenforschung GmbH,
Planckstr. 1, 64291 Darmstadt, Germany, <http://www.gsi.de>
GSI is a member of the Helmholtz association of national research centres <http://www.helmholtz.de>.
E-only-edition: DOI:10.15120/GR-2016-1

Editor: Katrin Große,
Contact: gsilibrary@gsi.de, phone: +496159 712610, fax: +496159 713049.
Cover photograph: Gabi Otto.
Publication date: August 2016

For the production of this report templates and scripts of the JACoW collaboration (Joint Accelerator Conferences on Web <http://www.jacow.org>) were used.

Contents

DOI:10.15120/GR-2016-1

DOI:10.15120/GR-2016-1

DOI:10.15120/GR-2016-1

DOI:10.15120/GR-2016-1

DOI:10.15120/GR-2016-1

DOI:10.15120/GR-2016-1

DOI:10.15120/GR-2016-1

DOI:10.15120/GR-2016-1

Pre-series production of microcables for STS detector modules at LTU Ltd

V.M. Borshchov[1], *Yu.A. Murin*[2], *C.J. Schmidt*[3], *M.A. Protsenko*[1], *I.T. Tymchuk*[1], *J.M. Heuser*[3], *R.A. Kushniruk*[1], *M.S. Tykhomirova*[1], *K.M. Liholitova*[1], *and L.V. Klimova*[1]

[1]LED Technologies of Ukraine (LTU) Ltd, Kharkov, Ukraine; [2]JINR, Dubna, Russia; [3]GSI, Darmstadt, Germany

Pre-series batches of microcables for CBM-STS detector modules have been developed, manufactured and delivered. They are being used for the development and verification of work flows and tooling for STS detector module assembly at GSI and JINR. The work was carried out within the STCU project P635 by the partners GSI and LTU, and additionally in cooperation with JINR.

Microcables for STS detector modules

Ultra-light micro-cables are the key component for the CBM-STS. They are employed to realize the analogue signal interconnection between silicon sensors and readout electronics, providing minimized material budget. For the detector modules two kinds of interconnection components will be employed [1, 2]:

- ultra-light interconnection microcables based on aluminium-polyimide adhesiveless dielectrics: connecting microcables, interstrip cables (optional), daisy-chain cables (optional), and shielding layers.
- meshed spacers based on Kapton or polyimide (narrow and wide meshed spacers).

The amount of microcables and meshed spacers required for the STS totals to more than 75 thousands.

Pre-series microcables

For working-off the assembly approaches test sets of microcables (100 pcs.) and 24 pre-series batches of microcables (about 900 pcs.) have been manufactured and delivered to JINR and GSI. Microcables and spacers have been manufactured at the microcables production site [3] and laminated with spacers at the assembly site of LTU Ltd. The length of the microcables is chosen as it was done for the first ladder mechanical mock-up, namely 111 mm, 212 mm and 252 mm. According to the base approach [1, 2] each pre-series set of microcables includes about 40 components – mainly those depicted in Fig. 1:

- analog connecting cable with glued narrow meshed spacer – 32 pcs (8 types);
- shielding layer with wide meshed spacer – 2 pcs. (2 types);
- wide meshed spacer – 2 pcs. (2 types);
- interstrip cable – 1 pc. or 2 pcs. (optional);
- daisy chain cable – 2 pcs. (2 types) (optional).

Figure 1: Analogue cable with narrow meshed spacer (top); shielding layer with wide meshed spacer (middle); wide meshed spacer (bottom).

The manufactured microcables are being used for developing and verifying work flow and tooling for the STS detector module assembly at GSI and JINR [4, 5].

Conclusions

The manufactured pre-series microcables allow verifying the assembly approaches for the STS detector modules. The obtained results will be applied for the forthcoming CBM STS detector modules series production.

References

[1] C.J. Schmidt et al., CBM Progress Report 2012, p. 18

[2] V.M. Borshchov et al., CBM Progress Report 2014, p. 47

[3] V.M. Borshchov et al., CBM Progress Report 2014, p. 45

[4] C. Simons et al., Development of a workflow for the STS module assembly, this report

[5] A. Sheremetev et al., Development of tooling for the STS module assembly at JINR's VB LHEP Assembly Laboratory, this report

DOI:10.15120/GR-2016-1

Progress with micro-strip sensors for the CBM Silicon Tracking System

J. Heuser[1], *Y. Murin*[2], *C.J. Schmidt*[1], *D. Soyk*[1], *and C. Sturm*[1]
[1]GSI, Darmstadt, Germany; [2]JINR, Dubna, Russia

The eight tracking layers of CBM's Silicon Tracking System will be comprised of double-sided silicon micro-strip sensors in four geometrical dimensions. All sensors have the same width and numbers of strips but differ in the lengths of the strip-shaped electrodes. Those are matched to the particle densities in the respective aperture of the detector. Short strips are located close to the beam line where the particle densities are highest [1]. The main sensor parameters are:

- n-type silicon
- thickness: 285/320 $\pm$15 μm (vendor dependent)
- double-sided segmentation
- 1024 strips per side of 58 μm pitch
- strip lengths: 2/4/6/12 cm
- strip angle w.r.t. vertical edge: 7.5 degree (p-side), 0 degree (n-side)
- AC coupled read-out
- read-out from top edge
- 2nd metal read-out routing lines interconnecting the AC layers of the corner strips
- outer dimensions: 6.2 cm width; 2.2, 4.2, 6.2 and 12.4 cm height

Near-final prototypes in all sizes have been designed in cooperation with two vendors: CiS, Erfurt, Germany [2], and Hamamatsu Phototonics, Japan [3]. Productions of small batches were ordered from GSI and JINR in close coordination at both companies. Figure 1 presents details of a recent sensor produced. The sensors with 12 cm long strips are new. They replace the initially foreseen daisy-chained pairs of 6 cm high sensors with monolithic sensors. This will facilitate the module assembly by making the double-sided attachment of daisy-chain cables unnecessary. Pre-requirement is the availability of 6" wafer processing capability at the fabrication lines. While this is the standard technology at Hamamatsu, the wafer processing at CiS is still based on 4", with 6" processing being in a development phase.

Progress has been made with unifying the layouts of the sensors in all four dimensions. Contact pads for bias delivery and signal read-out were placed in accordance with the emerging module assembly procedure, allowing best placement and attachment of the micro cables connecting the sensor to the read-out electronics and bias supplies. Thickest possible metal layers, ca. 800 nm, are realized on the sensors to minimize the resistive load on the read-out ASIC, resulting in minimized noise. The largest sensor can be contacted also in the middle of the strips, reducing the resistive term further. Contact pads and other marks like labels, strip numbers and fields for serial number encoding were placed such that various quality assurance procedures are facilitated. Final inspection is part of the product deliverable. Detailed test parameters, specifications and test protocols have been worked out with the vendors. They cover both global sensor performance as current-voltage behavior, and strip-by-strip tests.

The prototypes are in the course of being qualified in the STS laboratories at GSI and Univ. Tübingen, using dedicated equipment for optical and electrical inspection. Also verified is their charge collection performance prior and after exposure to a neutron equivalent irradiation as later in the experiment, under the anticipated thermal operating conditions of $\leq$ -5° C. The aim is to establish sensor production readiness towards the end of 2016.

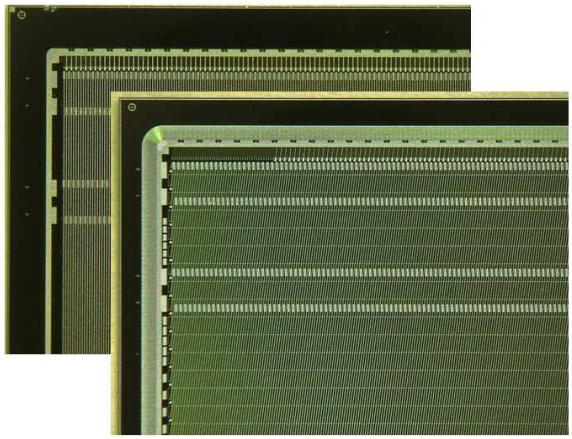

Figure 1: Microscope views of corners of two sides of a recent 6.2 by 2.2 cm prototype micro-strip sensor from CiS. Visible are the metal layers of the strips (lower photo: 0 degree orientation on the n-side, upper photo: 7.5 degree orientation on the p-side). The guard ring and bias ring structures surround the sensitive area. Rows of contact pads allow attaching the read-out cable. Horizontal routing lines on a second metal layer interconnect the read-out lines of the strips in opposite sensor corners for common read-out.

References

[1] CBM STS Technical Design Report, GSI Report 2013-4 (2013), chapter 2.3
[2] http://www.cismst.org
[3] http://www.hamamatsu.com

DOI:10.15120/GR-2016-1

Progress with the Integration of the CBM Silicon Tracking System

S. Belogurov[1], *D. Emschermann*[2], *M. Faul*[2], *U. Frankenfeld*[2], *J. Heuser*[2], *S. Koch*[2], *P. Koczon*[2], *J. Kunkel*[2], *J. Lehnert*[2], *T. Morhardt*[2], *W. Niebur*[2], *C.J. Schmidt*[2], *H.R. Schmidt*[3], *S. Schwab*[2], *O. Vassyliev*[2], *and J. Weinert*[2]

[1]ITEP, Moscow, Russia; [2]GSI, Darmstadt, Germany; [3]Univ. Tübingen, Germany

The STS system integration effort targets a detector that can be installed in the gap of the superconducting dipole magnet and taken out for system maintenance [1]. The current engineering activities address the detailed structure of the detector system, the space requirements of the mechanical STS building blocks along with technical solutions to their installation, geometrical precision, the cooling of electronics and sensors, and routing of the supplies and services within and through the thermal enclosure.

System design and mechanical units

The eight tracking stations of the STS are composed of 18 mechanical *half units*. The base of a half unit is a C-shaped frame onto which the detector ladders, assemblies of sensor modules mounted on carbon fiber carriers, are placed. The opening of the C-frames cover the detector's physics aperture, while at its perimeter the read-out electronics and power distribution boards are located and can be cooled. After optimization of the sensor placement in the units, the ladder structure and cable lengths have been defined, a pre-requisite for designing C-frames and cooling plates. Figure 1 depicts the current CAD design of a corner of detector half unit 7 in the most downstream station, the largest one with about 1 m height. Progress has been made with the arrangement of ladders, their detailed mounting on the C-frame, the cooling plates, the locations of electronics and powering boards and routing of signal and power cables. The dimensions of the STS main frame, receiving the half units and the thermal insulating walls, meet the spatial boundary conditions. The design aims at a mechanical precision of half unit/ ladder placement of better than 100 μm.

Cooling plates

The cooling system has to remove more than 40 kW of power dissipated by the front-end electronics located inside the thermal enclosure. The stacks of front-end electronics boards are to be mounted onto cooling plates. Those are aluminum plates with millimeter-diameter cooling channels through which bi-phase CO_2 will be circulated. The engineering team is currently prototyping such cooling plates in cooperation with industry using specific pressure-standing welding techniques.

Carbon fiber ladders

Prototypes of carbon fiber ladders have been manufactured at GSI in a winding technique. They were meant to prove the feasibility of a request for series production in aerospace industry. They are also used to explore a specifically low-mass construction of central ladders surrounding the beam pipe. A technical solution is depiced in Fig. 2, employing thin rods rather than a hollow cone as reported in [2] that turned out to involve too much material in the respective CBM arrangement.

Further tasks

The studies on the STS integration comprise further topics that are in different stages of completion: the rails for units and system, the base support plate, the realization of real-size models of C-frames with attached components, beam pipe and window towards target chamber/Micro Vertex Detector.

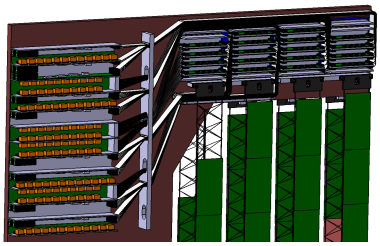

Figure 1: CAD design of a corner of a C-frame with detector ladders (center), front-end electronics (top), and powering and read-out boards (left), indicating also cable routing.

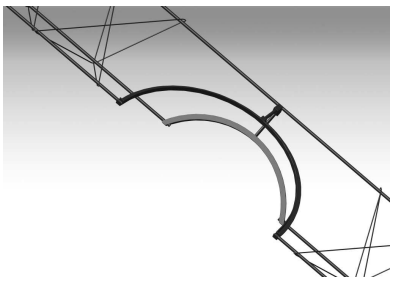

Figure 2: Design of a carbon fiber ladder with a particularly low-mass central region to surround the beam pipe.

References

[1] CBM STS Technical Design Report, GSI Report 2013-4 (2013), chapter 5.1

[2] S. Igolkin et al., CBM Progress Report 2014, p. 48

DOI:10.15120/GR-2016-1

Characterization of CBM silicon microstrip sensors bonded by microcables to Beetle readout chips

V. Dobishuk[1,2], *J. Heuser*[3], *V. Kyva*[1], *Ie. Momot*[1,3], *V. Pugatch*[1], *C. Sturm*[3], *and M. Teklishyn*[1,4]

[1]Institute for Nuclear Research NAS Ukraine, Kyiv, Ukraine; [2]Taras Shevchenko National University of Kyiv, Kyiv, Ukraine; [3]GSI, Darmstadt, Germany; [4]FAIR, Darmstadt, Germany

The CBM Silicon Tracking System will be assembled with double-sided silicon microstrip sensors connected to the readout electronics placed outside of the physics acceptance by microcables of different length. For connecting 58 μm pitch strips of the sensor two microcables with a pitch of 116 μm are to be used: the upper one for odd numbered strips, the bottom one for even numbered strips.

Characterization studies of prototypes of such assemblies are under way at KINR. First results are reported here for a silicon microstrip sensor (6 by 6 cm, CiS) bonded to the two readout $Beetle$ [1] chips mounted on the daughter board of an Alibava [2] system. The Alibava mother board digitizes analogue data from 256 charge-sensitive preamplifiers with 25 ns peaking time and provides control of the system. The sampled pulse is stored in an analogue pipeline with a fixed latency which is determined by the scintillator trigger adjusted for triggering from the MIP hits. A photo of the part of the daughter board with Beetle chips bonded by microcables to the microstrip sensor is shown in the left part of the Fig.1. Drawings of the connecting microcables are shown on the right part of Fig. 1.

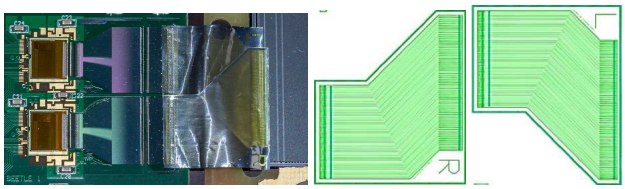

Figure 1: Left: Photo of the CBM microstrip sensor bonded by two microcables to Beetle chips of the Alibava Daughter Board. Right: Drawings of the microcables.

The sensor was operated at 80 V. Figure 2 (left, blue histogram) shows the noise distribution over the 256 channels of the readout microchips. The first Beetle chip accounts for the channels between 0 and 127, while channels from 128 to 255 correspond to the second chip. As one can see the noise grows up in both chips up to the channel no. 42. This is due to the fact that those channels are connected to the strips at the wafer edge where the length of the strips steadily increments accordingly to their layout at 7.5° stereo angle. The geometry of the microcable is such that the length of the connecting lines grows up here as well. The noise distribution as a function of the strip number on the wafer is shown by the red histogram. One may see that it goes abruptly down where the strip length as well as the length of the microcable lines becomes constant (from the strip-channel no. 85). The verification of the strip map (red histogram) has been performed by scanning focused laser beam (640 nm wavelength) with a diameter of 10 μm over the wafer. The response of operational strips was in accordance with the laser spot position.

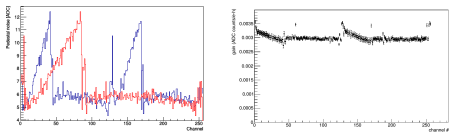

Figure 2: Left: Average noise of two Beetle chips as a function of their input channel number connected by microcables to the sensor (blue histogram); Noise assigned to the sensor strip number (red histogram). Right: Calibration histogram as a function of the readout chips' input channel.

In its left panel, Fig. 3 illustrates the two-dimensional amplitude distribution of the sensor response for two-strip clusters measured with the laser beam moving across the wafer. The right part shows similar data measured for cosmic rays, triggered by a scintillator detector on events with trajectories perpendicular to the sensor surface. Charge sharing in the interstrip gap is observable for the laser beam case. We shall accumulate more events for the cosmic rays with a statistics sufficient for making conclusion on the signal-to-noise performance in the interstrip gap.

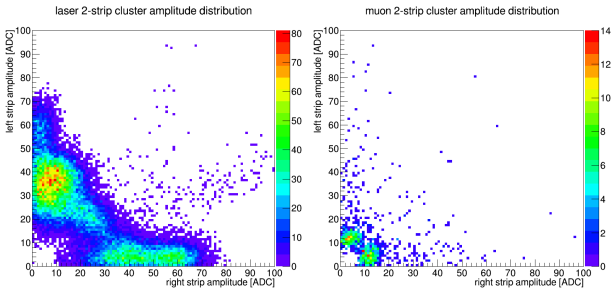

Figure 3: Left: Two dimensional amplitude distribution of the sensor response for two-strip clusters measured with the laser beam moving between adjacent strips. Right: Two-strip cluster data measured for cosmic rays.

References

[1] http://www.kip.uni-heidelberg.de/lhcb/Publications/BeetleRefMan_v1_3.pdf

[2] http://www.alibavasystems.com

DOI:10.15120/GR-2016-1

Development of a workflow for the CBM-STS module-assembly

C. Simons[1], *D. Soyk*[1], *R. Visinka*[1], *and I. Tymchuk*[2]
[1]GSI, Darmstadt, Germany; [2]LTU, Kharkiv, Ukraine

The Silicon Tracking system will consist of eight tracking stations that are built from different types of basic functional modules. Those are made from a double-sided silicon microstrip sensor that is connected via microcables to two front-end electronics boards. For one module 32 polyimide microcables, each with 64 aluminum traces, have to be connected on one end to 16 STS-XYTER ASICs, and on the other end to the p and n sides of the sensor, in two staggered layers with TAB-bonding. Additionally, the chips have to be wire-bonded to the front-end electronics boards and shielding layers have to be fixed. The aim was to find the best order for the process steps and to optimize aligning, bonding and glueing processes to obtain reliable and reproducable results. Fixtures had to be developed to facilitate the work and to make results as independant as possible from the personnel involved. UV-curing glues for the protection of the ASICs were tested to reduce the curing time of the glue to a minimum and to accelerate the workflow.

Assembly workflow

Having tried different orders of process steps we agreed on one workflow that turned out to be the most workable one. At the beginning the necessary material has to be arranged and a process slip is prepared for the module to keep records.

Step 1: The 32 microcables for p and n sides have to be TAB-bonded to the 16 STS-XYTER-ASICs in two layers. After bonding a quality measurement is performed with a pogo pin testsocket to find out if each bond has electrical contact. Reworking in case of failure is possible. Finally a protective glue is applied on the TAB-bonds (Fig. 1).

Step 2: These semi-modules now have to be TAB-bonded to the p side of the silicon sensor in two layers. After bonding quality measurements are performed with a pogo pin testsocket that puts the STS-XYTER in minimal operation and tests the electrical contact of the TAB-bonds. The application of glue protects the TAB-bonds at the end (Fig. 2).

Step 3: Now four STS-XYTER ASICs are die and wire bonded to the first row of the front-end board. If measurement results are ok, this first row is protected with globtop glue. Afterwards the procedure is repeated for the second ASIC row on the board (Fig. 3).

Step 4: At the end shielding layers and spacers are glued onto the microcables. Then the module has to be turned over to the n side of the sensor and the four steps have to be repeated for the this side (Fig. 4).

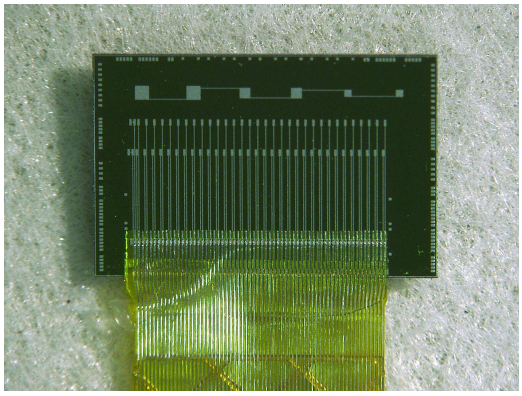

Figure 1: Microcables TAB-bonded to the ASIC.

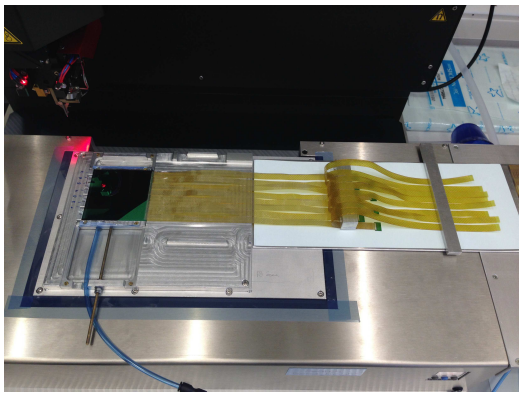

Figure 2: Microcables TAB-bonded to the sensor.

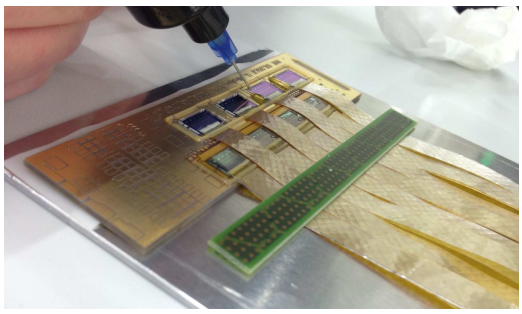

Figure 3: Globtop on the STS-8 board.

Figure 4: Dummy module with a 62x62 sensor.

DOI:10.15120/GR-2016-1

Test sockets for quality measurements during the CBM-STS module assembly

C. Simons[1], *V. Kleipa*[1], *C. J. Schmidt*[1], *D. Soyk*[1], *K. Kasinski*[2], *and I. Tymchuk*[3]
[1]GSI, Darmstadt, Germany; [2]AGH University of science and technology, Krakow, Poland; [3]LTU, Kharkiv, Ukraine

During the CBM-STS module assembly quality measurements need to be performed to assure electrical contact of the TAB-bonds that connect the microcables with the STS-XYTER chips as well as the silicon microstrip sensor. Non-destructive, easy and fast procedures for a large amount of microcables can be realized with Pogo Pin test sockets that are well adapted to the needs. In case of failure rebonding is possible while the devices are on the machine. Bonds are then finally protected with a globtop glue.

Test socket for the STS-microcables

After having TAB-bonded the Aluminum traces of the microcables to the pads of the STS-XYTER chip, the contacts can be checked through a test socket that provides easy connection to a dedicated testfan on the microcables (see Fig. 1). This testfan increases the pitch of the 42 μm wide traces from 116 μm to 200 μm. The testpads are staggered in two rows and have an approximately size of 200 by 600 μm. Because of the very thin microcables (thickness 24 μm) the company could only deliver the top socket with the Pogo Pins. The bottom socket will be designed in-house, a draft already exists (see Fig. 2). The microcable will be fixed by vacuum on a plate and aligned with pins.

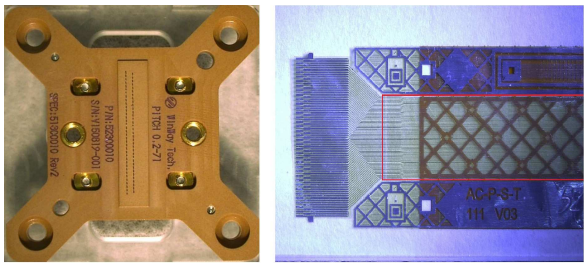

Figure 1: Top Pogo Pin socket (WinWay Technology) and testfan of the microcable.

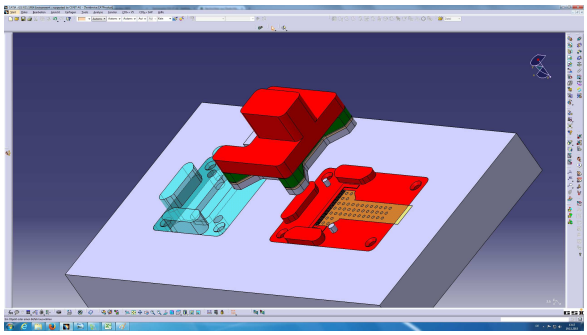

Figure 2: Draft design of the bottom socket.

For the bond connectivity test the Aluminum traces of the microcables are connected through a 64-pin adapter. The test consists of applying a small current to a single wire while the ASIC substrate is grounded. Testing neighboring wires will indicate shorts. The amount of current is measured and will indicate the quality of wire and ASIC-connection. The test needs to be done separately on each wire.

Test socket for the STS-XYTER chip

The electrical contact of the TAB-bonds that connect the semi-modules (STS-XYTER chips with two layers of microcables) with the silicon microstrip sensors can be put into practice by taking the chip into operation. A satisfactory bond will show through an increase in noise level attributed to the additional capacitance on the pre-amplifier input. The chip designers have elaborated a minimal set of 50 larger test pads for essential connectivity, that are placed near to the ordenary bonding pads. It allows full operation of the chip and to perform a rapid noise level estimate. Procedures for this estimate are wired into the ASIC. The testpad for a Pogo Pin has to be at least 150 μm x 150 μm in size, the pitch should be at least 200 μm (see Fig. 3, red marked pads). The design for the socket was made by *aps Solutions GmbH*, Munich, in cooperation with *WinWay Technology*, Taiwan. The socket will be manufactured after forwarding the final coordinates of the testpads to aps Solutions.
The chip by itself is placed upside down into the socket that will have an opening for the microcable. Further tasks for this test procedure are the development of a modified STS-XYTER board and suitable software.

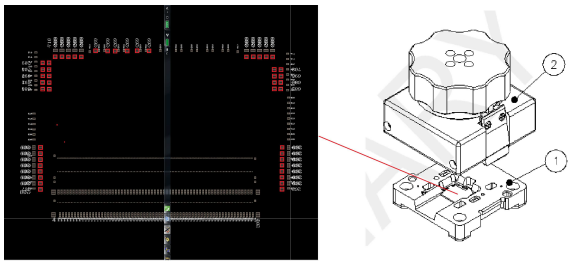

Figure 3: STS-XYTER with test pads and test socket by WinWay Technology.

DOI:10.15120/GR-2016-1

STS-XYTER2, a prototype detector readout chip for the CBM-STS and -MUCH

K. Kasinski[1], *R. Kleczek*[1], *R. Szczygiel*[1], *P. Otfinowski*[1], *and C. J. Schmidt*[2]

[1]AGH University of Science and Technology, Cracow, Poland; [2]GSI, Darmstadt, Germany

STS-XYTER2 is a 128 channel full-size prototype IC dedicated for the STS and MUCH detectors' readout. After tests of the previous prototype, the chip design was revised.

The analog front-end was modified to reach the noise requirements, improve testability, ensure fail-safe operation and support gas detectors of MUCH. The charge amplifier (CSA) was re-designed. As a result of amplifier-cable-detector co-design and optimization [1] [2], a NMOS input transistor and direct cascode amplifier was used for the input stage. This architecture results also in a significant improvement of the CSA amplifier PSRR from the positive power supply rails. The amplifier's buffer structures are configurable for best usage of available output voltage swing while working with holes or electrons as input charge. The CSA gain is configurable to support STS (7.5 mV/fC $\pm$20%) and MUCH (1.32 mV/fC $\pm$3%) detectors. The channels have 58 μm pitch, but the detector-side pads are staggered. The channels associated with 1^{st} row and 2^{nd} row of pads have individual control of CSA input branch current. Therefore it is now possible to switch off every second channel (feature used in MUCH mode). Detailed post-layout studies towards front-end susceptibility to cross-talk and instability caused by external parasitic components (especially series resistance of power rails, wire-bond resistance and inductance, PCB components etc.) were performed. The resistance of power rails of the FE amplifiers were reduced by factor of 2 (shapers) and 4 (CSA) compared to the previous prototype. By n-well shielding of all pads and splitting the protection diodes rings and connecting them to different potentials (1.2 V low-noise VDDM, and 1.8 V VDD_ADC) the crosstalk between back- and front-side of the AFE and the leakage current of the protection diodes (significant at larger temperatures) are reduced. The reference potentials distribution was improved by adding more on-chip capacitors and by using separate output drivers if more than one processing stage is to be driven from a single reference (to cut the possible feedback path). Shaper amplifiers and CSA enable individual switching-off the buffer branches in each channel to cut the signal path (and prevent interferences) of faulty channels. Slow shaper enables selection of shaping time (90 ns – 280 ns in 4 steps) to trade between speed and noise. Fast discriminator was supplied with output gating and a counter to enable fast signal path characterization. The analog-to-digital converter was modified to increase temperature stability and to speed up the calibration procedure (by adding global threshold and direct driving of the ADC input).

The layout and circuit modifications include many improvements towards microassembly of cables, wafer-level and post-assembly test procedures and FEB boards design. In particular: the front part of the ASIC was extended by 200 μm, adding 150 μm $\times$ 150 μm pads for pogo-probing, using fiducial markers on the visible 6^{th} metal layer; the power supply pads support multiple wire-bonds or ribbon-bonding (to reduce resistance and inductance). A 64-bit eFuse cell was implemented to assign individual ID at wafer-level testing stage. The number of power domains was reduced to make FEB design easier. The bulk connection quality was improved to reduce cross-talks through the bulk.

The digital back-end has been completely re-designed. A new read-out protocol and interface was designed and implemented. It is scalable (bandwidth: 9.4 – 47 MHit/s/chip) and is optimized for operation with the GBTx data concentrator [3] in the presence of AC-coupled, multidrop electrical SLVS links. The most interesting features of the protocol are: fully deterministic delay from DPB to ASIC, link synchronization procedure which does not require any phase regulation at the ASIC, lossless data compression optimized for the payload and expected front-end load. The protocol was verified in hardware (Kintex FPGA boards). A 15-bit address space in the front-end registers was used to accommodate additional counters (working with fast discriminator) and registers for controlling in-channel features. Based on the beam-tests [4], the DICE-based register cells layout was improved towards even better SEU immunity. SEU protection of the digital back-end is enhanced by using logic triplication in the control path and data parity in FIFO-based circuits of the data path. Radiation tolerance of the AFE part is increased by using NMOS transistors in the enclosed-layout geometry.

The STS-XYTER2 ASIC is currently being under development. It is expected to be taped-out in Q1 of 2016 via IMEC engineering run services.

References

[1] K. Kasinski *et al.*, "Optimization of the microcable and detector parameters towards low noise in the STS readout system", Proc. SPIE, vol. 9662 (2015).

[2] K. Kasinski *et al.*, "Front-end readout electronics considerations for Silicon Tracking System and Muon Chamber", JINST vol. 11, C02024.

[3] K. Kasinski, W. Zabolotny, R. Szczygiel, "Interface and protocol development for STS read-out ASIC in the CBM experiment at FAIR", Proc. SPIE 9290, doi: 10.1117/12.2074883.

[4] J. Lehnert et al., "SEU Tests with the STS-XYTER Version1 ASIC", this report

DOI:10.15120/GR-2016-1

Investigation on low mass copper flex cables for the CBM-STS detector

T. Blank[1], *C.J. Schmidt*[2], *C. Simons*[2], *and D. Soyk*[2]
[1]KIT, Karlsruhe, Germany; [2]GSI, Darmstadt, Germany

The silicon sensors of the Silicon Tracking System (STS) will be connected to the read-out chips (RoC) with up to 0.5 m long and 100 μm thin flex cables. The aluminium conductors of these cables are 30 μm wide and 14 μm high. The conductor pitch is 100 μm. The production of theses cables is demanding. The cables will be tab-bonded to the sensors and the RoCs in two overlapping layers, which is a time-consuming process. Thus, an alternative based on a double-layered copper flex cable with vias is under investigation, having the potential to ease and accelerate the manufacturing processes. This paper presents the current development status of the cable and the planned production steps.

Silicon Tracking System Design – Micro Cable Interconnects

The silicon sensor measures 62 $\times$ 62 mm^2 and is a double-sided strip sensor with 1024 signal channels and a bias ring on both sides of the sensor, top and bottom. The signal and sensor bias lines are connected to eight RoCs with eight flex cables, which are staggered in two rows. As the distance between the RoCs and the sensors varies due to layout restrictions of the read-out PCB carrying the RoCs, two different staggered cable length are required. Furthermore, due to the placement of the bias connector pads on the edges of the sensor two different bias cables are needed. Therefore, eight different cable types are used to connect the signal of both signal contact rows of the sensor to the RoCs. Figure 1 shows a cross section through the sensor and the tab bonded micro cables. The aluminium signal lines are bonded to the pads of the sensor through openings in the cable. The tab-bonding process is reliable and can be performed at room temperature. Alignment of the cables prior to the bonding process is an elaborate process, however. Thus, an alternative cable design based on copper instead of aluminium is proposed.

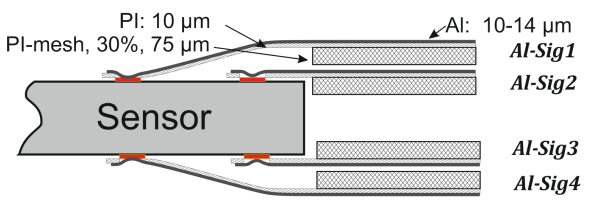

Figure 1: Connection scheme of the tab-bonded micro-cables with aluminium signal traces to the top and bottom side of the sensor.

Copper Micro Cable Design

Copper offers higher conductivity in comparison to aluminium, it is widely used for the production of PCBs and can be readily structured by subtractive (etching) or additive (galvanic) methods. Disadvantages of smaller radiation length can be compensated through narrower signal lanes maintaining line resistivity. The copper process allows to route the signals over various planes, as they can be connected electrically by means of micro-vias. Thus, the two different layers “Al-Sig1” and “Al-Sig2” can be combined in a single layer, reducing the amount of total cables required for the silicon tracking system by a factor of two. Figure 2 depicts a cross section of the cable mounted on the RoC. The bottom and top copper lines are 6-10 μm thick and will be coated with an EPIG-layer (Electroless Palladium Immersion Gold). The top and bottom PI-layers are 12.5 μm thick. They are laminated to a meshed PI-layer with a filling factor of 30% by a 12.5 μm thick epoxy-glue layer. The low fill factor reduces the capacity of the cable and the signal noise.

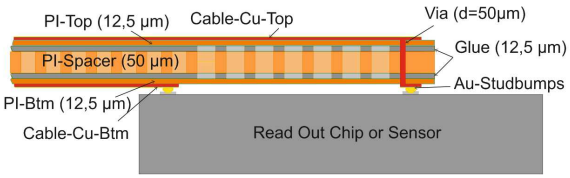

Figure 2: Cross section through the copper cable mounted on the RoC or sensor.

The cable will be connected by means of gold stud bumps to the pads of the sensor. The stud bumping process is very reliable and fast. More than 15 bumps can be placed per second; hence, the bumps required for one sensor side can be produced in less than two minutes. As a main source of noise linearly depends on the capacitance of the cable, various designs have been simulated with the tool “TNT” to evaluate its capacitance. The capacitance of the cable shown in Fig. 2 aggregates to 0.82 pF/cm. If the thickness of the meshed layer is increased to 150 μm as indicated in Fig. 1, the capacity reduces to 0.67 pF/m. In the simulation, the ground-plane is assumed to be located 165 μm below the bottom PI-layer.

Status and outlook

A batch of four different test cables with a length of 200 mm and 186.5 mm with and without bias lines was ordered. The cables will allow the validation of the succeeding manufacturing processes as the attachment of the cable to the RoCs and the sensor.

DOI:10.15120/GR-2016-1

SEU tests with the STS-XYTER version 1 ASIC

J. Lehnert[1] *and P. Kozcon*[1]
[1]GSI, Darmstadt, Germany

The sensors of the CBM Silicon Tracking System (STS) are connected to 8 STS-XYTER frontend ASICs with 128 channels each developed at AGH Cracow [1]. The ASICs are located just outside of the active area of the STS and exposed to high charged particles rates and total integrated doses over the full lifetime up to 100 kRad. In order to ensure proper functionality in this environment and to reduce single event upsets (SEU) which manifest as bit flips, the ASIC design implements a DICE (Dual Interlocked Storage) cell architecture for the configuration settings of each channel as well as for critical global settings.

SEU Testing of DICE Cells at COSY

During the CBM electronics beam test at COSY Jülich[1] in October 2015, the first version of the STS-XYTER frontend ASIC, produced in a UMC 180 nm process, was characterized for the first time with respect to single-event effects in its DICE cell architecture. Goal was the quantitative assessment of SEU cross sections for the DICE cells, which may strongly depend on the actual cell architecture, and the comparison to the regular flip flops in the design [2]

Tests were performed in a dedicated high-intensity proton beam used in parallel for multiple irradiation studies within CBM, which allowed running at rates up to 3×10^9 protons per spill on the setup, which provided a good compromise between sufficient statistics for the SEU investigations and a stable (not fully DICE protected) readout interface. Device under test was a single STS-XYTER version 1 ASIC bonded to a prototype frontend board (FEB). The ASIC was centered in the proton beam. The FEB was connected to a standard readout and control chain with a SYSCORE3 readout board and a data aquisition PC with a HTG-K7 board and a FLESnet based readout. For the purpose of the test only the control functionality of the system was used, i.e. reading and writing to ASIC registers. The test used 32240 bits each of DICE cells and flip flops respectively, arranged in a two-dimensional structure of 8bit DICE discriminator threshold values and 8bit flip-flop counters for 130 channels with 31 discriminators each. The test procedure consisted in a continuous readback of a predefined pattern from the DICE cells and of fixed random values from the read-only counters and a check for bit flips in the expected register values. Repeated readback allows to distinguish SEUs from readout errors. An ionisation chamber from GSI detectorlab (B. Voss) with QFW based readout was placed behind the ASIC to provide an accelerator-independent and continuous measurement of beam intensities[2] .

SEU Test Results

The test was done for a total of 48 hours of effective irradiation. In this period, 3467 bit flips for the flip flops were observed and 116 bit flips for the DICE cells. These numbers provide a direct quantification of the relative SEU rate of the DICE cells with respect to flip flops. The factor of 29.9 is in the expected range for DICE cells. With a preliminary estimate of the proton fluence larger than $2 \times 10^7/\mathrm{cm}^2/\mathrm{s}$, the SEU counts translate in an SEU cross section below 1.1×10^{-15} cm^2/bit for the DICE cells which is consistent with literature values.

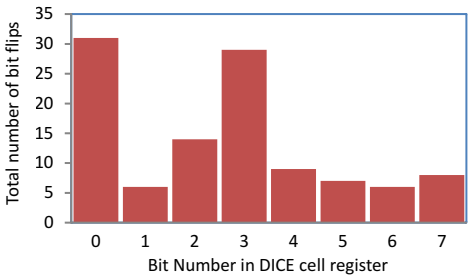

Figure 1: SEU counts for the individual bits of the DICE cell threshold registers

The DICE cells exhibit significant differences in bit flip count over the 8 bits of the individual DICE registers (see Fig. 1). This observation could be correlated with different distance from bulk/well contacts for the individual bits in the DICE cell layout. Consequently the upcoming revision 2 of the STS-XYTER ASIC [3] will implement an modified DICE cell layout. The expected improvement in DICE SEU rate by a factor of up to 3 will be verified in a forthcoming beam test.

References

[1] K. Kasinski et al., “STS-XYTER, a High Count-Rate Self-Triggering Silicon Strip Detector Readout IC for High Resolution Time and Energy Measurements”, IEEE NSS/MIC, 2014

[2] S. Löchner et al., “Radiation Studies on the UMC 180 nm CMOS Process at GSI”, RADECS 2009 Proceedings, p. 614

[3] K. Kasinski et al., ”STS-XYTER2, a prototype detector readout chip for the STS and MUCH”, CBM Progress Report 2015, Darmstadt 2016

[1]Various support by IKP, FZ Jülich is acknowledged.

[2]Various support by S. Löchner, GSI, is acknowledged.

Background rejection in the dielectron analysis with the CBM Micro-Vertex Detector*

E. Krebs[1], *T. Galatyuk*[2,3], *and J. Stroth*[1,3]

[1]Goethe-Universität, Frankfurt, Germany; [2]Technische Universität Darmstadt, Germany; [3]GSI Darmstadt, Germany

The leptonic decay channels of the light vector mesons ρ, ω and ϕ are excellent probes of the strongly interacting matter under extreme conditions. This study aims at exploring the use of the CBM Micro-Vertex Tracker (MVD) to reduce the background from π^0-Dalitz decays and γ-conversions.

To do so, electron pairs from meson decays have been simulated from a thermal source for central Au+Au reactions at SIS-100 energies such that the meson spectra are consistent with p_T and rapidity distributions measured by NA49 [1]. The decays of various sources simulated with the Pluto [2] event generator are embedded into the hadronic environment generated with UrQMD. In-medium modifications of the ρ spectral functions calculated by Rapp and Wambach [4] and dileptons from QGP radiation have been included in the Pluto cocktail [5]. The magnetic field was set to 100% strength. Particle identification is only based on the acceptance of Monte-Carlo tracks in the RICH and TRD detectors. No δ-electrons have been added.

The strategy of background rejection comprises several steps. In order to identify leptons from photon conversions that were produced outside of the target region, each reconstructed track is extrapolated to the primary decay vertex and removed from the analysis depending on its deviation to the vertex. One characteristic for conversion pairs is their small opening angle. A wedge-cut is applied taking into account the opening angle of an identified electron to its closest neighbor without particle identification and the product of the momenta of the two tracks [3].

The MVD of the CBM experiment can further contribute to reduce this background by including points from the MVD into the track reconstruction. An improved rejection of pairs originating from the target region could be observed. Previous studies have shown that the MVD stations are also a source for γ-conversions which can not be effectively rejected by the vertex extrapolation cut, especially in the first two stations closest to the target. Extrapolating tracks to the first MVD station and requiring that they are in its acceptance improved the suppression off-vertex tracks from γ-conversions.

Adding the MVD into the analysis results in a higher signal-to-background ratio. However, the cut efficiency is around 12% lower. As the significance is higher there is still a gain with the MVD (see Tab. 1). The signal-to-background as a function of invariant mass of the full cocktail after all analysis steps is presented in Fig. 1.

*This work has been supported by BMBF (05P12RFFC7), HIC for FAIR, HGS-HIRe, H-QM, and GSI.

Mass Range $\left[\frac{\text{GeV}}{c^2}\right]$	Cut Efficiency	S/B	$S/\sqrt{S+B}$
Without MVD			
$0-0.15$	$(25\pm1)10^{-2}$	4.7 ± 0.1	238 ± 1
$0.15-0.5$	0.75 ± 0.01	0.19 ± 0.01	57.2 ± 0.4
$0.5-1.2$	0.81 ± 0.01	0.26 ± 0.01	46.6 ± 0.4
$\omega\rightarrow e^+e^-$	0.81 ± 0.02	0.73 ± 0.01	42.8 ± 0.5
$\phi\rightarrow e^+e^-$	0.83 ± 0.07	0.20 ± 0.01	6.3 ± 0.4
With MVD			
$0-0.15$	$(21\pm1)10^{-2}$	5.8 ± 0.1	234 ± 1
$0.15-0.5$	0.67 ± 0.01	0.28 ± 0.01	64.4 ± 0.4
$0.5-1.2$	0.69 ± 0.01	0.46 ± 0.01	53.4 ± 0.5
$\omega\rightarrow e^+e^-$	0.68 ± 0.01	1.3 ± 0.1	45.4 ± 0.6
$\phi\rightarrow e^+e^-$	0.71 ± 0.06	0.38 ± 0.03	7.5 ± 0.5

Table 1: Signal-to-background ratios and significance (with statistical errors) for dilepton decays in different mass regions. A cut efficiency of 1 corresponds to the amount of dielectrons after PID.

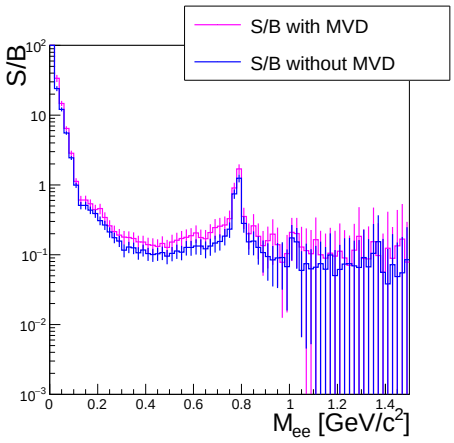

Figure 1: Signal-to-background ratio over invariant mass spectrum after all cuts are applied for central AuAu collisions at 8AGeV, with statistical error bars.

References

[1] C. Alt et al. (NA49 Collab.), Phys. Rev. C 78, 044907 (2008)

[2] I. Froehlich et al., arXiv:0708.2382

[3] T. Galatyuk, PhD Thesis, Goethe-Universität, Frankfurt am Main, (2009)

[4] R. Rapp and J. Wambach, Adv. Nucl. Phys. 25(2000) 1

[5] F. Seck et al., Towards a realistic even generator for in-medium and QGP dileptons, CBM Progress Report 2014

DOI:10.15120/GR-2016-1

Radiation hardness tests of electronic components for CBM-STS low voltage power supply

S. Löchner[1], *P. Koczoń*[1], *and A. Rost*[1]
[1]GSI, Darmstadt, Germany

Electronic components installed in the field of reaction products in future experiments at FAIR have to be radiation hard. At present, selected parts like DC/DC converters and LDO voltage stabilisers undergo exhaustive tests with use of intense minimum ionising particles' beams, mostly about 3 GeV protons at the COSY facility, Jülich[1].

Test setup

For components like DC/DC converters or LDO voltage stabilisers the output voltage level as well as the expected transient voltage spikes rate due to single event upsets have to be monitored during irradiation. Voltage level monitoring (input and output) requires relatively low readout frequency below 1 Hz and can be implemented on the inexpensive ARDUINO system [1]. Fast transients have been monitored on a 4-trace digital oscilloscope Rhode-Schwarz RTO1044 [2] . Measurement results have been recorded in nonvolatile memory and analysed.

Selected ASICs

For the radiation hardness tests several DC/DC converters have been chosen. Selection criteria like circuit efficiency, chip size, coreless inductivity, apropriate output voltage and sufficient output power as well as voltage setting flexibility have been applied.

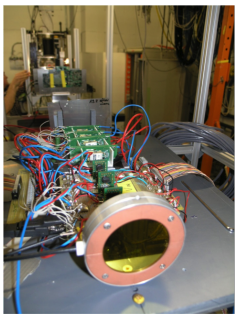

Figure 1: Base plate with PCB card holder and wiring. In the front an IC for beam current monitoring.

Only one model of the LDO stabilizer produced in rad hard technology has been examined until now. Alltogether 10 test boards with LTC3605, 3 boards with LTC3610 (Linear Technology), 4 boards containing LM2596S (Texas Instruments) as well as 4 FEASTMP boards [3] have been tested in two beam times. All tested ASICs were powered on during the irradiation runs. The test boards were placed in a holder fixing their positions with respect to the proton beam during the measurement as shown in Fig. 1.

Test results

The PCBs with tested chips were placed in a row along the beam axis such that the irradiating beam punched through all of them. A small ionisation chamber placed on the beam axis behind tested chips was used to monitor the beam intensity (Fig. 1).

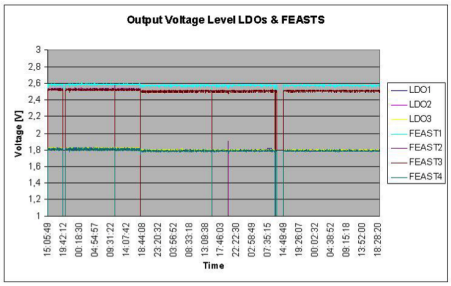

Figure 2: Output voltages of DUTs in time (short voltage drops are due to hardware changes).

The beam profile has been investigated with Gafchromic dosimetric film [4]. In the course of the irradiation the film developes a spot corresponding to the shape of the proton beam with the optical density corresponding to the integrated beam intensity. The total dose is known from the measurement with the ionisation chamber and the position of the irradiated chips marked on the film. A fractional dose can be estimated for each point on the film by scanning the optical density. This allows to estimate precisely the beam intensity integral and - consequently - the dose at the ASICs' positions. Out of the tested DC/DC converters only FEASTMP survived more than 10^{13} protons which corresponds to a dose of 4×10^{12} cm^{-2}. No fast transients were observed on LDO voltage stabilisers.

References

[1] S. Löchner and P. Koczoń, GSI Annual Report 2014
[2] http://www.rohde-schwarz.de/de/Produkte/messtechnik-testsysteme/aerospace-and-defense/messtechnik/oszilloskope-fuer-ad/RTO.html
[3] http://project-dcdc.web.cern.ch/project-dcdc/public/Documents/FEASTMod_Datasheet.pdf
[4] http://www.ashland.com/products/gafchromic-radiotherapy-films

[1]Various support by IKP, FZ Jülich is acknowledged.

Estimation of the hit position error in the CBM-STS

H. Malygina[*1,2,3], *V. Friese*[2], *and M. Zyzak*[1,2,4]
[1]Goethe University, Frankfurt, Germany; [2]GSI, Darmstadt, Germany; [3]KINR, Kyiv, Ukraine;
[4]FIAS, Frankfurt, Germany

Relevant physical processes which occur in the detector should be taken into account for its numerical modelling. In the current implementation of the STS digitization model [1], such processes can be included separately. This allows investigating their individual influence on the reconstructed hit positions and their errors. A reliable estimate of the hit position error is important to obtain a proper track χ^2, which is used to discard ghost track candidates. This affects the signal-to-background ratio of the reconstructed physical signals and the corresponding efficiencies.

In this report we present a procedure of hit error estimation which is obtained from first principles and is independent of measured spatial resolution or simulated residuals. For verification of the prodecure, we use the pull distribution ($\mathrm{pull} = \mathrm{residual}/\mathrm{error}$) of the hit position. Its width must be ≈ 1, and its shape must reproduce the shape of the residuals distribution.

There are several contributions to the total hit position error:

$$\sigma^2 = \sigma^2_{\mathrm{alg}} + \sum_i \left(\frac{\partial x_{\mathrm{rec}}}{\partial q_i}\right)^2 \sum_{\mathrm{sources}} \sigma^2_j. \qquad (1)$$

Here, σ_{alg} is the error of the cluster position finding algorithm (CPFA) and x_{rec} the reconstructed hit position. The index $i = 1...n$ denotes the strip number in the cluster with n being the cluster size. Among the already included other error sources σ_j are the detector noise (the equivalent noise charge), the charge discretization, and the non-uniformity of energy loss.

The derivatives $\partial x_{\mathrm{rec}}/\partial q_i$ in (1) depend on the chosen CPFA. We here use the unbiased algorithm described in [2]. This yields e.g. for a 2-strip cluster

$$\left|\frac{\partial x_{\mathrm{rec}}}{\partial q_i}\right| = \frac{p}{3}\frac{q_1 q_2}{\max(q_1,q_2)^2}\frac{1}{q_i}.$$

To single out σ_{alg}, we consider the simplest model of an ideal detector response: the charge distribution is proportional to a geometrical projection of an incident particle trajectory onto the read-out plane. The CPFA of [2] yields the following errors σ_{alg} for different cluster sizes:

$$\sigma_1 = \frac{p}{\sqrt{24}}, \quad \sigma_2 = \frac{p}{\sqrt{72}}\left(\frac{q_2 - q_1}{max(q_1,q_2)}\right), \quad \sigma_{n>2} = 0\,.$$

The estimate of the signal discretization error is given by $\sigma_{\mathrm{discr}} = \frac{\text{dynamic range}}{\sqrt{12}\ \text{number of ADC}}$.

* Work supported by HIC-for-FAIR, H-QM and HGS-HIRe.

The contribution from the non-uniformity of energy loss is more difficult to take into account because the actual energy deposit along the track is not known. The following approximations allow a straightforward solution:

- the registered charge corresponds to the most probable value (MPV) of energy loss;
- the incident particle is ultrarelativistic ($\beta\gamma \gtrsim 100$).

The second assumption is very strong but it uniquely relates the MPV and the distribution width [3]

$$MPV = \xi[\mathrm{eV}] \times \left(\ln\left(1.057 \times 10^6 \xi[\mathrm{eV}]\right) + 0.2\right).$$

Solving this with respect to ξ gives the estimate for the FWHM [4]

$$\sigma_{\mathrm{non}} = w/2 = 4.018\xi/2.$$

Figure 1 shows the verification of the error estimation procedure with simulated Au+Au events in the STS. The pull width exceeds unity. This can be a consequence of an artificial increase in the residuals caused by the discretization of the trajectory in Geant, such that the coordinates of the entry and exit points of the track do not perfectly coincide with the actual sensor surfaces.

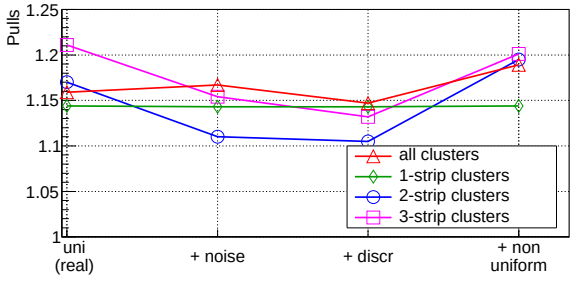

Figure 1: Widths of pull distributions when taking into account different physical effects. The label "uni (real)" corresponds to the perfect detector model affected by the trajectory discretization in Geant.

References

[1] H. Malygina, V. Friese and J.M. Heuser, CBM Progress Report 2013, Darmstadt 2014, p. 96

[2] H. Malygina and V. Friese, *Determination of the cluster position in the CBM-STS*, this report

[3] K. A Olive *et al.* (Particle Data Group), Chin. Phys. **C 38** (2014) 090001

[4] S. Meroli, D. Passeri and L. Servoli, JINST **6** (2011) P06013

DOI:10.15120/GR-2016-1

Determination of the cluster position in the CBM-STS

H. Malygina[*1,2,3] *and V. Friese*[2]

[1]Goethe University, Frankfurt, Germany; [2]GSI, Darmstadt, Germany; [3]KINR, Kyiv, Ukraine

In the double-sided silicon strip sensors of the CBM-STS, a charged particle activates a number of adjacent strips ("cluster"). From the charge measurements q_i of the strips in the cluster, the particle position has to be reconstructed. An algorithm for such position reconstruction should be unbiased and provide minimal position residuals, i.e., it should minimise the measurement error. Moreover, it should be computationally efficient.

A commonly used method is the centre-of-gravity (COG), which defines the cluster centre as $x_{\rm rec} = \sum_i x_i q_i / Q$, where x_i is the centre coordinate of strip i and $Q = \sum_i q_i$ the total charge in the cluster. This prescription, however, does in general not provide a bias-free measurement nor does it result in the smallest residuals.

In order to develop a better-suited algorithm, we note that to first order, the detector response in the silicon sensors is a uniform charge distribution, corresponding to the projection of the particle trajectory on the readout (strip) edge. This charge distribution, which is then integrated on the readout strips, can be characterised by two independent variables, namely the entry and exit coordinates of the track in the sensor, $x_{\rm in}$ and $x_{\rm out}$. Since the thickness of the sensors is small, the trajectory within the sensor can be approximated as a straight line, and we can define the true coordinate $x_{\rm true} = 0.5(x_{\rm out} - x_{\rm in})$. The proper algorithm can now be derived from the requirement that the average residual $\langle x_{\rm rec} - x_{\rm true} \rangle$ vanishes:

$$\int dx_{\rm true}\, P(x_{\rm true})\, (x_{\rm rec} - x_{\rm true}) \stackrel{!}{=} 0 \ .$$

Here, $P(x_{\rm true})$ is the probability density for $x_{\rm true}$, which can be derived from that of $x_{\rm in}$ and $x_{\rm out}$. We assume both variables, for a given cluster size, to be uniformly distributed, which was verified by simulations.

The resulting measurement prescriptions are:

- For single-strip clusters, the centre of the strip is taken: $x_{\rm rec} := x_i$. The corresponding error is $\sigma_x = p/\sqrt{24}$, with p being the strip pitch.
- For two-strip clusters with strips i and $i+1$:

$$x_{\rm rec} := \frac{1}{2}\,(x_i + x_{i+1}) + \frac{p}{3}\frac{q_{i+1} - q_i}{\max(q_i, q_{i+1})} \ .$$

  The corresponding error is

$$\sigma_x = \frac{p}{\sqrt{72}}\frac{q_{i+1} - q_i}{\max(q_i, q_{i+1})} \ .$$

- For clusters with $n > 2$ strips, extending from strip i to j:

$$x_{\rm rec} := \frac{1}{2}\,(x_i + x_j) + \frac{p}{2}\frac{q_j - q_i}{q};\ q := \frac{1}{n-2}\sum_{k=i+1}^{j-1} q_k .$$

  This prescription exactly reproduces the true coordinate, i.e., the corresponding error vanishes.

Several effects lead to deviation from a uniform charge distribution on the readout edge, such as fluctuations in the charge creation along the trajectory, noise, threshold, diffusion and charge discretization. The currently implement STS digitizer software allows to add those one-by-one [1]. These effects increase the position resolution as demonstrated in Fig. 1, such that the residual distribution alone does not favour the new algorithm over the COG. However, as shown in [2], the new algorithm has the advantage that the hit position errors can be estimated a-priori, which is important for the correct determination of the track parameters.

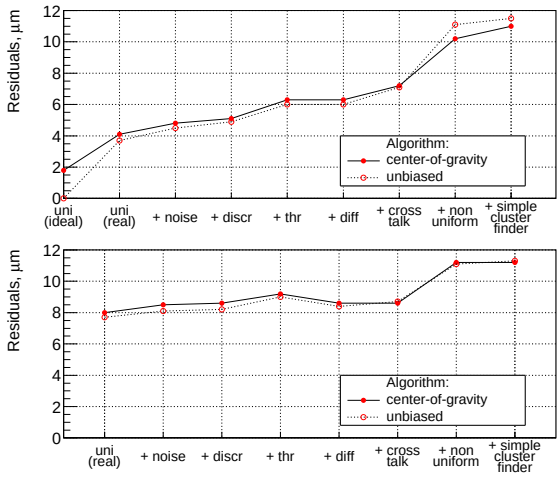

Figure 1: Width of the residual distribution from simulation for 3-strip clusters (top) and all clusters with cluster size distribution as expected for Au+Au events at 10A GeV (bottom) when taking into account different processes (see text). For the difference of "uni (ideal)" and "uni (real)", see [2].

References

[1] H. Malygina, V. Friese and J. M. Heuser, CBM Progress Report 2013, Darmstadt 2014, p. 96

[2] H. Malygina and V. Friese, *Estimation of the hit position error in the CBM-STS*, this report

* Work supported by HIC-for-FAIR, H-QM and HGS-HIRe.

Test of prototype components for the CBM-STS readout chain

A. Rodriguez Rodriguez[1] *and J. Lehnert*[2]
[1]Goethe University, Frankfurt, Germany; [2]GSI, Darmstadt, Germany

The front-end board (FEB) with STS-XYTER ASICs and the read-out board (ROB) with GBTX and *Versatile Link* components are main elements of the STS read-out chain [1]. A FEB with a single prototype of STS-XYTER v1 and a Versatile Link Demonstrator Board (VLDB), implementing 4 custom radiation hard devices to be used on the ROB, are currently available in the STS laboratory. Several test have been carried out to check their performance, system integration and functionalities. A brief description about devices tests, experimental setup and results are presented here.

Test of STS-XYTER v1

One of the goals of the STS-XYTER [2] design is to achieve a low level noise performance (below 1000 e^- rms in noise charge in the final system). Realistic post-layout simulations for the prototype version of the chip estimate an Equivalent Noise Charge (ENC) around 1600 e^-. Noise measurements were carried out using different sensor modules. The FEB with 1 ASIC and 14 connected channels is linked to a Syscore3 v1 board; the system is configured over the CBMnet protocol.

The chip response in connected and non-connected channels was studied. During the measurements two-stages LC and RC filters are used to reduce the noise ripple in the sensor bias and common mode noise. A significant reduction in the system noise can be achieved by shielding low-voltage cables and properly grounding the system. Sensor and FEB were placed inside a shielded box made of steel of 2 mm thickness. The box and FEB board share a common ground point which is connected to the ground potential of the low-voltage supplies.

Figure 1 shows the equivalent noise charge (ENC) in the 128 channels of the chip; these correspond to average values over the 31 comparators of every channel. Values for each comparator are estimated from the respective S-curves. Results are shown for 2 daisy-chained sensors of 6.2 cm $\times$ 6.2 cm readout by a 30 cm polyimide microcable. The measurements have shown noise levels around 1800 e^- for connected channels. This value is higher than the requirements but still consisted with simulations. The redesigned revision 2 of the STS-XYTER will have significantly reduced noise.

VLDB tests

The VLDB is an evaluation board for the radiation hard GBT and Versatile Link ecosystem [3]. It implements 4 custom designed modules: a GBTx ASIC, a VTRx, GBT-SCA and FEAST_MP DC-DC converters. The VLDB can be configured and controlled by I^2C. A Java Programmer Tool allows to configure the GBTx. The experimental setup for system tests is shown in Fig. 2. It consists of the VLDB with the AFCK board as optical backend. The setup allows to check the optical data path and to develop and test firmware and software tools. Furthermore, the addition of an STS-XYTER emulator to the AFCK gives the possibility to test the full data round trip with the VLDB electrical front-end interface and the STS-XYTER communication protocol. The setup allows to have a test bench ready upon availability of the STS-XYTER v2.

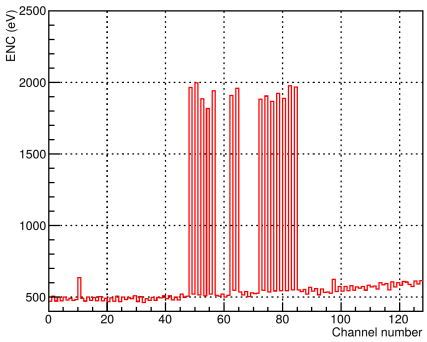

Figure 1: *ENC in every channel estimated as an average value for all channel's discriminators.*

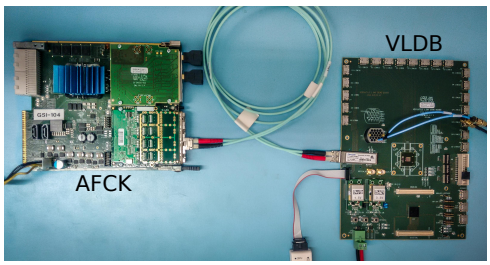

Figure 2: *Experimental setup for VLDB system test.*

References

[1] J. Lehnert et al., GSI-SR2014-NQM-CBM-26, GSI Report 2015-1, DOI:10.15120/GR-2015-1-MU-NQM-CBM-26

[2] K. Kasinski et al., "STS-XYTER, a High Count-Rate Self-Triggering Silicon Strip Detector Readout IC for High Resolution Time and Energy Measurements", IEEE NSS/MIC, 2014

[3] P. Moreira et al., "The GBT Project", Proceedings of Topical workshop on electronics for particle physics, TWEPP, Paris, France, 21-25 September 2009, p. 342

DOI:10.15120/GR-2016-1

Charge collection of n-irradiated prototype CBM-STS microstrip sensors

I. Momot[2,3], H. Malygina[2,3], M. Singla[1], P. Larionov[2], M. Teklishyn[1,3], J. Heuser[1], and C. Sturm[1]
[1]GSI, Darmstadt, Germany; [2]Goethe University, Frankfurt, Germany; [3]KINR, Kyiv, Ukraine

The STS will employ double-sided silicon microstrip sensors to detect the space-points of ionizing particles originating in beam-target interactions. The strips on the p side of the sensors are tilted with respect to the n side by 7.5°. To read out the sensor only from one edge, as required by the detector ladder structure, the end strips from one edge are connected to the end strips on the other edge. This interconnection can be provided via double metallization (DM) or using external interstrip cables (SMwC). The central strips are the full-length strips without any interconnection.

Current prototype sensors were tested for their charge collection performance both before and after a non-ionizing radiation dose corresponding to twice the end-of-life criterion defined for the STS detector: 1 MeV neutron equivalent fluence of 2×10^{14} $n_{eq}cm^{-2}$. The irradiatons were performed at Karlsruhe Institute of Technology (KIT), Germany [1]. All measurements were made in a light-tight set-up with temperature control, operating the sensors at -5° C. The signals from a β-source (^{90}Sr) to mimic minimum ionizing particles (MIP) were read out with an n-XYTER based acquisition system. Four sensors were selected for the measurement of variation of leakage current with bias voltage (IV), bulk capacitance versus bias voltage (CV), and for charge collection tests with a ^{90}Sr source. The list of the sensors under test is given in Table 1 along with their sizes, thickness, types of the connections and full depletion voltage before irradiation (extracted from the capacitance-voltage measurements).

Table 1: Specifications for the sensors under tests. The naming convention in the left column encodes the prototype generation (5 or 6), the manufacturer (H = Hamamatsu, C = CiS), the sensor height/strip length in cm (4 or 6), and the wafer number.

name CBM0-	size cm × cm	thickness μm	inter-connection	V_{fd} ±5 V
5H4-W18	6 × 4	327	SMwC	68
5H4-W10	6 × 4	331	DM	75
6C6-W14	6 × 6	293	SMwC	94
5C6-W6	6 × 6	291	DM	98

A coincidence scheme with a pin diode as trigger was used. A 2 mm Aluminum absorber behind the sensor cut away the low-energy β-spectrum. The obtained signal from MIPs was fitted with a Landau-Gauss convolution and the most probable value is interpreted as the collected charge. The results for charge collection efficiency, based on an ADC-to-charge calibration and the expected charge in the detector according to the wafer thickness, are shown in Fig. 1.

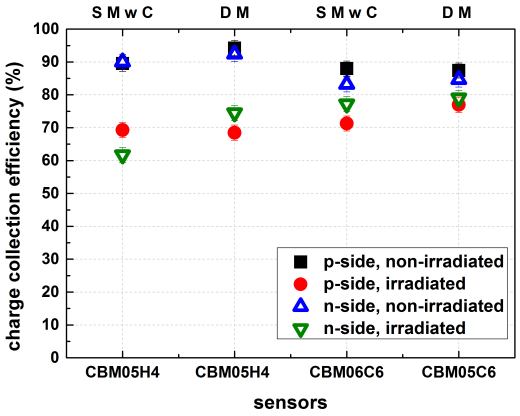

Figure 1: Charge collection results with ^{90}Sr.

The sensors were also tested with 2 GeV proton beams at COSY (Jülich) in December 2014. The result of charge collection efficiency which is defined from the simulation taking into account interstrip and coupling capacitance are shown in Fig. 2 for Hamamatsu sensors only.

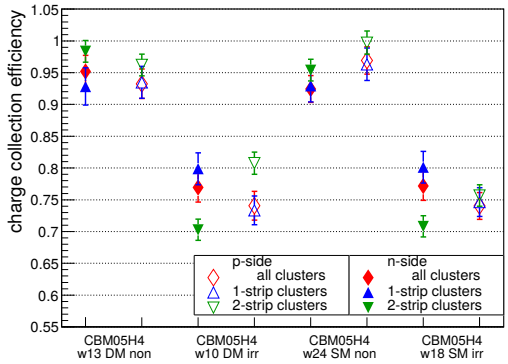

Figure 2: Charge collection results with proton beam.

The prototype sensors from two vendors, in two technological configurations, show a reduction of charge collection by 15% to 25% after irradiation to twice the maximum neutron fluence expected in the CBM experiment. New series of sensors from CiS and Hamamatsu are under preparation to forthcoming irradiation studies.

References

[1] http://www.ekp.kit.edu/english/irradiation_center.php

DOI:10.15120/GR-2016-1

Online reconstruction of multi-strange hyperons at SIS-100

H. Cherif[*1], *I. Vassiliev*[2], *and A. Toia*[1,2]
[1]Goethe-Universität, Frankfurt, Germany; [2]GSI, Darmstadt, Germany

The Compressed Baryonic Matter (CBM) experiment at the future Facility for Antiproton and Ion Research (FAIR) in Darmstadt is designed for precision measurements of observables which are sensitive to high density effects and phase transitions, using the high intensity heavy ion beams provided by the SIS 100/300 accelerators at FAIR. One among the possible signatures of the phase transition from nuclear matter to deconfined phase and formation of the Quark Gluon Plasma (QGP) is the enhanced production of multi-strange particles. As those observables are very rare probes, interaction rates up to 10 MHz are needed to guarantee high-statistics measurements, and the experimental task to identify hadrons, leptons and secondary vertex in collisions with up to about 1000 charged particles requires complex global triggers selections. In this report we investigate the performance of multi-strange hyperons measurement in CBM experiment at SIS 100 the first phase of FAIR project.

Multi-strange hyperons are reconstructed via their weak decay into charged hadrons ($\Lambda \rightarrow p\pi, \Xi \rightarrow \Lambda\pi, \Omega \rightarrow \Lambda K$). The momentum and the topology of the tracks is measured by the Silicon Tracking System (STS) detector which is installed in a large acceptance dipole magnet. Identification of the decay products is performed by a time-of-flight measurement with TOF detector located at a distance of 6 to 10 m behind the target. We studied the hyperons reconstruction in Au-Au collisions at different energies achievable with SIS 100. We used the UrQMD event generator, coupled to a Geant3-based description of the CBM detector. Tracks were reconstructed with a Cellular Automaton and a Klaman filter algorithms using the KF Particle Finder package [1]. An example of reconstructed invariant mass spectra of $\Xi^-, \bar{\Xi}^+, \bar{\Lambda}$ and Ω^- is shown in Fig. 1 for Au-Au central collisions at 10 AGeV. The red line indicates the fit by the sum of a polynomial and Gaussian function. The reconstruction efficiency is shown in Table 1.

Table 1: Reconstruction efficiency of $\bar{\Lambda}, \Xi^-, \bar{\Xi}^+, \Omega^-$ and $\bar{\Omega}^+$ in Au-Au central collisions at 10A GeV

	$\bar{\Lambda}$	Ξ^-	$\bar{\Xi}^+$	Ω^-	$\bar{\Omega}^+$
Efficiency(%)	20.6	8.5	6.3	5.1	2.3

The measurement of multi-strange hyperons requires a high interaction rates up to 10 MHz. With the high multiplicity of charged particles produced in heavy ions collisions, this leads to huge data rates of up to 1 TB/s. In this

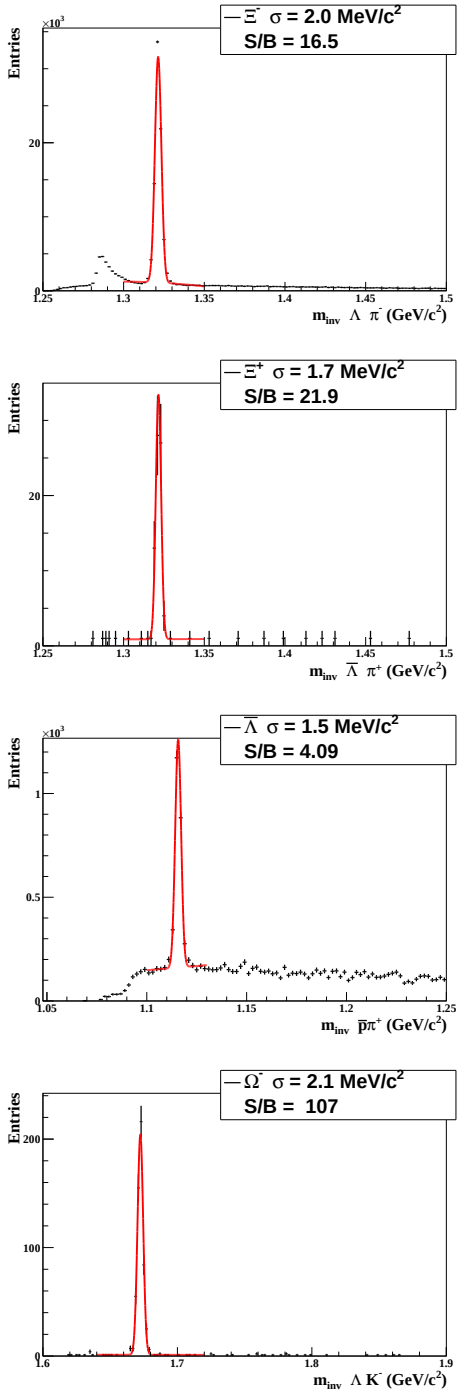

Figure 1: Invariant mass distrbution of $\Xi^-, \bar{\Xi}^+, \bar{\Lambda}$ and Ω^- reconstructed from their charged weak decays products in Au-Au central collisions at 10 AGeV.

*h.cherif@gsi.de

DOI:10.15120/GR-2016-1

environment, the CBM experiment requires a Rejection Factor (RF) of 400 or more. The online event selection is performed by the First Level Event Selector (FLES), a scalable high performance computer with a high-bandwidth interconnect network, the flexibility of which allows the implementation of a large variety of trigger signatures.

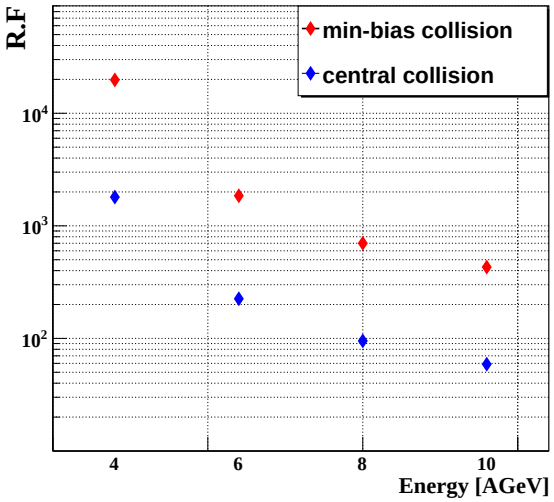

Figure 2: Rejection factor calculated for central and minimum bias collisions at different energies.

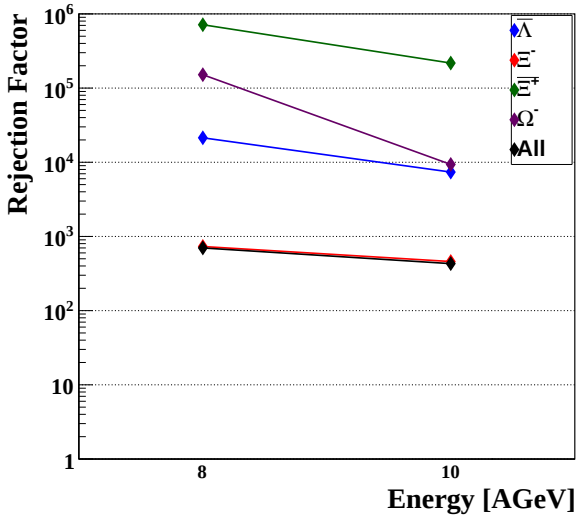

Figure 3: The rejection factor calculated for individual hyperons, compared to the one calculated for all hyperons, in minimum bias Au-Au collisions at 8A and 10A GeV.

The rejection factor for a software trigger on multi-strange hyperons at SIS 100 energies was studied. The results are shown in Fig. 2 and Table 2. The rejection factor is calculated by dividing the total number of events by the number of selected events containing at least one of the multi-strange hyperons in Table 1. As shown in Fig. 2, the rejection increases with the decreasing energy since multi-strange hyperons become increasingly rare at low energy, thus we achieve the CBM requirement on the RF. Fig. 3 shows the rejection factor for minimum bias Au-Au collisions at 8A and 10A GeV, calculated separately for events containing Ξ^-, $\bar{\Xi}^+$, $\bar{\Lambda}$ and Ω^-. From the comparison to the rejection obtained when selecting events containing at least one of those hyperons, we conclude that selection is dominated by the Ξ^-.

Table 2: Rejection factor calculated at SIS 100 energies for central and minimum bias collisions

	4A GeV	6A GeV	8A GeV	10A GeV
min. bias	19800	1850	700	430
central	1800	225	95	59

References

[1] I. Kisel, I. Kulakov and M. Zyzak, IEEE Trans. Nucl. Sci. **5** (2013) 3703

Automated strip quality assurance for the STS sensors of the CBM experiment

P. Larionov[1]
[1]Goethe Universität, Frankfurt, Germany

The Silicon Tracking System (STS) surves as the main tracking detector of the Compressed Baryonic Matter (CBM) experiment providing tracking information of charged particles propogation and determination of their momenta. The STS will be assembled with approximately 1220 double-sided silicon microstrip sensors in four different sizes.

Complicated fabrication technology of double-sided sensors and large-scale sensor production demands a reliable and efficient quality assurance of the STS sensors to ensure decent operation of the whole system [1]. Three quality test centers are being equipped in GSI and EKU Tübingen, Germany and in JINR, Russia to perform full-scale quality assurance of the STS sensors including optical inspection, bulk electrical tests and strip quality tests. The strip quality tests are particulary important to identify strip defects that can be developed during fabrication, transportation or handling of sensors. The most commonly occuring strip defects include:

- pinholes, i.e. ohmic connections between an implant and a readout strip;
- leaky strips;
- strip “shorts” - ohmic connections between two or more readout strips;

Herewith, the first two defects, if connected to the readout electronics, pose a danger for latter, therefore, must be identified and charged off for the readout coupling. The last one does not constitute a serious threat for the readout chain but degrades the spacial resolution of the system thus have to be determined as well.

A test stand has been assembled in the cleanroom environment at GSI, Darmstadt to provide efficient strip defects identification. The setup, featuring a probe station, several measurement instruments and a software for testing automation, provides a full scan of the quality of each strip. By making use of the switching matrix three tests in a row are performed taking 4 seconds for each strip to test providing the required strip quality information. The software prints the results of the scan online to the user interface and also saves them in an ASCII file. Figure 1 illustrates the results of the full strip quality scan for the junction side of one of the STS prototype sensors demonstrating the strip leakage current distribution, the pinhole and the readout strip short scans. During the scan one pinhole defect was identified showing the current throught the coupling capacitor over 200 nA under 20 V test voltage applied. The setup will be used to perform full or partial scans of the STS sensors during mass production according to tests done by manufacturers.

This work is supported by HGS-HIRe, H-QM, HIC for FAIR.

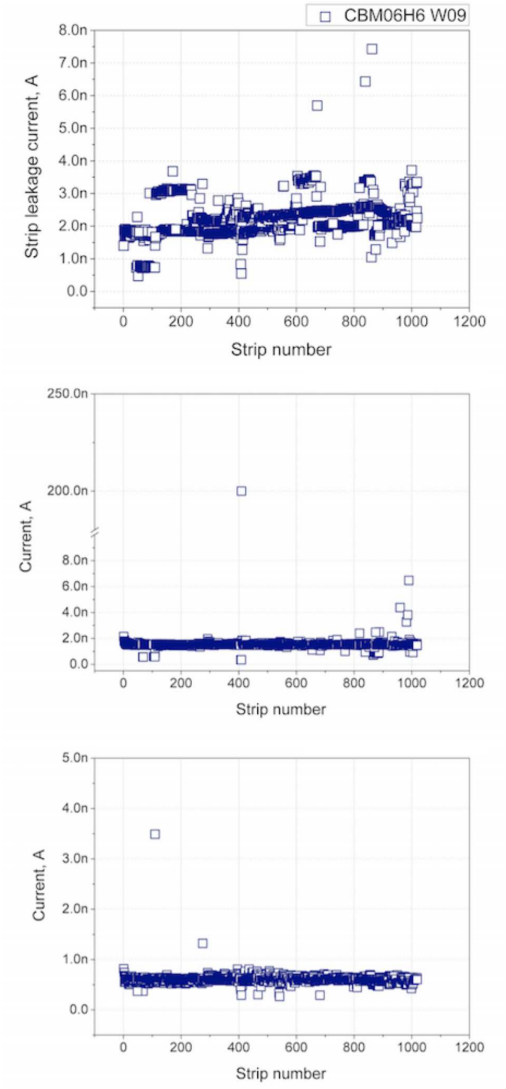

Figure 1: Output of the automated strip quality scan. Top: strip leakage current distribution; center: pinhole test scan; bottom: readout strip short scan.

References

[1] P. Larionov and P. Ghosh, GSI Scientific Report 2012, p. 47

DOI:10.15120/GR-2016-1

Improvements to the CBM TOF simulation in CBMROOT*

P.-A. Loizeau[1], *N. Herrmann*[2], *and the CBM ToF working group*
[1]GSI, Darmstadt, Germany; [2]Physikalisches Institut, Universität Heidelberg, Germany

Charged hadrons will be identified in CBM through the Time-Of-Flight method (TOF), using measurements from a wall built out of Resistive Plate Chambers (RPC). This report presents the improvements done to the simulation of this TOF wall in the CBMROOT framework.

First, new QA data containers and analysis classes were added in CBMROOT, to measure the quality of the TOF simulation and to quantify the performance changes when new TOF wall geometries or software are used. The new data containers are arrays of CbmMatch and CbmLink objects, which provide for each TofHit (reconstructed signal on detector) the indices of the corresponding TofDigis (simulated electronic signals) and TofPoints (Monte Carlo points on detector active area). Each index is associated to a weight indicating its contribution to the TofHit properties (position and time). This allows to build comparisons of the expected (derived from the TofPoints) and reconstructed properties of the TofHit. Examples of such comparisons are the residuals (quality of measurement) and pulls (quality of errors). The new CbmTofHitFinderQa class provides these comparisons and all distributions needed to calculate the efficiency of the simulation steps as function of position, momentum or phase space.

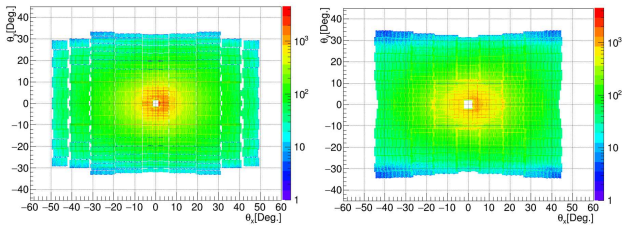

Figure 1: TofHits distribution in angular coordinates for old (v13-5b, top) and new (v16a_1e) geometries (both at Z = 6 m) with 100k Au+Au URQMD events at 10 AGeV.

These QA improvements were used to validate new geometries for the CBM TOF wall in CBMROOT: the generation v16a. This new geometry generation provides the following improvements: (i) a realistic description of the inner wall (low angles around the beam pipe), (ii) improved modules positions (better coverage for all wall positions), (iii) an extended outer wall. Five versions of the 16a geometry were produced, 16a_1h (4.5 m from target), 16a_1e (6 m), 16a_1m (6.5 m), 16a_3e (8.5 m) and 16a_3m (10 m), for use in the CBM SIS 100 hadron, electron and muon setups and the SIS 300 electron and muon setups, respectively. A comparison of the simulated hit distributions with the old and new geometries at 6 m from target (SIS100 electron setup) can be found in Fig. 1. Using the CbmTofHitFinderQa task, the distributions of the residuals and pulls in X, Y, Z and T for both geometry generations were compared and no difference (or slight improvements) were observed. The efficiency of the TOF wall (from MC tracks to hits) gained a few percent with the new geometries thanks to the improved angular coverage. Therefore the generation 16a is the default TOF geometry starting from the NOV15 release of CBMROOT.

TOF QA was also used to check that the more realistic event-based digitizer and clusterizer chain for TOF [1] provides reasonable results. For this, a comparison was made between the residuals, pulls and efficiency obtained with this simulation chain and those obtained with the idealistic TOF simulation task (direct TofHits production from MC points, default in NOV15 release). Figure 2 presents for example the comparison for the residuals on the X coordinate. The effect of the more realistic "cluster" description of the new chain can be seen in the wider distribution, as the direct production is limited at the width of a single channel. For the hit time, the new method is closer to the MC "truth" thanks to the averaging effect of multiple channel clusters, as expected from real data. For all

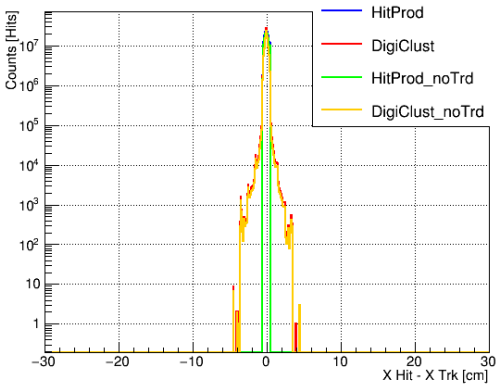

Figure 2: Comparison of the residuals in X between TofHit and TofPoint for the old simulation chain ("HitProd") and the new ("DigiClust") one, with and without TRD.

available comparisons, results are more realistic and either equivalent or better with the Digitizer+Clusterizer simulation chain. Therefore it is the TOF default simulation chain starting from CBMROOT release FEB16.

References

[1] P.-A. Loizeau *et al.*, CBM Progress Report 2013, Darmstadt 2014, p. 100

* Work supported by BMBF (05P12VHFC7)

Configuration, monitoring and data acquisition with the IPbus-AFCK readout chains *

P.-A. Loizeau[1], *D. Emschermann*[2], *W. F. J. Müller*[2], *and the CBM DAQ working group*
[1]GSI, Darmstadt, Germany; [2]FAIR, Darmstadt, Germany

In previous years, CBM used for some of its readout chain prototypes a combinations of the SYSCORE FPGA boards and the CBMnet communication protocol. On the data receiver side were used either the ABB board, DABC as interface framework and the "rocutil" library as configuration framework [1], or the FLIB board with a dedicated FLESnet version as interface and a `ROOT` based control library [2]. This was especially the case for the nXYTER based systems used for the STS tests.

The readout chain prototype which will be used by CBM in the coming years is based on the CERN GBT and SCA ASICs [3], the AFCK FPGA board [4] as Data Pre-processing Board (DPB), the IPbus protocol and interface software developed by CMS [5] for controls and the FLESnet acquisition framework [6]. Therefore a set of new software is needed to maintain functionality equivalent to the "rocutil" and `ROOT` based libraries, to easily add new ones as well as new hardware, and to prepare with test setups the final configuration and monitoring environment of the CBM experiment.

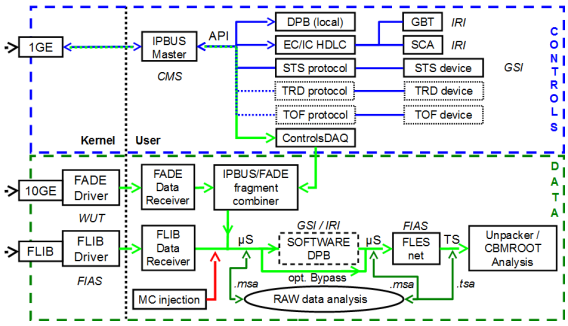

Figure 1: Planned organization of the control and acquisition software with the new readout chain. Update of [7].

Figure 1 presents the software organization being currently prepared. The top part describes the control and configuration interfaces, while the bottom part shows the data acquisition path. The control part communicates with the hardware through an IPbus master. The framework will reflect the modular DPB firmware organization [7], with common functionality in a base library (DPB) and separate libraries and classes for the CBM sub-systems and the protocols of their front-end. In addition a "Control DAQ" is planned to dump test data from the DPB through the control path, allowing access to raw data and easier debugging of the various hardware components. The acquisition part is organized around the FLESnet interfaces called microslice (μS in the figure) and time-slice (TS). All data sources fill μS containers, which can either be directly combined in TS containers or go first through an optional software preprocessing stage performing tasks later implemented in the DPB. The unpacking and analysis of the data is then done within the `CbmRoot` framework.

As a first step toward the construction of this new environment, the "rocutil" software was converted from the DABC interface to the IPbus interface. This was tested with an nXYTER 2.0 based setup, hooked to an AFCK loaded with the nDPB firmware. Most functionality from the original software are now available. It was also extended to support all new elements on the nXYTER 2.0 FEB, such as temperature probes or external control voltages, and to allow easy scan of the configuration parameters, forming the "ndpbutil". Figure 2 shows as an example a comparison of the median ADC values measured during a scan of the Vs control voltage at different temperatures.

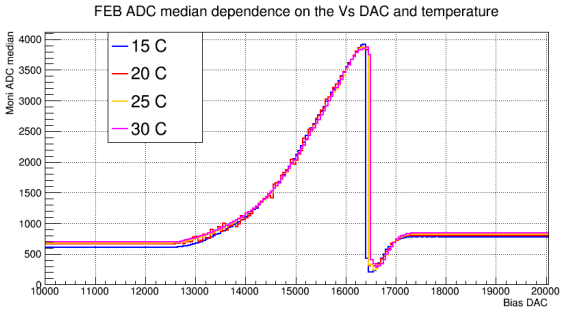

Figure 2: Median ADC value as function of the Vs bias voltage, at 15, 20, 25 and 30 °C

References

[1] S. Linev *et al.*, CBM Progress Report 2009 (2010) p. 56
[2] I. Sorokin *et al.*, CBM Progress Report 2014 (2015) p. 41
[3] J- Lehnert, W. F. J. Müller and C. Schmidt, Proc. SPIE **9662** (2015) 96622S, doi:10.1117/12.2205623
[4] W. Zabołotny *et al.*, *The AFCK Board as the Data Processing Board prototype for the CBM experiment*, this report
[5] The CMS Collaboration, Cactus: uHAL and IPbus website, https://svnweb.cern.ch/trac/cactus
[6] D. Hutter *et al.*, *CBM FLES input interface developments*, this report
[7] P.-A. Loizeau *et al.*, Proc. SPIE **9662** (2015) 96622X, doi:10.1117/12.2205820

* Work supported by GSI(SIS)/GSI(ESR)/GSI(UNILAC)/GSI(PHELIX) /HI Mainz/HI Jena/HIC4FAIR/HGShire/EU, EURONS contract No. 506065/GSI cooperation with university Mainz/Helmholtz-Nachwuchsgruppe

DOI:10.15120/GR-2016-1

Charge collection studies for prototypes of CBM-STS sensors with the Alibava readout system

M. Teklishyn[1,3], *I. Momot*[2,3], *V. Pugatch*[3], *and J. Heuser*[4]
[1]FAIR, Darmstadt, Germany; [2]Goethe University, Frankfurt, Germany; [3]KINR, Kyiv, Ukraine;
[4]GSI, Darmstadt, Germany

The CBM-STS front end electronics is currently under development. Before the dedicated STS-XYTER ASIC becomes available for tests of the sensor prototypes, front-end electronics based o the n-XYTER chip [1] is applied. However, in order to cross check the results one can include measurements performed with yet another read out system. The Alibava system [2] is a portable readout system for scientific purposes. It uses the *Beetle* readout chip which was developed for the tracker system of the LHCb experiment [3]. It is suitable for characterizing the properties of irradiated and non-irradiated microstrip sensors.

The Alibava readout system mainly consists of the two separate parts: the mother board and the daughter board. The primary analogue readout system is placed on the daughter board. It comprises two *Beetle* chips that operate in analogue readout mode. The Beetle chip is used for the readout and amplification of the collected charge from the individual sensor strips. It has 128 channels with an amplifier and a shaper. The readout, amplification and shaping of the collected signal pulses is then sampled into an analogue pipeline with a bunch-crossing frequency of 40 MHz. The analogue data is measured in analogue-digital-counts (ADC). The data that is brought off the chip is transferred via a flat cable to the mother board, where it is processed and digitized. The mother board communicates with the data acquisition software on a computer.

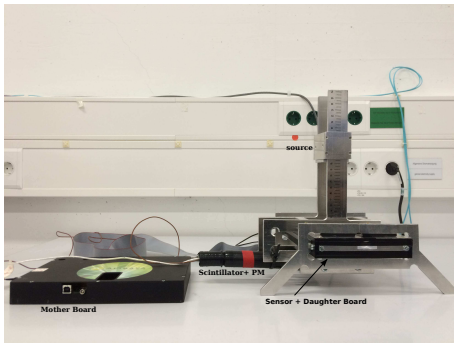

Figure 1: Set-up with the Alibava system.

A view of the set-up in the STS laboratory is shown in Fig. 1. Scintillator connected to photomultiplier tube is used as a trigger system. The scintillator, sensor and collimated source are aligned in such way that mostly perpendicular particles can penetrate. The source and the scintillator are mechanically interconnected and can move simultaneously in the X and Y direction. The height of the source above the sensor can be independently adjusted. Electrons with energies in the range between 1 MeV and 2.28 MeV (^{90}Y β-decay energy) can be considered as minimum ionized particles. In order to avoid triggering on the soft component $<$1 MeV we applied a threshold for the signals from the photo multiplier. We assume the total electron energy to be absorbed in the plastic scintillator. The resulting spectrum was fitted with a Landau-Gaussian convolution and the most probable value interpreted as collected charge. An example of the obtained spectra is shown in Fig. 2.

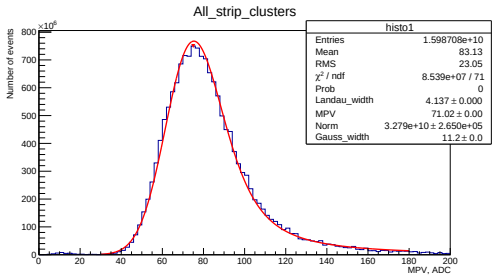

Figure 2: Signal of MIPs from the ^{90}Sr source fitted by Landau-Gaussian convolution, $\Delta_p \simeq 71$ ADC counts.

Two types of 6$\times$6 cm^2 sensors were already studied with this system: single metal sensors without interconnection between short and long inclined strips (SM) and single metal with microcable interconnection (SMwC). They shown almost the same charge collection result for long strips; the signal-to-noise ratio is $\geq$20 for each case. The Alibava setup has an internal calibration procedure. By injecting test charge pulses to the preamplifier input and observing the response in the ADC units, one can later convert the output signal from the β-source in units of electron charge. Different sensor read-out schemes were examined: (1) one strip connected to one read-out channel; (2) every second strip is readout; (3) two strips connected to one read-out channel. For the moment we performed the measurements with only perpendicular tracks. The data is in the process of being analyzed in terms of signal for different cluster sizes yielded, and signal-to-noise ratios.

References

[1] A.S. Brogna et al., NIM A568 (2006) 301-308

[2] http://www.alibavasystems.com

[3] S. Löchner and M. Schmelling, *The Beetle reference manual for Beetle version 1.3/1.4/1.5*, LHCb note 2005-105, August 22, 2006.

DOI:10.15120/GR-2016-1

Test and optimization of the PaDiWa-AMPS TDC and QDC front-end electronics for PMT and Si-PM read-out applications*

W. Koenig[1], *A. Rost*[†2], *and the HADES and CBM collaborations*[1]

[1]GSI Helmholtzzentrum für Schwerionenforschung GmbH, Darmstadt, Germany; [2]Technische Universität Darmstadt, Germany

A Charge-to-Digital-Converter (QDC) and Time-to-Digital-Converter (TDC) based on a commercial FPGA (Field Programmable Gate Array) was developed [1] to read out PMT signals of the planned HADES electromagnetic calorimeter (ECAL). The main idea is to convert the charge measurement of a detector signal into a time measurement, where the charge is encoded in the width of a digital pulse. The PaDiWa-AMPS front-end board for the TRB3 (General Purpose Trigger and Readout Board - version 3) which implements this conversion method was developed. The well-established TRB3 platform will take over the precise time measurement and serves as data acquisition. The main purpose of the proposed board is to read-out the HADES ECAL PMTs. The board showed good performance in laboratory and also during several beam times. A time precision of 20 ps and a relative charge resolutions below 0.5% (for ECAL pulses ∼1 V) was reached. SPICE simulations have been done to optimize the front-end in terms of charge and time resolution, dynamic range and signal-to-noise ratio. In a beam time with secondary photons at the MAMI accelerator in Mainz the read-out concept was successfully used to read-out PMTs of HADES ECAL modules [2]. It showed excellent precision in providing charge and time measurement compared to much more complex read-out systems. During the HADES pion beam experiment the flexibility of the front-end was shown [3]. The additionally installed Hodoscope detector was successfully read out by the PaDiWa-AMPS board. For that the analog part was adapted to the pulse shapes of small 1” PMTs. It is planned to use the PaDiWa-AMPS board to read-out Si-PM signals of the CBM PSD detector. With the help of simulations and laboratory measurements it has been shown that an adjustment of the concept is possible. Challenging is the large dynamic range which has to be covered, in addition one has to deal with minimizing the external noise which is introduced by the Si-PM and its pre-amplifier. By optimizing the low and high frequency cut-off filters of the PaDiWa-AMPS board (see Fig. 1) the signal-to-noise ratio could be significantly improved (see Fig. 2). Further improvements and tests are currently ongoing. A beam test with the NA61/SHINE PSD detector at the CERN SPS is planned for the mid of 2016. Further improvements regarding, in particular, the rate capability need an implementation of several features in the FPGA. A redesign and manufacturing is planned for the first half of this year.

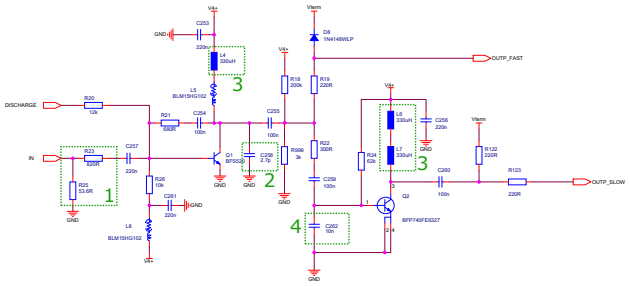

Figure 1: Schematics for one channel, excluding FPGA. The elements which have been investigated are labeled: 1) Attenuation part, 2) Low-pass filter, 3) High-pass filter, 4) Integrator gain.

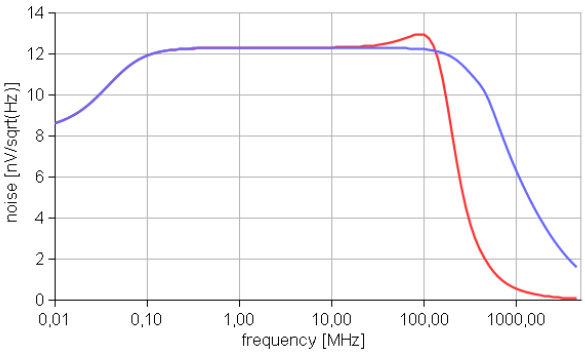

Figure 2: Frequency dependence of the normalized noise at the output of the FAST amplification stage for two values of the filter capacitor C258 (Low-pass filter). Blue curve: 2.7 pF, Red curve: 47 pF. High frequency noise could be reduced by almost a factor of two.

References

[1] M. Traxler et al., “A Precise Multi-Channel QDC FEE utilizing FPGAs as Discriminators and Delay Elements Based on the TRB3 as TDC and Readout Platform”, GSI Scientific Report 2013

[2] O. Svoboda et al., “Test of the HADES Electromagnetic Calorimeter modules on photon beam”, GSI Scientific Report 2013

[3] A. Rost et al., “Optimizing the PaDiWa-AMPS TDC and QDC front-end electronics for the HADES pion beam Hodoscope”, GSI Scientific Report 2014

* Work supported by VH-NG-823, HA216/EMMI, HIC for FAIR, GSI.

† a.rost@gsi.de

DOI:10.15120/GR-2016-1

Centrality determination in heavy-ion collisions with the CBM experiment

V. Klochkov and I. Selyuzhenkov
GSI, Darmstadt, Germany

The size and evolution of the medium created in a heavy-ion collision depends on collision geometry which is defined by the impact parameter vector, number of participants and binary collisions. The geometric quantities cannot be measured directly. Experimentally collisions are characterized by the measured particles multiplicities around midrapidity or energy measured in the forward rapidity region, which is sensitive to the spectator fragments. For this, collisions are grouped into centrality classes with the most central class defined by events with the highest multiplicity (smallest forward energy) which corresponds to small values of the impact parameter. In the CBM experiment the multiplicity of produced particles is measured with the silicon tracking system (STS) [1] with an acceptance in polar angle $2.5^\circ < \Theta < 25^\circ$. For this analysis we used the total number of reconstructed tracks with at least 3 hits in 8 STS stations. The projectile spectator detector (PSD) [2], which covers the range in x (y) of $0.21^\circ < \Theta < 5.7^\circ$ (4.3°) at the distance of 8 m from the target, is sensitive mostly to spectator fragments (outer modules are also sensitive to produced particles). For this analysis the PSD modules were grouped into PSD1, PSD2 and PSD3 as shown in the Fig. 1.

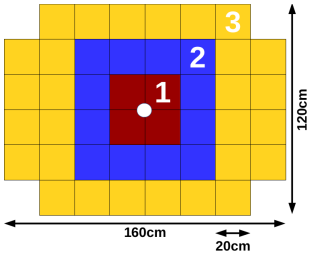

Figure 1: Transverse to the beam layout of the PSD modules. Colors show groups used in the analysis: PSD1 (red), PSD2 (blue) and PSD3 (yellow).

To study the performance of the centrality determination, 10K Au+Au collisions with beam energy of 10 AGeV simulated with DCM-QGSM (see Ref. [18–28] in [2]) and UrQMD [3] event generators were used. CBM setup (simulated with CBMRoot version Jul15) includes the beam pipe, standart STS and magnet configurations and PSD geometry with 44 modules elongated in x direction with 6 cm hole in the center. Event-by-event centrality is determined with the following procedure:

1. STS multiplicity (M_{STS}) and energy deposition in PSD subgroup (E_{PSD}) scaled by their maximal value (M^{max}_{STS} and E^{max}_{PSD}).
2. Parameterise 2D correlation between multiplicity and/or PSD subgroup energies (see Fig. 2 right panel):
   (a) initial fit of profile (red circles) of the correlation using a polynomial function (red line);
   (b) recalculate profile (black triangles) according to the fit slope and refit (red line).
3. Slice 2D correlation perpendicular to the fit (Fig. 2 left panel) or 1D distribution (not shown) in percentiles of total number of events.

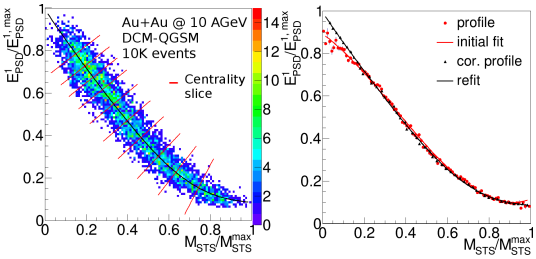

Figure 2: Illustration of the centrality determination procedure (left) with equal percentiles. The correlation between the energy deposited in the PSD1 and the STS multiplicity overlays with the result of the fit procedure (right).

For each centrality class the mean value of the impact parameter and its corresponding standart deviation was found using simulated information. In the Fig. 3 centrality dependence of the impact parameter resolution for different centrality estimators and two different models is shown.

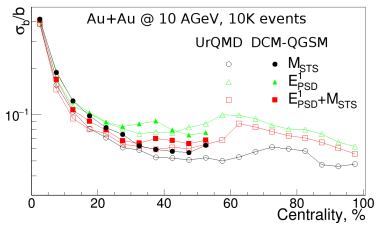

Figure 3: The impact parameter resolution with different centrality estimators calculated with UrQMD and DCM-QGSM models. Centrality class 0-5% corresponds to most central events, while 95-100% to the most peripheral.

In summary, we observe that the impact parameter resolution obtained with the PSD is comparable to that of the STS. Using correlations between STS and PSD slightly improves the resolution in central (0-30%) collisions. In the future the procedure for centrality determination will be extended to estimate the total cross-section and determine the absolute scale of the centrality using a Glauber model.

References

[1] J. Heuser et al. [CBM Collaboration], TDR for the CBM STS, http://repository.gsi.de/record/54798.

[2] F. Guber et al. [CBM Collaboration], TDR for the CBM PSD, https://repository.gsi.de/record/109059.

[3] M. Bleicher et al., J.Phys. G25, 1859 (1999).

DOI:10.15120/GR-2016-1

Status of the CBM-MVD PRESTO project *

M. Koziel[1], *T. Tischler*[1], *P. Klaus*[1], *C. Müntz*[1], *and J. Stroth*[1,2] *for the CBM-MVD collaboration*[1]
[1]Institut für Kernphysik, Goethe-Universität, Frankfurt, Germany; [2]GSI Darmstadt, Germany

This report summarizes the status of full-size prototyping the 2^{nd} and 3^{rd} station quadrants of the CBM Micro-Vertex Detector (MVD). The PRESTO project discussed in reference [1] aims at double-sided integration of 15 ultra-thin CMOS pixel sensors onto a 380 μm thin TPG carrier, representing a station quadrant. To limit possible risks related to integration, testing and vacuum compatibility, only the back side of the module has been integrated yet (6 MIMOSA-26 sensors plus 4 FPCs [2]), see figure 1a.

Yield: During a probe test campaign [3] working sensors were identified and then glued on the TPG carrier. Bonding of the sensors to the FPCs was done using a manual bonder. After wire bonding, 5 sensors are operating but with higher threshold values for each bank compared to the probe test setup. This can be associated with a voltage drop on the power supply lines of the sensor, caused by the length of the FPC of about 250 mm. With time, an additional sensor started to exhibit malfunctioning that can point to a problem with the reference voltage generation for each pixel due to the corresponding not ESD-protected sensor pad.

FPC quality:

Parameter	Test result
Eye diagram @ 40 MHz	passed
Cross-talk between sensors	not observed
Power ON/OFF influence	not observed
Voltage drop over the power lines	about 180 mV
Trace resistivity	1.68 10^{-6} Ω·cm

Heat sink quality: In-vacuum the heat evacuation was addressed with a 500 μm thin TPG plate using a flexible Kapton heater glued on one side of the carrier. The heater was providing 350 mW/cm^2 of dissipated heat. The TPG carrier was clamped into a heat sink that was directly cooled by a cooling liquid with a temperature of -40 °C. The temperature of the plate was measured by the means of 12 PT-100 temperature sensors uniformly distributed on the other side of the plate. The temperature gradient did not exceed the accepted limit of 8 K/cm and was in fact by a factor of about two lower.

Vacuum compatibility: The PRESTO sensors were also exposed to an ^{55}Fe source. In figure 1a the corresponding hit pattern is overlayed. Between the source and one of the sensors, metal wires forming the letters "MVD" were positioned, that can also be seen in the same picture. Several pressure cycles (standard pressure / 10^{-5} mbar) were performed together with measurements of the sensor current consumption and noise (temporal and fixed-pattern), employing a TRBv3-based customized read-out. After several pressure cycles, the main sensor parameters remained unchanged, see figure 1b.

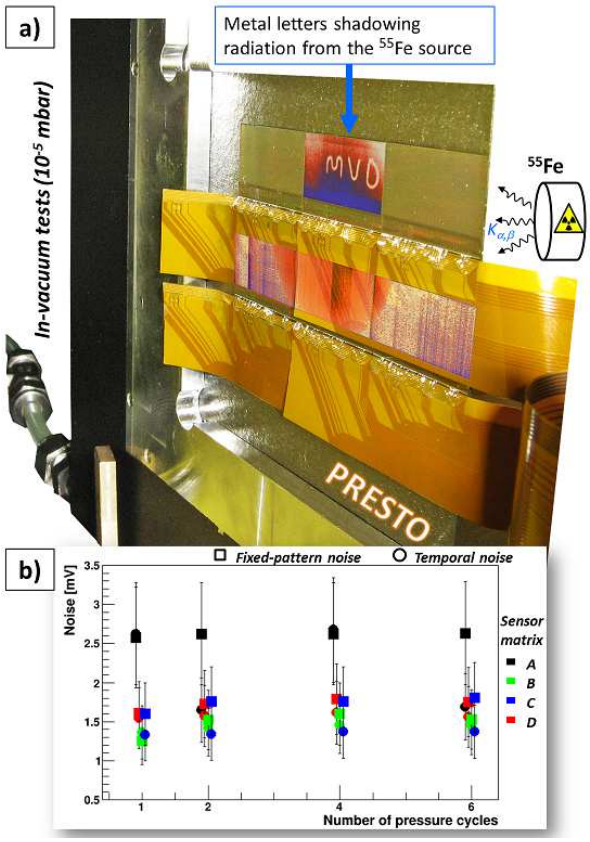

Figure 1: PRESTO: (a) The back side of the module clamped into an Al-based heat-sink and installed inside a vacuum chamber. The hit pattern from a radioactive ^{55}Fe source on four sensors is overlayed. (b) Measured sensor noise as a function of the pressure cycle number.

References

[1] M. Koziel et al., "PRESTO: PREcursor of the Second sTatiOn of the CBM-MVD." GSI annual report 2014.

[2] P. Klaus et al., "Ultra-low material budget Cu flex cable for the CBM-MVD. "GSI annual report 2014.

[3] M. Koziel et al., "The CBM-MVD: Progress in Mechanical Integration." GSI annual report 2014.

*This work has been supported by BMBF (05P12RFFC7), EU-FP7 HadronPhysics3, HGS-HIRe, GSI and HIC for FAIR.

DOI:10.15120/GR-2016-1

CBM MVD simulation - performance and status*

S. Amar-Youcef[1], *M. Deveaux*[1], *E. Krebs*[1], *B. Linnik*[1], *B. Milanovic*[1], *C. Muentz*[1], *P. Sitzmann*[1], *T. Tischler*[1], *and J. Stroth*[1,2]

[1]Goethe-Universität, Frankfurt, Germany; [2]GSI, Darmstadt, Germany

With the new realistic description of the CBM Micro-Vertex Detector (MVD) improved performance and physics case studies have been conducted.

The MVD is the dedicated detector to track particles with high precision in close vicinity to the target in CBM. It improves the tracking capabilities of the CBM Silicon Tracking System (STS) in the low momentum range (below 0.5 GeV/c) and allows applying keen topological criteria, needed as distinctive factor to reduce the combinatorial background. Topological cuts represent an integral part of different analyses. E.g. in the open charm analysis they allow to identify and favor potential decay particles indicating a definite displaced decay vertex. In the dielectron spectrometry (single) electron and positron tracks particularly from (incompletely detected) γ-conversion and π_0-Dalitz decays need to be discriminated. Here, the topological features of particles not originating from the primary vertex or exhibiting small opening angles to its closest partner can be exploited. However, in this analysis the discriminating power has to be traded off against the additional background effected by the additional detector material close to the target, as further elaborated in [1].

Tracking capability

Monte Carlo (MC) simulations were carried out in order to access the tracking capability including the MVD. To this end a simple simulation task was defined using the box generator. Events with each 100 pions (uniformly distributed in emission angle, and momentum between 0.05 and 1.5 GeV/c) are transported at full magnetic field through the detector setup.

The setup including 4 MVD (geometry version v15a) and 8 STS (v15c) stations was compared to a setup with 8 STS (v15c) stations only. Just primary tracks are considered. The impact parameter resolution, the momentum resolution, the tracking efficiency (see fig.1) and hit mapping efficiency (see fig.2 for particles with momentum smaller than 0.5 GeV/c) serve as measures for the tracking performance. As a result, adding the MVD improves these performance parameters, as this detector provides additional spatial resolution as well as geometrical acceptance especially for low-momentum particles. Thus, as it can be seen in fig.2, the MVD supplements the tracking performance also in the STS. Here, the Monte Carlo tracks are compared to the reconstructed tracks hit by hit. The upper block shows the case when no MC hit is registered, and the lower block shows the case when a MC hit is registered in the respective station.

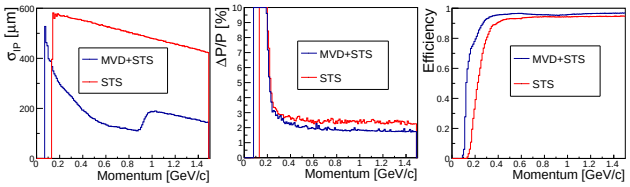

Figure 1: Impact parameter and momentum resolution, and tracking efficiency as a function of the momentum for a setup with STS and MVD (blue), and STS only (red). Only primary tracks originating from the primary vertex are considered.

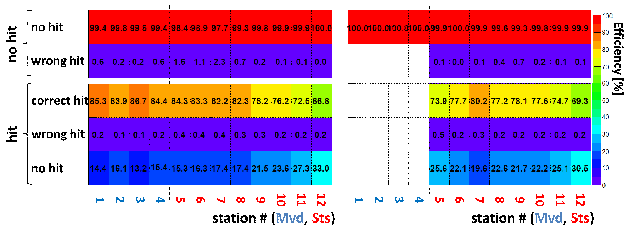

Figure 2: Hit mapping efficiency with STS and MVD (lhs) and STS only (rhs): Monte Carlo (MC) tracks are compared to the reconstructed tracks hit by hit and each station separately. Two cases are distinguished: No MC hit was detected (upper block), and a MC hit was detected (lower block) in the respective station. The different rows indicate the results from tracking.

Summary

The tracking performance was investigated using the new realistic description of the MVD. It was found that the MVD improves the CBM tracking capability due to the added value w.r.t. spatial resolution and geometrical acceptance. This result is completed by the findings reported in [1] on improving the signal-to-noise ratio in the dielectron invariant mass spectrum by adding the MVD in the analysis.

References

[1] Erik Krebs, this report.

* Work supported by BMBF (05P12RFFC7), HIC for FAIR and GSI

Reconstruction of dimuons with KF Particle Finder*

I. Kisel[1,2,3], *D. Radevych*[4], *I. Vassiliev*[1], *and M. Zyzak*[† 1,2,3]

[1]GSI, Darmstadt, Germany; [2]Goethe-Universitaet Frankfurt, Frankfurt am Main, Germany; [3]Frankfurt Institute for Advanced Studies, Frankfurt am Main, Germany; [4]Taras Shevchenko National University of Kyiv, Kyiv, Ukraine

One of the most promising observables for the CBM experiment are J/ψ and low mass vector mesons (LMVM), which are extremely important for investigation of the dense baryonic matter. The probability of the charmonium creation strongly depends on the properties of the baryonic medium formed in the collision, that makes it well suited for the QCD phase diagram exploration. LMVM are perfectly suited for investigation of early stages of the collision because of their extremely low lifetime.

J/ψ and LMVM can be reconstructed through the dimuon channel. Muons do not interact strongly, therefore they pass through the baryonic matter that is formed during the collision without interaction and carry out exactly the information about the parent particle and its properties.

Reconstruction of dimuons using MuCh PID was added to the KF Particle Finder package. The low multiplicities (J/ψ) and branching ratio of the dimuon channel (LMVM) require tight cuts on the PID stage. Tracks which are used for reconstruction of dimuon should fulfill additional criteria of being primary, the STS track should be matched with a MuCh track, both STS and MuCh tracks should pass cuts on χ^2 value and on the minimum number of hits. In case of J/ψ the cut on the number of hits in MuCh track is tighter since muons produced in its decay are more energetic. Also, as it follows from the decay topology, muons from J/ψ decay should have $p_t > 1.5$ GeV each.

Particle	ε_{method}, %	$\varepsilon_{4\pi}$, %	S/B	σ, MeV/c^2
$J/\psi \to \mu^+\mu^-$	15.1	6.9	0.79	29.3
$\rho \to \mu^+\mu^-$	45.4	1.2	0.007	149.0
$\omega \to \mu^+\mu^-$	42.1	1.1	0.147	8.5
$\phi \to \mu^+\mu^-$	48.5	2.1	0.045	4.2

Table 1: J/ψ and LMVM reconstructed by the dimuon channel: efficiency, width of the signal peak, and S/B.

Due to the low multiplicities of the muons and tight cuts, analysis of the background can not be performed on the event-by-event level. For simulation of the background the mixed event technique implemented in the KF Particle Finder is used: tracks produced in different UrQMD collisions are mixed and combined with each other, that gives the number of arbitrary combinations growing quadratically with the number of events. Such technique allows to estimate the background for the several orders higher statistics then a usual event-by-event analysis.

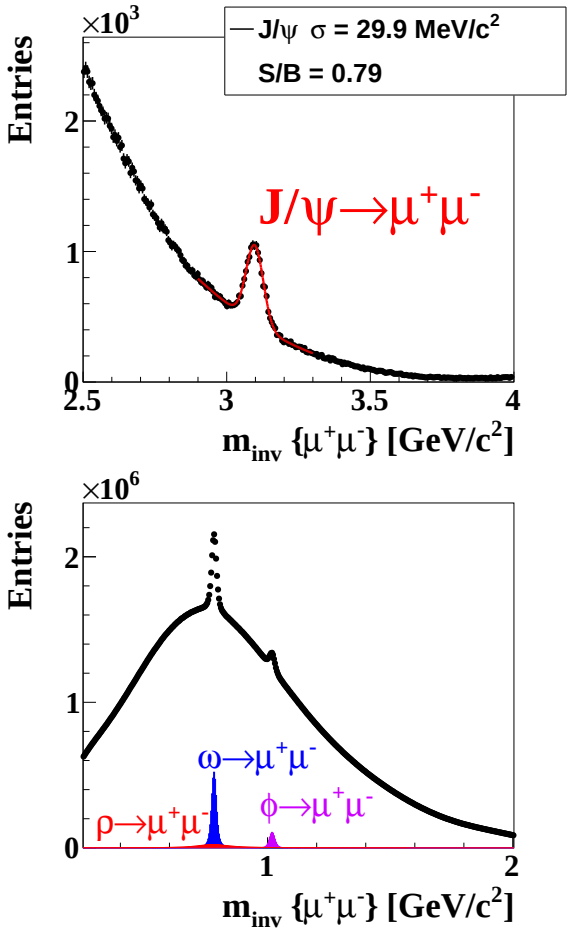

Figure 1: Mass spectra of J/ψ and LMVM together with their signal to background (S/B) ratios in dimuon channel for 10^{11} simulated central AuAu events at 25 AGeV using MuCh PID and mixed event technique.

The mass spectra of J/ψ and LMVM decaying by the dimuon channel obtained by the KF Particle Finder for 10^{11} central AuAu events at 25 AGeV using MuCh PID is shown in Fig. 1. Corresponding efficiencies, signal to background (S/B) ratios, and widths of the peaks are given in Table 1.

Summarizing, tools for dimuon analysis with MuCh PID are added to the KF Particle Finder package.

* Work supported by HICforFAIR, FIAS and HGS-HIRe for FAIR.

† m.zyzak@gsi.de

DOI:10.15120/GR-2016-1

Hypernuclei reconstruction at the CBM experiment*

I. Kisel[1,2,3], *I. Vassiliev*[1], *and M. Zyzak*[1,2,3]

[1]GSI, Darmstadt, Germany; [2]Goethe-Universitaet Frankfurt, Frankfurt am Main, Germany; [3]Frankfurt Institute for Advanced Studies, Frankfurt am Main, Germany

In the CBM experiment at FAIR ultra-high net-baryon densities and moderate temperatures will be reached in heavy-ion collisions. Model calculations predict structures in the QCD phase diagram at large baryon chemical potentials, like the critical endpoint followed by a first order phase transition. Moreover, new phases are predicted, such as quarkyonic matter.

Theoretical models predict that single and double hypernuclei are produced via coalescence in heavy-ion collisions with the maximum yield in the region of SIS100 energies. Discovery and investigation of new hypernuclei and of hypermatter will shed light on the hyperon-nucleon and hyperon-hyperon interactions, which are essential ingredients for the nuclear equation-of-state at high densities and moderate temperatures. Beam energies available at SIS100 appear to be especially well suited for generating signals of the phase transition. To study the performance of multi-strange hyperon and hypernuclei reconstruction, several sets of $5 \cdot 10^6$ central Au+Au UrQMD events (Fig. 1) at the FAIR energy range have been simulated.

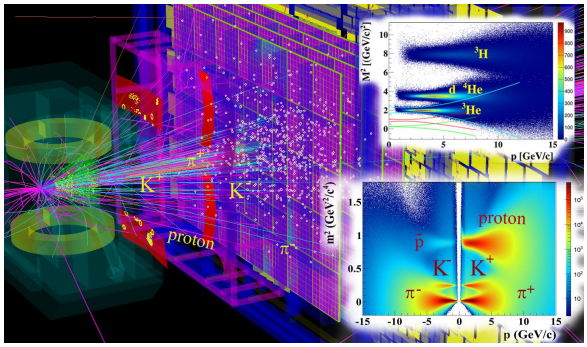

Figure 1: A simulated CBM event of a Au + Au collision at 15 AGeV. The TOF detector identifies hadrons i. e. pions, kaons, protons and fragments.

The combination of MVD and STS segmented strip detectors, cables and support frames was used for event simulation and reconstruction. The TOF detector identifies hadrons i.e. pions, kaons, protons, and fragments, i. e. d, t, ^3He and ^4He in the angular range covered by the STS detector.

The current KF Particle package includes searching for the bound state $\{\Lambda n\}_b$, ${}^3_\Lambda H$, ${}^4_\Lambda H$, ${}^4_\Lambda He$, ${}^5_\Lambda He$ and corresponding anti-particles. Searching for double hypernuclei ${}^4_{\Lambda\Lambda}H$ and ${}^6_{\Lambda\Lambda}He$ is under development. Hypernuclei will be reconstructed in the CBM experiment by their detached from the primary vertex decays into charged hadrons and fragments, like $d, t, {}^3He$ and ${}^4He$. A reconstructed ${}^4_\Lambda He \to \pi^- p^3He$ decay is shown in Fig. 2.

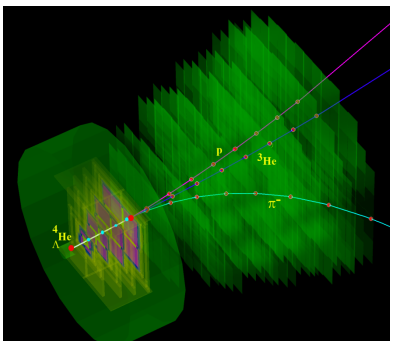

Figure 2: A reconstructed ${}^4_\Lambda He \to \pi^- p^3He$ decay topology.

${}^4_\Lambda He$ hypernuclei are created at the primary vertex and decay to $\pi^- p^3He$ several centimeters downstream of the target. Presence of the ^3He fragment in a 3-prong vertex is a unique signature of such decay. The reconstructed invariant-mass spectrum of $\pi^- p^3He$ is shown in Fig. 3.

Small amount of background events in the high-mass region is due to misidentified high-momentum hadrons in the sample of ^3He selected particles.

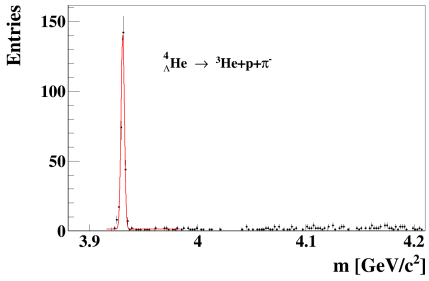

Figure 3: The reconstructed invariant-mass spectrum of $\pi^- p^3He$ in $5 \cdot 10^6$ central Au+Au collisions at 10 AGeV. The red line indicates the signal plus background fit by a polynomial plus Gaussian function.

Assuming the ${}^4_\Lambda He$ production multiplicity for minimum bias Au+Au events at 10 AGeV about $5 \cdot 10^{-4}$, the branching ratio of 20% to $\pi^- p^3He$ decay, taking into account the 14.7% ${}^4_\Lambda He$ detection efficiency, one would expect the ${}^4_\Lambda He$ collection rate of up to $5.4 \cdot 10^5$ per hour.

* Work supported by HICforFAIR, FIAS and HGS-HIRe for FAIR.

Reconstruction of D^0 with KF Particle Finder*

I. Kisel[1,2,3], *I. Vassiliev*[1], *and M. Zyzak*[† 1,2,3]

[1]GSI, Darmstadt, Germany; [2]Goethe-Universitaet Frankfurt, Frankfurt am Main, Germany; [3]Frankfurt Institute for Advanced Studies, Frankfurt am Main, Germany

Investigation of the charm production is one of the main tasks for the CBM experiment. According to the current theoretical models charm is expected to be an extremely sensitive probe of the properties of the dense matter created in heavy ions collisions. Moreover, charm production mechanisms at the CBM energies are not studied yet. At these energies charm quarks are expected to be produced in primary hard scattering processes, thus, providing a possibility to study the early phases of the collision. Depending on the interaction with the medium, they hadronize into D mesons, charmed baryons, or charmonium.

Open charm is considered as one of the possible triggers for the CBM experiment. Therefore reconstruction of the open charm was added to the KF Particle Finder package, which will be run at the CBM online computing farm as a part of the FLES package.

Because of the low multiplicity, studies of open charm reconstruction can not be performed on the event-by-event level. Therefore the mixed event technique for the background simulation was added to the KF Particle Finder: tracks produced in different UrQMD collisions are mixed and combined with each other, that gives the number of arbitrary combinations growing quadratically with the number of events. Such technique allows to estimate the background for the several orders higher statistics then a usual event-by-event analysis.

With the new tools feasibility of D^0 and $\overline{D}^0$ reconstruction was studied in central NiNi events at 15 AGeV. For the studies CBM configuration including realistic geometries of the MVD (version 14b), STS (version 13d) and TOF (version 13b) detectors was used. Tracks were reconstructed by the Cellular Automaton based track finder in STS and MVD, their identification was performed using TOF information. In order to reproduce the realistic response of the MVD detector, the simulation also includes delta electrons produced by the ions passing through the target and pileup events corresponding to the interaction rate of 100 kHz.

Particle	ε_{method}, %	$\varepsilon_{4\pi}$, %	S/B	σ, MeV/c^2
D^0	7.6	1.7	0.4	10.6
$\overline{D}^0$	7.6	1.7	0.7	11.1

Table 1: Efficiency of D^0 and $\overline{D}^0$ reconstruction, widths of the signal peaks, and S/B for 10^{11} simulated central NiNi events at 15 AGeV using TOF PID.

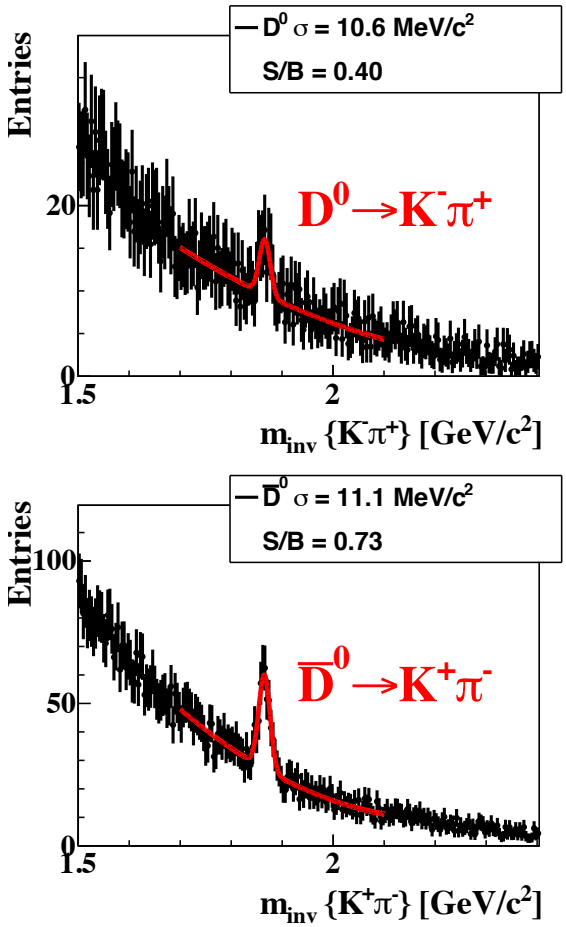

Figure 1: Mass spectra of D^0 and $\overline{D}^0$ mesons obtained by the KF Particle Finder package together with their signal to background (S/B) ratios for 10^{11} simulated central NiNi events at 15 AGeV using TOF PID. The mixed event technique is used for the background estimation.

The mass spectra of D^0 and $\overline{D}^0$ obtained by the KF Particle Finder for 10^{11} central NiNi events at 15 AGeV using TOF PID are shown in Fig. 1. Corresponding efficiencies, signal to background (S/B) ratios, and widths of the peaks are given in Table 1. A small lifetime ($c\tau$ of hundreds μm) together with a low multiplicities of open charm particles require tight cuts in order to achieve high S/B ratio, that leads to a smaller reconstruction efficiency.

Summarizing, tools for open charm analysis are added to the KF Particle Finder package.

* Work supported by HICforFAIR, FIAS and HGS-HIRe for FAIR.

† m.zyzak@gsi.de

DOI:10.15120/GR-2016-1

Σ^+ and Σ^- reconstruction by the missing mass method*

I. Kisel[1,2,3], *P. Kisel*[† 1,2,4], *P. Senger*[1], *I. Vassiliev*[1], *and M. Zyzak*[1,2,3]

[1]GSI, Darmstadt, Germany; [2]Goethe-Universität Frankfurt, Frankfurt am Main, Germany; [3]Frankfurt Institute for Advanced Studies, Frankfurt am Main, Germany; [4]Joint Institute for Nuclear Research, Dubna, Russian Federation

One of possible signals of QGP formation is enhanced strangeness production. Being abundant particles (several particles per collision are produced at the CBM energies), Σ^+ and Σ^- carry out large fraction of produced strange quarks. Reconstruction of Σ-particles together with other strange particles completes the picture of strangeness production and allows to compare yields of Σ and Σ^*. Reconstruction of Σ-particle will open a possibility to investigate H-dybarion objects, if such exist, by the decay channel $\Sigma^- p$, which is expected to be the dominant one.

All strange mesons and hyperons, except Σ-particles, can be either registered directly by the tracking system and identified by the PID detectors or have decay modes with all charged particles and, as a result, can be reconstructed through their daughters. Σ^+ and Σ^- have all decay modes with at least one neutral daughter, which can not be registered by the CBM detector at all (decay modes with n or ν) or can be registered with an efficiency on the 10^{-7} level (decay modes with π^0). The main channels of Σ^+, Σ^- and their antiparticles together with the corresponding branching ratios (BR) are:

$\Sigma^+ \to p\pi^0$	$\overline{\Sigma}^+ \to \overline{p}\pi^0$	BR 51.57%
$\Sigma^+ \to n\pi^+$	$\overline{\Sigma}^+ \to \overline{n}\pi^-$	BR 48.31%
$\Sigma^- \to n\pi^-$	$\overline{\Sigma}^- \to \overline{n}\pi^+$	BR 99.8%

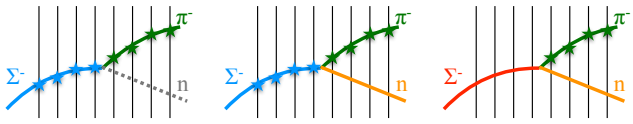

Figure 1: The missing mass method for reconstruction of $\Sigma^- \to n\pi^-$.

Having a lifetime sufficient to be registered by the tracking system ($c\tau_{\Sigma^+} = 2.4$ cm and $c\tau_{\Sigma^-} = 4.4$ cm), these particles can not be identified by the PID detectors. The missing mass method can be applied for their identification, as illustrated in Fig. 1:

1. tracks of the mother (Σ^-) and the charged daughter (π^-) particles are reconstructed in the tracking system;
2. the neutral daughter particle (n) is reconstructed from these tracks;
3. a mass constraint is set on the reconstructed neutral daughter, that modifies also its momentum;
4. the mother particle is constructed out of the charged and reconstructed neutral daughter particles and the mass spectrum is obtained, by which the particle can be identified.

True Σ particles form a peak, while the background will form a continuous structure (Fig. 2).

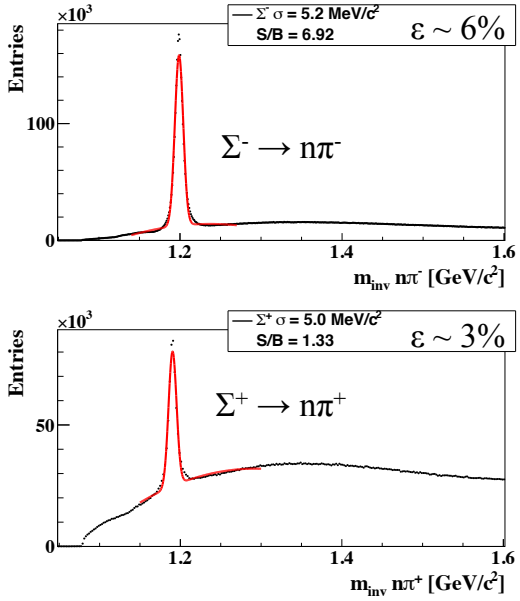

Figure 2: Reconstructed $\Sigma^- \to n\pi^-$ and $\Sigma^+ \to n\pi^+$.

The method can be applied for reconstruction of other strange particles, such as:

$$\Xi^- \to \Lambda\pi^- \quad \text{with} \quad \Lambda \to n\pi^0;$$
$$\overline{\Xi}^+ \to \overline{\Lambda}\pi^+ \quad \text{with} \quad \overline{\Lambda} \to \overline{n}\pi^0;$$
$$\Omega^- \to \Lambda K^- \quad \text{with} \quad \Lambda \to n\pi^0;$$
$$\overline{\Omega}^+ \to \overline{\Lambda}K^+ \quad \text{with} \quad \overline{\Lambda} \to \overline{n}\pi^0;$$
$$\Omega^- \to \Xi^0\pi^-;$$
$$\overline{\Omega}^+ \to \overline{\Xi}^0\pi^+.$$

Their investigation will allow to increase the efficiency of the corresponding particles and to investigate systematic errors comparing yields of different decay channels.

Another possible application of the method is suppression of the $\mu^+\mu^-$ background by identifying muons produced in $\pi^\pm$ and $K^\pm$ decays.

* Work supported by BMBF, HICforFAIR and HGS-HIRe for FAIR.
† P.Kisel@gsi.de

Design of a control and monitoring system for the mirror alignment of the CBM RICH detector*

J. Bendarouach† [1] *and C. Höhne*[1]

[1]Justus Liebig University, Gießen

An important aspect to guarantee a stable operation of a RICH detector is the alignment of the mirrors. A first method to qualitatively assess whether misalignment is present, CLAM (Continuous Line Alignment Monitoring [1]), has been implemented in the RICH prototype and successfully tested during a beamtime at CERN. A correlation has been highlighted between reflected stripes appearing broken and corresponding reconstructed rings [2].

In order to quantify the highlighted misalignment, a second method, inspired by the HERA-B experiment [3], was developed and uses recorded data. The principle of the method is as follow. When a particle enters the RICH vessel, it emits Cherenkov light, which is reflected by one or several mirror tiles to the PMT plane, see red crosses on Fig. 1. These photon hits are then reconstructed together

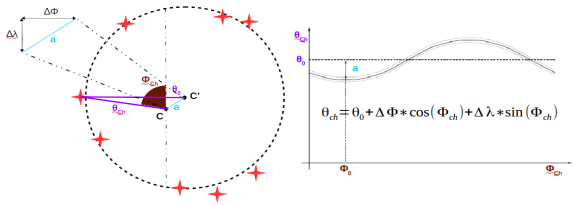

Figure 1: A sinusoidal behaviour between Cherenkov distances and angles has been demonstrated [3], allowing a misalignment quantification of mirror tiles.

as a ring, whose center C' differs in case of misalignment from the point C, representing the extrapolated particle hit to the PMT plane, if the incident particle had been reflected by the same aligned mirror tiles. Measuring Cherenkov distances (θ_{Ch}) and angles (Φ_{Ch}) for each photon hit, a sinusoidal dependence has been demonstrated between these two parameters (see formula Fig. 1). For a sufficient number of accumulated events hitting a particular mirror tile, those measurements can reveal and quantify potential misalignments of the considered tile (via $\Delta\Phi$ and $\Delta\lambda$, see Fig. 1) [4].

This technique has been adapted and tested for the CBM RICH detector with simulations in the CbmRoot framework. It produces good results for misalignments ranging from 0.2 mrad up to 12 mrad, as seen in Fig. 2. If possible mirror misalignment is revealed, it can be subsequently included and rectified by correction routines. A first correction cycle has been successfully implemented. A mirror tile has been artificially misaligned by 5 mrad around its

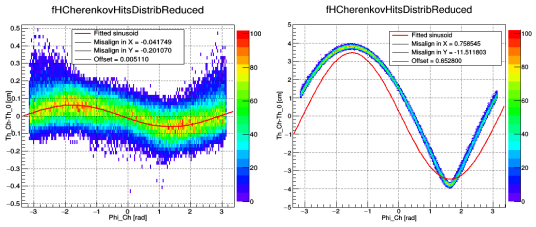

Figure 2: Plot of (θ_{Ch} - θ_0) as function of Φ_{Ch}. For a 0.2 (left) and 12 (right) mrad rotation around the horizontal axis, a fit of the sinusoid (red curves) returns 0.2 and 11.5 mrad misalignment respectively.

horizontal axis and this misalignment has been evaluated using the described method. The extracted misalignment is 5.26 mrad around the horizontal axis and 0.37 mrad around the vertical one. A new simulation using the corrected mirror geometry has then been run and at the reconstruction level the mean position between the points C and C' has been compared before and after corrections were applied (see Fig. 3).

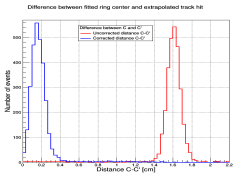

Figure 3: Distance between the fitted ring center C' and the extrapolated track hit to the PMT plane C. For the uncorrected case (red), the mean distance was 1.6 cm, whereas once the correction has been calculated and applied (blue), it was reduced to 0.15 cm.

It is foreseen to use these correction routines to compare ring reconstruction and ring-track matching efficiencies. In a next step, the CLAM technique will also be used to quantify misalignment via photogrammetry.

References

[1] L. Steiger et al., Nucl. Instr. Meth. Phys. Res. A 639 (2011) 219

[2] J. Bendarouach et al., CBM Progress Report 2014, p.56

[3] A. Gorisek et al., Nucl. Instr. Meth. Phys. Res. A 433 (1999) 408

[4] M. Staric et al., Nucl. Instr. Meth. Phys. Res. A 586 (2008) 174

*Work supported by HGS-HIRe, the GSI F&E cooperation with Gießen and BMBF grants 05P15RGFCA and 05P12RGFCG.

† jordan.bendarouach@exp2.physik.uni-giessen.de

DOI:10.15120/GR-2016-1

Deriving the effective focal plane for the CBM-RICH detector *

I. Kres[1], *K.-H. Kampert*[1], *and C. Pauly*[1]
[1]University of Wuppertal, Germany

The RICH detector is designed to provide identification of electrons and suppression of pions in the momentum range below 10 GeV/c. This will be achieved using a gaseous RICH detector with focusing mirror elements and a photon detector consisting of a plane of MAPMTs. In our current "standard" design, the photon detector has a "wing-shaped" construction consisting of 4 individual plane elements, two of them above and two below the beampipe respectively. This design approximates the ideal focal sphere, and is the result of a detailed optimization procedure [1].

The detailed mechanical design, however, shows that this geometry introduces significant dead space regions between the two tilted halfs of each wing. This is due to the required additional volume behind the PMTs needed for electronic readout components. It turns out that a continously curved detection plane might be mechanically easier to implement, and would help to overcome the dead space limitation. In this report we present a study to derive the ideal 3-dimensional shape of the focal plane based on full Monte Carlo simulations, using the ring sharpness as optimization criterion.

To obtain the optimal focal position, the tilted wing-shaped PMT planes were rotated back, such that a single, flat detection plane is used in the simulation. Using individual Monte Carlo simulations, this flat plane was moved upstream and downstream along the beam direction such, that the optimal focal position will be crossed for each point (x, y). For each step, the dR-value (based on ellipse fitting of the Cherenkov rings) was mapped as a function of (x, y). dR, the mean distance of each individual hit to the fitted ellipse, is used here as criterion for ring sharpness. Finding the minimum dR value along z for a given point in (x,y) yields a 3d shape of the optimal focal plane.

The study was carried out for two different mirror rotation angles of $-1°$ with respect to the beam axis (rich_v14a_1e geometry version) and for $10°$ (rich_v16a_1e). Single electrons and positrons were generated uniformly on all planes, with transverse momenta ranging from 0.75 to 3 GeV/c. Due to bending of low momentum electrons in the magnetic field the different energies might lead to different focal spheres. Figure 1 shows the derived shape of the ideal focal plane.

Figure 2 shows a fit of these data with a cylindrical shape aiming to derive the optimal radius and tilt angle of this shape. This simplified form was chosen because it will be easier to implement in the Monte Carlo simulation, and also for the later mechanical design. As a result,we find a cylinder basis radius of 2m, and a cylinder tilt angle of $11.5°$ with respect to beam axis.

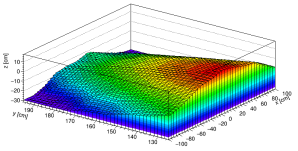

Figure 1: Ideal focal plane, based on the calculation of dR for geometry rich_v16a_1e.

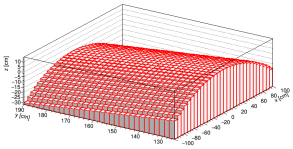

Figure 2: Fit, based on data from figure 1.

Based on these parameters, we performed a comparison between the extracted optimal focal shape and the currently implemented "standard" wing-shaped geometry. Figure 3 shows, that the currently used geometry roughly matches the "optimal" focal plane. However, there is a striking difference in the tilt angle. The tilt angle of the standard geometry is not only based on ideal focussing, but the result of a more involved optimization procedure taking into account also the size of focal plane, the ring ellipticity A/B, and the photon incident angle α. A similar optimization procedure now also has to be done to determine the optimal tilt angle in the cylindrical focal plane geometry.

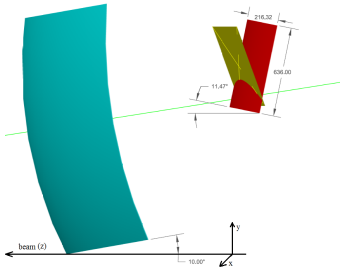

Figure 3: Comparison of the extracted geometry (red) with a wing-shaped (yellow).

References

[1] T. Mahmoud et al. CBM Progress Report (2015)

* Work supported by BMBF 05P15PXFCA, and GSI

Time and position resolution of high granularity, high counting rate MRPC for the inner zone of the CBM-TOF wall *

M. Petriş[1], D. Bartoş[1], G. Caragheorgheopol[1], I. Deppner[3], V. Duţă[1], J. Frühauf[2], N. Herrmann[3], M. Kiš[2], P-A. Loizeau[2], M. Petrovici[1], L. Rădulescu[1], V. Simion[1], and C. Simon[3]

[1]NIPNE, Bucharest, Romania; [2]GSI, Darmstadt, Germany; [3]PI, Heidelberg University, Germany

Two in-beam tests using heavy ion induced reactions were focused on the counter behaviour in high counting rate and multiplicity environment. The one performed at GSI using a Sm beam of 1.1·A GeV was followed by one at CERN with an Ar beam of 13·A GeV. In both cases the detector under test, called Buc2013 [1, 2], was positioned at polar angles of a few degrees relative to the beam axis in order to get the maximum exposure. A narrow strip MGM-SRPC, called BucRef, described in [3], positioned behind the detector under test, was used as time reference. Both of them were sandwiched between two plastic scintillators for rate estimates. The counting rate estimate using the plastic scintillators gives a value of $\sim$1 kHz/cm^2 for the GSI in-beam test and $\sim$5 kHz/cm^2 for CERN in-beam test for the runs used in the present analysis.

The signals delivered by Buc2013 prototype were processed by a new front-end electronics (FEE), called PADI8 [5], developed within the CBM-TOF collaboration. For BucRef an older version of PADI, called PADI3, was used in the GSI beam time and PADI8 FEE in CERN SPS beam time. The digital conversion of the LVDS signals was performed by FPGA based TDCs [6]. An overview of the GSI in-beam experimental setup and the steps followed in the data analysis, based on cbmroot softare, are comprehensively described in [7].

The efficiency obtained with Buc2013 as a function of the PADI8 thresolds for two applied high voltages ($\pm$5.5 kV and $\pm$5.6 kV), is sown in Fig. 1 (left side). The efficiency remains larger than 98% at the largest value of the threshold used in these measurements, of 240 mV. The statistical errors are within marker size. At the highest applied threshold (240 mV) the mean cluster size value is of 3 strips. As it was already shown in reference [4], this gives the possibility to reconstruct the position across the strip with a position resolution better than the one based on the pitch size (pitch/$\sqrt{12}$), in addition to the position information along the strip (obtained from the difference of the times measured at the both ends of the strip).

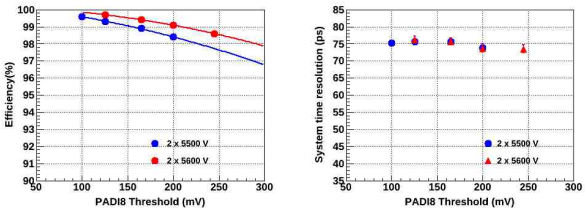

Figure 1: Efficiency(left side) and system time resolution (right side) as a function of PADI8 threshold at two applied HV ($\pm$5.5 kV and $\pm$5.6 kV).

The system time resolution (contributions of both Buc2013 and BucRef) corrected for slewing effect, reaction product velocity spread and hit position, (Fig. 1 - right side) improves slightly increasing threshold, the best value being of 74 ps$\pm$1 ps, including the electronics contribution.

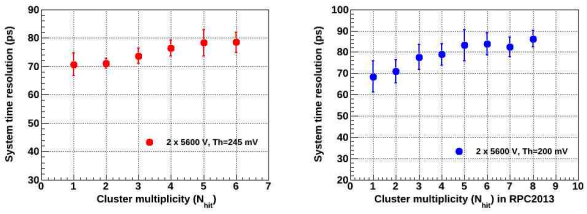

Figure 2: System time resolution as a function of hit multiplicity in Buc2013 for GSI beam test - left side and CERN SPS beam test - right side.

The dependence on the hit multiplicity of the system time resolution is shown for GSI in-beam test in the left side of Fig. 2 and for CERN SPS beam test in the right side of Fig. 2. As it is expected, the best time resolution is obtained for single hit events, a slight increase with the hit multiplicity in Buc2013 prototype being observed.

The obtained efficiency for Buc2013 prototype in the CERN-SPS beam test was of 99% and the corresponding mean cluster size of 3.6 strips for 5.6 kV applied HV and 200 mV FEE threshold. The difference in the hit multiplicity and counting rate between the two mentioned experiments could explain the slight observed differences in the cluster size and time resolution.

References

[1] V. Aprodu et al., CBM Progress Report 2013 (2014), p.79

[2] M. Petriş et al., GSI Scientific Report 2014, (2015), p.88

[3] M. Petrovici et al., JINST 7 (2012) P11003

[4] M. Petriş et al., CBM Progress Report 2011 (2012), p.5

[5] CBM-TOF Collaboration, CBM-TOF TDR, October 2014

[6] TRB3 Homepage: http://trb.gsi.de/

[7] I.Deppner et al., CBM Progress Report 2014 (2015), p.86

*Romanian NASR/contract RO-FAIR F02 and NASR/NUCLEU Project PN09370103

DOI:10.15120/GR-2016-1

J/ψ detection via di-muon channel in 15 A GeV Ni+Ni collisions with the CBM detector at FAIR

P. P. Bhaduri[*] *and A. Toia*
GSI, 64291 Darmstadt

The goal of the Compressed Baryonic Matter (CBM) experiment [1], at FAIR is the investigation of the strongly interacting matter at high net baryon densities produced in relativistic heavy-ion collisions. In the first phase of FAIR, the SIS-100 accelerator ring will be operational, which will provide beams up to an energy of 30 GeV for protons, 12 A GeV for heavy ions (eg:Pb, Au, In, ...) and 15 A GeV fo light ions (eg:C, Ca, Ni, ...). The proposed key observables include the measurement of J/ψ mesons. In this article we report our latest results based on realistic simulation, on performance of J/ψ detection via di-muon channel in 15 A GeV central Ni+Ni collisions. Depending on the collision energy, different MUCH configurations are proposed in [2]. For our present investigations, we have employed the SIS-100-C set up of the muon system, along with TRD as the trigger station and TOF wall. The muon system comprises of 5 hadron absorbers and 4 tracking stations. The first absorber made of carbon (graphite), has a thicknes of 60 cm. The other four are made of iron of variable thickness (20 + 20 + 30 + 100 cm), total thickness (iron) being 170 cm. Each tracking station consists of three layers of high resolution Argon + CO_2 based gaseous chambers. In our study, the event generators PLUTO and UrQMD-3.3 have been used for generating signals and background particles respectively. PLUTO generates the J/ψ mesons following a thermal fireball model with thermal m_T (T=170 MeV) and Gaussian rapidity ($\sigma_y = 0.16$) distributions. For central Au+Au collisions, HSD model predicts the J/ψ multiplicity in 15 A GeV as $m_{J/\psi} = 2.44 \times 10^{-6}$. The corresponding value for Ni+Ni system is obtained by scaling the value down by factor of 5, the ratio of average number of binary collisions for Ni+Ni and Au+Au systems, and comes out to be 5×10^{-7}. We simulated 1M central Ni+Ni collisions at 15 A GeV. The particles from the event generators have been transported through the CBM detector set up using GEANT 3 and reconstructed using standrad reconstruction procedure of CBMROOT package. Reconstructed global tracks are selected having i) more than 6 STS hits ii) more than 10 muon hits iii) more than 2 TRD hits iv) track STS $\chi^2 \leq 1.5$ iv) track much $\chi^2 \leq 1.5$ v) track TRD $\chi^2 \leq 6$ vi) vertex $\chi^2 \leq 2$ and vii) TOF mass $m^2 \leq 0.6$. The invariant mass spectra for the J/ψ mesons along with the combinatorial background is shown in the top panel of Fig. 1. The signal extracted from the embedded events is normalized according to the J/ψ multiplicity calculated above. The combinatorial background is calculated with the mixed event technique applied to 10^6 events generated by UrQMD. The J/ψ mass peak is visible over the background. The bottom panel shows the acceptance of the reconstructed signals. The pair reconstruction efficiency (including the geometrical acceptance of the detector) and S/B ratio are respectively found to be $3.32 \pm 0.02\%$ and 1.37 ± 0.05. The J/ψ mass resolution is found to be $\sigma_M \simeq 33$ MeV. For minimum bias collisions, J/ψ multiplicity will be factor of 4 lower compared to central collisions. With the maximum foreseen event rate of 10 MHz, the J/ψ yield in di-muon channel, comes out to be 2.62×10^{-3} per second.

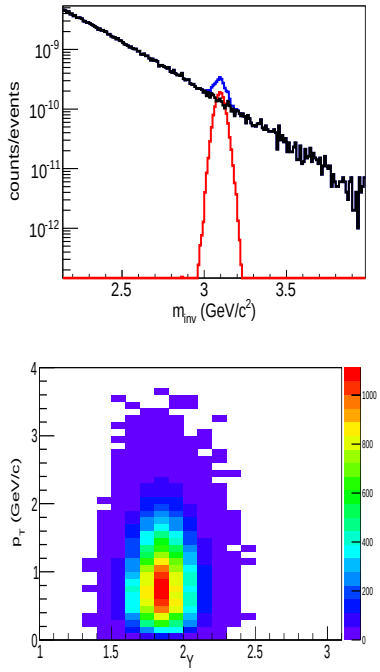

Figure 1: (Top) J/ψ invariant mass spectra in di-muon channel reconstructed in 15 A GeV central Au+Au collisions. The properly mormalized spectra for signal (red line) and combinatorial background (black line) are shown separately in addition to the total spectrum (blue line). (Bottom) Acceptance distribution of the reconstructed J/ψ mesons in the (y, p_T) plane. Mid-rapidity is at y $\simeq 1.73$.

References

[1] P. Senger, Nucl. Phys. A **862-863**, 139 (2011).

[2] MUCH Technical Design Report.

[*] p.bhaduri@gsi.de

DOI:10.15120/GR-2016-1

Simulation of di-muon continuum from correlated open charm decay at FAIR

Partha Pratim Bhaduri[*1] *and Alberica Toia*[1]
[1]GSI, 64291 Darmstadt, Germany

In relativistic heavy-ion collision, various processes of different physical origins contribute to the di-muon invariant mass spectrum measured experimentally. To isolate different sources from the total spectrum and to estimate their respective experimental acceptances, each process needs to be studied independently using input Monte Carlo (MC) simulation method within given experimental conditions. In the continuum region of the invariant mass the relevant contributions arise from the Drell-Yan process, dominating at large di-muon masses and semi-muonic simulatenously decays from two open charm hadrons ($D\bar{D}$ pairs or $\Lambda_C\bar{D}$ pairs). Simulation efforts for development of a MC code to generate muon pairs from Drell-Yan (DY) process, in the FAIR energy regime, was described earlier [1]. In addition to DY di-muons, another component of the physical continuum comes from the electro-weak decays of open charm mesons, which are beleived to induce a substantial background to the potentially overwhelming thermal radiation in the intermediate mass region. They also contribute to the J/ψ mass region as well. In this report we describe our first results on the modelling and reconstruction of the di-muon continuum originating from open charm decays, at FAIR energy domain.

In Table 1 we list the possible elementary recations to produce open charm hadrons, along with the kinematic production thresholds. At FAIR energies, open charm hadrons are produced close to their kinematic production threshold. Thus in addition to D mesons the open charm baryons are also important, owing to smaller production threshold. Note that Σ_c immediately undergoes strong decay to Λ_c via: $\Sigma_c \rightarrow \Lambda_c + \pi^0$. Charm quark distrbutions are unknown at FAIR energies due to unavailability of data. A standard practice would be to simulate the di-muon distributions from open charm decays with PYTHIA event generator, for generation of the open charm hadrons and their decay into muonic channel. However PYTHIA is based on pQCD calculations and direct use of PYTHIA in the FAIR energy domain is debated. In the present report we developed a toy MC using the momentum and rapidity distributions from HSD [2], and a uniform azimuthal distribution, to create a open charm hadron pair. Two inpdepedent production channels are considered namely the $D\bar{D}$ and $\Lambda_C\bar{D}$, relative occurance of which are decided according to the respective multiplicities of D and Λ_C hadrons. The multpilicities of different open charm mesons, in 25 A GeV central $Au + Au$ collisions, from HSD model are shown in Table 2. Owing to much smaller yield, we neglect the contribution from strange-charm mesons. During random production, open charms hadron pairs are thus produced via $\Lambda_C\bar{D}$ channel with 69% probability and via $D\bar{D}$ channel with 31% probability.

Table 1: Different processes yielding open charm hadrons, relevant at FAIR energy domain. These charmed hadrons further contribute to di-muon mass spectrum via semi-muonic decay channels. N stands for both proton (p) or neutron (n).

Reaction	$\sqrt{s_{th}}$ (GeV)
$N + N \rightarrow N + N + D^+ + D^-$	5.62
$N + N \rightarrow N + N + D^0 + \bar{D^0}$	5.62
$N + N \rightarrow N + N + D_S^+ + D_S^-$	5.82
$N + N \rightarrow N + \Lambda_C^+ + D^0(D^-)$	5.2
$N + N \rightarrow N + \Sigma_C^+ + D^0(D^-)$	5.3

Table 2: Multpilicities of different charmed mesons, in 25 A GeV central Au + Au collisions from HSD [2].

Particle	Multiplicity
D^0	3.74×10^{-5}
$\bar{D^0}$	1.15×10^{-4}
D^+	4.17×10^{-5}
D^-	8.91×10^{-5}
Λ_c	12.5×10^{-5}

The produced pairs are then independently decayed via semi-muonic channel, weighted by their respective branching ratios, with isotropic decay angular distributions. For D mesons both 3 body (eg: $D^+ \rightarrow \bar{K^0}\mu^+\nu_\mu$) and 4 body (eg: $D^+ \rightarrow K^-\mu^+\pi^+\nu_\mu$) decay schemes are implemented with 55% and 45% respective probabilities. The resulting di-muon spectrum form a continuum where the yield depends on the product of the branching ratios of two decaying open charm hadrons and the pair multiplicity. The same code can be used to generate the di-electron continuum from open charm decays. Fig. 1 shows the di-muon (top panel) and di-electron (bottom panel) normalized invariant mass spectra from charm decays, generated using our toy MC, for 25 AGeV Au+Au collisions. The di-muon distribution has a mean around 760 MeV, whereas the di-elctron distribution peaks around 626 MeV. The single muons from this input di-muon continuum, have also been tracked in GEANT along with all other partcles from UrQMD, and reconstructed with the CBMROOT analysis package. The SIS-300 muon detector set up, optimized for J/ψ detection has been used for this purpose. The standard muon analysis

* p.bhaduri@gsi.de

DOI:10.15120/GR-2016-1

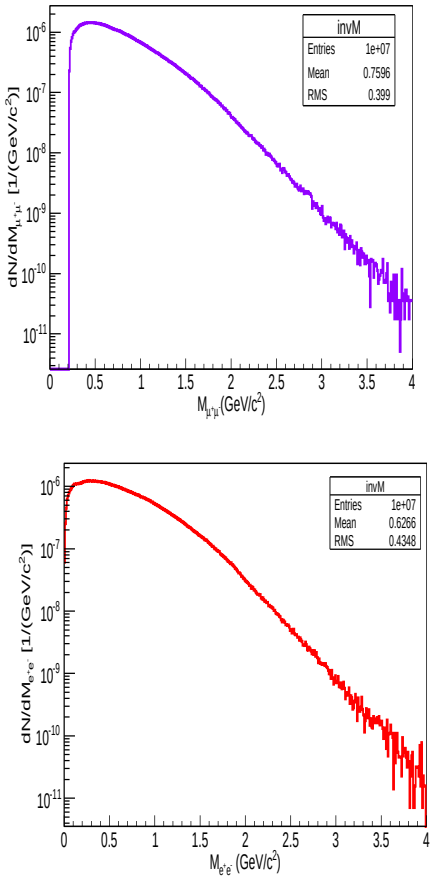

Figure 1: Invariant mass distrbution of the di-muons (top panel) and di-electrons (bottom panel), originating from correlated decay of open charm hadrons in 25 A GeV Au+Au collisions.

framework has been employed, to select muon tracks from charm decays. The reconstructed invariant mass spectra, is calculated from 100,000 simulated events. The contribution of charm to the di-muon spectra is found to be a few orders of magnitude smaller than that of combinatorial background and even than the Drell-Yan process. For all realistic di-muon analysis at CBM energies, the contribution from open charm deacys thus can be safely neglected. At SIS-100 open charm contribution will be absent, as the relevant beam kinetic energies are below the production threshold.

Acknowledgement

We would like to thank Subhasis Chattopadhyay and Tetyana Galatyuk for many stimulating discussions. PPB is supported by the research grant of Prof. A. Toia.

References

[1] P. P. Bhaduri and S. Chattopadhyay, CBM Progress Report 2014, Darmstadt 2015, p. 131

[2] W. Cassing, E. Bratkovskaya, and A. Sibirtsev, Nucl. Phys. A **691**, 753 (2001); arXiv:nucl-th/0010071 [nucl-th].

Extraction of moments of net-particle event-by-event fluctuations in the CBM experiment*

V. Vovchenko[1,2,3] *and I. Kisel*[1,2,4]

[1]FIAS, Frankfurt, Germany; [2]Goethe University, Frankfurt, Germany; [3]Taras Shevchenko University, Kiev, Ukraine; [4]GSI, Darmstadt, Germany

The future CBM experiment at FAIR will employ high intensity beams and large acceptance detectors in order to study the properties of the strongly interacting matter produced in heavy-ion collisions at high baryon densities. The search for the conjectured critical point of QCD is one important task. It is predicted from statistical physics that higher moments of event-by-event fluctuations are very sensitive to the proximity of the critical point. Thus, it was suggested that higher moments of fluctuations of conserved charges can be used as probes for the critical behavior.

The cumulants of a higher order require statistical samples of increasingly bigger size in order to allow for a reliable determination. In order to explore the rate of the statistical convergence of cumulants of different order a Monte Carlo simulation is performed. For this purpose the sample of 10^{12} Poisson-distributed random numbers is analyzed. The dependence of the statistical uncertainty of the normalized skewness $S\sigma$, the normalized kurtosis $\kappa\sigma^2$, and the 6th normalized moment C_6/C_2, on the size of the statistical sample is shown in Figure 1. The results, which were obtained for three different values of σ^2 of the distribution, indicate that, in order to reduce the statistical uncertainty down to a few percent level, it is necessary to collect data from around 10^4–10^5 events for skewness, 10^6–10^7 for kurtosis, and 10^{10}–10^{11} for C_6/C_2. This is well within the designed capabilities of the CBM experiment.

The extraction of scaled variance, skewness, and kurtosis of proton distribution from simulated UrQMD and PHSD events is also explored. We test the validity of the efficiency correction described by binomial distribution [1], particularly in the case when there are deviations from the binomial distribution in the detector response. First the ideal case is investigated. For this purpose the detector response for each proton is simulated by performing a Bernoulli trial with a given efficiency of 80%, same for all protons in all events. Then the binomial efficiency correction is performed, and the obtained results are shown in Fig. 2a. For all three considered kinematic windows the correction allows to properly reconstruct the original value. In the second case it is assumed that the efficiency is different in each event and fluctuates around 80% with a Gaussian width of 3%. In this case (Figure 2b) the efficiency correction does not allow to recover exactly the original value for skewness and kurtosis, and thus, the more elaborate efficiency correction is likely needed. Such a statement is also supported by the preliminary simulations performed within the CBMROOT framework, which includes a realistic CBM detector response.

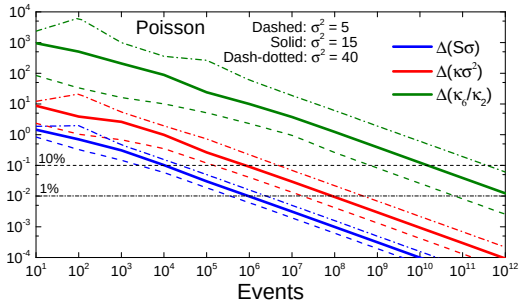

Figure 1: Dependence of statistical errors of various cumulants on the size of statistical sample. Three samples containing 10^{12} Poisson-distributed numbers were analyzed.

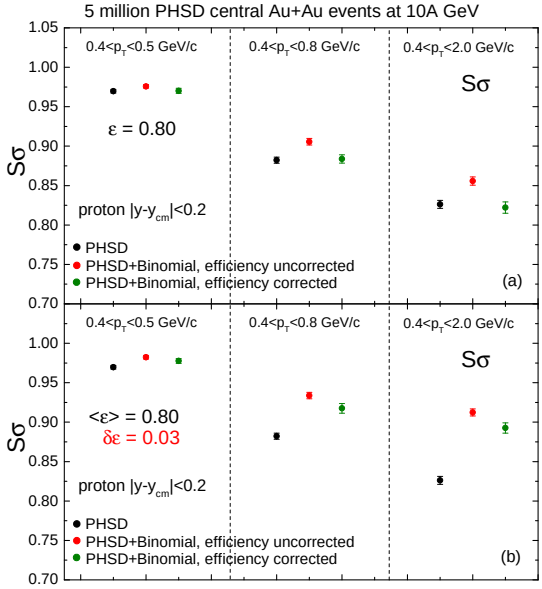

Figure 2: The original (black circles), efficiency uncorrected (red circles), and efficiency corrected (green circles) skewness $S\sigma$ of the proton number fluctuations. The detector response is simulated by binomial distribution with (a) fixed and (b) fluctuating event-by-event efficiency.

References

[1] A. Bzdak and V. Koch, Phys. Rev. C **86**, 044904 (2012).

* Work supported by HIC for FAIR and HGS-HIRe

DOI:10.15120/GR-2016-1

The AFCK Board as the Data Processing Board prototype for CBM experiment*

W. Zabolotny[†1], *G. Kasprowicz*[1], *A. Byszuk*[1], *M. Guminski*[1], *K. Pozniak*[1], *and R. Romaniuk*[1]
[1]Institute of Electronic Systems, Warsaw University of Technology, Warszawa, Poland

The Data Processing Boards (DPB) are important part of the CBM readout and detector control systems, providing concentration (possibly combined with local preprocessing) of readout data before they are sent to the First Level Event Selector (FLES). Additionally, DPBs should provide fast and slow control for the Front End Electronics (FEE), distribute the reference clock, and time-critical information, like synchronization and flow control messages from the Timing and Fast Control system (TFC). In the 2014 year, the AFCK boards were proposed as the prototyping platform for DPB [1]. In the 2015 year, the second revision of the AFCK boards was manufactured and tested. Thanks to improvements in the PCB design and use of another PCB substrate (ISOLA FR408HR), the 10 Gbps transmission speed was achieved in both FMC connectors, improving the connectivity features of the board. The tests were performed using the FADE-10G protocol [2].

The AFCK boards were used to test firmware blocks implementing the future DPB functionality, by different CBM groups [3, 4].

In particular, different options of Ethernet connectivity were successfully tested (via the AMC backplane, via the SFP transceiver placed in the SFP cage on the FMC board and via SATA type connector). The IPbus compatible controller has been tested in various scenarios, including difficult cases where gigabit transceivers belonging to the same block ("quad") were used for different functionalities using different transmission speed. The packaged version of the IPbus board controller was prepared by Junfeng Yang from GSI.

The Ethernet interface is characterized by relatively high round-trip latency, which may impair efficiency of control algorithm. Therefore preliminary studies on adaptation of control procedures to such conditions were undertaken [5].

The AFCK communication interfaces require appropriate configuration of the board flexible clocking system. To allow testing of different communication variants without reprogramming of the MMC processor, a special JTAG-controlled firmware was created that allows to configure the AFCK clock crossbar and programmable clock oscillators located on the board itself or on the additional FMC board (e.g., the FM-S14 board [6]).

In certain possible uses of the DPB board (e.g. in certain implementations of the TFC slave or in the GBTx emulator mode used in the development), it is necessary to recover the high-quality clock from the communication links. The preliminary results show that it is possible [7]. however, further research aimed at optimization of the locking speed is necessary. The desired solution should be based on firmware based PLL with phase detector inside the FPGA and the external digitally controlled programmable clock generator.

The work on usage of the GBT-FPGA cores in the AFCK board was also continued. The visit of Swagata Mandal from VECC was used to cooperate at the development of the GBTx emulator [8]. Additionally, studies on implementation of multiple GBT-FPGA cores in AFCK were performed. The first result is the core, which may be used for testing of the VLDB board. Further research is still required on packaging the GBT-FPGA cores in a way allowing to share the same GTX quad between the GBT-FPGA and 1 Gbps or 10 Gbps Ethernet.

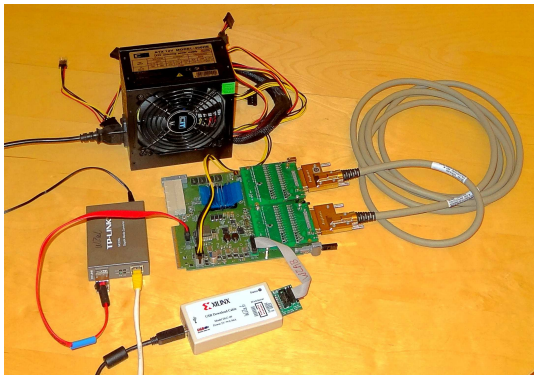

Figure 1: The AFCK board used in a stand-alone mode with ATX power supply. The Ethernet connectivity is provided by the self-made SATA-SFP cable and media converter. Two FMC VHDCI cards provide the LVDS link between the STX-XYTER controller and the STS-XYTER model implemented separately in the same FPGA. The external JTAG programmer is used to configure the FPGA and clocking system.

An important topic in the 2015 year was the development of the STS-XYTER protocol tester. The STS-XYTER controller and model were successfully ported to the AFCK platform. The dedicated FMC cards were designed and manufactured, that allow connecting the STS-XYTER controller with the STS-XYTER model via a VHDCI cable providing the true LVDS link. This allows to perform protocol tests using a single AFCK board (as shown in Figure 1), or two AFCK boards, ensuring that the clocks in the STS-XYTER controller and in the STS-XYTER model are

* Work partially supported by GSI
† wzab@ise.pw.edu.pl

truly independent.

New versions of the STS-XYTER model provided by the AGH team were successfully tested. Further progress in the development of the STS-XYTER communication protocol was achieved in the cooperation with the GSI and AGH teams [9].

The current implementation of the STS-XYTER controller uses the black-box emulator of the GBT e-link. Therefore, the current and future work is aimed on allowing the controller to operate via the true e-link, which introduces additional clock-domain crossing issues.

As the complexity of firmwares implemented in the AFCK board increases, it becomes obvious that it is necessary to split them into manageable components. One of possible solutions is the use of the standard IP packager available in the Xilinx Vivado environment. However this approach has also some disadvantages. For example it is not possible to use complex data types in the I/O ports of the modules, which is a standard solution used e.g. in the IPbus modules. Additionally, this approach limits the possibilities of inter-block logic optimization.

Therefore, another Tcl script based approach was proposed. The structure of the design is described with a hierarchy of "extended project files" which may contain HDL sources, associated constraint files and nested "extended project files". This solution minimizes amount of information which must be stored to preserve the structure of the design, and therefore is better suited for version control systems. The disadvantage of this approach is an incompatibility with Xilinx "Out of Context" compilation mode, that significantly increases the speed of design recompilation.

The optimal method to handle continuously evolving complex firmware projects requires further research.

References

[1] W.M. Zabołotny and G. Kasprowicz, "Data processing boards design for CBM experiment", November 2014, Proc. SPIE, vol. 9290, pp. 929023-929023-11

[2] W. M. Zabolotny, "Low latency protocol for transmission of measurement data from FPGA to Linux computer via 10 Gbps Ethernet link", July 2015, Journal of Instrumentation, vol. 10, pp. T07005

[3] P.A. Loizeau and D. Emscherman and J. Lehnert and W.F.J. Müller and J. Yang, "The prototype readout chain for CBM using the AFCK board and its software components", September 2015, Proc. SPIE, vol. 9662, pp. 96622X-96622X-11

[4] W.M. Zabołotny and G. Kasprowicz and A.P. Byszuk and D. Emschermann and M. Gumiński and B. Juszczyk and J. Lehnert and W.F.J. Müller and K. Poźniak and R. Romaniuk, "Versatile prototyping platform for Data Processing Boards for CBM experiment", February 2016, Journal of Instrumentation, vol. 11, pp. C02031

[5] W. Zabołotny, "Improvement of FPGA control via high speed but high latency interfaces", September 2015, Proc. SPIE, vol. 9662, pp. 96623G-96623G-8

[6] "FM-S14 Quad SFP/SFP+ transceiver FMC", http://www.fastertechnology.com/products/fmc/fm-s14.html

[7] M. Gumiński and W. Zabołotny and G. Kasprowicz and K. Poźniak and R. Romaniuk, "Time and clock synchronization with AFCK for CBM", September 2015, Proc. SPIE, vol. 9662, pp. 96622V-96622V-6

[8] S. Mandal and W. Zabolotny and S. Sau and A. Chkrabarti and J. Saini and S. Chattopadhyay and S.K. Pal, "Internal monitoring of GBTx emulator using IPbus for CBM experiment", September 2015, Proc. SPIE, vol. 9662, pp. 96622Q-96622Q-11

[9] K. Kasinski, "STS-HCTSP: Silicon Tracking System Hit & Control Transfer Synchronous Protocol using GBT's e-link for the CBM experiment at FAIR", Poster presentation at iWoRiD-2015 - 17th International Workshop on Radiation Imaging Detectors, 28 June - 2 July 2015, DESY, Hamburg, Germany, https://www-alt.gsi.de/documents/DOC-2015-Oct-10.html

DOI:10.15120/GR-2016-1

Narrowing down the MRPC design with heavy-ion beams at CERN/SPS *

C. Simon[1], I. Deppner[1], N. Herrmann[1], A. Akram[1], E. Bao[1], J. Frühauf[2], M. Kiš[2], P.-A. Loizeau[2], P. Weidenkaff[1], and the CBM ToF working group[1]

[1]Ruprecht-Karls-Universität Heidelberg, Heidelberg, Germany; [2]GSI, Darmstadt, Germany

By the end of 2016, the ToF working group plans to freeze the design of their MRPC prototypes for mass-producing detector components to be used in the actual CBM setup. Therefore, the in-beam performance of prototypes needs to be evaluated against—not limited to—the criteria formulated on detection efficiency ($> 95\,\%$), system time resolution ($< 80\,\mathrm{ps}$) and rate capability (from 1 to several tens of $\mathrm{kHz/cm^2}$, depending on the foreseen module position in the ToF wall). To get the full picture, conditions at test-beam facilities should reflect the SIS100 environment as closely as possible, i.e. should allow for a flood illumination of the detector surfaces with particle fluxes of $10\,\mathrm{kHz/cm^2}$ and above. Such realistic conditions can only be achieved by heavy-ion beams impinging on a dedicated target creating secondary particles at small angles and high track densities.

As in October 2014 at GSI/SIS18 [1][2] particle fluxes of only several hundreds of $\mathrm{Hz/cm^2}$ could be reached and GSI accelerators were not available in 2015, the ToF working group decided to continue their prototype testing efforts at CERN/SPS in February and in November 2015. Since 2011 CBM is a CERN recognized experiment under the name RE21. ToF and TRD working groups of CBM jointly operated their prototypes in a dedicated concrete cave (dimensions: $2.6\,\mathrm{m} \times 2.4\,\mathrm{m} \times 9.6\,\mathrm{m}$) at the H4 beam line of the North Area. While in February $13A\,\mathrm{GeV}$ Ar ions hit a Pb target, the November beam consisted of $30A\,\mathrm{GeV}$ Pb ions which is close even to SIS300 conditions. Particle fluxes of a few $\mathrm{kHz/cm^2}$ were observed on the detectors under test.

In the February in-beam test, the ToF working group essentially extended the measurement program of the prototypes already tested in the October 2014 beam time to higher particle fluxes. Prototype designs were not modified. Based on these results, for November, the group agreed on systematically assessing certain MRPC engineering design aspects by developing a set of new prototypes differing from each other only by single components. This way, an unbiased evaluation of the following questions was aimed at:

- single HV stack or double HV stack
- impedance matching to the front-end electronics
- design of the high-voltage electrode
- benefits of gas-tight designs (sealing)

As the data analysis is ongoing, final conclusions cannot be drawn yet.

Figure 1 depicts the setup during the November campaign comprising 20 MRPC detectors including 10 newly developed ones. Several boxes housing the counters are visible. The beam enters the setup from the right side. The target was placed about $4\,\mathrm{m}$ in front of the setup. The setup is arranged in two levels (cf. Fig. 2), one above the beam height of $1.2\,\mathrm{m}$, one below. Foreseen for the higher-rate regions of the ToF wall, the prototypes on the lower level are positioned closer to the beam and exposed to a three times higher particle flux than the detectors on the upper level. The counters on both levels are arranged in several detection stations (8 on the upper level, 7 on the lower level) to allow for charged-particle tracking. The properties of the prototypes can be studied in much greater detail if single detector hits can be matched to global particle tracks. The lower-rate counters numbered #2, #3 and #4 in Fig. 2 are equipped with resistive plates made of float glass. The prototypes numbered #14 use ceramics as resistive material to withstand the rate conditions close to the beam pipe [3]. All other counters contain low-resistive glass from China as electrodes.

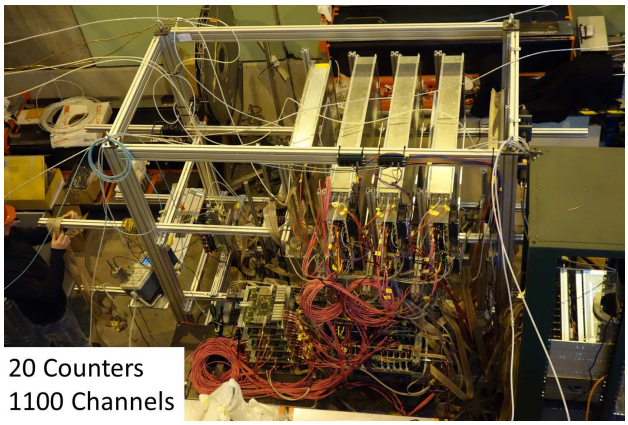

Figure 1: CERN November 2015 setup photography. The beam enters the setup from the right side.

An offline event display of the setup is shown in Fig. 3. The detection stations of the upper and lower levels are marked in pink. Red dots symbolize hits on a counter's active area. Hit-to-track matching with different detection stations leads to the extrapolated track lines. In this event, the tracking algorithm found several tracks which, however, cannot be shown all for readability reasons. Only tracks with hit multiplicities of 5 (lower pink line), 7 (green lines) and 8 (upper blue line) are visualized.

* This project was partially funded by BMBF 05P12VHFC7 and by EU/FP7-HadronPhysic3/WP19 and has received funding from the European Union's Horizon 2020 research and innovation program under grant agreement No 654168.

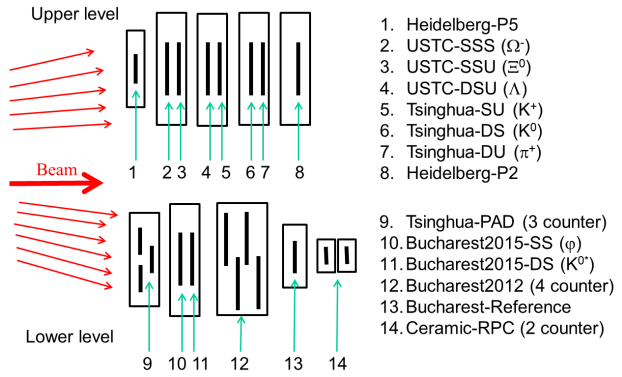

Figure 2: CERN November 2015 setup sketch. Lower-rate prototypes sit on the upper level, higher-rate prototypes on the lower.

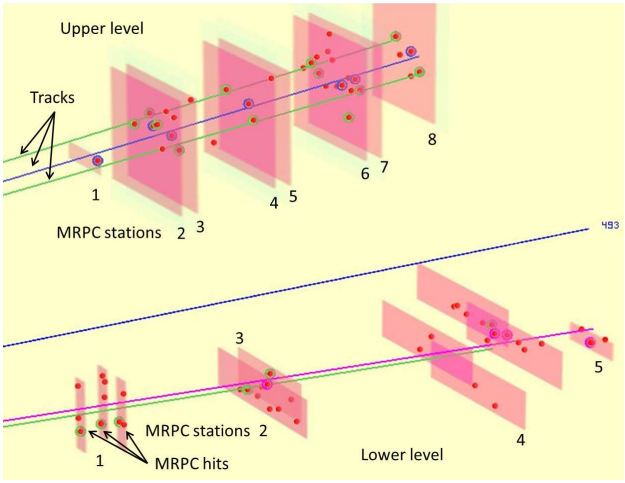

Figure 3: Exemplary event display of the CERN November 2015 setup showing fitted particle tracks with 8 (blue) and 7 (green) associated hits.

Complementing the MRPC prototype studies, two 16-strip pcCVD-DDs [4] (polycrystalline Chemical Vapor Deposition diamond detector) and a 4-segment mosaic scCVD-DD [5][6] (single crystalline) were placed in beam for trigger purposes and to improve the tracking of particles in the MRPC setup.

Signal arrival time digitization was based on a 32-channel FPGA-TDC [7] residing on front-end cards (CBM-TOF-FEE) hooked up in close vicinity to the MRPCs. The readout process took place via TRB3 [8] data hubs. Analog MRPC signals of most prototypes under test were preamplified and discriminated by the final iteration of the PADI ASIC [9]. In total, more than 1000 electronics channels (1 % of the final ToF channel count) were successfully operated during the beam time. The data taking period was about 4 days. In total, about 1 TByte of data were acquired.

First preliminary results are presented in Figure 4. It shows the time difference spectrum between the counters *Bucharest2015-SS* and *Bucharest2015-DS* (numbered #10 and #11 in Fig. 2). The width (Sigma) of a Gaussian fit (red line) denotes the time resolution of this system which amounts to 84 ps. The single counter resolution including all electronic contributions can be obtained by dividing the system time resolution by the square root of 2 assuming both counters contribute equally. By comparing the time resolutions obtained with different such MRPC pairs the individual counter resolutions can be teased out. In order to get an estimate of the distribution tails the RMS value can be compared to the Gaussian sigma. In Figure 4, these two quantities are very similar.

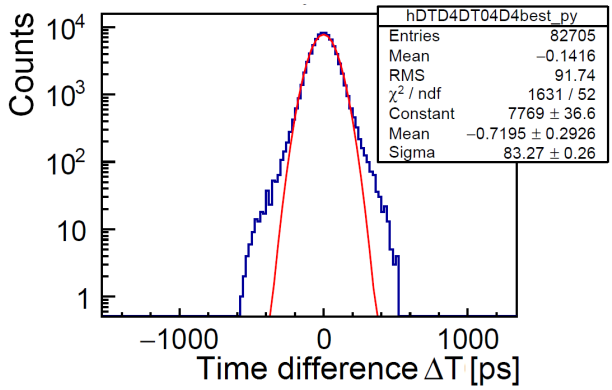

Figure 4: Time difference spectrum between the *Bucharest2015-SS* and the *Bucharest2015-DS* prototypes. The Gaussian sigma and the histogram's RMS are very similar.

References

[1] I. Deppner et al., "MRPC performance evaluation in a heavy ion beam test at GSI", CBM Progress Report 2014 (2015) 86

[2] M. Petriş et al., "Performance of MGMSRPC for the inner zone of the CBM-TOF wall in heavy ion beam tests", CBM Progress Report 2015 (2016)

[3] R. Sultanov et al., "Progress in Ceramic RPCs for the Beam Fragmentation T0 Counter", CBM Progress Report 2015 (2016)

[4] F. Schirru et al., "Development of large area diamond detectors for time-of-flight measurements of heavy ions", GSI Scientific Report 2014 (2015) 502

[5] J. Pietraszko et al., "Low-purity IIa scCVD diamond material for high-current heavy-ion experiments in HADES/CBM at FAIR", GSI Scientific Report 2014 (2015) 31

[6] J. Pietraszko et al., "High-resolution tracking based on sc-CVD diamond detector for straw tube detector tests", GSI Scientific Report 2014 (2015) 32

[7] C. Ugur et al., "FPGA based multi-channel TDC development", GSI Scientific Report 2014 (2015) 212

[8] M. Traxler et al., "Applications of the TRB3 and Associated Front End Electronics in Recent Beam Times", GSI Scientific Report 2014 (2015) 514

[9] M. Ciobanu et al., "PADI-8 – a new ASIC prototype for the CBM ToF Wall", CBM Progress Report 2013 (2014) 84

DOI:10.15120/GR-2016-1

Statistical model at SIS energies *

M. Lorenz †[1] *and the HADES collaboration*[*]
[1]GU, Frankfurt, Germany

In the last 30 years statistical hadronization models have been established as a successful tool to fit particle yields or yield ratios from relativistic and ultrarelativistic heavy-ion collisions [1, 2, 3] with only a few parameters. The extracted freeze-out parameters show a striking regularity, lining up on a curve in the temperature-baryochemical potential plane, connecting smoothly data from the GeV to the TeV regime [4]. These findings have been widely interpreted as a hint that (local) chemical equilibrium is achieved in such collisions. However, especially in the relativistic energy regime it is unclear how this apparent equilibrium is established microscopically. Therefore, in order to interpret these results, it is important to test the model also in small systems and at low energies, where the number of produced particles is small and hence no classical equilibration process is expected to occur.

Recently two groups applied their respective statistical model, which successfully describe hadron yields in heavy-ion collisions, also to elementary reactions and reached different conclusions. While the authors of [5, 6] found good agreement for yields and even transverse momentum spectra obtained in elementary $e^+ + e^-$, the authors of [7] found significantly worse agreement between model and experimental yields.

In order to investigate this issue, we use the yields of hadrons produced in elementary p+p collisions at $\sqrt{s_{NN}}$= 3.2 GeV measured with HADES, which have recently become available [8, 9, 10].

We apply a similar fit as in our previous work [11] but use an updated version of THERMUS (v3.0) [12]. We use the mixed canonical ensemble where strangeness is exactly conserved while all other quantum numbers are calculated grand-canonically and constrain the charge chemical potential μ_Q using the ratio of the baryon and charge numbers of the collision system.

We state that the yield of the ϕ meson is of particular interest in this context, because of its different sensitivity to the strangeness suppression parameters γ_s and R_c. As the ϕ conserves strangeness by definition as a $s\bar{s}$ state its yield is not suppressed in the R_c formalism, while strongly suppressed when γ_s is used. We found in [11] that the ϕ yield is well described using R_c and therefore stick to this way of quenching strange particle production in our statistical model calculations.

We simultaneously fit the yields of the neutral pions, the η, the ω and the kaons, as well as the mean number of participants $\langle A_{part} \rangle$ and constrain the charge chemical potential μ_Q by the initial charge to baryon ratio. We find the following values for chemical freeze-out parameters: $T_{chem} = (100 \pm 6)$ MeV, $\mu_b = (560 \pm 29)$ MeV, the strangeness correlation radius results as $R_c = (0.8 \pm 0.4)$ fm and the radius of the whole fireball $R = (2.0 \pm 0.4)$ fm with χ^2/d.o.f.=2.9.

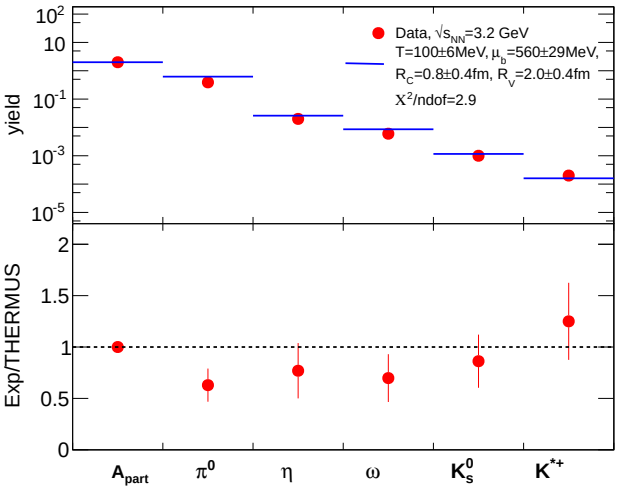

Figure 1: Comparison of hadron yields ratios and of model and data in the p+p system at $\sqrt{s_{NN}}$= 3.2 GeV. Values obtained for the free parameters of the statistical model fit, are given as well as details in the text.

A detailed comparison of the data with our statistical model fit is shown in the upper part of Fig. 1, while the lower part of this figure depicts the ratio of data and fit. The overall agreement between model and data is comparable to the outcome of our previous work where we fitted hadron yields obtained from Ar+KCl collisions at $\sqrt{s_{NN}}$= 2.6 GeV. Furthermore, the p+p freeze-out point fits quite well to the previously observed regularity of freeze-out points in the $T - \mu_b$ plane, displayed in Fig. 2, where the extracted point of this work is displayed together with similar points extracted in [13] and [4].

As argued in the beginning, this finding is rather surprising when thinking in terms of classical equilibration processes. Therefore we next extend our studies to the slightly larger collision system p+Nb where more hadron yields are

* Work supported by GSI, HIC4FAIR
† m.lorenz@gsi.de

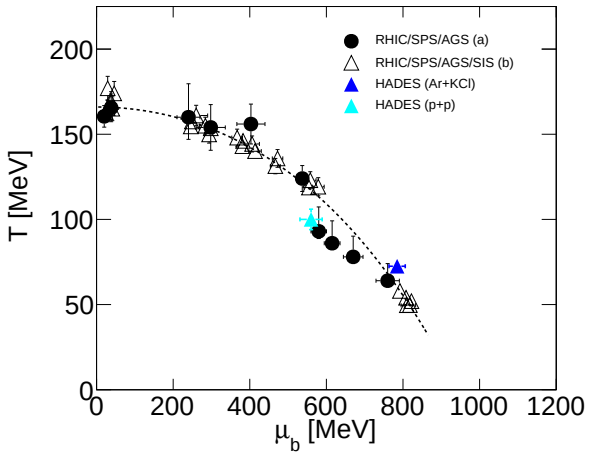

Figure 2: Freeze-out points in the $T - \mu_b$ plane obtained from statistical model fits to hadron yields or yield ratios [13] (filled symbols) and [4] (open symbols). In addition, the HADES points for Ar+KCl [11] (blue triangle) and the p+p point (cyan triangle) from this work are displayed. The dotted line corresponds to a common freeze-out condition of 1 GeV fixed energy per baryon.

available. Details of this study and an in-depth comparison to the Ar+KCl fit can be found in [14]. In addition, we point the interested reader to a recent investigation where hadron yields resulting of a transport model simulation have been compared to statistical hadron rates [15].

References

[1] P. Braun-Munzinger, K. Redlich and J. Stachel, arXiv:nucl-th/0304013 (2003).

[2] A. N. Tawfik, Int. J. Mod. Phys. A **29** 17, 1430021 (2014).

[3] M. Floris, Nucl. Phys. A **931** 103 (2014).

[4] J. Cleymans, H. Oeschler, K. Redlich and S. Wheaton, Phys. Rev. C **73**, 034905 (2006).

[5] F. Becattini, G. Passaleva, Eur. Phys. J. C **23** 551 (2002).

[6] F. Becattini, P. Castorina, J. Manninen, H. Satz, Eur. Phys. J. C **56** 493 (2008).

[7] A. Andronic, F. Beutler, P. Braun-Munzinger, K. Redlich, J. Stachel, Phys. Lett. B **675**, 312, (2009).

[8] G. Agakishiev *et al.* [HADES Collaboration], Eur. Phys. J. A **48**, 64, (2012).

[9] G. Agakishiev *et al.* [HADES Collaboration], Phys. Rev. C **90**, 015202, (2014).

[10] G. Agakishiev *et al.* [HADES Collaboration], Phys. Rev. C **92**, 024903, (2015).

[11] G. Agakishiev *et al.* [HADES Collaboration], Eur. Phys. J. A **47** 21 (2011).

[12] S. Wheaton, J. Cleymans, Comput. Phys. Commun. **180** 84 (2009).

[13] A. Andronic, P. Braun-Munzinger and J. Stachel, Nucl. Phys. A **772**, 167 (2006).

[14] G. Agakishiev *et al.* [HADES Collaboration], arXiv:1512.07070 [nucl-ex].

[15] J. Steinheimer, M. Lorenz, F. Becattini, R. Stock and M. Bleicher, arXiv:1603.02051 [nucl-th].

DOI:10.15120/GR-2016-1

Strangeness production in Au+Au collisions at 1.23 AGeV measured with HADES*

H. Schuldes[1†] *for the HADES Collaboration*
[1]Goethe-University Frankfurt, Germany

The High Acceptance Di-electron spectrometer HADES [1] is devoted to study rare and penetrating probes in heavy-ion and elementary collisions with beams provided by the SIS18 accelerator. In Au+Au collisions at 1.23 AGeV incident energy all particles carrying open and hidden strangeness are produced below their respective nucleon-nucleon threshold. As a consequence, the production cross sections are very sensitive to medium effects like momentum distributions, two- or multi-step processes and modification of the in-medium spectral distribution of the produced states [2]. For the first time at such low energies, a close to complete set of open and hidden strange hadrons has been reconstructed including the following hadron yields: $K^{\pm}, K^0, \phi, \Lambda$.

In total 7.3 billion of the 40% most central Au(1.23 GeV per nucleon)+Au collisions have been analyzed for this investigation. The data has been recorded with HADES and a substantially improved analysis method has been employed to reconstruct the hadrons with high purity in a wide phase space region. In this contribution we focus on the production of charged kaons and ϕ mesons.

The kaons are identified using the velocity measured in the time-of-flight detectors and the momentum. To enhance the signal to background ratio, the specific energy loss information in the drift chambers and the TOF-scintillator wall are used. The resulting mass spectra are shown in Figure 1. The residual background can be subtracted using a polynomial parameterization.

For the first time at such low energies it was possible to reconstruct also the neutral ϕ meson, which was done calculating the invariant mass of the charged kaon pairs. The distribution is shown in Figure 2. The combinatorial background was subtracted using the mixed-event method.

With this high statistics data sample it is possible to do a multi-differential analysis in transverse mass, rapidity and different centrality classes. Especially the ratio of ϕ to K^- is of special interest, as it is has been observed to strongly increase towards lower energies by the HADES [3] and FOPI collaboration [4, 5, 6] in smaller systems and for higher beam energies. This high contribution has influences on the interpretation of the observed K^- kinematics and the conclusion that the strangeness exchange mechanism should be the most dominant production channel for K^- at sub threshold energies as suggested from transport models [2].

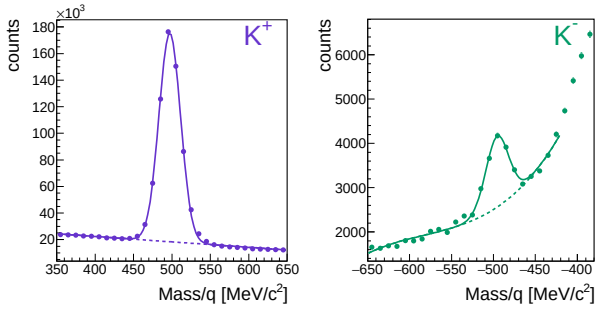

Figure 1: Zoom into the charged particle mass spectrum in the regions of the K^+ (left) and K^- (right) signal. The residual background is subtracted using a polynomial parameterization.

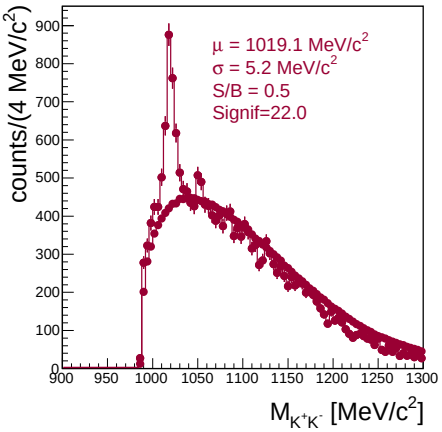

Figure 2: Invariant mass distribution of charged kaons. The combinatorial background is subtracted using the mixed-event method, a beautiful ϕ signal is emerging.

References

[1] G. Agakishiev et al. [HADES Collaboration], Eur. Phys. J. A 41 (2009).

[2] C. Hartnack et al., Phys. Rept. 510, 119 (2012). (2013) 56

[3] G. Agakishiev et al. [HADES Collaboration], Phys. Rev. C80:025209 (2009).

[4] A. Mangiarotti et al. [FOPI Collaboration], Nucl. Phys. A714 (2003) 89-123.

[5] K. Piasecki et al. [FOPI Collaboration], Phys. Rev. C91 (2015) no.5, 054904.

[6] P. Gasik et al. [FOPI Collaboration], arXiv.1512.06988 [nucl-ex].

* Work supported by GSI, HIC for FAIR, HGS-Hire, HQM
† h.schuldes@gsi.de

Λ and K^0_S reconstruction in Au+Au at 1.23A GeV with HADES *

T. Scheib[1†] *for the HADES Collaboration*
[1]Goethe Universität, Frankfurt, Germany

In April and May 2012 HADES recorded a high statistic data sample of Au(1.23 AGeV)+Au events. At this energy the production of strange particles is investigated below the free NN threshold. Due to the steep excitation function of strange particle yields towards SIS beam energies they become very sensitive probes for the strangeness production mechanisms and in-medium propagation. In this work analysis details of the two strange hadrons Λ and K^0_s are presented.

The High Acceptance Di-Electron Spectrometer covers almost the full azimuthal angle ϕ and largely the polar angle θ ($18° - 85°$). With two planes of Multi-wire Drift Chambers (MDC) in front and two behind a superconducting magnet, the tracks of charged particles can be reconstructed and their momenta determined. These detected particles can be identified by using the energy-loss information in MDC and TOF and/or the time-of-flight measurements from the META detectors TOF and RPC. A more detailed description of the HADES detector can be found in [1].

In total HADES collected 7.3x10^9 reactions at beam intensities of (1.2 - 1.5) $\cdot 10^6$ ions/s. The beam was incident on a 15-fold segmented Au target. From the triggered events (requiring a multiplicity in the outer detector region (TOF wall) $M > 20$ corresponding to 47% most central events) the 40% most central reactions with a mean number of participating nucleons $< A_{Part} > = 191$ were analyzed.

The two particles investigated in this work, Λ and K^0_s, decay via the weak interaction leading to relatively long life-times compared to strong and electromagnetic decays and are reconstructed via the following channel:

$$\Lambda \rightarrow \pi^- + p \ \ (63.9\%)$$

$$K^0_S \rightarrow \pi^- + \pi^+ \ \ (69.2\%).$$

The charged particles are identified by selecting the mass in a window from 40 to $300 MeV/c^2$ for pions and 700 to $1200 MeV/c^2$ for protons. Then the invariant mass of the respective pairing in the final state is calculated leading to a peak structure at the expected mass for Λ and K^0_S respectively. However, the background in the invariant mass spectrum is dominated by contributions from uncorrelated pairs. In order to suppress this contribution, cuts on the decay topology are applied. Here pairs of daughter particles originating from the primary vertex are separated from the ones coming from a (weak) decay. The remaining background after application of topology cuts is described by the mixed event method. Subtracting the background results in highly significant Λ and K^0_S signals which are sufficient to do a triple-differential analysis as a function of rapidity, transverse mass and centrality.

To draw any conclusions on the production of the investigated hadrons and therefore on strangeness itself the reconstructed signal has to be corrected for acceptance and efficiency of the detector. For this purpose particles are produced thermally in a full Monte-Carlo simulation using Pluto [2] and then propagated through a realistic modeling of the detector response using GEANT3 [3]. After that the particles are subjected to the same analysis chain as used for the recorded data. The fraction of input to remaining particles gives the correction factor which is applied on the signals extracted in the data analysis, resulting in the initially produced particle yields.

In order to guarantee a similar behaviour as the one of the real detector, an accurate knowledge of all possible detector effects is mandatory and has to be modeled in simulation as precisely as possible. A way to test the accuracy of the correction are lifetime measurements. The mean particle lifetime τ is indeed a well-known quantity which our measured result can be compared to. Since the constraints put on the decay topology in the secondary vertex analysis are strong, they significantly reduce the efficiency. Therefore the measurement of the mean lifetime for different sets of topology cuts gives a quantitative estimation of the robustness of our efficiency correction. The time-of-flight t_P of a particle can be calculated from the observables flight distance l, mass m and reconstructed momentum p via:

$$t_P = \frac{l \cdot m}{|p|}. \quad (1)$$

The t_P distribution for K^0_S is shown in figure 1. The exponential decay law

$$N(\Delta t) = N_0 \cdot exp^{\frac{-\Delta t}{\tau}} \quad (2)$$

can be fitted to the distribution and the inverse slope parameter gives the mean lifetime τ. The indicated measured lifetimes are obtained for different cut settings that are later used in a triple-differential analysis. They agree very well with the PDG value [4]. The same procedure is repeated for the Λ hyperon.

The described results are a solid foundation for the subsequent analysis which relies on the precision of the acceptance and efficiency correction.

* Work supported by GSI, HIC for FAIR, HGS-Hire, HQM
† t.scheib@gsi.de

DOI:10.15120/GR-2016-1

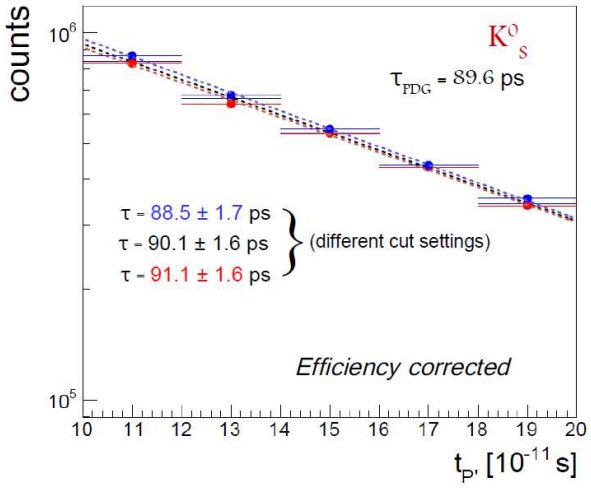

Figure 1: Efficiency corrected time-of-flight t_P of K^0_S for different topology cut settings. Indicated are the mean lifetimes from fits of the exponential law to the respective distribution. Also indicated is the well-known mean lifetime τ_{PDG} taken from the PDG which agrees within uncertainties with the values measured with HADES [4].

References

[1] G. Agakishiev *et al.* [HADES Collaboration], Eur. Phys. J. A 41 243 (2009).

[2] I. Froehlich, L. Cazon, T. Galatyuk, V. Hejny, R. Holzmann, M. Kagarlis and W. Kuhn *et al.*, PoS ACAT 2007 (2007) 076 [arXiv:0708.2382 [nucl-ex]].

[3] GEANT. Detector Description and Simulation Tool, 2004. http://cont.cern.ch/writeup/geant/, Online User Guide.

[4] K.A. Olive et al. (Particle Data Group), Chin. Phys. C, 38, 090001 (2014).

Towards high-rate experiments with the HADES drift chambers

C. Wendisch [*1], *L. Lopes*[2], *M. Wiebusch*[3], *C. Müntz*[3], *and J. Stroth*[1,3] [†]
[1]GSI, Darmstadt, Germany; [2]LIP, Coimbra, Portugal; [3]Goethe-Universität, Frankfurt, Germany

The future physics program of HADES at FAIR demands high detection standards, also in the operation stability of the tracking system comprising four layers of planar drift chambers (MDC-I - IV). Due to the expected increase in beam intensities already at FAIR phase 0, stable operation of the wire chambers has to be ensured for factors 2-3 higher particle load than the maximum so far. Hence, long term high rate detector tests were performed, in addition for different counting gas mixtures of argon and CO_2 to determine the optimal fraction of CO_2 by testing the limits of stability for the HADES drift chambers.

High rate stability tests.

To mimic the detector response to a heavy-ion collision, a powerful x-ray source is well suited, matching the total load and occupancy distribution along the chamber expected from heavy-ion collisions. Utilizing this, a long term irradiation of 3 weeks was conducted, achieving a detector ionization current of 5 μA per wire layer corresponding to 2 times the load resulting from Au+Au reactions at 1.23 AGeV and a beam intensity of 10^7 ions/s (beam-time 2012). An overall stable operation was observed from 30-10% of CO_2, while 10 % proved to be the lower limit since at very high rates frequent sparks indicated incipient instability. Trading risks, stable operation and signal quality, 15-20 % fraction of CO_2 will be the optimal gas mixture for high rate experiments, likely optimized individually for chambers before and behind the magnetic field.

Advanced readout by upgrading front-end-electronics.

For ensuring future fast readout with improved sensibility, also the Front-End-Electronics (FEE) is being reviewed. Data from high rate heavy-ion reactions and x-ray tests revealed channel-crosstalk (congruent signals in adjacent channels), amounting to 1.2 % of signals on average, biasing the tracking efficiency. As depicted in figure 1 most of the channels receive crosstalk with a rate less than 1%, but due to certain FEE modules the crosstalk rate of very few single channels is higher than 10 %. Additionally, broken single channels (< 5%), instability and low bandwidth of Fiber-Optical-Transceivers, and the missing TDC multi-hit capability are drawbacks resulting in the need of a full redesign of the MDC-FEE, for which these flaws should be prevented. Thus, the development of state of the art analog and digital FEE was started. Since the original analogue signal processing ASIC (ASD8 [1]) is no longer available, current alternatives have to be considered, focussing on optimal drift time resolution (1 ns for spatial resolution < 100 μm) and a precise charge measurement (detecting the particles energy loss).

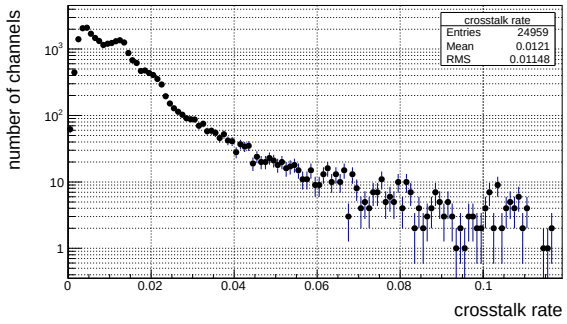

Figure 1: Crosstalk rate distribution across all active MDC channels, for Au(1.23 AGeV)+Au.

Available ASICs are being evaluated in view of these needs, like PADI (ASIC for CBM RPC)[2], PASTTREC (ASIC for PANDA straw tube tracker)[3] as well as discrete amplifiers like PADIWA. PASTTREC was applied and operation parameters tuned to MDC-I, see figure 2. The two concepts ASIC and discrete solution will be adapted to the HADES-MDC and finally tested using a proton beam.

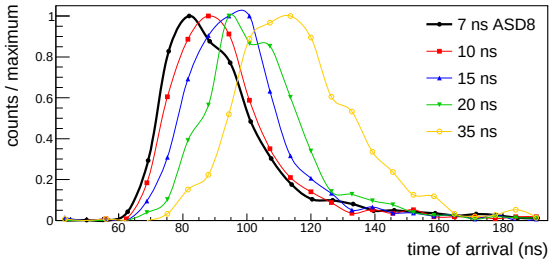

Figure 2: Arrival time distributions of signals from MDC-I (Sr-90 source) by PASTTREC ASIC [3] (peaking time variation: 10, 15, 20, 35 ns) and ASD8 [1] as reference.

References

[1] F. M. Newcomer et. al., IEEE Trans. Nuc. Sci. 40 (1993) 630.
[2] M. Ciobanu et. al, IEEE Trans. on Nuc. Sci., 61 (2014) 1015.
[3] "The Straw Tube Trackers of the PANDA Experiment", Proc. ANIMMA Conf. 2013, [arXiv:1307.4537].

* c.wendisch@gsi.de
† Work supported by BMBF, HIC for FAIR and GSI.

DOI:10.15120/GR-2016-1

Analysis of pion induced interactions with neutron in final state*

L. Chlad[† 1,2], *A. Kugler*[1], *and the HADES collaboration*

[1]Nuclear Physics Institute of the CAS, Řež, Czech Republic; [2]Charles University in Prague, Czech Republic

Recent interest of scientific community in a study of nucleon-nucleon short range correlations in nuclei [1] and [2] triggered HADES collaboration interest in this topic [3].

In a first approach we decided to test response of the HADES spectrometer to neutrons exploiting data obtained with π^- beam in summer 2014 [4]. Ideal interaction where we can test the neutron detection is $\pi^- + \mathrm{p} \rightarrow \pi^- + \pi^+ + \mathrm{n}$ as we can determine completely the neutron momentum from kinematics (1). For the purpose of our analysis it is important that the neutron passes through the HADES spectrometer without interaction with the exception of TOF and RPC detectors [5]. From previous experiments and simulations [6] and [7] we know that the interaction probability within these detectors would be in the order of a few percent, that is confirmed as one can see on the left side of figure 1.

To cross-check the selected hits in TOF and RPC we take a look on the difference between measured and expected neutron momentum. The so called expected momentum is defined as

$$\vec{p}_{\mathrm{expect}} = \vec{p}_{\mathrm{beam}} + \vec{p}_{\mathrm{target}} - \vec{p}_{\pi^-} - \vec{p}_{\pi^+}. \qquad (1)$$

The measured neutron momentum is calculated from straight distance between reconstructed vertex (from both pion tracks) and the position of hit in TOF or RPC detector and measured time of flight

$$\beta c = \frac{l_{\mathrm{path}}}{t_{\mathrm{tof}}} \Rightarrow p_{\mathrm{measure}} = \frac{\beta c\, m_{\mathrm{n}}}{\sqrt{1-\beta^2}}. \qquad (2)$$

The difference $\Delta p = |\vec{p}_{\mathrm{expect}}| - p_{\mathrm{measure}}$ is shown on figure 1 right. As one can see the real data peak is a bit broader probably due to contamination of carbon events within the polyethylene target.

In the next step we decided to focus on interactions with a neutron and one neutral meson in the final state

$$\pi^- + \mathrm{p} \rightarrow \mathrm{n} + \pi^0/\eta/\omega. \qquad (3)$$

From these mesons we chose η because in the measured energy region ω production would be highly sub-threshold and π^0 detection with present HADES spectrometer is complicated due to its decay branching ratio into two photons. For η meson the energy region is around the threshold and we can use its decay $\eta \rightarrow \pi^-\pi^0\pi^+$ for event selection

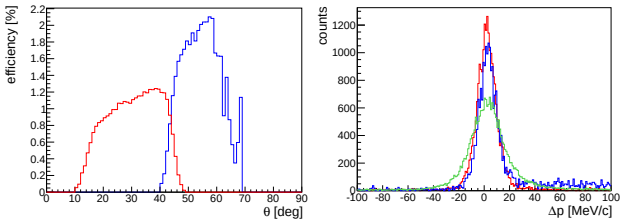

Figure 1: **Left:** Detection efficiency of neutrons within RPC (red) and TOF (blue) detectors. **Right:** Difference of measured and expected neutron momentum for real data (green), simulations using GCalor (red) and Geisha (blue) hadron package for Geant3.

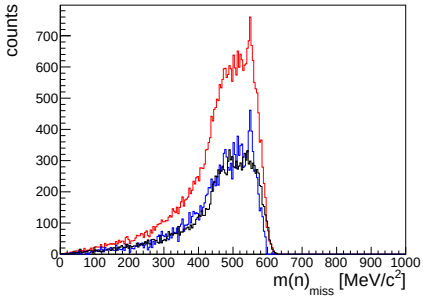

Figure 2: Measured neutron missing mass spectra for polyethylene (red) and carbon (black) targets. Data for carbon are appropriately scaled. The difference which corresponds to hydrogen contribution in polyethylene is showed with blue line.

(reconstructed two charged pions). The kinematics of interaction (3) with η only in the measured energy region tells us also restrictions on polar angle ($\theta < 40°$) and time of flight ($11\,\mathrm{ns} < t_{\mathrm{tof}} < 28\,\mathrm{ns}$). These cuts plus the veto signal from MDC gives us a set of hits that we presume to be caused by a neutron and we calculate the missing mass which is plotted on figure 2. The peak around $550\,\mathrm{MeV/c^2}$ is in very good agreement with $m_\eta = 547.9\,\mathrm{MeV/c^2}$.

References

[1] R. Subedi et al., Science 320 (2008) 1476.

[2] O. Hen et al., Science 364 (2014) 614.

[3] R. Holzmann, GSI Report 2014, MU-NQM-HADES-20.

[4] HADES collab., GSI Report 2014, MU-NQM-HADES-16.

[5] G. Agakishiev et al., Eur. Phys. J. A **41** (2009) 243.

[6] H. Klein and F. D. Brooks, PoS (FNDA2006) 097.

[7] J. Machado et al., JINST **8** (2013) P07020.

* Work supported by GACR 13-06759S of the Czech Science Foundation and grant LM201549 of the MEYS of the Czech Republic.

† chlad@ujf.cas.cz

Analysis of charge-dependent azimuthal correlations in Au+Au collisions with HADES *

F. Kornas[1], *I. Selyuzhenkov*[2], *T. Galatyuk*[1,2], *and the HADES collaboration*[2]
[1]TU, Darmstadt, Germany; [2]GSI

The chiral magnetic effect (CME) in heavy-ion collisions (HIC) allows to experimentally search for possible local parity violation of the strong interaction. In HICs, most of the particle spins are aligned due to the strong magnetic fields created. Fluctuations in chirality would lead to a charge seperation along the magnetic field which could be measured through two-particle correlations.
To determine the direction of the magnetic field the reaction plane (RP) has to be reconstruct for each event. In the absence of fluctuations, the magnetic field should be perpendicular to the RP and provides a good reference to look for further particle correlations. The particle correlations are considered with respect to the reaction plane. Two different correlators are proposed to disentangle the charged-particle motion with respect to each other [1]:

$$\gamma_{\alpha\beta} = \langle \cos\left(\phi_\alpha + \phi_\beta - 2\Psi_{\mathrm{RP}}\right)\rangle \quad (1)$$

$$\delta_{\alpha\beta} = \langle \cos\left(\phi_\alpha - \phi_\beta\right)\rangle\,. \quad (2)$$

ϕ is the azimuthal angle of the charged particle, Ψ_{RP} is the angle of the reaction plane, α, β account for the different particle charges and the brackets $\langle ... \rangle$ denote the average over particles and events.
Both correlators as a function of centrality have been measured by ALICE [2] and STAR [3] for like- and unlike-sign pairs. All correlators show a clear enhancement towards peripheral collisions. This is expected since in peripheral collisions there are more spectators and the magnetic field for the participants is much stronger than in central collisions. While the measured γ are very similar for ALICE and STAR the δ looks different. This can be explained by the fact that the γ correlator removes all background which is not related to the reaction plane. For the δ this is not the case. Therefore, a good understanding of the background is needed.
In April 2012, seven billion Au+Au collisions at $\sqrt{s}_{NN} = 2.42\,\mathrm{GeV}$ have been measured with HADES. For the recent analysis only one day of the data is used where all six sectors of HADES were active ($\sim 1/30$ of the total statistics). The analysed particles are protons, positively and negatively charged pions which are identified using their measured velocity as a function of momentum. A kinematical cut on the phase space distribution is applied to select regions where acceptance and reconstruction efficiency are smooth. The rapidity range is chosen to be around $y = y_{\mathrm{mid}} \pm 0.3$ with $y_{\mathrm{mid}} = 0.74$ being the midrapidity. The transverse momentum is reduced to $400 \leq p_t \leq 1000\,\mathrm{MeV}$ for protons and $200 \leq p_t \leq 600\,\mathrm{MeV}$ for pions.
The reconstruction of the reaction plane is done by the Forward Wall detector which is placed 7 m downstream the target and covers an angular range from $0° \leq \theta \leq 7°$. It is done by a Q-vector analysis which is a simple sum over all unit vectors of all particle hits weighted by their deposit charge.

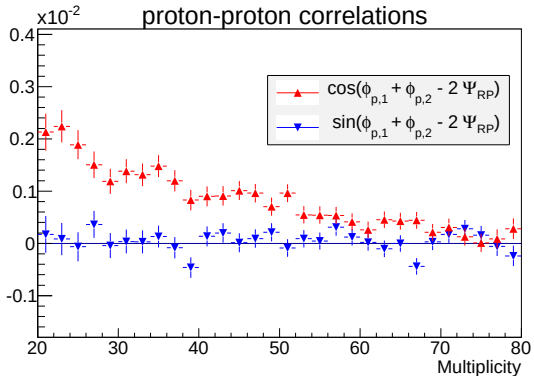

Figure 1: First results of the two-particle correlator γ for proton-proton correlations as a function of the multiplicity as measured with HADES. The lower curve shows the corresponding sine term.

Figure 1 shows the first results of the γ correlator for proton-proton correlations as a function of multiplicity. The multiplicity is defined by the number of selected particle candidates in an event. Additionaly, the sine term $\langle \sin\left(\phi_\alpha + \phi_\beta - 2\Psi_{RP}\right)\rangle$ is shown as a measure for possible detector effect. From the physics consideration this sine term should lie at around zero. This is not exactly fulfilled but the value is much smaller than the signal, so the first results look promising.
Further systematic studies are ongoing to check if all the contributions to the γ correlator are taken into account.

References

[1] S. A. Voloshin, Phys. Rev. C70 (2004) 057901.
[2] B. Abelev *et al.*, Phys. Rev. Lett. 110 (2013) 1.
[3] B. Abelev *et al.*, Phys. Rev. Lett. 103 (2009) 251601.

* Work supported by VH-NG-823, Helmholtz Alliance HA216/EMMI and GSI.

DOI:10.15120/GR-2016-1

Anisotropic production of charged pions in Au+Au collisions at 1.23 A GeV*

M. Gumberidze[1], *P. Tlusty*[2] *and H. Schuldes*[3] *for the HADES Collaboration*

[1]Technische Universität Darmstadt, Germany; [2]Nuclear Physics Institute, Academy of Sciences, 25068 Rez, Czech Republic; [3]Goethe-Universität, Frankfurt am Main, Germany

The High Acceptance DiElectron Spectrometer HADES [1] is designed mainly to study production of dielectron pairs from elementary and heavy-ion collisions at 1-2 A GeV. At the same time, the spectrometer provides detection and high quality identification of charged particles with a large solid angle. In this contribution we focus on the analysis of charged pion production in Au + Au collisions at 1.23 A GeV, and especially on pion anisotropy.

For the symmetric collision system Au + Au the polar distributions in the center-of-mass system can be fitted employing the function of form: $\frac{dN}{d(cos\theta_{cm})} = const * (1 + A_2 cos^2\theta_{cm})$. The parameter A_2 characterizes the anisotropy of the pion source.

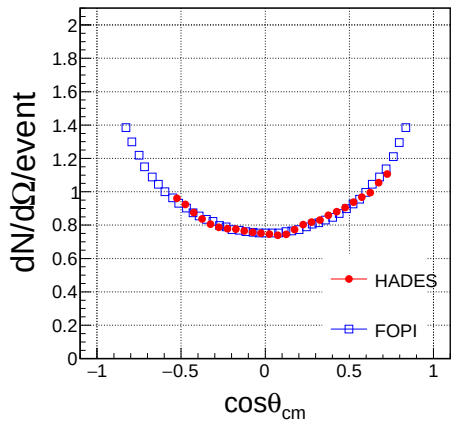

Figure 1: Center-of-mass polar angle distribution of π^- produced in Au+Au collisions. Open squares correspond to a FOPI measurement at 1 A GeV, closed points to HADES at 1.23 A GeV for semicentral events (6% - 21%).

The measured center-of-mass polar angular distribution of pions is shown in Fig. 1 in comparison with FOPI result from Au + Au at 1A GeV [2]. Data have been normalized to the same yield at midrapidity and are found to be in good agreement. Pions with center-of-mass momenta between 100 and 800 MeV/c have been selected. No losses in acceptance occure in this phase space region. As visible in Fig. 1 data show strong anisotropies quantified by A_2 = 0.97 $\pm$ 0.10. Similar effects are observed in the ^{12}C + ^{12}C system [3], where A_2 = 0.88 $\pm$ 0.12 and 1.19 $\pm$ 0.16 for beam energies of 1A GeV and 2A GeV, respectively.

The anisotropy is stronger in peripheral than in central collisions. This effect is attributed to pion reabsorption and reemission which occur more frequently in central events.

We also observe a strong dependence of the pion anisotropy on center-of-mass momentum (see Fig. 2). One can see that the anisotropy is increasing with center-of-mass momentum up to A_2 = 1.5, and around 400 MeV/c it has a tendency to level off. This phenomenon can be explained as high momenta pions keeping asymmetry from 2-body nucleon-nucleon collisions (inside nuclei), while the anisotropy of low momenta pions is damped by multiple regeneration ($\pi N \rightarrow \Delta \rightarrow \pi N$) and rescattering processes.

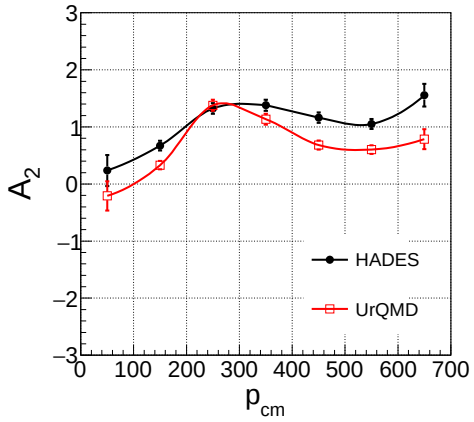

Figure 2: The anisotropy parameter A_2 of π^- as a function of the momentum in the center-of-mass system for HADES (closed points) and UrQMD (open squares).

Anisotropy results extracted from our data are in agreement with a systematic study of pion production in Au + Au collision at similar beam energies measured by FOPI [2]. The asymmetry has a non-trivial momentum dependence, well described by UrQMD transport calculations.

References

[1] G. Agakishiev *et al.* (HADES Collaboration), Eur. Phys. J. A 41 (2009) 243.

[2] W. Reisdorf *et al.* (FOPI Collaboration) Nucl. Phys. A 781 (207) 459-508.

[3] G. Agakishiev *et al.* (HADES Collaboration) Eur. Phys. J. A 40 (2009) 45-59.

* Work supported by TU Darmstadt: VH-NG-823, GSI, Czech Republic: GACR 13-067595, HGS-HIRe and H-QM.

Reconstruction of broad signals in heavy ion collisions *

G. Kornakov[†1] *for the HADES Collaboration*
[1]Technische Universität Darmstadt, Germany

The unambiguous identification of hadron modifications in hot and dense QCD matter is one of the important goals in nuclear physics. In the regime of 1 - 2 GeV kinetic energy per nucleon, HADES has measured rare and penetrating probes in elementary and heavy-ion collisions. The main creation mechanism of mesons is the excitation and decay of baryonic resonances throughout the fireball evolution. Furthermore, the excitations of baryons make a significant contribution to the dilepton emission but also play an important role in the production of strange particles. In this report we show the progress made on the calculation of the combinatorial background for broad resonances with signal to background ratios less than 1 %.

The direct reconstruction of baryon resonances in heavy ion collisions is a challenging task. As pointed out by several authors [1], the shape and the normalization of the combinatorial background obtained by the event mixing technique do not allow always to extract the correct line shapes and yields. We have developed a new iterative algorithm, which builds the best hypothesis of signal and background by distortion of individual particle properties. This allows us to extract signals with signal-to-background ratios below 1 %.

Here we show the results of the validation of the explained technique. First in simulated events which mimic true central Au+Au collisions at 1.23A GeV generated by PLUTO [2]. The cocktail consists out of thermally produced protons with radial expansion, and a 10 % $\Delta^{++}(1232)$ and thermal positively charged pions. The expected signal in the p-π^+ invariant mass spectrum has a signal to background ratio below 2 % around Δ pole mass, fading to values of 10^{-4} in the tail of the $\Delta^{++}(1232)$ resonance. In Fig. 1 we show the result of applying the abovementioned technique to the simulation.

The same method was also applied to the real data recorded with HADES in 1.23 GeV/u Au+Au collisions. In Fig. 2 the efficiency corrected signal for the 10 % most central collisions is shown. The statistics presented here corresponds to 5 % of the total sample measured. The signal of $\Delta^{++}(1232)$ is clearly visible, as well as a contribution of overlapping $N*$ resonances. The high statistic signal allows for double differential analysis.

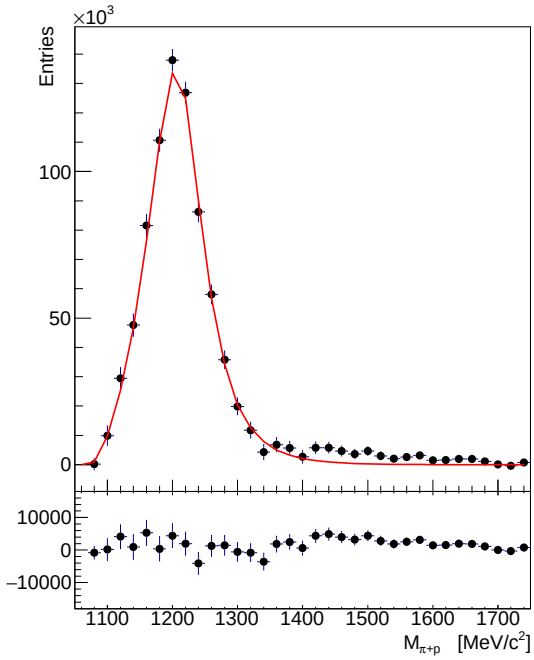

Figure 1: Reconstructed $\Delta^{++}(1232)$ signal (full circles) simulated by PLUTO in a environment similar to those of central Au+Au collisions at 1.23A GeV. The line is the input signal in the cocktail. The bottom figure represents the residuals between the reconstructed and the input.

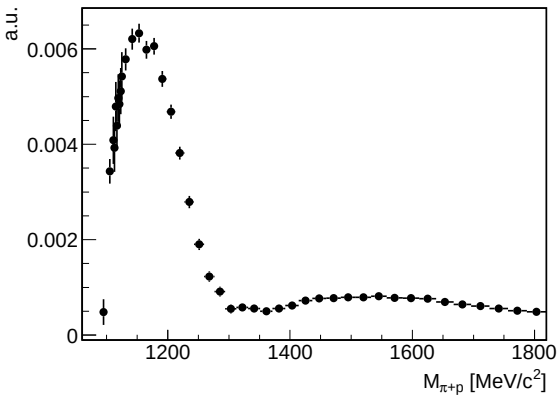

Figure 2: Reconstructed invariant mass of π^+p after background subtraction in the 10 % most central Au+Au events. The $\Delta^{++}(1232)$ dominates the distribution. The second enhancement of the spectra corresponds mainly to the N* and D* resonances.

References

[1] D. L'Hote, NIMA337 (1994) 544-556
[2] I. Fröhlich et at., PoS(ACAT)076 (2007)

* Work supported by VH-NG-823 and GSI.
† g.kornakov@gsi.de

DOI:10.15120/GR-2016-1

Modeling thermal dilepton radiation for SIS experiments *

F. Seck[†1], *T. Galatyuk*[1,2], *P. M. Hohler*[4], *R. Rapp*[4], *and J. Stroth*[2,3]

[1]Technische Universität Darmstadt, Darmstadt, Germany; [2]GSI, Darmstadt, Germany; [3]Goethe-Universiät, Frankfurt, Germany; [4]Texas A&M University, College Station (TX), USA

Electromagnetic probes are radiated during the whole time evolution of a heavy-ion collision. They decouple from the collision zone once they are produced and carry valuable information about the properties of matter created inside the hot and dense fireball to the detector.

In particular, the yield of low-mass dileptons is sensitive to the fireball lifetime, while the slope in the intermediate-mass region of the dilepton invariant-mass spectrum can serve as a thermometer which is unaffected by blue-shift effects caused by the collective expansion of the medium [1].

Realistic thermal dilepton emission rates and an accurate modeling of the fireball's space-time evolution are needed to properly describe the contribution of in-medium signals to the dilepton invariant-mass spectrum. At SIS energies hadronic transport models are commonly used to describe the fireball evolution. The incorporation of in-medium effects is however challenging. A complete hydrodynamic description as employed at high energies is, in general, also not possible since the incoming nuclei need a long time to fully overlap which raises the question if local thermalization occurs and if so, over which period it time. As a compromise between the microscopic transport and macroscopic hydro approach a coarse-graining procedure was proposed [2] and applied to the SIS energy regime [3,4]. By dividing the space-time evolution into 4-dimensional cells and averaging over an ensemble of simulated transport events one obtains smooth particle distributions. Meaningful temperatures, baryon and pion densities can than be determined in the cells which fulfill certain criteria for the occurrence of local thermalization. Figure 1 shows the trajectories of the inner 27 cells in the temperature-baryon density plane for central Au+Au collisions at 1.23 A GeV. The extracted bulk properties serve as an input for the calculation of the thermal dilepton radiation based on Eq. (1) with an in-medium ρ spectral function that describes available spectra at ultrarelativistic collision energies [5].

$$\frac{d^8N}{d^4x\,d^4p} = \frac{\alpha_{\rm EM}^2}{\pi^2\,M^2}\,f_B(p_0,T)\,\varrho_{\rm EM}(M,p;T,\rho_{\rm eff},\mu_\pi) \quad (1)$$

M is the mass of the virtual photon, f_B denotes the the thermal Bose distribution function and $\varrho_{\rm EM}$ is the electromagnetic spectral function of the QCD medium which depends on the temperature T, the effective baryon density $\rho_{\rm eff}$ and the effective chemical potential of pions μ_π. To get to the pertinent dilepton spectrum the rates are integrated over the whole space-time evolution, i.e., the contributions from the different cells are summed up.

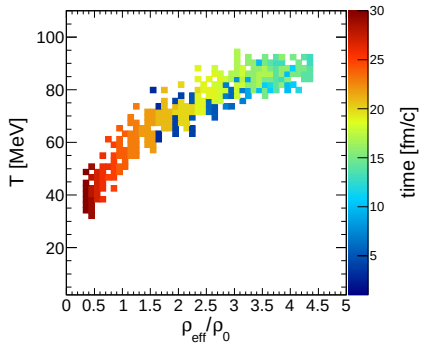

Figure 1: Trajectories of the inner 3x3x3 cells (1 fm^3 each) for central Au+Au collisions at 1.23 A GeV in the temperature T and effective baryon density $\rho_{\rm eff}$ plane indicated by colors for the different time steps.

Figure 2 shows such a differential dilepton yield for different masses and transverse momenta. Besides the gain of several insights into the fireball evolution at SIS energies [4], the resulting histogram is implemented into the Monte Carlo event generator Pluto and used for the sampling of dileptons. The output can be utilized by the HADES and CBM collaborations for feasibility studies and acceptance corrections.

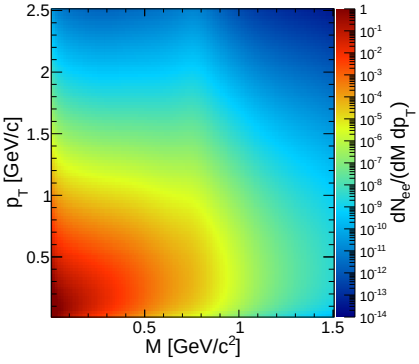

Figure 2: Differential yield of dileptons in central Au+Au collisions at 1.23 A GeV.

References

[1] R. Rapp and H. van Hees, Phys. Lett. **B** 753 (2016) 586.

[2] P. Huovinen *et al.*, Phys. Rev. **C** 66 (2002) 014903.

[3] S. Endres *et al.*, Phys. Rev. **C** 92 (2015) 014911.

[4] T. Galatyuk *et al.*, arXiv:1512.08688 [nucl-th], accepted for publication in Eur. Phys. J. **A**.

[5] R. Rapp, Adv. High Energy Phys. 2013 (2013) 148253.

*This work was supported by the U.S. National Science Foundation under grant PHY-1306359, by the Humboldt foundation (Germany), by the Helmholtz-YIG grant VH-NG-823 at GSI and TU Darmstadt (Germany), and by the Hessian Initiative for Excellence (LOEWE) through the Helmholtz International Center for FAIR (HIC for FAIR).

† fseck@gsi.de

Dilepton reconstruction in pion induced reactions with HADES*

F. Scozzi[1,2] *and the HADES Collaboration*[1]
[1]TU Darmstadt, Germany; [2]IPNO, Orsay, France

The High-Acceptance Di-Electron Spectrometer (HADES) operates at the GSI with pion, proton and heavy-ion beams provided by the synchrotron SIS18. In summer 2014 HADES took data from pion-induced reactions using carbon and polyethylene (PE), at several pion beam momenta. The largest statistics was recorded at a pion beam momentum of 0.69 GeV/c with a target of PE in order to explore the second resonance region and the sub-threshold coupling of the ρ to baryonic resonances. The main purpose for measuring dielectrons is to study the channel $\pi N \rightarrow R \rightarrow e^+e^-N$, for the understanding of the electromagnetic baryon-resonance transition form factors in the time-like region.

Electrons and positrons are identified using appropriate cuts on time-of-flight and RICH observables so that it is possible to achieve a high purity in lepton selection [1]. A big challenge of this type of analysis is usually to maximise the signal to background ratio. Signal is defined as the number of unlike pairs minus the combinatorial background (CB), estimated as $CB = \sqrt{N_{++}N_{--}}$ in which N's are the number of the like sign pairs. Two additional cuts are applied: the opening angle between the two leptons larger than 9° and the tracks having a fitted or unfitted segment in an angle of 4° are rejected from the analysis. In fig.1 the raw inclusive spectrum of dielectrons is shown together with the signal to background ratio: around 2500 pairs with invariant mass larger than π mass are reconstructed and it is possible to see how the last mentioned cut is effective for the maximation of signal to background ratio, that is higher than 1, except that around 120-130 $\frac{MeV}{c}$.

We aim at comparing the experimental mass spectrum with a e^+e^- cocktail (fig. 2), formed by the different known components: π^0 Dalitz decay, η Dalitz decay, Δ Dalitz decay and $N(1520)$ Dalitz decay. The cross sections for $1\pi^0$, $2\pi^0$ and η channels are taken from the previous data [2] and they are known with only quite large uncertainties (an analysis of the reconstruction of π^0 and η using full conversion method is actually on going to constrain these values), while for $N(1520)$ the contribution is deduced from $1\pi^0$ channel rescaled for branching ratio and isospin coefficient. The calculation is made using the PLUTO generator [3] for both proton and carbon, then the two components are added according to the ratio, taken from the data, 1:2. No ρ contribution is shown, but actually it seems necessary to describe the data. Anyway efficiency

* Work supported by VH-NG-823, Helmholtz Alliance HA216/EMMI and GSI

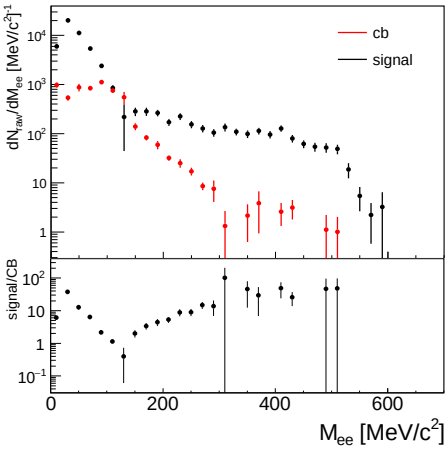

Figure 1: Di-electron invariant mass reconstructed from π^- + PE target and signal to background ratio

corrections are at the moment under investigation to make the direct comparison with the cocktail possible.

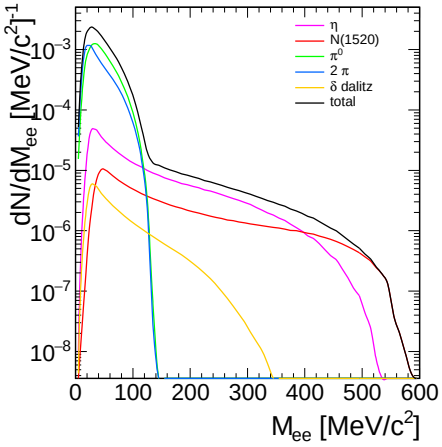

Figure 2: Dilepton cocktail in HADES acceptance

References

[1] F.Scozzi (HADES), "Importance of the HADES RICH for di-electron analysis in pion induced reactions", GSI Scientific Report 2014

[2] H.Landolt, R.Börnstein, Landolt-B.12, (1988)

[3] I. Fröhlich et al., Pluto: A Monte Carlo Simulation Tool for Hadronic Physics, PoS ACAT2007 (2007) 076

DOI:10.15120/GR-2016-1

Origin of the asymmetry factor in the dilepton combinatorial background calculation *

S. Harabasz[1,2] *for the HADES collaboration*

[1]Technische Universität Darmstadt, Darmstadt, Germany; [2]Jagiellonian University, Kraków, Poland

Invariant mass spectra of e^+e^- reconstructed in heavy-ion collisions provide a direct information on the fireball life-time and temperature. When plotting them, it is not possible to recognize which electron and positron belong to a true pair. The only solution is to combine all e^- with all e^+ in the event, and try to estimate the amount of uncorrelated pairs, so called combinatorial background (CB).

It can be shown [1], that the CB contribution to the total e^+e^- yield can be estimated as the geometric average of total like-sign yields:

$$N_{+-}^{\mathrm{CB}} = R \cdot 2\sqrt{N_{++}N_{--}}, \tag{1}$$

where

$$R := \frac{[\epsilon_{+-} + \epsilon_+(1-\epsilon_{+-})][\epsilon_{+-} + \epsilon_-(1-\epsilon_{+-})]}{[\epsilon_{++} + \epsilon_+(1-\epsilon_{++})][\epsilon_{--} + \epsilon_-(1-\epsilon_{--})]} \tag{2}$$

and ϵ_+, ϵ_- are the probabilities to reconstruct single e^+ or e^-, while ϵ_{+-}, ϵ_{++}, ϵ_{--} are probabilities of reconstructing pairs of respective signs. Note, that this form is different from the previously quoted [2]

$$R' := \epsilon_{+-}/2\sqrt{\epsilon_{++}\epsilon_{--}}, \tag{3}$$

which was obtained after making implicitly an assumption, that electrons and positrons in the event are produced fully independently [3]. In fact, it is intuitively plausible, that $R' = 1$, but even in this case $R \neq 1$ unless $\epsilon_{+-} = \epsilon_{++} = \epsilon_{--}$.

The ratio R does not need to be computed directly from Eq. 2, since Eq. 1 holds in event mixing as well, and R is equal to the ratio of mixed-event spectra (there is no signal in this case):

$$R = N_{+-}^{\mathrm{mix}}/2\sqrt{N_{++}^{\mathrm{mix}}N_{--}^{\mathrm{mix}}}.$$

For this reason, the correct form of the factor R (Eq. 2 instead of Eq. 3), although very important for the understanding of concepts, has no influence on the practical application and final dilepton spectra.

The result of the calculation is shown in Fig. 1 as a function of dilepton invariant mass. Black points were obtained using particle tracks reconstructed in AuAu at 1.23A GeV measured by HADES [4, 5]. Red points were calculated from tracks reconstructed in full Monte Carlo simulation of the same reactions. Very good agreement of the two shows that the dilepton reconstruction efficiency is very well reproduced in the MC simulation of HADES. Blue points were computed with ideal simulated particles filtered by the HADES acceptance. The clear deviation of the variant that takes into account only acceptance effects from all the others proves, that a correctly computed ratio R involves also efficiency and it is incorrect to attribute it only to different acceptances for pairs of different signs, as it is also evident from the Eq. 2. Finally, green points were obtained with particles filtered both by acceptance and reconstruction efficiency, calculated separately. The much smaller discrepancy visble in this case originates most probably from the different methodologies and still has to be understood.

The results reported in [2, 6] correspond to the black points in Fig. 1 and they remain valid.

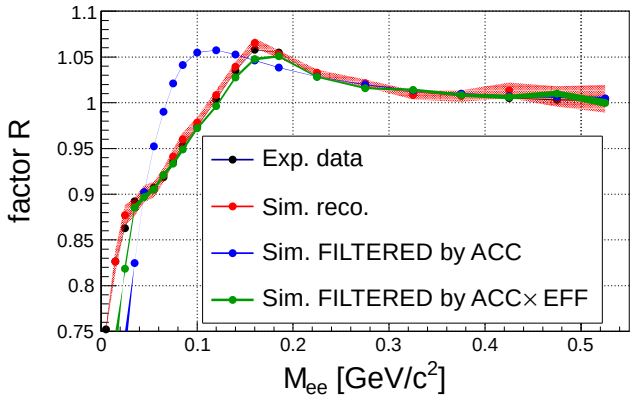

Figure 1: Factor R as a function of lepton pair invariant mass, computed for different data sets and with different ways of taking HADES acceptance and/or reconstruction efficiency into account. Details are given in the text.

References

[1] A. Adare et al. (PHENIX), Phys.Rev.C81(2010)034911

[2] S. Harabasz et al. (HADES), "Acceptance correction for the dilepton combinatorial background in HADES", GSI Scientific Report 2014

[3] T. Hemmick et al. "Measurements of Continuum Electron Yield", BNL 2002

[4] G. Agakishiev et al. (HADES), Eur.Phys.J.A41:243-277,2009

[5] S. Harabasz et al. (HADES), "Electron identification in Au+Au collisions at 1.23 GeV/u in HADES using multivariate analysis", GSI Scientific Report 2013

[6] S. Harabasz et al. (HADES), "Reconstruction of virtual photons with HADES", GSI Scientific Report 2014

* Work supported by VH-NG-823, EMMI, GSI, HGS-HIRe and H-QM.

Design of a new photon detector for the HADES RICH*

M. Faul[1], J. Friese[†2], C. Höhne[3], T. Kunz[2], S. Lebedev[1], W. Niebur[1], C. Pauly[4], M. Traxler[1]
[1]GSI Darmstadt, [2]TU München, [3]JLU Gießen, [4]BU Wuppertal

The promising feasibility study [1] for a new HADES RICH photon detector based on multi anode photo multiplier tubes (MAPMTs) with enhanced BA cathodes and the purchase of 1100 of such 8x8 pixel tubes (Hamamatsu H12700) for the CBM experiment [2] have initiated a joint effort of both collaborations to realize such a detector together with a new signal read-out on a short time scale. The goal of this enterprise is twofold. First, the replacement of the still operational MWPC in the HADES RICH will yield a significant enhancement of the e^+e^- - pair identification efficiency in forthcoming HADES runs and second, the new device will provide a realistic testbed environment for the commissioning of the CBM RICH detector.

The mechanical design of the new device is governed by the detector position upstream of the interaction target with related beam tube constraints as well as by the existing radiator volume and mirror geometry. To achieve optimum ring image reconstruction the photo cathodes have to nearly match the strongly curved focal surface of the mirror (R = 870 mm). Based on dedicated simulation studies the photo tubes will be arranged in 2 planes placed at z1 = - 80 mm and z2 = -200 mm and cover an illuminated area of D = 1230 mm diameter. Altogether 74 super modules with 3x2 individual MAPMTs each on a common PCB backplane are mounted on an aluminium carrier frame such as to provide gas tight enclosure of the inner detector volume and to allow for nitrogen filling at $\Delta P \sim$ 15 hPa overpressure. The design is depicted in figure 1.

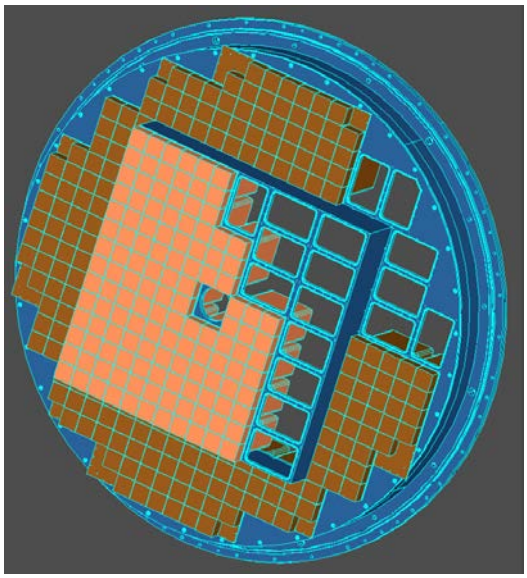

Figure 1: Front view of the photon detector with 428 multi anode phototubes and 27.392 pixels of 6x6 mm^2.

Each PCB backplane (156 x 105 mm^2) will host 12 front end cards (DiRICH) for signal read-out and a data combiner module for connection to the TRB based DAQ system. Details of the read out chain and its current design status are reported in [3]. The thermal power load of all 856 DiRICH cards and 74 combiner modules is expected to be $P_{th} < 2$ kW and will be dissipated by fan supported airflow.

The new detector geometry and the versatile CBM ring finder algorithm have been implemented in the HGEANT / HYDRA simulation and analysis package. Simulations for fully propagated e+/e- tracks show nearly constant ring radii for all polar emission angles (see figure 2, left).

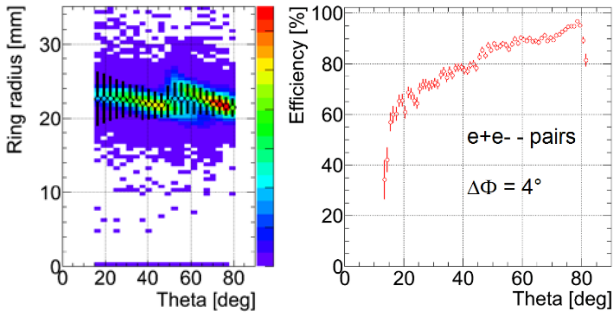

Figure 2: Radii of single Cherenkov rings (left) and individual ring reconstruction efficiencies for close e+/e- - track pairs at opening angles of $\Delta\phi = 4°$.

The reconstruction and identification efficiency for individual overlapping rings of close pair tracks ($D\Phi = 4°$) is depicted in the right panel of figure 2 assuming very conservative estimates for the quantum efficiency of the enhanced BA photo cathode. The separation of the two MAPMT planes visible in the radius distribution does not affect the pair recognition efficiency. Simulations for high track multiplicities in Au+Au collisions including radiator scintillation background are under way.

A first batch of MAPMTs is currently undergoing quality assessment tests [4]. The detector frame is under construction and will soon be installed in a dedicated test chamber for full system measurements. After the arrival of new prototype read out cards and assembly of first MAPMT super modules we will start with commissioning measurements utilizing single photon light sources at high trigger rates.

[1] K. Schmidt-Sommerfeld, Mast. Th., TUM 2014P, Sc. Rep. 2014 GSI Report 2015-1, 33 p. (2015)
[2] J. Eschke et al., CBM Progress Report 2015
[3] C. Pauly et al., CBM Progress Report 2015
[4] J. Förtsch et al., CBM Progress Report 2015

* Work supported by GSI, BMBF 05P15RGFCA, 05P15PXFCA
† juergen.friese@ph.tum.de

DOI:10.15120/GR-2016-1

Efficiency corrections to particle number fluctuations *

M. Szala[1], *R. Holzmann*[2], *and the HADES collaboration*[1]
[1]J. W. Goethe Universität, Frankfurt am Main, Germany; [2]GSI, Darmstadt, Germany

Investigations of heavy-ion collisions at low beam energies give access to the thermodynamics of QCD in the low T and high μ_B region of the phase diagram. In particular, higher order moments of conserved quantities (e.g. baryon number, charge, strangeness) are predicted to be sensitive to a first order phase transition and especially to the critical point of the QCD phase diagram. Indeed, fluctuations characteristic of the latter features would modify these moments. Measuring at SIS18, the HADES detector allows to extend data taken in the RHIC beam-energy scan to bombarding energies in the few-GeV regime. Here we discuss our investigations of efficiency corrections to the observed fluctuation signal.

The first four moments of a particle number distribution are its mean (M), its variance (σ), its skewness (S) and its kurtosis (K). To cancel the volume effect of the collision system the products of the higher order moments $S \cdot \sigma$ and $K \cdot \sigma^2$ are often used.

Investigations of the energy dependence of moments of net-proton multiplicity distributions were published in 2013 by the STAR Collaboration [1][2]. In the Beam Energy Scan (BES) at RHIC the center-of-mass energy of the Au+Au collisions was varied from $\sqrt{s_{NN}} = 7.7 - 200$ GeV ([1]STAR2).

The HADES experiment has recorded about seven billion Au+Au collisions at a bombarding energy of 1.23 GeV/u ($\sqrt{s_{NN}} = 2.41$ GeV). With this large statistics, the higher order moments of proton number distributions can be investigated in great detail. The main goal of this analysis is to expand the STAR measurement to lower center-of-mass energy.

In analysing experimental data, the efficiency correction is an important step in obtaining the higher order moments of the proton number distributions. For this purpose, we have done detailed investigations on the efficiency correction using Au+Au UrQMD events and GEANT simulations.

Two different efficiency correction methods were tested: correcting the moments (as proposed by [4], [3]) and unfolding of the distributions [5].

The first method consists in correcting the measured moments for efficiency. The local efficiency corrections include a dependence of efficiency on the phase-space (e.g. transverse momentum, rapidity). The proton number distributions were analysed in a centrality dependent way within a fixed phase space bin of p_t = 400 - 1600 MeV and $|y_{cm}|\pm$ 0.2.

The first results of the correction using [4],[3] indicate problems with this approach which assumes constant track reconstruction efficiencies. Therefore, the method was expanded to an event-by-event efficiency correction depending on the track multiplicity in the different sectors of the HADES spectrometer (see Fig. 1).

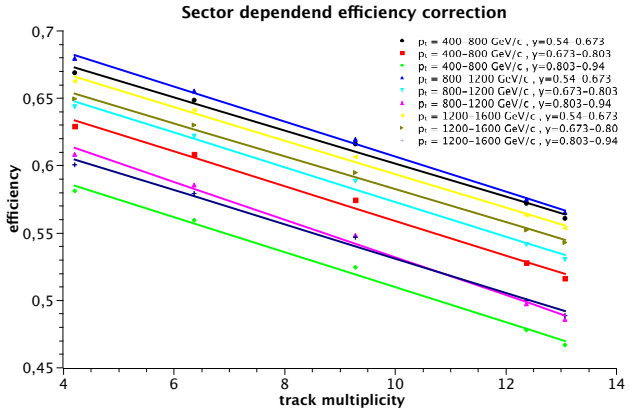

Figure 1: Centrality dependent efficiency in different p_t-y bins for one sector of the HADES spectrometer. With this correlation a sector and centrality depending event-by-event efficiency correction is performed.

As a result this method corrects the higher order moments of semi-peripheral collisions rather well, whereas in the most central collisions it still falls short of correcting moments (see Fig. 3).

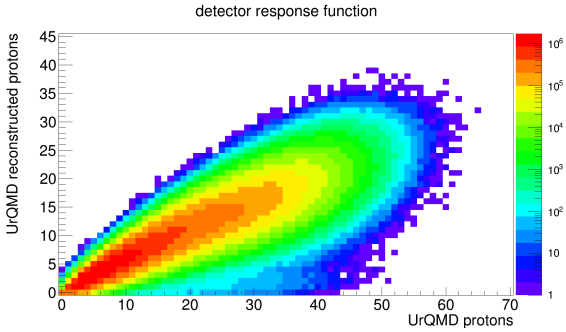

Figure 2: Simulated response matrix for the unfolding correction method

As a second method of efficiency correction the unfolding was introduced. This was realized with the ROOT TUfold package which is based on a least square fit with

* Supported by GSI and EMMI.

DOI:10.15120/GR-2016-1

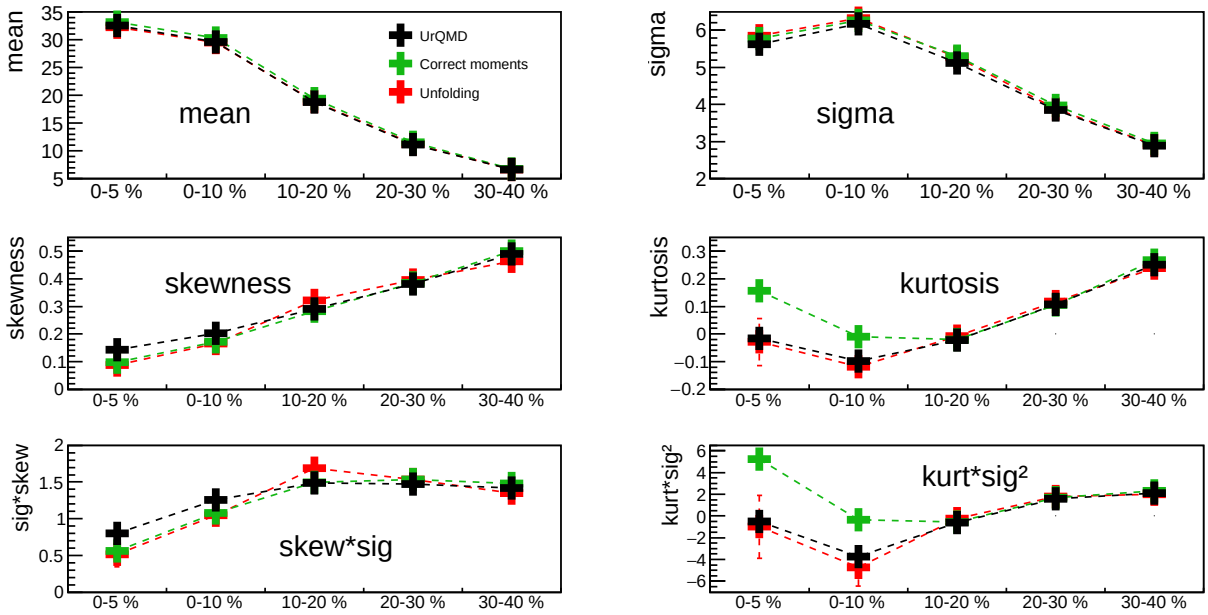

Figure 3: Comparison of the efficiency correction of higher order moments of the proton distributions in Au+Au UrQMD simulation. The black points are the UrQMD reference. The green points describe the results of correcting the moments and shows discrepancies at the most central collisions. The unfolding results are shown in red and reproduce the reference within the error bars quite well.

Tikhonov regularisation and an optional area constraint [5]. The detector response matrix is obtained from out UrQMD simulation (see Fig. 2).

To compare the two methods of efficiency correction the unfolding method was analysed in the same centrality classes and the same phase space bin. Within error bars the unfolding method delivers a reliable result and is also reproducing the moments for the most central collisions (see Fig. 3).

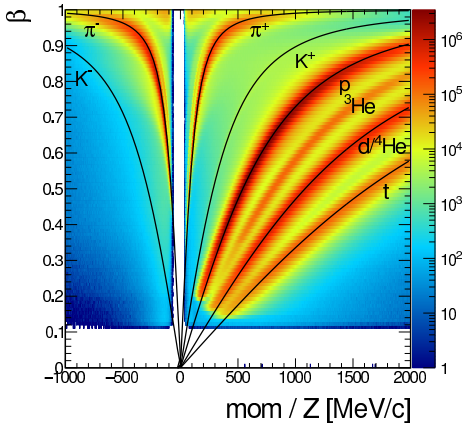

Figure 4: Particle identification in Au+Au data

As the fully conserved quantity is the baryon number, further investigations will focus on including the fragments (see Fig. 4) produced in Au+Au collisions at $\sqrt{s_{NN}} = 2.41$ GeV to the efficiency correction. Our ultimate goal is to apply the correction methods to real Au+Au data and compare with the STAR systematics.

References

[1] STAR Collaboration, Phys. Rev. Lett. 112 (2014) 32302.

[2] STAR collaboration, Phys. Rev. Lett. 113 (2014) 092301

[3] A. Bzdak, V. Koch, Phys.Rev. C86 (2012) 044904.

[4] A. Bzdak, V. Koch, Phys.Rev. C91 (2015) 027901.

[5] S. Schmitt, JINST 7 (2012) T10003.

DOI:10.15120/GR-2016-1

Dilepton reconstruction in Au+Au collisions at 1.23A GeV with HADES*

P.Sellheim[1] *and the HADES collaboration*[1]
[1]Goethe-Universität, Frankfurt am Main, Germany

In continuation of a systematic investigation of the emissivity of strongly interacting matter, HADES has recently measured the dielectron emission in $Au + Au$ collisions at 1.23A GeV beam energy. Due to the high track density reached for this collision system, different reconstruction strategies have been pursued to achieve optimal reconstruction efficiencies and purities. Electron (positron) candidates have been identified by means of a multi-variate analysis, where the neural network has been trained alternatively based on clean signal and background tracks from data and by simulated tracks. Moreover, the electron track candidates have been matched to rings using ring parameters of found rings [1]. Alternatively, track candidates identified by time-of-flight only have been matched to ring signatures without running the ring finder prior [2] (the so-called backtracking).
Leptons identified with both methods are used for dilepton reconstruction. The signal is reconstructed as combination of all unlike-sign pairs whereof the background needs to be subtracted. The background is estimated with two methods. The mixed event unlike-sign background is used in the mass region $M > 0.25\ GeV/c^2$, since a high statistics background is needed to reduce statistical errors. However, the mixed-event background is not intrinsically normalized and is therefore adjusted to the background contribution at lower masses $M < 0.25\ GeV/c^2$. In this region a same-event like-sign background is evaluated by the geometric mean of like-sign pairs. It provides naturally the normalization and takes care of correlated combinatorial background. This is essential since a correlated background of cross combinations from Dalitz decays is present in the low mass region. However, a multiplicative factor correcting differences of efficiency and acceptance for different pair signs is needed as well [3].
The spectrum of unlike-sign pairs, background and signal shown in figure 1 reveals the small signal to background ratio as the main challenge for a precise signal reconstruction. A signal up to a mass of around 1 GeV/c^2 is reconstructed. In order to compare the quality of both lepton identification methods the significance of their reconstructed spectra is compared in figure 2. Both histograms show a similar mass dependent trend but the significance obtained with backtracking is higher. This is resulting from a more efficient lepton identification in combination with a strong close pair rejection capability due to the ability to reconstruct overlapping rings.

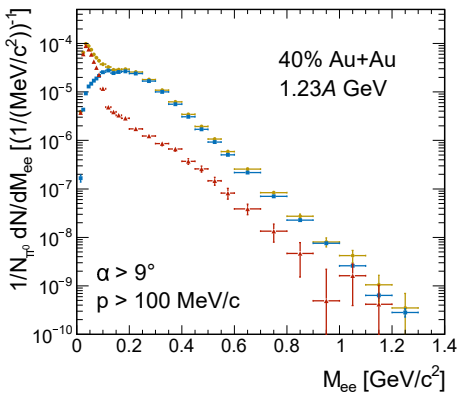

Figure 1: The signal (triangles) is reconstructed by subtraction of the background contribution (squares) from the spectrum of all reconstructed unlike-sign pairs.

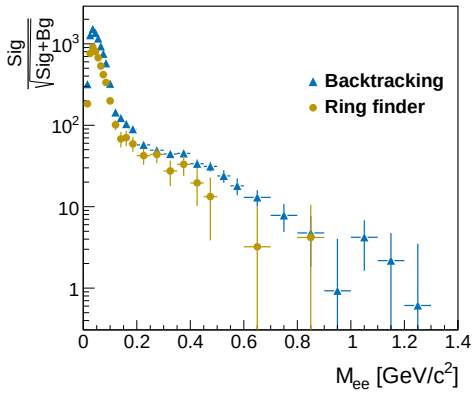

Figure 2: The significance estimated from the spectrum obtained from the ring finder (circles) is compared to the one obtained with the backtracking (triangles) approach.

References

[1] J. Lehnert, J. and the HADES collaboration", Nucl. Instrum. Meth. A433 (1999) 268-273

[2] P. Sellheim and the HADES collaboration, J. Phys. Conf. Ser. 599 (2015) no.1 012027

[3] S.Harabasz, this report

* Supported by BMBF(05P12RFGHJ,05P15RFFCA), GSI, HIC for FAIR, HGS-HIRe and H-QM.

Electromagnetic calorimeter for HADES experiment - progress report

O. Svoboda[1,#], C. Blume[2], W. Czyżycki[3], E. Epple[4], L. Fabbietti[4], T. Galatyuk[5], M. Golubeva[6], F. Guber[6], S. Hlaváč[7], A. Ivashkin[6], M. Kajetanowic[8], B. Kardan[2], W. König[9], A. Kugler[1], K. Lapidus[4], E. Lisowski[3], J. Pietraszko[9], A. Prakash[1], P. Ramos[1], A. Reshetin[6], A. Rost[5], P. Salabura[8], Y. G. Sobolev[1], P. Tlustý[1],M. Traxler[9]

[1]NPI CAS, Řež, Czech Republic; [2]Goethe-Universität, Frankfurt, Germany; [3]Institute of Technology, Kraków, Poland; [4]TU München, Germany; [5]TU Darmstadt, Germany; [6]INR RAS, Moscow, Russia; [7]IP SAV, Bratislava, Slovakia; [8]UJ Kraków, Poland; [9]GSI, Darmstadt, Germany

Experimental studies of di-lepton as well as of hadron production in AA, pA, pp and pion induced reactions were successfully carried out during the last decade by the High Acceptance Di-electron Spectrometer (HADES). With the approaching operation of the FAIR SIS100 accelerator, HADES is under extensive upgrade program. The electromagnetic calorimeter (ECAL) is being built to extend HADES possibility for measurements of neutral meson production in heavy ion collisions in the energy range of 2–10 AGeV, to be running already within FAIR module 0 beginning in 2018 on the beams of SIS18. The calorimeter will also improve the electron-hadron separation of the spectrometer, and will be used for the detection of photons from strange hadron resonances.

The R&D of the ECAL detector was crowned by the approval of the TDR [1]. The full setup will consist of 978 modules divided into 6 sectors, and it will cover forward angles of $16^\circ < \Theta < 45^\circ$ and almost full azimuthal angle. Each module is composed of a lead glass Cherenkov counter covered in TYVEK paper, photomultiplier (PMT) surrounded by a magnetic shielding, HV divider and an optical fiber for monitoring. Two types of PMTs were selected, namely 1.5” EMI 9903KB and 3” Hamamatsu R6091. The high voltage power supply system will consist of CAEN SY1527LC HV crates with 24-channel A1535 cards providing a voltage up to 3.5 kV and a current up to 3 mA per channel. Control of the high voltage will be done remotely using the EPICS control system. A charge-to-width based PaDiWa AMPS board connected to TRB3 was developed and tested for ECAL readout.

Parallel to the currently running build-up of the detector, further research is being performed in order to fully understand the properties and behaviour of the single ECAL modules as well as of the whole detector.

Several ECAL modules were tested at MAMI Mainz [2], [3]. Wide range of measurements using cosmic muons were performed in order to understand the light behavior inside the modules. Simulations using Geant3 based HADES software environment (HGeant+Hydra) were performed and crosschecked with the measured results, in order to tune the light transport description in the simulations. A stand-alone code for transport of Cherenkov photons developed by M. Prokudin [4] was used to produce look-up tables for fast photon transport inside the modules. Dedicated software libraries are being developed to fully include ECAL to the HADES tracking software environment.

A specialized monitoring system (see Figure 1) was developed to control the stability of the ECAL detector. Short light pulses (10 ns) from a laser LED are distributed equally to all modules in one sector (163 pieces). Part of the system for one sector was already purchased.

Figure 1: Optical divider for the ECAL detector.

Single parts of the detector are currently under construction: support structure is under production, over 1000 lead glass modules from OPAL experiment (CERN) were already disassembled and prepared for final assembly, out of them 150 modules were already fully assembled; a part of the high voltage system was purchased. The main aim is to have the ECAL (possibly not all PMTs eguipped) running in 2018 for physics runs at SIS18.

References

[1] HADES Collaboration, Technical Design Report for the HADES ECAL, GSI Darmstadt 2014

[2] O. Svoboda et al., GSI Scientific Report 2013 (2014)12

[3] O. Svoboda et al., GSI Scientific Report 2014 (2015)27

[4] A.V. Arefev et al., A study of light collection in “Shashlik” calorimeters, Instrum. Exp. Tech. 51 2008) 511

* Work supported by the MEYS of the CR - projects LM2015049, LG12007, GACR 13-06759S and AS CR M100481202 grants, by GSI, HIC for FAIR, EMMI, and by European Community FP7 – Capacities, contract HadronPhysics3 n. 283286.

#svoboda@ujf.cas.cz

DOI:10.15120/GR-2016-1

Search for a Σ^0 Signal in p + Nb at E_{kin} = 3.5 GeV *

L. Fabbietti[1,2], J. Friese[1] and T. Kunz[†1,2] for the HADES collaboration
[1]Physik Department E62, Technische Universität München, D-85748 Garching; [2]Excellence Cluster 'Origin and Structure of the Universe', D-85748 Garching

The production of Λ^0 – baryons (M = 1115.7 GeV/c^2) has been investigated by the HADES collaboration in various collision systems ranging from p + p to Au + Au at SIS energies. In this context it is of interest, to which amount feeding from Σ^0 (M = 1192.6 GeV/c^2) decays via the processes $\Sigma^0 \rightarrow \Lambda^0\gamma$ (BR = 100 %) and $\Sigma^0 \rightarrow \Lambda^0 e^+e^-$ (BR = 0.005 %) contribute to the observed Λ yields [2]. While at low collision energies close to the NN threshold the production cross sections $\sigma_\Lambda/\sigma_\Sigma \approx 10$ [1] suggest a feeding of ~ 10% it is expected that at energies around 1 GeV above threshold this contribution increases to ~30% [3]. For even higher energies it may reach up to 50%.

We have therefore started an attempt to identify Σ^0 – decays in the reaction p + Nb at E_{kin} = 3.5 GeV ($\sqrt{s_{NN} - s_0} \approx 1.6$ GeV). In the collected data sample of 4.21· 10^9 events around 1.1 million Λ particles have been reconstructed through their weak decay $\Lambda \rightarrow p\pi^-$ and utilizing momentum, dE/dx and track vertex information [4]. Coincident γ detection is achieved through conversion pair $\gamma \rightarrow e^+e^-$ identification, due to the absence of an electromagnetic calorimeter. The design of the HADES detector is optimized for low conversion probability. Furthermore, the momentum measurement for electrons is limited to $p_e \geq 60$ MeV/c because of the strong magnetic field between the two tracking stations MDCI/II and MDCIII/IV. GEANT simulations show that the conversion probability for γ´s (E_γ ~ 80 MeV) from Σ^0 decays is only ~3.5% while the acceptance and detection efficiency for their conversion pairs is 6.7%.

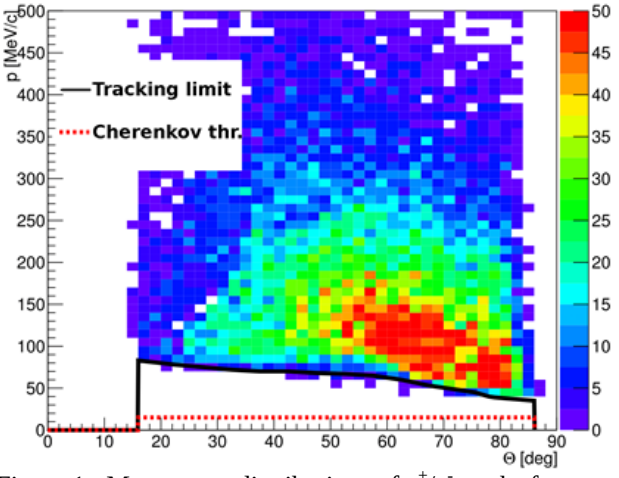

Figure 1: Momentum distributions of e^+/e^- tracks from reconstructed $\pi^0 \rightarrow e^+e^-\gamma$ decays. The given limits define the un-accessible momentum region (see text).

In the present analysis we require for each event with Λ content at least the momentum vector of one fully reconstructed electron/positron with a good quality RICH ring. For the identification of the converted photon we search for a second electron/positron candidate characterized by at least a RICH signal with hits in the inner tracking detectors only. The momentum of the latter is then determined from a MC estimate in the un-accessible phase space region. While the lower limit of this region is determined by the Cherenkov threshold, the upper limit is given by a polar angle dependent function obtained from e^+/e^- pairs from identified π^0 Dalitz decays in the same reaction (see fig.1).

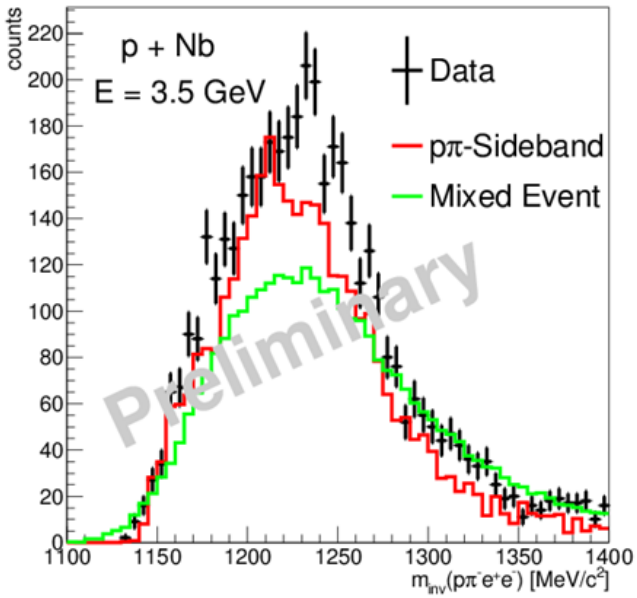

Figure 2: Invariant mass distribution for all $p\pi^-ee$ candidates with combinatorial backgrounds from mixed event and sideband analysis.

The reconstructed four particle invariant mass spectrum is presented in figure 2. The combinatorial background has been determined via event mixing and sideband analysis techniques. Around 600 - 1100 Σ^0 candidates become visible, albeit at a slightly shifted pole mass. This shift is attributed to the incomplete momentum determination of one of the two electrons.

Further background studies and refined detection efficiency calculations are presently underway.

[1] P.Kowina et. al, Eur. Phys. J. A 22, 293-299 (2004)
[2] K.A. Olive et al., Chin. Phys. C, 38, 0900001 (2014)
[3] H.Landolt, R.Börnstein, Landolt-B.12, (1988)
[4] G.Agakishiev et. al, Eur. Phys. J. A 50 (2014) 81

* Work supported by BMBF 05P15WOFCA, GSI TMLFRG 1316
† tobias.kunz@tum.de

Measurement of the pΛ correlation function in p+Nb reactions at 3.5 GeV*

O. Arnold[1,2]*, L. Fabbietti*[1,2]*, and the HADES collaboration*[1]

[1]Physik Department E62, Technische Universität München, James-Franck-Str. 1, D-85748 Garching, Germany;
[2]Excellence Cluster Universe, Technische Universität München, Boltzmannstr. 2, D-85748, Garching, German

Motivation

In 2008, the reaction $\mathrm{p} + ^{93}\mathrm{Nb}$ was measured with a kinetic proton energy of $3.5\ \mathrm{GeV}$ and about $3.2 \cdot 10^9$ were recorded. This large event sample allows to study correlation properties in terms of two-particle correlation functions between particles that were produced in the above mentioned p+A reaction. The general definition of the two particle correlation function reads as follows:

$$C(\mathbf{p}_1, \mathbf{p}_2) = \frac{P(\mathbf{p}_1, \mathbf{p}_2)}{P(\mathbf{p}_1) \cdot P(\mathbf{p}_2)}, \qquad (1)$$

where $P(\mathbf{p}_1, \mathbf{p}_2)$ is the conditional probability of finding a particle pair in the same event normalized to the product of the single-particle probabilities finding such particles independently. Experimentally, the two-particle correlation function of Eq. 1 was evaluated in the pair rest frame (PRF) defined as $\mathbf{P} = \mathbf{p}_1 + \mathbf{p}_2 = 0$ as a function of the relative momentum in the PRF $k = \mathbf{p}_1^* = \mathbf{p}_2^*$. At small relative momenta $k < 100\ \mathrm{MeV/c}$ the correlation function is sensitive to the size of the particles emission region of the niobium nucleus. Assumed that the interaction between the particles is known, the source size can be extracted by comparing the data to model calculations. In the low energy regime proofed by such a technique the collision energy $E = \hbar k^2/2\mu$ is quite small therefore the full information about the scattering thus interaction (e.g. of $p\Lambda$) is contained in the (s-wave) expansion of the scattering amplitude $f(k) = (-a^{-1} + 1/2 d_0 k^2 - ik)^{-1}$, footing on two parameters the scattering length a and the effective range d_0. This makes the topic rather interesting. By knowing the source size of the system e.g. by measuring it with an independent pair, one is able to test different sets of scattering parameters e.g. for $p\Lambda$. An example of a theoretical $p\Lambda$ correlation function can be found in [1].

Data analysis

To study the $p\Lambda$ correlation function, in the first step the Λ hyperon was identified via the decay $\Lambda \rightarrow p\pi^-$ and the invariant mass of the two decay products. To suppress the combinatorial background of $p\pi^-$ pairs stemming from other sources than Λ, topological cuts were used to reach a large purity sample. In the second step of the analysis the correlation function was constructed creating a relative momentum distribution of pairs from the same event $A(k)$ and a reference sample $B(k)$ using the event mixing method which results in the experimentally constructed correlation function:

$$C(k) = \frac{A(k)}{B(k)}. \qquad (2)$$

To have a measure of the source size of the system the correlation function was independently constructed using pairs of protons. For protons the interaction is well established and many protons are produced at SIS 18 energies. We obtained an invariant source size for proton pairs of $r_{0,pp} = 2.02 \pm 0.01(\mathrm{stat})\ \mathrm{fm}$.
To study interaction parameters of the $p\Lambda$ pair, the size of the emission region of this pair has to be determined. We used for this purpose the simulation data from the Ultrarelativistic Quantum Molecular Dynamics (UrQMD) [2] transport model. The reaction p+Nb was simulated and the relative distances r at the moment of the freeze-out were calculated, which is the relevant information for the source size determination. Together with the measurement of the proton-proton source size it was possible to fix in this way the source size for the $p\Lambda$ pair.
In a final step, two different sets of scattering parameters were tested, which were calculated in a chiral effective field theory approach [3]. It was shown that the two-particle $p\Lambda$ correlation function develops a sensitivity to the scattering parameters for rather low relative momenta $k < 50\ \mathrm{MeV/c}$ if using the result from leading-order (LO) or next-to-leading-order (NLO). The experimental sensitivity in terms of the available statistics was not enough to constraint further theoretical models. However, it was shown that the method is a tool to understand the final state interaction of particle pairs, where the knowledge about their interaction in terms of experimental data is rather scarce. The results of this work was contained in a recent publication by HADES.

References

[1] F. Wang, S. Pratt, "Lambda-Proton Correlations in Relativistic Heavy Ion Collisions", Phys. Rev. Lett. 83 (1999) 3138

[2] S. A. Bass *et. al.*, "Microscopic Models for Ultrarelativistic Heavy Ion Collisions", Prog. Part. Nucl. Phys. 41 (1998) 225-370

[3] J. Haidenbauer *et. al.*, "Hyperon-nucleon interaction at next-to-leading order in chiral effective field theory", Nucl. Phys. A 915 (2013) 24-58

* Work supported by HIC4FAIR

DOI:10.15120/GR-2016-1

Efficiency Correction Map for pion-induced reactions measured with HADES*

L. Fabbietti[1,2], *S. Maurus* †[1,2], *J. Wirth*[1,2], *and the HADES collaboration*

[1]Excellence Cluster "Origin and Structure of the Universe", 85746 Garching, Germany; [2]Physik Department, TU München, 85746 Garching, Germany

In the field of modern experimental nuclear physics the study of strangeness production in hadronic matter is a major topic. The HADES spectrometer at GSI provides excellent identification capabilities for strange hadrons as $K^{\pm}$, $\overline{K^0_s}$ and π^--induced reactions are well suited to study the properties of these hadrons within nuclear matter. For the reconstruction of these states and the extraction of their in-medium properties, it is mandatory to know precisely the detection efficiency (ϵ) of all sub-detectors of the HADES setup. Typically, full-scale simulations are performed to correct for the limited ϵ and acceptance. In order to verify these simulations, a correction procedure based on experimental data collected during the experimental secondary π^--beam campaign at a central beam momentum of 656, 690, 748 and 800 MeV/c impinging on a polyethylene (C_2H_4, PE) target was developed. Based on the kinematic constraints introduced by elastic scattering (ES) a correction map in Φ, Θ and momentum was derived. In this procedure one of the two particles (π^- or p) is selected as a reference. By calculating the missing mass of this reference particle it is possible to identify the second one originating from an ES event. Taken the kinematical information of the reference particle the expected properties of the missing particle can be calculated as follows:

$$\Phi_{missing} = \Phi_{reference} - 180^{\circ} \quad (1)$$

$$\Theta_{missing} = arctan\left(\frac{P_{ref} \cdot sin(\Theta_{ref})}{P_{beam} - P_{ref} \cdot cos(\Theta_{ref})}\right) \quad (2)$$

This allows to determine the expected yield for ES events in Φ, Θ and momentum. By applying 3σ cuts on the kinematic characteristics of the ES system in $\Delta\Phi = \Phi_{expected} - \Phi_{measured}, \Delta\Theta$ and energy conservation the missing particle can be tracked. Figure 1 shows the experimental distribution of the missing mass as a function of the momentum together with the ES selection cuts. Depicted in green are the σ extracted from the fit of the Y-projected distribution for different momentum slices. These σ are fitted with a parabola to extract the cut, which is indicated with the black line. After applying these 2D cuts the measured yield can be determined and the final ϵ map is shown in Fig. 2. Blue represents the experimental ϵ with statistical errors and depicted in green the ϵ of the simulation. As a comparison the black histogram shows the simulated single track ϵ, which uses the GEANT track information and verifies if this track has been reconstructed. There is a good agreement between the simulated single track and experimental ϵ. The peak in the experimental ϵ arises from the carbon subtraction. The deviation to the simulated ϵ is under investigation. To cope with the background arising from quasi ES events of the carbon contained in PE, a dedicated run with a carbon target was used for subtraction. In order to scale the carbon run to the PE run, the missing mass of both systems is integrated in a carbon dominated region to extract the scaling factor. By applying the same procedure as for the PE target as well as the scaling factor, the contribution from the carbon background can be subtracted resulting in a clean p - π^- sample.

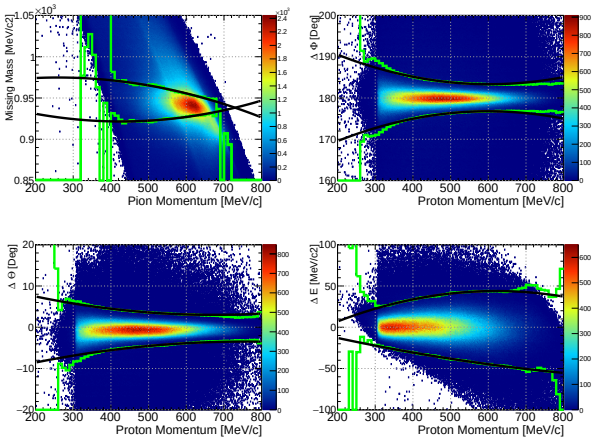

Figure 1: Experimental distributions of the missing mass, $\Delta\Phi$, $\Delta\Theta$ and ΔE as a function of the π^- and proton momentum. The green and black line correspond to the applied cut.

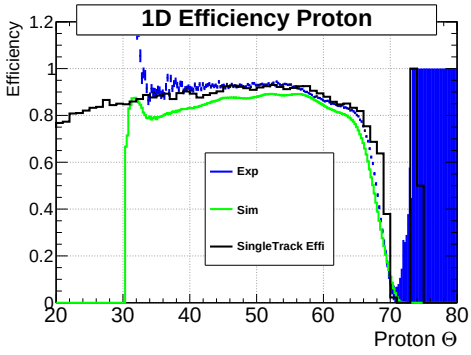

Figure 2: Φ integrated ϵ. Blue: experimental data with statistical errors. Green: simulation using this method. Black: simulated single track ϵ. Good agreement between the simulated single track and experimental ϵ.

* Work supported by BMBF 05P2015 and 05P15WOFCA.

In-medium kaon absorption in pion-induced reactions*

L. Fabbietti[1,2], A. Scordo[3], J. Wirth[1,2], and the HADES collaboration

[1]Excellence Cluster "Origin and Structure of the Universe", 85746 Garching, Germany; [2]Physik Department, TU München, 85746 Garching, Germany; [3]INFN Laboratori Nazionali di Frascati, 00044 Frascati (Roma), Italy

In 2014 the HADES collaboration performed two pilot experimental campaigns with secondary pion beams. Hereby, the investigation of the production as well as the properties of K^- in cold nuclear matter generated in pion-nucleus reactions ($\pi^- + W$, $\pi^- + C$) at $p_{\pi^-} = 1.7$ GeV/c is of particular interest.

The K^0 production in pion-induced reactions mainly takes place at the surface of the nuclei ($\sigma \sim A^b, b = 2/3$) as already verified by the FOPI collaboration [1]. While K^- can be absorbed in nuclear matter through resonance production processes ($K^-N \rightarrow Y\pi$), no conventional absorption mechanism exists for K^0 and K^+. Therefore the K^+ is expected to behave analogue to the K^0 [2]. The situation of the K^- is more involved and has not been measured in pion-induced reactions until now. If an increase of the absorption with A would be dominant, a $b < 2/3$ should be observed. Although, a drop of the effective mass [3] and thus a decrease of the kinematical threshold would lead to $b > 2/3$.

In the course of the K^- cross-section extraction as a function of A, a systematic study of the K^- absorption is carried out on the basis of the comparison of K^-/K^+ ratios produced off light (C) and heavy (W) nuclei.

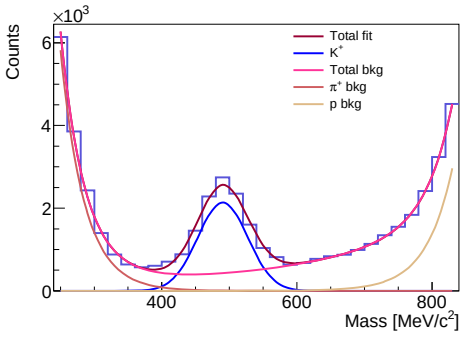

Figure 1: Reconstructed K^+ mass distribution (RPC: (500-570/27.5-40) [MeV/c,°]). The fit consists of a Gaussian for the K^+ signal together with the background described by a polynomial and two exponential functions taking into account the pion and proton signature, respectively.

In total about 99.7×10^3 and 4.2×10^3 K^- were reconstructed for ^{12}C as well as 100×10^3 K^+ and 6.9×10^3 K^- for ^{184}W allowing for a double-differential analysis of the kaon in phase space separately for the two detector systems, RPC and TOF, to obtain two independent measurements of the K^-/K^+ ratios. Moreover, this statistics combined with the large acceptance of the HADES setup offers a large part of the kaon phase space allowing the extrapolation of the kaon yield to the full solid angle and therefore the extraction of production cross-sections after applying efficiency correction. Both charged kaons are reconstructed by means of time-of-flight (RPC/TOF) and momentum measurements combined in the mass observable pictured in Fig. 1 for one phase space bin.

Figure 2 depicts the comparison of the K^-/K^+ ratios measured off the tungsten target divided by the same ratio measured off the carbon target as a function of momentum for both detector systems (RPC/TOF). A clear K^- disappearance for a higher effective density is observed, which is even more pronounced for low momenta. The slight discrepancy between RPC and TOF will later on be covered by the systematic error, which is not applied yet.

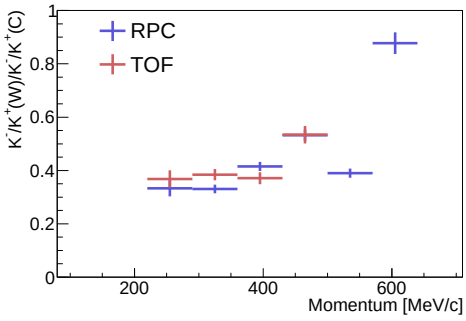

Figure 2: K^-/K^+ ratio in pion-tungsten collisions compared to pion-carbon as a function of momentum separately for the two detector systems RPC and TOF. No efficiency and acceptance has been applied.

References

[1] M. L. Benabderrahmane et al., Measurement of the in-medium K0 inclusive cross section in π^--induced reactions at 1.15 GeV/c, Phys. Rev. Lett. 102, 182501 (2009)

[2] G. Agakishiev et al.: Medium effects in proton-induced K0 production at 3.5 GeV. Phys. Rev., Bd. C90: S. 054906 (2014)

[3] J. Schaffner et al., In-medium production of kaons at the mean field level, Nucl. Phys. A625: S. 325 346 (1997)

* Supported by the DFG cluster of excellence "Origin and Structure of the Universe"

DOI:10.15120/GR-2016-1

Λ production in 3.5 GeV energy p-p reactions at HADES*

R. Lalik[1,2], L. Fabbietti[1,2], and the HADES collaboration

[1]Physik Department E62, Technische Universität München, 85748 Garching, Germany; [2]Excellence Cluster 'Origin and Structure of the Universe', 85748 Garching, Germany

The understanding of Λ hyperon production in proton-proton reactions is important for further studies of strangeness interactions in nuclear matter and it has been studied by HADES at a beam energy of 3.5 GeV. To be able to compare the experimental results with theoretical predictions, resonant and non-resonant contributions to the total production spectrum have been considered, also employing several exclusive Λ-channel analyses from the same reaction. In particular the influence of intermediate resonances like Λ^*, Σ^* , Δ^{++} or N^* to the inclusive Λ production has been considered. Pinning down all contributions will help in tuning transport models (GiBUU and UrQMD) as well will serve in the understanding of the production mechanism of Λ in proton-nucleus reactions. These result will also help to understand future measurements at SIS100 at FAIR.

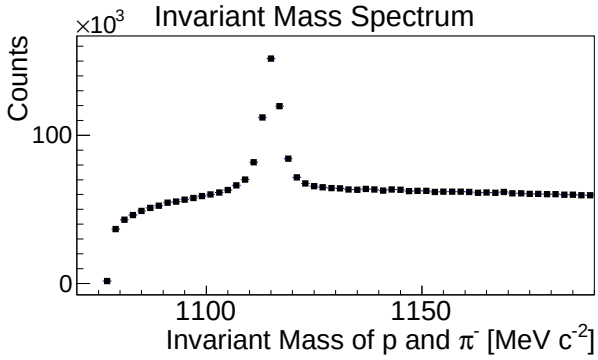

Figure 1: Reconstructed Λ signal yield in pp reaction.

The Λ hyperon is reconstructed in HADES by its charged hadronic decay into a proton and a negative pion pair. These particles are measured using MDC gas chambers, arranged in four layers of a tracking device immersed in a toroidal magnetic field. Bending of the track in the magnetic field allows to reconstruct the momentum and the polarity of the particle. These quantities, together with the energy deposition in the MDC gas volume, are uniquely correlated for each particle species by the Bethe-Bloch equation, allowing for particle identification. Using the invariant mass technique for combined proton and pion tracks, the mother particle is reconstructed (Fig. 1). The Λ production vertex is reconstructed by intersecting the Λ track with all other tracks leaving the reaction region. By applying several topological cuts on the production and decay vertexes, the misidentification background is reduced

* Work supported by BMBF 05P12WOGHH.

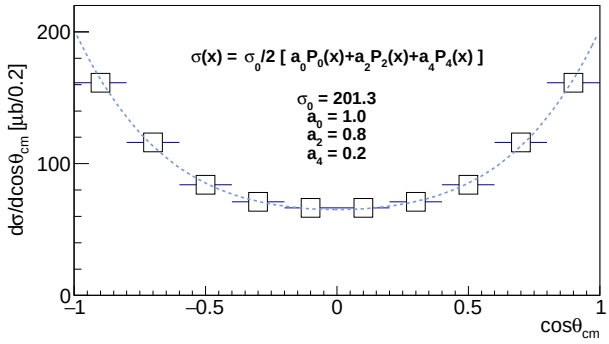

Figure 2: Differential cross-section of the Λ-hyperon production in the proton-proton center of mass frame in the proton-proton collisions at HADES.

and the final yield results in about 260×10^3 Λ-hyperons with statistical error below 1%. The signal to background ratio (S/B) is estimated to be around 0.5.

Experimental data have been corrected for the geometrical acceptance and reconstruction efficiency using a model produced with a Pluto [1] event generator. Each exclusive channel of the model has been simulated separately and all channels are added coherently. The simulation model is based on set of all known production channels, most of them measured with HADES [2, 3, 4, 5, 6], COSY-TOF [7] or estimated using the resonance model [8, 9].

The total Λ production cross-section was estimated to $\sigma(\mathrm{pp} \rightarrow \Lambda + X) = 201.3 \pm 1.3\,\mu\mathrm{b}$ with no systematical errors evaluated yet. The production anisotropy is described in terms of first three even Legendre polynomials P_0, P_2 and P_4 as shown in Fig. 2. Statistical and systematical evaluation of the anisotropy is under calculation.

References

[1] I. Frohlich et al. PoS ACAT2007 (2007)

[2] G. Agakishiev et al. PL B742 (2015)

[3] G. Agakishiev et al. PR C90 (1 2014)

[4] G. Agakishiev et al. PR C85 (3 2012)

[5] G. Agakishiev et al. PR C87 (2 2013)

[6] G. Agakishiev et al. PR C90 (5 2014)

[7] M. Abdel-Bary et al. EPJ A46 (2010). [Erratum: Eur. Phys. J.A46,435(2010)]

[8] K. Tsushima et al., Phys. Lett. B 390 (1997)

[9] K. Tsushima et al., Phys. Rev. C 59 (1999)

DOI:10.15120/GR-2016-1

DOI:10.15120/GR-2016-1

Track point resolution of a GEM TPC *

M. Berger[1,2], *L. Fabbietti*[1,2], *and the FOPI collaboration*[1]
[1]Physik Departement E62, Technische Universität München; [2]Excellence Cluster 'Origin and Structure of the Universe'

In past experiments, Time Projection Chambers (TPCs) have been equipped with a gating structure to prevent the migration of avalanche ions created during gas amplification – traditionally realized with Multi Wire Proportional Chambers (MWPCs) – in order to maintain drift field homogeneity. This, however, limited the application of TPCs to experiments with trigger rates smaller than $\mathcal{O}(10^3\,\mathrm{Hz})$. To overcome this limitation a TPC with GEM (Gas Electron Multiplier) foils [1], exploiting their intrinsic ion backflow suppression, has been built [2]. This GEM-TPC has a drift length of 728 mm, an inner radius of 50 mm and an outer radius of 155 mm. For tests with cosmic tracks and different heavy ion beams as well as for a physics experiment with an pion beam the GEM-TPC was employed together with the FOPI spectrometer [3].
To reduce the data rate and to introduce the possibility of an early noise suppression, pad hits are collected in entities called clusters which are defined by an amplitude, a position and an position uncertainty. This is done by a full 3D local minima search which is independent of the pad shape or pad plane geometry. The clusters are then passed to the pattern recognition algorithm performing track finding employing a conformal mapping method [4]. Finally, a track can be fitted to these clusters. For this the Kalman Filter implementation provided by the GENFIT [5] framework is used.
For track fitting it is mandatory to have a precise knowledge of the uncertainty on the cluster position. The uncertainty of this position is strongly dependent on the track topology. For example, along the track the pad hits are uniformly distributed while perpendicular to the track the pad hit distribution is broadened by diffusion. Therefore the uncertainty has to take the track topology into account. Furthermore, the position uncertainty along the track is note taken into account by the track fitting since no additional information is gained. In order to incorporate the track topology a prefit has to be performed. After this prefit new clusters are created by stepping through the track and collecting the pad hits. These pad hits are projected onto a plane perpendicular (see left side of Fig.1) to the track and a covariance matrix representing the distribution of the pad hist on this plane is calculated. To properly take all effects contributing to the position uncertainty into account, the eigenvalues and therefore the size of the previously calculated covariance matrix are scaled according to a parametrization. This parametrization takes effects introduced by the discrete pad size, by diffusion and by the projection of the tracks onto either the padplane or the z-axis into account. After applying various corrections concerning the effect of the discrete pad size and static drift field distortions these parameters are determined by fitting the residual distributions of the individual clusters with the log-likelihood method. Figure 2 shows the final resolution for the TPC operated with a Ar/CO_2 drift gas at a drift field of 360 V/cm and a gain of approximately 5100 obtained from a measurement of cosmic muons.

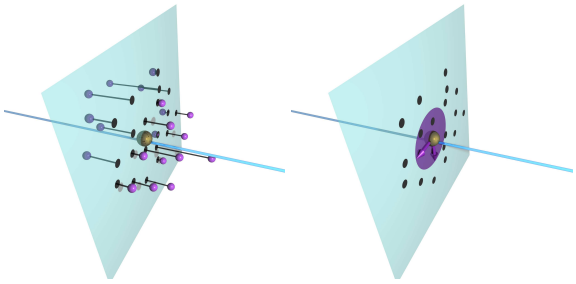

Figure 1: Left panel: Pad hits (purple spheres) projected onto a plane (turquoise) perpendicular to the track (light blue). The projected pad hits are depicted as black disks and the resulting cluster position is shown in gold. Right panel: Final resulting uncertainty of the cluster is shown as transparent purple ellipse. The eigenvectors (scaled by the eigenvalue) are shown as purple arrows.

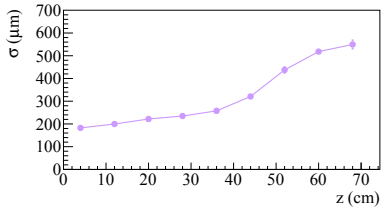

Figure 2: Space point resolution as a function of the drift length.

References

[1] F. Sauli, NIM A, 386 (1997), 531
[2] L. Fabbietti et al., NIM A, 628 (2011), 204-208
[3] K. Hildenbrand, GSI Nachr. 91-02, 6 (1992)
[4] J. Rauch, Journal of Physics: Conference Series 396 (2012) 022042
[5] C. Höppner et al., NIM A 620 (2010) 518

*This work was supported by the DFG cluster of excellence 'Origin and Structure of the Universe'.

Understanding the production Mechanism of pK^+ Λ in elementary proton-proton collisions*

R. Muenzer[1,2,3,4], S. Lu[1,2], L.Fabbietti[1,2], and the FOPI and HADES collaboration[1]

[1]Physik Department E62, TUM,D-Garching; [2]Excellence Cluster Universe 'Origin and Structure of the Universe',D-Garching; [3]Institut für Kernphysik, Goethe Unversität,D-Frankfurt; [4]CERN,CH-Geneve

The production of strangeness in elementary proton-proton collisions is of interest for different field in hadron physics. On the one hand an accurate description of the production mechanism is required for transport model calculations. The major ingredient for the description of strangeness production are the energy dependent cross section, the branching ratio and non-isotropic production distributions. Especially at energies in the low GeV range the production of the p+K^++Λ final state can occur through deveral different resonant and non-resonant intermediate channels, especially N^{*+} resonances [1]. Furthermore, a better understanding of the non-resonant production mechanism also including p-Λ final state interaction is necessary.

Recently the last years a campaign was started to analysis the production mechanism using Partial Wave Analysis methods, to understand the contributions of different possible production channels including also interference between the different waves. The approach of a combined analysis is to fit e measured data from several experiments for the p$K^+\Lambda$ final state, to determine a description of all data sample with one set of transition amplitudes.

The experimental data and the corresponding beam energy used for this analysis are listed in Table 1. The extraction

experiment	E_{Beam} (GeV)
DISTO [2]	2.14
COSY-TOF -TOF [3]	2.16
DISTO [2]	2.5
DISTO [2, 4]	2.85
FOPI [5]	3.1
HADES [6]	3.50

Table 1: List of available experimental data for the reaction p+p→p$K^+\Lambda$.

of the exclusive events are explained elsewhere [2, 3, 5, 6]. The analysis of these experimental data is performed using the Bonn-Gatchina PWA Framework (BG-PWA) [8]. In this framework non-resonant and resonant production channels are included. The main resonant contribution is via intermediate N^{*+} , which are parametrized by a relativistic Breit-Wigner formula. The N^{*+} resonances, which are used in the analysis are given in Table 2. In case the final state consists of three particle the Λ and the proton form

Resonance	J^P	M (GeVc^{-2})	Γ (GeVc^{-2})
$N^{*+}(1650)$	$\frac{1}{2}^-$	1.655	0.150
$N^{*+}(1710)$	$\frac{1}{2}^+$	1.710	0.100
$N^{*+}(1720)$	$\frac{3}{2}^+$	1.720	0.250
$N^{*+}(1875)$	$\frac{3}{2}^-$	1.875	0.220
$N^{*+}(1880)$	$\frac{1}{2}^+$	1.870	0.235
$N^{*+}(1895)$	$\frac{1}{2}^-$	2.090	0.090
$N^{*+}(1900)$	$\frac{3}{2}^+$	1.900	0.250

Table 2: N^{*+} resonances included in the Partial Wave Analysis written in the spectroscopic notation with their the mass and the width, taken form [7].

a two particle pΛ -subsystem. Via this formalism, the final state interaction can be parametrized by an effective range parametrization:

$$A^{\beta}_{2b} = \frac{\sqrt{s_i}}{1 - \frac{1}{2} r^{\beta} q^2 a^{\beta}_{p\Lambda} + \mathrm{i} q a^{\beta}_{p\Lambda} q^{2L}}, \qquad (1)$$

where q is the relative momentum between the baryons in the two particle subsystem and multi index β denotes possible combinations of quantum numbers.. $a^{\beta}_{p\Lambda}$ is the pΛ-scattering length and r^{β} is the effective range of the Λ-p system. F(q,r,L) is the Blatt-Weisskopf factor, which is used for normalization (with F(q,r,L=0)=1)[8]. For this analysis only Wave with p-Λ in L=0 are consider for final state interaction.

This Analysis allows to extract the excitation function of N^{*+} resonances. The results of this analysis of the successful analysis will be published in the near future.

References

[1] S. Abd El-Samad, et al: Phys.Lett. B688 (2010)

[2] M.Maggiora et al.: Nucl.Phys. A835 (2010); M.Maggiora et al: Nucl.Phys. A691 (2001)

[3] M.Roeder et al: Eur. Phys. J. A49 (2013)

[4] F.Balestra et al: Phys.Rev.Lett. 83 (1999)

[5] R.Muenzer: PhD Thesis, TU Munich (2014);

[6] E.Epple: PhD Thesis, TU Munich (2014);G. Agakishiev et al.: Physics Letters B742 (2015)

[7] K.A. Olive et al., Chin. Phys. C38 (2014)

[8] Anisovich, A.V. and Sarantsev, A.V.: Eur.Phys.J. A30 (2006); A.V. Anisovich, et al.: Eur.Phys.J. A47 (2011); K.N. Ermakov et al.: Eur.Phys.J. A47 (2011)

*Work supported by supported by the DFG Project FA 898/2-1, BMBF 05P12WOGHH, Excellence Cluster Universe, GSI(HADES),GSI(HADES)

DOI:10.15120/GR-2016-1

PWA study of cusp in p + p → p + K^+ + Λ with Flatté distribution*

S. Lu[1,2], *R. Münzer*[1,2], *E. Epple*[1,2], *L. Fabbietti*[1,2], *J. Ritman*[3], *E. Roderburg*[3], *F. Hauenstein*[3], *and M. Maggiora*[4]

[1]Physik Department E62, Technische Universität München, 85748 Garching; [2]Excellence Cluster 'Origin and Structure of the Universe', 85746 Garching; [3]Forschungszentrum Jülich; [4]University of Torino

In the last years, the strangeness production in nucleon-nucleon collisions has attracted interest. In a new analysis campaign, a combined PWA analysis of the HADES and FOPI data togehter with data sets measured at the DISTO and COSY-TOF experiment will be performed. The description of all the production channels, that can contribute to the p K^+ Λ final state, requires a special analysis framework. For the analysis, the Bonn-Gatchina Partial Wave Analysis (PWA) framework is used [3]. In this framework the transition amplitude from an initial wave to a final state is parameterized as a function of the energy and phase. The wave functions of different transitions with the same quantum numbers can mix, which leads to interference. Amplitudes and phase parameters of these transitions have to be determined by PWA.[4]

In addition to the Λp FSI and N^* resonance excitation effects a pronounced narrow structure is observed in the Dalitz plot and in its projection on the pΛ-invariant mass. This peak structure appears at the p + p → N + K^+ + Σ threshold and is interpreted as ΣN cusp effect. For a description of the experimental data by using the BG-PWA, the first approach was to use a Breit-Wigner parametrization. Since Breit-Wigner is a rather simplified approximation, Flatté-like parametrization[1] has been considered too. This takes into account the coupling strength of Λp and Σp. The amplitudes A of partial waves are then parametrized by:

$$A = \frac{C\sqrt{\Gamma_{p\Lambda}\Gamma_0}}{(M^2 - s - \mathrm{i}(\Gamma_{p\Lambda} + \Gamma_{p\Sigma})M)}, \quad (1)$$

$$\Gamma_{\Lambda p} = g_{\Lambda p} * q_{\Lambda p}, \Gamma_{\Sigma p} = g_{\Sigma p} * q_{\Sigma p}. \quad (2)$$

In our work, we are using PWA to simulate the cusp structre and trying to explore the influence of ratio of two coupling strength, which may help to contribute the deeper physical understanding of this peak structure. In the single data analysis it was shown that no unique solution can be derived but ambiguities appear for the weights of the contributing channels. However, more than one data sample is used and processed by PWA at same time, one can reduce ambiguieties. This method is called combined data analysis.

In figure 1 the invariant mass of pΛ of the experimental distribution (black data points) and the results of the PWA fit (red histogram) are shown. Only statistical errors are shown. A good agreement between experimental data and PWA simulation where the cusp contribution has been parametrized with a Flatté function is shown and a combined data analysis for four data samples has been carried out.

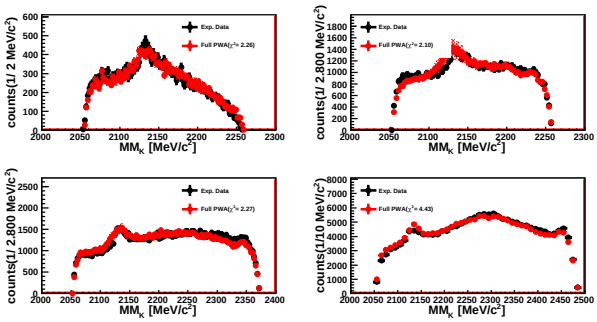

Figure 1: Invariant-mass systems of pΛ for COSY-TOF@2.16GeV, DISTO@2.14GeV, DISTO@2.5GeV and DISTO@2.85GeV in a combined data analysis.The black dots are experimental results and blue solid curve is the analysis in BG-PWA using Flatté paramtriztion.[5]

The present work is dedicated to the PWA analysis of the exclusive events from pp collision measured by various collaborations. The main work is focused on describing the NΣ cusp phenomenon, which appears in the experimental data, by using Flatté paramaterization on BG-PWA Framework. The PWA analysis give a nice agreement with experimental data for various data sets, however, it can be seen that the PWA results obtained for a single energy are not unique between several data sets. The combined data analysis has shown a good fitting result and it offers a consistent parameters like coupling constants and resonant mass, which could be further used to calculate the scattering lengths for production channels, etc.

References

[1] S.Abd El-Samad *et al.*, arXiv nucl-ex (2012) 1206.0426

[2] S. M. Flatté, Phys. Lett. B 63 (1976) 224

[3] A.V. Sarantsev et. al., Eur.Phys.J. A25,2005,441-453

[4] R. Muenzer, GSI report (2015)

[5] S,Lu, Master thesis, TUM,(2016)

* Work supported by DFG Projekt FA 898/2-1

DOI:10.15120/GR-2016-1

Measurements of the low mass dielectron continuum in pp and Pb-Pb collisions with the ALICE experiment at the LHC*

A. Chauvin[1,2], *T. Dahms*[†1,2], *A. Dashi*[1,2], *O. Vázquez Doce*[1,2], *and I. Vorobyev*[1,2]

[1]Excellence Cluster Universe, Technische Universität München, Garching, Germany; [2]Physik Department, Technische Universität München, Garching, Germany

Introduction

Heavy-ion collisions at ultrarelativistic energies allow us to study nuclear matter under extreme conditions and explore the QCD phase diagram for new and possibly deconfined states of matter. Electron-positron pairs (dielectrons) are created during all stages of such collisions. As they do not possess colour charge, they carry information about the medium properties at the time of production unperturbed by strong final-state interactions to the detector. They are hence the only probe of a possible chiral-symmetric phase, predicted by lattice QCD calculations to exist at temperatures similar to the deconfinement temperature. The most prominent signature would be a modification of the ρ spectral function, as observed at lower collision energies by CERES and NA60 at the SPS [1, 2] as well as PHENIX and STAR at RHIC [3, 4]. Furthermore, thermal dilepton radiation provides access to the earliest temperatures of the system.

The extraction of interesting physics signals in the dielectron continuum requires not only a precise understanding of the physics background from hadron decays—Dalitz decays of light pseudoscalar mesons, resonance decays of vector mesons, and semileptonic decays of heavy flavour mesons— but also of the much larger combinatorial background of correlated and uncorrelated origin. The opposite-sign background yield (B_{+-}) is determined via the geometric mean of the same-sign pair yields (N_{++} and N_{--}):

$$B_{+-} = 2\sqrt{N_{++}N_{--}}. \quad (1)$$

Small acceptance differences between same-sign and opposite-sign pairs introduced by the detector geometry can be corrected utilising the fact that any deviation from (1) in mixed events must originate from acceptance differences. Thus, the signal is calculated as:

$$S = N_{+-} - 2\sqrt{N_{++}N_{--}} \times \frac{M_{+-}}{2\sqrt{M_{++}M_{--}}}, \quad (2)$$

where M denotes mixed event pair yields.

The measurement of the dielectron continuum in pp collisions serves as crucial reference and test of our understanding of the hadron decay background, estimated by a "hadron cocktail".

Ongoing Efforts

The dielectron measurements are performed in the central barrel spectrometer of ALICE [5] and utilise the excellent PID capabilities of ALICE by combining energy loss information in the time projection chamber and the inner tracking system with time-of-flight measurements. Our group is leading the analyses on the data samples of pp collisions at a centre-of-mass energy of $\sqrt{s} = 13\,\text{TeV}$, including a triggered sample of events with high charged-particle multiplicities, and Pb-Pb collisions at $\sqrt{s_{NN}} = 5.02\,\text{TeV}$, collected in 2015. It should be highlighted that the pp data were also stored at the GSI storage facility, which allowed us to perform the analysis of these data at the GSI National Analysis Facility.

Our group is actively involved in all aspects of the dielectron analysis. For the first time, the hadron contamination of the dielectron signal was measured as a function of the invariant mass. We have studied possibilities to further improve the rejection of photon conversion pairs using, e.g. their particular angular distributions. The hadron cocktail, used to estimate the signal contribution from hadron decays, was improved in various ways, e.g. by including the possibility to polarise the hadrons. A dedicated pp run with lowered magnetic field ($B = 0.2\,\text{T}$) was analysed with goal to increase the low-momentum electron acceptance in the time-of-flight detector relative to the nominal field strength of $B = 0.5\,\text{T}$. This serves as feasibility study for a dedicated future heavy-ion run with such a field configuration to increase the low mass and p_T dielectron acceptance. First raw signal spectra in pp collisions at $\sqrt{s} = 13\,\text{TeV}$ and Pb-Pb collisions at $\sqrt{s_{NN}} = 5.02\,\text{TeV}$ were produced. While in pp collisions, the invariant-mass spectrum was measured up to $3.5\,\text{GeV}/c^2$, only 10% of the Pb-Pb data have been reconstructed so far. On this sample, one can already achieve a statistical signal significance of $\approx$1, comparable to the one achieved on the full 2011 Pb-Pb sample.

References

[1] CERES Collaboration, Phys. Rev. Lett. **75** (1995) 1272.

[2] NA60 Collaboration, Phys. Rev. Lett. **96** (2006) 162302.

[3] PHENIX Collaboration, Phys. Rev. C **93** (2016) 014904.

[4] STAR Collaboration, Phys. Rev. Lett. **113** (2014) 022301. Addendum: [Phys. Rev. Lett. **113** (2014) 049903].

[5] ALICE Collaboration, JINST **3** (2008) 08002.

* Work supported by the DFG cluster of excellence "Origin and Structure of the Universe".

† torsten.dahms@cern.ch

Transverse momentum spectra in pp collisions at $\sqrt{s} = 13$ TeV*

A. Andronic[1], *T. Drozhzhova*[1,4], *J. Gronefeld*[1,2], *M. Ivanov*[1], *M.L. Knichel*[3], *P. Lüttig*[4], *S. Masciocchi*[1], *J. Otwinowski*[5], *E. Perez Lezama*[1,4], *K. Schweda*[1], *F. Sozzi*[1], *A. Toia*[1,4]
for the ALICE Collaboration

[1]EMMI & GSI Darmstadt; [2]Technical University Darmstadt; [3]University of Heidelberg; [4]Goethe University Frankfurt; [5]Institute of Nuclear Physics, PAS, Cracow

We present the transverse-momentum ($p_{\rm T}$) distributions of primary charged particles measured in proton-proton collisions at the centre-of-mass energy $\sqrt{s} = 13$ TeV with the ALICE detector at the LHC. Primary particles are defined as prompt particles produced in the collisions, including all decay products, with the exception of those from weak decays of strange particles. The measurement has been performed [1] in events having at least one charged particle produced with $p_{\rm T} > 0$ in the pseudorapidity interval $|\eta| < 1$ (an event class denoted INEL>0).

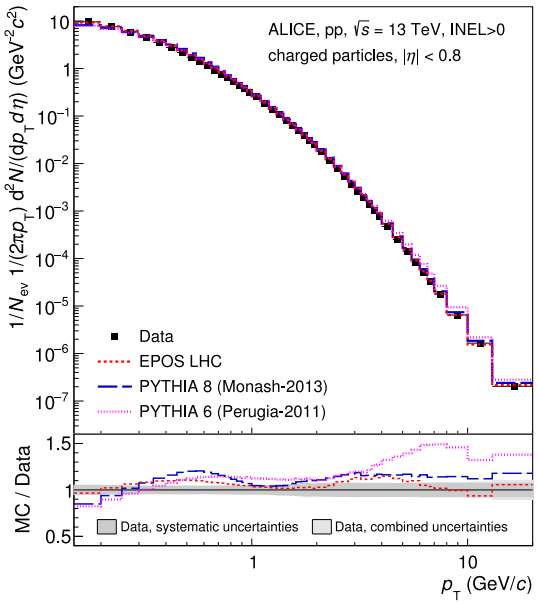

Figure 1: Invariant charged-particle yield as a function of $p_{\rm T}$ normalised to INEL>0 events. The data are compared to calculations with Monte Carlo event generators [2, 3].

Figure 1 presents the measured $p_{\rm T}$ spectrum and its comparison with calculations with PYTHIA 6 (Perugia-2011 tune), PYTHIA 8 (Monash-2013 tune) and EPOS LHC. For bulk particle production, the mechanism of colour reconnection is an important one in the PYTHIA models [2]. EPOS is a model based on the Gribov-Regge theory at parton level. Collective (flow-like) effects are treated via parametrisations in the EPOS LHC version [3]. These event generators, benefitting from the tuning performed on the LHC data in Run 1, describe the $p_{\rm T}$ spectrum reasonably well, although not in detail. It is interesting to note that both PYTHIA 8 and EPOS LHC models show a similar pattern in the ratio to data, with discrepancies up to 20% and that PYTHIA 6 overestimates particle production at high $p_{\rm T}$.

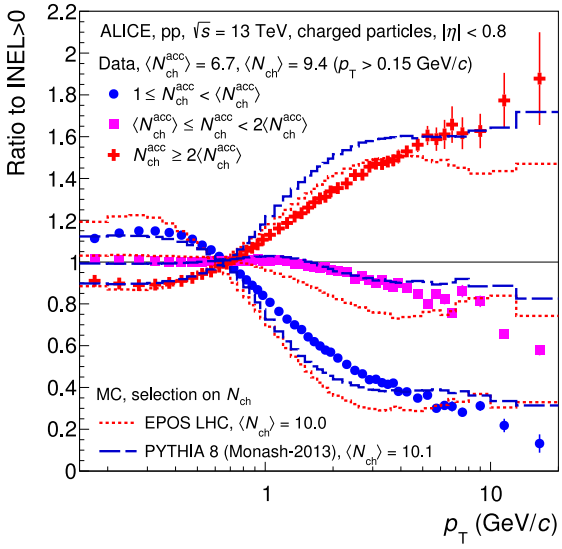

Figure 2: Ratios of transverse-momentum distributions of charged particles in three intervals of multiplicities to the respective one for inclusive (INEL>0) collisions. The spectra were normalised by the integral prior to division.

Figure 2 shows the ratio of spectra measured in three intervals of multiplicity to the inclusive (INEL>0) spectrum. The selection is performed on the multiplicity measured in the same kinematic region as the spectrum, $|\eta| < 0.8$ and $0.15 < p_{\rm T} < 20$ GeV/c , using the measured track multiplicity $N_{\rm ch}^{\rm acc}$ for data and the true value of $N_{\rm ch}$ known in Monte Carlo events. The data in Fig. 2 show that the correlation of the spectrum with multiplicity is prominent for the whole $p_{\rm T}$ range and in particular that it is stronger at high $p_{\rm T}$. In first order, this correlation arises naturally from jets, giving the leading high-$p_{\rm T}$ hadron and a significant contribution to multiplicity. The general features seen in the data are reproduced by PYTHIA 8 and EPOS LHC fairly well, but some disagreements are noticeable too, in particular in the $p_{\rm T}$ region of a few GeV/c .

References

[1] ALICE Collaboration, Phys. Lett. **B753** (2016) 319.

[2] T. Sjöstrand, arXiv:1310.8073.

[3] T. Pierog et al., Phys. Rev. **C92** (2015) 034906.

* Work supported by GSI, BMBF, EMMI, H-QM, and HGS-HIRe

DOI:10.15120/GR-2016-1

Charged-particle multiplicity density at mid-rapidity measured by ALICE in LHC Run 2 *

A. Toia[†1,2], *F. Sozzi*[1,3], *T. Drozhzhova*[1,2], *E. Perez Lezama*[1,2], *J. Gronefeld*[1], *and the ALICE Collaboration*

[1]GSI, Darmstadt; [2]Goethe University, Frankfurt; [3]FIAS, Frankfurt

The measurement of the inclusive production of charged hadrons in high-energy proton-proton or nucleus-nucleus interactions is a key observable to characterise the global properties of the collision. Particle production at collider energies originates from the interplay of perturbative (hard) and non-perturbative (soft) QCD processes. Soft scattering processes and parton hadronisation dominate the bulk of particle production at low transverse momenta and can only be modelled phenomenologically. Hence, these measurements provide constraints for a better tuning of models and event generators. Moreover, in case of nucleus-nucleus collisions, it carries an important relation to the collision geometry, i.e. the overlap region of the colliding nuclei.

The data presented here were recordered in 2015, when after a two-year long shutdown, the Large Hadron Collider (LHC) restarted operation delivering pp collisions at $\sqrt{s}$ = 13 TeV and Pb–Pb collisions at $\sqrt{s_{\rm NN}}$ = 5.02 TeV, which are the highest energies ever achieved in the laboratory. The data were collected using a minimum-bias trigger based on the coincidence of hits in two scintillator detectors (called V0), covering the full azimuth and more than 4 units of pseudorapidity, in the ranges $2.8 < \eta < 5.1$ and $-3.7 < \eta < -1.7$, respectively. Their timing information is also used offline to remove contamination from background events. Events used for the data analysis are further required to have a valid reconstructed vertex within $|z| < 10$ (7) cm in pp (Pb–Pb) collisions. The measurement relies on the Silicon Pixel Detector (SPD), two arrays of pixels arranged with an approximate cylindrical geometry at radii of 3.9 and 7.6 cm covering intervals of $|\eta| < 2.0$ and $|\eta| < 1.4$ for the inner and outer layers, respectively. The $\mathrm{d}N_{\rm ch}/\mathrm{d}\eta$ measurement is performed using short track segments, called tracklets, built using the position of the reconstructed primary vertex and two hits, one in each SPD layer. The charged-particle pseudorapidity density is obtained from the measured distribution of tracklets, corrected for the acceptance and efficiency for a primary particle to produce a tracklet, and the contamination of reconstructed tracklets from combinations of hits not produced by the same primary particle.

For pp collisions, we report a measurement for inelastic events (INEL) and events having at least one charged particle in the pseudorapidity interval $|\eta| < 1$ (INEL>0). Figure 1 shows the average charged-particle density distribution $\langle \mathrm{d}N_{\rm ch}/\mathrm{d}\eta \rangle$ measured in pp collisions for INEL and INEL>0 events in the pseudorapidity range $|\eta| <$ 1.8. Also shown in the Figure are the results recently published by the CMS Collaboration for inelastic collisions, which agree, within the uncertainties, with the ALICE measurement. We compare our measurement to Monte Carlo calculations performed with PYTHIA 6 (Perugia-2011), PYTHIA 8 (Monash-2013) and EPOS LHC in both the INEL and INEL>0 event classes. PYTHIA 6 calculations are in better agreement with the data than PYTHIA 8 in both classes. EPOS LHC calculations are sligthly higher than the data both in INEL and INEL>0 events [1]. Figure 2 shows a compilation of results on pseudorapidity density of charged particles measured at central rapidity ($|\eta| < 0.5$) at different collider energies for pp and A–A collisions. The energy dependence of $\langle \mathrm{d}N_{\rm ch}/\mathrm{d}\eta \rangle$ is parametrised by the power law function fitted to data. Although the fit results assume that uncertainties at different centre-of-mass energies are independent, which is not strictly the case, the new measuremnt seems to be in line with the expectations from the data measured at lower energy.

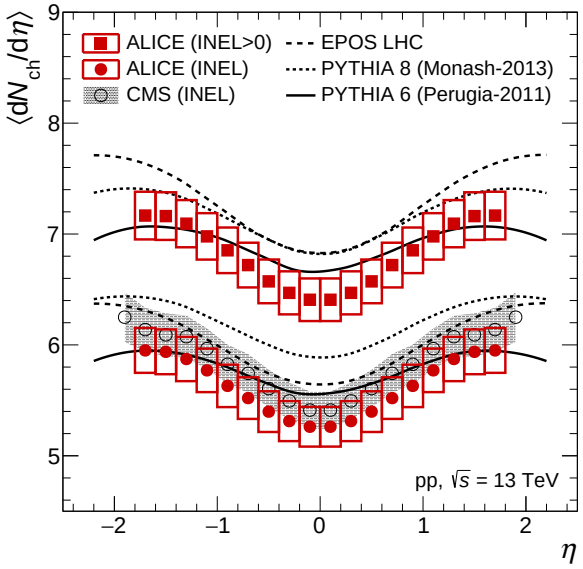

Figure 1: Average pseudorapidity density of charged particles as a function of η produced in pp collisions at $\sqrt{s}$= 13 TeV. The ALICE results are shown in the normalisation classes INEL and INEL>0 and compared to Monte Carlo calculations and to the results from the CMS Collaboration [3]. The uncertainties are the quadratic sum of statistical and systematic contributions. [1]

For Pb–Pb collisions, the charged particle multiplicity

* Work supported by GSI/BMBF/Goethe University Frankfurt/EMMI/HIC4FAIR/HGS-HIRe/H-QM

† a.toia@gsi.de

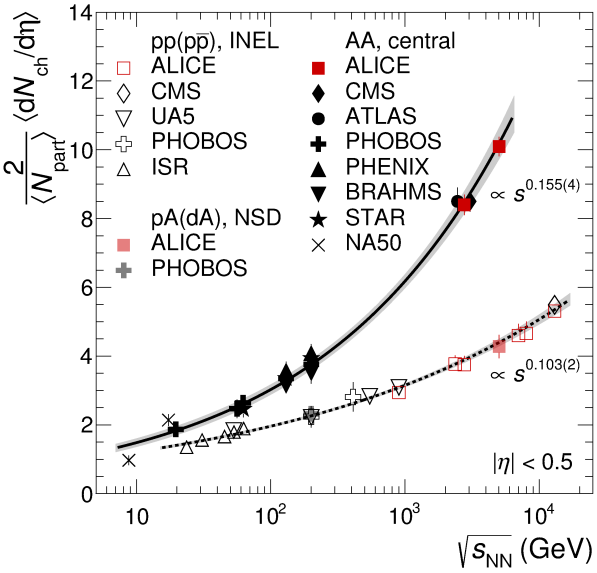

Figure 2: Values of $\frac{2}{\langle N_{\rm part}\rangle}\langle {\rm d}N_{\rm ch}/{\rm d}\eta\rangle$ for central Pb–Pb and Au–Au collisions (see text) as a function of $\sqrt{s_{\rm NN}}$. Measurements for inelastic pp and p$\overline{\rm p}$ collisions as a function of $\sqrt{s}$ are also shown along with those from non-single diffractive p–A and d–A collisions. The s-dependences of the AA and pp (p$\overline{\rm p}$) collision data are well described by the functions $s_{\rm NN}^{0.155}$ (solid line) and $s_{\rm NN}^{0.103}$ (dashed line), respectively. The shaded bands show the uncertainties on the extracted power-law dependences. The central Pb–Pb measurements from CMS and ATLAS at 2.76 TeV have been shifted horizontally for clarity [2].

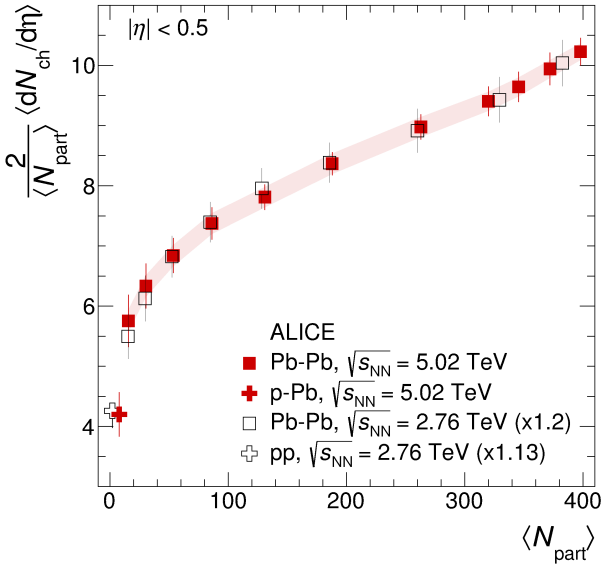

Figure 3: The $\frac{2}{\langle N_{\rm part}\rangle}\langle {\rm d}N_{\rm ch}/{\rm d}\eta\rangle$for Pb–Pb collisions at $\sqrt{s_{\rm NN}}$ = 5.02 TeV in the centrality range 0–80%, as a function of $N_{\rm part}$ in each centrality class. The error bars indicate the point-to-point centrality-dependent uncertainties whereas the shaded band shows the correlated contributions. Also shown is the result from non-single diffractive p–Pb collisions at the same $\sqrt{s_{\rm NN}}$. Data from lower energy (2.76 TeV) Pb–Pb and pp collisions , scaled by a factor of 1.2 and 1.13 respectively, are shown for comparison. The error bars for p–Pb at $\sqrt{s_{\rm NN}}$ = 5.02 TeV and lower energy Pb–Pb and pp collisions indicate the total uncertainty [2].

is studied as a function of the centrality. The classification of events into centrality classes is done by using the amplitudes of the signals in the V0 detector. The V0 distribution is fitted using a phenomenological approach based on the Glauber Monte Carlo plus a convolution of a model for the particle production and a negative binomial distribution. This creates a connection between an experimental observable and the geometrical model of nuclear collisions used in the MC-Glauber, from which we can access the number of nucleons participating in the collision, $N_{\rm part}$. The analysis is restricted to the 80% most central events, to avoid trigger inefficiency and contamination by electromagnetic processes.

In order to compare bulk particle production at different energies and in different collision systems, the charged-particle density calculated with the tracklet method in various centrality classes, defined by V0, is divided by the average number of participating nucleon pairs, $\langle N_{\rm part}\rangle/2$, calculated with the MC-Glauber for centrality classes defined by classifying the events according to their impact parameter. In Figure 2 we also show a compilation of data for central Pb–Pb and Au–Au collisions from experiments at LHC, RHIC and SPS, together with the new measurement at 5.02 TeV. The dependence of $\frac{2}{\langle N_{\rm part}\rangle}\langle {\rm d}N_{\rm ch}/{\rm d}\eta\rangle$ on the center-of-mass energy confirms the trend established by lower energy data. It is much stronger than the one measured for pp and even for p–Pb collisions, which fall on the curve for proton–proton collisions, indicating that the strong rise in AA is not solely related to the multiple collisions undergone by the participants since the proton in p–A collisions also encounters multiple nucleons [2].

The multiplicity shows a strong dependence on the centrality (Figure 3) with $\frac{2}{\langle N_{\rm part}\rangle}\langle {\rm d}N_{\rm ch}/{\rm d}\eta\rangle$ decreasing by a factor 1.8 from the most central collisions, large $\langle N_{\rm part}\rangle$, to the most peripheral, small $\langle N_{\rm part}\rangle$, and a smooth trend towards the value measured in minimum bias p–Pb collisions. The centrality dependence of ${\rm d}N_{\rm ch}/{\rm d}\eta$ is nearly identical to that measured at $\sqrt{s_{\rm NN}}$ = 2.76 TeV, which showed to be very similar to those measured at RHIC, pointing to a similar mechanism of particle production independent of energy.

References

[1] ALICE Collaboration, Phys. Lett. B 753 (2016) 319-329, 2015.

[2] ALICE Collaboration, arXiv:1512.06104, 2015.

[3] CMS Collaboration, arXiv:1507.05915, 2015.

DOI:10.15120/GR-2016-1

Upgrade of the ALICE Time Projection Chamber*

D. Miśkowiec†, J. Hehner, L. Karayan, S. Masciocchi, T. Morhardt, C. J. Schmidt, and B. Voss
GSI, Darmstadt, Germany

ALICE (A Large Ion Collider Experiment) is one of the four large experiments at the CERN LHC. It was designed and built with the aim of studying collisions between lead ions and learning about the properties of the extreme matter created therein. The experiment successfully took data from pp, Pb–Pb, and p–Pb collisions during the LHC Run 1 at half of the nominal LHC beam energy, and continues its studies at (nearly) full energy in the Run 2. A significant increase of luminosity is planned for Run 3 (Table 1).

run	period	$\sqrt{s_{\mathrm{NN}}}$	rate
LHC Run 1	2009–2013	2.76 TeV	4 kHz
LHC Run 2	2015–2018	5.02 TeV	10 kHz
LHC Run 3	2021–2023	∼5 TeV	50 kHz

Table 1: Energy and rate of Pb–Pb collisions at the LHC.

The ALICE Time Projection Chamber (TPC) is the main tracking and particle-identification detector of the Central Barrel which covers midrapidity $-0.9 < \eta < 0.9$ and the full azimuth $0 < \varphi < 2\pi$ (Fig. 1). Charged particles traversing the TPC volume ionize gas (Ne–CO_2). The ionization electrons drift away from the central electrode to one of the two endplates, each equipped with 18 inner and 18 outer readout chambers (IROCs and OROCs). The chambers measure the position, arrival time, and charge of the arriving electron cloud.

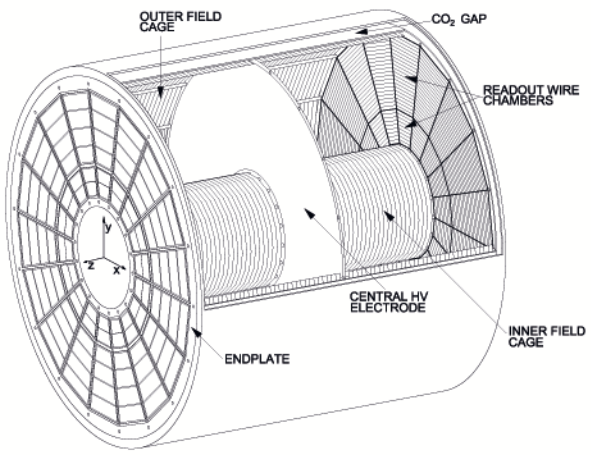

Figure 1: The ALICE TPC at the Large Hadron Collider. Each endplate is equipped with 36 readout chambers.

The present readout chambers are of the multiwire type (Fig. 2). The gating grid is made transparent (by setting it to a voltage matching the drift potential) after each trigger. 100 μs later, when all ionization electrons reached the anode plane, the gating grid is closed (by applying to its wires alternating voltages) and blocks slow positive ions created around the anode wires from entering the sensitive volume of the TPC and distorting the drift field. The gating grid is fully transparent to electrons and suppresses the backflowing ions by a factor of 800, but the pulsing mode of operation limits the event-taking rate to 3 kHz.

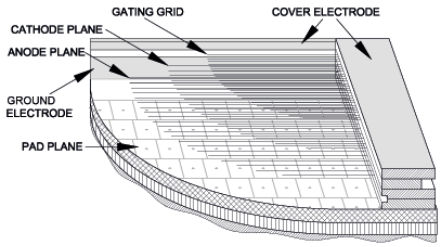

Figure 2: Readout chambers of the ALICE TPC used in Run 1 and Run 2. The gating grid is opened for the arriving electrons and subsequently closed, preventing the ions produced at the anodes from entering the drift volume.

In order to avoid the dead time caused by the gating grid and to record the data at rates appropriate for the LHC Run 3, the existing wire chambers will be replaced by GEM-based ones [1, 2]. GEM, Gas Electron Multiplier, is a kapton foil with thin layers of Cu coating on both sides to which a voltage of 200-400 V is applied. The electrons are accelerated and multiplied in the holes of the GEMs (Fig. 3). A stack of 4 GEMs results in a gas gain of 2000 and, by a special configuration of voltages across the GEMs

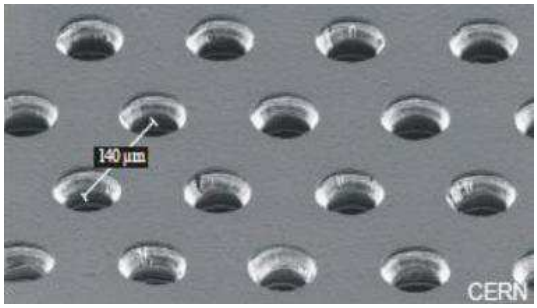

Figure 3: Gas Electron Multiplier (GEM) foil.

* Work supported by GSI, BMBF, EMMI, H-QM, and HGS-HIRe.
† d.miskowiec@gsi.de

DOI:10.15120/GR-2016-1

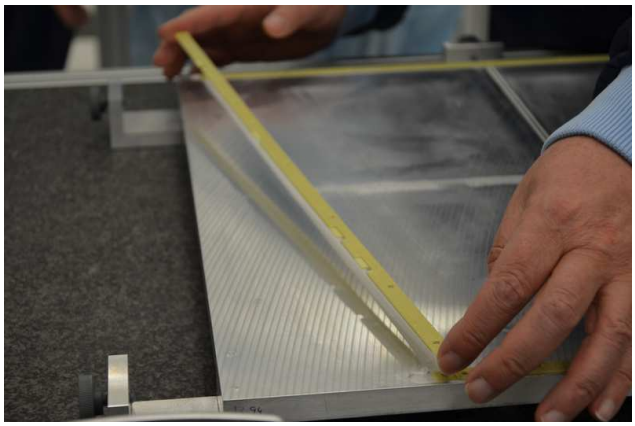

Figure 4: GEM framing - preparation of the Vetronit frame. An aluminum jig ensures alignment and stability during curing.

and between them, suppresses the back-flowing ions by a factor of 100.

The production of the new readout chambers will take two years and is about to start. Building the outer readout chambers (OROCs) will involve a lot of logistics. The GEM foils will be produced at CERN and subsequently travel to Helsinki or Budapest for quality assurance tests. Certified foils will be sent to Munich, Bonn, and GSI where they will be glued to thin frames made of Vetronit. The leakage current of the foils will be checked before and after gluing. In parallel, the aluminum bodies with padplanes will be produced, assembled, and tested for gas tightness in Heidelberg and Frankfurt. Finally, complete OROCs will be assembled at two sites, in Bucharest and at GSI. The smaller IROC chambers will be built in the USA.

GSI assumes two important roles in the chamber production chain. The framing of all GEM foils of type OROC3 (the largest foils in the project) and the assembly of half of all OROC chambers will be performed here. A working group consisting of members of the ALICE group and the

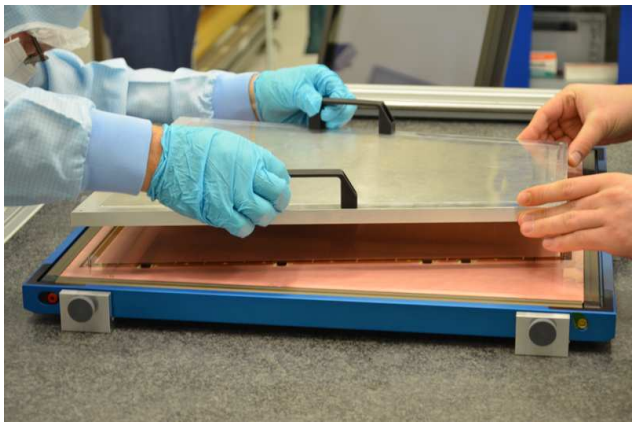

Figure 5: GEM framing - gluing of the GEM foil to the frame. The foil is stretched and pressed against the frame.

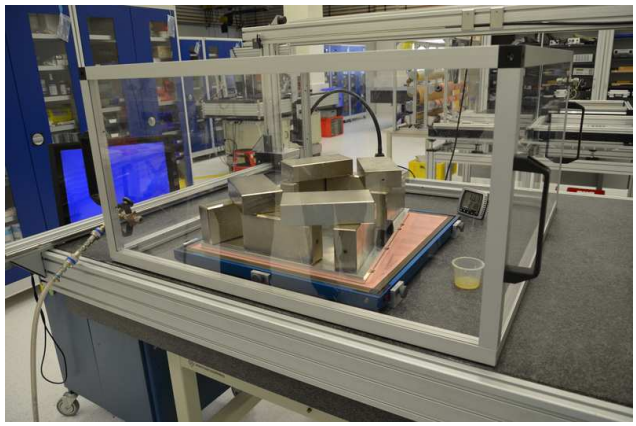

Figure 6: GEM framing - curing. The foil is kept under tension. The humidity is reduced by flushing with nitrogen.

detector lab is currently defining the procedures and acquiring/setting up the necessary equipment. In December 2015 a first framing session took place in the GSI detector lab. Two IROC foils (smaller than the planned OROC3 foils) were framed (Figs. 4, 5, 6).

The leakage current measurement is essential to assess the quality and cleanliness of a GEM foil. It is performed by applying 500 V to each of the sectors of the GEM and measuring the current (Fig. 7). A current of 1 nA is acceptable for a sector of 100 cm^2. The test will be automatized during the main production.

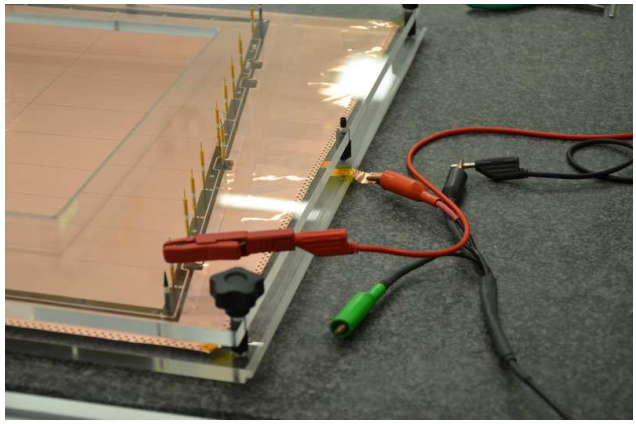

Figure 7: GEM framing session at GSI in December 2015: leakage current test. With 500 V applied to the GEM, the leakage current should be of the order of 1 nA.

References

[1] ALICE Collaboration, Technical Design Report for the Upgrade of the ALICE TPC, CERN-LHCC-2013-020, https://cds.cern.ch/record/1622286

[2] ALICE Collaboration, Addendum to the Technical Design Report for the Upgrade of the ALICE TPC, ALICE-TDR-016-ADD-1, https://cds.cern.ch/record/1984329

DOI:10.15120/GR-2016-1

ALICE in the first year of Run 2 at the LHC*

The ALICE Collaboration

After a very successful first running period CERN's Large Hadron Collider (LHC) was turned off in 2013 for a planned long shutdown (LS1) during which not only the accelerator itself but also the experiments went through a substantial consolidation process in preparation for Run 2 which started in spring 2015.

The dedicated heavy-ion experiment ALICE was completed in terms of detector installation during LS1. The last five super modules of the transition radiation detector (TRD) were installed during LS1 such that now the TRD covers the full azimuth. Six super modules of the new dijet calorimeter and one additional module of the photon spectrometer calorimeter were integrated into ALICE extending the electromagnetic calorimeter system substantially. Also the key detector for the measurement of charged-particle trajectories in ALICE, the time projection chamber (TPC), for which the ALICE group at GSI holds major responsibility, was subject to important consolidation work during LS1. The gas mixture in the TPC was changed from Ne(90):CO_2(10) to Ar(90):CO_2(10) which results in a more stable performance in high particle-flux operation without a significant degradation of momentum resolution. Also the TPC read-out electronics was redesigned. With the new hardware, which was installed during the winter shutdown, the read-out rate will increase substantially in 2016, in particular for heavy-ion running.

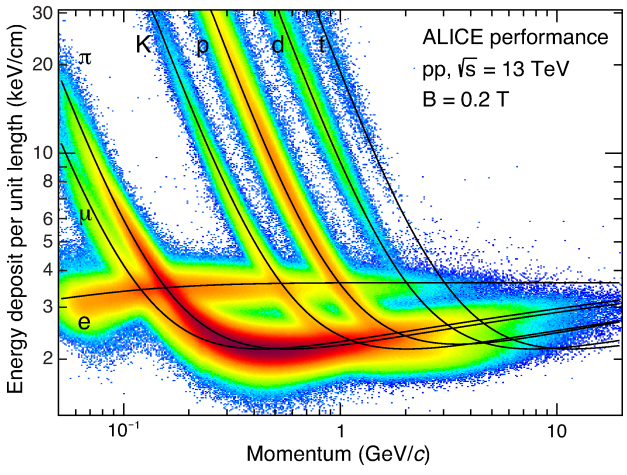

Figure 1: Specific energy loss $\mathrm{d}E/\mathrm{d}x$ measured as a function of charged-particle momentum with the ALICE TPC [1]. The solid lines indicate parametrizations of the expected mean energy loss.

The physics program was restarted at the LHC in June 2015 with proton collisions at $\sqrt{s} = 13$ TeV, the highest collision energy ever reached in the laboratory. During this running period with proton beams until October 2015 the consolidated ALICE apparatus has performed exceptionally well. As an example, Fig. 1 shows the specific energy loss measured with the TPC as a function of charged-particle momentum in an exploratory run at reduced magnetic field (B = 0.2 T, instead of the nominal 0.5 T).

The first heavy-ion running period in Run 2 took place during three weeks in November and December 2015. For the first time, lead nuclei were brought to collision at an energy above one PeV (see Fig. 2). In the most central Pb-Pb collisions, in which an unprecedented energy density above 20 GeV/fm^3 is reached, more than 25.000 charged particles are produced [2] and substantial anisotropic flow coefficients are measured [3].

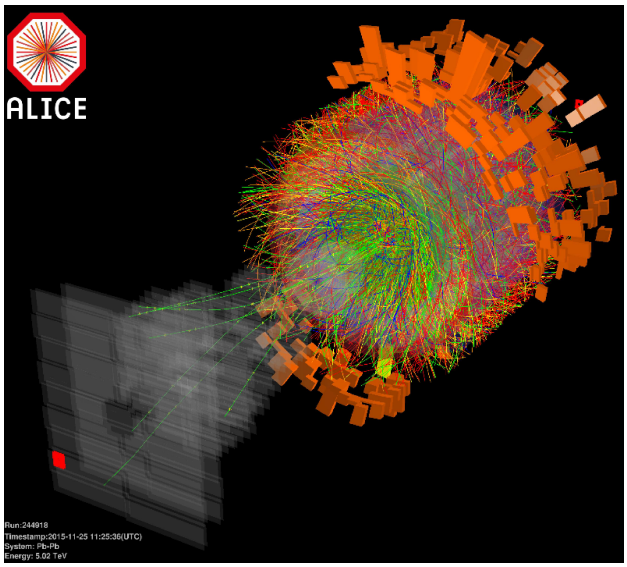

Figure 2: ALICE event display of a central Pb-Pb collision at $\sqrt{s_{\mathrm{NN}}} = 5.02$ TeV.

References

[1] ALICE Collaboration, ALICE-PUBLIC-2015-004

[2] ALICE Collaboration, arXiv:1512.06104

[3] ALICE Collaboration, Phys. Rev. Lett. **116**, 132302 (2016)

* Work supported by GSI, BMBF, EMMI, H-QM and HGS-HIRe

Influence of N_2 and H_2O admixtures on the mobility of ions in Ne-CO_2

A. Deisting[*1,2], *C. Garabatos*[1], *A. Szabo*[3], *and D. Vranic*[2]

[1]GSI Helmholtzzentrum für Schwerionenforschung GmbH, Darmstadt, Germany; [2]Physikalisches Institut, Ruprecht-Karls-Universität Heidelberg, Heidelberg, Germany; [3]Faculty of Mathematics, Physics and Informatics, Comenius University, Bratislava, Slovakia

Introduction

In gaseous detectors ions are created during the primary ionisations as well as during the gas amplification. Accumulating ions and the corresponding space charge can impose a great challenge to such detectors, as they are operated at high rates. For example the ALICE Time Projection Chamber (TPC) at LHC will face such conditions during run 3[1]. Creating models of space charge relies on the knowledge of the ion mobility K and these models can help to correct for field distortions created by ions.

Experimental set-up

To the end of a mobility measurement a small detector, utilising three stacked Gas Electron Multiplier (GEM) foils[2] to amplify the primary ionisations, was built and commissioned. Above the GEM stack a wire grid is located. Together with the first GEM (GEM1) it encloses the drift gap. A well defined potential above the grid is provided by an additional electrode. K of ions created during the gas amplification is then measured: A signal read out at the lower side of GEM1 provides the information that these ions leave the GEM stack into the drift gap, indicating the start of the ion drift. Throughout their movement in the gap the ions induce a signal on the grid. Since the polarity of this signal changes as the ions pass the wire grid, the inflection point in the read out grid signal marks the ion arrival time at the grid. For each gas mixture the two signals defining the drift time were read out for different electric fields E. Since only low drift fields were applied, a constant mobility as function of the field is assumed: $v = K \cdot E$[3]. From the mobility, using the ambient pressure (P_{Meas}) and temperature (T_{Meas}) during the measurement, the reduced mobility K_0 is calculated: $K_0 = K \times \frac{273.15\,\text{K}}{T_{\text{Meas}}} \times \frac{P_{\text{Meas}}}{1\,\text{atm}}$. Averaging over the individual K_0 obtained for different fields gives the final mobility for each gas mixture.

Water admixtures to Ne-CO_2 (90-10)

Different water contents were achieved by varying the gas flow. In Ne-CO_2 (90-10) the mobility at water contents between $50\,$ppm and $800\,$ppm was measured. Our measurements confirm the previously observed trend[4] of water lowering the ion mobility. At H_2O contents higher than about $500\,$ppm the decrease was found to level off. In the wet gas, compared to the same gas mixture without water, larger ion clusters develop. While in the dry gas only CO_2 ions remain after few $\mathcal{O}(10\,\text{ns})$ and clusters consisting out of C and O form, different clusters build up in the presence of H_2O[5]. The formation probabilities of such clusters rise with increasing water content until the effect saturates as the water content is high enough.

Nitrogen in Ne-CO_2 (90-10)

Adding nitrogen to Ne-CO_2 (90-10) decreases the reduced mobility. K_0 is lowered by $\sim 0.9\,\%$ as the N_2 concentration is increased by $1\,\%$ (compared to the mixture of Ne, CO_2 and N_2). From the measured data K_0 of CO_2 ions in Ne, CO_2 and N_2 is extracted according to Blanc's law[6]. For Ne $4.0(2)\,\text{cm}^2\,\text{V}^{-1}\,\text{s}^{-1}$, for CO_2 $1.0(3)\,\text{cm}^2\,\text{V}^{-1}\,\text{s}^{-1}$ and for N_2 $1.9(2)\,\text{cm}^2\,\text{V}^{-1}\,\text{s}^{-1}$ is found. The mobilities of neon and carbon-dioxide are in agreement with the previous results obtained in Ne-CO_2[4].

Conclusions

The ion mobility in Ne-CO_2 (90-10) was studied for different admixtures of water and nitrogen. It was observed that adding $100\,$ppm of H_2O decreases K_0 by $5\,\%$ in this gas mixture. However, the effect levels off at $\sim 500\,$ppm. Compared to the effect of water, admixtures of N_2 play a minor role. For Ne-CO_2 (90-10) the mobility was found to be $3.0(1)\,\text{cm}^2\,\text{V}^{-1}\,\text{s}^{-1}$, hence adding N_2 to this mixture leads to a lower mobility. The mobility of the drifting (CO_2) ions in the dedicated gas mixture of the ALICE TPC (Ne-CO_2-N_2, 90-10-5) was measured to be $2.9(1)\,\text{cm}^2\,\text{V}^{-1}\,\text{s}^{-1}$.

References

[1] ALICE Collaboration, *Technical Design report for the Upgrade of the ALICE Time Projection Chamber* (CERN-LHCC-2013-020).

[2] F. Sauli, *GEM: A new concept for electron amplification in gas detectors* (Nuclear Instruments and Methods in Physics Research Section A: Accelerators, Spectrometers, Detectors and Associated Equipment, 386, 2, p. 531–534) 1997.

[3] W. Blum et al., *Particle detection with drift chambers* (Springer Science & Business Media) 2008.

[4] A. Deisting et al., *Measurements of ion mobility in argon and neon based gas mixtures* (Proceedings of the VCI 2016, Submitted to NIMA) 2016.

[5] Y. Kalkan et al.,*Cluster ions in gas-based detectors* (Journal of Instrumentation, IOP Publishing, 2015).

[6] M. A. Blanc, *Mobilité des Ions*, (J. Phys. Theor. Appl., 1908).

* alexander.deisting@cern.ch

DOI:10.15120/GR-2016-1

Measurement of D mesons as a function of multiplicity in p–Pb collisions at $\sqrt{s_{\rm NN}} = 5.02$ TeV with ALICE*

J. Wilkinson[1], *K. Schweda*[2], *and the ALICE Collaboration*

[1]Physikalisches Institut, Ruprecht-Karls-Universität Heidelberg, Germany; [2]Research Division, GSI Helmholtzzentrum für Schwerionenforschung, Darmstadt, Germany

Heavy quarks (charm and beauty) serve as unique probes of the medium formed in ultrarelativistic heavy-ion collisions. Their large masses mean that they are only formed during initial hard scatterings in a heavy-ion collision, and not in thermal processes in the Quark-Gluon Plasma (QGP). In addition, they retain their large masses even after the partial restoration of chiral symmetry experienced in QGP formation.

pp and p–Pb collisions serve as a baseline for Pb–Pb measurements, as no long-lived medium is expected to be formed in these systems. One particularly interesting measurement to make in these systems is the production rate of heavy-flavour particles as a function of charged-particle multiplicity. Multiplicity-dependent measurements give insight into the role of multi-parton interactions (MPI) in charm production, and in particular comparisons between the results in pp and p–Pb collisions allow these effects to be disentangled from the effect of multiple binary nucleon-nucleon collisions. Previous measurements in pp collisions showed a faster-than-linear increase of the D-meson yield as a function of multiplicity at both mid-rapidity and forward and backward rapidity [1].

The charged-particle multiplicity was sampled in two regions: mid-rapidity ($|\eta| < 1.0$) from the number of track segments reconstructed by the Silicon Pixel Detector, and backward rapidity ($2.8 < \eta < 5.1$, the Pb-going direction) based on the signal measured by the V0A hodoscope. The measured observable was the so-called 'self-normalised yield': the efficiency-corrected yield in each multiplicity interval was normalised by the number of events in that interval and then divided by the corresponding value for the multiplicity-integrated case. At mid-rapidity, the multiplicity was taken relative to the mean multiplicity of charged particles measured in inelastic p–Pb collisions in ALICE, $\langle {\rm d}N_{\rm ch}/{\rm d}\eta \rangle = 17.64 \pm 0.01\,({\rm stat.}) \pm 0.68\,({\rm syst.})$ [2].

D mesons were reconstructed in the central barrel of ALICE through the hadronic decay channels $\rm D^0 \rightarrow K^-\pi^+$, $\rm D^+ \rightarrow K^-\pi^+\pi^+$ and $\rm D^{*+} \rightarrow D^0\pi^+$ (and respective charge conjugates). The analysis made use of the Inner Tracking System (ITS) for topological selections on the decay vertices, and the Time Projection Chamber (TPC) and Time Of Flight detector (TOF) for particle identification. The D-meson yields were extracted via fits to the invariant mass distributions in each multiplicity interval.

Figure 1 shows the measured results averaged over all D-meson species for pp and p–Pb collisions for the multiplicity estimated at forward and backward rapidity [3].

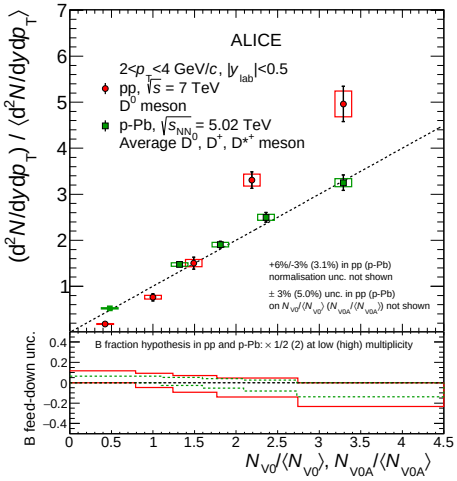

Figure 1: Relative D-meson yields in pp and p–Pb collisions as a function of charged-particle multiplicity at backward rapidity [1, 3].

The measurements as a function of mid-rapidity multiplicity [3] show a largely similar trend between the pp and p–Pb results, whereas the results at backward rapidity show a roughly linear increase for the p–Pb case and a faster-than-linear increase for pp collisions. The results for p–Pb collisions in both rapidity regions were also found to be consistent with EPOS3 calculations, both with and without viscous hydrodynamics, within uncertainties [3, 4, 5].

References

[1] **ALICE** Collaboration, "Measurement of charm and beauty production at central rapidity versus charged-particle multiplicity in proton-proton collisions at $\sqrt{s} = 7$ TeV," *JHEP* **09** (2015) 148, arXiv:1505.00664 [nucl-ex].

[2] **ALICE** Collaboration, "Pseudorapidity density of charged particles in p–Pb collisions at $\sqrt{s_{\rm NN}} = 5.02$ TeV," *Phys. Rev. Lett.* **110** (2013) 032301, arXiv:1210.3615 [nucl-ex].

[3] **ALICE** Collaboration, "Measurement of D-meson production versus multiplicity in p–Pb collisions at $\sqrt{s_{\rm NN}} = 5.02$," arXiv:1602.07240 [nucl-ex].

[4] H. Drescher, M. Hladik, S. Ostapchenko, T. Pierog, and K. Werner, "Parton based Gribov-Regge theory," *Phys.Rept.* **350** (2001) 93–289, arXiv:hep-ph/0007198 [hep-ph].

[5] K. Werner, B. Guiot, I. Karpenko, and T. Pierog, "Analysing radial flow features in p-Pb and p-p collisions at several TeV by studying identified particle production in EPOS3," *Phys.Rev.* **C89** (2014) 064903, arXiv:1312.1233 [nucl-th].

* Work supported by HGS-HIRe, BMBF, GSI and EMMI

η and π^0 meson production in Pb–Pb collisions at $\sqrt{s_{\rm NN}}$ = 2.76 TeV *

L. Leardini[1], *A. Morreale*[2], *A. Marín*[†3], *F. Bock*[4,1], *M. Germain*[2], *P. González*[5], *P. Ladrón de Guevara*[5], *D. Mühlheim*[6], *A. Passfeld*[6], *K. Reygers*[1], *J.Stachel*[1], *J.P. Wessels*[6], *and the ALICE Collaboration*[1]

[1]Physikalisches Institut, Ruprecht-Karls-Universität Heidelberg, Germany; [2]Laboratoire de Physique Subatomique et des Technologies Associées SUBATECH, Nantes, France; [3]Research Division and ExtreMe Matter Institute EMMI, GSI Helmholtzzentrum für Schwerionenforschung, Darmstadt, Germany; [4]Lawrence Berkeley National Laboratory, Berkeley, United States; [5]Centro de Investigaciones Energéticas, Medioambientales y Tecnológicas (CIEMAT), Madrid, Spain; [6]Institut für Kernphysik, Westfälische-Wilhems-Universität Münster, Münster, Germany

The measurement of π^0 and η mesons in a broad $p_{\rm T}$ range is important to understand particle production in pp and and Pb–Pb collisions, as well as energy loss mechanisms in central Pb–Pb collisions due to the formation of the QGP. In addition, it is essential for the measurement of the direct photons as they constitute the main source of photon background. During the year 2011, the ALICE experiment took a large data sample of central (0-10%) and semi-central (20-50%) Pb–Pb collisions. The analysis of 1.6×10^7 (1.1×10^7) events for central (semi-central) collisions made possible the first η meson measurement in Pb–Pb collisions at $\sqrt{s_{\rm NN}}$ = 2.76 TeV [2, 3] and the extension of the π^0 results from $p_{\rm T}$ = 12 GeV/c to 20 GeV/c.

ALICE measures photons using two complementary techniques: the photon conversion method (PCM) and the photon calorimeters (PHOS and EMCal) [1]. Neutral mesons are reconstructed in the 2γ decay channel. π^0 and η raw yields are obtained for each $p_{\rm T}$ bin integrating the clear peaks observed in the two-gamma invariant mass spectra on top of a combinatorial background. Efficiency and acceptance corrections obtained in Monte Carlo simulations are applied independently to the PCM and EMCal results. The final invariant differential yields (see Fig. 1) are obtained by combining the PCM and EMCal ones using as weights the statistical and systematic errors. A suppression in Pb–Pb collisions is observed compared to the NLO pQCD predictions scaled by $\langle N_{\rm coll}\rangle$. The η/π^0 ratio has been measured (see Fig. 2). With the current accuracy the η/π^0 ratio is consistent with the η/π^0 ratio in pp collisions, with the $K^{\pm}/\pi^{\pm}$ ratio and with pQCD (jet-quenching based) predictions [4].

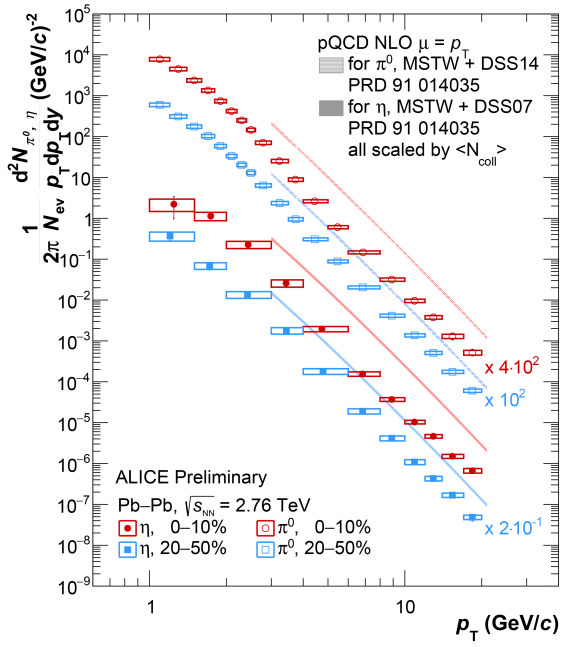

Figure 1: Invariant differential yields of π^0 (open symbols) and η (closed symbols) mesons in the two centrality classes in Pb–Pb collisions at $\sqrt{s_{\rm NN}}$ = 2.76 TeV compared to NLO pQCD predictions scaled by $\langle N_{\rm coll}\rangle$.

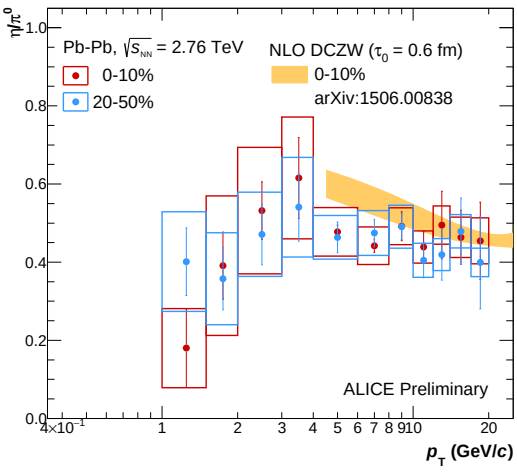

Figure 2: η/π^0 ratio in two centrality classes in Pb–Pb collisions at $\sqrt{s_{\rm NN}}$ = 2.76 TeV compared to theoretical jet quenching predictions.

References

[1] Abelev, B. *et al.* (ALICE Collaboration)Int. J. Mod. Phys. A29 (2014)1430044

[2] L. Leardini [ALICE Collaboration], https://indico.mitp.uni-mainz.de/event/56/session/9/contribution/11

[3] A. Morreale [ALICE Collaboration], arXiv:1512.05250

[4] W. Dai, X. F. Chen, B. W. Zhang and E. Wang, Phys. Lett. B **750** (2015) 390 [arXiv:1506.00838 [nucl-th]].

* Work supported by GSI, EMMI, BMBF, HGS-HIRe, HGSFP and IN2P3

† a.marin@gsi.de

DOI:10.15120/GR-2016-1

J/ψ measurements in p-Pb collisions at $\sqrt{s_{\mathrm{NN}}} = 5.02\,\mathrm{TeV}$ exploiting the TRD trigger *

S. Weber[1,2]

[1]GSI, Darmstadt, Planckstraße 1, 64291 Darmstadt, Germany; [2]Technische Universität Darmstadt, Karolinenplatz 5, 64289 Darmstadt, Germany

Quarkonium has long been proposed as an excellent probe for the deconfined medium created in high energy heavy-ion collisions. Both a suppression mechanism due to the screening of the potential by free color charges in the medium [1], as well as an enhancement at higher collision energies through (re)combination of independently produced charm and anticharm quarks [2, 3] have been proposed. In addition to hot medium effects charmonium production is subject to cold nuclear matter effects (CNM), such as shadowing or gluon saturation and parton energy loss [4]. These effects are already present in hadron-nucleus collisions, which thus can be used to disentangle them from hot matter effects.

ALICE has performed measurements of J/ψ production in p-Pb collisions at $\sqrt{s_{\mathrm{NN}}} = 5.02\,\mathrm{TeV}$ at mid-rapidity in the dielectron decay channel and at forward and backward rapidity in the dimuon decay channel [5, 6, 7]. For the data at midrapidity minimum bias events were used so far. By exploiting the trigger capabilities of the transitition radiation detector (TRD) [8], it is expected that the significance of the measurement can be improved for higher momenta. This work presents an analysis of J/ψ production in p-Pb collisions at $\sqrt{s_{\mathrm{NN}}} = 5.02\,\mathrm{TeV}$ taken with two different TRD triggers requiring an electrons with $p_{\mathrm{T}} > 2\,\mathrm{GeV/c}$ or $p_{\mathrm{T}} > 3\,\mathrm{GeV/c}$, respectively.

A sample of electrons from photon conversions, making use of particle identification and topological cuts for the track selection, was used to estimate the trigger efficiency. It is composed to equal parts of the tracking and PID requirements. The p_{T} dependence is shown in figure 1.

Figure 2 shows the invariant mass distribution of the electron positron pairs together with the background estimated from combining particles from different events, and the extracted signal after background subtraction.

The presented study proves the feasibility of the usage of the TRD to trigger on high momentum electrons. A first estimate on the p_{T} integrated inclusive J/ψ cross-section is in agreement with the results obtained in the analysis conducted on minimum-bias triggered data [6]. In the LHC Run 2 the TRD is now fully installed, while in Run 1 only 13 out of 18 supermodules were present. Furthermore the contamination from electrons from photon conversions in outer regions of the detector is now reduced by taking the local curvature of the tracks inside the TRD into account. Thus, an increased TRD performance is expected.

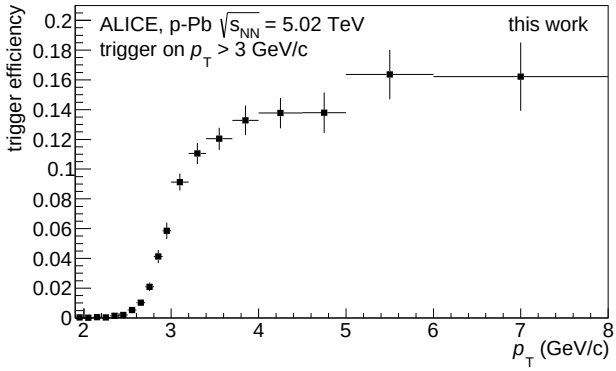

Figure 1: Trigger efficiency for electrons as function of p_{T}.

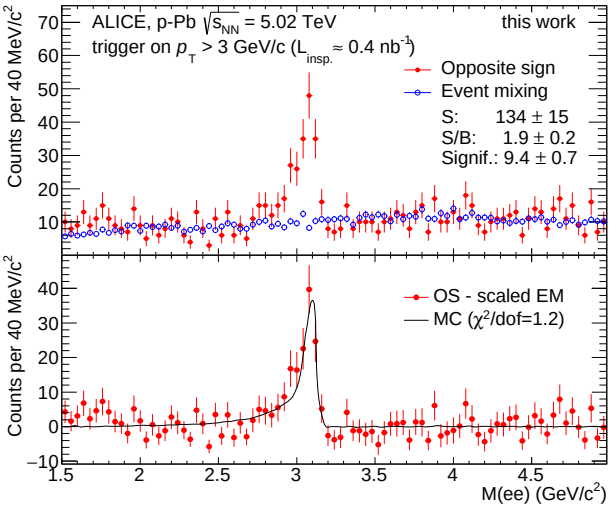

Figure 2: Invariant mass distribution, extracted signal and expected signal shape from Monte Carlo simulations.

References

[1] Matsui T. and Satz H., Phys. Lett. B 178 (1986) 416

[2] Braun-Munzinger P. and Stachel J., Phys. Lett. B 490 (2000) 196–202

[3] Thews R. L., Schroedter M. and Rafelski J., Phys. Rev. C 63(5) (2001) 054905

[4] F. Arleo and S. Peigné, JHEP 1303 (2013) 122

[5] ALICE collaboration, JHEP 02 (2014) 073

[6] ALICE collaboration, JHEP 06 (2015) 055

[7] ALICE collaboration, JHEP 11 (2015) 127

[8] ALICE Collaboration, CERN-LHCC 2001-021

*Work supported by GSI, BMBF, Helmholtz Alliance HA216/EMMI, H-QM, and HGS-HIRe

Studies of the baryon-(anti)baryon interaction with ALICE at the LHC*

M. Nicassio†[1], *P. Braun-Munzinger*[1,2], *S. Masciocchi*[1,3], *and D. Miśkowiec*[1]

[1]GSI Helmholtzzentrum für Schwerionenforschung, Darmstadt, Germany; [2]ExtreMe Matter Institute EMMI, Darmstadt, Germany; [3]Physikalisches Institut, Ruprecht-Karls-Universität Heidelberg, Heidelberg, Germany

Motivation and formalism

The interaction among baryons is currently the subject of intense theoretical study, but nonetheless it is still poorly known or not known at all for most of the baryon systems in the strangeness sector. There is a clear need for experimental constraints to make progress on its understanding [1] since there are only few scattering data with large uncertainties as constraints to theory. By measuring baryon-(anti)baryon momentum correlations in heavy-ion collisions, the interaction can be studied via femtoscopic techniques inverting the traditional approach in which the knowledge of the interaction is used to extract the space-time extent of the region emitting particles. It is a unique tool, especially to study baryon-antibaryon annihilation. This type of analysis is carried out here for the pΞ systems for the first time, measured in Pb–Pb collisions, recorded with the ALICE detector at the LHC.

The correlation function is defined as the ratio between the two-particle momentum distribution and a reference distribution in absence of correlation, obtained in heavy-ion collisions by correlating particles which come from different events. It is analyzed as a function of the difference between the three-momenta of the two particles in the pair rest frame ($Q_{\rm inv}$=2k*). Any deviation of this function from unity indicates effects due to quantum symmetrization for identical particles and final state interaction between the two particles (Coulomb and strong interaction). A model developed by Lednicky and Lyuboshitz [2] allows the correlation function in presence of final state interaction to be calculated analytically with a parametrization of the strong interaction which is independent of the actual potential and expressed with two parameters: the scattering length and the effective radius. Those are complex numbers and the imaginary part of the scattering length accounts for annihilation.

Analysis details

For this analysis, data from the LHC Pb–Pb run collected in 2011 have been used with about 20 M events in the most central class (0-10%). To build the denominator of the correlation function, the two particles are selected from different events with similar topology (position of the vertex and centrality class). Primary protons are identified using the Time Projection Chamber (TPC) and the Time Of Flight detector. The purity of the sample is about 95%. Charged Ξ baryons are measured through the reconstruction of the cascade topology of their dominant decay channel ($\Xi^- \rightarrow \Lambda + \pi^- \rightarrow p + \pi^- + \pi^-$ and charge conjugate). Identification of daughter tracks is crucial in this case as well to reduce the combinatorial background. With the current selection criteria a purity of about 75% is obtained for Ξ candidates in the most central class of events.

Due to the finite detector resolution, two-track resolution effects can bias the correlation functions: particles which travel close in space might be reconstructed as one track (track merging) or a single particle as two distinct tracks (track splitting). To check the presence of such effects, the angular distances in the transverse plane and in pseudorapidity ($\Delta\varphi^*\Delta\eta^*$) between the proton track and each of the cascade daughter tracks were calculated at a certain radius in the TPC (1.2 m). Correlation functions are obtained for all primary-secondary track combinations. Like-sign pair correlation functions show a dip, an overall loss of pairs, at small distances ($|\Delta\varphi^*|<0.04$ and $|\Delta\eta^*|<0.05$). Such pairs are not used to build the correlation functions. The magnitude of the correction at low k* (k*$<$ 0.05 GeV/c) is about 5%.

Results and outlook

A strong correlation is observed both for baryon-baryon pairs ($p\Xi^- + \overline{p}\overline{\Xi}^+$) and for baryon-antibaryon pairs ($p\overline{\Xi}^+ + \overline{p}\Xi^-$), positive and negative respectively, as expected from the attractive and repulsive Coulomb interaction. A first evaluation of the systematic uncertainties has been carried out varying track and pair selection criteria. It ranges from 5 to 20% in the low k* region.

The correlation functions obtained have to be corrected for momentum resolution and purity. Furthermore, contributions from residual correlations have to be estimated and taken into account. Those are produced by parent particles that feed-down to the system under study and smear the correlation function. Correlation functions will be fitted using the analytical model mentioned above to extract the parameters of the strong interaction, ideally fitting simultaneously correlation functions obtained for different centrality classes, to better constrain the fit.

References

[1] J. Haidenbauer et al., arXiv:1511.05859v1 [nucl-th]

[2] R. Lednicky and V. L. Lyuboshitz, Sov. J. Nucl. Phys. 35 (1982)

* Work supported by Alexander von Humboldt Stiftung, GSI, BMBF, EMMI, H-QM and HGS-HIRe.

† m.nicassio@gsi.de

DOI:10.15120/GR-2016-1

Detector non-uniformity corrections for collision symmetry plane estimates*

V. Gonzalez[1], *J. Onderwaater*[2,3], *and I. Selyuzhenkov*[2]
[1]CIEMAT, Madrid, Spain; [2]GSI, Darmstadt, Germany; [3]TU Darmstadt, Darmstadt, Germany

We briefly discuss a software framework [1] that extracts corrections for azimuthal non-uniformity [2] in the calculation of flow vectors $Q_n = \Sigma_{i=0}^{M} w_i e^{in\varphi_i}$, where φ is an azimuthal angle and w a weight (multiplicity).

The general part of the framework is designed to be utilized within the scope of any experimental setup, only requiring tuning of an external piece of software interface. Other key points of its design are performance and flexibility of incorporating new Q-vector corrections or new combinations of them with a minimum design impact. For this, an object oriented approach without sacrificing performance is applied. The framework models any experimental setup as a set of detectors handled by a manager (Fig. 1).

Each detector can have multiple configurations for the

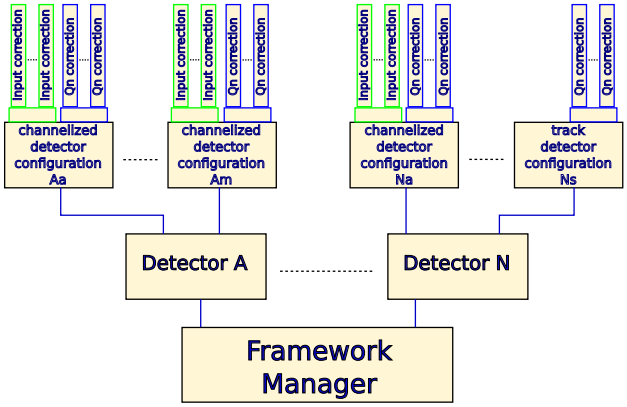

Figure 1: Framework functional architecture.

construction and correction of flow vectors. Detector configurations can handle tracking detectors, as well as channelized detectors while allocating a set of channels numbers. The user can define a set of corrections to be applied on each of these detector configurations. Corrections for Q-vectors are included as well as for individual elements of Q-vectors, such as gain equalization for channelized detectors. Any detector configuration has a socket where the desired Q-vector corrections plug in. When a new Q-vector correction is designed, information on the order in which it is applied is fixed. The Q-vector correction should follow a predefined template.

To demonstrate the functionality of the framework for a specific combination of subevents and detector non-uniformities a simple Monte-Carlo routine is employed. Particles for three subevents A, B, and C are generated

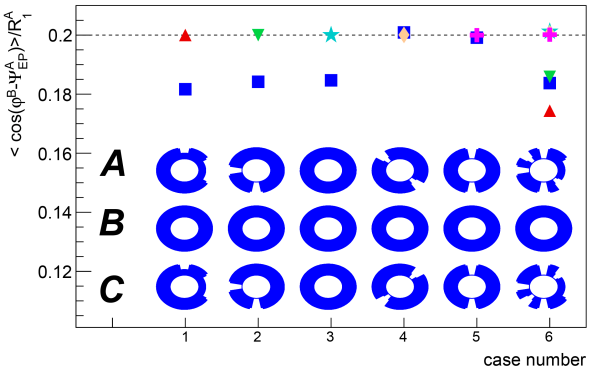

Figure 2: Estimates of input v_1 (dashed line) from simulated azimuthal angle distributions before (blue squares) and after different corrections (other markers).

with $v_1 = 0.2$ and respective multiplicities 50, 200, and 50. In the simulation, subevent B consists of an ideal tracker, while subevent A and C are radially segmented in 16 equal parts. From simulated angles after detector acceptance the $\langle v_1 \rangle = \langle cos(\varphi^B - \Psi^A_{EP}) \rangle / R^A_1$ is extracted where the resolution correction R^A_1 is calculated using the 3-subevent method [3]. The azimuthal acceptance of A, B and C is represented by the disks in Fig. 2. Case 1 (triangle up) demonstrates the gain equalization, where for A and C four segments have 50% of the ideal gain (which mimics four miscalibrated channels). Case 2 (triangle down) demonstrates recentering, where two orthogonal segments are disabled. Case 3 (star) demonstrates the alignment correction. Here the subevents A and C have uniform acceptance, but the coordinate systems are rotated by $\pi/8$ to mimic misalignment. Case 4 (diamond) and 5 (cross) have gaps that maximize the twist and rescaling corrections respectively. However, these non-uniformities don't affect our observable and the corrections don't change the result. Case 6 is a superposition of cases 1-5. In all cases 1-6 the input value of v_1 is accurately reconstructed. Limitations for the applicability of the corrections and the impact of multiplicity correlations are currently being studied.

References

[1] https://github.com/FlowCorrections/FlowVectorCorrections available under GNU General Public License v.3

[2] I. Selyuzhenkov and S. Voloshin, Phys. Rev. C **77** (2008) 034904

[3] A. Poskanzer and S. Voloshin Phys. Rev. C58 (1998) 1671-1678

* Work supported by GSI, TU Darmstadt, BMBF, EMMI, H-QM, and HGS-HIRe

Building a GEM-based Outer Readout Chamber prototype for the ALICE TPC upgrade *

P. Gasik[†1,2], *L. Fabbietti*[1,2], *A. Mathis*[1,2], *R. Muenzer*[1,2], *and the ALICE TPC collaboration*

[1]Physik Department E62, TU München, 85748 Garching, Germany; [2]Excellence Cluster 'Origin and Structure of the Universe', 85748 Garching, Germany

A large Time Projection Chamber (TPC) is the main device for tracking and charged-particle identification in the ALICE experiment at the CERN LHC [1]. After the second long shutdown in 2019-2020, the LHC will deliver Pb beams colliding at an interaction rate up to 50 kHz, which is about a factor of 100 above the present read-out rate of the TPC. To fully exploit the LHC potential the TPC will be upgraded based on the Gas Electron Multiplier (GEM [2]) technology.

In order to check the feasibility of the upgrade solution, a full-scale prototype of an Outer Readout Chamber (OROC) has been built. It was equipped with twelve large-size GEM foils as amplification stage and with a total area of $\sim$0.76 m^2 it is the largest GEM-based detector built to date.

The chamber is of trapezoidal shape of 114 cm length and 47 cm (87 cm) width of the short (long) parallel sides. The prototype is assembled on a spare OROC of the ALICE TPC. The mechanical structure of the chamber consists of GEM stacks, a pad plane, an additional 3 mm Stesalit insulation plate (so called 'strong back') and an aluminium frame (alubody). A schematic view of a prototype is shown in fig. 1.

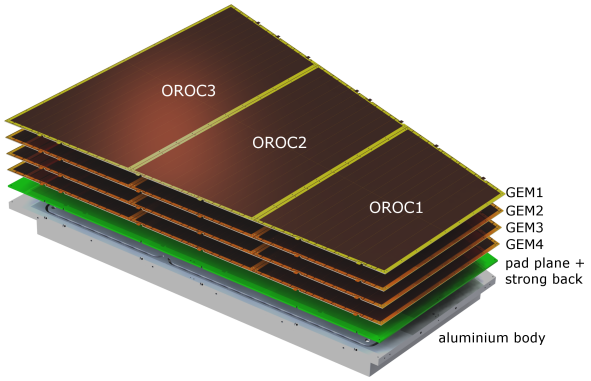

Figure 1: Exploded view of the 4-GEM OROC.

Three independent quadruple GEM stacks are mounted on top of the pad plane employing GEM foils with a pitch of 140 μm ("Standard" - S) and 280 μm ("Large Pitch" - LP). The subsequent GEM foils in a stack have been installed according to the S-LP-LP-S configuration.

The prototype in a test vessel containing a field cage was tested with an Ar-CO_2 (82-18) gas mixture and irradiated with a ^{55}Fe X-ray source. For the commissioning of the detector, 256 pads ($\sim$75 cm^2) were connected to a charge-sensitive preamplifier and the signal was digitised with a multi-channel analyser for measuring the X-ray spectrum. The detector gain is estimated by comparing the current, measured with a picoammeter, at the anode to the primary current deduced from a rate of X-rays.

Figure 2 shows an example of the energy spectrum of ^{55}Fe obtained at a gain of around 80000. Both argon peaks are visible together with a low intensity peak, corresponding to the aluminium fluorescence X-rays (the source was placed in front of the aluminised drift electrode). The energy resolution of the main peak is σ/E(^{55}Fe) = 11.8%. It should be noted that the drift field used in these studies was set to $\sim$180 V/cm, which is a factor more than twice lower than the nominal ALICE drift field (400 V/cm).

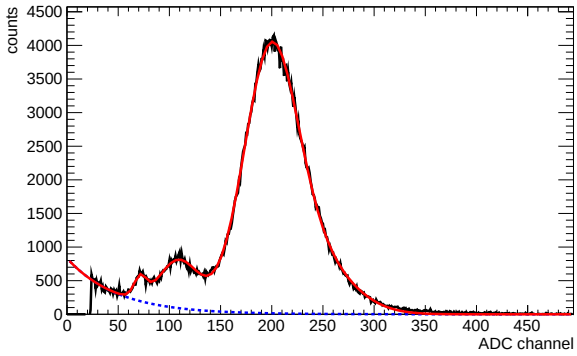

Figure 2: ^{55}Fe spectrum obtained in Ar-CO_2 (82-18) with OROC2 stack.

We therefore demonstrate the feasibility of replacing the current Multi Wire Proportional Chambers with the new GEM technology. The start of the mass production of the readout chamber for the upgraded ALICE TPC is planned in the middle of 2016. All the readout chambers are planned to be assembled until Q1.2019, when the LS2 is supposed to start and the TPC will be moved to the surface. Installation and commissioning of the chambers will last until the end of 2020.

References

[1] J. Alme et al. (ALICE TPC Collaboration), Nucl. Instr. Meth. A **676** (2010) 316.

[2] F. Sauli, NIM **A386** (1997) 531

* Work supported by GSI, BMBF, BMBF 05P12WOGHH, Excellence Cluster 'Universe'

† p.gasik@tum.de

DOI:10.15120/GR-2016-1

d*E*/d*x* resolution studies of a full-size GEM-based readout chamber prototype for the upgrade of the ALICE TPC*

A. Mathis[†1,2], *L. Fabbietti*[1,2], *P. Gasik*[1,2], *R. Münzer*[1,2], *and the ALICE TPC collaboration*

[1]Physik Department E62, Technische Universität München, 85748 Garching, Germany; [2]Excellence Cluster 'Origin and Structure of the Universe', 85748 Garching, Germany

Introduction

The ALICE Collaboration is planning major upgrades of the spectrometer to benefit from the significantly enhanced luminosity of the Large Hadron Collider beyond 2019 [1]. In particular, the ALICE Time Projection Chamber (TPC), the main device for charged-particle tracking and particle identification (PID) in ALICE, is foreseen to be operated in an ungated mode with continuous readout. Therefore, the currently used gated Multi-Wire Proportional Chambers (MWPC) will be replaced by readout chambers based on the Gas Electron Multiplier (GEM) [2], while retaining the present tracking and PID capabilities via measurement of the specific energy loss dE/dx.

The baseline solution for the TPC upgrade consists of a stack of four GEM foils as amplification stage containing both Standard (S, 140 μm pitch) and Large Pitch (LP, 280 μm pitch) GEMs arranged in the order S-LP-LP-S [3].

d*E*/d*x* resolution studies at the CERN PS

The dE/dx performance of a full-size prototype of the ALICE Inner Readout Chamber (IROC) equipped with such a stack was evaluated at the CERN Proton Synchrotron with a secondary beam containing electrons and negative pions with a momentum of 1 GeV/c. The detector was equipped with 10 EUDET front-end cards, based on the PCA16 [4] and ALTRO [5] chips.

The specific energy loss dE/dx is determined by the truncated mean of the 70% lowest charges Q_{tot} of the ionization clusters along the track. The charge of individual clusters is corrected for local gain variations on a pad-by-pad basis according to a normalized gain map. The observed gain spread is ∼10.5%. The relative dE/dx resolution is then defined as $\sigma(\mathrm{d}E/\mathrm{d}x)/\langle \mathrm{d}E/\mathrm{d}x\rangle$, where $\langle \mathrm{d}E/\mathrm{d}x\rangle$ corresponds to the mean of the energy loss distribution and $\sigma(\mathrm{d}E/\mathrm{d}x)$ to its width. Figure 1 shows an exemplary dE/dx spectrum of 1 GeV/c electrons and pions recorded at a gain of about 2000 and depicts the corresponding separation power, defined as

$$S_{AB} = \frac{2|\langle \mathrm{d}E/\mathrm{d}x\rangle_A - \langle \mathrm{d}E/\mathrm{d}x\rangle_B|}{\sigma(\mathrm{d}E/\mathrm{d}x)_A + \sigma(\mathrm{d}E/\mathrm{d}x)_B} \qquad (1)$$

for two particle species A and B.

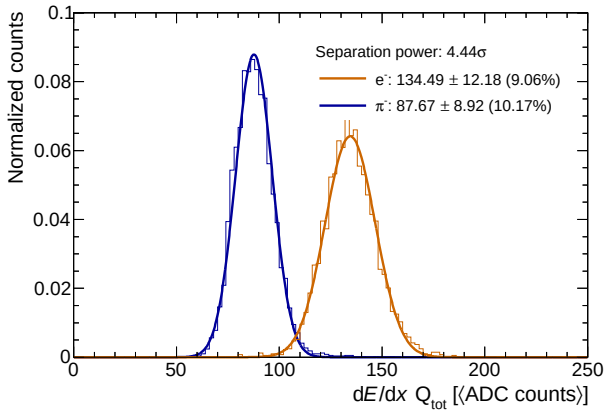

Figure 1: Truncated (0–70 %) energy loss distributions for electrons and pions with a momentum of 1 GeV/c measured with the IROC GEM prototype at a gain of 2000.

The dE/dx resolution measured with the GEM IROC prototype, under a voltage configuration fulfilling the demanding requirements of the ALICE TPC in particular with respect to ion backflow suppression and energy resolution, is fully consistent with that of the current MWPC IROC.

Summary and outlook

The dE/dx resolution of a GEM-based prototype for the ALICE TPC has been evaluated. The excellent PID capabilities of the current MWPC-based ALICE TPC will be preserved after the upgrade.

The production of the readout chambers for the TPC upgrade is planned to start mid of 2016 and will last until 2019, when installation and commissioning of the chambers will take place.

References

[1] B. Abelev *et al.*, "Upgrade of the ALICE Experiment: Letter of Intent", CERN-LHCC-2012-012 (2012).

[2] F. Sauli, "GEM: A new concept for electron amplification in gas detectors" NIM A **386** (1997) 531.

[3] B. Abelev *et al.*, "Upgrade of the ALICE Time Projection Chamber", CERN-LHCC-2013-020 (2013).

[4] A. Kaukher, O. Schäfer, H. Schröder, and R. Wurth, "Status of TPC-electronics with Time-to-Digit Converters", EUDET-Memo-2009-08 (2009).

[5] R. Esteve Bosch, A. Jimenez de Parga, B. Mota and L. Musa, "The ALTRO Chip", IEEE Transactions on Nuclear Science **50** (2003) 2460.

* This research was supported by the DFG cluster of excellence 'Origin and Structure of the Universe' and BMBF Verbundprojekt 'ALICE at high rate' 05P15WOCA1.

† andreas.mathis@ph.tum.de

Baryon femtoscopy in proton-proton collisions at 7 TeV with ALICE*

O. Arnold[1,2], *D. Mihaylov*[1,2], *L. Fabbietti*[1,2], *A. Bilandzic*[1,2], *and the ALICE collaboration*

[1]Physik Department E62, Technische Universität München, James-Franck-Str. 1, D-85748 Garching, Germany;
[2]Excellence Cluster Universe, Technische Universität München, Boltzmannstr. 2, D-85748, Garching, Germany

Motivation

The investigation of baryon-baryon interactions has been an important topic in high-energy physics [1]. Being able to describe the hyperon-nucleon interaction (HNI) is e.g. of great importance to understand the composition of astrophysical objects such as the core of neutron stars. Experimental data on the HNI has been provided mostly by scattering experiments. However, modern high-energy experiments provide much higher statistics. A method to study interactions between hyperon-nucleon pairs is femtoscopy. It is based on a two-particle correlation function at low relative momenta:

$$C(\mathbf{p}_1, \mathbf{p}_2) = \frac{P(\mathbf{p}_1, \mathbf{p}_2)}{P(\mathbf{p}_1) \cdot P(\mathbf{p}_2)}, \quad (1)$$

where $P(\mathbf{p}_1, \mathbf{p}_2)$ is the conditional probability of finding a particle pair in the same event. $P(\mathbf{p}_{1,2})$ is the single-particle probability of finding such particles independently. In the kinematic region of low relative pair momenta, the two-particle correlation function (1) is sensitive to both the emission source size of the two particles and the interaction between the pair. If the source size of the system is known beforehand e.g. by using another baryon pair with a well established interaction, the interaction of hyperons with nucleons can be studied. This is usually done using the Lednicky model [2], which describes the two-particle correlation function for baryon-pairs, based on an effective range expansion of the complex scattering amplitude in terms of scattering length and effective range. These parameters describe the interaction for low relative momenta between the pair and can be calculated by theoretical models making it possible to compare such predictions to experimental data.

Analysis strategy

For the femtoscopy study, the pp 7 TeV ALICE data sample was analyzed using minimum bias events. The z-position of the primary vertex was required to be within $10\ \mathrm{cm}$ of the center of the ALICE detector. The goal of the analysis was to construct experimentally, the two-particle correlation functions of pp, pΛ and pΞ^- pairs. To have a proton sample with large purity, the specific energy loss signal from the TPC and the time-of-flight signal from the TOF detector were combined for proton momenta larger than $p > 0.75\ \mathrm{GeV}$, because above this momentum threshold the specific energy loss signals for the individual charged particles start to overlap. For lower proton momenta only the TPC was used. The hyperons were identified by their decays involving charged particles $\Lambda \rightarrow p\pi^-$ and $\Xi^- \rightarrow \Lambda(p\pi^-)\,\pi^-$ using the invariant mass technique. To reject contributions from combinatorial background, several topological cuts were applied to reduce the source of particles not stemming from the hyperons. Around 6M Λ ($S/B \sim 20$) and 430k Ξ ($S/B \sim 6$) hyperons were reconstructed. The experimental correlation function was calculated by constructing a sample $A(k)$, which contains the distribution of particle pairs from the same event as a function of their relative momenta $k = \frac{1}{2}|\mathbf{p}_1 - \mathbf{p}_2|$ in the pair rest frame $\mathbf{p}_1 + \mathbf{p}_2 = 0$. A reference sample $B(k)$ containing only the product of the single-particle probabilities of Eq. (1) was obtained with the event mixing technique and the correlation function calculated by

$$C(k) = \frac{A(k)}{B(k)}. \quad (2)$$

In the region where the particles are correlated by femtoscopic effects we were able to reconstruct around 7000 pΛ ($k < 150\ \mathrm{MeV/c}$) and around 100 pΞ pairs ($k < 100\ \mathrm{MeV/c}$). For pΛ and pp pairs femtoscopy is feasible in terms of statistics. This will be continued and the source size extracted and the interaction between pΛ studied. For the pΞ case, the number of pairs at low relative momenta is not enough to draw any conclusion. The goal is to use LHC Run2 data for pp collisions at 13 TeV. With an expected integrated luminosity which will be around 10 times larger compared to LHC Run 1 conditions, the number of $p\Xi$ pairs below $100\ \mathrm{MeV/c}$ could reach a number around 1000 thus making $p\Xi$ femtoscopy feasible in pp collisions.

References

[1] J. Adam *et al.*, "One-dimensional pion, kaon, and proton femtoscopy in Pb-Pb collisions at $\sqrt{s_{\mathrm{NN}}}$=2.76 TeV", Phys. Rev. C 92 (2015) 054908

[2] R. Lednicky, V.L. Lyuboshits, "Final State Interaction Effect on Pairing Correlations Between Particles with Small Relative Momenta", Sov. J. Nucl. Phys. 35 (1982) 770

* Work supported by HIC4FAIR, HGS-HIRe, BMBF

DOI:10.15120/GR-2016-1

Multiparticle correlation techniques*

A. Bilandzic[1,2], *L. Fabbietti*[1,2], *and the ALICE Collaboration*

[1]Physik Department E62, Technische Universität München, 85748 Garching, Germany; [2]Excellence Cluster 'Origin and Structure of the Universe', 85748 Garching, Germany

Multiparticle azimuthal correlations are nowadays utilized regularly by all major collaborations worldwide which are analyzing heavy-ion data. Most notably, correlation techniques are used to explore the collective properties of the new state of matter, the Quark-Gluon Plasma (QGP), composed of deconfined quarks and gluons, by performing measurements of anisotropic flow phenomena in heavy-ion collisions. Anisotropic flow provides direct information on the QGP properties because it develops from the earliest stages in heavy-ion collisions, when the produced matter is still hot and dense enough for the QGP to exist. With the recent advent of a generic framework developed in [1], which enables exact and efficient evaluation of any multiparticle azimuthal correlation, such studies can be performed with unprecedented precision.

Cumulant analysis with LHC Run 2 data

The exploration of QGP properties has broken new ground with the recent heavy-ion collisions from Run 2 operations at the Large Hadron Collider. With the heavy-ion data taken at the end of 2015, the ALICE Collaboration has made the first observation of anisotropic flow of charged particles in lead–lead collisions at the record breaking energy of 5.02 TeV per nucleon pair [2]. When the anisotropic flow harmonic v_n is estimated with the k-particle correlator, the statistical spread of that estimate scales to leading order as $\sigma_{v_n} \sim \frac{1}{\sqrt{N}} \frac{1}{M^{k/2}} \frac{1}{v_n^{k-1}}$, where M is the number of particles in an event (multiplicity), and N is the total number of events. The observed increase of both the multiplicity [3] and of anisotropic flow (see Fig. 1) in Run 2 when compared to Run 1 results, leads to the best sensitivity ever for analyses with multiparticle correlation techniques. This will enable for the first time at Run 2 energies at the LHC precision studies of higher moments of higher order flow harmonics, event-by-event flow fluctuations and correlations and flow of rare particles.

Multiparticle correlations and femtoscopy

Theoretical models predict the existence of a QGP also in the core of neutron stars. When the neutrons are under sufficiently large pressure from the neutron star's own gravity, they break down into their constituent quarks forming a QGP. However, experimental data suggest that not only neutrons but also other hadrons are relevant for the neutron star structure. One popular candidate are hyperons (baryons containing at least one strange quark in addition to up and down quarks). The appearance of hyperons in the core of a neutron star have dramatic effect on its equation of state [4]. The nature of both the two-body hyperon-nucleon [5] and the three-body hyperon-nucleon-nucleon interactions is at the moment poorly understood mostly due to the lack of experimental constraints for the parameters entering the theoretical models. The adaption and utilization of the above mentioned multiparticle correlation techniques for the study of genuine three-body interactions between hyperons and nucleons is under way.

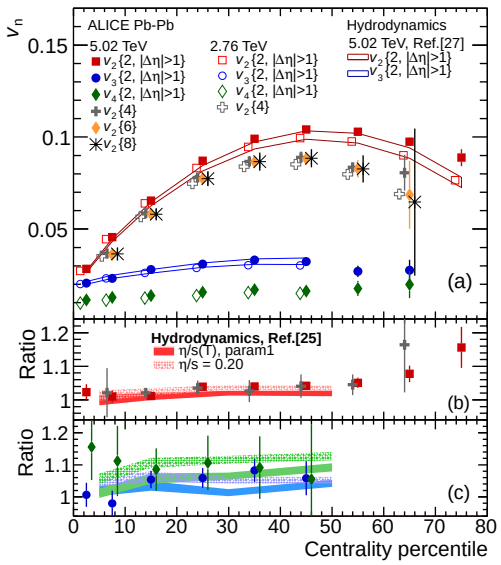

Figure 1: Centrality dependence of anisotropic flow harmonics v_n in lead–lead collisions at record breaking collision energy of 5.02 TeV per nucleon pair [2].

References

[1] A. Bilandzic *et al.* Phys. Rev. C **89** (2014) 064904 [arXiv:1312.3572 [nucl-ex]].

[2] J. Adam *et al.* [ALICE Collaboration], Phys. Rev. Lett. **116** (2016) 132302 [arXiv:1602.01119 [nucl-ex]].

[3] J. Adam *et al.* [ALICE Collaboration], arXiv:1512.06104 [nucl-ex].

[4] D. Lonardoni *et al.* Phys. Rev. Lett. **114** (2015) 9, 092301 [arXiv:1407.4448 [nucl-th]].

[5] H. Beck [ALICE Collaboration], arXiv:1502.00848 [nucl-ex].

*Supported by BMBF Verbundprojekt ALICE at HIG rate 05P15WOCA1

DOI:10.15120/GR-2016-1

Test of the PANDA Barrel DIRC prototype in a hadron beam at CERN *

C. Schwarz[†1], *L. Allison*[3], *A. Belias*[1], *R. Dzhygadlo*[1], *A. Gerhardt*[1], *K. Goetzen*[1], *G. Kalicy*[3], *M. Krebs*[1,2], *D. Lehmann*[1], *F. Nerling*[2], *M. Patsyuk*[1,2], *K. Peters*[1,2], *G. Schepers*[1], *J. Schwiening*[1], *M. Traxler*[1], *and M. Zühlsdorf*[1,2]

[1]GSI, Darmstadt, Germany; [2]Goethe Universität Frankfurt, Germany; [3]Old Dominion University, Virginia, USA

In 2015 the focus of the DIRC detector group was on the assembly and test of a large prototype for the PANDA Barrel DIRC [1] with hadronic beams at the CERN PS with the goal of validating the design concepts and establishing the baseline design. Experiments were undertaken at

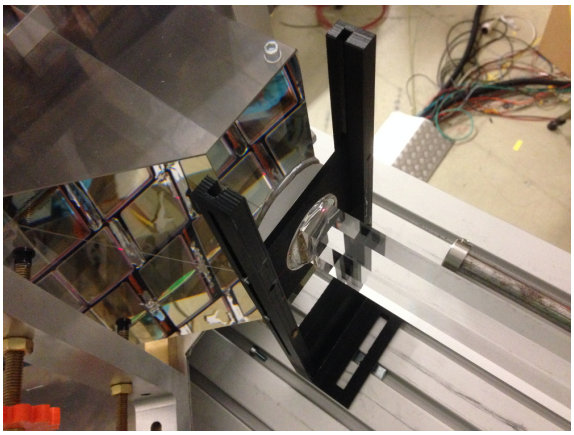

Figure 1: The lens prototype between the expansion prism and the radiator.

CERN-T9 with hadron beams in the summer of 2015. The charged particle beam produced Cherenkov photons in a radiator bar (17 mm × 35 mm ×1225 mm) or in a radiator plate (17 mm × 160 mm ×1250 mm), both made from synthetic fused silica. The angles of the photons were measured by an array of 3×5 PHOTONIS PLANACON MCP-PMTs XP85012 [2] after exiting the radiator via a focusing system in a prism-shaped expansion volume. Between the expansion volume and the radiator a lens system (Fig. 1) made from fused silica and lanthanum crown glass (LaK33B) focused the Cherenkov pattern onto the photon detector plane. The radiator, lens, and prism were coupled to each other using optical grease and placed into a light-tight container on a remote-controlled rotating stage. The data acquisition was performed using PADIWA front end cards and TRB3 boards reading out about 1500 electronic channels. During 34 days of data taking a total of some 500M triggers were recorded for a wide range of particle angles and momenta, similar to the expected PANDA phase space, in different optical configurations. The narrow bar and wide plate were coupled to cylindrical or spherical lenses, with and without anti-reflective coating, including a complex lens-system, or coupled directly to the prism.

* Work supported by HGS-HIRe, HIC for FAIR, and EU FP7 grant #227431.

† C.Schwarz@gsi.de

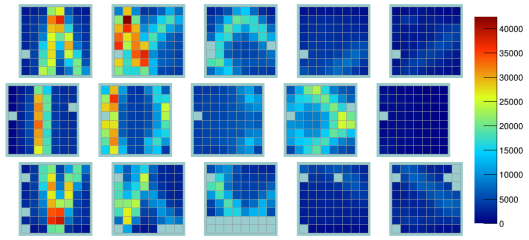

Figure 2: Array of 3 × 5 photon detectors with 960 pixels with a Cherenkov pattern from p = 7 GeV/c beam particles.

The example of such a pattern, accumulated over many events, is shown in Fig. 2. Sharply focused structures are observed over the entire photon detector plane. The analysis of the data from the narrow bar geometry found a single photon Cherenkov angle resolution of 10–12 mrad and a yield of 15-80 detected Cherenkov photons per particle, depending on the polar angle. These values are consistent with detailed Geant simulations (Fig. 3) of the experimental setup and validate this geometry as baseline design for the PANDA Barrel DIRC Technical Design Report, due in the summer of 2016.

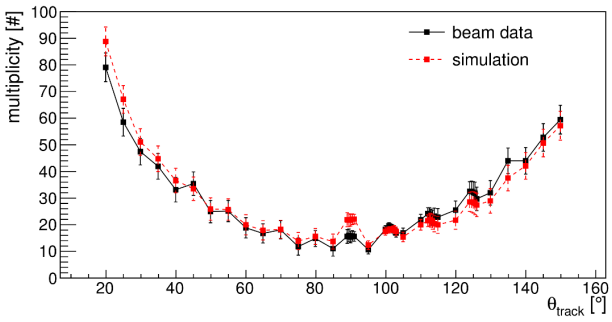

Figure 3: Photon yield as function of the track polar angle for data and simulation results as black and red symbols, respectively.

References

[1] M. Hoek et al., The PANDA Barrel DIRC detector, Nucl. Instr. and Meth. Res. Sect. A 766 (2014) 9.

[2] http://www.photonis.com.

Quality Assurance measurements for the PANDA Barrel DIRC prototype radiator bars*

M. Krebs† [1,2], *K. Peters*[1,2], *G. Schepers*[1], *C. Schwarz*[1], *and J. Schwiening*[1]
[1]GSI, Darmstadt, Germany; [2]Goethe-Universität, Frankfurt, Germany

In the barrel region of the target spectrometer of the PANDA experiment, a fast focusing Cherenkov counter using the DIRC (Detection of Internally Reflected Cherenkov light) principle will be used to provide charged hadronic particle identification (PID). In order to meet the PANDA-PID requirements, the Barrel DIRC has to provide precise measurements of the Cherenkov angle, which is the crucial quantity for identifying charged particles that traversed the radiators. The Cherenkov photons propagate through the radiators by total internal reflection until they reach the detection plane, which is equipped with an array of optical sensors. The radiators, rectangular bars made from synthetic fused silica, have to fulfill very strict optical and mechanical requirements. Properties like squareness and parallelism of the sides, very smooth polished surfaces, sharp corners and rectangularity have to meet the requirements to ensure that the Cherenkov photons reach the optical sensors without angular distortions. In order to determine the surface roughness of a radiator bar, it is necessary to measure firstly the bulk transmission and secondly the transmitted intensity after many internal reflections. Hence an optical setup with a multi-wavelength laser system and a computer controlled motion system was built in the optics lab. For measuring the bulk transmission, the laser beam travels straight through the radiator, while for internal reflection measurements the laser is coupled into the radiator at the Brewster angle (see Fig. 1). Depending on the

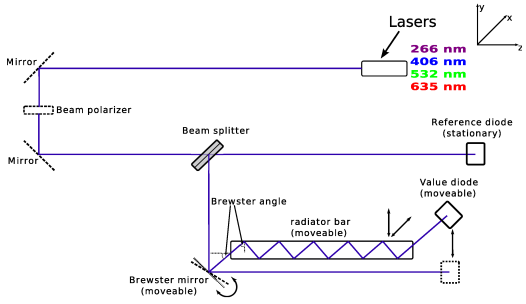

Figure 1: Current setup in the Barrel DIRC optics lab.

length and orientation of the bar, the beam is reflected from the faces up to 50 times, until it leaves the bar and impinges on the (value) photo diode. The reference diode is used to cancel out possible fluctuations from the laser system. The fraction of light lost during the internal reflections is related to the coefficient of total internal reflection, which in turn can be related to the surface roughness via the scalar scattering theory. Figure 2 shows the results from three different prototype bars built by two different manufacturers, Carl Zeiss Jena GmbH and InSync Inc. The calculated reflection coefficients and thus the corresponding surface roughness values are found to be in good agreement with the data from the vendors. For instance, with a fitted surface roughness of 4.4 Å, bar No. 2 (InSync Inc.) exceeds the PANDA Barrel DIRC radiator specifications of 10 Å for the large sides of the radiator.

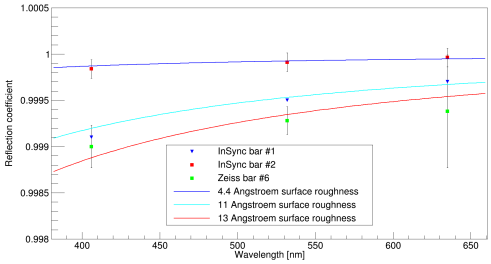

Figure 2: Reflection coefficients with corresponding surface roughness values for three prototype radiator bars

In order to reduce angle smearing, the parallelism and squareness of the long radiator sides and faces, due to the high number of reflections, have to fulfill strict requirements. The squareness must not exceed a value of 0.25 mrad for side-to-face angles. For the quality assurance of the radiator bars an auto collimator from the company Nikon (see the sketch in Fig. 3) is used. It has an accuracy of ≈ 0.002 mrad. In combination with a pentaprism, the reticule deviation in x- and y-direction could be precisely measured with respect to the reticule in the ocular of the auto collimator. The first prototype bar measured in this setup was produced by Carl Zeiss Jena GmbH and all angles were found to deviate from the nominal 90 deg value by less than 0.024 mrad, thus meeting the production specifications and proving the QA data of the company.

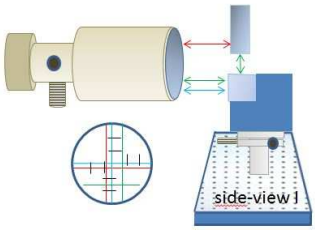

Figure 3: Representation of the measurement with the auto collimator

* Work supported by EU FP7 grant, contract no. 227431, Hadron-Physics2, and HGS-HIRe
† m.krebs@gsi.de

DOI:10.15120/GR-2016-1

New developments with microchannel plate PMTs*

A. Lehmann[†1], *M. Böhm*[1], *W. Eyrich*[1], *M. Pfaffinger*[1], *F. Uhlig*[1], *and PANDA Cherenkov Group*

[1]Physikalisches Institut IV, Universität Erlangen-Nürnberg, Erwin-Rommel-Str. 1, D-91058 Erlangen

The detection of single photons in the PANDA DIRC detectors for π/K separation will be done with microchannel-plate (MCP) PMTs. With a time resolution of <50 ps they are very fast and with $\leq$10 μm pores they can be used in magnetic fields of 2 Tesla. As compact multi-anode devices (e.g., the 8×8 pixel 2-inch PHOTONIS XP85112 MCP-PMT) they reach an active area ratio of ∼80%. Recently their main obstacle of a very limited lifetime due to serious photo cathode (PC) aging [1] was overcome by coating the MCPs with an innovative atomic layer deposition (ALD) technique. This prevents atomic desorption from the MCP material and reduces the flux of feedback ions which damage the PC. The lifetime of an MCP-PMT is usually determined by measuring the quantum efficiency (QE) as a function of the integrated anode charge (IAC).

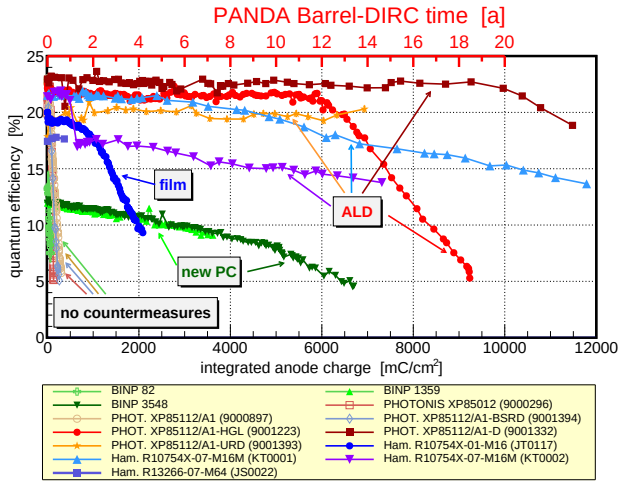

Figure 1: Results of our lifetime measurements for different MCP-PMTs: QE as a function of the IAC at 400 nm.

Our group is studying aging effects of MCP-PMTs since about five years. A simultaneous long-term illumination of all new lifetime-enhanced MCP-PMT models with a single photon rate comparable to that expected in PANDA is performed [2, 3]. The spectral QE, the gain and the dark count rate are measured every several weeks and position scans across the PC surface are performed every few months to identify regions where the QE starts decreasing. The results in Fig. 1 show that, compared to MCP-PMTs without any countermeasures, there is a tremendous improvement of up to a factor 50 in the lifetime of MCP-PMTs, especially for those with ALD coating. At full luminosity the best tubes will be usable in PANDA for more than 20 years.

To improve the active area ratio compared to their 1-inch tubes Hamamatsu was developing new 2-inch MCP-PMTs (8×8 and 128×6 pixels) with ALD coating for the PANDA DIRCs. The first prototypes were delivered early in 2015. Before these tubes can be included in our lifetime setup their performance characteristics have to be measured. The results are mixed: on the negative side we find a rather inhomogeneously distributed QE across the PC and a significantly reduced rate stability of only ∼500 kHz/cm^2 single photons (compared to ∼10 MHz/cm^2 for the 1-inch MCP-PMTs); on the positive side the time resolution of ∼22 ps with almost no backscattering tail is excellent and the cross talk among adjacent anode pixels is clearly lower than that of the 2-inch PHOTONIS XP85112 MCP-PMTs (see Fig. 2). The latter is an important aspect for the Barrel DIRC.

The new Hamamatsu tubes with 128×6 pixels are interesting for the PANDA Endcap DIRC. However, the high pixel density required the design of special frontend boards to enable a parallel readout of all pixels simultaneously. The first measurements show a very good position resolution of down to 0.5 mm. This will soon be further tested inside a B-field of 2 Tesla to study the gain behavior and in particular focusing effects on the position resolution. Afterwards these tubes will be included in our lifetime setup.

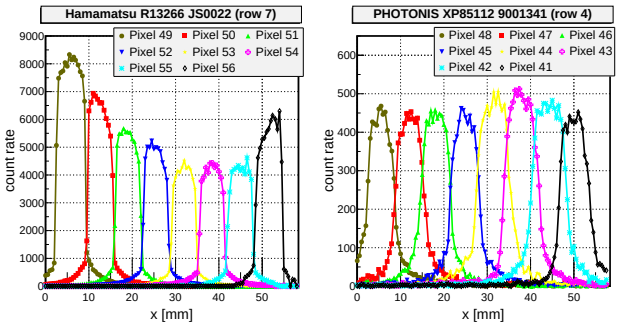

Figure 2: Comparison of the crosstalk among the anode pixels for a PHOTONIS and the new Hamamatsu 2-inch MCP-PMTs with ALD coating both with 10 μm pore size.

References

[1] A. Britting, et al., 2011 JINST 6 C10001

[2] F. Uhlig, et al., Nucl. Instr. and Meth. A 787 (2015) 105

[3] A. Lehmann, et al., DIRC2015 Proceedings

* Work supported by GSI (contracts EREYRI1416 and ERANTO1419) and BMBF

† Albert.Lehmann@physik.uni-erlangen.de

Cooling system of the $\overline{\text{P}}$ANDA-EMC forward endcap*

S. Leiber† [1], *M. Albrecht*[1], *M. Fink*[1], *F.-H. Heinsius*[1], *T. Held*[1], *T. Holtmann*[1], *B. Kopf*[1], *M. Kümmel*[1], *M. Kuhlmann*[1], *P. Musiol*[1], *A. Mustafa*[1], *M. Pelizäus*[1], *J. Pychy*[1], *M. Richter*[1], *C. Schnier*[1], *T. Schröder*[1], *C. Sowa*[1], *M. Steinke*[1], *T. Triffterer*[1], *and U. Wiedner*[1]

[1]Ruhr-Universität Bochum, Germany

Introduction

The Electromagnetic Calorimeter (EMC) of the $\overline{\text{P}}$ANDA target spectrometer is placed inside a superconducting solenoid and consists of two endcaps and a barrel part.

Lead tungstate crystals ($PbWO_4$) will be used as scintillator material because of its fast response, compactness, adequate radiation hardness and a sufficient energy resolution over the large range of photon energies.

The operation temperature of the $\overline{\text{P}}$ANDA-EMC is set to -25°C. Compared to room temperature at +25°C the light yield is increased by a factor of ≈ 4. The light yield dependency at -25°C amounts to dLY/dT = 3.0% [1] and requires a temperature stability of ± 0.1°C [2].

The Forward Endcap Cooling System

In order to achieve a stable operating temperature, a system of different cooling substructures is necessary. A cooling unit with adjacent pump provides the cooling liquid for both endcap cooling systems and the barrel cooling, then the circuit is split into individual cooling substructures. The forward endcap cooling system is divided into four substructures: the main cooling, the front cooling, the side cooling, and the air cooling. The first three cooling substructures are operated with a methanol-water mixture (50:50) and the air cooling is provided by cleaned, dried and cooled compressed air.

Main Cooling

All alveoli, which contain the scintillator crystals with photo detectors and their preamplifiers, are directly mounted to the aluminium backplate. The preamplifier heat output (≈ 650 W) is transferred to the backplate. Into this backplate, holes for the cooling liquid with a diameter of 13 mm are drilled along its entire length to remove the heat. The backplate consists of 22 straight holes and 14 U-turn holes above and below the beam pipe feedthrough in order to achieve a uniform cooling.

Front and Side Cooling

Both the front and side cooling are set up to minimize the temperature gradient inside the forward endcap. The front cooling is directly connected to the front plate in front of the scintillator crystals and is made of two pipes with an outer diameter of 10 mm. Each pipe follows a winding route to cover one half of the front plate and is made of methanol resistant synthetics to reduce the material density compared to aluminium in front of the scintillation crystals.

The side cooling is mounted on the inner side of the stiffener ring flanking the alveoles and is divided into two vertical segments to split the cooling of the stiffener ring into equal halves. Both segments consist of three parallel aluminium pipes to cover the overall width of the stiffener ring.

Air Cooling

Compressed air is used to reduce the air humidity inside the forward endcap in order to prevent condensation and icing. In order to cool down the air its feed pipe is running inside the cooling liquid supply pipe for the other cooling substructures [3]. The supply of cooled air is split into several inlets to create a uniform air exchange within the cooled area of the forward endcap.

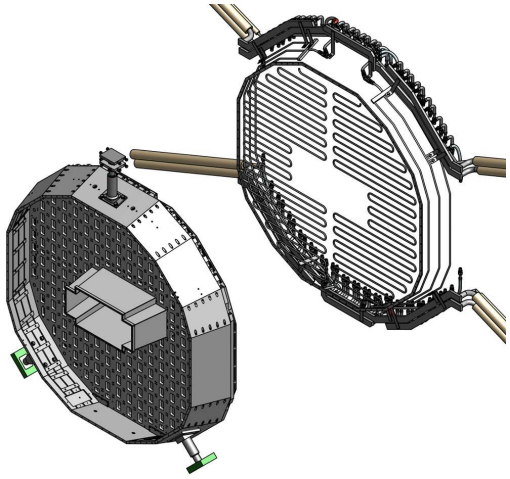

Figure 1: Forward endcap backplate with stiffener ring (left) and cooling pipes of the front and side cooling (right).

References

[1] $\overline{\text{P}}$ANDA Collaboration, EMC Technical Design Report, 2008.

[2] J. Becker, Analyse des Zerfalls $\chi_{cJ} \rightarrow K^+K^-\eta$ bei BES-III und Entwicklung eines Kühlsystems für den Prototypen des PANDA-EMC, Dissertation, Ruhr-Universität Bochum, 2012.

[3] C. Schnier et al., Inlet and Outlet of the Main Cooling for the $\overline{\text{P}}$ANDA-EMC Forward Endcap, GSI Scientific Report 2015.

* Work supported by BMBF and EU

† E-mail: stephan@ep1.rub.de

DOI:10.15120/GR-2016-1

Inlet and outlet of the main cooling for the $\overline{\text{P}}$ANDA EMC forward endcap*

C. Schnier†[1], *M. Albrecht*[1], *M. Fink*[1], *F.-H. Heinsius*[1], *T. Held*[1], *T. Holtmann*[1], *B. Kopf*[1], *M. Kümmel*[1], *M. Kuhlmann*[1], *S. Leiber*[1], *P. Musiol*[1], *A. Mustafa*[1], *M. Pelizäus*[1], *J. Pychy*[1], *M. Richter*[1], *T. Schröder*[1], *C. Sowa*[1], *M. Steinke*[1], *T. Triffterer*[1], *and U. Wiedner*[1]

[1]Ruhr-Universität Bochum, Germany

Introduction

The $\overline{\text{P}}$ANDA EMC will use $PbWO_4$-crystals as scintillator. This material achieves a fast response, sufficient energy resolution and efficiency and an adequate radiation hardness. The light yield of $PbWO_4$ can be improved by a factor of four if it is cooled down from $+25°\text{C}$ to $-25°\text{C}$ [1]. To achieve a stable operation temperature at $-25°\text{C}$, the forward endcap of the $\overline{\text{P}}$ANDA EMC will have a thermal insulation [2] combined with a multi part cooling system [3].

Main Cooling

One part of the cooling system is the main cooling. It consists of an eight-piece manifolds which is connected on top and below the forward endcap backplate with 72 hoses. A methanol/water mixture (50/50) is used as cooling liquid. It is forseen to adjust individually the cooling flow of each hose by reduction shim between the connection of the backplate and each hose. The backplate is cooled down through bores whereby the main part of the rejected heat is dissipated through the main cooling. In combination with the other cooling parts a $PbWO_4$-crystal temperature gradient along the crystal length of $\Delta T \leq 0,1°\text{C}$ can be achieved [4].

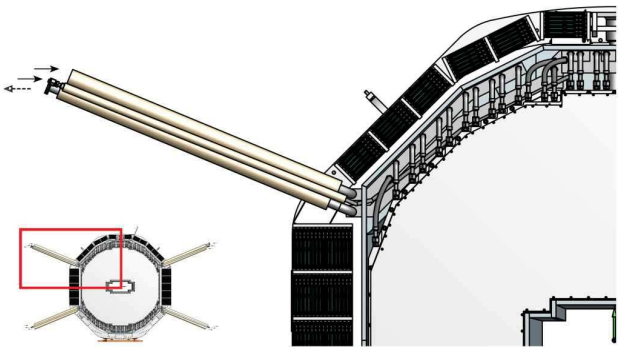

Figure 1: Back view of the EMC forward endcap with removed parts to show the main cooling (filled arrow=inlet, dotted arrow=outlet).

Developement of the Inlet and Outlet

The $\overline{\text{P}}$ANDA EMC is located inside a solenoid yoke with restricted space inside the feedthrough holes for cooling, cables and fibres. In order to fulfill the thermal requirements with a minimum of cross-sectional area, a combination of PU and vacuum insulated inlet and outlet is forseen.

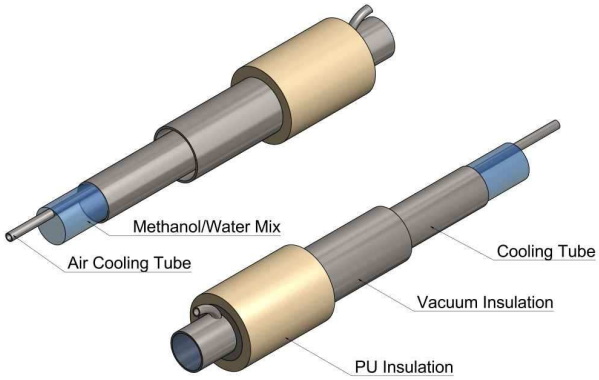

Figure 2: Scheme of the insulated main cooling inlet of the forward endcap.

In order to have an optimal use of the available space, inside the inlet and outlet of the main cooling respectively one air cooling pipe is carried. Therefore no additional heat exchanger is required. Thus a cross-sectional area of about $111\,\text{cm}^2$ of the cooling pipes inside the solenoid feedthrough can be achieved and fullfill the tight space requirements.

In Order to ensure a stable flow inside the cooling system and therefore a stable temperature, air pockets have to be removed from the pipes. To realize this, it is forseen to create a venting at the top side of the manifold. Due to shortage of space just a few millimeters distance is available between the manifold and the insulation. Outside the solenoid yoke the vent valve will be located to give a good accessibility.

References

[1] $\overline{\text{P}}$ANDA-Collaboration, EMC Technical Design Report, 2008.

[2] S. Leiber et al., "Development of the Insulation for the $\overline{\text{P}}$ANDA EMC", GSI Scientific Report 2014.

[3] S. Leiber et al., "Cooling System for the $\overline{\text{P}}$ANDA EMC Forward Endcap", GSI Scientific Report 2015.

[4] J. Schulze, "Prototypentwicklung für das elektromagnetische Kalorimeter des $\overline{\text{P}}$ANDA-Experimentes", Diploma Thesis, Ruhr-Universität Bochum, April 2009.

* Work supported by BMBF and EU

† E-mail: cschnier@ep1.ruhr-uni-bochum.de

Monte Carlo simulation for the PANDA GEM-tracker detector

N.Divani-Veis[1, 2, 3], A.Ehret[1], R.Karabowicz[1], T.R.Saito[1, 2], B.Voss[1]
[1]GSI, Darmstadt, Germany; [2]HIM, Mainz, Germany; [3]University of Birjand, Iran

A gas electron multiplier (GEM) is a type of a gaseous ionization detector, and it will be used as a first forward tracking detector behind the central tracker in the PANDA set-up [1, 2, and 3]. The system will provide measurements of charged particle trajectories with high precision over a large solid angle between 3º and 20º. In the former simulation studies [4], only the sensitive volumes acting mostly as detectors and readout systems were implemented in the PANDA Monte Carlo simulation program. Based on the technical design recently all the materials associated with the GEM-tracker detector have now been included in the simulations for the present work.

The GEM-tracker detector system consists of three stations. The first station is mounted approximately at about 1m behind the target along the beam axis in the solenoid magnet. Each station realizes a complex series of multi-layers with detector windows, cathodes, GEM foils, sensitive pad planes, Ar/CO_2 gas containers, cooling support and electronic devices. The double-sided read-out pad planes are located in the centre of each station providing strip information about crossing particles in 4 projections: radial and circular (in front), horizontal and vertical (in back). Each station consists of 47 layers, and the material and the shape of all the layers are implemented in the simulation program. The Riddle shell with its rigid and light-weight support structures which holds all the GEM-tracker stations have also been implemented. In this work, it is tried to get close to GEM realistic geometry as far as possible. Figure 1 shows the mechanically designed GEM-tracker by CAD (left) and GEM-tracker system implemented in the PANDARoot the simulation (right).

In the present geometry of the GEM-tracker system, we looked into mass reconstruction of J/ψ and Ψ (2s) with simulated events in order to check an enhancement of the background due to implementing more materials as described above. Figure 2 shows one of the results for J/ψ (left) and Ψ (2s) (right), with the former geometry (blue line) and with the present geometry (red line). It exhibits almost no difference indicating that there is no significant enhancement in the invariant mass reconstruction by putting all materials associated with the GEM-tracker system. Investigations on the detailed performance of the GEM-tracker system are in progress.

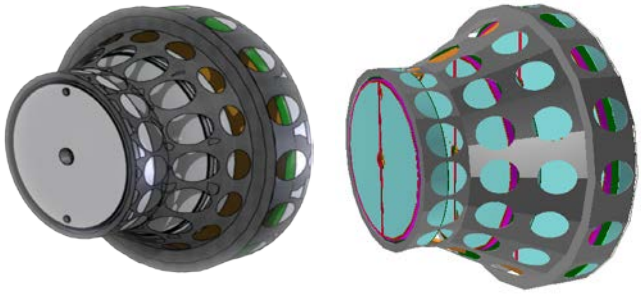

Figure 1: PANDA GEM-Tracker realistic geometry (left: as CAD design, right: implemented in the PandaRoot simulation).

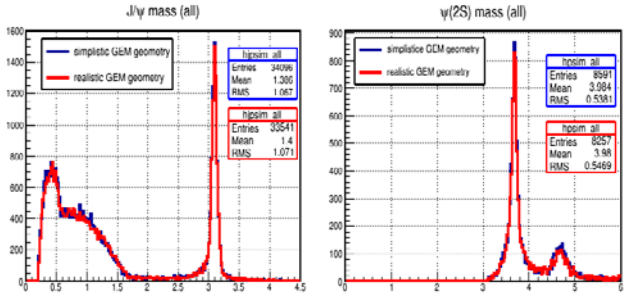

Figure 2: The reconstructed invariant mass distributions of J/ψ (left) and Ψ (2s) (right) with the former geometry (blue histogram) and with the present implementation (red histogram).

References

[1] B.Voss et al., GSI Scientific Report 2008, page 242.
[2] R.Karabowicz et al., GSI Scientific Report 2009, page 12.
[3] B.Voss et al., GSI Scientific Report 2009, page 338.
[4] R.Karabowicz, GSI Scientific Report 2012, page 301.

DOI:10.15120/GR-2016-1

Initial operation of the cluster-jet target for $\overline{\text{P}}$ANDA*

A.-K. Hergemöller†[1], *D. Bonaventura*[1], *S. Grieser*[1], *B. Hetz*[1], *E. Köhler*[1], *and A. Khoukaz*[1]
[1]Westfälische Wilhelms-Universität, Münster, Germany

For the $\overline{\text{P}}$ANDA experiment the day-one target is planned to be a cluster-jet target. The prototype of this target has already been built up at the University of Münster in 2008 [1] and operates successfully since then. With this device it is routinely possible to achieve target thicknesses of more than $2 \times 10^{15}\ \frac{\text{atoms}}{\text{cm}^2}$. Based on the experiences with the prototype the final cluster-jet target for $\overline{\text{P}}$ANDA was designed [2] and set successfully into operation in Münster recently (see Fig. 1). The cluster beam is produced due

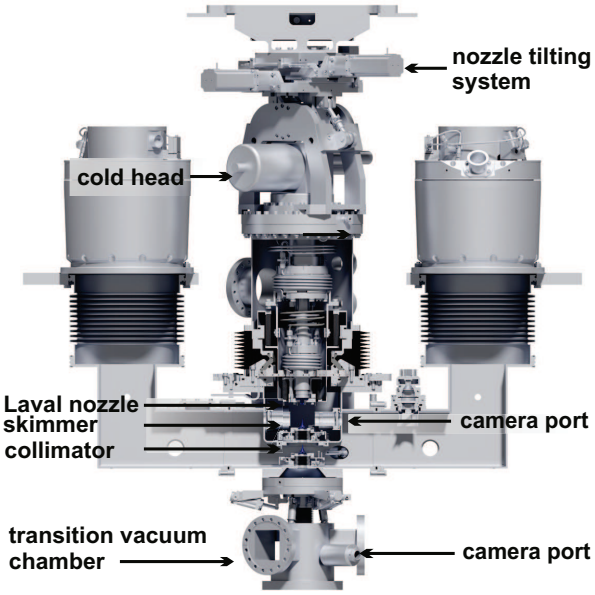

Figure 1: Main components of the cluster-jet source.

to the expansion of pre-cooled gases within a Laval nozzle (further information on Laval nozzles can be found in [3]). The extraction of the beam from the surrounding gas jet and the definition in size and shape is done via two orifices, the so called skimmer and collimator. Furthermore, the cluster source includes a nozzle tilting system consisting of a spherical joint with the narrowest point of the Laval nozzle as point of rotation. With this feature it is possible to extract highly intensive core beams [4], which correspond to regions of higher thicknesses within the cluster beam. The presence and position of these core beams mainly depend on the stagnation conditions in front of the nozzle. A first measurement series of the cluster beam at the final $\overline{\text{P}}$ANDA target directly behind the nozzle is shown in

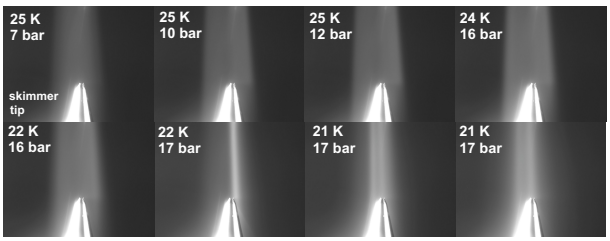

Figure 2: Cluster beam at different stagnation conditions. The beam direction is from top to bottom.

Fig. 2. By tilting the nozzle systematically, it is possible to extract different regions of the cluster beam. A measurement of the beam thickness in dependence of the nozzle orientation then leads to a two-dimensional scan of the whole cluster beam. For that purpose, initial measurements were already performed at low target thicknesses. With the future integration of the final beam dump of the cluster-jet target, it will be possible to perform the cluster beam scans at highest thicknesses, as well. The integration is planned for the first half of 2016. After extensive tests of the cluster source, the beam dump and all corresponding components, it is planned to install the target at the COSY accelerator in Jülich for first test operations in an experimental environment. Above that, further investigations on the cluster size and mass (cf. [4]) are planned. Therefore, a Mie scattering setup was designed, consisting of a diode laser, which can be moved around the cluster beam, and a glass fiber in combination with a photon counting module to measure the scattering distribution in almost $360°$ around the cluster beam. Currently, the setup is tested and optimized with regard to possible stray light coming from the setup itself.

References

[1] A. Täschner et al., Nucl. Instr. and Meth. A660 (2011) 22-30, doi: 10.1016/j.nima.2011.09.024.

[2] A.-K. Hergemöller, "Design and Special Features of the Cluster-Jet Target for $\overline{\text{P}}$ANDA", GSI Scientific Report 2014 (2015).

[3] S. Grieser, "Glass Laval Nozzle Prototypes for Cluster-Jet Targets", GSI Scientific Report 2015 (2016).

[4] E. Köhler, "Mass spectroscopy of hydrogen cluster-jets and beam density optimisation studies", PhD Thesis, University of Münster, 2016.

* Work supported by HGS-HIRe for FAIR, BMBF and GSI.
† a.hergemoeller@wwu.de

Glass Laval nozzle prototypes for cluster-jet targets*

S. Grieser†[1], *D. Bonaventura*[1], *A.-K. Hergemöller*[1], *B. Hetz*[1], *E. Köhler*[1], *L. Lessmann*[1], *C. Westphälinger*[1], *and A. Khoukaz*[1]

[1]Institut für Kernphysik, Westfälische Wilhelms-Universität Münster, Germany

Cluster-jet targets provide high and constant beam densitiesand are by this highly suited for storage ring experiments. A cluster source generates a continuous flow of cryogenic solid clusters by the expansion of pre-cooled gas, i.e. hydrogen, within fine Laval nozzles. The geometry of the nozzle is crucial for the cluster production prozess (see Fig. 1). The production of such nozzles with their fine complex inner geometry represents a major technical challenge. Our possibility to produce new Laval nozzles ensures the operation of cluster-jet targets, e.g. for the $\overline{\text{P}}$ANDA experiment, and allows via systematic tests a better insight in the production of clusters to match the required target performance [1]. Up to now metal nozzles were used routinely [2]. Latest, investigations on precise

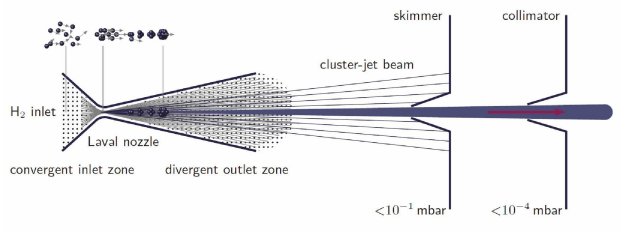

Figure 1: Sketch of the cluster production process [3].

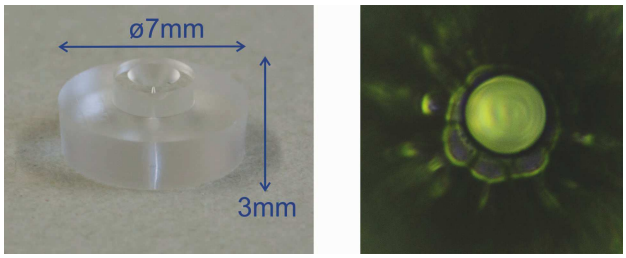

Figure 2: Left: The new glass nozzle. Right: Microscopic view of the narrowest inner diameter of about 30 μm.

nozzles manufactured by selective laser etching of glass are performed. This manufacturing process is currently limited by the used optics components which results currently in a maximal length of 3 mm of the glass nozzle (see Fig. 2). Furthermore, an extension for the glass nozzle to enlarge the outlet zone was produced, so that the new combined nozzle has the same length (18 mm) as the previous metal ones. An adapation system was developed to adapt the new nozzles to the currently used geometry. In this context a new self manufactored polymid sealing was developed as an excellent alternative for indium sealing (see Fig. 3). A

Figure 3: From left to right: Polymid ring for sealing between nozzle adaptor and cold head, aluminium ring to adapt the nozzle to the currently used geometry, polymid cone for sealing between nozzle and aluminium ring, new glass nozzle, aluminium part to fix the glass nozzle in the nozzle adaptor.

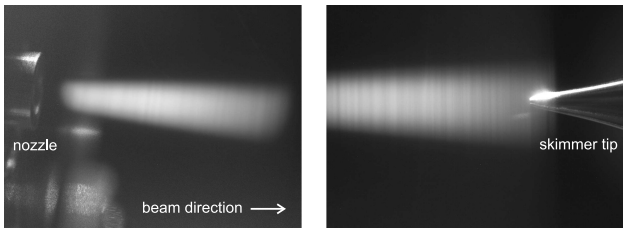

Figure 4: Cluster beam produced with the glass nozzle.

cooling test with 18 bar helium down to 19.5 K was successfully performed. Different to indium the new sealing also ensures an accurate and clean extraction of the sealing and above that, it is non-poisonous and reusable. Measurements with the new glass nozzle at the $\overline{\text{P}}$ANDA cluter-jet target prototype show a defined, stable, and reproducible cluster beam in a distance of 2.1 m from the nozzle (see Fig. 4). Further systematic studies and an optimisation of the target thickness by the adjustment of the nozzle tilting system, skimmer, and collimator as well as investigations on different nozzle geometries and their influence on the cluster beam will be performed.

References

[1] A.-K. Hergemöller, Initial Operation of the Cluster-Jet Target for $\overline{\text{P}}$ANDA, GSI Scientific Report 2015 (2016).

[2] S. Grieser, A new Production Process for Laval Nozzles, GSI Scientific Report 2014 (2015).

[3] E. Köhler, PhD Thesis, University of Münster, 2015, Germany.

* Work supported by HGS-HIRe for FAIR, BMBF, and GSI

† s.grieser@uni-muenster.de

DOI:10.15120/GR-2016-1

New results from IMS of uranium fission fragments with FRS-ESR*

M. Diwisch[1], R. Knöbel[1,2], H. Geissel[1,2], Yu. A. Litvinov[2], Z. Patyk[3], W. R. Plaß[† 1,2], C. Scheidenberger[1,2], B. Sun[2,4], H. Weick[2], F. Bosch[2], D. Boutin[2], L. Chen[1,2], C. Dimopoulou[2], A. Dolinskii[2], B. Franczak[2], B. Franzke[2], M. Hausmann[5], C. Kozhuharov[2], J. Kurcewicz[2], S. A. Litvinov[2], G. Martinez-Pinedo[2,6], M. Matoš[2], M. Mazzocco[2], G. Münzenberg[2], S. Nakajima[7], C. Nociforo[2], F. Nolden[2], T. Ohtsubo[8], A. Ozawa[9], J. Stadlmann[2], M. Steck[2], T. Suzuki[7], P. M. Walker[10], M.-R. Wu[6], M. Winkler[2], and T. Yamaguchi[7]

[1]Justus-Liebig-Universität Gießen; [2]GSI Helmholtzzentrum für Schwerionenforschung GmbH, Darmstadt; [3]National Centre for Nuclear Research - NCBJ Swierk, Warsaw, Poland; [4]Beihang University, Beijing, China; [5]Michigan State University, East Lansing, USA; [6]Technische Universität Darmstadt; [7]Saitama University, Saitama, Japan; [8]Niigata University, Niigata, Japan; [9]University of Tsukuba, Ibaraki, Japan; [10]University of Surrey, Guildford, United Kingdom

A novel data analysis method has been applied to two Isochronous Mass Spectrometry (IMS) experiments [1, 2, 3]. In these, a 410 MeV/u ^{238}U projectile beam was fast extracted from the synchrotron SIS-18 with an average intensity of 10^9/spill. The projectiles were focused on a 1 g/cm^2 beryllium target at the entrance of the FRS to create neutron-rich isotopes via abrasion-fission. The fission fragments were spatially separated with the FRS and injected into the isochronous storage ring ESR for fast mass measurements without applying cooling. IMS was performed under two different experimental conditions, with and without Bρ-tagging [4] at the high-resolution dispersive central focal plane of the FRS. In the experiment with Bρ-tagging the magnetic rigidity of the injected fragments was determined with an accuracy of $2 \cdot 10^{-4}$.

The new method of data analysis, which uses a correlation matrix for the combined data set from both experiments, has provided experimental mass values of 25 neutron-rich isotopes in the element range from Se to Ce for the first time (Fig. 1) and improved values for 6 isotopes [5, 6, 7]. The high sensitivity and selectivity of the method have given access to nuclides detected with a rate of a few atoms per week. Figure 2 shows the difference of the experimental mass values for Te, Sn and Cd isotopes and the prediction of the liquid drop model. The liquid-drop parameters have been deduced from a fit to the tabulated values of the Atomic Mass Evaluation 2012 (AME2012). The experimental mass values of Te, Cd and Sn isotopes show a pronounced shell effect towards and at N=82.

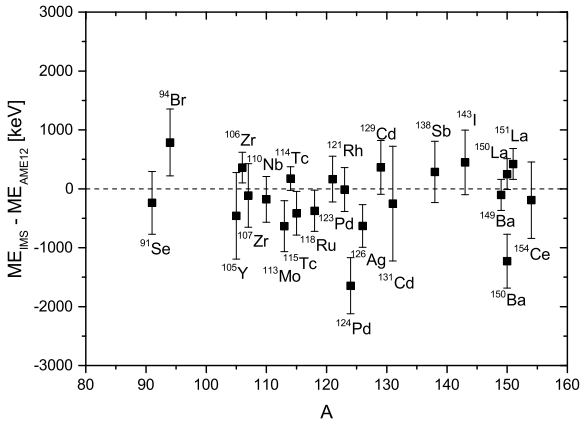

Figure 1: Measured new mass values compared with the corresponding extrapolated AME2012 values.

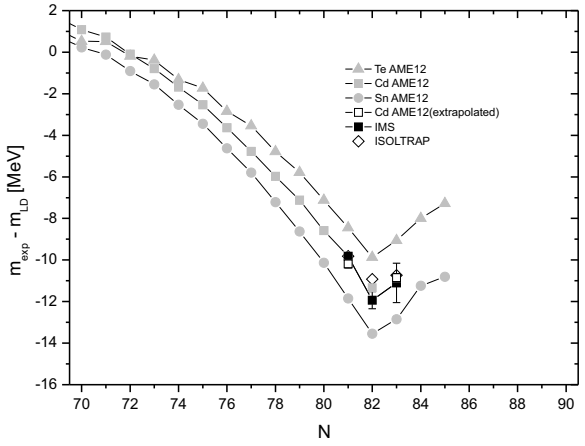

Figure 2: Difference between measured mass values including values of this work (IMS) and that of a recent publication (ISOLTRAP) [8] and the prediction of the liquid drop model for the elements Te, Sn and Cd.

References

[1] M.Matos, PhD Thesis, JLU Giessen, (2004).

[2] R. Knöbel, PhD Thesis, JLU Giessen, (2008).

[3] B. Sun et al., Phys. Lett. B 688 (2008) 294.

[4] H. Geissel et al., Hyperfine Interact. 173 (2006) 49.

*Work supported by the BMBF (06GI9115I, 06DA7047I), the Helmholtz Association (HGF) through the Nuclear Astrophysics Virtual Institute (VH-VI-417), the Helmholtz International Center for FAIR (HIC for FAIR) within the framework of the LOEWE program launched by the State of Hesse, and the UK Science and Technology Facilities Council.

† Wolfgang.R.Plass@exp2.physik.uni-giessen.de

[5] R. Knöbel et al., Phys. Lett. B 754 (2016) 288.

[6] R. Knöbel et al., Eur. Phys. J. A (in press).

[7] M. Diwisch, PhD Thesis, JLU Giessen, (2015).

[8] D. Atanasov et al., Phys. Rev. Lett. 115 (2015) 232501.

Charge changing cross sections of neutron-rich carbon isotopes*

R. Kanungo[1] F. Ameil[2], J. Atkinson[1], Y. Ayyad[3], D. Cortina-Gil[3], I. Dillmann[2], A. Estradé[1,2], A. Evdokimov[2], F. Farinon[2], H. Geissel[2,4], G. Guastalla[2], R. Janik[5], R. Knöbel[2], J. Kurcewicz[2], Yu. A. Litvinov[2], M. Marta[2], M. Mostazo[3], I. Mukha[2], C. Nociforo[2], H.J. Ong[6], S. Pietri[2], A. Prochazka[2], C. Scheidenberger[2,4], B. Sitar[5], P. Strmen[5], M. Takechi[2], J. Tanaka[6], I. Tanihata[6,7], S. Terashima[7], J. Vargas[3], H. Weick[2], J. S. Winfield[2]

[1]Saint Mary's University, Halifax, Canada; [2]GSI, Darmstadt, Germany; [3]Universidad de Santiago de Compostela , Santiago de Compostella, Spain, [4]University of Giessen, Giessen, Germany, [5]Comenius University, Bratislava, Slovakia, [6]RCNP, Osaka University, Osaka, Japan, [7]Beihang University, Beijing, China,

The measurement of charge changing cross sections of $^{12-19}$C performed at the FRS, is reported.

The root mean square radius of point proton density distribution (herefater referred to as proton radius) is one of the fundamental properties of a nucleus. Its importance for neutron-rich nuclei is for determining the neutron skin thickness and in halos, for finding the correlation between the halo neutron(s) and the core nucleus. The proton radii are also sensitive observables to test nuclear theories, in particular the nuclear interactions.

The matter radii of the light neutron-rich nuclei in the *p-sd* shell have been derived from measurements of interaction cross sections [1,2] and for some by proton elastic scattering [3] as well. There is however very limited information on the proton radii. This is largely because the traditional techniques like electron scattering are still not feasible for the short-lived nuclei approaching the neutron drip-line.

A new approach that has recently been employed is the determination of proton radii from charge changing cross sections analyzed in a Glauber model framework [4-6]. The charge changing cross section is a sum of all interactions between the protons and neutrons of the target and the protons of the projectile (nucleus of interest).

Here we report accurate measurements of charge changing cross sections (σ_{cc}) for $^{12-19}$C at energies of ~ 900*A* MeV performed using the fragment separator, FRS at GSI [7]. Secondary beams of these isotopes were produced via projectile fragmentation of ^{20}Ne and ^{40}Ar primary beams on a Be target. The FRS was used to separate and identify the incident beam. This was accomplished using energy-loss information from a multi-sampling ionization chamber (MUSIC), magnetic rigidity measured using position sensitive TPC detectors. These detectors were located at the final achromatic focus F4. The time-of-flight between two plastic scintillators placed at the dispersive focus F2 and at F4 provided the velociy of the secondary beam. The number of incident nuclei (N_{in}) of interest were identified and counted event by event using the Z vs A/Q correlation obatined from the above-mentioned detectors.

After interaction of the beam with a reaction target (carbon or polyethylene target) at F4 the number of un-interacted nuclei (N_{out}) with the same Z number as the incident beam were identified and counted using another MUSIC detector placed immediately downstream of the reaction target. In order to eliminate the cross section arising from change of charge due to processes like charge exchange where the interaction occurs with the neutrons in the target, the Z=7 events populated from the reaction of the carbon isotopes with the target were subtracted. The ratio N_{out}/N_{in} is used to obtain σ_{cc}.

Figure 1 shows the measured σ_{cc}. The cross section shows an increase for ^{15}C. This is a associated with the effect of the one-neutron halo in this nucleus. A gradual increase is observed beyond that until ^{17}C. The cross section does not show much increase after that. The σ_{cc} clearly show that the proton radii do not evolve following $A^{1/3}$ dependence along an isotopic chain.

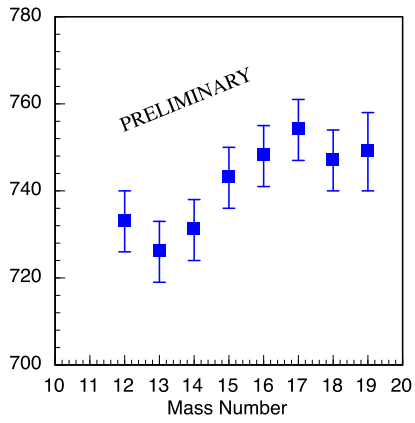

Figure 1 : Charge changing cross sections of ^{A}C+C.

References

[1] A. Ozawa, T. Suzuki and I. Tanihata, Nucl. Phys. A 693 (2001) 32.
[2] I. Tanihata, H. Savajols and R. Kanungo, Prog. Part. Nucl. Phys. 68 (2013) 215.
[3] P. Egelhof et al., Euro. Phys. Jour. A 15 (2002) 27.
[4] T. Yamaguchi et al. Phys. Rev.C 107 (2011) 032502.
[5] A. Estrade et al., Phys. Rev. Lett. 113 (2014) 132501.
[6] S. Terashima et al., Prog. Theor. Exp. Phys. (2014) 101D02.
[7] H. Geissel et al., Nucl. Instrm. Meth. Res. B 70 (1992) 286.

DOI:10.15120/GR-2016-1

Understanding effect of tensor interactions in light nuclei via high-momentum one-neutron-transfer reaction *

H.J. Ong† [1] *and the S436 Collaboration*
[1]RCNP, Osaka University, Osaka, Japan

The tensor interactions which originate from the pion exchange are essential interactions that provide the most significant two-body attraction in nuclear interactions. Theoretically, ab-initio calculations [1] have pointed out the essential importance of the tensor interactions for binding nuclei up to mass number A=12. However, while it is generally accepted that the tensor interactions play a dominant role in nuclei, experimental evidence has been scarce and was limited to the lightest nuclei up to ^{4}He. In an earlier work [2], we reported a possible evidence on the effect of the tensor interactions in ^{16}O based on the observation of a large component of high-momentum neutrons. The high-momentum neutron-transfer ^{16}O(p,d) reactions were performed at energies between 200 – 400 MeV and at finite angles between 10 – 25 degrees. However, the observed "enhanced high-momentum components" at these finite angles could have been falsely caused by reaction mechanisms, which may become important at these angles.

Here, we report measurements of high-momentum one-neutron transfer (p,d) reactions centered at 0 degree at the FRS (i) to investigate the effect of reaction mechanisms, and (ii) to search for supporting evidence for the observed "effect of tensor interactions" in ^{16}O.

The experiment was performed using proton beams at

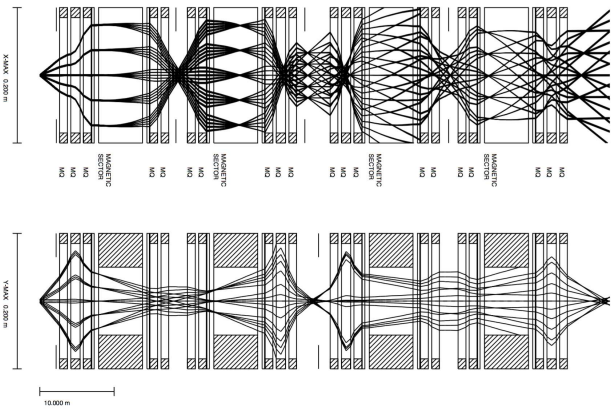

Figure 1: Beam envelopes for scattered deuterons from the target station to the S4 area of the FRS in the newly devised momentum-dispersive mode.

four energies, 403, 604, 907, and 1209 MeV, to cover momentum transfer around 2 fm^{-1}. The proton beams bombarded a POM (^{16}O) target placed in the target station at the entrance of the FRS. We used a 100- and 308-mg/cm^2-thick POM target for the measurements with the two lower-energy and two higher-energy proton beams respectively. The scattered deuterons were momentum analyzed by the FRS, operated in a momentum-dispersive mode, and detected at the focal plane using two multi-wire drift chambers (MWDCs) and a plastic scintillator. Fig. 1 shows the beam envelopes in the horizontal (top panel) and vertical (bottom panel) axes respectively. The dispersion from the target position to the S4 focal plane was about 17 m.

Figure 2 shows the measured angle and horizontal position at the first (upstream) MWDC. The three loci on the left correspond to three discrete states in ^{15}O and ^{11}C, while the locus on the right corresponds to the admixture of the excited 3/2$^-$ state in ^{15}O and the excited 1/2$^-$ state in ^{11}C. Measurements with a $^{\rm nat}$C target were also performed to subtract the contributions from the ^{12}C contaminant in the POM target. Preliminary results for the measurements at 403 MeV are consistent with the previous measurement at finite angles [2], indicating that the effect of reaction mechanisms is negligible. Detailed data analyses for other energies are in progress.

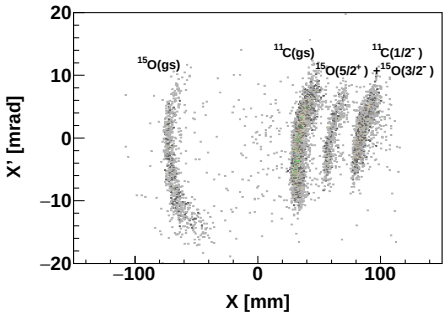

Figure 2: The horizontal position and angle of the scattered deuterons at the first (upstream) MWDC for the measurements with 403-MeV proton beam. The three loci on the left correspond to the ground state (1/2$^-$), the excited 5/2$^+$ state in ^{15}O, and the ground state (3/2$^-$) in ^{11}C. The locus on the right corresponds to the admixture of the excited 3/2$^-$ state in ^{15}O and the excited 1/2$^-$ state in ^{11}C.

References

[1] S. C. Pieper and R. B. Wiringa, Annu. Rev. Nucl. Part. Sci. 51, 53 (2001).

[2] H.J. Ong, et al., Phys. Lett. B725, 277 (2013).

* The experiment was performed within the framework of the NUSTAR Super-FRS Collaboration.

† onghjin@rcnp.osaka-u.ac.jp

DOI:10.15120/GR-2016-1

Observation and spectroscopy of new proton-unbound isotopes ^{30}Ar and ^{29}Cl

I. Mukha * [1], *L.V. Grigorenko*[2,3], *X. Xu*[1,4], *L. Acosta*[5], *E. Casarejos*[6], *A.A. Ciemny*[7], *W. Dominik*[7], *J. Duénas-Díaz*[8], *V.Dunin*[2], *J. M. Espino*[9], *A. Estradé*[10], *F. Farinon*[1], *A. Fomichev*[2], *H. Geissel*[1,4], *T.A. Golubkova*[11], *A. Gorshkov*[2], *Z. Janas*[7], *G. Kamiński*[12], *O. Kiselev*[1], *R. Knöbel*[1,4], *S. Krupko*[2], *M. Kuich*[7], *Yu.A. Litvinov*[1], *G. Marquinez-Durán*[8], *I. Martel*[8], *C. Mazzocchi*[7], *C. Nociforo*[1], *A. K. Ordúz*[8], *M. Pfützner*[7,1], *S. Pietri*[1], *M. Pomorski*[7], *A. Prochazka*[1], *S. Rymzhanova*[2], *A.M. Sánchez-Benítez*[8], *C. Scheidenberger*[1,4], *P. Sharov*[2], *H. Simon*[1], *B. Sitar*[13], *R. Slepnev*[2], *M. Stanoiu*[14], *P. Strmen*[13], *I. Szarka*[13], *M. Takechi*[1], *Y.K. Tanaka*[1,15], *H. Weick*[1], *M. Winkler*[1], *J.S. Winfield*[1], *and M.V. Zhukov*[16]

[1]GSI, Darmstadt, Germany; [2]JINR, Dubna, Russia; [3]Kurchatov Institute, Moscow, Russia; [4]University of Gießen, Germany; [5]Universidad de México, Mexico; [6]University of Vigo, Spain; [7]University of Warsaw, Poland; [8]University of Huelva, Spain; [9]University of Seville, Spain; [10]University of Edinburgh, UK; [11]University of Moscow, Russia; [12]INP PAN, Kraków, Poland; [13] Comenius University, Bratislava, Slovakia; [14]IFIN-HH, Bucharest, Romania; [15]University of Tokyo, Japan; [16]Chalmers University, Göteborg, Sweden

We report on the discovery and spectroscopic study of the $2p$ emitter ^{30}Ar and its neighbor ^{29}Cl by use of a ^{31}Ar beam at the fragment separator FRS of GSI.

The experiment is based on in-flight decay of the $2p$ emitters and the tracking of the decay-product trajectories by micro-strip silicon detectors (its first application can be found in Ref. [1]). First, radioactive ^{31}Ar ions were produced by fragmenting a 885 *A*MeV ^{36}Ar primary beam in a 8 g/cm^2 ^{9}Be target. To separate the ^{31}Ar fragments, a thick wedge degrader was installed at the first focal plane of the FRS. The wedge was shaped for an achromatic focusing of the 620 *A*MeV ^{31}Ar beam on the secondary 4.8-g/cm^2-thick ^{9}Be target located at the mid-plane of the FRS. The ^{31}Ar intensity was 50 ions s^{-1}, and the ^{30}Ar ions of interest were produced via one-neutron knockout reactions in the secondary target. A set of 4 large-area micro-strip silicon detectors was positioned downstream of the target to measure positions of all ^{30}Ar in-flight decay products, e.g., coincident two protons and a heavy-ion recoil. The detectors allowed a reconstruction of all fragment and decay-product trajectories, angles and the position of the corresponding decay vertex [2]. Optical Time-Projection Chamber was used in parallel to observe beta decays of stopped ^{31}Ar ions, which passed the secondary target intact. With this implantation-decay detector, β-delayed $3p$ emission from ^{31}Ar was observed [3]. Previously unknown isotopes ^{30}Ar and ^{29}Cl have been identified by measurement of the trajectories of their in-flight decay products ^{28}S+p+p and ^{28}S+p, respectively. The analysis of angular correlations of the fragments provided information on decay energies and structure of the parent states [2]. The derived decay scheme is shown in Fig. 1.

The discovered new isotopes ^{30}Ar and ^{29}Cl are unbound. The lowest states in ^{30}Ar, ^{29}Cl point to large Thomas-Ehrman shifts with respect to their mirror nuclei, which gives an evidence on a violation of isobaric symmetry in structure of these unbound nuclei. The two-proton decay has been identified in a transition region between simultaneous two-proton and sequential proton emissions from the ^{30}Ar ground state, which is characterized by an interplay of three-body and two-body decay mechanisms [2]. Such a phenomenon, never observed before, may be common in $2p$-unbound nuclei, and could be of interest for other disciplines dealing with few-body systems. The indicated dramatic change of odd-even mass staggering in $2p$-unbound nuclei and the fine structure in the $2p$ decay of the ^{30}Ar*(2.9 MeV) state call for further investigations.

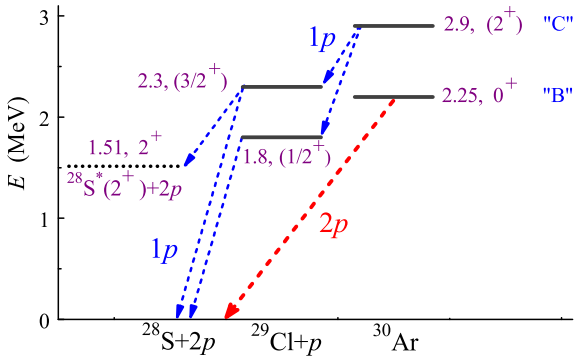

Figure 1: Decay scheme of ^{30}Ar and ^{29}Cl states [2], given relative to the $2p$ and $1p$ thresholds, respectively.

This experiment has demonstrated success of two detection techniques (implantation-decay and decay-in-flight) which are suggested by the EXPERT (EXotic Particle Emission and Radioactivity by Tracking) working group to the Super-FRS physics program [4] of the NUSTAR Collaboration of FAIR.

References

[1] I. Mukha *et al.*, Phys. Rev. Lett. **99** (2007) 182501.

[2] I. Mukha *et al.*, Phys. Rev. Lett. **115** (2015) 202501.

[3] A.A. Lis *et al.*, Phys. Rev. C 91 (2015) 064309.

[4] J. Äysto *et al.*, Nucl. Instr. Meth. B **376** (2016) 111.

* I.Mukha@gsi.de

DOI:10.15120/GR-2016-1

Analysis status of missing-mass spectroscopy of the ^{12}C(p,d) reaction near the η' emission threshold*

Y. K. Tanaka[1,2] and the η-PRiME collaboration
[1]The University of Tokyo, Tokyo, Japan; [2]GSI, Darmstadt, Germany

We investigate in-medium properties of the η' meson by means of missing-mass spectroscopy of the (p,d) reaction [1]. Since the large mass of the η' meson in vacuum (958 MeV/c^2) is theoretically understood by the $U_A(1)$ anomaly effect under the presence of spontaneous breaking of chiral symmetry, the η' mass may be reduced at normal nuclear density [2]. Actually, some model calculations predict a 4–15% reduction relative to the in-vacuum mass [3, 4, 5, 6]. Such a mass reduction would induce an attractive potential between an η' and a nucleus, suggesting possible existence of η' meson-nucleus bound states (η' mesic nuclei), which may be observed with the (p,d) reaction [7].

In 2014, we performed an inclusive measurement of the ^{12}C(p,d) reaction to obtain an excitation spectrum of ^{11}C around the η' emission threshold, in which we aimed at achieving an extremely good statistical sensitivity with a relative error size of $\sim$ 1%. A 2.5 GeV proton beam from SIS-18 impinged on to a 4 g/cm^2 thick carbon target. Deuterons ejected by the (p,d) reaction were momentum-analyzed by the FRS used as a spectrometer. A newly developed ion-optics mode was applied to the FRS with an achromatic focus at F2 and a dispersive focus at F4. Trajectories of the deuterons were measured at F4 with multi-wire drift chambers and time projection chambers. Time of flight (TOF) between the two focal planes were measured by plastic scintillation counters. A detailed experimental setup is described in Ref. [8]

For data analysis, firstly, deuterons were identified by the measured TOF and rejection of accidental multiple hits based on waveform analysis of signals from the scintillation counters. We achieved contamination probability of other background particles, mainly protons, of the order of 10^{-4} in the deuteron identified events. Secondly, the momenta of the deuterons were obtained from the measured tracks at F4 by taking into account ion-optical properties of the spectrometer, which were calibrated by measuring the d(p,d)p elastic scattering at a proton energy of 1.6 GeV.

An acceptance-uncorrected raw spectrum corresponding to $\sim$ 1% of the total data is shown in Fig. 1. The excitation energy in the horizontal axis was calculated from the momentum of the deuteron, a deduced energy of the primary beam, and an estimated energy loss in the target. The experimental energy resolution was evaluated to be < 3 MeV (σ) from the elastic d(p,d)p measurements. Since a relative error size around a central acceptance region is $\lesssim$ 10% for the $\sim$ 1% data, an extremely good statistical sensitivity at a level of $\sim$ 1% is expected to be achieved for the total accumulated data as intended.

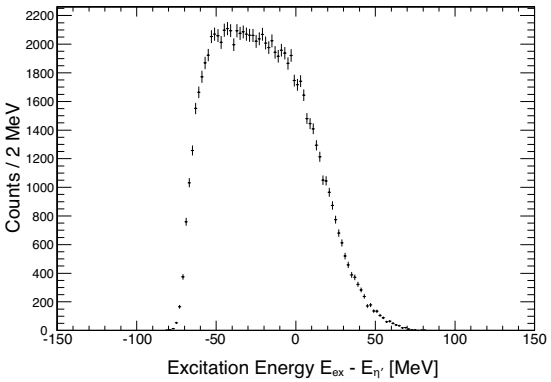

Figure 1: An acceptance-uncorrected raw spectrum for $\sim$ 1% of the total data. The horizontal axis is the excitation energy $E_{\rm ex}$ of ^{11}C referring to the η' emission threshold $E_{\eta'}$.

Further analysis is ongoing to obtain a final spectrum combining whole data sets, including a correction of acceptance and making normalization of the cross section. Existence of a peak structure originating from formation of η' mesic nuclei will be examined in a statistical method.

In the future, we plan a semi-exclusive measurement of the (p,dp) reaction in order to extend the experimental sensitivity. While an ejected deuteron will be measured by a forward spectrometer, a proton emitted from the decay of the η' mesic nuclei will be detected around a reaction target. Tagging such a proton is expected to improve the signal-to-noise ratio of the spectrum, which was very small in the present inclusive measurement. R&D for the future plan is in progress.

References

[1] K. Itahashi *et al.*, Prog. Theor. Phys. **128**, 601 (2012).
[2] D. Jido *et al.*, Phys. Rev. C **85**, 032201(R) (2012).
[3] P. Costa *et al.*, Phys. Rev. D **71**, 116002 (2005).
[4] H. Nagahiro *et al.*, Phys. Rev. C **74**, 045203 (2006).
[5] S. D. Bass and A. W. Thomas, Phys. Lett. B **634**, 368 (2006).
[6] S. Sakai and D. Jido, Phys. Rev. C **88**, 064906 (2013).
[7] H. Nagahiro *et al.*, Phys. Rev. C **87**, 045201 (2013).
[8] Y. K. Tanaka *et al.*, GSI scientific report (2015).

*The experiment was performed in the framework of the Super-FRS collaboration for FAIR.

DOI:10.15120/GR-2016-1

Baryon resonances investigated in isobaric charge-exchange reactions

J. Benlliure[1], H. Lenske[2], J.L. Rodríguez-Sánchez[1], J. Vargas[1], I. Vidaña[3], J. Atkinson[4], T. Aumann[4], Y. Ayyad[1], S. Beceiro[1], K. Boretzky[4], A. Chatillon[5], D. Cortina[1], P. Diaz[1], A. Estrade[4], H. Geissel[4], A. Kelic[4], Y. Litvinov[4], C. Paradela[1], S. Pietri[4], A. Prochazka[4], C. Scheidenberger[4], M. Takechi[4], J. Taieb[5], H. Weick[4], and J. Winfield[4]

[1]University of Santiago de Compostela, Spain; [2]University of Giessen, Germany; [3]University of Coimbra, Portugal; [4]GSI, Germany; [5]CEA DAM, Bruyeres-le-Chatel, France

Nucleonic excitations play an important role in many and divers facets of nuclear science such as the definition of three body forces [1], the quenching of the Gamow-Teller strength [2], or the description of relativistic heavy-ion collisions by using transport codes [3]. More recently, it has been pointed out the direct role of the lowest-energy nucleon excitations, the Δ-isobars, in the composition of neutron stars. Recent constraints of the symmetry energy at saturation density and its density derivative favor the appearance of Δ-isobars in β-stable nuclear matter at densities, between two and three times the saturation density, even below the limit for hyperon formation [4, 5].

Following the pioneering experiments performed at Saturne (France) [6] and KEK (Japan) [7], we investigated the excitation of nucleon resonances in isobaric charge-exchange reactions of projectile nuclei at relativistic energies. In the present experiment we accelerated beams of ^{112}Sn and ^{124}Sn at 400A, 700A and 1000A MeV. Isobar charge-exchange projectile residues were produced in reactions induced on thin targets of C, CH_2, Cu and Pb. Those (A,Z$\pm$1) residues were unambiguously identified by using the Fragment Separator [8] and the corresponding energy-loss spectra determined from the accurate measurement of their magnetic rigidity. Moreover, the measurement of the primary beam rigidity made it possible to unfold the response function of our experimental device, improving the resolution of the final missing-energy spectra [9].

In Fig. 1 we display the missing-energy spectra obtained for ^{112}In projectile residues produced in reactions induced by ^{112}Sn projectiles on a carbon target at 400A (solid line) and 1000A MeV (dashed line). In both spectra we observed to clear contributions, one for very small missing-energy values associated to the quasielastic or Gamow-Teller charge-exchange process, and a second one for missing-energy values above 150 MeV corresponding to inelastic charge-exchange reactions mediated by the excitation of the nucleon resonance.

Fig. 1 also shows that the inelastic component produced at 400A MeV is formed by a single structure with missing-energy values between 150 and 400 MeV that we associate to the excitation of the Δ(1232) isobars. At 1000A MeV we observe and inelastic process with several components, one with a maximum around 280 MeV corresponding to

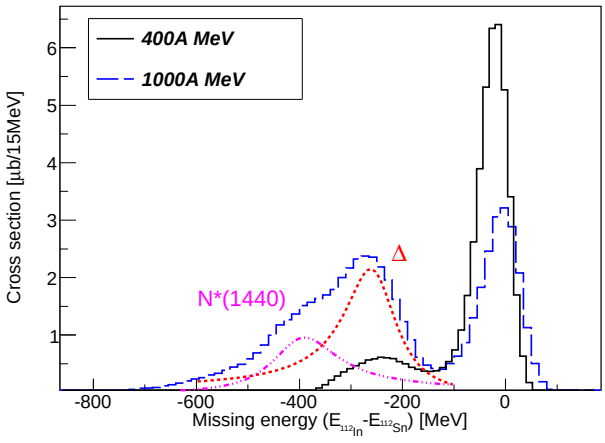

Figure 1: Missing-energy spectra corresponding to the ^{112}In production in reactions induced by ^{112}Sn projectiles on a carbon target at 1000A (dashed line) and 400A MeV (solid line).

the Δ isobars and a second one with a maximum around 400A MeV that we tentatively assign to the excitation of the N*(1440) resonance. A third structure is even observed around 600 MeV.

These results support the recent proposal for a dedicated experiment by using the SuperFRS at FAIR to investigate the in-medium excitation of nucleon resonances in isospin asymmetric nuclear matter.

References

[1] W. Zuo et al., Nucl. Phys. A **706**, 418 (2002).

[2] A. Arima, Prog. Part. Nucl. Phys. **46**, 119 (2001).

[3] Gao-Chan Yong, Phys. Rev. C **93**, 044610 (2016).

[4] A. Drago et al., Phys. Rev. D **89**, 043014 (2014).

[5] B. Cai et al., Phys. Rev. C **92**, 015802 (2015).

[6] C. Ellegard et al., Phys. Rev. Lett. **50**, 1745 (1983).

[7] J. Chiba et a., Phys. Rev. Lett. **61**, 1982 (1991).

[8] A. Kelic et al., Phys. Rev. C **70**, 064608 (2003).

[9] J. Vargas et al., Nucl. Instrum. Methods A **707**, 16 (2013).

DOI:10.15120/GR-2016-1

Rate capability of the prototype Cryogenic Stopping Cell for the Super-FRS*

M. P. Reiter[1], *A.-K. Rink*[1], *T. Dickel*[1,2], *E. Haettner*[1,2], *F. Heiße*[1,2,3], *W. R. Plaß*[†1,2], *S. Purushothaman*[2], *F. Amjad*[2], *S. Ayet San Andrés*[1,2], *J. Bergmann*[1], *D. Blum*[2], *P. Dendooven*[4], *M. Diwisch*[1], *J. Ebert*[1], *H. Geissel*[1,2], *F. Greiner*[1], *C. Hornung*[1], *C. Jesch*[1], *N. Kalantar-Nayestanaki*[4], *R. Knöbel*[1,2], *J. Lang*[1], *W. Lippert*[1], *I. Miskun*[1,2], *I.D. Moore*[5], *C. Nociforo*[2], *M. Petrick*[1], *S. Pietri*[2], *M. Pfützner*[1,6], *I. Pohjalainen*[5], *A. Prochazka*[2], *C. Scheidenberger*[1,2], *M. Takechi*[2], *Y. K. Tanaka*[2], *H. Weick*[2], *J. S. Winfield*[2], *and X. Xu*[1,2]

[1]Justus-Liebig-Universität Gießen; [2]GSI Helmholtzzentrum für Schwerionenforschung GmbH, Darmstadt; [3]Technische Universität Dresden; [4]KVI-Center for Advanced Radiation Technology, University of Groningen, The Netherlands; [5]University of Jyväskylä, Finland; [6]University of Warsaw, Poland

At the Low-Energy Branch (LEB) of the Super-FRS at FAIR, projectile and fission fragments will be produced at relativistic energies, separated in-flight, energy-bunched, slowed down and thermalized in a cryogenic stopping cell (CSC) filled with ultra-pure He gas. The fragments are extracted from the stopping cell using a combination of DC and RF electric fields and gas flow. A prototype CSC for the LEB has recently been developed and successfully commissioned at the FRS Ion Catcher at GSI [1,2,3].

Ionization of He buffer gas atoms during the stopping of energetic ions creates a region of high space charge in the stopping cell. The space charge decreases the extraction efficiency of stopping cells since the high amount of charge distorts the applied DC electric drag fields. Thus the understanding of space charge effects is of great importance to make full use of the high yields at future RIB facilities such as the Super-FRS at FAIR. For this purpose a detailed study of space charge effects in the CSC was performed [4].

The extraction efficiencies, extraction times and extraction profiles of the prototype CSC were studied in experiments and simulations using ^{238}U projectile fragments produced at 1000 MeV/u at the FRS. The extraction efficiencies for ^{221}Ac and ^{213}Fr measured as a function of the beam rate are shown in Fig. 1. Up to a rate of about 10^4 ions/s injected into the CSC the extraction efficiencies and extraction times are constant; at higher rates the extraction efficiencies and extraction times decrease. This behavior can be explained by space charge effects, which cause a deflection of the ions in the CSC towards the electrodes, such that with increasing beam rate only ions stopped closer to the extraction nozzle can be extracted. Good agreement between experiments and simulations was found.

The conditions chosen for the study are challenging (i) since the high energy of the ions leads to a large energy straggling after slowing-down and consequently requires a high stopping gas density and (ii) because of the high nuclear charge of the fragments. Since the energy deposition roughly scales with the square of the nuclear charge, the rate capability of the CSC for lighter elements will be much higher. We have developed a novel concept of a CSC with orthogonal extraction [5]. Besides much higher areal density and shorter extraction times, this CSC will have a rate capability exceeding 10^7 ions/s as predicted by simulations. This concept will be realized for the stopping cell for the LEB of the Super-FRS at FAIR.

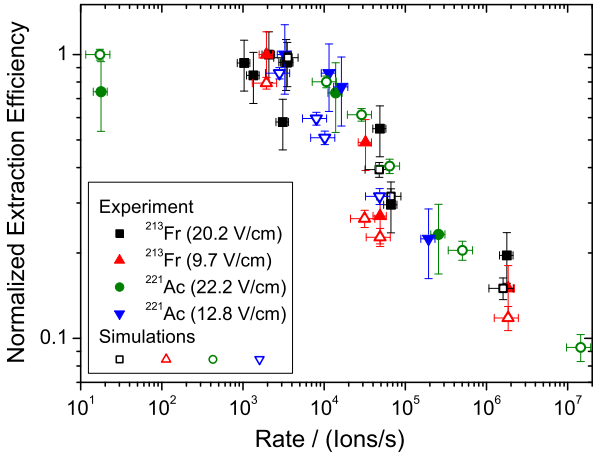

Figure 1: Extraction efficiencies for ^{221}Ac and ^{213}Fr as a function of the beam rate from experiments (solid symbols) and simulations (open symbols) for two different electric DC field strengths each. Every data series has been normalized independently to a maximum extraction efficiency of unity.

References

[1] M. Ranjan et al., Europhys. Lett. 96 (2011) 52001.

[2] W.R. Plaß et al., Nucl. Instrum. and Methods B 317 (2013) 457–462.

[3] S. Purushothaman et al., Europhys. Lett. 104 (2013) 42001.

[4] P. Reiter et al., Nucl. Instrum. and Methods B (2015), http://dx.doi.org/10.1016/j.nimb.2015.12.016.

[5] T. Dickel et al., GSI Sci. Rep. 2013 (2014), p. 106.

*Work supported within the collaboration agreement between GSI and KVI, University of Groningen, by the BMBF under contract no. 05P12RGFN8, by the Hessian Ministry for Science and Art (HMWK) through the LOEWE Center HICforFAIR, by HGS-HIRe, by the Justus-Liebig-Universität Gießen and GSI under the JLU-GSI strategic Helmholtz partnership agreement, and by the European Community FP7 - Capacities, contract ENSAR no. 262010.

† Wolfgang.R.Plass@exp2.physik.uni-giessen.de

Expected invariant mass hypernuclear spectroscopy within FRS

C.Rappold[*1,2] *and T.R. Saito*[1,3,4]

[1]GSI, Darmstadt, Germany; [2]Justus-Liebig-Universität Giessen, Germany; [3]Johannes Gutenberg-Universität, Mainz, Germany; [4]The Helmholtz Institute Mainz, Mainz, Germany

The first experiment of the HypHI collaboration demonstrated the feasibility of the hypernuclear spectroscopy by means of heavy ion beam induced reactions. The phase 0 experiment was performed with a ^{6}Li beam at 2AGeV impinged on a stable ^{12}C target material. The main results of the experiment showed the reconstruction and identification of decay vertexes of Λ particle and $^{3}_{\Lambda}$H, $^{4}_{\Lambda}$H [1, 2, 3].

The future experiment aims to product and study the proton-rich hypernuclei within the FRS and SuperFRS fragment separator. The decay channel of interest is mainly the mesonic weak decay involving π^- mesons of the proton-rich hypernuclei. Therefore an experimental apparatus that allow to separate the π^- from the positively charged particles and fragments is necessary to perform such spectroscopy experiment at FRS or SuperFRS.

Two different approaches are under development and their designs have been already reported [4, 5]. In order to assess if this experimental method is viable, a test experiment based on the previously successful experiment will be performed in the near future. Light hypernuclei $^{3}_{\Lambda}$H, $^{4}_{\Lambda}$H and nnΛ will be the species of interest that will be aimed to be reconstructed and identified by invariant mass method. After the two-body decay, selecting a narrow magnetic rigidity acceptance window of the FRS or SuperFRS, while detection a large portion of the emitted π^-, one can expect no dependency of the invariant mass of the hypernucleus of interest as a function of the magnetic rigidity of the positively charged fragment.

The top panel of Fig.1, shows the invariant mass spectra of $^{3}_{\Lambda}$H of the reconstructed simulated event and mixed event as a function of the magnetic rigidity of ^{3}He. It shows the clear independence of the invariant mass $^{3}_{\Lambda}$H from each ^{3}He magnetic rigidity bin that could represent the acceptance window of the FRS or SuperFRS. It shows also that the mixed event invariant mass distribution actually is dependent of the magnetic rigidity. A magnetic rigidity acceptance window can then be selected to optimize the background contribution to the measured invariant mass distribution. Once a such acceptance window is selected, the projected the invariant mass spectra could be comparable to the one shown in the bottom of Fig.1, where a signal-to-background ratio was set to be around 0.24, similarly to the ratio observed in the first experiment for a realistic expectation. A clear and narrow signal distribution in red color can be observed on the top of the background distribution simulated by the mixed event.

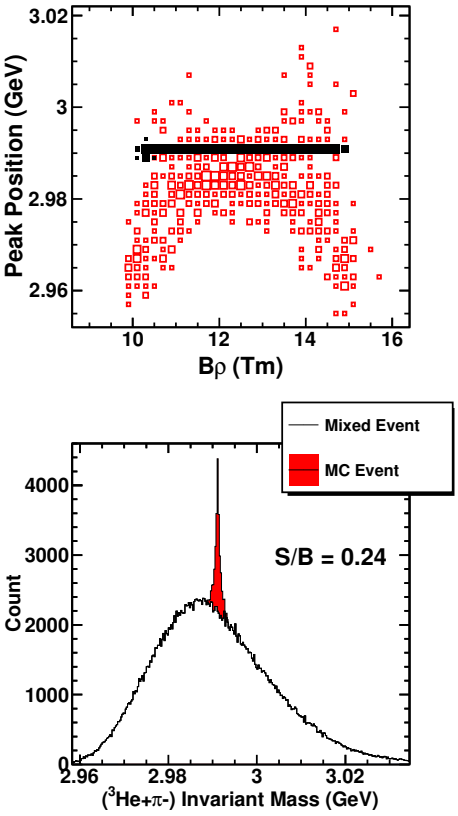

Figure 1: Invariant mass spectra as a function of the magnetic rigidity Bρ of the decayed fragment ^{3}He of $^{3}_{\Lambda}$H$\rightarrow$ π^-+^{3}He in the top panel. The invariant mass spectra of the simulated event is shown in black and of the mixed event in red. The projection within the FRS fragment separator selected magnetic rigidity acceptance of the figure of the top panel. The ratio between the simulated event and the mixed event was set have a signal-to-background ratio of 0.24.

References

[1] C. Rappold *et al.*, Nucl. Phys. A **913**, 170 (2013).

[2] C. Rappold *et al.*, Phys. Rev. C **88**, 041001 (2013).

[3] C. Rappold *et al.*, Phys. Lett. B **747**, 129 (2015).

[4] C. Rappold *et al.*, GSI Scientific Report 2014 [GSI Report 2015-1] (2015) p. 135.

[5] C. Rappold *et al.*, GSI Scientific Report 2014 [GSI Report 2015-1] (2015) p. 136.

* c.rappold@gsi.de

DOI:10.15120/GR-2016-1

Experimental conditions for exotic hypernuclear production

C.Rappold[*1,2], *T.R. Saito*[1,3,4], *C. Scheidenberger*[1,2], *and H. Geissel*[1,2]

[1]GSI, Darmstadt, Germany; [2]Justus-Liebig-Universität Giessen, Germany; [3]Johannes Gutenberg-Universität, Mainz, Germany; [4]The Helmholtz Institute Mainz, Mainz, Germany

The HypHI collaboration demonstrated the feasibility of the hypernuclear spectroscopy by means of heavy ion beam induced reactions after the publications of the results of first experiment. During this first experiment, a ^{6}Li beam at 2AGeV on a Carbon target was used. The final results showed that the experimental method is viable for the study of hypernuclei [1, 2, 3].

A new set of experiments at FRS and SuperFRS fragment separator is under consideration. Two different experimental apparatus for this purpose is under development [4, 5]. Additionally to the detection setup design, the optimal experimental conditions for the production of the proton-rich and neutron-rich hypernuclei has been investigated. A secondary exotic beam produced and transported by the FRS or SuperFRS can be used to increase the production yield of exotic hypernuclei. Theoretical calculation of the heavy ion collisions can predict those production yield and cross section of exotic hypernuclei as a function of the beam energy, the exotic or stable beam and target species. Additionally, in the case of an exotic beam for the hypernuclear production, the production yield of this exotic beam is a function of the reaction of the primary beam and the production target and its thickness. The yield of exotic beam also depends of the transport transmission between the exotic beam production area and the hypernuclear production area. A multivariate analysis was implemented for taking into account the results from the EPAX, and DCM-QGSM calculations and MOCADI simulations.

The transport optics calculated and simulated by MOCADI, is used in order to determine the momentum and geometrical acceptance of the fragment within the second part of the FRS. The EPAX calculation is used to estimate the production cross section of exotic beam from stable primary beam and target species. The MOCADI simulation also is used to determine the production yield from the EPAX calculation in which the thickness of the production target provide the nuclear absorption. DCM-QGSM theoretical calculations provide the hypernuclear production cross sections from the proton and neutron-drip line. Thanks to the multivariate analysis, an optimization procedure allows to find the best experimental conditions that can maximize the hypernuclear yield.

Table 1 summarizes the results of this optimization procedure. Several proton-rich and neutron-rich hypernuclei and their yield per second are shown with the primary beam, primary target, target thickness, secondary beam energy and intensity necessary to obtain such a production yield. More details can be found in [6].

Table 1: Summary of all results from the optimization procedure. Some Λ-hypernuclei up-to Carbon isotopes are presented, and for each, the optimal experimental conditions are reported: The reaction necessary to procedure the exotic beam, the target thickness, the exotic beam selected to produce the hypernuclei of interest on a 4-centimeter ^{12}C target, the exotic bean kinetic energy and the intensity, and the resulting hypernuclear yield.

	Reaction	Target (cm)	2^{nd} beam	E_k (AGeV)	I (10^6/s)	Yield (/s)
$^{8}_{\Lambda}$C	^{14}N+^{9}Be	5.5	^{12}N	1.94	5.1	0.2
$^{9}_{\Lambda}$C	^{14}N+^{9}Be	5.5	^{12}N	1.94	5.1	0.8
$^{10}_{\Lambda}$C	^{14}N+^{9}Be	5.5	^{12}N	1.94	5.1	1.5
$^{11}_{\Lambda}$C	^{14}N+^{9}Be	5.5	^{12}N	1.94	5.1	0.9
$^{7}_{\Lambda}$B	^{14}N+^{9}Be	5.5	^{12}N	1.94	5.1	0.7
$^{8}_{\Lambda}$B	^{14}N+^{9}Be	5.5	^{12}N	1.94	5.1	2.7
$^{9}_{\Lambda}$B	^{14}N+^{9}Be	5.5	^{12}N	1.94	5.1	3.5
$^{10}_{\Lambda}$B	^{14}N+^{9}Be	5.5	^{12}N	1.94	5.1	2.5
$^{11}_{\Lambda}$B	^{20}Ne+^{9}Be	2	^{17}F	1.97	5.7	1.2
$^{9}_{\Lambda}$Be	stable beam		^{16}O	2.	10.	4.4
$^{11}_{\Lambda}$Be	^{23}Na+^{11}B	15.5	^{12}B	1.79	1.2	0.6
$^{5}_{\Lambda}$Li	^{12}C+^{9}Be	6	^{10}C	1.94	5.1	2.5
$^{6}_{\Lambda}$Li	^{14}N+^{9}Be	5.5	^{12}N	1.94	5.1	4.3
$^{7}_{\Lambda}$Li	stable beam		^{14}N	2.	10.	5.2
$^{8}_{\Lambda}$Li	^{20}Ne+^{9}Be	2	^{17}F	1.97	5.7	3.7
$^{9}_{\Lambda}$Li	^{16}O+^{9}Be	5.5	^{14}O	1.93	5.5	2.2
$^{3}_{\Lambda}$He	^{14}N+^{9}Be	5.5	^{12}N	1.94	5.1	1.8
$^{7}_{\Lambda}$He	^{20}Ne+^{9}Be	2	^{17}F	1.97	5.7	2.9

References

[1] C. Rappold *et al.*, Nucl. Phys. A **913**, 170 (2013).

[2] C. Rappold *et al.*, Phys. Rev. C **88**, 041001 (2013).

[3] C. Rappold *et al.*, Phys. Lett. B **747**, 129 (2015).

[4] C. Rappold *et al.*, GSI Scientific Report 2014 [GSI Report 2015-1] (2015) p. 135.

[5] C. Rappold *et al.*, GSI Scientific Report 2014 [GSI Report 2015-1] (2015) p. 136.

[6] C. Rappold *et al.*, e-Print: arXiv:1601.03930 (2015).

* c.rappold@gsi.de

DOI:10.15120/GR-2016-1

Simulation on the performance of the DEGAS gamma detector array

G. S .Li[*1], *C. Lizarazo*[1,2], *I. Kojouharov*[1], *J. Gerl*[1], *and H. Schaffner*[1]
[1]GSI, Darmstadt, Germany; [2]Technische Universität Darmstadt, Darmstadt, Germany

In the DESPEC project the rare isotopes produced by the Super-FRS will be stopped in an active implanter AIDA surrounded by the DEGAS array to measure gamma rays from alpha, beta, proton, neutron and isometric decays [1]. The full DEGAS system is a key instrument of DESPEC and is envisioned to be operated with high detection efficiency and high ability in the discrimination of the prevailing intense background radiation. In order to optimize the DEGAS setup and get detailed information of its performance, a corresponding Geant4 simulation framework is developed and verified using the experimental data from EUROBALL Cluster and BGO back-catcher detectors. On this basis, further simulation is performed using simplified geometries.

The DEGAS configurations used for the simulation are shown in Figure 1. The left consists of 26 triple clusters in a box shape. The Ge capsules are the same as the ones in the EUROBALL Clusters previously employed at GSI in the RISING campaign [2]. For each triple cluster a 20 cm long cooling finger, comprised of 3 cm diameter Cu inside and 0.5 cm thickness Al outside, is assumed. In the middle, 5 cm thickness active BGO with hexagonal shape is added to each Ge capsules as back-catcher. On the right, 5 cm thickness active CsI and 1 cm passive Pb are added to the corners and upstream of the box shape as side-catcher. At the same time, 3 cm Pb is used to cover remaining holes from the BGO back-catcher as passive shield. In the simulation, a Pb wall of 5 cm thickness and 1 m long is assumed upstream of the array for all the three configurations.

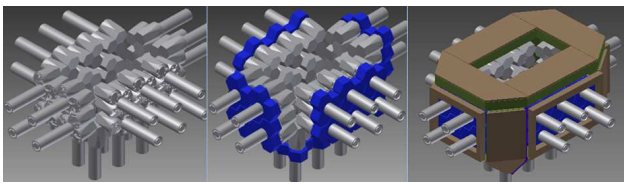

Figure 1: Simplified DEGAS configurations used in the simulations (see text).

Figure 2 shows the background reduction factor, comparing the non-shielded Ge array (Figure 1 left) with back-catcher shielding (blue line) and additional side shielding (magenta line). In the simulation, the background is assumed as exponential distribution, ranging from 10 keV to 5000 keV, isotropically emitted from the outside of the DEGAS system. One can see from the figure that if the active BGO back-catcher is installed, about 50% of the background that accumulated in the Ge detectors could be suppressed, while with active CsI and passive Pb even 90% of the background in Ge could be suppressed.

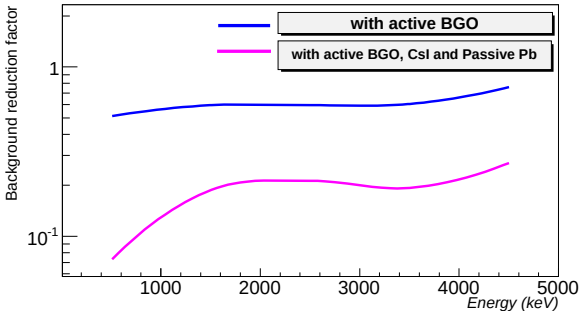

Figure 2: Background reduction factor for different types of DEGAS shielding (see text).

Figure 3 shows the energy spectra of Ge detectors in the three configurations. In the simulation, a mono-energetic gamma-ray source at 1000 keV is considered. The gamma rays are isotropically emitted from a plane with an area of 24×8 cm^2 in the center of DEGAS. The ratio between the mono-energetic gamma-ray source and the background radiation is 1:10000. The results show that the peak to total (P/T) ratio in the unshielded configuration is 1.4% (green line), with active BGO back-catcher it increases to 2.1% (blue line), and if the active CsI and passive Pb are included the ratio reaches 8.2% (magenta line).

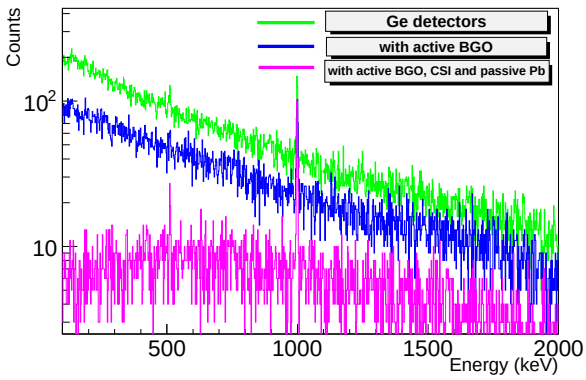

Figure 3: Energy spectra of Ge detectors in the three configurations (see text).

The Geant4 simulation of the DEGAS gamma-ray detection system using simplified geometries demonstrates the

* G.Li@gsi.de

DOI:10.15120/GR-2016-1

essential function of the BGO back-catcher and CsI side-catcher. Further studies will be performed using more detailed geometries.

References

[1] Alexander Herlert, PJ Web of Conferences 71, 00064 (2014)

[2] H. J. Wollersheim *et al.*, Nucl. Instr. and Meth. Phys. Res. A537 (2005) 637

DOI:10.15120/GR-2016-1

3D positron sensitivity with large volume lyso crystal

T. Arici[1,2], *T. Habermann*[1], *I. Kojouharov*[1], *J. Gerl*[1], *and C. Scheidenberger*[1,2]
[1]GSI, Darmstadt, Germany; [2]Justus-Liebig-University, Gießen, Germany

Position sensitive gamma detectors are employed for a wide range of applications from physics research, biomedicine to applications in the civil sector like oil investigations. A development of a technology is needed to localize the interaction points of a gamma rays also inside a large volume crystal to extend the usage of existing systems.

Introduction

The aim of this project was to investigate the 3D position resolution of a thick scintillation crystal employing a novel approach different to what is being used in gamma cameras. Usually, thin scintillation materials, with few mm thickness, are used to determine the depth dependent response of the scintillation light arriving at the light read-out. The light read-out is generally a single position-sensitive photomultiplier (PSPMT) or an array of PMTs and one can investigate the interaction position in the material in 2D by analyzing the light distribution created. Depending on the depth of the interaction position the width of the light distribution will vary. Interactions closer to the PMT surface would have less spread light at the photo cathode than those interactions further away. The spatial distribution of the light along the crystal is then determined up to a resolution of a few mm. The principal idea of this approach is to cover several faces of a cubic and thick scintillator crystal with position sensitive photo-sensors in order to determine the interaction points of penetrating gamma-rays in 3D.

Material and Method

To investigate the potential of the multi-face photon-detection, the system has been built, using a 34x34x34 mm^3 LYSO crystal coupled to position-sensitive PMTs (Hamamtsu 8500C series). Truncated square plastic pyramids served as light guides between crystal and PSPMT as shown in Figure 1. The centroid of the light distribution on each side was obtained employing a conventional resistive chain network on each PSPMT. The obtained centroids and the relative light intensity provides a measure of the interaction position in 3D. Demanding one 511 keV gamma-ray to be detected in the reference detector in coincidence with the signals of the cube detector allowed to study the pure response of the other 511 keV gamma-ray in the cube. Absorption in the PMT material was negligible. The PSPMT amplitude signals were first calibrated by uniformly illuminating the crystal with the ^{22}Na source. Collimation is done by a pyramidal 8 cm thick tungsten collimator, placed at the front face of the gamma camera window, emitting gammas in z-direction to create the optical photons. The amplitudes are then used to construct the interaction position. We investigated how the amplitudes of the channels differ by moving the source across the x/y-plane in steps of 5 mm.

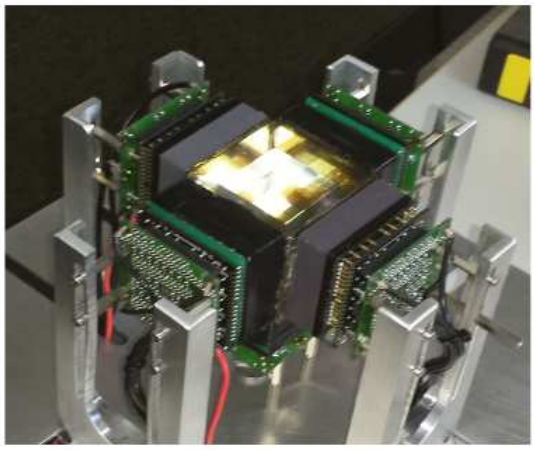

Figure 1: 3D imaging detector system, one surface open. The crystal is shown in the middle, covered with plastic windows coupled to PSPMTs. The open surface was covered later

The algorithm that is used to determine the interaction position is based on a mathematical model considering the charge collection on anodes which was published by H.O. Anger and is still a basic principle of image reconstruction [1]. The Anger algoritm calculates the position of the event as a mean value of the measured charge distribution, which represents the light distribution in the imaging plane depending on the source position assuming a constant amplification of the photomultiplier tube.

Undesired effects at the edges seen as a worse spatial resolution. Even if the light reflections at the edges were perfectly uniform, the boundaries will widen the light distribution and shift the centroid of the light far from the real interaction position. This is illustrated in Figure 2.

Conclusion

The light distribution of a cubic LYSO scintillation crystal with 3.4 cm side length and the position sensitivity de-

DOI:10.15120/GR-2016-1

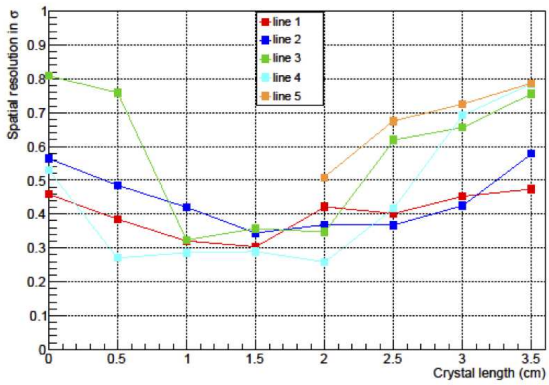

Figure 2: Position resolution distribution across the surface of the crystal.

pending on the interaction position of gamma rays was studied. Employing the Anger formalism with corrections for the interaction depth an average resolution of 8 mm (FWHM) was obtained. The results demonstrate that the new approach indeed provides position information in 3D. The limitation in resolution comes mainly from pincushion effects. A way-out might be individual anode pixel gain calibrations and fitting of theoretical light distribution curves. Optimizing the surface treatment may also be important to improve the resolution further.

References

[1] H. Anger."A new instrument for mapping gamma-ray emitters" Biology and Medicine Quarterly Report UCRL, 1957, 3653: 38. (University of California Radiation Laboratory, Berkeley)

DOI:10.15120/GR-2016-1

Decay spectroscopy at SHIP using a new focal plane detection system

A.K. Mistry[*1,2], *F.P. Heßberger*[1,2], *D. Ackermann*[1,4], *B. Andel*[5], *S. Antalic*[5], *M. Block*[1,2,3], *P. Chhetri*[6], *Ch.E. Düllmann*[1,2,3], *F. Giacoppo*[1,2], *J. Hoffmann*[1], *J. Khuyagbaatar*[1,2], *N. Kurz*[1], *F. Lautenschläger*[6], *M. Laatiaoui*[1,2], *J. Maurer*[1], *P. Mosat*[5], *J. Piot*[4], *S. Raeder*[1,2], *I. Rusanov*[1], *M. Vostinar*[4], *and A. Yakushev*[1]

[1]GSI, Darmstadt, Germany; [2]Helmholtz Insitute Mainz, Germany; [3]Johannes Gutenberg University, Mainz, Germany; [4]GANIL, Caen, France; [5]Comenius University, Bratislava, Slovakia; [6]TU Darmstadt, Germany

Nuclear structure experimental studies in the heavy and superheavy element regime at the extremes of sensitivity require continuous advancements in detector development. A focal plane detection system was designed and developed in-house at GSI, Darmstadt, to explore this region in decay spectroscopy studies [1]. Initially, a study was performed on the superheavy nucleus ^{257}Db with the LISE filter at GANIL, France, with the data currently under analysis. To assess the performance and capabilities of the apparatus in combination with the SHIP separator, an experimental campaign over a variety of heavy nuclei was completed in October 2015 at GSI.

The measurement apparatus comprises a double sided silicon strip detector (DSSD) of 60x60 strips (1 mm strip pitch, 300 μm thickness) for the detection of recoil implantations and subsequent α/e^-/spontaneous fission decays surrounded in a box formation by four single sided silicon strip detectors (SSSD) upstream, to measure α-decay escapes and conversion electron emission. The detection arrangement had one Ge clover detector (behind the DSSD and separated by a thin 1.5 mm Al cap) for γ-ray/X-ray decay measurements (up-to 5 Ge detectors are possible). The electronics readout system used was charge sensitive preamplifiers coupled to the FEBEX3A/B digitisers [2] developed at GSI and previously employed by the TASCA group [3].

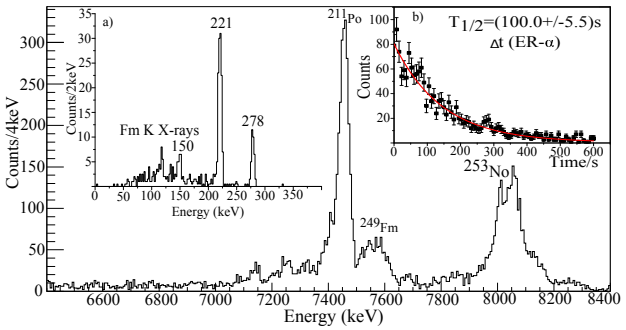

Figure 1: Alpha-decay of ^{253}No measured in the DSSD. Inset a) Gamma rays in coincidence with the α-decay of ^{253}No, inset b) time difference between evaporation residues (ER) implantation and subsequent α decay.

The primary beam of $^{48}Ca^{10+}$ in parasitic mode (5 Hz macropulse, 5 ms wide) was impinged on a variety of targets. Initially, the previously measured [4] heavy odd-A actinide ^{253}No was produced in the reaction ^{207}Pb(^{48}Ca,2n)^{253}No. In coincidence with the α-decays from ^{253}No, γ-rays from excited states in ^{249}Fm were measured. In this deformed mid-shell region of the nuclear chart, ^{254}Lr and ^{255}No were also produced. The data analysis is ongoing.

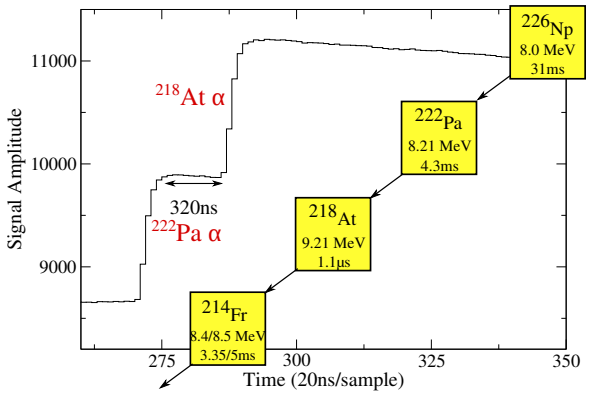

Figure 2: ^{226}Np decay chain measured in the reaction ^{181}Ta(^{48}Ca,3n)^{226}Np. The relatively fast decay of ^{218}At can be measured through examination of individual traces correlated to the ms decay of ^{226}Np and ^{214}Fr.

In order to study the evolution of the N=126 shell closure above protactinium, which is not yet well understood [5], neutron deficient isotopes in the uranium-plutonium region were studied in addition. To that end, the reaction ^{48}Ca + ^{181}Ta→^{229}Np* was selected with a two-fold purpose of populating neutron deficient neptunium isotopes to improve on data in this region, while at the same time testing the performance of the electronics in a region with known relatively fast decays. An example of a decay chain correlated to ^{226}Np is shown in Fig 2. The fast decay of ^{218}At measured demonstrates the capability of detecting events in the sub-microsecond range with an almost dead time free system. In conclusion, the new SHIP focal plane detection system has been successfully tested at GSI, with a broad collection of data taken.

References

[1] D. Ackermann *et al.*, GSI Scientific Report 2014, 169, (2015)

[2] J. Hoffmann *et al.*, GSI Scientific Report 2011, 253, (2012)

[3] J. Khuyagbaatar *et al.*, PRL 112, 172501, (2014)

[4] F. P. Heßberger *et al.*, EPJ A 48, 5, (2012)

[5] J. Khuyagbaatar *et al.*, PRL 115, 242502, (2015)

* a.k.mistry@gsi.de

Laser spectroscopy of nobelium

P. Chhetri[1], *D. Ackermann*[2], *H. Backe*[3], *M. Block*[2,3,4], *B. Cheal*[5], *Ch. E. Düllmann*[2,3,4], *P. V. Duppen*[6], *J. Even*[4], *R. Ferrer*[6], *F. Giacoppo*[2,4], *S. Götz*[3], *F.P. Heßberger*[2,4], *M. Huyse*[6], *O. Kaleja*[1], *J. Khuyagbaatar*[2,4], *P. Kunz*[7], *M. Laatiaoui*[2,4], *F. Lautenschläger*[1], *W. Lauth*[4], *A. K. Mistry*[2,4], *S. Raeder*[2,4], *E. Minaya Ramirez*[4], *Th. Walther*[1], *C. Wraith*[5], *and A. Yakushev*[2,4]

[1]TU Darmstadt, Germany; [2]GSI Helmholtzzentrum, Darmstadt; [3]Univ. Mainz, Germany; [4]Helmholtz-Institut Mainz, Germany; [5]Univ. Liverpool, UK; [6]KU Leuven, Belgium; [7]TRIUMF Vancouver, Canada

Relativistic effects influence the valence electron configuration of the heaviest elements affecting their physical and chemical properties. These effects can be described using state-of-the-art numerical approaches for highly correlated, relativistic many-electron systems, such as Multi Configuration Dirac-Fock and Relativistic Coupled-Cluster calculations [1]. To benchmark these calculations, a comparison between measured and predicted atomic properties is needed. At present, no laser spectroscopy data is available for the transfermium elements (Z>100). Thus, laser spectroscopic studies of these elements are of great interest.

In our experiments we aim to search for atomic levels in the element nobelium (Z=102) applying the Radiation Detected Resonance Ionization Spectroscopy (RADRIS) [2] technique. For such studies the isotope ^{254}No, $t_{1/2}$ = 51s was chosen. It was produced via the fusion evaporation reaction ^{208}Pb(^{48}Ca,2n)^{254}No using the ^{48}Ca ion beam provided by the UNILAC. The fusion-products were separated by the velocity filter SHIP and about four ^{254}No ions/s entered a buffer gas cell where they were stopped in 95 mbar argon gas of 99.9999% purity and were subsequently collected on a tantalum filament. After an appropriate collection time, the primary beam was blocked and the accumulated ions were re-evaporated as neutral atoms by a short heating pulse. We then employ a two-step photoionization process to ionize the atoms. In case of resonant excitation and final photoionization, the ions were transported by suitable electric fields to a silicon detector where they were identified by their characteristic α decay.

Laser light for the first excitation-step was provided by four tunable dye lasers and an optical parametric oscillator (OPO) system and transported to the experimental setup using UV-fibers. The dye lasers were pumped by two excimer lasers operated at 248 nm and 308 nm. The OPO, pumped by a frequency-tripled Nd:YAG laser, was operated in a frequency mixing mode, delivering laser light in the wavelength range below 410 nm. The 351 nm light for the second, non-resonant step was provided by a high power excimer laser and was transported to the experimental setup by highly reflective UV-mirrors. The laser wavelengths were measured with a high precision.

Different theoretical models predict the *7s7p* ^{1}P$_1$ atomic level in the range of 322-385 nm [3]. The large spectral range to be covered and the low production rate makes the experiment challenging. After the level search in 2007 and 2014, the setup was further optimized [4]. In summer 2015, a resonance was observed at a wavelength of about 333.8 nm and the resulting α-decay spectrum is shown in Fig. 1. Baking the filament increased the effieciency of the setup increased by about a factor of two, cf. 1 (c). These results will be published soon. In addition, some Rydberg states were identified in the 2015 beamtime. This enables the determination of the first ionization potential of No with high accuracy in future beamtimes.

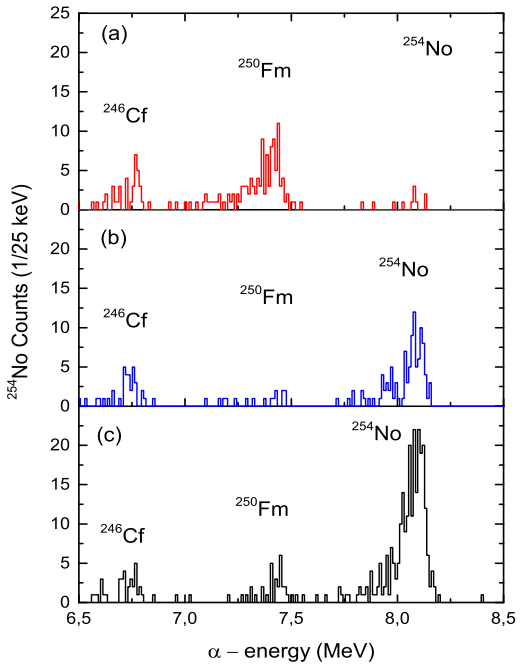

Figure 1: α-decay spectrum of ^{254}No. The measurements with laser off (a), lasers on (b) and after conditioning the filament(c). The laser excitation energy λ_1= 333.8 nm, λ_2= 351 nm with laser pulse energy E_{λ_1} = 200 μJ and E_{λ_2} = 36 mJ. The measurement time was 300 s for (a) and (b) and 600s for (c)

Acknowledgements: This work was supported by the BMBF (FAIR NuSTAR 05P09RDFN4, 05P12RDFN8, 05P15RDFN1) and the Helmholtz- Institut Mainz.

References

[1] E. Eliav et al. Nucl. Phys. A **944** 518–550 (2015)

[2] H. Backe et al. Nucl. Phys. A **944** 492–517 (2015)

[3] M. Laatiaoui et al. Eur. Phys. J. D **68** 71-77 (2014)

[4] F. Lautenschläger et al. Nucl. Instrum. Methods B (2016), (submitted)

DOI:10.15120/GR-2016-1

On-line commissioning of the cryogenic buffer-gas stopping cell at SHIPTRAP

O. Kaleja[*1,2], *K. Blaum*[3], *M. Block*[2,4,5], *P. Chhetri*[1,2], *S. Eliseev*[3], *F. Giacoppo*[2,4], *F.-P. Heßberger*[2], *M. Laatiaoui*[2,4], *F. Lautenschläger*[1,2], *E. Minaya Ramirez*[6], *A. Mistry*[2,4], *S. Raeder*[2,4], *L. Schweikhard*[7], *and P. G. Thirolf*[8]

[1]TU Darmstadt; [2]GSI Helmholtzzentrum Darmstadt; [3]MPIK Heidelberg; [4]Helmholtz-Institut Mainz; [5]Universität Mainz; [6]IPN Orsay; [7]Universität Greifswald; [8]LMU München

Introduction

The Penning-trap mass spectrometer SHIPTRAP allows for direct mass measurements of the heaviest elements, created in fusion-evaporation reactions and separated by the velocity filter SHIP. In previous experiments the masses of $^{252-255}$No (Z=102) and ^{255,256}Lr (Z=103) had been measured directly for the first time [1,2]. In order to proceed to even heavier elements with lower production rates, the overall efficiency of the setup has to be improved further. It is currently mainly limited by the combined stopping and extraction efficiency of the buffer-gas stopping cell [3]. Therefore, a new buffer-gas stopping cell has been developed (CryoCell). It features a larger stopping volume and is operated at 40 K [4]. Its overall efficiency was recently measured on-line using ^{254}No ions.

Experiment

The on-line commissioning of the CryoCell took place in fall 2015. Nobelium ions were produced in the fusion-evaporation reaction ^{208}Pb(^{48}Ca,2n)^{254}No by use of a 0.58 mg/cm^2 lead target and separated from the primary beam by the velocity filter SHIP. A cross section of about 2 μb at a beam energy of 4.55 AMeV resulted in an ion count rate $\dot{n}_{\mathrm{SHIP}}$ of up to 3.0(4) ions/s, as measured at the focal plane of SHIP using silicon strip detectors.

The nobelium ions entered the CryoCell filled with 50 mbar ultra-pure helium gas through a 3.8 μm-thick titanium foil. Within the gas the ions were thermalized and then extracted by means of direct-current voltages and radio-frequency oscillating fields. After extraction, the ions were implanted into an 0.8 μm thick aluminium foil placed in front of a silicon detector, where their characteristic alpha decay energy was recorded.

Results

After optimization, the overall efficiency of the CryoCell setup

$$\epsilon = \frac{\dot{n}_{\mathrm{extr}}}{\dot{n}_{\mathrm{SHIP}}}, \qquad (1)$$

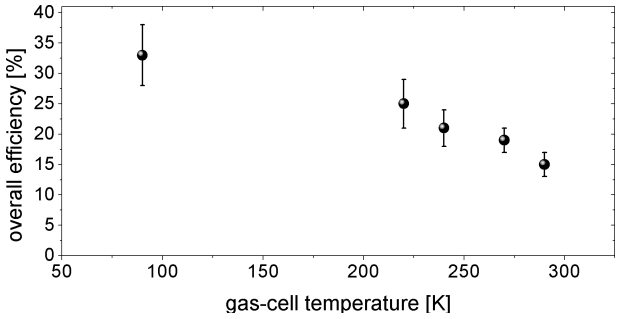

Figure 1: Overall efficiencies of the buffer-gas stopping cell for ^{254}No ions at different temperatures. The helium density was equivalent to 50 mbar at room temperature. The incoming ion rate was 3.0(4) ions/s for all measurements.

was determined, where $\dot{n}_{\mathrm{SHIP}}$ and $\dot{n}_{\mathrm{extr}}$ are the incoming and extracted ion rate (containing all charge states), respectively. The latter can be deduced from the detected alpha count rate and the known detector efficiency. Figure 1 shows the obtained overall efficiency as a function of the operating temperature of the CryoCell. An increasing efficiency for lower temperatures was observed, which is attributed to freeze-out of impurities of the helium buffer gas. Due to extraction problems the data point with the lowest achieved temperature was limited to 90 K.

At this temperature a maximum effienciency of 33(5) % was obtained, which corresponds to an extracted ion rate of about one ion/s. This is an improvement by a factor four in comparison with the previous buffer gas cell [5] and paves the way for investigating heavier and more exotic nuclides in future experiments. To give an example, the first direct mass measurement of rutherfordium (Z=104) with a production cross section of 15 nb now becomes feasible.

Further improvements are expected at lower operating temperatures with an optimized combination of the gas pressure and entrance window thickness.

References

[1] M. Block et al., Nature 463 (2010) 785
[2] E. Minaya Ramirez et al., Science 337 (2012) 1207
[3] J.B. Neumayr et al., NIM B 244 (2006) 489
[4] C. Droese et al., NIM B 338 (2014) 126
[5] S. Eliseev et al., NIM B 258 (2007) 479

* o.kaleja@gsi.de

DOI:10.15120/GR-2016-1

DOI:10.15120/GR-2016-1

Predictions of Adsorption of Cn, Fl and their homologs Hg and Pb, respectively, on a Hydroxylated Quartz Surface

V. Pershina
GSI Helmholtzzentrum, Darmstadt, Germany

Both experimental and theoretical research in the area of chemistry of the superheavy elements (SHE) have recently been focusing on investigations of properties of elements 112 (Cn) and 114 (Fl): their unusually high volatility was expected due to the strongest relativistic effects on their electron shells and a closed-shell, $6d^{10}7s^2$, and a quasi-closed shell, $7s^27p_{1/2}{}^2$, electronic ground states, respectively [1]. First experimental studies of their volatility as adsorption on a gold surface of detectors of a chromatography column have indeed shown that these elements are very volatile [2-4]. They, however, disagree on the trend in volatility between Cn and Fl: Cn < Fl [3] while Cn > Fl [4]. Further experiments are under way to solve this contradiction and to differentiate between these elements and their lighter homologs Hg and Pb [5]. This aim should be achieved with the use of two types of detector surfaces – quartz and gold – presumably giving very different adsorption enthalpies, ΔH_{ads}(M).

Earlier, we have predicted ΔH_{ads} of these elements on gold via 4c-DFT cluster calculations [6] and on quartz using a van der Waals (vdW) adatom-slab model and atomic DCB CC calculations [7]. In this work, we predict ΔH_{ads} of Hg, Cn, Pb, and Fl on a quartz surface at ~ 21 °C using the periodic ADF BAND code [8].

Two types of the hydroxylated α-quartz (001) surface were considered; vicinal and germinal silanols. Various adsorbate coverage - from the full till a very low one - was modeled by the (1x1), (2x2) and (4x4) supercells. Also, various adsorption positions were tested. Fig. 1 shows, e.g., adsorption of adatom M on the (2x2) supercell simulating the vicinal silanol (80% at 21 °C).

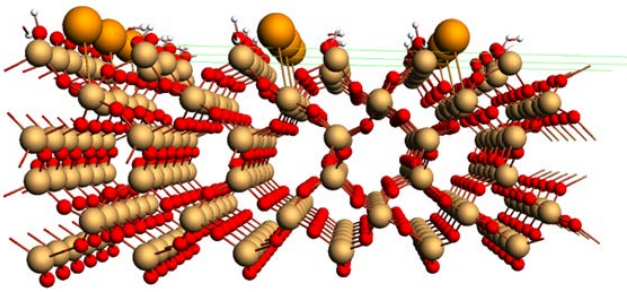

Fig. 1. Atom M (M = Hg, Cn, Pb, and Fl) adsorbed on a hydroxylated quartz surface, a (2x2) supercell (a side view).

Results of the calculations have shown that adsorption on vicinal silanols is stronger than on germinal, and that the preferred adsorption position of all the adatoms is a hollow one, on top of the Si atoms in the second row from the top (Fig. 1).

Table 1 summarizes the calculated ΔH_{ads} of Hg, Cn, Pb, and Fl on the hydroxylated (001) α-quartz surface for the (4x4) supercell, as well as our earlier calculations of ΔH_{ads} of these elements on quartz using a vdW model [6], also in comparison with experimental data. One can see that the ADF BAND data agree pretty well with experiment for Hg and Pb at zero coverage, which gives credit to the results for Cn and Fl: these elements should not adsorb on quartz by chemical forces. However, the vdW adsorption should give positive ΔH_{ads} values [7]. A high inertness of Cn and Fl towards quartz is a result of strong relativistic effects.

Thus, according to the present calculations and those of [6,7], the following behavior can be predicted for the coming experiments: Pb should adsorb on quartz at 21 °C; Hg should not adsorb on quartz and should adsorb on gold at 21 °C; Cn should not adsorb on quartz and should adsorb on gold at $T_{ads} \approx$ -20 °C, while Fl should not adsorb on quartz at 21 °C and should adsorb on gold at 21 °C showing a smooth distribution along the detectors' area.

Table 1. Predicted $-\Delta H_{ads}$ (kJ/mol) of Hg, Cn, Pb, and Fl on a hydroxylated α-quartz (001) surface and experimental data at zero coverage

Method	Hg	Cn	Pb	Fl	Ref.
ADF	54	-38	152	-22	This
vdW[a]	(26.3)	26.0	(27.3)	21.0	7
Exp.	42 ± 2	-	165 ± 4	-	9

[a] a vdW model plus atomic DCB CC calculations.

References

[1] K. S. Pitzer, J. Chem. Phys. **63**, 1032 (1975).
[2] R. Eichler, et al. Nature **447**, 72 (2007).
[3] R. Eichler, et al. Radiochim. Acta **98**, 133 (2010).
[4] A. Yakushev, et al. Inorg. Chem. **53**, 1624 (2014).
[5] A. Yakushev, an experimental proposal (2016).
[6] V. Pershina, et al, J. Chem. Phys. **131**, 084713 (2009).
[7] V. Pershina, et al. J. Chem. Phys. **128**, 024707(9) (2008).
[8] ADF BAND, see http://www.scm.com.
[9] R. Eichler, private communication.

DOI:10.15120/GR-2016-1

Improvements for superheavy element chemistry behind TASCA

L. Lens[1,2], A. Yakushev[2,3], Ch.E. Düllmann[1,2,3], M. Asai[4], M. Block[1,2,3], H.M. David[2], J. Despotopulos[5], A. Di Nitto[1,2], K. Eberhardt[1,3], M. Götz[1,2,3], S. Götz[1,2,3], H. Haba[6], L. Harkness-Brennan[7], F.P. Heßberger[2,3], R.-D. Herzberg[7], D. Hinde[8], J. Hoffmann[2], A. Hübner[2], E. Jäger[2], D. Judson[7], J. Khuyagbaatar[2,3], B. Kindler[2], Y. Komori[6], J. Konki[9], J.V. Kratz[1], J. Krier[2], N. Kurz[2], M. Laatiaoui[2,3], S. Lahiri[10], B. Lommel[2], M. Maiti[11], A.K. Mistry[2,3], C. Mokry[1,3], K. Moody[5], Y. Nagame[4], J.P. Omtvedt[12], P. Papadakis[9], V. Pershina[2], D. Rudolph[13], J. Runke[1,2], M. Schädel[2,4], P. Scharrer[1,2,3], T. Sato[4], D. Shaughnessy[5], B. Schausten[2], J. Steiner[2], P. Thörle-Pospiech[1,3], N. Trautmann[1], K. Tsukada[4], J. Uusitalo[9], A. Ward[7], M. Wegrzecki[14], E. Williams[8], N. Wiehl[1,3], V. Yakusheva[2,3]

[1]Univ. Mainz, Germany; [2]GSI, Darmstadt, Germany; [3]Helmholtz-Institut Mainz, Germany; [4]JAEA, Tokai, Japan; [5]LLNL Livermore, USA; [6]RIKEN, Wako-shi, Japan; [7]Univ. Liverpool, UK; [8]ANU Canberra, Australia; [9]Univ. Jyväskylä, Finland; [10]SINP Kolkata, India; [11]IITR Uttarakhand, India; [12]Univ. Oslo, Norway; [13]Lund Univ., Sweden; [14]ITE, Warsaw, Poland

Experiments on the chemical properties of flerovium (Z=114, Fl), produced in the reaction ^{244}Pu(^{48}Ca, 3-4n)^{288,289}Fl, were performed at GSI, Darmstadt using the COMPACT gas-chromatography setup coupled to the gas-filled recoil separator TASCA [1]. The first experimental investigations of Fl at GSI were performed in 2009 and two radioactive decays of Fl were observed with negligible background [1]. The two most long-lived known Fl isotopes are ^{289}Fl ($T_{1/2}$ =$2.1^{+0.8}_{-0.4}$ s) and ^{288}Fl ($T_{1/2}$ = $0.69^{+0.17}_{-0.11}$ s) [2]. Due to their relatively short half-lives a fast transport time from TASCA to COMPACT is crucial. The transport time is directly linked to the volume of the Recoil Transfer Chamber (RTC) [3], which in turn is attached at the TASCA the focal plane. During the experiment reported in [1], TASCA was operated in its Small Image Mode (SIM) [4]. Relative to the High Transmission Mode (HTM), the SIM has a smaller image size at the focal plane at the cost of a lower transmission.

For experimental investigations on Fl, performed in 2014/15 several improvements to the experimental set-up have been performed, to optimize the overall efficiency. Initially this was studied with short-lived Hg and Pb isotopes:

1) Optimizations of i) the quadrupole magnets focusing in HTM and ii) window size of the RTC resulted in a higher overall efficiency.

2) Several RTCs were developed and tested to identify the minimum transport time. For Fl studies, a fully Teflon®-covered RTC and direct connection to COMPACT appears to be the best suited. It suppresses encounters of Fl with any reactive surfaces prior to those in COMPACT. SRIM simulations showed a gas mixture of 50% He and 50% Ar and an RTC depth of 20 mm to ensure complete stopping of Fl isotopes inside the RTC. In addition, the transport time as function of the gas flow rate was optimized, leading to faster flush-out and hence an improved overall efficiency. Online experiments with ^{183}Hg ($T_{1/2}$ = 9.4 s) produced in the ^{48}Ca+^{142}Nd reaction showed that 62% of all Hg entering the RTC were deposited in COMPACT. The amount of Hg entering the RTC was measured in a separate experiment by placing a Si focal plane detector, behind the RTC window in the RTC position. Using a chopped beam (0.1 s beam on and 5 s beam off), a flush-out profile for Hg was measured. Based on the Hg decay-in-flight observation in a SiO_2-covered COMPACT array, 50% of Hg entering the RTC reached COMPACT within 0.4 s, at a gas flow rate of 2 L/min.

3) Different combinations of COMPACT detectors with either a Au or SiO_2 surface, can be used in an isothermal or thermochromatography mode. This broadens the range of experimentally accessible chemical reactivity. Preparatory experiments have shown, that Pb deposits on SiO_2, whereas Hg deposits only on Au [5]. To distinguish between Pb- and Hg-like behavior, a first section of the COMPACT detector is covered with a SiO_2 surface (cf. Fig. 1).

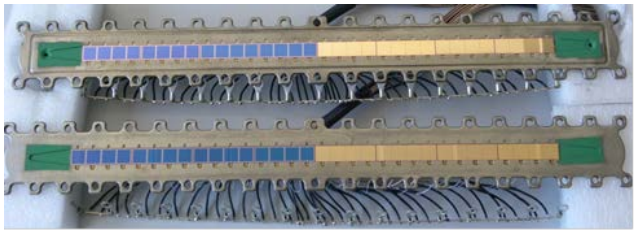

Fig. 1: COMPACT detector array with SiO_2 and Au surfaces.

Experiments on Fl using this improved system have been performed and are currently under analysis. The setup is also suitable for chemical studies of element 113, where the isotope ^{284}113 ($T_{1/2}$ = $0.97^{+0.12}_{-0.10}$ s) [6, 7, 8] can be produced as daughter after α-decay of ^{288}115 in the reaction ^{243}Am(^{48}Ca,3n)^{288}115.

References

[1] A. Yakushev *et al.*, Inorg. Chem. 53, 1624 (2014)
[2] Ch. E. Düllmann, et al., PRL 104, 252701 (2010)
[3] J. Even *et al.*, NIM A 638, 157-164 (2011)
[4] A. Semchenkov *et al.*, NIMB 266, 4153 (2008)
[5] L. Lens, *et al.*, GSI Sci. Rep. 2014, p. 183(2015)
[6] Yu. Ts. Oganessian, *et al.*, Nucl. Phys. A 944 (2015)
[7] D. Rudolph *et al.*, PRL 111, 112502 (2013)
[8] J.M. Gates *et al.*, PRC 92, 021301 (2015)

DOI:10.15120/GR-2016-1

Radiochemical investigation of the kinematics of multi-nucleon transfer reactions

M. Götz[1,2,3], S. Götz[1,2,3], J. V. Kratz[1], Ch. E. Düllmann[1,2,3], J. Ballof[1], H. Dorrer[1], J. Grund[1], E. Jäger[2], O. Keller[1], J. Krier[2], J. Khuyagbaatar[2,3], L. Lens[1,2], B. Lommel[2], M. Mendel[1], Ch. Mokry[1,3], K. J. Moody[5], J. Runke[1,2], M. Schädel[2], B. Schausten[2], D. Shaughnessy[5], J. Steiner[2], P. Thörle-Pospiech[1,3], N. Trautmann[1], N. Wiehl[1,3], A. Yakushev[2,3], and V. Yakusheva[2]

[1]Institute of Nuclear Chemistry University Mainz, 55099 Mainz, Germany; [2]GSI Helmholtz Center for Heavy-Ion Research, 64291 Darmstadt, Germany; [3]HIM Helmholtz Institute Mainz, 55128 Mainz, Germany; [4]Advanced Science Research Center JAEA, Tokai-mura Ibaraki 319-1195, Japan; [5]Lawrence Livermore National Laboratory, Livermore CA, USA

Multi-nucleon transfer reactions have attracted renewed attention as a promising tool for the production of neutron-rich transactinide isotopes [1-3]. Based on this renewed interest we performed a ^{48}Ca + ^{248}Cm bombardment at an incident energy 10% above the Coulomb barrier at TASCA to investigate angular-resolved distributions and recoil energies of isotopes between Cf and Fm. Identification of isotopes of these elements was performed within the offline radiochemical separation technique. Thus, only long-lived isotopes with atomic mass numbers between 246 and 256 were accessible. For the analysis of the reaction kinematics, the estimation of the most probable number of evaporated neutrons and the recoil energies as function of the angular distribution was evaluated for each nuclide. We used the stacked catcher foil technique to recieve information about the penetration by using several few μm thin Ni-foils, which were arranged behind one another. Each foil was divided into four arc-segments thus collecting reaction products emitted at different angles. This allowed to simultaneously measuring both, recoil ranges and angular distributions.

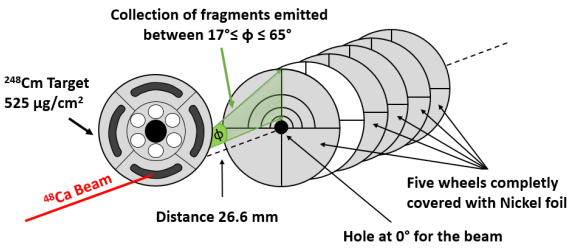

Figure 1: Schematic of the experimental setup: Five frames were completely covered with Ni-catcher foils of different thicknesses (1x3 μm, 3x1 μm and 1x5 μm). The first wheel was designed to stop sputtered ^{248}Cm target material. On the second wheel, only one quadrant was covered with a 5μm nickel foil to catch all transfer products emitted into this quadrant to provide a 100 % reference.

Irradiation of ^{248}Cm with ^{48}Ca ions was performed at the TASCA target position at a beam energy of 5.78 MeV/u, which corresponds to a center of mass energy of 220 MeV in the center of target. The target was irradiated for 10 hours with an average beam intensity of 4.6 x 10^{12} particles/s. The transfer products were stopped in the Ni catcher foils covering laboratory angles from ϕ = 17° - 65°. After end of bombardment, the foils were dissolved in dilute nitric acid, and a scavenger precipitation with $Fe(OH)_3$ using ammonia was performed. Different elements were separated on a cation-exchange column with 0.12 M α-HiB and 0.14 M α-HiB at pH=4.80 into a combined Fm/Es fraction and a Cf/Bk fraction, respectively. This allowed seperating nuclides with adjacent atomic numbers by subsequent column chromatographic treatment. The identification of Bk-, Cf-, Es-, and Fm-isotopes was achieved by detecting α-particles, considering known cross-section ratios for different isotopes of a given element [4], and their characteristic decay properties as well as precursor effects.

Kinetic energies corresponding to recoil range in the stopping material were evaluated using the stopping power systematics of ions in matter [5]. The data will be investigated within Volkov's generalized Q_{gg} systematics including corrections for the breaking of nucleon pairs in the multi-nucleon transfer process [3,6]. Information of the angular distributions, and the total kinetic energy loss (TKEL) can be used to generate deflection functions for the visualisation of the rotational movement through the nucleon-transfer process.

References

[1] V. Zagrebaev et al,. Nucl.Phys. A834, 366c (2010)

[2] W. Greiner et al., Nucl. Phys. A834, 323c (2010)

[3] J.V. Kratz et al., Phys. Rev. C88, 054615 (2013)

[4] D.C. Hoffman et al., Phys. Rev. C31, 1763 (1985)

[5] J.F. Ziegler, Interactions of ions with matter, http://www.srim.org, (2015)

[6] V.V. Volkov, Int. Conf. on Reactions between Complex Nuclei, Nashvillle 1974, (North Holland, Amsterdam) Vol. II, 363 (1974)

DOI:10.15120/GR-2016-1

DOI:10.15120/GR-2016-1

Investigations of the ^{17}Ne continuum structure

J. Marganiec[1,2,3], F. Wamers[1,2], T. Aumann[1,2], L.V. Chulkov[5,2], M. Heil[2], B. Jonson[6], R. Plag[2], H. Simon[2], and the R^{3}B collaboration

[1]TU Darmstadt, Darmstadt, Germany; [2]GSI, Darmstadt, Germany; [3]EMMI@GSI, Darmstadt, Germany; [5]NRC Kurchatov Institute, Moscow, Russia; [6]Chalmers Tekniska Högskola, Göteborg, Sweden

Nuclear and Coulomb excitations of ^{17}Ne using CH_2, C, and Pb targets were studied in relativistic ($\approx$ 500 MeV/u) breakup reactions at GSI, employing the R^{3}B-LAND setup for measurements in inverse and full kinematics. Excited states in the ^{17}Ne continuum were observed as event-wise coincidences between final-state ^{15}O and two protons. The experimental excitation spectra, reconstructed from the relative kinetic energy between the final-state partners ^{15}O-p-p, are well described as resulting from the contribution of several excited states in ^{17}Ne, superimposed on a smooth physical background. The example of the CH_2 target data is shown in Fig. 1. Five resonance-like structures corresponding to excitations of narrow resonant states in ^{17}Ne are observed in the data from the CH_2 and C targets, while only three are identified in the data from the Pb target. The results of previous spectroscopic studies of ^{17}Ne together with the available experimental information about the structure of excited states in the mirror nucleus ^{17}N were used as a first guidance in our interpretation. The spectroscopic information for the members of the A = 17, T = 3/2 isobaric multiplet were also used for the classification of the states, together with the isobaric multiplet mass equation (IMME) and the Thomas-Ehrman shifts (TES).

The first peak in the spectrum is due to an unresolved doublet consisting of two narrow states, $I^\pi = 5/2^-$ and $1/2^+$. The relative contributions of these two states were obtained from an analysis of the three-body correlations. The second peak at E^* = 2.652 MeV was interpreted as an unresolved doublet of $5/2^+_1$ and $3/2^-_2$ states. The level structures in the T = 3/2 isobaric multiplets allow a prediction for the positions of these states: $5/2^+_1$ at 2.614(20) MeV and $3/2^-_2$ at 2.692(21) MeV, respectively. A value of TES($3/2^-_2$) = 380(16) keV was found. A comparison with the level scheme of mirror nucleus, ^{17}N, suggests that the third peak, at E^* = 3.415(38) MeV could be the second $5/2^-_2$ state. The TES($5/2^-_2$) = 359(40) keV is close to the TES($3/2^-_2$) and is thus in support of the $5/2^-_2$ assignment. Two additional resonances at 5.210(79) MeV and 10.06(16) MeV were observed in the present experiment, the latter only for the light targets. The partial decay scheme of ^{17}Ne with dominating decay branches is shown in Fig. 2.

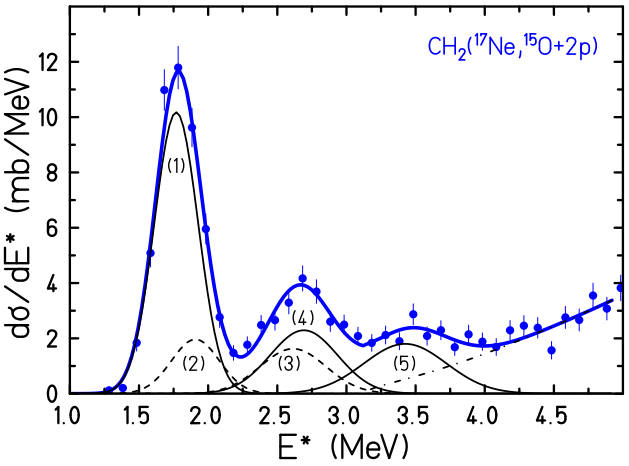

Figure 1: Narrow resonance states in the low-energy region, $0 < E_{fpp} < 4$ MeV excited in the CH_2 target. The thin solid lines show negative-parity states, dashed lines stem for positive-parity states, and the dash-dotted line is physical background.

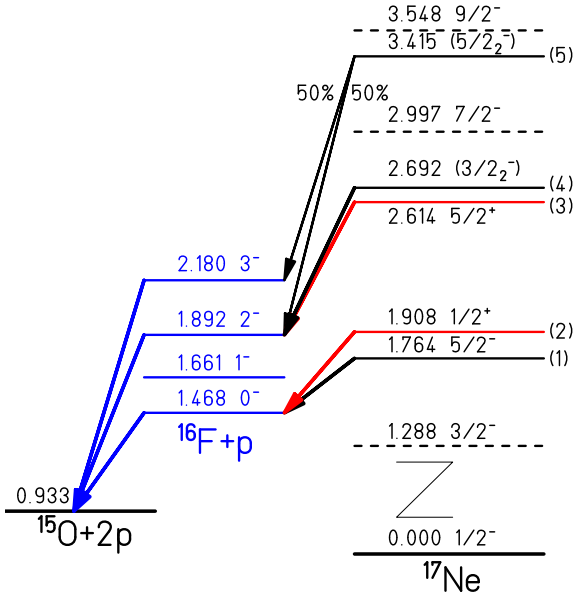

Figure 2: Narrow resonance states above the two-proton separation energy in ^{17}Ne. Positive-parity states are drawn as red, negative-parity states as black, and unobserved states as dashed lines. Dominant decay branches via intermediate resonant states in ^{16}F are shown with arrows.

DOI:10.15120/GR-2016-1

Dissipative effects in fission by using complete kinematics measurements

J.L. Rodríguez-Sánchez[1], *J. Benlliure*[1], *J. Taïeb*[2], *H. Álvarez-Pol*[1], *L. Audouin*[3], *Y. Ayyad*[1], *G. Bélier*[2], *G. Boutoux*[2], *E. Casarejos*[4], *A. Chatillon*[2], *D. Cortina-Gil*[1], *T. Gorbinet*[2], *A. Heinz*[5], *A. Kelić-Heil*[6], *B. Laurent*[2], *J.F. Martin*[2], *C. Paradela*[1], *E. Pellereau*[2], *B. Pietras*[1], *D. Ramos*[1], *C. Rodríguez-Tajes*[7], *D.M. Rossi*[6], *H. Simon*[6], *J. Vargas*[1], *and B. Voss*[6]

[1]University of Santiago de Compostela, Spain; [2]CEA DAM DIF, Arpajon, France; [3]IPN Orsay, Orsay, France; [4]University of Vigo, Spain; [5]University of Chalmers, Sweden; [6]GSI, Darmstadt, Germany; [7]GANIL, Caen, France

In this work complete kinematics measurements of the two fission fragments, obtained for the first time by using the SOFIA setup [1, 2], are used to study the deformation dependence of the dissipation parameter. For this purpose, we introduce a new experimental observable sensitive to dissipative effects at large deformations: the neutron excess of the final fission fragments. This observable was used to deduce the value of the dissipation parameter after the saddle point. The new approach should help us solving the questions concerning the value of the dissipation parameter and its dependence on deformation and temperature.

In Ref. [3], we used the partial fission cross sections and the width of the charge distributions of the final fission fragments to investigate dissipative effects at small deformations. These observables cover a large range in excitation energies (up to 350 MeV), providing us with the possibility to investigate the temperature dependence of the dissipation parameter. We concluded that a constant value of the ground-to-saddle dissipation parameter (β_{gs}) of (4.5 ± 0.5) $\times$ 10^{21} s^{-1} provides the best description of this set of data. The overall description of the data by using a constant value of the dissipation parameter confirmed the conclusions obtained in previous works with respect to the magnitude and temperature independence of the reduced dissipation parameter at small deformations [4, 5]. In addition, these calculations also provide an accurate description of the fissioning nuclei at the saddle-point deformation and can be considered as a suitable tool to investigate the dissipative effects at large deformations by using additional observables sensitive to the saddle-to-scission dynamics.

In this sense we propose the use of the neutron excess of the two final fission fragments ($<N>/Z$), obtained for the reaction ^{208}Pb($500A$ MeV) + p, to investigate dissipative effects at large deformation because this observable also depends on the prescission neutron evaporation. Furthermore, in our experiment the neutron excess of the final fission fragments is measured very accurately and with high efficiency, resulting in an excellent constraint for model calculations.

The average neutron excess of the final fission fragments is displayed as a function of the atomic number of the fissioning nuclei in Fig. 1, where we also show the results of our model calculations [6] assuming β_{gs} = 4.5 $\times$ 10^{21} s^{-1} and different values for the saddle-to-scission dissipation parameter (β_{ss}): 4.5 $\times$ 10^{21} s^{-1} (solid line), 6.5 $\times$ 10^{21} s^{-1} (dot-short-dashed line), and 20 $\times$ 10^{21} s^{-1} (dot-long-dashed line). The accuracy in the measurement of the neutron excess of the final fission fragments confirms the sensitivity of this observable to the saddle-to-scission dissipation. This benchmark also allows us to establish that calculations considering a saddle-to-scission dissipation parameter between 4.5 $\times$ 10^{21} s^{-1} (solid line) and 6.5 $\times$ 10^{21} s^{-1} (dot-short-dashed line) can describe the average neutron excess for the full range of fissioning systems.

The similitude between the values of the dissipation parameter required to describe the fission dynamics before and after the saddle point excludes any strong dependence on deformation as previously though [7]. Moreover, the large range in excitation energy covered by the present data and their description using a constant value of dissipation also exclude any strong dependence on temperature.

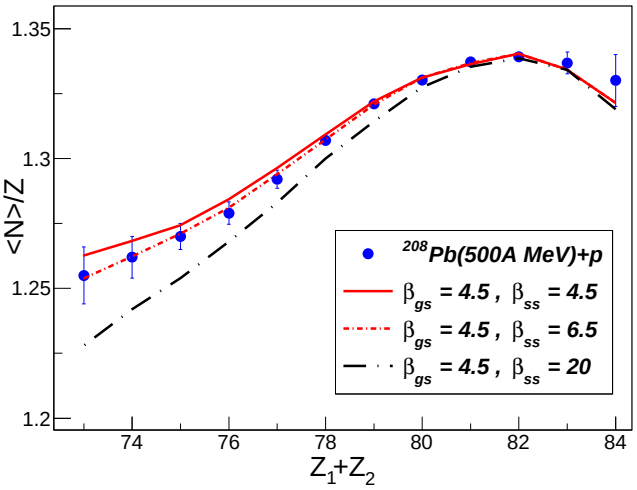

Figure 1: Average neutron excess of the final fission fragments as a function of the atomic number of the fissioning nuclei. The lines represent model calculations for different values of the dissipation parameters in units of 10^{21} s^{-1}

References

[1] J. F. Martin et al., Eur. Phys. J. A **51**, 174 (2015).
[2] J. L. Rodríguez et al., Phys. Rev. C **91**, 064616 (2015).
[3] J. L. Rodríguez et al., Phys. Rev. C **92**, 044612 (2015).
[4] B. Jurado et al., Phys. Rev. Lett. **93**, 072501 (2004).
[5] Y. Ayyad et al., Phys. Rev. C **91**, 034601 (2015).
[6] J. L. Rodríguez et al., Phys. Procedia **64**, 157 (2015).
[7] I. Diószegi et al., Phys. Rev. C **63**, 014611 (2000).

DOI:10.15120/GR-2016-1

Dissipative effects investigated by using light-charged particle multiplicities

J.L. Rodríguez-Sánchez[1], *J. Benlliure*[1], *C. Paradela*[1], *H. Álvarez-Pol*[1], *L. Audouin*[2], *Y. Ayyad*[1], *G. Bélier*[3], *G. Boutoux*[3], *E. Casarejos*[4], *A. Chatillon*[3], *D. Cortina-Gil*[1], *T. Gorbinet*[3], *A. Heinz*[5], *A. Kelić-Heil*[6], *B. Laurent*[3], *J.-F. Martin*[3], *E. Pellereau*[3], *B. Pietras*[1], *D. Ramos*[1], *C. Rodríguez-Tajes*[7], *D.M. Rossi*[6], *H. Simon*[6], *J. Taïeb*[3], *J. Vargas*[1], *and B. Voss*[6]

[1]University of Santiago de Compostela, Spain; [2]IPN Orsay, Orsay, France; [3]CEA DAM DIF, Arpajon, France; [4]University of Vigo, Spain; [5]University of Chalmers, Sweden; [6]GSI, Darmstadt, Germany; [7]GANIL, Caen, France

Light-charged particles are one of the most widely used observable to investigate the dynamics of the fission process in direct kinematics. However, in direct kinematics is very difficult to obtain correlations between this observable and the fission fragments due to the fact that fission fragments cannot always be detected, and even less, their identification in atomic or mass number [1]. To overcome this problem, we have used the inverse kinematics technique together with the SOFIA setup [2]. Thanks to the inverse kinematics the fission fragments and light-charged particles are emitted at high kinetic energies in the forward direction, facilitating their detection with high efficiency and precision. Then the state-of-the-art detectors of the SOFIA setup allowed us for the first time to determine additional correlations between the light-charged particles and fission fragments for investigating dissipation in fission.

In this work, we use the light-charged particles emitted in proton-induced fission reactions on ^{208}Pb at different kinetic energies to study fission dynamics. In this kind of reaction, light-charged particles can be emitted from the first stage of the reaction, the so-called intranuclear cascade, or through the deexcitation of the compound nucleus. In the latter case we can assume that light-charged particles are only emitted before the saddle point because of the shorter saddle-to-scission paths, where the most probable deexcitation channels are the emission of neutrons and γ-rays. Thus these measurements represent an ideal scenario to study the presaddle fission dynamics.

In Fig. 1 we represent the average value of the multiplicity distribution of particles measured with atomic number $Z = 1$ [3] as a function of the projectile bombarding energy. The data are also compared with model calculations based on the Kramers approach [4] and ABLA07 [5], where fission is described as a diffusion process across the fission barrier. ABLA07 also takes into account transient time effects in fission by using an analytical description of the time-dependent fission decay width, obtained from the solution of the Fokker–Planck equation [6].

These calculations reveal that this observable is sensitive to transient time effects. As can be observed, dynamical calculations based on the Kramers approach for a value of the reduced dissipation parameter of $\beta = 4.5 \times 10^{21}$ s^{-1} (long-dashed line) overestimate the data, while ABLA07 calculations considering dissipative and transient time effects for the same value of the reduced dissipation parameter (solid line) provide a good description. On the other hand, ABLA07 calculations assuming values of $\beta = 10 \times 10^{21}$ s^{-1} (dotted line) and $\beta = 20 \times 10^{21}$ s^{-1} (dot-dashed line) underestimate our measurements.

The overall good description of the light-charged particles multiplicities allows us to confirm the conclusions obtained in previous works [7, 8, 9, 10] with respect to the magnitude and temperature independence of the reduced dissipation parameter at small deformations, leading to a constant value of $\beta = 4.5 \times 10^{21}$ s^{-1}.

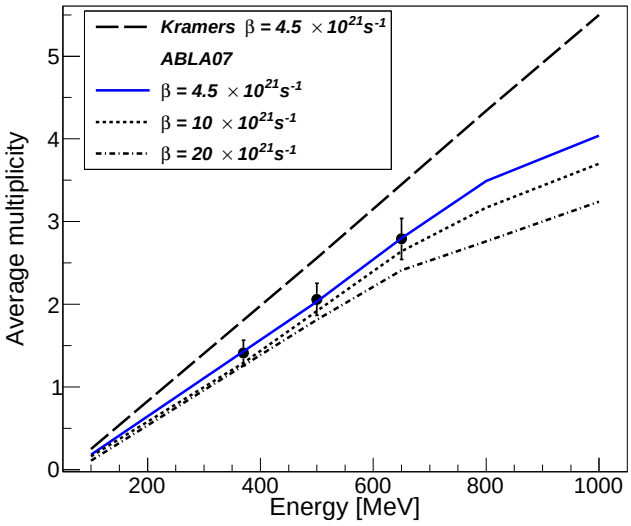

Figure 1: Average multiplicity of particles with $Z = 1$ as a function of the projectile bombarding energy for the reaction ^{208}Pb + p. The lines represent different model calculations.

References

[1] B. Lott et al., Phys. Rev. C **63**, 034616 (2001).

[2] J. F. Martin et al., Eur. Phys. J. A **51**, 174 (2015).

[3] J. L. Rodríguez et al., GSI Sci. Rep. 2014, p. 189.

[4] H. A. Kramers, Physica **7**, 284 (1940).

[5] A. Kelić et al., arXiv:0906.4193v1.

[6] B. Jurado et al., Phys. Lett. B **553**, 186 (2003).

[7] B. Jurado et al., Phys. Rev. Lett. **93**, 072501 (2004).

[8] C. Schmitt et al., Phys. Rev. C **81**, 064602 (2010).

[9] Y. Ayyad et al., Phys. Rev. C **91**, 034601 (2015).

[10] J. L. Rodríguez et al., Phys. Rev. C **92**, 044612 (2015).

DOI:10.15120/GR-2016-1

Constraining the level densities from proton-induced fission reactions

J.L. Rodríguez-Sánchez[1], J. Benlliure[1], J. Taïeb[2], H. Álvarez-Pol[1], L. Audouin[3], Y. Ayyad[1], G. Bélier[2], G. Boutoux[2], E. Casarejos[4], A. Chatillon[2], D. Cortina-Gil[1], T. Gorbinet[2], A. Heinz[5], A. Kelić-Heil[6], B. Laurent[2], J.-F. Martin[2], C. Paradela[1], E. Pellereau[2], B. Pietras[1], D. Ramos[1], C. Rodríguez-Tajes[7], D.M. Rossi[6], H. Simon[6], J. Vargas[1], and B. Voss[6]

[1]University of Santiago de Compostela, Spain; [2]CEA DAM DIF, Arpajon, France; [3]IPN Orsay, Orsay, France; [4]University of Vigo, Spain; [5]University of Chalmers, Sweden; [6]GSI, Darmstadt, Germany; [7]GANIL, Caen, France

The nuclear level density is one of the main ingredients for the statistical description of the fission process. In this work, we propose to constrain the description of this parameter by using fissioning systems with low angular momentum and high excitation energies ($E^* > 100$ MeV). These conditions represent a good approach to study the impact of the level densities on the experimental observables, such as the fission cross sections and width of the atomic-number distribution of the fission fragments, because the effect of the rotational and vibrational excitations on the level densities washes out at excitation energies ~ 40 MeV [1].

For this propose we use fission reactions induced by protons on ^{208}Pb at high kinetic energies. These measurements were performed with the combination of the inverse kinematics technique and the SOFIA detection setup [2] that allowed us to measure the fission cross sections and the charge distribution of the fission fragments [3, 4].

In Fig. 1 we display the width of the atomic-number distribution of the fission fragments (σ_Z) as a function of the atomic number of the fissioning system ($Z_1 + Z_2$) for the reactions measured in this work: ^{208}Pb + p at 370A MeV (open crosses), 500A MeV (open circles), and 650A MeV (open diamonds). As can be seen, the width of the atomic-number distribution increases with decreasing $Z_1 + Z_2$. Moreover, for all the reactions we obtain very similar values for the width of each $Z_1 + Z_2$. This result indicates that for a given fissioning system $(Z_1 + Z_2)$ the width of the atomic-number distribution of the final fragments depends on neither the entrance channel nor on the bombarding energy of the projectile. The range in $Z_1 + Z_2$ covered in each reaction is different because it reflects the initial violence of the reaction, and consequently the evaporation probabilities from the increase of excitation energy. Therefore, this observable clearly provides an important constraint for model calculations describing the evolution of the fissioning system from the ground state to the saddle-point deformation.

We also compare these measurements with ABLA07 calculations [5] assuming different descriptions for the level-density parameter ($\tilde{a}$). The solid line represents a calculation based on the deformation-dependent level-density parameter proposed by Ignyatuk et al. [6] while the dotted and dashed lines correspond to deformation-independent parametrizations according to $\tilde{a}$=$A/8$ and $\tilde{a}$=$A/12$, respectively.

The first conclusion is that for the heaviest fissioning nuclei with the lowest excitation energies there is no sensitivity to the parameters used in the model calculations. The same conclusion was also obtained when this observable was used to constrain ground-to-saddle disipative effects [7]. On the other hand, for fissioning systems lighter than $Z_1 + Z_2 < 80$ we observe a sensitivity to the different descriptions of the level-density parameter. As can be seen, only calculations considering a deformation-dependent level-density parameter following Ignyatuk's parametrization provide a satisfactory description of the width of the charge distributions of the fission fragments (solid line). Thus these results reveal that this observable could be used in future works to study the fissility and/or temperature dependence of the level-density parameter [8].

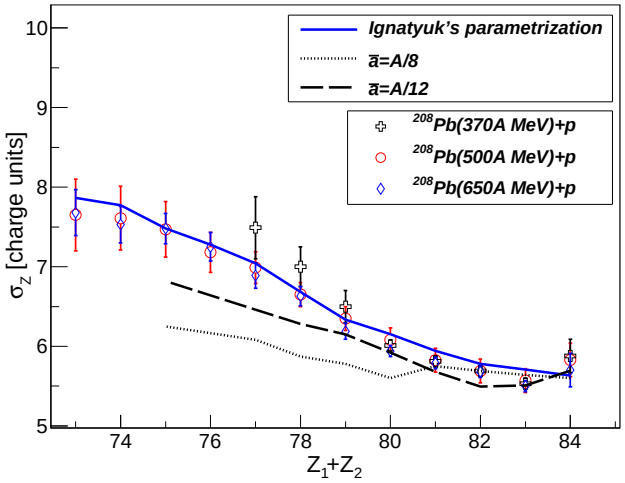

Figure 1: Width of the charge distribution of the fission fragments as a function of the fissioning system. The lines correspond to different calculations.

References

[1] A.R. Junghans et al., Nucl. Phys. A **629**, 635 (1998).
[2] J.F. Martin et al., Eur. Phys. J. A **51**, 174 (2015).
[3] J.L. Rodríguez et al., Phys. Rev. C **90**, 064606 (2014).
[4] J.L. Rodríguez et al., Phys. Rev. C **92**, 044612 (2015).
[5] A. Kelić et al., arXiv:0906.4193v1.
[6] A.V. Ignatyuk et al., Sov. J. Nucl. Phys. **21**, 612 (1975).
[7] Y. Ayyad et al., Phys. Rev. C **91**, 034601 (2015).
[8] J.P. Lestone, Phys. Rev. C **52**, 1118 (1995).

DOI:10.15120/GR-2016-1

Systematic measurement of knockout reaction cross sections in medium mass nuclei

J. Díaz-Cortés[1], J.L. Rodríguez-Sánchez[1], J. Benlliure[1], D. Dragosavac[1], D. Pérez[1], H. Álvarez-Pol[1], B. Blanck[2], E. Casarejos[1], V. Fohr[3], M. Gascón[1], W. Gawlikowicz[4], A. Heinz[5], K. Helariutta[6], L. Pienkowski[4], M. Staniou[3], K. Subotic[7], K. Summerer[3], B. Pietras[1], J. Taieb[8], A. Trzcinska[4], D. Rossi[6], H. Simon[6], J. Vargas[1], and B. Voss[6]

[1]University of Santiago de Compostela, Spain; [2] Centre d'Etudes Nucleaires,Bordeaux-Gradignan Cedex, France; [3]GSI, Darmstadt, Germany; [4]University of Warsaw, Poland; [5]University of Chalmers, Sweeden; [6]University of Helsinki, Finland; [7]Institute of Nuclear Science Vinca, Belgrade, Serbia; [8]CEA DAM, Bruyeres-le-Chatel, France

Nucleon knockout reactions have being largely used to investigate structural effects [1] and halo radial nucleon distributions [2] in nuclei far from stability. However, most of the available information concerns light systems. In the present report we present an attempt to systematically investigates neutron and proton knockout cross sections in medium-mass nuclei covering a large range in isospin.

The experiment took place at the GSI facility where we used primary beams of ^{124}Sn and ^{112}Sn, and secondary beams produced in the fragmentation of ^{132}Xe and fision of ^{238}U at energies around 1000 MeV/A to produce nuclei between Cadmium and Xenon over a broad range in isospin. The FRagment Separator was used as a two-independent magnetic spectrometers, each with a different magnetic setting. In the first part of the FRS, fission and fragmentation fragments produced by the primary beams were unambiguosly identified in mass and charge. At the intermediate focal plane of the FRS, a beryllium target of 2591 $\pm$ 7 mg/cm^2 was placed in order to induce the knockout reactions. Then, the second part of the FRS was used to identify, the fragmentation products.

In Fig. 1 we depict the preliminary 1-neutron (upper panel) and 1-proton (lower panel) removal cross sections for different tin isotopes measured in this work (points) as a function of the projectile mass number. We have also included some existing measurments from other works. As can be seen, our data are in good agreement with those obtained before. Moreover, we provide a rather complete scan over a broad range in isospin.

For stable and neutron-rich tin isotopes we observe that neutron knockout is much favoured with respect to the proton knockout. For neutron-deficient isotopes the situation changes. The observed cross sections for these reaction channels do not follow the linear evolution one would expect just from the evolution of the relative abundaces of protons and neutrons or from the separation energies. Therefore, the systematic evolution of the cross sections is affected by structural effects.

In Ref. [5] the evolution of similar cross sections were discussed by using calculations based on the intranuclear cascade concept. The results are that those model calculations describe rather well the knockout of loosely bound systems but largely overestimate these cross sections for deeply bound ones. More recently, the knockout of light systems has been investigated using abrasion-ablation model calculations [6]. In this case the abrasion model also fails the description of these cross sections unless the excitation energy gained in the knockout is arbitrarily modified. We expect that the new data obtained in this work will contribute to put some light into this puzzling situation.

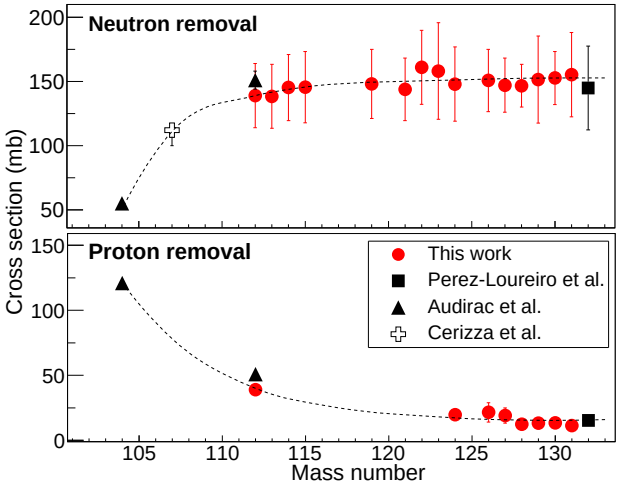

Figure 1: Knockout reaction cross section of different tin isotopes (Z=50) from N = 63 to N = 82. The dashed lines are to guide the eye.

References

[1] R. Kanungo et al., Phys. Rev. Lett. **102**, 152501 (2009).

[2] D. Bazin et al., Phys. Rev. Lett. **74**, 3569 (1995).

[3] D. Pérez-Loureiro et al., Phys. Lett. B **703**, 552(2011).

[4] G. Cerizza et al., Phys. Rev. C **93**, 021601 (2016).

[5] L. Audirac et al., Phys. Rev. C **88**, 041602 (2013).

[6] S. Ronja et al. submitted to Phys. Rev. C

DOI:10.15120/GR-2016-1

The role of EPICS in NUSTAR*

B. Löher[1], *M. Heil*[1], *H. Simon*[1], *and H. T. Törnqvist*[1,2]
[1]GSI, Darmstadt, Germany; [2]Technische Universität Darmstadt, Darmstadt, Germany

The experiments conducted within the Nustar collaboration make use of many different and inhomogeneous types of machinery and detectors. In addition, the detectors are meant to be interchangeable to allow for flexible customized experimental setups. Therefore, the need arises for a common, highly scalable, and highly customizable experiment control system, which will not interfere with an often changing experiment environment.

Additional requirements for such a control system include: Support for a variety of devices, and the possibility to add support for new devices. The software should run on all major operating systems, be open source and have extensive documentation available. The software should allow for fine-grained access security, have support for engineering units (SI units) and automatic validity and range checks. Visual and acoustic warnings in case of system failure or when critical values are reached should be provided. The system should be fast to reconfigure, robust, and allow for saving and restoring complete parameter sets. These requirements are fully satisfied either directly or via the use of extensions by EPICS [1], the experiment control system co-created by the Argonne National Laboratory.

Today, EPICS is already successfully in use in several experiments throughout GSI, mainly in the HADES, R3B, CBM and PANDA groups. However, the EPICS servers (IOC) and related software are mainly tailored to a specific use case and either no or only isolated infrastructural components exist. What is needed for future operations in the Nustar collaboration besides the IOCs and user interfaces for the individual device are therefore common infrastructural components.

The role of EPICS in Nustar is, therefore, to provide a set of centralised services to create a common infrastructure for all related experiments. These components should provide convenience functionality on top of the pure control and monitoring tasks performed by the IOCs. As such, great synergetic effects are to be expected. Figure 1 shows a schematic overview of the dual-layer network structure and the infrastructural components.

Gateway processes provide a number of related functions: Each gateway represents a bridge between two separate networks. Therefore, the gateway has full control over traffic sent from EPICS clients to IOCs and vice versa. This allows to enforce access restrictions for clients to specific process variables (PV), by either completely hiding the PV or allowing readonly access. Another important functionality is PV mapping via the use of aliases. Using aliases

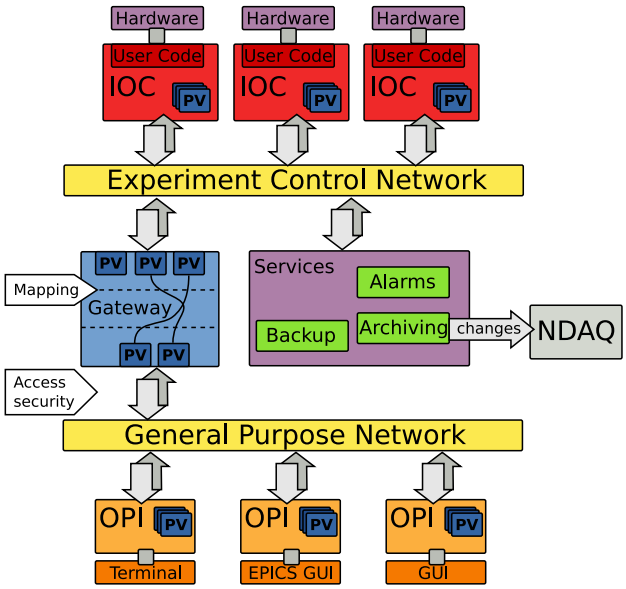

Figure 1: Schematic layout of planned Nustar EPICS infrastructure.

it is possible to give physical (channel) names to the actual PVs in each IOC, and then in the gateway translate the physical names to logical names. The client will then only see the mapped logical names. This is important, e.g. in case a piece of hardware needs to be replaced. Then it is sufficient to update the mapping rules instead of having to update all clients. In Nustar gateways are supposed to represent access points to the closed EPICS network from the general purpose GSI/FAIR network.

An option for saving and restoring the current state is to use the existing BURT extension. It saves the state of each IOC to plain text files. These can be versioned and tagged using git. Such saved states can e.g. mark important points in the timeline of an experiment and therefore represent 'trusted' settings.

The existing Channel Archiver extension for EPICS provides a way to record and replay the history of selected PVs with high performance. It is foreseen to provide an interface from the Channel Archiver to the Nustar Data Acquisition (NDAQ), which allows for recording IOC state changes as part of the main NDAQ data stream in the form of 'sticky events'. For additional information on the matter see the Nustar DAQ TDR [2].

[1] A. Johnson, et al., Epics - experimental physics and industrial control system (2011).

[2] NUSTAR Common DAQ WG, DAQ TDR, to be submitted

* Work supported by RBRB and the R^{3}B collaboration

DOI:10.15120/GR-2016-1

TRB readout of a thin silicon tracker for $(p, 2p)$ reactions*

S. Reichert[1,2], M. Sako[2], H. Baba[2], M. Böhmer[1], R. Gernhäuser[1], L. Maier[1], D. Mücher[3,9], M. Sasano[2], C. Berner[1], N. Chiga[2], W. F. Henning[4], T. Kobayashi[5], Y. Kubota[2,5], R. Lang[1], V. Panin[2], L. Stuhl[2], E. Takada[7], T. Uesaka[2], L. Werner[1], J. Yasuda[8], and the TRB collaboration[10]

[1]Physik Department, Technische Universität München; [2]RIKEN Nishina Center; [3]Department of Physics, University of Guelph; [4]ANL; [5]Department of Physics, Tohoku University; [6]Center for Nuclear Studies, University of Tokyo; [7]NIRS; [8]Kyushu University; [9]TRIUMF; [10]trb.gsi.de

A detector setup with high position and energy resolution is the essential key component for inverse kinematics experiments to study heavy exotic nuclei in $(p, 2p)$ reactions. A collaboration between RIKEN and TUM is presently developing a thin silicon tracker array [1] for an experiment at at the SAMURAI spectrometer of the Riken Nishina center in Tokio (Japan). The readout concept discussed here is based on a development by the TRB collaboration with a strong contribution from GSI and will be applicable for a wide range of future NUSTAR experiments.

Three layers of 100 μm thick single-sided strip detectors with a pitch of 100μm [1] are arranged in a two-arm setup (see fig.1). The strips of the first two layers are oriented vertically while the third layer strips are oriented horizontally. Additional beam tracking with drift chambers in front of the target allows for high resolution reconstruction for both, polar and azimuthal angles. Covering a polar angular range of $33° < \Theta < 55°$, typical energies of the detected protons will range from 80 MeV$< E_p <$ 200 MeV, resulting in an energy loss in those thin active layers ranging from 60 keV to 150 keV only. This small energy loss makes the noise level the most challenging issue for the performance of the readout electronics.

To avoid thermal stress the 51 x 78 mm large silicon wafers were mounted on d = 0.64 mm thin aluminum nitride frames and connected to 6 layers PCBs. The latter are equipped with up to 16 APV25s [3] chips and newly developed high density ceramics pitch adapters. Each APV25s chip is connected through one FPC cable to the vacuum interfaces of the detector chamber.

For the digital integration of up to 16 APV25s readout chains one ADCM [2] module per detector is used. This FPGA based electronics originally developed for the HADES RICH detector read-out at GSI features 16 channels of 12 bit ADCs including gain and offset adjustment. The firmware implementation already containes the APV protocol decoding, zero suppression, common mode handling and a high speed TRBnet [2] interface. This configuration allowed to read the full silicon tracker setup with a single TRB3 board at trigger rates up to 120 kHz, depending on the individual channel threshold. While unconnected reference channels provide a measure for the performance of the full electronics chain ($\sigma = 5$ LSB) more than 98% of the detector channels feature a distribution of $\sigma < 10$ LSB in their random signal amplitudes. Using an average calibration of 0.55 keV/LSB this allows for a signal to noise ratio of S/N > 10.

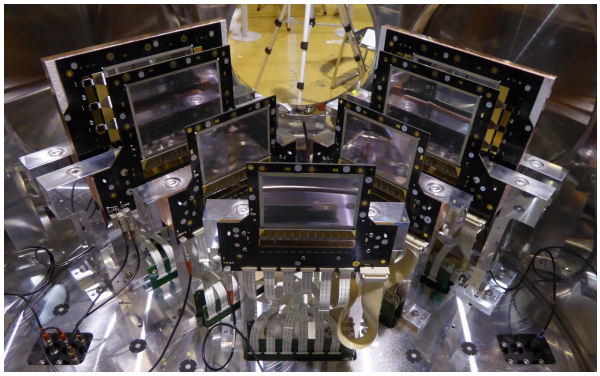

Figure 1: Front view of the two arm silicon detector setup with an additional reference detector at target position.

The complete new setup was tested in February 2016 at the HIMAC facility in Japan using the reactions ^{16}O$(p, 2p)^{15}$N and ^{132}Xe$(p, 2p)$, each with beam energies of E = 290 MeV/nucleon and intensities of several 10^5 pps. By exchanging trigger information and synchronizing the systems with a 40 MHz time stamp for each triggered event the TRB based readout was integrated into the RIKEN BABIRL DAQ system used for an also newly developed TOF system and further ancillary detectors. The TRB based DAQ system with 8700 channels was operated stably over several days at individual trigger thresholds of about 15-20 keV and typical event rates of up to 5 kHz. Already online the particle tracks in the two arms gave a clear signature for the expected (p,2p) kinematics. The measured data for thin d = 150μm fiber targets and a stack of d = 80μm foil targets (polypropylene) will show the tracking resolution of the new setup. Data analysis has just started with the implementation of a new tracking algorithm.

References

[1] S. Reichert et al.: RIKEN Accel. Prog. Rep. 48 (2015).

[2] J. Michel et al., IEEE Trans. Nuc. Sci., VOL. 58,4, (2011)

[3] M.J. French et al., Nuc. Inst. and Meth. A 466 (2001) 359–365

* Work supported by GSI (TMLFRG1316),Outstanding Individual Research Grant at RIKEN (M. Sasano) and DFG cluster of excellence 'Origin and Structure of the Universe'

Development of a TEGIC-detector for beam diagnostics *

L. Bierwirth, R. Gernhäuser, S. Maurus and S. Winkler
Physik Department, Technische Universität München

The intensities of primary and secondary beams will increase significantly with the upcoming GSI/FAIR accelerator facility. To cope with such increased intensities also in experiments, new detector systems for beam monitoring and particle identification are required, since established systems are limited with respect to their rate capabilities.
A well known technique for monitoring and identifying the charge of beam particles is the precise measurement of their energy loss as they traverse the active volume of a detector. Solid state detectors (SSDs) are often used for particle tracking especially in evacuated beam lines. But these detectors suffer from radiation damage which can alter their properties or even lead to a destruction of the devices. Gas detectors however are not affected by this degradation as their active volume is continuously exchanged, which makes these kind of detectors radiation hard by design and the perfect candidate for a stable and long-term operating detector especially for heavy ions. Standard gas detectors for element identification like MUlti Sample Ionization Chambers (MUSIC) face a limited rate capability due to the variable drift time needed for the secondary charge cloud to reach the electrodes of the detector. In addition the slowly drifting gas ions partly screen the electrical field in the active volume and may lead to recombination effects. This can result for high particle densities in a significant degradation of the achievable energy resolution.
In order overcome these limitations a reduction of the drift path may increase the rate capability and stability of such devices. About a decade ago the Tilted Electrode Gas Ionization Chamber (TEGIC) [1] has been introduced and first results looked very promising [2, 1]. The TEGIC detector is based on planar electrodes tilted by several degrees with respect to the beam axis to avoid a large overlap of electron and ion clouds as well as to reduce the drift length with respect to the effective detector length [3].
We have designed and assembled a new TEGIC detector, that is integrated in a standard CF100 beam pipe segment. It allows for a fast and easy integration in many established applications. Figure 1 illustrates the internal component of the detector using 33 electrodes and 16 independent anode channels with individual readout. The electrodes have an active diameter of D = 50mm and are built from d = 2 μm Mylar foils. These are plated on both sides with a conductive layer of aluminum and bonded to circular shaped standard PCB frames.
To achieve short signal paths and precise positioning of neighboring frames with alternating potentials a set of standard SMD connectors has been used. Additional precision combs guarantee for the alignment and coplanarity of the electrodes at distances of $l = 9.25 \pm 0.05$ mm . The stack of electrodes is mounted on a base PCB directly connecting the signal lines to a Mesytec MPR-16 pre-amplifier without additional vacuum feed-through or cables. Combined

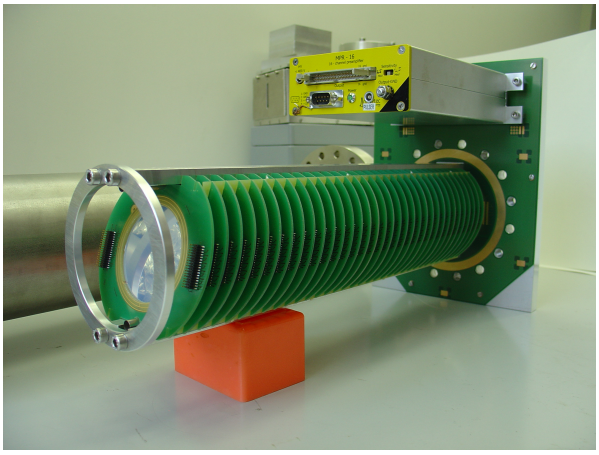

Figure 1: The beamline TEGIC consists of 33 tilted electrodes. The interface PCB (right side) is directly connected to the MPR-16 pre-amplifier.

with a state-of-the-art fully digital readout based on the FEBEX platform developed at GSI we will be able to use complex algorithms for pileup discrimination and energy reconstruction.
First tests in the lab showed a very good performance of the full system with an ENC of about 800 electrons per channel only. The full setup will be tested with a Xenon beam in June 2016 in CAVE C at GSI to demonstrate the expected resolution $\Delta Z < 0.3$ (FWHM) and evaluate optimum parameters for gas mixture and operating pressure at different rates. Variable pressure will allow for a flexible operation of the device with very different ion species or beam intensities without changing the electronics chain. Such a highly integrated detector, with a long-term high rate capability can be used in future experiments, like the R^3B at FAIR.

References

[1] K. Kimura et al., NIM A 538 (2005), 608-614
[2] S. Maurus et al., GSI Scientific Report (2014), 143
[3] S. Maurus, Development of a Large Area TEGIC-Detector for Heavy Ions, MSc thesis, TU-München (2015).

* Work supported by GSI (TMLFRG1316)

DOI:10.15120/GR-2016-1

Application of calorimetric low temperature detectors for the investigation of Z-yield distributions of fission fragments

P. Grabitz[1,2], *S. Dubey*[1,2], *A. Echler*[1,2,4], *P. Egelhof*[1,2], *M. Mutterer*[1], *S. Stolte*[2], *A. Blanc*[3], *H. Faust*[3], *U. Köster*[3], *S. Kraft-Bermuth*[4], *P. Scholz*[4], *S. Bishop*[5], *J.M. Gomez-Guzman*[5], *and F. Gönnenwein*[6]

[1]GSI, Darmstadt, Germany; [2]University of Mainz, Germany; [3]Institut Laue-Langevin, Grenoble, France; [4]University of Giessen, Germany; [5]Technical University Munich, Germany; [6]University of Tübingen, Germany

Precise data on the characteristics of fission-fragment yields, element distributions, kinetic-energy distributions, excitation-energy distributions and correlations of these quantities are of great interest for a better understanding of the fission process and of open questions concerning reactor physics and neutrino oscillations. The thermal neutron induced fission typically leads to a multitude of different nuclei ($>$ 400) with different kinetic energies.

One of the leading instruments for the investigation of fission fragment properties is the LOHENGRIN recoil separator at the High-Flux-Reactor ILL Grenoble. The LOHENGRIN spectrometer separates fission fragments according to their mass-to-ionic-charge ratio and their kinetic energy by a magnetic and an electrostatic field, but has no selectivity with respect to nuclear charges Z. For Z-yield determination of the mass-separated fragments different methods are used. Gamma spectroscopy or radiochemical methods, for instance, enable measurements in the complete range of fragment masses, but are limited to specific radioactive isotopes, depending on their decay or chemical properties. A principally universal method evolved in the 1980th at the LOHENGRIN is the passive absorber method that exploits the Z-dependent energy loss of fission fragments passing through an energy degrader [1,2]. This separation requires detector systems with high energy resolution for the residual energy and negligible pulse height defect, as well as degrader foils which are optimized with respect to thickness, homogeneity and energy-loss straggling, and was limited up to now to the region of light fission fragments (Z$<$43, A$<$107) [1-3].

Due to its good energy resolution and energy linearity a new and innovative detection system, namely calorimetric low temperature detectors (CLTDs) [4,5], promises, in combination with an adequate absorber material, an improvement in nuclear-charge resolution. Consequently, a new experimental system using a CLTD array for energy measurement and silicon nitride (Si_3N_4) foils as passive absorbers has been set up for the first time for Z-yield determination at the LOHENGRIN spectrometer [6]. The CLTD array, consisting of 25 sapphire absorber pixels equipped with aluminum transition-edge temperature sensors [5,7], has an active area of 15$\times$15 mm^2 and is operated at a temperature of 1.5 K. Previous test measurements at the tandem accelerator at MLL Garching with stable ^{109}Ag and ^{127}I ion beams have shown very promising results concerning the Z-resolving power (Z/ΔZ=55 at Z=50, see fig. 1)

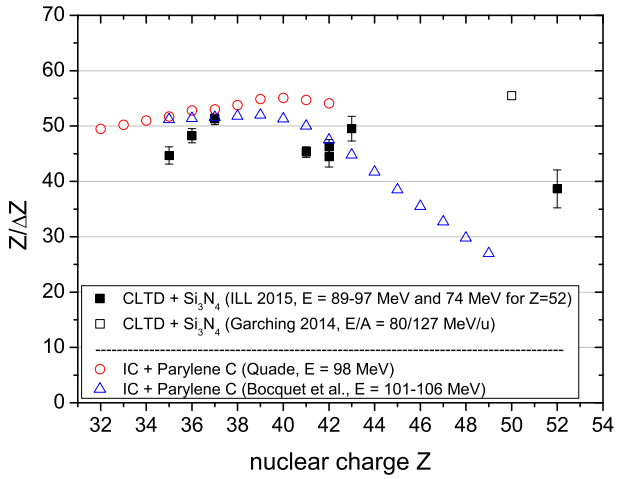

Figure 1: Z-resolution Z/ΔZ as function of nuclear charge obtained with CLTDs and Si_3N_4 absorbers for fission fragments from ^{235}U(n$_{th}$,f) at LOHENGRIN and for heavy ions at MLL Garching as compared to data measured with ionization chambers and Parylene-C absorbers on ^{233}U(n$_{th}$,f) by Quade et al. [1,2] and on ^{249}Cf(n$_{th}$,f) by Bocquet et al. [3]. The present data were measured with different absorber thicknesses (6.5 μm for Z = 35–43, 4 μm for Z = 50 and 4.4 μm for Z = 52). ΔZ is defined as the ratio of FWHM of an individual Z in the residual-energy spectra and the separation of the adjacent Z (see fig. 2).

of the new system [6]. Moreover, these tests have shown better performance of Si_3N_4 foils as compared to the previously used Parylene-C absorbers.

Preliminary results with regard to the Z-resolving power of the new experimental system obtained in the first experiments at ILL and MLL are summarized together with results from previous measurements and predictions performed with conventional detection techniques in fig. 1. In addition, examples of residual-energy spectra for light (A=92) and heavy (A=132) fission fragments from ^{235}U(n$_{th}$,f) are displayed together with Gaussian fits performed for deducing the individual Z-yields in fig. 2. For light fission fragments (Z$<$43, A$<$107) we could already match the historically best Z-resolutions achieved with Parylene-C absorbers and conventional ionization chambers [1-3] (see figs. 1 and 2a), even under not yet optimized conditions. Towards higher masses, where we profit even more from the outstanding properties of CLTDs (en-

DOI:10.15120/GR-2016-1

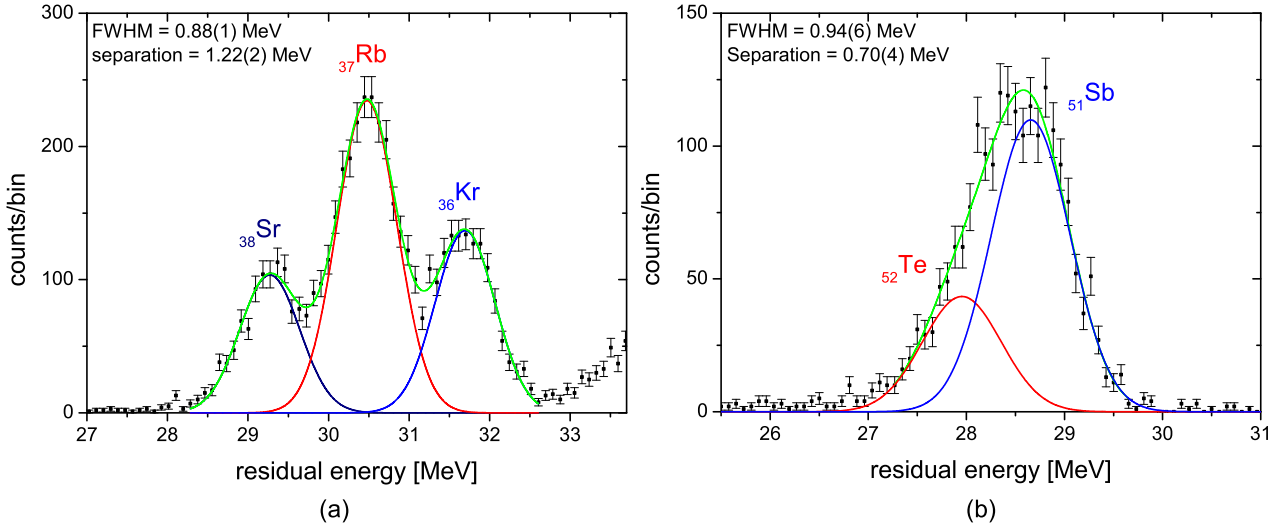

Figure 2: Residual-energy spectra for fission fragments from ^{235}U(n$_{th}$,f) mass-separated by the LOHENGRIN, after passing through a stack of Si_3N_4 degrader foils. (a) A = 92, initial energy E = 97 MeV with 6.5 μm of Si_3N_4. (b) A = 132, E = 74 MeV with 4.4 μm of Si_3N_4.

ergy resolution, energy linearity even at high ionization density), we could demonstrate significant improvements as compared to previous measurements with conventional techniques (figs. 1 and 2b). The fact that the quality in Z-resolution achieved with heavy ions at the Tandem at MLL Garching, has up to now not been reached in the measurements at ILL, indicates that there is still potential for improving the experimental conditions at ILL.

For a precise determination of cumulative yields of fission fragments it is mandatory to measure systematically the element distributions for various ionic charge states, as well as for various kinetic energies. In the present experiment this has been done for mass 92, and partly for masses 106–109. Of particular interest was the isotopic fission yield of ^{92}Rb from ^{235}U(n$_{th}$,f) for which, according to recent work [8,9], more precise data are urgently needed for a better understanding of reactor neutrino oscillations and the reactor neutrino anomaly. The investigation of Z-yield distributions for the heavier masses A$\geq$106 was started with the aim to study possible even-odd effects in the transition region from the light fragment group towards the symmetry region, which is of high interest for our understanding of the fission process. The data analysis concerning both burning topics is presently in progress.

For future investigations we plan to improve the detection technique concerning the detection efficiency, flexibility and nuclear-charge resolution. Such an improvement should enable us to continue systematic investigations in the symmetry region of nuclear fission and towards heavier masses.

References

[1] U. Quade, *PhD thesis*, University of Munich (1983).

[2] U. Quade et al., *Nucl. Phys. A* **487** (1988) 1.

[3] J.P. Bocquet et al., *Nucl. Instr. Meth. A* **267** (1988) 466.

[4] P. Egelhof and S. Kraft-Bermuth, *Topics Appl. Phys.* **99** (2005) 469.

[5] S. Kraft-Bermuth et al., *Rev. Sci. Instrum.* **80** (2009) 103304.

[6] P. Grabitz et al., *Jour. Low Temp. Phys.* (2016) DOI: 10.1007/s10909-016-1566-0.

[7] A. Echler et al., *Jour. Low Temp. Phys.* **167**, 5-6 (2012) 949.

[8] A.A. Sonzogni et al., *Phys. Rev. C* **91** (2015) 011301.

[9] D.A. Dwyer and T.J. Langford, *Phys. Rev. Lett.* **114** (2015) 012502.

DOI:10.15120/GR-2016-1

Mesoscopic Coulomb crystals in the planar limit confined in the SpecTrap Penning trap

S. Schmidt[1,2], T. Murböck[3], Z. Andelkovic[4], G. Birkl[3], W. Nörtershäuser[1], and M. Vogel[4]

[1]Institut für Kernphysik, TU Darmstadt; [2]Institut für Kernchemie, Johannes Gutenberg-Universität, Mainz; [3]Institut für Angewandte Physik, TU Darmstadt; [4]GSI Helmholtzzentrum für Schwerionenforschung, Darmstadt

Stable, low-temperature Coulomb crystals confined in a Penning trap are of particular interest for quantum information processing experiments [1], sympathetic cooling of highly charged ions [2] or the physics of quantum-many-body systems and quantum phase transitions [3]. They are formed when their thermal energy is small compared to their Coulomb potential energy. Depending on their size, ranging from small Coulomb clusters [4] to large plasmas, they show qualitatively different behaviour [5].

Here, we report on the formation of mesoscopic Coulomb crystals in a cylindrical Penning trap. The presented studies include the investigations of the static and dynamic properties of shell structures that occur in the planar limit $\alpha \rightarrow 0$, where α is the aspect ratio (axial/radial) of the cloud. We compare our results with the theory of a planar shell model [5] and find good agreement with our experimental observations. The results present an important step towards sympathetic cooling and precision laser spectroscopy of highly charged ions.

The presented measurements have been performed with the SpecTrap Penning trap experiment [2], where magnesium ions are created inside a home-build compact source for bunches of singly-charged atomic ions [6]. The ion source has proven simple and reliable, and has been used to produce μs-bunches of up to 10^6 magnesium ions at kinetic energies of a few hundreds of eV. Ion detection has been accomplished using a low-noise, non-destructive ion detection system [7]. After transport and capture, the ions

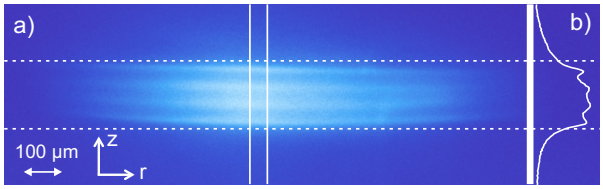

Figure 1: Image (a) and y-projection (b) of the central region of the planar ion crystal.

are prepared inside the trap in a state of low rotation frequency $\omega_r \approx 74\,\mathrm{kHz}$ and low temperature $T < 5\,\mathrm{mK}$, by laser Doppler cooling via the $^2\mathrm{S}_{1/2} \rightarrow {}^2\mathrm{P}_{3/2}$ transition at 279.8 nm. For a density of $n_0 \approx 3.35 \cdot 10^7\,\mathrm{cm}^{-3}$, we expect the Coulomb coupling parameter Γ to be in the range of $170 \leq \Gamma \leq 870$. Due to the low rotation frequency ω_r, the ions are weakly bound in radial direction, leading to a large radial extend of the ion cloud. As can be seen in Figure 1, for the given conditions, the ions arrange themselves to a crystal with planar geometry of equally spaced lattice planes. The number of lattice planes depends on the total areal density σ of the ion crystals. Since the shell curvature is small compared to the Wigner-Seitz radius $a_{\mathrm{WS}} = (3/4\pi n_0)^{1/3} \approx 19.2\,\mu\mathrm{m}$, the structure of the planar Coulomb crystal can be predicted by a planar shell model described in [5]. To compare our results with this

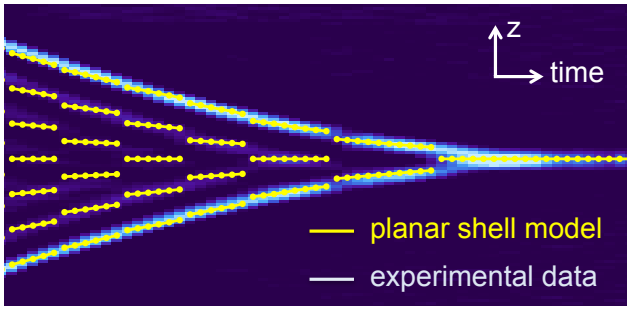

Figure 2: Time-evolution of the y-projections of the ion Coulomb crystals prepared in the Penning trap setup.

theory, we have evaluated the total number of lattice planes and the distance between each plane as a function of the total number of ions and thus as a function of σ. The time-evolution of an ion crystal with initially about $5 \cdot 10^4$ ions is shown in Fig. 2. The change of the areal density over time caused by ion loss was calculated from the fluorescence data and was used for the comparison of the theoretical predictions with our results. The agreement between experiment and theory is very good, giving a comprehensive description of the properties of the confined Coulomb crystals, that will be used in future for sympathetic cooling of highly charged ions.

This work has been supported financially by BMBF (05P12RDFA3, 05P15RDFAA, and 05P12PMFAE), DFG, GSI, and HIC for FAIR.

References

[1] M. J. Biercuk et. al., Nature **458**, 996 (2009)

[2] Z. Andelkovic et. al, Phys. Rev. A **87**, 033423 (2013)

[3] A. Retzker et. al., Phys. Rev. Lett. **101**, 260504 (2008)

[4] S. Mavadia et. al., Nature communications **4** (2013)

[5] D. H. E. Dubin et. al, Rev. Mod. Phys. **71**, 87 (1999)

[6] T. Murböck et. al., submitted to Rev. Sci. Inst. (2016)

[7] S. Schmidt et. al., Rev. Sci. Inst. **86**, 113302 (2015)

Linear polarization measurement in elastic hard x-ray scattering*

K.-H. Blumenhagen[†1,2,3], *S. Fritzsche*[1,2], *T. Gassner*[1,2,3], *A. Gumberidze*[3,4], *R. Märtin*[1,3], *N. Schell*[5], *D. Seipt*[1], *U. Spillmann*[3], *A. Surzhykov*[1], *S. Trotsenko*[1,3], *G. Weber*[1,3], *V. A. Yerokhin*[1,6], *and Th. Stöhlker*[1,2,3]

[1]HI-Jena, Germany; [2]University of Jena, Germany; [3]GSI, Darmstadt, Germany; [4]EMMI, GSI Darmstadt, Germany; [5]HZG, Geesthacht, Germany; [6]Peter the Great St. Petersburg Polytechnic University, Russia

The elastic scattering of photons from atoms has been studied experimentally. While previous studies on elastic scattering covered a broad range of photon energies and target materials [1, 2], they mostly considered unpolarized photon beams in the hard x-ray regime. A few experiments, where the photon polarization was taken into account [3], were limited to the following scenarios (excluding magnetic scattering [4], where one uses oriented targets): (1) Measuring the elastic scattering differential cross section when the incident photon beam is partially linearly polarized. (2) Measuring the linear polarization of the elastically scattered beam when the incident beam is unpolarized. Both these types of experiment suffered from low statistics due to technological shortcomings: Low-intensity polarized x-ray sources on the one hand and inefficient x-ray polarimeters on the other. These problems could be reduced with the advent of novel technologies, so a new type of elastic scattering experiment became feasible, which is presented in this report: Measuring the linear polarization of the scattered beam, when the incident beam is highly linearly polarized. To observe relativistic effects, a scenario with strong electromagnetic fields was chosen, namely the scattering of 175 keV hard x-rays from a high-Z target (gold). An intense, highly linearly polarized photon beam at that energy was provided by the High Energy Materials Science Beamline P07 [5] at the third-generation synchrotron radiation source PETRA III at DESY, Hamburg. The polarization of the scattered beam was analyzed with a dedicated silicon strip Compton polarimeter [6] at three scattering angles θ in the polarization plane of the incident beam (coplanar geometry). For this, the Compton polarimetry technique [7] was applied, which involves a measurement of the φ_C-distribution, where φ_C is the azimuthal scattering angle of Compton scattering events inside the polarimeter. Fitting the φ_C-distribution allows to extract the polarization of the beam incident on the polarimeter surface. In the present work, a non-analytical fit function based on Monte Carlo simulations was employed. The reason for this procedure (instead of using the analytical Klein-Nishina Compton scattering cross section) was to include detector effects. An example of a φ_C-distribution together with the corresponding fit is shown in figure 1 (a). Preliminary results for the polarization of the elastically scattered beam are presented in figure 1 (b).

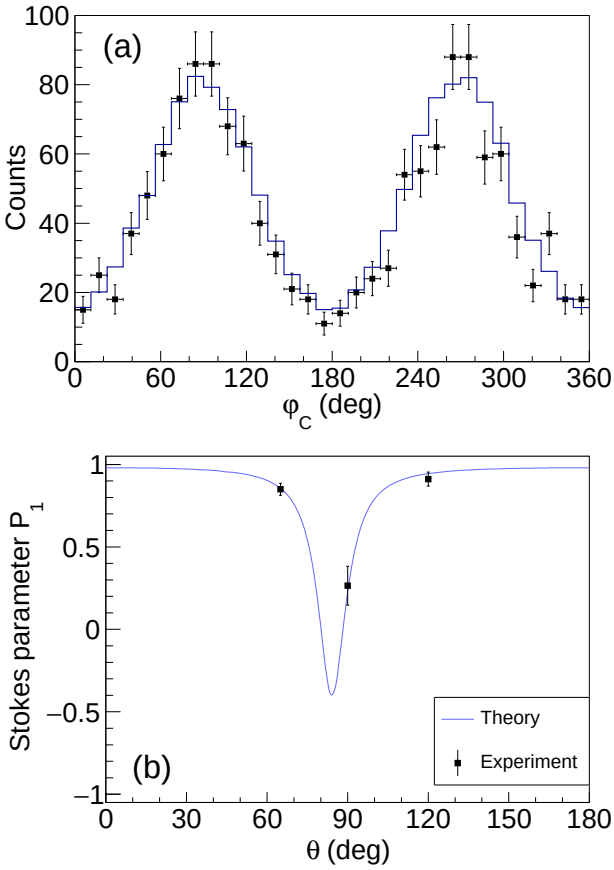

Figure 1: Preliminary results: (a) φ_C-distribution with fit from Monte Carlo generated spectra at $\theta = 65°$. (b) Stokes parameter P_1 of the elastically scattered photon beam. Theory from [8] which is based on [9, 10].

References

[1] P. P. Kane et al., Phys. Rep. 140, 75-159 (1986).

[2] D. A. Bradley et al., Radiat. Phys. Chem. 56, 125-150 (1999).

[3] S. C. Roy et al., Phys. Rev. A 34, 1178-1187 (1986).

[4] M. Cooper and W. Stirling, Radiat. Phys. Chem. 56 85–99 (1999)

[5] N. Schell et al., Mater. Sci. Forum 772, 57-61 (2014).

[6] D. Protic et al., IEEE Trans. Nucl. Sci. 53, 3181-3185 (2005).

[7] F. Lei et al. Space Sci. Rev. 82 309–388 (1997).

[8] A. Surzhykov et al., private communication (2014).

[9] A. Surzhykov et al., Phys. Rev. A 88 062515 (2013).

[10] A. Surzhykov et al., J. Phys. B 48 144015 (2015).

* Work supported by HGS-HIRe / Helmholtz Alliance (HA216/EMMI) / DESY and HZG support at beamline P07.

† k.-h.blumenhagen@gsi.de

DOI:10.15120/GR-2016-1

Status of the ARTEMIS experiment

M. Wiesel[1,2,3], *G. Birkl*[1], *M.S. Ebrahimi*[2,3], *A. Martin*[1], *W. Quint*[2,3], *and M. Vogel*[1,2]
[1]Institut für Angewandte Physik, TU Darmstadt; [2]GSI, Darmstadt; [3]Ruprecht Karls-Universität Heidelberg

We are currently revising and upgrading ARTEMIS, a Penning trap experiment designed for precision microwave spectroscopy of highly charged ions [1]. In combination with optical spectroscopy this will be used to determine the magnetic moment of the electron in the presence of the extreme fields in the vicinity of the core of a highly charged ion. Within the theory of bound-state quantum electrodynamics, magnetic moments can be calculated to high accuracies. With the foreseen measurements at relative accuracies on the ppb level and beyond, it is possible to test such calculations with high stringency. The method of choice is the so-called laser-microwave double-resonance spectroscopy, utilizing the fact that for some medium-charged ions the fine-structure, and for some heavy highly-charged ions the hyperfine-structure splitting is in the optical regime. These ions, such as $^{207}Pb^{81+}$ and $^{209}Bi^{82+}$, for example, are foreseen to be available within the framework of the HITRAP facility that ARTEMIS is being connected to. For first off-line tests, the $^{40}Ar^{13+}$ ion has been chosen. It has a spinless nucleus, so that the magnetic moment (g-factor) of the $2p$-electron can be measured. Due to the high magnetic field of 7 T also first laboratory measurements of higher-order Zeeman effects can be performed [2]. To that end, we have successfully and routinely operated an in-trap source of highly charged ions, similar to a miniature electron beam ion trap, and have created ions up to Ar^{16+}. We

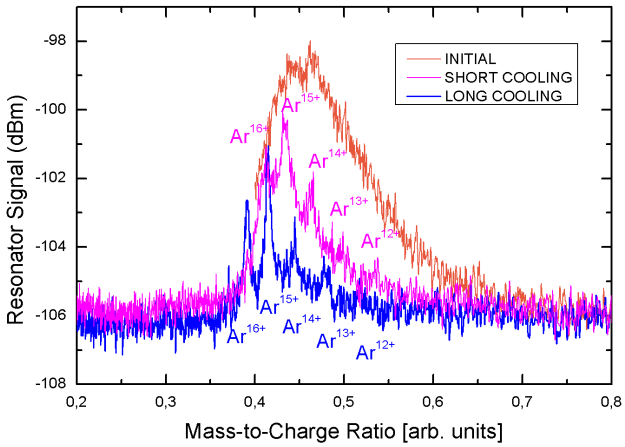

Figure 1: Detected argon ion charge state spectrum for different cooling times.

are able to store these ions over the course of days, detect them non-destructively by use of dedicated radio-frequency resonators, and to cool their motion, as depicted in figure 1. Attempts at optical spectroscopy have been made using the existing laser setup at 441 nm, but background fluorescence has been found to overcast the possible ion signal. Hence, the system has been revised and several improvements have been implemented, mainly with respect to the imaging of the fluorescence from the trap to the outside detector. We have further set up and installed the complete system for production and irradiation of microwave radiation at 65 GHz. At the same time, a new superconducting resonator for non-destructive detection has been built and characterized in detail. As an example, figure 2 shows the measured

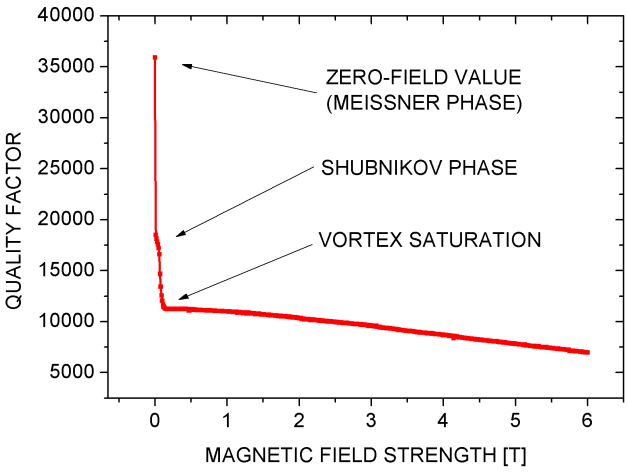

Figure 2: Superconducting resonator quality factor as a function of the magnetic field strength.

quality factor of the superconducting resonator as a function of the magnetic field strength. It becomes obvious that the values achieved in absence of an external field (when the superconductor is in the Meissner phase) are substantially modified once it enters the Shubnikov phase, in which there is resistive loss due to the interaction of magnetic field vortices with the alternating current in the resonator. The curve flattens when the vortex-vortex interaction in the superconductor leads to a saturation behaviour. The measured characteristics represent valuable information for the design of future non-destructive detection schemes. The upgraded experiment will now further be commissioned.

This work has been supported in part by DFG (Grants VO 1707/1-2 and BI 647/4-1), by GSI, HGS-HIRe, and by the IMPRS for Quantum Dynamics Heidelberg.

References

[1] W. Quint, D. Moskovkin, V.M. Shabaev and M. Vogel, Phys. Rev. A **78** (2008) 032517.

[2] D. von Lindenfels et al., Phys. Rev. A **87** 023412 (2013).

Status of the HILITE Penning trap experiment

M. Vogel[1], *N. Stallkamp*[1,4], *S. Ringleb*[3], *W. Quint*[1,2], *G. Paulus*[3], *and Th. Stöhlker*[1,3,4]
[1]GSI, Darmstadt; [2]Ruprecht Karls-Universität Heidelberg; [3]Universität Jena; [4]Helmholtz-Institut Jena

We are currently devising a dedicated Penning trap setup for the preparation of ion targets to be irradiated with high-intensity laser light, and the study of subsequent reactions. Of particular interest is the detailed investigation of multiphoton-ionisation by highly intense laser light. The central function of the setup is to provide control of the confined particles species, its density, localization and optimized overlap with the laser light. Also, the non-destructive detection of reaction products is a central property. Details on the physics case have been given in [1].

We have brought forward the functionality of the setup by building the Penning trap [2], its mounting to the cryostat, the thermal shielding and a pulsed drift tube for deceleration of externally produced ions. Measurements have shown that the required temperatures of 4 K at the trap and 45 K at the thermal shielding are indeed reached. We have performed simulations showing that ions from external sources can be decelerated in our setup from energies up to 5 keV per charge and captured in the trap with high efficiency. The components of the deceleration system have been built, together with a destructive ion detection system for testing the setup functionality, and the components for incoupling of the laser and dumping of the residual laser pulse [3]. Also, we have designed and built a non-

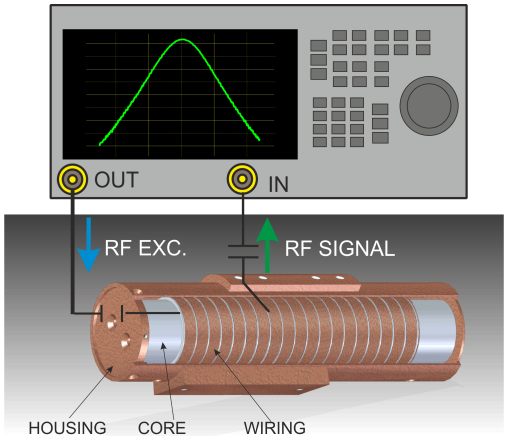

Figure 1: Schematic of the resonator.

destructive ion detection system by signal pick-up in the Penning trap with a radio-frequency resonator as seen in figure 1.

We have equipped the system with a cryostat that allows the cooling of probes in the centre of the magnetic field to a temperature of 4 Kelvin, see the schematic in figure 2. The magnet is capable of producing well-defined field strengths of up to 6 Tesla. We have installed a control system based on LabView which allows to scan the field strength at a given rate. We have used this to measure the behaviour of a superconducting resonator in strong magnetic fields. The measurements have given valuable information on the

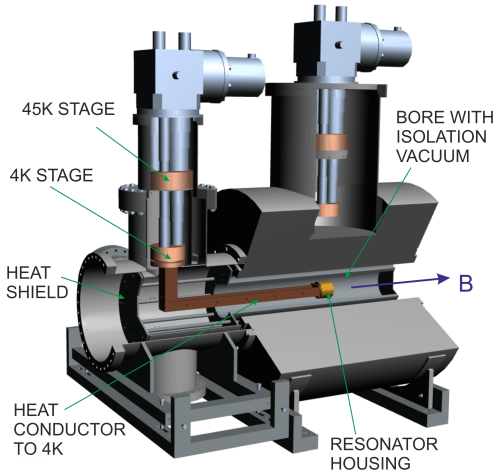

Figure 2: Resonator located in the centre of the magnet

dependence of the resonator signal on the magnetic field strength, see figure 3, which is of interest to a multitude of Penning trap experiments which feature such resonators.

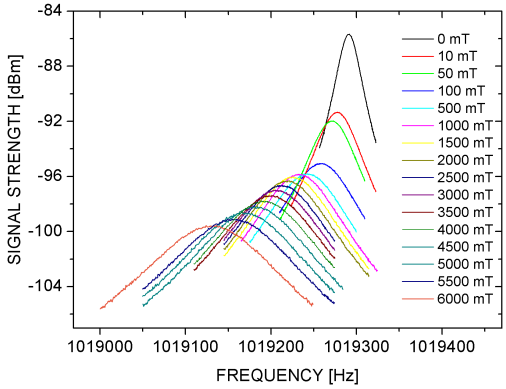

Figure 3: Resonator signal vs. magnetic field strength.

References

[1] M. Vogel, W. Quint, Th. Stöhlker and G.G. Paulus, Nucl. Inst. Meth. B **285**, 65 (2012)

[2] S. Kumar, M. Vogel, W. Quint, S. Ringleb, Th. Stöhlker, C.P. Safvan, Journal of Physics Conference Series **635** (2015) 092070

[3] S. Ringleb, M. Vogel, S. Kumar, W. Quint, G. Paulus, Th. Stöhlker, Journal of Physics Conference Series **635** (2015) 092124

DOI:10.15120/GR-2016-1

Electron spectroscopy in collisions of U^{28+} projectiles with gaseous targets*

P.-M. Hillenbrand†[1], *S. Hagmann*[1], *J. M. Monti*[2], *R. D. Rivarola*[2], *K.-H. Blumenhagen*[1,3,4], *C. Brandau*[1,5], *W. Chen*[1], *R. D. DuBois*[6], *A. Gumberidze*[1], *D. L. Guo*[7], *M. Lestinsky*[1], *Yu. A. Litvinov*[1], *A. Müller*[5], *S. Schippers*[5], *U. Spillmann*[1], *S. Trotsenko*[1,3], *G. Weber*[3], *and Th. Stöhlker*[1,3,4]

[1]GSI, Darmstadt, Germany; [2]CONICET, Rosario, Argentina; [3]Helmholtz-Institut, Jena, Germany; [4]FSU, Jena, Germany; [5]JLU, Giessen, Germany; [6]Missouri University S&T, Rolla, USA; [7]IMP, Lanzhou, China

The interest in studying the ionization of U^{28+} ions colliding with gaseous targets at near-relativistic projectile energies is twofold: Firstly, the fundamental atomic collision process with a heavy multi-electron projectile is characterized by a comparably low ionization threshold. This collision system far from charge-state equilibrium poses a challenge to theoretical descriptions beyond first-order perturbation. Secondly, U^{28+} is planned to be one of the main beams used in the accelerator chain of FAIR. Therefore, a reliable knowledge of ionization cross sections of U^{28+} is required for calculating ion-beam lifetimes, which are limited by collisions with the atoms of the residual gas.

Total projectile ionization cross sections for U^{28+} colliding with various gaseous targets have recently been reported [1]. In comparison to total cross sections, experimental data of differential cross sections provide considerably more stringent tests to *ab initio* theories. Within this study, the energy distribution of the emitted electrons has been studied both experimentally and theoretically [1]. The experiment was performed using the magnetic forward-angle electron spectrometer installed at the ESR. Measurements were performed for the collision systems U^{28+} + H_2 at 50 MeV/u (see Figure 1), U^{28+} + N_2 at 30 MeV/u, and U^{28+} + Xe at 50 MeV/u.

Experimentally, a significant asymmetry in the electron energy distribution was observed, which increases towards heavier targets. As can be seen in Figure 1, the currently available theory and the experimental data are not yet consistent. The challenge for theory is illustrated in Figure 2: The impact parameters (in atomic units) contributing most to the ionization of the projectile, are given by $\hat{b} \approx \gamma v_p/(E_p^b + E_e') \approx 1.1$ a.u., since the binding energy of the most abundant $4f^{14}$ electrons in U^{28+} is only $E_p^b = 1.1$ keV. At these impact parameters, the potential of the neutral target atom, described by the Green-Sellin-Zachor (GSZ) potential $V_{\mathrm{GSZ}}(r)$, is significantly screened as compared to a pure Coulomb potential $V_{\mathrm{Coulomb}}(r)$.

The experimental findings motivate the further development of theoretical descriptions for projectile ionization at large impact parameters and corresponding experiments. With the present experimental setup at the ESR, measurements at similar impact parameters will be accessible, e.g., for K-shell ionization of Ar^{17+} at 400 MeV/u.

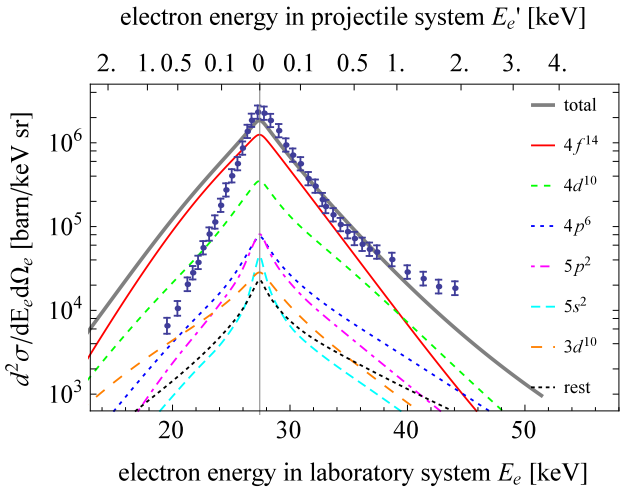

Figure 1: Experimental and theoretical results for collisions $U^{28+} + H \rightarrow U^{29+} + H^* + e^-$ at 50 MeV/u: energy distribution of electrons observed at an angle of $\vartheta_e = 0°$ with respect to the projectile beam [2].

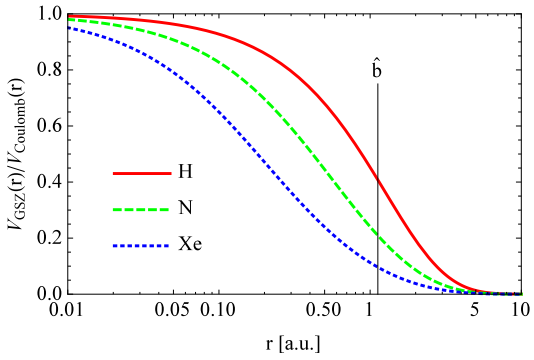

Figure 2: Screening factor of the target potential for three neutral targets and the characteristic impact parameter $\hat{b}$ for the dominating $4f^{14}$-ionization of U^{28+} at 50 MeV/u [2].

References

[1] G. Weber *et al.*, Total projectile electron loss cross sections of U^{28+} ions in collisions with gaseous targets ranging from hydrogen to krypton, Phys. Rev. ST Accel. Beams **18**, 034403 (2015).

[2] P.-M. Hillenbrand *et al.*, Strong asymmetry of the electron-loss-to-continuum cusp of multi-electron U^{28+} projectiles in near-relativistic collisions with gaseous targets, Phys. Rev. A, *submitted* (2016).

*This work was supported by HIC-for-FAIR through HGS-HIRe, the Helmholtz-CAS Joint Research Group HCJRG-108, and by BMBF (contracts 05P12R6FAN and 05P15RGFAA).

† p.m.hillenbrand@gsi.de

Triple ionization of atomic Cd involving $4p^{-1}$ and $4s^{-1}$ inner-shell holes *

R. Beerwerth[†1,2], *J. Andersson*[3], *P. Linusson*[4], *J. H. D. Eland*[3,5], *V. Zhaunerchyk*[3], *R. Feifel*[3,6], *and S. Fritzsche*[1,2]

[1]Helmholtz Institute Jena, Jena, Germany; [2]Theoretisch-Physikalisches Institut, Universität Jena, Jena, Germany; [3]Department of Physics, University of Gothenburg, Gothenburg, Sweden; [4]Department of Physics, Stockholm University, Stockholm, Sweden; [5]Department of Chemistry, Physical and Theoretical Chemistry Laboratory, Oxford University, Oxford, United Kingdom; [6]Department of Physics and Astronomy, Uppsala University, Uppsala, Sweden

The creation of inner-shell holes leads to a cascade of Auger decays if the binding energy of the hole is above the ionization threshold for at least two higher charge states. Experimentally, these processes can be investigated by Augerelectron photoelectron coincidence spectroscopy, where the emitted electrons are measured in coincidence. The total kinetic energy of the electrons associated to one event allows to obtain precise information on the spectrum of the final states. Additionally, the energy of individual electrons provides information about intermediate states and thus the decay pathways. We provided a theoretical analysis of the triple ionization of atomic cadmium, which was studied experimentally [1]. This study extends the previously performed analysis of the formation of doubly-ionized cadmium [2].

We performed numerical computations to understand the two-step Auger cascade that emerges upon the photo ionization of a $4s$ or $4p$ electron from the $4d^{10}5s^2$ ground-state configuration of atomic cadmium. To this end, we utilize the RATIP toolkit [3] to compute the photo-ionization cross sections as well as the Auger transition rates between all major intermediate states. As a result, we obtain spectral information about the emitted electrons and on the population of the final states in triply-charged cadmium.

Our computed final-state spectrum at a photon energy of $200\,\mathrm{eV}$ is shown in figure 1. The lower part of the figure shows the computed spectrum, where the energy scale is relative to the ground-state energy of atomic cadmium.

We find that Auger cascades leading to triply-ionized final states are strongly influenced by shake-up transitions, where either the initial photo ionization or one of the Auger decays is accompanied by the excitation of a valence electron. Since the $4d^85p$ configuration does not appear in any pathway emerging from singly-ionized cadmium with an inner-shell hole, it is clear that the population of this configuration happens completely due to shake-up transitions. Computationally, we treat this by including configuration mixing between $5s^2$ and $5p^2$ configurations. As a result, as can be seen in figure 1, we find that $4d^85p$ states receive a similar population by shake-up transitions as the $4d^85s$ configuration.

Another important conclusion of our calculations is that a $4s$-hole predominantly decays to the excited state configuration $4d^75s^2$, while the ground configuration does almost not get populated by this path. Furthermore, its population is energetically forbidden by any path emerging from a $4p$-hole, if no shake-up transition is involved. However, we find that if one of the valence $5s$ electrons is excited to a higher s-orbital, this path becomes energetically possible and also very likely, such that the ground-state configuration receives a significant population. To estimate the contribution of higher s-orbitals to this decay path, we performed the same calculation with additional shake-up transitions into the $7s$ orbital. In Fig. 1, it can be seen that the population of the ground configuration increases slightly, while the excited states get less populated. Higher shells are therefore expected to have almost negligible contribution, while other classes of shake-up transitions may be more important.

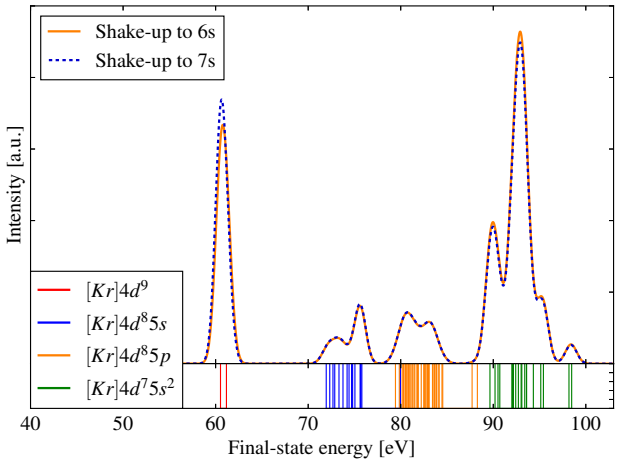

Figure 1: Calculated final-state spectrum of triply ionized cadmium. We consider two sequential Auger steps that follow the removal of an inner-shell $4s$ or $4p$ electron in atomic cadmium by a $200\,\mathrm{eV}$ photon.

Our study shows that shake-up transitions are very important for the considered cascade processes. They become more important when longer decay paths, and hence higher ionization stages, are involved. In this particular case, we found that the population of the ground state of triply-ionized cadmium is predominantly driven by shake-up transitions in either the photo ionization or the first Auger step.

References

[1] Andersson, J. et al., Phys. Rev. A 92, 023414 (2015)
[2] Linusson, P. et al., Phys. Rev. A 83, 023424 (2011)
[3] Fritzsche, S., Comp. Phys. Comm. 183, 1525–1559 (2012)

*This work has been supported by the BMBF (Grant No. 05P15SJCIA).

† Randolf.Beerwerth@uni-jena.de

DOI:10.15120/GR-2016-1

The effect of bound-state dressing in laser-assisted radiative recombination*

R. A. Müller† [1,2], *D. Seipt*[1], *S. Fritzsche*[1,2], *and A. Surzhykov*[1]
[1]Helmholtz-Institute Jena, Jena, Germany; [2]Friedrich-Schiller-University Jena, Jena, Germany

The radiative capture of a continuum electron into a bound state of an atom or ion in the presence of a laser field is commonly called *laser assisted radiative recombination* (LARR). This process can be observed for example as the last step in high harmonic generation (HHG) as well as in storage ring experiments [1, 2]. Besides the practical application in HHG there are moreover indications that LARR might support the generation of neutral antihydrogen [3].

While in most analytical treatments of LARR it is assumed that the incident electron moves solely in the laser field and recombines into a bound Coulomb state that is unaltered by the external laser, we devoted a recent work to the effects arising due to the laser dressing of the residual bound state [4]. In this work we performed calculations accounting for the influence of both, the laser and the Coulomb field on the initial continuum as well as the final bound state. We found that the angle-differential cross section can be split up into so called partial cross sections each describing LARR for a particular number of photons N exchanged between the recombining electron and the external laser field:

$$\frac{d\sigma_{1s}^{(N)}}{d\Omega_k} = \frac{4\pi^2}{c^2 p}\omega_k(N)\sum_{\lambda}\left|M^{(N)}\right|^2, \qquad (1)$$

where $M^{(N)}$ is the matrix element of the process and $\omega_k(N) = E_i - E_{1s} + N\omega_L$ the *discrete* energy of the emitted recombination photon.

In Fig. 1 we display the cross section (1) as a function of the recombination photon energy $\omega_k(N)$ (solid lines and circles) for two laser intensities I_L. In comparison we show results where we artificially excluded the bound state dressing (dashed lines and triangles). It can be seen in Fig. 1 that the spectrum is not just a single line, as it would be for the laser-free radiative recombination, but a distribution of photon energies. The width of this distribution is approximatively given by $\Delta\omega_k = 2E_L p/\omega_L^2$ [4], therefore $\Delta\omega_k$ increases the stronger the laser becomes.

As seen from Fig. 1, the dressed and undressed results behave quite differently as a function of $\omega_k(N)$. The results obtained without bound-state dressing are almost symmetric around the field-free photon energy where $N = 0$. A slight increase of $d\sigma_{1s}^{(N)}/d\Omega_k$ towards higher photon energies is caused by the prefactor $\omega_k(N)$ in Eq. (1). If, in contrast, the bound-state dressing is included in the computations, the photon distribution becomes strongly asymmetric. For higher intensities these asymmetries become more pronounced. This can be explained by the fact that the influence of the bound-state dressing increases with the number of photons involved in the process [4]. This number N, of course, is larger for a more intense external laser. Even though the dressing effects are often neglected we have shown that they can become important even for medium laser intensities ($I_L \sim 10^{13}$W/cm^2).

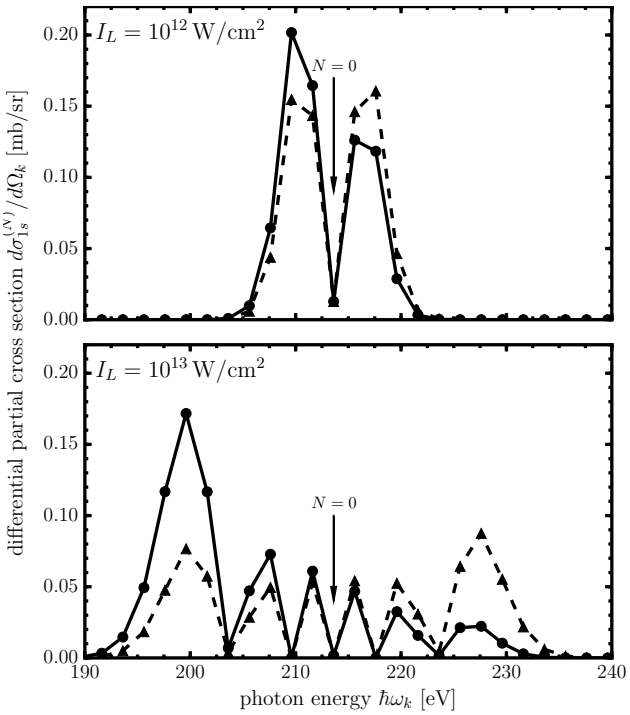

Figure 1: Angle-differential partial cross section for the laser-assisted recombination of a $E_i = 200$eV electron and a hydrogen nucleus as a function of the recombination photon energy $\omega_k(N)$. Dashed lines and triangles refer to results where the dressing of the target bound states is neglected. For details see text and Ref. [4]

References

[1] A. L'Huillier and Ph. Balcou, Phys. Rev. Lett. **70**, 774 (1993)

[2] U. Schramm, et al. Phys. Rev. Lett. **67**, 22 (1991).

[3] M. L. Rogelstad, F. B. Yousif, T. J. Morgan, and J. B. A. Mitchell, J. Phys. B **30**, 3913 (1997).

[4] R. A. Müller, D. Seipt, S. Fritzsche, and A. Surzhykov, Phys. Rev. A **92**, 053426 (2015)

* Work supported by HI Jena and Studienstiftung des Deutschen Volkes.

† robert.alex.mueller@gmail.com

The magnetic toroidal sector: a broad-band electron-positron pair spectrometer

S. Hagmann[1], P.M. Hillenbrand[1, 3], Y. A Litvinov[1], U. Spillmann[1], K. Stiebing[2], Th. Stöhlker[1, 4, 5]
[1] GSI Helmholtzzentrum Darmstadt, [2] Inst. für Kernphysik, Universität Frankfurt, [3] Universität Giessen, [4]Helmholtz Institut Jena, [5]Fakultät für Physik, Universität Jena

Electron–positron pair production has evolved into a central topic of QED in extreme fields as the coupling between the lepton field and the electromagnetic field is close to one[1, 2]. Most recently the surprisingly high cross sections observed for pair production in relativistic heavy-ion atom collisions have aroused new interest in this process even in the accelerator design community as capture from pair production has been identified as a critical, potentially luminosity limiting process in relativistic heavy ion colliders. The enormous cross sections observed can be traced[1] to the large transverse electric fields $E_{transv}\sim\gamma$. Theory predicts a scaling of the total cross section for free-free pair production [1,3] $\sigma_{free\text{-}free}\sim(Z_{proj})^2(Z_{tar})^2 \ln^3\gamma$ and a very complex relation between the angular emission patterns of electron and positron[4]. The future relativistic storage ring HESR at FAIR with a collision energy range up to $\gamma\sim6$ will be best suited to study for ion-induced pair-production all channels which may be distinguished experimentally[3].

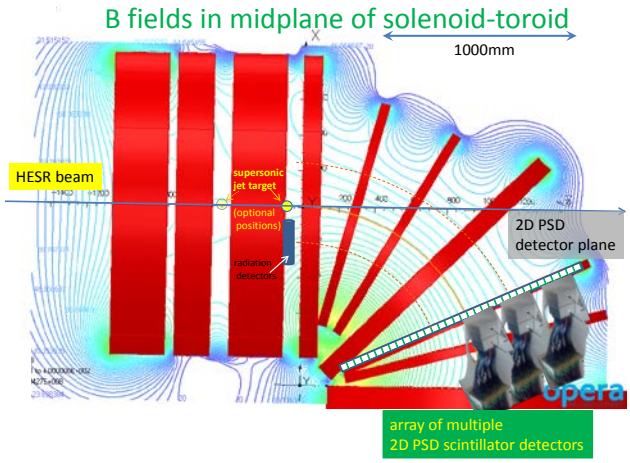

Figure 1: Cut through the midplane of the coil assembly of a toroidal magnetic lepton spectrometer for lepton energies up to 20 MeV.

A corresponding future experimental investigation of the dynamics of the heavy-ion induced free-free pair creation up to $\gamma\sim6$

$$X^{Z+} + A \longrightarrow X^{Z+} + \{A^*\} + e^+ + e^- \qquad (1)$$

is the motivation for the current spectrometer design study: a coincident detection of both outgoing leptons and their vector momenta as constitutive in a complete description of free-free pair production is not practically possible with instruments covering only a small solid angle for each lepton.

We have therefore employed OPERA-3D[5] to study the electro-optical properties of a magnetic toroidal spectrometer with very large effective solid angle enabling coincident detection of the vector momenta of electrons and positrons from a free-free pair (see fig. 1).

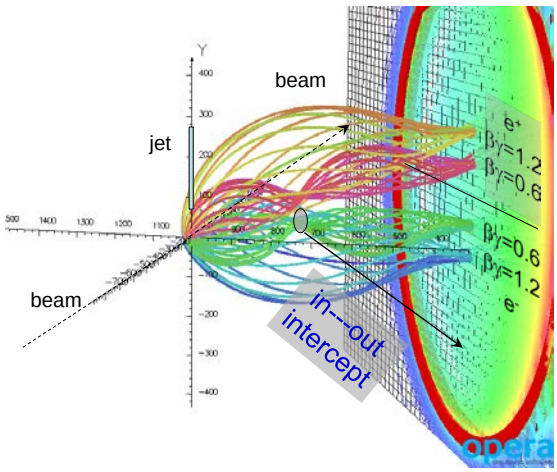

Figure 2: Electrons and positrons launched at the jet target with polar angles $\Theta_L\leq20^0$ and azimuthal angels $0^0\leq\varphi\leq360^0$. In the given configuration with B=107 G and the detector plane located at 66^0 all lepton trajectories with $\beta\gamma=1.2/n$, n=1, 2, are intersecting at well distinguishable locations X_n in the detector plane. The lepton kinetic energies corresponding to the trajectories given here are 85 keV ($\beta\gamma=1.2/2$) and 287 keV ($\beta\gamma=1.2/1$), respectively.

In a toroidal B-field e^- and e^+ are momentum-dispersed perpendicular to the bend plane of the toroid. For a given B-field one can find lepton momenta $\beta_0\gamma_0/n$, $n\geq1$, for which all trajectories independent of their forward laboratory emission angle will intersect in a point X_n on the detector plane (fig. 2). For all other lepton momenta $\beta\gamma$ the parallel and perpendicular momenta can be determined by 2D-PSD detectors; the complete emitter frame emission pattern of a lepton pair may thus be determined by coincident detection of leptons in the detector plane for a choice of a few appropriate B-field settings.

References

[1] Ionescu, D. Habilitationsschrift, FU-Berlin (1997).
[2] A. Voitkiv, J. Ullrich, Relativistic Collisions, Springer Series AOPP, Vol. 49 (2008)
[3] D. Ionescu et al. Phys. Rev. A54 4960 (1996)
[4] R. Tenzer et al. Eur. Phys. J. D 11 347-353 (2000)
[5] OPERA-3D User Guide, Vector Fields Limited, 24 Bankside, Kidington, Oxford OX5 1JE, UK

DOI:10.15120/GR-2016-1

Geometrical characterization of a position-sensitive germanium detector *

T. Gassner[1,2,3], *H.F. Beyer*[3], *and U. Spillmann*[3]
[1]Helmholtz Institute Jena, Germany; [2]IOQ Jena, Germany; [3]GSI, Darmstadt, Germany

The FOCAL experiment is an ambitious x-ray crystal spectrometer project aiming for an accurate determination of the 1s Lamb shift in highly charged heavy ions, like hydrogen-like (H-like) gold Au^{79+} [1, 2]. The ions are provided by the accelerator chain of the GSI Helmholtz Centre and stored in the experimental storage ring ESR. In the ESR the ion beam can be overlapped with a supersonic gas-jet target, acting as a quasi-free electron source for the ions which may capture target electrons into an excited state during a collisional process. During the deexcitation of the ions numerous x rays are emitted and may be detected by the position sensitive semiconductor detectors of the FOCAL spectrometer. Since the measurement principle of a crystal spectrometer is of geometrical nature, all relevant dimensions having an influence on the final result have to be accurately specified. One of the last remaining unknowns of the assembly is the actual position of the semiconductor crystal inside the housing of the position sensitive x-ray detector [3]. For its determination a dedicated measurement campaign has been conducted at the European Synchrotron Radiation Facility ESRF in Grenoble, France, where an intense and narrow x-ray beam can be provided. The measurement made use of the fact that the anode of the semiconductor crystal is segmented into 48 vertical strips, where each strip acts as an independent x-ray detector. In the experimental hutch the detector was mounted on a horizontally movable platform facing directly the x-ray beam coming from the synchrotron. In fine steps the detector was moved horizontally while at the same time the count rate of an arbitrarily chosen vertical strip was recorded. The count rate was zero if the x-ray beam missed the selected strip (see red data points in figure 1). As soon as the beam started to intersect with the strip, the count rate increased until the whole footprint of the beam was inside the strip dimensions. The count rate did not change while the beam was moved completely inside the strip leading to a plateau like region. After reaching the opposing boundary of the strip the count rate started to fall again until the beam completely left the strip. To determine the centre of the peaking distribution a model function was fitted onto the data points. Since both, the response function of a strip as well as the x-ray beam profile, are well described by a rectangular function, the convolution of two rectangular functions, which is a trapezoidal function, was used as the fitting model (blue curve in figure 1). To relate the local coordinate system of the x-ray beam position with the outer fiducial mark, also used during the original assembly procedure, a sheet of photosensitive paper, which darkens when being irradiated, had been attached to the detector front. After being irradiated for a while an optical telescope with cross hairs was aligned to the dark spot and the distance to the fiducial mark was measured be moving the detector with the aid of the platform and noting the covered distance. This optical alignment procedure was afflicted with an uncertainty of approximately 0.3 mm, which is the only limiting factor for this kind of position determination. With this measurement the last remaining geometrical unknown of the FOCAL assembly could be determined, resulting in a completely defined system for precision x-ray spectroscopic investigations.

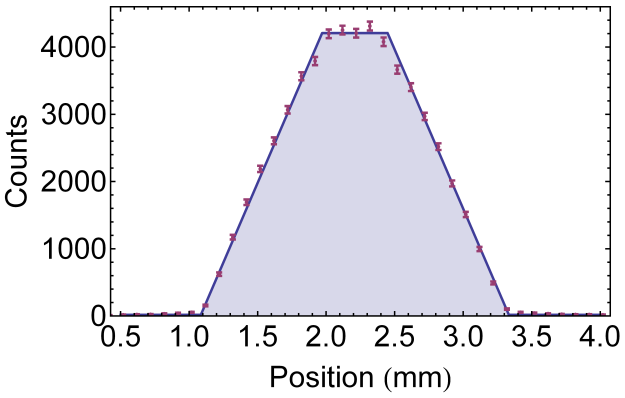

Figure 1: *Red points:* Number of triggered x-ray events in an arbitrary strip of the segmented x-ray detector as a function of position. *Blue curve:* Best fit of a trapezoidal function onto the data points, used to extract the barycentre.

References

[1] H.F. Beyer *et al.*, *Crystal optics for precision x-ray spectroscopy on highly charged ions - conception and proof*, Journal of Physics B: Atomic, Molecular and Optical Physics **48**, p. 144010 (2015)

[2] H.F. Beyer *et al.*, *Crystal optics for hard-X-ray spectroscopy of highly charged ions*, Spectrochimica Acta Part B: Atomic Spectroscopy **64**, p. 736 – 743 (2009)

[3] D. Protić *et al.*, *Two-dimensional microstrip Germanium detector for the spectroscopy of hard X-ray transitions*, IEEE Trans. Nucl. Sci. **52**, p. 319 (2005)

*This report is also part of the GSI Scientific Report 2015 DOI:10.15120/GR-2016-1

Linear polarization of fluorescence photons emitted from two-step radiative cascade via overlapping resonances of highly charged ions

Z. W. Wu[1,2], *A. Surzhykov*[1], *N. M. Kabachnik*[3,4], *C. Z. Dong*[2], *and S. Fritzsche*[1,5]

[1]Helmholtz Institute Jena, Germany; [2]Northwest Normal University, Lanzhou, China; [3]European XFEL, Hamburg, Germany; [4]Moscow State University, Moscow, Russia; [5]University of Jena, Germany

In the past several decades, angular distribution and polarization of characteristic fluorescence photons emitted from highly charged ions (HCI) have been studied extensively both in theory and in experiment. Compared to total decay rates, these angle- and polarization-resolved properties have been found much more sensitive to various atomic effects, such as, the Breit interaction, the hyperfine interaction, or the multipole mixing of radiation fields. However, up to the present, almost all the angular distribution and polarization studies were made for the fluorescence photons emitted from well-isolated (fine-structure) energy levels of atoms or ions, while little attention was paid to their counterparts from (partially) overlapping resonances. In contrast to the case of well-isolated atomic levels, an overlap of two (or more) atomic resonances may lead to a depolarization of themselves due to the spin-spin and spin-orbit interactions. The effect of such a depolarization was studied very recently for the angular distribution and angular correlation of the fluorescence photons emitted in a two-step radiative cascade $1s2p^2\ J_i = 3/2 \rightarrow 1s2s2p\ J = 1/2, 3/2 + \gamma_1 \rightarrow 1s^22s\ J_f = 1/2 + \gamma_1 + \gamma_2$ of lithium-like W^{71+} ions [1]. For this particular case, due to the depolarization, a quite strong dependence of angular anisotropy of the emitted fluorescence photons upon the splitting of the intermediate $1s2s2p\ J = 1/2, 3/2$ overlapping resonances were found.

In this contribution, we follow our previous work [1] and further study linear polarization of the fluorescence photons emitted in the same radiative cascade [2]. Special attention was paid how the splitting of the intermediate resonances affects the linear polarization and whether modifications of the linear polarization can be utilized for extracting such splittings, if analyzed along the isoelectronic sequence of lithium-like ions. For this purpose, we employed the density matrix theory to derive general expression for the linear polarization of the emitted fluorescence photons. While the derived formalism can be applied to any atomic or ionic system, we here consider again the two-step radiative cascade of lithium-like W^{71+} ions.

In Fig. 1, we display linear polarization of the second-step γ_2 photons as functions of the level splitting of the intermediate $1s2s2p\ J = 1/2, 3/2$ overlapping resonances. Results are shown for photons that are emitted perpendicular to the quantization axis (as defined in the prior excitation process) and for assumed alignment parameters $\mathcal{A}_2 = -1.0$, -0.5, 0.5, and 1.0 of the initial $1s2p^2\ J_i = 3/2$ level. Similar to the case of angular distribution, a quite strong effect of the level splitting upon the linear polarization of the photons is obtained at small splittings $\Delta\omega \lesssim 0.2$ a.u. ≈ 5.4 eV. Moreover, for given small level splittings, the linear polarization also depends sensitively upon the initial alignment of the $1s2p^2\ J_i = 3/2$ level [2]. This finding strengthens our recent suggestion that angle-resolved measurements of characteristic fluorescence photons may help identify small level splittings.

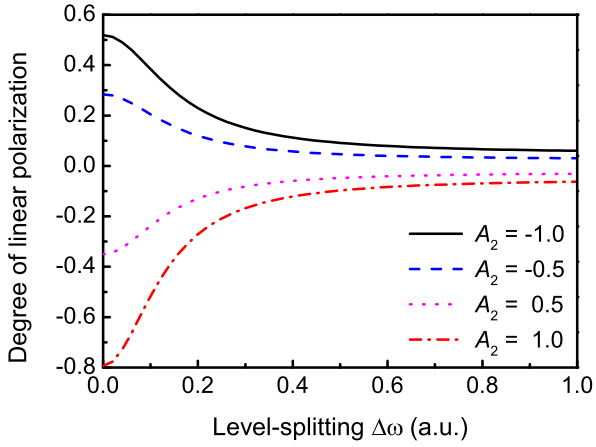

Figure 1: Degree of linear polarization of the second-step γ_2 photons as functions of the level splitting $\triangle\omega$ of the intermediate overlapping resonances. Results are shown for photons that are emitted perpendicular to the quantization axis and for assumed alignment parameters $\mathcal{A}_2$ of the initial $1s2p^2\ J_i = 3/2$ level: $\mathcal{A}_2 = -1.0$ (black solid line), -0.5 (blue dashed line), 0.5 (magenta dotted line), and 1.0 (red dash-dotted line).

Owing to this sensitivity of the linear polarization with regard to the level splitting of the intermediate overlapping resonances, we conclude that accurate measurements of photon polarization may alternatively serve as a tool as well for determining small level splittings in HCI. Such measurements are experimentally accessible by using present-day solid-state or crystal-based photon detectors and could be carried out at heavy-ion storage rings or electron beam ion trap facilities.

References

[1] Z. W. Wu, *et al.*, *Phys. Rev. A* **90**, 052515 (2014).

[2] Z. W. Wu, *et al.*, *J. Phys. Conf. Ser.* **635**, 012020 (2015).

DOI:10.15120/GR-2016-1

Proposal for a new electrode design of the HITRAP cooling trap

Z. Andelkovic[1], *F. Herfurth*[1], *N. Kotovskiy*[1], *B. Maaß*[2], *J. Steinmann*[3], *and G. Vorobyev*[1]

[1]GSI Darmstadt; [2]Technische Universität Darmstadt; [3]Hochschule Darmstadt

After the beamtime of 2014 and the successful commissioning of the last linear deceleration stage, the HITRAP radio-frequency quadrupole (RFQ), only one step is missing for the planned preparation of bunches of cold, heavy, highly charged ions (HCI) - the HITRAP cooling trap. In the previous years the cooling trap was commissioned offline, using locally produced highly charged O^{8+}, Ar^{12+} ions and electrons [1].

The major challenge for the dynamic capture, storage and cooling of ions from the RFQ is the necessary combination of high voltage, cryogenic temperature, high magnetic field and ultra-high vacuum. It turned out that the complexity of the system was preventing a reliable operation of the trap at voltages higher than a few kV. This was sufficient for ions from the EBIT, but for capturing online ion bunches from the GSI accelerator stable operation of the trap up to 20 kV is needed. To that end, a new design, was proposed that would simplify the trap at the expense of its flexibility. An overview can be seen in Fig. 1.

The classical approach to constructing a precision Penning trap is to use a ring electrode which defines the potential, two endcaps to confine the particles axially and two compensation electrodes to harmonize the potential to a high degree. Several such sets of electrodes can be used for creating the so-called nested traps. Finally, two additional capture electrodes facilitate external ion injection. Although well proven in experiments, this design is not necessarily the goal of the cooling trap which needs to store and cool ions without performing high precision measurements at the same time.

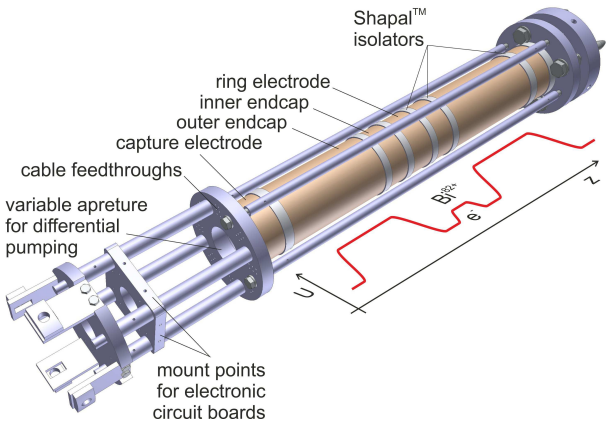

Figure 1: Overview of the suggested simplified design of the cooling trap. The drawing shows the stack of seven electrodes, the stabilization cylinders and the mount points for the electronic components.

In order to simplify the design but keep the functionality, one can use a mechanically compensated Penning trap [2] with only two additional endcaps for trapping ions and electrons at the same time. That way the stack of electrodes reduces to only seven pieces, dragging also the number of necessary electrical connections from the outside from 52 to around 15. Due to the availability of new materials in the recent years, such as Shapal™, which offer low electrical and high thermal conductivity at the same time, one can construct more complex electrode mounts without compromises in stability. A comparison of the technical properties of the two trap designs is given in Table 1.

Table 1: Comparison of some important aspects of the existing and the suggested new design of the HITRAP cooling trap.

	old	new
no. electrodes	21	7
no. cables	52	15
size	$d = 14.8$ mm	$d = 15.8$ mm
max. E field	5 kV/mm	1 kV/mm
mounting from	both sides	one side
configurations	multiple	single
$C_2/C_4/C_6$	$0.26/10^{-4}/0.055$	$0.55/10^{-3}/0.048$

Detailed simulations of the trapping and the cooling process [3] show that optimized arrangement of the electrodes could improve the trap performance and accelerate the resistive cooling by almost an order of magnitude. Although a large cylindrical trap expansion coefficient C_4 from Table 1 is generally not desirable, in this case it facilitates the distribution of energy among all degrees of freedom, including the energy exchange between ions and electrons, as planned for the electron cooling technique. This is of special interest for a rapid cooling of HCI, since the electron capture cross-section, i.e. the lifetime of ions in the trap, is highly dependant on the ion temperature.

References

[1] Z. Andelkovic, et al.: *Deceleration of ions in the HITRAP facility*, GSI Scientific Reports 2014

[2] G. Gabrielse and F.C. Mackintosh, Int. J. Mass Spectrom. Ion Proc. **57**, 1 (1984)

[3] J. Steinmann, PhD Thesis, University Erlangen-Nürnberg, to be submitted, 2016

DOI:10.15120/GR-2016-1

BREIT: A new computer code for calculating charge-state fraction evolutions in media

N. Winckler[1], *M. Al-Turany*[1], *T. Kollegger*[1], *A. Rybalchenko*[1], *V.P. Shevelko*[2], *and Th. Stöhlker*[1]
[1]GSI, Darmstadt, Germany; [2]P.N. Lebedev Physical Institute, Moscow, Russia

Introduction The evolution of the charge state distribution of an ion beam passing in gaseous or solid target is a relevant quantity in many research fields, such as accelerator, plasma, atomic, and nuclear physics. The evolution of the charge state fractions $F_i(x)$ in the i^{th} charge state can be obtained by solving the rate balance equations [1] :

$$\frac{d}{dx}F_i = \sum_j \sigma_{ji}F_j - \sum_j \sigma_{ij}F_i, \qquad (1)$$

where σ_{ij} is the electron-loss or electron-capture cross-section from state i to state j, and x is the penetration depth. There exists several computer codes allowing the computation of the non-equilibrium charge-state fractions. However, these codes compute both, the cross-sections and the rate equations, and force the user to be bound to a particular physics model in the computation of the cross-sections. Moreover, these codes usually use a Runge-Kutta approach to solve the system of differential equations which requires additional setting to handle the convergence of the solutions, and sometimes, several iterations. In this contribution, we present a short description of a newly created computer code BREIT (Balance Rate Equations for Ion Transportation) which uses a set of charge-changing cross sections as input data, solves the rate equations analytically by the matrix-diagonalization method.

Solving analytically the differential equation sytem Considering the eq. 1 for a finite dimention N and the normalization condition $\sum_{q_i=q_1}^{q_N} F_q = 1$, we can show that equation 1 can be written as follow:

$$\frac{d}{dt}F_k = \sum_{i=1}^{N-1} a_{k,i}\ F_i + g_k \qquad (2)$$

where $q_1 \leq k \leq q_{N-1}$, $a_{k,i}$ is a linear combination of the cross-sections $\sigma_{i,j}$, and $g_k = \sigma^{EC}_{N,k}$ is the contribution from the last state q_N to the state k. We can easily recognize that eq. 2 is a typical differential equation system with a second constant member, which has solution of the form $F(x) = F^h(x) + Z(x)$, where $Z(x)$ is the particular solution of eq. 2 and $F^h(x)$ is the solution of the homogeneous equation, $\frac{d}{dx}F = AF$, with A the matrix system of dimension $N-1$, and F the charge state vector. As a particular solution, we use the equilibrium fractions, i.e. the solution of $AF + g = 0$. The solution to this equation is trivial : $Z = -A^{-1}g$. The homogeneous equations can be solved using the eigenvalue decomposition method. If A can be diagonalized then $A = PDP^{-1}$ where D is diagonal (with eigenvalues λ_i) and P is the eigenvector matrix. With the change of variable: $Y = P^{-1}F$ the homogeneous equation becomes: $\frac{d}{dx}Y = DY$. If the eigenvalues $\lambda_i \in \mathbb{R}$ then the solution is trivial, and consists of a vector with elements $C_i \exp(\lambda_i)$. If some eigenvalues $\lambda_i \in \mathbb{C}$ then the algorithm sorts the eigenvalues and eigenvectors by pair of complex conjugates and forms a new eigenvector basis, linear combinations of cosine and exponential functions, whose arguments are the imaginary and real eigenvalue parts, respectively. The unknown coefficients C_i are determined by the required initial condition $Y(x=0) = C_i = P^{-1}F^h_0$. The homogeneous solution is then obtained by $F^h(x) = PY(x)$. The solution of the system is the sum of the homogeneous and particular solution. Once all matrix and vector components are calculated, a formula factory forms the solutions analytically and stores them in a string container.

Software The BREIT code takes as input the cross-section coefficients as well as the initial conditions as described in the BREIT documentation available at the GitHub repository [2] . The output is created on demand as text file containing the analytical solution, or as ROOT or pdf files containing the figures of the distributions. In addition to the offline installation, an online BREIT application is available[3].

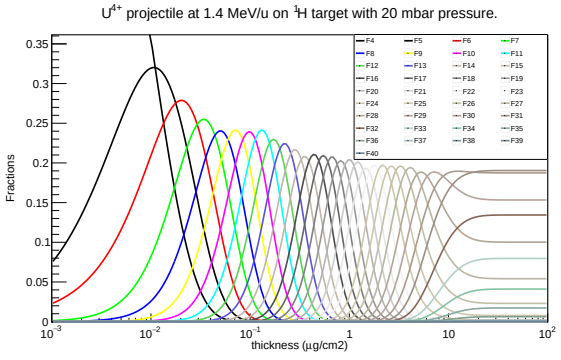

Figure 1: Output figure example of the non-equilibrium $F_i(x)$ using 37 charge states of uranium ions (q = 4–40) and 104 input loss and capture cross sections.

References

[1] H.-D. Betz, Rev. Mod. Phys. 44, 465 (1972).
[2] https://github.com/FAIR-BREIT
[3] http://breit.gsi.de

DOI:10.15120/GR-2016-1

Detection system for forward emitted XUV photons from relativistic ion beams at ESR*

C. Egelkamp[1], *V. Hannen*[1], *H.-W. Ortjohann*[1], *J. Vollbrecht*[1], *Ch. Weinheimer*[1], *D. Winzen*[1], *B. Lommel*[2], *D. Winters*[2], *A. Hoffmann*[3], *and Ch. Spielmann*[3]

[1]WWU Münster, Institut für Kernphysik, Wilhelm-Klemm-Str. 9, 48161 Münster; [2]GSI Helmholtzzentrum für Schwerionenforschung GmbH, Planckstr. 1, 64291 Darmstadt; [3]Friedrich-Schiller-Universität Jena, Institut für Optik und Quantenelektronik, Max-Wien-Platz, 07743 Jena

The Institut für Kernphysik in Münster developed a detection system for XUV photons in the wavelength region of about 10 nm. The system is designed to collect forward emitted fluorescence photons created in laser-spectroscopy experiments with highly-charged ions at the experimental storage ring (ESR). It will be used for a measurement of the $^3P_0 - {}^3P_1$ splitting in beryllium-like krypton ($^{84}Kr^{32+}$) in an anti-collinear laser spectroscopy experiment [1]. After excitation to the $^3P_1$ state by a dye laser, the ions deexcite under the emission of XUV photons at a wavelength of about 17 nm which are blueshifted to wavelengths down to 7 nm. The detector consists of a movable cathode plate that can be driven into the beam line via a pressured air motor. Therefore the plate has a central slit to not disturb the ions while moving the plate into the beam. Photons that hit the cathode will produce mostly secondary electrons that will be guided electromagnetically onto a microchannel plate (MCP) detector. A similar detection system for optical photons making use of a movable parabolic copper mirror and a photomultiplier outside the vacuum, has already successfully been applied in the LIBELLE experiment [2].

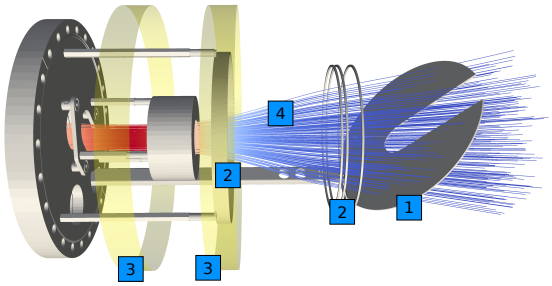

Figure 1: Electromagnetic setup with cathode plate (1), ring electrodes (2), coils (3) and indications for the magnetic field lines (4)

Figure 1 shows a schematic view of the whole setup with all the electromagnetic components as it was implemented for simulations in SIMION 8.1 [3]. The photocathode is coated with a 300 nm thick layer of caesium iodide (CsI), vacuum evaporated onto the cathode surface in the target laboratory at GSI to enhance the secondary electron yield at the wavelengths of interest (compare figure 2). First measurements with a XUV laser source at the Institut für Optik und Quantenelektronik in Jena and with a gamma source in the keV region in Münster indicate a significantly higher electron yield for the CsI coated cathode in comparison to the uncoated stainless steel surface. However, at this point no quantitative statement can be made. Figure 2 shows the cathode plate with the rainbow-colored CsI coating.

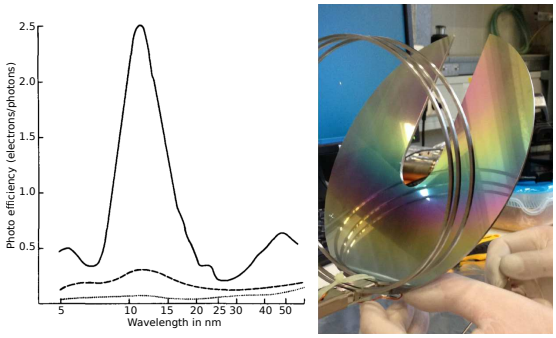

Figure 2: Left: electron yield with 300 nm CsI coating according to [4]; right: coated cathode plate

The solenoid coil system (mounted outside the vacuum) and thereby the magnetic field plays a crucial role in the electron guiding. The simulations resulted in an optimum configuration of a two coil system with opposing currents to have the field lines tightly concentrated at the MCP while still covering the complete cathode plate. The field shown in figure 1 is created by such a coil design.

In the beginning of 2016 the detector has been mounted at the ESR after successful vacuum tests and is currently being prepared for a test beamtime in summer 2016 with carbon ions ($^{12}C^{3+}$). The experiment with beryllium-like krypton can hopefully take place in 2018.

References

[1] D.F.A. Winters *et al.*, *Laser spectroscopy of the* $(1s^2 2s2p)$ $^3P_0 - {}^3P_1$ *level splitting in Be-like krypton*, GSI Experiment E104

[2] V. Hannen *et al.*, Jinst 8 (2013) P09018

[3] SIMION package, Scientific Instrument Services, Inc., http://simion.com

[4] J.A.R. Samson, *Photocathodes: Their efficiency and stability*, Nuclear Instruments and Methods in Physics Research 222, 1984

* Work supported by BMBF under contract number 05P15PMFAA

Precision high voltage divider for the electron cooler at CRYRING *

D. Winzen[†1], *I. Denesjuk*[1], *V. Hannen*[1], *W. Nörtershäuser*[2], *H.-W. Ortjohann*[1], *O. Rest*[1], *and Ch. Weinheimer*[1]

[1]WWU Münster, Institut für Kernphysik, Wilhelm-Klemm-Str. 9, 48161 Münster;
[2]Technische Universität Darmstadt, Institut für Kernphysik, Schlossgartenstraße 9, 64289 Darmstadt

The low energy storage ring CRYRING is currently being set up as the first storage ring of the upcoming accelerator facility FAIR at GSI. CRYRING features an electron cooler in order to cool stored ions and thus achieve a low momentum spread of the beam. To determine the velocity of the ions a precise knowledge of the acceleration voltage of the electron cooler is essential. In earlier measurements of hyperfine transitions in hydrogen- and lithiumlike ions at Experimental Storage Ring (ESR), the limiting uncertainty was the voltage measurement of the electron cooler [1]. That uncertainty could be removed by an in-situ precision measurement of the cooler voltage using a precision high voltage divider provided by PTB on a temporary basis.

Since commercially available high-voltage dividers do not offer the desired precision and stability for use at CRYRING, we construct a high-precision divider for voltages up to 35 kV which will be similar to the ultrahigh-precision voltage dividers which have been constructed in Münster in cooperation with PTB for use at the KATRIN experiment [2, 3] (figure 1). The precision of the divider will be in the low ppm range and will, if other sources of systematic uncertainties like e.g. space charge effects are under control, allow for measurement uncertainties in the $< 10^{-5}$ region.

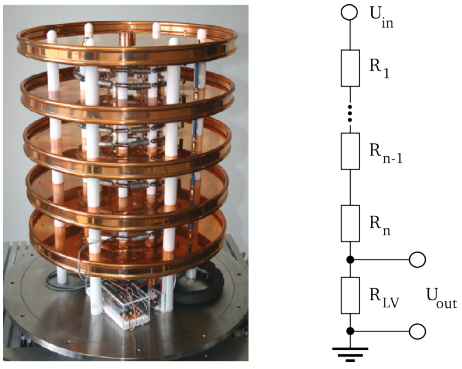

Figure 1: Left: KATRIN high voltage divider K35. Right: High voltage divider principle.

The simplest version of a voltage divider consists of two resistors connected in series. For high-voltage dividers the high voltage resistance R_{HV} usually consists of many resistors R_i connected in series to allow for the requested maximum voltage. The output voltage U_{out} is measured using a high-precision digital voltmeter over the low voltage resistor R_{LV}. Voltage dividers are characterized by their scale factor:

$$M = \frac{U_{in}}{U_{out}} = \frac{\sum_i R_i + R_{LV}}{R_{LV}} \quad (1)$$

This scale factor describes the factor between input and output voltage and has to be matched to the high-voltage range of interest and the most sensitive range of the applied digital voltmeter (< 20 V for commercially available precision 8.5 digit voltmeters). For measurement ranges from 1 kV up to 35 kV the high voltage divider will therefore provide different scale factors by implementing different low voltage outputs.

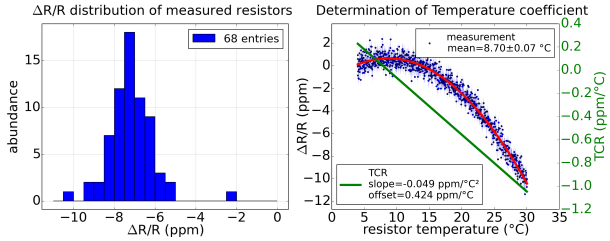

Figure 2: Left: Distribution of warm up deviations of precision HV resistors at 600 V load and 25 °C ambient temperature. Right: TCR measurement of sample resistor.

To achieve the desired accuracy and stability, the thermal behaviour of the HV resistors to be used has to be considered. The available Vishay VHA518-11 resistors [4] have been characterized by applying the maximum nominal load (600 V) at an ambient temperature of 25 °C and measuring the relative change in resistance $\frac{\delta R}{\delta T}/R$ until thermal equilibrium is reached (figure 2, left). As a result of the resistors showing similar thermal characteristics, it is possible to minimize the change in resistance by stabilizing the ambient temperature to the temperature with minimal temperature coefficient (TCR) of the resistors (figure 2, right). The thermal and mechanical design of the divider is currently being finalized and construction will start in summer 2016.

References

[1] M. Lochmann *et al.*, Phys. Rev. A 90, (2014) 030501(R)
[2] T. Thümmler *et al.*, New J. Phys. 11 (2009) 103007
[3] S. Bauer *et al.*, JINST 8 (2013) P10026
[4] Vishay, http://www.vishaypg.com/docs/63006/hmetlab.pdf

* Supported by BMBF under contract number 05P15PMFAA
† d.winzen@uni-muenster.de

DOI:10.15120/GR-2016-1

Flexible picosecond master oscillator fiber amplifier system for ion beam laser cooling at ESR/SIS100*

D. Kiefer[1], *T. Beck*[1], *and T. Walther*[1]
[1]Institute of Applied Physics, TU-Darmstadt, Darmstadt, Germany

We are developing a flexible picosecond master-oscillator fiber amplifier system for laser cooling relativistic ion beams at the ESR/SIS100. In this contribution, we present first data regarding its spectral properties.

Laser cooling of relativistic ion beams was successfully demonstrated at the ESR during beam times in 2004, 2006 and 2012 [1]. With this technique a relative longitudinal momentum spread of less then $\Delta p/p = 10^{-6}$ was achieved [2]. It was shown that intra beam scattering is a potential source of heating [3]. Simultaneous cooling with cw and pulsed lasers is a possible solution to overcome this limitation. The required spectral bandwidth of the pulsed coherent laser radiation is determined by the relative momentum distribution of the ion beam. For the best performance flexible bandwidths are preferable. Our laser system will provide pulses with adjustable pulse lengths between approx. 70 and 740 ps and thus, due to the pulses being Fourier transform limited, bandwidths between ca. 1.3 and 16.7 GHz.

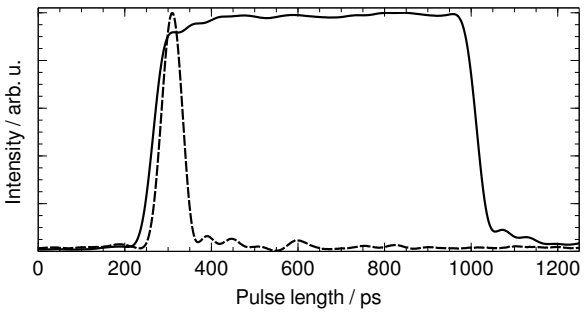

Figure 1: Pulse shape in the time domain. Intensities are normalized. Dashed line: shortest possible pulse with a length of ca. 70 ps. Solid line: longest possible pulse with a length of approx. 740 ps.

The basic laser system was introduced in [4]. Pulses of variable duration are cut out of narrow linewidth cw-laser radiation (1028 nm, 0.5-1.5 MHz rep. rate) using a fiber based electro optical modulator (c.f. figure 1) and then amplified. The corresponding FFT calculated spectra are shown in figure 2. Measured spectra obtained by a Fabry-Perot-spectrometer (c.f. figure 3) demonstrate that our pulses are indeed Fourier transform limited. Thus, we have demonstrated production of Fourier transform limited pulses with a duration between 70 and 740 ps.

* Work supported by BMBF Grant No. 05P12RDRB2

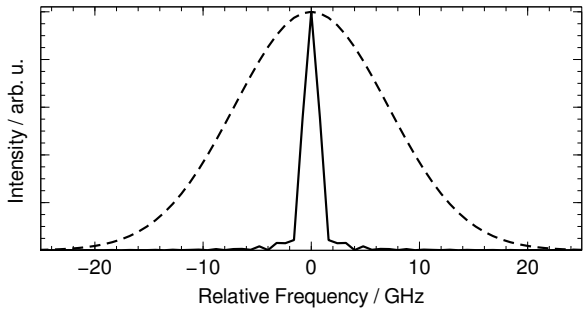

Figure 2: Fourier-transformed spectra in the frequency domain calculated from the pulse shape. Intensities are normalized. Dashed line: shortest possible pulse with a bandwidth of ca. 16.7 GHz. Solid line: longest possible pulse with a bandwidth of approx. 1.7 GHz.

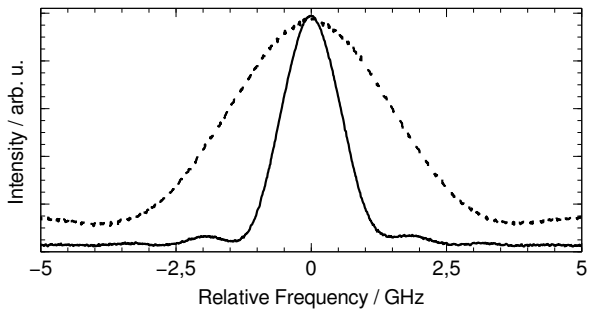

Figure 3: Spectra in the frequency domain taken with a Fabry-Perot spectrometer. Intensities are normalized. Dashed line: pulse with a length of ca. 240 ps and a bandwidth of ca. 3.5 GHz. Solid line: longest possible pulse with a length of ca. 740 ps and a bandwidth of approx. 1.3 GHz.

References

[1] D. Winters et al, "Laser cooling of stored relativistic C^{3+} ions at the ESR", GSI Scientific Report 2013

[2] T. Beck, B. Rein and Th. Walther, "An all solid-state based laser system for laser cooling of relativistic ion beams", GSI Scientific Report 2013

[3] S. N. Atutov, R. Calabrese, R. Grimm, V. Guidi, I. Lauer, P. Lenisa, V. Luger, E. Mariotti, L. Moi, A. Peters, U. Schramm and M. Stößel. "White-light Laser Cooling of a Fast Stored Ion Beam", Phys. Rev. Lett. **80** (1998) 2129

[4] T. Beck and Th. Walther, "A flexible pulsed ps/ns laser system for ion beam cooling at the ESR/SIS100", GSI Scientific Report 2014

DOI:10.15120/GR-2016-1

Schottky beam time "logbook" for laser spectroscopy of Bi^{82+} and Bi^{80+} *

C. Trageser[1,2], *C. Brandau*[†1,2], *C. Geppert*[2], *Yu.A. Litvinov*[2], *J. Meisner*[3], *A. Müller*[1], *W. Nörtershäuser*[4], *R. Sanchez*[2], *S. Sanjari*[2], *S. Schippers*[1], *M. Schmidt*[3], *and J. Ullmann*[4,5]

[1]Justus-Liebig-Universität Gießen, Germany; [2]GSI Helmholtzzentrum für Schwerionenforschung, Darmstadt, Germany; [3]Physikalisch-Technische Bundesanstalt, Braunschweig, Germany; [4]Technische Universität Darmstadt, Germany; [5]Helmholtz-Institut Jena, Germany

During 2014, a new data acquisition (NTCAP-DAQ) was successfully commissioned [1, 2] that can sample ("time-capture") the signals of the new Schottky probe in the ESR [3] continuously with a high bandwidth. Sustained rates of Schottky signals demodulated to its in-phase (I) and quadrature (Q) components exceeding $35 \cdot 10^6$ IQ-Samples s^{-1} (data rate 140 MByte s^{-1}) were achieved. With this high rate several harmonics of the ion beam circulating in the storage ring are covered allowing a redundancy check to be performed. In addition, the raw-IQ-data storage with a high sampling rate offers many options for the offline analysis such as a flexible partition of the of data with priorities on either time- or frequency-resolution but also allows decimation and filter algorithms to be used for improved signal-to-noise ratios [2].

One of the primary applications of such a continuous, broadband Schottky DAQ is the use as a "beam logbook" during storage ring experiments: in a recent ESR laser spectroscopy experiment on the hyperfine splitting of Bi^{82+} and Bi^{80+} [4, 5] the NTACP-DAQ was utilized to monitor the ion beam properties. In these experiments the ion velocity is determined due to the electron cooling, i.e., by the velocity of the cooler electrons. For best experimental results the velocity of the electrons needs to be known precisely [6]. Using the Schottky-frequency technique the constancy of beam quality, e.g., the energy deviation of the ion beam was monitored down to relative changes of $\Delta E_i/E_i \sim 10^{-7}$. The absolute value of the ESR cooler voltage was measured with a precision high-voltage divider [7] provided by the Physikalisch-Technische Bundesanstalt, Braunschweig. An important correction to this voltage is the space charge potential of the cooler electron-beam. In order to experimentally determine this correction (Fig. 1) the cooler electron-current is changed in steps from its initial value of 250 mA to further values with small space-charge potential, here, to 10 mA (at around t=1100 s) and finally to 50 mA. The voltage of the cooler is adjusted in such a way that the revolution frequency matches the initial Schottky frequency. The voltage differences yield the corresponding values for the space-charge potential.

The present example nicely demonstrates the capabilities of this NTCAP-DAQ. In these first experimental runs only the Schottky signals were recorded by the NTCAP-DAQ. The slow control data such as the electron current and the cooler voltage were recorded with a different setup and were merged later. Meanwhile, the NTCAP-DAQ also features up to 22 DMA scaler channels that can record slow control data such as accelerator control-signals, experimental parameters and even detector signals synchronously with the Schottky signals.

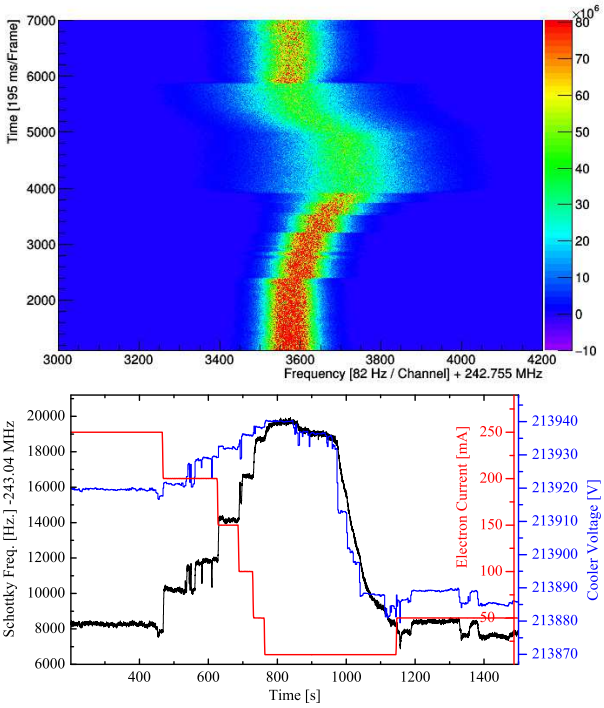

Figure 1: Precision determination of the space-charge potential of the cooler electron-beam. Upper panel: 2D Schottky spectrum (124th harmonics) of Bi^{82+} ions in the ESR. Lower panel: Schottky Frequency (black line, left y-axis), cooler voltage (blue line, right y-axis) and cooler electron current (red line, 2nd right y-axis).

References

[1] C. Trageser et al., GSI Scientific Report 2014, p. 220.
[2] C. Trageser et al., Phys. Scr. **T166** (2015), 014062.
[3] F. Nolden et al., Nucl. Instrum. Meth. A **659** (2011), 69.
[4] J. Ullmann et al., J. Phys. B **48** (2015), 144022.
[5] J. Ullmann, PhD thesis, in preparation.
[6] M. Lochmann, Phys. Rev. A **90** (2014), 030501(R).
[7] J. Hällström et al., IEEE Trans. Instrum. Meas. **63** (2014), 2264.

*Work is supported by BMBF (contracts 06GI911I, 06GI7127/05P12R6FAN and 05P15RDFAA), by the Helmholtz-CAS Joint Research Group HGJRG-108 and by HIC for FAIR.

† c.brandau@gsi.de

DOI:10.15120/GR-2016-1

Towards electron-ion collision experiments at CRYRING@ESR using a sheet-beam electron-target in "crossed-beams" geometry *

C. Brandau[†1,2], *S. Geyer*[3], *M. Lestinsky*[2], *B. Ebinger*[1], *A. Borovik, Jr.*[1], *O. Kester*[2,3], *C. Kozhuharov*[2], *O. Meusel*[3], *A. Müller*[1], *S. Schippers*[1], *Th. Stöhlker*[2,4,5] *for the SPARC working group "Electron Targets"*

[1]Justus-Liebig-Universität Gießen, Germany; [2]GSI Helmholtzzentrum für Schwerionenforschung, Darmstadt, Germany; [3]Goethe Universität Frankfurt am Main, Germany; [4]Friedrich-Schiller-Universität Jena, Germany; [5]Helmholtz-Institut Jena, Germany

As a part of the program of the SPARC collaboration (working group "Electron Targets") it is planned to install a transverse electron target at the storage ring CRYRING@ESR [1, 2, 3], i.e., a sheet-like electron beam that collides with the ion beam under an angle of $90°$. The new electron gun will feature a multi-electrode design (Fig. 1) [1, 4, 5, 6] that allows for a flexible control of beam properties such as electron density, electron-energy, trapping/non-trapping of slow ions in the electron beam space charge potential in the interaction region etc.

Although well-established in low-energy single-pass experiments [7] such a transverse electron target has never been realized at a heavy-ion storage ring, yet. Compared to a merged-beams arrangement for electron-ion collision studies at a storage ring electron cooler, comparatively easy spectroscopic access to the interaction region is possible in a crossed-beams setup allowing photon or even electron spectroscopy experiments to be performed. In contrast to an internal gas-jet target, the electrons are free and not bound to a nucleus. Therefore, atomic processes such as electron-impact excitation, ionization, radiative recombination and nuclear excitation by electron capture can be studied at high experimental resolution and without the difficulties due to competing processes that involve the target nucleus such as proton-impact excitation, non-radiative (kinematic) capture or Coulomb excitation. In addition, the collision energy can be easily changed in well-defined small steps over a broad range of without changing the ion beam energy [1, 7]. The experimental program was recently presented at the latest SPARC workshop [8] and is partly described also in [1, 3].

The optimal layout of the electrode geometry and the gun performance are presently being studied theoretically as well as experimentally at test set-ups at the Universities of Giessen and Frankfurt. The outcome of these studies will lead to a design that is optimally adapted to the experimental environment at the storage ring CRYRING@ESR and to photon and electron spectroscopy at the target. First results of our test measurements are encouraging, but they also bare witness of the complexity of such a multi-electrode sheet-beam gun.

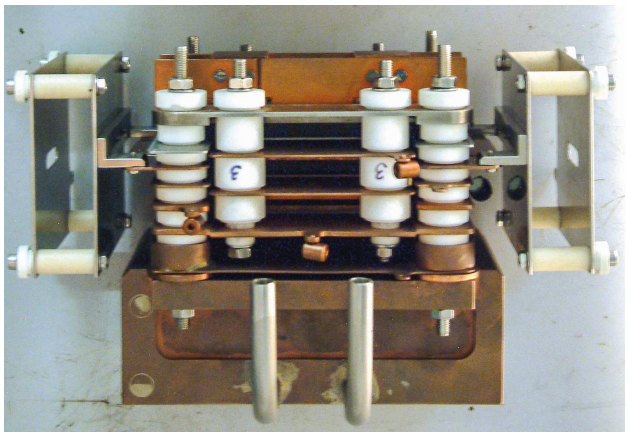

Figure 1: Giessen sheet-beam multi-electrode gun [4, 6]. The electron beam propagates from the top to the bottom, the ion beam direction is from the left to the right. The gun is used in the Giessen single-pass low-energy electron-ion collision experiment [7]. This gun, as well as a similar type at the University of Frankfurt [5] are used to study the properties of multi-electrode high-density electron guns. Such a type of electron gun that is further optimized for a storage ring environment and for photon spectroscopy will be used in the CRYRING@ESR collision setup [1].

References

[1] Z. Andelkovic et al., *Technical Design Report: Experimental Instrumentation of CRYRING@ESR*, 2015, http://www.fair-center.eu/en/en/for-users/experiments/appa/documents.html.

[2] M. Lestinsky et al., Phys. Scr. **T166** (2015), 014075.

[3] M. Lestinsky et al., *Physics book: CRYRING@ESR*, in preparation.

[4] W. Shi et al., Nucl. Instrum. Meth. B **205** (2003), 201.

[5] S. Geyer et al., Phys. Scr. **T156** (2013), 014093.

[6] A. Borovik Jr. et al., J. Phys.: Conf. Ser. **488** (2014), 142007.

[7] A. Müller, Adv. At. Mol. Opt. Phys. **55** (2008), 293.

[8] C. Brandau et al., SPARC 2015 workshop, Fodele, Crete, 2015/09/24.

*Work is supported by BMBF (contracts 05P12R6FAN and 05P15RGFAA), and by HIC for FAIR. PSP code:1.3.1.5.9

† c.brandau@gsi.de

Cross sections for collisional K-shell excitation of hydrogenlike uranium ions*

A. Gumberidze[1], *A. Markowska*[2], *A. Surzhykov*[3], *D. B. Thorn*[4], *C.J. Fontes*[5], *B. Najjari*[6], *H.L. Zhang*[5], *A. Voitkiv*[7], *S. Fritzsche*[3,8], *D. Banaś*[2], *H. Beyer*[1], *W. Chen*[1,9], *R. D. DuBois*[10], *S. Geyer*[11], *R. Grisenti*[1,11], *S. Hagmann*[1,11], *M. Hegewald*[11], *R. Hess*[1], *S. Hess*[1,11], *C. Kozhuharov*[1], *R. Märtin*[3], *N. Petridis*[1,11], *A. Simon*[12], *U. Spillmann*[1], *M. Trassinelli*[13], *S. Trotsenko*[1,3], *G. Weber*[1,3], *D. F. A. Winters*[1], *N. Winters*[1], *D. Yu*[14], *and Th. Stöhlker*[1,3,8]

[1]GSI, Darmstadt, Germany; [2]Institute of Physics, Jan Kochanowski University, Kielce, Poland; [3]Helmholtz-Institut Jena, Jena, Germany; [4]LLNL, Livermore, CA, USA; [5]Computational Physics Division, Los Alamos National Laboratory, Los Alamos, USA; [6]University of Strasbourg, France; [7]University of Düsseldorf, Germany; [8]IOQ, Friedrich-Schiller-Universität Jena, Jena, Germany; [9]IHEP, CAS, Dongguan, China; [10]Missouri University of Science and Technology, Rolla, USA; [11]University of Frankfurt, Frankfurt am Main, Germany; [12]NSCL Michigan State University, East Lansing, USA; [13]Inst. des NanoSciences de Paris, CNRS UMR7588 and UMPC-Paris 6, Paris, France; [14]Institute of Modern Physics, Lanzhou, China

In the current work, we extended/complemented our study [1] of the electron- and proton-impact excitation processes (EIE and PIE) for hydrogen-like uranium (U^{91+}) in collisions with H_2 target with the energy of 212.9 MeV/u. Namely, We extracted the total excitation cross sections into $2s_{1/2}$, $2p_{1/2}$ and $2p_{3/2}$ levels by normalizing intensities of the corresponding spectral lines on those due to the Radiative Electron Capture (REC) process and using the theoretical REC cross sections.

The experiment was carried out at the internal gas jet of the Experimental Storage Ring (ESR). The detailed description of the experimental setup and the used detection techniques can be found in e.g. [1, 2]. Briefly, we looked at the x-rays generated by the excitation (and the subsequent decay) and the REC processes. Utilizing coincidences with the charge-changed projectiles we can clearly separate the spectral lines corresponding to those two processes. Namely, for excitation we observe the following lines: Lyα_2: $2s_{1/2} \rightarrow 1s_{1/2} + 2p_{1/2} \rightarrow 1s_{1/2}$, Ly$\alpha_1$: $2p_{3/2} \rightarrow 1s_{1/2}$ and for the REC (forming Helium-like uranium): Kα_2: $^3S_1 \rightarrow {}^1S_0 + {}^3P_1 \rightarrow {}^1S_0$, K$\alpha_1$: $^3P_2 \rightarrow {}^1S_0 + {}^1P_1 \rightarrow {}^1S_0$. The experimental excitation (EIE+PIE) cross sections were obtained as the ratio of the number of counts in the Ly$\alpha_{1,2}$ lines to those of the K$\alpha_{1,2}$ and multiplying them by the corresponding theoretical REC cross sections. This was done for different x-ray emission angles and the final results were obtained as weighted means. Here, we make use of the fact that both the Ly and K radiation was found to be isotropic for this collision system. The REC process has been extensively studied for such collision systems in the past decades both theoretically and experimentally [2] and meanwhile its cross sections can be calculated with an accuracy of 5%.

A comparison of our experimental cross sections for the excitation processes with the state-of-the-art theoretical predictions is presented in table 1. The experimental uncertainties comprise the statistics, the detector efficiencies (3%) and the theoretical REC cross sections (5%). The theoretical values for the both processes (PIE + EIE) have been calculated within the fully relativistic framework including the Generalized Breit Interaction (GBI) for the EIE [3, 4]. The comparison shows that the experimental results obtained by normalization on the Kα_1 line are in good agreement with the theoretical values, whereas the results for the normalization on Kα_2 are deviating. Possible reasons for this, such as missing cascade contributions in the REC theory, have to be further investigated.

Theoretical cross section values			
Level	PIE	EIE	Total
$2p_{3/2}$	0.988	1.107	**2.095**
$2p_{1/2} + 2s_{1/2}$	1.153	2.549	**3.702**
Experimental cross section values			
Level	Normalization on Kα_2		
$2p_{3/2}$	**2.78±0.2**		
$2p_{1/2} + 2s_{1/2}$	**4.97±0.4**		
Level	Normalization on Kα_1		
$2p_{3/2}$	**2.01±0.2**		
$2p_{1/2} + 2s_{1/2}$	**3.60±0.3**		

Table 1: Experimental results in comparison with theoretical predictions for the K-shell excitation of U^{91+} in collisions with H_2 target at 212.9 MeV/u.

References

[1] A. Gumberidze et al. Phys. Rev. Lett. **110**, 213201 (2013).

[2] J. Eichler and Th. Stöhlker, Phys. Rep. **439**, 1 (2007).

[3] C.J. Fontes, D.H. Sampson, and H.L. Zhang. Phys. Rev. A **51**, R12 (1995).

[4] Najjari and A. B. Voitkiv, Phys. Rev. A **85**, 052712 (2012).

* Work supported by Helmholtz Alliance EMMI.

DOI:10.15120/GR-2016-1

An improved Si(Li)-Compton polarimeter for the SPARC collaboration

U. Spillmann[1], K.H. Blumenhagen[2,3], T. Krings[4], R. Märtin[2], M. Vockert[2,3], G. Weber[2], and Th. Stoehlker[1,2,3], on behalf of the SPARC collaboration

[1]GSI, Darmstadt, Germany; [2]HI Jena, Germany; [3]IOQ, Friedrich Schiller Universität Jena, Germany; [4]Semikon Detector GmbH, Jülich, Germany.

X-ray spectroscopy and x-ray polarimetry technology is essential for the experiment program of the SPARC collaboration [1] at GSI and FAIR.

Polarization of x-rays coming from recombination processes induced by collisions of heavy and highly charged ions at relativistic energies with electrons or low-density gaseous targets provides a unique insight into the dynamics of charged particles in extremely strong and temporally short electromagnetic fields. Detailed knowledge of this field has, besides atomic physics itself, a great relevance for plasma- and astrophysics.

To strengthen the instrumentation portfolio of SPARC a dedicated Si(Li)-Compton polarimeter *) was ordered at Semikon Detector GmbH (see figure 1). It is based on a planar double-sided strip detector (Li-drifted silicon bulk) with a thickness of 9.2 mm. The strip structure was defined with 32 strips on each side with a pitch of 1mm and a length of 32 mm. To achieve a good energy resolution not only the detector crystal itself has a working temperature close to 110 K but also the input stages of the preamplifiers are cooled. Laboratory tests demonstrated a spectroscopic resolution of ~850 eV (p^+-side) and ~1300 eV (HV-side) at a γ-ray energy of 60 keV (Am-241). To demonstrate the homogenous spectroscopic performance the spectra of all strips of the p^+-side irradiated with an Am-241 source are presented in figure 2. The improved resolution of the system compared to our present ones [2] gives us enhanced possibilities for studying atomic transitions at lower energies and lower Z-systems as well as other systems where polarisation transfer can be observed [3].

To gain best physics performance also at higher x-/γ-ray energies the design of the system foresees a possible upgrade to a telescope system (Compton telescope) by installing a second planar detector (HPGe) behind the Si(Li)-detector. The mechanical design chosen, allows an arbitrary orientation of the detector without loss of LN_2.

Figure 1: The Si(Li)-Compton Polarimeter

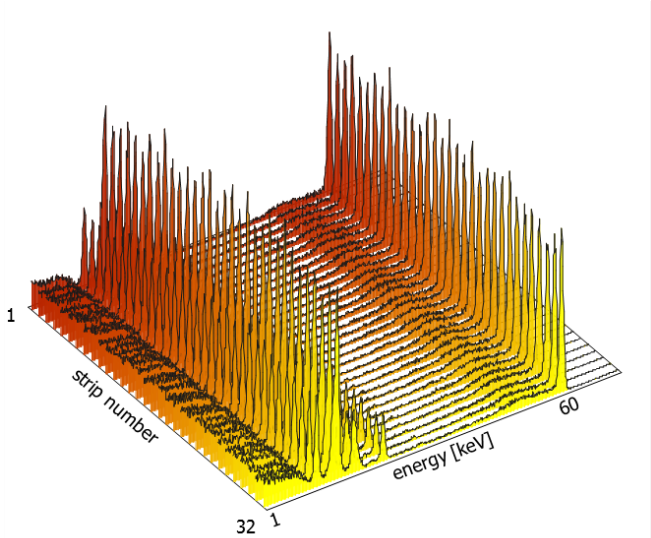

Figure 2: Energy spectra of a Am-241 source detected by the strip structure on the p^+-side of the Si(Li) Compton polarimeter.

References

[1] Technical Report of the SPARC collaboration http://www.gsi.de/fair/experiments/sparc/index_e.html

[2] G. Weber et al., "Performance of a position sensitive Si(Li) x-ray detector dedicated to Compton polarimetry of stored and trapped highly-charged ions", JINST 5,C07010 (2010)

[3] R. Märtin et al., "Polarization Transfer of Bremsstrahlung Arising from Spin-Polarized Electrons" Phys. Rev. Lett. 108, 26480 (2012)

*) financed by Friedrich Schiller Universität Jena

Efficiency of parallel computing for ions stored in Penning traps*

A. Henkel[1,2,3], *F. Herfurth*[1], *R. Pinnau*[2], *and T-K. Strempel*[3]

[1]GSI Helmholtzzentrum, Darmstadt, Germany; [2]University, Kaiserslautern, Germany; [3]University of Applied Sciences, Darmstadt, Germany

With the HITRAP (Highly charged Ions Trap) facility at the GSI it is possible to explore slow highly charged ions up to U 92+. The most important part of the facility is the Penning trap, which allows the trapping of charged ions.

Because of the ion-ion interactions, the simulation of ion clouds in the penning trap has a computational effort of $O(N^2)$ in a brute force simulation scheme. For a system of 10^5 ions, as it occurs in the Penning trap, solving the equations of motion in a straightforward manner leads to long computing times.

A hybrid MPI/OpenCL implementation has been developed to run the simulation on CPU/GPU cluster to distribute the computational effort. To compare the same parallelized code on two kind of parallel systems (SYS1 and SYS2), a GPU and a multicore processor cluster were considered. The system SYS1 is the GSI HPC cluster "Kronos" consisting of 200 nodes. Each node is equipped with a Intel Xeon E5-2660 (40 cores) and 128GB RAM. The system SYS2 is a single PC which is equipped with four Tesla c2050 computing processors.

Figure 1 shows a comparison between the architecture of a CPU and GPU.

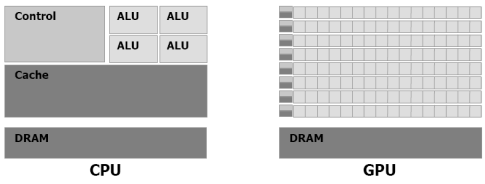

Figure 1: Comparison between the architecture of CPU and GPU

The efficiency of parallelization was tested in the following way. The speed-up s is the quotient of the computation time for one processor $T(1)$ and the computing time for p processors T(p).

$$s(p) = \frac{T(1)}{T(p)}$$

In Figure 2 we see the run-time measurements of a cloud of $2^{17} \approx 130.000$ ions for one iteration on the two systems. The simulation was run with 2^{17} ions, because the number of processors increases with the power of two. In Figure 3 we see the predicted speed-up for the parallel implementation, following by Amdahl's law [2].

The maximum speed-up, which can be expected, is the limit of the two functions, shown in the Figure 3 above.

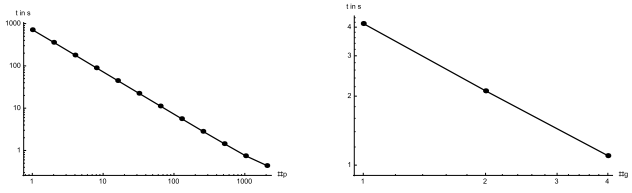

Figure 2: Run-time left: SYS1, right: SYS2

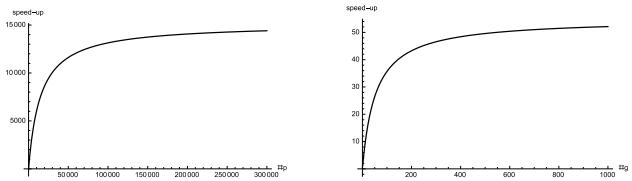

Figure 3: Speed-up: left (SYS1), right (SYS2)

The limits are $s_\infty^{CPU} \approx 16400$ and $s_\infty^{GPU} \approx 55$. If we want to simulate a system of 2^{17} ions, the time for one iteration is 715.72 s for one processor in SYS1 and 4.15 s for one GPU in SYS2. On a CPU cluster and with an infinity number of processors we can calculate one iteration in 0.048 s. If we use an infinite number of GPU we can calculate one iteration in 0.076 s.

Due to the strong magnetic field in the HITRAP Penning trap the step size is at least restricted to the cyclotron frequency. The step size should be choosen about 10^{-10} s. Therefore, a simulation of a cloud of 2^{17} ions for a duration of 1 s lasts approximately 15 years on the CPU cluster. The same simulation on the GPU cluster needs approximately 24 years. Therefore, further research is spend to modify the integrator to increase the step size and to decrease the computing time.

References

[1] Karp, Alan H., and Horace P. Flatt. "Measuring parallel processor performance." Communications of the ACM 33.5 (1990): 539-543.

[2] Amdahl, Gene M. "Validity of the single processor approach to achieving large scale computing capabilities." Proceedings of the April 18-20, 1967, spring joint computer conference. ACM, 1967.

[3] http://docs.nvidia.com

* Work supported by FE, Project-Number DAGROS1416.

DOI:10.15120/GR-2016-1

Preparing first experimental installations at CRYRING@ESR*

M. Lestinsky[†1], *A. Bräuning-Demian*[1], *F. Herfurth*[1], *S. Schippers*[2], *R. Schuch*[3], *Th. Stöhlker*[1,4], *and the SPARC collaboration*[1]

[1]GSI, Darmstadt, Germany; [2]JLU Gießen, Germany; [3]Stockholm University, Sweden; [4]HI Jena, Germany

CRYRING@ESR is a new heavy ion storage ring facility at GSI/FAIR and is presently under construction [1-4]. The former Swedish CRYRING is presently refitted and adapted to its new location. Commissioning of ring operation will soon start. CRYRING@ESR will be able to store all classes of ions available at ESR but at much lower ion energies. Moreover, it features excellent vacuum conditions for the storage of the highest charge states. CRYRING was conceived as a synchrotron, thus stored ions may be de- and accelerated internally to energies between ~ 0.05 and 15 MeV/u. The research collaborations SPARC, FLAIR, and NuSTAR have formulated extensive research programmes for this facility [5]. Ion-storage at low energies is ideally suited for precision spectroscopy and thus allows one, e.g., to test non-perturbative strong field QED terms, or to study transient quasi-molecular systems. Furthermore, at the border between atomic and nuclear physics, nuclear size effects, hyperfine interactions or exotic couplings between the electronic shell and the nucleus of an ion may be explored. In nuclear physics, storage of bare nuclei at low energies permits to determine fragment distributions unmasked by atomic physics. Under these conditions, e.g., nuclear reactions at the Coulomb barrier or the nucleosynthesis of heavy elements in the Gamow window of the p-process may be analyzed.

The construction is rapidly advancing, see Figure 1 for an impression of the present project status. In particular, all ring sections have been installed and the precision alignment of ion-optically active elements is currently underway. Media installations have been completed. A small ion source and a RFQ accelerator were installed as a local injector system for independent test operation of CRYRING@ESR. This injector has been commissioned and a H_2^+ beam could be accelerated to 300 keV/u [6].

In order to prepare a first generation of experiments at CRYRING@ESR, the German APPA R&D collaboration has applied for and received substantial funding within the BMBF Verbundforschung scheme [7]. An accompanying TDR for planned experimental instrumentation was drafted in parallel and has been accepted recently [8]. This instrumentation comprises various installations for a wide range of atomic physics experiments: Electron-ion collision spectroscopy with high-resolution at the electron cooler or at a high-density transverse electron target for high energies, laser spectroscopy, as well as energy-resolved determination of target radiation from the visible to the vacuum ultraviolet (VUV) regime. A number of experimental infrastructure measures were addressed as well: Particle detector mounts, and a precision voltage divider for an accurate determination of the ion velocity under cooling conditions. The current BMBF funding period runs from 2015–2018 and fits to the present timeline for the FAIR construction, which foresees a major shutdown of the GSI accelerator infrastructure after summer 2016 until early 2018. In this situation, the local injector at CRYRING@ESR is extremely valuable, as it allows for testing and optimizing of the new experimental infrastructure. This will be decisive for ensuring that the experiments at CRYRING@ESR will be ready when the GSI accelerator facility resumes operation.

Figure 1: The CRYRING construction area in Dec. 2015.

*CRYRING@ESR is supported by GSI, HI Jena, Stockholm Univ., Jagiellonian Univ. Kraków, and BMBF Verbundforschung under various contracts.

† m.lestinsky@gsi.de

References

[1] `http://www.gsi.de/cryring/`

[2] H. Danared, et al., “Technical Design Report: LSR - Low-energy Storage Ring”, 2011, Manne-Siegbahn-Laboratory, Stockholm University

[3] M. Lestinsky, et al., “CRYRING@ESR: A study group report”, 2012, GSI Darmstadt

[4] M. Lestinsky, et al., “CRYRING@ESR: Present Status and Future Research”, 2015, Phys. Scr. T166, p. 014075

[5] M. Lestinsky, et al., “Physics book: CRYRING@ESR”, in preparation.

[6] F. Herfurth, et al., “The status of the CRYRING@ESR project”, GSI annual report 2015, GSI Darmstadt, in print.

[7] `http://appa-rd.fair-center.eu`

[8] Z. Andelkovic, et al. and the SPARC collaboration, “Technical Design Report: Experimental Instrumentation of CRYRING@ESR”, 2015, FAIR Darmstadt

S-EBIT facility: status report*

S. Trotsenko[1,2], N. Bauer[2], W. Chen[2], J. Menssen[1,2,3], G. Vorobjev[2], D. Racano[2], A. Gumberidze[2,4], C. Kozhuharov[2], S. Purushothaman[2], F. Herfurth[2], R. Schuch[6], and Th. Stöhlker[1,2,4,5]

[1]Helmholtz-Institut Jena, D-07743 Jena, Germany; [2]GSI Helmholtzzentrum für Schwerionenforschung, D-64291 Darmstadt, Germany; [3]Hochschule Rhein Main, University of Applied Sciences, D-65428 Rüsselsheim, Germany; [4]ExtreMe Matter Institute EMMI, GSI, D-64291 Darmstadt, Germany; [5]Friedrich-Schiller-Universität Jena, D-07743 Jena, Germany; [6]Department of Physics, Stockholm University, SE-10691 Stockholm, Sweden

One of the goals of Helmholtz Institute Jena with respect to the Facility for Antiproton and Ion Research is to provide highly-charged, low-energy ions by using the S-EBIT facility currently being installed at GSI [1]. This is of particular importance during the FAIR construction related shutdown period of the GSI accelerator complex, when little to no beam time can be provided. During this period the S-EBIT shall facilitate research and development works for SPARC experiments at FAIR. This accelerator-independent source of HCI will not only provide ions necessary for R&D of HITRAP [2] experimental stations but also serve as a standalone device for research and R&D activities (e.g. development of x-ray spectrometers, calorimeter detectors, x-ray optics etc. [3]). Furthermore, the combination of S-EBIT with the available laser infrastructure e.g. JETI200 will be a unique platform for the study of highly charged ions subject to intense laser radiation [4] as it is planned at a later stage once the S-EBIT facility has been moved to Jena.

Currently, for the S-EBIT facility, two independent setups are being built: EBIT-I and EBIT-II. The first one, represents an EBIT with electron energies of up to 40keV (and ~150mA), and thus in combination with the 3T magnet it will be able to efficiently produce highly-charged ions with the charge state of up to Th^{80+}. In the case of the second EBIT, main efforts are concentrated on constructing the system able to provide electrons with highest possible energy, up to 260keV, and few hundreds mA, which in combination with 4T magnet shall produce high-Z HCI, up to bare uranium. Both EBITs will not only serve as sources of HCI but also work in a standalone operation.

The construction of the EBIT-I has been accomplished. A brand-new vacuum interlock system has been built in order to enable the EBIT to be connected to the GSI vacuum system, which would be necessary for the experiments that require extraction of the produced ions towards the HITRAP experiments. The vacuum and cryogenic tests of the system have been successfully carried out. The superconducting magnet was powered up with 60A, thus providing the magnetic field in the trap region of 3T. The high-voltage line has been built up and the first test of the system has been performed, where the voltage of 20kV (limited by the HV-supply) has been applied to the drift tubes. The supplies for the electron gun (cathode filament, bucking magnet, anode- and focus-electrode) as well as for the electron collector parts have been tested. The work on conditioning the e-gun is currently on-going; so far it has been possible to reach 3mA electron current.

The EBIT-II was equipped with the new superconducting magnet, designed to provide magnetic fields of up to 4T as well as the newly constructed drift tubes. The new shielding to separate the 4K SC-magnet from the room temperature EBIT chamber has been manufactured hosting the temperature sinking couplings for the SC-magnet current leads. The first vacuum and cryogenic tests were successfully carried out. The current leads of the SC-magnet have been optimized to minimize heat load of the system. The preparation for the first magnet test is ongoing. A new bucking coil for the electron gun has been manufactured. The new high-voltage feedthrough system for ramping the trap is currently being constructed. The vacuum system is being modified for coupling with the GSI (HITRAP) beamline.

References

[1] R. Schuch et al., JINST5, C12018 (2010)
[2] F. Herfurth et al., Phys. Scr. T166, 014065 (2015)
[3] D. Hengstler et al., Phys. Scr. T166, 014054 (2015)
[4] M. Vogel et al., Nucl. Instr. Meth. B 285, 65 (2012)

**Also a part of the HI-Jena Scientific Report 2015*

DOI:10.15120/GR-2016-1

Many-electron projectile stripping cross section studies at the ESR gas target*

G. Weber[1,2], *M. O. Herdrich*[2,3], *R. D. DuBois*[4], *P.-M. Hillenbrand*[1,5], *S. Sanjari*[1,7], *D. F. A. Winters*[1], *N. Petridis*[1,6], *and Th. Stöhlker*[1,2,3]

[1]GSI, Darmstadt, Germany; [2]HI-Jena, Germany; [3]IOQ, Univ. Jena, Germany; [4]Missouri S&T, Rolla, MO, USA; [5]IAMP, Univ. Giessen, Germany; [6]IKF, Univ. Frankfurt, Germany; [7]EMMI, Darmstadt, Germany

Charge-changing processes, i. e. loss or capture of electrons, occurring in ion-atom and ion-ion collisions belong to the most basic interactions in all types of plasmas. Moreover, in accelerators interactions between projectile ions and the residual gas can lead to a change of the projectile charge state. In the presence of dispersive ion optical elements, the trajectories of up- or down-charged ions do not match the one of the reference charge state, resulting in a successive defocussing and, as a consequence, loss of beam intensity. Moreover, ions impinging on the beam line walls give rise to several unwanted effects, such as increased radiation levels and significant degraded vacuum conditions due to ion-impact induced desorption. For the FAIR project, in order to reach highest beam intensities, while minimizing the limitations induced by space charge, and avoiding losses in stripper targets, the use of low- to medium-charged, many-electron ions is planned [1]. However, in the relevant energy region from 10 MeV/u up to a few GeV/u the number of bound electrons of these ions is far above that of the corresponding equilibrium charge state, making projectile stripping, sometimes also referred to as electron loss, the dominant beam loss process. Thus, for the planning of future accelerators and ion beam experiments, precise knowledge of the stripping cross sections of many-electron projectiles is necessary. As the theoretical treatment of such many-body atomic physics problems is quite challenging, experimental benchmarks are needed to test the various predictions of different theory models [2].

Recently, two electron loss studies covering beam energies up to 50 MeV/u for U^{28+} ions was presented [3,4]. We now report on a follow-up experiment using again U^{73+} projectiles which was performed at a higher beam energy of 150 MeV/u at the ESR gas target and covering a broad range of the target atomic number Z. After injecting the beam into the ESR the ions were stored and electron cooling was applied. After a few seconds, when stable beam conditions were reached, the shutter of the internal gas target was opened and a gas jet being perpendicular to the ion beam axis was formed inside the interaction chamber of the ESR. Up- or down-charged ions produced in interactions with the target were subsequently lost due to collisions with the beam line walls or dedicated scrapers after passing the bending magnets. N_2, Ar, Kr, and Xe were used as target gases with densities between a few times 10^9 and a few times 10^{11} particles/cm^3. The beam lifetime, which is dominated by the electron loss cross section (i. e. projectile ionization), was deduced from measuring the ion beam intensity as a function of time using a DC current transformer (DCCT) and the integrated Schottky signal of the new resonant pickup.

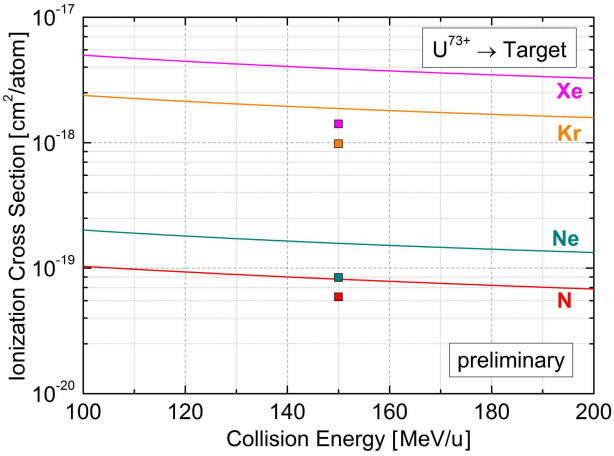

Figure 1: Preliminary: Compilation of the total electron-loss cross section for U^{73+} ions in collisions with various target gases.

A detailed analysis of the obtained data in order to extract the projectile electron loss cross section for the various target gases has been performed. Preliminary results are shown in Fig. 1 together with theoretical predictions by V. P. Shevelko et al. [5]. As already found in previous studies, the electron loss in collisions with heavy targets is significantly overestimated by theory. This issue will be discussed in detail in an upcoming publication.

References

[1] FAIR - Baseline Technical Report (2006)

[2] V. P. Shevelko et al., *Electron Loss and Capture Processes in Collisions of Heavy Many-Electron Ions with Neutral Atoms*, in: Atomic Processes in Basic and Applied Physics **68**, 125-152, Springer (2012)

[3] G. Weber et al., Phys. Rev. ST AB **12**, 084201 (2009)

[4] G. Weber et al., Phys. Rev. ST AB **18**, 034403 (2015)

[5] V. P. Shevelko, private communication (2015)

*Work supported by the Alliance Program of the Helmholtz Association (HA216/EMMI) and by HIC-for-FAIR through HGS-HIRe and Helmholtz-CAS Joint Research Group HCJRG-108.

DOI:10.15120/GR-2016-1

Dramatic radial fluctuations of ion tracks in Gd_2TiZrO_7*

R. Sachan[1], E. Zarkadoula[1], M.F. Chisholm[1], Y. Zhang[1], M. Lang[2], C. Trautmann[3], and W.J. Weber[2,1,#]

[1]ORNL, Oak Ridge, TN 37831, USA; [2]University of Tennessee, Knoxville, TN 37996, USA; [3]GSI and Technische Universität Darmstadt, Germany

We report unexpected dramatic radial variations in the ion tracks formed by GeV heavy ions at a constant electronic energy-loss in pyrochlore structured Gd_2TiZrO_7. High angle annular dark field (HAADF) was used to image the atomic track structure at 1 nm incremental depth steps. Along a track length of about 20 nm, the radial variations are up to 40% . Molecular dynamics simulations are consistent with these observations.

Experimental details

In this study, polycrystalline samples of Gd_2TiZrO_7 were irradiated at room temperature with 2.3 GeV energy ^{208}Pb ions at the beamline X0 of the UNILAC linear accelerator of GSI. The ion fluence was 5×10^{10} ions/cm^2 in order to create isolated ion tracks.

Plan-view scanning transmission electron microscope (STEM) samples were prepared to characterize the track morphology at a depth of 10 µm from the irradiated surface. Nanoscale depth-dependent HAADF imaging of plan-view ion tracks in a 5th order aberration corrected STEM, which provided the incoherent images and a simplified atomic-resolution three-dimensional morphology of the tracks [1]. This method possesses an advantage over cross-sectional TEM imaging, which is limited to qualitative track morphology information.

Significant variation in track radii at the same depth is shown in Figure 1. To understand this variation in track radii, a focal series of HAADF images were taken at 1 nm incremental depths by changing the electron beam focus.

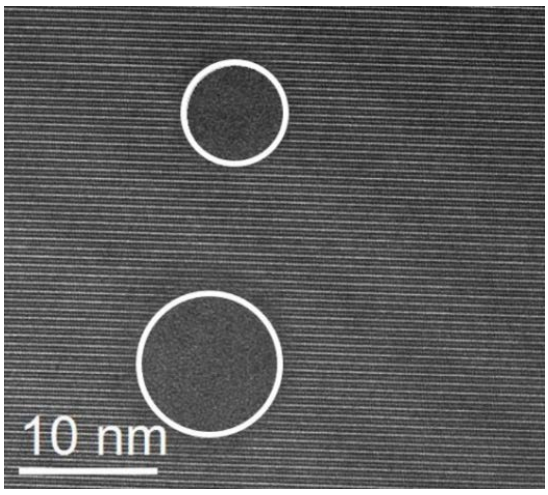

Figure 1: HAADF image of two ion tracks in Gd_2TiZrO_7 at depth of 10 µm.

Molecular dynamics simulations

Molecular dynamics (MD) simulations were performed to confirm the experimental variation of track radii at nanoscale increments in track length in Gd_2TiZrO_7. Figure 2(a) illustrates a slice along the z direction of the system after 340 ps of simulation time, where the variation of the ion track diameter is clearly seen along the track length. The ion track consists of an amorphous core, and the rearranged (defect-fluorite) shell structure, in agreement with the experimental findings. The MD images in Figure 2(b) and (c) show the cross section of the ion track at the two different depths indicated in Figure 2(a). In agreement with the experimental observations, the core diameters have different size along the incremental length of track.

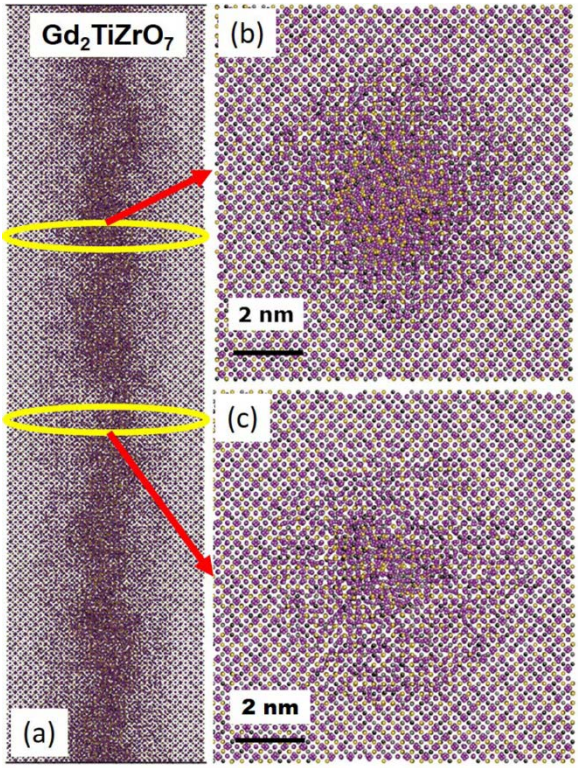

Figure 2: MD simulation of 2.3 GeV Pb ion track in Gd_2TiZrO_7, along ion trajectory (a) and cross sections at two different depths (b,c)

References

[1] S. J. Pennycook *et al.*, Philosophical transactions. Series A 367 (2009) 3709.

* Work supported by U.S. Department of Energy, Office of Science, Basic Energy Sciences, Materials Science and Engineering Division.
#wjweber@utk.edu

Ion track density profiles in amorphous Si_3N_4 and SiO_2*

P. Mota-Santiago[1,#], T. Bierschenk[1], A. Nadzri[1], D. Schauries[1] C. Trautmann[2,3], M.C. Ridgway[1], and P. Kluth[1]

[1] ANU, Canberra, Australia; [2]GSI Helmholtzzentrum, Darmstadt, Germany; [3]Technische Universität Darmstadt, Darmstadt Germany.

When amorphous dielectrics are irradiated with swift heavy ions, intense electron excitations in narrow regions around the ion trajectories are produced. Part of the exchanged energy is later transferred to the lattice via electron-phonon coupling increasing the local temperature rapidly and can lead to the formation of molten regions. The effect of local heating leads to non-uniform thermal stress and internal mass transfer [1, 2]. As the cooling down period lasts from 10^{13}-10^{11} s, such features are frozen in leading to a concentrically cylindrical ion track with a core-shell density profile [3]. Using small angle X-ray scattering (SAXS) it is possible to measure the local density variations in these ion tracks [3].

In this work we present a study on the morphology of ion tracks in 1-µm thick a-Si_3N_4 and a-SiO_2 layers grown by plasma enhanced chemical vapour deposition (PECVD) on c-Si (100) wafers using SAXS. The films were irradiated at the Heavy Ion Accelerator Facility at the Australian National University with 185 MeV Au ions, and at the X0-beamline of the UNILAC of GSI with 2.3 GeV Au ions at fluences of 1×10^{11} and 5×10^{11} ions/cm^2 where track overlap effects are negligible.

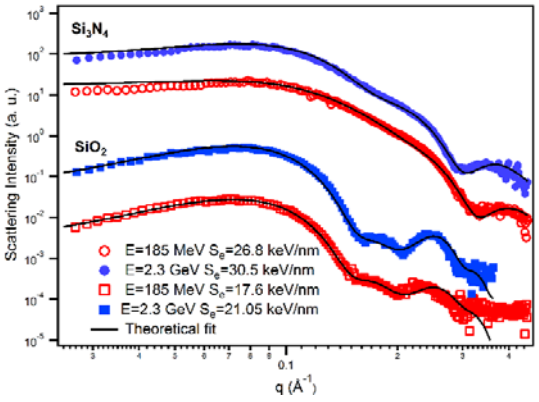

Figure 1: SAXS spectra of a-Si_3N_4 and a-SiO_2 irradiated with 185 MeV (open symbols) and 2.3 GeV Au ions (full symbols) with a fluence of 5×10^{11} ions/cm^2. Solid lines represent numerical fits to experimental data.

The corresponding electronic stopping powers were calculated with the SRIM-2013 code [4], resulting in 26.8 and 30.5 keV/nm for Si_3N_4, and 17.6 and 21.05 keV/nm for SiO_2, for ANU and UNILAC irradiation, respectively. Over the thickness of the layer, the stopping powers vary by less than 1.5%.

* Work supported by Consejo Nacional de Ciencia y Tecnologia (CONACyT) and the Australian Research Council (ARC). This work was performed at the SAXS/WAXS beamline at the Australian Synchrotron.

#pablo.mota@anu.edu.au

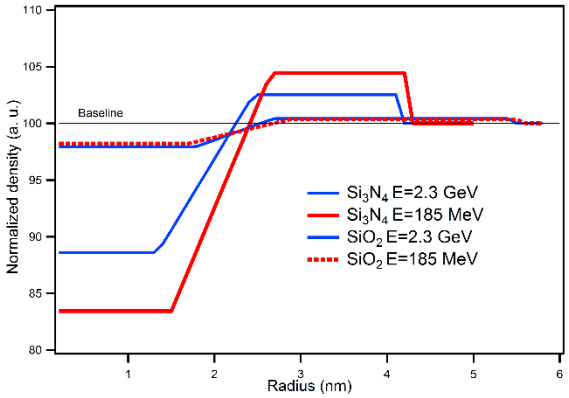

Figure 2: Corresponding density profile of ion tracks formed in a-Si_3N_4 and a-SiO_2. The density misfit is larger for a-Si_3N_4 than for a-SiO_2.

SAXS measurements were carried out at the Australian Synchrotron with an X-ray energy of 12 keV and a camera length of 900 mm. Fig. 1 shows the SAXS patterns from all four samples. The scattering intensity can be theoretically modelled assuming cylindrical geometry of the tracks considering a radial density variation ρ(r) around the track centre [3]. The best fits were obtained using a core shell structure with an under dense core and over dense shell defining a linear transition between both. The resulting density profiles are shown in Fig. 2. While the total track radii in a-SiO_2 (~5.5 nm) are larger than those in Si_3N_4 (~4.2 nm), the density changes in the latter are far greater, exceeding 10% (compared to about 2% in SiO_2). This difference may be related to lower density values of CVD materials compared to bulk, i.e. ~16 % for a-Si_3N_4 and 5% in a-SiO_2. While we observed an important difference in the absolute density, there is little difference in the total track radius between irradiation conditions despite the discrepancy in the electronic stopping powers of~20 %, which can possibly be related to the velocity effect.

The information on the transition region between core and shell is contained in the high q regions (see Fig. 1) and constitutes an improvement on previous measurements on ion tracks in a-SiO_2 [3].

[1] S. Klaumünzer, Nucl. Instr. Meth. B 41 (1990) 1144

[2] V.A. Borodin *et al.*, Nucl. Instr. Meth. B 209 (2003) 122

[3] P. Kluth *et al.*, Phys. Rev. Lett. 101 (2008) 175503

[4] J.F. Ziegler *et al.*, *The Stopping and Range of Ions in Solids*. Stopping and ranges of ions in matter. Pergamon, 1985

DOI:10.15120/GR-2016-1

Raman study of swift heavy ion induced changes of calcite ($CaCO_3$) *

Nicole Schöppner[1#], Sebastian Dedera[1], Ulrich A. Glasmacher[1], Christina Trautmann[2]
[1]Institut für Geowissenschaften, Univ. Heidelberg; [2] TU Darmstadt and GSI Helmholtzzentrum Darmstadt, Germany

The objective of this research project is the characterization and quantification of material changes in calcite caused by the irradiation with swift heavy ions. Calcite ($CaCO_3$) is a member of the carbonate mineral group. In nature calcite contains uranium concentrations in the range of <168 µg/g [1-3]. The occurrence of tracks from spontaneous fission of uranium in calcite has been reported in several studies [4]. Since Raman spectra of natural calcite grains are well documented [5-8], we used this technique as a nondestructive analytical tool to determine ion-beam induced changes of calcite. Structural changes are generally visible in the shift of band position as well as in changes of the band width and intensity, and sometimes in the occurrence of new bands. Here we focus on the change of the band intensity I given by [9]

$$I \sim v^4 I_0 N (\partial\alpha/\partial q)^2$$

where v and I_0 are the frequency and intensity of the stimulating laser, respectively, N is the number of scattering molecules, and $(\partial\alpha/\partial q)$ the changing of polarizability where α is the polarizability and q is the normal vibrational coordinate of the molecule. To monitor beam-induced changes in calcite, the T(Ca, CO_3) lattice modes at ~155 and ~283 cm^{-1} as well as the υ_4-symmetric CO_3 deformation mode at ~714 cm^{-1} and the υ_1-symmetric CO_3 stretching mode at ~1088 cm^{-1} (internal modes) [8] were chosen.

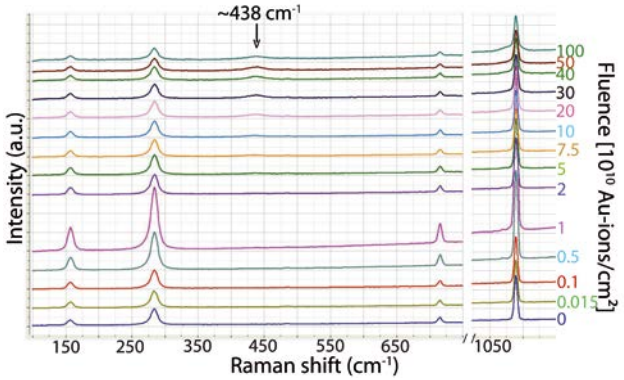

Fig. 1: Uncorrected Raman spectra of colorless calcite before and after irradiation with 4.8 MeV/u Au-ions of different fluences. The spectra are stacked vertically for better visibility. The arrow marks the appearance of a new Raman band at ~438 cm^{-1}.

The irradiation experiments combined with in-situ Raman spectroscopy were performed at the M3 beamline of GSI benefitting from the newly installed Horiba Jobin Yvon iHR 320 spectrometer (grating with 1800 grooves/mm and stimulating laser of 532 nm (Quantum Ventus)) [10, 11]. The wave number accuracy of the system is 1 cm^{-1}.

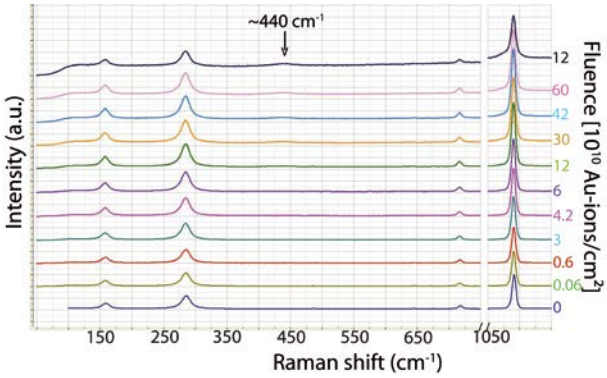

Fig. 2: Uncorrected Raman spectra of yellow calcite before and after irradiation with 4.8 MeV/u Au-ions of different fluences. The spectra are stacked vertically for better visibility. The arrow marks the appearance of a new Raman band at ~440 cm^{-1}.

As samples we selected colorless calcite (CC) and yellow calcite (CY) containing different impurities: 0.22 wt% magnesium (CC) and 1.01 wt% Mg and in addition 0.38 wt% sulfur (CY). The crystals were irradiated with 4.8 MeV/u Au ions applying fluences between 1.5×10^8 – 2×10^{12} ions/cm^2. Raman spectra were acquired in-situ before and after each irradiation step on the same sample position (Figs. 1, 2).

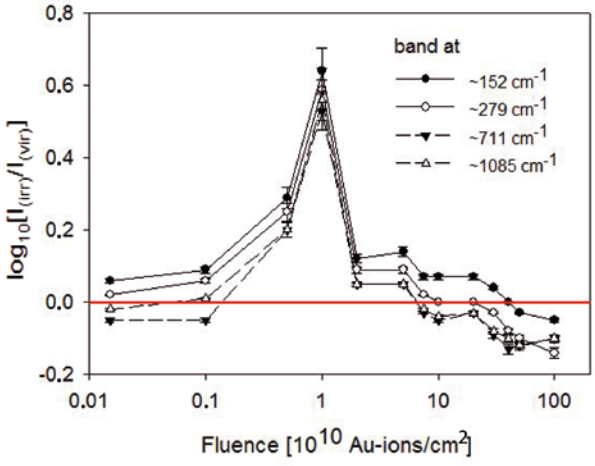

Fig. 3: Normalized Raman band intensities of calcite CC as a function of fluence in double log presentation. Lattice modes T (Ca, CO_3) (~152 and ~279 cm^{-1}) and internal modes υ_4 and υ_1 (~711 and ~1085 cm^{-1}) are displayed. The red line marks the value of the pristine sample.

In comparison to the Raman spectra of CC, all Raman bands of the yellow calcite CY are shifted to slightly higher wavenumbers (~6 cm^{-1} in average) probably a consequence of the different Mg content [7]. The CY spectra

*Work supported by HGS-HIRe
#nicole.schoeppner@geow.uni-heidelberg.de

also contain an extra band at ~1020 cm^{-1} that might be related to the υ_1 (SO_4) vibration mode [12].

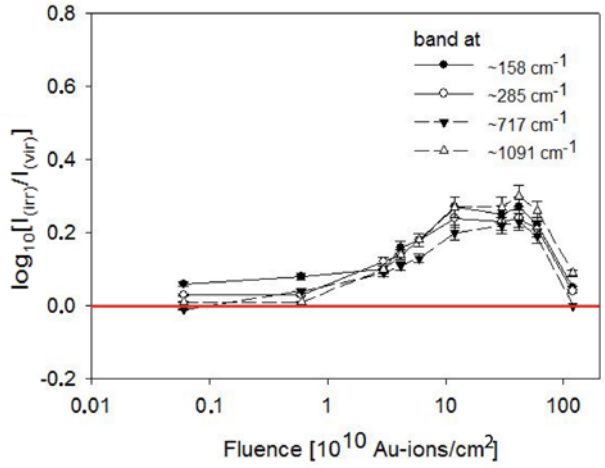

Fig. 4: Normalized Raman band intensities of calcite as a function of fluence in double log presentation. Lattice modes T (Ca, CO_3) (~158 and ~285 cm^{-1}) and internal modes υ_4 and υ_1 (~717 and ~1091 cm^{-1}) are displayed. The red line marks the value of the pristine sample.

For quantitative analysis of beam-induced effects, the band intensities of the irradiated samples were normalized by the corresponding band intensity of the virgin sample (I_{irr}/I_{vir}). For both crystals the I_{irr}/I_{vir} data of the lattice and internal modes of calcite increase with fluence in the initial stage of the irradiation, reach a maximum and finally decrease to a value below unity (Figs. 3 and 4).

For the CC sample, the maximum is reached at a fluence of 1×10^{10} Au-ions/cm² much earlier compared to 1×10^{11} Au-ions/cm² for the CY crystal. In the latter case, the maximum has a more pronounced plateau.

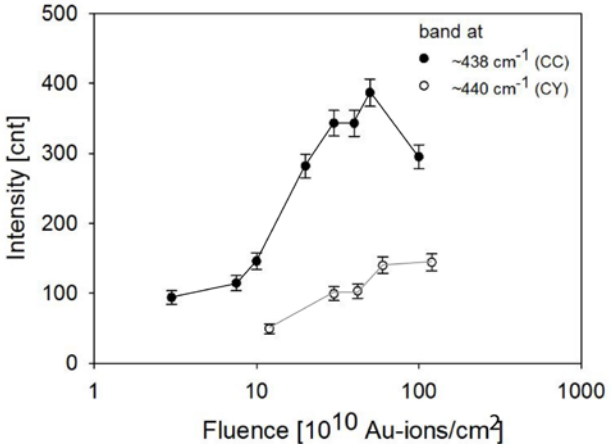

Fig. 5: Absolute intensities of new Raman band at ~438 and ~440 cm^{-1} as a function of fluence observed when irradiating CC and CY calcite.

The above described initial increase of the Raman band intensities up to a maximum is unexpected as the irradiation with heavy ions normally destroys the crystal lattice and this would cause a steady decrease of the normalized intensity with increasing fluence. Within our experiments this was clearly not the case. If we assume that the frequency (ν) and the intensity (I_{vir}) of the stimulating laser were kept constant, either the number of scattering molecules and/or the polarizability must have changed.

For both crystals, a new Raman band is observed above a critical fluence appearing at ~438 cm^{-1} (5×10^{10} Au-ions/cm²) for CC and at ~440 cm^{-1} (5×10^{11} Au-ions/cm²) for CY (Fig. 1 and 2). For CC, the intensity increases until a fluence of 5×10^{11} Au-ions/cm² and then decreases at 1×10^{12} Au-ions/cm², whereas for CY the band intensity steadily increases and saturates at the highest fluence (Fig. 5).

At present, the assignment of this new Raman band is unclear. None of the known vibrations modes for CaC_2 [14], $Ca(OH)_2$ [15], CH_x, C=C, CO [16], CO_2 [17], O_2 [18], CaO are compatible with the observed frequency of this band. Model calculations in cooperation with the Department of Chemistry at the University Heidelberg are in progress.

References

[1] M.B. Andersen et al., Earth and Planetary Science Letters 265 (2008) 229.
[2] D.L. Hoffmann et al., Chemical Geology, 259 (2009) 253.
[3] J.M. Alcaraz-Pelegrina et al., Applied Radiation and Isotopes 65 (2007) 798.
[4] D. Macdougall, P.B. Price, Science 185 (1974) 943.
[5] A. Dandeu et al., Chem. Eng. Technol. 29 (2006) 221.
[6] G. Behrens et al., Spectroscopy Letters 28 (1995) 983.
[7] U. Wehrmeister et al., J. Raman Spect. 41 (2010) 193.
[8] S. Gunasekaran et al., J. Raman Spect., 37 (2006) 892.
[9]http://www.chemgapedia.de/vsengine/vlu/vsc/de/ch/3/anc/ir_spek/ra_messparameter.vlu/Page/vsc/de/ch/3/anc/ir_spek/raman_spektroskopie/raman_geraetetechnik/ra_1_7_3/laslei_m45ht1201.vscml.html
[10] S. Dedera et al., Nucl. Instr. Meth. B 365 (2015) 564.
[11] S. Dedera, Dissertation, Univ. Heidelberg (2015).
[12] N. Buzgar et al., Anal. Şt. Univ. "Al. I. Cuza" Iaşi, Geologie. 55/1, 5-23 (2009).
[13] W. Bolse, Nucl. Instr. Meth. B, 244 (2006) 8.
[14] http://www.patent-de.com/20070913/DE102006011427A1.html
[15] Z.V. Padanyi, Solid State Communications, 8 (1970) 541.
[16] W. Otting, Der Raman-Effekt und seine analytische Anwendung, Springer Verlag, 161 p. (1952).
[17] http://www.chem.purdue.edu/gchelp/vibs/co2.html
[18] http://www.chem.purdue.edu/gchelp/vibs/o2.html

DOI:10.15120/GR-2016-1

In situ Raman spectroscopy of heavy ion irradiated gypsum ($CaSO_4$*$2H_2O$)*

Nicole Schöppner[1#], Sebastian Dedera[1], Ulrich A. Glasmacher[1], Christina Trautmann[2]
[1]Institute of Earth Sciences, Univ. Heidelberg; [2] TU Darmstadt and GSI Helmholtzzentrum Darmstadt, Germany

Gypsum is a constituent of nuclear repositories and is located on the surface of Mars. In both situations, it is exposed to highly ionizing radiation including energetic ions [1]. Our research is triggered by the question if ion irradiation of natural gypsum ($CaSO_4$*$2H_2O$) leads to the release of crystal water and if radiation can induce a phase-transition. In this context, our special interest is to test up to which limit radiation-induced effects can be detected by means of Raman spectroscopy.

To answer these questions, samples were prepared by manually cleaving a large polycrystalline crystal. The cleaved surfaces are very smooth, thus no polishing was applied. The samples were irradiated at the M3 beamline of the UNILAC with 4.8 MeV/u ^{197}Au and ^{131}Xe ions under normal beam incidence. The sample exposed to Au ions (electronic energy loss dE/dx=23 keV/nm [2]) received fluences between 3×10^9 – 2×10^{12} ions/cm^2. For the irradiation with Xe ions (dE/dx=17 keV/nm) fluences between 3×10^9 and 5×10^{11} ions/cm² were applied. Both samples were analyzed before irradiation and after each irradiation step using in-situ confocal Raman spectroscopy available at the M3 beamline [3,4]. This procedure has the great advantage that the sample remains for all measurements in vacuum on its fixed position. Orientation effects are thus avoided and for each fluence step, the same sample spot is analyzed. The Raman spectrometer is a Horiba Jobin Yvon iHR 320 instrument using grating with 1800 grooves/mm. The laser system consists of a Laser Quantum Ventus (green laser, 532 nm). The wave number accuracy is 1 cm^{-1}.

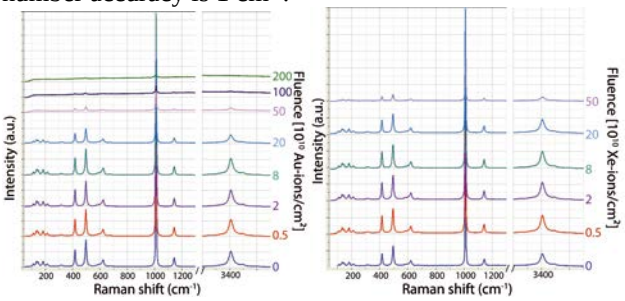

Fig. 1: Raman spectra of gypsum before and after irradiation with 5×10^{11} Au-ions/cm² (left) and Xe-ions/cm² (right).

The Raman spectra of the irradiated samples do not show any band shifts compared to the spectra of the unirradiated sample (Fig. 1). However, the normalized intensities (band intensity of irradiated compared to unirradiated sample, I_{irr}/I_{vir}) of the different Raman bands significantly decrease above a critical ion fluence of about 8×10^{10} Au-ions/cm² (Fig. 2). At a fluence of about 7×10^{11} Au-ions/cm² the Raman band of the υ_3 (H_2O) mode [5,6] is no longer visible. The υ_1 (H_2O) mode [5,6] vanishes at a slightly higher fluence of about 2×10^{12} Au-ions/cm². Under the irradiation with Xe ions, the behavior is rather similar but the critical fluences are shifted to higher values due to the lower dE/dx of Xe ions compared to Au ions.

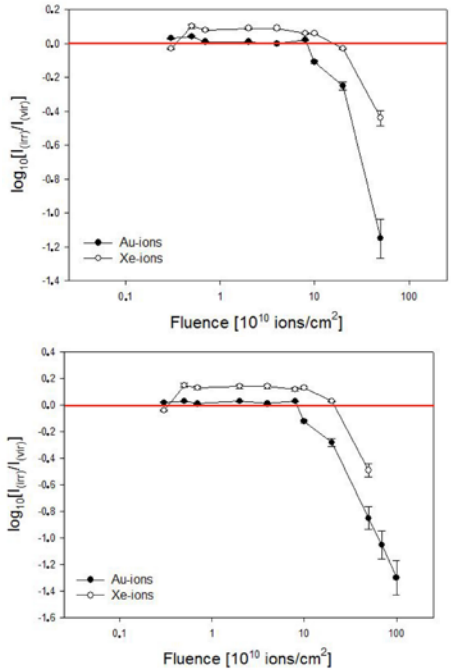

Fig. 2: Normalized intensities of antisymmetric stretching mode υ_3 (H_2O) at ~3493 cm^{-1} (top) and symmetric stretching mode υ_1 at ~3403 cm^{-1} (bottom) as a function of fluence for the irradiation with 4.8 MeV/u Au and Xe ions. The red line marks the value of the pristine sample.

Our results clearly show, that gypsum irradiated with high energy heavy ions loses crystal water creating monocline anhydrous Ca-sulfate. Based on our Raman spectroscopy data, there is no indication of a beam-induced phase transition. We conclude that gypsum exposed to cosmic radiation may steadily release water at the surface of Mars.

[1] Y. Liu et al., 40th Lunar and Planetary Science Conference (2009)
[2] J.F. Ziegler et al., *The Stopping and Range of Ions in Solids*, Pergamon, 1985
[3] S. Dedera et al., Nucl. Instr. Meth. B 365 (2015) 564
[4] S. Dedera. Dissertation, Univ. Heidelberg (2015)
[5] H. Nagabhushana et al., J. of Alloys and Compounds 482, (2009) 308
[6] B.J. Berenblut et al., Spectrochim. Acta 27A (1971) 1849

*Work supported by HGS-HIRe
#nicole.schoeppner@geow.uni-heidelberg.de

Ion-induced desorption and cleaning processes

A. Warth[1], *M. Bender*[*1], *L. Bozyk*[1], *D. Severin*[1], *F. Völklein*[2], *and C. Trautmann*[1]
[1]GSI, Darmstadt, Germany; [2]Hochschule RheinMain, Wiesbaden, Germany

Ion-induced desorption affects the performance of modern high intensity particle accelerators by decreasing the vacuum quality. In the past decade it was intensively investigated and could be described as enhanced thermal desorption after an ion impact [1]. The situation changes in next generation accelerators such as FAIR or Spiral2 where intensive ion beams directly impact on production targets resulting in critical vacuum breakdowns. For example, Spiral2 will deliver 5e14 ions/sec onto an unbaked target.

Goal and Experiments

We have measured desorption yields of gold coated copper targets with intermediate diffusion barrier of chromium, which is supposed to be the best system[1]. We tested in-situ cleaning methods to reduce the desorption yields from unbaked targets. Samples were precleaned with isopropanol, acetone and purified water. Subsequently, they were transferred into the UHV system of M1 through a load lock. Irradiation was carried out with Ca^{10+} ions of 4.8 MeV/u and with an ion current between 10^{-9} and 10^{-8}A. The background residual gas pressure was in the low 10^{-10} mbar regime and the subsequent pressure rise was determined by means of an ionizing vacuum gauge. Basically three in-situ cleaning-procedures have been applied and compared:

- thermal bake-out at different temperatures
- a 5 keV-Ar-Sputtergun at the exposition area
- the ion beam itself (beam-scrubbing) [2]

Figure 1 shows the evolution of the desorption yield subjected to the applied cleaning methods. For simplicity and comparision, the values are given in arbitary units of pressure rise per beam current (mbar/A) and normalized to the respective startingpoint of the measurement. Absolute yields are between 30 000 and 50 000 [3]. For each measured value Δp was recorded directly after reaching steady state. This short irradiation time was chosen to avoid target cleaning by the ion beam except for the beam scrubbing run, where the target was ought to be cleaned by the ion beam. The x-axis of the plot represents the total duration the cleaning was applied. Each set of values was fitted by a shifted exponential decay, resulting in an offset-value y_0. This value represents the lowest desorption yield that can be achieved with the respective cleaning method.

Conclusion

According to the results, shown in in fig. 1, thermal bake out is the most effective cleaning procedure. Sputter-

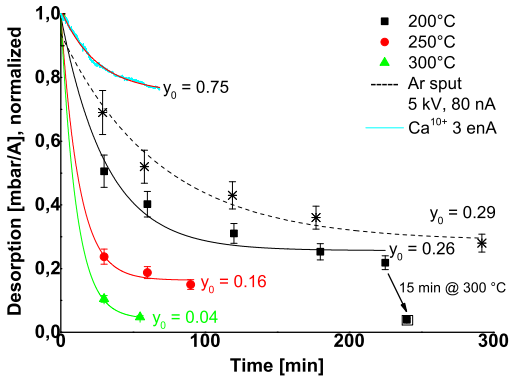

Figure 1: Normalized desorption yield (in a.u.) as function of different cleaning procedures and -time

cleaning can be as effective as a bake out at rather low temperatures (200° C) but only after several hours of sputtering. Optical investigations showed that by this method, even the metal coating was removed in large amounts. Most ineffective is the beam-scrubbing. The efficiency could be enhanced by increasing dE/dx with a heavier beam. Among the different temperatures, the cleaning is most efficient at higher temperatures. Within the error bars, it seems that the remaining desorption value y_0 is the lowest for highest temperatures. It will not become this low at lower temperatures. This conclusion is further supported by one value at 240 min, indicated by the arrow. Here, the sample, which was heated at 200° C for totally 225 min, was afterwards heated to 300° C for only 15 minutes. The result is a desorption yield comparable to 300° C samples. Finally, a further result shall be mentioned briefly. Another sample which has been baked at 200° C for in total 200 min has been exposed to atmosphere for a few hours. Afterwards it was reinserted into the UHV-system again and irradiated. The measured desorption yield was the same as before the exposure to atmosphere. That means that ion induced desorption of unbaked samples has a high contribution from gas diffusion out of the bulk. It further explains the above mentioned high yields. In the upcoming beam time it will be tested, if the samples can be treated ex-situ and the sustainability of the treatments under atmosphere.

References

[1] M. Bender et al., NIM **B** 267 (2009) 885–890

[2] E. Mahner, et al., Phys. Rev. ST AB 6, (2003) 013201

[3] M. Bender et al., J. Phys. Conference Series **599** (2015) 012039

* m.bender@gsi.de

DOI:10.15120/GR-2016-1

Swift heavy ion irradiation of interstellar dust analogues*

E. Dartois †[1], *M. Chabot*[2], *Th. Pino*[3], *K. Beroff*[3], *M. Godard*[4], *D. Severin*[5], *M. Bender*[5], *and C. Trautmann*[5, 6]

[1]Institut d'Astrophysique Spatiale (IAS), CNRS, Univ. Paris Sud, Université Paris-Saclay, F-91405 Orsay, France; [2]Institut de Physique Nucléaire d'Orsay, IN2P3-CNRS, Univ. Paris Sud, Université Paris-Saclay, F-91405 Orsay, France ; [3]Institut des Sciences Moléculaires d'Orsay (ISMO), CNRS, Univ. Paris Sud, Université Paris-Saclay, F-91405 Orsay, France; [4]Centre de Sciences Nucléaires et de Sciences de la Matière (CSNSM), CNRS/IN2P3, Univ. Paris Sud, Université Paris-Saclay, F-91405 Orsay, France; [5]GSI, Darmstadt, Germany; [6]TU Darmstadt, Germany

Motivation & Experiments

Interstellar cold dust grain particles are immersed in VUV and cosmic ray radiation environments influencing their physico chemical composition. As a result of these energetic interactions, carbonaceous dust particles evolve and release fragments feeding the interstellar gas phase chemistry. Cosmic ray ion irradiation of interstellar carbonaceous dust analogues is simulated experimentally at GSI, at high energies, to explore the species formed and potentially released in the gas phase. The dust analogues evolution is monitored in situ as a function of fluence at 40, 100 and 300 K, simultaneously with infrared spectroscopy (solid phase) and mass spectrometry (for the species released in the gas phase). The radiolytic CH stretch destruction and chemical species produced are measured. The cross-sections derived for the swift heavy ions irradiations are implemented in an astrophysical context.

Hydrogenated interstellar amorphous carbon and polyaromatic analogues films were prepared at IAS and ISMO (Orsay) by a plasma-enhanced chemical vapor deposition method (PECVD, IAS) and a low pressure premixed flat flame (ISMO), and deposited on a IR transmitting substrate under vacuum. This method has been described in previous works [1-4]. Swift ion irradiation experiments were performed at the M3-branch with $^{197}Au^{25+}$ (at $4.8 MeV/u$), $^{132}Xe^{21+}$ (at $4.8 MeV/u$) and $^{12}C^{2+}$ (at $3.6\ MeV/u$) projectiles in campaigns on July 2014 (Au), September 2014 (Xe) and September 2015 (C). These beams were coupled to the M3 beamline, a high vacuum chamber (a few 10^{-8} mbar) holding an infrared transmitting substrate, cryocooled down to about 40 K. The low temperature irradiations where followed by a post-irradiation temperature programmed desorption (TPD), to sublimate the species formed and trapped in the irradiated film. Gas phase species were monitored with mass spectra recorded with a quadrupole mass spectrometer (MKS MicroVision Plus, Fig.1). A ThermoFisher Scientific FTIR spectrometer (Nicolet 6700) was used to record the infrared film transmittance as a function of fluence during the irradiations, at 45° from the a-C:H film normal. Infrared spectra were also recorded during the TPDs.

* Work supported by GSI(UNILAC). Part of the equipment and missions, have been financed by the ANR and French INSU-CNRS program "Physique et Chimie du Milieu Interstellaire" (PCMI).

† emmanuel.dartois@ias.u-psud.fr

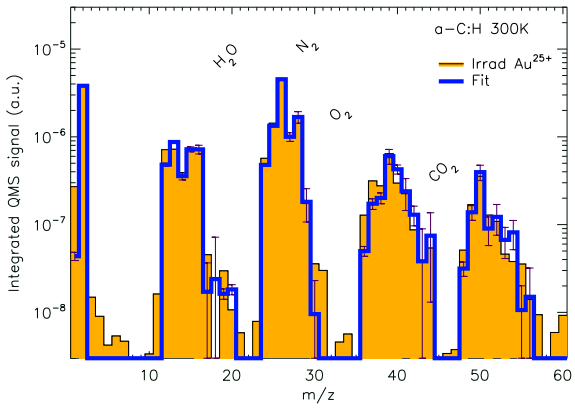

Figure 1: QMS integrated signal for the interstellar analogue a-C:H sample, irradiated ($^{197}Au^{25+}$) at 300K (orange bars). The best model fit for the retrieved carbonaceous species contributions is shown in blue. These species measured are then included in an astrophysical model

Results

The inclusion of the cross section measurements into an astrophysical CR model show that the hydrogenated amorphous carbon interstellar dust analogue are relatively resilient against cosmic rays, with astrophysical destruction time scales of 5×10^7 years and above, of the same order as the interstellar lifetime of an interstellar cloud. The experimentally observed release of small hydrocarbons (from CH_y to C_4H_y, e.g. Fig.1) upon CR interactions with dust will contribute to replenish the large hydrocarbons reservoir of the gas phase, and help in reconciling the actual discrepancies between astronomical observations and models in dense cloud interfaces. This work is submitted for publication in the Astronomy & Astrophysics journal.

References

[1] Alata, I., Jallat, A., Gavilan, L., et al. 2015, Astronomy & Astrophysics, 584, A123

[2] Carpentier, Y., Féraud, G., Dartois, E., et al. 2012, Astronomy & Astrophysics, 548, A40

[3] Godard, M., Féraud, G., Chabot, M., et al. 2011, Astronomy & Astrophysics, 529, A146

[4] Pino, T., Dartois, E., Cao, A.-T., et al. 2008, Astronomy & Astrophysics, 490, 665

Phase field simulation of fracturing of solids caused by heavy-ion beams*

A. Schlüter[†1,4], *C. Kuhn*[1], *R. Müller*[4], *M. Tomut*[3], *H. Weick*[3], *C. Trautmann*[2,3], *and P. Simon*[2,3]

[1]Computational Mechanics, University of Kaiserslautern, Germany; [2]Fachbereich Material- und Geowissenschaften, TU Darmstadt, Germany; [3]GSI, Darmstadt, Germany; [4]Institute of Applied Mechanics, University of Kaiserslautern, Germany

Intense high-energy particle beams that hit a solid almost instantaneously deposit a large amount of energy in the irradiated material. This causes thermal expansion and consequently mechanical loading of the body, which may even lead to disastrously macroscopic fracturing. The development of reliable numerical models that can predict such failure mechanisms is of primary interest for high-power accelerator facilities. The intention of the discussed phase field model is to predict and analyze this type of structural failure. The model regards the irradiated body as a linear elastic solid and neglects effects like phase transitions, i.e. melting, vaporization or ionization. In order to calculate the energy loss of the beam - which enters the energy balance equation of the model - the software ATIMA [1] is used. The thermomechanical behavior is described in terms of the displacement and temperature fields and the corresponding partial differential equations. An additional scalar phase field variable is introduced in order to represent cracks. The crack propagation law is found by a variational principle, that resembles Griffith's energy criterion of fracture mechanics. Eventually, this approach yields a set of coupled Euler-Lagrange equations that is solved with the finite element method.

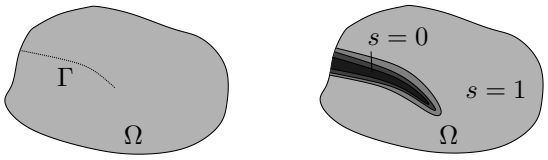

a) b)

Figure 1: a) Body with crack Γ and b) approximation of the cracks by a phase field $s(\boldsymbol{x}, t)$.

In order for the current model to be a suitable tool, three fundamental assumptions have to be justified:

- failure is due to brittle fracture,
- material parameters are assumed to be independent of temperature
- the energy loss of the ions is completely transformed into heat.

Under these assumptions, the thermomechanics of the regarded body Ω are described in terms of the displacements $\boldsymbol{u}(\boldsymbol{x}, t)$ and the temperature $\theta(\boldsymbol{x}, t)$. The body also might contain cracks Γ, see Fig. 1 a), which are approximated by a continuous phase field $s(\boldsymbol{x}, t) \in [0, 1]$. A value of $s = 1$ indicates undamaged material, whereas $s = 0$ represents broken material.

The governing partial differential equations that determine the evolution of the primary fields $\boldsymbol{u}$, θ and s can be found from Hamilton's principle. They are: the balance of momentum, the balance of energy and a phase field equation that describes crack growth. The energy equation contains a heat source term that models the effect of the beam on the solid. It is assumed that this heat source term is equal to the stopping power of the ions.

a) b)

Figure 2: a) Finite element setup and b) contour plot of the phase field $s(\boldsymbol{x}, t)$ for a cross section of the cylinder after exposure to an uranium beam.

The set of partial differential equation is solved by means of a finite element approach, see [2] for details. Fig. 2 a) shows the setup for a numerical experiment in which a cylinder (radius 5.5 mm) made of polycrystalline graphite is subjected to a 60 ns pulse of $5 \cdot 10^{11}$ ^{238}U ions with an energy of 1000 MeV/u. The resulting damage is concentrated in the center of the specimen as can be observed in the contour plot of the phase field parameter s, see Fig. 2 b).

References

[1] H. Geissel, C. Scheidenberger, P. Malzacher, J. Kunzendorf and H. Weick, "ATIMA" [Software], GSI, Available from *https://web-docs.gsi.de/ weick/atima/*

[2] A. Schlüter, C. Kuhn, R. Müller, M. Tomut, C. Trautmann, H. Weick and C. Plate, "Phase Field Modelling of Dynamic Thermal Fracture in the Context of Irradiation Damage", Continuum Mechanics and Thermodynamics (2015), p. 1

* Work supported by GSI

† aschluet@rhrk.uni-kl.de

DOI:10.15120/GR-2016-1

SAXS measurements of etched and un-etched ion tracks in apatite*

A. Nadzri[1,#], D. Schauries[1], P. Mota-Santiago[1], C. Trautmann[2,3], A. Hawley[4], P. Kluth[1]
[1]Australian National University, ACT, Australia; [2]GSI Helmholtzzentrum, Darmstadt, Germany; [3]Technische Universität Darmstadt, Darmstadt, Germany; [4]Australian Synchrotron, VIC, Australia

Small angle x-ray scattering (SAXS) is a non-destructive technique yielding information on the geometry and size distribution of nanometer sized objects in a sample. It can be used to study the morphology of etched and un-etched ion tracks in natural apatite with great precision [1-2]. In nature, track formation in apatite results from the spontaneous fission of inclusions of uranium. Etched tracks of fission fragments are used for dating and constraining the thermal history of geological samples.

This project investigates how differences in the un-etched track morphology translate into etched ion track dimensions, in particular the influence of different mineral compositions and crystal orientation of the tracks. Natural apatite [$Ca_5(PO_4)_3F$] samples from Durango, Mexico (DA) were irradiated at room temperature at the X0-beamline of the UNILAC of GSI with 2.3 GeV ^{209}Bi ions to simulate fission tracks. Irradiation fluences of 10^8 ions/cm^2 and 10^{11} ions/cm^2 were used to create well separated tracks. The former was applied to samples used for chemical etching experiment. Following the irradiation, the samples were chemically etched for 10 s in 0.55 M HNO_3. The resulting track morphology was investigated using SAXS at the Australian Synchrotron in Melbourne.

Scattering images from the SAXS measurements of the un-etched tracks in DA are illustrated in figure 1. Figure 1(a) shows an isotropic scattering image when the tracks axis is aligned with the x-ray beam confirming a circular track cross section while the highly anisotropic scattering image in figure 1(b) with two narrow streaks was observed when the sample was tilted by 10°, indicating the high aspect ratio of the ion tracks. Figure 1(c) presents the scattering image of the etched tracks in DA. The etched tracks exhibit hexagonal pattern when aligned with the x-ray beam indicating an etch-anisotropy in apatite yielding faceted etch pits with 6-fold symmetry. The streaks in figure 1 (b) and (c) can be extracted (by masking one of the streak as it is symmetric) to plot the scattering intensities as a function of scattering vector *q* as shown in figure 2. The strong oscillating scattering intensities yield information about the track radius and indicate monodisperse tracks with a sharp density change between the tracks and matrix material [3]. The hard cylinder fit (solid line) yields an average radius of 5.2 nm for the un-etched tracks and 25.5 nm for the etched tracks.

* Work supported by Australian Research Council (ARC) and the Australian Synchrotron (AS)
#allina.nadzri@anu.edu.au

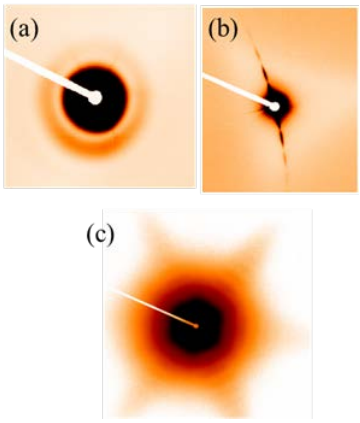

Figure 1: SAXS images of un-etched (a) and (b) and etched (c) ion tracks in Durango apatite. (a) and (c) correspond to the ion tracks aligned and (b) to the tracks when tilted by 10° with respect to the x-ray beam.

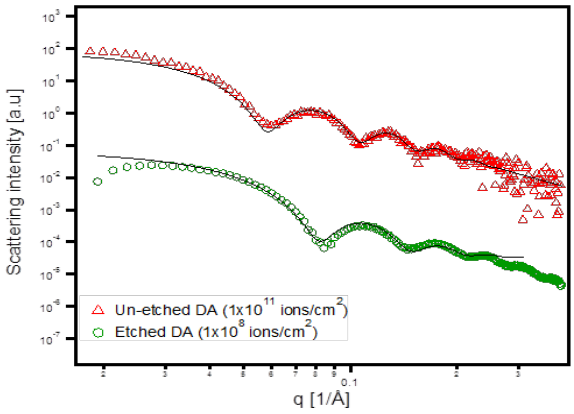

Figure 2: Scattering intensites as a function of scattering vector *q* for un-etched and etched ion tracks in Durango apatite. The spectra are offset for clarity.

These results show that SAXS can reveal details about the morphology of ion tracks in minerals and may help to understand the correlation between un-etched and etched ion tracks in natural samples and their dependence on mineral composition and track orientation.

References

[1] B. Afra *et al.*, Phys. Rev B 83 (2011) 064116
[2] P. Kluth et al., J. Appl. Phys. 110 (2011) 123520
[3] B. Afra et al., Nucl. Meth. Phys. Res. B 326 (2014)

DOI:10.15120/GR-2016-1

Chemical track etching of ion-irradiated dolomite

Baldur Knörr[1,#], Ulrich A. Glasmacher[1], Sebastian Dedera[1], Michael Burchard[1], Christina Trautmann[2]

[1]Institute of Earth Sciences, Heidelberg University; [2]GSI and Technische Universität Darmstadt, Germany

In geosciences, fission-track dating is one of the main methods of thermochronological analysis. Mineral samples are etched to convert tracks of fission fragments into surface etch pits with a channel that can be viewed and quantified under an optical microscope. Below a mineral specific temperature tracks accumulate over time due to the mineral's natural uranium content [1].

Dolomite ($CaMg(CO_3)_2$) is an important mineral formed in lacustrine environments and during diagenetic processes. To test the viability of the track etching method, we used dolomite crystals from Binntal, Switzerland and irradiated them with 11.1 MeV/u ^{197}Au ions to a nominal fluence of 1×10^6 ions/cm^2. During irradiation the crystals were covered with a hexagonal mask to create irradiated and non-irradiated areas on the crystal surface. A thin polycarbonate foil simultaneously irradiated was etched to determine the exact fluence applied.

Track etching of the irradiated dolomite samples was performed with a solution of hydrochloric acid (0.001 ± 0.0001 mol/l). The temperature of the etchant was thermally stabilized to 20 (± 0.1) °C using a heated water bath. The etchant was stirred with a magnetic stir bar. The etch pits were counted and their dimensions measured once every 15 min (± 10 s), using a reflected light Olympus BX 50 microscope and Stream Enterprise software. The etch pits exhibited a triangular shape and reached a diameter of 1-2 µm after 120 min of etching (Figs. 1, 2).

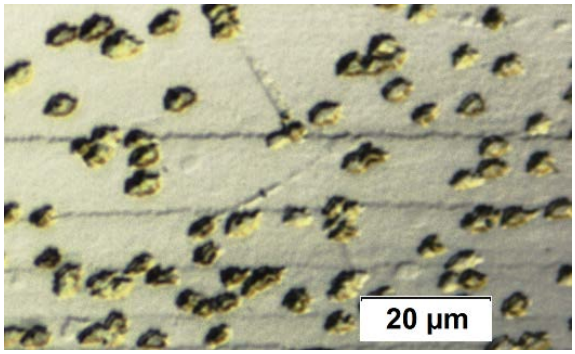

Figure 1: Etch pits on surface of irradiated dolomite (120 min, 20°C, 0.001 mol/l HCl, 50x magnification).

The polymer reference foil covering the dolomite samples during irradiation was etched in aqueous 6 mol/l NaOH solution for 90 min at 50 (± 0.1) °C. When exposed to the etchant, all ion tracks in the foil are converted into open channels that can easily be counted (Fig. 3).

The analysis of several microscope images yields an areal density of 1.75 (± 0.13) × 10^6 etch pits/cm^2 for dolomite and 1.76 (± 0.12) × 10^6 pores/cm^2 for the polymer foil. Within the experimental error, the amounts of etch pits matches the fluence applied.

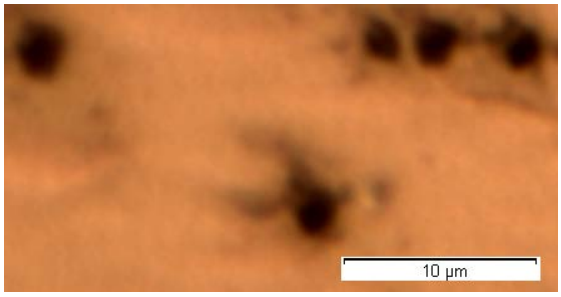

Figure 2: Etch pits on surface of irradiated dolomite (120 min, 20°C, 0.001 mol/l HCl, 200x magnification).

In conclusion, hydrochloric acid is a useful etchant for visualizing ion tracks in dolomite created by swift heavy ions. The etching solution applied converts all tracks into countable etch pits. Based on this result, a method of visualizing natural radiation damage in dolomite for the purposes of fission-track dating is currently under investigation. Experiments with fission tracks induced by covering dolomite samples with zircon grains, which emit fission fragments when irradiated with thermal neutrons, are in progress.

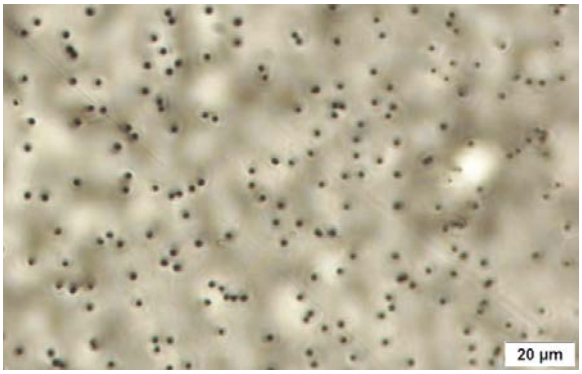

Figure 3: Etch pits on surface of irradiated polymer foil (90 min, 50 °C, 6 mol/l NaOH, 50x magnification).

[1] K.G. Bell, Uranium in carbonate rocks, Shorter contributions to general geology, 474-A (1963).

Acknowledgement

We would like to thank the Material Science section of GSI Darmstadt, Drs. M.E. Toimil-Molares and I. Schubert for sample irradiations and M. Brückner for the priceless support in the chemistry lab.

* Work supported by BMBF-Verbundprojekt 05KK7VH1 and 05K13VH1.

#Baldur.Knoerr@geow.uni-heidelberg.de

DOI:10.15120/GR-2016-1

Development of novel semiconductor process compatible nanopore membrane technologies*

A. Hadley[1,#], A. Nadzri[1], P. Mota-Santiago[1], D. Schauries[1], A. Hawley[2], C. Trautmann[3], P. Kluth[1]
[1]Australian National University, ACT, Australia; [2]Australian Synchrotron, VIC, Australia; [3]GSI Helmholtzzentrum and Technische Universität Darmstadt, Darmstadt, Germany

The ion track etching technique has become an established method for the industrial production of polymer nanoporous membranes [1]. Ion track etched membranes may also be fabricated in thin films typically used in semiconductor processing such as silicon dioxide (SiO_2) and silicon nitride (Si_3N_4), however the processes needed to reliably produce these structures are not well established. The ability to produce nanoporous structures in SiO_2 and Si_3N_4 is highly desirable as this provides the opportunity to integrate etched ion track membranes with standard semiconductor fabrication processes.

The aim of this work is to develop a better understanding of the ion track etching process in SiO_2 and Si_3N_4 and its dependence upon the un-etched track structure by using a novel combination of advanced electron microscopy and synchrotron based small angle x-ray scattering (SAXS) combined with Monte-Carlo (MC) simulation techniques. Functionalizing the pores using atomic layer deposition (ALD) will also be studied.

Free-standing SiO_2 and Si_3N_4 membranes were irradiated with 1.1 GeV ^{179}Au ions at the X0-beamline of the UNILAC. Additional irradiations with 185 MeV ^{179}Au ions were carried out at the ANU swift heavy ion accelerator facility. Low fluence (1×10^8 or 5×10^8 ions/cm^2) is chosen to avoid significant overlap of etched pores. Figure 1(a) shows nanopores etched in an SiO_2 film. The outer diameter of the pores is approximately 200 nm, and the thickness of the film is 1.8 μm. Figure 1(b) shows the surface of a Si_3N_4 membrane with etched nanopores. The outer diameter of the pores is approximately 100 nm. Both these samples were irradiated at GSI using the irradiation conditions given above.

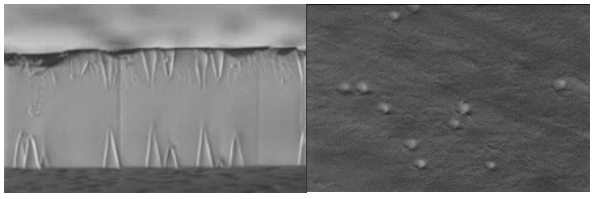

(a) (b)

Figure 1: (a) Cross-section SEM image of etched pores in an SiO_2 membrane. (b) SEM image of etched pores in Si_3N_4.

SiO_2 membranes were etched in a solution of 4% HF to form the nanopores. The membranes were etched from both sides to produce paired conical structures like those shown in Figure 1(a), and from one side to produce single cones (not shown). Pores in Si_3N_4 membranes were formed by etching in 85% H_3PO_4 at 150°C from both sides of the membrane. Using this technique pores with radii from around 10 nm (inner radius) up to 200 nm (outer radius) and with very uniform size distributions were formed.

SAXS is well suited for the characterisation of these structures because it allows us to leverage statistics since many uniform structures may be measured at once [2]. It also allows us to extract information about the morphology of the entire length of the nanopores. Figure 2(a) is an example of a SAXS image obtained from conical etched pores in a SiO_2 membrane etched from both sides to produce pairs of double cones. The highly complex image contains details about the pore morphology. Figure 2(b) is the calculated scattering intensity from a preliminary MC simulation of a double conical structure like that shown in Figure 1(a), with outer radius 105 nm, and inner radius 5 nm.

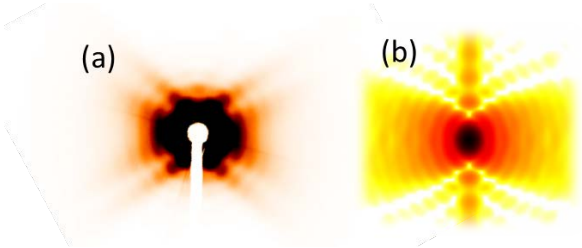

Figure 2. (a) SAXS image of double conical pores obtained at the SAXS/WAXS beamline of the Australian Synchrotron. (b) MC simulation of scattering intensity.

The fitting of SAXS images as a function of the orientation of the pores in the x-ray beam, and their simulation using Monte-Carlo simulation methods will enable us to accurately reconstruct complex 3D pore geometries. This will enable the dependence of the etched track upon the un-etched track structure to be studied, and will help to gain an understanding of the etching kinetics. The pores will then be able to be tailored for specific applications, like nano scale filtration and bio sensing.

References

[1] M.E. Toimil-Molares, Beilstein J Nanotechnology 2 (2012) 860
[2] P. Kluth et. al., Phys. Rev. Lett. 101 (2008) 175503

* Work supported by the Australian Research Council (ARC) and the Australian Synchrotron.
# andrea.hadley@anu.edu.au

Non-covalent functionalization of nanofluidic diodes

G. Pérez-Mitta[1], L. Burr[2,3], C. Trautmann[2,3], M.E. Toimil-Molares[2] and O. Azzaroni[1]*
[1]INIFTA, UNLP, La Plata, Argentina; [2]GSI, Darmstadt, Germany, [3]TU Darmstadt, Germany

Inspired by the capacity of biological systems to control the motion of fluids through protein channels, the field of nanofluidics has continuously grown during the past decade. One of its goals is designing artificial pores that are capable of mimicking the behaviour of their biological counterparts, exhibiting higher selectivity and functionality [1]. Their design requires the combination of various nanofabrication techniques to chemically and/or physically modify the channel in a controlled manner.

In this report, we show the construction of a nanofluidic ionic diode, whose ionic current output can be modulated with the pH of the solution. This was obtained by sputtering gold over the small opening of a conical polycarbonate nanochannel and then using this gold layer to deposit a monolayer of an amphoteric-amphipilic polymer (Amphipol) [2].

Single nanochannel membranes were fabricated by irradiating 30-µm thick polycarbonate foils with single Au ions (E ~ 2 GeV) at the UNILAC, and subsequently removing the created ion track by asymmetric selective chemical etching [3]. After etching, the nanochannel surface was functionalized first by sputtering a thin Au layer on the surface of the small channel opening, and then immersing the foil in a 1mg/ml amphipol aqueous solution for 2 hours. The film was subsequently thoroughly rinsed with water several times (Fig. 1).

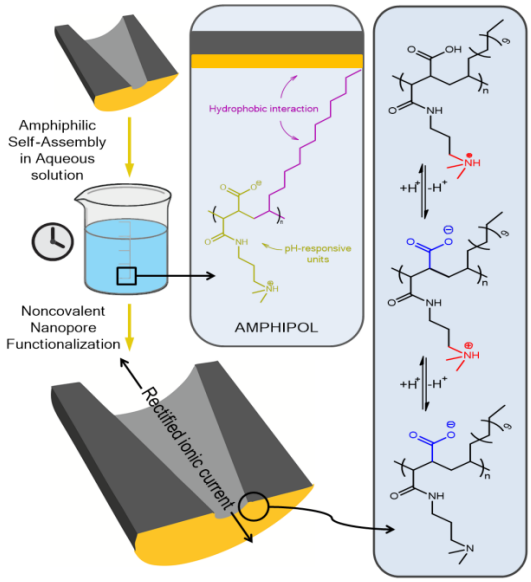

Figure 1: Modification of polycarbonate conical nanopore with a thin gold layer and amphipol molecules. The three different protonation states are shown.

The amphipol molecules interact hydrophobically with the surface exposing their protonable groups towards the surface. Further experiments using surface plasmon resonance (SPR) confirmed the modification process and also provided a value for the thickness of the amphipol layer of ~1 nm which is consistent with the formation of a monolayer over the surface.

Each amphipol monomer contains a tertiary amine and a carboxylic acid group (marked in red and blue in Fig. 1, respectively), which bear positive and negative charges in a proton concentration dependant manner. This is important because the surface charge of the modified channels can then be modulated with the pH of a contacting solution.

After functionalization of the nanochannels, current-voltage characteristics were measured at different pH values to explore the ionic transport across the channels (Fig. 2). The results showed a gating effect, reducing the current at positive voltages and increasing the current at negative voltages by increasing the pH.

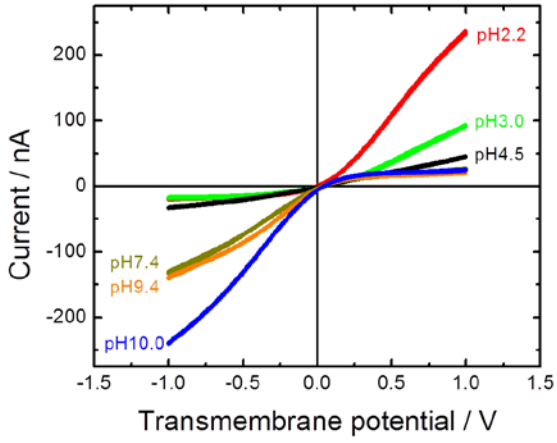

Figure 2: Current-voltage characteristics of an amphipol-modified nanochannel measured at different pH.

The importance of these results is that with a simple one-step modification the ionic transport across a nanochannel can be fully modulated by simply changing the pH of the electrolyte solution. Furthermore, by cycling the pH many times from pH 10 to pH 2 the reversibility of the system was proved.

[1] X. Hou et al., Chem. Rev. 40 (2010) 2385.
[2] Pérez-Mitta et al., Nanoscale 8 (2016) 1470.
[3] P. Serbun et al., Eur. Phys. J. Appl. Phys. 58 (2012) 10402.

* Work supported by DFG FOR1583
# gperezmitta@inifta.unlp.edu.ar

DOI:10.15120/GR-2016-1

Pyrophosphate sensing with bis(dipicolylamine) modified nanopores

M. Ali[1,2,#], S. Nasir[2], C. Trautmann[1,2], and W. Ensinger[2]

[1]GSI, Darmstadt, Germany; [2]TU Darmstadt, Germany.

Nanopores have gained remarkable attention as miniaturized sensing devices because of their unique ion transport properties. These nanosensors have been used for the detection of a variety of analytes [1]. The working principle is based on the modulation of transmembrane ion currents and electrical signals originated either by the passage of an analyte through the pore under an applied voltage or on the ligand-receptor interaction occurring when the analyte is introduced in the environment of the ligand-modified pore.

During recent years, much attention has been devoted to miniaturize the sensing devices for the selective detection of biologically important anions. Amongst the various phosphate anions, pyrophosphate (PPi) anion plays a vital role in different biological processes. PPi is a small negatively charged ($P_2O_7^{4-}$) analyte produced in the living organisms as a by-product of adenosine triphosphate (ATP) hydrolysis in the cellular system. This anion participates in a variety of enzymatic reactions controlling metabolic and energy transduction processes.

Fluorescent and colorimetric chemo-sensors exploit metal chelator ligands which transduce changes in the corresponding fluorescent or colorimetric signals on binding with PPi anion. Among the various metal complexes, zinc complexes based on two di(2-picolyl)amine [bis(DPA)] moieties have proved effective binders for the PPi sensing.

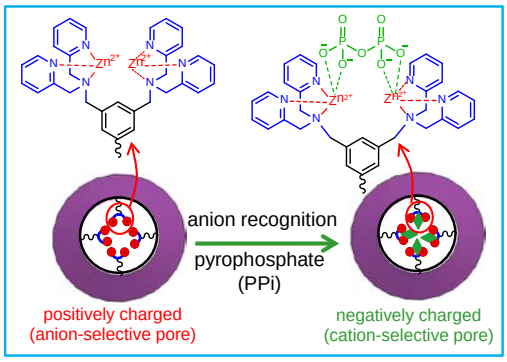

Figure 1: Cartoon representing changes in pore surface chemistry before and after binding of PPi anion with immobilized zinc complexes based on bis(DPA) moieties.

Single conical nanopores were fabricated in 12-µm thick polyethylene terephthalate (PET) membranes by asymmetric track-etching technique [2]. The pore surface is chemically functionalized with bis(DPA) ligands via carbodiimide coupling chemistry. Subsequently, the complexation of zinc ions is achieved by exposing the modified pore to a solution of zinc(II), leading to the formation of bis(Zn^{2+}–DPA) complexes (Fig. 1) [3]. The as-prepared (unmodified) conical pore preferentially transported cations due to the presence of $–COO^-$ groups and shows current rectification. Upon complexation, the bis(Zn^{2+}–DPA) complexes imparted positive charges to the pore surface, leading to the inversion of current rectification (Fig. 2a) [3].

After the successful anchoring of bis(Zn^{2+}–DPA) complexes, we studied the sensing capability of the sensor towards phosphate anions, particularly PPi. Figure 2b shows the changes observed in the *I–V* curves when the bis(Zn^{2+}-DPA)-modified pore was exposed to different phosphates (sodium salts) such as monohydrogen phosphate (HPO_4^{2-}), dihydrogen phosphate ($H_2PO_4^-$), adenosine monophosphate (AMP), adenosine diphosphate (ADP), adenosine triphosphate (ATP) and pyrophosphate (PPi). From the *I–V* characteristics, we conclude that the modified pore displays a remarkable specificity towards PPi anions: no significant changes were observed in the *I–V* characteristics of the single pore exposed to HPO_4^{2-}, $H_2PO_4^-$, AMP, ADP and ATP (phosphates concentrations of 1 µM in the background electrolyte were not recognized by the bis(Zn^{2+}–DPA) moieties). On the contrary, PPi selectively bound with the bis(Zn^{2+}–DPA) moieties under these conditions, imparting negative charge to the pore surface, with the resulting ionic current rectification.

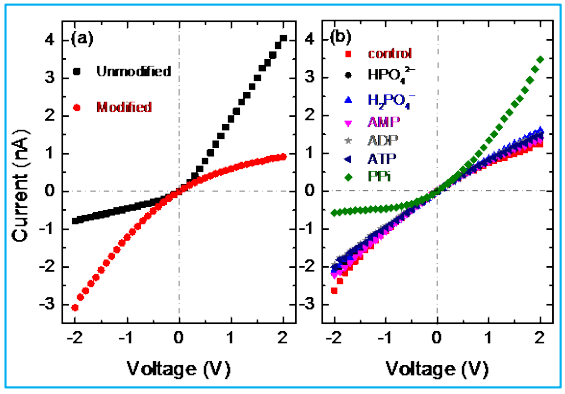

Figure 2: *I–V* curves of a single conical nanopore (*d* ~19 nm and *D* ~480 nm), (a) with carboxylate groups and bis(Zn^{2+}–DPA) moieties on the pore surface and (b) bis(Zn^{2+}–DPA)-modified nanopore on exposure to 1.0 µM concentration of various phosphates.

In summary, label-free specific detection of PPi anion using a nanofluidic sensing device based on a single asymmetric pore was demonstrated experimentally. Such nanofluidic sensors could readily serve as a monitor of biological important reactions, *e.g.*, real-time DNA sequencing.

[1] S. Howorka and Z. Siwy, *Chem. Soc. Rev.* 38 (2009) 2360.
[2] P. Y. Apel *et al. Nucl. Instr. Meth. B* 184 (2001) 337.
[3] M. Ali *et al. Small;* DOI: 10.1002/smll.201600160

M.Ali@gsi.de

Synthesis and application of ZnO nanowire-based 3D networks for enhanced photo-electrochemical water splitting*

L. Movsesyan[1,2,#], A.W. Maijenburg[1], G. Mul[3], W. Sigle[4], C. Trautmann[1,2], M.E. Toimil-Molares[1,†]
[1]GSI, Darmstadt, Germany; [2]TU Darmstadt, Germany; [3]University of Twente, The Netherlands, [4]MPI for Solid State Research, Stuttgart, Germany

By combining ion-track nanotechnology and electrochemical deposition, three-dimensional (3D) ZnO nanowire networks were synthesized in specifically designed track-etched membranes. Polycarbonate (PC) foils (thickness 30 µm) were irradiated with ~2 GeV Au ions at the UNILAC X0-beamline. As each ion passing through the foil produces an individual ion track along its path. Intersecting tracks were obtained by irradiating the foils four times in consecutive steps, each time from a different direction under an angle of 45˚ to the PC surface normal. In total a fluence of four times 2×10^9 ions/cm^2 were applied.

The irradiated foils were symmetrically etched in 6M sodium hydroxide (NaOH) at 50˚C for 7 min. The etching resulted in the formation of a network of nanochannels (diameter 150 nm). Replicates of the channels were formed by electrodeposition of ZnO inside the membranes. The deposition was performed in an aqueous electrolyte (0.1 M $Zn(NO_3)_2{\cdot}6H_2O$) and by applying a potential of -1 V vs Ag/AgCl at 60 ˚C. After membrane dissolution in dichloromethane (CH_2Cl_2), free standing ZnO nanowire networks were obtained [1] as shown in the scanning electron microscopy (SEM) image in Fig. 1a.

These structures were tested as photoanodes in a photo-electrochemical (PEC) cell for water splitting. Due to their one-dimensional shape and geometrical orientation, nanowire networks promise more efficient light absorption and charge carrier separation as well as improved transport to the surface of the electrode compared to bulk material. To protect ZnO from photo(electro)chemical corrosion, the samples were coated with a very conformal 20-nm thick layer of TiO_2 by atomic layer deposition (ALD). The thickness of the ALD layer was confirmed by electron energy loss spectroscopy (Fig. 1b). PEC measurements were performed using bare and coated ZnO networks and corresponding films (electrochemically deposited by applying cyclic voltammetry) as reference. The samples were immersed in a 0.1 M K_2SO_4 aqueous solution (pH 5.6) and served as photoanodes. The photoresponse was recorded by applying linear sweep voltammetry (LSV) sequentially in the dark and under illumination. In Fig. 1c, LSVs under chopped light are shown. Networks with and without TiO_2 coating produced higher photocurrents than the corresponding reference films due to better transport properties and large surface of the wires. The addition of TiO_2 increased the photocurrent significantly for both cases. Since TiO_2 is an n-type semiconductor material, more charge carriers can be generated in ZnO/TiO_2 system. The ZnO/TiO_2 network has a lower dark current for the complete potential range as compared to the bare ZnO network. The increase of dark current for the uncoated system is related to photocorrosion of ZnO, as well as the direct access of electrolyte to the gold substrate at the bottom of the network. After PEC measurements, all samples were analyzed by SEM in order to investigate the morphology changes arising from corrosion. Our ZnO/TiO_2 nanowires did not undergo significant changes, although empty TiO_2 nanotubes were observed in a small area of the sample, indicating dissolution of ZnO wires through the TiO_2 shell. In contrast, the diameter of the wires in the bare ZnO network was reduced from 150 to 120 nm, and the height decreased from 25 to 15 µm. This decrease is an obvious consequence of photocorrosion of ZnO. In some areas of the network the nanowires turned into flakes with dimensions in the micrometer range. So, besides enhancing the photocurrent, TiO_2 also serves as a protection layer. The high surface-to-volume ratio makes these 3D nanowire networks promising photoelectrodes for enhanced water splitting.

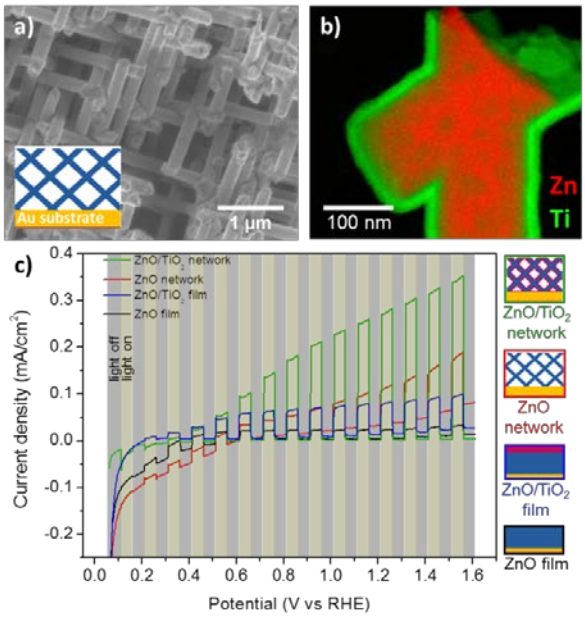

Figure 1: a) SEM image of ZnO nanowire network with an inset showing a cross-sectional scheme of the network on a gold substrate, b) EELS image of a junction of two crossing ZnO/TiO_2 nanowires, c) linear sweep voltammograms of bare ZnO, core/shell ZnO/TiO_2 nanowire networks and corresponding films under chopped light.

[1] L. Movsesyan, *et. al.*, Semicond. Sci. Technol., 31 (2016) 14006.

* Work supported by Beilstein Institute and by DFG, SPP 1613.
# L.Movsesyan@gsi.de
† M.E.ToimilMolares@gsi.de

DOI:10.15120/GR-2016-1

Thermoelectric transport measurements on antimony nanowire networks

M.F.P. Wagner[1,2,3,#], *M.E. Toimil-Molares*[1], *C. Trautmann*[1,3], *F. Völklein*[2]
[1]GSI Helmholtzzentrum, Darmstadt, [2] RheinMain University of Applied Sciences, Rüsselsheim, [3]Technische Universität Darmstadt, Darmstadt, Germany

Nanowire networks (NWNW) are ideal candidates to be used as elements in thermoelectric microsystems. They exhibit a highly improved mechanical stability compared to arrays of parallel oriented nanowires [1]. Theoretical calculations predict a decrease of thermal conductivity in nanostructures with an concurrent enhancement of the thermoelectric figure of merit ZT of 20%-150% [2]. To synthesize antimony NWNWs the ion-track nanotechnology is applied. In a first step, polycarbonate foils are irradiated at the X0-beamline of the UNILAC under 45° incidence angle from four directions. After each tilt angle, the foil is turned by 90° around the foil normal. The irradiated foils are then chemically etched in 6M NaOH at 50°C, converting the ion tracks into cylindrical pores. These pores are filled with Sb using a pulsed electrodeposition process [3]. This method allows homogeneous growth of the network and complete control over structural parameters such as wire density, wire diameter, wire alignment, etc.. In order to characterize the Seebeck coefficient, as well as the electrical and thermal conductivity of a sample in cross plane, a layer system as in Fig. 1 is used [3]. A thin stripe (4 mm x 1 mm) is cut from the prepared network. The stripe with the network embedded in the template, is glued onto a silicon wafer using a silver filled epoxy. The silver epoxy as well as a thin layer of gold on the backside of the sample, is used as electrical contacts. To generate a temperature gradient a $Bi_{0.9}Sb_{0.1}$ heater is evaporated on top of the stack after preparing a thin electrical isolation layer of Al_2O_3 using atomic layer deposition. Figure 2 presents normalized resistance (a), Seebeck coefficient (b) and thermal conductivity (c) of two different nanowire arrays. Also shown are reference measurements (c) of the thermal conductivity of unirradiated 30-µm thick PC foil (green triangles) as well as of 100-µm thick borofloat glass (blue diamonds) [3]. Both measurements fit well to literature values (0.21 W/mK for polycarbonate and 1.15 for borofloat glass). First complete sets of thermoelectric measurements were performed on the following two samples: (i) cross-linked NWNW (length 30 µm, average wire diameter ~150 nm, wire density ~2.8×10^9 cm^{-2}) (red squares) and (ii) parallel nanowire array (thickness 30 µm, average wire diameter ~125 nm and wire density ~1×10^8 cm^{-2}) (black dots). Figure 2c displays the thermal conductivities of the NWNWs between 290 and 370 K. The thermal conductivity values of the nanowire-polymer composites are very low, only slightly above the thermal conductivity of pure polycarbonate. For the system consisting of a parallel nanowire array we see an increase in the thermal conductivity for increasing temperatures compared to NWNW.

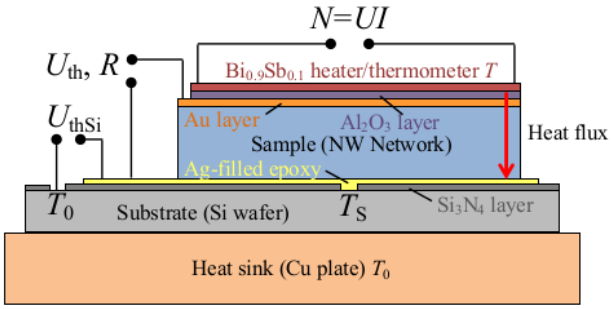

Figure 1 Experimental setup for the characterization of cross-plane thermoelectric properties of nanowire arrays.

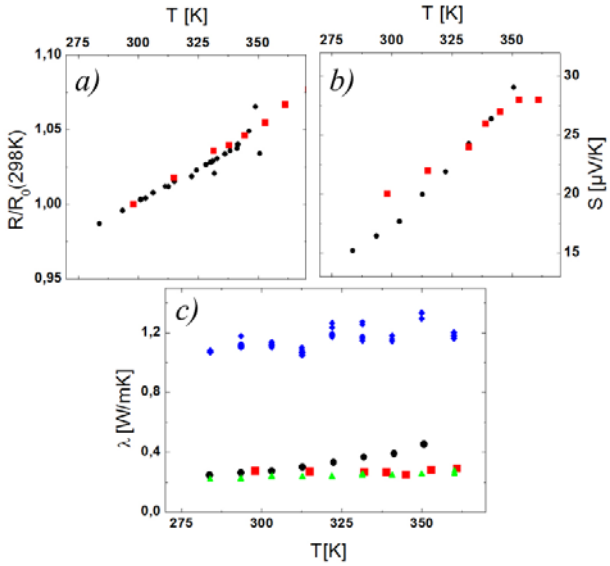

Figure 2 Properties of different Sb nanowire arrays as a function of temperature. The nanowire arrays embedded in a 30 µm thick PC template consist of nanowire network with average wire diameter ~150 nm and nanowire density ~2.8×10^9 cm^{-2} (red squares) and of a parallel nanowire array (average wire diameter ~125 nm and nanowire density ~1×10^8 cm^{-2} (black dots): a) electrical resistance R (normalized to the resistance R_0 at room temperature), b) Seebeck coefficient and c) thermal conductivity including also data of an unirradiated 30-µm thick PC foil (green triangles) and 100-µm thick borofloat glass (blue diamonds).

[1] Rauber et al., Nano Lett. 11 (2011) 2304
[2] O. Roslyak and A. Piryatinski, cond-mat.mes-hall, arXiv:1501.03229v1 (2015)
[3] Wagner et al., Phys. Status Solidi A 213 (2016) 610

* Work supported by DFG, SPP 1386
# F.M.Wagner@gsi.de

Vibrational response of single copper-nanowires using an optical pump and probe approach

C. Jean[1], L. Belliard[1,], T.W. Cornelius[2], B. Perrin[1], L. Becerra[1], O. Thomas[2], M.E.Toimil-Molares[3], M. Cassinelli,[3,4]*

[1]Institut des NanoSciences de Paris, France; [2]Aix-Marseille Universite, France;[3]GSI, Darmstadt, Germany, [4]TU Darmstadt, Germany.

The vibrational resonances of a certain object can be tuned by its size, shape, and local environment. In nanoscale systems, the eigenmodes exhibit frequencies from few 10 GHz up to 1 THz, and time-resolved optical spectroscopy is a powerful method to address such high frequencies. In these experiments, ultra-short femtosecond pump pulses induce a fast lattice heating by electron-phonon coupling, and the associated thermal expansion in the investigated object is optically detected by a time delayed probe pulse. Initially measurements were performed on nanoparticle ensembles to work with high signal to noise ratios. However, even though the nanoparticles synthesis processes are nowadays more and more controlled, the vibrational response of the assemblies is always strongly affected by the inherent size and shape distribution of the nanoparticles. In order to overcome this drawback, measurements on single nanoparticles have been recently reported. In the case of supported nanoparticles, there is an acoustic energy transfer into the substrate, and as a direct consequence the resonators exhibit low quality factors. Even if the measurements are performed on a single nanoparticle, broad peaks are revealed on the Fourier spectrum, and thus a fine estimation of the elastic properties is very challenging.

In this work, copper nanowires were synthesized by electrodeposition in polycarbonate (PC) etched ion-track membranes, prepared at GSI by heavy ion irradiation and subsequent chemical etching. After PC dissolution in dichloromethane, the wires were dispersed onto Si wafers which had been previously structured with periodic trenches (Figure 1). In this way, any mechanical coupling to the substrate is supressed increasing the elastic confinement of the first and second breathing modes, and leading to quality factors of one order of magnitude larger than previously reported for supported wires [1]. Figure 2 shows the transient sample reflectivity (ΔR/R) measured on a single freestanding Cu nanowire with diameter 200 nm. The fast Fourier transform reveals the first and second acoustic features located around ~ 15.6 and ~ 39.6 GHz associated with the excitation of the first and second harmonic breathing modes. Additionally, we have reported GHz acoustic phonon wave guiding in free standing single copper nanowires [2].

These experiments provide a unique way to independently obtain geometrical and mechanical nanomaterial characterization.

#laurent.belliard@upmc.fr

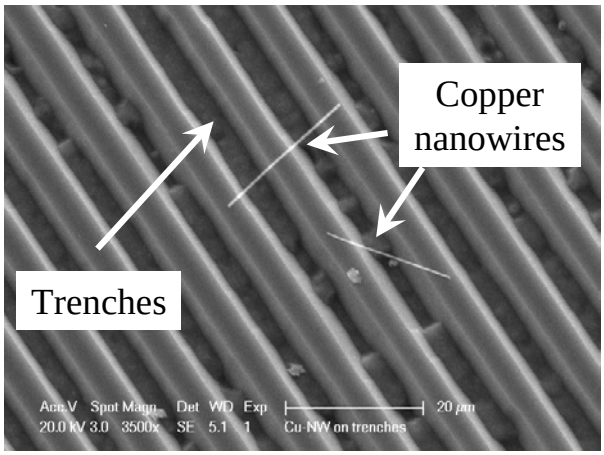

Figure 1: Scanning electron microscopy image of single copper nanowires suspended over trenches.

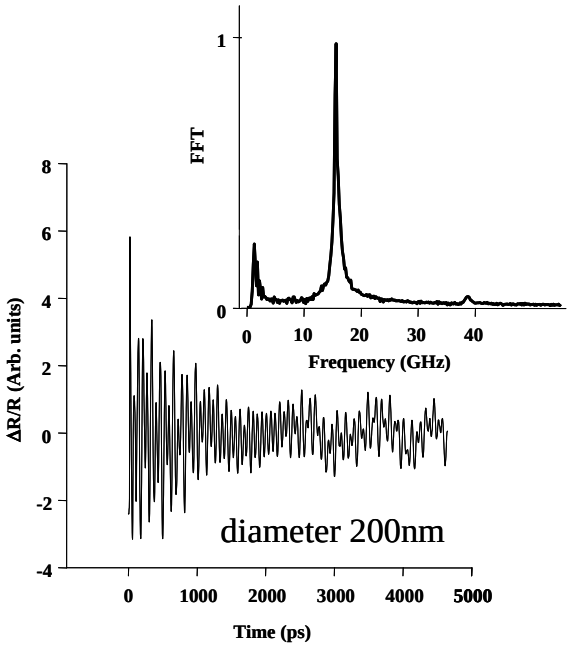

Figure 2: Transient sample reflectivity obtained on a single 200-nm diameter copper nanowire and the associated FFT spectrum.

References

[1] L. Belliard et al., J. of Appl. Phys. 114 (2013) 193509
[2] C. Jean et al., J. Phys. Chem. Lett. 5 (2014) 4100.

DOI:10.15120/GR-2016-1

High energy density physics problems related to the Future Circular Collider*

N.A. Tahir[1], *F. Burkart*[2], *R. Schmidt*[2], *A. Shutov*[3], *D. Wollmann*[2], *and A.R. Piriz*[4]

[1]GSI, Darmstadt, Germany; [2]CERN, Geneva, Switzerland; [3]IPCP, Chernogolovka, Russia; [4]UCLM, Ciudad Real, Spain

In this contribution we report simulation results of physical conditions induced in a solid copper cylindrical target by the Future Circular Collider (FCC) proton bunches. These simulations have been carried out using an energy deposition code FLUKA and a 2D hydrodynamic code, BIG2, iteratively. Although the protons will be accelerated to a maximum energy of 50 TeV in the FCC, for the present calculations we considered 40 TeV protons. The bunch intensity is 10^{11} protons, the bunch length is 0.5 ns, bunch separation is 25 ns and the focal spot size is characterized with standard deviation, σ = 0.2 mm. We consider a solid copper cylindrical target that is 5 m long and has a radius of 2 cm. The beam is incident perpendicular to one face of the cylinder so that the beam and the target axis coincide. At t = 1250 ns, when only 50 out of 10600 bunches have been delivered, a maximum specific energy of about 220 kJ/g has been deposited along the target axis. This high energy deposition leads to strong heating of the target material.

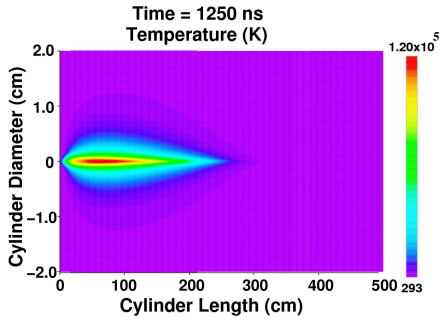

Figure 1: Temperature distribution after delivery of 50 bunches.

Fig. 1 shows that the maximum temperature induced by the energy deposition is about 10^5 K while Fig. 2 shows a pressure of around 45 GPa and the pressure has been distributed in the target due to the shock propagation. Fig. 3 shows the density reduction along and around the axis due to the shock propagation. The physical state of the target at this time is presented in Fig. 4. It is seen that due to the extreme conditions of temperature and pressure, the target material has gone through phase changes including melting, liquid phase and a weakly ionized plasma state. This can cause pollution of the accelerator components and the accelerator environment. These calculations clearly show that an accidental release of even a very small fraction of the FCC beam energy can lead to serious problems. It is therefore extremely important to design a robust machine protection system.

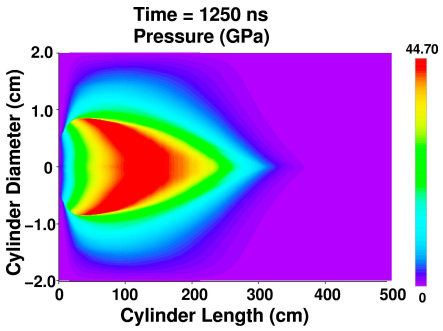

Figure 2: Pressure distribution corresponding to Fig. 1.

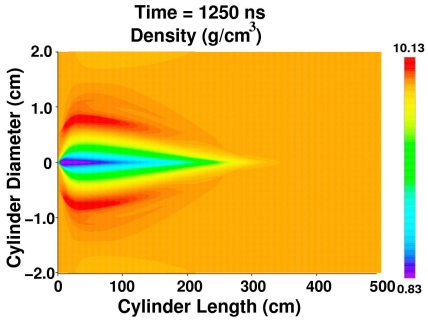

Figure 3: Density distribution corresponding to Fig. 1.

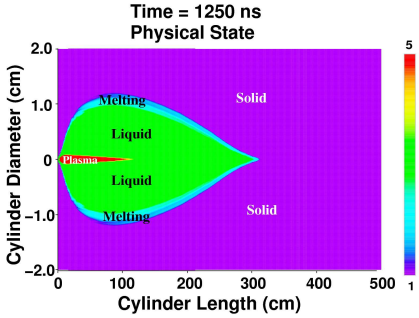

Figure 4: Target physical state corresponding to Fig. 1.

* Work supported by GSI and CERN

DOI:10.15120/GR-2016-1

Metallic target emission in the 0.5-6 GHz range after irradiation by an ultra-high intensity laser

S. Hulin[1], J-L. Dubois[1], J. Ribolzi[2], M. Bailly-Grandvaux[1], J. J. Santos[1], A. Poyé[3], B. Cassany[2] and V. Tikhonchuk[1]

[1]Univ. Bordeaux, CNRS, CEA, CELIA, FR-33405 Talence, FRANCE; [2]CEA-CESTA, 33114 LeBarp, FRANCE;
[3] Laboratoire de Physique, CNRS UMR-5672, Ecole Normale Supérieure de Lyon, 69364 Lyon Cédex 07, FRANCE

We are interested in understanding the process of intense electromagnetic emission during laser-solid interaction on powerful laser system [1]. To that purpose we have developed a specific experiment based on a simple target fixed to a specific target holder which allows us to unambiguously measure both the electromagnetic emission and the current circulating inside the target. Previously we have realized several experiments on low energy laser systems (<1 J) and shown that the integration of the measured current gives the charge of the target (the amount of electrons that escape from the target), that the electromagnetic emission is proportional to this charge and that it is spectrally shaped by the target holder geometry [2][3]. Our main goal in performing an experiment on PHELIX is to prove that all these observations remain valid on high energy laser systems.

The difficulty in reproducing experiments initially performed at low energy on a high energy laser system such as PHELIX is that most of the techniques used before have to be adapted. We expect signals which can be 400 higher than what was previously measured. Moreover, the electromagnetic emission we want to characterize is the source of an important noise. To perform valid measurements it is then necessary to strongly and correctly shield the measure chain.

During the 5 days that were devoted to our experiment we have been able to perform 28 shots among which 20 were completely successful. The 8 “lost” shots were mainly due to the difficulty we had in finding a correct configuration to efficiently shield the detectors, cables and oscilloscope against the strong electromagnetic perturbation. However, this work was worth to be done because the shape of the electromagnetic perturbation is very similar to the shape of the expected signal as can be seen on Figure 1. It is then very easy to make the mistake of considering the measurement as valid whereas it is just noise.

The laser energy was tuned from 10 J to 200 J with a fixed duration of 500 fs but we also performed few shots at 10 ps for 200 J. With this exploration we have been able to validate our model and our setup. At maximum energy and for the shortest duration we measured a maximum current of 4360 A for a maximum charge of 1.5 µC, and a magnetic field that could reach 3000A/m (equivalent electric field E = 1.13 MV/m) at 20 cm of the target. We have also discovered that the shunt which helps for measuring the current is behaving differently on high energy laser systems and that saturation effects occur for laser energies over 10 J even if the measurements remain valid. It was also the first time that the two components of the magnetic field (radial and tangential) were measured simultaneously. The result is in total agreement with what was expected (no radial component as can be seen on Figure 2 bottom) and reinforce the validity of our description of the process.

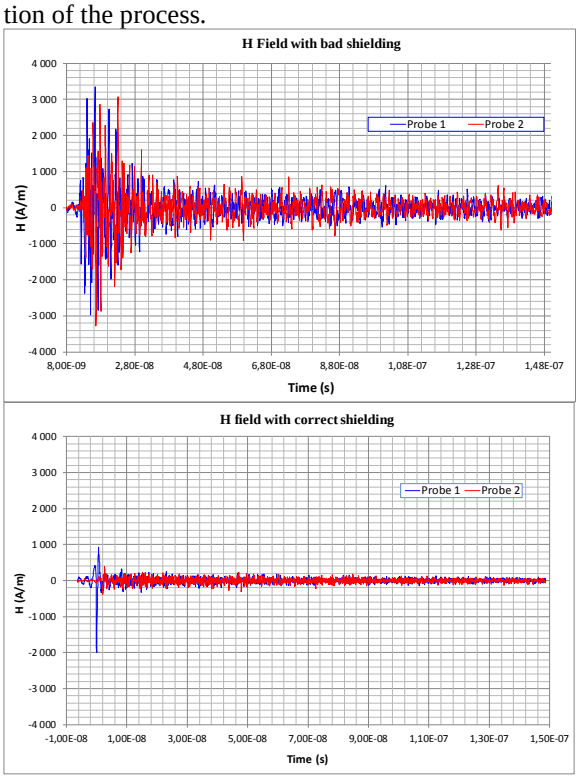

Figure 1 : *comparison of two equivalent laser shots with a bad (top) and a correct (bottom) shielding.*

Acknowledgments

We are very grateful to GSI for the access to the PHELIX laser facility and have strongly appreciated the professionalism of the PHELIX laser team. We acknowledge financial support from the French National Agency (ANR) in the framework of the “Investments for the future” program IDEX Bordeaux-LAPHIA (ANR-10-IDEX-03-02)

References

[1] Mead *et al.* , Rev. Sci. Instr. **75**, 4225 (2004)
[2] Dubois *et al.* , Phys. Rev. E **89**, 013102 (2014)
[3] Poyé *et al.* , Phys Rev. E **91**, 043106 (2015)

DOI:10.15120/GR-2016-1

Operation and improvements of PHELIX

S. Götte[1], *C. Brabetz*[1], *C. Bruske*[1], *U. Eisenbarth*[1], *M. Kreutz*[1], *S. Kunzer*[1], *D. Reemts*[1], *T. Stöhlker*[1,2], *L. Tymura*[1], *F. Wagner*[1,2], *B. Zielbauer*[1,2], *and V. Bagnoud*[*1,2]

[1]GSI, Darmstadt, Germany; [2]Helmholtz Institute Jena, Germany

The *P*etawatt *H*igh *E*nergy *L*aser for heavy *I*on E*x*periments (PHELIX) is a user facility of GSI that has been serving the international user community since 2008 and acts as one of the main experimental capability of the plasma physics department. PHELIX is a versatile nanosecond and sub-picosecond laser delivering pulses above 100 J and in a peak-power range up to 500 TW that are particularly well suited to generate hot nanosecond plasma, accelerate particles or study novel x-ray sources. In 2015, PHELIX mainly focused on providing beam-time granted by the GSI director for experiments recommended after a peer-review process by the PHELIX committee. In total, thirteen experiments were conducted: four of these were made at the UNILAC experimental area, where one was done in combination with the ion beam available at this site and another one used the high frequency equipment of the UNILAC. The rest was done at the in-house experimental area at the PHELIX building. Details about the various experimental beam times delivered by the laser are described in the plasma physics section of this annual report [1 ... 9]. Several peer-reviewed articles were published in 2015 based on results of experiments performed at PHELIX [10 ... 19]. Since it takes time to publish results afterwards, most of these took place in the year(s) before.

Operation and improvements

As in the past, about half of the 260 working days were spent to prepare and to perform external beam times (see fig. 1). The PHELIX shot data base registered 709 shots on target. Only 3.4 % of these are marked as failed which again shows the good performance of the laser system in its eighth year of operation. To keep this reliability, 37 % of the time had to be spent to maintenance. Two internal beam times took 9 % of the available time while the shutdown period was reduced to a few days only.

One of the internal beam times were done in order to gain better control of the wavefront quality. This effort lead to an increase of the encircled energy in the laser focus on target which has direct impact to laser ion acceleration techniques as pointed out in [9]. As a result, new work procedures have been established and came to daily operation in between.

Outlook

PHELIX continues its quality -improvement effort to deliver reliable and accurately measured laser parameters for external experiments in 2016. Besides this, it is planned to increase the repetition rate of the pre-amplifier section to somewhat of a few shots per minute for dedicated high repetition rate experiments with energies at the Joule level [20].

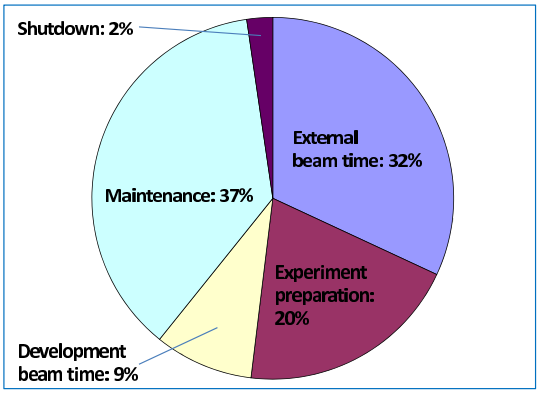

Figure 1: PHELIX usage in 2015

References

[1] O. Deppert et al., this report
[2] A. Kleinschmidt et al., this report
[3] B. Landgraf et al., this report
[4] D. Khaghani et al., this report
[5] R. Benocci et al., this report
[6] J. Y. Mao et al., this report
[7] D. Jahn et al., this report
[8] R. Wilson et al., this report
[9] F. Wagner et al., this report, and Phys. Rev. Lett., accepted
[10] S. Busold et al., Scientific Reports, 5:12459, DOI: 10.1038/srep12459 (2015)
[11] R. S. Belikov et al., Quantum Electron. **45**, 5 (2015)
[12] W. Cayzac et al., Phys. Rev. E **92**, 053109 (2015)
[13] C. Brabetz et al., Phys. Plasmas **22**, 013105 (2015)
[14] B. Ecker at. al., J. Phys. B **48**, 133009 (2015)
[15] B. Landgraf et al., Opt. Express 23(6):7400-6, DOI: 10.1364/oe23.007400 (2015)
[16] A. Ortner et al., NIM B 343 (2015), and Phys. Rev. E **91**, 023104 (2015)
[17] D. R. Rusby et al., J. Plasma Phys. 81.05: 475810505 (2015)
[18] G. G. Scott et al., New J. Phys. **17**, 033027 (2015)
[19] F. Wagner et. al., Phys. Plasmas, **22**, 063110 (2015)
[20] U. Eisenbarth et al., this report

* v.bagnoud@gsi.de

Upgrade of the PHELIX Pre-Amplifier towards higher repetition rates *

U. Eisenbarth[†1], *S. Götte*[1], *S. Kunzer*[1], *D. Reemts*[1], *B. Zielbauer*[1], *and V. Bagnoud*[1]
[1]GSI, Darmstadt, Germany

The PHELIX Pre-Amplifier is a flashlamp-based Nd:glass laser amplifier system with a typical pulse output energy of up to 10 J and a repetition rate of one shot every 3 minutes. This limitation mainly arises from thermal wavefront deformations such as defocus, astigmatism and higher order aberrations as well as birefringence effects. Nowadays several experiments such as X-ray generation or laser particle acceleration demand higher shot rates allowing more systematic studies on the investigation of the acceleration processes as well as improvements of the used targets.

In the past year, significant progress has been achieved on the way towards higher pulse repetition rates. Based on detailed studies on the characterization of a flashlamp-based amplifier head an improved pre-amplifier system has been designed. These studies also represent an important milestone for the first stage of a system upgrade towards higher performance.

In order to increase the repetition rate, the 45 mm amplifier head as well as a new pulsed power system driving the flashlamps have been developed in a separate test setup. New Nd:glass laser materials (Schott APG1 and Siom W31) exhibiting higher heat conductivity coefficients have been tested with respect to wavefront aberrations and gain while operated at repetition rates up to one shot every 15 s.

If the waiting time between two shots is shorter than the typical time constants for cool-down a pile-up behavior can be observed. As it turns out, the overall wavefront aberration (peak to valley value) over many shots however does not increase exceeding all limits but approaches a steady state, whose absolute value is determined by the repetition rate (see figure 1). Due to this steady state, stable operation can be achieved employing adaptive optics in order to compensate for these aberrations. A more detailed wavefront analysis shows that the defocus aberration contributes to more than than 80 % of the overall wavefront error. Fortunately this error can easily be compensated using a motorized lens in the optical setup. The remaining terms are compensated using a deformable mirror. Both, the wavefront measurement as well as the active compensation have been significantly improved in the test setup.

Another effect during operation with increasing repetition rates is birefringence which also arises from thermal gradients in the active laser material. This effect leads to local depolarization of the laser beam passing the laser rod.

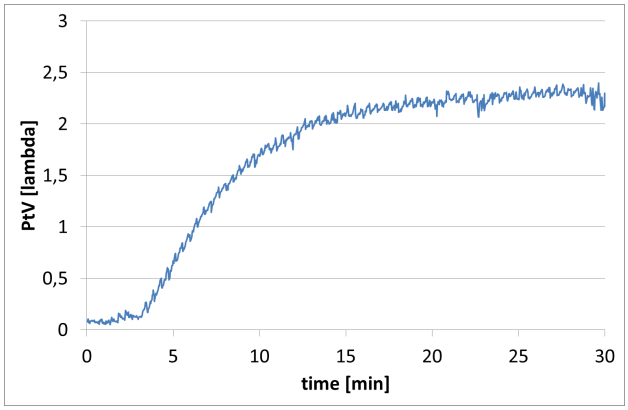

Figure 1: Evolution of the laser wavefront aberration (PtV) over time. The repetition rate was one shot every 25 s.

In combination with polarization optics this would result in a significant loss of output energy. In order to overcome this limitation, the amplifier head is operated in a double-pass configuration in combination with a Faraday rotator.

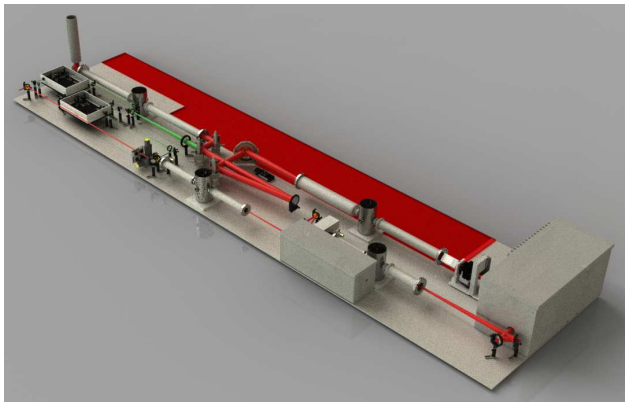

Figure 2: View of the planned Pre-Amplifier upgrade

Based on the above tests and improvements a new Pre-Amplifier system has been designed (figure 2) delivering pulses with output energies up to 20 J at a nominal repetition rate of one shot every 25 s. The integration of the new PHELIX Pre-Amplifier setup is planned for summer 2016. This upgrade and the experiences gathered also represent an important step forward for the planned 100 J APPA laser system at the FAIR project.

* This report is also published in the HI Jena Scientific Report 2015
† u.eisenbarth@gsi.de

DOI:10.15120/GR-2016-1

Development of new diagnostic for temporal contrast measurement at PHELIX *

V.A. Schanz[1,2], *F. Wagner*[3], *and V. Bagnoud*[1,3]
[1]GSI, Darmstadt, Germany; [2]TU Darmstadt, Darmstadt, Germany; [3]HI Jena, Jena, Germany

Requirement and issues of temporal contrast

PHELIX is able to create laser-intensities of 10^{20} W/cm^2. Before the maximum intensity is reached minor side-pulses and amplified spontaneous emission (ASE) arrive at the target. These can be intense enough to ionize the target. Thin targets, e.g. for experiments aiming at laser-particle-acceleration can be destroyed and the experiment fails. Therefore several techniques are used to prevent side-pulses and to decrease the ASE-level [1]. At the moment the ratio between the ASE-level and the level of the main peak – the ASE-contrast – is between eleven and twelve orders of magnitude. Because no device is able to resolve more than eleven orders of magnitude in intensity, this could not be confirmed yet. For more than a decade there has been no advancement in the improvement of direct high contrast measurement. In the context of a master thesis, a new third order scanning cross-correlator is developed to measure the best ASE-contrast at PHELIX and later on all high energy lasers.

Pulse measurement by cross-correlation

To measure the temporal intensity profile the pulse is splitted into two beams. One part is frequency doubled (by SHG in a BBO-crystal) and then both beams are overlapped onto another BBO-crystal. By the nonlinear effect of sum-frequency-generation (SFG) a signal beam with frequency (3ω), which intensity depends on the intensity of the overlapping pulse parts. By varying the delay τ between the arrival of both pulses at the crystal, different parts of the pulses overlap. Scanning through the delay leads to the temporal pulse profile. The delay τ is varied by a changeable length of one of the beam's path by a motorized stage. The setup is shown in figure 1.

The geometry of the green beam path leads to a delay of the green pulse which equals eight times the distance over which a linear stage moves the retroreflecting mirrors. So a temporal window of 2.8 ns is obtained, which exceeds any existing cross-correlators by a factor of two and more.

The dynamic range of a cross-correlator is limited by the noise level of the used detector. In this setup a CCD-camera with very low dark noise, combined with techniques to reduce electronic noise [2] and frequency filtering methods are used. Proof of principle measurements (Fig. 2) show that the dynamic range already reaches 10^{11}. Further improvements are ongoing.

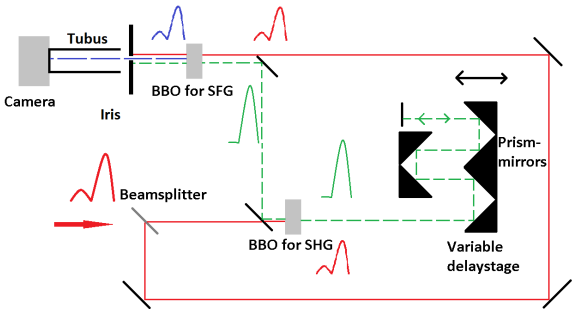

Figure 1: This schematics shows the optical paths in the developed cross-correlator. The line desribes the laserpulses with the fundamental frequency (ω), dashed the green path (2ω) and the long dashed line the blue light at (3ω)

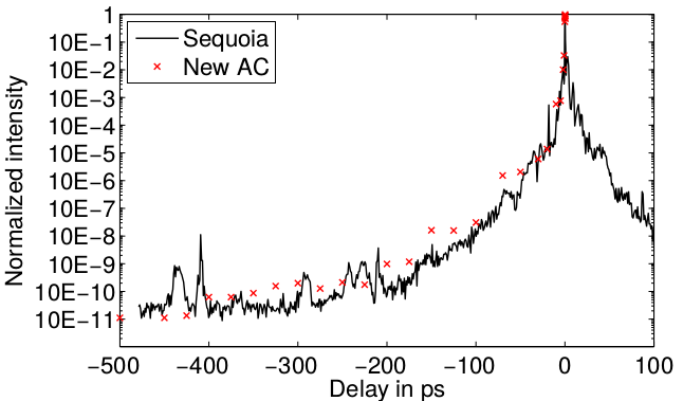

Figure 2: The black curve shows the pulse profile measured by the cross-correlator *Sequoia* from *Amplitude Technologies*. Crosses show the proof of principle measurement with the new cross-correlator

References

[1] F. Wagner et al., Appl. Phys. B **116**, 2013, p.429-435

[2] D. Javorkova and V. Bagnoud, Opt. Exp. **15** 2007, p.5439-5444

* Work supported by GSI(PHELIX)

Optimized laser ion acceleration at the PHELIX laser facility *

F. Wagner †[1,2], *C. Brabetz*[1], *U. Eisenbarth*[1], *B. Zielbauer*[1], *and V. Bagnoud*[1,2]
[1]GSI, Darmstadt, Germany; [2]Helmholtz Institut Jena, Germany

Laser driven ion acceleration is one of the main applications of the PHELIX short pulse system. Since the commissioning of the PHELIX laser in 2008 several experiments have been undertaken, aiming at optimized properties of laser-accelerated ion beams e.g. beam collimation, spectral shape and maximum energy. Besides specific developments of sophisticated target compositions and geometries, the laser system has been continually improved.

One important achievement in recent years has been the implementation of an ultrafast optical parametric amplifier (uOPA) which enables a temporal contrast level better than 10 orders of magnitude up to an instant of 100 ps before the peak intensity [1,2]. Thanks to this ultra-high contrast the use of micrometer and sub-micrometer thick targets for laser ion acceleration experiments has become possible. It is well known that the use of such thin targets along with a sufficiently high temporal contrast of the laser pulse is particularly favorable for ion acceleration via the target normal sheath acceleration (TNSA) mechanism and could lead to enhanced cutoff energies. Furthermore, for a certain match of laser and target conditions alternative acceleration mechanisms could come into play, e.g. the laser breakout afterburner (BOA) mechanism [3].

The feasibility of applying sub-micrometer thick targets at PHELIX for ion acceleration has been studied in several experiments in 2013 and 2014. Fig. 1 shows a TNSA spectrum obtained from the interaction of the PHELIX pulse with a 700 nm thick target (shot 7451). The spectrum was measured using radiochromic film in stack configuration as we described in detail in [3]. High particle numbers between 10^9 and 10^{12} protons per MeV for energies above 5 MeV as well as the relatively high cutoff energy of 38 MeV confirmed the achieved temporal contrast.

During that experiment, the maximum achievable ion energy was limited due to on-shot aberrations that reduced the intensity on the target. In 2015 we undertook a dedicated internal beamtime to improve the beam quality of the fully amplified PHELIX pulse. Three active elements were used to reduce aberrations: a lens which was switched between a position for alignment and one for full energy shots to compensate for defocus aberration, a mirror after the main amplifier that was actively bent to compensate for astigmatism and a deformable mirror to reduce remaining aberrations. The beam quality was monitored using a Shack-Hartmann wavefront sensor. In addition we mapped the far field after the main amplifier during a full energy shot with a newly commissionned 16-bit CMOS camera (Hamamatsu model C11440-22CU).

Three representative far field images are shown in Fig. 2. Using these images the maximum on-target intensity could be estimated to be $5*10^{20}$, $2*10^{20}$ and $5*10^{19}$ W/cm^2 for the cases **a**, **b** and **c**, respectively. In conclusion a much higher maximum intensity is achieved when the full active control of the on-shot aberrations is applied. This was also confirmed by the proton yield. A typical spectrum obtained from a sub-micrometer thick target is shown in Fig. 1 (shot 11831). Particle numbers and the cutoff energy have improved significantly. In Particular, the cutoff energy of 85 MeV is a new world record for laser ion acceleration via the TNSA mechanism.

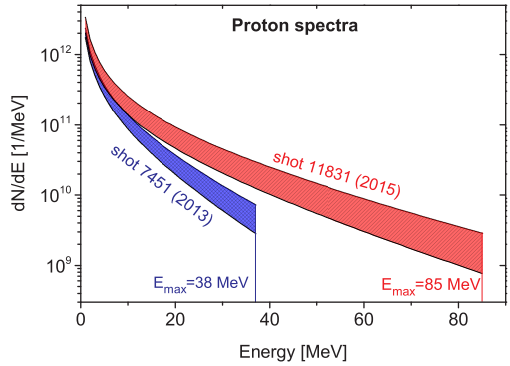

Figure 1: Spectra of protons accelerated via the TNSA mechanism from a shot on a 700 nm thick target after the implementation of the uOPA in 2013 (shot 7451) and from a shot on a 900 nm thick target using active control of the on-shot aberrations in 2015 (shot 11831).

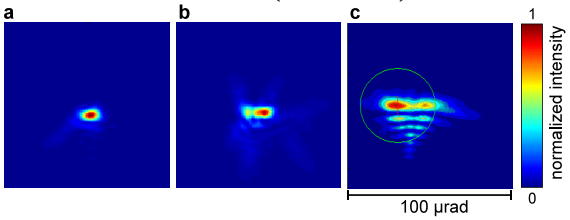

Figure 2: Far field images of the PHELIX pulse for **a**: the cold system, **b**: full active aberration control (lens, bent mirror and deformable mirror) and **c**: reduced aberration control (just lens)

References

[1] F. Wagner et. al., Appl. Phys. B **116**, 2013
[2] F. Wagner et. al., Opt. Expr. **22**, 2014
[3] F. Wagner et. al., Phys. Plasmas **22**, 2015
[4] F. Wagner et. al., submitted to Phys. Rev. Lett. 2016

* This report is also published in the HI Jena Scientific Report 2015
† f.wagner@gsi.de

DOI:10.15120/GR-2016-1

Technical report for P073, stimulated Raman Backscattering at PHELIX*

B. Landgraf[1,2], *F. Gärtner*[3,4], *D. Kartashov*[2], *A. Hoffmann*[1], *Z. Samsonova*[1,2], *G. Vieux*[5], *G. McKendrick*[5], *D. Jaroszynski*[5], *J. Jacoby*[4], *T. Kühl*[1,3], *and C. Spielmann*[1,2]

[1]Helmholtz Institute Jena, Jena, Germany; [2]Institute of Optics and Quantum Electronics, Abbe Center of Photonics, Friedrich-Schiller University Jena, Jena, Germany; [3]GSI, Darmstadt, Germany; [4]Institute for Applied Physics, Plasmaphysics, Goethe-University Frankfurt/Main, Frankfurt/Main, Germany; [5]University of Strahclyde, Glasgow, United Kingdom

Introduction

Stimulated Raman Backscattering (SRBS) is a promising way to upgrade existing high intensity systems beyond the Petawatt(PW) level [1]. To overcome scaling limitations in state of the art chirped pulse laser amplifiers the intensity has to be increased after passing the last solid state device. SRBS describes a three wave interaction in laser plasmas in which a plasma wave is generated due to the ponderomotive force of a beatwave originating from two counter-propagating frequency shifted laser pulses. The frequency difference is crucial because it defines the optimal plasma frequency.

Experimental Setup

Here we report about the results obtained during project P073 in the granted beamtime in March 2015. In the experiment the 25 cm diameter beam of PHELIX was split into two 100 cm^2 quadratical, vertically aligned beams (Fig. 1). The pulse duration of both beams was independently controlled by a grating compressor assembled by the PHELIX laser team. The measurement of the pulse duration is shown in Fig. 2 and is 31 ps. It conforms with the in the technical preparation report specified pulse parameters. The energy ratio of both beams is variable and can be tuned up to 50J per beam. Additionally the temporal overlap of both beams can be changed by an integrated delay stage. Both beams could be easily separated spatially in the target chamber and the focussed at the end of two beamlines. The beam shows strong dependance on the vertical alignment related to thermal effects. This limits the shot rate to around 1 shot per 6h for phase sensitive measurements.

Diagnostics

As both beams are overlapped under 0.5° they can be spatially separated and extracted for pulse characterization measurements. In our case we installed a 2nd order Autocorrelator, a Pyroelectric head for energy measurements, a 2D-GaAs near- and farfield detector and an InGaAs MidIR spectrometer. On side of the pump beam, plasma transmission and beam profile were recorded.

* Work supported by GSI(PHELIX), GSI(HIJ), HGShire/European Regional Development Fund (EFRE)/state of Thuringia (TMBWK) under Grant No. B 715-08008/TR, U Strathclyde

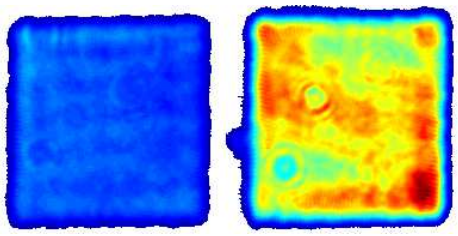

Figure 1: Beamprofile of two spatially separated beams. For convenience the picture is transposed. Both pulses are aligned vertically in the laser and are amplified in the same laser chain with different pulse duration.

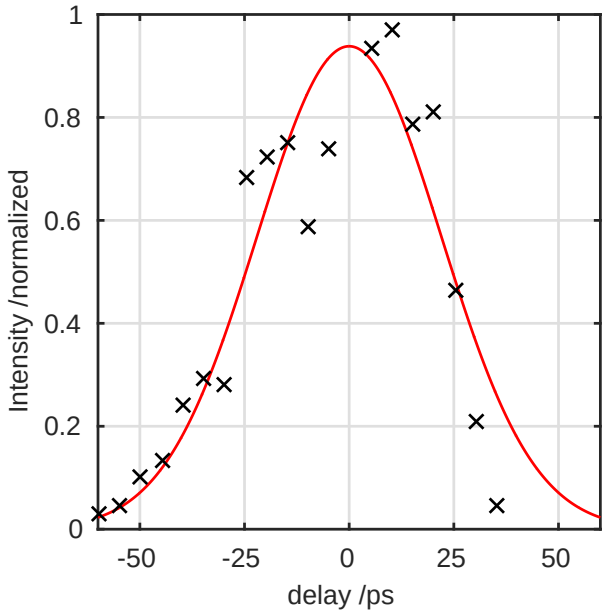

Figure 2: Autocorrelation measurement of the installed compressor. The stretched pulse was scanned with a 500 fs probe. The resulting best fit is achieved with $\exp -(t - \tau_0)^2/\omega^2$ and ω = 31 ps.

References

[1] V. M. Malkin, G. Shvets, and N. J. Fisch. Physical Review Letters 82.22 (1999): 4448.

DOI:10.15120/GR-2016-1

Laser-driven proton acceleration with cone-guided hemispherical targets*

O. Deppert[†1], *C. Brabetz*[2], *S. Busold*[1], *D. Jahn*[1], *A. Kleinschmidt*[1], *K. Philipp*[1], *P. Poth*[1], *G. Schaumann*[1], *D. Schumacher*[2], *A. Blazevic*[2], *V. Bagnoud*[2], *and M. Roth*[1,2]

[1]Technische Universität Darmstadt, Germany; [2]Helmholtzzentrum für Schwerionenforschung GmbH - GSI, Germany

In the FI scheme, the compression and ignition of the fuel capsule are decoupled, leading to moderate pressures which minimize potential instabilities. **P**roton-driven **F**ast **I**gnition (pFI) makes use of laser-driven protons which are dumped into the hot spot to ignite a burn wave. The upcoming ARC laser-system at NIF will be a short-pulse, petawatt, 10 kJ class laser which allows for the first time the realization of a combined ICF and pFI scenario. In order to scale the laser-driven proton acceleration concept, the key mechanism of pFI, detailed laser-parameter studies on realistic pFI target geometries need to be carried out at high energy petawatt laser-systems worldwide. First steps have been made by an experimental campaign in 2015 at the PHELIX laser-system at the Helmholtzzentrum für Schwerionenforschung GmbH (GSI) at Darmstadt. During this campaign several important pFI parameters, e.g. the focusing behavior of the laser-driven proton beam, the influence of the laser-pulse length onto the conversion efficiency as well as the spatial and angular proton beam profile have been studied in detail.

A PHELIX short pulse laser beam with varying pulse length and energy for constant intensities of the order of 10^{19} W/cm^2 was used to primarily accelerate protons from the surface of a complex cone-guided hemispherical target geometry (Fig. 1, a)) by the **T**arget **N**ormal **S**heath **A**cceleration (TNSA) mechanism. The target consists of a hemispherical part which produces a focusing proton beam and a cone part to guide and further modify it. In a typical pFI scenario the fuel capsule would be attached close to the outlet port. The targets been investigated additionally alter the angular distribution of the guided proton beam due to the interaction with strong electric ($\sim$TV/m) as well as azimuthal magnetic fields ($\sim$kT) inside the geometry, thus allowing to produce an annular shaped proton beam. This scheme is proposed to be more efficient to ignite the pre-compressed hot spot by reducing the total required ignition energy by almost a factor of two [**?**]. To diagnose the emerging ion beam three Thomson Parabola spectrometers, a newly developed **I**on **W**ide-**A**ngle **SP**ectrometer (iWASP) as well as **R**adiochromic film **I**maging **S**pectroscopy (RIS) and **N**uclear **A**ctivation based **I**maging **S**pectroscopy (NAIS) were applied. The interaction of the proton beam with the electric and magnetic fields inside the cone produces an annular proton beam for higher ($\geq$ 9 MeV) (Fig. 1, c)) and a typical TNSA beam profile for lower proton energies (b)). Additionally, a complementary spectral measurement with a newly developed iWASP allows for angular and energy resolved proton beam characterization from a larger solid angle to determine more precisely the proton conversion efficiency. Fig. 2 shows the energy resolved angular distribution for proton energies between 3.3-28 MeV for the half emission cone of the beam. The annular structure can be clearly seen for energies $\geq$ 9 MeV due to the hole of the distribution for small emission angles left hand side. The time-stamps shown in Fig. 2 corresponds to a time-of-flight (ToF) distance of 1 mm behind the outlet port where the compressed fuel capsule would be placed. In the first 14-24 ps the high energy part of the proton beam will deposit its energy circular around the hot spot to drive a shock wave to further compress the core. Between 24-40 ps the low energy, but high intensity part of the spectrum then will be used to ultimately ignite the hot spot. The preliminary results presented here show the first time the experimental realization of this promising concept.

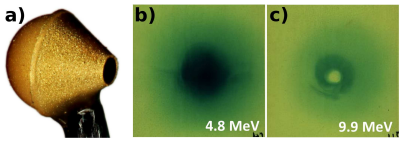

Figure 1: a) Dedicated target design for pFI; b) Typical TNSA and c) annular proton beam measured with RIS.

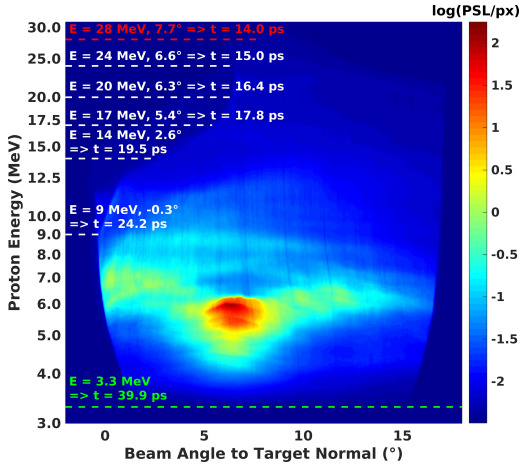

Figure 2: Angular and energy resolved proton distribution with ToF marks for passing the target outlet port.

References

[1] M. Temporal *et al.* , Plas. Phys. Contr. Fus. **51**, 035010 (2009).

* This report is also published in *News and Reports from High Energy Density generated by Heavy iOn and Laser Beams 2015.*

† O.Deppert@gsi.de

DOI:10.15120/GR-2016-1

A laser-driven neutron source at PHELIX *†

A. Kleinschmidt‡[1], *V. Bagnoud*[2], *O. Deppert*[1], *A. Favalli*[3], *S. Frydrych*[1], *J. Hornung*[1], *D. Jahn*[1], *G. Schaumann*[1], *A. Tebartz*[1], *F. Wagner*[2], *G. Wurden*[3], *and M. Roth*[1]

[1]Institut für Kernphysik, TU Darmstadt, Germany; [2]GSI Helmholtzzentrum für Schwerionenforschung GmbH, Darmstadt, Germany; [3]Los Alamos National Laboratory, New Mexico, USA

Neutrons can be used in a wide field of applications to probe and alter materials. Laser-driven neutron sources have the potential to complement common accelerator-based spallation sources because of their compact design and the possibility of easy impelementation in other facilities.

The principle of laser-driven neutron sources has already been demonstrated at different laser systems like, amongst others, the Trident laser facility at Los Alamos National Laboratory, New Mexico, USA [1] or the VULCAN laser at Rutherford Appleton Laboratory, Harwell Oxford, UK [2].

These neutron sources are based on laser-ion acceleration and their subsequent conversion into neutrons. The acceleration of deuterons in the transparency regime is of particular interest for the generation of neutrons, because of the so-called *deuteron break-up* reaction. Therefore such sources require a high energy short pulse laser with intensities above 10^{18} W/cm^2 and high temporal contrast. The improvement of the PHELIX laser during the last years, especially with respect to temporal contrast [3], made it possible to perform a first neutron experiment at GSI.

Neutron generation at PHELIX

Using the PHELIX short pulse beam with an energy of 200 J and intensities between 10^{20} and 10^{21} W/cm^2 within a pulse length of 0.5 ps, protons and deuterons were accelerated from thin deuterated plastic foils in the thickness range of a few hundred nanometers and characterized with Thomson parabolas and RadioChromic Films (RCF). The ions were driven into a beryllium catcher that was built out of several beryllium disks of various thicknesses and layers of RCF inbetween. The sandwich type catcher was wrapped in tungsten foil with an overall thickness of 1 cm to reduce the number of neutrons scattered out of the catcher.

Neutrons are produced via nuclear reactions of the accelerated ions in the catcher material. (p,n) or (d,n) reactions generate a homogeneous angular neutron distribution, whereas pre-equilibrium emissions or the deuteron break-up result in a more forward directed emission with higher energies. This results in an angular neutron distribution with a 4π component and an overlapping forward directed neutron beam.

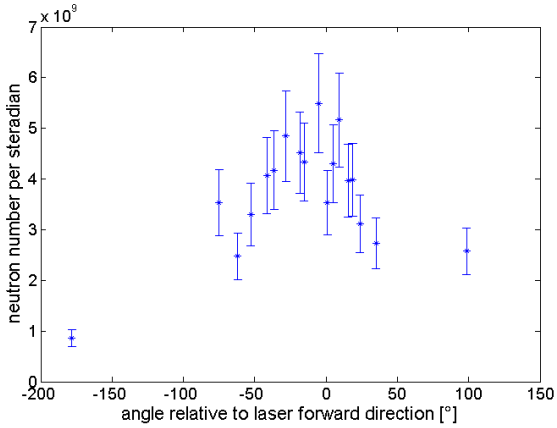

Figure 1: Angular neutron distribution with respect to the laser forward direction (0°).

The energy spectrum of the neutrons, their flux, and angular distribution were measured with three neutron time of flight detectors, using liquid scintillators coupled to photomultiplier tubes, and BD-PND Bubble Detectors. Both detector types were set up in different angles around the target chamber.

Especially the simultaneous measurement with up to 30 Bubble Detectors per shot allowed a detailed analysis of the angular neutron distribution. An example of such a distribution can be seen in Figure 1 showing neutron number per steradian over angle with respect to the laser forward direction defined as 0°. The laser incident angle on target was -10°. The data clearly reflects the forward directed characteristics of neutron emission from non-equilibrium reactions.

The maximum dose measured in the laser forward direction scaled to a distance of 1 m to the center of the beryllium catcher was about 43 mrem, which is the highest neutron flux measured at a laser-driven neutron source so far.

References

[1] M. Roth et al., Phys. Rev. Let., 110 (4), (2013)

[2] S. Kar et al., Phys. Plasmas (2015)

[3] F. Wagner et al., Appl. Phys. B, 116 (2) pp. 429-435., (2013)

* Work supported by GSI(PHELIX) /HIC4FAIR

† This report is also published in 'News and Reports from High Energy Density generated by Heavy Ion and Laser Beams 2015'

‡ a.kleinschmidt@gsi.de

Laser-driven acceleration of helium ions at PHELIX*

I. Engin [†1], *O. Deppert* [2], *S. Frydrych* [2], *A. Kleinschmidt* [2], *M. Roth* [2], *F. Schlüter* [1], *F. Wagner* [3], *and M. Büscher* [1,4]

[1] FZ Jülich, DE; [2] TU Darmstadt, DE; [3] GSI Darmstadt, DE; [4] HHU Düsseldorf, DE

An unsolved question in the context of laser-driven ion acceleration is the influence of the strong magnetic laser/plasma fields on the spins of the accelerated particles. Two scenarios are possible here: either these fields change the spin direction of those particles, or the spins are sufficiently robust that the short laser pulse has no effect on the spin alignment of a polarized target [1]. For the second scenario, there is no data on the behavior of nuclear spins ($\omega_{\mathrm{Larmor},^3\mathrm{He}} = 32.4\,\mathrm{MHz\,T^{-1}}\,B$) in magnetic laser/plasma fields ($\mathcal{O}\left(10^3 - 10^5\,\mathrm{T}\right)$). It has to be experimentally investigated if the polarization can be conserved inside plasmas during laser–acceleration processes, which would also open up the possibility of nuclear fusion with polarized fuel, in which the cross-sections for nuclear fusion reactions theoretically can be enhanced, leading to higher energy yields compared to the case of unpolarized fuel. In order to investigate the polarization of laser-accelerated ^{3}He ions from a pre-polarized ^{3}He gas–jet target, the feasibility of laser-induced ion acceleration out of underdense gas–jet targets had to be demonstrated at PHELIX. As laser target, both ^{4}He and unpolarized ^{3}He gas were used. The laser–acceleration process was simulated with EPOCH 2D on the FZJ supercomputer JURECA. The simulated as well as experimental laser parameters were set to: $I_\mathrm{L} = 1.4\times10^{19}\,\mathrm{W\,cm^{-2}}$, $\lambda_\mathrm{L} = 1.053\,\mu$m, $\tau_\mathrm{L} = 0.8\,$ps, $n_\mathrm{c} = 10^{21}\,\mathrm{cm^{-3}}$, $a_0 \approx 3.3$. Different backing pressures were applied: ^{4}He at 30 bar ($n_\mathrm{gas}^\mathrm{max} \approx 0.06\,n_\mathrm{c}$) and 15 bar ($n_\mathrm{gas}^\mathrm{max} \approx 0.03\,n_\mathrm{c}$), and unpolarized ^{3}He at 8 bar ($n_\mathrm{gas}^\mathrm{max} \approx 0.02\,n_\mathrm{c}$). As main ion diagnostics, a removable *GAFCHROMIC HD-V2* RCF wrap-around detector was mounted close to the interaction region cylindrically around the nozzle in order to measure the angular ion distribution qualitatively. The RCFs were wrapped in 5 μm thick Al foil. Hence, both $\mathrm{He}^{1+,2+}$ ions with $\mathcal{E}_\mathrm{He} > 1.6\,$MeV were able to irradiate the RCFs. In addition, three Thomson parabola spectrometers (TP) were placed at three angles relative to the laser axis ($HV = 3\,$kV, $B \approx 0.6\,$T, $170 - 370\,$nsr). The TPs were armed with *Agfa MD4.0* IPs and for one laser shot with pre-etched *TASTRAK* CR-39 SSNTDs. Results: Figure 1 illustrates a lineout of the BG-corrected angular $\mathrm{He}^{1+,2+}$–ion distribution on the height of the laser focus, obtained from the scanned RCF-raw data. In transversal direction (around $\pm90°$), a peak in ion signal with a FWHM of $\varphi_\mathrm{fwhm} = 23°$ indicates the ion–emission angles for the TP measurements: $-\{80°, 90°, 100°\}$. The IPs could not be calibrated with $^{3,4}\mathrm{He}^{1+,2+}$ ions beforehand. The ion–energy spectra, *i.e.* the normalized signal intensity (per MeV sr) against the ion energy in MeV, could be extracted from the detector raw data, *cf.* Fig. 2: both $^4\mathrm{He}^{1+,2+}$ Thomson parabolas are imaged on the IP. The high- and low-energy cut-offs in case of $^4\mathrm{He}^{2+,1+}$ are given with 4.6 MeV (normalized energy uncertainty of $\Delta\mathcal{E}\,\mathcal{E}^{-1} = 0.032$) and 0.84 MeV ($\Delta\mathcal{E}\,\mathcal{E}^{-1} = 0.014$), respectively. The single CR-39 measurement ($-80°$, 356 nsr) in total yielded $1.4\times10^{11}\,\mathrm{sr^{-1}}$ He^{1+} and $5.7\times10^{10}\,\mathrm{sr^{-1}}$ He^{2+} ions. A proper layout of a polarized ^{3}He gas–jet target is currently being developed. Two weeks of beamtime at PHELIX (2016/2017) was granted for the polarization measurement of laser-accelerated ^{3}He ions from a polarized target.

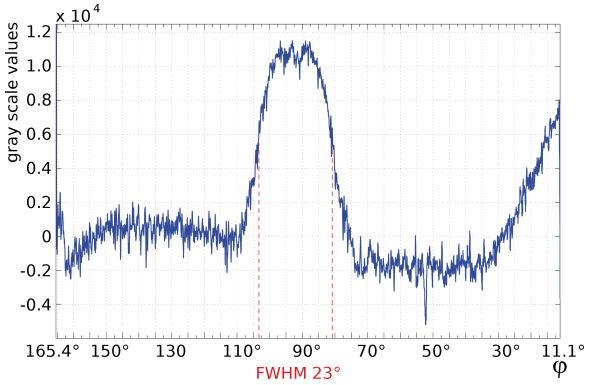

Figure 1: BG-corrected angular ion distribution.

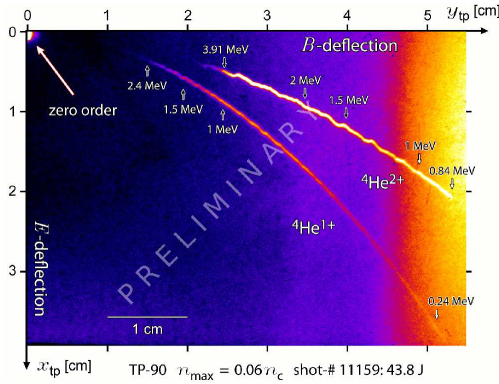

Figure 2: IP raw data, $^4\mathrm{He}^{1+,2+}$ Thomson parabolas

References

[1] N. Raab *et al.*, Phys. Plasmas **21**, 023104 (2014)

* A similar version of this report is also published in IKP Annual Report 2015, FZ Jülich.

† i.engin@fz-juelich.de

DOI:10.15120/GR-2016-1

Absorption of ultra-intense laser pulses in near-critical density plasma *

R. Wilson[1], *R.J. Gray*[1], *R.J. Dance*[1], *C. Armstrong*[1,2], *S. Williamson*[2], *C. Brabetz*[3], *F. Wagner*[3], *D. Neely*[2,1], *and P. McKenna*[† 1]

[1]SUPA, Department of Physics, Universtiy of Strathclyde, Glasgow, G4 0NG, United Kingdom; [2]Central Laser Facility, STFC Rutherford Appleton Laboratoty, Didcot, Oxfordshire, OX11 0QX, United Kingdom; [3]PHELIX Department, GSI Helmholtz Center for Heavy Ion Research, Planckstrasse 1, D-64291, Germany

Introduction

The degree to which laser energy is coupled to electrons in a laser-plasma interaction, and subsequently to ions and other radiation forms, is fundamentally important to all applications of intense laser-plasma interactions.

We report on an experiment which aims to achieve direct measurements of total absorption, and the correlated energy coupling to fast electrons, in the transition from surface to volumetric interactions, utilising near-critical density targets. Volumetric interactions arise as a result of hole-boring and the onset of relativistic induced transparency, and can give rise to significantly increased absorption.

Additionally, this investigation aims to determine if the upper limit of absorption in solid targets, as predicted by Levy et al [1], can be overcome by employing near-critical density targets.

Experiment

The experiment was conducted using the PHELIX laser, GSI. This system is ideal for conducting absorption measurements primarily due to its high shot-to-shot energy stability, vital for consistent measurements. This system can delivered 200 J pulses ($\sim$155 J on-target) with duration of 700 fs (FWHM). With selective pulse energy, or laser defocus, results were taken for intensities between 10^{17}-10^{20} W/cm^2. The high temporal intensity contrast delivered by this system ($\sim 10^{11}$ [2]) is also vital for experimentation using ultrathin and foam targets, to prevent significant preplasma or target expansion prior to the arrival of the peak laser energy.

To directly quantify the laser energy deposited in interaction targets one can measure all unabsorbed light, taking four distinct forms; scattered, transmitted, reflected and backscattered laser light. To collect the first two forms a custom-designed integrating sphere, with an inner wall coated by a Lambertian scattering material, was employed. Scattered/transmitted light was then measured using two visible to near-infrared spectrometers coupled to either hemisphere.

As targets were irradiated at normal incidence (0°), reflected and backscattered light become a single measurement. Its energy content was quantified by imaging the reflected/backscattered light leaving the sphere entrance port incident on a fully calibrated diffuse scatter screen.

A curved stacked detector [3], consisting of image plate and steel filters, is placed around the sphere equator. This provides a high resolution angular and low resolution energy measurement of the escaping electron distribution. This measurement is key for comparing laser absorption to the subsequent coupling to electrons.

A schematic/picture of this set-up in the PHELIX target chamber is shown in Fig. 1.

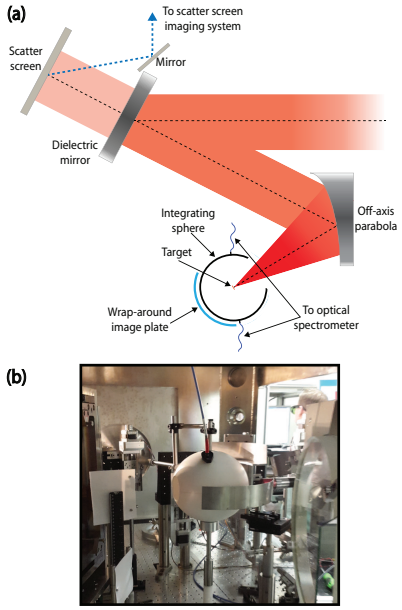

Figure 1: (a) Schematic of experimental set-up used to measure laser absorption, and subsequent coupling to fast electrons (b) Image of this set-up.

The targets selected for exploring absorption were either, relatively thick (6 μm) aluminium foils, to explore surface-dominated absorption, or thin nm-scale (40-1000 nm) and low density plastic based foam targets (5-1000 mg/cm^3), to explore the transition to volumetric absorption.

Analysis of the collected data is underway, and results will be reported in a future publication.

References

[1] M.C. Levy *et al*. Nature Comm., DOI: 10.1038/ncomms5149.

[2] F. Wagner *et al*. Appl. Phys. B **116**, 429 (2014).

[3] R.J. Gray *et al*. Appl. Phys. Lett. **99**, 171502 (2011).

* We acknowledge financial support from EPSRC (Grant Nos. EP/J003832/1, EP/L001357/1 and EP/K022415/1)

† paul.mckenna@strath.ac.uk

Surface parallel electron acceleration using ultra-intense sub-picosecond pulses

J. Y. Mao[1], O. Rosmej[2,3,], M. H. Li[4], J. Urbancic[1], F. Gaertner[2,3], K. Dimitri[2], S. Zaehter[2,3], D. Aslituerk[2,3], M. Z. Tao[4], C. Brabetz[2], V. Bagnoud[2,5], F. Wagner[2,3], B. Zielbauer[2], P. Neumayer[2], S. Mattias[1], M. Aeschlimann[1], L. M. Chen[4], T. Kuehl[2,5,6]*

[1]University of Kaiserslautern and Research Center OPTIMAS, Kaiserslautern, Germany; [2]GSI Helmholtzzentrum, Darmstadt, Germany; [3]Goethe University, Frankfurt, Germany; [4]Beijing National Laboratory for Condensed Matter Physics, Institute of Physics, CAS, Beijing 100190, China; [5]Helmholtz Institute Jena, Jena, Germany; [6]Johannes-Gutenberg University, Mainz, Germany, *contact o.rosmej@gsi.de

As a continuation of the experiment P090, we investigated the optimization of highly collimated target surface electron (TSE) beams with high electron energy and monoenergetic property. The interaction of a Cu bulk target irradiated by an ultra-intense laser at PHELIX could make it possible to generate high-energy Gamma rays for backlighting of HIHEX (up to 300 μm Pb).

The experiments were using the fundamental wavelength of 1053 nm with a peak power of around 40 TW. The s–polarized laser beam with a duration of τ_0 = 500 fs was focused by an f40 off-axis paraboloidal mirror at a grazing incidence angle onto a Cu bulk target with the focus diameter of 5 μm. An additional prepulse with adjustable intensity from 1×10^{-4} to 1×10^{-8} was applied 3ns-5ns in advance of the main pulse. A schematic picture of the experimental setup is shown in Figure 1. Also, 1% leakage of the main beam was frequency-doubled and applied as a probe beam to monitor the preplasma scale and density by using the M-Z interferometry method .

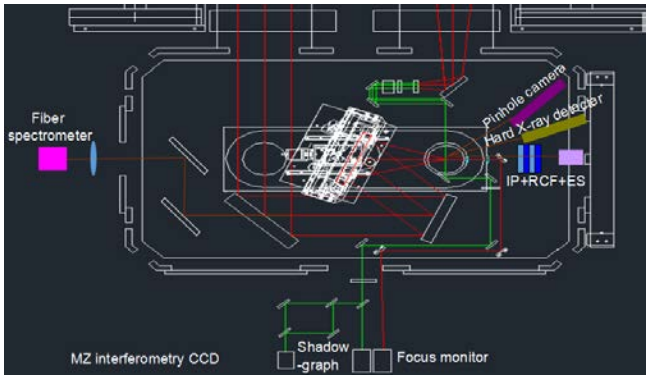

Figure 1: Experiment setup.

We investigated the prepulse dependence on the TSE generation, including the prepulse intensity ratio and the delay time. According to our previous experimental results [1], an optimized intensity ratio of the prepulse is essential to achieve an effective underdense preplasma. In the experiment, we found that when the laser power is lower, the required preplasma density is correspondingly lower. The phenomena are supported by numerical simulations [2]. In detail, both the intensity ratio of the prepulse and the delay time between the prepulse and the main beam were controlled, while the consequent preplasma density and scale were simultaneously monitored. At the optimized intensity ratio between prepulse and main pulse of around 5×10^{-7}, well concentrated and intense TSE electron jets with low divergence were observed at a laser incident angle of 72o, as shown in Figure 2(a). The divergence of the TSE electron jet was measured to be around 3° (FWHM). And the corresponding electron spectrum is detected, as shown in Figure2(b). Compared to the last experiment, the electron energy becomes lower. It might suggests that the generated TSE beam quality depends more on the laser power, than the laser intensity.

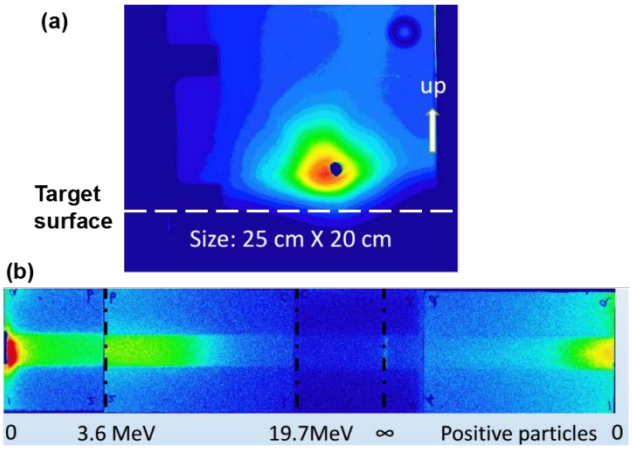

Figure 2(a): Spatial angular distribution of the TSE beam in the case with the prepulse intensity ratio of 5×10^{-7}. Figure 2(b): Corresponding electron spectrum. The hole has a diameter of 5 mm.

[1] J. Y, Mao, L. M. Chen, K. Huang *et al.*, Appl. Phys. Lett. 106, 2015, p.131105.

[2] W. M. Wang, L. M. Chen, J. Y. Mao *et al.*, High Energy Density Physics 9, 2013, p. 578.

DOI:10.15120/GR-2016-1

Proton acceleration and matter at high energy density in laser-irradiated micro-pillar experiments

D. Khaghani[*1,2], *B. Borm*[1,2], *L. Burr*[1,3], *F. Gärtner*[1,2], *L. Gremillet*[4], *M. Lobet*[4,5], *L. Movsesyan*[1,3], *O. Rosmej*[1], *M.E. Toimil-Molares*[1], *F. Wagner*[1,6], *and P. Neumayer*[1]

[1]GSI, Darmstadt, Germany; [2]Goethe-Universität, Frankfurt am Main, Germany; [3]Technische Universität, Darmstadt, Germany; [4]CEA, Arpajon, France; [5]CELIA, Bordeaux, France; [6]HIJ, Jena, Germany

Increasing laser absorption is a crucial point in the enhancement of several processes initiated by hot electrons, such as proton acceleration, isochoric heating of solid matter or hard x-ray emission. Shaping the interaction surface has the potential to increase laser-matter coupling significantly. It has been demonstrated that surface roughness of solid targets contributes to an increase in laser absorption. For example, laser irradiated glass targets covered with E. Coli bacteria led to a strong enhancement of the x-ray flux [1]. In this context, arrays of free-standing pillars are seen as a promising candidate [2]. Along with a wider interaction surface, such targets allow deep penetration of the laser field in the target structure as vacuum gaps exist between the pillars (Fig. 1.a). Moreover, when the laser beam comes at normal incidence on the target, both magnetic and electric fields point towards the pillar lateral surface, which ensures a strong coupling. Last but not least, since hot electrons have a range much larger than the pillar diameter, they can isochorically heat the whole volume of the sample and generate ultra-high energy densities [3]. To explore these processes, we have irradiated metallic micro-pillar arrays at the high-energy short pulse PHELIX laser.

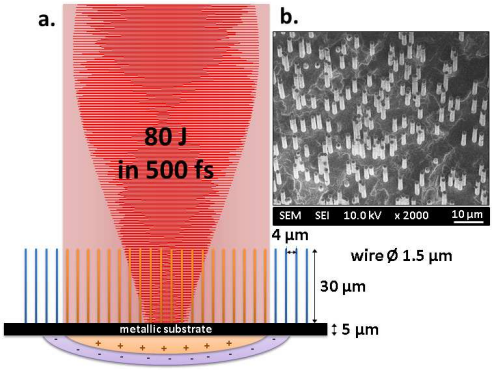

Figure 1: Experimental scheme of a micro-pillar array irradiated by a pulse from the PHELIX laser (a), representative SEM image of a target (b)

Targets were developed in collaboration with the Materials Research department of GSI with the ion track technology and the template method. Polymer membranes were irradiated by fast Au^{25+} ions at the UNILAC, and then etched to high-aspect ratio pores, in which metallic micro-pillars were grown by electrodeposition (Fig. 1.b). The advantage of this method is that each target has a relatively thin metallic substrate layer of about 5 μm. Thicker substrates would not permit proton acceleration because of the hot electrons being damped. Pillars and substrates are systematically made of two distinct materials in order to distinguish them via x-ray spectroscopy. We investigated micro-pillars of different elements (Cu, Ag and Au) with a length of 30 to 60 μm and a diameter of 1.5 μm. The pillar density was a sixth of solid density.

Targets were irradiated with 500 fs pulses at intensities ranging from 3×10^{16} to 2×10^{18} W/cm^2. The laser contrast was improved using the new uOPA-module of PHELIX in conjunction with plasma mirrors, avoiding this way premature destruction of the delicate target structure. Proton spectra emitted from the rear-side (substrate) of the target were measured using a Thomson parabola. In addition, a magnet-spectrometer measured MeV electrons escaping the targets. We have observed a significant increase in particle yields, temperatures and maximum energies of both protons and hot electrons.

Another important part of the study concerned x-ray emission. We developed a broadband spectrometer (Fig. 2) using a large cylindrically curved graphite crystal (HOPG) in a van Hámos configuration, looking at photon energies from 8 to 12 keV. We have obtained evidence of ultra-high energy density conditions at gigabar pressure.

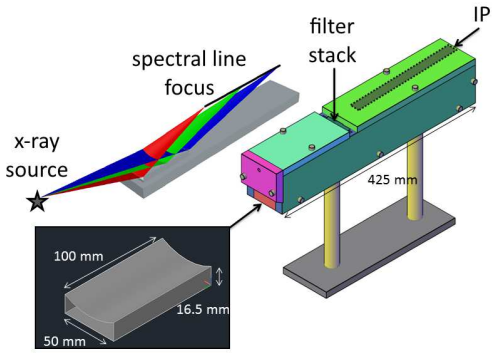

Figure 2: Broadband x-ray spectrometer

References

[1] M. Krishnamurthy *et al.*, Opt. expr. **20**(5), 5754–5761 (2012).

[2] Z. Zhao *et al.*, Physics of Plasmas **17**(12), 123108 (2010).

[3] M.A. Purvis *et al.*, Nature Photonics **7**(10), 796–800 (2013).

* d.khaghani@gsi.de

DOI:10.15120/GR-2016-1

Improvement of contrast-to-noise in short-pulse hard x-ray radiographic imaging using detector stacks

B.Borm[1,2], F. Gärtner[1,2], D. Khaghani[1,2], and P. Neumayer[1]
[1]GSI, Darmstadt, Germany; [2]Goethe-Universität Frankfurt, Germany

Since its discovery, one of the most prominent uses of x-ray radiation has been to reveal the interior of otherwise optically opaque objects. In experiments producing high energy density conditions in the laboratory (e.g. [1]) x-ray radiography is enabled by the availability of powerful high-energy laser driven x-ray sources, providing the required number of photons within nanosecond to picosecond exposure times. This allows for example direct measurements of the mass density for equation-of-state measurements on the shock hugoniot [2] or the release adiabate [3].

While x-ray energies below 10 keV are suitable to penetrate low-Z targets at moderate (few times solid) densities, probing samples compressed to highest densities, as e.g. the mm-size high-Z targets intended to be used at FAIR (e.g. [4]), requires photons with energies well above 100 keV and of high intensities to provide sufficient transmission through the target and high signal-to-noise ratios, respectively. These prerequisites can be obtained by focusing high-energy short-pulse lasers onto solid targets to intensities of order 10^{18} W/cm², generating both characteristic line radiation and a continuum of bremsstrahlung, extending up to MeV photon energies [5].

Besides the spatial resolution a crucial quality figure of a radiographic image is the image contrast. Here, the contrast-to-noise ratio determines whether two different areal densities can be discriminated. Obtaining a high density discrimination, or density-contrast, requires maximizing the number of detected photons.

In addition to providing a large number of backlighting photons in the first place, the efficient detection of the transmitted radiation is equally important. In laser-plasma experiments imaging plates (IP) are widely used as detectors for keV x-rays. While for photon energies up to few tens of keV imaging plates have quantum efficiencies close to unity, at photon energies of 100 keV and above, the quantum efficiency is significantly reduced. As a consequence, a significant flux of energetic photons is still present behind the plate. This suggests that placing a second detector will yield a further measurement of the same image, effectively doubling the detection efficiency. This is a small investment compared to for example doubling the laser energy.

To verify the benefit of this idea, we have tested the method of stacking imaging plates (IPs) to detect hard x-rays during an experiment performed at the PHELIX laser at GSI.

Gold foils of 5 µm thickness were irradiated under normal incidence with laser pulses of approx. 80 J energy at a duration of 600 fs, focused to 100 µm focal spot diameter resulting in intensities of 10^{18} W/cm².

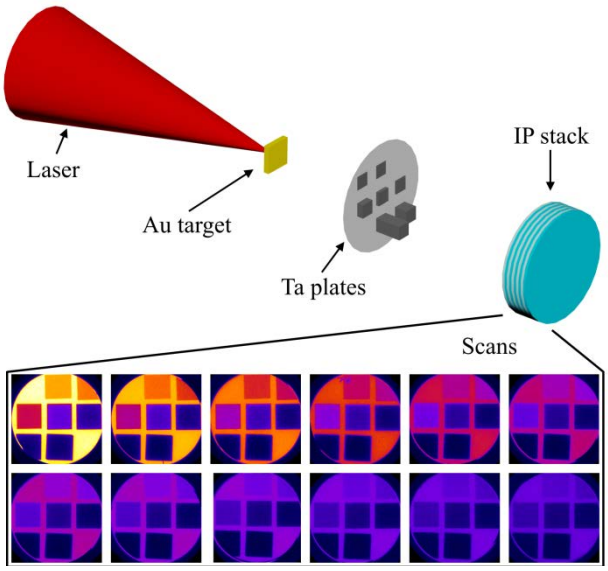

Figure 1: Experimental setup

The hard x-ray radiation emitted by the target was recorded in a distance of 420 mm by a stack of 12 imaging plates (type Fuji BAS-SR), placed directly on top of each other.

A set of square tantalum plates of different thicknesses was placed as radiographic test objects in the path between backlighter and detector. A schematic of the experimental setup is shown in Fig. 1 together with the raw images recorded by the 12 IPs in a single shot.

Analysis showed that compared to a single IP the detector stack achieved an improvement of the contrast-to-noise ratio of a factor ranging between 2-3, close to the theoretical limit for the shot noise dominated image.

Simulations using the Monte-Carlo code Geant4 with a one-temperature photon energy distribution yielded quantitative agreement with the observed scaling. Our results show that multiple exposures by detector stacking lead to a significant noise reduction, equivalent to that of a 4-9x more powerful backlighter source.

References

[1] B. A. Remington et al., Mod. Phys. **78**, 755 (2006).
[2] A. Kritcher et al., High Energy Density Physics **10**, 27 (2014).
[3] M. E. Foord et al., Review of Scientic Instruments **75**, 2586 (2004).
[4] K. Li et al., Laser and Particle Beams **32**, 631 (2014).
[5] H. Schwoerer et al., Phys. Rev. Lett. **86**, 2317 (2001).

DOI:10.15120/GR-2016-1

Spatially resolved temperature diagnostic of a thin Ti-wire heated by laser-accelerated relativistic electrons* †

A. Schönlein[1], *G. Boutoux*[2], *S. Pikuz*[3], *L. Antonelli*[2], *D. Batani*[2], *A. Debayle*[4], *L. Giuffrida*[2], *J. Honrubia*[5], *J. Jacoby*[1], *D. Khaghani*[6], *P. Neumayer*[6], *O. Rosmej*[1,6], *J. J. Santos*[2], *and A. Sauteray*[2]

[1]Goethe Universität, Frankfurt, Germany; [2]Univ. Bordeaux, CNRS, CEA, CELIA; [3]JIHT, Moscow, Russia; [4]CEA DAM DIF, Bruyères-le-Chatel, France; [5]ETSI Aeronauticos, Universidad Politécnica de Madrid, Madrid, Spain; [6]GSI, Darmstadt, Germany

In the reported experiment, warm dense matter (WDM) was generated by irradiating a wire target with a high intensity PHELIX-laser pulse. The wire geometry lead to a confinement of relativistic electron currents which are generated during the laser-matter interaction. Due to this confinement, the process of volumetric heating by the relativistic electrons is maintained in large target depths.

The experiment was carried out at the PHELIX-laserbay. Ti-wires with a diameter of $50\,\mu m$ and a length of $3-4\,mm$ were irradiated. The laser was focused on the tip of the wires to intensities up to $10^{21}\,W/cm^2$, with a contrast of 10^{-10}.

High spatial resolution K-shell X-ray spectroscopy was used to measure the isochoric heating process induced by the laser-accelerated relativistic electrons propagating along the Ti-wire. Radiation of highly charged He- and H-like Ti-ions and Kα-satellites have been measured with high spectral resolution ($2\,m\mathring{A}$) using a focusing spectrometer with spatial resolution (FSSR). The FSSR consists of a spherically bend quartz crystal as a dispersive element and X-ray films as detectors.

The energy of photons emitted due to K-shell tranistions depends on the charge state of the atom. Inside the matter rather a charge state distribution than a single charge state is present. This leads to a broadening of the observed Kα-line (fig. 1).

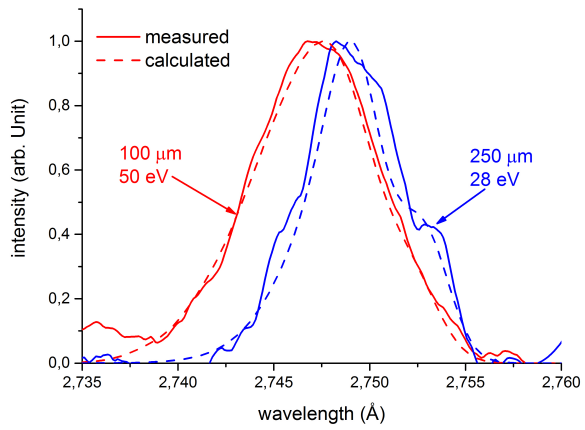

Figure 1: Comparison of modelled and measured Kα broadening.

The observed line is a superposition of all lines emitted by atoms of different charge states, which appear at a corresponding temperature of plasma bulk electrons. The broadening of the Kα-line is modelled by superposition of every charge state transistion energy, weighted with a charge state distribution. The charge state distribution for different temperatures is calculated using FLYCHK[1]. Figure 1 shows a comparion of the modelled and the measured broadening of the Kα-line. It is shown that the measured broadening can be modelled very satisfactorily by variing the charge state distribution by means of temperature.

The comparison of modelled and measured broadening can be used to determine the temperature of the heated target along the wire axis. The results are presented in figure 2.

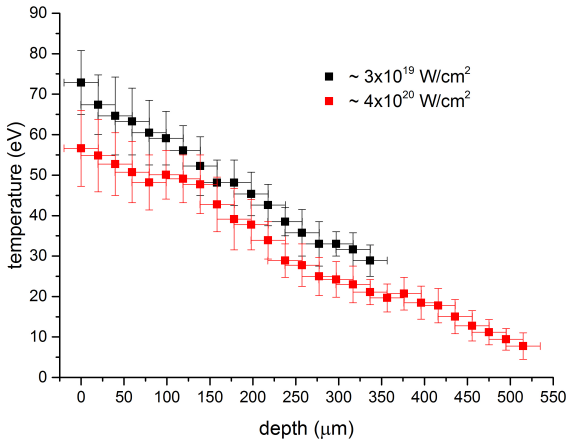

Figure 2: Temperature profile of warm dense matter heated by relativistic electrons.

It is observed, that the wire is heated to WDM temperatures of $10-70\,eV$ into a depth of $500\,\mu m$. We conclude, that using a wire geometry of high aspect ratio in laser-matter experiments, gives the possibility to generate WDM with volumetric character.

Our results are compared to simulations [2] that highlight both the role of electron confinement inside the wire and the importance of resistive stopping powers in warm dense matter.

References

[1] http://nlte.nist.gov/FLY/

[2] G. Boutoux in this report

* Work supported by GSI(PHELIX) / HIC4FAIR / HGSHire.

† This report is also submitted to 'News and Reports from High Energy Density generated by Heavy Ion and Laser Beams 2015'

X-ray emission from laser-induced plasma with ZnO nanostructured targets *

Z. Samsonova[†1,2], *E. Förster*[1,2], *S. Höfer*[1], *A. Hoffmann*[1], *D. Kartashov*[1], *D. Khaghani*[3], *B. Landgraf*[1], *P. Neumayer*[3], *R. Röder*[4], *C. Ronning*[4], *O. Rosmej*[3], *C. Spielmann*[1,2], *L. Trefflich*[4], *I. Uschmann*[1,2], *and M. Zürch*[1]

[1]Institute of Optics and Quantum Electronics, Abbe Center of Photonics, FSU Jena, Germany; [2]Helmholtz Institut Jena, Germany; [3]GSI, Darmstadt, Germany; [4]Institute of Solid State Physics, FSU Jena, Germany

Utilization of nanostructured targets for laser-produced plasma sources allows one to overcome the limited absorption of laser energy [1, 2] and to archive simultaneously very hot and dense plasma by volumetric heating [3]. Generation of such plasmas is of particular interest for both astronomical studies and table-top hard X-ray laser development. In this contribution we present the results of experimental investigation of hard X-ray generation from nanostructured solid targets irradiated by relativistically intense ultrashort laser pulses. The targets are made of zinc oxide, a dielectric, trasparent in the visible and NIR/MID range.

Experiment

The experiment was carried out at the Ti:Sapphire laser system in Jena (JETi-40). Ultra-short (45 fs) 130-mJ laser pulses at 400 nm wavelength are focused close to the normal incidence on a nanostructured target providing the peak intensity of 2.7×10^{19} W/cm^2. To minimize preplasma formation and ablation of nanostructures before the arrival of the main pulse, it is essential to have a high pulse contrast, which is about 10^{-10} on 1-ps scale in our case. The main diagnostics of X-ray emission from the plasma is a bent crystal spectrometer, based on LiF 220 crystal with a CCD camera. The samples have morphology of a disordered array of single crystalline nanowires ("grass-like") with diameters of 100-400 nm and a length of 1-5 μm (Fig. 1). For investigating the influence of the morphology on the X-ray yield, we have also measured X-ray spectra emitted from polished single crystalline ZnO.

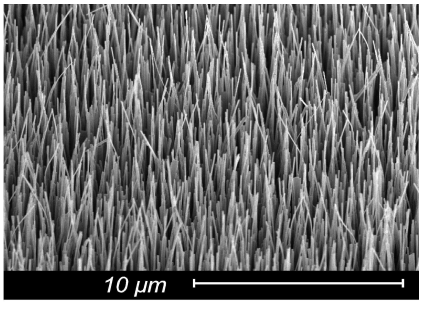

Figure 1: SEM image of "grass-like" nanostructured ZnO sample.

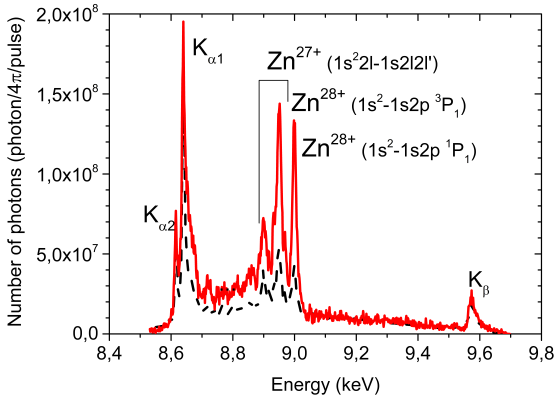

Figure 2: Calibrated spectra of X-ray emission obtained from "grass-like" (red solid line) and polished (black dashed line) ZnO targets.

Results and discussions

The observed characteristic lines in the spectral energy region 8.7-9.0 keV demonstrate generation of highly charged states of Zn up to He-like Zn from both, nanostructured and polished sample (Fig. 2). However, in comparison with a polished sample, the obtained flux of photons at the Kα transitions in He-like Zn is more than 2.5 times higher for nanostructured targets. Remarkably, the intensity of observed K$_\alpha$ emission from Zn^{28+} generated in nanostructured target is almost equivalent to the intensity of the K$_\alpha$ emission from neutral Zn, pointing on the possibility to achieve very high density of highly charged plasma. Measurements with samples having different length and diameter of nanowires have shown that the longer and the thinner wires are advantageous for the production of hot and dense plasma. To investigate the temporal evolution of generated plasma, we are currently working on simulations of experimental spectra using FLYCHK code with time-dependent electron density and temperature.

References

[1] A. A. Andreev and K. Yu. Platonov, Contr. to Plasma Phys. 53, 2 (2013)

[2] G. Kulcsar et al., Phys. Rev. Lett. 84, 22 (2000)

[3] A. Purvis et al., Nature Photonics 7 (2013)

* This report is also published in the HI Jena scientific report 2015

† zhanna.samsonova@uni-jena.de

DOI:10.15120/GR-2016-1

Collisional versus resistive energy losses of laser-accelerated electrons in a warm dense titanium wire

G. Boutoux[1], A. Schönlein[2], S. Pikuz[3], L. Antonelli[1], D. Batani[1], A. Debayle[4], A. Franz[2], L.Giuffrida[1], J.J. Honrubia[5], J. Jacoby[2], D. Khaghani[6], P. Neumayer[6], O.N. Rosmej[2, 6], T. Sakaki[1], J.J. Santos[1]
[1]CELIA, Université de Bordeaux, France; [2]Goethe University, Frankfurt, Germany; [4]JIHT RAS, Moskau, Russland; [4]CEA DAM DIF, France; [5]ETSI Aeronauticos, UPM, Madrid, Spain; [6]GSI, Darmstadt, Germany

Ultrahigh intensity laser interactions with dense targets stand out as an effective way to produce high-current relativistic electron beams (REB). In this context, it is important to understand the REB transport, at high electron current densities and through warm dense and highly resistive plasmas. To investigate this topic, we studied the interaction of the PHELIX laser (E_L=120 J on target, t_p=500 fs, λ=1064 nm) with a free-standing mass-limited Ti-wire (experiment P-077). In this report, we consider a laser shot with a ns-contrast up to 10^{-10} and with a focal spot size down to 6 µm, leading to a laser intensity on target of I_L=7.10^{20} W/cm^2. The REB, accelerated during interaction between relativistic laser pulse and short scale length preplasma, penetrate the wire and deposit energy therein. In [1,2], we have already discussed how isochoric heating due to laser-accelerated electrons can generate Warm Dense Matter (WDM) in depth and how we can diagnose this extreme state of matter. In this report, we focus on hot electrons and how they lose energy in WDM. When electrons propagate the wire, they ionize it and subsequent K-shell and Bremsstrahlung emission occurs, making the electrons propagation experimentally traceable. To characterize their energy distribution as well as their transport, we used two main diagnostics and a comprehensive set of simulations. First, a "Bremsstrahlung cannon" acted as a hard X-ray spectrometer. It was made of a stack of image plates (IP) and differential filtering at the front and rear sides. Monte-Carlo modelling of the Bremsstrahlung dosimetry was then used to infer the internal hot electron energy distribution. Both experimental data from this diagnostic and from dedicated "Particle-In-Cell" calculations (using the code PICLS-2D [3]) demonstrate that hot electrons with temperature of about 2 MeV were generated. Secondly, a Focusing Spectrometer with Spatial Resolution (FSSR) enabled highly spatially and spectrally resolved X-ray spectroscopy. In particular, the Kα emission intensity profile along the wire gives rather direct information on the REB propagation. The Kα signal was surprisingly found to decrease exponentially up to ~0.8 mm deep, though a stopping range of 1.8 mm was expected in cold Ti, see Fig. 1(a). Energy losses of an electron beam propagating within a material are commonly associated with inelastic collisions with bound and free electrons in the matter. However, this process is insufficient at the extremely high current density j_h achieved in relativistic laser-plasma experiments, where resistive losses induced by the neutralizing return current, of density j_e, become important. Indeed, while the rate of collisional energy loss by the electron beam per unit volume is proportional to $\rho.j_h$, with ρ the material density, by assuming a perfect current neutralization j_e=-j_h, the rate for the resistive energy loss is around $\eta.j_h^2$, with η the material resistivity. This last process has been recently experimentally evidenced in the warm dense matter regime [4]. To quantify the resistive losses, we performed hybrid PIC simulations [5]. Our simulations are able to reproduce the Kα emission intensity profile along the wire, see Fig.1(a). The predicted electron current density inside the wire is up to 10^{12} A.cm^{-2} (time-averaged), which is higher than in [4]. Resistive effects are found to be dominant in the first 200 µm of the target, where the electron current density is important. In total, resistive losses exceed collisional losses by a factor 2.35, hence justifying the observed reduction of the electron stopping range. Fig. 1(b) illustrates the competition between collisional and resistive losses as a function of the wire depth. As expected, the resistive losses, proportional to the square of the current density, are dominant near the laser-plasma interaction region. Yet, in comparison to experiments on foils, e.g. [4], the collective effects remain dominant over a relatively larger distance.

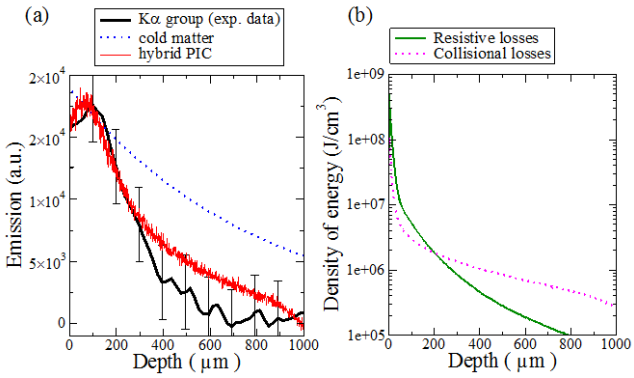

Figure 1: (a) Experimental Kα emission intensity profile along the wire using the FSSR compared to hybrid PIC simulations and a standard Monte-Carlo simulation in cold matter. (b) Resistive and collisional density of deposited energy as a function of wire depth predicted by the hybrid PIC code.

References:

[1] GSI Sci. Report 2014, APPA-MML-PP-11, p. 285
[2] GSI Sci. Report 2014, APPA-MML-PP-08, p. 282
[3] Y. Sentoku et al., J. Comput. Phys., 227, 6846 (2008)
[4] X. Vaisseau et al., Phys. Rev. Lett. 114, 095004 (2015)
[5] J.J. Honrubia et al., Laser and Particle Beams 24, 217 (2006)

DOI:10.15120/GR-2016-1

Generation of subnanosecond, intense ion bunches with the laser-driven LIGHT beamline*

D. Jahn[1], *D. Schumacher*[2], *C. Brabetz*[2], *J. Ding*[1], *S. Weih*[1], *F. Kroll*[3,4], *U. Schramm*[3,4], *T. E. Cowan*[3,4], *V. Bagnoud*[2,5], *A. Blazevic*[2,5], *and M. Roth*[1]

[1]Technische Universität Darmstadt, Darmstadt, Germany; [2]GSI Helmholtzzentrum für Schwerionenforschung, Darmstadt, Germany; [3]Technische Universität Dresden, Dresden, Germany; [4]Helmholtzzentrum Dresden-Rossendorf, Dresden, Germany; [5]Helmholtz-Institut Jena, Jena, Germany

Within the Laser Ion Generation Handling and Transport (LIGHT) project at GSI laser-driven ion acceleration and, especially, ion beam shaping with conventional accelerator technology are investigated using the worldwide unique LIGHT test beamline in the Z6 experimental area [1]. The project is based on a Target Normal Sheath Acceleration (TNSA) source driven by the Petawatt High-Energy Laser for Heavy Ion EXperiments (PHELIX) 100 TW beam resulting in a continuous proton energy spectrum up to a maximum energy of 28.4 MeV. The ions of the TNSA source are captured by a high-field solenoid for energy selection of protons in a range of 8 to 10 MeV via chromatic focusing. In a distance of 2 m from the source, an implemented radiofrequency (rf) double spiral resonator operating at -90 degrees synchronous phase is used for phase rotation of the accelerated single bunch. This way, the bunch can be either energy-compressed or longitudinally phase-focused down to a subnanosecond pulse [2]. Behind the resonator, the beam is transported through two permanent quadrupole doublets (50 mm, 25 T/m) into a second target chamber. In this second target chamber located at 6 m distance from the source, a second high-field solenoid system was installed for steep focusing to access highest peak intensities. Behind this solenoid, the diagnostic instruments are placed.

The LIGHT project dealing with proton acceleration follows two main objectives: The longitudinal phase focusing should be improved and the focal spot size should be minimized. For the first objective, a newly developed fast diamond detector based on a $5 - 7$ μm thin membrane with a time resolution up to (65 ± 5.5) ps and a field gradient of 5 V/μm was positioned at 6 m distance from the source. With this device a new optimum in phase focusing was reached: The shortest measured proton bunch lasted (209 ± 18) ps (FWHM) with a proton energy of 8 MeV. For comparison, a bunch duration of (462 ± 40) ps (FWHM) was measured in 2014. Figure 1 shows the temporal bunch profile. For the second objective, the second solenoid was installed at 6 m distance for steep focusing: A focal spot size of 2.3 mm x 2.3 mm with 2.5×10^8 protons was achieved resulting in a current of 1.2×10^9 1/ns $\sim$ 190 mA and an intensity of 2.3×10^{19} 1/(s cm^2). In the next experimental campaign in 2016, the beam homogeneity will be improved. After this crucial step, this beam can be applied for proton imaging.

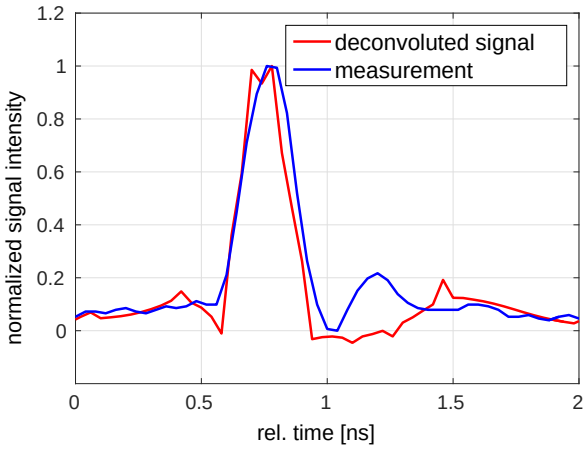

Figure 1: Measured temporal profile of the shortest proton bunch with a duration of (209 ± 18) ps after deconvolution.

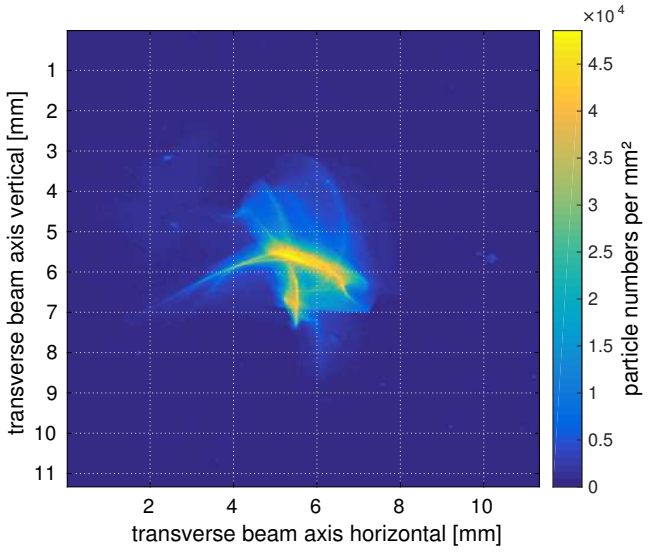

Figure 2: Measured focal spot size of 2.3 mm x 2.3 mm.

References

[1] S. Busold *et al.*, NIMA **740**, 94-98 (2014)

[2] S. Busold *et al.*, Scientific Reports **5**, 12459 (2015)

*This report is also published in *GSI Scientific Report 2015*.

DOI:10.15120/GR-2016-1

First steps towards the generation of intense, subnanosecond heavy ion bunches at LIGHT *

J. Ding[1], *D. Schumacher*[2], *D. Jahn*[1], *O. Deppert*[1], *C. Brabetz*[2], *S. Weih*[1], *F. Kroll*[3,4], *U. Schramm*[3,4], *T.E. Cowan*[3,4], *V. Bagnoud*[2,5], *A. Blazevic*[2,5], *and M. Roth*[1]

[1]TU Darmstadt, Darmstadt, Germany; [2]GSI, Darmstadt, Germany; [3]TU Dresden, Dresden, Germany; [4]HZDR, Dresden, Germany; [5]HI Jena, Jena, Germany

The LIGHT collaboration, consisting of several Helmholtz institutes and universites, has been founded for the purpose of Laser Ion Generation, Handling and Transport. For this a test beam line has been established at the Z6 experimental area at GSI [1]. The laser ion generation is based on the Target Normal Sheath Acceleration (TNSA) mechanism and driven by the PHELIX 100 TW beam line. A pulsed solenoid captures and collimates a part of the divergent ion beam with a continous energy spectrum by means of achromatic focusing [2]. The resulting collimated beam with a much narrower energy spread can then be compressed in phase or energy in a radiofrequency cavity, which is situated two meters behind the ion source. Two quadrupole doublets transport the ion beam to a second target chamber. The resulting ion beam is then diagnosed with a diamond detector for a temporal depiction of the achieved phase focus or with a stack of radiochromatic films for an energy spectrum.

Two campaigns in 2015 examined the acceleration of fluorine ions with TNSA and the handling and transport of the resulting ion beams. The first campaign focused on the generation of fluorine ions. For this purpose a 13 μm tungsten foil with a submicrometer coating of CaF_2 on the rear side was heated to 1100 degrees celsius in order to get rid of water and hydrocarbons. By removing these pollutions an efficient acceleration of fluorine ions of varying charge states was achieved. In figure 1 an extrapolation of the energy spectrum of the observed fluorine ions and their charge states can be found. It was measured with a Thomson parabola, which was set up at 0.12 m behind the target. Since the pinhole of the Thomson parabola covers only a very small solid angle of 1.1 mrad in the centre of the beam, the spectrum of the whole beam can only be extraced by extrapolating the measured part of the beam. This was done by assuming a two dimensional Gaussian beam distribution with an energy dependent standard deviation. The divergence of the fluorine ion beams as a function of their energy was taken to be the same as the divergence of TNSA proton beams [3]. In addition the photo-stimulated luminescence values from the image plates had to be converted to particle numbers by means of energy loss calculations with GEANT and fitting to existing models [4].

In the second campaign the transport and phase focusing of a part of the fluorine ion spectrum in the LIGHT beamline was approached. Six metres behind the target a diamant detector recorded time of flight (TOF) data. Figure 2 shows the comparison of TOF data of a phase focused fluorine ion and proton beam, converted to energy per nucleon. The central energy of the transported fluorine ion bunch was 0.85 MeV/u with an energy spread of $\pm$0.3 MeV. The relative energy spread of the fluorine ion bunch is much bigger than that of the proton bunch. Therefore the fluorine ion beam is longitudinaly much longer at the entrance of the rf cavity than the proton beam and exceeds the cycle duration of the rf cavity. This leads to the formation of multiple phase focused ion bunches. Simulations with TraceWin suggest, that the fluorine ion tof data in figure 2 stem from F^{7+} and F^{6+} only, because the particle numbers of the other accelerated charge states are strongly suppressed at the selected energy range.

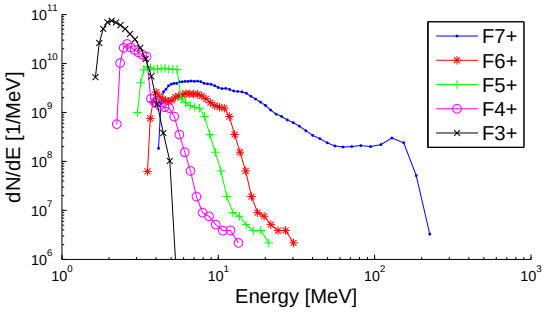

Figure 1: Energy spectrum of TNSA fluorine ions

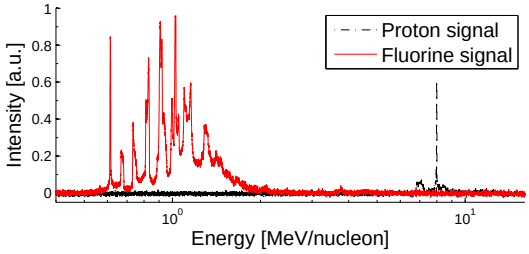

Figure 2: Diamond detector signal of phase focused ions

References

[1] S. Busold et al., NIMA 740, 94-98 (2014).

[2] S. Busold et al., PRSTAB 16, 101302 (2013).

[3] E. Bambrink et al., Phys. Rev. Lett 96, 154801 (2006).

[4] P. Poth, Master thesis (2015).

* also published in annual report 'News and Reports from High Energy Density generated by Heavy iOn and Laser Beams 2015'

Pepperpot emittance measurements for LIGHT beam characterization *

S. Weih[1], D. Jahn[1], J. Ding[1], D. Schumacher[2], C. Brabetz[2], A. Blazevic[2,3], V. Bagnoud[2,3], F. Kroll[4,5], U. Schramm[4,5], T. E. Cowan[4,5], and M. Roth[1]

[1]Technische Universität Darmstadt, Darmstadt, Germany; [2]GSI Helmholtzzentrum für Schwerionenforschung, Darmstadt, Germany; [3]Helmholtz-Institut Jena, Jena, Germany; [4]Helmholtz-Zentrum Dresden-Rossendorf, Dresden, Germany; [5]Technische Universität Dresden, Dresden, Germany

The Laser Ion Generation, Handling and Transport (LIGHT) project at the Z6 experimental area investigates the possibility of beam transport and shaping of laser- accelerated protons and heavier ions with conventional accelerator technology [1]. In the past experiments, ultra-short bunches with an energy of 8 MeV were generated and measured for protons [2], and the transport of fluorine and carbon ions along the 6 m long beamline was shown. During the experiments in October 2015, first emittance measurements were performed for protons to characterize the beam quality and transverse beam dynamics. Since the TNSA particle bunches are only provided in single-shot mode, the pepperpot measurement method was suited the best.

The measurement was realized with a conventional beam diagnostics pepperpot device which was placed directly behind the first solenoid in the beamline, which is used to collect and focus the diverging particles directly behind the source. Since this is the main transverse focusing element, its influence on the emittance was of major interest. A radiochromatic film (RCF) stack was used 60 cm behind the pepperpot as screen.

To measure the emittance of the TNSA source (based on a 0.01 mm gold target), at first, the solenoid stayed turned off during the shot. The pattern on the RCF screen showed a magnified image of the pinholes with the magnification corresponding to the geometrical distances of the setup. The TNSA source can therefore be seen as an almost ideal point source. The evaluation of the phase space was performed in the radial dimension (r - r') and confirmed this result (fig. 1), but since the obtained numerical value of $\epsilon = 2.7$ mm mrad was already the resolution limit of the experimental setup, the measured value yields only an upper limit for the source emittance. The real source emittance might be much lower, like [3] indicates.

The second measurement was carried out with the solenoid turned on during the shot, which is the operation mode for the 6 m long transport along the beamline. Since there is no energy selection in front of the solenoid, the protons enter it with their full energy spectrum and get separated radially due to the solenoid chromaticity. On the screen, the image of the pinholes therefore becomes radially streaked. The radial positions within one streak can be assigned to the corresponding proton energies (fig. 2), which allows an energy-resolved emittance analysis. In practice, due to small signals, it was difficult to analyze the RCF images for the solenoid emittance measurement. It could be seen qualitatively, that the solenoid field distorts the symmetry of the pattern on the screen (fig. 2). This explains the measured emittance blow-up of a factor around 10 compared to the upper limit of the source emittance. Further investigations on this effect will be performed following the aim to maintain the small source emittance along the beamline. Additionally, the resolution of the source emittance measurement setup will be improved.

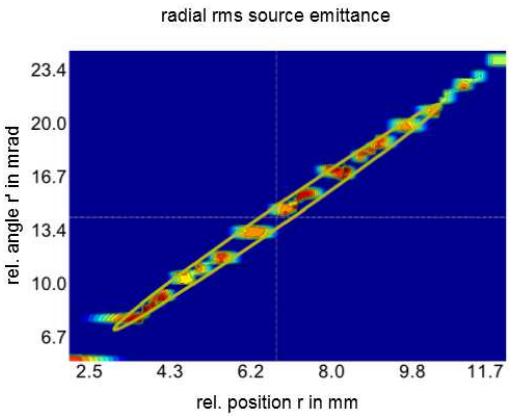

Figure 1: Radial phase space diagram of the TNSA proton source with rms emittance ellipse.

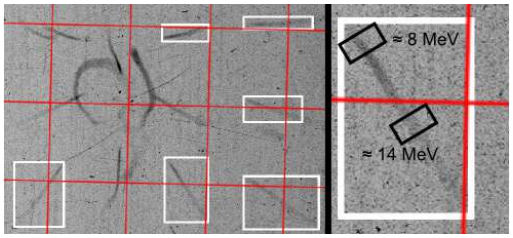

Figure 2: Section of the RCF image from the measurement with the solenoid turned on (left). The grid shows the calibration of the setup. Some streaks are shifted away from their original position in a non-radial way, which disturbs the symmetry. On the right, the energy selection within one streak is illustrated.

References

[1] S. Busold et al., NIM-A **740**, 94-98 (2014)

[2] S. Busold et al., Scientific Reports 5, 12459 (2015)

[3] T. E. Cowan et al., Phys. Rev. Lett. **92**, 204801 (2004)

* This report is also published in *News and Reports from High Energy Density generated by Heavy iOn and Laser Beams 2015*

DOI:10.15120/GR-2016-1

Study of water and carbon at high pressures generated by laser-driven shocks

R. Benocci[1], K. Jakubowska[2], D. Batani[2], Y. Maheut[2], T. Sakaki[2], J. Trela[2], B. Borm[3], P. Neumayer[3], A. Molineri[3], O.N. Rosmej[3, 4], P. Barroso[5], C. Verona[6]

[1]Università di Milano Bicocca, Milan, Italy; [2]CELIA, Université de Bordeaux, France; [3]GSI, Darmstadt, Germany; [4]Goethe University, Frankfurt, Germany; [5]Observatoire de Paris, Paris, France; [6]Universita Degli Studi di Roma-Tor Vergata, Rome, Italy

Modelling the internal structure of icy planets requires a precise knowledge of the behaviour of water and carbon over a broad range of pressures and temperatures. Material properties at extreme conditions are predicted by highly computing intensive ab-initio calculations coupled to molecular dynamics (e.g. [1,2]). This motivates experimental testing of equation of state and phase transitions of these materials in the Megabar pressure range.

We have conducted an experiment at the PHELIX laser facility, using the high-energy laser pulse to drive strong shocks into water and diamond samples. A phase plate was used to produce a flat focal intensity profile over a 1mm diameter, ensuring a homogenous planar drive. An important part of the experiment consisted in the optimization and the spatial and temporal calibration of the VISAR and self-emission diagnostic systems available at GSI. These were used to infer the thermodynamics of the driven state, providing sub-ns time resolution by using fast streak cameras.

The water targets, shown in figure 1, have been tested and revealed a few drawbacks due to the presence of ghost-reflected beams from the rear surface. This was most likely due to the presence of a poor antireflective coating on the rear side of the targets. Also many targets had problems of water leakage once put under vacuum. For these reasons, we could not get significant results on water targets but we could indeed get information on how to improve target design.

As for carbon, the target scheme is shown in Fig. 2 with a nickel step deposition of about 20 µm thickness on the side of the VISAR laser probe beam and 5 um of CH and 20 µm nickel deposition thickness on the side of the main laser beam. The intermediate layer was a diamond monocrystal with thickness between 90 and 280 µm. This target scheme allows observing the shock breakout times at the interface between Ni and diamond, diamond and vacuum, Ni and vacuum. Also, VISAR allows to continuously monitor the motion of the reflecting surface in time: in our case this is the Ni surface because at the pressures reached in the experiment diamond is not expected to metallize. Hydrodynamics simulations reproducing experimental data allow getting the pressure and density at each time. These were performed with the code CHIC [3].

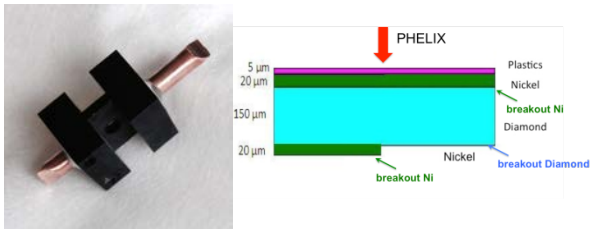

Figure 1: Water target assembly (left), and diamond target structure (right).

An example VISAR trace is shown in Fig. 2. For this shot hydro simulations reproducing the measured shock breakout times predict a shock velocity $D_{Ni} \approx 11.1$ km/s in nickel, corresponding to a pressure $P \approx 5.6$ Mbar. Impedance mismatch upon shock breakout into the diamond then yields pressures of $P \approx 4.5$ Mbar and a shock velocity $D \approx 15.7$ km/s in the diamond.

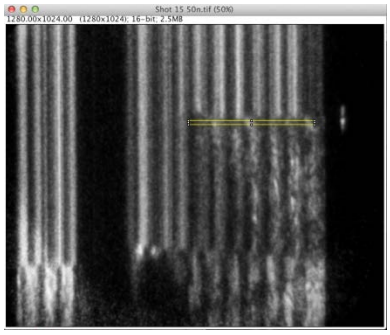

Figure 2: VISAR image from a diamond target.

Measuring of the VISAR fringe shifts in conjunction with measured shock velocities and hydrodynamic calculations enables us to extract the refractive index in the shocked material. This will allow for direct comparison with predictions from ab-initio calculations. Currently, a detailed analysis of all obtained shots is underway, and a detailed comparison with hydro simulations using different state-of-the-art EOS-models.

The authors acknowledge partial funding for this experiment by Laserlab Europe.

References

[1] Redmer *et al.* Icarus **211,** 798 (2011)
[2] Cavazzoni *et al.*, Science **283**, 44 (1999).
[3] J. Breila, et al., Computers & Fluids **46**, 161 (2011).

Investigation of plasma-accelerated flyer plates*

S. Sander[1], *J. Helfrich*[1], *S. Frydrych*[1], *J. Ohland*[1], *C. Bläser*[1], *G. Schaumann*[1], *D. Schumacher*[2], *A. Blazevic*[2], *and M. Roth*[1]

[1]Technische Universität Darmstadt, Institut für Kernphysik, Schlossgartenstraße 9, 64289 Darmstadt, Germany;
[2]GSI Helmholtzzentrum für Schwerionenforschung GmbH, Planckstraße 1, 64291 Darmstadt, Germany

Introduction

Man-made space debris is exponentially increasing in the low earth orbit, posing a big threat on current and future space missions [1]. To remove the space debris, high velocity impacts ($v > 10$ km/s) of tungsten balls with a presumed momentum transfer of $\sim 10 - 15$ are proposed to slow down space debris [2]. Thereby, it will decrease in orbit and burn up in the atmosphere earlier.

Experiment

The first objective is to reach a high velocity with a tungsten flyer plate that remains in a solid state. For preliminary experiments, a special target design has been developed as seen in figure 1.
The first layer is a $270\,\mu$m thick polyethylene (PE) sample. A tungsten thumbtack construction with a $50\,\mu$m thick and $600\,\mu$m long stalk and a head diameter of $600\,\mu$m and $25\,\mu$m thickness is glued on the PE rear side. In this setup, the accelerated head is free and not glued to any structure other than the PE itself.
The experiments are performed at the target area *Z6* at GSI, where the *nhelix* laser system is used to drive a shock wave into the PE. After the shock breakout, the expanding material hits the disk of the thumbtack. This is supposed to accelerate the thumbtack to high velocities, while retaining the solid state of the disk.
With a streak camera the shock breakout on the rear side of the PE is determined to calculate the shock velocity in the PE. This information is used to benchmark future simulations. The temporal behaviour of the plate is measured with two *DICAM Pro* in a side view configuration (see figure 1). Over several shots, a time evolution of the flyer plates reaction has been obtained (see figure 2).
In figure 2a, the tungsten disk can be seen undisturbed. 100 ns after the *nhelix* impact, the expanding material reaches the flyer plate (2b). In figure 2c, at $t = 150$ ns, the flyer plate starts to expand and eventually breaks apart as seen in figure 2d. Over multiple shots an average expansion velocity of the PE was estimated to ~ 1 km/s. A rough estimate of the expansion of the tungsten in figure 2c and d results in $v_{\text{expansion}} \approx 7$ km/s. A movement of the flyer plate prior to break up could not be confirmed. This phenomenon is currently under investigation. Possible explanations are a pre heat of the flyer plate due to radiation from the *nhelix*-PE interaction or a generation of a strong shock wave in the tungsten.

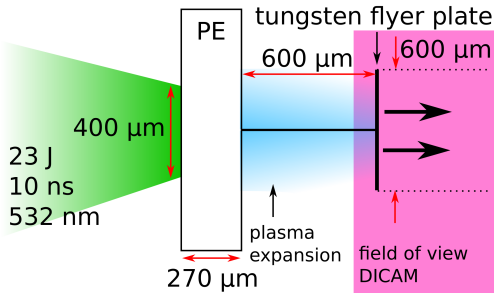

Figure 1: Schematic setup of experiment: The shock wave is driven with the *nhelix* laser (with 23 J, 532 ns, 10 ms, spotsize 400μm and intensity homogenized flat top) into 270μm thick PE samples. A streak camera determines the shock breakout on the PE rear side. The flyer plate is observed with two *DICAM Pro* in a side view configuration.

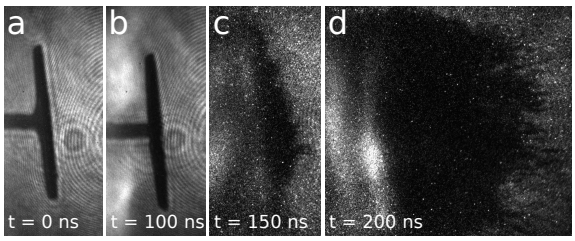

Figure 2: *DICAM Pro* measurements show the temporal development of the impacting plasma expansion on the flyer plate and the reaction of the plate.

Simulation

Simultaneously, hydrodynamic fluid simulations are prepared to further study possible target designs. In a first step, the FEOS code has been analysed and is now used to produce the equations of state (EOS) for tungsten and PE which are required for the simulations. These simulations will be benchmarked with the already received experimental results.

References

[1] McKnight, Darren and Donald Kessler, IEEE Spectrum, Retrieved (2012).

[2] G. Ganguli, C. Crabtree, L. Rudakov, S. Chappie, Aerospace Conference, 2012 IEEE (2012).

*This report is also published in *News and Reports from High Energy Density generated by Heavy iOn and Laser Beams 2015.*

DOI:10.15120/GR-2016-1

Simulations of hydrodynamic tunneling of the Future Circular Collider protons in solid copper target*

N.A. Tahir[1], *F. Burkart*[2], *R. Schmidt*[2], *A. Shutov*[3], *D. Wollmann*[2], *and A.R. Piriz*[4]

[1]GSI, Darmstadt, Germany; [2]CERN, Geneva, Switzerland; [3]IPCP, Chernogolovka, Russia; [4]UCLM, Ciudad Real, Spain

After the unprecedented success of the Large Hadron Collider (LHC), the international community (with CERN taking the leading role) is involved in a design study of a new, much bigger and much more powerful accelerator complex named the Future Circular Collider (FCC). This new machine will accelerate two counter rotating proton beams to a maximum energy of 50 TeV in a 100 km circumference tunnel, before they will be made to collide. According to the nominal design parameters, each beam will comprise of 10600 bunches with a bunch intensity of 10^{11} protons which means 1.06×10^{15} protons per beam. The bunch length is 0.5 ns while separation between two neighboring bunches is 25 ns so that the total length of the bunch train is 265 μs. The intensity distribution in the focal spot is a Gaussian in the transverse direction with a standard deviation, σ = 0.2 mm.

It is to be noted that each FCC beam carries an awesome energy of around 8.5 GJ which is equivalent to airbus A380 (560 t) flying at a speed of 850 km/h. Safety of operation with such extremely powerful beams is a critically important issue, as off–nominal beam deflection can have serious consequences for the accelerator components, accelerator environment and other equipment. To estimate the consequences of such an accident, we carried out simulations of full impact of one FCC beam beam with a solid copper cylinder. The beam is incident perpendicular to one face of the cylinder so that the beam axis coincides with the target axis. In these calculations we assume that the target is 5 m long and has a radius of 2 cm. The simulations have been carried out using an energy deposition code, FLUKA [1] and a 2D hydrodynamic code, BIG2 [2], iteratively. First, the FLUKA code is used to calculate the energy loss of the protons considering solid material density. This energy loss data is used as energy input to BIG2, which then calculates the thermodynamic and the hydrodynamic response of the target. The high energy deposition in the target by only a few bunches leads to strong heating that generates extremely high pressure in the absorption region. The high pressure launches a radially outmoving shock wave that leads to strong density depletion along, and around the axis. The protons that are delivered in the subsequent bunches therefore penetrate much deeper into the target and continuation of this process (proton hydrodynamic tunneling) leads to a substantial prolongation of the penetration depth of the projectile particles. We note that when the density along the axis decreases by about 15 %, the hydro calculations are stopped and the modified density distribution is used in FLUKA to calculate the modified energy loss distribution, which is then used in the BIG2. This process is continued iteratively untill the end of the calculation. We note that when this work started, the FCC beam parameters were not finally fixed and at that time 40 TeV was considered. Of course these calculations can be extrapolated to 50 TeV, which is considered today.

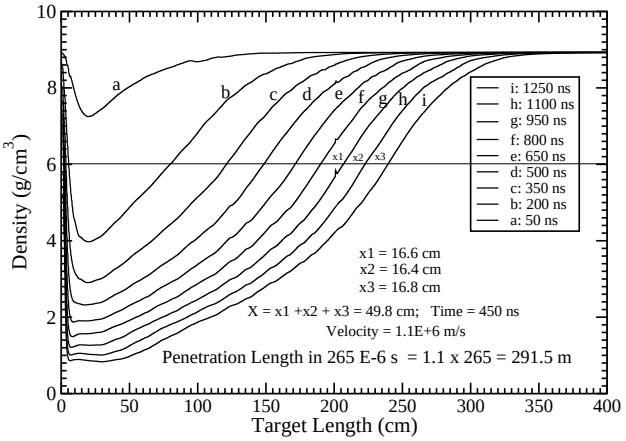

Figure 1: Density vs target axis at different times for calculation of the penetration depth of the protons.

It is to be noted that due to the storage and time limitations of the computer, it is not possible to carry out simulations of the interaction of all the 106000 bunches with the target. Nevertheless, one can have a very good estimate of the penetration depth of the proton beam as follows. In Fig. 1, we present density vs axis at different times during irradiation. Curve "a" represents the time when 2 bunches have been delivered while later curves are plotted using an interval of 150 ns. We consider 6 g/cm^3 as the reference point on the density curve and calculate the speed with which this point moves towards the right. It is seen that at 800 ns, the depletion front achieves a steady average speed of 1.1 x 10^6 m/s. The total beam duration considering all 10600 bunches is 265 μs that leads to a penetration distance of about 290 m. If one considers 50 TeV proton beam, the penetration distance could be up to 350 m.

References

[1] A. Fasso et al., in Conf. on Computing in High Energy and Nuclear Physics, La Jolla, USA, 2003.

[2] V.E Fortov et al, Nucl. Sci. Eng., vol. 123, p. 169, 1996.

* Work supported by GSI and CERN

Simulations of beam–matter interaction experiments at the CERN HiRadMat Facility*

N.A. Tahir[1], *F. Burkart*[2], *R. Schmidt*[2], *A. Shutov*[3], *D. Wollmann*[2], *and A.R. Piriz*[4]

[1]GSI, Darmstadt, Germany; [2]CERN, Geneva, Switzerland; [3]IPCP, Chernogolovka, Russia; [4]UCLM, Ciudad Real, Spain

Figure 1: Three target assemblies used in three different experiments, each comprised of 15 solid Cu cylinders, every cylinder has radius, r = 4 cm, length, L = 10 cm and 1 cm gap in between.

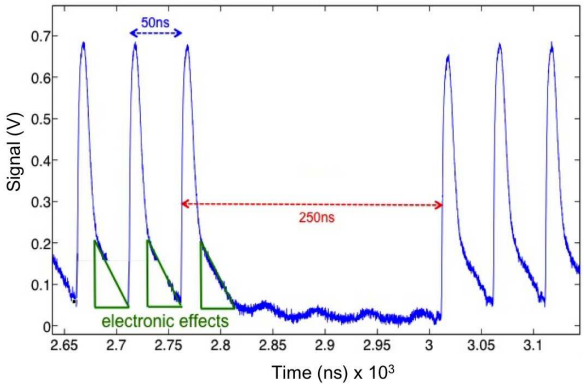

Figure 2: Time structure of the proton beam.

Beam–matter interaction experiments were performed at the CERN HiRadMat facility in which solid copper cylindrical targets were irradiated with 440 GeV, bunched proton beam delivered by the Super Proton Synchrotron [1,2]. The three target assemblies used in three different experiments are shown in Fig. 1. Each assembly is comprised of 15 Cu cylinders, each 10 cm long with a radius of 4 cm and a gap of 1 cm in between to allow for diagnostic. The beam is incident vertical to the left face of the first cylinder so that the beam axis coincides with the cylinder axis. The temporal profile of the beam is presented in Fig. 2. In fact the protons were delivered in sets of 36 bunches each, while a separation of 250 ns was considered between the neighboring bunch packets. The beam parameters used in the experiments are given in Table 1.

Detailed numerical simulations were also carried out in order to understand the experimental measurements. These simulations were done using an energy deposition code FLUKA and a 2D hydrodynamic code, BIG2, iteratively. In the simulations, we used the exact experimentally used beam parameters, but for the simplicity of the calculations, we considered a single copper cylinder with a length of 150 cm and a radius of 4 cm. Previously [3], we reported simulations of Experiment number 2 and 3, which showed that the penetration depth of the protons and the shower was in excellent agreement with the experimental measurements (unlike the static simulations excluding the hydrodynamics). In the present contribution, we report simulation results of Experiment number 1, which again is in very good agreement with the experimental measurements, as seen in Table 2 which provides a comparison between the experimental measurements and the simulations for all the three experiments.

Table 1: Beam Parameters Used in the Three Experiments

Experiment Number	Number of Bunches	Beam σ (mm)	Beam Energy (MJ)
1	144	2.00	1.52
2	108	0.20	1.14
3	144	0.20	1.52

Table 2: Comparison between simulated and measured penetration length.

Target	Simulated (cm)	Measured (cm)	Measure to Simulated(cm)
1	56	58	-2.0
2	80	79.5	0.5
3	90	85	5.0

References

[1] R. Schmidt et al., Phys. Plasmas 21 (2014) 080701.

[2] F. Burkart et al., J. Appl. Phys. 118 (2015) 055902.

[3] N.A. Tahir et al., Phys. Rev. E 90 (2014) 063112.

* Work supported by GSI and CERN

DOI:10.15120/GR-2016-1

Energy dependence of the radiation exposure of electronics for the plasma physics experiments studied with FLUKA

S. Damjanovic[1] and A. Tauschwitz[1]
[1]GSI, Darmstadt, Germany

The energy dependence of the radiation environment due to the interaction of intense U-ion beams with lead targets has been simulated with FLUKA with the goal to estimate the radiation damage to electronic equipment planned to be installed within and near the target chamber. Electronics exposed to a radiation field could experience three different types of radiation damage: damage from the total ionising dose, displacement damage and single event errors. The first two have a cumulative nature and can be assessed through the dose and 1MeV-neutron-equivalent fluence. The third has a stochastic nature and can only be evaluated in terms of probability vs. high-energy hadron fluence. All three quantities have been studied, but only the results for the physical dose are presented in this report.

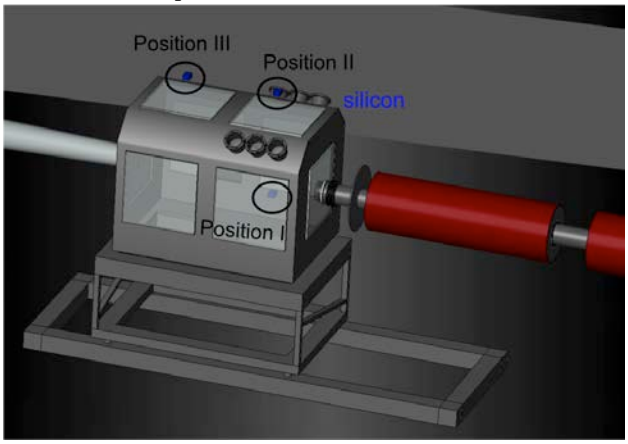

Figure 1: FLUKA geometry of the target chamber with three selected locations for the installation of electronics

The simulations are based on a focussed uranium beam of maximum intensity (5×10^{11} particles per pulse) and kinetic energies of 0.4, 1.0 and 2.0 GeV/u. The length of the lead targets is defined as 60% of the beam range in the target: 2.7 mm for 0.4 GeV/n, 9.7 mm for 1 GeV/n and 23 mm for 2 GeV/n, assuring about the same fraction of the total beam energy deposited in the lead target.

A closer look at the target chamber in terms of physical dose distributions for a single shot of U-ions is shown in Fig.2. The dose delivered to silicon is then quantified for three different locations of electronics indicated in Figs. 1 and 2 (labelled as Positions I-III). A summary of the beam energy- and electronic location dependence of the dose per single shot is shown in Fig.3. The final results are presented with the closed markers. As visible there, nearly independent of energy the dose at the Position I (in the immediate vicinity of the target) is found to be larger by about factors of 130/70 than at the Positions II and III (outside of the chamber), respectively. Depending on the equipment position, the dose for the highest beam energy considered (E_k=2 GeV/n) is larger by factors of 4-5 than for E_k=1 GeV/n, and by factors of 40-140 than for E_k=0.4 GeV/n. In order to better understand the energy dependence and to distinguish the effects from the primary beam and the secondaries produced, the dose values are normalized to the total energy deposited in the targets and plotted in the same Fig.3 with the open markers.

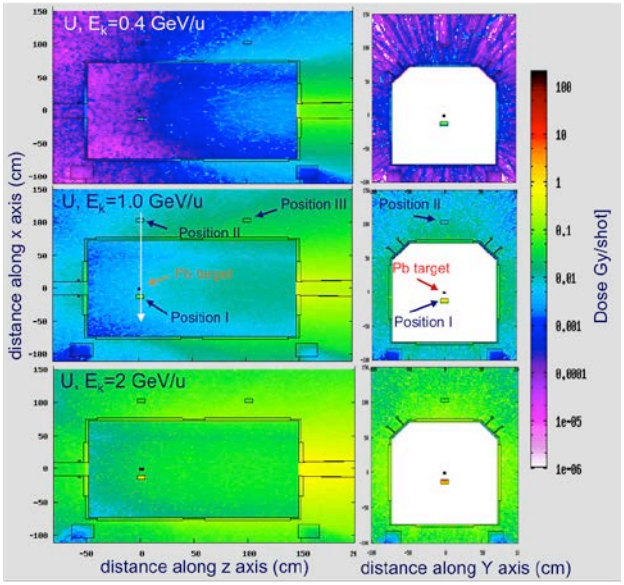

Figure 2: Dose distribution for a single shot of U-ions at E_k=0.4, 1.0 and 2.0 GeV/n

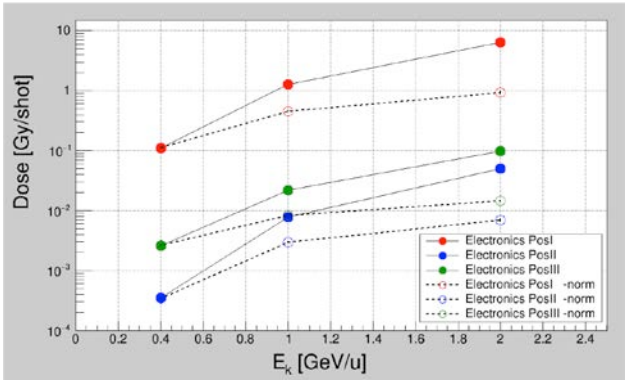

Figure 3: Dose in electronics vs. beam energy for the same fraction of energy deposited in the target (closed) and normalized to the total energy deposited (open points)

The sensitivity of electronics to radiation strongly depends on the used technology and the construction of the device. As a very rough guideline commercially available electronics must be expected to fail if the cumulated dose reaches 10^2 to 10^5 Gy.

DOI:10.15120/GR-2016-1

Design of a 5 GeV Proton Microscope for FAIR*

M. Schanz†[1], *D. Varentsov*[2], *and D.H.H. Hoffmann*[1]
[1]TU Darmstadt, Darmstadt, Germany; [2]GSI, Darmstadt, Germany

The PRIOR-I (Proton Microscope for FAIR) prototype facility has recently been commissioned at GSI with 3.6 GeV proton beams delivered by the SIS-18 heavy ion synchrotron [1]. The design of this microscope is based on compact high-gradient (120 T/m) NdFeB permanent magnet quadrupole (PMQ) lenses which can facilitate imaging with protons up to 4.5 GeV. This system is capable of providing a magnified image of a dense object and correcting the most significant terms of the chromatic aberrations, which led to the achievement of micrometer-level spatial and nanosecond-scale temporal resolution with a remarkable density sensitivity during the beam time commissioning. Despite the success of the first experiments, a continuous degradation of the image quality and spatial resolution due to a severe radiation damage of the PMQ lenses has been observed [1]. It was concluded that PMQ lenses are not an appropriate choice for a radiographic facility with high-energy and high-intensity proton beams. Therefore the final design of the PRIOR proton microscope (PRIOR-II) will employ small but strong and radiation-resistant normal conducting electromagnets in order to assure high imaging quality for future experiments at GSI and FAIR.

Since the PRIOR-II microscope has to fulfill a lot of different requirements which will mainly be determined by the future experiments, new simulation tools were developed to estimate the performance of the new system [2]. The respective ion optical simulations were based on COSY Infinity 9.1 taking into account high order image aberration effects which determine the image quality of a radiographic setup. By the observation of the geometrical moments of a point spread function an entirely new approach to the calculation of the spatial resolution performance of radiographic facilities was introduced [2].

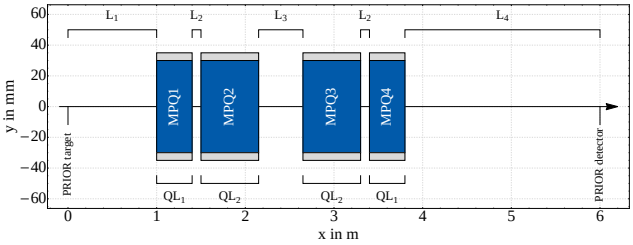

Figure 1: Geometrical layout of the PRIOR-II setup.

The PRIOR-II setup was optimized regarding the length of the individual magnets QL_1 - QL_4 as well as the distances between the magnets L_1 - L_4 (see Fig. 1) in order to obtain a compromise between the resolution and the constraints of the construction process. The shape of the yoke was chosen to guarantee an overall field deviation $\Delta G/G$ of less than $4 \cdot 10^{-4}$ and to suppress higher multipole orders ($B_n/B_2 < 4 \cdot 10^{-4}$), especially $n = 6, 10, 14$, between 80% and 90% load. The two layered coil with just 14 turns per pole will provide high field gradients up to G= 43.3 T/m (30 mm pole tip radius) while being driven by 1.7 kA current [3].

When PRIOR-II will be installed at FAIR utilizing 5 GeV protons, a magnification of 7.98 with a micrometer-level spatial resolution ($CR_x = 7.26$ μm, $CR_y = 3.83$ μm) and the maximum field of view of 26.9 x 21.5 mm^2 can be provided (see Fig. 2).

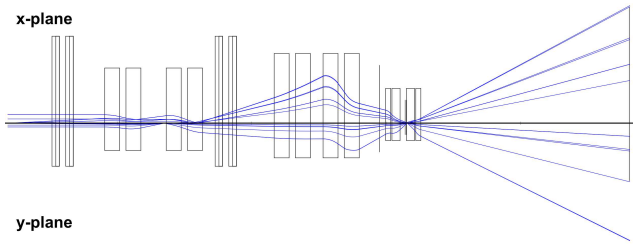

Figure 2: Ion optical layout of PRIOR-II.

It is foreseen that during the construction of FAIR, PRIOR-II will be installed first at the HHT cave at GSI and provide a magnification of 2.5 ($CR_x = 9.67$ μm, $CR_y = 6.51$ μm).

The design of PRIOR-II will offer simultaneously a variable geometry and a variable field gradient, enabling a wide range of proton energies to be used for various investigations on high energy density states in matter as well as on medical applications with an impressive image quality.

References

[1] D. Varentsov et al., Rev. Sci. Instrum. **87**, 023303 (2016)

[2] M. Schanz, "High Energy Proton Microscopy at FAIR", Master thesis, TU Darmstadt (2016)

[3] A. Kalimov, "Quadrupole for PRIOR-M", intl. Tech. Rep. GSI (2015)

* Work supported by BMBF, grant agreement ID 05K13RDB. This report is also submitted to *'News and Reports from High Energy Density generated by Heavy Ion and Laser Beams 2015'*.

† m.schanz@gsi.de

DOI:10.15120/GR-2016-1

Demagnetization of PRIOR Permanent Magnet Quadrupoles*

M. Endres †[1], *M. Schanz*[1], *P. M. Lang*[2], *D. Varentsov*[3], *and D.H.H. Hoffmann*[1]
[1]TUD, Darmstadt, Germany; [2]European XFEL, Hamburg, Germany; [3]GSI, Darmstadt, Germany

The PRIOR-I Proton Microscope was commissioned at GSI in 2014. [2] The setup consists of four Permanent Magnet Quadruople (PMQ) Lenses, each one assembled from several Halbach-Style arrays (PMQ modules). The PMQ modules itself consist of 48 single NdFeB wedges arranged in two (inner and outer) circles with 24 segments each (see fig. 1). During the beam time with 4.5 GeV protons the lenses were hit and therefore damaged by radiation, resulting in a decreased quality of the magnetic field and a worse image quality. Measurements of the magnetic field after the first experiments showed a degradation of the field gradient by $10-13\%$, in addition an increase of higher multipole components was observed. Following those investigations, various NdFeB magnetic material was deliberately irradiated and analyzed.

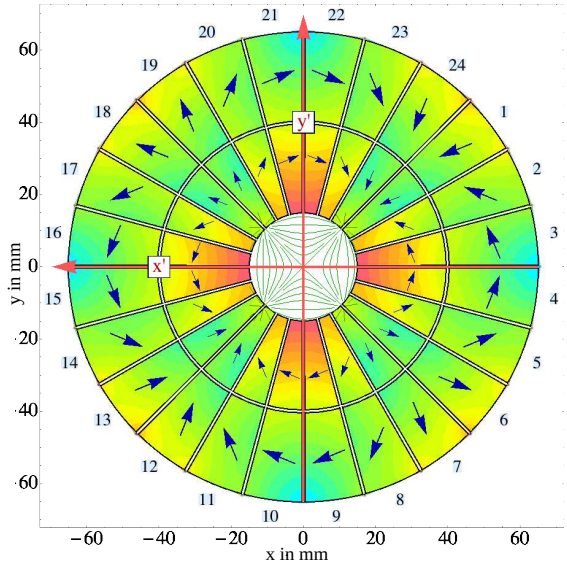

Figure 1: Geometry of the PRIOR PMQ Modules. The colour shows the internal Field H.

At first single wedges were irradiated with protons with different doses. The irradiated ones and one non-irradiated wedge were cut into small samples to scan the magnetic properties. Here a correlation between the absorbed dose and degradation was already visible [1]. To investigate the influence of the $\vec{H}$-Field inside an assembled module a PMQ module was deliberately irradiated. The module was irradiated with approximately $8.3 \cdot 10^{11}$ protons at 3.6 GeV. The dose for each wedge was measured with radiochromatic films (RCF). The field gradient was measured on the x' and y' axes each on five points (see figure 1).

The RCF showed that wedge 23 and 24 from the inner ring had absorbed the highest dose while wedge 11 and 12 from the inner ring were barely affected by radiation. These wedges were replaced with non-irradiated ones. The "repaired" module was scanned again. No increase of the field gradient in comparison with the measurement directly after the irradiation was visible. The disassembled wedges were individually scanned for their magnetic properties. No correlation between the dose and the observed degradation could be proved. This led to the conclusion that – assembled in an array – the wedges which absorbed the highest dose are not the most damaged ones.

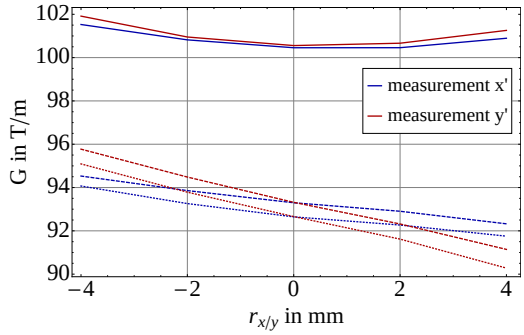

Figure 2: Gradient before (solid), after irradiation (dashed) and after exchange of segments with highest dose (points).

The replaced and analyzed wedges were located in regions which are the magnetic poles of the quadrupole. This are regions with a low $\vec{H}$-Field. It seems possible that the influence of the this field is higher than the the influence of the dose. To proof this hypothesis, more wedges have been disassembled and will be analyzed.

To overcome the issue of demagnetization, a new mircoscope facility (PRIOR-II) – based on electromagnetic quadrupoles – has been developed at GSI in 2015. [3] Simultaneously a setup for the remagnetization of the PRIOR-I facility is assembled at the collaborating institute ITEP.

References

[1] P. Lang, Dissertation TU Darmstadt 2014.

[2] D. Varentsov et al., Rev. Sci. Instrum. arXiv:1512.05644, (submitted) (2016).

[3] M. Schanz, GSI Report 2015.

* Work supported by BMBF. This report is also submitted to *News and Reports from High energy Density generated by Heavy Ion and Laser Beams 2015*

† m.endres@gsi.de

State of development of the inductive coupled plasma stripper device *

K. Cistakov[1#], A. Fedjuschenko[1], G. Xu[1,2,3], Ph. Christ[1], M. Iberler[1], T. Ackermann[1], T. Rienecker[1], A. Blazevic[4], K. Weyrich[4], O. Rosmej[4], A. Schönlein[1], J. Wiechula[1], T. Manegold[1], S. Zähter[1] and J. Jacoby[1]

[1]Goethe University of Frankfurt, Frankfurt am Main, Germany; [2]IMP, Lanzhou, China; [3]UCAS, Beijing, China; [4]GSI, Darmstadt, Germany;

At the present time gas and solid foils are mainly used as stripper in accelerator facilities like GSI to achieve an increase in the charge state of the ions. As an alternative to these methods a dense pinch plasma is proposed as stripper medium. Compared to a gas stripper, which shows much less effectiveness, and a foil stripper, which has a shorter life time, a plasma stripper has both higher efficiency and longer lifetime. As a consequence, this novel stripper is recommended for the requirements at FAIR.

The effect of a plasma for the increase of the equilibrium charge states has been already proved in experiments with a Z-pinch [1]. However, a disadvantage of the Z-pinch is the erosion of the electrodes, which has a negative impact in the lifetime of the systems. Apart from that, the high magnetic fields have an adverse effect in the beam optic. In contrary to the Z-pinch a Theta-pinch has no erosion and the magnetic field of the coil is mainly in the center of the coil. The magnetic field distribution is mainly parallel to the beam and has therefore no influence to the beam dynamics [2] [3] [4]. For the ignition of a dense plasma, a spherical Theta-pinch was developed and successfully tested at a beam time at GSI. A major feature of the Theta-pinch is the use of a large spherical discharge vessel surrounded by a multi-turn induction coil, which is connected to a capacitor bank via low inductance transmission line, thus forming a resonant circuit. The stored energy in the capacitors was 3.6 kJ. As switch a high power thyristor stack was used. During the pinch a maximum electron density of about $3.5 \times 10^{22} m^{-3}$ (Figure 1) were achieved.

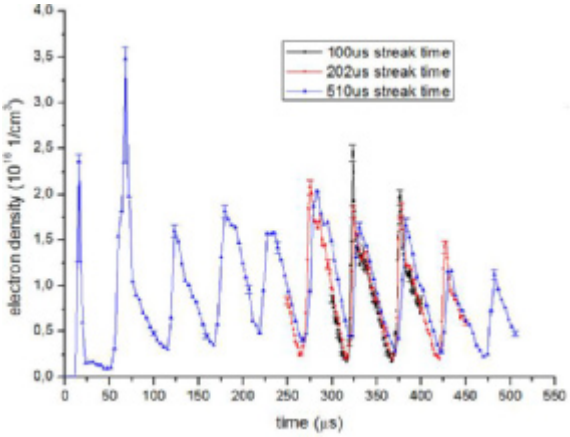

Figure 1. Electron density of a 14 kV, 110 Pa discharge, measured with different streak times [5].

The charge state of the ion beam was increased. In experiment on Z6 Area during beam time 2014, the initial state of the ion beam Au^{26} was increased to the final state of Au^{31}.The measurements made with the spherical Theta-pinch during the beam time showed, however, a negative impact in the beam optic due to distortion of the magnetic field at the ends of the coil. The reason is an asymmetrical current flow at the connecting elements of the coil. Therefore, a maximum ion transmission of about 58% was achieved. A modified form of the Theta-pinch is being developed to increase the electron density and the transmission.

A new stripper cell with cylindrical coil and symmetrical power connection was designed, in order to eliminate asymmetric magnetic fields. Through the diamagnetism of the plasma along the entire z-axis, the ion beam will be sufficiently protected from the influence of asymmetric magnetic fields.

Because of the cylindrical design of the coil, the efficiency of the energy transfer will be decreased from 85% to a maximum of 50%. Due to the new coil design the energy storage system has been increased from 3.6 kJ to 49 kJ. Thus, the energy deposition into the plasma is expected to be increased by a factor of 8. Within this configuration the expected plasma densities are of $3 \times 10^{23} m^{-3}$.

References

[1] J. Jacoby et al., „Stopping of Heavy Ions in a Hydrogen Plasma“ Physical Review Letters 74, Nr. 1550, 1995.

[2] C. Teske et al., „Energy transfer efficiency of a spherical theta pinch“ Physics Plasmas 17, Nr. 043501, 2010.

[3] C. Teske et al., „Electron density and plasma dynamics of a spherical theta pinch”, Physics of Plasmas 19, Nr. 033505, 2012.

[4] G. Loisch et al., „ Review of the State-of-the-Art Development of the Spherical Theta Pinch Plasma Source“, Plasma Science 42, Issue 5, 2014.

[5] G. Loisch et al., „Hydrogen Plasma Dynamics in the Spherical Theta Pinch Plasma Target for Heavy Ion Stripping“ Physics of Plasmas 22, Nr. 053502, 2015.

* Work supported by BMBF contract No 05P2015.
* This report is also submitted to 'News and Reports from High Energy Density generated by Heavy Ion and Laser Beams 2015
*cistakov@iap.uni-frankfurt.de

DOI:10.15120/GR-2016-1

Regulation of heterochromatic DNA double strand break relocation*

A. Heselich[1], N.P. Benz[1], K.O. Voss[1], C. Sauter[1], N. Özguen-Korkusuz[1], G. Taucher-Scholz[1,2] and B. Jakob[1]

[1]GSI, Darmstadt, Germany; [2] TU Darmstadt, Darmstadt, Germany

Motivation

Repair of DNA damage in heterochromatic areas (HC) is a challenge for cells, but eukaryotic cells have developed mechanisms to enable efficient repair of heterochromatic DNA double strand breaks (HC-DSBs). These damages are moved to the euchromatic-heterochromatic border, and at the same time decondensation of the chromatin takes place. This process was first shown in Drosophila by Chiolo *et al.* [1] and in mammalian cells by our group [2] and might support further repair. In order to identify possible factors involved in these processes we analyzed DSB-relocation in wild-type and deficient /knock-down murine fibroblasts cells after targeted irradiation at the GSI microprobe.

Materials & Methods

We generated knock-out cell lines of murine fibroblasts (NIH/3T3) via the so-called CRISPR/Cas9 system with knock-out of either HP1 alpha or beta. For irradiation experiments siRNA mediated knock-down of the corresponding HP1 isoform was performed as well. Chromocenters representing the HC areas in murine cell nuclei were irradiated with heavy ions (Au 4,8 MeV/u) using targeted ion irradiation at the microbeam facility. Recruitment of DNA repair factors and kinetics of relative occurrence of DNA DSBs at three positions in/at chromocenters (central, intermediate and peripheral) were evaluated after immunofluorescence staining against γH2AX and HP1alpha or beta.

Results

A potential candidate to play a role in relocation of heterochromatic DSBs was HP1 (heterochromatin protein 1), which facilitates the condensation of HC. In addition it is known to be recruited to laser-, ultrasoft X-ray- or alpha particle-induced DNA damage independent from H3K9 methylation [3]. In first heavy ion irradiation experiments we detected the accumulation of HP1alpha at the DNA damage sites in chromocenters (Fig. 1), which interestingly stayed localized at the DSB during its transport out of HC and afterwards. DSB relocalization kinetics after microbeam irradiation with Au (4,8 MeV/u) showed a fast relocalization to the periphery of chromocenters in WT NIH/3T3. Despite the relocation of HP1alpha together with damage sites in WT cells, up to now no significant influence on the relocation process could be found in HP1 knock-out cells, neither for HP1 alpha knock-out cells with HP1 beta knock-down (Fig. 2) nor for HP1 beta knock-out cells with knock-down of HP1 alpha (data not shown).

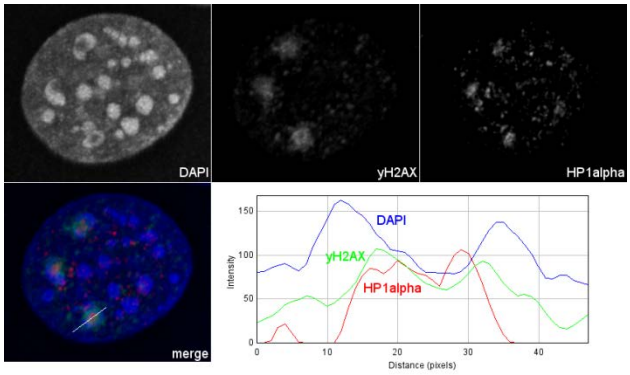

Figure 1: DNA damage induced in chromocenters by targeted heavy ion irradiation gets relocated to the euchromatic/heterochromatic border over the time. Co-localization analysis via signal profile blots showed that HP1 alpha (red) accumulates at these damages (green) and stays at the damage site during the relocation process.

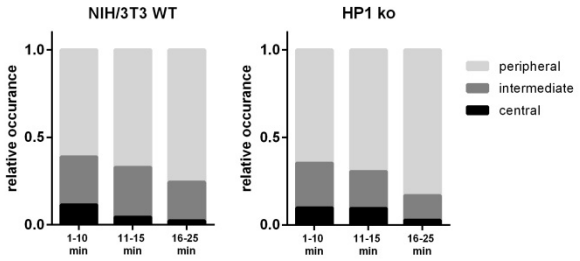

Figure 2: Relocation of HC DNA DSBs over time after targeted irradiation in WT and HP1alpha knock-out/HP1 beta knock-down cells. Data represent rel. occurrence of the 3 different positions in hit chromocenters. Irradiation: Au 4,8 MeV/u, microbeam facility GSI.

Summary

We observed accumulation of HP1alpha at HC damages that stayed at the damage site even during the relocation. However, we saw no significant influence on relocation of DNA DSBs in HP1 knock-out/knock-down cells compared to WT NIH/3T3. We therefore conclude that HP1 has no major role in the relocation of heterochromatic DNA damage in mammalian cells despite its proposed role in *Drosophila* [1]. We are now looking for alternative factors capable of influencing the relocation of DNA DSBs to the euchromatic/heterochromatic border to elucidate its influence on DNA repair.

References

[1] Chiolo, I., *et al.* Cell 144, 2011.
[2] Jakob, B., *et al.* Nucleic acids research 39, 2011.
[3] Luijsterburg, M.S., *et al.* JCB 185, 2009.

* This work is supported by the German federal ministry of education and research (BMBF). Grant#: 02NUK037A.

Detection and spatial correlation of radiation induced DSB using SEM and Fluorescence Microscopy

S.Tonnemacher[1], G.Becker[1], G. Taucher-Scholz [1, 2] and B. Jakob[1]
[1]GSI, Darmstadt, Germany; [2]Technical Universität Darmstadt, Germany

Introduction

The resolution of electron microscopy (EM) is significantly superior compared to standard fluorescence microscopy (FM). A major dis-advantage of transmission EM (TEM) for radiobiological studies is the loss of 3D context due the need of ultrathin layers. In contrast, using Scanning EM (SEM) it is possible to get information on the 3D topology which is due to its high depth of sharpness. However, to observe the inner structure of cells or cell nuclei in SEM, the biological samples need to be dried and ruptured in a way which preserves the ultrastructure. In this study we show the possibility of correlative imaging by SEM and FM of cellular chromatin preparations. For visualisation of radiation induced DNA damage, antibodies against repair proteins and detection by combined immunogold and organic chromophores were used.

Materials and Methods

NIH-3T3 cells were cultured on 7x5mm silicon wafers with engraved marks. Cells were irradiated (1Gy x-ray), fixed 30 min post-irradiation in MeOH (30 min, -20°C) and permeabilised in ice cold acetone (1 min). For immunocytochemical staining γH2AX monoclonal AB was used. The secondary AB carried two labels (10 nm colloidal gold and Alexa 488). After staining, samples were dried using an ethanol extraction series and subsequent critical point drying (CO_2). FM was done at a Leica BM LA using a 63x 0.9 NA water lens. SEM was done at a Jeol ISM-7401F at an acceleration voltage of 5 kV. Two different detectors were used for the detection of back scattered electrons (gold beads) or secondary electron emission (topology, not shown).

Results

To establish the detection of DNA double-strand breaks (DSBs) with SEM it was necessary to show the correlation of the nanogold marker with known radiation induced signals in FM. By co-staining with the conventional AB (Alexa 568), we could prove that the double labelled secondary AB binds correctly to the desired biological target (not shown). Conditions were established for dry-rupturing the cell nuclei to get access to the chromatin in the SEM. To obtain correlated images, opened up nuclei were rehydrated, imaged in FM (Fig. 1a) and dried again for the vacuum conditions of the SEM. The engraved marks on the silicon wafers (337 nm N_2 laser) enabled revisiting these nuclei in the SEM (Fig. 1b). Fig. 1 shows exemplarily the correct retrieval of chromatin areas damaged by radiation (γH2AX) using our approach. Owing to the high resolution of SEM the gold beads are detected individually (Fig. 1b).

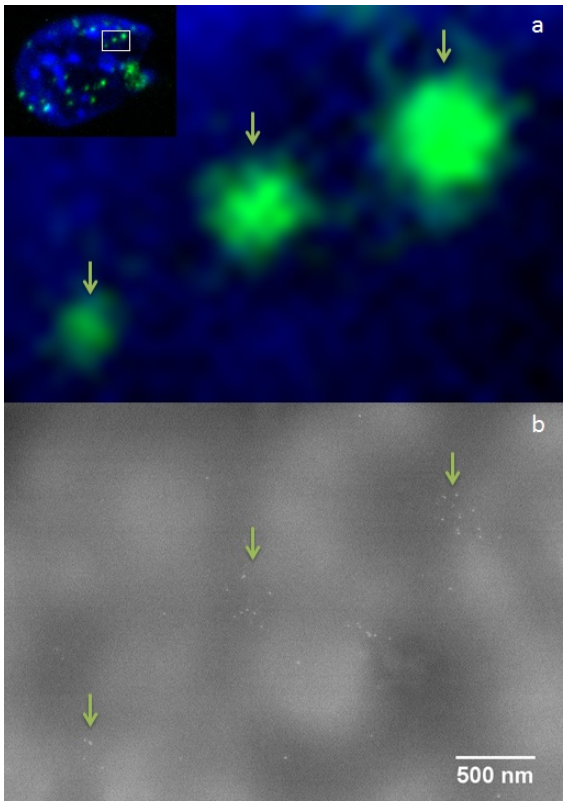

Figure1. a) Fluorescence image of an area of nucleus of NIH-3T3cell irradiated with 1 Gy x-rays. Blue: DNA; green Alexa 488 bound to γH2AX as a DSB marker. Insert: whole ruptured nucleus showing the enlarged area of (a) (rectangle). b: SEM image of the same area after repositioning. White dots represent individual gold beads at the chromatin surface.

Conclusions

We could demonstrate the possibility to correlate images of the DNA DSB marker γH2AX in irradiated cell nuclei using FM and SEM by introducing fiducial marks on the wafers for repositioning. SEM allows the detection of individual 10 nm gold beads as well as the chromatin topology when cells have been dry ruptured. As SEM detection of the nanogold is limited to the surface, the next step will be to obtain a 3D distribution utilizing a FIB-SEM.

Funding: This work was supported by BMBF Grant 02NUK037A and the graduate school HGS-Hire.

DOI:10.15120/GR-2016-1

Polymerase Θ plays no crucial role in the repair of complex DNA double-strand breaks induced by carbon ions*

C. Barent[1,2] , G. Becker[1], G. Taucher-Scholz[1,2], and N. B. Averbeck[1]
[1]GSI Helmholtzzentrum für Schwerionenforschung, Darmstadt, Germany; [2]TUD, Darmstadt, Germany

DNA double strand breaks (DSBs) represent severe lesions, which can compromise genomic integrity and even be lethal. Different DSB repair pathways exist and several factors influence their choice, e. g. enzymatic digestion of the 5' strand of the DNA molecule, i. e. resection.

Resection is important for the repair of heavy-ion induced DSBs independent of the cell-cycle phase [1]. Which repair pathway repairs these processed ends in G1-phase cells is still under investigation. The major repair pathway throughout the cell cycle, classical non-homologous-end-joining (NHEJ), cannot deal with resected ends. It is discussed that the PARP1-dependent alternative NHEJ pathway is involved, of which polymerase Θ (PolΘ) represents a factor [2].

We depleted cells of PolΘ to study whether it is involved in the repair of ion-induced DSBs in G1-phase cells. To analyse whether the chosen conditions of PolΘ depletion are effective, we treated mock- and PolΘ-depleted cells with H_2O_2. The selected conditions proved to be effective; they caused decreased cell survival after treatment with H_2O_2 as it was described earlier [3] (Fig. 1).

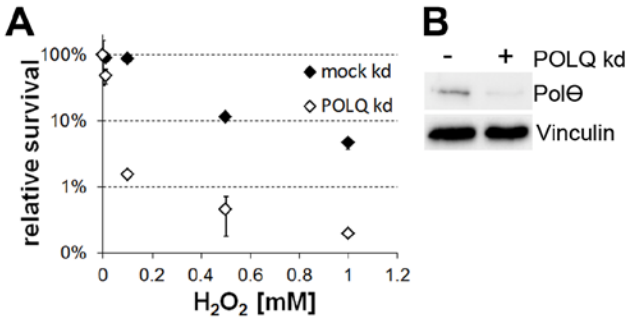

Figure 1: Survival of polymerase Θ-depleted cells is significantly decreased after induction of oxidative DNA lesions. (A) Human, immortalized fibroblasts (NFFhTERT) were depleted or mock depleted for PolΘ by RNAi mediated knockdown (kd) of POLQ and treated with different concentrations of H_2O_2 (0-1 mM). Cell survival was analysed by a clonogenic survival assay. Error bars: Standard deviation of three biological replicates. (B) The PolΘ depletion was proven by a western blot analysis. Vinculin served as a loading control.

Upon induction of complex DNA lesions after carbon-ion irradiation, cells depleted for PolΘ show no clear DSB-repair defect (Fig. 2), neither in G1- nor in G2-phase cells. Since PolΘ depletion also did not cause altered clonogenic cell survival (data not shown), these preliminary data suggest that PolΘ is not required for the repair of complex, ion-induced DSBs.

* This work is supported by BMBF grant 02NUK037A.

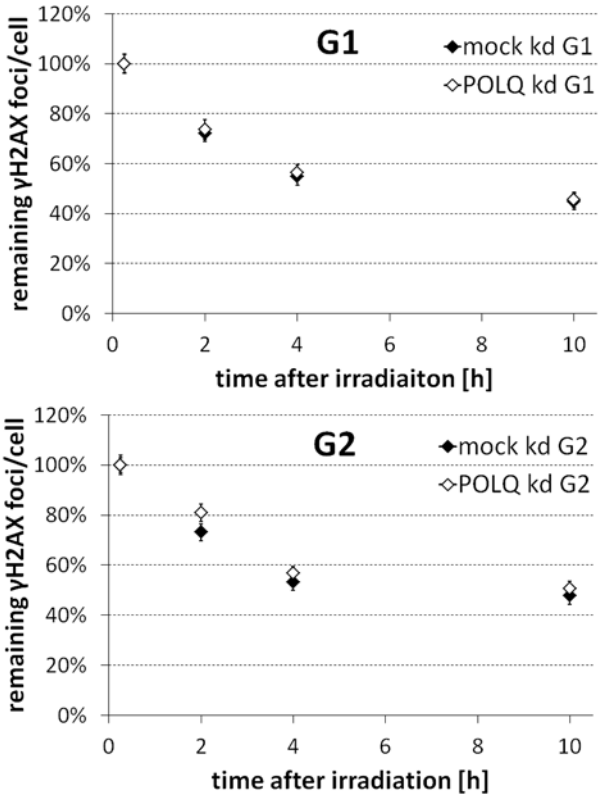

Figure 2: Repair of complex DSBs is polymerase Θ independent. Human, immortalized fibroblasts were depleted or mock depleted for PolΘ and irradiated with carbon ions (6.5 MeV/u, LET 325 keV/µm). Aphidicolin treatment prevented G1-cells from moving on to G2 and allowed to discriminate S-phase cells. DSB-repair kinetics were measured by the γH2AX (DSB marker)-foci assay [4] in G2- (CENP-F positive) and G1-cells (CENP-F negative). The numbers of γH2AX foci were normalized to the γH2AX foci number 15 min after irradiation, which served as the number of DSBs induced. Error bars: Standard deviation of three biological replicates.

References

[1] N. Averbeck *et al.*, Cell Cycle (2014) 13: p. 2509-2516
[2] P. Mateos-Gomez *et al.*, Nature (2015) 518: p. 254–257
[3] M. Yoshimura *et al.*, Mol Cell (2006) 24: p. 115-125
[4] M. Löbrich *et al.*, Cell Cycle (2010) 9: p.662-669

The recruitment of the resection regulators RIF1 and BRCA1 to complex DNA double-strand breaks in G1 cells after heavy-ion irradiation

T. Syzonenko[1], B. Jakob[1], G. Becker[1], M. Durante[1,2], G. Taucher-Scholz[1,2], and N. B. Averbeck[1]
[1]GSI Helmholtzzentrum für Schwerionenforschung, Darmstadt, Germany; [2]TUD, Darmstadt, Germany

Resection is an enzymatic degradation of DNA double stand breaks (DSBs), which with increasing LET exceedingly occurs at heavy-ion-radiation induced DSBs [1]. Resection represents an important step in the DSB-repair pathway choice. Cells have developed a cell-cycle dependent mechanism to control the DNA-DSB resection. In the G1 phase of the cell cycle the DSBs are widely protected from resection, in contrast, in S- and G2 phase DSB resection is permitted. However, after heavy-ion irradiation the induced complex DNA DSBs are resected not only in S- and G2- but also in G1-phase [1].

To study the regulation of resection in G1-phase cells after heavy-ion irradiation, we performed immunofluorescence staining against RPA, a resection marker, and BRCA1 and RIF1, two regulatory factors of resection. The latter prevents resection of simple DNA DSBs in G1-phase cells and the former promotes their resection in S- and G2-phase cells [2-4]. We found both factors are recruited to heavy ion-induced DSBs in G1-phase cells. However, they never co-localize (Fig. 1). Only BRCA1 but not RIF1 co-localizes with the resection marker RPA (Fig. 2).

These results conform to the finding that RIF1 and BRCA1 are antagonistic [2-4]. From this data we further conclude that only a subset of heavy-ion induced DSBs become resected in G1-phase cells. Since we find BRCA1 co-localizing with the resection marker RPA in G1-phase cells, our findings suggest that BRCA1's resection promoting activity is not limited to the G2-cell-cycle phase. Further studies will clarify the roles of RIF1 and BRCA1 and their interplay in the regulation of resection of heavy-ion-radiation induced DNA DSBs.

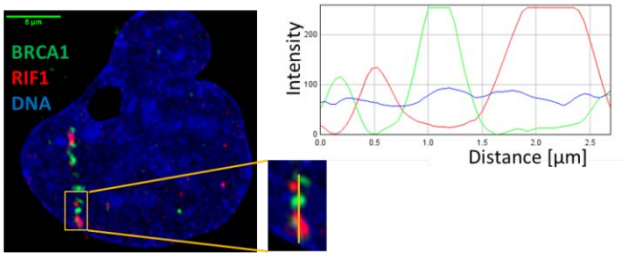

Figure 1: RIF1 and BRCA1 are recruited to complex DSBs induced in G1-phase cells. Human osteosarcoma cells (U2OS) were irradiated with Uranium-ions in a low angle (LET 15,000keV/µm, fluence $3x10^6$ p./cm^2). The cells were fixed 1 h after irradiation and immuno-stained against RIF1 and BRCA1. To discriminate G1 and S/G2 phase, the cells were additionally immuno-stained against CENP-F. G1-phase cells lack CENP-F and hence are negative for this staining. DNA was visualized by DAPI staining.

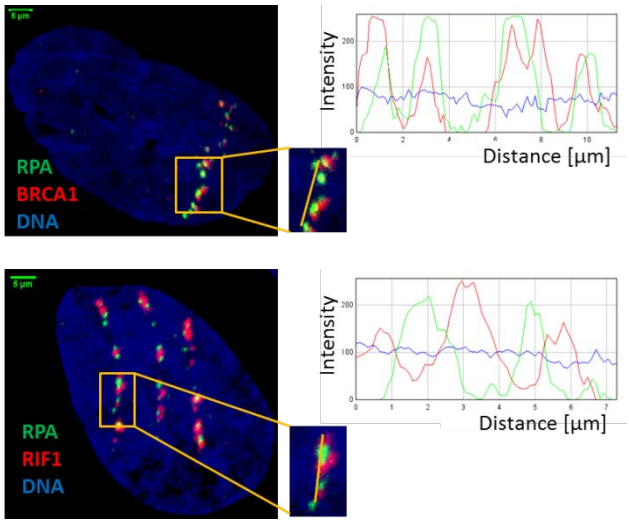

Figure 2: BRCA1 and RPA co-localize at ion-induced DSBs in G1-phase cells, but RIF1 and RPA do not. Human osteosarcoma cells (U2OS) were irradiated with Uranium-ions in a low angle (LET 15,000keV/µm, fluence $3x10^6$ p./cm^2) and fixed 1h after irradiation. They were immuno-stained against RPA and BRCA1 (top) or RPA and RIF1 (bottom). To discriminate G1 and S/G2 phase, the cells were additionally immuno-stained against CENP-F. G1-phase cells lack CENP-F and hence are negative for this staining. DNA was visualized by DAPI staining.

Acknowledgements

This work is part of the Helmholtz Graduate School for Hadron and Ion Research "HGS-HIRe for FAIR" and supported by the DFG funded Graduate College 1657 "Molecular and cellular responses to ionizing radiation".

References

[1] N. Averbeck *et al.*, "DNA end resection is needed for the repair of complex lesions in G1-phase human cells", Cell Cycle (2014) 13 (16), 2509-16
[2] J. R. Chapman *et al.*, "RIF1 is essential for 53BP1-dependent Nonhomologous End Joining and suppression of DNA double-strand break resection", Molecular Cell (2013) 49 (5), 858-71
[3] C. Ecsribano-Díaz *et al.*, "A cell cycle-dependent regulatory circuit composed of 53BP1-RIF1 and BRCA1-CtIP controls DNA repair pathway choice", Molecular Cell (2013) 49 (5), 872-83
[4] L. Feng *et al.*, "RIF1 counteracts BRCA1-mediated end resection during DNA repair", J. Biol. Chem. (2013), 288 (16), 11135-43

DOI:10.15120/GR-2016-1

Analysis of the influence of the ubiquitin ligase RNF8 on decondensation at heterochromatic damage sites after ion irradiation

N. P. Benz[1], A. Heselich[1], K.O. Voss[1], N. Özgün-Korkusuz[1], G. Taucher-Scholz[1,2] and B. Jakob[1]
[1]GSI, Biophysics, Darmstadt, Germany; [2]TU Darmstadt, Biology, Germany

Motivation

Accessibility of DNA damage is essential for DNA repair processes especially in highly condensed heterochromatin (HC) where DNA relaxation might be necessary for the efficient repair of DNA double strand breaks (DSBs). Taking advantage of the localized induction of DSBs specifically within murine HC compartments (chromocenters) using the GSI heavy ion microprobe, two processes were revealed in relation to HC-DSB repair: one is the fast decondensation of chromatin around the damage site, and the other is the relocation of DNA DSBs to the euchromatic border [1]. It is still unknown which process starts first and if or how they are influencing each other. One potential candidate in radiation induced chromatin decondensation is the ubiquitin ligase RNF8 which has been shown to play a role in this regard after laser microirradiation [2]. After laser-induced DSB induction RNF8 binds to the phosphorylated repair factor MDC1 and mediates ubiquitylation as well as the recruitment of the chromatin remodeler CHD4 to the DNA damage site. Here we investigate if RNF8 is also an important factor for ion-irradiation induced heterochromatin decondensation .

Materials & Methods

Heterochromatic components, so-called chromocenters, of murine embryonic fibroblasts were irradiated with heavy ions (Xe 4,8 MeV/u or Au 4,8 MeV/u) using targeted ion irradiation at the microbeam facility. Chromatin decondensation at sites of ion traversals in chromocenters – indicated by γ-H2AX immunostaining of DSBs – was evaluated microscopically in postirradiative fixed cells based on a local intensity drop of DAPI- DNA staining.

Results

To test if the local heterochromatic decondensation triggered by charged particle irradiation depends on RNF8 signaling, we targeted murine chromocentres (HC) after RNF8 depletion by siRNA at the GSI microprobe and compared the depletion of DAPI staining at sites of ion traversals with wild type cells. After Xe or Au ion (4.8 MeV/u) irradiation, the vast majority (~ 90%) of targeted and hit chromocenters showed a local decondensation, thus indicating a robust damage signaling. However, no significant difference between RNF8 k.d. and mock regarding the fraction of decondensed chromocenters could be observed (Fig. 1A). RNF8 depletion was verified using Western blot analysis (Fig. 1B) and the absence of efficient 53BP1 recruitment (Fig. 2).

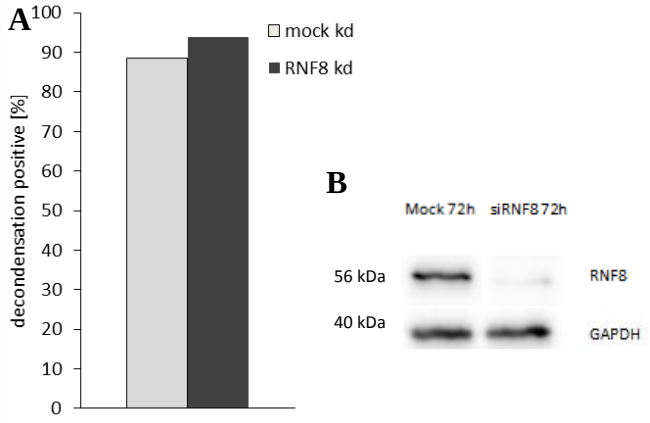

Figure 1: (A) HC decondensation events after targeted single ion irradiation using Au or Xe ions (4.8 MeV/u). Hit chromocenters were evaluated after fixation and immunostaining of the phosphorylated histone H2AX (DSB marker). Intensity profiles of the DNA counterstain DAPI served as readout for HC decondensation. (B) Western blot analysis showing the efficiency of the siRNA mediated RNF8 knockdown.

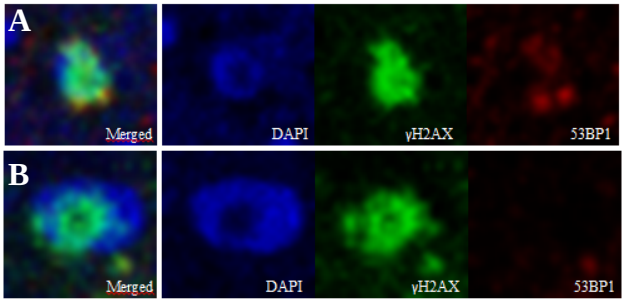

Figure 2: Decondensation and 53BP1 recruitment in chromocenters irradiated with Au ions (4.8 MeV/u); (A) control cells: 53BP1 colocalizes with γH2AX. (B) RNF8-depleted cells: 53BP1 accumulates only at the periphery of decondensed area and does not completely colocalize with γH2AX.

These results indicate, that RNF8 is necessary for efficient recruitment of 53BP1 to ion induced damage sites in HC, but not substantially involved in the observed ion induced HC decondensation. Other posttranslational modifications or remodeling factors might be responsible for the observed local regulation of chromatin compaction after charged particles.

References

1. Jakob, B., *et al.* Nucleic acids research 39, 2011.
2. Luijsterburg, M.S., *et al.* EMBO journal 31, 2012.

Funding: This work is supported by the German federal ministry of education and research (BMBF). Grant: 02NUK037

Repositioning and targeting irradiation of offline preselected single cell nuclei for chromatin decondensation measurements using the heavy ion microprobe *

E. Abdollahi[1], N. Özgün-Korkusuz[1], K.O. Voss [1], M. Durante [1, 2], G. Taucher-Scholz [1, 2] and B. Jakob[1]

[1]GSI, Darmstadt, Germany; [2]Technical Universität Darmstadt, Germany

Introduction

Compacted heterochromatin (HC) provides a challenge for the cellular double strand break (DSB) repair system, particularly in combination with the induction of complex lesions as produced by ion particle irradiation. Exposure of cells to ion radiation revealed a local chromatin decompaction in heterochromatin compartments like murine chromocenters [1]. This chromatin decondensation is accompanied by damage relocation to the hetero-/euchromatin interface for further processing [1]. The mechanism of DSB movement and its relation to the radiation induced chromatin decompaction is not clear. Employing FLIM setup, we recently established chromatin compaction sensitive probes and showed HC decondensation in ion irradiated and subsequently fixed cells [2]. Here we established conditions for multiple repositioning between our FLIM setup and the GSI microprobe for targeted irradiation of chromocenters and measurements of chromatin state in living cells.

Materials and Methods

NIH-3T3 cells were cultured and stained with 1 µM Nuclear Violet (NV). FLIM measurements and irradiation were done as described in [2]. Irradiation was done using gold ion (4.8 MeV/u). For immunostaining 53BP1 rabbit polyclonal (Calbiochem, 1:500) and Atto 647 goat-anti rabbit (Sigma, 1:200) as primary and secondary antibody were used.

Results

In this study, we aimed at utilizing FLIM technique for monitoring radiation-induced chromatin decompaction in living murine cells. Therefore, we did repetitive FLIM measurements of NIH-3T3 cells stained with 1µM NV, which allows a pronounced readout of chromatin compaction [2]. Single nuclei showing well distinguishable chromocenters in FLIM (Fig. 1A,B) were selected and by the aid of a precise sample holder and coordinate transfer repositioned at the microprobe, where the targeted irradiation took place (Fig. 1C). The precision of the repositioning procedure was in the order of 100 µm. Images of the selected nuclei served for identification. After irradiation, cell were transferred to the FLIM setup again, repositioned and a post-irradiation FLIM image acquired (Fig. 1 C,D). Cells were subsequently fixed and immunostained for a DSB marker for hit verification. Surprisingly, a pan-nuclear damage pattern could be observed (Fig. 1 H), indicating phototoxicity of NV. This was later confirmed in additional experiments (not shown). The NV/UV induced pan-nuclear damage most probably prevented a localized damage response including the chromatin decondensation (Fig. 1C-F); however we can't exclude the applied ions being off target due to the impeded hit verification.

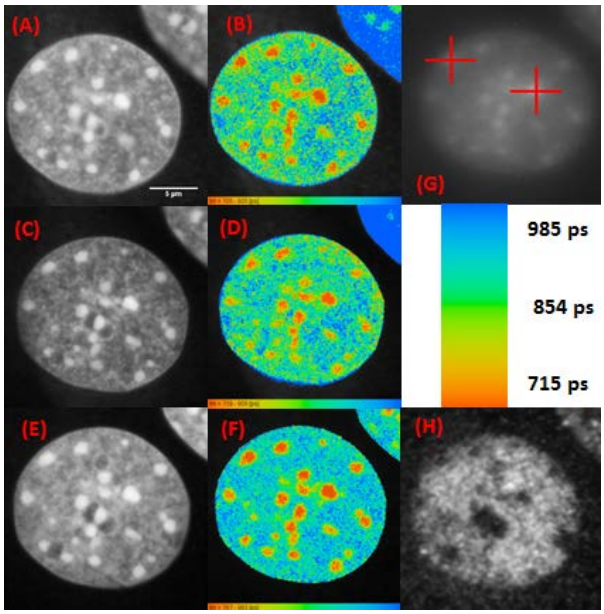

Figure1. Fluorescence lifetime imaging (FLIM) of preselected and irradiated NIH3T3 cell stained with 1µM NV. (A-B) Intensity and lifetime images of living NIH3T3 cell before irradiation. (C-D) Intensity and lifetime images of repositioned cell after offline irradiation using gold ions (4.8 MeV/u). (E-F) Intensity and lifetime images of preselected cell after fixation and immunostaining. (G) Targeted chromocenters at the microprobe. (H) Intensity image of DNA DSB marker 53BP1.

Conclusions

Our results show that our FLIM setup enables us to preselect targets for irradiation at the microprobe using the established repositioning procedure. Although the promising NV can't be used as a chromatin compaction probe in living cells due to its phototoxicity, it still might be functional in fixed samples where a clear lifetime-contrast could be obtained. Future experiments will apply the established procedures using alternative pretested non-phototoxic chromatin compaction probes.

References

[1] B. Jakob et al. NAR, 39, 6489-99 (2011).
[2] E. Abdollahi et al. NIMB,365,626-30(2015).

* Work supported by DFG GRK1657 and BMBF 02NUK037A.

DOI:10.15120/GR-2016-1

Establishment of human embryonic neural stem cells as in vitro model for radiation risk assessment*

O. Arrizabalaga[1], S. Sadeghi, M. Mayer [2], J. Baur[1] and S. Ritter[1,#]
[1]GSI, Darmstadt, Germany, [2]University of Applied Sciences Aschaffenburg, BioMEMS Lab, Germany.

Pre- and postnatal exposure to ionizing radiation (IR) may perturb brain development and lead to cognitive dysfunction (e.g. [1]). However, little is known about the underlying mechanisms. To address this topic we chose human neural stem cells (NSC) as a model system. NSC have the capacity to self-renew and can differentiate into neurons, astrocytes and oligodendrocytes providing a versatile tool to study radiation effects on the developing brain. First, a fast and efficient protocol to generate NSC from human embryonic stem cells (hESC) was established using Gibco PSC neural induction medium (Life Technologies) [2]. Already seven days after differentiation initiation, NSC were ready for expansion using neural expansion medium supplemented with FGF2 and EGF. Immunofluorescence staining confirmed that the generated NSC were positive for common neural markers. Examples are shown in **Fig. 1**. Another powerful method to characterize cells is gene expression analysis by means of real-time quantitative PCR (qPCR). To minimize technical variations PCR-data have to be normalised using stable reference/house-keeping genes. To identify those, RNA samples from control and irradiated cells (1 Gy X-rays) were isolated, because IR may affect gene expression [3]. Gene expression profiling was performed using the RT^2 Profiler Array for human housekeeping genes (Qiagen) and genes were ranked by the NormFinder software [4]. Out of the 12 genes studied, the expression of HPRT1 and PGK1 were found to be the most stable. Hence, the geometric mean of HPRT1 and PGK1 was used in subsequent studies for normalisation.

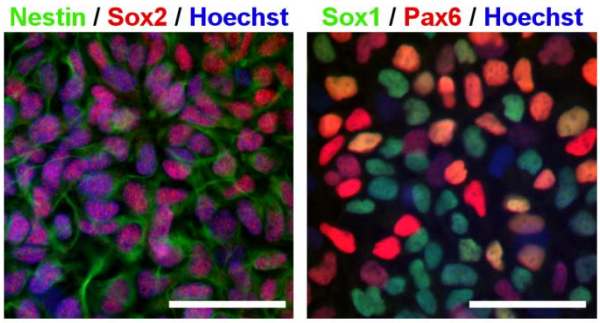

Figure 1: Immunostaining of hESC-derived NSC. NSC were stained against Nestin, Sox2, Sox1 or Pax6 (Life technologies). DNA was counterstained with Hoechst. Scale bar = 50 µm.

In a first experiment NSC were exposed to 1 or 2 Gy X-rays (1,5 Gy/min, 250 kV, 16 mA) and RNA samples were collected 1 and 7 days post-irradiation. Neural marker expression was measured by qPCR. The results show a decreased expression of all markers (NES, SOX1, SOX2 and PAX6) 1 day after exposure for both doses compared to the control. At day 7, the levels of neural markers in samples exposed to 1 Gy were close to control levels, whereas 2 Gy exposed samples still expressed lower levels than the control. Additionally, the cell cycle progression of NSCs was studied by flow cytometry up to 24 hours after irradiation (**Fig. 2**). In control cultures about 40 % of cells were in G1, 43 % in S and 17 % in G2/M phase. The exposure to 1 Gy X-rays resulted in a G2/M- block between 8 and 12 hours after exposure (with 43% and 27% in G2/M, respectively) preventing the division of cells with damaged DNA. Another mechanism that limits the transmission of DNA damages to the progeny is apoptotic cell death. Hence, the percentage of cells that underwent apoptosis was measured using the TUNEL Assay (Roche). Exposure to 1 Gy X-rays resulted in an up to fourfold higher apoptotic level at day 2 and 3 post-irradiation compared to control cells, decreasing steeply on day 4. In summary, data obtained so far show that X-irradiation affects the cell cycle progression of NSC and increases significantly the apoptotic rate. Moreover, the expression of neural markers was decreased compared to the control. These alterations may affect lineage differentiation and further maturation of NSC and their progeny. Currently, the differentiation pattern and electrophysiological activities of irradiated NSC are being investigated in more detail.

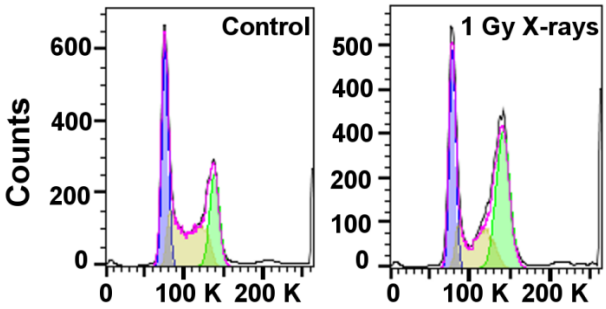

Figure 2: DNA content measured by flow cytometry. NSC were fixed, stained with DAPI and the DNA content was analysed. Exemplarily, data obtained 8 hours after exposure to 1 Gy X-rays are sown. Cells in G1, S and G2/M phases are shown in purple, yellow and green respectively.

References

[1] Verreet et al., JNeurodevDisord. (2015) **7**:3, 17-21.
[2] Yan et al., StemCellsTranslMed. (2013) 11: 862-870.
[3] Arrizabalaga et al., GSI Scientific Report (2014) APPA-Health-38.
[4] Andersen et al., Cancer Res. (2004) 64: 5245-5250.

* Work supported by BMBF (02NUK025 and 02NUK034C)
#s.ritter@gsi.de

Cardiomyocytes derived from human embryonic stem cells respond with functional and transcriptional alterations to chemical stress and ionizing radiation*

I. Schroeder[1], S. Nitsch[1], F. Braun[1/2], M. Scholz[1], and S. Ritter[#,1]
[1]GSI, Darmstadt, Germany, [2]Hochschule Darmstadt, Germany

Cardiotoxicity induced by ionizing radiation is a health concern not only during early embryogenesis when the heart forms. It is also seen as a late effect in patients diagnosed with cancer that have been subjected to radiation therapy. As donor tissue is scarce or even impossible to obtain, studies on the mechanisms and pathways involved in radiation-induced cardiotoxicity mainly rely on *in vitro* cell models. One particular suitable one is the human embryonic stem (hES) cell model that allows mimicking cardiac *in vivo* development generating functional cardiomyocytes. However, as it includes all intermediate/progenitor stages seen *in vivo*, it can easily be used to identify those stages of development and regeneration most sensitive to ionizing radiation.

We differentiated H9 hES cells into cardiomyocytes using two different protocols [1, 2]. Both led to the generation of beating clusters within 15 days and the expression of cardiac markers such as cardiac troponin (cTNT) and alpha and beta myosin heavy chain (a/bMHC). Subjecting the cells to isoprenaline, a β1 and β2 adrenoreceptor agonist, induced tachycardia-like effects (**Figure1**) leading to a two-fold increase of the beat rate. This suggests that the cardiomyocytes generated *in vitro* are able to respond to exogenous stress.

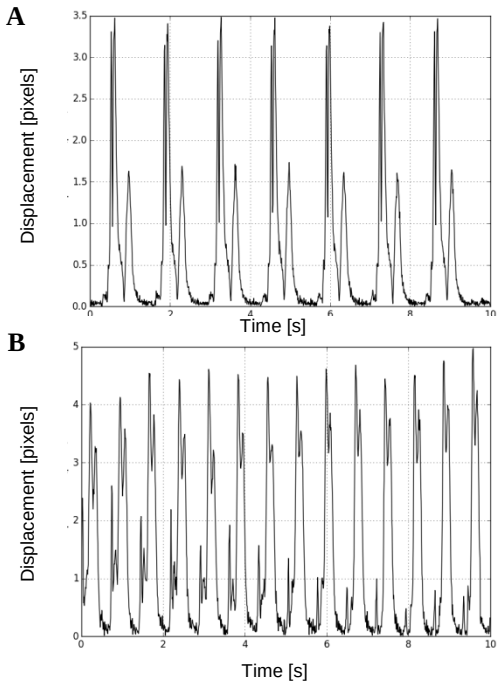

Figure 1: Beat rate (Displacement/time [s]) in cardiomyocytes generated in vitro. A: spontaneous beating in control cells. B: Beat rate after treatment with 1µM isoprenaline.

The impact of ionizing radiation was analyzed by subjecting hES cells to 1Gy X-rays. Differentiation of the surviving cells was initiated 4 days after irradiation using the protocol of Lian et al. [1]. Preliminary results indicate that irradiated cells formed smaller clusters compared to their non-irradiated counterparts and either displayed no or impaired beating capability. mRNA analyses revealed that irradiation of hES cells led to transcriptional alterations in all subsequent developmental stages. Early mesoderm formation, a prerequisite of heart development was affected as judged by lower levels of brachyury (Figure 2A) at d1, the stage when differentiation into mesoderm occurs. Likewise, cardiac markers such as bMHC, which characterizes mature cardiomyocytes, were negatively affected (Figure 2B).

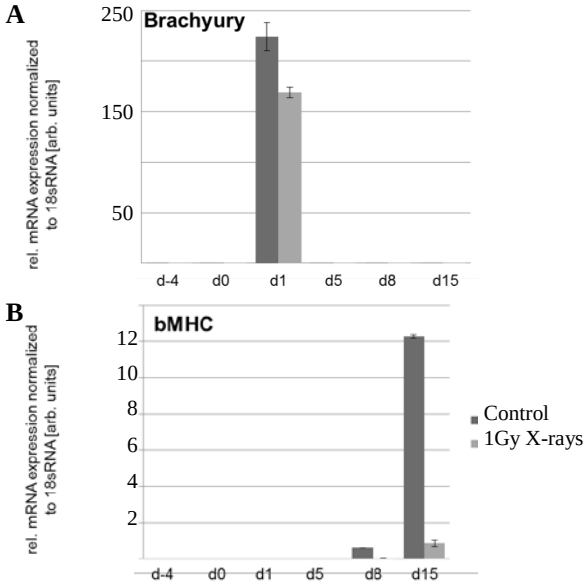

Figure 2: Relative mRNA expression during cardiac differentiation of brachyury (A) and bMHC (B) in control and irradiated cells. d=days, d-4: day of irradiation, d0: differentiation initiation.

In summary, the radiation–induced impairment may indicate a negative impact on the positional and temporal patterning of the cardiomyocytes during early development *in vivo*.

References

[1] Lian et al., Nature Protocols 8 (2013), 162
[2] Kadari et al., Stem Cell Rev and Rep 4 (2014), 560

* Work supported by BMBF (02NUK025A), # s.ritter@gsi.de

 DOI:10.15120/GR-2016-1

Detection of specific translocations in human lymphocytes using a break-apart probe*

K. Sievers[1,2], N.Paz[1], E. Nasonova[3] and S. Ritter[1]

[1]GSI, Darmstadt, Germany; [2]Justus-Liebig-Universität Gießen, Germany, [3]JINR, Dubna, Russia

Chromosome aberration analysis in peripheral blood lymphocytes is an established method to quantify past radiation exposures and to assess possible health risks of ionizing radiation. Among the different types of aberrations produced translocations are of great interest because they are common in human cancer.

In a recent pilot study on putative genetic effects of radon spa therapy for chronic inflammatory disease we analyzed chromosome aberrations in lymphocytes from 2 patients before and after therapy by means of 24-color fluorescence in situ hybridization (mFISH). The patients did not show any change in the frequency of aberrations before and after therapy, but in one patient who underwent already the fifth radon therapy we detected 2 cells with an identical (clonal) translocation between chromosome 7 and 14 (i.e. [t(7; 14) (q34; q11)] affecting the genes coding for the α-/δ-chain and the γ-chain of the T-cell receptor (TCR). Since the clone size is small (<0.2% of lymphocytes carry this specific translocation), we chose an interphase FISH technique to gain statistical power. Specifically, a dual-color break-apart probe (Vysis) was applied which hybridizes to the flanking regions of the TCR A/D locus at 14q11. A spectrum green labeled probe targets the telomeric (3´) region of the locus, while a spectrum orange labeled probe hybridizes to the centromeric (5´) region. For automated image acquisition and subsequent evaluation the Metafer/Metacyte software (MetaSystems) was used.

To validate the specificity and sensitivity of the probe, blood samples were taken from three healthy donors (HD) and lymphocytes were isolated by centrifugation in Vacutainer cell preparation tubes (Beckton Dickinson). Directly after isolation an aliquot of each sample was fixed in methanol/acetic acid (3:1). The remaining cells were stimulated with 1 % phytohemagglutinin and cultured for 48h at 37°C. Colcemid was added to the samples 3h before harvest to accumulate metaphase cells. Subsequently lymphocytes were collected and slides were prepared as described elsewhere [1]. The break-apart probe was hybridized to unstimulated and stimulated cells according to the manufacturer's protocol. First, 60 metaphases per HD were examined. All metaphases showed the expected signal pattern, i.e. signals are in close proximity or overlap commonly referred to as fusion signal (Fig. 1, left). Accordingly, the analytical specificity of the probe is 100%. Next, the "normal" pattern was evaluated in interphase cells by measuring the distance between signals in relation to both signal diameter and nuclear radius length. This is particularly important, because the extension of the gap between red and green signals depends for example on probe design, the locus under study and chromatin condensation [2]. Based on the analysis of about 500 cells per HD, a distance less than 40% of nuclear radius length was defined as normal. Accordingly, in a translocated chromosome the signals are expected to show a larger distance usually termed split signal (Fig. 1, right). Using this criterion up to 2500 nuclei per sample (n=6) were analyzed. For stimulated and unstimulated lymphocytes of HD the split rate was 4,7 % (Fig. 2) leading to a cutoff value of 5,4 % calculated as mean value of false positive nuclei plus three times the standard deviation [2]. This relatively high cutoff level renders the probe unsuitable for the analysis of rare translocations involving the TCR A/D locus.

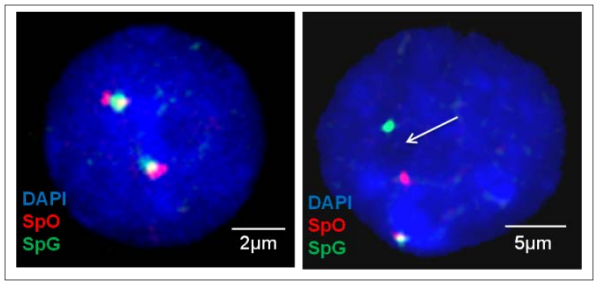

Fig. 1: Break-apart FISH with two probes (SpO: spectrum orange; SpG: spectrum green) flanking the TCR A/D locus at 14q11. Representative nuclei showing a fusion (left) and a split (right) pattern in lymphocytes of a healthy donor (HD2).

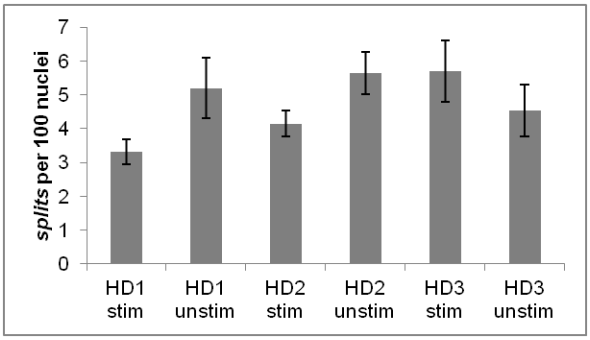

Fig. 2: Frequency of stimulated (stim) or unstimulated (unstim) lymphocyte nuclei exhibiting a split pattern.

References

[1] R. Lee et al., Mutation Research 701 (2010) 52.
[2] J.I. Martín-Subero et al., International Journal of Cancer 98 (2002) 470.

* Work supported by BMBF, grant 02NUK017A.

Complex chromosome exchanges in human lymphocytes*

C. Hartel[1], J. Baur[1], P. Hessel[1], N. Paz[1], E. Nasonova[1,2] and S. Ritter[1]
[1]GSI, Darmstadt, Germany; [2] JINR, Dubna, Russia.

Chromosomal aberrations in peripheral blood lymphocytes (PBLs) are a widely used biomarker for exposure to ionizing radiation. We applied the full-genome painting technique mFISH (multiplex fluorescent in-situ hybridization) to analyse chromosomal aberrations in PBLs. While sparsely ionizing radiation predominantly induces "simple exchange" type aberrations (i.e. rearrangements resulting from two breaks), densely ionizing radiation produces an increased amount of "complex exchanges" (i.e. aberrations resulting from three or more breaks in at least two chromosomes). The ratio of complex to simple exchanges, called *C*-ratio, is often used as a biomarker for exposure to high-LET radiation.

We exposed human PBLs *in vitro* to 2 Gy of alpha particles (^{241}Am alpha source, energy on Target 3.66 MeV). Immediately afterwards, cell growth was stimulated and chromosome spreads were prepared after 48 h and 72 h. After mFISH hybridization, the chromosomal aberrations were analysed. The resulting *C*-ratio is shown in Figure 1, together with previously published data for 2 Gy X-rays and 2 Gy extended Bragg peak C-ions [1]. The *C*-ratio is higher after alpha particle exposure, compared to both C-ions and X-rays. Moreover, it is higher 72 h after alpha-particle exposure compared to 48 h. This is in line with the observation, that high-LET exposure induces a severe delay of heavily damaged cells [2].

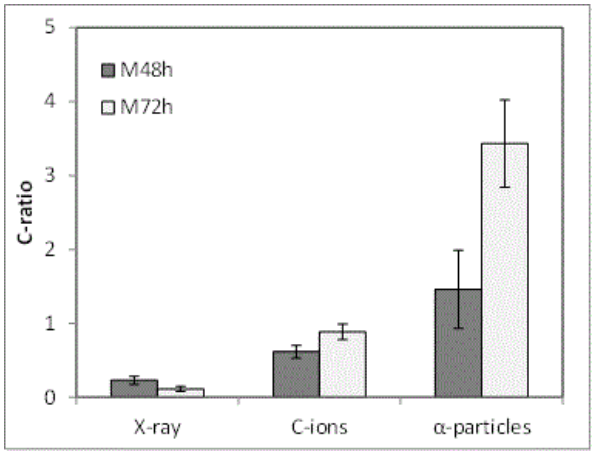

Figure 1: C-ratio (ratio of complex to simple exchanges) in human lymphocytes exposed in vitro to a dose of 2 Gy X-ray (250 kV), extended Bragg peak C-ions and Alpha particles.

As part of the project GREWIS, we aim to determine the cytogeneic risk of low doses of densely ionizing radiation, as applied during therapeutic radon baths. While *in vitro* data show an enhanced C-ratio for a high dose of alpha particle radiation (see fig 1), it is unclear whether the therapeutic radon exposure has any detectable effect *in vivo*. To determine this, the background level of chromosomal aberrations in healthy individuals as well as in patients with arthritic/rheumatic diseases have to be known before any attempt can be made to identify additional aberrations induced by low doses of high-LET radiation. We therefore applied the mFISH method to analyze chromosomal aberrations in PBLS from two healthy donors of similar age. In the first donor, 27 aberrations were observed in 1838 metaphases, (0.015±0.003 per cells), while in the second donor, 20 aberrations were found in 1189 cells (0.017±0.004 per cell). While these values are similar, the aberration spectrum (i.e. the frequencies of different aberration types) was surprisingly different between the two donors (see figure 2). While terminal deletions and simple reciprocal translocations were found in both individuals, donor 1 also had several simple dicentric exchanges as well as complex aberrations.

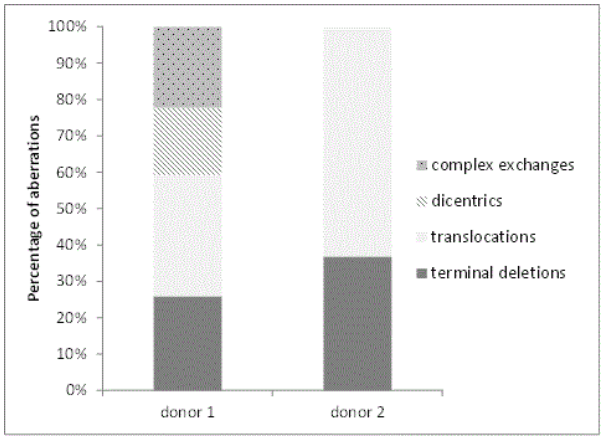

Figure 2: Relative frequencies of different aberration types observed two healthy donors of similar age.

In the upcoming part of the GREWIS study, PBLs from patients undergoing a radon bath treatment will be analysed. The current results underline the importance of a careful analysis of the background level of chromosomal aberrations, especially the frequency of complex aberrations, for each individual patient before therapy in order to detect potential small increases in the aberration rate after the radon treatment.

References

[1] C. Hartel et al, Radiother Oncol 2010.
[2] R. Lee et al, Radiat Environ Biophys 2011.

* Work supported by BMBF, contract Nr 02NUK017A

DOI:10.15120/GR-2016-1

Human embryonic stem cell derived neurospheres form functional networks on microelectrode arrays*

M. Mayer[1], *O. Arrizabalaga*[2], *S. Ritter*[2], *and C. Thielemann*[1]

[1]University of Applied Sciences, BioMEMS Lab, Aschaffenburg, Germany; [2]GSI, Biophysics, Darmstadt, Germany

Various studies have shown that the developing central nervous system (CNS) is particularly sensitive against ionizing radiation (IR) leading to abnormal CNS development that could cause mental retardation and behavioural disorders [1]. Yet, there is hardly any information about the impact of IR on neuronal network communication.

To address this topic we differentiated human embryonic stem cells (hESC, line WA09) to neuronal stem cells (NSC), and these into three dimensional neurospheres (NS). The functionality of NS was characterized using microelectrode arrays (MEA). This method allows assessing the electrical activity of neuronal tissue in a non-invasive way. Briefly, after 18 days in culture, NS were plated on the MEA chips coated with polyethyleneimine and laminin (Fig. 1a). NS attached and cells migrated radially out of the NS. In order to characterize the outgrowing cells, immunofluorescence staining against the protein beta-III tubulin was performed demonstrating that these cells are terminally differentiated neurons (Fig. 1b).

A previous study has shown that the development of neuronal signalling typically proceeds in three phases [2]. First, electrical activity can be detected as random, single spikes. After some days, train-like spiking activity evolves that further develops into burst-like activity. These bursts represent the mature signalling activity of the network.

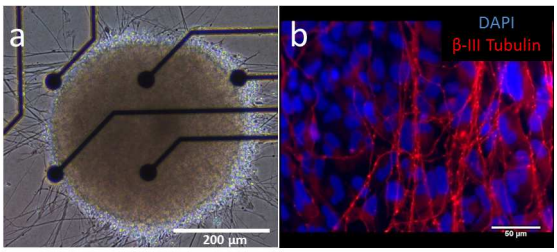

Figure 1: hESC derived NS were cultured on MEA chips to examine their electrical activity (a) or on coverslips to investigate their morphological properties by immunofluorescence staining against the protein beta-III tubulin (red). Nuclei were counterstained with DAPI (blue) (b).

Our electrophysiological studies showed that signals were either detected within the first week of culturing on MEA chips or did not appear at all. Initial signals were random single spikes (Fig. 2a) with occasional burst-like events. A significant increase in the number of bursts was detected five days after onset of the spikes (Fig. 2b). Burst-like activity was defined as at least three spikes with a maximum interspike interval of 100 ms. In first experiments NS were formed from the progeny of X-ray irradiated hESC or NSC (1 Gy X-rays, 250 kV, 16 mA). These experiments showed, that irradiated cells are still able to form NS and that the resulting NS are electrophysiologically active. However, the evaluation of the data showed a lower network activity compared to the control. Currently, experiments on the effect of carbon ions on network signalling are being carried out.

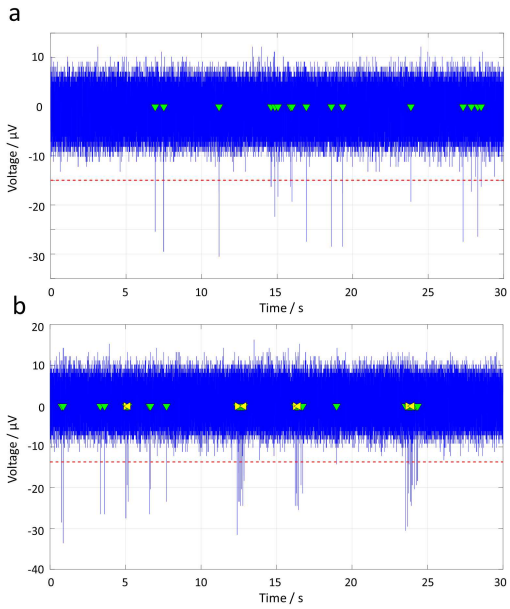

Figure 2: Development of neuronal signalling of neurospheres cultured on MEA chips. The first signs of electrical activity are random single spikes (a, green arrows) that further develops into burst-like activity (b, yellow arrows).

References

[1] Schull, W.J. et al., Teratology 1999, 59: 222-226

[2] Heikkilä, T.J. et al., Exp. Neurol. 2009, 218: 109-116

* Funding for this project was provided by the Federal Ministry of Education and Research (02NUK025C and 02NUK034C).

Measurement of radon diffusion in matter

A. Maier[1], J. Dickmann[1,2], P. van Beek[1,2], G. Kraft[1], C. Fournier[1], U. Weber[1]
[1]GSI, Darmstadt, Germany; [2]TU Darmstadt, Germany

Introduction

A basic working hypothesis of the GREWIS project is the assumption of fast radon diffusion into the body and accumulation in the different compartments of the organism. Therefore, the knowledge of solubility and diffusion of radon and its decay products in the human body is important. In a biological organism, the radon concentration seems not to be distributed homogeneously, yielding an inhomogeneous dose to different organs. In order to improve the accuracy of the measurement of the radon uptake, we started direct radon diffusion measurements through thin slabs of different materials using the α-decay as monitor of the penetrating radon.

Measurement setup

For these measurements a special setup was installed inside the radon exposure chamber which has been described before [1]. In the experiment, radon from a large volume diffuses through the test sample into the small test volume above a surface barrier detector where the α-particles of the radon decay and the decay of daughter nuclei are measured. The major challenge of these measurements is the complexity of the energy spectra of the radon decay and of the Po-218 and Po-214 isotopes. The polonium isotopes aggregate mainly at the surface of the detector yielding narrow lines with small low energy tails.

In contrast, radon stays in gas phase. Consequently, the alpha particles undergo energy loss and straggling according to their travel path from the (isotropically emitting) radon-gas atoms to the detector surface. This yields broad continua in the alpha spectrum in which also a part of the counting rate gets lost (see fig. 1).

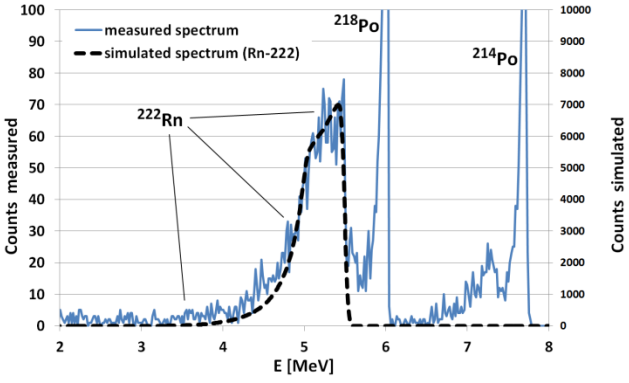

Fig. 1: Alpha energy spectrum from the radon atoms in the test volume above the detector. The polonium lines are at 7.7 MeV and 6 MeV. The radon continuum extends below 5.5 MeV. The dashed line shows the theoretical spectrum for Rn-222 alpha particles only.

Data analysis

In an analytical simulation of the geometry, of energy loss and straggling, we could reproduce the α-continuum for our detector geometry and determine the correction factor for the energy range of interest below 5.5 MeV. The simulated spectrum qualitatively agrees with the experimental data (see fig. 1). Therefore, from the simulation an efficiency factor can be calculated for the alpha particles that hit the detector (not lost in the surrounding walls or stuck in the volume). For the given cylindrical geometry of the test volume (H=5mm, R=10 mm) the theoretical efficiency factor is 32%.

In order to count the radon-222 particles diffusing through the test sample into the test volume, the part of the alpha spectrum in the energy range of 4.5-5.5 MeV should be selected.

Derived from Fick's law of diffusion, every concentration gradient produces a particle flux, which is proportional to the diffusion constant D. The concentration gradient is also proportional to the partial pressure of radon in the test sample. The partial pressure at the lower surface of the test sample can be determined by measurement of the α-activity in the test volume.

In fig. 2 the numerical solution of the diffusion model is given together with an analytical approximation, which shows good conformity. With this approximation, the radon diffusion constant can be calculated from the measurement of the time dependency of the alpha activity in the energy range given above.

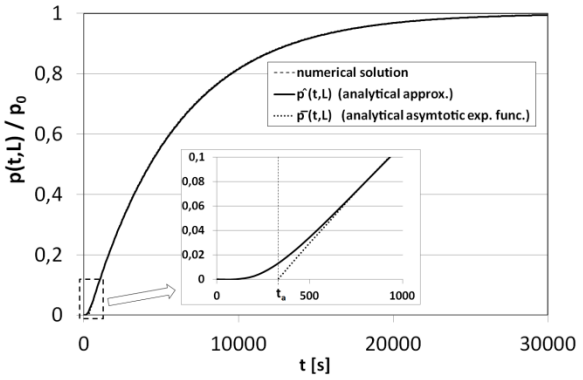

Fig. 2: Calculated time dependency of the partial radon pressure in the test volume.

References

[1] J. Baasner, A. Maier, D. Schardt, J. Breckow, M. Durante, C. Fournier, G. Kraft, Radon diffusion through tissue, GSI Scientific report 201
[2] A. Fick, Über Diffusion, Annalen der Physik, 170 (1): 59-86, 185.

* Work is supported by BMBF project funding reference number 02NUK017A

DOI:10.15120/GR-2016-1

Alpha irradiation setup*

A. Maier[1], *A. Zipf*[1,2], *G. Kraft*[1], *C. Fournier*[1]
[1]GSI, Darmstadt, Germany; [2] TU Darmstadt, Germany.

Introduction

In the GREWIS project the biological effects of ionizing radiation, especially α-particles, are studied. For cell experiments, the therapeutic radon concentrations are too low because the hit probability of individual cells is very small. The majority of non-hit cells will cover the few affected cells. To get clear effects in irradiated cells, they have to be exposed directly to α-particles from a radioactive source with higher doses.

Experimental setup

In the experimental setup, a commercial plan radiation source of Americium-241 is used which has a half life time of 432.2 years and emits α-particles with an energy of 5.49 MeV. This energy is similar to the energies of α-particles emitted during radon decay. The americium is evaporated on a metal disc, covered by a 2 µm thick gold plating and is inserted in the basis of the irradiation chamber. In order to guarantee a precise exposure, a fast mechanical shutter between the source and the target, capable of blocking the α-irradiation, was installed. The low range of these particles requires a short distance between source and target, which could be minimized to 2.7 mm. The cells grow on 2 µm thick mylar foil in rings of stainless steel. The whole setup, including the ring can be seen in Fig. 1. [1]

Fig. 1: Irradiation setup

Dosimetry

For any biophysics experiment it is of extreme importance to know the dose deposited on the cells during experiment and the linear energy transfer LET. The dose can be calculated from the particle fluence F by:

$$D = F \cdot \frac{1}{\rho} \cdot LET$$

The fluence was determined by CR-39 dosimetry. CR-39 plates were exposed, etched and the etch pits were counted as traversals of α-particles. The LET was calculated by measuring the energy spectra of the α-particles hitting a detector at the same distance as the cells. With the energy loss program Atima, the corresponding LET for different energies could be calculated and was weighted with the energy spectrum. Fig. 2 shows the dependency of the LET on the α-energy with a track averaged LET and in the middle of a 8 µm thick cell.

From these results, a dose-rate for a cell monolayer with a thickness of 8 µm was determined as:

$$D = 8.2 \pm 2.4 \text{ Gy/min}$$

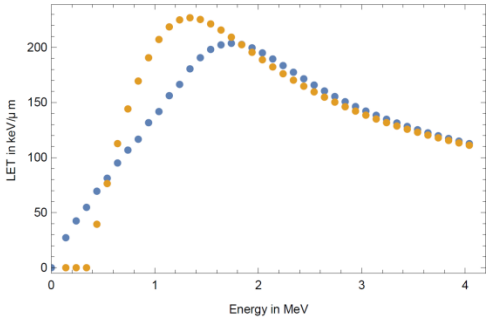

Fig. 2: LET dependency on the α-energy, of a track averaged LET between 1-8 µm in the cell (blue) and in the middle of a 8 µm thick cell (orange)

Experimental validation

For experimental validation, a survival curve with CHO (Chinese hamster ovary) cells was performed. The results were compared with a calculation done with the local effect model (LEM) and are shown in Fig. 3. [2]

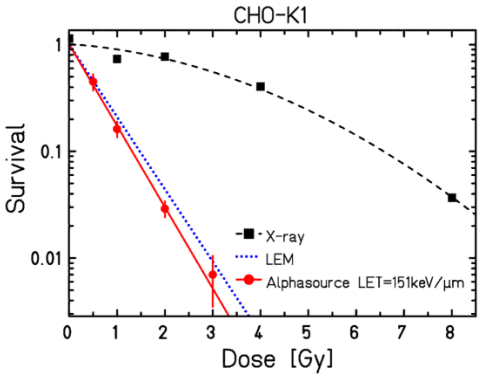

Fig. 3: Survival curve of CHO cells with α-particles, x-ray and the model prediction by LEM

References

[1] J. Adrian, Etablierung einer α-Bestrahlungseinrichtung für Zellen – Konstruktion und strahlenbiologische Experimente, Bachelorthesis, TU Darmstadt, 2014

[2] A. Zipf, Dosimetrie an einer Americium-241 Zell-Bestrahlungs-Apparatur, Bachelorthesis, TU Darmstadt, 2015

* Work is supported by BMBF project funding reference number 02NUK017A

Changes in homeostasis and tissue organization in human skin after exposure to ionizing irradiation*

J. Wiedemann[1,2], *P. Simoniello*[1], *E. Thönnes*[1], *K. Gand*[1], *C. Caliendo*[1], *P. G. Layer*[2], *M.Durante*[1,2], *M. Kovacs*[4], *M. Podda*[4], *and C. Fournier*[1,3]

[1]GSI, Darmstadt, Germany; [2]TU Darmstadt, Germany; [3]Hochschule Darmstadt, Germany; [4]Department of Dermatology, Darmstadt Hospital

Introduction

The increasing application of charged particles in radiotherapy requires a better understanding of homeostasis and organisation of tissue exposed to carbon ions compared to X-rays. Especially the skin is exposed during all radiation treatments but the cellular and molecular mechanisms related to early occuring side effects are not well understood.

Material and Methods

Human full-thickness skin equivalents (EFT400; MatTek) were irradiated using low versus high X-ray and carbon ion (110–145 MeV/μm; LET 100 keV/ μm) doses. Samples were fixed and processed 3 days after irradiation for histochemistry. The sections were stained with Hematoxylin and Eosin and parakeratosis, hyperkeratosis and a changed morphology in the basal layer was analysed.

Results and Discussion

The occurance of pyknotic nuclei in the stratum corneum (parakeratosis), the thickening of the stratum corneum (hyperkeratosis) and a change in the polarity of the basal cells are effects which are observed after irradiation (Figure 1).

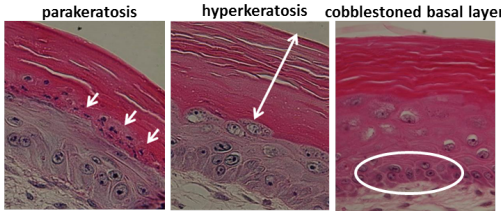

Figure 1: Hematoxylin & Eosin staining of human skin equivalents showing parakeratosis, hyperkeratosis and a changed morphology in the basal layer

The number of pyknotic nuclei per field of view where counted (parakeratosis) and the thickness of the stratum corneum was measured and related to the thickness of the epidermi (hyperkeratosis)(Figure 2). The results show that parakeratosis occurs mainly after carbon ion irradiation whereas hyperkeratosis was enhanced to a similar extend after both irradiation types.

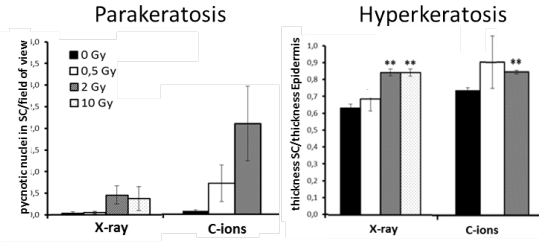

Figure 2: Quantitative analysis of parakeratosis and hyperkeratosis 3 days after X-ray and carbon ion irradiation; N=2, n=4; SEM, p $\leq 0,05$ =*, p $\leq 0,01$=**

A semi-quantitative analysis was established for the morphological changes in the basal layer, 20 pictures per sample where categorized according to the morphology of the basal cells. A change in the polarity (cobblestoned morphology) is mainly observed after low X-ray doses and less pronounced after C-ion irradiation (Figure 3).

Our results show that irradiation with high doses of heavy

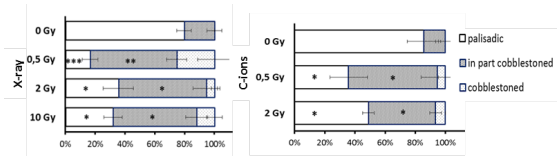

Figure 3: Semi-quantitative analysis of the morphology of the cells in the basal layer 3 days after X-ray and carbon ion irradiation; N=2, n=4; SEM, p $\leq 0,05$=*, p $\leq 0,01$=**, p $\leq 0,001$=***

ions and x-rays accelerate the differentiation process to a similar extend comparing the same physical doses. High doses of carbon ions where more effective than X-rays in inducing abnormal differentiation reflected in a more pronounced parakeratosis. In contrast, changes identified following low dose exposure (0,5 Gy), like the polarity of the basal cells, were induced more effectively after X-ray exposure [1].

References

[1] Simoniello P. and Wiedemann J. et al; 2016; Front. Oncol. 5:294.doi: 10.3389/fonc.2015.00294

* Work supported by GREWIS No. 02NUK017A; DFG (GRK 1657) and HGS-HIRe.

DOI:10.15120/GR-2016-1

Impact of Radon and low-dose X-ray exposure on adipokine induced inflammation in rheumatoid arthritis*

K. Shreder[1], A.Cucu[1], P.Rühle[2], U. Gaipl[2], M. Durante[1], C. Fournier[1]

[1] Helmholtzzentrum für Schwerionenforschung GSI, Darmstadt, [2] Department of Radiation Oncology, Universitätsklinikum Erlangen, Friedrich-Alexander-Universität Erlangen-Nürnberg

Introduction

Rheumatoid arthritis (RA) is a chronic inflammatory disease of the joints. RA patients are treated primarily with drugs, but also ionizing radiation is used. The patients are exposed either locally to low doses of photons or to Radon. The levels of adipokines, mainly produced by adipose tissue, are elevated in the serum of RA patients (1). Some adipokines increase the expression of inflammatory and bone destructive factors in synovial fibroblasts which are key players in RA (2). In this study we investigated the effect of radon spa treatment on adipokine levels in the serum of patients, suffering from musculoskeletal diseases. In additional *in vitro* experiments we examined the effect of recombinant adiponectin on the release of IL-6 in synovial fibroblasts (SF) following irradiation.

Materials and methods

Serum samples were collected from patients before and 3 months after radon spa treatment (600 to 1.200 Bq/l for nine times á 20 minutes). Adipokine levels were measured by ELISA. Human SF from RA patients (RASF) and healthy donors (NSF) were pretreated or not with adiponectin (5µg/ml) for 24h and then irradiated with X-rays. Cell culture supernatants were collected 24h after irradiation and IL-6 was measured by ELISA (eBiosience).

Results and discussion

Adipokine levels in serum of patients

Serum levels of visfatin were significantly decreased three months after treatment with radon baths compared with baseline (before therapy) (Fig.1). Serum levels of adiponectin were reduced roughly half of the patients after the therapy (Fig.2). Since it is known that elevated circulating adipokines positively correlate with serum levels of inflammatory factors IL-6 and C-reactive protein (CRP) in RA patients (3), we hypothesize, that the observed decrease in serum adipokine levels after low-dose irradiation inhibits the inflammation process in the joint.

Effect of adiponectin on IL-6 release in human synovial fibroblasts

After stimulation of SF (NSF and RASF) with recombinant adiponectin, the release of IL-6 was significantly elevated in SF. In turn, X-ray irradiation of SF with 0.5Gy or 2.0Gy reduced the adiponectin induced IL-6 release in RASF. No radiation induced changes were observed in NSF stimulated with adiponectin (Fig.3).

Our results demonstrate the radiation induced reduction of adiponectin induced IL-6 release by SF of RA patients. Decrease of adipokine levels in serum of radon treated patients could therefore be an important feature for the therapy of RA patients.

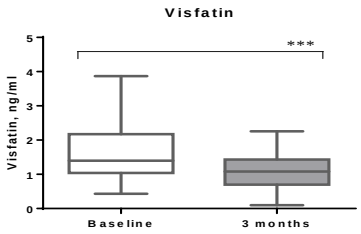

Fig.1 Visfatin level in serum of patients, treated with radon baths, Mean±SEM, N=27

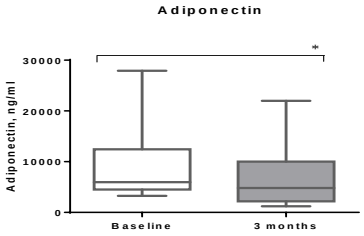

Fig.2 Adiponectin level in serum of patients, treated with radon baths, Mean±SEM, N=13

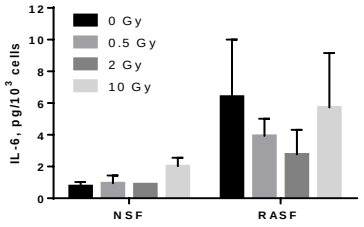

Fig.3 Effect of adiponectin on IL-6 release in human synovial fibroblasts following irradiation, Mean±SEM, N=2

References

1. Sglunda et al, PlosOne 2014
2. Schäffler et al, Endocrine reviews 27(5):449-467
3. Oki et al, Clin. Endocr. 2007 Nov; 67(5):796-800

*Work supported by BMBF (02NUK017A GREWIS)

(Low-dose) irradiation and anti-inflammatory effects in endothelial cells*

Nadine Erbeldinger[1], Felicitas Merz[1], Stephanie Hehlgans[3], Svetlana Ktitareva[1], Stephanie Meyer[2], Bianca Bertulat[2], M. Cristina Cardoso[2], Laura Babel[4], Miriam Grunewald[4], Tobias Meckel[4], Franz Rödel[3], Claudia Fournier[1]

[1]GSI, Biophysik; [2] Fachbereich Biologie, Zellbiologie und Epigenetik, TU Darmstadt; [3]Klinik für Strahlentherapie und Onkologie, Molekulare Strahlenbiologie, Goethe-Universität Frankfurt, [4]Fachbereich Biologie, Membrandynamik, TU Darmstadt

Introduction

Under the influence of stress factors like inflammatory cytokines (e.g. TNF-α) or irradiation, endothelial cells (EC) differentially express surface molecules, leading to adhesion of peripheral blood lymphocytes (PBL), followed by transmigration through the blood vessel wall into injured tissue [1]. Treatment of patients with chronically inflammatory diseases with low doses of irradiation has pain relieving and anti-inflammatory effects [2]. In this work, we investigate adhesion of PBL to EC after low dose exposure under shear stress (blood flow) conditions, and potentially underlying mechanisms; e.g. the ROS-(reactive oxygen species) production, NFκB signaling and activation of adhesion molecules on cell surfaces.

Methods

The adhesion of PBL to TNF-α stimulated EC was investigated under static [2] or laminar conditions. The production of ROS was measured in a first step in endothelial hybridoma cells (Ea.hy926) via flow cytometry using an intracellular dye (2‘,7‘-Dichloro-dihydrofluorescein-diacetate, H_2DCFDA) [3]. The amount of NF-κB translocation was measured in Ea.hy926 and EC by a high-content/high-throughput imaging routine (Operetta) 1 or 3 h after addition of TNF-α and /or photon irradiation [4]. In parallel, we analyze the clustering of adhesion molecules (ICAM-1 and VCAM-1) qualitatively by fluorescence microscopy according to [5].

Results

The dose effect on ROS production in Ea.hy cells is discontinuous with a maximum at 0.5 Gy for He- ions (89 keV/µm) (Fig. 1). Reduced adhesion was found at low doses, and even more pronounced under laminar conditions for He ions at 0.1 and 0.5 Gy (Fig. 2).

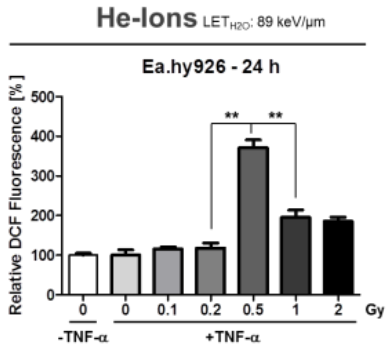

Fig. 1: Ea.hy926 cells were irradiated with He-ions (89 keV/µm) and analyzed for intracellular ROS production by flow cytometry 24 h later. ROS production peaks at 0.5 Gy.

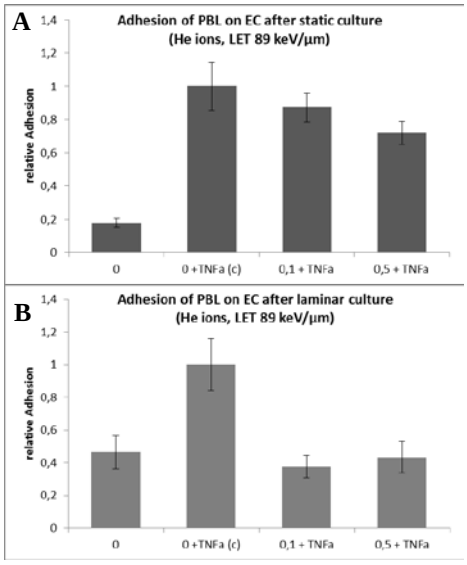

Fig. 2: Reduced adhesion of PBL on EC under static (A) and laminar (B) conditions after low doses of He ions (89 keV/µm, 0.1 and 0.5 Gy, 24h). Laminar culture conditions seem to enhance the anti-inflammatory effect of low dose irradiation. N=1, n=3

Discussion

We found previously that low doses of photons (0.1 to 2 Gy, [2]) reduced PBL adhesion onto EC caused by TNF-α. This was also observed for He-ions, and depending on the cultivating system (static or laminar, Fig. 2), which implies essential physiological mechanisms. Regulation or expression of components of the antioxidative system and the resulting ROS production is related to reduced adhesion after photon exposure [3]. Similar patterns of ROS production were detected after He-ion exposure (Fig. 1). Previous results obtained with photons and C-ions revealed that NF-κB p65 nuclear translocation is enhanced in the presence of TNF-α, but not further modified by low dose exposure [2]. Also, no change in the surface expression of adhesion molecules after photons was detected [5]. Investigations on the respective impact of He-ion exposure, as well as on the activation of adhesion molecules, are under work.

References

[1] Schnoor et al., (2015) Mediators Inflamm. 2015:946509.
[2] Erbeldinger et al., GSI report 2013
[3] Large M et al., (2015) Strahlenther Onkol. 191(9):742-9.
[4] Erbeldinger et al., GSI report 2014
[5] Lauer et al., (2014) Adv Drug Deliv Rev. 79-80:79-94.

* Financed by BMBF (GREWIS 02NUK017A and 02NUK17D), DFG (GRK 1657) and HGS-HIRe

DOI:10.15120/GR-2016-1

X-ray irradiation triggers immune-stimulation of lymphocytes*

P. Voos[1], S. Fuck[1], O. Rauh[1], D. Tandl[1], A. Spahn[1] C. Fournier[2], G. Thiel[1]
[1]Membran Biophysics, FB Biology, TU Darmstadt, Darmstadt, [2]Department of Biophysics, GSI, Darmstadt

Introduction

Radiobiology is mostly concerned with the effects of ionizing irradiation (IR) on DNA and the nucleus. Recently it was however realized that also extra nuclear targets are relevant for understanding the full impact of IR on cells. Here we report on the impact of x-ray irradiation on a potential immune-activation of lymphocytes.

Material and Methods

Images were obtained on a confocal microscope (TCS SP, Leica Heidelberg) with a 63x oil immersion objective (HCX PL APO 63x/ 1,32-0,6). Images were recorded with LAS AF software Version 2.60. Cell diameter of Jurkat cells was determined with an automatic cell counter (NanoEnTek, Seoul, Korea). Cells were irradiated from an x-ray source (Philips MCN 165/796704); dose was varied by adjusting cell/ x-ray distance.

Results

The starting point of this project was the observation that Jurkat cells, a tumor cell line derived from T-lymphocytes, undergoes a change in morphology after treatment with ionizing irradiation. Fig. 1A shows typical images of Jurkat cells before and 48 h after irradiation with 2 Gy x-ray. The data show that this treatment causes an increase in the size of these lymphocytes. The effect is dose dependent; the plot in Fig. 1B shows that a mean irradiation induced increase in cell size is achieved 48 h after treatment by a dose of ca. 2 Gy. This dose of X-ray irradiation is medically important since it is the most frequently used does in clinical tumor therapy.

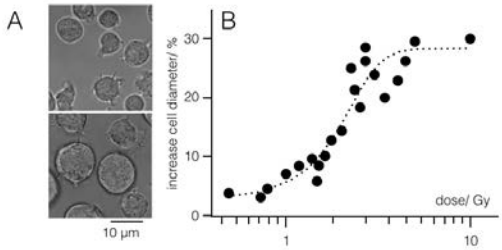

Figure1: A: Images of Jurkat cells before (top) and 48 h after irradiation with 2 Gy x-ray (down). B: increase in cell diameter as a function of irradiation with different doses of x-ray. Diameters were measured 48h after irradiation. Fitting data with logistic equation yields a half maximal effect at 2.5 Gy.

*funded by DFG (GRK1657) and BMBF (project 02NUK017A GREWIS).

Scrutiny the lymphocytes shows that the increase in size is to a great extend achieved by an adhesion of the cells to the surface of the culture chamber. Fig. 2 shows confocal images of Jurkat cells before and after irradiation with 2 Gy x-ray. The confocal sections of the cells in the Z-direction illustrate that the cells are generally round before treatment; they generate a flat contact with the glass surface after irradiation treatment.

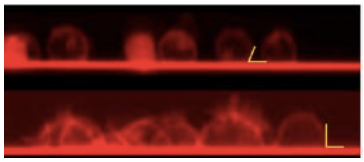

Figure 2: Confocal images of Jurkat cells in z-plane before (top) and 48 h after irradiation with 2 Gy x-ray (down). Yellow bars show contact angles.

It is well established that lymphocytes adhere to other cells in the process of immunological recognition and recirculation [1]. The morphological alteration of Jurkat cells hence suggests that x-ray irradiation is able to trigger an immune-activation. To test this hypothesis we investigated the expression of the IL-2 receptor alpha chain CD25 after x-ray stimulation. This protein is an established marker for the activation state of T-cells [2]. An analysis of CD25 expression in Jurkat cells by FACS analysis shows that this marker protein is significantly up-regulated in response to X-ray irradiation. This finding is further supported by western blot analysis, which also shows an up-regulation of the marker protein CD25.

Conclusion

The data advocate the hypothesis that x-ray irradiation causes a stimulation of lymphocytes. This occurs in response to radiation doses, which are relevant in tumor therapy. This may contribute to the known effect of ionizing radiation on the immune status of patients.

References

[1] S Letourneau et al. IL-2- and CD25-dependent immunoregulatory mechanisms in the homeostasis of T-cell subsets. J Allergy Clin Immunol. 2009, 123:758-762

[2] ML Dustin, TA Springer. Role of lymphocyte adhesion receptors in transient interactions and cell locomotion. Annu. Rev. Immunol. 9:27-66

DOI:10.15120/GR-2016-1

Vascular and fibrotic changes in irradiated myocard after cardiac ablation with carbon ions in a pig model

N. Erbeldinger[1,4]; F. Merz[1]; P. Simoniello[1]; H. I. Lehmann[2]; P. Lugenbiel[3]; A. Eichhorn[1]; D. Thomas[3]; D. L. Packer[2]; M. Durante[1,4]; C. Graeff[1] and C. Fournier[1]

[1]GSI, Darmstadt, Germany; [2]Mayo Clinic/St. Marys Hospital, Rochester, MN, USA; [3]Heidelberg University Hospital, Heidelberg, Germany; [4]Darmstadt University of Technology, Darmstadt, Germany

Introduction

Cardiac arrhythmias (CA) are wide-spread diseases among the elderly population thus constituting a global burden[1,2]. Treatment of CA is in most cases anti-arrhythmic and anti-coagulant medication[3]. In case of recurrence despite medication, the established therapy is a catheter ablation [3]. However, ablation often has limited efficiency (60-75%) and carries risks for complications[4].

This motivates the investigations of alternative, non-invasive treatments. The favorable properties of carbon ion irradiation are well established in cancer therapy. Based on studies using high frequency, x-ray- or β-irradiation ablation of cardiac tissue, ablation can be achieved using irradiation techniques[4,5,6]. In this studies, induction of fibrosis after irradiation is accompanied by diverse tissue remodeling processes[7,8]

Our aim within this study is to relate the observed biological effects elicited by scanned carbon ions to cardiovascular changes in irradiated heart tissue.

Material and Methods

Effects of high dose carbon ion irradiation, e.g. induction of fibrosis, were investigated in a porcine model. Cardiac substructures were targeted with single doses of 25-55 Gy (as depicted in Figure 1).

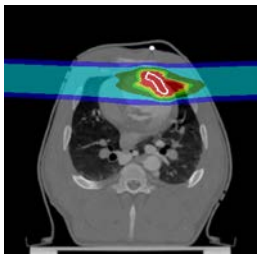

Figure 1: 4D-dose distribution to a free-wall left ventricular target to a dose of 40 Gy.

Animals were monitored up to six months after irradiation. Tissue biopsies from irradiated and non-irradiated areas were obtained three and six months after irradiation during final follow-ups and were either processed for histological or protein analyzes.

Results

The comparison of sham-control with irradiated target areas revealed replacement of cardiomyocytes with fibrotic tissue. Fibrosis progression continues up to 6 months (data not shown). Furthermore, bleeding in targeted areas was observed after three months (Figure 2 A, B), which is most likely caused by damaged blood vessels. After six months, the amount of bleeding recedes (not shown). In parallel, decreased capillary density was observed after three months (Figure 2 C, D), which persisted until six months after irradiation (not shown).

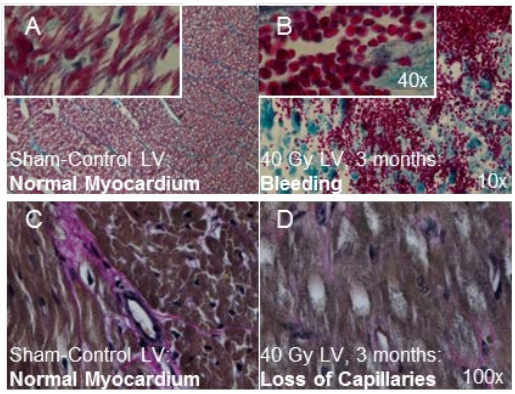

Figure 2: Bleeding and decreased capillary density. LVs from sham and 40Gy irradiated pigs were stained with trichrome (A,B) and Verhoeff van Gieson staining (C,D) after three and six months. Bleeding occurs only after irradiation and diminishes over time (not shown). Amount of capillaries decrease up to three months after irradiation (not shown).

Discussion

In our study, we could show extensive tissue remodeling in the target area, finally leading to fibrosis. Persisting vascular damage indicates ongoing tissue altering processes, which contribute most likely to the observed electrophysiological changes.

References

1 Verdino J Saudi Heart Assoc. 2015; 27(1): 44–49.

2 Chugh et al. Circulation. 25, 2014; 129(8): 837–847.

3 Kim, Korean J Thorac Cardiovasc Surg. 2014; 47(6): 499–503.

4 Cappato, Circ Arrhythm Electrophysiol. 2010; 3(1):32-8.

5 Bode, Europace. 2015;17(12):1868-74.

6 Guerra, Circulation. 2004;110:911-914.

7 Boerma, Curr Drug Targets. 2010;11(11):1405-12.

8 Schultz-Hector, Int J Radiat Oncol Biol Phys. 2007; 67(1):10-8.

Work is supported by HGS-HIRe and financed by GRK 1657 and BMBF (GREWIS, 02NUK017A)

DOI:10.15120/GR-2016-1

Pharmacological augmentation of heavy ion cancer therapy *

Norman Reppingen[1], *Aljona Cucu*[2], *Marco Durante*[1,2], *and Claudia Fournier*[2,3]
[1]TU Darmstadt; [2]GSI Helmholtzzentrum für Schwerionenforschung; [3]University of Applied Sciences Darmstadt

In the previous report[1] **we pesented data showing the pharmacological optimization of the response to X - ray to increase the surface presence of immune relevant molecules on murine tumor cells. We confirmed the pharmacological concept to be useful also for augmenting carbon ion therapy.**

Surface Molecules

The interaction of the immune system with tumor cells is partly governed by surface molecules, steering recognition and cell killing of tumor cells by immune cells. Therefore, increasing surface presence of certain molecules could help to optimize these interactions. The surface presence of the cell death inducing receptor CD95, also known as Fas, was increased by Carbon Ion Irradiation after 24 and 48 h. Using our pharmacological approach, the surface presence of this molecule was increased more than 4 fold on CT26.WT murine colon carcinoma cells after irradiation with up to 6 Gy of High LET (300 keV/μm Carbon, which is not possible with carbon ion irradiation alone at least in this cell type (Figure 1 A).

Signalling

We explored our pharmacological approach consisting of a triterpenoid, the anti malarial drug chloroquine and a Tyrosine Kinase Inhibitor. We found our approach to decrease the abundance of molecules known to support cancer cell survival and to increase radioresistance[2] (e.g. Mcl-1, Survivin, Bcl-XL, data not shown). Interestingly, we found carbon ion irradiation to decrease the phosphorylation of Akt in CT26.WT cells, a molecule amongst the ones involved in treatment resistance and cancer progression (Figure 1 B). This is different to X - ray, which generally is increasing the activity of this pathway. With X - ray, we also found decreased Akt - activity under influence of our drugging approach, suggesting utility for supporting carbon ion irradiation (not shown).

Outlook

The efforts in the murine colon carcinoma model CT26.WT are currently being extended to the aggressive murine breast cancer model 4T1 and the murine melanoma model B16-F10. The design of *in vivo* experiments following our tenet[2] in preclinical, immune competent animal models is ongoing.

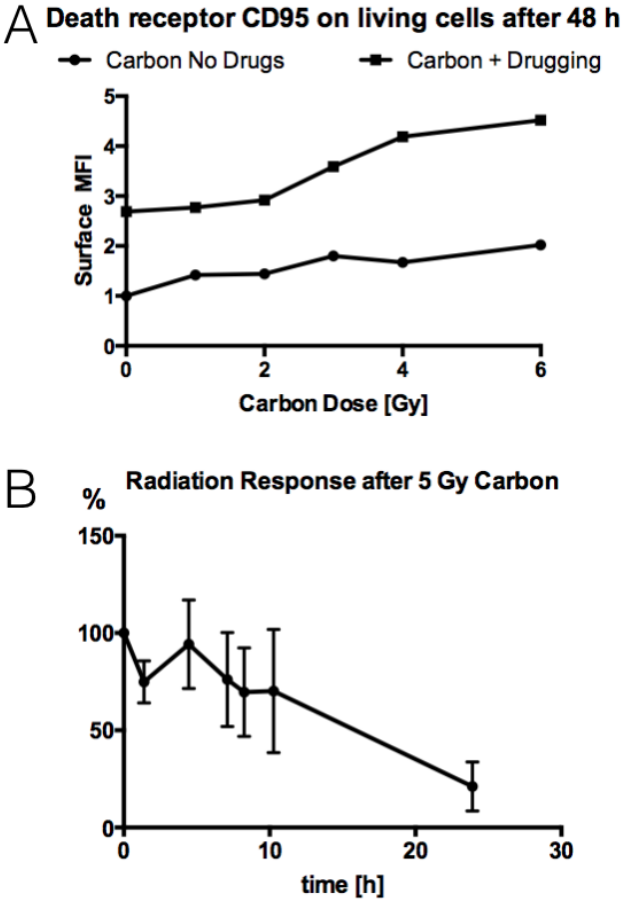

Figure 1: Results in CT26.WT murine colon carcinoma cells. **A** (flow cytometry): Dose dependent surface translocation of CD95 after High LET carbon ion irradiation increased by the influence of chloroquine, a triterpenoid and a Tyrosine Kinase Inhibitor. **B** (western blot densitometry): Decrease of Akt phosphorylation in CT26.WT cells in the hours following Carbon Ion Irradiation.

References

[1] N. Reppingen, M. Durante, C. Fournier, Scientific Reports 2015

[2] M. Durante, N. Reppingen and K. Held, "Immunologically augmented cancer treatment using modern radiotherapy", Trends in Molecular Medicine, Vol. 19, No. 9, 565-582, http://dx.doi.org/10.1016/j.molmed.2013.05.007

* Work supported by HGShire

Impaired differentiation of osteoclasts following irradiation

A.Groo[1], N.Hoenig[3], K.Lischka[2], M.Durante[1,2], C.Fournier[1]
[1]Helmholtzzentrum für Schwerionenforschung GSI, [2]Technische Universität Darmstadt,
[3]Universitätsmedizin Göttingen, Georg-August-Universität Göttingen

Introduction

Ionising radiation is not only used for treatment of malignant tumors but also for relief of symptoms during chronic-inflammatory diseases of the musculoskeletal system. However, doses vary from 0. Gy (5-10 Gy total dose) for Low-Dose Radiotherapy (LD-RT) up to 60 Gy during tumor treatment (1,2). LD-RT leads to contained inflammation and consequently to reduced bone destruction (3). However, bone destruction after high dose exposure during tumor therapy is often attributed to increased activity of bone resorbing osteoclasts (OCs). The exact cellular and molecular mechanism of bone metabolism following ionising radiation is still unclear. In the present work we investigated the impact of ionising radiation on the differentiation process of bone resorbing osteoclast cells.

Materials and Methods

Human OCs were generated from buffycoats of healthy donors (blood donor service Frankfurt/Main). After X-ray exposure, differentiation of OCs from monocytes was initiated by adding RANKL (45 ng/ml) and M-CSF (25 ng/ml). Differentiation was assessed by staining of TRAP, F-actin ring and nucleus with DAPI. Protein expression was assessed by Western blot.

Results

The numbers of differentiated OCs were remarkably decreased following exposure of precursor OCs (monocytes) to moderate und high doses of X-rays, whereas irradiation with a low dose (0.5 Gy, data not shown) did not impair the differentiation (Fig.1).

A key regulatory molecule of the differentiation process in OCs is TRAF6, which induces the osteoclastogenic transcription factor NFATc1. NFATc1 in turn controls the expression of bone resorptive enzyme cathepsin K. The important structural arrangement of cytoskeleton in OCs is c-Src mediated (4). The protein level of these proteins were decreased following irradiation with 2 Gy and 10 Gy (Fig.2), only cathepsin K was only downregulated following a high dose (10 Gy). The low dose (0.5 Gy) did not affect the expression of osteoclasteogenic proteins, except a trend for NFATc1, in line with unchanged cell number of differentiated osteoclasts after irradiation with 0.5Gy (data not shown).

Conclusions

Our data indicate that differentiation of human osteoclasts *in vitro* is impaired following high dose irradiation, whereas following low dose exposure only a trend is observed. However, our previous results revealed that the resorptive activity of OCs on bone substrate is also inhibited after low dose irradiation (5).The inhibition of the differentiation process could be explained by the lowered expression of TRAF6protein, which could reduce further signalling after irradiation.

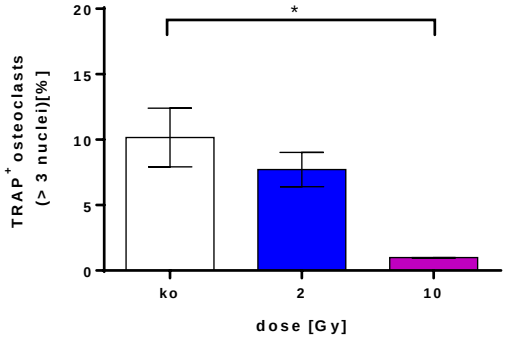

Fig. 1: Differentiated osteoclasts (TRAP$^+$, >3 nuclei, F-actin ring) 14 days after exposure to X-rays (2; 10 Gy). Mean, SEM (N=6). *P<0.05

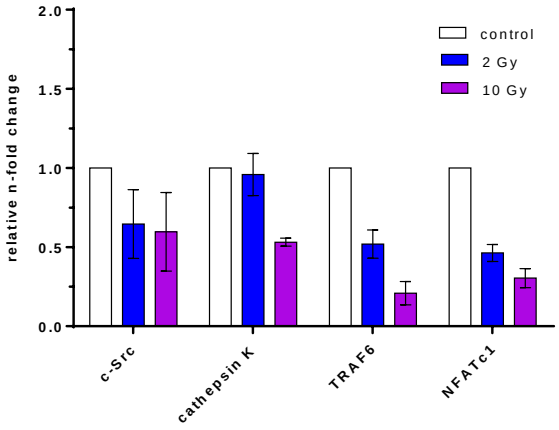

Fig. 2: Expression of osteoclastogenic proteins in irradiated osteoclasts after 14 days. Cathepsin K, NFATc1, TRAF6 and c-Src were detected by Western blot analysis. GAPDH served as loading control. Mean, SEM (N=3)

References

[1] Seegenschmiedt MH et al , Strahlenther Onkol. 2004 Nov; 180(11)
[2] Schmeler KM et al, Cancer 2010; 116:625-30.
[3] Rödel F et al, Front Oncol. 2012 Sep 25;2:120
[4] Sanjay A et al, J Cell Biol. 2001 Jan 8;152(1):181-95
[5] Groo A et al, GSI Scientific Report 2014

*Work supported by BMBF (02NUK017A Grewis)

DOI:10.15120/GR-2016-1

Low doses of ionizing radiation reduce osteoclast numbers and increase osteoblast mineralization

Lisa Deloch[1], Aljona Cucu[2], Benjamin Frey[1], Claudia Fournier[2], Udo S. Gaipl[1]
[1]Department of Radiation Oncology, Universitätsklinikum Erlangen, Friedrich-Alexander-Universität Erlangen-Nürnberg, Germany
[2]GSI Helmholtzzentrum für Schwerionenforschung GmbH, Darmstadt, Germany

Introduction

Rheumatoid Arthritis (RA) is a chronic inflammatory autoimmune disease with a prevalence of about 1%. It is, amongst others, characterized by synovial infiltration and invasion of the synovium. This, in most cases, leads to a local as well as systemic osteoclast (OC) –mediated destruction of cartilage and bone as well as an inhibition of bone formation by osteoblasts (OB) (1). Today's treatment options offer a good disease control in RA and other degenerative inflammatory musculoskeletal diseases. Nevertheless, not all patients sufficiently respond to these options. In those cases low-dose radiotherapy (LD-RT) might be a promising approach to reduce experienced pain levels, attenuate inflammation, and improve the quality of life (2-6). However, a lack of randomized trials and *in/ex vivo* experiments often restrains health professionals from routine usage. We therefore have aimed to investigate the effects of LD-RT on bone homeostasis in a RA mouse model (7).

Materials and Methods

OCs were generated by isolating bone marrow (BM) from the long bones of 5-6 week old h*TNF-α*tg mice. 24h after seeding in triplicate in medium containing 10 ng/ml M-CSF and 50 ng/ml RANK-L, cells were irradiated with 0.5 Gy of X-rays. TRAP positive cells with 3 or more nuclei were considered as OCs. OBs were isolated from the calvariae from 3-6 days old h*TNF-α*tg pubs. Cells were cultured until P2 and then seeded in triplicates onto 24-Well plates. At 100% confluency mineralization media (PromoCell) was added and irradiation was carried out 24h after. At d21 Alizarin Red staining was performed and analysed using ImageJ. Human primary OBs were differentiated from mesenchymal stem cells from healthy donors.

Results

While numbers of differentiated h*TNF-α* tg OCs were significantly reduced (Fig.1A), the amount of mineralized aerials was increased after 0.5 Gy of X-rays (Fig.1B). Also mineralization process in human primary OBs was significantly enhanced following irradiation with 0.5 Gy of X-rays. Additionally irradiated OBs showed a trend for increased ALP content (Fig.1C).

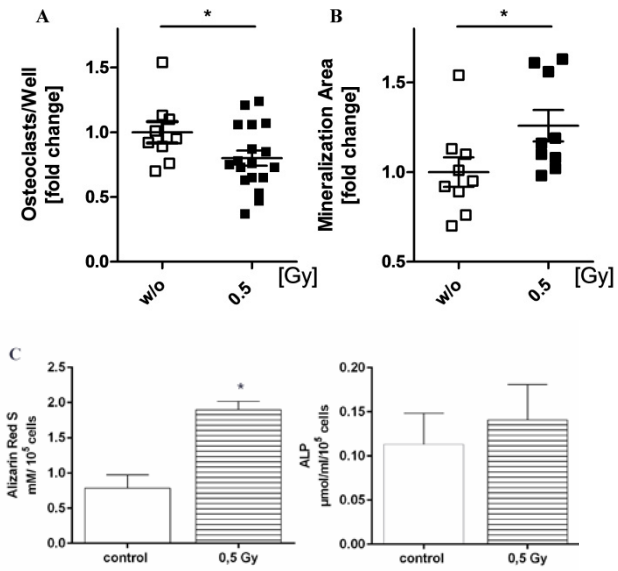

Figure 1: A) Numbers of TRAP pos. h*TNF-α*tg BM-derrived OCs (n=6) and B) Alizarin Red stained mineralized OB deposits from h*TNF-α*tg calvariae (N=2, n=3) after irradiation with 0.5 Gy of X-rays. C) Alizarin red S and ALP concentration in human primary OBs at 14 days after irradiation with X-rays. Data presented as mean ±SEM and analysed by Mann-Whitney-U test in comparison to non-irradiated controls. (*p<0.05, **p<0.01, ***p<0.001)

Conclusion

Our findings support a positive decelerating effect of LD-RT on bone erosion in TNF-driven arthritis. A dose of 0.5 Gy seems to partially restore a healthy bone homeostasis in this experimental animal model of chronic inflammation. The results from *in vitro* experiments with human primary OBs confirm that findings.

References

1. G. Schett and J. P. David, *Nat Rev Endocrinol*, 6(12), 698-706 (2010)
2. L. Keilholz et al, *Strahlenther Onkol*, 174(5), 243-50 (1998)
3. O. J. Ott et al, *Strahlenther Onkol*, 188(12), 1108-13 (2012)
4. O. J. Ott et al, *Strahlenther Onkol*, 190(4), 394-8 (2014)
5. O. J. Ott et al, *Strahlenther Onkol*, 190(3), 293-7 (2014)
6. M. H. Seegenschmiedt and L. Keilholz, *Radiother Oncol*, 47(1), 17-28 (1998)
7. J. Keffer et al, *Embo j*, 10(13), 4025-31 (1991)

* Work supported by BMBF (GREWIS, 02NUK017A)

Choice of DNA repair pathways and transmission of chromosomal rearrangements in hematopoietic cells exposed to different radiation qualities*

M. Rall[1], D. Kraft[2], A. Cucu[2], G. Taucher-Scholz[2], H. Bönig[3], M. Volcic[1], D. Salles[1], L. Wiesmüller[1], C. Fournier[2]

[1]Gynecological Oncology, Ulm University, Germany, [2]GSI, Darmstadt, Germany;
[3]Institute for Transfusion Medicine, Frankfurt University, Germany

Introduction

Hematopoietic stem and progenitor cells (HSPC), that is, the cell population giving rise not only to all mature hematopoietic lineages but also the presumed target for leukemic transformation, can transmit genetic events, such as generated by ionizing radiation if DNA double-strand breaks (DSB) are not faithfully repaired. In our collaboration we explored the quality and molecular components of DSB repair as well as the transmission of chromosomal changes in human HSPC compared to mature peripheral blood lymphocytes (PBL).

DSB repair

Actively cycling human HSPC and PBL [1] were nucleofected with a DSB repair substrate designed for the analysis of homologous recombination (HR) [2], representing error free DSB repair. DSB within the substrate were induced with 2 and 5Gy of X rays, carbon (60-85keV/µm) or calcium ions (180keV/µm). Reconstitution of wild-type *EGFP* was measured 24h post-irradiation [3]. Results from our previous study showed that HSPC were compromised in HR compared to mature lymphocytes, which could be explained by diminished NF-κB signalling [4 and GSI report 2011]. As can be seen in figure 1B after irradiating the cells HR deficiency for HSPC compared to PBL was confirmed. Furthermore for both cell types a dose (fig.1A, HSPC data not shown) and a trend for LET (fig. 1B) dependent increase in HR could be observed [3].

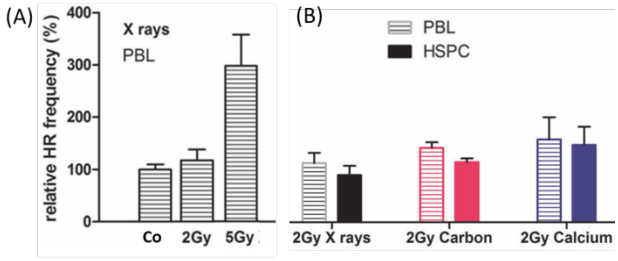

Figure 1: DSB repair analysis [figure modified from 3]. After exposure of (A) PBL with X rays and (B) HSPC and PBL with different radiation qualities (carbon or calcium ions) the fraction of EGFP+ cells was quantified (FACS Calibur®, BD). HR data were individually normalized to unirradiated controls representing 100% (PBL: 0.043 × 10^{-2} and HSPC: 0.048 × 10^{-2}). Mean values and SEM are indicated (X-rays: n = 3 from 1-3 independent experiments; carbon ions: n = 3 from 1experiment).

Transmission of chromosomal rearrangements

In the context of diminished HR and potentially inaccurate repair pathways in HSPC, the transmission of chromosomal rearrangements to daughter cells have been analyzed. As depicted in figure 2A irradiated HSPC (X rays or 60-85keV/µm carbon ions) were cultivated in a 3D matrix (colony-forming-unit-assay) for 14 days. From single myeloid colonies, metaphase spreads were prepared and stained using mFISH technique [5 and GSI report 2009]. With respect to clonal aberrations, all colonies derived from unirradiated HSPC showed a normal karyotype (fig. 2B). In both X-rays and carbon ion derived colonies clonal chromosome aberrations were observed, i.e., detected in all metaphases of an individual colony. Incorrect repair in HSPC was reflected by clonal aberrations in 40% of their progeny irrespective of the radiation quality. Taking the frequency of colonies with clonal aberrations as a surrogate marker of the late leukemia risk, carbon ion versus photon radiotherapy is not expected to lead to an increased leukemia risk, even though HSPC show a deficiency in homologous repair preferentially targeted by ion radiation damage.

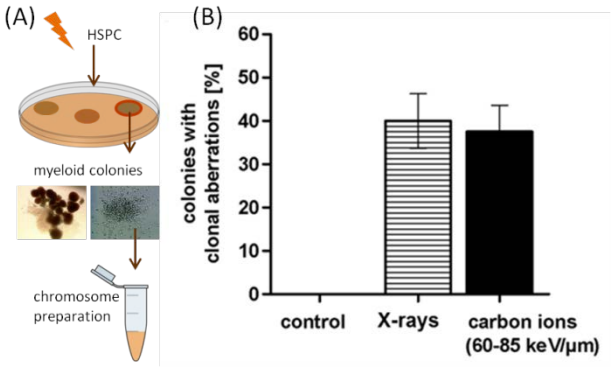

Figure 2: (B) Frequency of myeloid colonies with clonal aberrations after exposure to different radiation qualities (X rays or carbon ions) [figure modified from 5]. For every radiation quality data for all applied doses (between 1 and 3 Gy) were pooled (7 controls, 30 colonies from irradiated HSPC). The Mean values and SEM are indicated

References

[1] Becker et al (2009), Int J Radiat Biol, 85(11):1051-1059
[2] Keimling et al (2011), FASEB J, 25(11):3849-3860
[3] Rall et al (2015), Frontiers in Oncology, 5(250)
[4] Kraft et al (2015), Leukemia 29 (7): 1543–54
[5] Kraft et al (2015), Mutation Research 777: 43–51

* Work financed by DLR/BMWi contract No. 50 WB 1225.

DOI:10.15120/GR-2016-1

Inflammatory effects of TNFα are counteracted by X-ray irradiation and AChE inhibition in mouse micromass cultures

G. Thangaraj[1], V. Manakov[1], A. Cucu[2], C. Fournier[2] and P.G. Layer[1]
[1]Technische Universität Darmstadt, Germany; [2] GSI Darmstadt, Germany.

Introduction

As a means to analyse anti-inflammatory effects by radiation and/or by cholinergic mechanisms, we found that cultured primary human osteoblasts express most cholinergic components (Fig. 1). After X-ray irradiation, their level of acetylcholinesterase (AChE) was strongly elevated. As a 3D model, we cultured mesenchymal stem cells isolated from E11 mouse embryos as micromass nodules (Fig. 2), and differentiated them into chondro- and osteoblasts. They were stimulated by the inflammatory cytokine TNF-α, before exposure to 2 Gy X-rays. Effects on chondro- and osteoblasts of TNF-α, of X-rays, or both were analysed by Alcian Blue, or Alizarin Red staining, respectively; acetylcholinesterase (AChE) activity was visualized histochemically (further details in ref. 1).

Results

Human osteoblast cells express radiation-sensitive cholinergic components (Fig. 1E). Moreover, irradiation with 2Gy of X-rays drastically increased the expression of AChE, as shown by RT-PCR (Fig. 1A). The effects of cholinergic, inflammatory and radiation-sensitive effects in mesenchymal micromass cultures are presented in Fig.2**.**

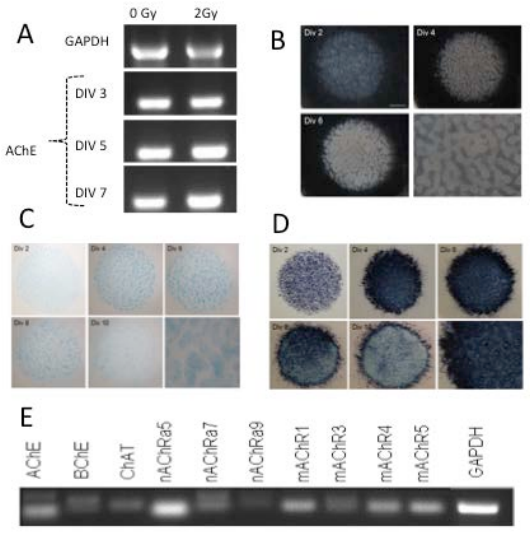

Fig.1**.:**(A) RT-PCR of control and X-ray-irradiated human osteoblast cells; (B) Formation of nodules from mesenchymal cells from embryonic E11.5 mice limbs; (C) Cartilage formation in nodules revealed by Alcian blue staining after 2-10 days in vitro (div); (D) Mineralization of bony materials indicated by alkaline phosphatase (dark blue); B-D present mouse cultures between div 2-10 from E11.5 mouse limb buds; the lower right frames show magnifications of respective div6 samples; (E) RT-PCR for cholinergic components of human osteoblast

Conclusion

Using micromass cultures, this study revealed that i) blocking AChE activity inhibits differentiation of chondro- and osteoblasts, ii) X-rays advance differentiation of chondro- and osteoblasts in vitro, iii) TNF-α inhibits chondro- & osteoblast differentiation, which is reversed by X-rays, and iv) AChE inhibition masks in vitro effects of TNF-α in vitro.

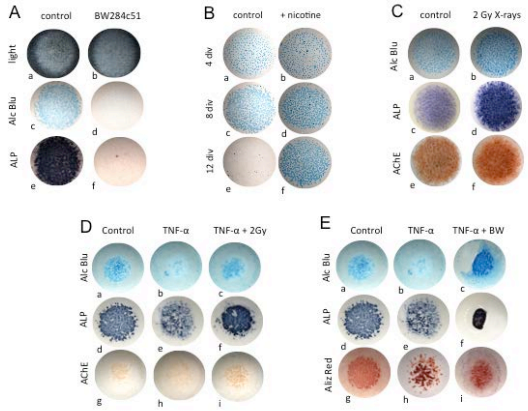

Fig. 2.: (A) Mesenchymal micromass cultures (MMC) were treated for 12 days in vitro (div) with 100 µM BW284c51, a specific AChE inhibitor. Nodule formation were disturbed under BW treatment (b, cf. control in a). (B) Effect of 20 µM nicotine on MMC after 4-12 div. (C) X-rays advance differentiation of cartilage and bone at div3 in MMC. ALP and AChE activity were strongly increased by X-rays. (D) Action of 5 ng/ml TNF-α alone, or together with 2Gy X-rays on MMC. (E) Effect of 5 ng/ml TNF-α is counter-acted by AChE inhibition

Acknowledgement: We thank H. Bonig for providing bone marrow samples. This work was funded by BMBF (Project 02NUK017A and C). H.B. was funded by LOEWE, III L 4-518/17.004, 2010.

Reference 1: Thangaraj et al. (2016), Chemico-Biol. Interactions, http://dx.doi.org/10.1016/ j.cbi.2016.03.027.

Experimental validation of the relative biological effectiveness along the proton spread out Bragg peak with the Local Effect Model*

R. Grün[1], T. Friedrich[1],M. Krämer[1] and M. Scholz[1]
[1]GSI, Darmstadt, Germany

Introduction

The purpose of this study is to compare the predictions of the local effect model (LEM IV) in an extensive analysis with relative biological effectiveness (RBE) experiments along the proton spread out Bragg peak (SOBP) found in the literature [1]. The analysis demonstrates the capabilities and limitations of the model and underlines experimental systematics.

Methods

19 publications with in-vitro experiments focusing on proton RBE along the SOBP were considered [2], covering in total more than 100 depth positions. The treatment planning software TRiP98 [3] was used to optimize the passive proton SOBP of each experiment. Together with the physical dose distribution the RBE was calculated based on the LEM and compared to the measurements. The input parameters of the LEM are the linear-quadratic parameters of the reference irradiation evaluated in the experiments and the transition dose D_t, describing the dose for which the linear quadratic behaviour of the dose-response curve transits into a purely linear shape. This transition dose D_t was evaluated from an empirical relationship in order to resign from any free parameter and demonstrate the predictive power of the LEM [4].

Results

A clear increase of RBE on the dose-averaged linear energy transfer (LET_D) was observed. This can be seen from the experimental data and is underlined by the LEM predictions (fig. 1). For therapy relevant doses (2 Gy (RBE)), RBE of experiments and LEM predictions increase above the clinically applied constant value of 1.1 for LET_D values higher than 2 keV/µm which roughly corresponds to the proximal part of the SOBP. The RBE prediction of the LEM is in good agreement with the experimental data within the 95 % confidence interval for LET_D values up to 10 keV/µm, which corresponds to the distal end or penumbra of the SOBP. For LET_D values above 15 keV/µm the observed deviation needs to be taken with caution since experimental data is scarce in this region. The deviation of the LEM prediction to the experimental RBE are further decreasing with decreasing survival level, i.e., increasing dose level.

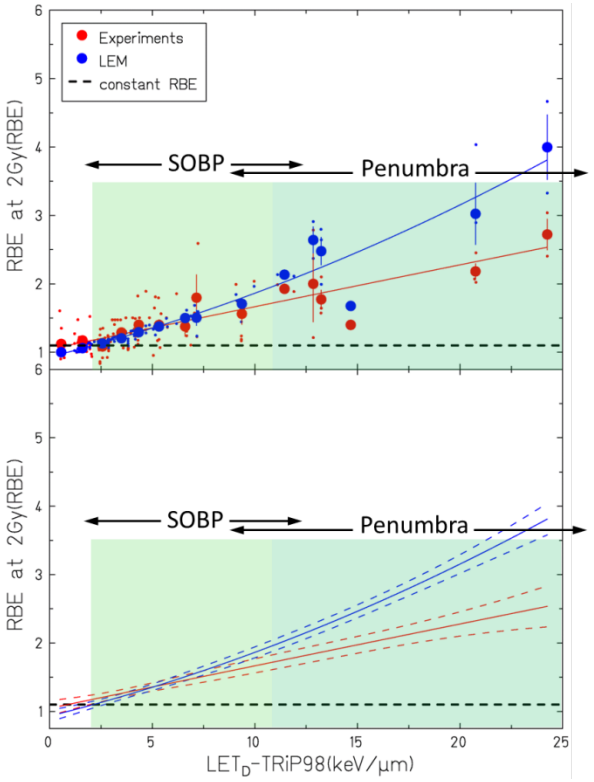

Figure 1: Measured and LEM predicted RBE_{2Gy} vs. LET_D. Red: Experimental RBE values; Blue: LEM prediction. Upper: The large circles are mean RBE values evaluated in 1 keV/µm bins. The mean LET_D of each bin is used as reference. The small circles show the original RBE values. The fit to the data is performed for the original RBE values without consideration of error bars. Lower: complemental to a) the 95 % confidence interval of the fit curves.

Conclusion

The LEM adequately describes the RBE inside the SOBP even though it predicts a slightly steeper slope of RBE with LET_D.

References

[1] T. Elsässer et al., Int J Radiat Onc Biol Phys, (2010) **78**:1177.
[2] H. Paganetti, Phys Med Biol, (2014) **59**:R419.
[3] M. Krämer and M. Scholz, Phys Med Biol, (2000) **45**:3319.
[4] T. Friedrich et al., J Rad Res, (2013) **54**:494.

* Work supported by RaySearch Laboratories AB

DOI:10.15120/GR-2016-1

Cell survival-curve shapes of exponential growing cells based on cell-cycle specific survival-curves

P. Günther[1], T. Friedrich[1], M. Durante[2] and M. Scholz[1]
[1]GSI, Darmstadt, Germany [2]TIFPA, Trento, Italy

The dose D dependent effect $\nu = -\ln(S)$ of cell survival S for asynchronous cell cultures is described by the linear-quadratic model (LQ) $\nu = \alpha \cdot D + \beta \cdot D^2$ with the linear parameter α, and quadratic ter β. This primary empirical observation is reflected by the mechanistic GLOBLE model [1] for cell survival in the low dose range. A recently published extension to this model [2] is able to describe survival-curves of cells in different stages of their replication cycle. Taking into account cell-cycle specific sensitivities for an exponentially growing, asynchronous cell culture leads to substantial deviations from the pure LQ shape at high doses.

Material and Methods

The basic GLOBLE model [1] predicts the survival probability of cells after photon irradiation based on the DNA damage pattern. The distribution of DSBs on a higher order chromatin structure is evaluated, which consists of subunits called loops. A loop with one DSB is classified as isolated DSB (iDSB). Two or more DSBs within one loop are counted as a complex DSB (cDSB). Cell inactivation probabilities, so called lethalities, are assigned to these damage classes. The influence of the cell-cycle on the survival in the cell-cycle specific GLOBLE model [2] is considered by the local replication status of the loops, which is assumed to determine the available repair pathways. The survival probability can be calculated by

$$S = \exp\left(-\left[\#iDSB_1 \cdot \epsilon_{i,1} + \#iDSB_2 \cdot \epsilon_{i,2} + \#cDSB \cdot \epsilon_c\right)\right]$$

with the number of iDSBs on unpaired (paired) loops $\#iDSB_{i,1}$ ($\#iDSB_{i,2}$) , the lethality $\epsilon_{i,1}$ ($\epsilon_{i,2}$), the number of cDSBs $\#cDSB$, and the lethality ϵ_c. The cell survival S for asynchronously growing cells at the dose D is given by

$$S(D) = \int d\phi \, S(D,\phi) \cdot \rho(\phi)$$

with the cell-cycle dependent survival $S(D,\phi)$, at the cell-cycle position ϕ and the distribution of cells within the cell-cycle $\rho(\phi)$. In the following this survival model is called asynchronous GLOBLE model. In this work we analyze the properties of asynchronous, exponentially growing cells, based on the assumption that the total cell population consists of subpopulations, whose survival probabilities are described by the cell-cycle specific GLOBLE model [2].

Results and Conclusion

An example calculation with typical parameters for CHO cells ($\alpha = 0.17\ \mathrm{Gy}^{-1}, \beta = 0.026\ \mathrm{Gy}^{-2}$) is shown in fig. 1. The first derivative of a LQ shaped effect ν, as a function of dose D, is a straight-line (fig. 1, light grey). The asynchronous GLOBLE model effect curve shows this behavior for doses up to ~7 Gy for CHO cells, but a substantial deviation from that shape for higher doses. According to this model the dose at which the deviation occurs is cell type dependent, and is in the range of 5 to 15 Gy.

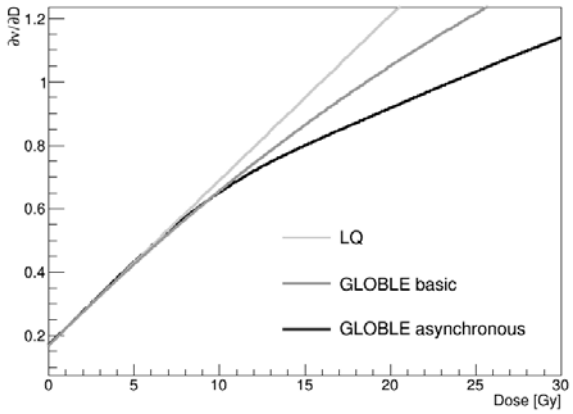

Figure 1: First derivative of the effect the LQ, basic GLOBLE and asynchronous GLOBLE model.

A less pronounced deviation from the LQ shape was already observed with the basic GLOBLE model [1] (fig. 1 grey line), which arises from DNA damage saturation. The additional deviation in the asynchronous GLOBLE model comes from a heterogeneous radiosensitivity of the cell population and is in the order of magnitude of already observed [3,4] deviations, which are considered by empirical approaches. The innovation of the asynchronous GLOBLE model is that it predicts this deviation and allows for a mechanistic interpretation. This could consolidate the assumption of the empirical linear-quadratic-linear survival curve that is used in the local effect model [3] to represent the photon reference dose response curve.

References

[1] Friedrich T, et al. *Radiation Research* 2012 Sept; 178(5): 385-394
[2] Hufnagl A, et al. *DNA Repair* 2015 March; 27(1): 28-39
[3] Elsässer T, et al. *Int. J. Radiat. Oncol. Biol. Phys.* 2010 Nov; 78(4): 1177–83
[4] Astrahan M, *Med. Phys* 2008 Aug; 35(9): 4161-72

Founded by DFG (Graduiertenkolleg 1657)

Extension of the Particle Irradiation Data Ensemble

A.M. Bothe[1,2], M. Scholz[1], T. Friedrich[1]
[1]GSI, Darmstadt, Germany; [2]Goethe Universität, Frankfurt, Germany

A compilation of parameters describing survival probability of cultured cells after both photon and ion irradiation was presented by GSI within the Particle Irradiation Data Ensemble (PIDE) for different experimental settings in 2013 [1]. By considering large data sets rather than individual experiments this tool allows investigating the characteristics of enhanced ion effects with high precision. Recent work enhanced this data base and also included raw data of underlying experiments. This allows a sound uncertainty analysis of derived quantities, which was lacking before.

PIDE

Ion radiation in general leads more effectively to biologic damage as photon irradiation. This is usually expressed within the relative biological effectiveness (RBE), defined as the ratio of photon and ion dose required to achieve the same effect. Despite its simple definition, the RBE is a quantity depending on several factors: Besides energy (and thus LET) it depends on particle species, dose (or effect) level, as well as the intrinsic radiosensitivity of the cells or tissues under investigation. The colony forming assay is frequently used for systematic studies of RBE dependencies; it is based on the assessment of the proliferative capacity of cultured cells after irradiation. Typically, only intra-laboratory comparisons for different radiation qualities are performed. A concurrent view / meta-analysis on all available data allows for an even deeper insight, providing a higher precision and measures of data fluctuation and uncertainties.

Inspired by this the PIDE data base was created in 2013, comprising over 800 experiments taken from the literature. From these experiments, linear quadratic parameters describing the shape of the dose response curves are tabled within the data base for both photon and ion irradiation, allowing the evaluation of RBE for any effect level. The PIDE was made accessible to the research community via the GSI website [1], and first evaluations of open questions concerning the RBE systematics were presented in [2]. Currently, PIDE is used by more than 100 researchers worldwide.

Extension of the data base

Including more data, in particular emerging from the recent years, the PIDE has been enhanced. It now contains 1110 ion experiments with corresponding photon experiments, taken from 115 scientific publications. Instead of only having parameters tabled, the raw data (i.e. survival probability for each dose point) were added, if the data was available. Figure 1 presents the amount of data of the original and extended PIDE version. Availability of the raw data facilitates the rigorous derivation of error measures for all derived quantities of interest. Figure 2 presents the abundance of the various ion species in the two versions. Remarkably, the extension increased the fraction of proton experiments, driven by the current discussion about the importance of proton RBE [3]. The extended version of PIDE will give rise for substantiating the results of [2] with much higher accuracy. Furthermore, it will help to set uncertainties of RBE model predictions in relation of accuracy of experimental data.

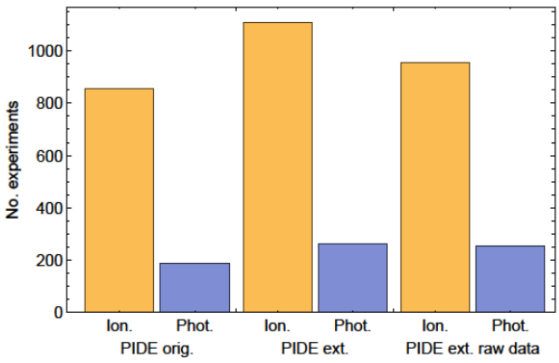

Figure 1: Number of survival experiments in the original and extended version of the PIDE. For almost all experiments raw data are available now.

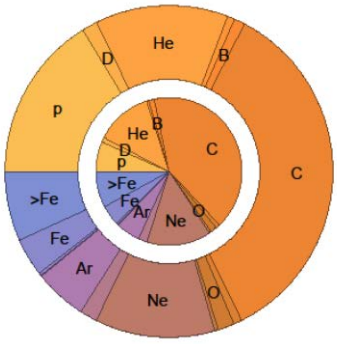

Figure 2: Species subdivision of ion experiments contained in PIDE in the original and extended version (inner and outer ring, respectively).

References

[1] www.gsi.de/bio-pide
[2] Friedrich *et al.*, J. Radiat. Res. **54,** 494 (2013).
[3] Grün *et al.*, Med. Phys. **40**, 111716 (2013).

DOI:10.15120/GR-2016-1

Simulating the effect of focused ion beams

T. Friedrich[2], M. Scholz[1]

[1]GSI, Darmstadt, Germany

Heavy ion radiation is more effective in inactivating cells due to their highly localized energy deposition along the ion track, which gives rise to the emergence of complex damage. Hence, the local ionization density is a key quantity in the description of the biologic effect. This is exploited within the Local Effect Model (LEM) for the calculation of ion effects in comparison to low LET radiation as X-rays or hard γ rays. Such effects can also be achieved by focusing low LET particle radiation to small spots, as this results in high local ionization densities as well. An extension of LEM predicts the associated effect enhancements.

LEM for particle spots

To determine the biologic effects of radiation, the local ionization density is the ultimate key quantity of interest. This justifies a classification of different radiation qualities in sparsely or densely ionizing. A dense ionization pattern can be either realized by high LET ion radiation or by focusing low LET radiation to small spot sizes in the order of a micron, thus cumulating up local dose.

To implement the latter in the LEM [1], the full simulation approach used to calculate the effects of uniformly distributed particle hits was modified to reflect a Gaussian beam spot distribution, implying a Gaussian density distribution of the particles across the beam. The widths in x- and y-directions as well as the number of particles in the spot can be chosen as input parameters of the calculations, c.f. Fig. 1a. Then, with the methods of LEM, the effect of a spot hitting a cellular nucleus can be derived.

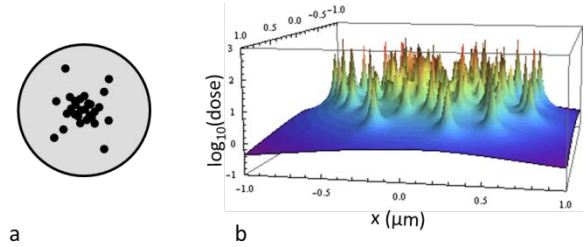

Figure 1: LEM was modified to calculate the effect of spot irradiations of a specified number of ions focused to a Gaussian spot (a). The dose profile of 117 protons focused to a beam spot of 0.7 µm width is shown in (b).

Mechanism of effect enhancement

Figure 1b illustrates the local dose deposition of 117 protons with energy of 20 MeV, focused to a beam width of 0.7 µm (FWHM). As protons of this energy still have a low LET and cause typically none or one DSB along their track, a uniform irradiation with these protons would be comparable to photon radiation, where the DSB pattern is homogeneously spread out over the entire cell nucleus. In contrast, in the spot irradiation, all tracks are in close proximity. This gives rise to a higher probability for the formation of DSB clustering on the micrometer scale. In the LEM, these clustered DSB are interpreted as multiple lesions within a DNA chromatin loop [2]. They are harder to repair for the cells, thus implying a higher effect of the radiation. As an example, a dose of 0.62 Gy given to CHO cells (α = 0.139 Gy^{-1}; β = 0.0268 Gy^{-2}) results in about 91 % cell survival for x-ray irradiation, 90 % for a broadbeam irradiation of the same dose (117 protons), and 75% for a spot irradiation of the same number of pro tons as indicated in Fig. 2. While the entire energy and thus the dose the nucleus is exposed to is equal in these cases, the biologic effect is predicted to be clearly enhanced in the spot irradiation.

Outlook

Spot irradiation on the micrometer scale can be realized in microbeam experiments with protons and also heavier ions. A verification of the effect enhancement was already found in [3] for the endpoint of chromosomal aberrations. Impressively, simply by focussing particles, they get more harming to biologic targets. Further experiments are carried out considering cell inactivation, where a one-to-one comparison of experimental data with the LEM is aimed at. This will help to better understand the importance of the µm-scale for the formation of complex damage.

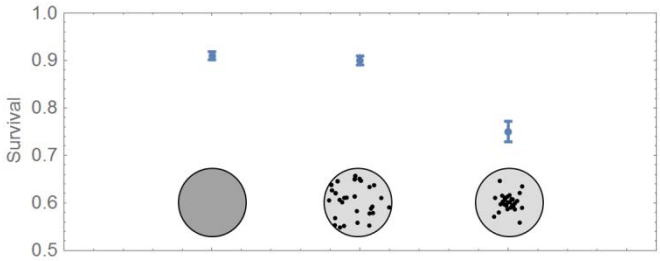

Figure 2: Predicted survival of CHO cells after 0.62 Gy photon radiation, proton radiation (broadbeam) and focused proton beams.

Acknowledgements

This work is funded by BMBF within research grant 02NUK031D.

References

[1] Friedrich et al., Int. J. Radiat. Biol. **88**, 103 (2012).
[2] Schmid et al., Phys. Med. Biol. **57**, 5889 (2012).

Advances in OER-driven biological optimization with ion beams

E. Scifoni[1], W. Tinganelli[1,2], M. Durante[1,2], O. Sokol[1] and M. Krämer[1]

[1]GSI, Biophysics Dept., Darmstadt, Germany; [2] INFN-TIFPA, Trento Institute for Fundamental Physics and Applications, Dept.of Physics, Trento University, via Sommarive 14, 38123, Povo (Trento), Italy;

One of the major indications, for which ion beam therapy may act as a first therapeutic choice, is the fight against hypoxic tumors, i.e. tumors where the lack of oxygen induces an increased radioresistance, quantified by the oxygen enhancement ratio (OER). While this potential benefit has been demonstrated, due to the LET dependent decrease of the OER, it is also clear that the amount of reduction of this radioresistance can be quite limited, if the irradiation is not properly tuned to the specific and usually highly heterogeneous oxygen distribution within a target tissue.

In recent years, our group developed the first approach to include explicitly the oxygen enhancement ratio in treatment planning [1], extending the GSI research treatment planning system TRiP98 [2].

The oxygen distribution was used to drive directly the optimization of the ion fields [3]. The refinement of this concept lead to the development of the *kill painting* method, where, beyond the accounting of a RBE weighted dose, the objective function of the biological optimization engine was modified including also an isoeffect in the local microenvironment [4], until restoring a flat survival level over the whole irradiated tumor.

For carbon ions a clear advantage was shown for OER–optimized plans,where the concept of kill painting was employed, as compared to conventional plans, and it was also experimentally verified [4].

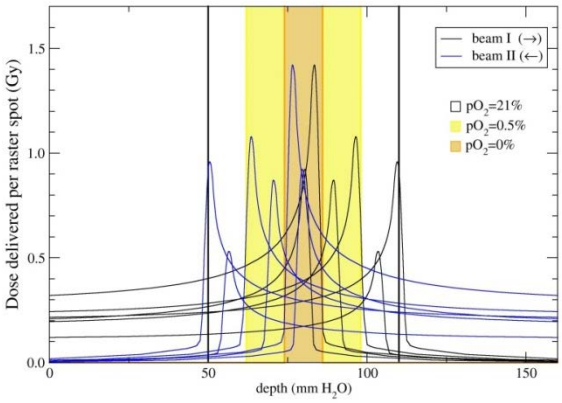

Figure 1: Example of fluence distribution for OER-optimized plans with two opposed fields of carbon ions on a differently oxygenated tissue (see Ref.[4] for details).

In the last year, firstly, the code was adjusted allowing to perform OER-driven optimization also with ions different from carbon, like oxygen, which is potentially a better candidate for fighting hypoxia. It was then possible to perform treatment planning studies including this option, to assess the differential advantages of the various ions in normoxic and in partially hypoxic tumors. A clear advantage was found for the use of oxygen in the latter case, which was also experimentally proved [6].

Among the ongoing developments, there is the inclusion of an OER model based on a more mechanistic basis [7,8]. Further outlook, include the consideration of other forms of biological intra-tumour heterogeneities (e.g. *stem-ness* of tumor cells) as driving force for the optimization, beyond the oxygenation effect.

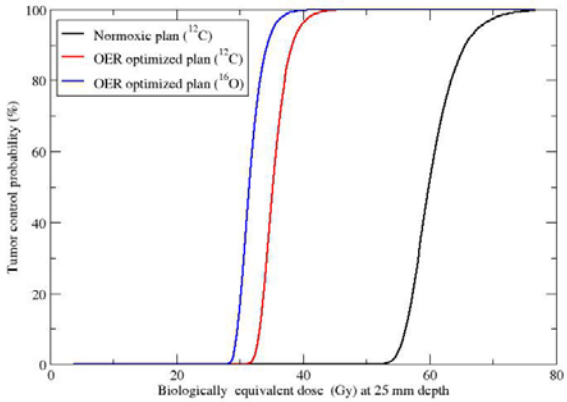

Figure 2: Advantages of OER optimized plans for carbon and oxygen ions in terms of tumor control probability dependence on an equivalent dose in the entrance channel [4,9].

References

[1] E. Scifoni, W. Tinganelli, W. K. Weyrather, M. Durante, A. Maier and M. Krämer, Phys. Med. Biol. 58, 3871-3895 (2013).

[2] M. Krämer and M. Durante, Eur. Phys. J. D 60, 195 (2010).

[3] M. Krämer, E. Scifoni, F. Schmitz, O. Sokol and M. Durante, Eur. Phys. J. D 68, 306 (2014).

[4] W. Tinganelli, M. Durante, R. Hirayama, M. Krämer, A. Maier, Y. Furusawa, W. Kraft-Weyrather, and E. Scifoni, Sci. Rep. 5, 17016 (2015).

[6] O. Sokol et al., this Report.

[7] E. Scifoni, Mod. Phys. Lett. A 30, 1540019 (2015).

[8] D. Boscolo et al., this Report

[9] E.Scifoni, M. Krämer, W. Tinganelli, R. Hirayama, W. Kraft-Weyrather, A. Maier, Y. Furusawa and M. Durante, Poster presented at ICRR (Kyoto) 2015.

DOI:10.15120/GR-2016-1

Biological characterization of therapeutic oxygen beams

O. Sokol[*1,2], *E. Scifoni*[1], *W. Tinganelli*[1,3], *S. Brons*[4], *T. Friedrich*[1], *M. Durante*[1,3], *and M. Krämer*[1]

[1]GSI, Darmstadt, Germany; [2]Technische Universität Darmstadt, Darmstadt, Germany; [3]TIFPA Trento Institute for Fundamental Physics and Applications, Trento, Italy; [4]HIT, Heidelberg, Germany

Some of the modern accelerator facilities allow testing ion modalities for therapy, beyond currently used protons and carbon (^{12}C) ions. In particular, oxygen (^{16}O) ions are of big interest as a possible alternative to ^{12}C ions for cases of poor oxygenation of the tumor tissue (hypoxia) [1]. The current TRiP98 physical beam model for ^{16}O was recently updated using attenuation and fragmentation measurements for the primary beam as well as the generated nuclear fragments; it already returns precise absorbed dose profiles. More tests are required to benchmark the present physical and biological model in order to perform reliable comparative treatment planning studies. Biological characterization implying survival measurements, RBE-weighted dose profiles verification and tests in the hypoxic microenvironment is performed in the experimental cave of HIT, Heidelberg.

Relative biological effectiveness

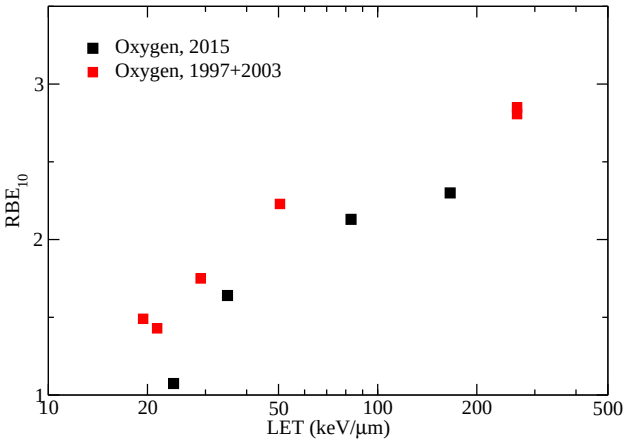

Figure 1: RBE for 10% survival level vs. dose averaged LET of oxygen ion for CHO-K1 cell line.

Figure 1 represents the set of RBE_{10} measurements for LET values of 24, 35, 83 and 166 keV/μm (CHO-K1 cell line) together with data from PIDE database [2]. Recent values tend to be lower along all LET range; this tendency can be explained by changes in the cell line properties (in particular, changes in parameters of the reference X-ray curve). Considering the generally observed fluctuations for RBE values and lack of ^{16}O data, more measurements are required to characterize the dependency precisely, especially in the region of higher LET values.

* o.sokol@gsi.de

Tumor hypoxia

With regard to patient treatment planning, the proper choice of ion modality remains one of the main challenges. If the plan is optimised for a flat RBE-weighted dose without considering the tumour microenvironment, one should not expect the benefit of using ^{16}O ions as compared to ^{12}C. An example is shown on Figure 2, which represents the dose-volume histograms for plans with different ions (data for ^{1}H, ^{4}He and ^{12}C taken from [3]). Prescribed dose to the skull-base chordoma was 3 Gy(RBE) per fraction (patient CT taken from the GSI pilot project).

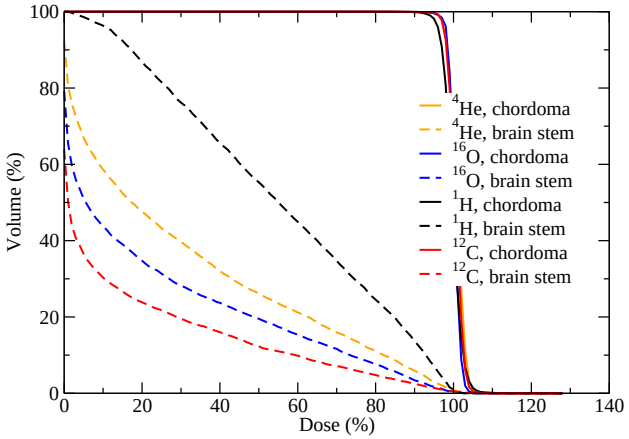

Figure 2: DVH for different double opposed fields plans with prescribed target dose 3 Gy(RBE).

However, in case of inhomogeneous target oxygenation, use of ^{16}O may result in a better peak-to-entrance ratio compared to ^{12}C. The corresponding model study was already presented in [4]; the comparison of ^{12}C data [1] with recent ^{16}O measurements for the same plan proves the concept (manuscript in preparation).

References

[1] W. Tinganelli et al, Kill-painting of hypoxic tumours in charged particle therapy, Scientific reports 5 (2015).

[2] T. Friedrich et al, Systematic Analysis of RBE and Related Quantities Using a Database of Cell Survival Experiments with Ion Beam Irradiation, Journal of Radiation Research 54.3: 494–514 (2013)

[3] R. Grün et al, Assessment of potential advantages of relevant ions for particle therapy: a model based study, Medical Physics. 42: 1037–47 (2015)

[4] F. Tommasino, E. Scifoni, and M. Durante, New Ions for Therapy, International Journal of Particle Therapy (2015).

DOI:10.15120/GR-2016-1

Chemical stage implementation in TRAX*

D. Boscolo†[1], *E. Scifoni*[1,2], *M. Krämer*[1], *and M. Durante*[1,2]
[1]GSI, Darmstadt, Germany; [2]TIFPA, Trento Italy

Tumors in hypoxic conditions can be up to three times more radioresistant compared to the well oxygenated ones. To ensure the success of a radiation therapy treatment this effect must be taken into account and models able to predict the tumour response in different irradiation condition for different oxygen levels are absolutely needed. In particular one of the main hypothesis imputes this effect to the amount of the DNA damage mechanism mediated by free radicals.TRAX is a Monte Carlo particle track structure code developed at GSI. The original version of the code has been adapted to handle the chemical module and is now able to reproduce the radical production and diffusion. A description of the chemical model will be presented in this report and some intermediate results will be shown.

According to the standard paradigm of radiation damage, the effect of radiation is described as a three stages process. These stages are characterized by different time scale and are identified as: the physical stage, the pre-chemical stage and the chemical stage.

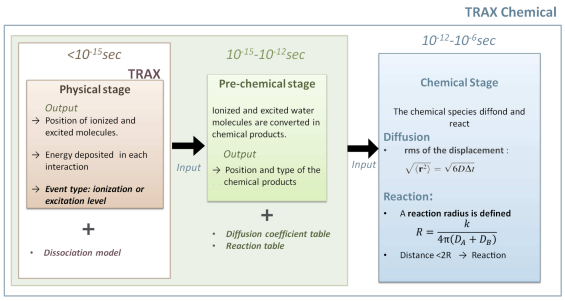

Figure 1: Schematic view of the approach followed for the implementation of the pre-chemical and chemical stage of radiation damage in the track structure code TRAX.

Physical stage: it last for the first 10^{-15} s after the irradiation. The primary particles and secondary electrons excite and ionise the water molecules. This phase corresponds to the direct effect of radiation and is already fully implemented in the original TRAX code.

Pre-chemical stage: In this stage the ionised and excited water molecules dissociate or relax to the ground state. Many dissociation channels exist and the probability of dissociation in a particular channel changes whether the water molecule has been ionised or excited and, if excited, on the molecular excitation level involved [3]. This stage ends with the thermalisation of all the chemical species around 10^{-12}s after the irradiation and has been recently implemented on TRAX.

Chemical stage: it includes the Brownian diffusion and the reactions between all the chemical species generated during the pre-chemical stage. The track evolution is described with a step by step approach. For each time step of the simulation, t, the chemical species diffuse randomly with a mean step size calculated according to the Smoluchowski diffusion equation :$< l >= \sqrt{(6Dt)}$. The reaction model implementation is presently in progress. The idea is to make two chemical species react when they are closer than a reaction radius. This kind of approach has been already used in [3, 4, 5], these three very similar methods differ by the definition of the reaction radius. The chemical stage lasts up to 10^{-6}s, after that time the chemical development of the track is supposed to be over and the radical yields are assumed to be constant.

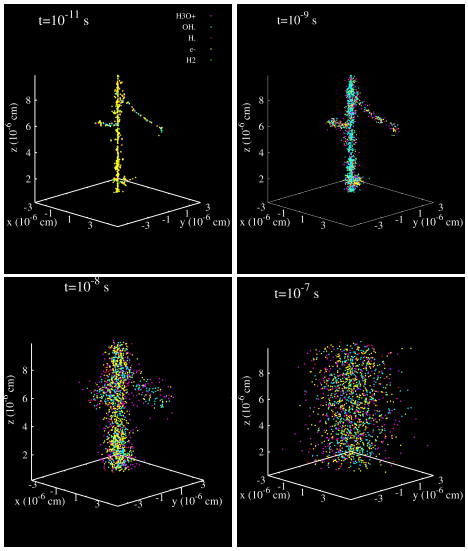

Figure 2: Simulation of radical diffusion for a 10MeV carbon ion generated with the new version of TRAX.

References

[1] M.Krämer et al.,Radiat Environ Biophys,33:91-109(1994).
[2] C.Wälzlein et al., Phys. Med. Biol. ,59:1441-1458(2014).
[3] M.S.Kreipl et al., Radiat. Environ. Biophys. ,48:11-20(2009).
[4] M.Karamitros et al., J. Comp. Phys. ,274:841-882(2014).
[5] H.Nikjoo et al., Radiat. Prot. Dosim. , 99:77-80(2002).

*The research leading to these results has received funding from the European Union Seventh Framework Programme [PEOPLE 2013 ITN-ARGENT project] under grant agreement n [608163].
† d.boscolo@gsi.de

DOI:10.15120/GR-2016-1

Backscattered electron emission after protons impact on gold foils: Experiments and simulations.

F. Hespeels[1], P. Sekovsky[2], S. Lucas[1], E. Scifoni[2] and M.Kraemer[2]
[1]University of Namur , Namur, Belgium; [2]GSI, Darmstadt, Germany;

It has been shown that the presence of gold nanoparticles (GNPs) can increase cell damage during radiotherapy treatment, possibly due to emission of low energy electron around GNPs [1, 2]. Reproducing the interaction between protons beam and GNPs by Monte Carlo simulation requires cross section data which are still incomplete. In this context, theoretical models need experimental validation. This work aims at a comparison of simulation results calculated with the TRAX code and with experimental data obtained from irradiation of thin foils akin to GNPs.

The TRAX code is dedicated to the description of low-energy electron emission and transport in solids after proton irradiation [3, 4]. Sets of interaction cross sections for electron with energies down to 1 eV are available for different materials and allows us to reproduce ionization, excitation and elastic scattering. Standard elastic scattering cross sections can be calculated using the screened Rutherford approximation or the Partial Wave Analysis method, respectively, for low and high Z. Ionization induced by electron is taken into account by applying the binary encounter Bethe model. Auger electron emission probabilities are implemented in the code using Livermore Evaluated Atomic Data Library.

Experimental data were gathered at the University of Namur. The incident proton beam is generated with the ALTAIS accelerator, a 2 MV Tandem accelerator. Beam intensity is measured continually with a faraday cage. During irradiation, backscattered electrons are collected within an angle of 102° by a Retarding Field Analyser (RFA) which is based on the principle of a high-pass energy filter (Fig.1). Only electron with higher energy than the retarding grid potential applied can reach the collector screen and are measured by a Keithley picoammeter. By measuring the collector current as a function of the potential we can obtain the energy spectrum of the secondary electrons emitted from our target. Preliminary measurements were performed with two different samples: Carbon 50 nm thin film (ACF-METALS) and gold 200 nm thin film. Study of carbon thin film is essential as it will be used as a support for GNPs in future irradiation experiments. The energy of the proton beam has been set to 2 MeV. Spectra were acquired within an energy range from 0 to 600 eV in steps of 10 eV. Electron energy spectra resulting from 2 MeV proton bombardment on carbon and gold are displayed on figure 1. For 50 nm carbon, it turns out that the simulation is quite similar to the experimental results on an absolute scale. The Auger peak at ~270 eV appears slightly shifted and more pronounced in TRAX simulation. For gold, we obtained a much higher yield of low energy electron in the simulation than in the experiment. This observation can be due to a contamination of the gold foil with a thin carbon film. This hypothesis can be corroborated by XPS analysis which indicated high level of carbon in the first nanometer of the sample. Moreover, by simulating a little thin film of carbon pollution (2 nm thick) placed above the gold thin film, the calculated yield of electron decreases to the experimentally observed level. A cleaning procedure is under development to reduce such “dirt” effect. For future experiments, GNPs will be deposited on thin Carbon films using the magnetron sputtering method developed in Namur [5].

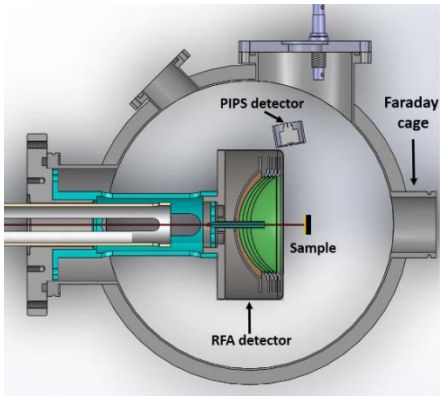

Figure 1: Experimental Setup

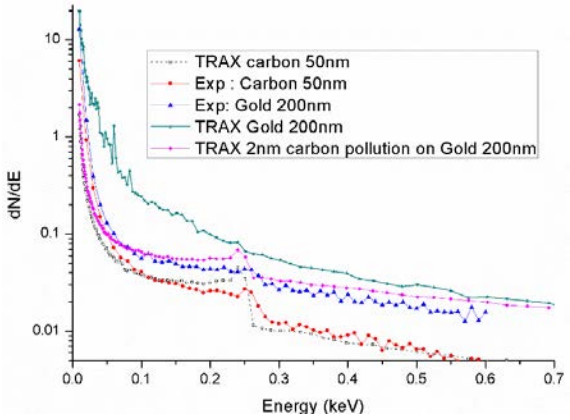

Figure 2: TRAX and experimental secondary electron spectrum of carbon tin film and gold thin film.

References

[1] J.F. Hainfeld et al, J. Pharm. Pharmacol.67, 977 (2008)
[2] J.F. Hainfeld et al, Phys. Med. Biol. 49, 39 (2004).
[3] C. Wälzlein et al, Phys. Med. Biol. 59, 1441 (2013).
[4] M. Krämer and G Kraft, Radiat. Environ. Biophys. 33, 91 (1994).
[5] V.Bouchat et al, Surf. Coat. Tech. 205, 4964 (2011).

DOI:10.15120/GR-2016-1

Speed-up of scanned beam particle therapy by splitting iso-energy slices to optimize particle beam intensities

A. Eichhorn[1], *S. Hild*[1], *K. Anderle*[1], *and C. Graeff*[1]
[1]GSI, Darmstadt, Germany

Introduction and Background

In particle therapy (PT) the total target dose is composed of multiple contributions from individual beam spots. During radiation delivery the maximum beam intensity is limited by the minimal time needed for beam spot monitoring. For synchrotron-based systems without dynamic intensity control (DIC), the intensity is preset for each spill and is hence restricted by the smallest spot in an iso-energy slice (IES). Depending on the homogeneity of spot weights, this procedure can cause extremely long treatment times and hence can lead to low patient numbers and less cost efficient therapy. Especially severe is this problem in hypofractionated plans, or when rescanning is used as a method of motion compensation. In both cases, IESs can contain spots of very different spot weights. We developed a method to separate beam spots based on their associated weight into two independent IESs, which permits higher intensities for the strongly weighted spots, and therefore significantly reduces treatment times.

Material and Methods

In a first step a reasonable threshold was determined to separate the points in two IESs, calculating mean weight and standard deviation. The threshold was slightly adjusted for optimal use of the available discrete intensity levels. After dividing the IES corresponding to the point weights for both IESs a new scan path was calculated using a genetic algorithm [1][2]. To ensure integrity of the new scan paths, i.e. taking into account the maximum allowed scanner jump, selected large spots were divided in two parts and partly moved to the lower intensity IES, enabling a irradiation of both IESs. Therefore a grid of possible supporting points was calculated, consisting of spots with weights higher than the threshold plus the minimum particles per point. Finally the shortest possible way, taking into account all constraints, was found through the grid to the next raster point in the new IES with low intensities. The method was tested for 4D treatment plans such as single fraction lung cancer therapy and cardiac arrhythmia ablation in pigs. Irradiation times as well as target coverage and doses deposited in organs at risk (OAR) were investigated.

Results

The results depend on the plan structure and the homogeneity of beam weights in every plan. In total we found substantial reduction of the delivery time with a mean reduction of (43±12)% and (47±15)%, respectively. Changes in the resulting 4D dose distributions were negligible for the target volume as well as for the OARs.

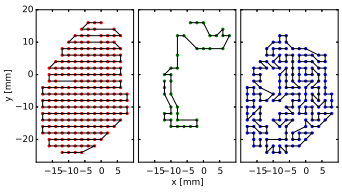

Figure 1: Exemplary iso-energy slice (IES) before and after separation according to beam intensities. On the left the original IES is shown. In the middle and on the right the two separate IESs are shown. The middle one shows the beam spots with low weight, while the right one shows the high weighted beam spots.

Discussion and Conclusion

The separation of IES based on spot weight offers a simple way of greatly reducing treatment times for moving target applications and can be easily implemented in facilities without DIC. Nevertheless, an experimental validation of the method is necessary, to ensure that no additional dosimetric changes will occur in the dose distribution compared to the simulations. Beside facilities without DIC also facilities using DIC could benefit from this technique, as gradients between spots weights are minimized, which could lead to an additional reduction of treatment times.

References

[1] M.F. Dias et al.,'*Scan path optimization with/without clustering for active beam delivery in charged particle therapy*', Physica Medica, 2015

[2] M.F. Dias, '*Scan path optimization for active beam delivery in charged particle therapy*', Master thesis, University of Lisbon, 2012

[3] J. Pardo et al., '*Heuristic optimization of the scanning path of particle therapy beams*', Medical Physics, 2009

DOI:10.15120/GR-2016-1

Treatment planning with an adaptive dose grid

M. Prall[*1], *K. Anderle*[1], *C. Graeff*[1], *and S. Hild*[1]
[1]GSI, Darmstadt, Germany

Introduction

In treatment plan optimization for scanned particle beams, the dose is evaluated on a regular, typically densely sampled dose grid. Employing an adaptive grid both speeds up and improves the optimization by focusing on relevant volumes such as volume borders or intra-field dose gradients.

Material and Methods

A two-step process was implemented in the in-house treatment planning software TRiP [1]. First, a coarse IMPT (intensity modulated particle therapy) optimization is used to identify regions with negligible dose and with dose gradients between fields. For this purpose, only every third grid point is considered in each direction and a small number (usually five) conjugate gradient iterations are performed. This results in a preliminary dose distribution allowing to identify regions with negligible dose or regions potentially containing dose gradients. The latter can result from volume borders or field edges. A new grid with an inhomogeneous density is set up and a second conjugate gradient optimization is performed in order to obtain the final treatment plan. Both simple geometries and patient CTs were used to test this method using a range of parameters (low dose threshold, grid density, dependence on dose gradients).

Results

In Figure 1 field edges and therefore also a potential gradient region lie in the target volume, as the beams are obstructed by two OARs (organs at risk). Low-dose regions are removed from the grid; while gradient regions and regions of volume borders are assigned a high grid density. Depending on parameters and geometry, this strategy reduces the grid density by a factor of 3 to 20. Satisfactory target coverage (V95>95%) could be achieved in all cases. Figure 2 shows dose volume histograms (DVHs) of treatment plans for a non small cell lung cancer (NSCLC) patient case with the heart as OAR. These plans were derived with and without the adapted dose grid. The adapted plan has somewhat better dose coverage than the standard plan and OAR sparing is comparable. On average, memory consumption and computation time was was reduced by approximately a factor of five.

* m.prall@gsi.de

Outlook

Adaptive dose grid treatment planning could be interesting for complex anatomies with a large number of constraints, or also for robust optimization with a large number of scenarios.

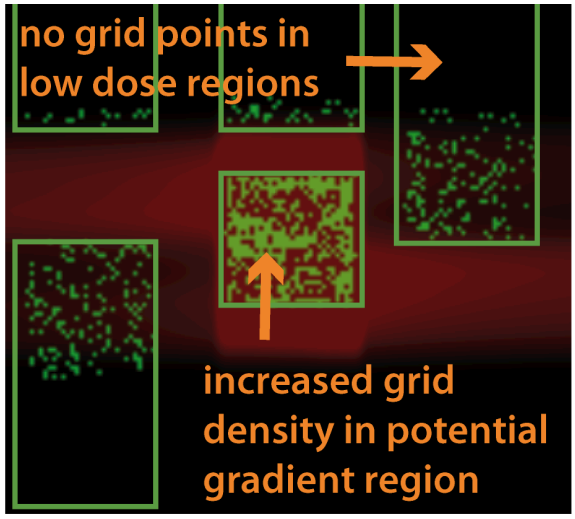

Figure 1: Adapted strategy for a simplified geometry. Grid points used for the optimization are skipped if the dose is negligible in the OARs. The density of grid points is increased in potentially inhomogeneous regions.

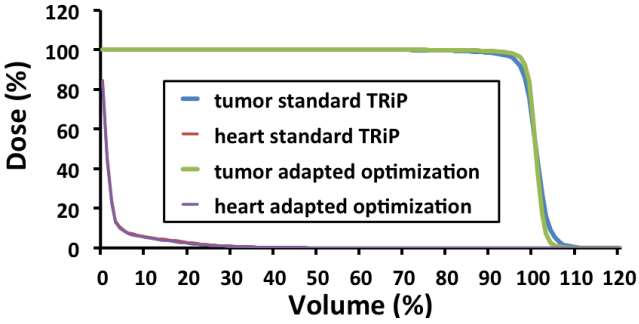

Figure 2: DVHs of treatment plans derived with standard TRiP and with the adaptive dose grid for a NSCLC case.

References

[1] M. Krämer, et al., “Treatment planning for heavy-ion radiotherapy: physical beam model and dose optimization”, Phys. Med. Biol. 48(14):2063-2070

DOI:10.15120/GR-2016-1

Validation of tissue equivalent materials for particle therapy phantoms*

S. Hild[†1], *I.Yohannes*[2], *S. Vasiliniuc*[2], *C. Schuy*[1], *O. Langner*[3], *C. Bert*[2], *and C. Graeff*[‡1]

[1]GSI, Darmstadt, Germany; [2]Department of Radiation Oncology, Universitätsklinikum Erlangen, Friedrich-Alexander-Universität Erlangen-Nürnberg, Germany; [3]QRM - Quality Assurance in Radiology and Medicine GmbH, Germany

Introduction

Accelerated charged particles, in contrast to high energy photons, have a finite maximum range when traversing matter. In particle therapy for cancer treatments, the finite range and the increased dose deposition towards the end of a particle track (Bragg Peak) features highly tumor conform dose deposition. This advantage however also represents one of the major challenges, as uncertainties in patient positioning or uncertainties in converting tissue densities to particle stopping power directly influence the particle penetration depth. Therapy planning is realized on the basis of a three dimensional computed tomography (CT) scan representing the internal patient geometry. The CT values (Hounsfield units (HUs)) are thereby converted into the equivalent range of the respective particle in water (water equivalent path length (WEPL)) using an experimentally validated look up table. Existing tissue substitutes do not show the typical HU-WEPL relation of real tissues [1]. In collaboration with Altropol Kunststoff GmbH, QRM GmbH and the Universitätsklinikum Erlangen, we developed and validated five tissue equivalent materials for particle therapy to further be used in phantom construction.

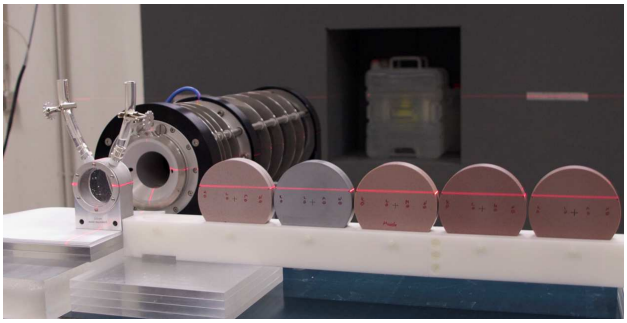

Figure 1: Experimental setup for WEPL measurements at the Heidelberg Ion Beam Therapy Center. Final measurements of the 5 tissue equivalent materials and a reference probe using a PTW PeakFinder.

Materials and Methods

The HU and the corresponding WEPL for carbon ions, of 31 different material combinations have been measured at the Universitaetsklinikum Erlangen and the Heidelberg Ion Beam Therapy Center (fig. 1). The results of these measurements have further been used to optimize five tissue equivalent materials as described in Yohannes et al. [2].

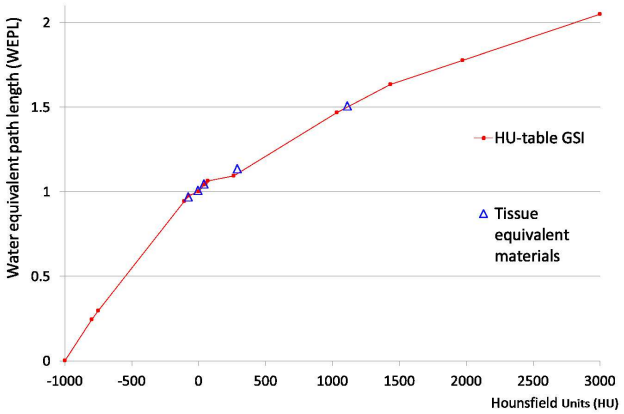

Figure 2: Measured WEPL and HU of the five final materials (blue, triangles) compared to GSI's look up table used during the pilot project (solid line).

Results and Conclusion

The final materials showed good agreement with the Hounsfield look up table which was used at GSI during the particle therapy pilot project (fig. 2). Not only can these new tissue equivalent materials be used for general phantom construction, but also calibration of individual CTs should be feasible. To fully characterize these materials further scattering experiments have to be performed. Initial measurements have already been carried out in the beginning of this year and are currently analyzed.

References

[1] M. Witt et al., "Optimization of the stopping-power-ratio to Hounsfield-value calibration curve in proton and heavy ion therapy", Z Med Phys. 25(3) (2015) 251-63

[2] I. Yohannes et al., "Radiation properties of tissue- and water-equivalent materials formulated using the stoichiometric analysis method in charged particle therapy", Med. Phys. 43 (2016) 308

* Work supported by Bundesministerium fur Wirtschaft und Energie ZIM - KF2137107AK4

† The authors thank M. Rovituso, D. Richter and S. Brons for their support during WEPL measurements and the GSI-Workshop for building the needed equipment

‡ c.graeff@gsi.de

DOI:10.15120/GR-2016-1

Accelerated calculation of radiological path length for 4D dose calculation*

M. Wolf[1,2], *S. Hild*[1], *and C. Graeff*[†,1]
[1]GSI, Darmstadt, Germany; [2]TUD, Darmstadt, Germany

Introduction

In contrast to photon therapy the particles in ion beam therapy are stopped within the patient. Their penetration depth depends on the radiological density of the traversed tissue. Like other treatment planning systems TRiP4D uses water equivalent path lengths (WEPLs) to model tissue inhomogeneities. During dose calculation using a typical three-dimensional computed tomography image (3DCT), the WEPLs for 10^5 to 10^6 voxels are computed [1]. For 4D dose calculations using time resolved CT (4DCT) the voxel number increases by the number of recorded respiration phases (usually 10). Going from 3D to 4D dose calculation, code profiling showed that the WEPL computation time increased from about $10\,\%$ to more then $65\,\%$ of the total time. Especially ray tracing was detected to cause major time consumption.

Materials and methods

The originally implemented ray tracing algorithm in TRiP4D is based on the Siddon algorithm [2]. It uses basic vector calculus to compute all intersections of the beam with the 3DCT represented by a three-dimensional (3D) grid. Those exceeding the CT boundaries are omitted. The geometrical intersection length through every voxel is calculated, scaled with the tissue density. The WEPL from entry to target point is then determined by interpolation. By omitting table entries behind the target point in beam's eye view, a preliminary time reduction could be achieved [3] (fig. 1, gray bars).

The new implemented algorithm uses a revised version of the Siddon algorithm. Instead of computing all intersections with the 3D grid, the calculations are restricted to the region where the beam actually intersects the CT. This reduces the number of calculated intersections by a factor of at least 2 [4]. A further time reduction is reached by directly calculating the WEPL as a weighted sum during the ray tracing process, instead of interpolating afterwards.

All approaches calculate the indices of the traversed voxels for scaling with their corresponding CT value (in Hounsfield units). Those floating-point calculations can be transferred to simple integer iterations of consecutive voxel indices by calculating the index of the start voxel and performing the ray tracing in reverse order. The beam direction is internally inverted and the algorithm strides back from target to entry point, yielding the same WEPL.

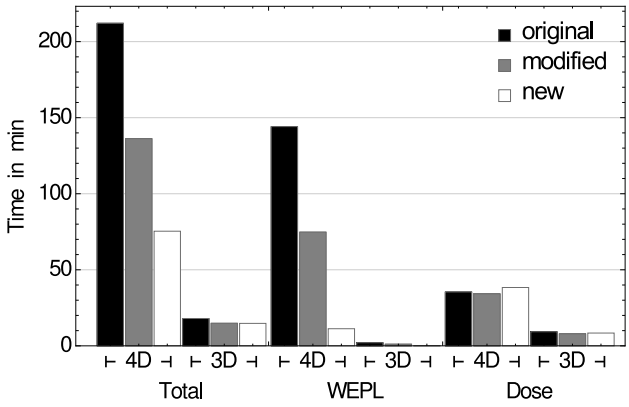

Figure 1: Profiling results for a biological 4D and 3D dose calculation (single threaded) for a lung tumor patient and a prostate patient respectively, with three different implementations for WEPL calculation.

Results and conclusion

The profiling results are shown in Figure 1. For the 3D prostate case, the total time is in the same range for all three implementations. In 4D dose calculation the new ray tracing approach (fig. 1, white bars) substantially reduces the total time by $\approx 65\,\%$ compared to the original algorithm (black bars). The WEPL calculation time is decreased by $\approx 90\,\%$ and by $\approx 50\,\%$ relative to the original and the modified algorithm respectively. The remaining dose calculation needs approximately the same amount of time for all three implementations. Getting more efficient the more WEPLs are to be computed, the new algorithm is especially beneficial in 4D dose calculation.

References

[1] M. Krämer et al., "Treatment planning for heavy-ion radiotherapy: physical beam model and dose optimization", Phys. Med. Biol. (2000) 45, p.3299-3317

[2] R. Siddon, "Fast calculation of the exact radiological path for a threedimensional CT array", Med. Phys. (1985) 12, p.252-255

[3] S. Hild et al., "Fast optimization and dose calculation in scanned ion beam therapy", Med. Phys. (2014) 41

[4] M. de Greef et al., "Accelerated ray tracing for radiotherapy dose calculations on a GPU", Med. Phys. (2009) 36, p.4095-4102

* Work in part supported by HGS-HIRe.
† c.graeff@gsi.de

Lateral scattering of 120 and 200 MeV/u ^{4}He ions in water

M. Rovituso[*1], *C. Schuy*[1], *S. Brons*[2], *S. Fabiano*[3], *A. Gonzalez Montoro*[4], *and U. Weber*[1]
[1]GSI, Darmstadt, Germany; [2]HIT, Heidelberg, Germany; [3]University of Catania, Italy; [4]University of Valencia, Spain

At energies of several hundred MeV/u required in ion therapy, ion beams passing through the beam line components (i.e. exit window, beam monitors) and the patient's body is affected by multiple scattering and by nuclear processes. These phenomena lead to a broadening of the lateral beam profile that needs a good parametrization to describe not only the core of the pure electromagnetic part of the multiple scattering process (Molière's theory) but also the tail characterized by the nuclear interactions processes (Glauber's theory).

Due to a growing interest for ^{4}He ions in cancer therapy, aim of this work was to investigate the lateral scattering of 120 and 200 MeV/u ^{4}He beams impinging on water targets. All the measurements were done in the Ion Beam Therapy Center (HIT) of Heidelberg in the experimental cave (QS-cave).

The ^{4}He beams were delivered in resonance mode from the synchrotron accelerator of HIT. The experimental setup is shown in Fig. 1. Water targets of 4.5 cm and 14 cm thickness were used for 120 and 200 MeV/u beam, respectively. The detectors of the experiment were EDR2- films [1] and a PTW 2D array detector [2]. When using the PTW detector, a single spot beam was delivered with intensity of 1.5x10^{10} particle in order to get a good signal on the halo of the distribution. For the EDR2-films, instead, the intensity was 1.6x10^9, intensity that allowed a good noise to signal ratio in the halo region. The films were developed and scanned.

Figure 1: Scheme of the experimental setup of the scattering measurement of 120 and 200 MeV/u ^{4}He ions in water. The film and the PTW array were placed at the same position.

After a calibration procedure from grey value to fluence, a vertical and horizontal profile were extracted. The 2D array, instead, gives as output a matrix already calibrated in dose. The matrix was filtered by assuming a radial symmetric distribution in order to reduce the noise level and a 1-dimensional profile was extracted. The lateral profile of the 2D array and the film were compared. Both distributions were fitted using the approach of Bellinzona et al. [3], that proposed, for strong scattered distribution, a fit with the sum of a Gauss and a Rutherford hyperbolic function with equation:

$$\frac{f(y)}{N} = (1-W)\frac{1}{\sqrt{2\pi}\sigma} exp\left[-\frac{y^2}{2\sigma^2}\right] + W\frac{2b^{3/2}}{\pi}\frac{1}{(y^2+b)^2} \quad (1)$$

where σ is the width of the Gaussian core, W a relative weight, N a normalization factor and b represents the horizontal shift of the hyperbolic function. This function takes into account the multiple scattering that occurs at small angles and the single nuclear scattering at wide angles.

The results are shown in Fig. 2. A single Gaussian approach describes only the core of the distribution, while the Gauss+Rutherford approach well describes not only the core but also the tail of the distribution, strongly underestimate from the single Gauss approach. The comparison

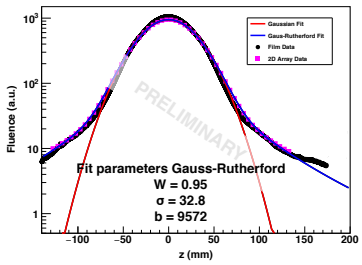

Figure 2: Lateral beam profile of 200 MeV/u ^{4}He scattered at 14 cm of H_2O. The 2D array and the film data were compared to each other and fitted with a Gaussian and a Gauss-Rutherford fit.

between the EDR-2 films and the PTW 2D array response showed that even though the films have a really high spatial resolution the response in the tail region is more noisy respect to the PTW 2D array.

References

[1] M.E. Moyers, "EDR-2 film response to charged particles", Phys Med Biol, vol.53, pp.N165-73, May 2008 (2013) 56

[2] A. Van Esch et al., "The octavius 1500 2D ion chamber array and its associated phantoms: dosimetric characterization of a new prototype", Med Phys, vol.41,p.091708, Sep 2014

[3] V.E. Bellinzona et al., "On the parametrization of lateral dose profiles in proton radiation therapy", Phys Medica, vol.31,pp.484-492, February 2015

* Work supported by HGS-HIRe

DOI:10.15120/GR-2016-1

Measurement of the dose distribution produced by a 3D range modulator for fast ion beam therapy

U. Weber [1], Y. Simeonov[2], C. Schuy [1], T. Printz-Ringbaek [2], S. Brons [3], K. Zink [2]
[1]GSI, Darmstadt, Germany; [2]Technische Hochschule Mittelhessen, IMPS; [3] Heidelberger Ionenstrahl-Therapie (HIT)

Introduction

Treatment time in intensity modulated particle therapy with raster scanning depends mainly on the number of different iso-energy layers used. In this project a treatment concept using only one energy and a so called *3D range modulator* (RM) is proposed in order to achieve a conformal dose distribution in irradiation times of a few seconds only. This could reduce interplay effects and should provide a more reliable dose delivery to moving targets (e.g. lung cancer).

The RM modulates a sharp Bragg- Peak [1] to a broad Spread-Out BP (SOBP). The extension and depth of the SOBP is varied in dependence of the lateral position. This concept has already been proposed [2], but a good target-conformal dose distribution couldn't be measured yet.

Recently, the *Technische Hochschule Mittelhessen* has developed a highly improved RM in cooperation with GSI. This RM consists of a large number of sharp pins each with a diameter of only 1.5 mm and different lengths (up to 50 mm) to modulate the necessary shift of the BP. Thus, a homogeneous dose can be delivered for arbitrary target volumes (Fig. 2). The technique is designed for small and medium sized targets.

This report describes a fast and efficient dose measurement using a RM for an isodose sphere with a radius of 5 cm. It serves as a proof of concept for this new RM technique.

Experiments

The measurements were performed with a scanned 400 MeV/u ^{12}C pencil beam at the HIT accelerator in Heidelberg. The RM was positioned in a distance of 95 cm from an ion chamber array with 1000 chambers with a spatial resolution of 3 mm (*PTW Octavius 1000, Starcheck*). A binary range shifter of 10 plates and 6 additional PMMA plates of 50 mm were used to adjust the depth in fine steps. The combination of the PTW array plus the range shifter allows a full 3D dose measurement (Fig. 3) with very high resolution (ca. 50.000 points). The acquisition for one dose plane takes only a few seconds.

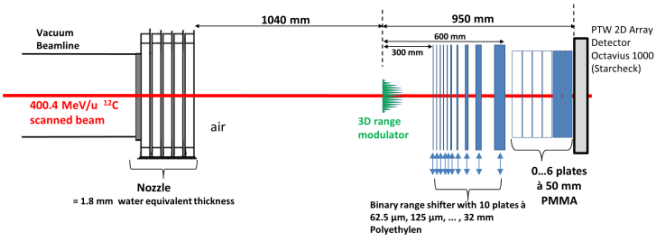

Figure 1: Setup of the 3D dose measurement for a RM.

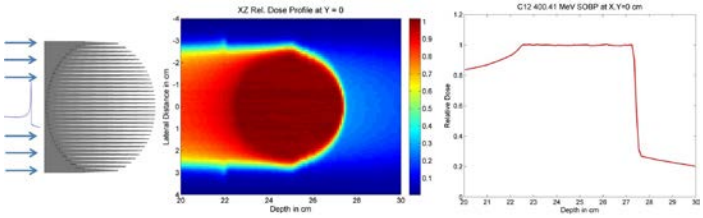

Figure 2: Schematic principle of the 3D Range Modulator and simulated dose from FLUKA

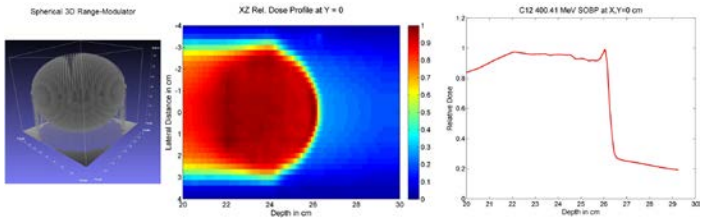

Figure 3: Design of a spherical RM and measured dose

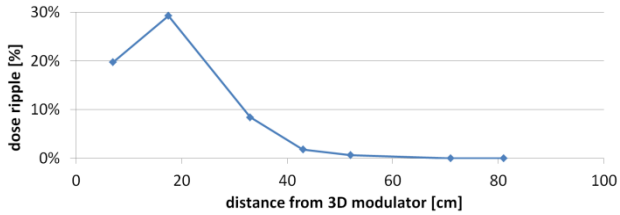

Figure 4: Dose ripple [3] induced by the fine structures of the RM. The ripple was measured with a series of X-ray films at different distances from the RM.

Conclusion

The proof-of-concept experiment could be successfully performed. The 3D dose measurements show that a spherical isodose can be produced. A RM requires a distance of typically 60 cm from the patient, agreeing with the findings in [3].

References

[1] U. Weber and G. Kraft, Design and construction of a ripple filter for a smoothed depth dose distribution in conformal particle therapy, Phys. Med. Biol., 44: 2765–75, (1999).

[2] T. Sakae, et al., Conformal irradiation by proton beam scanning and multilayer energy filter, Rev. Sci. Instrum., Vol. 74, No. 3, (2003).

[3] T. P. Ringbæk et al., Monte Carlo simulations of new 2D ripple filters for particle therapy facilities Acta Oncol. 53, 40–9, N2014 (2014).

DOI:10.15120/GR-2016-1

Monte Carlo simulations for Bragg curve measurements in PMMA

F. Horst[*1,2], *C. Schuy*[1], *K. Zink*[2], *and U. Weber*[1]
[1]GSI, Darmstadt, Germany; [2]IMPS/THM, Giessen, Germany

Introduction

For the precise determination of Bragg curves in PMMA, a novel measurement method using two large area ionization chambers (ICs) with absorber material of variable thickness ("binary range shifter") in between was applied at the Heidelberg Ion-Beam Therapy Center (HIT) for 220 MeV protons and 430 MeV/u carbon ions [1]. Although the expected Bragg curve progression was clearly visible in the recorded data, they were superimposed by sudden steps in the entrance region.

Methods

To understand the origin of these steps, extensive Monte Carlo simulations using the FLUKA code [2, 3] and the Geant4 code [4] were carried out. The experimental setup was modeled within both codes and the radiation transport through the different components was simulated. The energy deposited within the active volume of both ICs was scored and the ratio between the two was taken as a measure for the signal ratio measured at HIT.

Results and Discussion

The experimentally observed steps could be reproduced by both Monte Carlo codes and their origin could be identified as a loss of delta electrons and nuclear fragments emitted in large angle along the air gap between absorber and IC which was present for some settings. A comparison of experimental and simulation data for 220 MeV protons is shown in Figure 1. The loss of delta electrons causes a big step while the impact of the nuclear fragment loss is not that large. The small differences between the predictions of FLUKA and Geant4 might be due to slightly different geometrical models of the beamline within the two codes. The effect of electron and nuclear fragment buildup on absorbed dose curves behind air-material boundaries has already been described by Carlsson and Carlsson in 1977 [5]. Due to the electrons' and fragments' broad angular distributions with respect to the narrow focused primary particle beam, some of them will get lost along an air gap. This effect is illustrated in Figure 2.

Outlook

For future experiments, the setup might be improved in a way so that the mentioned perturbation by the gaps gets reduced or even fully eliminated. This could e.g. be done by a more compact arrangement of the absorbers or by using larger ICs. However, such a setup of a binary range shifter free of gaps would be more complex, expensive and it has to be considered if this is reasonable.

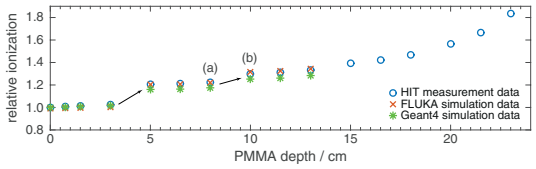

Figure 1: The entrance region of the depth dose profile of 220 MeV protons stopping in PMMA measured at HIT using the setup described elsewhere in this report [1] in comparison to FLUKA and Geant4 simulation results. The steps in the curve due to delta electron or nuclear fragment loss are marked with arrows. The datapoints (a) and (b) refer to the setup schematics shown in Figure 2.

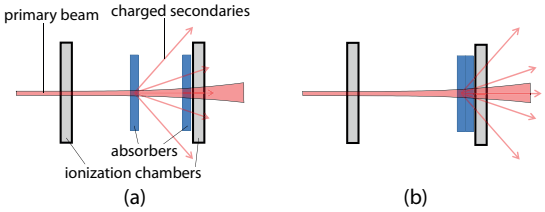

Figure 2: Schematic illustration of the loss of delta electrons or nuclear fragments on their way through an air gap between absorber and IC due to their broad angular distribution. Setup (a) generates a data point before and setup (b) a datapoint behind the steps shown in Figure 1.

References

[1] C. Schuy et al., "Precision Bragg curve measurements in PMMA ", this report

[2] T.T. Böhlen et al., "The FLUKA Code: Developments and Challenges for High Energy and Medical Applications", Nuclear Data Sheets 120, 211-214 (2014)

[3] A. Ferrari et al., "FLUKA: a multi-particle transport code", CERN-2005-10 (2005)

[4] S. Agostinelli et al., "Geant4 - a simulation toolkit", NIM A 506, 250-303 (2003)

[5] C.A. Carlsson and G.A. Carlsson, "Proton dosimetry with 185 MeV protons. Dose buildup from secondary protons and recoil electrons", Health Physics 33, 481-483 (1977)

* f.horst@gsi.de

DOI:10.15120/GR-2016-1

Precision Bragg curve measurements in PMMA

C. Schuy[1], *F. Horst*[1], *S. Brons*[2], *and U. Weber*[1]
[1]GSI, Darmstadt, Germany; [2]HIT, Heidelberg, Germany

Motivation

Standard dosimetry in clinical particle therapy protocols relies mainly on water as tissue equivalent target material [1]. Nevertheless there are certain conditions where the usage of water is impractical and solid tissue equivalent materials would offer a considerable advantage. Therefore an experimental setup to measure highly precise Bragg curves and dose attenuation in different materials was developed and tested at the Heidelberg Ion-Beam Therapy Center (HIT) with 430 MeV/u ^{12}C and 220 MeV p impinging on PMMA.

Experimental setup

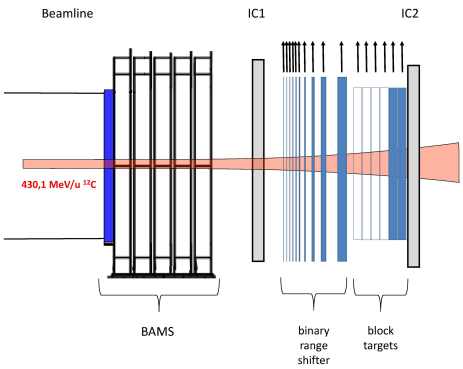

Figure 1: Schematic of the experimental setup consisting of a reference ionization chamber (IC1), a binary range shifter, up to six PMMA block targets and a measurement ionization chamber (IC2).

A schematic of the experimental setup is shown in figure 1. The setup consists of two parallel plate ionization chambers directly connected to Keithley Model 6517 electrometers, a binary range shifter composed of ten plates of PMMA (minimum range shift of 0.013 g/cm^2) that can be individually introduced in the beam and up to 6 blocks of PMMA (range shift of ≈5.8 g/cm^2 each). Data collection, control of the range shifter and synchronization with the particle beam is controlled by a LabVIEW application and additional NI-DIO hardware.

Results

An example of a measured depth dose distribution (DDD) of 430 MeV/u ^{12}C impinging on PMMA using the described setup is presented in figure 2. For target thicknesses bigger than ≈15 g/cm^2 the measured DDD shows the expected behavior with a sharp Bragg peak followed by a fragmentation tail. Smaller thicknesses, especially the measurement points switching from a thick range shifter setting to the first block target, show a step in the measured relative dose due to geometrical restrictions of the currently used setup. This behavior is described in more detail in [2].

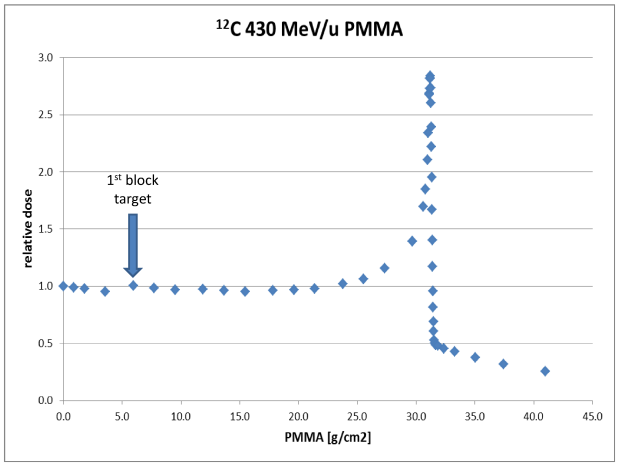

Figure 2: Measured DDD of 430 MeV/u ^{12}C impinging on PMMA. The measurement point of the first block target is indicated by an arrow.

Outlook

The current iteration of the described experimental setup shows the ability to perform precision Bragg curve and dose attenuation measurements in solid materials. Future iterations will include an updated geometry based on the considerations presented in [2], an automated and motorized change of block target thickness using computer controlled linear axes to improve measurement time and fully modularized software controlling and analyzing the experiment online.

References

[1] D. Schardt et al., Heavy-ion tumor therapy: Physical and radiobiological benefits, Rev. Mod. Phys. (2010) 82

[2] F. Horst et al., Monte carlo simulations for Bragg curve measurements in PMMA, GSI Scientific Report (2016) submitted

DOI:10.15120/GR-2016-1

Dose attenuation measurements in the ROSSINI-2 project for space research*

U. Weber [1], *C. Schuy* [1], *M. Rovituso* [1], *M. Giraudo* [2], *C. La Tessa* [3] *and M. Durante* [4]

[1]GSI, Darmstadt, Germany; [2]Thales Alenia Space - Domain Exploration and Science, Italy; [3]Brookhaven National Laboratory, USA; [4]TIFPA - Trento Institute for Fundamental Physics and Applications, Italy

Introduction

One of the most serious challenges in space exploration is the health risk related to the exposure of a radiation field extremely different from Earth's [1]. Therefore, the project ROSSINI-2* aims at designing, manufacturing and testing innovative materials with high shielding capability against the challenging radiation environment created by Galactic Cosmic Rays and Solar Particle Events in space [2]. This study is the continuation of ROSSINI, an ESA-funded project [3].

Experiments

The aim of the experiment was the measurement of the reduction (attenuation) of the dose for a beam passing through a certain target. A number of different target materials have been proposed in the ROSSINI2 cooperation for these tests (see fig. 2). Some of these materials have no special shielding function, but are commonly used for the construction of a space craft (e.g. aluminium Al2024, polyphenylsulfone, kevlar or carbon fiber epoxy composites, etc.). Other materials like Lithiumhydrid[1] or PE with NdFeB-nanoparticles[2], etc. only serve as shielding material. PMMA and water are used as reference materials - and for some particle-therapy related measurements in parallel.

For the experimental setup (see fig. 1) we used two parallel plate ionization chambers (air filled), that measured the laterally integrated dose before and behind the target. It has to be noted, that a 20 mm PMMA plate was always positioned directly in front of the IC2 in order to achieve constant conditions for the electron build-up effect. The electronics and ionization chambers ensured a very low noise and a reproducibility of < 0.5 ‰. The measurements were performed with a 430 MeV/u ^{12}C pencil beam at the HIT accelerator in Heidelberg.

The dose reduction of the targets is then given as the ratio of the measured charges Q_{IC2}/Q_{IC1} with a target (to be measured) divided by this ratio without a target. Because this experiment is mainly focussed on the dose attenuation by nuclear effects, a correction was introduced, where the influence of the increasing electronic energy loss (dEdx from Bethe-Bloch) by the target was eliminated. This correction is designed to obtain results that are comparable to the more common measurements using higher energies (of typ. 1 GeV/u), where the influence of the increasing energy-loss is much less pronounced. The correction was calculated by LISE++. The results of the dose attenuation measurements with and without dEdx-correction are presented in figure 2.

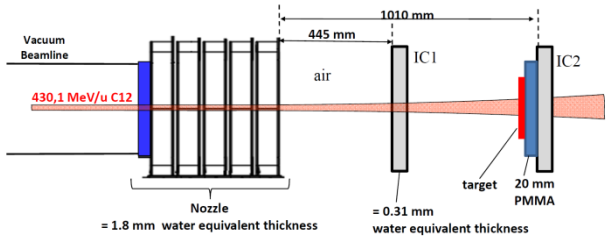

Figure 1: Setup of the dose attenuation measurements

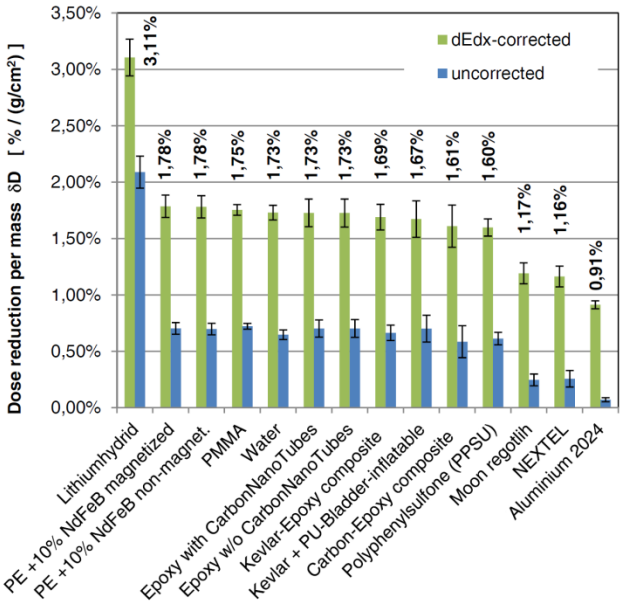

Figure 2: Relative dose reduction for different target materials. The values of the different targets are all normalized to their thicknesses in [g/cm^2].

Conclusion

Lithiumhydrid is a very effective material for dose shielding in space and shows a much higher dose attenuation compared to the polymer-based materials. The applicability in space crafts has to be examined separately.

References

[1] M. Durante and A. Cucinotta, Physical basis of radiation protection in space travel, Rev. Mod. Phys. 83, 1245 (2011)

[2] M. Durante, Space radiation protection: Destination Mars, Volume Life Sci. Space Res. 1 (2014)

[3] C. Schuy et al., The ROSSINI project at GSI, GSI Sci. Rep. 2014-1, Biophysics-46, 248 p. (2014).

* ROSSINI-2 is supported by ESA (Contr. No.4000112525/14/NL/LF)

[1] Targets were provided by University of Turin, Department of Chemistry and NIS, Italy

[2] Targets were provided by the National Centre for Scientific Research "Demokritos", Greece

DOI:10.15120/GR-2016-1

Initial four-body forces from chiral effective field theory in ab initio many-body methods*

S. Schulz[1] *and R. Roth*[1]

[1]Institut für Kernphysik - Theoriezentrum, Technische Universität Darmstadt, Germany

In recent years there has been tremendous progress in the ab initio description of nuclei. One of the reasons for this development is chiral effective field theory (EFT), which establishes a systematic connection to the underlying theory, quantum chromodynamics. It allows to construct the interactions between nucleons in a systematic and improvable way [1].

However, almost all calculations of nuclei so far have neglected the four-nucleon (4N) force that is appears at fourth order of chiral EFT, even though NN forces are included to that same order. Given their order in chiral EFT, they are expected to be small, but they are necessary for precision studies and consistent order-by-order calculations. While there are estimates of their effect on the ground-state energy of ^{4}He [2], their contribution in heavier-mass nuclei is currently unknown. We perform the partial-wave decomposition for the 4N forces to attain a representation of the force usable for many-body calculations.

The framework for including the initial four-body forces involves multiple steps (see fig. 1). Interactions from chiral EFT are often represented using a cartesian plane-wave basis. For handling the forces in the similarity renormalization group (SRG) transformation, we require a partial-wave decomposition (PWD). Specifically, we need a representation in a harmonic oscillator (HO) basis depending on Jacobi coordinates and coupled to total angular momentum and isospin. The advantage of such a basis is the comparatively small storage space, as the center-of-mass part is decoupled and the Hamiltonian becomes block-diagonal in total isospin, angular momentum, and parity.

Using this basis, we perform the SRG transformation, which softens the interaction and improves the convergence of a subsequent many-body calculation. Even if we do not include initial four-body forces, the SRG induces irreducible many-body forces. Especially in medium-mass and heavy nuclei the contributions of induced four-body forces are sizable [3].

For a subsequent many-body calculation the interactions must be available in a single-particle HO basis, which requires a non-trivial basis transformation. Afterwards, the interaction can be included in many-body methods directly, but most methods cannot handle four-body forces explicitly. Therefore, an approximation like normal-ordering can be used to reduce the particle rank.

Starting from the SRG transformation and excluding the normal-ordering, we have already established a working framework [4]. Our latest efforts aim at the PWD of initial 4N forces.

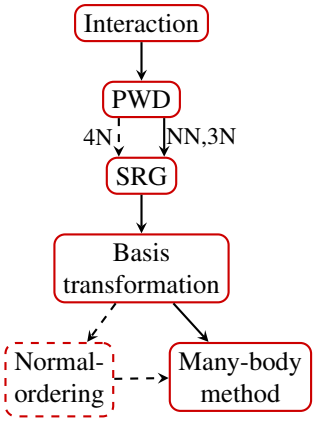

Figure 1: Required steps for including few-body forces in many-body calculation. Dashed lines indicate unfinished parts.

The 4N forces have been derived in a cartesian plane-wave basis [5] and need to be transformed to the Jacobi HO basis. Decomposing the 4N force in partial waves requires 12 integrals over the angular part of the Jacobi coordinates, of which 7 can be performed analytically. Obtaining an expression in a HO basis requires an additional six integrals over the absolute momenta, totaling 11 integrals that have to be performed numerically for every single matrix element. This integration takes up most of the computation time and limits us to small model space sizes in our current implementation. First proof-of-concept calculations with small model spaces for the 4N interaction have been performed for ^{4}He, but convergence with respect to the model space size has not yet been achieved.

This limitation will be overcome in future implementations by using a two-step process and storing intermediate results.

References

[1] R. Machleidt et al., Phys. Rep. 503, 1, 1 (2011).

[2] A. Nogga et al., EPJ Web Conf. 3, 05006 (2010).

[3] S. Binder et al., Phys. Lett. B 736, 119 (2014).

[4] A. Calci, Ph.D. thesis, TU Darmstadt (2014).

[5] E. Epelbaum, Eur. Phys. J. A 34, 2, 197 (2007).

* Work supported by GSI, DFG (SFB 1245), HIC for FAIR, and BMBF (05P15RDFN1)

Ab initio spectroscopy of open-shell medium-mass nuclei: merging no-core shell model and in-medium similarity renormalization group *

E. Gebrerufael[1], *H. Hergert*[2], *R. Roth*[1], *and K. Vobig*[1]

[1]Institut für Kernphysik, TU Darmstadt, Schlossgartenstr. 2, 64289 Darmstadt, Germany; [2]National Superconducting Cyclotron Laboratory, Michigan State University, East Lansing, MI 48824-1321, USA

We merge two of the most successful ab initio many-body techniques, the No-Core Shell Model (NCSM) [1] and (multi-reference) In-Medium Similarity Renormalization Group (IM-SRG) [2,3]. On the one hand, NCSM is limited to light nuclei due to the factorial growth of the model space, while the IM-SRG provides access to heavy nuclei due to soft computational scaling with the particle number A. On the other hand, IM-SRG is initially designed only for ground-state observables, while in the NCSM spectroscopic observables can be obtained readily. Merging these techniques leads to a powerful method that combines the advantages of NCSM and IM-SRG, while eliminating the main disadvantages.

The merging of these two many-body techniques is described the following: An initial NCSM calculation in a limited model space, here $N_{\max} = 0$, is used to define a reference state $|\Psi\rangle$ for the multi-reference IM-SRG evolution of the Hamiltonian for the target nucleus. The resulting IM-SRG evolved Hamiltonian $H(s)$ is employed in a second NCSM calculation to extract ground and excited states as well as spectroscopic observables. The IM-SRG evolution of the Hamiltonian causes a decoupling in A-body space which accelerates the model-space convergence.

For the calculations presented here, we use the chiral nucleon-nucleon plus three-nucleon Hamiltonian in (multi-reference) normal-ordered two-body approximation [4, 5]. To soften the interaction a free-space SRG evolution is applied with $\alpha = 0.08\,\mathrm{fm}^4$ [6].

Figure 1 shows the expectation value of the Hamiltonian with respect to the reference state $\langle H(s)\rangle_\Psi$ (solid line) as a function of the flow parameter s which should converge against the eigenvalue of the initial Hamiltonian (horizontal dashed line). This is not the case since the generator used for the IM-SRG evolution is truncated in practical calculations such that the reference state is not completely decoupled from its excitations. Subsequent NCSM calculations in different model spaces show that the eigenvalues of the IM-SRG evolved Hamiltonian are still useful. Remarkably, the NCSM eigenvalues converges very fast with increasing flow parameter s. This is a direct consequence of the IM-SRG evolution and the decoupling of the Hamiltonian in A-body space. Going to large value of the flow parameter we observe that the induced many-body contribution beyond three-body level become significant. Fortunately, there is a wide plateau around $s = 0.1\,\mathrm{MeV}^{-1}$ appearing already in $N_{\max} = 2$ which makes an identification of an optimal value of the flow parameter possible. Still a small discrepancy at the level of $1.5\,\mathrm{MeV}^{-1}$ can be seen due to neglected induced many-body contributions in the IM-SRG evolution.

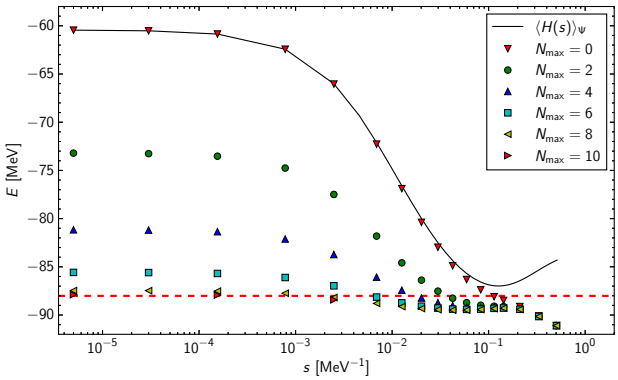

Figure 1: Eigenvalues obtained in different model spaces and expectation value $\langle H(s)\rangle_\Psi$ w.r.t. to the reference state $|\Psi\rangle$ of the IM-SRG evolved Hamiltonian $H(s)$ as function of the flow parameter s for ^{12}C (see also legend). The horizontal dashed line represents the $N_{\max}$-extrapolated result of the initial Hamiltonian.

Since we have already diagonalized the IM-SRG evolved Hamiltonian for ^{12}C using NCSM, we can extract excitation energies without additional cost. First results are very promising. For forthcoming investigations, we will perform a consistent IM-SRG evolution of electromagnetic operators to get further important observables for different isotopes. A particular focus will be put on the Hoyle state in ^{12}C. Since the new technique allows us to tackle all medium-mass nuclei at moderate computational cost, we will also investigate open-shell nuclei up to calcium isotopes.

* Work supported by GSI, DFG (SFB 1245), HIC for FAIR, and BMBF (05P15RDFN1)

References

[1] P. Navratil *et al.*, Phys. Rev. Lett. 84, 5728 (2000).

[2] K. Tsukiyama *et al.*, Phys. Rev. Lett. 106, 222502 (2011).

[3] H. Hergert *et al.*, Phys. Rev. C 90, 041302 (2014).

[4] R. Roth *et al.*, Phys. Rev. Lett. 109, 052501 (2012).

[5] E. Gebrerufael *et al.*, Phys. Rev. C 93, 031301 (2016).

[6] R. Roth *et al.*, Phys. Rev. Lett. 107, 072501 (2011).

DOI:10.15120/GR-2016-1

Short-range correlations studied with unitary transformations

T. Neff[1] *and H. Feldmeier*[1,2]
[1]GSI, Darmstadt, Germany; [2]FIAS, Frankfurt, Germany

Realistic nucleon-nucleon interactions feature a strong short-range repulsion and a strong tensor force. These components of the interaction induce corresponding short-range correlations in the nuclear wave function. The most direct evidence for short-range correlations is found in triple-coincidence experiments where one knocks out a nucleon pair with electrons at high-momentum transfer [1].

A popular approach for dealing with short-range correlations when solving the many-body problem is to transform the bare interaction by means of unitary transformations into an effective low-momentum interaction. With this softened interaction the many-body problem can be solved for example in the no-core shell model (NCSM) employing an harmonic oscillator basis. In [2] we employed this strategy to study short-range correlations in ^{4}He. In this paper we compared results for the Argonne V18 interaction and the N3LO interaction obtained in a chiral EFT. Both interactions fit the nucleon-nucleon scattering data but differ in their short-range behavior.

In the similarity renormalization group (SRG) the unitary transformation is given by a flow equation

$$\frac{d\widehat{H}_\alpha}{d\alpha} = \left[\widehat{\eta}_\alpha, \widehat{H}_\alpha\right]_- , \quad \frac{d\widehat{U}_\alpha}{d\alpha} = -\widehat{U}_\alpha \widehat{\eta}_\alpha \,, \tag{1}$$

with the standard generator given by the commutator of the Hamiltonian with the intrinsic kinetic energy:

$$\widehat{\eta}_\alpha = (2\mu)^2 \left[\widehat{T}_{\rm int}, \widehat{H}_\alpha\right]_- . \tag{2}$$

In practical applications the flow equation is solved in two-body approximation

$$\widehat{H}_\alpha = \widehat{U}_\alpha^\dagger \widehat{H} \widehat{U}_\alpha = \widehat{T}_{\rm int} + \widehat{V}_\alpha^{[2]} + \ldots + \widehat{V}_\alpha^{[N]} \approx \widehat{T}_{\rm int} + \widehat{V}_\alpha^{[2]} , \tag{3}$$

neglecting three- and higher-body terms of the transformed Hamiltonian. This breaks the unitarity of the transformation in many-body systems. The resulting flow-dependence of many-body results can be used to judge the importance of the omitted higher order terms.

The SRG will drive the transformed Hamiltonian to a band diagonal form in momentum space, decoupling low- and high-momenta. With increasing flow parameter α the interaction gets more and more softened. This is reflected in the elimination of high-momentum components in the wave function. We have solved the Schrödinger equation with the SRG evolved Hamiltonian

$$\widehat{H}_\alpha \left|\Psi_\alpha\right\rangle = E_\alpha \left|\Psi_\alpha\right\rangle \tag{4}$$

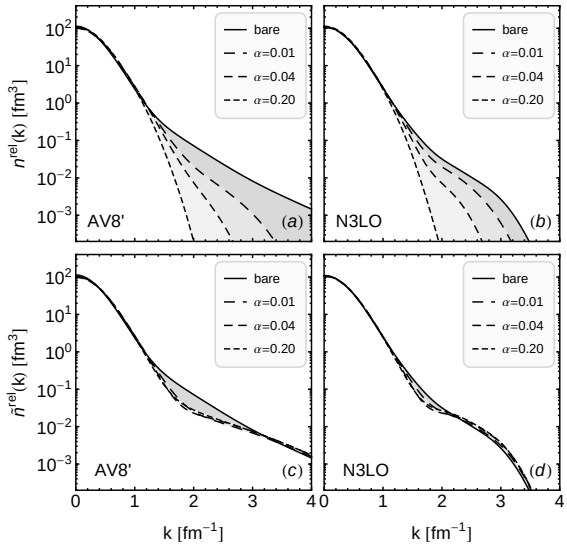

Figure 1: Relative momentum distributions in ^{4}He obtained with SRG transformed AV8' and N3LO interactions. On top with bare density operators, on bottom with SRG transformed density operators.

and calculated the relative momentum distribution $n^{\rm rel}(k)$, the probability to find a pair of nucleons with relative momentum k for the bare and SRG evolved AV18 and N3LO interactions. As is show in the top panel of Fig. 1 the momentum distributions for the bare AV18 and N3LO interactions differ significantly for large relative momenta. With increasing flow parameter the high-momentum components get eliminated and the results for the SRG transformed AV18 and N3LO interactions are very similar.

The information about the high momentum components is however not lost but contained in the unitary transformations $\widehat{U}_\alpha$. If we consider the momentum distribution as an observable we have to apply the unitary transformation also to the two-body density operator. This is shown in the bottom part of Fig. 1 where the density operator has been transformed in two-body approximation. The results are now only very weakly depending on the flow parameter α. This remaining flow dependence indicates the missing contributions of three- and four-body terms.

References

[1] R. Subedi *et al.*, Science **320**, 1476 (2008).

[2] T. Neff, H. Feldmeier, W. Horiuchi, Phys. Rev. C **92**, 024003 (2015).

DOI:10.15120/GR-2016-1

Hartree-Fock many-body perturbation theory for ab initio nuclear structure *

A. Tichai[1] *and R. Roth*[1]

[1]Technische Universität Darmstadt, Schlossgartenstraße 2 , 64289 Darmstadt, Germany

The development of novel techniques for the solution of the Schrödinger equation pushed the frontiers of modern ab initio calculations using realistic nuclear interactions towards the medium-mass regime. In the past years different methods like the coupled cluster (CC) framework, or the in-medium similarity renormalization group (IM-SRG) have proven their reliability in providing an accurate description of binding energies for closed-shell systems. However, both approaches are numerically challenging and the extension to open-shell systems is rather involved.

A conceptually more simple method is many-body perturbation theory (MBPT). Starting from a nuclear Hamiltonian H we define a so-called partitioning by introducing an auxilliary parameter λ yielding a one-parameter family of operators,

$$H_\lambda = H_0 + \lambda W,$$

where $W = H - H_0$ defines the perturbation and H_0 the unperturbed part. We assume that the nuclear observable of interest can be written as a power series expansion in terms of λ and evaluate the expansion coefficients order by order. In principle there is an infinite number of different partitionings and the proper choice of H_0 strongly effects the quality of the results.

The reason why MBPT is typically not considered as an ab initio approach are the underlying convergence issues of the perturbation series. Prior studies based on Slater determinants constructed from harmonic oscillator single-particle states (HO-MBPT) revealed a divergent sequence of partial sums [2,3]. We are able to overcome this issue by optimizing the partitioning. We choose H_0 to be the Hartree-Fock (HF) Hamiltonian arising from an initial NN+3N interaction. The use of HF single-particle states a yields rapidly convergent power series expansion (HF-MBPT). A recursive formulation allows us to calculate energy-corrections up to high orders and to investigate the convergence characteristics in depth. Figure 1 shows a comparison of the convergence behaviour of the perturbation series in light nuclei up to order 30. While the perturbation series in HO basis is divergent, the power series converges exponentially fast when using HF single-particle states and the converged value agrees with the exact result obtained from a configuration interaction (CI) calculation. From this we expect low-order partial sums to be a reasonable approximation to the converged result.

Employing normal-ordering techniques enables for deriving second- and third-order energy corrections explicitly

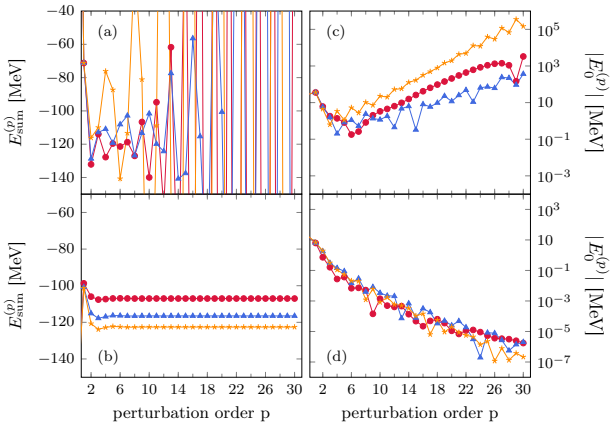

Figure 1: Partial sums of ^{16}O in HO basis (a) and HF basis (b) for the NN+3N-full interaction with $\alpha = 0.08\text{fm}^4$ and truncation parameters $N_{\text{max}} = 2$ (circle), 4 (triangle) and 6 (star). The corresponding energy corrections for each order are displayed in (c) and (d), respectively. All calculations are performed at oscillator frequency $\hbar\Omega = 24\,\text{MeV}$.

in terms of two-body matrix elements, thus circumventing the computational issues one has to resolve when working on a many-body level instead. The corresponding third-order partial sums from HF-MBPT are in excellent agreement with recent CC reults over the entire nuclear chart (see Fig. 3 and 4 in [1]). We further remark that our third-order perturbative calculations require only $1 - 3\%$ of the runtime compared to state-of-the-art CC calculations. This allows for a fast and cheap benchmark of modern nuclear interactions.

The use of multi-configurational reference functions enables the extension of MBPT to open-shell systems. First investigations show that MBPT yields also a robust framework in this more general setting.

References

[1] A. Tichai *et al.*, Phys. Lett. B756, 283 (2016)

[2] S. Binder *et al.*, Phys. Lett. B736, 119 (2014)

[3] J. Langhammer *et al.*, Phys. Rev. C86, 5 (2012)

[4] R. Roth *et al.*, Phys. Lett. B683, 272 (2010)

* Work supported by GSI, DFG (SFB 1245), HIC for FAIR, and BMBF (05P15RDFN1)

DOI:10.15120/GR-2016-1

Large-scale HFB calculation with exact blocking for odd-A nuclei *

A. Arzhanov[1,2], *G. Martínez Pinedo*[1,2], *L. M. Robledo*[3], *and T. R. Rodríguez*[3]

[1]Institut für Kernphysik, TU Darmstadt, D-64289 Darmstadt, Germany; [2]GSI Helmholtzzentrum für Schwerionenforschung, D-64291 Darmstadt, Germany; [3]Departamento de Física Teórica, UAM, E-28049 Madrid, Spain

Exact blocking calculation

In order to properly describe a system with odd number of particles a blocked wavefunction (wf) is required. As blocked level is not known beforehand, we need to start from the even-even wf and have one of the low-lying quasiparticle (qp) levels blocked in the fully-paired state:

$$|\Phi_{\mu_i}\rangle = \beta^\dagger_{\mu_i}|\Phi_e\rangle \sim \alpha^\dagger_{\mu_i}\prod_{l>0}^{l\neq\mu_i}\left(u_l + v_l\alpha^\dagger_l\alpha^\dagger_{-l}\right)|-\rangle\,,$$

where $|\Phi_e\rangle$ is the fully-paired HFB trial wf of BCS form that properly describes an even-even nucleus, the $\beta^\dagger_{\mu_i}$ is the Bogolyubov creation operator for a qp characterized by a set of quantum numbers μ_i, the $\alpha^\dagger_l$ and $\alpha^\dagger_{-l}$ are the conjugate pair of canonical single-particle (sp) creation operators with u_l and v_l being the corresponding occupansies ($u_l^2 + v_l^2 = 1$), and $|-\rangle$ is the bare sp vacuum. The wf $|\Phi_{\mu_i}\rangle$ then properly describes the odd-mass system, as it is built from odd Slater determinants. $|\Phi_{\mu_i}\rangle$ is spin-polarized, and is no more invariant under T-inversion. A non-zero T-odd density matrix appears and so do the associated T-odd fields. In practice the blocked wf $|\Phi_{\mu_i}\rangle$ can very conveniently be contructed by swapping the appropriate columns in the U and V matrices (related to u_l and v_l entries by Bloch and Messiah theorem) of a fully-paired state. Furthermore, imposed axial symmetry in our calculation preserves K-quantum number and parity was found to be conserved as well, meaning that the blocked state μ_i can be characterized by these two quantum numbers. However, initially blocking a qp with the lowest energy is not guaranteed to lead to the lowest ground-state (gs) energy after variation, because the re-minimization rearranges all qp levels self-consistently. Therefore several low-lying quasiparticles have to be considered. In addition, owing to the presence of potentially coexisting prolate, oblate, and spherical minima in the nuclei, blocked configurations with several quadrupole deformations have to be explored as well.

Results

The exact blocking calculations were carried out with codes developed in the Nuclear Physics Group at the Universidad Autónoma de Madrid. However, having to carry out so many variational calculations with additional degree of freedom in form of T-odd components is very computationally demanding. Therefore, to reduce the computational cost, one usually reverts to different approximative blocking techniques that preserve T-symmetry.

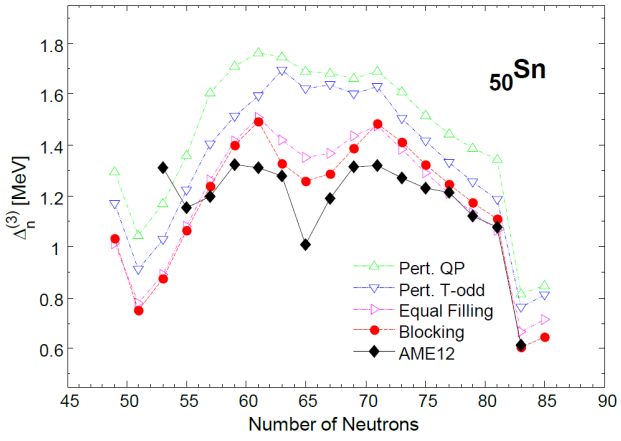

Figure 1: Neutron pariring gaps of tin isotopes. Approximative blocking methods: perturbative qp addition (green), perturbative T-odd field (blue), and equal filling approximation (magenta) compared to exact blocking calculations (red), as well as to experimental values from Atomic Mass Evaluation 2012 (black).

Fig. [1] shows how such approximations compare to the calculation with exact blocking in terms of the neutron pairing gaps for tin isotopes. Studying the results for tin isotopes, seen in Fig. [1], as well as a selection of other isotopic chains, we notice only a slight difference between EFA and exact blocking, which is evident of a rather small, but still noteceable, impact of T-odd terms in current EDFs. In the meantime, the implemented perturbative treatments tend to alsways give larger pairing gaps, coming from systematically underbound total binding energies by $\sim 100 - 300$ keV. Despite this, one clearly notices that the main qualitative features are reproduced in all schemes, but one should be careful comparing the calculations directly to the experimental values, as the odd-mass nuclei were not properly included in the fitting protocols of the existing EDFs. Therefore, by performing exact blocking calculations, we directly probe the T-odd terms that were completely neglected in the current Gogny and Skyrme parametrizations. Detailed analysis of such calculations will help to constrain the existing and identify the new terms in effective interaction to better describe various ground state and spectroscopic observables.

* Work supported by Helmholtz Association through Nuclear Astrophysics Virtual Institute (VH-VI-417 /HGF/ NAVI GSI).

New evidences on the existence of pygmy quadrupole resonance in ^{124}Sn *

N. Tsoneva[1,2] *and H. Lenske*[2,3]

[1]Frankfurt Institute for Advanced Studies (FIAS), 60438 Frankfurt am Main, Germany; [2]Institut für Theoretische Physik, Universität Gießen; [3]GSI Darmstadt

Here, we report on recent results on pygmy quadrupole resonance (PQR), which we predicted theoretically a while ago [1] and now it is being confirmed by three independent experiments [2, 3]. Our theoretical approach is based on density functional theory as the appropriate theoretical scheme of high predictive power for systematic investigations of nuclear ground and excited states by energy-density functional (EDF) methods and advanced QRPA and multi-phonon techniques in the frame of the quasiparticle-phonon model (QPM) [4, 5], respectively.

The first experimental evidence for the existence of pygmy quadrupole states in the neutron rich nucleus ^{124}Sn is provided by the (^{17}O, ^{17}O' γ) reaction at 340 MeV [2]. The measured energy and intensity distributions of the 2^+ states below E= 5 MeV, are found very similar to the predictions based on our EDF+QPM approach as it is shown in Fig.1 and in [2]. The analysis of these experimental data confirms the theoretical predictions of almost pure isoscalar nature of PQR excitations [1].

More evidences on the dominance of single-particle contributions to the E2 ground state transitions from the PQR region are obtained by further experimental studies using $(\alpha, \alpha'\gamma)$ and (γ, γ') reactions, performed on ^{124}Sn nucleus [3]. From analysis of transition densities these single-particle components are found to be strongly connected to neutron skin oscillations. These studies were also able to distinguish the genuine PQR mode from multi-phonon excitations [3].

The obtained from EDF+QPM calculations cumulative $E2$ strength and the one extracted from the (γ, γ') and $(\alpha, \alpha'\gamma)$ experiments is discussed in [3]. It was found that the EDF+QPM theory predicts a higher fragmentation of the $E2$ strength but agrees with the (γ, γ') total PQR strength after this has been corrected for feeding as described in [3]. The comparison could be further improved when the contribution of adopted $E2$ strength seen as well in the $(\alpha, \alpha'\gamma)$ experiment is also included [3]. These experiments were also able to study γ decays leading to different final states and, thus, to determine γ-decay branching ratios $b_0 = \Gamma_0/\Gamma$, where Γ_0 is the ground state decay width and Γ is the total decay width [3]. Therefore, in order to obtain a clearer picture and to test the PQR wave functions further, we compare the theoretical and experimental ground state γ-decay branching ratio b_0 [3]. As in the experiment, the EDF+QPM calculations confirm the predominant decay of 2^+ states above 3 MeV to the ground state. This is due to the fact that the state vectors of these states

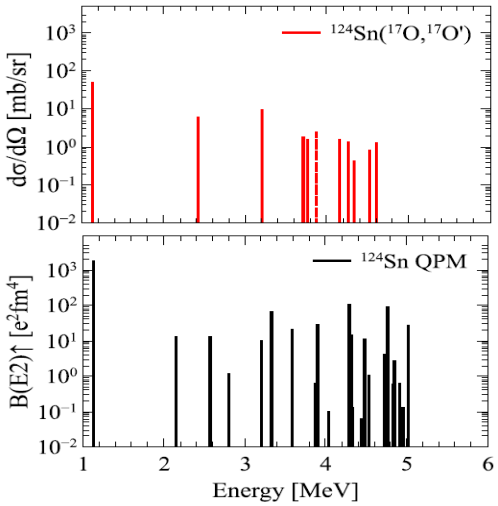

Figure 1: (Color online) Cross sections measured in (^{17}O, ^{17}O' γ) reaction at 340 MeV on ^{124}Sn nucleus, compared with B(E2) values, obtained from EDF+three-phonon QPM calculations [2].

contain a substantial part of collective one-phonon components related to the QRPA states at E =3-4MeV. The latter supports the conclusion that large b_0 values exclude a statistical origin of the PQR strength and they are a possible experimental signature for a PQR mode. In a few cases, comparable contributions of one-phonon and two-phonon transition matrix elements into the total $B(E2)$ transition probability are found, which can explain the experimental observation of large b_0 values and comparably small $E2$ strength at energies above 3.5 MeV, as observed from the combined data of the $(\alpha, \alpha'\gamma)$ and (γ, γ') experiments [3].

In conclusion, the independent measurements of low-energy quadrupole states with different probes and theoretical predictions within the EDF+QPM approach allow to identify a new mode of nuclear excitation, namely PQR in ^{124}Sn nucleus. The spectroscopic features of the PQR are well described by the theory which is confirmed from the comparison with novel experiments [1, 2, 3].

References

[1] N. Tsoneva, H. Lenske, Phys. Lett. **B695** 174 (2011).

[2] L. Pellegri *et al.*, Phys. Rev. C **92**, 014330 (2015).

[3] M. Spieker *et al.*, Phys. Lett. B **752**, 102 (2016).

[4] N. Tsoneva *et al.*, **B586**, 213 (2004).

[5] N. Tsoneva, H. Lenske, Phys. Rev. C **77**, 024321 (2008).

* Work supported by the HIC for FAIR

DOI:10.15120/GR-2016-1

Fission and evaporation of heavy hypernuclei formed in relativistic ion collisions

A. Botvina[1], *M. Bleicher*[1], *and J. Pochodzalla*[2]

[1]ITP and FIAS, Goethe University, Frankfurt am Main, Germany; [2]IKP and HIM, Gutenberg University, Mainz, Germany

It was intensively discussed in previous years that hypernuclei can be abundantly produced in relativistic ion collisions at the GSI and FAIR energies [1, 2, 3]. In the peripheral collisions the residual (target- and projectile-like) nuclei can capture the produced Λ hyperons and become excited hyper-residues. Their subsequent decay results in formation of hyper-nuclei and normal ones. This reaction is analogous to the fragmentation and multifragmentation processes investigated sometimes ago in GSI by FRS and ALADIN collaborations. Since the reaction mechanisms favouring the Λ formation leads usually to high excitation of residues, more than 2–3 MeV per nucleon, then the multifragmentation break-up will dominate in this case [4]. However, low excitation energies are typical for big residues, and, similar to non-strange nuclei, it can bring their to the disintegration via fission and evaporation.

We have generalized the fission and evaporation models developed previously to describe these reaction processes in normal nuclei [5, 6] for the hyper-matter case. The connection with multifragmentation at high energy is also included. The hyperon–nucleon interaction is slightly smaller than the nucleon-nucleon one, therefore, we have introduced the corresponding corrections for the binding and separation energies in the nuclei. The fission barrier for hypernuclei is also a little bit higher (up to 0.3–1 MeV) that reflects a larger binding energy of Λ in big nuclei. We believe a small admixture of hyperons should not change the main properties of nuclei. Therefore, we have assumed that the level density structure remains the same as in normal nuclei, and it depends only on the mass number and the isospin. The inverse cross-section for emission of a Λ hyperon is taken approximately as for the neutron emission. As we have checked the reasonable variations of these parameters (for example, consistent with the geometrical cross-sections) do not change the picture qualitatively, and lead only to small quantitative differences. We think our approximation is reliable as a starting estimate for probabilities of these reactions.

In Figure 1 we demonstrate preliminary calculations for evaporation and fission obtained within our new models. The selected source of ^{223}Ra can be easily obtained as a residue in collisions of relativistic heavy nuclei after loosing few nucleons and getting the excitation energy. In the both cases, with and without a captured Λ, the nucleus undergoes fission which reaches a maximum at excitations around 1 MeV per nucleon. Similar calculations for normal nuclei provide a very good description of produced fragments in the fission and evaporation processes [5, 6, 7]. The fast evaporation of Λ and other particles becomes important at higher excitation and this suppresses the slow fission mode. We have also obtained a very broad distribution of remnant masses, therefore, a great variety of hypernuclear states is expected in such reactions. This heavy-ion method for obtaining hypernuclei considerably extends the opportunities existing in traditional hyper-nuclear studies with hadron interactions.

We thank BMBF for support of this work.

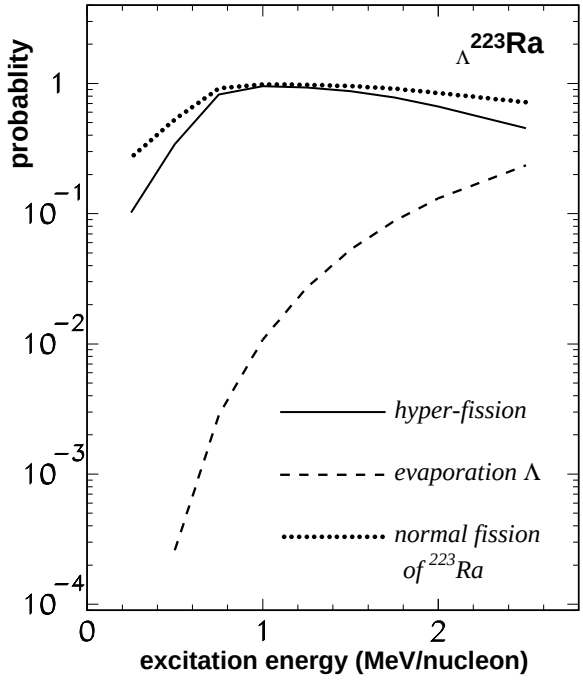

Figure 1: Probabilities of ^{223}Ra fission, and hyper-fisiion of $^{223}_{\Lambda}$Ra in competition with evaporation of Λ from this hypernucleus versus its excitation energy.

References

[1] A.S. Botvina *et al.*, Phys. Rev. C **84**, (2011) 064904.

[2] T.R. Saito *et al.*, Nucl. Phys. A **881**, (2012) 218.

[3] A.S. Botvina *et al.*, Phys. Lett. B **742**, (2015) 7.

[4] A.S. Botvina and J. Pochodzalla, Phys. Rev. C **76**, (2007) 024909.

[5] J.P. Bondorf *et al.*, Phys. Rep. **257**, (1995) 133.

[6] N. Eren *et al.*, Eur. Phys. J. A **49**, (2013) 48.

[7] H. Imal *et al.*, Phys. Rev. C **91**, (2015) 034605.

DOI:10.15120/GR-2016-1

Charged-current neutrino-nucleus cross-sections for the ν process *

A. Sieverding[†1], *T. Marketin*[2], *G. Martínez-Pinedo*[1,3], *and K. Langanke*[3,1]

[1]Institut für Kernphysik (Theoriezentrum), Technische Universität Darmstadt, Schlossgartenstraße 2, 64289 Darmstadt, Germany; [2]Physics Department, Faculty of Science, University of Zagreb, 10000 Zagreb, Croatia; [3]Gesellschaft für Schwerionenforschung Darmstadt, Planckstr. 1, D-64259 Darmstadt, Germany

Core-collapse supernova explosions of massive stars are a major contributor to the chemical enrichment of the galaxy as they represent a means to release the products of stellar hydrostatic burning into the interstellar medium. Therefore CCSNe are responsible for the production of most of the elements up to iron. The final composition of the ejecta depends on the nucleosynthesis induced by the shock-heating of the explosion itself. The explosion is accompanied by large neutrino fluxes emitted from the collapsing stellar core. The neutrino irradiation affects the shock-heated nucleosynthesis in the ν process [1].

Assuming very high neutrino energies, mainly neutral-current spallation reactions have a significant impact on the nucleosynthesis. These reactions can be computed with sufficient accuracy using simple nuclear models, since they are mainly sensitive to collective excitations. As state-of-the-art SN simulations tend to predict neutrino energies to be lower than expected in the past, charged current channels gain in relative importance. since they are often determined by a few low-energy Gamow-Teller and Fermi transitions. Strengths for these transitions are in some cases known from experiments.

The reactions ^{26}Mg(ν_e,e$^-$) ^{26}Al and ^{22}Ne(ν_e,e$^-$)^{22}Na affect the production of the radioactive isotopes ^{26}Al and ^{22}Na which are interesting for γ-ray astronomy [2].
At low neutrino energies ^{26}Mg(ν_e,e$^-$) is dominated by Gamow-Teller transitions and the Fermi transition to the short lived 0^+ state in ^{26}Al. The strength of the Gamow-Teller transitions B(GT) has been measured with high precision by Zegers et al. [3] . For the reaction ^{22}Ne(ν_e,e$^-$)^{22}Na data from the β-decay of the mirror nucleus ^{22}Mg can be used for the dominant transitions.
The cross-sections derived from the measured transition strengths have been supplemented by forbidden transitions calculated with RPA as in [2].
Table 1 compares the cross-sections obtained in that way with the results of a calculation by Marketin et al. using a relativistic Quasiparticle Random Phase Approximation (QRPA) [4]. We find that the cross-sections are higher by almost a factor of two at the lowest energies that are expected to be found in Core-Collapse Supernovae. Implementing these rates in nucleosynthesis calculations we expect to see a slight increase in the production of ^{26}Mg and ^{22}Na.

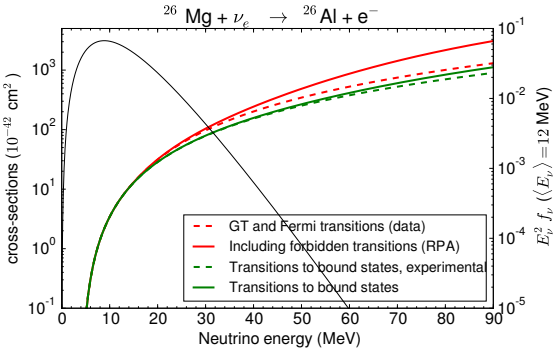

Figure 1: Cross section for the reaction ^{26}Mg(ν_e,e$^-$) as a function of neutrino energy. At very low energies the cross section is dominated by the experimentally known transitions.

Reaction	Method	T_{ν_e} in MeV		
		2.8	4.0	6.4
^{26}Mg+ν_e	QRPA	3.14	12.01	52.76
	incl. exp	5.28	16.11	67.02
^{22}Ne+ν_e	QRPA	3.90	13.28	50.03
	incl. exp	6.61	18.04	67.03

Table 1: Cross sections averaged assuming Fermi-Dirac distributions of different temperatures T_ν and $\mu = 0$ in units of 10^{-42} cm^2.

References

[1] A. Heger, E. Kolbe, W. C. Haxton, K. Langanke, G. Martínez-Pinedo, S. E. Woosley, *Neutrino nucleosynthesis*, Physics Letters B **606** 258.

[2] A. Sieverding, L. Huther, G. Martinez Pinedo, K. Langanke, *Neutrino nucleosynthesis of radioactive nuclei in supernovae*, vol. 2015-1 of *GSI Report* (GSI Helmholtzzentrum für Schwerionenforschung, Darmstadt, 2015), p. 341 p., URL `https://repository.gsi.de/record/184067`.

[3] R. G. T. Zegers, *et al.*, *The (t,He3) and (He3, t) reactions as probes of Gamow-Teller strength*, Phys. Rev. C **74** (2) 024309.

[4] N. Paar, H. Tutman, T. Marketin, T. Fischer, *Large-scale calculations of supernova neutrino-induced reactions in $Z = 8$˜82 target nuclei*, Phys. Rev. C **87** 025801.

* Work supported by NAVI
† a.sieverding@gsi.de

DOI:10.15120/GR-2016-1

Nuclear robustness of the r-process in neutron-star mergers*

M.-R. Wu† [1], *J. Mendoza-Temis*[1,2], *K. Langanke*[3], *G. Martínez-Pinedo*[1,3], *A. Bauswein*[4,5], *and H.-T. Janka*[6]

[1]TU Darmstadt, Germany; [2]ICN, UNAM, Mexico; [3]GSI, Germany; [4]Aristotle University of Thessaloniki, Greece; [5]HITS, Germany; [6]MPA Garching, Germany

Binary neutron star mergers are expected to be the major sources for future gravitational wave detections [1] and are connected with the observations of short Gamma-ray bursts [2]. They are also considered as promising astrophysical sites where the rapid neutron-capture process (r-process) takes place to produce nearly a half of the elements heavier than iron in the Universe [3]. Moreover, the decay of radioactive nuclei produced during the r-process may power astrophysical transients, the so-called kilonovae, that may have been observed recently [4].

The r-process nucleosynthesis in matter ejected dynamically during the initial phase of ~ 10 ms after the merger has been extensively studied. Due to the large initial neutron excess, fission cycling takes places during the r-process and is responsible for the robustness of the resulting abundance pattern against the variation of the mass ratio of the two merging neutron stars [5] and the assumed equation of state of dense matter [6].

In this work, we aim to explore the effect of different theoretical mass predictions for extremely neutron-rich nuclei on the outcome of the r-process. We have used a complete set of ejecta trajectories of $\approx 1.70 \times 10^{-3}\ M_\odot$ from the numerical simulation of a merger system consisting of two 1.35 $M_\odot$ non-spinning neutron stars [6]. For the nuclear reaction network, we have calculated the neutron capture and its reverse rates for nuclei with $Z \leq 83$ based on four different nuclear mass models: FRDM, WS3, DZ31, and HFB21 while keeping the other nuclear physics inputs to be the same (see [7] for a detailed description and references).

As shown in Fig. 1, different nuclear mass models give rise to different abundance position and height for the third peak nuclei with $A \approx 195$. This is related to the fact that some mass models such as FRDM and HFB21 predict additional drops of the neutron separation energy at neutron number $N = 129$ above the neutron shell closure, when compared to the DZ31 and WS3 models. As a result, nucleosynthesis flow is halted longer at nuclei with larger N and Z where the peak forms during the r-process. For example, in the case of FRDM model, the third peak is at $(N, Z) = (128, 68)$ while it is located at $(N, Z) = (126, 66)$ in the DZ31 model.

Similar drops in neutron separation energy also appear in the region above neutron number $N \gtrsim 82$ for mass models of FRDM and HFB21. However, the final nucleosynthesis abundances around the second peak ($A \sim 130$) is nearly unaffected by the mass models. This is because during the r-process, due to the different beta-decay half-lives, matter piles up at the super-heavy nuclei ($A \sim 280$) but not around the region of the second peak. The second peak is only produced by fission of those super-heavy nuclei during the r-process freeze-out. Since we have used the same nuclear physics input for nuclei with $Z > 83$, this leads to very similar abundance shape in the $A \sim 130$ peak.

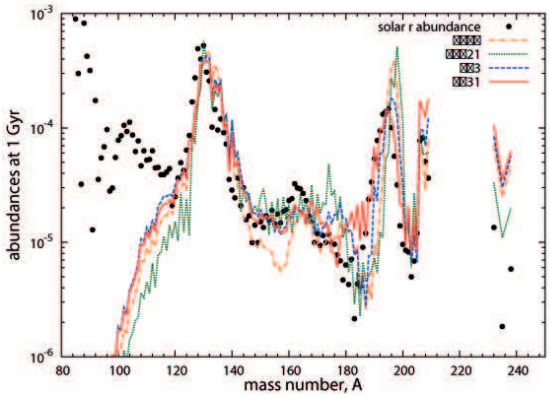

Figure 1: Abundance as a function of mass number, A, of the neutron star merger ejecta at the time of 10^9 year after merger for different nuclear mass models.

The above results also point to the importance of exploring the effect of other nuclear physics inputs such as the beta-decay half-lives, fission rates, and fission yield distributions. We plan to further investigate these facets in the future and eventually evaluate their impact on the resulting abundances and the lightcurves of kilonovae.

References

[1] B. P. Abbott et. al., (LIGO Scientific Collaboration and Virgo Collaboration) Living Rev. Relativity **19**, 1 (2016).

[2] E. Berger, Ann. Rev. Astron. Astrophys., **52**, 43 (2014).

[3] C. Freiburghaus, S. Rosswog, and F.-K. Thielemann, Astrophys. J. **525**, L121 (1999).

[4] N. R. Tanvir et. al., Nature **500**, 547 (2013).

[5] O. Korobkin, S. Rosswog, A. Arcones, and C. Winteler, Mon. Not. Roy. Astron. Soc **426**, 1940 (2012).

[6] A. Bauswein, S. Goriely, and H.-T. Janka, Astrophys. J. **773**, 78 (2013).

[7] J. Mendoza-Temis, M.-R. Wu, K. Langanke, G. Martínez-Pinedo, A. Bauswein, and H.-T. Janka, Phys. Rev. **C92**, 055805 (2015).

*Work supported by DFG through SFB 634, HIC for FAIR, NAVI, EMMI, European Community Framework Program, DFG through ST7, and the Cluster of Excellence EXC153.

† mwu@theorie.ikp.physik.tu-darmstadt.de

Systematic of fission properties of r-process nuclei*

S. A. Giuliani†[1], *G. Martínez-Pinedo*[1], *and L. M. Robledo*[2]

[1]Institut für Kernphysik (Theoriezentrum), Technische Universität Darmstadt, Schlossgartenstraße 2, 64289 Darmstadt, Germany; [2]Departamento de Física Teórica, Universidad Autónoma de Madrid, E-28049 Madrid, Spain.

Fission plays a crucial role in r-process nucleosynthesis occurring in neutrons star mergers. As it was shown in a recent publication [1], the main requirement for achieving a robust r- process is that at the freeze out the amount of material accumulated in the fissioning region ($A \sim 250$) must be much larger than around the second peak and above $A \sim 120 - 180$. Therefore, a proper description of the fission properties of superheavy nuclei including fission barrier heights, cross sections and fragment distributions, is crucial for obtaining reliable r-process calculations.

In the previous GSI report [2] we studied the fission properties of superheavy nuclei obtained using the Barcelona-Catania-Paris-Madrid (BCPM) Energy Density Functional (EDF) [3, 4, 5]. In this work, we present the systematic of binding energies and fission barriers of the BCPM EDF using the Perturbative Nucleon Addition Method (PNAM) [6]. Within this phenomenological scheme, the self-consistent energy of the nucleus is obtained by constraining the many-body wave function to have the desired particles number. After that, the overbinded energy is corrected by adding the lowest quasiparticle excitation. In order to test the validity of this approach with the BCPM EDF, we computed the Potential Energy Surface (PES) of oe and oo nuclei in the region $84 \leq Z \leq 120$ and $120 \leq N \leq 250$ and the binding energies from neutron to proton drip line for nuclei with $8 \leq Z \leq 120$, and we compared our predictions with the available experimental data. All aspects of the mean-field calculations are identical to the ones presented in Ref. [2].

Regarding the nuclear binding energies, the BCPM EDF reproduces the experimental data of ee nuclei with a rms deviation of 1.49 MeV. Considering oo and oe nuclei computed with the PNAM this deviation slightly increases up to 1.52 MeV. Regarding the neutron separation energy S_n, the BCPM+PNAM reproduces the experimental data with a rms deviation of 0.760 MeV, that is slightly lower than the rms deviation for ee nuclei (0.768 MeV). As a benchmark of the fission properties of BCPM+PNAM, we compared our predictions of the inner ($\mathrm{B_I}$) and outer ($\mathrm{B_{II}}$) fission barrier heights and isomer excitation energies ($\mathrm{E_{II}}$) with the experimental data of Ref [7]. For the even-even nuclei we got a rms deviation of $\sigma(\mathrm{B_I}) = 1.44$ MeV,

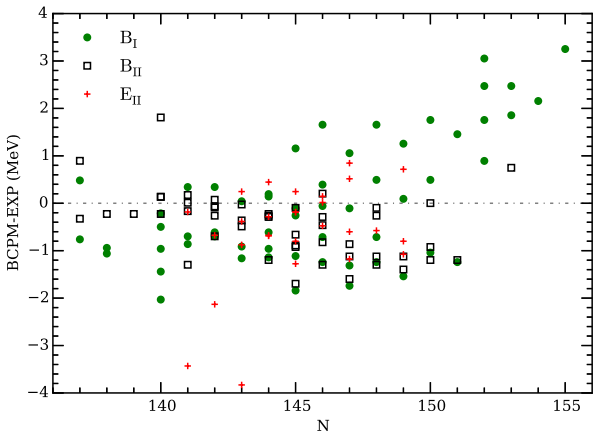

Figure 1: Deviations between BCPM predictions and experimental data [7] for $\mathrm{B_I}$, $\mathrm{B_{II}}$ and $\mathrm{E_{II}}$ as a function of neutrons number.

$\sigma(\mathrm{B_{II}}) = 0.77$ MeV and $\sigma(\mathrm{E_{II}}) = 0.98$ MeV. When oe an oo nuclei are included, the rms deviations change to $\sigma(\mathrm{B_I}) = 1.29$ MeV, $\sigma(\mathrm{B_{II}}) = 0.81$ MeV and $\sigma(\mathrm{E_{II}}) = 1.22$ MeV. These values are rather satisfying, specially considering that the uncertainties related with the experimental measurements of $\mathrm{B_I}$, $\mathrm{B_{II}}$ and $\mathrm{E_{II}}$ can be as large as 0.7 MeV. The PNAM clearly improves the description of $\mathrm{B_I}$, that is general overestimated in our calculations due to the preservation of axial symmetry. On the other, the $\mathrm{E_{II}}$ deviation increases when oe and oo nuclei are considered. This is mainly due to the Thorium isotopic chain, where the isomer excitation energies of BCPM have been found to be 3-4 MeV lower than the experimental data.

These results show that for oe and oo nuclei, BCPM+PNAM maintain the level of accuracy obtained with the BCPM EDF for ee nuclei, giving us the confidence for a robust calculation of the fission rates. A work in this direction is already in progress.

References

[1] J. J. Mendoza-Temis et al., Phys. Rev. **C92**, 055805 (2015).
[2] S. A. Giuliani et al., GSI Report 2015-1, 348 p. (2015).
[3] M. Baldo et al., Phys. Rev. **C87**, 064305 (2013).
[4] S. A. Giuliani et al., Phys. Rev. **C90**, 054311 (2014).
[5] S. A. Giuliani et al., Phys. Rev. **C88**, 054325 (2013).
[6] T. Duguet et al., Phys. Rev. **C65**, 014310 (2001).
[7] S. Bjørnholm et al., Rev. Mod. Phys. **52**, 725 (1980).

* The work of SAG and GMP was supported by the Helmholtz Association through the Nuclear Astrophysics Virtual Institute (VH–VI–417) and the BMBF–Verbundforschungsprojekt number 06DA7047I. The work of LMR was supported by the Spanish MICINN Grants No. FPA2012–4694 and No. FIS2012–34479 and by the Consolider–Ingenio 2010 MULTIDARK CSD2009-00064.

† giuliani@theorie.ikp.physik.tu-darmstadt.de

DOI:10.15120/GR-2016-1

Accretion-induced collapse of ONe cores *

H. Möller[1] *and G. Martínez-Pinedo*[1,2]
[1]TU Darmstadt, Darmstadt, Germany; [2]GSI, Darmstadt, Germany

Introduction

Electron-degenerate cores composed of oxygen and neon are mainly formed through carbon burning in super asymptotic giant branch (SAGB) stars with initial masses between about 7 and 9 solar masses [1]. They can become oxygen-neon white dwarfs (ONe WD), they can undergo electron-capture supernovae (ECSN) or they might even proceed towards explosive oxygen-burning and a subsequent thermonuclear explosion. For details, see e.g. [2]. Additionally, in the accretion induced collapse scenario (AIC), the white dwarf can proceed towards collapse by accreting matter from a companion star in a binary system.

The collapse of the ONe core is triggered by electron captures (EC) on ^{20}Ne [3], simultaneously leading to a strong increase in temperature in the stellar core, thereby igniting oxygen and forming a thermonuclear burning front. Ultimately, the fate of the star (i.e. collapse or explosion) will be determined by a competition between the deleptonization of the NSE-ashes, resulting in a pressure loss, and the oxygen deflagration wave moving outwards.

MESA models

Here, we perform calculations with the stellar evolution code MESA [4] of accreting ONe cores to study the behavior of the core prior to the ignition of oxygen. We quantify the impact of the nuclear physics input on the ignition density as well as the possible development of convection. Figure 1 shows the size of the nuclear reaction network that we use in the calculations compared to a previous study of the AIC of ONe cores by [5].

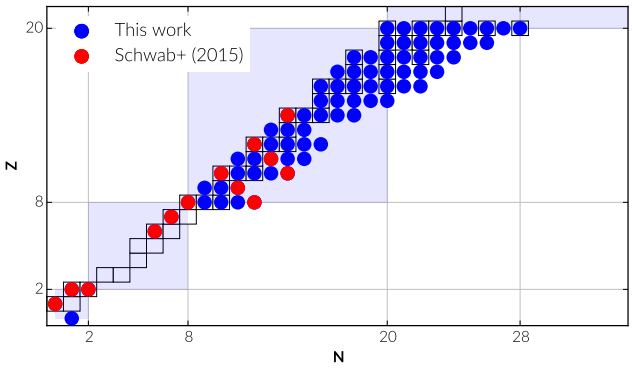

Figure 1: Reaction network used in our calculations.

We show that an accurate description of the nuclear reactions is crucial for the determination of the pre-supernova structure of these stars and point out that weak rates involving sd-shell nuclei are especially important. Most crucial is the ^{20}Ne-EC, where taking into account the second forbidden transition to the ground state of ^{20}F has a significant impact of the evolution of the star in general and the ignition density in particular. This can be seen in the T_c-ρ_c-diagram in Figure 2. It should be noted that experimental as well as theoretical advances in the determination of this rate are currently being made. Also, the choice of the network size as well as the inclusion of the α-capture rate on ^{20}O have an impact on the ignition density (See Figure 2 and [6] for details).

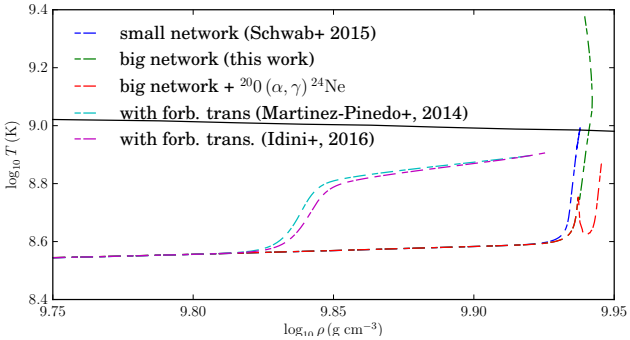

Figure 2: T_c-ρ_c-diagram of the calculated MESA models.

Outlook

Modeling the oxygen deflagration requires a hydrodynamic description coupled to a reaction network including EC reactions up to iron-group nuclei. We are currently performing hydrodynamic simulations that capture the onset of the oxygen-flame ignition and follow it towards a possible core-collapse, describing the deflagration based on a level-set approach (see e.g. [7] for more details).

References

[1] Jones, S., *et al.* 2013, ApJ **772**, 150
[2] Isern, J., *et al.* 1991, ApJ, **372**, L83
[3] K. Nomoto, ApJ **322** (1987), 206–214.
[4] Paxton, B., *et al.* 2011, ApJS, **192**, 3
[5] Schwab, J., *et al.* 2015, MNRAS, **453**, 1910
[6] Möller, H., *et al.* 2014, PoS(NIC XIII)125
[7] Reinecke, M., *et al.* 1999, A&A, **347**, 724

* supported by the Helmholtz Association through NAVI

DOI:10.15120/GR-2016-1

4Dim numerical general relativity, hydrodynamics and the roles of the hadron and quark matter EOS in neutron star mergers *

M. Hanauske† [1,2,3], *H. Stöcker*[1,2,3], *L. Rezzolla*[2,3], *K. Takami*[4,2], *A. Zacchi*[2], *J. Schaffner-Bielich*[1,2], *and J. Papenfort*[1,2,3]

[1]GSI, Darmstadt, Germany; [2]Institute for Theoretical Physics, Max-von-Laue-Straße 1, 60438 Frankfurt, Germany; [3]Frankfurt Institute for Advanced Studies, Ruth-Moufang-Straße 1, 60438 Frankfurt, Germany; [4]Kobe City College of Technology, 651-2194 Kobe, Japan

One hundred years after Albert Einstein developed the field equations of general relativity and predicted the existence of gravitational waves, his theory triumphantly corroborates all experimental and observational tests it has been put through to date. Gravitational waves (GW) have been recently observed from a pair of merging black holes by the LIGO detectors [1] and GWs emitted from merging neutron star binaries are on the verge of their first detection.

The results of 4-dimensional numerical simulations of merging neutron star binaries in full general relativity show that the emitted GWs of the merger and post-merger phase are strongly determined by the high density region of the equation of state (EOS). The underlying general-relativistic hydrodynamical evolution of the produced hypermassive neutron star (HMNS) depends on the hadronic and quark matter properties.

Fig.1 depicts the GW-amplitude of an equal-mass neutron star binary merger simulation ($M_{\rm tot} = 2.7 M_\odot$), wherein the used EOS (ALF2 [2]) has incorporated a phase transition to color-flavor-locked quark matter at $\rho_{\rm trans} = 3\,\rho_0$ (for details see [3]). The absolute maximum of $|h|$ marks the time of the merger (i.e., $t = 0$ ms) and the last peak of h_+ corresponds to the time where the HMNS collapses to a black hole (i.e., $t = 14.16$ ms). The upper part of Fig.1 shows the logarithm of the rest mass density profiles for three different time snap-shots ($t = -0.17, 4.05, 13.16$ ms), whereat the boundary of the hadron-quark phase transition (HQPT) is marked with a red curve. For the used ALF2-EOS with $M_{\rm tot} = 2.7 M_\odot$, the maximum density reached within the inspiral phase is below the onset of the HQPT, but soon after the merger the density reaches values above $\rho_{\rm trans}$, forming a mixed phase inner region of deconfined quark matter.

In Ref. [3] it has been shown that the detection of GWs from merging neutron star binaries can be used to determine the high density regime of the EOS. The power spectral density profile of the post-merger emission is characterized by the four distinct frequencies f_1, f_2, f_3 and f_{2-0} and with the knowledge of the total mass the system, the GW signal can set tight constraints on the EOS.

The underlying hybrid star model of the ALF2-EOS uses a Gibbs construction to model the HQPT, whereat the EOS

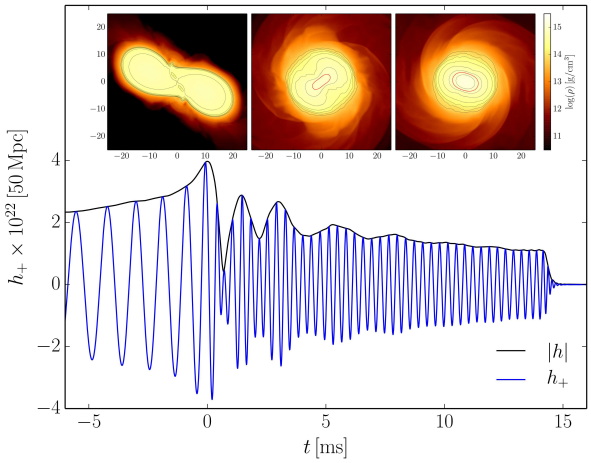

Figure 1: Rest mass density profiles and gravitational wave amplitude $|h|$ and h_+ at a distance of 50 Mpc for the ALF2-EOS with $M_{\rm tot} = 2.7 M_\odot$.

softening in the mixed phase region is extremely moderate and as a consequence the EOS is hardly distinguishable from a neutron star model having e.g., hyperonic degrees of freedom. Assuming a higher surface tension of quark matter, the hadron-quark phase transition behaves more in accordance with a Maxwell construction having a density jump at the phase transition boundary. In some particular models [4], the appearance of a disconnected mass-radius relation implies the existence of a third family of compact stars, so called twin stars. Usually it is assumed that the loss of stability of a neutron star, exceeding its maximum mass, leads to the collapse into a black hole - however, within these models a collapse could be, at first, stopped before the black hole forms. Due to the strong softening at the QCD - phase transition region, the emitted gravitational waves profile of a merging system within such EOSs will be easy distinguishable from a neutron star model.

References

[1] Abbott, B. P., et al., *Phys. Rev. Lett.* **116**, p. 061102 (2016).

[2] M. Alford, M. Braby, M. Paris and S. Reddy, *The Astrophysical Journal* **629**, p. 969 (2005).

[3] K. Takami, L. Rezzolla and L. Baiotti, *Phys. Rev. D* **91**, p. 064001 (2015).

[4] A. Zacchi, M. Hanauske and J. Schaffner-Bielich, *Phys. Rev. D* **93**, p. 065011 (2016).

* Work supported by the Hadron and Ion Research Facility for Antiproton and Ion Research (HIRe for FAIR), the Helmholtz International Center for FAIR (HIC for FAIR), the Karin und Carlo Giersch Foundation and the Frankfurt Institute for Advanced Studies (FIAS).

† hanauske@th.physik.uni-frankfurt.de

DOI:10.15120/GR-2016-1

Investigations of the chiral phase transition with (axial-)vector mesons within the functional renormalization group approach*

J. Eser† [1] *and D. H. Rischke*[1]

[1]Institut für Theoretische Physik, Goethe-Universität, Max-von-Laue-Str. 1, D-60438 Frankfurt am Main, Germany

Introduction

The restoration of chiral symmetry in quantum chromodynamics for high temperatures and/or net-baryon densities modifies the spectral properties of light vector mesons. Such in-medium modifications generated during heavy-ion collisions, e.g. in the upcoming CBM experiment, affect the measurable dilepton spectra via mesonic decay processes. A study of vector mesons is therefore crucial for the understanding of the characteristics of the produced quark-gluon plasma. We investigate the chiral phase transition including vector and axial-vector mesons within the functional renormalization group (FRG) approach.

Extended linear sigma model

We use the so-called extended linear sigma model (eLSM) as a low-energy description of the strong interaction in terms of hadronic degrees of freedom. More precisely, we consider a two-flavor version of the eLSM that is similar to the Sakurai model [1]. Besides scalars (σ, a_0) and pseudoscalars (η, π), the eLSM also involves vector and axial-vector mesons, namely the ω and the ρ as well as the f_1 and the a_1 mesons.

Functional renormalization group

The FRG approach focuses on the scale (k-)dependence of the effective average action Γ_k, which is the generating functional for one-particle irreducible vertex diagrams in the theory at hand. The interpolation of Γ_k between the classical action in the ultraviolet and the full effective action in the infrared is described by the FRG flow equation [2]. We solve this equation for the corresponding effective action of the eLSM in the local potential approximation and tune the ultraviolet parameters such that physical values for the mesonic screening masses and for the chiral order parameter, the chiral condensate, are achieved in the infrared.

We want to emphasize that the (axial-)vector mesons are treated beyond mean field, i.e. their quantum and statistical fluctuations were explicitly taken into account by the FRG flow.

Results

In Ref. [3], we have shown that in the chiral limit and if the axial anomaly is neglected the chiral phase transition for vanishing quark-chemical potential is of first order. Still for massless quarks but in the presence of the axial anomaly, however, the transition becomes second order. Finally, this second-order transition is smeared out into a crossover as soon as the quarks are considered to be massive, leading to an explicit breaking of chiral symmetry. These results are consistent with many previous studies such as Ref. [4].

The first-order transition takes place at a temperature of 147.4 MeV. For the second-order transition and for the crossover we found (pseudo-)critical temperatures of 276.5 and 354.8 MeV, respectively. These values are extremely high compared to lattice results of around 160 MeV [5].

In the first two cases the masses of chiral partners degenerate at the phase boundary and beyond, a phenomenon which is lost in the last case due to the crossover character of the transition. Here, the masses of chiral partners approach each other but do not become identical. The mass of the ρ meson was found to be increasing towards the chiral transition temperature, while the mass of a_1 meson decreases. Moreover, our results favor the $f_0(500)$ resonance to be the measured equivalent of the σ meson.

Outlook

In order to obtain more "realistic" chiral transition temperatures we are currently working on an extension of this investigation by introducing quark fields to the eLSM by means of a Yukawa coupling to the mesonic degrees of freedom. Closely related to this will be the study of the phase transition for nonvanishing quark-chemical potentials. Furthermore, the presented work is going to serve as a basis for computing the spectral functions of (axial-)-vector mesons within the FRG.

References

[1] J. J. Sakurai, "Theory of strong interactions", Ann. Phys. 11, 1 (1960).

[2] C. Wetterich, "Exact evolution equation for the effective potential", Phys. Lett. B 301, 90 (1993).

[3] J. Eser, M. Grahl, and D. H. Rischke, "Functional renormalization group study of the chiral phase transition including vector and axial-vector mesons", Phys. Rev. D 92, 096008 (2015).

[4] R. D. Pisarski and F. Wilczek, "Remarks on the chiral phase transition in chromodynamics", Phys. Rev. D 29, 338 (1984).

[5] A. Bazavov *et al.*, "Chiral and deconfinement aspects of the QCD transition", Phys. Rev. D 85, 054503 (2012).

* J. E. thanks F&E GSI/GU, HIC for FAIR, and the German Academic Scholarship Foundation for funding.

† eser@th.physik.uni-frankfurt.de

Spectral functions and in-medium properties of hadrons*

R.-A. Tripolt†[1], *C. Jung*[2], *L. von Smekal*[2], *and J. Wambach*[1,3]
[1]ECT*, Italy; [2]JLU Giessen, Germany; [3]TU Darmstadt, Germany

We present results on in-medium spectral functions and transport coefficients of hadrons. Our non-perturbative approach is based on the Functional Renormalization Group (FRG) framework and applied to the (Polyakov-) quark-meson model. In particular, we show results for the pion spectral function and for the mesonic shear viscosity over entropy density ratios.

The investigation of in-medium properties of strongly interacting hadrons is a long-standing and very challenging problem. In the following, we use the method put forward in [1,2] to calculate spectral functions and transport coefficients at finite temperature and chemical potential. This method is based on the non-perturbative FRG framework and has been applied to the quark-meson model as well as to the Polyakov quark-meson model which act as effective models for QCD at low energies.

The resulting pion spectral function is shown in Fig. 1 at $T = 50$ MeV and vanishing chemical potential. Due to the interactions with the heat bath, the pion is unstable at this temperature, as indicated by the finite width of the peak. The peak as well as the thresholds of the available decay channels are boosted to higher energies as the spatial momentum increases.

Using the momentum dependence of the pion and sigma spectral functions as input, we were able to calculate the corresponding shear viscosities using the Green-Kubo formula,

$$\eta = \frac{1}{24} \lim_{q_0 \to 0} \lim_{|\vec{q}| \to 0} \frac{1}{q_0} \int d^4x \; e^{iqx} \left\langle \left[T_{ij}(x), T^{ij}(0) \right] \right\rangle ,$$

where $T_{ij}(x)$ is the energy-momentum tensor. In the case of the quark-meson model, the dominant contribution to the shear viscosity is given by

$$\eta_{\sigma,\pi} \propto \int \frac{d\omega}{2\pi} \int \frac{d^3p}{(2\pi)^3} \; p_x^2 \, p_y^2 \, n'_B(\omega) \, \rho^2_{\sigma,\pi}(\omega, \vec{p}).$$

In Fig. 2 we show η/s for the pions and the sigma mesons as a function of temperature at $\mu = 0$. Towards small temperatures, the shear viscosity of the pions increases drastically which is due to a decreasing width of the pion peak, cf. Fig. 1. A comparison with chiral perturbation theory (χPT) [3] shows good agreement for intermediate temperatures. The difference at small temperatures is due to the fact that two-pion scattering processes are not yet included in our truncation. Towards the crossover transition, which occurs at $T \approx 160$ MeV, we observe an increase of η/s.

In future works, we will further improve and extend our method. In particular, we aim at calculating the quark spectral function and the corresponding shear viscosity as well as extending our model by including vector and axial-vector mesons.

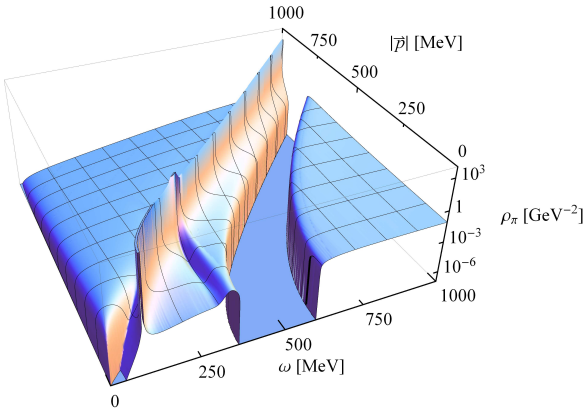

Figure 1: The pion spectral function ρ_π is shown vs. energy ω and spatial momentum $\vec{p}$ at $T = 50$ MeV and $\mu = 0$.

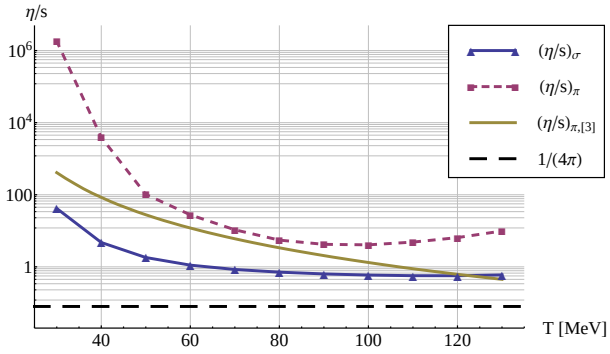

Figure 2: The shear viscosity over entropy density ratio η/s of the pions and of the sigma mesons is shown vs. T at $\mu = 0$ in comparison to results from χPT [3].

References

[1] R.-A. Tripolt, L. von Smekal, and J. Wambach, Phys. Rev. D90, 074031 (2014).

[2] R.-A. Tripolt, N. Strodthoff, L. von Smekal, and J. Wambach, Phys. Rev. D89, 034010 (2014).

[3] R. Lang, N. Kaiser, and W. Weise, Eur. Phys. J. A48, 109 (2012).

* Supported by BMBF, project number 05P12RDGHD, and HIC4FAIR. R.-A. T. was supported by GSI through the cooperative agreement with TU Darmstadt.

† tripolt@ectstar.eu

DOI:10.15120/GR-2016-1

Modeling chiral criticality and its consequences for heavy-ion collisions*

G. A. Almasi†[1], *B. Friman*[1,2], *and K. Redlich*[2,3,4]

[1]Gesellschaft für Schwerionenforschung, GSI, D-64291 Darmstadt, Germany; [2]ExtreMe Matter Institute (EMMI), D-64291 Darmstadt, Germany; [3]University of Wrocław - Faculty of Physics and Astronomy, PL-50-204 Wrocław, Poland; [4]Department of Physics, Duke University, Durham, NC 27708, USA

In this work we report on the study of baryon number cumulants in effective field theories of QCD. A main goal of heavy-ion physics is to prove or disprove the existence of a chiral critical point of QCD, the endpoint of a first order chiral phase transition. If it exists, an enhancement of fluctuations of conserved charges are expected in its vicinity on the phase diagram [1]. Due to this fact calculation of correlations and fluctuations of conserved charges has been proposed to study the existence and location of the chiral critical endpoint of QCD.

Our calculations are carried out using the Polyakov–Quark-Meson (PQM) model [2] with the help of the Functional Renormalization Group (FRG) [3]. This model lies in the same universality class as QCD, and hence has the same critical behavior. The FRG formalism guarantees that the critical fluctuations of the bosons are taken into account in a consistent way. The Polyakov-loop extension is needed to suppress the low temperature single quark fluctuations and provide reasonable baryon number cumulants at all temperatures.

In our studies we calculated the baryon number cumulants up to fourth order in the whole phase diagram. Following the ideas in [4, 5] for comparison with experiment we do not take a heavy-ion freeze-out line to carry out calculations on, but rather we define a freeze-out line self-consistently within the model. This is done by looking for a line on the phase diagram, on which the calculated χ_B^3/χ_B^1 cumulant ratio agrees with the experimental measurements as a function of μ_q/T. The experimental data on net-proton cumulants where provided by the STAR collaboration [6]. We found that the cumulant ratios χ_B^1/χ_B^2, χ_B^3/χ_B^1 and χ_B^3/χ_B^2 can be very well reproduced on this self-consistently defined freeze-out line, but the χ_B^4/χ_B^2 model calculations show the opposite behavior compared to the experimental data. From this we conclude that the available χ_B^4/χ_B^2 net-proton data cannot be understood as a signal of criticality in this current setup. In the future we plan to study the model parameter dependence of these results, as well as the effect of a repulsive vector interaction between quarks.

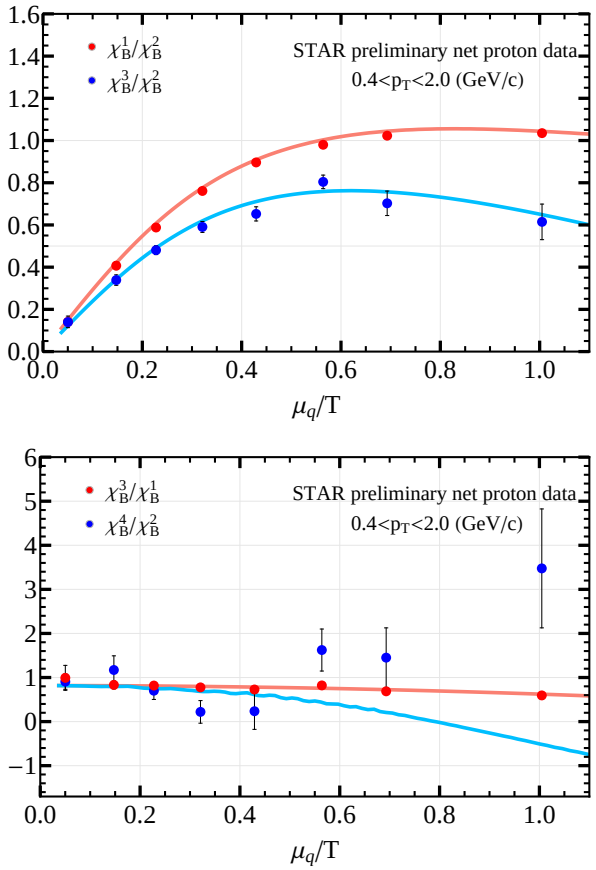

Figure 1: Top figure: χ_B^1/χ_B^2 (red) and χ_B^3/χ_B^2 (blue) plotted against μ_B/T. Bottom figure: χ_B^3/χ_B^1 (red) and χ_B^4/χ_B^2 (blue) plotted against μ_B/T.

References

[1] M. Stephanov, K. Rajagopal, E. V. Shuryak Phys. Rev. Lett. **81** 4816-4819 (1998)

[2] B.-J. Schaefer, J. M. Pawlowski, and J. Wambach, Phys. Rev. **D76**, 074023 (2007).

[3] C. Wetterich, Phys. Rev. **B301**, 90-94 (1993).

[4] A. Bazavov *et al*, Phys. Rev. Lett. **109** 192302 (2012).

[5] G. A. Almasi, B. Friman and K. Redlich, Quark Matter 2015 Proceedings (2015).

[6] X. Luo and the STAR Collaboration, **PoS CPOD2014** 019 (2015).

*The work of B.F. and K.R. was partly supported by the Extreme Matter Institute EMMI. K. R. also acknowledges partial supports of the Polish Science Foundation (NCN) under Maestro grant DEC-2013/10/A/ST2/00106, and the U.S. Department of Energy under Grant No. DE-FG02-05ER41367. G. A. acknowledges the support of the Hessian LOEWE initiative through the Helmholtz International Center for FAIR (HIC for FAIR).

† g.almasi@gsi.de

Particle number fluctuations in the van der Waals model*

V. Vovchenko[1,2,3,4], *D.V. Anchishkin*[1,5], *M.I. Gorenstein*[1,5], *and R. Poberezhnyuk*[1,5]

[1]FIAS, Frankfurt, Germany; [2]Goethe University, Frankfurt, Germany; [3]GSI, Darmstadt, Germany; [4]Taras Shevchenko University, Kiev, Ukraine; [5]BITP, Kiev, Ukraine

The van der Waals (VDW) equation of state is a simple and popular model to describe the pressure function in equilibrium systems of particles with both repulsive and attractive interactions. This equation predicts the existence of a first-order liquid-gas phase transition and contains a critical point. Two steps to extend the VDW equation and make it appropriate for new physical applications in high-energy physics are carried out: (i) the grand canonical ensemble (GCE) formulation [1] and (ii) the inclusion of the quantum statistics [2]. The former allows one to calculate the particle number fluctuations, in particular in the vicinity of the critical point, while the latter makes it possible to describe the nuclear matter as a van der Waals system of nucleons, which obey the Fermi-Dirac statistics.

For the nuclear matter, the VDW parameters a and b are fixed to reproduce the ground state properties. This results in $a \simeq 329$ MeV·fm^3 and $b \simeq 3.42$ fm^3 ($r_p \simeq 0.59$ fm). The model predicts a location of the critical point for the symmetric nuclear matter at temperature $T_c \simeq 19.7$ MeV and nucleon number density $n_c \simeq 0.07$ fm^{-3}.

The scaled variance $\omega[N]$, skewness $S\sigma$, and kurtosis $\kappa\sigma^2$ of particle number fluctuations are calculated for both the classical VDW equation [3] and for the nuclear matter [4]. They are depicted in Figs. 1 and 2. For the classical case we succeed to obtain the analytical expressions which have a universal form, i.e., they do not depend on particular values of the VDW parameters a and b. For the nuclear matter case we explicitly obtain the T-μ dependence of the fluctuations. In both cases the fluctuations measures show a very similar qualitative behavior: (i) they all diverge at the critical point, (ii) the crossover region of the phase diagram is characterized by the large values of the scaled variance, the almost zero skewness, and the significantly negative kurtosis and (iii) the rich structures of the skewness and kurtosis are observed in the wide region around the critical point; namely, they both may attain large positive or negative values.

The strongly intensive measures of particle number and energy fluctuations are also considered. Similarly to the cumulants of particle number fluctuations, they show a singular behavior in the vicinity of the critical point.

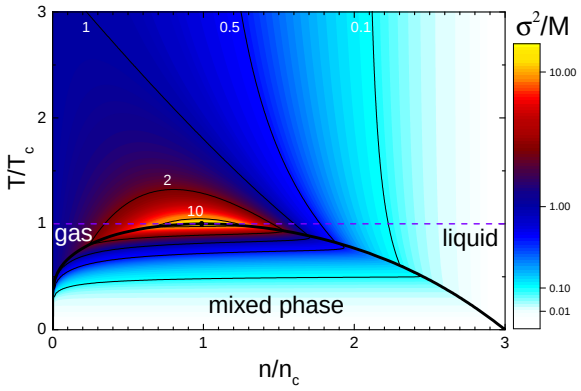

Figure 1: The temperature and density dependence of the scaled variance $\omega[N]$ of particle number fluctuations for the classical VDW equation.

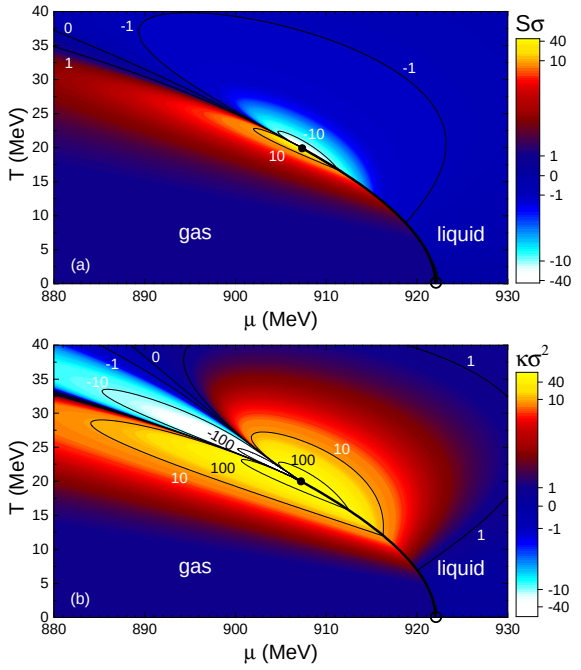

Figure 2: The (a) skewness $S\sigma$ and (b) kurtosis $\kappa\sigma^2$ calculated for the symmetric nuclear matter in (T, μ) coordinates within the VDW equation of state for fermions.

References

[1] V. Vovchenko, D. V. Anchishkin, and M. I. Gorenstein, J. Phys. A **48** (2015) 305001.

[2] V. Vovchenko, D. V. Anchishkin, and M. I. Gorenstein, Phys. Rev. C **91** (2015) 064314.

[3] V. Vovchenko, R. V. Poberezhnyuk, D. V. Anchishkin, and M. I. Gorenstein, J. Phys. A **49** (2016) 015003.

[4] V. Vovchenko, D. V. Anchishkin, M. I. Gorenstein, and R. V. Poberezhnyuk, Phys. Rev. C **92** (2015) 054901.

* Work supported by HIC for FAIR

DOI:10.15120/GR-2016-1

Excluded volumes and the thermodynamics of a hadron gas*

Pok Man Lo† [1], *Bengt Friman*[2], *and Krzysztof Redlich*[1]
[1]University of Wroclaw, Wrocław, Poland; [2]GSI, Darmstadt, Germany

Based on phenomenological nucleon-nucleon interactions, it is commonly assumed that all hadrons repel each other at short distances. In the equation of state of hot and dense strongly interacting matter, this is often implemented by introducing an excluded volume [1, 2, 3]. This leads to an equation of state similar to that of van der Waals for a non-ideal gas, where the particle eigenvolume, v_0, is a model parameter.

On the other hand, the S-matrix approach to thermodynamics provides a consistent framework for handling both attractive and repulsive interaction channels [4, 5]. Within this approach, the thermodynamic pressure is, to leading order in the relativistic virial expansion, determined by the relevant scattering phase shifts [4]. These may be obtained empirically from scattering experiments or computed within a microscopic theory or a phenomenological model.

In this project we study the effect of short-ranged repulsive forces on the thermodynamics of the $\pi N\Delta$ system using the two approaches. Within the excluded volume approximation, we follow Ref. [2], and employ a spherical eigenvolume v_0,

$$v_0 = \frac{16}{3}\pi r_0^3, \tag{1}$$

with $r_0 = 0.3\,\mathrm{fm}$ for all particle species.

In the S-matrix approach, we obtain the interaction contribution to the pressure of the $\pi\,N\,\Delta$ system using empirical P_{33} phase shifts [5]. To account for an additional repulsive interaction, we add a P-wave hard-core phase shift

$$\begin{aligned}\delta_{rc}(x = qa_S) &= \arctan\left(\frac{j_1(x)}{n_1(x)}\right)\\ &= \arctan\left(\frac{x - \tan x}{1 + x\tan x}\right),\end{aligned} \tag{2}$$

to the empirical one. Here $a_S = 2r_0 = 0.6\,\mathrm{fm}$ is the distance between the centers of two touching spheres of radius r_0.

In Fig. 1 we show the pressure obtained in the various approximation schemes, at vanishing baryon chemical potential. We note that the pressure of a free gas of pions, nucleons and Δ-resonances agrees quite well with that obtained in the S-matrix approach. However, when we add the short-range repulsion, we observe an appreciable difference in the temperature dependence of the pressure between the two approaches. The excluded volume approximation yields a much stronger effect than the S-matrix approach. This is partly due to the fact that in the S-matrix approach the repulsion acts only in the P-wave channel, where the effect of short-ranged interactions is suppressed by the angular momentum barrier.

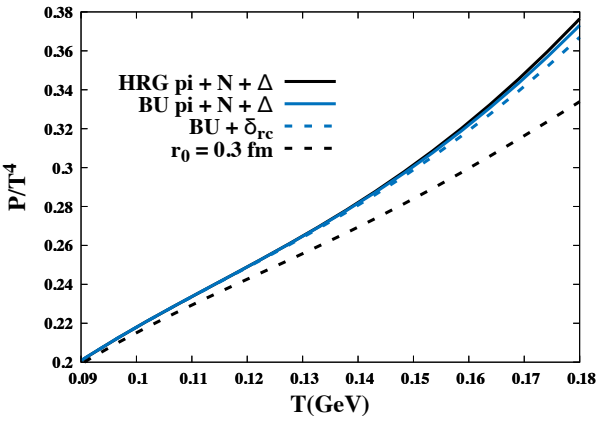

Figure 1: The pressure of the pion-nucleon-Delta system in the various schemes versus temperature at vanishing baryon chemical potential.

Finally, we point out that the introduction of an excluded volume between pions and nucleons in addition to the interaction that generates the Δ resonance distorts the phase shift in the P_{33} channel. As seen above, the effects of the interaction in the resonant P_{33} channel are well approximated by introducing a free gas of Δ resonances [4]. We conclude that the introduction of an excluded volume, at least in resonant channels, leads to an inconsistent description of the interaction contribution to the thermodynamics.

References

[1] D. H. Rischke, M. I. Gorenstein, H. Stoecker and W. Greiner, Z. Phys. C **51**, 485 (1991).

[2] A. Andronic, P. Braun-Munzinger, J. Stachel and M. Winn, Phys. Lett. B **718**, 80 (2012).

[3] K. Redlich and K. Zalewski, Phys. Rev. C **93**, no. 1, 014910 (2016).

[4] R. Dashen, S. K. Ma and H. J. Bernstein, Phys. Rev. **187**, 345 (1969).

[5] W. Weinhold, B. Friman and W. Nörenberg, Phys. Lett. B **433**, 236 (1998).

* Work supported in part by FIAS, EMMI, and Polish Science Foundation, under Maestro grant 2013/10/A/ST2/00106.

† pmlo@gsi.de

Generalizations of the excluded-volume mechanism*

S.Typel† [1]
[1]GSI, Darmstadt, Germany

The excluded-volume mechanism (EVM) is a simple means to incorporate a short-range repulsive interaction between particles in models for the equation of state (EoS) of strongly interacting matter. This approach is based on a geometric picture, introducing a finite volume for the particles, which effectively corresponds to a hard core interaction and leads to an stiffening of the EoS known, e.g., from the van-der-Waals EoS. The available volume $V_i = \Phi_i V$ for the motion of a particle i is reduced as compared to the total volume V of the system. In the conventional approach, the available-volume fraction Φ_i is a linear function of the particle densities. It approaches zero at some point and thus the particle i cannot appear any more. E.g., the EVM is used in EoS models for astrophysical applications in order to describe the dissolution of nuclear clusters with increasing density [1].

The standard EVM is generalized in Ref. [2] in several aspects. Any functional form of Φ_i is allowed and thus it is possible to consider both repulsive and attractive interactions in an effective way. The available-volume fraction can depend on vector and scalar particle number densities, which naturally appear in relativistic models. Thermodynamic consistency requires the appearance of rearrangement contributions in the scalar and vector potentials of the particles and thermodynamic quantities. The general form of these rearrangement terms was derived in Ref. [2] keeping the quasi-particle picture and standard thermodynamic definitions of densities. For classical Maxwell-Boltzmann statistics, the EVM can be formulated as a medium dependence of the particle degeneracy factors or as a particular temperature dependent mean-field potential of the particles. These two approaches are no longer equivalent if quantal Fermi-Dirac or Bose-Einstein statistics are considered. Changing from the classical to the quantal description in the rigid-sphere model, the consistency with the virial EoS at low densities demands to introduce an effective temperature dependence of the individual particle volume parameters. This effect is most important for small masses and low temperatures.

The standard and general forms of the EVM are applied in Ref. [2] to three different systems to exemplify the major effects. The supression of cluster formation with increasing total particle density is demonstrated for the simple case of a non-interacting neutron-proton-deuteron mixture. It is shown that the conventional choice of the excluded-volume fraction Φ_i causes a divergence of the system pressure at the dissolution point of the deuteron. Hence the construction of an EoS in such an approach requires to treat the phase transition from the phase with deuterons to the unclusterd phase.

Besides the phenomenological description of the suppression of particles with increasing density, such as nuclear clusters in the previous example, the removal of degrees of freedom with decreasing densities can be modeled in the generalized EVM using the formulation with density dependent effective degeneracy factors. In Ref. [2] the case of symmetric two-flavor quark matter is considered in a simple toy model assuming a dependence of the available-volume fractions on the total scalar density. With a particular choice of the Φ_i functions that vanish for low densities, the non-existence of quark degrees of freedom at low densities is generated with an increase of the effective quark masses close to the disappearance density due to the rearrangement terms in the scalar potentials. This is accompanied by a reduction of the system pressure similar as in simple bag models for the quark matter EoS. At high densities the usual Stefan-Boltzmann limit of a gas of light non-interacting quarks is obtained.

The generaizedl EVM is combined in Ref. [2] with a relativistic mean-field description of nuclear matter with density dependent meson-nucleon couplings in order to modify the stiffness of the EoS at densities above nuclear saturation. The specific choice of the excluded-volume fractions of the nucleons allows to keep the original parameterization of the model with a successful description of nuclear matter at subsaturation densities and of properties of finite nuclei respecting a number of constraints. A systematic variation of the Φ_i functions in this model and thus the stiffness of the EoS of hadronic matter is used in Ref. [3] in combination with an extended Nabu–Jona-Lasinio model for quark matter to study the consequences for the properties of compact stars. In particular the twin-star phenomenon was considered, i.e. the possibility for the existence of compact stars with identical masses but different radii with and without a quark matter phase in the core.

* Work supported by NAVI (VH-VI-417), NewCompStar (COST Action MP1304) and the Heisenberg-Landau program.

† s.typel@gsi.de

References

[1] H. Pais and S. Typel, "Comparison of equation of state models with different cluster dissolution mechanisms," to be published in the special-topics issue on Nuclear Particle Correlations and Cluster Physics, Int. J. Mod. Phys.

[2] S. Typel, Eur. Phys. J. A **52**, no. 1, 16 (2016).

[3] S. Benic, D. Blaschke, D. E. Alvarez-Castillo, T. Fischer and S. Typel, Astron. Astrophys. **577**, A40 (2015)

DOI:10.15120/GR-2016-1

Influence of the modeling of the eigenvolume corrections on the extraction of the chemical freeze-out properties*

V. Vovchenko[1,2,3] *and H. Stoecker*[1,2,4]

[1]FIAS, Frankfurt, Germany; [2]Goethe University, Frankfurt, Germany; [3]Taras Shevchenko University, Kiev, Ukraine; [4]GSI, Darmstadt, Germany

The hadron-resonance gas (HRG) model have been rather successfully used to extract the chemical freeze-out properties of matter created in heavy-ion collisions, by fitting the rich data on mean hadron multiplicities in various experiments. In most of these analyses, however, the short-range repulsive interactions between hadrons are either neglected, or it is assumed that the eigenvolumes of all hadrons are the same. In the latter case the eigenvolume correction factors essentially cancel out in the ratios of hadron yields and, thus, the extracted freeze-out parameters are the same as in the point-particle case.

In order to test the sensitivity of the modeling of the eigenvolume corrections in the multi-component hadron gas we employ the conventional HRG model with the Particle Data Group (PDG) hadron input and the hadron type dependent eigenvolume corrections to fit the ALICE hadron mid-rapidity yield data on the most central Pb+Pb collisions [1]. For the case of the point-like hadrons a well-known fit result of $T \sim 155$ MeV is reproduced. However, the situation changes if hadrons have different eigenvolumes. In the case when all mesons are taken to be point-like while all baryons have a hard-core radius of 0.3 fm the temperature dependence of the χ^2 has a broad minimum in the temperature range of $155 - 210$ MeV, with fit quality comparable to the $T \sim 155$ MeV minimum in the point-particle case (see Fig. 1). When we apply the eigenvolume corrections with the mass-proportional eigenvolume $v_i \sim m_i$, fixed to the particular proton hard-core radius r_p, we observe a second minimum in the temperature dependence of the χ^2, located at the significantly higher temperatures. For instance, at $r_p = 0.5$ fm the fit quality is better than in the point-particle HRG case in a very wide temperature range of $170 - 320$ MeV, with the global minimum located at $T \simeq 275$ MeV and $\chi^2/N_{\rm dof} \simeq 1.5$. These results imply that the extracted value of the chemical freeze-out temperature is very sensitive to the modeling of the short-range repulsion between hadrons, and that it cannot be extracted with high reliability from the LHC hadron yield data.

We also perform a similar analysis [2] at the finite (baryo)chemical potential by considering the data on hadron yields in central Pb+Pb collisions of the NA49 collaboration in the energy range $\sqrt{s_{\rm NN}} = 6.3 - 17.3$ GeV. For this analysis we additionally consider an alternative formulation of the multi-component eigenvolume model from Ref. [3], referred to as the "cross-terms" model. When we apply the same eigenvolume corrections with the mass-proportional eigenvolume $v_i \sim m_i$, fixed to different values of the proton hard-core radius of $r_p = 0.4 - 0.6$ fm, we obtain a noticeably better description of the data at all five collision energies in very wide high-T, high-μ_B regions within both considered models as shown in Fig. 2 for $r_p = 0.5$ fm. The results show that, similarly to the temperature, the determination of the chemical potential at freeze-out is very model-dependent. On the other hand, we find that the entropy per baryon contour lines approximately correspond to the χ^2 minimum valleys (solid lines in Fig. 2), and are significantly less model-dependent.

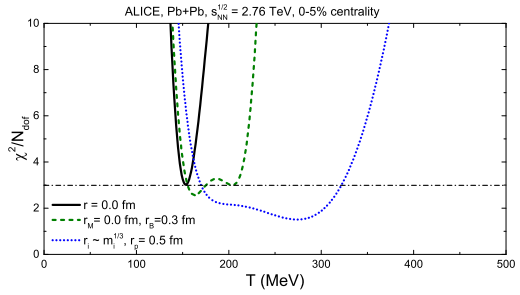

Figure 1: The temperature dependence of $\chi^2/N_{\rm dof}$ of fit to ALICE data on hadron yields in 0-5% most central Pb+Pb collisions at 2.76 TeV within the three different parametrizations of hadron eigenvolumes.

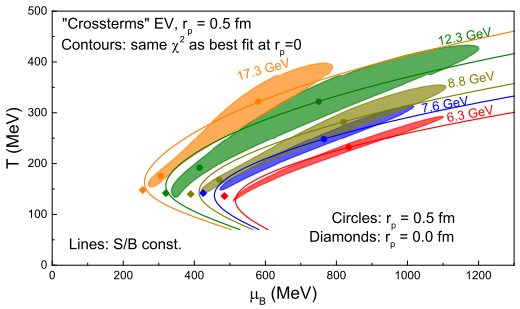

Figure 2: Regions in the T-μ_B plane where the eigenvolume HRG model with mass-proportional eigenvolume yields a better fit to the NA49 data than the point-particle HRG model.

References

[1] V. Vovchenko and H. Stoecker, arXiv:1512.08046 [hep-ph].

[2] V. Vovchenko and H. Stoecker, in preparation.

[3] M. I. Gorenstein, A. P. Kostyuk, and Y. D. Krivenko, J. Phys. G **25** (1999) L75.

* Work supported by HIC for FAIR and HGS-HIRe

Hadron resonance gas with eigenvolume corrections and Hagedorn mass spectrum versus lattice QCD*

V. Vovchenko[1,2,3,4], *D.V. Anchishkin*[4,5], *M.I. Gorenstein*[1,5], *and H. Stoecker*[1,2,3]

[1]FIAS, Frankfurt, Germany; [2]Goethe University, Frankfurt, Germany; [3]GSI, Darmstadt, Germany; [4]Taras Shevchenko University, Kiev, Ukraine; [5]BITP, Kiev, Ukraine

The lattice QCD results for the pressure and energy density at zero baryonic chemical potential of the Wuppertal-Budapest collaboration [1] are analyzed within the hadron resonance gas (HRG) model. Two popular extensions of the ideal HRG are considered: the excluded volume model, which describes a repulsion of hadrons at short distances, and the Hagedorn model with an exponential mass spectrum. We consider two different strategies for our analysis.

In the first analysis [2] we consider only the small temperatures $T < 155$ MeV below the crossover-type transition. There we assume that all hadrons, including the Hagedorn states, have identical eigenvolumes, characterized by the hard-core radius r. This effect is modeled by the excluded-volume (EV) model [3]. For the Hagedorn mass spectrum we use the parameterization $\rho(m) = C\,\theta(m - M_0)\,(m^2 + M_0^2)^{-a}\,\exp(m/T_H)$ with $M_0 = 2$ GeV, $T_H = 160$ MeV, $m_0 = 0.5$ GeV, and $a = 5/4$. Normalization parameter C is fixed by fitting lattice data.

Results of the calculations for the temperature dependence of the scaled pressure and energy density for different values of r are depicted in Fig. 1. The excluded-volume corrections decrease both the pressure and the energy density while the inclusion of the Hagedorn mass spectrum leads to their enhancement. If both the excluded-volume corrections and the Hagedorn mass spectrum are considered simultaneously we find that the lattice data can be well fitted for $r \lesssim 0.4$ fm and $C \lesssim 0.2$ GeV$^{3/2}$ with $\chi^2/N_{\rm dof} \lesssim 1$. These results indicate that neither the excluded-volume parameters neither nor the Hagedorn mass spectrum can be extracted in a definitive way from the lattice data.

In the second analysis a different strategy is adopted: instead of considering a limited temperature range we rather simply analyze how far can the HRG alone go in describing the available lattice data. The commonly used point-particle HRG can describe the lattice data up to $T \sim 150$ MeV but then significantly overshoots the data due to the increasing number of hadronic degrees of freedon and shows signs of the Hagedorn divergence. In the present analysis we consider a HRG with the conventional PDG hadron input and the mass-proportional eigenvolumes $v_i = m_i/\varepsilon_0$. We do not consider the Hagedorn states which are suppressed due to their large eigenvolumes. In Fig. 2 the temperature dependence of the scaled pressure and energy density for the point-particle HRG and for the EV-HRG with $\varepsilon_0 = 11.4$ GeV/fm^3 is depicted. It is seen that the inclusion of the eigenvolume correction leads to a significant improvement of the aggreement between HRG and the lattice QCD: the data is described fairly well by the EV-HRG up to $T = 250$ MeV. This gives an alternative possibility to interpret the lattice results above $T = 150$ MeV, which remains a rather challenging task.

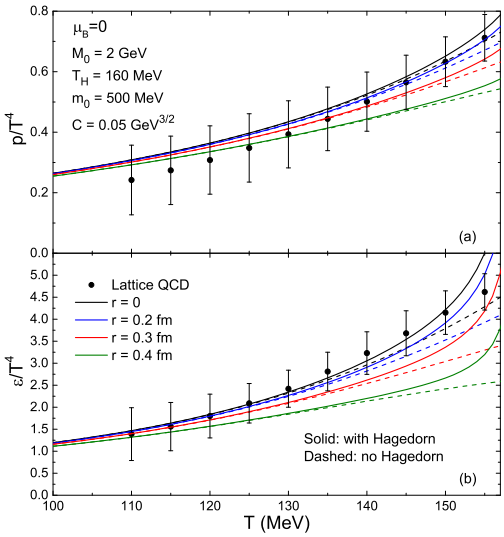

Figure 1: Results of the EV-HRG + Hagedorn model for different values of r compared to the lattice data for (a) p/T^4 and (b) ε/T^4.

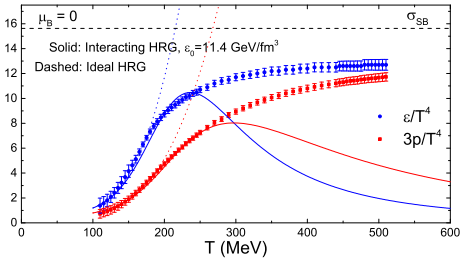

Figure 2: Results of the EV-HRG model for p/T^4 and ε/T^4 employing the mass-proportional eigenvolumes.

References

[1] S. Borsanyi et al., Phys. Lett. B **730**, (2014) 99.

[2] V. Vovchenko, D. V. Anchishkin, and M. I. Gorenstein, Phys. Rev. C **91** (2015) 024905.

[3] D. H. Rischke, M. I. Gorenstein, H. Stoecker and W. Greiner, Z. Phys. C **51** (1991) 485.

* Work supported by HIC for FAIR

DOI:10.15120/GR-2016-1

Equation of state of a hadronic gas with a hard-core interaction*

L.M. Satarov[†1,2], *K.A. Bugaev*[1,3], *and I.N. Mishustin*[1,2]

[1]FIAS, Frankfurt am Main, Germany; [2]Kurchatov Institute, Moscow, Russia; [3]BITP, Kiev, Ukraine

Realistic calculations of the equation of state (EoS) of a hot and dense hadronic matter should take into account finite sizes of hadrons. We investigate [1] thermodynamic properties of a hadronic gas with a hard sphere interaction (HSI) of particles. In the Boltzmann approximation pressure of a one-component matter can be written as $P = nTZ(n)$ where T and n are the temperature and rest-frame density of hadrons, respectively. The compressibility factor Z is a function of the packing fraction $\eta = nv$ where v is a hard-core volume of a single hadron. One can use the same expression for multi-component systems if all particles have equal hard-core radii. In this case n equals the total density of all species.

We demonstrate that the van-der-Waals parametrization used in the excluded volume models [2] (EVM), $Z_{\rm EVM} = (1-4\eta)^{-1}$, strongly overestimates pressure at $\eta \gtrsim 0.2$. On the other hand, the Carnahan-Starling approximation [3] (CSA), $Z_{\rm CSA} = (1+\eta+\eta^2-\eta^3)(1-\eta)^{-3}$, agrees well with numerical calculations of Z in a wider domain $\eta \lesssim 0.5$. Note that the relative difference between the EVM and CSA diminishes at $\eta \to 0$. Up to now the attempts to include finite size effects in hydrodynamic and statistical models of heavy-ion collisions were based mostly on the excluded volume approach.

We consider first the EoS of the chemically equilibrated $N+\Delta+\pi$ mixture, assuming that hadronic hard-core radii are equal: $R_N = R_\Delta = R_\pi$. For comparison, the limiting case of point-like pions ($R_N = R_\Delta, R_\pi = 0$) are studied additionally. In the second case one can write the total pressure as $P = T\left[n_\pi^{\rm id}(T) + n_B Z(n_B)\right]$, where $n_\pi^{\rm id}(T)$ is the equilibrium density of the ideal gas of pions and $n_B = n_N + n_\Delta$. Note, that in this case the pion to baryon ratio is larger than in the ideal $N+\Delta+\pi$ gas (at the the same temperature and baryon chemical potential).

The results of the sound velocity calculations are shown in Fig. 1a for the case $T = 150$ MeV. One can see that the CSA predicts a softer EoS (with smaller sound velocity at given temperature and baryon density) as compared to the EVM. Moreover, the acausal states ($c_s > 1$) in the CSA are shifted to very high baryon densities, which presumably correspond to the deconfinement phase transition. Comparison of the solid and dashed lines in Fig. 1a shows that the transition to point-like pions reduces the c_s values. We have checked that this effect becomes stronger at higher temperatures.

Additional calculations are made to consider the EoS of an extended set of baryons, antibaryons and mesons with masses $m < 2$ GeV. In this study we apply the zero-width approximation and assume equal hard-core radii for all hadrons. According to Fig. 1b, inclusion of heavier hadrons and antibaryons gives rise to smaller sound velocities as compared to the $N+\Delta+\pi$ system.

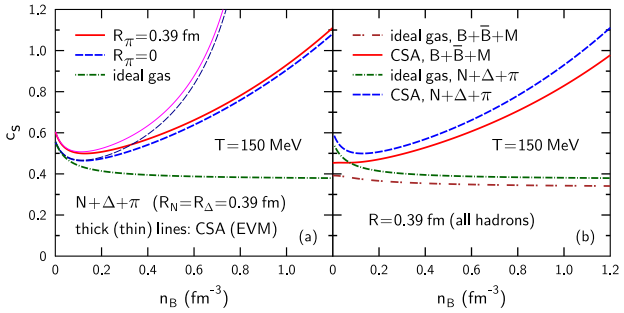

Figure 1: Sound velocity of hadronic matter at temperature $T = 150$ MeV as a function of net baryon density. Panel (a) shows the results for chemically equilibrated system, composed of nucleons (N), Δ-isobars and pions (π). The solid lines correspond to equal sizes of baryons and π-mesons, the dashed lines are calculated in the limit of point-like pions. The solid line in panel (b) corresponds to extended set of (anti)baryons and mesons with equal hard-core radii $R = 0.39$ fm.

Finally, we estimate the corrections to the EoS due to the quantum-statistical effects. Our conclusion is that they are small unless the baryon chemical potential exceeds the nucleon mass and temperature is below 100 MeV. Therefore, these corrections can be safely neglected under conditions expected in relativistic heavy ion collisions.

References

[1] L.M. Satarov, K.A. Bugaev, I.N. Mishustin, Phys. Rev. C 91 (2015) 055203

[2] D.H. Rischke, M.I. Gorenstein, H. Stöcker, W. Greiner, Z. Phys. C 51 (1991) 485

[3] N.F. Carnahan, K.E. Starling, J. Chem. Phys. 51 (1969) 635

* Work supported by HIC4FAIR

† satarov@fias.uni-frankfurt.de

Excluded volume corrections in the multi-component hadron gas within the thermodynamic mean-field approach*

D. Anchishkin[1,2] *and V. Vovchenko*[2,3,4,5]

[1]BITP, Kiev, Ukraine; [2]Taras Shevchenko University, Kiev, Ukraine; [3]FIAS, Frankfurt, Germany; [4]Goethe University, Frankfurt, Germany; [5]GSI, Darmstadt, Germany

A mean-field approach for the thermodynamic description of interacting multi-component gas in the grand canonical ensemble is formulated. The approach is based on the partition of the canonical ensemble (CE) density of free energy into "free" (ideal gas) and interacting parts as $\phi(n,T) = \phi_0(n,T) + \phi_{\rm int}(n,T)$. It follows that the system pressure can then be partitioned as [1]

$$P(n,T) = P^{\rm id}(n,T) + P^{\rm ex}(n,T) \qquad (1)$$

into sum of the ideal gas pressure and the *excess* pressure $P^{\rm ex}$, which appears in the presence of interactions. It follows basic from thermodynamic identities that in the grand canonical ensemble (GCE) the particle density $n(T,\mu)$ in the interacting system is determined as the solution to the following transcendental equation

$$n(T,\mu) = n^{\rm id}[T, \mu - U(n,T)], \qquad (2)$$

where $U(n,T)$ is the *thermodynamic mean-field*, and is related to the excess pressure by the condition of thermodynamic consistency as $n\,\partial U/\partial n = \partial P^{\rm ex}/\partial n$. These relations can be straightforwardly generalized to the multi-component case [2].

The obtained formulation is especially convenient for transforming classical equations of state given in the CE in form $P = P(n,T)$ to the GCE. Indeed, the excess pressure is determined in a straightforward way as $P^{\rm ex} = P - nT$, while the mean-field $U(n,T)$ can then be calculated from thermodynamic consistency relation. Solving the transcendental equation (2) gives the GCE particle density Finally, substituting $n(T,\mu)$ into Eq. (1) one obtains the system pressure as a function of its natural variables T and μ.

As an example we consider the GCE formulation of different classical excluded-volume models In particular we are focusing on the simple van der Waals parameterization, $P = nT/(1-4\eta)$, and on the Carnahan-Starling model

$$P = Tn\,\frac{1+\eta+\eta^2-\eta^3}{(1-\eta)^3}\,. \qquad (3)$$

Here $\eta = bn/4$ is the packing fraction. Compared to the van der Waals parameterization, the Carnahan-Starling model can describe the Monte Carlo data [3] on the equation of state for hard spheres for much higher values of the packing fraction, as demonstrated in Fig. 1.

The mean-field approach is used to model the hard-core repulsion in hadron-resonance gas model used for description of chemical freeze-out in heavy-ion collisions. We calculate the collision energy dependence of several quantities, in particular the net-baryon density, for different values of hard-core hadron radius and for different EV models. It is shown that the precision of the commonly used van der Waals excluded-volume model is sufficient for realistic values of hard-core hadron radius ($r \lesssim 0.5$ fm). We note, however, that the situation may change if one considers hadrons of different radii, which may push the freeze-out temperature upwards [4].

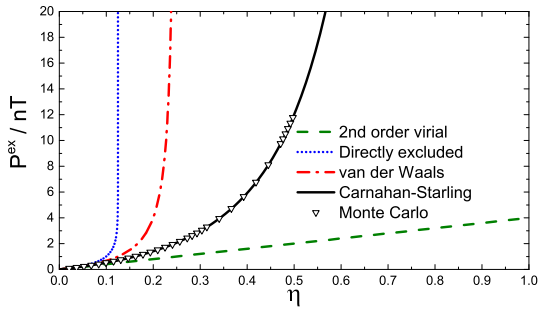

Figure 1: The dependence of the quantity $P^{\rm ex}/nT$ on the packing fraction η for four different excluded-volume models. Monte Carlo data from Ref. [3] is depicted by triangles.

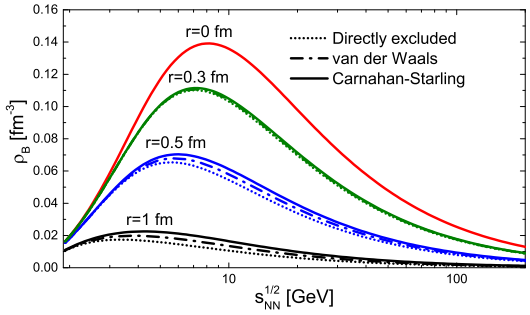

Figure 2: Energy dependence of the net-baryon density at chemical freeze-out calculated using three different excluded-volume models.

References

[1] D. Anchishkin, Sov. Phys. JETP **75** (1992) 195; D. Anchishkin and E. Suhonen, Nucl. Phys. A **586** (1995) 734.

[2] D. Anchishkin and V. Vovchenko, J. Phys. G **42** (2015) 105102.

[3] G.-W. Wu and R.J. Sadus, AIChE J. **51**, (2005) 309.

[4] V. Vovchenko and H. Stoecker, arXiv:1512.08046 [hep-ph].

* Work supported by HIC for FAIR

DOI:10.15120/GR-2016-1

Second-order dissipative fluid dynamics at finite chemical potential*

Amaresh Jaiswal† [1], *Bengt Friman*[1], *and Krzysztof Redlich*[1,2]
[1]GSI, Darmstadt, Germany; [2]University of Wroclaw, Wroclaw, Poland

High-energy heavy ion collisions create strongly interacting matter under extreme conditions of high temperature and density. At such conditions, quarks and gluons are deconfined to form a new state of matter, the quark-gluon plasma (QGP), which behaves as a strongly coupled fluid having the smallest shear viscosity-to-entropy density ratio, η/s [1, 2]. Relativistic dissipative fluid dynamics has been applied quite successfully to describe the space-time evolution of the QGP and estimate its transport coefficients [1]. However, relativistic generalization of the Navier-Stokes theory suffer from acausality and numerical instability. Consistent formulation of a causal theory of relativistic dissipative fluid dynamics is therefore important and is currently an active research area [3, 4, 5].

Fluid dynamic equations are the conservation equations for energy-momentum tensor, $\partial_\mu T^{\mu\nu} = 0$, and particle four-current, $\partial_\mu N^\mu = 0$. In the case of massless partons (no bulk viscosity), the energy-momentum tensor and the net-quark current can be written as

$$T^{\mu\nu} = \epsilon u^\mu u^\nu - P\Delta^{\mu\nu} + \pi^{\mu\nu}, \quad N^\mu = n u^\mu + n^\mu, \quad (1)$$

where ϵ, P, and n are the energy density, pressure, and the net quark number density. The projection operator $\Delta^{\mu\nu} = g^{\mu\nu} - u^\mu u^\nu$ is orthogonal to the fluid four-velocity u^μ defined in the Landau frame: $T^{\mu\nu}u_\nu = \epsilon u^\mu$. The shear stress tensor, $\pi^{\mu\nu}$, and the particle diffusion current, n^μ, are the dissipative quantities.

Within the framework of kinetic theory, we obtain the relaxation equations for $\pi^{\mu\nu}$ and n^μ as [5]

$$\dot{\pi}^{\langle\mu\nu\rangle} + \frac{\pi^{\mu\nu}}{\tau_\pi} = 2\beta_\pi\sigma^{\mu\nu} + 2\pi_\gamma^{\langle\mu}\omega^{\nu\rangle\gamma} - \frac{4}{3}\pi^{\mu\nu}\theta - \frac{10}{7}\pi_\gamma^{\langle\mu}\sigma^{\nu\rangle\gamma}, \quad (2)$$

$$\dot{n}^{\langle\mu\rangle} + \frac{n^\mu}{\tau_n} = \beta_n\nabla^\mu\alpha - n_\nu\omega^{\nu\mu} - n^\mu\theta - \frac{9}{5}n_\nu\sigma^{\nu\mu}. \quad (3)$$

Here τ_π and τ_n are the relaxation times corresponding to the dissipative quantities, $\sigma^{\mu\nu}$ is the velocity stress tensor, $\omega^{\mu\nu}$ is the vorticity tensor and θ is the expansion scalar. The coefficients β_π and β_n are obtained as [5]

$$\beta_\pi = \frac{\epsilon + P}{5}, \quad \beta_n = \frac{\pi^2 + 3\alpha^2}{3\alpha\,(\pi^2 + \alpha^2)}\,n - \frac{n^2\,T}{\epsilon + P}, \quad (4)$$

where $\alpha = \mu/T$ is the ratio of quark chemical potential to temperature.

*Work supported in part by FIAS, EMMI, and the Polish Science Foundation, under Maestro grant DEC-2013/10/A/ST2/00106.

† a.k.jaiswal@gsi.de

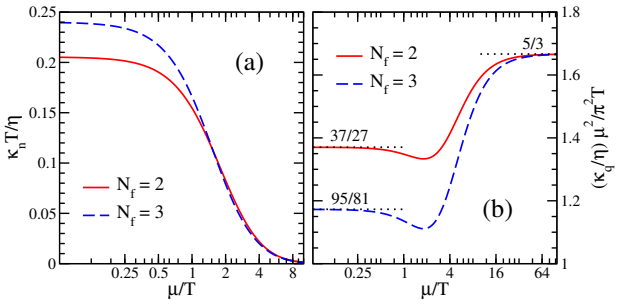

Figure 1: (a): The ratio of charge conductivity to shear viscosity scaled by the temperature, $\kappa_n T/\eta$, and (b): The ratio of thermal conductivity to shear viscosity, κ_q/η, scaled by the factor $\mu^2/\pi^2 T$, for two flavor (solid line) and three flavor (dashed line) massless quarks, plotted against μ/T.

The dimensionless ratio $\kappa_n T/\eta = \beta_n T/\beta_\pi$ is a measure of the relative importance of the charge conductivity and the shear viscosity. In Fig. 1 (a), we observe that while $\kappa_n T/\eta$ is almost constant for small μ/T, it drops rapidly for larger values indicating that the conductivity of the QGP is small relative to the shear viscosity at low temperature and high density. Another interesting quantity is the ratio of thermal conductivity to shear viscosity $\kappa_q/\eta = \left(\frac{\epsilon+P}{n\,T}\right)^2(\beta_n/\beta_\pi)$, which in the limit of both small and large μ/T reduces to $\kappa_q/\eta = C\,\pi^2\,T/\mu^2$; see Fig. 1 (b). This behaviour is typical to that of a strongly coupled system [6]. We conclude that the behaviour of transport coefficients, obtained within a simple kinetic theory model, shows intriguig similarity to that of a conformal fluid in the strong coupling regime.

References

[1] U. Heinz and R. Snellings, Ann. Rev. Nucl. Part. Sci. **63**, 123 (2013).

[2] R. S. Bhalerao, A. Jaiswal and S. Pal, Phys. Rev. C **92**, 014903 (2015).

[3] C. Chattopadhyay, A. Jaiswal, S. Pal and R. Ryblewski, Phys. Rev. C **91**, 024917 (2015).

[4] W. Florkowski, A. Jaiswal, E. Maksymiuk, R. Ryblewski and M. Strickland, Phys. Rev. C **91**, 054907 (2015).

[5] A. Jaiswal, B. Friman and K. Redlich, Phys. Lett. B **751**, 548 (2015).

[6] D. T. Son and A. O. Starinets, JHEP **0603**, 052 (2006).

Bulk and shear viscosities of a confining gluon plasma *

Wojciech Florkowski[1], *Radoslaw Ryblewski*[1], *Nan Su*[†2], *and Konrad Tywoniuk*[3]

[1]The H. Niewodniczański Institute of Nuclear Physics, Polish Academy of Sciences, PL-31342 Kraków, Poland;
[2]Frankfurt Institute for Advanced Studies, Goethe-Universität Frankfurt, D-60438 Frankfurt am Main, Germany;
[3]Theory Devision, CERN, CH-1211 Geneva 23, Switzerland

Introduction

Transport coefficients, such as bulk (ζ) and shear (η) viscosities, characterize crucial transport properties of the quark-gluon plasma (QGP) studied in ultra-relativistic heavy-ion collision experiments currently carried out at RHIC@BNL and LHC@CERN as well as the forthcoming one at FAIR@GSI. The strongly coupled nature of the QGP indicates a tiny η, while the existence of the QCD transition indicates an increasing ζ near the transition region due to the breaking of conformal symmetry, and these have posed critical challenges for the theory community since the launch of the heavy-ion program. Here we review the results of ζ and η from a kinetic approach inspired by the Gribov-Zwanziger (GZ) quantization [1, 2].

Gribov dispersion relation

The GZ quantization is an improvement over the conventional Faddeev-Popov quantization in the infrared (IR) region. As a result of the GZ qauntization, an IR scale $\gamma_{\rm G}$ named the Gribov parameter is generated and the gluon dispersion relation in the Coulomb gauge consequently reads

$$E(\boldsymbol{k}) = \sqrt{\boldsymbol{k}^2 + \frac{\gamma_{\rm G}^4}{\boldsymbol{k}^2}}\,, \tag{1}$$

where $\boldsymbol{k}$ is the three-momentum of a gluon. It is straightforward to see $E(\boldsymbol{k}) \to \infty$ as $\boldsymbol{k} \to 0$ that indicates the suppression of the IR phase space. The resulting gluon plasma is thus confining in the IR.

Viscosities of a confining gluon plasma

In order to apply hydrodynamical considerations, we first rewrite Eq. (1) in the Lorentz covariant form, $E(k\cdot u) = \sqrt{(k\cdot u)^2 + \gamma_{\rm G}^4/(k\cdot u)^2}$, where $k^0 = |\boldsymbol{k}|$, and u^μ is the four-velocity of the rest frame. For the calculation of transport coefficients, without loss of generality, we may impose the Bjorken symmetry of the system. Considering small perturbations around the equilibrium distribution function, $f = f_{\rm GZ} + \delta f$ where $f_{\rm GZ} = \{\exp[\gamma_{\rm G}\sqrt{y^2+y^{-2}}/T] - 1\}^{-1}$, and making use of the first-order viscous hydrodynamical expressions for bulk and shear viscous pressure corrections, we find the following expressions in the relaxation time approximation (with c_s being the speed of sound, g_0 being the degeneracy factor, and $\tau_{\rm rel}$ being the relaxation time.).

Bulk viscosity ζ

$$\zeta = \frac{g_0\gamma_{\rm G}^5}{3\pi^2}\frac{\tau_{\rm rel}}{T}\int_0^\infty {\rm d}y\,\left[c_s^2 - \frac{1}{3}\frac{y^4-1}{y^4+1}\right] f_{\rm GZ}(1+f_{\rm GZ})\,. \tag{2}$$

Shear viscosity η

$$\eta = \frac{g_0\gamma_{\rm G}^5}{30\pi^2}\frac{\tau_{\rm rel}}{T}\int_0^\infty {\rm d}y\,\frac{\left(y^4-1\right)^2}{y^4+1} f_{\rm GZ}(1+f_{\rm GZ})\,. \tag{3}$$

ζ/η scaling

One interesting finding in our study is about the ratio ζ/η in the relaxation time approximation that reads

$$\frac{\zeta}{\eta} = \kappa_{\rm GZ}\left(\frac{1}{3} - c_s^2\right)\,, \tag{4}$$

where $\kappa_{\rm GZ} = 5/2$. This is in line with the predictions of strongly coupled theories based on the gauge-gravity duality and in contrast to the perturbative QCD predictions $\zeta/\eta \propto \left(1/3 - c_s^2\right)^2$. As a comparison, the same ratio of a massive Bose-Einstein plasma reads

$$\frac{\zeta}{\eta} = \kappa_{\rm BE}\left(\frac{1}{3} - c_s^2\right)^{3/2}\,, \tag{5}$$

where $\kappa_{\rm BE} = 3\sqrt{15}/2$. Our exploratory study has shown interesting features of a confining gluon plasma inspired by the GZ quantization that may be in line with the expectation of a strongly coupled plasma.

References

[1] W. Florkowski, R. Ryblewski, N. Su and K. Tywoniuk, "Bulk viscosity in a plasma of Gribov-Zwanziger gluons", arXiv:1504.03176 [hep-ph].

[2] W. Florkowski, R. Ryblewski, N. Su and K. Tywoniuk, "Transport coefficients of the Gribov-Zwanziger plasma", arXiv:1509.01242 [hep-ph].

* Work supported in part by GSI and HIC4FAIR.

† nansu@fias.uni-frankfurt.de

DOI:10.15120/GR-2016-1

Entropy production in chemically nonequilibrium quark-gluon plasma created in central Pb+Pb collisions at LHC energies*

V. Vovchenko[1,2,3], *M.I. Gorenstein*[1,4], *L.M. Satarov*[1,5], *I.N. Mishustin*[1,5], *L.P. Csernai*[6], *I. Kisel*[1,2], *and H. Stoecker*[1,2,7]

[1]FIAS, Frankfurt, Germany; [2]Goethe University, Frankfurt, Germany; [3]Taras Shevchenko University, Kiev, Ukraine; [4]BITP, Kiev, Ukraine; [5]Kurchatov Institute, Moscow, Russia; [6]IPT, Bergen, Norway; [7]GSI, Darmstadt, Germany

The evolution of chemically nonequilibrium quark-gluon plasma (QGP) created in central Pb+Pb collisions at LHC is described [1,2] by the Bjorken-like ideal hydrodynamics with the time-dependent quark fugacity λ. It is assumed that initially the deconfined matter consists mostly of gluons (i.e. $\lambda \simeq 0$), but quarks and antiquarks are produced at later times. We use the explicit parametrization for fugacity, $\lambda(\tau) = 1 - \exp\left(\frac{\tau_0-\tau}{\tau_*}\right)$, where τ is the proper time, τ_* is the quark chemical equilibration time, τ_0 is the initial time of hydro evolution. The chemically equilibrium scenario ($\lambda = 1$) corresponds to the limit $\tau_* \to 0$.

The pressure (P) and energy density (ε) of undersaturated quark-gluon plasma (uQGP) are found by considering it as an ideal gas of massless partons. We get the relations $\varepsilon = 3P = \frac{\pi^2}{60}\,(32 + 21 N_f \lambda)\, T^4$, where T is temperature and N_f is the number of quark flavors. The corresponding expression for the entropy density is $s \simeq \frac{32\pi^2}{45} T^3\,[1 + N_f \lambda (0.66 - 0.16 \ln \lambda)]$. In the case of a purely central collision of equal nuclei, one can estimate the total entropy of created matter per unit space-time rapidity as $dS(\tau)/d\eta = \pi R^2 s \tau$ where R is the geometrical radius of initial nuclei. In our calculations we fix the value of $dS/d\eta$ at the decoupling (freeze-out) temperature $T_f = 155$ MeV from the observed charged pion multiplicity at midrapidity.

In the case of ideal uQGP, the Bjorken hydrodynamics leads to the relation $\varepsilon \propto \tau^{-4/3}$. Using further the above expressions for ε and s, one can show that temperature (entropy density) drops with τ faster (slower) as compared to the equilibrium QGP, where $T \propto \tau^{-1/3}$ and $s \propto \tau^{-1}$. The calculation results for T and $dS/d\eta$ are shown in Figs. 1a, b for different values of τ_*. One can see that deviations from the equilibrium scenario are most significant at early times $\tau \lesssim \tau_*$. Higher temperatures of uQGP follow from a lower number of degrees of freedom as compared to chemical equilibrium.

According to Fig. 1b, the entropy of uQGP increases gradually with time and about 25% of its final value is generated during the hydrodynamic expansion. The total amount of the produced entropy changes weakly with the variation of τ_*. Note that this effect is present in ideal hydrodynamics and occurs due to increasing number of degrees of freedom in deconfined matter. This is different from the entropy growth due to dissipative processes in viscous fluid dynamics.

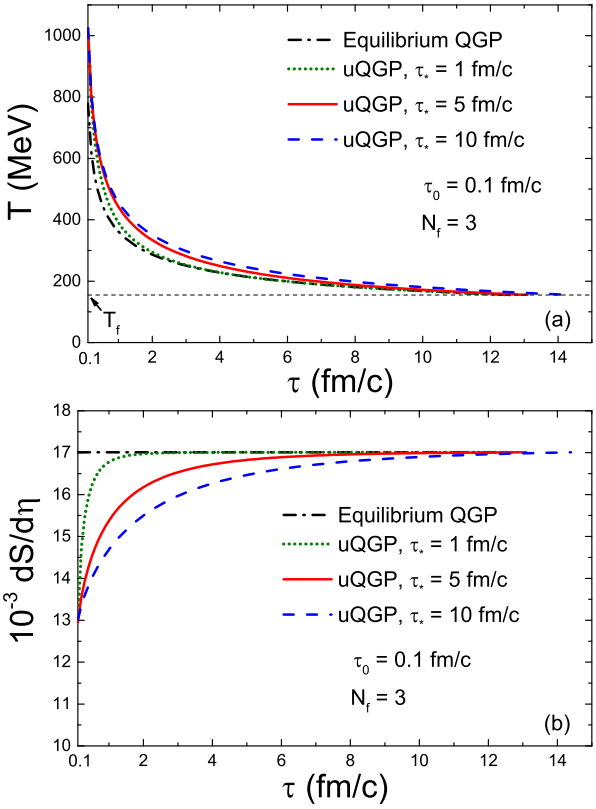

Figure 1: Temperature (a) and entropy per unit space-time rapidity (b) as functions of the proper time in a purely central Pb+Pb collision at $\sqrt{s_{\rm NN}} = 2.76$ TeV. Different lines are calculated for different values of quark equilibration time τ_*. The horizontal line in (a) corresponds to the decoupling temperature.

Our calculations show that the (anti)quark fugacity remains smaller than unity even at the hadronization stage. It is natural to assume that this will result in suppressed (anti)baryon-to-meson ratios. Such a suppression has been recently observed [3] at LHC energies.

References

[1] H. Stöcker *et al.*, Astron. Nachr. 336 (2015) 744

[2] V. Vovchenko, M.I. Gorenstein, L.M. Satarov, I.N. Mishustin, L.P. Csernai, I. Kisel, and H. Stöcker, Phys. Rev. C 93 (2016) 014906; arXiv: 1510.01235 [hep-ph]

[3] B. Abelev *et al.* (ALICE Collaboration), Phys. Rev. C 88 (2013) 044910

* Work supported by HIC for FAIR and HGS-HIRe

Consequences of an initial gluon overpopulation in heavy ion collisions*

K. Zhou[1,3] *and H. Stoecker*[1,2,3]

[1]Frankfurt Institute for Advanced Studies, D-60438 Frankfurt am Main, Germany; [2]GSI Helmholtzzentrum für Schwerionenforschung GmbH, D-64291 Darmstadt, Germany; [3]Institut für Theoretische Physik, Goethe Universität Frankfurt, D-60438 Frankfurt Main, Germany

The pre-equilibrium evolution in heavy ion collisions is complicated but important for our undertanding of the hot and dense QCD matter formed there. To date, it's belived that in this early stage there is a rather dense system of gluons emerging from the initially quark-free color glass condensate, CGC, through a strong glasma field stage into isotropization till time scale $\sim 1/Q_s$ (Q_s is the saturation scale). The CGC model even predicts that this early gluonic matter might be overpopulated thus containing more gluons than those a "simple" Bose-Einstein distribution can accommodate when the system is weakly coupled.

We discuss here consequences of this initial highly occupied gluonic matter: gluon BEC (Bose-Einstein condensate) formation and a pure gluo scenario for the system's dynamic evolution.

Since the overpopulation, it's argued that dynamically the emergence of a gluon BEC (at least transiently) can help reconciling the excessive gluons [1]. But for now it's still unclear how this happens from realistic simulation for heavy ion collisions.

Just being suitable for this topic, BAMPS [2] is a well developed and tested parton cascade aiming at understanding the early stage evolution in heavy ion collisions. By correctly implementing the quantum statistics for boson interaction into cascade simulation in BAMPS, we indeed observed that the gluon BEC emerge and grow kinetically (see Figure. 1 (a)) under an overpopulated inital condition provided the elastic collisions are dominant[3]. It's the first study to show the gluon BEC using parton cascade simulation for relativistic system (massless gluon). We found that during the thermalization process, there's a continuous increase of soft mode gluons being followed by a subsequent decrease to approach equilibrium distribution while the condensation occurs. The times for the completion of the gluon condensation and of the entropy production are found to scale inversly with the energy density.

The gluon dominance also means less quarks in the very initial stage, and many transport simulations[3, 4] show that only very few soft quarks are present during the subsequent pre-equilibrium evolution, because compared to the growth of soft gluon population, the quark production is relatively slow. See Figure. 1 (b) for example.

It has been proposed to take two-step equilibration [5] to mimic this stage, in where the gluon equilibration time is much less than the quark's. Consequently the yields of

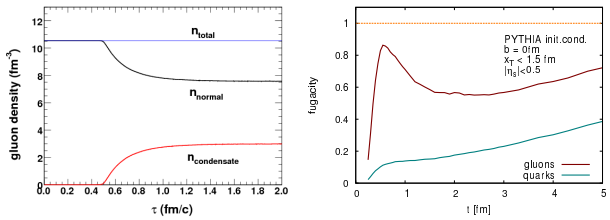

(a) (b)

Figure 1: (a)time evolution for number density of gluons and gluon BEC under initial condition $f_0 = 0.4\theta(p - Q_s)$ within BAMPS box calculation. (b)time evolution for fugacity of gluons and quarks within BAMPS for Au+Au $\sqrt{s_{NN}} = 200GeV$ at b=0 fm in mid-rapidity.

hard thermal photons and dileptons would be suppressed sine the reduction of the electric charge density compared to chemically equilibrated QGP. Moreover this can also influence the fireball further evolution dynamically. Being reminded that, in pure SU(3) gauge theory, there's a sharp first order phase transition from pure gauge phase into confined glueball phase at critical temperature $T_c = 270MeV$. We can imagine this could be taken as the extreme but not far case for heavy ion collisions since in the quarkless "pure" glue plasma the virtual quark-antiquark loops are also suppressed by $1/N_c$ [6]. Then after a 1-st order phase transition into a confined glueball Hagedorn states, the glueballs and glueball-Hagedorn resonances there can decay cascadely into final hadronic states. The realistic description for AA collisions might be in between this new pure glue scenario [7] and the conventional paradigm with fully chemically equilibrated QGP experiencing crossover phase transition at $T_{cs} = 155 \pm 20MeV$, and a time dependent fugacities until chemical saturation for quark should be considered in the phase structure and also its dynamical evolution.

References

[1] J.P. Blaizot, et al., Nucl. Phys. **A 873**, 68(2012).

[2] Z. Xu and C. Greiner, Phys. Rev. **C 71**, 064901(2005).

[3] Z. Xu, K. Zhou, C. Greiner and P. Zhuang, Phys. Rev. Lett **114**, 182301(2015).

[4] J.-P. Blaizot, et al, Nucl. Phys. **A 904**, 829(2013).

[5] E. Shuryak, Phys. Rev. Lett **68**, 3270(1992); L.D. McLerran and R. Venugopalan, Phys. Rev. **D 49**, 2233(1994).

[6] B. Lucini and M. Panero, Phys. Rept.**526**, 93(2013).

[7] H. Stoecker, et al., J. Phys. G **43**(2016)1, 015105.

* Work supported by the LOEWE Initiative HIC for FAIR of the state of Hesse, by the Helmholtz Graduate School HIRE for FAIR, by the Frankfurt international graduate school for science, FIGSS at FIAS, by the Karin and Carlo Giersch Foundation, Frankfurt, by HGF and by BMBF.

DOI:10.15120/GR-2016-1

About the early degrees of freedom in ultra-relativistic nucleus-nucleus collisions*

P. Moreau[1], *W. Cassing*[2], *O. Linnyk*[2], *and E. L. Bratkovskaya*[1]

[1]Frankfurt Institute for Advanced Studies, Johann Wolfgang Goethe Universität, Frankfurt am Main, Germany; [2]Institut für Theoretische Physik, Universität Gießen, Germany

The 'Big Bang' scenario implies that in the first microseconds of the universe the entire state has emerged from a partonic system of quarks, antiquarks and gluons – a quark-gluon plasma (QGP) – to color neutral hadronic matter consisting of interacting hadronic states (and resonances) in which the partonic degrees of freedom are confined. Nowadays this early phase can be regenerated in relativistic heavy-ion collisions which show that such a QGP can exist for a couple of fm/c and that it interacts more strongly than hadronic matter. Effective approaches have to be employed to theoretically describe this medium, such as hydrodynamics and hybrid models, or kinetic approaches. But in the case of hydrodynamic based approaches, nothing can be said about the effective degrees of freedom of the QGP. For this purpose, we propose to study the influence of the early degrees of freedom on the final hadronic observables in Au+Au collisions at $\sqrt{s_{NN}}$ = 200 GeV [1] within the PHSD transport approach [2, 3]. In this approach the partonic dynamics is based on Kadanoff-Baym equations for Green functions with self-energies from the Dynamical QuasiParticle Model (DQPM) which describes QCD properties in terms of 'resummed' single-particle Green functions [4]. Based on the lattice QCD results the critical energy density of $\epsilon_c \approx 0.5\ \mathrm{GeV.fm}^{-3}$ separates the hadronic and partonic phases.

The issue about the initial degrees of freedom has been of actual discussion. We find that a non-perturbative system of initially massive gluons (scenario I) and a system of initially dominantly quarks and antiquarks (scenario II) lead to different hadronic observables when imposing the same initial energy-momentum tensor $T_{\mu\nu}(x)$ just after the passage of the impinging nuclei. In case of the gluonic initial condition I the formation of $s, \bar{s}$ pairs in the QGP proceeds rather slow [5] such that the anti-strange quarks and accordingly the K^+ mesons do not achieve chemical equilibrium even in central Au+Au collisions at $\sqrt{s_{NN}}$ = 200 GeV. Accordingly, the K^+ rapidity distribution is suppressed in the gluonic scenario and in conflict with the data from the BRAHMS Collaboration. Furthermore, whereas the abundance of pions is not very sensitive to the initial degrees of freedom, the proton and antiproton rapidity distributions also disfavor the scenario I. The data from the RHIC Collaborations [6] clearly favor the scenario II with dominantly initial quarks and antiquarks as seen in Fig. 1.

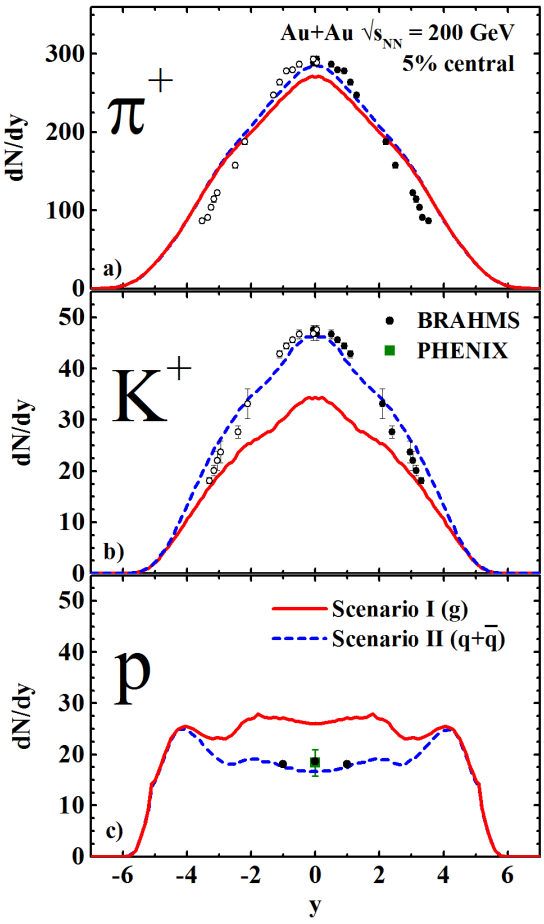

Figure 1: Rapidity distributions for π^+ (a) and K^+ (b) mesons and protons (c) from PHSD for the scenarios I and II in comparison to the results of the BRAHMS and PHENIX Collaboration [6] for 5% central Au-Au collisions at $\sqrt{s_{NN}} = 200$ GeV .

References

[1] P. Moreau *et al.*, arXiv:1512.02875.

[2] W. Cassing and E. L. Bratkovskaya, Nucl. Phys. A **831**, 215 (2009).

[3] O. Linnyk *et al.*, Prog. Part. Nucl. Phys. 87 (2016) 50.

[4] W. Cassing, Eur. Phys. J. ST **168**, 3 (2009).

[5] V. Ozvenchuk *et al.*, Phys. Rev. C 87 (2013) 024901

[6] I. G. Bearden *et al.* [BRAHMS Collaboration], Phys. Rev. Lett. 94 (2005) 162301; I. Arsene *et al.* [BRAHMS Collaboration], Phys. Rev. C 72 (2005) 014908; S. S. Adler *et al.* [PHENIX Collaboration], Phys. Rev. C 69 (2004) 034909

* Work supported by HIC4FAIR/HGS-HIRe.

Charm production at LHC in the Parton-Hadron-String-Dynamics (PHSD) *

Taesoo Song[1], *Elena Bratkovskaya*[1], *Hamza Berrehrah*[1], *and Wolfgang Cassing*[2]

[1]Frankfurt Institute for Advanced Studies and Institute for Theoretical Physics, Johann Wolfgang Goethe Universität, Frankfurt am Main, Germany; [2]Institut für Theoretische Physik, Universität Gießen, Gießen, Germany

Ultrarelativistic heavy-ion collisions are the experiments to create hot and dense matter in the laboratory. The Large Hadron Collider (LHC) is presently the most powerful heavy-ion accelerator with collision energies up to several TeV per nucleon. The properties of the matter created in such high energy collisions are expected to have occured also in the early universe. There are several promising probes to investigate the properties of these systems; heavy flavor such as charm or bottom is one of the very promising observables.

In order to study the production and interaction of heavy flavor in relativistic heavy-ion collisions, the hot dense matter should be described in time and space. The Parton-Hadron-String-Dynamics (PHSD) is a microscopic transport approach that describes heavy-ion collisions by using partons, hadrons, and strings (continuum states) as degrees-of-freedom with off-shell spectral functions for partons and hadrons. The PHSD has been applied to a wide range of collision energies, system sizes and observables with good success [1].

We have studied the production and interaction of charm in relativistic heavy-ion collisions as described in more detail in Refs. [2, 3]: Initial charm quark pairs are produced through hard nucleon-nucleon binary collisions by using the PYTHIA event generator. The transverse momentum and rapidity of charm and anti-charm quarks are slightly adjusted such that they are similar to those from the Fixed-Order Next-to-Leading Logarithm (FONLL) calculations. Since the parton distributions in the nucleon are modified in a heavy nucleus, charm quark pairs – which are mainly produced through gluon fusion in high-energy collisions – are also modified by the (anti-)shadowing effect which is taken into account in our study by using the EPS09 package. The produced charm and anti-charm quarks then interact with off-shell partons in the PHSD. The scattering cross sections are calculated in the Dynamical Quasi-Particle Model (DQPM) on the basis of the same propagators and couplings as in the PHSD. As the matter expands and the temperature decreases, charm and anticharm quarks hadronize into D and $\bar{D}$ mesons through either coalescence or fragmentation. The hadronized D and $\bar{D}$ mesons finally interact with light hadrons in the hadron gas phase with scattering cross sections calculated in an effective lagrangian approach. After several hundreds of $\mathrm{fm/c}$, the D and $\bar{D}$ mesons all are frozen out and can be compared with experimental spectra or related observables.

Fig. 1 shows a comparison of the R_{AA} of D mesons in 0-10 % and the elliptic flow v_2 of D^0 mesons in 30-50 % central Pb+Pb collisions at $\sqrt{s_{NN}}$=2.76 TeV with the experimental data from the ALICE collaboration. We find that the R_{AA} as well as the v_2 of D mesons from the PHSD reproduce the experimental data very well when including the shadowing effect.

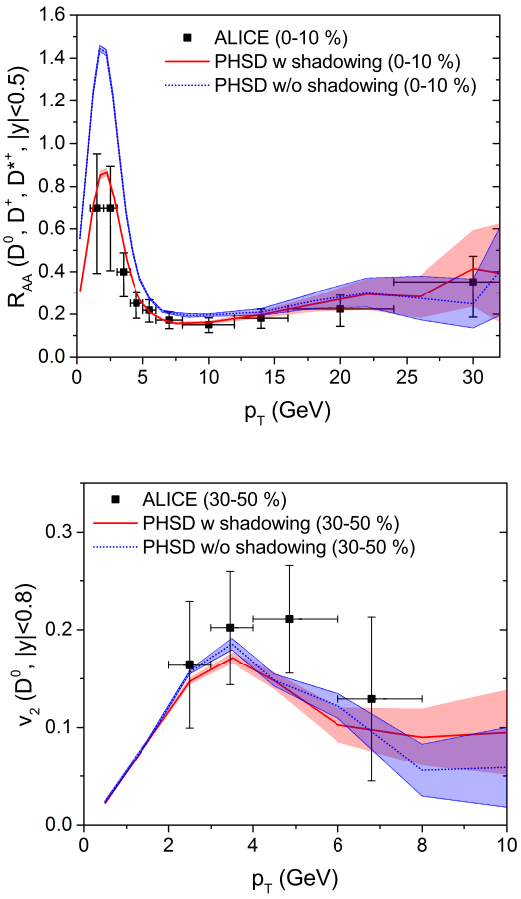

Figure 1: R_{AA} of D mesons in 0-10 % and v_2 of D^0 mesons in 30-50 % central Pb+Pb collisions at 2.76 TeV compared with the experimental data from the ALICE collaboration.

References

[1] O. Linnyk *et al.*, Prog. Part. Nucl. Phys. 87 (2016) 50

[2] T. Song *et al.*, Phys. Rev. C 92 (2015) 014910

[3] T. Song *et al.*, arXiv:1512.00891 [nucl-th]

* Work supported by HIC4FAIR/DFG.

DOI:10.15120/GR-2016-1

The interplay of the jet-energy loss with the jet-medium coupling and the medium*

B. Betz†[1], *F. Senzel*[1], *C. Greiner*[1], *and M. Gyulassy*[2,3,4]

[1]Goethe-University, Frankfurt, Germany; [2]Columbia University, New York, USA; [3]CCNU, Wuhan, China; [4]LBNL, Berkeley, USA

We are presenting a study that addresses the impact of the background medium, the transverse flow fields, and the jet-medium coupling on the pion nuclear modification factor R_{AA} and the high-pT elliptic flow for relativistic heavy-ion collisions.

This study is based on a generic pQCD-like, jet-energy loss model [1]

$$\frac{dE}{d\tau} = -\kappa\, E^0(\tau)\, \tau^1\, e^{3/4}\, \zeta_q\, \Gamma_f \qquad (1)$$

with the jet energy E, the path length τ, the energy density of the background medium e, and jet-energy loss fluctuations ζ_q. This model is coupled to state-of-the-art hydrodynamic descriptions [2].

Here, we report on a model extension to medium backgrounds generated by the parton cascade BAMPS [3] which allows for a direct comparision of jet observables for two different background media: While the hydrodynamic description assumes an equilibrated system, the parton cascade BAMPS also includes non-equilibrium effects in the bulk medium evolution.

We find that both medium backgrounds show a remarkable similarity, especially for the pion nuclear modification factor, see Fig. 1. Nevertheless, there is an impact of the background medium and the background flow on the high-pT elliptic flow.

In addition, we point out (see the lower panel (b) of Fig. 1) that for event-averaged, non-fluctuating initial conditions studied here the simultaneous description of the pion nuclear modification factor and high-pT elliptic flow requires to consider both the background flow fields (via the flow factor $\Gamma_f = \gamma_f[1 - v_f \cos(\phi_{\rm jet} - \phi_{\rm flow})]$ with the background flow velocities v_f and the γ-factor $\gamma_f = 1/\sqrt{1-v_f^2}$)) as well as a jet-medium coupling that depends on the energy of the jet, the temperature of the medium, and non-equilibrium effects around the phase transition as introduced in Ref. [4].

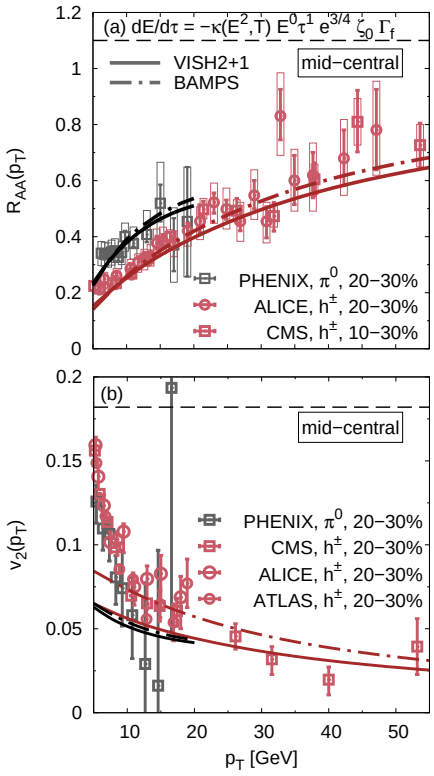

Figure 1: The pion nuclear modification factor (upper panel) and the high-p_T pion elliptic flow (lower panel) for mid-central events at RHIC (black) and LHC (red). The measured data [5, 6, 7, 8] are compared to a pQCD-based energy loss, including a jet-medium coupling of $\kappa = \kappa(E^2, T)$, jet-energy loss fluctuations (ζ_0), and transverse flow fields (Γ_f). The medium background is either described by VISH2+1 [2] (solid lines) or BAMPS [3] (dashed-dotted lines).

References

[1] B. Betz and M. Gyulassy, JHEP **1408**, 090 (2014) [JHEP **1410**, 043 (2014)]; Phys. Rev. C **86**, 024903 (2012).

[2] C. Shen, U. Heinz, P. Huovinen and H. Song, Phys. Rev. C **84**, 044903 (2011); Phys. Rev. C **82**, 054904 (2010).

[3] Z. Xu and C. Greiner, Phys. Rev. C **71**, 064901 (2005).

[4] J. Xu, J. Liao and M. Gyulassy, Chin. Phys. Lett. **32**, no. 9, 092501 (2015).

[5] A. Adare *et al.* [PHENIX Collaboration], Phys. Rev. C **87**, 034911 (2013); Phys. Rev. Lett. **105**, 142301 (2010).

[6] B. Abelev *et al.* [ALICE Collaboration], Phys. Lett. B **720**, 52 (2013); Phys. Lett. B **719**, 18 (2013).

[7] S. Chatrchyan *et al.* [CMS Collaboration], Eur. Phys. J. C **72**, 1945 (2012); Phys. Rev. Lett. **109**, 022301 (2012).

[8] G. Aad *et al.* [ATLAS Collaboration], Phys. Lett. B **707**, 330 (2012).

*This work was supported by the Helmholtz International Centre for FAIR, the Bundesministerium für Bildung und Forschung, the US-DOE Nuclear Science Grant No. DE-AC02-05CH11231 within the framework of the JET Topical Collaboration, the US-DOE Nuclear Science Grant No. DE-FG02-93ER40764, and IPP/CCNU, Wuhan. Numerical computations have been performed at the Center for Scientific Computing (CSC).

† betz@th.physik.uni-frankfurt.de

Dynamics of K^* resonances in heavy-ion collisions*

Andrej Ilner[†1,2], *Daniel Cabrera*[‡1,2], *and Elena Bratkovskaya*[§1,2]

[1]Frankfurt Institute for Advanced Studies, Ruth-Moufang-Straße 1, Frankfurt am Main, Germany; [2]Institut für Theoretische Physik, Johann Wolfgang Goethe-Universität, Max-von-Laue-Straße 1, Frankfurt am Main, Germany

Strange vector meson resonances $K^* \equiv (K^{*+}, K^{*-}, K^{*0}, \bar{K}^{*0})$ are considered as one of the sensitive probes for the hot and dense nuclear medium. At relativistic energies K^*'s are produced at the freeze-out and can provide information about the Quark-Gluon-Plasma (QGP) formed in heavy-ion collisions (HIC). On the other hand, they are short leaving resonances, dominantly decaying to pions and kaons ($K^* \to K+\pi$), which makes them difficult to reconstruct experimentally since the final pions and kaons suffer from final state interaction in the expending hadronic phase, i.e. can rescatter or are absorbed. Moreover, the recreation of the K^* by fusion of $K + \pi \to K^*$ 'overshines' the signal from the QGP and leads to an additional complication for using the strange vector mesons as a clean probe for the phase transition.

As follows from chiral model calculations or coupled-channel G-matrix approaches, the K^* resonances change their properties when propagating in a hot and dense medium: Moreover, the properties of 'daughter' kaons/antikaons are also affected by the in-medium modifications [1]. All that has to be accounted for when modelling the K^* production in HIC.

We investigate the K^* dynamics in a dense and hot nuclear medium using the PHSD (Parton-Hadron-String-Dynamics) transport model which incorporates the hadronic and partonic degrees-of-freedom and their interaction, hadronization and further off-shell dynamics for the hadronic stage which incorporates in a consistent way in-medium effects for hadrons.

The in-medium effects for K^*'s are included in the PHSD in the form of temperature and density dependent effective masses and widths which enter the relativistic Breit-Wigner spectral function of K^* (see [1]) at the hadronization as well as in the hadronic production by $K + \pi$ fusion. Due to the in-medium effects, the spectral functions of K^{*+} and K^{*0} are shifted to the higher masses, i.e. they become slightly heavy in the medium, while the K^{*-} and $\bar{K}^{*0}$ resonances become lighter and their spectral functions show a visible broadening.

In Figure 1 we show the PHSD results for the transverse momentum spectra of $K^{*0} + \bar{K}^{*0}$ at midrapidity $|y| < 0.5$ for central Au+Au collisions at an invariant energy 200 GeV in comparison to the STAR data (red circles) [2]. The upper line with open black squares shows the K^* spectra taken directly at their decay point while the lower line with the green stars indicates the 'reconstructed' K^*'s from the final kaons and pions. One can see that the reconstructed spectrum is strongly suppressed at low p_T and much harder compared to the 'true' one taken at the decay point of the K^*'s. The sizeable distortion of the reconstructed K^* spectra can be attributed mainly
1) to the rescattering and absorption of the final pions and kaons which spoil the reconstruction procedure;
2) to the experimental cuts on the pion and kaon transverse momenta, total momenta, rapidity distribution as well as the general mass cut for the reconstructed K^* ($M = [0.8, 0.95]$ GeV) which sizeably decrease the spectra at low p_T and artificially increase the slope of the reconstructed spectra. We note that the in-medium effects on K^* play an minor role since they are mainly produced by $K+\pi$ fusion in the later stage of the reaction where the baryonic density is low due to the rapid expansion.

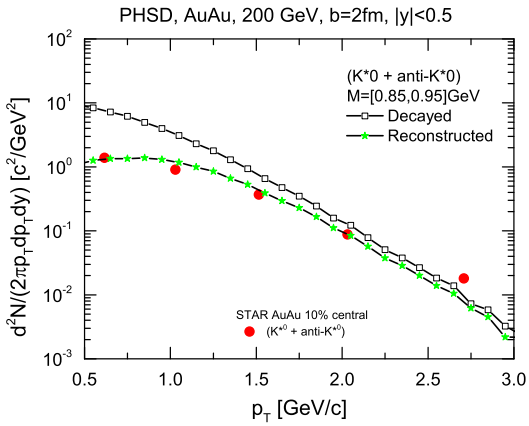

Figure 1: The transverse momentum spectra of $K^{*0} + \bar{K}^{*0}$ at rapidity of $|y| < 0.5$ for central Au+Au collisions at invariant energy of 200 GeV.

References

[1] Andrej Ilner, Daniel Cabrera, Pornrad Srisawad, Elena Bratkovskaya, *Properties of strange vector mesons in dense and hot matter*, Nucl. Phys. A 927 (2014) 249-265

[2] J. Adams et al. (STAR COLLABORATION), $K(892)^*$ *Resonance Production in Au+Au and p+p Collisions at* $\sqrt{s_{NN}} =$ 200 *GeV at RHIC*, PhysRevC.71.064902

*Work supported by the Helmholtz International Center for FAIR within the framework of the LOEWE program. A.I. acknowledges support by GSI, HGS-HIRe for FAIR and H-QM. D.C. acknowledges support by BMBF (Germany).

† ilner@fias.uni-frankfurt.de
‡ cabrera@fias.uni-frankfurt.de
§ Elena.Bratkovskaya@th.physik.uni-frankfurt.de

DOI:10.15120/GR-2016-1

Chiral symmetry restoration versus deconfinement in heavy-ion collisions at high baryon density *

A. Palmese[1], *W. Cassing*[1], *P. Moreau*[2], *and E. L. Bratkovskaya*[2]

[1]Institut für Theoretische Physik, Universität Gießen, Gießen, Germany; [2]Frankfurt Institute for Advanced Studies and Institute for Theoretical Physics, Johann Wolfgang Goethe Universität, Frankfurt am Main, Germany.

The study of the deconfinement phase transition and of the Quark-Gluon-Plasma (QGP) is a topic of major interest in heavy-ion physics especially at the future FAIR (Facility for Antiproton and Ion Research). Lattice QCD (lQCD) calculations show that along the deconfinement phase transition a restoration of chiral symmetry (CSR) takes place at roughly the same critical temperature and energy density. At finite baryon density both the properties of the QGP and the features of the CSR are not fully understood. As the baryon density and temperature increase, the scalar quark condensate $< \bar{q}q >$ is expected to decrease from a nonvanishing value in the vacuum to $< \bar{q}q > \approx 0$ which corresponds to CSR. The challenge is to find signatures for CSR and for the deconfinement phase transition. Our study is carried out within the PHSD transport approach [1], which incorporates explicit partonic degrees-of-freedom in terms of strongly interacting quasiparticles (quarks and gluons) in line with an equation-of-state from lQCD as well as dynamical hadronization and hadronic elastic and inelastic collisions. At low bombarding energy the dominant particle production in nucleus-nucleus reaction proceeds via the formation and decay of excited color singlet states, i.e. "strings". In Ref.[2] we have extended PHSD including CSR in the hadronic sector via the Schwinger mechanism, which rules the string decay fixing the ratio between strange and light quark production according to:

$$P(s\bar{s})/P(q\bar{q}) = \gamma_s = \exp\left(-\pi \frac{m_s^{*2} - m_q^{*2}}{2\kappa}\right),$$

with $\kappa \approx 0.176$ GeV^2 as the string tension and m_s^*, m_q^* as the strange and light quark effective masses. In each space-time cell we compute the scalar nucleon density and $< \bar{q}q >$, which modifies the effective masses of the quarks and consequently the strange to non strange quark fraction. In Fig.1 we show the ratios K^+/π^+, K^-/π^- and $(\Lambda + \Sigma^0)/\pi^-$ at midrapidity from 5% central Au+Au collisions as a function of the invariant energy $\sqrt{s_{NN}}$ computed within PHSD and HSD (HSD does not include partonic degrees-of-freedom). The inclusion of CSR is an essential ingredient in order to reproduce the rise of the K^+/π^+ and $(\Lambda + \Sigma^0)/\pi^-$ ratios at low bombarding energies. Comparing the HSD and PHSD results, it is clear that the onset of deconfinement is responsible for the drop in this ratio. In conclusion, the K^+/π^+ and $(\Lambda + \Sigma^0)/\pi^-$ ratios in A+A collisions are suitable probes for the deconfinement phase transition as well as for the CSR and our model provides a microscopic explanation of their excitation functions.

* Work supported by HIC4FAIR and HGS-HIRe.

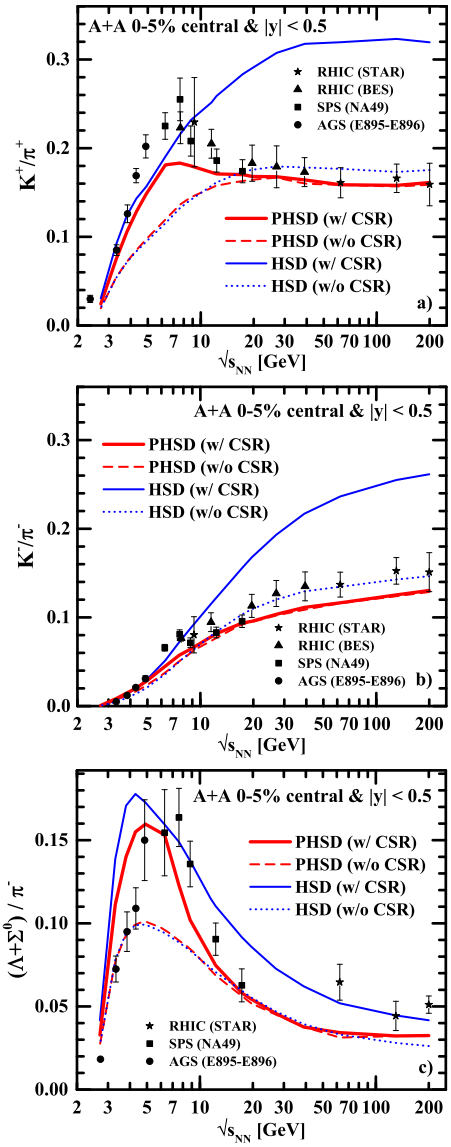

Figure 1: The ratios K^+/π^+ (a), K^-/π^- (b) and Λ/π^- (c) at midrapidity from 5% central Au+Au collisions as a function of the invariant energy $\sqrt{s_{NN}}$ in comparison to the experimental data from [3]. See legend for the individual lines from HSD and PHSD.

References

[1] W. Cassing *et al.*, Nucl. Phys. A **831**, 215 (2009).

[2] W. Cassing *et al.*, Phys. Rev. C **93**, 014902 (2016).

[3] B. I. Abelev *et al.* [STAR Collaboration], Phys. Rev. C **81**, 024911 (2010); M. M. Aggarwal *et al.* [STAR Collaboration], Phys. Rev. C **83**, 024901 (2011).

Dilepton and photon production across collision energies

O. Linnyk[*1], *W. Cassing*[1], *and E. Bratkovskaya*[2]
[1]Justus Liebig University of Giessen, Giessen, Germany; [2]GSI, Darmstadt, Germany

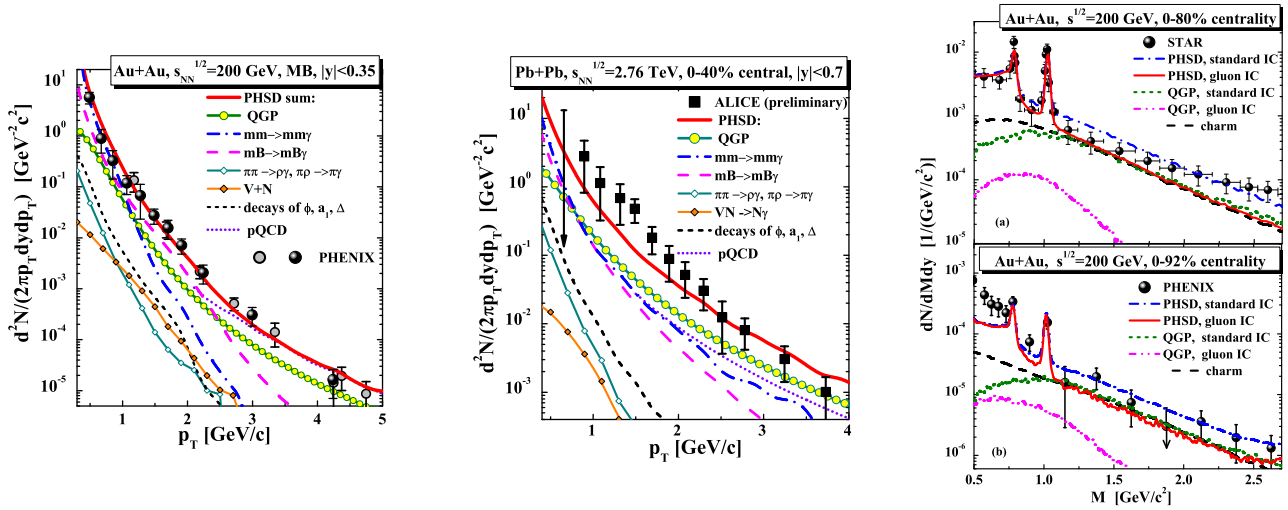

Left: PHSD results for the spectrum of *direct* photons produced in 0-40% most central Au+Au collisions at $\sqrt{s_{NN}} = 200$ GeV. **Center:** The yield of *direct* photons at midrapidity in Pb+Pb collisions at the invariant energy $\sqrt{s_{NN}} = 2.76$ TeV for 0-40% centrality. **Right:** The mass spectra of e^+e^- pairs from Au-Au reactions at $\sqrt{s_{NN}} = 200$ GeV for 0-80% centrality (a) and 0-92% (b). The solid red lines reflect the dilepton spectrum for the gluon dominated initial state while the dash-dotted blue line represents the same quantity for the quark-dominance in the initial state. **All:** Figures are taken from Refs. [1, 2, 3]. See references therein for the experimental data.

Our results on the dilepton and photon probes of the hot QCD matter produced in the heavy ion collisions at various collision energies from AGS to LHC were summarized and discussed in the scope of a recently published review [1]. The non-equilibrium evolution of strongly interacting relativistic particles is calculated using the theory of Kadanoff and Baym in the first gradient approximation. The properties of the QCD matter in equilibrium are based on the lattice QCD results parametrized by the dynamical quasiparticle model (DQPM). The resulting off-shell transport approach is called Parton-Hadron-String Dynamics (PHSD).

The description of the data is adequate from lower SPS energies up to LHC energies for p-p, p-A as well as A-A collisions, i.e. over a range of more than two orders in $\sqrt{s_{NN}}$. Our results on *direct photons* suggest that the role of such sources as mm and mB bremsstrahlung has been underestimated in the past and was found to be dominant at low photon p_T. The dynamics of the initial phases of the reaction might turn out to be important (pre-equilibrium flow, Glasma effect etc.). In a 'glasma' phase the photon/dilepton production is suppressed by about an order of magnitude since the gluon fields do not carry electric charge. In this case the direct photons would practically stem for the hadronic stages and carry the full hadronic elliptic flow v_2, see [3].

The main messages from our *dilepton* studies are: (i) at low masses ($M = 0.2 - 0.6$ GeV/c^2) the dilepton spectra show sizable changes due to hadronic in-medium effects, these effects can be observed at all energies from SIS to LHC but are most pronounced in the FAIR/NICA energy regime; (ii) at intermediate masses the QGP ($q\bar{q}$ thermal radiation) dominates for $M > 1.2$ GeV/c^2. (iii) The tension between the PHENIX and STAR dilepton data at the top RHIC energy (as well as PHSD predictions) no longer persists. (iv) Finally, the dilepton measurements within the future experimental energy and system scan (pp, pA, AA) from RHIC and new ALICE data at LHC will extend our knowledge on the properties of hadronic and partonic matter via its electromagnetic radiation.

References

[1] O. Linnyk, E. L. Bratkovskaya, and W. Cassing. *Prog. Part. Nucl. Phys.*, 87:50–115, 2016.

[2] O. Linnyk, V. Konchakovski, T. Steinert, W. Cassing, and E. L. Bratkovskaya. *Phys. Rev.*, C92(5):054914, 2015.

[3] Pierre Moreau, Olena Linnyk, Wolfgang Cassing, and Elena Bratkovskaya. arXiv:1512.02875

* olena.linnyk@theo.physik.uni-giessen.de

DOI:10.15120/GR-2016-1

Angular distribution of dilepton production in pion-nucleon collisions*

Enrico Speranza[1,2], *Miklós Zétényi*[3], *and Bengt Friman*[1]

[1]GSI Helmholtzzentrum für Schwerionenforschung, Darmstadt, Germany; [3]Technische Universität Darmstadt, Darmstadt, Germany; [2]Wigner Research Center for Physics, Budapest, Hungary

Dileptons are an important probe in heavy-ion collisions since they do not interact strongly and, therefore, they carry information about the hot and dense matter created. Dileptons are also important for studying elementary hadronic collisions.

The HADES collaboration at GSI has recently studied pion-induced reactions, including dilepton production. Preliminary results have been presented [1].

The goal of our work is to investigate the reaction $\pi N \to R \to Ne^+e^-$, where R is the intermediate baryon resonance, using effective Lagrangian models [2] at the energy of the center-of-momentum (CM) frame of the HADES experiment ($\sqrt{s} = 1.49$ GeV). By studying angular distributions, one can extract information on the total spin and parity of the baryon resonances and that can be useful in order to disentangle different production channels.

The angular distribution of the lepton pair is given by [3]

$$\frac{d\sigma}{dM d\cos\theta_{\gamma^*} d\cos\theta_e} \propto 1 + B\cos^2\theta_e, \qquad (1)$$

where θ_{γ^*} is the polar angle of the momentum of the virtual photon in the CM frame measured from the beam axis, θ_e is the polar angle of one of the two leptons measured from a chosen polarization axis in the rest frame of the virtual photon and M is the invariant mass of the lepton pair. B is the anisotropy coefficient and it is defined as

$$B = \frac{\Sigma_\perp - \Sigma_\parallel}{\Sigma_\perp + \Sigma_\parallel}, \qquad (2)$$

in which $\Sigma_\perp$ and $\Sigma_\parallel$ are the contributions of the transverse and parallel polarizations of the virtual photon to the cross section. B provides information on the polarization of the virtual photon and hence of the baryon resonance. In general, B depends on θ_{γ^*} and M.

In Fig. 1 we plot the anisotropy coefficient for $M = 0.5$ GeV for different spin parity cases for the baryon resonance as a function of θ_{γ^*}. The mass of the resonance is set to the CM energy. Fig. 1 shows that a given spin parity case for the baryon resonance gives rise to a characteristic shape for the anisotropy coefficient.

In Fig. 2 we plot the anisotropy coefficient calculated considering the most important resonances at HADES energy. The interference between the resonances is also included.

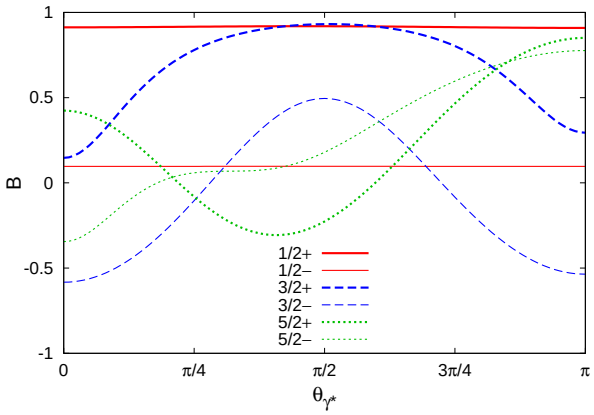

Figure 1: Anisotropy coefficient as a function of θ_{γ^*} for hypothetical resonances with different spin and parity at $M = 0.5$ GeV. The resonance masses coincide with $\sqrt{s} = 1.49$ GeV.

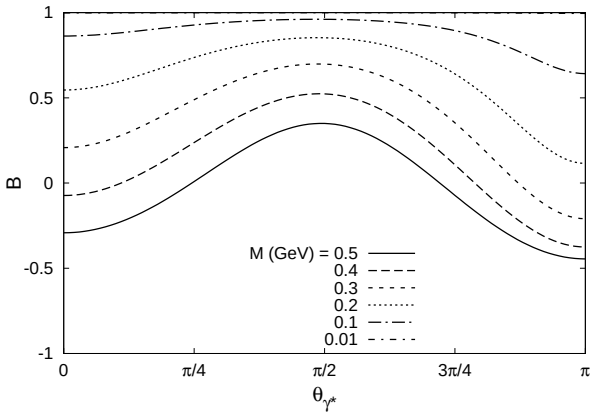

Figure 2: Anisotropy coefficient as a function of θ_{γ^*} for various dilepton masses. The contribution of the dominant resonances and their interference at $\sqrt{s} = 1.49$ GeV is taken into account.

References

[1] W. Przygoda (HADES Collaboration), talk presented at The 10th International Workshop on the Physics of Excited Nucleons, NSTAR2015, 25-28 May 2015, Osaka.

[2] M. Zétényi and Gy. Wolf, Phys. Rev. C **86** (2012) 065209.

[3] E. L. Bratkovskaya, O. V. Teryaev and V. D. Toneev, Phys. Lett. B **348**, 283 (1995).

*Work partially supported by VH-NG-823, Helmholtz Alliance HA216/EMMI and GSI.

Baryons within a three-flavor chiral effective model *

L. Olbrich[1], *M. Zétényi*[2], *F. Giacosa*[1,3], *and D. H. Rischke*[1]

[1]Institute for Theoretical Physics, Goethe University, Frankfurt am Main, Germany; [2]Wigner Research Center for Physics, Budapest, Hungary; [3]Institute of Physics, Jan Kochanowski University, Kielce, Poland

We consider the so-called extended linear sigma model (eLSM). For the case of $N_f = 3$, it features (pseudo)scalar and (axial-)vector mesonic degrees of freedom as well as glueballs [1]. In this work, we have extended this model by including three-flavor baryonic fields. To this end, we designed a mathematical framework to describe spin-$\frac{1}{2}$ baryon multiplets [2].

We constructed baryonic fields based on a chiral quark-diquark picture. In this process, we require a so-called mirror assignment, which will allow to construct chirally invariant mass terms within the Lagrangian. This naturally leads us to four octets, described by 3×3 matrices. Two of them, labeled N_1 and N_2, behave under chiral transformations as

$$N_{1R} \to U_R N_{1R} U_R^\dagger\,, \qquad N_{1L} \to U_L N_{1L} U_R^\dagger\,,$$
$$N_{2R} \to U_R N_{2R} U_L^\dagger\,, \qquad N_{2L} \to U_L N_{2L} U_L^\dagger\,.$$

The remaining two matrices M_1 and M_2 exhibit a chiral transformation from the left that is 'mirror-like' compared to the aforementioned fields:

$$M_{1R} \to U_L M_{1R} U_R^\dagger\,, \qquad M_{1L} \to U_R M_{1L} U_R^\dagger,$$
$$M_{2R} \to U_L M_{2R} U_L^\dagger\,, \qquad M_{2L} \to U_R M_{2L} U_L^\dagger\,.$$

This allows to write down a baryonic eLSM Lagrangian describing three-flavor octet baryons and their interaction with mesons. It is invariant under global chiral $U(3)_L \times U(3)_R$ as well as parity and charge-conjugation transformations. In combination with the mesonic part [1] it features the $U(1)_A$ anomaly, as well as explicit and spontaneous breaking of chiral symmetry, in order to reproduce known features of the strong interaction. The explicit form of the Lagrangian is presented in Ref. [2]. It contains twelve parameters, where ten of them describe interactions of baryonic fields with either (pseudo)scalar or (axial-)vector mesonic degrees of freedom. The remaining two constants $m_{0,1}$ and $m_{0,2}$ are mass-like parameters which formally break dilatation invariance. However, they can be assumed to arise from (dilatation-invariant) interactions of a glueball and/or a four-quark state with the baryonic fields, where the mechanism of spontaneous symmetry breaking induces a non-vanishing vacuum expectation value for the glueball and/or the four-quark state. This will allow to extract information about the origin of mass. Depending on the size of the obtained $m_{0,1}$ and $m_{0,2}$ values, all masses might originate not only from the breaking of chiral symmetry, but also from other sources, e.g. a glueball condensate.

Reducing the Lagrangian to two flavors, we are left with four doublets of nucleonic states which mix to produce the experimentally observed nucleon $N(939)$ and the resonances $N(1440)$, $N(1535)$, and $N(1650)$. In this limit, we used a standard χ^2 procedure to fit the parameters to ten experimental quantities and three quantities computed from lattice QCD: the four masses of the nucleonic states, the five kinematically allowed decay widths of a nucleonic resonance into a nucleon and a pseudoscalar meson, and the four axial coupling constants of the nucleonic states. In this way, we observe the existence of three acceptable and almost equally deep minima. Interestingly, while two of them show small values for $m_{0,1}$ and $m_{0,2}$, which indicates that all masses originate almost exclusively from chiral symmetry breaking, the third minimum exhibits values that are close to the vacuum mass of the nucleon, pointing to the existence of further contributions to the mass coming from other sources.

For all three sets of parameter values we obtain numerical results for experimentally observed quantities that are almost all in good agreement with experiment. The fitted values for the masses actually allow to trace them back to the limit where chiral symmetry is restored and to conclude that the pairs $N(939)$, $N(1535)$ and $N(1440)$, $N(1650)$ form chiral partners. However, the solutions of the model show one important mismatch, the $N(1535) \to N\eta$ decay width. In all three fits, this value is about an magnitude of order too small compared to experiment. Since this result is stable under parameter variations, further studies are needed. These might include the consideration of a possible $s\bar{s}$ contribution to the resonance $N(1535)$ or the effect of an anomaly term in the baryonic sector.

References

[1] D. Parganlija, P. Kovacs, G. Wolf, F. Giacosa and D. H. Rischke, Phys. Rev. D **87** (2013) 1, 014011 [arXiv:1208.0585 [hep-ph]].

[2] L. Olbrich, M. Zétényi, F. Giacosa and D. H. Rischke, Phys. Rev. D **93** (2016) 3, 034021 [arXiv:1511.05035 [hep-ph]].

* Work support by HGS-HIRe/HQM, the Hungarian OTKA Fund No. K109462 and HIC for FAIR.

DOI:10.15120/GR-2016-1

The scalar-isodoublet sector within an effective model*

T. Wolkanowski† [1], *M. Sołtysiak*[2], *and F. Giacosa*[1,2]

[1]Institut für Theoretische Physik, Goethe Universität Frankfurt am Main, 60438 Frankfurt am Main, Germany; [2]Institute of Physics, Jan Kochanowski University, 25406 Kielce, Poland

We study the light scalar sector for $I = 1/2$ by using a quantum field theoretical approach which includes a single kaonic seed state in a Lagrangian with both derivative and non-derivative interactions. A fit to πK phase shift data in the $J = 0$, $I = 1/2$ channel is performed, which demonstrates that within our model the $K_0^*(800)$ (or κ) emerges as a dynamically generated companion pole of $K_0^*(1430)$.

The scalar sector of hadron physics has been in the center of debate both from the theoretical and experimental side since a long time. There seems to be a consensus nowadays that at least the scalar states below 1 GeV are non-conventional mesons with respect to the ordinary $q\bar{q}$ picture [1]. For instance, a quarkonium can be constructed for the isodoublet case such that only one state is assigned to, which is often the heavier $K_0^*(1430)$ resonances. The existence and nature of the corresponding lighter $K_0^*(800)$, known as κ, is still controversial. In particular, the role of hadronic loop contributions to the self-energy has been found to be crucial in various studies and approaches.

Within our approach a single (quark-antiquark) seed state, roughly corresponding to the $K_0^*(1430)$, is described by an effective Lagrangian. We use a Lagrangian that contains – in agreement with chiral perturbation theory (chPT) and chiral models – both derivative and non-derivative interaction terms:

$$\begin{aligned}\mathcal{L}_{\text{int}} &= aK_0^{*-}\pi^0 K^+ + bK_0^{*-}\partial_\mu\pi^0\partial^\mu K^+ \\ &\quad + \sqrt{2}aK_0^{*-}\pi^+ K^0 + \sqrt{2}bK_0^{*-}\partial_\mu\pi^+\partial^\mu K^0 \\ &\quad + \dots\,, \end{aligned} \tag{1}$$

where dots represent analogous interaction terms for the other members of the isospin multiplets, as well as Hermitian conjugation. After computing the full one-loop resummed propagator of the seed state, we perform a fit to experimental πK phase shift data from Ref. [2]. The fit depends on four parameters of the model: the two coupling constants a and b, one bare mass, and one cutoff entering a Gaussian form factor for the loop integrals. The latter are obtained from the optical theorem for Feynman diagrams – however, care is needed when derivative interactions have to be included as in our case. For details see Ref. [3].

The $J = 0$, $I = 1/2$ phase shift for πK scattering up to 1.8 GeV is assumed to be dominated by the scalar kaonic resonances(s). Within our framework it therefore takes the form

$$\delta_{\pi K}(m) = \frac{1}{2}\arccos\left[1 - \pi\Gamma_{K_0^*}(m)d_{K_0^*}(m)\right]\,. \tag{2}$$

Here, the functions $\Gamma_{K_0^*}(m)$ and $d_{K_0^*}(m)$ are the tree-level decay width and the spectral function as determined by our Lagrangian (1).

As a result of our fit with $\chi^2/d.o.f. = 1.25$, we find that, besides the expected resonance pole of $K_0^*(1430)$, a pole corresponding to the light κ naturally emerges on the unphysical Riemann sheet. We determine:

$$K_0^*(1430): \ (1.413 \pm 0.002) - i(0.127 \pm 0.003)\,, \tag{3}$$

$$K_0^*(800) \ : \ (0.746 \pm 0.019) - i(0.262 \pm 0.014)\,. \tag{4}$$

It turns out that the light κ does not correspond to any peak in the scalar kaonic spectral function but only to an enhancement in the low-energy region at about 750 MeV. A large-N_c study shows that its pole disappears when N_c is large enough ($N_c \simeq 13$). As a consequence, this state is *not* predominantly a quarkonium but rather a dynamically generated meson. On the other hand, the pole of the corresponding state above 1 GeV tends to the real energy axis in the large-N_c, as expected for a predominantly quark-antiquark state.

For completeness, we also investigated the statistical significance of our results: we find that both derivative and non-derivative interactions are needed for a satisfactory fit. Variations of the models with only derivative or non-derivative interactions or with other form factors different from the Gaussian turn out to be not in agreement with the experimental results.

For the future, one should use more complete models than the one presented in this work. In particular, a model is desired which allows to study simultaneously the $I = 1/2$ and the $I = 3/2$ channels. For instance, the extended Linear Sigma Model of Ref. [4], that was used here as a motivation for our Lagrangian, can be applied for this purpose.

References

[1] K. A. Olive *et al.* (Particle Data Group), Chin. Phys. C **38**, 090001 (2014).

[2] D. Aston *et al.*, Nucl. Phys. B **296**, 493 (1988).

[3] T. Wolkanowski, F. Giacosa, and D. H. Rischke, Phys. Rev. D **93**, 014002 (2016) arXiv: 1508.00372 [hep-ph].

[4] D. Parganlija, P. Kovacs, G. Wolf, F. Giacosa, and D. H. Rischke, Phys. Rev. D **87**, 014011 (2013) arXiv: 1208.0585 [hep-ph].

*Work supported by HGS-HIRe, F&E GSI/GU, and HIC for FAIR Frankfurt. Full version can be found as arXiv: 1512.01071 [hep-ph]

† wolkanowski@th.physik.uni-frankfurt.de

Decay of a vector glueball

J. Sammet[1] *and F. Giacosa*[1,2]

[1]Goethe-Universiy, Frankfurt a.M., Germany; [2]Jan Kochanowski University, Poland

There are various experiments planned to produce glueball states. One example is the experiment PANDA, which is to be built at FAIR. When this experiment will be in operation, it should be able to form different glueball states via proton-antiproton collisions. In particular, it will be possible to produce glueballs in the energy-range 2.5 GeV - 5 GeV.

In our work we have constructed three effective Lagrangians which describe the decays of the vector glueball 1^{--}, and allow to make predictions about the ratios of decay. The Lagrangians (see Tab. 1) contain a glueball field and conventional mesons, which consist out of three light quarks u, d, s were considered. The underlying symmetry is flavour symmetry. The decay widths were determined for various decay channels.

Since the coupling constants g_1, g_2 and g_3 in the Lagrange densities from Tab. 1 were determined neither experimentally nor theoretically, all results are given as ratios w.r.t. a chosen decay channel.

The results are summarized in Tab. 1 and should be helpful for future experiments, which will investigate the decays of a vector glueball. If the vector glueball will be detected, the decay probabilities listed in Tab. 1 could be compared with those measured in experiments. Similarly, the coupling constants could be determined.

The experiment BES-III has already detected some mesons which are potential candidates to be a vector glueball. However, it was observed that this meson decays mainly in heavy quark states. On the contrary, we expect that glueballs should also have sizable decay widths in ligh quark-antiquark states.

An extension of this work will be to consider mesons composed of quarks u, d, s and c. This would also allow to caclulate decays in heavy quark-antiquark states.

Another interesting development is to take into account chiral symmetry of QCD which will provide additional constraints on decay widths.

Lagrangian	ratio of decay widths	results
$\mathcal{L}_1 = g_1\,\varepsilon_{\mu\nu\rho\sigma}\,\partial^\rho\,\mathcal{O}^\sigma\,\mathrm{Tr}[V^\mu A^\nu]$	$\frac{\Gamma_{\mathcal{O}\to K_{1,A}K^*}}{\Gamma_{\mathcal{O}\to a_1\rho}}$	1.085
	$\frac{\Gamma_{\mathcal{O}\to f_{1,N,A}\,\omega}}{\Gamma_{\mathcal{O}\to a_1\rho}}$	0.315
	$\frac{\Gamma_{\mathcal{O}\to f_{1,S,A}\,\phi}}{\Gamma_{\mathcal{O}\to a_1\rho}}$	0.203
$\mathcal{L}_2 = g_2\,\varepsilon_{\mu\nu\rho\sigma}\,\partial^\rho\,\mathcal{O}^\sigma\,\mathrm{Tr}[V^\mu\partial^\nu\,P]$	$\frac{\Gamma_{\mathcal{O}\to KK^*}}{\Gamma_{\mathcal{O}\to \pi\rho}}$	1.206
	$\frac{\Gamma_{\mathcal{O}\to \eta\omega}}{\Gamma_{\mathcal{O}\to \pi\rho}}$	0.203
	$\frac{\Gamma_{\mathcal{O}\to \eta'\omega}}{\Gamma_{\mathcal{O}\to \pi\rho}}$	0.092
	$\frac{\Gamma_{\mathcal{O}\to \eta'\phi}}{\Gamma_{\mathcal{O}\to \pi\rho}}$	0.155
	$\frac{\Gamma_{\mathcal{O}\to \eta\phi}}{\Gamma_{\mathcal{O}\to \pi\rho}}$	0.184
$\mathcal{L}_3 = g_3\,\mathcal{O}_\mu\,\mathrm{Tr}[P\,B^\mu]$	$\frac{\Gamma_{\mathcal{O}\to KK_{1,B}}}{\Gamma_{\mathcal{O}\to b_1\pi}}$	0.070
	$\frac{\Gamma_{\mathcal{O}\to \eta\,f_{1,N,B}}}{\Gamma_{\mathcal{O}\to b_1\pi}}$	0.016
	$\frac{\Gamma_{\mathcal{O}\to \eta'\,f_{1,N,B}}}{\Gamma_{\mathcal{O}\to b_1\pi}}$	0.003
	$\frac{\Gamma_{\mathcal{O}\to \eta'\,f_{1,S,B}}}{\Gamma_{\mathcal{O}\to b_1\pi}}$	0.003
	$\frac{\Gamma_{\mathcal{O}\to \eta\,f_{1,S,B}}}{\Gamma_{\mathcal{O}\to b_1\pi}}$	0.005

Table 1: decay width of a vector glueball.

References

[1] J.Sammet., *Decay of a vector glueball.* Bachelor thesis, Frankfurt am Main (2015). Available online at: Available online at: http://th.physik.uni-frankfurt.de/ giacosa/chiralgroup-Dateien/bachelor/BAJuliaSammet.pdf.

[2] Lutz M. et al., *Physics Performance Report for PANDA: Strong Interaction Studies with Antiprotons.* arXiv:0903.3905 (2009)

[3] Diego Bettoni., *The PANDA-Experiment at FAIR.* arXiv:0712.0186 (2007

[4] Wang, Zhiyong., *Recent Results at BESIII* Nucl. Part. Phys. Proc. 2015.01.028 (2015)

[5] K.A. Olive et al. (Particle Data Group), Chin. Phys. C 38, 090001, (2014) and 2015 update

DOI:10.15120/GR-2016-1

The low-energy constants of the extended linear sigma model at tree-level

F.Divotgey[1], *F.Giacosa*[1,2], *D.H.Rischke*[1], *and Peter Kovacs*[1,3]

[1]Institute for Theoretical Physics, Goethe University Frankfurt am Main, Germany; [2]Institute of Physics, Jan-Kochanowski University Kielce, Poland; [3]Institute for Particle and Nuclear Physics, Wigner Research Center for Physics Budapest, Hungary

The physics of strong interactions is theoretically very well described by Quantum Chromodynamics (QCD). In the limit of N_f flavors of massless quarks, QCD has a global chiral $SU(N_f)_L \times SU(N_f)_R$ symmetry, which is spontaneously broken to $SU(N_f)_{L+R}$ in the vacuum due to a nonvanishing quark condensate. Asymptotic freedom implies that the low-energy regime of QCD cannot be investigated by using perturbative methods. One possible approach to the low-energy spectrum that does not rely on a perturbative expansion in powers of α_S is provided by a systematical analysis of the low-energy properties of the hadronic n-point functions of QCD, chiral perturbation theory (ChPT) [1]. This approach makes use of the fact that the low-energy dynamics of QCD is fully determined by the self-interactions of the (pseudo-) Nambu-Goldstone bosons of spontaneous chiral symmetry breaking, which, for $N_f = 2$ are identified as the pions. On a Lagrangian level, those interactions are described by the most general chirally invariant Lagrangian, whose terms are organized as a series in pion momenta and quark masses coupled by the low-energy constants (LECs) of QCD. The pion fields enter this Lagrangian as the parametrization of the coset of the symmetry breaking pattern of chiral symmetry, yielding a nonlinear realization of the latter. Expanding the coset representative, the chiral Lagrangian may be written as

$$\begin{aligned}\mathcal{L}_{\chi PT} = &\frac{1}{2}\left(\partial_\mu \vec{\pi}\right)^2 - \frac{1}{2}M_\pi^2 \vec{\pi}^2 + C_{1,\chi PT}\left(\vec{\pi}^2\right)^2 \\ &+ C_{2,\chi PT}\left(\vec{\pi}\cdot\partial_\mu\vec{\pi}\right)^2 + C_{3,\chi PT}\left(\partial_\mu\vec{\pi}\right)^2\left(\partial_\nu\vec{\pi}\right)^2 \\ &+ C_{4,\chi PT}\left[\left(\partial_\mu\vec{\pi}\right)\cdot\partial_\nu\vec{\pi}\right]^2 + \mathcal{O}\left(\pi^6, \partial^6\right) \ , \qquad (1)\end{aligned}$$

where $M_\pi^2 = M^2 + \frac{2\ell_3}{f_\pi^2}M^4$ defines the tree-level pion mass and where in general the coupling constants $C_{i,\chi PT}$ are functions of the LECs.

An alternative approach to ChPT is provided by hadronic models featuring a linearly realized chiral symmetry, usually referred to as Linear Sigma Models (LSMs). In Refs. [2, 3] an extended version of this kind of models, the so-called extended Linear Sigma Model (eLSM), is presented. The eLSM incorporates all quark-antiquark mesons with quantum numbers $J^P = 0^\pm, 1^\pm$ and up to 2 GeV in mass, as well as the lowest lying scalar glueball [4]. The coupling constants and free parameters are fixed by fitting them to experimentally measured masses and decay widths.

The low-energy dynamics should not depend on whether chiral symmetry is linearly or nonlinearly realized. Therefore, in the low-energy limit, ChPT and the eLSM should have the same mathematical structure, helping us to determine the LECs of the eLSM. In order to find the low-energy limit of the eLSM one has to integrate out all fields of the theory that are heavier than the pion. However, due to complicated interaction terms this procedure is analytically only possible, if one imposes conditions on the interaction terms that restrict the analysis to tree-level. Integrating out all heavy fields, the eLSM Lagrangian can be brought into the form

$$\begin{aligned}\mathcal{L}_{eLSM} = &\frac{1}{2}\left(\partial_\mu \vec{\pi}\right)^2 - \frac{1}{2}m_{\vec{\pi}}^2 \vec{\pi}^2 + C_{1,eLSM}\left(\vec{\pi}^2\right)^2 \\ &+ C_{2,eLSM}\left(\partial_\mu\vec{\pi}\cdot\vec{\pi}\right)^2 + C_{3,eLSM}\left(\partial_\mu\vec{\pi}\right)^2\left(\partial_\nu\vec{\pi}\right)^2 \\ &+ C_{4,eLSM}\left[\left(\partial_\mu\vec{\pi}\right)\cdot\partial_\nu\vec{\pi}\right]^2 + \mathcal{O}\left(\pi^6, \partial^6\right) \ , \qquad (2)\end{aligned}$$

where in general the coupling constants $C_{i,eLSM}$ are functions of the model parameters of the eLSM.

The numerical values for the coupling constants $C_{i,\chi PT/eLSM}$ are listed in Tab. 1. One observes that the first two constants are in very good agreement in both approaches. On first sight the third and the fourth constant are only in qualitative agreement in both approaches. But in those cases one has to take into account that the explicit expressions for $C_{3,eLSM}$ and $C_{4,eLSM}$ contain model parameters that have not been determined up to now. These parameters can be estimated to be of order one, which would drive the third and the fourth low-energy coupling closer to the values obtained from ChPT. In order to improve our results, it will therefore be necessary to determine the missing model parameters in future studies.

Coupling Constant	$(N_f = 2)$-χPT	$(N_f = 2)$-eLSM
$C_{1,i}$	-0.279 ± 1.941	-0.268 ± 0.021
$C_{2,i} \cdot 10^5$ [MeV^{-2}]	5.882 ± 0.013	5.399 ± 0.081
$C_{3,i} \cdot 10^{11}$ [MeV^{-4}]	-5.606 ± 0.889	-9.302 ± 0.591
$C_{4,i} \cdot 10^{11}$ [MeV^{-4}]	2.517 ± 0.414	9.448 ± 0.589

Table 1: Comparison of the low-energy couplings of two-flavor ChPT and two-flavor eLSM.

References

[1] Jürg Gasser, Heinrich Leutwyler, Annals Phys. **158** (1984) 142,

[2] Denis Parganlija, Francesco Giacosa, Dirk H. Rischke, Phys. Rev. D **82** (2010) 054024,

[3] Denis Parganlija, Peter Kovacs, Gyorgy Wolf, Francesco Giacosa, Dirk H. Rischke, Phys. Rev. D **87** (2013) 1, 014011,

[4] Stanislaus Janowski, Francesco Giacosa, Dirk H. Rischke, Phys. Rev. D **90** (2014) 11, 114005.

DOI:10.15120/GR-2016-1

Relativistic spin-two fields: wave equations via Casimir operators of the Poincaré group

Adrian Koenigstein[1,2]*, Francesco Giacosa*[1,3]*, and Dirk H. Rischke*[1]

[1]Institut für Theoretische Physik, Johann Wolfgang Goethe-Universität; [2]Frankfurt Institute for Advanced Studies; [3]Institute of Physics, Jan Kochanowski University

Poincaré group

All relativistic classical and quantum field theories are constructed to fulfill the fundamental symmetry of invariance under Poincaré transformations. These are spacetime translations and Lorentz transformations, including boosts and rotations, which can be expressed in terms of four generators P^α for spacetime translations and six generators $I^{\alpha\beta}$ for the three boost directions and the three rotation axes. The generators obey the algebra of the Poincaré group

$$\begin{aligned}\left[I^{\alpha\beta},\, I^{\gamma\delta}\right] &= i\left(\eta^{\alpha\delta}I^{\beta\gamma} + \eta^{\beta\gamma}I^{\alpha\delta} - \eta^{\alpha\gamma}I^{\beta\delta} - \eta^{\beta\delta}I^{\alpha\gamma}\right),\\ \left[P^{\alpha},\, P^{\beta}\right] &= 0\,,\\ \left[P^{\gamma},\, I^{\alpha\beta}\right] &= i\left(\eta^{\gamma\alpha}P^{\beta} - \eta^{\gamma\beta}P^{\alpha}\right).\end{aligned}$$

The Poincaré algebra has two Casimir operators C_i, which are invariant under Poincaré transformations and commutate with the group generators

$$\begin{aligned}C_1 &\equiv P_\alpha P^\alpha = P^2\,,\\ C_2 &\equiv W_\alpha W^\alpha = W^2\,,\end{aligned}$$

where $W^\alpha = -\frac{1}{2}\epsilon^{\alpha\beta\gamma\delta}I_{\beta\gamma}P_\delta$ is the so-called Pauli-Lubanski pseudo-vector, see Ref. [1] for more details.

All properties which are uniquely classifying a theory should be invariant under all symmetry transformations of the theory. In consequence these characteristics are directly linked to the Casimir operators of the underlying symmetry group, since they are the objects remaining invariant under the symmetry transformations. In fact, the invariants are the eigenvalues of the Casimir operators and the fields in the theory have to be eigenfunctions of the Casimir operators. For fields Ψ, which are invariant under Poincaré transformations, this yields

$$P^2\,\Psi = m^2\,\Psi\,, \tag{1}$$

$$W^2\,\Psi = -m^2\,s(s+1)\,\Psi\,, \tag{2}$$

where m^2 and $-m^2 s(s+1)$ are the corresponding eigenvalues of C_1 and C_2. We conclude that the mass m and the spin s of a field Ψ are direct consequences of the Poincaré invariance and the information about the dynamics of the field Ψ, the wave equations, should be contained in the eigenvalue equations.

Massive spin-two field

The wave equations describing the massive relativistic spin-two field are the so-called Fierz-Pauli equations and were first published by Fierz and Pauli in Ref. [2]. The aim of our work [3] was to derive these relativistic wave equations via the Casimir operators of the Poincaré group.

Spin-two particles/fields are bosonic with five degrees of freedom, due to the five spin projections, and can be described via rank-two Lorentz tensors $T^{\mu\nu}$. In order to write down the eigenvalue equations (1) and (2) for spin-two fields we derive the generators P^α and $I^{\alpha\beta}$ and consequently the operators C_1 and C_2 in spin-two field representation, see Ref. [3]. The eigenvalue equations for $s = 2$ fields $T^{\mu\nu}$ read

$$\begin{aligned}(P^2)^{\mu\ \nu}_{\ \alpha\ \beta}\,T^{\alpha\beta} &= m^2\,T^{\mu\nu}\,,\\ (W^2)^{\mu\ \nu}_{\ \alpha\ \beta}\,T^{\alpha\beta} &= -6\,m^2\,T^{\mu\nu}\,.\end{aligned}$$

Using the explicit expressions for $(P^2)^{\mu\ \nu}_{\ \alpha\ \beta}$ and $(W^2)^{\mu\ \nu}_{\ \alpha\ \beta}$ and simplifying the equations yields

$$0 = (\Box + m^2)T^{\mu\nu}\,, \tag{3}$$

$$0 = T^{\mu\nu} - T^{\nu\mu}\,, \tag{4}$$

$$0 = \eta_{\mu\nu}T^{\mu\nu}\,, \tag{5}$$

$$0 = \partial_\mu T^{\mu\nu}\,, \tag{6}$$

which are the Fierz-Pauli equations for a massive spin-two field. Equation (3) is the Klein-Gordon equation describing the relativistic energy-momentum relation and the propagation of massive fields. The symmetry (4), tracelessness (5), and Lorentz condition (6) reduce the degrees of freedom of a rank-two tensor from sixteen to five.

Having this starting point all further aspects of massive spin-two fields, e.g. the Lagrangian, energy-momentum tensor, angular-momentum tensor, spin-tensor, classical solution, polarization tensors and their completeness relation, the tree-level propagator, quantization and respective commutation relations, as well as quantized energy, momentum, and spin, etc., can be derived, see Ref. [3].

References

[1] A. O. Barut and R. Raczka, "Theory Of Group Representations And Applications", Singapore, Singapore: World Scientific (1986).

[2] M. Fierz and W. Pauli, "On relativistic wave equations for particles of arbitrary spin in an electromagnetic field", Proc. Roy. Soc. Lond. A **173** (1939) 211.

[3] A. Koenigstein, F. Giacosa and D. H. Rischke, "Classical and quantum theory of the massive spin-two field", Annals Phys. **368** (2016) 16 doi:10.1016/j.aop.2016.01.024 [arXiv:1508.00110 [hep-th]].

DOI:10.15120/GR-2016-1

The CBM STS QA Database

Denis Bertini[1], *Anton Lymanets*[2], *Olga Bertini*[2], *and Evgeny Lavrik*[3]
[1]GSI, Darmstadt, Germany; [2]CBM-STS ,GSI, Darmstadt, Germany; [3]Tuebingen Universität , Germany

Introduction

The CBM STS QA Database will gather into one repository all relevant measurements obtained during the STS sensors tests performed by the STS QA responsible laboratories.
Any new or updated measurements will be stored in a dedicated database via the FairDB interface [1] and can then be directly accessed from any location using either a Web Interface or a ROOT macro.

Motivation

The FairDB interface will be used to store a large number sensor parameters such as their type, size, manufacturer and tracking information as well as results of different quality control checks.

One crucial aspect of the sensor control is the optical quality assurance which aims at inspecting the surface quality of the sensors including the information on various identified defect types such as surface scratches, metallization defects, photoresist residues, guard ring quality, sensor edge quality and parallelity. It is also possible to determine the integrity and/or presence of single electrical component on sensor surface, e.g., bias resistors, AC and DC pads, broken or shortened strips as well as foreign objects. The output of the inspection contains a lot of information to be stored. Defect information includes defect type, size, centre of mass, area, its position on the sensor surface, etc. This information is used to make decision on defect severity in order to accept or reject a sensor under test for future use in STS detector. The output of the inspection contains amongst others the raw source camera images for future analysis and quality control cross checks.
Another example of the optical inspection results to be stored is the sensor height map (also known as “warp” (see Fig. 1). Information on sensor warp allows to improve the tracking precision of the STS detector.

Design

Requirements

All new STS QA measurements as well as their history should be recorded and directly accessible from the analysis user code. For this purpose the STS QA Database is implemented using the FairDB SQL Interface [1] based on ROOT Library [3]. A Web User Interface that allow for quick access to the data should also be available.

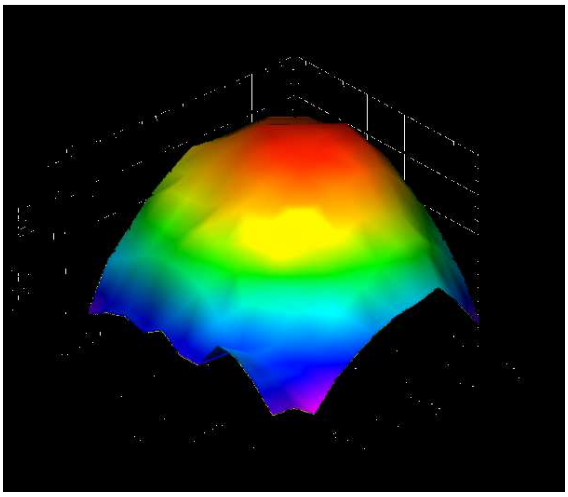

Figure 1: Height map for the central 5×5 cm^2 region of CBM06 silicon microstrip sensor.

QA Data Scheme

A main sensor table is mapped into a ROOT based QA Parameter manager which holds different lists of sensor features (Sensor geometry, IV measurement etc...) indexed via the sensor unique identifier.
All parameter classes are compatible with the FairRoot [2] framework initialisation scheme and could be used for the data analysis.

Web Interface

A Web Interface to the STS QA Database has been implemented. it will allow the user to quickly access the QA parameter data stored in the database without assuming any pre-installed library.

Conclusion

The STS QA Database and its Web Interface based on FairDB is available. It will be further tailored to the different STS activities.

References

[1] FairRoot Virtual Database (User Manual).

[2] The FAIR simulation and analysis framework 2008 J. Phys.: Conf. Ser. 119 032011

[3] R. Brun, F. Rademakers, P. Canal, I.Antcheva , D. Buskulic, O. Couet, A. and M. Gheata *ROOT User Guide* CERN, Geneva 2005.

DOI:10.15120/GR-2016-1

Status of FairMQ

A. Rybalchenko[1], *M. Al-Turany*[1], *and N. Winckler*[1]
[1]GSI, Darmstadt, Germany

The FairRoot framework provides a set of tools for simulation, reconstruction and data analysis for particle physics experiments [1]. In the last three years a message queue aware package (FairMQ) is introduced to FairRoot. FairMQ enables reconstruction and analysis of free streaming data [2] [4]. Moreover it makes it possible for user code to run in a distributed and heterogeneous environment with minimum effort from the user. FairMQ devices are independent processes that can be coordinated and synchronized (if needed) by an external mechanism through the internal state machine of the device. Furthermore, processes using FairMQ can be configured via extensible configuration system. The communication layer in FairMQ has an abstract interface that hides the transport implementation from the user code, which allows changing the transport layer without changing the user code. Currently two transport implementations are available in FairRoot: ZeroMQ [5] and nanomsg [6]. In the following a brief description of developments of sub-modules:

State machine

The internal state machine of the devices has been significantly improved to allow greater responsiveness and feedback during user task initialization, execution and shutdown. The state machine now runs user code in a separate thread, allowing the device to remain responsive to external queries and commands, independent of the user code condition. The chart in Fig. 1 shows the device states and allowed transitions, highlighting which states run in a separate thread. Additionally, if any errors occur, the device goes into an error state, halting the execution and leaving it open for debugging.

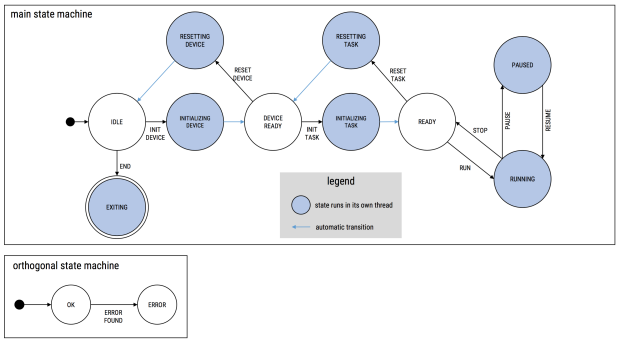

Figure 1: FairMQ State Machine

FairMQChannels

The communication channels between the devices have been reorganized to allow more flexible handling via names and indexes. External tools can be used to extract channel name information from the configuration and create execution graph for the device topologies.

Configuration

The configuration system of FairMQ [3] devices has been redesigned to provide greater reusability and flexibility. Common configuration definitions are now gathered in a single entity, significantly reducing code duplication. The configuration can now be easily extended to provide new settings and default values. Final device setup can be created from multiple sources, such as configuration files and command line parameters.

Multi-part API

FairMQ received new API and transport implementation interface for handling messages that consist of multiple parts. The new API provides more intuitive interface for the user, while at the same time offering greater flexibility for the transport implementation as to how to implement this feature with best performance. Transports that do not offer multi-part feature directly now have more freedom in implementing it. As a proof of concept, multi-part support has been added to the nanomsg transport implementation via MessagePack [7] library.

References

[1] M. Al-Turany et al.: The FairRoot framework, Journal of Physics: Conference Series (2012)

[2] M. Al-Turany, A. Rybalchenko: GSI Scientific Report: Streaming data processing with FairMQ (2013)

[3] M. Al-Turany, A. Rybalchenko, N. Winckler: GSI Scientific Report: Evolution and use cases of FairMQ (2014)

[4] M. Al-Turany, D. Klein, A. Manafov, A. Rybalchenko, F. Uhlig: Extending the FairRoot framework to allow for simulation and reconstruction of free streaming data. accepted for publication by, Journal of Physics: Conference Series (2013).

[5] ZeroMQ: http://zeromq.org/.

[6] nanomsg: http://nanomsg.org/.

[7] MessagePack: http://msgpack.org/.

DOI:10.15120/GR-2016-1

DDS: The Dynamic Deployment System

A. Manafov[1] *and A. Lebedev*[1]
[1]GSI, Darmstadt, Germany

The Dynamic Deployment System (DDS) [1] is a toolset that automates and significantly simplifies a deployment of user defined processes and their dependencies on any resource management system (RMS) using a given topology.

During 2015 the core and main modules of the DDS have been improved. A new **custom commands** feature has been implemented in DDS. Custom commnads API is an easy way to comunicate directly with user tasks. Two use cases were considered:

1. User task which connects to the DDS agent thus allowing direct comunication between user tasks.
2. External utility which connects to the DDS commander allowing to control user tasks from external process.

A custom command is a standard part of the DDS protocol. From the user perspective a custom command can be any text, for example, one can build a JSON or XML based protocol on top of it. A custom command recipient is defined by a condition allowing to send a command to a particular task or broadcast the command to a group of tasks or to all tasks. A simple developer API gives a smooth integration with user tasks.

A new **RMS plug-in architecture** has been implemented in DDS. It gives an external developers a possibility to create DDS plug-ins in order to cover different RMS. The new architecture gives isolated and safe execution of the plug-in. A plug-in must be a standalone processes - if it segfaults this won't effect DDS. Internally it uses the DDS protocol for communication between the plug-in and the DDS commander server - plug-ins speak the same language as DDS. The new RMS plug-in architecture is shown on Figure 1:

1. dds-commander starts a plug-in based on the dds-submit parameter,
2. plug-in contacts DDS commander server asking for submissions details,
3. plug-in deploys DDSScout fat script on target machines,
4. plug-in executes DDSScout on target machines.

The following RMS plug-ins are currently implemented in DDS: localhost, SSH, Slurm and MESOS.

The **documentation and the user manual** were considerably improved. Two new tutorials have been added.

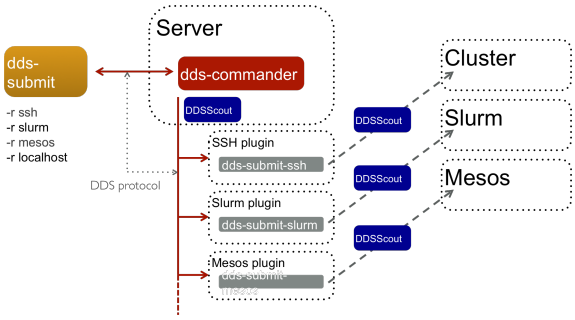

Figure 1: New RMS plug-ins architecture.

Tutorial1 shows an example usage of key-value property propagation feature and Tutorial2 shows how to use custom commands.

The DDS protocol was highly optimized for **massive key-value properties transport**. Internally small key-value messages are accumulated and transported as a single message. Additionally DDS agents use shared memory for local caching of key-value properties.

DDS has been tested on GSI Kronos cluster using 50 computing nodes with 200 processes per node. DDS's SSH plugin has been used to successfully distribute and manage 10081 AliceO2 user tasks (1 sampler, 5040 FLP and 5040 EPN [2]). Throughout the test, one DDS commander server has propagated more than 77M key-value properties. The total start up time of the whole system is 207 s.

Development

DDS is being actively developed using modern development tools, C++11, and Boost libraries [3]. As the continuous integration framework we use BuildBot [4]. The web site and DDS's users manual are based on DocBook [5]. We developed and maintain a unique Git workflow to simplify and secure the development [6].

References

[1] The Dynamic Deployment System (DDS), http://dds.gsi.de.
[2] A. Rybalchenko et al., Evolution and use cases of FairMQ, GSI Report 2014.
[3] BOOST C++ Libraries, http://www.boost.org.
[4] Buildbot. The Continuous Integration Framework, http://www.buildbot.net.
[5] DocBook, http://www.docbook.org.
[6] Git Workflow, https://github.com/AnarManafov/GitWorkflow.

DOI:10.15120/GR-2016-1

Task monitoring tool in FairRoot

R. Karabowicz
GSI, Darmstadt, Germany

Introduction

FairRoot [1] allows users to simulate and analyse physics data. The data analysis is performed using sets of FairTasks, written by software developers. The end-user executes ROOT [2] macro with a combination of FairTasks needed for the given analysis.

FairMonitor

The new addition to FairRoot, the *FairMonitor*, allows simple and coherent analysis of the code performance. The FairMonitor is storing information about the time spent on code execution (using ROOT's TStopwatch) and system memory change (using FairRoot's FairSystemInfo), based on a system of user-defined tags. Each piece of code, which time performance needs to be traced, should be enclosed in calls to the FairMonitor, as shown in 1.

```
FairMonitor::GetMonitor()
    ->StartMonitoring(this,"UniqueTag");
// piece of code to monitor
FairMonitor::GetMonitor()
    ->StopMonitoring(this,"UniqueTag");
```

Figure 1: Invoking monitoring using FairMonitor.

The FairMonitor is storing relevant information for each call with the given tag. If the given tag is used exactly once per event, it is possible to trace the code performance as a function of analysed event.

This functionality has been used internally in FairRoot, to keep track of performance of each user's task. To turn on the monitoring, user needs to enable monitoring in the macro (FairMonitor::GetMonitor()->EnableMonitor(kTRUE);).

The easiest way to see the results is to call FairMonitor::GetMonitor()->Print(); after the execution of the ROOT macro, as shown in Figure 2.

```
root [1] FairMonitor::GetMonitor()->Print()
[INFO   ] - Total Run Time: 9.56151 s ------------------------------------
[INFO   ] [  0.000006 s/ev |   6.397318 % ]  456k "FairTaskList"
[INFO   ] [  0.000034 s/ev |  35.289024 % ]    1M "  Pixel Digitizer"
[INFO   ] [  0.000022 s/ev |  23.073768 % ]  424k "  Pixel Hit Finder"
[INFO   ] [  0.000018 s/ev |  19.037301 % ]  448k "  Pixel Track Finder"
[INFO   ] [  0.000015 s/ev |  16.202588 % ]  432k "  Pixel Track Fitter"
[INFO   ] ----------------------------------------------------------------
```

Figure 2: Example output of the FairMonitor->Print() after macro execution.

The first information printed is the average time spent on task execution in seconds, then the ratio of this time to the total execution time. Subsequently, system memory change is printed, and, finally, the name of the task.

Alternatively, it is possible to draw this information in the ROOT canvas. Additionally, here, the data flow will automatically be presented, as in Figure 3.

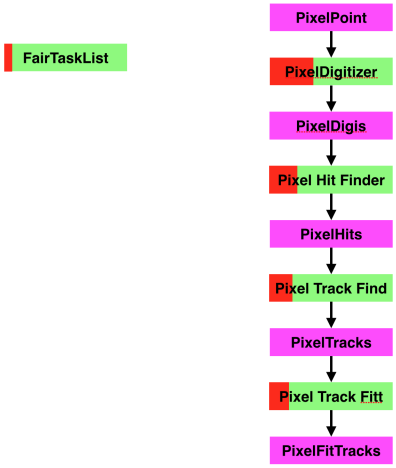

Figure 3: Data flow obtained with FairMonitor->Draw().

It is also possible to draw the dependence of the time (TIM) or memory (MEM) on the analysed event, using DrawHist() function of the FairMonitor. Example of this functionality is shown in Figure 4.

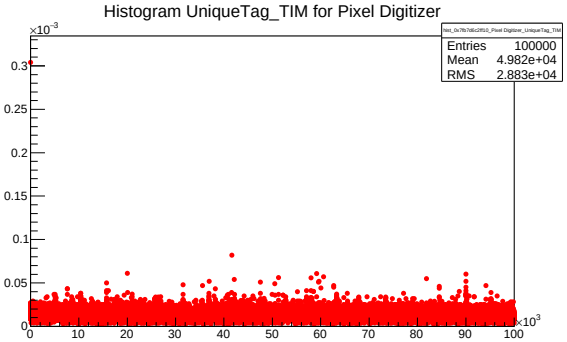

Figure 4: Example histogram obtained after execution of FairMonitor->DrawHist("UniqueTag_TIM").

Summary

With the introduction of the FairMonitor into FairRoot, the users and developers may now easily trace the implemented code time and memory performance. Graphical representation of the results is also available.

References

[1] Al-Turany M, Bertini D, Karabowicz R, Kresan D, Malzacher P, Stockmanns T and Uhlig F 2012 *J. Phys.: Conf. Series* **396** 022001

[2] ROOT: https://root.cern.ch

DOI:10.15120/GR-2016-1

Event reconstruction of asynchronous data stream in the R^{3}B experiment at FAIR

D. Kresan[1], *M. Al-Turany*[1], *F. Uhlig*[1], *the FairRoot group* , *M. Heil*[1], *and the R3B collaboration*
[1]GSI, Darmstadt, Germany

The future R^{3}B (Reactions with Rare Radioactive Beams) experiment at FAIR will cover a broad physics program of reaction studies with exotic nuclei far off stability, nuclear structure and dynamics, astrophysical aspects and technical applications. It is composed of complex detector sub-systems for precise measurements of heavy fragments, protons, neutrons and gammas. Development of a dedicated online reconstruction and analysis software, which has to handle asynchronous data streams from a sophisticated Data Acquisition System, is a challenging task. We will demonstrate in this paper how the R3BRoot framework performs as an online event builder, combining two not synchronised data streams from the gamma and proton calorimeter CALIFA [1] and the neutron time-of-flight spectrometer NeuLAND [2].

R3BRoot framework

The R3BRoot framework is a simulation, reconstruction and data analysis software for R^{3}B. It is based on FairRoot [3]. R3BRoot extends FairRoot with experiment specific detectors and algorithms implementation for R^{3}B. The R3BRoot framework was used for feasibility studies performed for Technical Design Reports of various detector sub-systems. It was also successfully tested in the online experimental operation during April 2014 beam-time at GSI [4].

Data flow and synchronisation

Data from detector prototypes in the 2014 test beam time was packed into sub-events by the DAQ server. Each sub-event corresponds to a physical reaction, which took place in the target (trigger value ”on-spill”), or measurement of cosmic particles (”off-spill”), i.e. sub-events were synchronised. On the other hand, in a later experiment in 2015 events from CALIFA and NeuLAND were built separately (i.e. sub-events are not synchronised). However, each sub-event is associated with a time-stamp value. This time-stamp was used in R3BRoot to reconstruct back real events and to look for correlations between detectors. The current implementation of such an event-builder allows both processing data from a remote-event server in online mode, or reading from a saved file in offline mode.
The synchronisation is implemented directly after the unpack stage of the raw data, and before any further reconstruction or analysis. On-the-fly stitching is realised by buffering of events from different data streams according to the detector list configuration in a steering macro within reasonably large time gap. After the buffering, time-stamp values of the events in buffer are analysed, a cut on the time difference is applied and matched events are written to the output.

Experimental results and summary

A matched event was defined as signal event, if at least one crystal in the CALIFA calorimeter was fired. The distributions of the NeuLAND trigger value before and after applying the CALIFA cut were compared. The results are shown in Fig. 1, where we conclude effective suppression of non-beam events and sufficient signal efficiency.

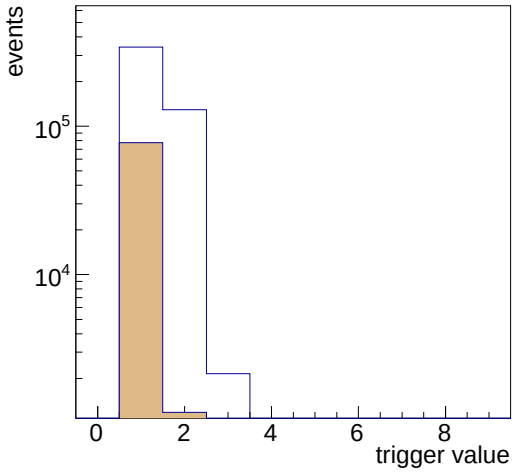

Figure 1: Illustration of gamma calorimeter (CALIFA at R^{3}B) performing as the software trigger. Events with values 1 - on-spill, 2 - off-spill, 3 - system clock. Line histogram shows distribution before applying the trigger, filled histogram - after.

References

[1] D. Cortina and the R^{3}B collaboration, “The CALIFA endcap”, GSI Scientific Report 2014 (2015) 194-198

[2] K. Boretzky and the R^{3}B collaboration, “NeuLAND - from double planes to the demonstrator”, GSI Scientific Report 2014 (2015) 200-202

[3] M. Al-Turany *et al.*, “The FairRoot framework”, J. Phys. Conf. Ser. 396 2 (2012) 022001

[4] D. Kresan *et al.*, “NeuLAND test beam data analysis with R3BRoot framework”, GSI Scientific Report 2014 (2015) 378-379

DOI:10.15120/GR-2016-1

FairDB Web Interface

Denis Bertini[1]
[1]GSI, Darmstadt, Germany

Introduction

The FairDB Web Interface eases the access and the visualization of the parameter data stored in SQL databases from any network connected computer only assuming the user to provide a web browser.

Design

The FairDB Web Interface is based on the Wt framework [1]. The web application uses only the C++ compiled language, from which the necessary HTML, Javascript, CGI and AJAX code are generated in order to ensure security and browser-portability.
A dedicated HTTP server easily integrates the ROOT [2] and the FairDB [3] libraries as they are written in the same programming language.

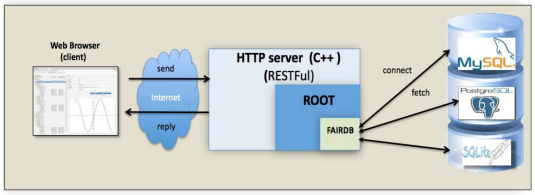

Figure 1: FairDB Web Interface Design

Security

The FairDB Web Interface uses internally the Wt built-in security module which includes, amongst others, protection against vulnerabilities such as Cross-Site Scritpting (XSS) or Cross-Site Request Forgery (CSRF).
A generic built-in authentication module implements best practices for authentication including third party providers (OAuth 2.0, Open ID Connect).
Once identified users successfully logged in, FairDB determines their privileges and access rights, so that it can audit their actions upon data stored in the database.

Tabular Data

To display tabular data, the FairDB Web Interface uses a Model View Controller strategy, where the **View** displays data provided by a **Model**. Only necessary items from the model will be loaded and rendered on the browser allowing display of any large table with low memory footprint.

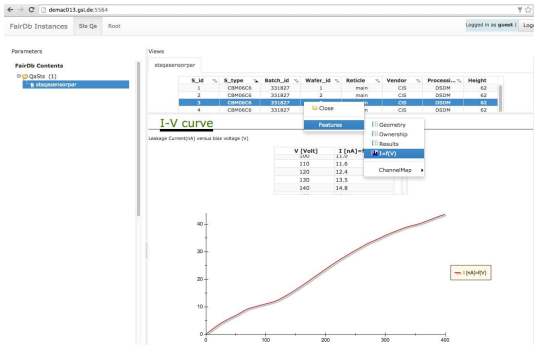

Figure 2: Tabular data visualization example

ROOT Graphics

The FairDB Web Inteface implements a complete ROOT object web browser via a dedicated interface to the Root javascript module [2].

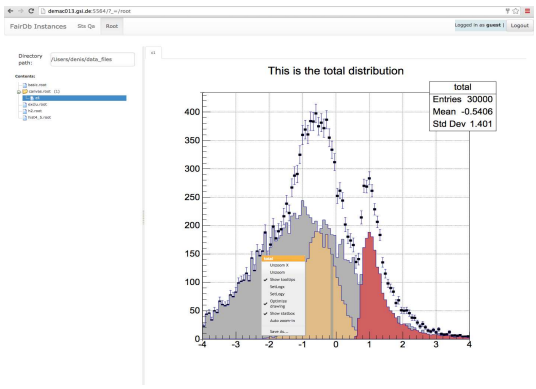

Figure 3: Visualization of ROOT Objects using FairDB Web Browser

Conclusion

A FairDB Web Interface has been implemented. It is currently used by the CBM STS group but can be tailored to any experiment or detector requirements.

References

[1] Wt Library web page (2016). Retrieved from http://www.webtoolkit.eu/wt

[2] R. Brun, F. Rademakers, P. Canal, I.Antcheva , D. Buskulic, O. Couet, A. and M. Gheata *ROOT User Guide* CERN, Geneva 2005.

[3] FairRoot Virtual Database (User Manual).

DOI:10.15120/GR-2016-1

Improved operation for the ALICE Tier2 Centre at GSI

K. Schwarz, S. Fleischer, R. Grosso, and J. Knedlik
GSI, Darmstadt, Germany

This article describes the improvements implemented in 2015 to increase the reliability and performance of the ALICE Tier2 Computing Centre at GSI.

ALICE Tier2 centre at GSI and ALICE Grid in Germany

The ALICE Tier2 centre and the National Analysis Facility at GSI provide a computing infrastructure for ALICE Grid and for the local usage of the German ALICE groups.

Throughout the year GSI participates in centrally managed ALICE Grid productions and data analysis activities, but also analysis jobs of individual users are running on the ALICE Tier2 centre. The overall job share of successfully computed jobs in 2015 contributed by the German Grid sites, the GSI Tier2 centre and Forschungszentrum Karlsruhe (ALICE Tier1 centre) has been 7.5% of all ALICE Grid jobs worldwide. This corresponds well with the pledged CPU resources for 2015: 13400 HEP-SPEC06 for GSI Tier2 (7% of the global Tier2 requirements) and 30000 HEP-SPEC06 for FZK (25% of the global Tier1 requirements)

The storage resources pledged to the global ALICE community (1000 TB) are provided via a Grid Storage Element which consists of a set of xrootd daemons running on top of the Lustre file system.

In this contribution we describe how local HPC resources can be integrated into the ALICE Tier2 centre at GSI. The work done in this context is also an important contribution to the Data Life Cycle Lab ”Structure of Matter/FAIR” within the portfolio project ”Large Scale Data Management and Analysis (LSDMA)”.

As can be seen in fig. 1 the main elements of the GSI storage setup are the xrootd redirector in combination with two xrootd data servers as well as the xrootd forward proxy server. The redirector of the GSI storage element uses the split directive of xrootd and redirects external clients to the external interfaces of the xrootd data server machines and internal clients to the internal interfaces which are directly connected to the local Infiniband - Cluster. The xrootd forward proxy server provides the possibility to Grid jobs running inside the protected HPC environment to read input data from external data sources using the proxy interface. Grid clients would receive the URL for external data sets from the Grid (AliEn) File Catalogue as well as the URL of the GSI xrootd forward proxy as a prefix. Instead of connecting directly to the external data sources clients would connect to the GSI xrootd proxy which in turn cuts out the prefix and enables the connection to the original destination. Thus all xrootd data traffic is tunneled through the xrootd forward proxy. Writing to external storage elements is possible via the same technique.

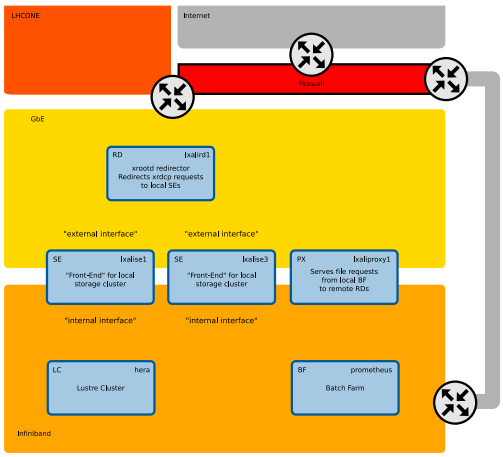

Figure 1: GSI storage setup

Improved technical infrastructure for the GSI ALICE Tier2 centre

In order to be able to guarantee at any given time a clearly defined state of all ALICE Tier2 services and service machines and also to be able to reproduce a given state and to add new machines to the system *Chef* as configuration management system has been introduced. Additionally *Monit* is being used as notification service and to ensure a fully automatic restart of ALICE Tier2 services in case problems would appear. Moreover all ALICE Tier2 computers and software services are being monitored by *MonaLisa* which includes also notification e-mails and a place to document issues of various kind. As High Level Service Monitoring the Key Performance Indicator monitoring introduced in 2014 is in use which shows the overall status of the ALICE Tier2 Centre by displaying wall time delivered, job error rate, compute efficiency, and storage element availability.

DOI:10.15120/GR-2016-1

Optimizing I/O performance by using an XRootD plug-in

J. Knedlik[1] *and K. Schwarz*[1]
[1]GSI, Darmstadt, Germany

Abstract

Accessing the scientific data stored on the ALICE Tier 2 centre suffered from infrastructure related bottlenecks. They are caused by the use of the XRootD - protocol for data access. This article describes the proposed solution, an XRootD plug-in, and the successfully performed tests while using it.

ALICE Tier 2 & XRootD

GSI is operating the only German ALICE Tier 2 centre, which provides a computing infrastructure and storage to the ALICE community. In ALICE's ALiEN grid framework specific data is accessed through the XRootD protocol. XRootD enables the use of of this data through a scalable federated storage system. At GSI, instead of operating XRootD servers with local storage, the shared HPC Lustre filesystem is used as storage backend of the XRootD servers.
In the ALICE - Framework, grid jobs requiring the same data are often scheduled on the same site to lower the need for traffic between sites. Additionally the German ALICE group at GSI often reuses data many times after it has been copied to GSI storage once. This means, that data stored at GSI remains for quite some time on site and it is essential to optimize the I/O performance.

Improving the I/O performance at GSI

With the current storage infrastructure at GSI, namely the access to Lustre through the XRootD data servers, the following room for improvement has been identified :

1. The current 2 XRootD dataservers can provide only limited I/O bandwidth

2. All data read locally from Lustre needs to be sent over the Network twice (Lustre to XrootD server & XrootD server to client) effectively doubling the network traffic for an I/O operation

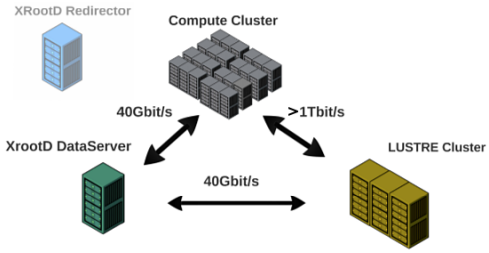

Figure 1: XRootD storage access at GSI
All Clients using XRootD to access ALICE grid data request it through XRootD data servers, this means that I/O traffic needs to go through the 40Gbit/s Link one dataserver can provide and that Lustre's full I/O speed cannot be utilized directly.

An XRootD client - plug-in to redirect to locally available files

Our proposed solution is to use the XRootD - client - plug-in - API to redirect underlying access to data on Lustre directly, bypassing the XRootD workflow if the data is locally available. The XRootD - client - plug-in - API comes with the advantage to change XrootD's underlying I/O operations, so that higher level software (e.g. ROOT, xrdcp,...) can use the plug-in without a need to know of its existence. Tests using the current plug-in show promising results, granting clients' access to Lustre with comparable I/O speeds without the need to use the full XRootD workflow.

Figure 2: A simplified example of the plug-in's "Open" call

```
  virtual XRootDStatus Open(params param){
{
    // use local file implementation if local file is available
  if(DataisLocal(param.path)){
XRootDStatus* return_stat;
    file->open(param);
  if(file->fail()) return_stat=new XRootDStatus( XrdCl::stError);
  else             return_stat=new XRootDStatus(XrdCl::stOK);
                   handler->HandleResponse(ret_st,0);
                   return *return_stat;
            }
            //use the XRootD standard implementation if not
            return xfile.Open(param);
}
```

Conclusion

In conclusion we have implemented an XRootD client - plug-in redirecting client I/O to data on Lustre, effectively improving the I/O performance by bypassing the need to read indirectly via the XRootD data server. The current Tests give promising results and show that such a plug-in can be used to tinker XRootD to our site's specific needs.

DOI:10.15120/GR-2016-1

GSI-HPC cluster

W. Schön[1], *T. Stibor*[1], *C. Huhn*[1], *V. Penso*[1], *T. Roth*[1], *J. Trautmann*[1], *HPC department*[1], *and IT-Security department*[1]

[1]GSI, Darmstadt, Germany

Abstract: The GSI HPC cluster is used by international collaborations to analyze experimental data. Recently the new Green IT Cube building is finished which accommodates the LCSC GPU cluster as well as number cruncher and storage systems. In the next years the cluster will be extended to be prepared for the needs of the large FAIR project.

Introduction

The FAIR project requires a significant growth in computing power in terms of FLOPs, I/O rates and online storage capacities. In an increasingly complex cluster, the tasks of monitoring, anomaly detection and management are accompanied by challenges of rack space, power density and cooling capacities. The new Green IT Cube computing center [1] meets these challenges, achieving a high energy and cost efficiency thanks to its special cooling system, but also providing space for up to 768 racks, with an energy supply of up to 12 Megawatts.

Compute Power

In an environment typical for GSI, LHC or FAIR experiments, demands for pure compute power are straightforward to meet. Due to the independence of the physics events, parallelization can be done easily by analyzing events simultaneously on a number of cores. The simplest solution is to increase the number of cores in the cluster to enhance the number crunching power. Hence, a new compute cluster comprised of 8000 cores has been taken into production. This cluster is managed by the the Slurm job scheduler, enabling the GSI batchfarm to scale out to the planned size of the FAIR T0-Computing, An increasing number of scientist is also employ more intricate programs, making use of MPI based code, different parallelization mechanisms and GPU-adapted algorithms. The latter is addressed by the L-CSC compute cluster, the nodes of which provide four AMD FirePro GPUs each, and which has reached no. 1 in the Green500 (http://www.green500.org/lists/green201411) in Fall 2014, with a compute power - efficiency of 5 GFlops/Watt.

I/O Capacity and Meta Data Perfomance

I/O is the crucial factor in analysing data of large experiments. The HPC department employs two Lustre file system deployments, with a total capacity of 15 PB. Lustre is an open source project under GNU public license that fuels several of the largest file systems world wide.

GSI participates in the development and testing of the Lustre (and is a founding member of the EOFS). Recently, GSI has become an Intel Parallel Computing Center with the goal of developing a Lustre Copytool for archiving data on TSM backend storage system [2].

In the past four years, the production cluster with about 125 file servers and a 7.3 Petabyte capacity has provided a fast and reliable storage for all of GSI's working groups. The next generation cluster running the current stable Lustre version and providing 7.7 PB has gone online in April 2015. Its new feature of storing the data object on disk using the ZFS file system has given good results, in particular with respect to reliability and stability. In addition work on efficient vectorized checksum computation for the ZFS file system has been contributed to the ZFS project [2].

Moreover, first steps toward metadata clustering have been taken. Distributing metadata across several servers will improving on one of the general bottleneck of Lustre, metadata performance. Heavy load on the meta data server can severely limit the overall cluster performance. Especially massively parallel concurrent access of jobs to one and the same file can cause problems, slowing down the entire cluster and thus the HPC farm. User code is often making very inefficient use of Lustre, e.g. by writing and reading huge numbers of small files instead of writing one large file. Excessive meta data usage can also be point to bad user code (e.g. nested infinite loops querying meta data). It is therefore necessary to monitor and detect anomal meta data operations to protect the whole system.

Managing the GSI Cluster

The GSI clusters are now being managed by the Chef configuration management tool with great success [3]. Meanwhile, old NFS services and servers have been phased out. Remaining physics data that was not moved to the Lustre clusters has been pooled up in few modern file servers, while distribution of scientific software has been entirely moved to CernVM-FS. The goal to improve stability by avoiding common shared resources for user code and system code apart from Lustre was attained, as was the goal to improve scalability by distributing the data in many instances.

References

[1] Trautmann et. al. GreenITCube - The new Data Center for FAIR & GSI, HEPIX'16

[2] Schoen et. al. GSI Site Report, HEPIX'16

[3] Huhn et. al. Chef@GSI revisited, HEPIX' 16

DOI:10.15120/GR-2016-1

Go4 Version 5.0 – web technologies for online monitoring

J. Adamczewski-Musch[1], *S. Linev*[1], *and the FAIR@GSI project*[1]
[1]GSI, Darmstadt, Germany.

Introduction

The GSI Object Oriented On-line Off-line system Go4 [1] provides a user environment for online monitoring of DAQ data with analysis code based on ROOT [2]. The acquired raw data files can be processed with the same code also offline in batch mode. The interactive graphical user interface (GUI) of Go4 combines ROOT and Qt [3] graphics and can control the parameters of the separate Go4 analysis process by means of a special inter-task communication and a user plug-in architecture [4]. Go4 is used at GSI and elsewhere for production data analysis of experiments in nuclear and atomic physics, for detector tests, and for characterization of frontend-electronics prototypes.

About 16 years after starting the Go4 project in 1999, Go4 version 5.0 has been released in June 2015. This new major release has been adjusted to support Qt version 5 and ROOT version 6. Besides, a new class of parametrized "shaped" conditions has been introduced to the analysis framework for easy definition of 2 dimensional regions of interest. What is more, the most recent ROOT HTTP server features have been employed for Go4 v5, opening up new possibilities of connectivity and GUI.

ROOT HTTP server

Already in previous versions of Go4 the analysis process could start a proprietary DABC [5] webserver to view the histograms in a web browser with JavaScript ROOT [6]. Since then this webserver implementation has been improved and fed into the *THttpServer* package [7] of the official ROOT distribution. As a consequence, the complete communication between the Go4 analysis and GUI processes could be re-implemented by means of the standardized *THttpServer* class. This does not only concern streaming of histograms to the GUI for visualisation, but also all Go4 objects like parameters and conditions, and the complete control and status traffic.

When launching the Go4 analysis from the Qt GUI, now the user can select if the GUI shall be connected to the analysis with the "classical" *Go4TaskHandler* (ROOT *TSockets)*, or via the *THttpServer*. This connection mode is almost transparent to the GUI user. The most important Go4 controls, like the analysis configuration, the parameter and condition editors, and the status and terminal display, work in the Qt GUI in the same way with both transport layers. However, the more lightweight and connectionless HTTP server starts up much faster than the old triple-socket connections which gives a benefit when the analysis is often restarted during code development.

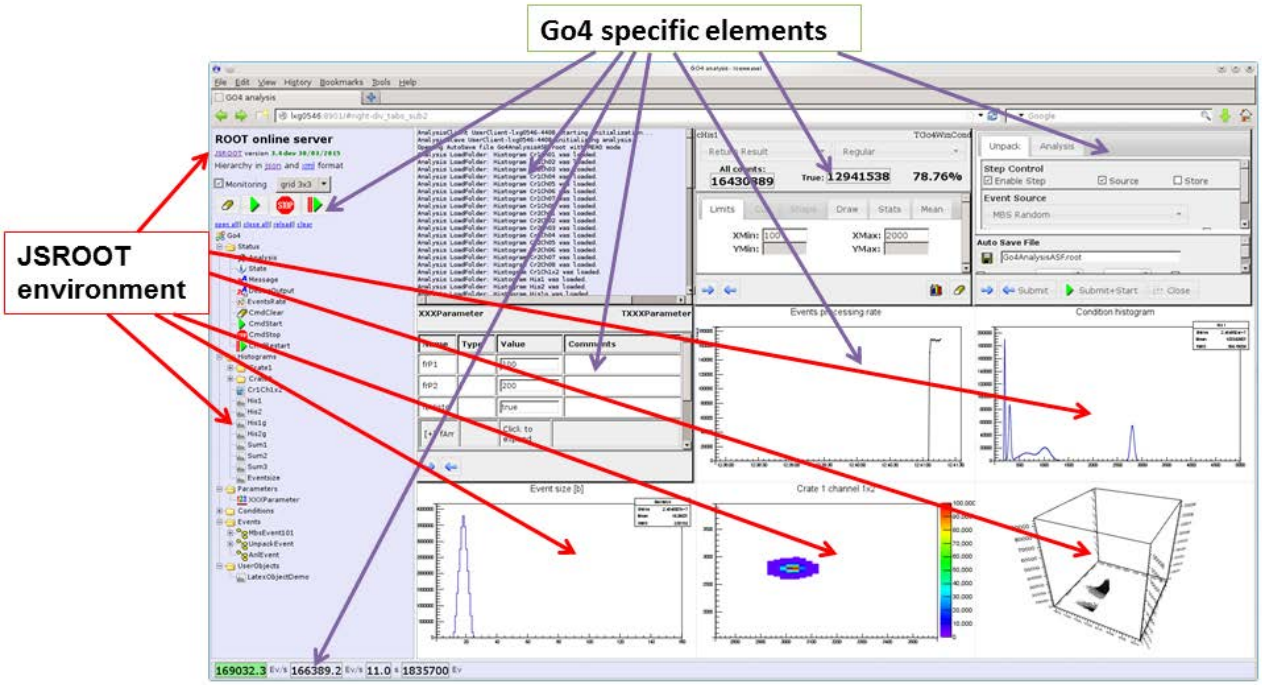

Figure 1: Go4 web client GUI in Firefox/Iceweasel browser. The arrows mark different layers of GUI framework.

DOI:10.15120/GR-2016-1

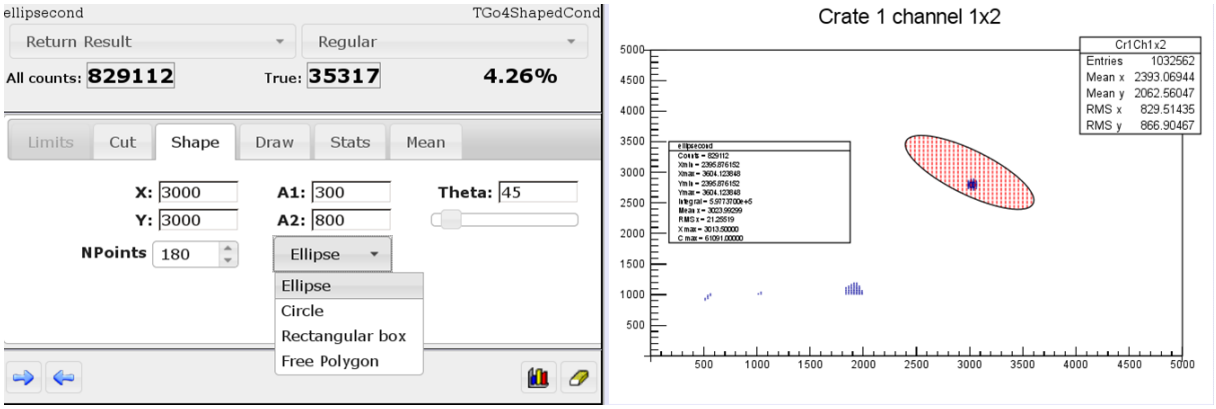

Figure 2: Go4 web client condition editor with a parametrized ellipsoidal *TCutG*.

Moreover, like the old Go4 analysis server, the HTTP server may inherently allow many Go4 GUIs at the same analysis process. Access protection is straightforward here by means of standard HTTP authentication techniques. Vice-versa, the Go4 Qt GUI may connect to several *THttpServers* and display and monitor their ROOT objects simultaneously. This works even for regular ROOT processes without any Go4 classes. Any connected *THttpServer* will appear as remote node in the Go4 object browser and may display its exported objects as icons in a hierarchical tree view. The Go4 GUI controls, however, can have effect on the first connected Go4 analysis only.

Besides this, if the *go4analysis* process is started with HTTP server, it is always possible to inspect the results with any web browser. This can be done concurrent to the controlling Go4 Qt GUI, or even without it during a batch analysis. Finally, in Go4 v5 the main control functionalities of the Go4 GUI have been implemented for a pure web browser client.

Web client GUI

The *go4analysis* process with ROOT *THttpServer* also offers an extended JavaScript-ROOT GUI dedicated for Go4 objects. Therefore any modern web browser may visualize and control the Go4 analysis with GUI elements similar to the established Go4 Qt-ROOT GUI. Figure 1 shows a screenshot of such Go4 web client GUI. It is based on the *jQuery.UI* [8] library for JavaScript and combines the generic JSROOT GUI [7] with specialized Go4 elements. On the left side of the browser window the object hierarchy in the Go4 analysis process is shown as an icon tree. By clicking or selecting an icon with the mouse menu, the corresponding object is displayed on the next active pad in the right browser frame, or in a new separate browser tab. In addition to the regular histogram displays available for any ROOT web server, Go4 specific editor widgets have been implemented to inspect and modify the analysis set-up, the parameter containers, or the condition/cut boundaries, resp. The layout of all control elements and the usage of these web GUIs is intentionally kept in the same way as known from the Qt GUI. Figure 2 shows as an example the Go4 web GUI condition editor together with the display of an ellipsoidal shaped cut (new Go4 class *TGo4ShapedCond*). Here the user may interactively modify the parameters of the ellipse (centroid, half axes and tilt angle) and apply the new region of interest to the *go4analysis* process.

The analysis text output and Go4 log messages may also be displayed in the browser workspace as a text view widget. Furthermore, the main Go4 analysis control buttons and the event rate meter appear in the web GUI similar to the known Qt GUI (see Figure 1). Of course the frequently refreshing of the displayed objects (“monitoring”) is also provided for the web client.

Outlook

The new release v5.0 maintains the established and widely requested Go4 framework for the next generation of ROOT and Qt. The additional HTTP server and Java Script GUI extend the online monitoring features to any regular web browser. On the other hand, the Go4 Qt GUI may visualize the webserver contents of any ROOT process with *THttpServer* in a most powerful way, using native ROOT graphics. Therefore Go4 can be even more applied as a flexible tool in various situations, for ROOT based physics analysis as well as for DAQ and electronics quality monitoring.

References

[1] *http://go4.gsi.de*
[2] *http://root.cern.ch*
[3] *http://www.qt.io*
[4] J. Adamczewski-Musch, H. G. Essel, and S. Linev “Online Object Monitoring With Go4 V4.4”, IEEE TNS Vol. 58, No. 4, August 2011, p. 1477-1481.
[5] *http://dabc.gsi.de*
[6] B. Bellenot and S. Linev, “JavaScript ROOT”, J.Phys.Conf.Ser.664(2015) doi:10.1088/1742-6596/664/6/062033
[7] J.Adamczewski-Musch and S.Linev, “THttpServer class in ROOT”, J.Phys.Conf.Ser.664(2015) doi:10.1088/1742 6596/664/6/062032
[8[*http://jqueryui.com/*

Software improvements for DAQ system MBS*

J. Adamczewski-Musch[1], N. Kurz[1], S. Linev[1], P. Zumbruch[1], and the FAIR@GSI project[1]

[1]GSI, Darmstadt, Germany.

The established data acquisition framework MBS (Multi Branch System) [1] is used for data taking since 20 years by several collaborations. This article reports the most recent improvements and developments for the MBS framework, as well concerning drivers and supplementary software.

MBS framework

64 bit support

The complete source code of the MBS framework has been remanufactured to work also on 64 bit Linux systems. This covers all data pointer types, the core data structures and the handling of the setup tables. At GSI a number of dedicated MBS nodes have been provided to run this platform.

New readout pipe type

A new readout pipe type 4 has been introduced to the MBS framework. For x86 Linux platforms this allows to allocate regular user space memory as readout buffer, instead of using coherent memory outside the kernel region reserved at boot time. Especially on 64 bit architectures this promises a larger pipe with more flexible set up. The DMA read out into such scatter gather memory pipe has been implemented for PEXOR-type boards in the *mbspex* device driver (see next section).

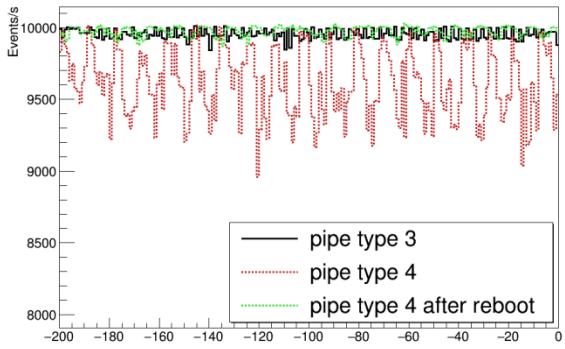

Figure 1: Event rate trending of different MBS readout pipe types: type 3 (coherent reserved memory), new type 4 (sg user space memory) and type 4 after fresh reboot. Time units on x axis are seconds.

A read out test of POLAND/QFW front-ends proved that pipe type 4 was working in principle (10 kHz event rate and 1.5 MB/s with 200 MB pipe length). However, due to fragmentation of the user memory, the performance of such scatter gather DMA was about 5% less than with the coherent pipe type 3, and showed larger event rate fluctuations in time. Only when MBS was started directly after rebooting the machine, pipe type 4 could achieve about the same performance as type 3, because of minimum initial user space page fragmentation (see Figure 1). The application and limits of the new pipe type are still to be explored.

Improvements and bug fixes

Several bugs have been fixed in 2015. For example, on Linux platforms a crash occurred when exiting the MBS dispatcher console by Ctrl-Z key. This was related to shared memory status structures and has been solved.

Additionally, the API for the tape archiving RFIO v8.0 has been implemented to MBS.

Device Drivers

White Rabbit timing receiver

The driver for the VMEbus based White Rabbit timing receiver board VETAR2 [2] has been ported also to the IPV Linux platform with fast extended local bus (ELB) mapping of the VMEbus address space. Therefore all MBS VME hardware (CES/RIO4 and IPV) under Linux is now able to import time stamp data from the future FAIR timing system into the experiment data acquisition when using MBS.

PEXOR/KINPEX

The *mbspex* driver [3] for the PCIe optical readout boards PEXOR and KINPEX has been further improved. In addition to the sequential readout mode from all connected chains of front-end boards, it now supports a driver intrinsic parallel data request from all chains. This means that even in this mode the MBS data acquisition is protected in the kernel module from concurrent slow control access to the front-end devices by other applications like the *gosipcmd* tool.

Furthermore, a pseudo scatter-gather DMA functionality has been implemented to the kernel module, since the DMA engine of the board's FPGA code is not yet capable to treat scatter-gather memory. This provides the functionality to use scattered user space allocated memory as new readout buffer pipe ("pipe type 4") in the MBS.

Auxiliary software

Control GUIs

On top of the *mbspex* driver software a number of graphical user interfaces (GUIs) for set-up and control of the optical front-end boards has been developed. The first of

* PSP codes: SFRS 2.4, ILIMA1.2.2.4, R3B 1.2.5.1.4, 1.2.6.6, 1.2.5.1.2.5, SPARC 1.3.1.3.11, SD -SEM 2.3.6.5.1.6.30

DOI:10.15120/GR-2016-1

them was designed for the POLAND beam diagnostic prototypes already in 2014 [3]. Similarly, for the set-up of GEMEX/NYXOR frontend-boards another GUI has been implemented, reflecting the features of the *nxyter* chip on these boards (Figure 2). Finally, in 2016 a graphical control tool for ADC baseline adjustments of the FEBEX/TUM boards is going to be deployed. All these GUIs are installed on the x86/PC MBS nodes capable of PCIe readout via PEXOR/KINPEX. They can be easily started by commands *poland*, *nyxor*, or *febex*, resp. They allow concurrent control access during MBS acquisition.

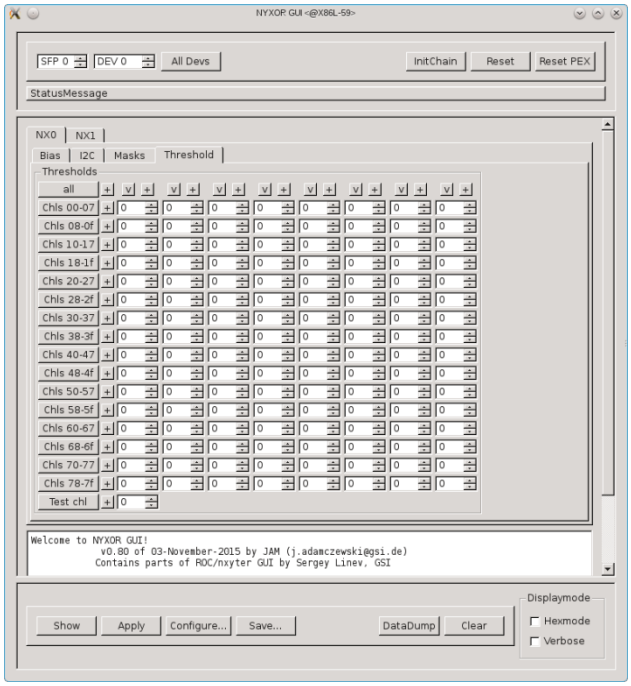

Figure 2: GUI for GEMEX/NYXOR frontend boards

Go4 and DABC installation

Besides the GSI IT Linux cluster, the analysis framework *Go4* [4] and the data acquisition framework *DABC* [5] have been installed also on the MBS dedicated Linux systems. These installations are available on the NFS mounted devices `/analysis` and `/dabc` after activating them by alias commands *go4login* or *dabclogin*, resp. Because of this, online monitoring and control of MBS with Go4, or by DABC web server tools, are possible without any additional Linux node. Moreover, new alias commands *webmbs*, *webprm*, and *webmbsrem* may immediately start DABC based web servers [6] for monitoring of different types of MBS processes on the local, or on remote nodes

EPICS

The EPICS [7] control system framework version 3.14.12.5 has been installed at all MBS dedicated Linux systems of GSI, for X86 , for IPV, and for RIO4 CPU. For this reason the standard EPICS release distribution has been adjusted to the previously not supported RIO and IPV power PC platform. The EPICS framework is available on all these platforms under the NFS mounted file system `/epics`. The environment can be set by sourcing the script `/epics/install/bin/epics` under bash shell. Porting and installation of EPICS to the not natively supported LynxOS platform is currently under investigation.

Outlook

All described MBS framework features are already available at GSI when activating the MBS developer installation. It is planned to release the improved MBS as new production version 6.3 in 2016. The device driver and auxiliary software like EPICS is also usable with current production version 6.2.

References

[1] *http://www.gsi.de/mbs*
[2] D. Beck et al., “Paving the Way for the FAIR General Machine Timing System”, GSI scientific report 2013, doi:0.15120/GR-2014-1-FG-CS-08
[3] J. Adamczewski-Musch, N. Kurz, S. Linev, “mbspex driver software for PEXOR/KINPEX readout boards” GSI scientific report 2014, doi:10.15120/GR-2015-1-FG-CS-06
[4] *http://go4.gsi.de*
[5] *http://dabc.gsi.de*
[6] J. Adamczewski-Musch, N. Kurz, S. Linev, “Status and developments for DAQ system MBS v6.3” GSI scientific report 2014, doi:10.15120/GR-2015-1-FG-CS-05
[7] *http://www.aps.anl.gov/epics/*

DOI:10.15120/GR-2016-1

Adaption of the Super Fragment Separator shielding layout for lowered beam intensities

I. Conrad, G. Fehrenbacher, E. Kozlova, R. Lang, H. Weick
GSI, Darmstadt, Germany;

The Super FRagment- Separator (Super-FRS) at the FAIR facility [1] will produce atomic nuclei with an exotic ratio of protons to neutrons. It demands highest standards of the constructional shielding and the handling process of activated components due to the required high intensities of the ion beam.

In the vicinity of the pre-separator beam line, a high level of radioactive activation of the target (approx. 1E11 Bq) and the beam catcher (approx. 1E13 Bq) is expected. With reduction of the accelerator beam intensity from 1E12 to 3E11 the main shielding geometry (see fig.1) was adjusted.

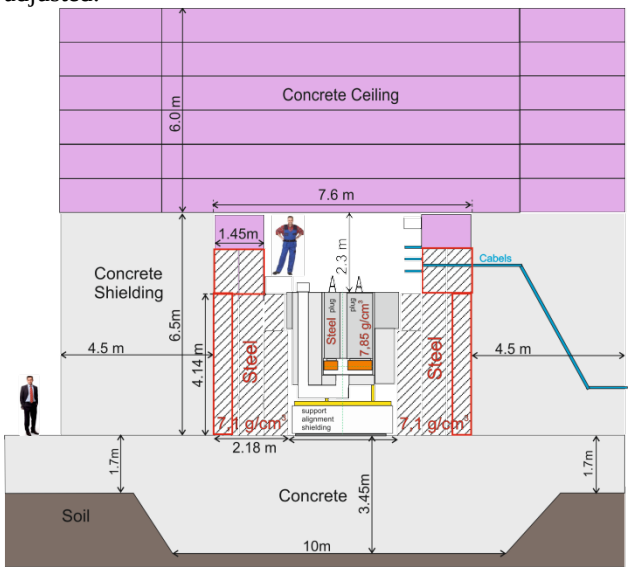

Figure 1: Old version of SFRS shielding design (2013) at the position of the dipole magnet with 3 layers of the steel bricks and concrete walls to the side and 6m concrete ceiling. Red framed parts were changed 2015.

Due to the lower intensity a reduction of the iron shielding was appropriate. Only two rows of iron bricks with the thickness of 80 cm remained instead of three rows with the 70 cm (see fig. 1 red framed parts). This last row will be replaced with a thicker concrete wall. The prompt dose behind the walls is still lower than 0.5 µSv/h. Also in the upper part of the SFRS shielding the concrete and iron layout were adjusted to adapt to the new parameters and to realise the cost savings.

The new geometry with reduced shielding layers was verified within the FLUKA-Models [2]. The residual dose in the service tunnel at the point N1 (fig.2) has to allow maintenance works soon after the beam shut down. On the top of the iron ceiling around the beam components a thin 20 cm layer of concrete was included to reduce the residual gamma radiation dose rate from the metal parts. On the basis of simulations this thickness was found to be the optimal shielding also for the neutron flux behind the iron.

The prompt dose at the point N2 behind the concrete walls is still lower than 0.5 µSv/h, however there is an additional iron shielding inside of the tunnel (see point N4) which represent the beam catcher or target chamber iron part. To reproduce a realistic geometry, up to 10 cm large gaps in the mobile ceiling were simulated. This calculation showed that such air gaps have no influence on the prompt dose on the top of the ceiling during the operation (see point N3).

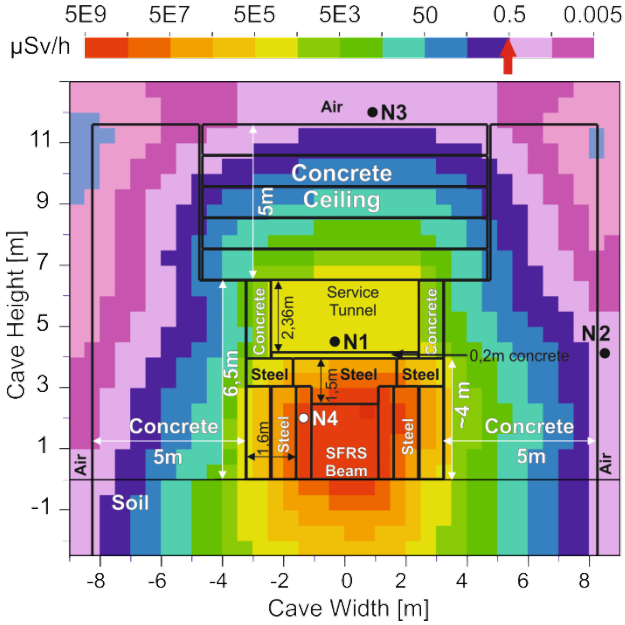

Figure 2: FLUKA prompt dose rate calculations for the new beam parameter with Uranium beam with the energy of 1.5 GeV/u and intensity of 3E11 U/s in the beam catcher. The cut is just behind the BC.

After the radiation protection application of the SFRS building in 2011 [3] by the hessian environmental authority and the successful permission granted in October 2012 the new changes have to be notified in the upcoming application.

References

[1] FAIR Baseline Technical Report, Editors H. H. Gutbrod (Editor in Chief), I. Augustin, H. Eickhoff, K.-D. Groß, W. F. Henning, D. Krämer, G. Walter, September 2006

[2] FLUKA: a multi-particle transport code, A. Fassò, A. Ferrari, J. Ranft, P. R. Sala; CERN-2005-10 (2005), INFN/TC 05/11, SLAC-R-773.

[3] Antrag für die Errichtungsgenehmigung von FAIR G18/T103, 2011.

DOI:10.15120/GR-2016-1

Update of the radiation protection permission for the supplement building (4a) and the transport tunnel GSI to FAIR (101)

R. Kissel, I. Conrad, G. Fehrenbacher, R. Lang, A. Sokolov
GSI, Darmstadt, Germany;

The construction of the future FAIR facility [1] requires an elaborated radiation protection scheme for the future accelerator complex to prevent considerable exposure of the public or employees. Shielding, labyrinth and ducts are approved from the radiation safety point of view using Monte-Carlo simulations with FLUKA code [2].

The tunnel 101 will serve as a transport beam line of the SIS18 beam towards the main SIS100 synchrotron of the future FAIR facility. This accelerator part is the first one to finish the construction and radiation protection permission procedure at the hessian environment authority (HMUKLV), which is necessary to consider changes in the layout since 2011. On the side of the tunnel there is a supplement technical building where the main personnel and transport access takes place.

The radiation protection application for this building 4a and tunnel 101 was released in September 2011 [3], see fig.1. The main changes in the planning since 2011 are smoke extraction lines which were the stipulations by the fire protection authority (Bauamt Darmstadt). Also there are some changes from user side to adjust the main transport path through the labyrinth in the tunnel to the further FAIR buildings.

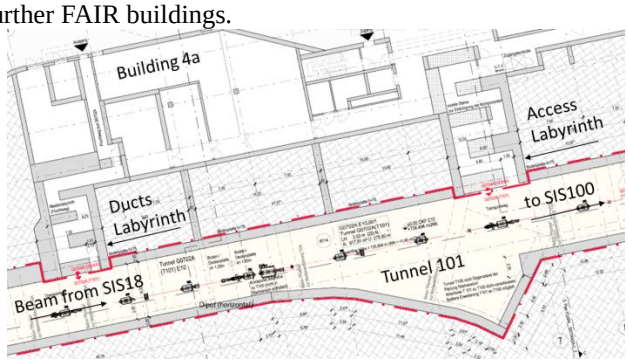

Figure 1: Old version of architectural plan for the application in 2011with building 4a (white) and the tunnel 101 (red framed). The beam comes from the left side out of SIS18 and goes towards injection part of the main SIS100 synchrotron. Left labyrinth is used for the air and water ducts, right one for the main personnel entrance and transport access.

Adjustment of the labyrinth geometry for the new smoke extraction lines was performed with the FLUKA calculations. The worst possible beam loss parameters at this point are 2% of 5E12 particles/s of proton beam and an energy of 4.7 GeV. The smoke extraction line is showed with the blue line in fig.2 top. It starts on the right side of the Labyrinth (point N1), goes along the tunnel till the labyrinth, bend to the point N2 and cross the labyrinth on the top of ceiling (see fig.2, bottom).

The geometry of the chicane was adjusted so that the prompt dose in the hall at the points N3 and N4 is less than 0.5µSv/h. This geometry was submitted in October 2015 to the hessian environment authority and the radiation permission was granted in March 2016.

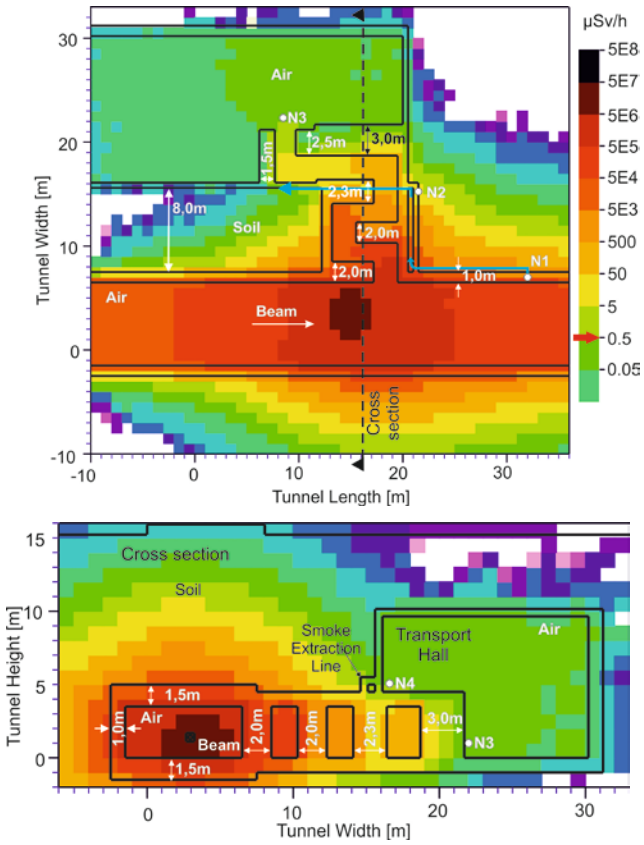

Figure 2: FLUKA prompt dose rate calculations for the new version of the labyrinth estimated with proton beam with the energy of 4.7 GeV and loss rate 1E11 p/s in tunnel 101 in front of the labyrinth, (top) horizontal and (bottom) vertical cross sections of the tunnel and adjacent building 4a.

References

[1] FAIR Baseline Technical Report, Editors H. H. Gutbrod (Editor in Chief), I. Augustin, H. Eickhoff, K.-D. Groß, W. F. Henning, D. Krämer, G. Walter, September 2006

[2] FLUKA: a multi-particle transport code, A. Fassò, A. Ferrari, J. Ranft, P. R. Sala; CERN-2005-10 (2005), INFN/TC 05/11, SLAC-R-773.

[3] Antrag für die Errichtungsgenehmigung von FAIR G4a/T101/T110, 2011.

DOI:10.15120/GR-2016-1

Measurements of the passive neutron dosimeter, ANDREA, at the CERN-EU High Energy Reference Field Facility CERF

I.A. Zahradnik[1, 2], G. Fehrenbacher[1], E. Kozlova[1], A. Sokolov[1], T. Radon[1]
[1]GSI, Darmstadt Germany; [2]THM, University of Applied Sciences Giessen

Introduction of the Neutron dosimeter

Accelerator facilities are sources of neutron radiation, assumed to be harmful to humans and the environment. Therefore, it is essential to measure the dose rates inside the accelerator tunnels, as well as outside of the beam line shielding and experimental area. The presence of high energy particles produces a great amount of neutron radiation which requires a neutron dose detection to be of the highest priority. At GSI Darmstadt, currently used and approved technique for environmental monitoring of neutron radiation implies the use of the GSI ball [1], which is appropriate for ambient dose equivalent measurements from 10 meV to 100 GeV energies. Nevertheless, this passive neutron dosimeter, with a weight of 20 kg and a diameter of 31 cm, is cumbersome for use in some cases. For the purpose of minimizing costs and dimensions as well as to improve the design and characteristics of the dosimeter, a compact neutron dosimeter ANDREA (**A** **N**eutron **D**osemete**R** for **E**fficient **A**rea monitoring) was developed [2]. The ANDREA dosimeter has three layers of different moderators. For the low energy neutrons, moderating outer layer material polyvinyl chloride (PVC) was used. In order to improve the response of the detector for high neutron energies a lead layer was applied. The neutrons with kinetic energies from several hundreds of MeV to several GeV interact with the heavy nucleus of the lead layer and cause an emission of some additional spallation neutrons. The final small layer of polyethylene (PE) moderates those spallation neutrons.

Measurements of the dosimeter response were performed at CERN reference field (CERF) facility to compare with FLUKA [3] simulation results.

Experimental Setup at CERF

The measurements with ANDREA at CERF with primary beam momentum of 120 GeV/c were performed at the center of 6 different squares on the top roof of the concrete shielding. The overall available irradiation time was divided in periods of 8 hours called runs. During each run, the TLD cards inside of ANDREA were exposed to neutrons at different exposure areas on the reference grid at different angles, either in frontal or in transversal direction (see Fig. 1).

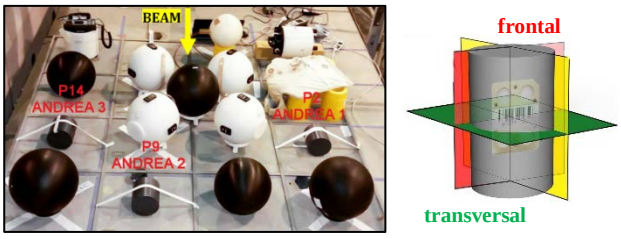

Fig. 1: The position of the ANDREA dosimeters at the 1st run (left) ANDREA directions (right)

Measurements and Simulation Results

The ratio of the experimentally determined dose with respect to the reference ambient dose equivalent is presented in Table 1, column 'CERF'.

TLD direction	CERF	FLUKA simulation	After calibration correction
Frontal	125%	99%	155%
Transversal	120%	100%	145%

Table 1: The results from CERF.

The dose experimentally determined at CERF shows an over estimation of 20-25% compared to the reference values at CERF. The ambient dose and measured results suggest that the polyethylene moderator layer of the ANDREA detector system might be slightly too small. The ANDREA response function would be closer to the H*(10) values if the diameter of ANDREA would be increased by few centimeters.

A difference of 5%, between the frontal and transversal values was found after analyzing the corresponding measurements at the CERN reference field. The neutron equivalent dose readings for these orientations of ANDREA dosimeter are almost the same, thus independent on orientation.

The Tab. 1, column 'FLUKA simulation', highlights that there is an agreement between the measurements and simulated dose reading at the high energy neutron fields at CERF. This means that the experimental measurements confirm the results of the Monte Carlo simulation.

Still the response calculations were done under an assumption of idealized conditions. Though a difficulty arises from the scattering of neutrons at the walls, on the ground and on the ceiling of the laboratory during calibration.

Therefore FLUKA simulations were carried out to determine the amount of scattering radiation and provide a corrected calibration. The comparison between the reference values at CERF and the measured CERF dose, Tab. 1, column 'After calibration correction', shows an overestimation of about 50%. The dosimeter reveals itself as an appropriate device for equivalent dose measurement, still the response to slow neutrons should be better analyzed.

References

[1] G. Fehrenbacher et al, Radiation Protection Dosimetry (2006), "Neutron dose measurements with the GSI ball at high energy accelerators", Oxford University Press.
[2] I. Zahradnik, Development of the Passive Neutron Dosimeter, ANDREA, Darmstadt 2015.
[3] A. Fasso et al, FLUKA: a multi-particle transport code, CERN-2005-10 (2005)

DOI:10.15120/GR-2016-1

DOI:10.15120/GR-2016-1

ROSE - a ROtating System for 4d Emittance measurements

M. Maier, X. Du, P. Gerhard, L. Groening, S. Mickat, H. Vormann, C. Xiao

GSI, Darmstadt, Germany

Introduction

A **RO**tating **S**ystem for **E**mittance measurements **ROSE** [1] has been developed and commissioned. It measures the full 4d transverse beam matrix of an ion beam. Different beams behind the HLI at GSI have been used in two commissioning beam times. All technical aspects of ROSE have been tested and ROSE has been benchmarked against existing emittance scanners for horizontal and vertical projections. The hard- and software to measure & evaluate the 4d beam matrix has been optimized and successfully commissioned.

Experimental setup

The ROSE (Fig. 1) detector is a standard slit-grid emittance scanner being rotatable around the beam axis.

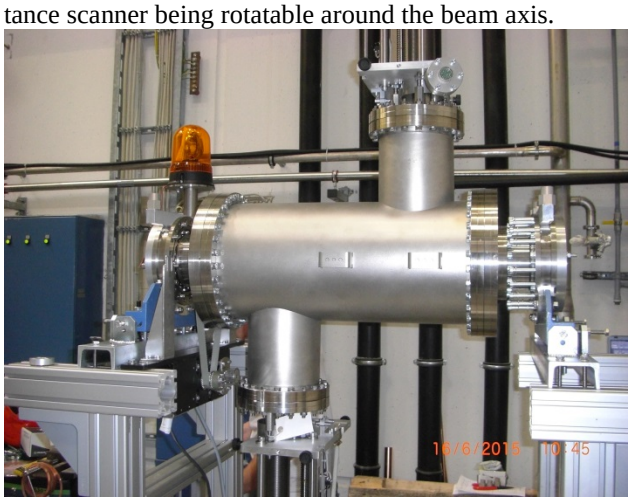

Figure 1 The ROSE detector during assembly.

Together with a magnetic quadrupole doublet it is possible to determine the full transverse 4d beam matrix with only four emittance scans at three different rotation angles [2].

For commissioning ROSE has been installed inside the UCW bunker behind the HLI beam line (Fig. 2).

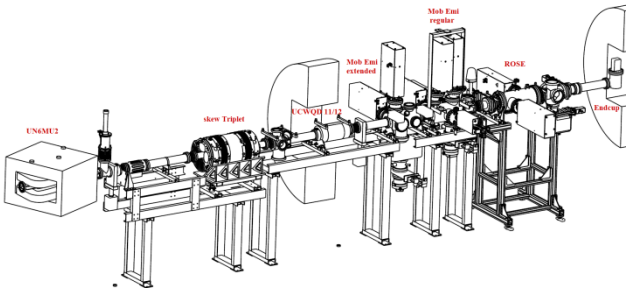

Figure 2: Beam line used for the commissioning of ROSE. The beam enters from the left.

In front of the bunker a skew triplet has been installed to apply controlled coupling or, in case that initial coupling of the ECR source is present, to remove that coupling.

Results

The measured emittances at 0° and 90° are in good agreement for all three emittance scanner set-ups. To commission ROSEs capability to measure the 4d transverse beam matrix the inter plane correlations of the HLI beam have been measured. As no significant initial correlations were found to be present in the HLI beam, controlled coupling of the planes by using a skew triplet has been applied and compared to the uncorrelated beam, as shown in Fig. 3. The expected effect of the skew triplet has been confirmed with ROSE very well. As the back-transformed beam parameters do agree very well, the reliability of the ROSE measurements is experimentally proven.

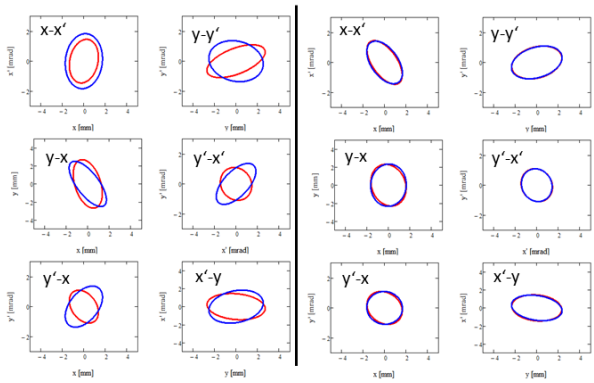

Figure 3: left: measured rms-ellipses of the six transverse projections as measured with ROSE behind a skew triplet. Right: Rms-ellipses after back-transformation to the skew triplet entrance. Measurements were done for two different triplet settings (red and blue).

Summary

ROSE has been commissioned successfully. To our knowledge it is the only device that can measure full 4d ion beam parameters for ions at energies beyond 150 keV/u.

The next step is to use ROSE to measure inter-plane correlations of an uranium beam before SIS18 injection and to attempt removing them using the skew triplet.

References

[1] Deutsche Patentanmeldung Nr. 102015118017.0

[2] C. Xiao et al., arXiv 1604.01909 (2016).

DOI:10.15120/GR-2016-1

Measurements at the cold model for the new post-stripper DTL

A. Seibel, X. Du, L. Groening, O. Kester, S. Mickat
GSI, Darmstadt, Germany

Introduction

In order to meet the challenges of the FAIR project concerning highest beam intensities, an upgrade of the existing Universal Linear Accelerator (UNILAC) is planned. The 108.408 MHz post-stripper section is recommended to be replaced. All activities are focused on substitution of this UNILAC section by an improved Alvarez DTL [1]. Simulations are done to improve the rf-properties. The geometry of the drift tubes is to be changed to improve the ratio of shunt impedance to maximum surface field [2]. This geometry allows a more homogeneous surface current distribution as well.

Setup

A test bench for low power rf measurements with a ten gap aluminum model (scale 1:3) was constructed (Fig. 1). The resonance frequency scales correspondingly to three times 108.408 MHz (= 325.224 MHz).

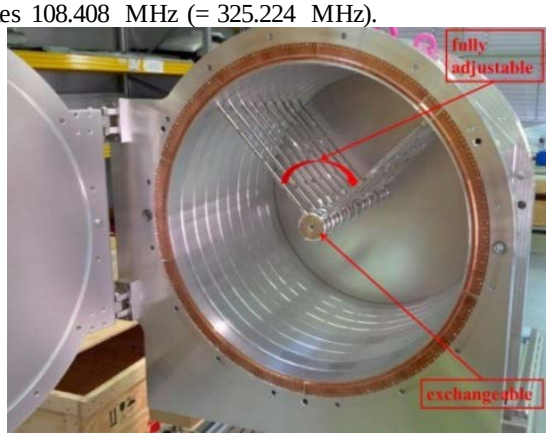

Figure 1: Ten gap Alvarez model for low power rf measurements.

The ten gap model with nine full and two half drift tubes at the tank caps allows the variation of the angle between the stems. The stem configuration of each drift tube has an influence on the field stability. In addition the drift tube caps are dismountable to compare different drift tube geometries.

Results

Measurements on the empty pillbox cavity have been performed. The simulated and measured resonance frequencies are in a very good agreement (better than 3‰). After mounting the drift tubes and stems inside the tank as shown in Fig. 1 the measured resonance frequency of the ten gap model is 326.78 MHz. As shown in Tab. 1 the simulated resonance frequency is just 0.6 MHz lower. The field distribution is recorded using the bead-pull method [3] and compared to the simulated field distributions in Fig. 2. The goal is to obtain the same modes for the ten gap model as for the simulations. In the existing Alvarez tanks of the UNILAC the frequency of the next higher order mode (TM011) is just about 0.5 MHz away from the resonance frequency of the TM010 mode, thus it disturbs the rf operation. To mitigate this effect new stem configurations, for example the alternating V-Stem configuration shown in Fig. 3, are tested in simulations and with measurements on the ten gap model.

Table 1: Frequencies for the ten gap model in MHz

Mode	Simulation	Measurement
TM010	326,18	326,78
TM011	415,82	414,76
TM012	566,11	566,30

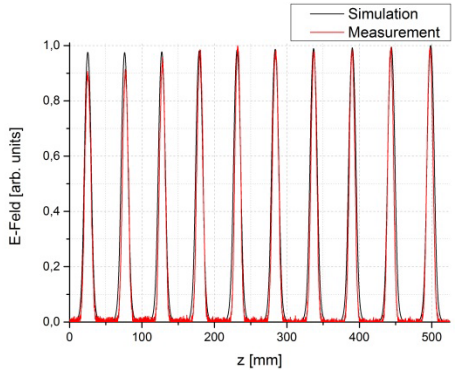

Figure 2: Electrical field distribution.

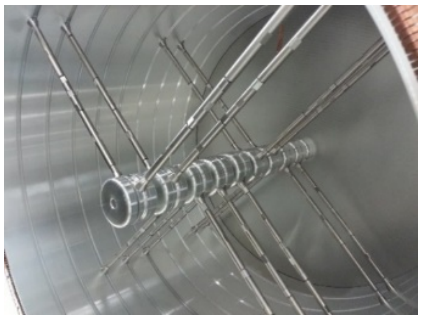

Figure 3: Alternating V-Stem configuration.

Outlook

It is planned to further improve the field stability by varying the stem configurations and probably to prolong the model to pronounce the effect on the field distribution.

References

[1] S. Mickat et al., internal report 2014
[2] X. Du et al. (this report)
[3] E. Müller, Disputation, Goethe Uni Frankfurt, 1977

DOI:10.15120/GR-2016-1

Status of beam dynamics design of the new post-stripper DTL

A. Rubin[1], *D. Daehn*[1], *X. Du*[1], *L. Groening*[1], *and S. Mickat*[1]
[1]GSI, Darmstadt, Germany

Introduction

The GSI UNILAC has served as injector for all ion species since 40 years. Its 108 MHz Alvarez DTL providing acceleration from 1.4 MeV/u to 11.4 MeV/u has suffered from material fatigue and has to be replaced by a new section [1]. The design of the new post-stripper DTL is now under development in GSI. An optimized drift tube shape increases the shunt impedance and varying stem orientations mitigate parasitic rf-modes [2]. This report is on the beam dynamics layout.

Beam dynamics simulations for the 1^{st} and the 2^{nd} Alvarez tanks

The beam dynamics simulations for the new model were done for $^{238}U^{28+}$ using the TraceWin code [3]. The behaviour of the beam in the proposed structure was investigated for different zero current phase advances, as without current, as for the current of 15 mA. Input emittances were chosen as E_x=E_y=0.175mm·mrad, E_z=16.57deg·MeV. Periodic solutions were found for each case and for each tank. The smallest transverse emittance growth along the 1^{st} tank A1 (15mA) was obtaned for a zero current phase advance of 55-90°. It confirms the results of the measurements in frame of the HIPPI experiments [4]. The initial zero current phase advances k_0 of 65-90° also correspond to the stability areas of the Hofmann stability chart (Fig.1).

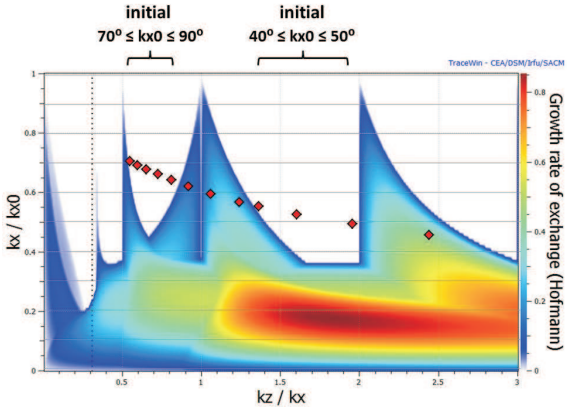

Figure 1: Hofmann stability chart for the new Alvarez-DTL.

Concerning the electric and magnetic field models the following cases for the tank A1 were studied:

- "hard edge" model for E-field and B-field with identical quadrupoles in each drift tube (effective length of 96 mm);
- 3D field maps for E-field, analytical field model for B-field with identical quadrupoles;
- 3D field maps for E-field and B-field with identical quadrupoles;
- "hard edge" model for E-field and B-field with three groups of quadrupoles (effective lengths 96 mm, 122 mm and 140 mm);
- 3D field maps for E-field, analytical field model for B-field with three groups of quadrupoles as above.

Beam dynamics simulations were done for k_0= 65° and for I=15 mA. The results of the simulations of all cases are basically identical. The transverse rms emittance growth for A1 is 2-4%, longitudinally it is about 5%. The same investigation for the 2^{nd} Alvarez tank (A2) shows almost no emittance growth.

Beam dynamics including intertank section

The intertank section for the presented design consists of quadrupoles, one buncher and spaces between them. These drifts can be filled with other elements (trafo, steerer, grid, probe etc.) The length of the intertank section is not finally determined at the moment and for the next example is taken as 157 cm. Four quadrupoles of an effective length of 96 mm and a buncher with voltage of 0.6 MV are proposed. The 1^{st} tank has 55 cells, the 2^{nd} 45 cells. The zero current phase advance for both tanks is 65°. The periodic solution was found as shown in Fig. 2. The transverse as well as the longitudinal rms emittance growth for the whole beam line is about 4%.

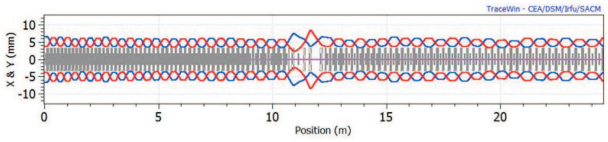

Figure 2: Transverse envelopes for A1, intertank and A2.

References

[1] L. Groening, et al. "Upgrade of the UNILAC for FAIR", HIAT 2015, Japan, 2015

[2] X. Du, et al. "Alvarez DTL Cavity Design for the UNLAC Upgrade", IPAC 2015, USA

[3] TraceWin http://irfu.cea.fr/Sacm/logiciels/index3.php

[4] L. Groening et al., "Experimental Evidence of the 90° Stop Band in the GSI UNILAC", Phis. Rev. Lett 102, 234801 (2009)

DOI:10.15120/GR-2016-1

High current proton and carbon beam operation via stripping of a molecular beam at GSI UNILAC

M. Heilmann[1], W. Barth[1,2], A. Adonin[1], C.E. Düllmann[1,2], R. Hollinger[1], E. Jäger[1], P. Scharrer[1,2], W. Vinzenz[1], H. Vormann[1]

[1]GSI, Darmstadt, Germany; [2]HIM, Mainz, Germany;

The experimental program of the future facility for Antiproton and Ion Research (FAIR) project requires a high number of cooled anti-protons per hour [1]. The FAIR proton injector linac has to deliver a 70 MeV, 35 mA pulsed proton beam at a repetition rate of 4 Hz [2].

During recent machine investigations at the GSI a high current proton beam was achieved in the Universal Lineral Accelerator (UNILAC) [3, 4]. In preparation for this the ion source was equipped with a newly developed 7-hole extraction system and optimized for single charged hydrocarbon beam (isobutane gas) operation. This beam was accelerated to 1.4 MeV/u and cracked in a new pulsed gas stripper into protons and charged carbon. The new stripper setup provides for high density gas pulses synchronous with the transit of the beam pulse close to the beam trajectory. With this setup a proton (up to 4.3 mA) as well a carbon-beam (up to 9.5 mA) intensity record at a beam energy of 1.4 MeV was achieved. The proton beam was accelerated up to 3.6 MeV/u inside the first Alvarez-section with full transmission.

MACHINE DEVELOPMENT

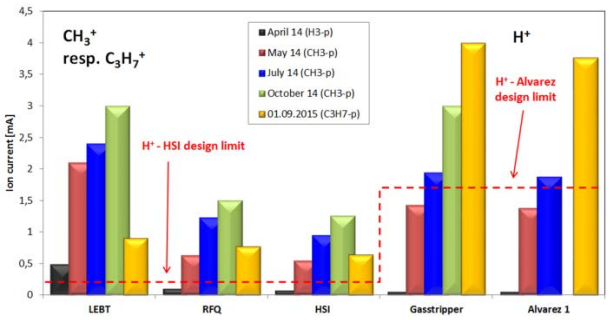

Figure 1: Measured beam current along HSI and Alvarez 1; the proton design limit was exceeded in the post stripper section.

The MUCIS ion source [5] was operated with isobutane (C_4H_{10}) gas, while a high-current $C_4H_7^+$-beam (0.7 emA) was delivered to the HSI. Due to the increased HSI design limitation for the $C_4H_7^+$-beam, an improved beam transmission compared to a pure proton beam is evident. The proton intensity should a theoretical increase by a factor of 7, while a factor of 6.4 was achieved (Fig. 1). The charge state distribution could be changed easily by varying the target density, while the proton beam intensity remains the same (Fig. 2). The proton beam transmission along the GSI-poststripper decreased to 70% (Fig. 3).

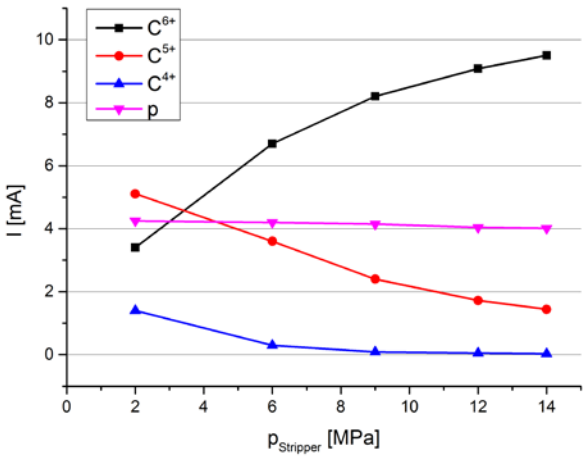

Figure 2: Measured ion current for proton- and carbon-beams (with different charge state) depending on stripper target density; stripping of an isobutane beam.

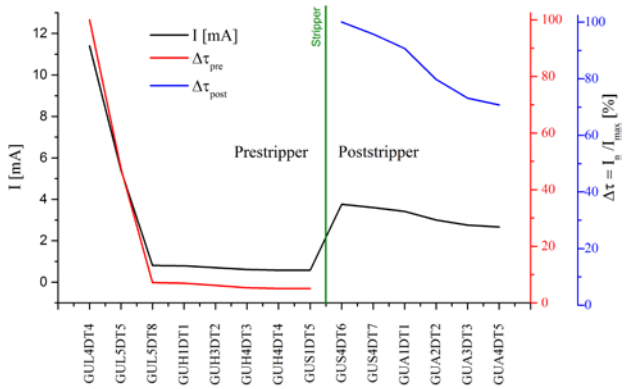

Figure 3: Measured (electrical) beam current of pre- ($C_4H_7^+$) and poststripper transmission (p) along GSI-UNILAC.

References

[1] O. Kester, et al., Status of FAIR Accelerator Facility, Proc. of IPAC, Dresden, Germany, p. 2084. (2014).

[2] R. Brodhage et al., First Coupled CH Power Cavity for the FAIR Proton Injector, Proceedings of IPAC, Dresden, Germany, p. 3232 (2014).

[3] W. Barth, et al., GSI Scientific Report 2015.

[4] W. Barth, et al., PRST-AB 18, 050102 (2015).

[5] R. Keller et al., Multicharged Ion Production with MUCIS, GSI Scientific Rep. 1987, p. 360. (1988).

DOI:10.15120/GR-2016-1

UNILAC status report

P. Gerhard[1]
[1]GSI, Darmstadt, Germany

Operation

UNILAC operation started with machine checkout and commissioning in July, regular operation began on July 27$^{\mathrm{th}}$ and ended on November 12$^{\mathrm{th}}$. Due to the upgrade activities regarding the rf transmitters of Alvarez 3, the maximum ion energy was restricted to 5.9 MeV/u. The SIS18 remained shut down for the whole year, therefore no beam for the synchrotron was accelerated. Furthermore, the number of active single gap resonators had been reduced to six, putting further constraints on the operation. For most of the time only one source at once was in use, thereby simplifying operation [1].

The regular beam time started with ^{12}C, followed by ^{197}Au and a long block of ^{48}Ca. This scheme was once repeated, followed by a short block of ^{238}U and ^{50}Ti, and two days of ^{3}He. ^{12}C, ^{48}Ca and ^{3}He were delivered by the ECR ion source via HLI, ^{197}Au and ^{50}Ti from the PIG, and ^{238}U from the high current terminal.

The main users for both ^{12}C and ^{197}Au were the material sciences at the M- and X-branch, biology, and the plasma physics (only ^{12}C). ^{48}Ca was used predominantly by SHE experiments (TASCA, SHIP, SHIPTRAP). Materials sciences used ^{48}Ca as well as ^{238}U, which was mainly requested by machine experiments. The latter also requested ^{197}Au and ^{50}Ti, and furthermore ^{40}Ar, ^{209}Bi, and CH_3^+. ^{3}He was exclusively accelerated for biology.

In spite of the restrictions mentioned above and in the shutdown section, all experiments could be served satisfactorily, not least thanks to the simplified beam time planning with only one source running most of the time and long periods for each ion species.

Shutdown Activities

Major shutdown activities at the UNILAC in 2015 were related to the main rf systems and cavities. The power converter for the Alvarez 3 transmitter is being renewed since November, this work is still ongoing. The rf transmitters for the single gap resonators 6 to 9 were dismantled beginning of 2015. The inter tank buncher BB6 was equipped with a spare spiral with lower aperture in 2014, recommissioning took place in May 2015. Drift tube no. 16 of Alvarez tank 1 had to be replaced due to water leakage in winter 2014/15. The drift tubes no. 30 of Alvarez 1 and no. 15 of Alvarez 3 had the same problem during the beam time of this year. Hence during the beam time several quadrupoles in the Alvarez drift tubes had to be disconnected, because the cooling water had to be switched off. Their replacement began in autumn.

In spring 2015 the kicker magnet UT1MK0 was equipped with a new hall probe for the zero field compensation. The existing probe was destroyed by heat from eddy currents. Water cooled cables, which power the main dipoles of the synchrotron SIS18 via the transfer channel, had to be replaced. This was started in September 2015 with the setup of scaffolding in the transfer channel and affected operation and other activities in the transfer channel.

Besides the highlights mentioned above, regular service and maintenance was scheduled, such as for cooling circuits, ventilation and control systems, and other infrastructure of the UNILAC. A larger number of turbo molecular vacuum pumps was replaced.

Machine Experiments

Already during commissioning, several machine experiments were conducted: The beam instrumentation department used ^{40}Ar (PIG) for bunch length measurements at US3, at the same time ^{40}Ar from the HLI was used for transverse emittance measurements at the CW demonstrator [2]. This was followed by the commissioning of the 4d-emittance measurement setup ROSE at UCW, again with ^{40}Ar from the HLI, and pulsed gas stripper investigations with high current ^{209}Bi and CH_3^+ as well as ^{40}Ar (PIG) [3]. This period was terminated with tests of the magnetic field feedback system of the dipole magnets of the charge state separator in the transfer channel with ^{1}H and ^{40}Ar in preparation of the upgrade of the hall probe setup.

Another two beam times with ^{40}Ar and ^{84}Kr for ROSE were executed in August and November respectively [4, 5]. High current proton beams made from CH_3^+ were investigated in September. The pulsed stripper was again tested with a ^{50}Ti beam (PIG, natural material) and high current ^{238}U in November. All machine experiments had been accomplished successfully.

References

[1] S. Reimann et al. (this report)
[2] M. Miski-Oglu et al. (this report)
[3] P. Scharrer et al. (this report)
[4] M. Maier et al. (this report)
[5] M. Maier et al., PRAB (submitted)

DOI:10.15120/GR-2016-1

UNILAC upgrade activities

L. Groening[*1]
[1]GSI, Darmstadt, Germany

In 2013 a review was held to evaluate the UNILAC's readiness w.r.t. the requirements imposed by FAIR [1]. This report confirmed the necessity to forge the project "UNILAC Upgrade" and defined its major pillars. After the last beam time in 2015 the directorate inquired a report on the achieved performance for uranium [2], which states that although considerable progress has been made, the UNILAC has achieved the FAIR design parameters to about 20%, i.e. the report re-stresses the relevance to push the upgrade of the machine.

Upgrade Activities

Provision of uranium will be concentrated at a dedicated new source terminal (terminal "West") to be installed between the existing terminals "North" and "South". It comes along with augmenting the repetition rate of the source from 1 to 2.7 Hz by shortening the source pulse length from 1000 to 500 μs and using an uranium/tungsten alloy as cathode material. The latter was fabricated successfully at the AREVA company. Beam matching to the HSI-RFQ will be through a newly designed LEBT [3, 4].
The beam dynamics of the existing HSI-RFQ is under redesign to reduce the electric surface field [5, 6]. New rods require the exchange of the carrier rings to preserve the resonant frequency. The subsequent matching section (MEBT) to the pre-stripper lacks operational flexibility. A new design [6] is well advanced and components are ready for tendering.
Remarkable progress has been made in increasing the efficiency of stripping U^{4+} to $U^{28+-31+}$ using a pulsed jet of hydrogen [7]. It allowed for provision of 9.5/7.9 emA (29+/28+) at the entrance to the post-stripper DTL [2]. Integration of the set-up into routine operation until 2019 has been started.
A round-to-flat adaptor for ion beams shall be integrated in front of the post-stripper. Its implementation for intense beams required the development of full 4d transverse beam diagnostics which was not at hand before. The ROSE set-up was successfully developed and commissioned at the HLI [8, 9].
The design of a completely new post-stripper DTL is ongoing. As FAIR is based on low duty cycle injectors, the beam quality provided by the latter is of utmost importance for the whole FAIR project. Following the recommendation of a dedicated review of the FAIR injector chain [1] not to sacrifice beam quality for rf efficiency, GSI gives preference to an Alvarez-type DTL instead of to an rf efficient KONUS-based design. The inner tank geometry is defined for all five tanks up to 11.4 MeV/u [10]. The design employs a novel scheme of rf field stabilization based on optimized orientations of the drift tube stems. Specially shaped drift tube end caps improved the ratio of shunt impedance per surface field w.r.t. existing tanks. A dedicated 1:3 cold rf model cavity has been built and rf measurements have started [11]. The beam dynamics design is under progress [12] relying on strong and periodic FDDF focusing together with systematic envelope matching. For an uranium beam of 15 emA the total 6d-rms-emittance growth up to 5.4 MeV/u is less than 2%. The beam dynamics design of the first inter-tank section is available. Integration of a phase probe, a beam current transformer, a profile grid, a valve, and a re-buncher cavity along each inter-tank section is foreseen. Re-bunchers are required to assure provision of all energies between 3 and 12 MeV/u with sufficiently low energy spread. Additionally, re-bunchers improve the periodicity of the longitudinal envelope along inter-tank transitions.

Acknowledgement

The work being presented here comprises contributions from many different departments at GSI, the Goethe University of Frankfurt, and the Helmholtz-Institute Mainz.

References

[1] Final report *GSI FAIR Injector Review*, Editor F. Gerigk, CERN, (2014).

[2] L. Groening and O. Kester, *Status der erreichten UNILAC-Parameter hinsichtlich der FAIR Anforderungen für* $^{238}U^{28+}$, (2015).

[3] C. Xiao et al. NIM A **788** 173 (2015).

[4] H. Vormann et al., this report.

[5] C. Zhang et al., this report.

[6] S. Mickat et al., this report.

[7] P. Scharrer et al., this report.

[8] C. Xiao et al., submitted to PRAB.

[9] M. Maier et al., this report.

[10] X. Du et al., this report.

[11] A. Seibel et al., this report.

[12] A. Rubin et al., this report.

* la.groening@gsi.de

DOI:10.15120/GR-2016-1

Status of the Compact LEBT project

H. Vormann, A. Adonin, P. Gerhard, L. Groening, R. Hollinger,

M. Maier, S. Mickat, A. Rubin, C. Xiao

GSI, Darmstadt, Germany

To fulfil the uranium beam current requirements for FAIR, an additional ion source branch must be built at the high current injector HSI. This injector beam line consists of a dedicated uranium ion source terminal and a straight LEBT section, the Compact LEBT [1]. Latest optimisations led to a relatively short LEBT, allowing installation of the terminal close to the existing ion source branches.

LEBT Design

Beam measurements have been used for beam dynamics simulations [2, 3]. They were performed at the existing high current ion source (North Terminal) and at the ion source test bench (HOSTI), providing more than 50 mA of total uranium beam current (typically 35 mA of U^{4+}, with approximately 15 mA of U^{4+} within an emittance of 280 mm mrad) (Fig. 1 and 2).

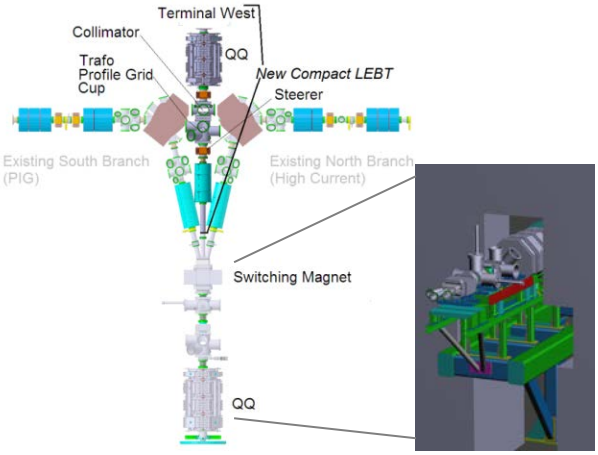

Figure 1: New HSI-LEBT with Compact-LEBT, LEBT model from switching magnet to quadrupole quartet.

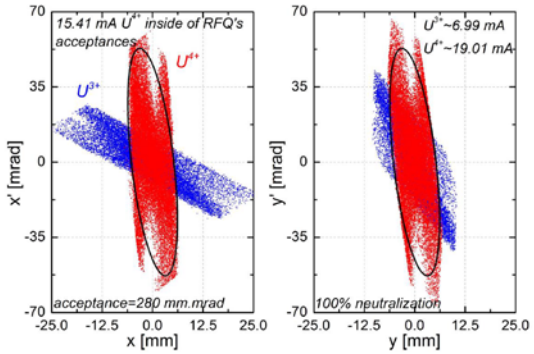

Figure 2: Uranium emittance at RFQ entrance, simulated from measured data (49 mA tot. beam current at ion source, 32 mA U^{4+}, 15 mA within 280 mm mrad).

As the two existing ion source branches will remain, a minimum distance between the new uranium terminal and the switching magnet must be kept (restricted space). Therefore two focusing elements must be used in this section, a quadrupole quartet (QQ) and a quadrupole triplet (QT).

For reducing the amount of the U^{3+} ions a collimator is used to scrape off this partition of the uranium beam (Fig. 3) [3]. Within the HSI, all U^{3+} ions will be scraped off in the collimator or lost in the following LEBT and RFQ at low energy.

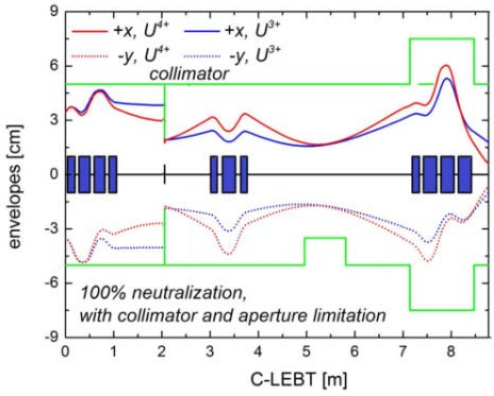

Figure 3: Beam envelopes $U^{3+/4+}$, with collimator.

Estimations showed that with upgrade measures at the UNILAC 18 emA of U^{4+} are sufficient to provide for the required 15 emA of U^{28+} behind the stripper (section between HSI and post stripper DTL).

In the new LEBT beam current transformers with large aperture are foreseen at the ion source, behind the first quadrupole quartet, and behind the collimator. A profile grid (width 94 mm) and a movable Faraday cup (diameter 80 mm) will be used for routine beam operation. An emittance measurement device is planned to be used during the commissioning phase.

Status of Components

The power supply for the new quadrupole quartet will be delivered in October 2016. For its SAT the new QQ will be installed in the beam line in Q3/2016. A fire protection concept for the new terminal has been set up recently, allowing now further planning steps.

References

[1] L. Dahl, proc. LINAC 2006
[2] S. Yaramyshev et al., proc. IPAC 2014
[3] C. Xiao et al., NIM A 788 (2015) 173-181.

DOI:10.15120/GR-2016-1

Rotating system for four-dimensional transverse rms-emittance measurements

C. Xiao[*], *M. Maier, X.N. Du, P. Gerhard, L. Groening, S. Mickat, and H. Vormann*
GSI, Darmstadt, Germany

A new method using a rotatable slit/grid emittance measurement device called ROSE (see Fig. 1) has been developed and commissioned to measure the four-dimensional second order moments. Comparing to the method using skew quadrupoles combined with a slit/grid emittance measurement device [1], it will allow fast and mobile four-dimensional emittance measurements without skew quadrupoles. A dedicated method which includes 15 algorithms has been developed to reconstruct the second moments. A minimum of four emittance measurements is sufficient to reconstruct the complete four-dimensional beam matrix.

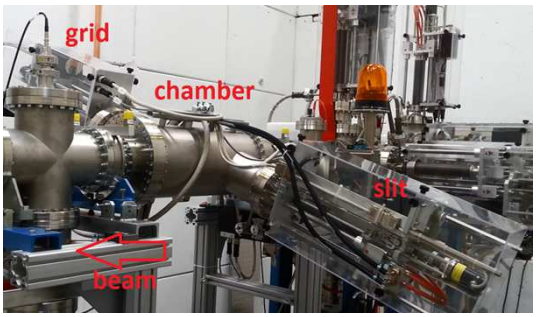

Figure 1: ROtating System for Emittance measurements (ROSE). The total length of ROSE is 833 mm.

Rotation by 0°/90° will just measure the usual uncoupled second moments. Rotation by θ° around the beam axis provides access to the coupled second moments [2]. The solution of the searched coupled matrix elements at location i can be summarized to a set of linear equations

$$\begin{cases} \Gamma_{11}\langle xy\rangle_i + \Gamma_{12}\langle xy'\rangle_i + \Gamma_{13}\langle x'y\rangle_i + \Gamma_{14}\langle x'y'\rangle_i = \Lambda_1 \\ \Gamma_{21}\langle xy\rangle_i + \Gamma_{22}\langle xy'\rangle_i + \Gamma_{23}\langle x'y\rangle_i + \Gamma_{24}\langle x'y'\rangle_i = \Lambda_2 \\ \Gamma_{31}\langle xy\rangle_i + \Gamma_{32}\langle xy'\rangle_i + \Gamma_{33}\langle x'y\rangle_i + \Gamma_{34}\langle x'y'\rangle_i = \Lambda_3 \\ \Gamma_{41}\langle xy\rangle_i + \Gamma_{42}\langle xy'\rangle_i + \Gamma_{43}\langle x'y\rangle_i + \Gamma_{44}\langle x'y'\rangle_i = \Lambda_4 \\ \Gamma_{51}\langle xy\rangle_i + \Gamma_{52}\langle xy'\rangle_i + \Gamma_{53}\langle x'y\rangle_i + \Gamma_{54}\langle x'y'\rangle_i = \Lambda_5 \\ \Gamma_{61}\langle xy\rangle_i + \Gamma_{62}\langle xy'\rangle_i + \Gamma_{63}\langle x'y\rangle_i + \Gamma_{64}\langle x'y'\rangle_i = \Lambda_6 \end{cases} \quad (1)$$

with

$$\Gamma_{11} = m^a_{11}m^a_{33},\ \Gamma_{12} = m^a_{11}m^a_{34},\ \Gamma_{13} = m^a_{12}m^a_{33},\ \Gamma_{14} = m^a_{12}m^a_{34}, \quad (2)$$

$$\Gamma_{21} = m^a_{11}m^a_{43} + m^a_{21}m^a_{33},\ \Gamma_{22} = m^a_{11}m^a_{44} + m^a_{21}m^a_{34},$$
$$\Gamma_{23} = m^a_{12}m^a_{43} + m^a_{22}m^a_{33},\ \Gamma_{24} = m^a_{12}m^a_{44} + m^a_{22}m^a_{34}, \quad (3)$$

$$\Gamma_{31} = m^a_{21}m^a_{43},\ \Gamma_{32} = m^a_{21}m^a_{44},\ \Gamma_{33} = m^a_{22}m^a_{43},\ \Gamma_{34} = m^a_{22}m^a_{44}, \quad (4)$$

and with the same procedure for setting b

$$\Gamma_{41} = m^b_{11}m^b_{33},\ \Gamma_{42} = m^b_{11}m^b_{34},\ \Gamma_{43} = m^b_{12}m^b_{33},\ \Gamma_{44} = m^b_{12}m^b_{34}, \quad (5)$$

$$\Gamma_{51} = m^b_{11}m^b_{43} + m^b_{21}m^b_{33},\ \Gamma_{52} = m^b_{11}m^b_{44} + m^b_{21}m^b_{34},$$
$$\Gamma_{53} = m^b_{12}m^b_{43} + m^b_{22}m^b_{33},\ \Gamma_{54} = m^b_{12}m^b_{44} + m^b_{22}m^b_{34}, \quad (6)$$

$$\Gamma_{61} = m^b_{21}m^b_{43},\ \Gamma_{62} = m^b_{21}m^b_{44},\ \Gamma_{63} = m^b_{22}m^b_{43},\ \Gamma_{64} = m^b_{22}m^b_{44}, \quad (7)$$

and finally

$$\Lambda_1 = \langle xy\rangle^a_f,\ \Lambda_2 = \langle xy'\rangle^a_f + \langle x'y\rangle^a_f,\ \Lambda_3 = \langle x'y'\rangle^a_f, \quad (8)$$

$$\Lambda_4 = \langle xy\rangle^b_f,\ \Lambda_5 = \langle xy'\rangle^b_f + \langle x'y\rangle^b_f,\ \Lambda_6 = \langle x'y'\rangle^b_f. \quad (9)$$

The algorithms offer the possibility to reconstruct the full beam matrix at location i from emittance measurements of different rotation angles through

$$\begin{bmatrix} \langle xy\rangle_i \\ \langle xy'\rangle_i \\ \langle x'y\rangle_i \\ \langle x'y'\rangle_i \end{bmatrix}^j = \Gamma_j^{-1}\Lambda^j, \quad j = 1, 2, \cdots 15. \quad (10)$$

A beam of $^{83}Kr^{13+}$ at 1.4 MeV/u has been used at the HLI. Evaluating four measurements the correlated second moments at the reference location. The averaged second moments matrix C at this location is calculated as (in units of mm and mrad)

$$C = \begin{bmatrix} 8.57 & -4.34 & -3.24 & -1.06 \\ -4.34 & 3.36 & -0.79 & 1.54 \\ -3.24 & -0.79 & 11.20 & -3.05 \\ -1.06 & 1.54 & -3.05 & 1.87 \end{bmatrix}. \quad (11)$$

The coupling was enforced by a skew triplet preceding ROSE. Evaluation of the rms projected and eigen emittances reveals that ε_x=3.15 mm mrad, ε_y=3.41 mm mrad, ε_1=2.36 mm mrad, and ε_2=2.06 mm mrad. The corresponding coupling parameter t is 1.20 and the beam through the skews is strongly coupled.

References

[1] C. Xiao, L. Groening, P. Gerhard, M. Maier, S. Mickat, and H. Vormann, Nucl. Instrum. Methods. Res. A 820 14 (2016).

[2] C. Xiao, M. Maier, X.N. Du, P. Gerhard, L. Groening, S. Mickat, and H. Vormann, submitted to PRAB.

[*] c.xiao@gsi.de

DOI:10.15120/GR-2016-1

Development and upgrade of the ECRIS facility

K. Tinschert, F. Maimone, R. Lang, J. Mäder, M. Endermann, P. T. Patchakui
GSI, Darmstadt, Germany

Investigation on pulsed mode operation with frequency tuning of the CAPRICE-ECRIS

Recent experimental results proved that the tuning of the operating frequency of the ECRIS is a promising technique to achieve higher ion currents of higher charge states [1]. On the other hand it is well known that the afterglow mode of the ECRIS operation can provide more intense pulsed ion beams in comparison with the continuous wave (cw) operation [2]. These two techniques can be combined by pulsing the variable frequency signal driving the Traveling Wave Tube Amplifier which provides the high microwave power to the ECRIS.

In order to analyse the effect of these two combined techniques on the ion source performance, several experiments were carried out on the pulsed frequency tuned CAPRICE-type ECRIS. In order to make a comparison between pulsed and cw operation, the first measurements were carried out by operating the ion source with a continuous wave (cw) microwave power of 350 W at 14.5 GHz. At this power level the other ion source parameters, mirror field and gas pressure, were optimized for the production of Ar^{12+}. After that a sweep of the microwave frequency, in the 13.5-15 GHz range (200 kHz steps with 20 ms dwell time), was performed. Figure 1 shows the variation of the Ar^{11+}, Ar^{12+} and Ar^{13+} currents for different microwave frequencies and one can see that the ion intensity can be strongly enhanced by tuning the frequency. For instance, with respect to 14.5 GHz, at 13.53 GHz the current of Ar^{12+} and Ar^{13+} is 3.3 and 5.2 times higher, respectively, and the charge state distribution shifts towards higher charge states (see Figure 3).

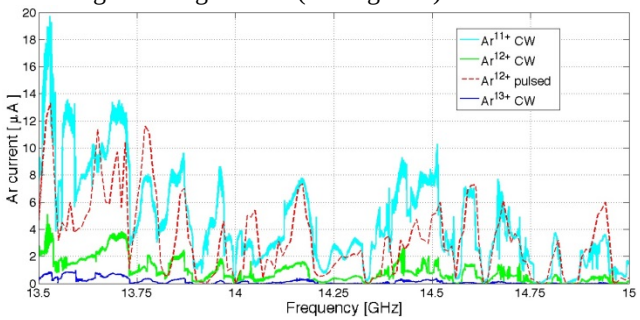

Figure 1: Argon beam currents measured during the frequency sweeps in the 13.5-15 GHz range

Then the afterglow mode was analysed at these two frequencies by pulsing the microwave power. Different pulse periods T_p and duty cycles $d=t_p/T_p$ (ratio between the pulse duration t_p and the pulse period) were investigated to find the best operating conditions for stable operation with maximum current. The best performance was found at 13.53 GHz pulsed with $d=30\%$ and T_p=100 ms. Figure 2 shows the increase of Ar^{12+} current by selecting the optimized frequency. Then the CAPRICE ECRIS was operated in pulsed mode again with T_p=100 ms and $d=30\%$ and, by manually stepping the frequency of 1 MHz within the 13.5-15 GHz range, the maximum of the afterglow current was measured. The intensity variation of the afterglow during the frequency tuning is shown in the dashed red line of the figure. 13.53 GHz remains the frequency where the maximum of the current was measured in pulsed mode, too. The measured charge states distributions are shown in Figure 3. In cw mode the tuning of the microwave frequency is effective for the higher charge states (i.e. $\geq 9^+$) while in pulsed mode there is a current gain for all the charge states when selecting an optimized frequency (e.g. 13.53 GHz for this ion source parameter setting). Furthermore the frequency tuning in pulsed mode doubles the intensity of the highest charge states, i.e. 13+ (see inset in Figure 3: zoomed view for Ar^{12+} and Ar^{13+}). This investigation experimentally showed that the frequency tuning combined with afterglow operation mode allow for a further enhancement of the intensity of pulsed highly charged ion beams [3].

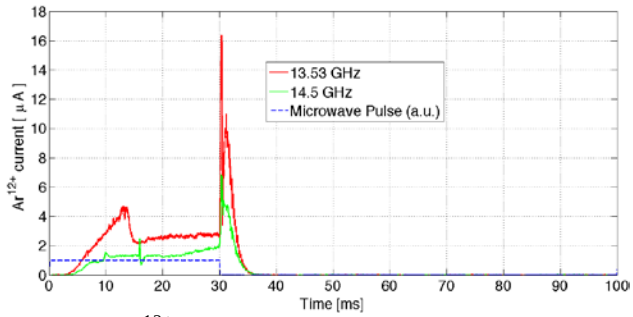

Figure 2: Ar^{12+} current (d=30%,T_p=100 ms) at 14.5 and 13.53 GHz

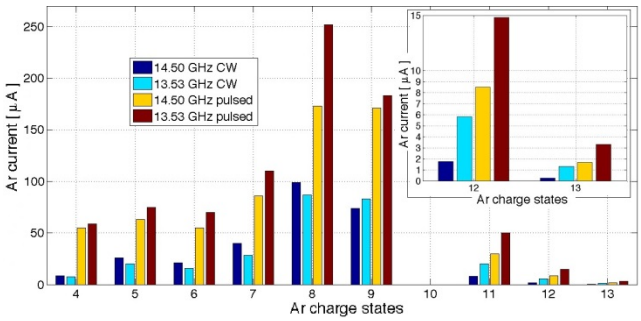

Figure 3: Ar charge states distribution

References

[1] F. Maimone *et al*, Rev. Sci. Instrum. 82 (2011) 123302
[2] R. Geller, *Electron Cyclotron Resonance Ion Sources and ECR plasmas*, IOP, Bristol (1996).
[3] F. Maimone *et al*, Rev. Sci. Instrum.82 (2016) 02A712

DOI:10.15120/GR-2016-1

Status of the IH-DTL poststripper linac proposal*

H. Hähnel†*, U. Ratzinger, and R. Tiede*
Institut für Angewandte Physik, Goethe Universität Frankfurt

For its role as dedicated injector for FAIR, several sections of the UNILAC have to be upgraded for high current uranium operation. The Alvarez linac in the poststripper section of the UNILAC is in operation since more than 40 years and therefore a replacement by a new linac would be beneficiary to FAIR operation. We propose an IH-DTL linac as replacement for the current GSI UNILAC Alvarez [1]. The new design is based on the KONUS beam dynamics concept and delivers high beam quality well within FAIR requirements. We report recent progress of the IH-DTL poststripper replacement design.

Layout and mechanical concept

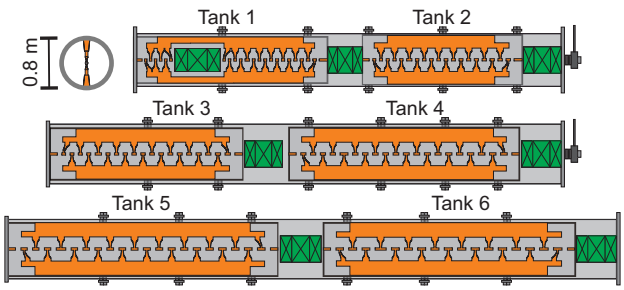

Figure 1: Sketch of the IH-DTL poststripper linac with the proposed modular tank layout.

The IH-DTL consists of six IH-DTL cavities with seven magnetic quadrupole triplet lenses. The linac features a modular tank concept (Figure 1), dividing each cavity into two to three modules with a cylindrical shape. The total length will be close to 25 m in contrast to more than 55 m of an Alvarez alternative.

Updated simulation results

The CST Microwave Studio simulations confirm, that the current design is well within the power design limit of $< 1.35MW$ per cavity. In fact, the cavities 1 & 2 should be operated from the same amplifier since their power need is very low. Another option would be to integrate the two into one cavity with two internal triplet lenses. The results of the CST simulations are summarized in the following table.

Further beam dynamics simulations were performed using voltage distributions provided by CST simulations of all cavities. Results show low emittance growth and high beam quality behind the poststripper linac. The emittance growth over the whole linac is shown in Figure 2. The total rms emittance growth in the transverse plane at 15 mA design current is 25 %.

	$Z_{eff} \cdot cos^2(\phi_s)$	Q	P_{total}
Tank 1	198 MΩ/m	$2.6 \cdot 10^4$	361 kW
Tank 2	209 MΩ/m	$2.7 \cdot 10^4$	532 kW
Tank 3	171 MΩ/m	$2.9 \cdot 10^4$	835 kW
Tank 4	141 MΩ/m	$3.0 \cdot 10^4$	1099 kW
Tank 5	116 MΩ/m	$3.0 \cdot 10^4$	1160 kW
Tank 6	103 MΩ/m	$3.0 \cdot 10^4$	970 kW

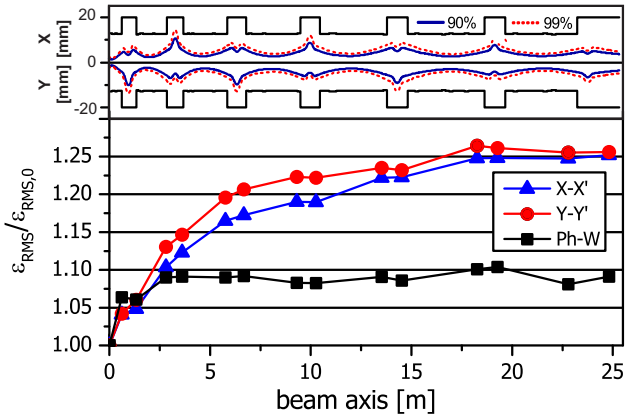

Figure 2: Emittance growth for the whole IH-DTL.

However it has to be noted, that this value cannot be directly compared to growth rates calculated with e.g. TraceWin. Extensive code comparison studies showed, that LORASR predicts higher emittance growth than TraceWin (see [2]). A cross check calculation using TraceWin is underway.

The proposed IH-DTL design is a viable option for the poststripper linac replacement. Further investigations, includiung extensive error studies, are currently ongoing at IAP Frankfurt.

References

[1] H. Hähnel, U. Ratzinger, R. Tiede, "Development of a KONUS based High Energy Linac for the UNILAC", GSI Scientific Report 2014, p. 408

[2] L. Groening et al., "Linac Code Benchmarking with High Intensity Experiments at the UNILAC", Proc. of PAC09, pp. 719-723, Vancouver, BC, Canada

* Work supported by BMBF05P15RFRBA
† haehnel@iap.uni-frankfurt.de

DOI:10.15120/GR-2016-1

RF-design of the new UNILAC post-stripper DTL *

X. Du[1], *L. Groening*[1], *S. Mickat*[1], *A. Seibel*[1,2], *and A. Rubin*[1]
[1]GSI, Darmstadt, Germany; [2]Goethe-University, Frankfurt, Germany

Abstract

Based on previous studies and optimization, the new 108 MHz Drift Tube Linac (DTL) of the UNILAC upgrade program at GSI [1] has finished the primary design. The energy from 1.4 MeV/u to 11.4 MeV/u will be provided by five tanks with similar power consumptions and tank lengths. The tube shape for every tank is specially designed for homogenous surface fields. The total power consumption is 10 percent lower w.r.t. the existing DTL. The field stabilization through stem configuration has been fully studied and should be applied.

Tank parameters

The tank diameters are kept constant in every tank for easier fabrication and the averaged fields E0(z) are about 2 MV/m with the Kilpatrick limit set to 1.0 for all cavities. Power consumption including beam load and safety margins are within a limit of 1.35 MW for each cavity. The total rf-length of all tanks should be not far from the present lengths (50 m) since the lengths of the inter-tank sections will not change significantly with the upgrade. The input and output energy are kept as before. Based on this background, we primarily designed five tanks that mostly meet the requirements; their basic rf-parameters are listed in Tab. 1. The beta profiles and 3d-electric field maps were ex-ported and to be plugged into design and simulations of the beam dynamics with TraceWin code [2].

Table 1: basic rf-parameters for the current design of the new post stripper Alvarez-DTL cavities.

cavity	energy (Mev)	total power	rf-length (m)	cell count
tank1	1.39-3.29	1.31	10.5	54
tank2	3.29-5.44	1.35	12.2	46
tank3	5.44-7.57	1.35	11.7	36
tank4	7.57-9.85	1.35	12.0	32
tank5	9.85-11.4	0.98	7.86	19
total	11.4	6.34	54.2	187

Field Stabilization

Former study shows that rotating specific stems by 180 degrees may change field stability [3]. In order to develop it as a new method to perform field stabilization, we built and analysed the transmission line equivalent circuit of an Alvarez-type cavity including the stems. With this equivalent circuit the differential equations of voltage distributions were established. Their standing wave solution delivered the dispersion curve of the cavity, which agrees very well to simulations for several cases with uniform stem configuration. The relationship between stem configuration, dispersion curve, and field flatness is analytically explained through these studies. Finally, standard procedures for such tuning methods are established. The method was applied to tank 1 of the new DTL design with simulations and the designed stem configuration for tank 1 is shown in Fig. 1. Due to increasing cell length, the stem configuration changes to assure that the local transversal admittance is as small as possible, such that the field distribution of the whole cavity will be much less sensitive to perturbations. The effect was checked by introducing an artificial geometric error near the first cell. Simulations showed that with the above stem configuration the field distribution with perturbation is much flatter w.r.t. a configuration with identical stem orientation all along the cavity. A 1:3-scale model rf-cavity with 10 gaps was built and tested to confirm the tuning effect [4]. Bead pull measurements and simulations both show that the dispersion curves are changed as expected by different stem configurations.

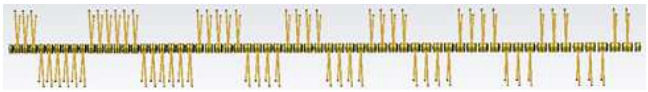

Figure 1: Stem configuration design for tank1 to achieve field stabilization

Further improvements

The total rf-length of the five tanks is four meters longer than the existing DTL, which might raise installation space issues. Further optimization aims for keeping the same total rf-length. Beta increasing in one cell will be taken into account in the cell by cell design VBA macro to obtain increased accuracy of the cell length. Tuners and couplers will be included in further rf design as well.

References

[1] L. Groening et al., this report.

[2] A. Rubin et al., this report.

[3] X. Du et al., Proc. of IPAC 2015, Richmond, USA, WEPMA017.

[4] A. Seibel et al., this report

*Work supported by GSI(UNILAC), EURONS contract No.506065 FAIR@GSI PSP code:1.3.4.2.

UNILAC High Current Injector (HSI) upgrade

S. Mickat[1], M. Baschke[2], L. Groening[1], H. Hähnel[2], M.S. Kaiser[1], H. Podlech[2], U. Ratzinger[2], R. Tiede[2], H. Vormann[1], M. Vossberg[1], C. Zhang[1]
[1]GSI, Darmstadt, Germany; [2]IAP, Frankfurt, Germany

The UNILAC is designated as the injector linac for the whole FAIR accelerator chain. Concerning the ambitious beam quality and intensity requirements an extensive upgrade program is in progress [1]. The existing High Current Injector (HSI) is known as a bottleneck from simulation for historical reasons, the tight boundary conditions during the Wideroe substitution in the nineties and the lower beam intensity requirements at this time. Especially after the RFQ upgrade in 2009 the transmission losses in front of the RFQ were shifted behind the RFQ [2]. The existing matching line between the RFQ and the IH (MEBT) is presently not able to match the beam to the IH properly. Regarding the HSI Upgrade the definition of the acceptance of the IH is crucial [3]. Every section in front of the IH up to the ion sources is checked with respect to match as good as possible into the IH, i.e. minimizing the transmission losses through the whole HSI by keeping the beam quality adequately.

New MEBT and RFQ electrodes

The existing inter-tank section (MEBT) between the HSI RFQ and the following IH comprises a combination of one quadrupole doublet and the superlens since 1999. The superlens is a 1m long RFQ cavity, which combines longitudinal and transverse focusing. In operation the coupling between the transverse and longitudinal focusing leads to less than the six necessary parameters for matching the beam into the IH adequately.

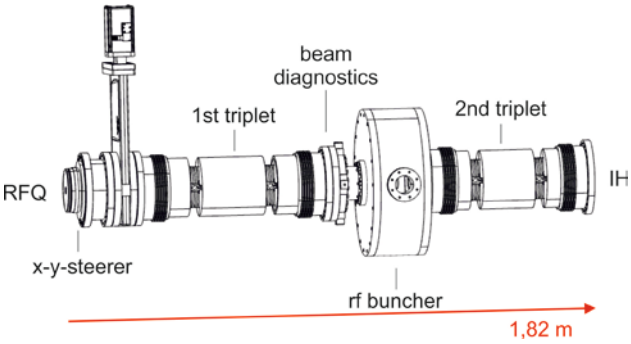

Figure 1: proposed MEBT section

The proposed MEBT comprises two triplet lenses for transverse and one buncher for longitudinal matching (fig.1).The decoupling of transverse and longitudinal focusing provides eight independent operating parameters, the six gradients assigned to the two triplets and the phase and amplitude of the buncher.

The trade-off with respect to the existing concept is the 50 cm longer installation length, which means a shift of the two existing IH tanks downstream. The cost-benefit analysis of such a MEBT redesign is positive towards the benefit. Simulations show no transmission losses through the IH as well as a reduction of the emittance growth, notably in the longitudinal plane (tab.1).

	Present MEBT	**New MEBT**
Transmission	*86 %*	*100 %*
Emittance growth (x/y/z)	*57 / 93 / 324 %*	*54 / 61 / 65 %*

Table 1: Comparison of the output beam parameters behind the IH between the present and new MEBT [4].

Another aspect in optimising the beam matching into the IH is the RFQ output beam parameters. The RFQ output beam parameters depend on the electrode design. Since the commissioning of the RFQ in 1999 every five years the electrodes were refurbished or rather renewed. The electrodes' surfaces are exhausted due to high power operation. The recent set of electrodes was mounted in 2009 [5]. Within this interval of servicing the opportunity of re-designing the electrodes is taken aiming for best beam matching into the new MEBT. Furthermore the inter-vane voltage is reduced for more reliability in operation [6].

For both subprojects the MEBT redesign and the RFQ upgrade, budget will be allocated in 2016. The components are ready for tender. The realisation of both measures, the new MEBT as well as the new RFQ electrodes, are feasible until 2018 from today's point of view.

References

[1] S. Mickat et al., "Status of the HE-LINAC project at GSI", Scientific Report 2014 GSI Report 2015-1, 407 p. (2015)
[2] L. Groening, "HE-Linac: Layout & preliminary (quasi) Front-to-End Simulations", GSI FAIR Injector Review, Darmstadt (2013)
[3] R. Tiede, internal note (2013)
[4] H. Hähnel et al., "Proposal of a Conventional Matching Section as an Alternative to the Existing HSI MEBT Superlens at GSI UNILAC", MOPP062, Proceedings of LINAC2014, pp. 196-198, Geneva, Switzerland (2014)
[5] H. Vormann et al., "Advanced UNILAC Upgrade for Fair", MOP040, Proceedings of LINAC2010, Tsukuba, Japan, 142 p., (2010)
[6] C. Zhang, "New Design of the HSI RFQ for UNILAC Upgrade", AKBP2, DPG Verhandlungen, Darmstadt (2016)

DOI:10.15120/GR-2016-1

New HSI-RFQ design for the UNILAC upgrade

Chuan Zhang[#], *Lars Groening, Sascha Mickat, Hartmut Vormann*
GSI Helmholtz Center for Heavy Ion Research, Planckstr. 1, Darmstadt, Germany
Markus Baschke, Holger Podlech, Ulrich Ratzinger, Rudolf Tiede
Institute for Applied Physics, Goethe-University, Frankfurt a.M., Germany

Abstract

As the main injector to the future FAIR facility, the UNILAC accelerator is required to deliver ion beams with high intensities as well as good beam quality. The electrodes of the current HSI RFQ are exhausted and the current RFQ together with the subsequent MEBT are assigned to be one bottle-neck for improving the brilliance performance of the whole linac. Based on the so-called NFSP (New Four-Section Procedure) method, a new RFQ electrode design has been developed and optimized for 20emA, U^{4+} beams at the RFQ-entrance. Since just the electrodes will be replaced, the RFQ length has been kept unchanged. Even with a lowered inter-vane voltage, the new RFQ design has achieved higher transmission efficiency and much better brilliance compared to previous designs.

Introduction

To meet the requirements for the injection to FAIR, UNILAC needs to deliver a 15emA U^{28+} beam. The current RFQ, which was designed in 2008 and has been put into operation in 2009, together with the subsequent MEBT are becoming one bottle-neck for improving the brilliance performance of the whole linac. After many years of operation, the electrodes have suffered from sparking. Therefore, an upgrade campaign for the HSI RFQ has been launched since 2015.

The design requirements for the new RFQ are:

- To reduce the max. surface electric field $E_{s,max}$
- To keep same length for adopting the same tank
- To improve the input and output matching
- To provide good beam performance

New Design Concepts

The new design (D2016) has been realized by using the NFSP method [1] with the following concepts:

- To drop the inter-vane voltage from 155kV to 125kV for lower $E_{s,max}$ at a cost of only 0.2mm smaller mid-cell aperture r_0
- To decrease the mid-cell aperture more slowly and smoothly at the beginning of the RFQ (see Fig. 1) in order to enlarge the transverse acceptance considerably
- To change the design philosophy for the bunching process completely. Fig. 2 shows that D2016 has a softer pre-bunching but much faster main bunching, which is just in opposite to the old design (D2008 [2]). The advantages are: 1) It will lead to a maximum longitudinal acceptance and make most particles bunched and accelerated. 2) During the main bunching process, the increased acceleration will help to overcome the increasing space-charge effects transversely.

The simulation results for D2016 are satisfying. Using the same input emittance and input Twiss parameters, the new RFQ is even 5 cm shorter, and increases the transmission efficiency from 89% to 94% with no emittance growth in the transverse plane and a longitudinal output emittance almost identical to the previous design.

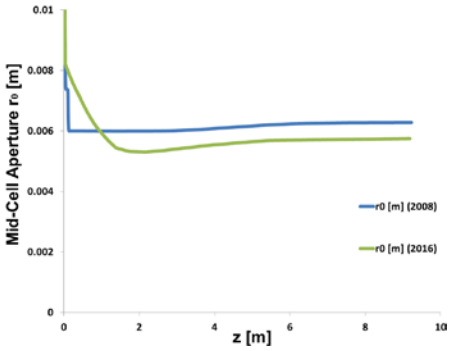

Figure 1: Mid-cell aperture along the RFQ (blue: D2008; green: D2016).

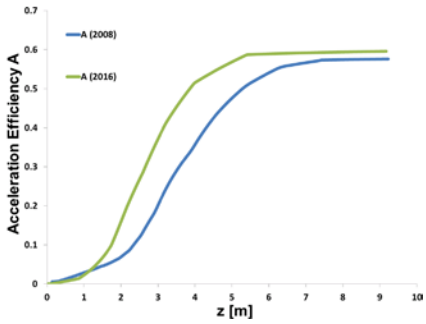

Figure 2: Acceleration efficiency along the RFQ (blue: D2008; green: D2016).

In short, the RFQ design itself is already ok. The work for input and output beam matching is ongoing.

References

[1] C. Zhang et al., Phys. Rev. ST Accel. Beams 7, 100101 (2004).
[2] A. Kolomiets et al., "Upgrade of the Unilac High Current Injector RFQ", LINAC'08, Victoria, BC, Canada, p. 136, http://www.JACoW.org

[#]c.zhang@gsi.de

DOI:10.15120/GR-2016-1

RF field simulations on the new Thales 1.8 MW amplifier resonant circuits

M. Müh, M. Hörr, B. Schlitt, A. Schnase, G. Schreiber, and W. Vinzenz
GSI, Darmstadt, Germany

RF pulse power levels up to 1.8 MW as required for the future UNILAC operation [1,2] demand clean and stable operation of the driving high power tube amplifier stages. To ensure sufficient stability, the output cavity of the RF amplifier - which defines the tube operating frequency band - is designed to strict specifications. Besides the desired fundamental operation mode, higher order modes (HOM) exist in the cavity and may cause breakdown if the local electric field exceeds the dielectric strength of the filling air. To prevent sparking in the amplifier cavity, adequate damping must be provided to dissipate energy of harmful modes without disturbing the fundamental. This can be achieved by loading the cavity with lossy materials in points of known high E- or H-field concentration, which is commonly used at existing RF systems [3].

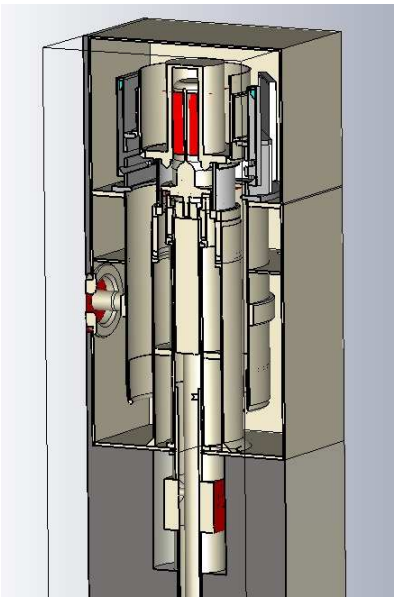

Figure 1: CST Microwave Studio amplifier model.

An eigenmode simulation of the complete cavity system was performed to allow evaluation of the pre-installed absorber and localization of the HOM field maxima. For this, the mechanical system was implemented as a detailed CST Microwave Studio model (Fig. 1). To enable fast calculation in spite of the high computational complexity, details negligible for simulation were simplified to optimize for model symmetries and accurate meshing. The model was parameterized for all built-in tuning elements, allowing for range sweeps during simulation. For the electron tube, a conductive material was added to emulate the anode current flow.

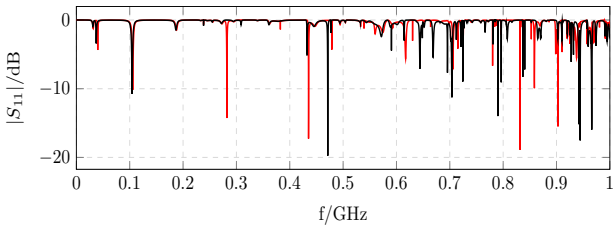

Figure 2: Reflected amplitude (S_{11}) of output cavity with (black) and without (red) HOM absorber.

Since losses are neglected in the eigenmode simulations and modes which cannot be excited by the amplifier tube are also found, a coaxial wave mode was coupled to the input and output by wave ports and the reflected amplitude S_{11} was determined by frequency domain analysis. The dominant resonant modes frequencies can be found in the S_{11} amplitude (Fig. 2) while the mode patterns at the exact frequencies are given by the eigenmode solutions (Fig. 3).

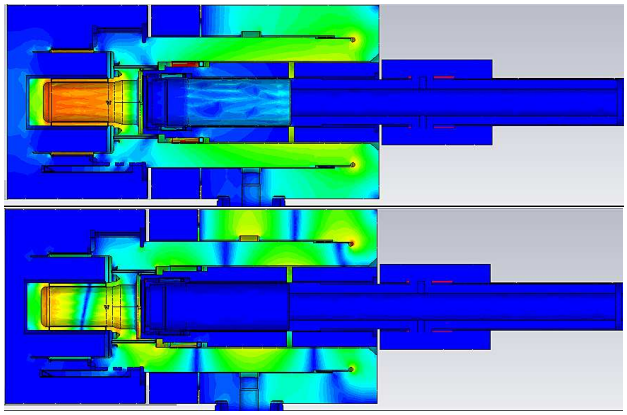

Figure 3: E-field distribution inside of the output cavity at 108 MHz fundamental (top) and 436 MHz HOM (bottom).

References

[1] B. Schlitt, M. Hoerr, A. Schnase, G. Schreiber, and W. Vinzenz, RF System Development for the New 108MHz Heavy Ion High-Energy LINAC at GSI, LINAC2014, Geneva, Switzerland, 2014, p. 556-558.

[2] B. Schlitt et al., this report.

[3] E. Feldmeier, G. Hutter, W. Vinzenz, and B. Schlitt, “Elimination of Parasitic Oscillations in RF Tube Amplifier for High Power Application”, LINAC08, Victoria BC, Canada, 2008, p. 981-983.

DOI:10.15120/GR-2016-1

Ion source operation at GSI

R. Hollinger, K. Tinschert*, A. Adonin*, R. Berezov*, D. Agahi, M. Brühl, M. Endermann, B. Gutermuth, F. Heymach, V. Ivanova, S. Jung, R. Lang, J. Mäder, F. Maimone, K. Ochs, P. T. Patchakui, M. Raupach, P. Schäffer, S. Schäffer, C. Vierheller, A. Wesp, S. Zulauf*
GSI, Darmstadt, Germany

High Current Ion Sources

The experimental program in 2015 has been focused on UNILAC experiments. The operation with high duty cycle (50 Hz) had the lion's share of a beam time. High current ion sources from Terminal North (MUCIS and VARIS) and Penning ion sources from Terminal South were supplying the experiments with various types of ions.

The following Table 1 gives an overview of the ion species, which were delivered for physics and accelerator development experiments. A representative value for delivered intensity to the linear accelerator UNILAC is the analysed current in front of the RFQ.

Table 1: Ion beam intensities generated with high current ion sources in 2015; filament driven volume type ion sources: MUCIS, Vacuum arc ion sources: VARIS, Penning type ion sources: PIG

Ion species	Duration (days)	Ion source	Analyzed intensity (emA)
$^{12}CH_3^+$	7	MUCIS	2.5
$^{12}C_3H_7^+$	3	MUCIS	0.8
$^{50}Ti^{2+}$	4	PIG	0.04
$^{197}Au^{8+}$	34	PIG	0.07
$^{209}Bi^{4+}$	4	VARIS	6
$^{238}U^{4+}$	11	VARIS	14

Mostly gold ion beam (Penning Ion Source) from the high current injector (HSI) was requested in 2015. The $^{197}Au^{8+}$ beam was operated with high duty cycle (50 Hz / 3 ms) and was used for material research (UMAT) and for biophysics (UBIO) experiments. The lifetime of the PIG source during the beam time was approximately 24 hours.

One of the main highlights of 2015 was the further development of molecular ion beams from Terminal North for production of intense proton and carbon beams behind the gas stripper [1,2,3]. Several molecular substances including alkane gases and volatile liquids have been tested using different ion source setups. Various plasma chambers, extraction systems and electrical connections (different plasma potential) have been tried out in order to achieve the best ion source performance and the maximum yield of protons behind the gas stripper. The best results have been achieved with methane (CH_4) and isobutane (C_4H_{10}) gases, providing molecular ion species CH_3^+ and $C_3H_7^+$ correspondingly. On Fig.1 a rather complicated mass-spectrum of isobutane is shown. One could see that the distribution maximum lies on propyle molecules (C_3H_X). The beam intensity in front of the RFQ reached 2.5 mA for CH_3^+ and 0.8 mA for $C_3H_7^+$, respectively [1]. As the result, the new record intensities of up to 4.3 mA for protons as well as of up to 10 mA for $^{12}C^{6+}$ ions in the post-stripper section have been achieved [3].

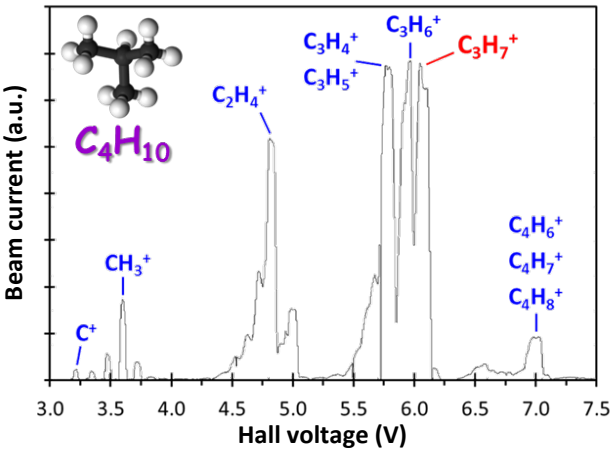

Figure 1: Mass spectrum of isobutane gas

Another notable highlight is the performance optimization of VARIS ion source with the new multi aperture (7-holes, ø 4 mm) extraction system for $^{238}U^{4+}$ beam. That results in combination with a pulsed gas stripper in a new record intensity for uranium in the post-stripper section (behind HSI) [5].

Further development of higher duty cycle (2.7 Hz) uranium operation for FAIR is ongoing. The new inductance free (L=0 H) resistances have been implemented into the discharge circuit of the ion sources at the Terminal North. That allows reducing the minimum operation pulse length of the VARIS ion source, which in turn reduces the thermal load on the cathode and generally could improve the ion source performance with duty cycles higher than 1 Hz. Also the concept of using U-W composite materials in the cathodes to increase the operation duty cycle for uranium is going to be proved. The recent investigations of the AREVA company have shown the possibility of manufacturing U-W(5% Wt.) and U-W(10% Wt.) alloys.

The further renewing and development of the PIG sources is in process. The four sputter PIG sources were successfully put into the operation after complete renewing and another two ion sources will be ready for the next beam time in 2016.

The construction of the new test bench for further investigation and development of compact PIG ion source is finished. The first test with Argon beam has been already performed. As a next step it is planned to measure

* Corresponding authors

DOI:10.15120/GR-2016-1

the current performance, the lifetime and the beam emittance.

High Charge State Injector HLI

The CAPRICE ECR ion source (ECRIS) at the High Charge State Injector (HLI) delivered the ion species listed in table 2 for various physics experiments in the regular beam time schedule as well as for dedicated ion beam development.

Table 2: Ion beam operation of the HLI-ECRIS in 2015; additional time for ion beam development in brackets.

Ion species	Auxiliary gas	Duration (days)	Analyzed intensity (eμA)
$^{3}He^{1+}$	He	2	320
$^{12}C^{2+}$	He	10	60
$^{40}Ar^{7+,8+,9+}$	He	15	30-140
$^{48}Ca^{10+}$	He	72	90
$^{84}Kr^{13+}$	O_2	7	30
($^{84}Kr^{6+...19+}$	O_2	1	2-33)

A $^{40}Ar^{7+}$ ion beam was used for machine commissioning at the HLI at the beginning of the beam time period. Subsequently this ion beam was used for two experiments scheduled at the local experimental area at the HLI working at beam energies of 1.4 MeV/amu. First emittance measurements as preparation for the commissioning of a prototype device of the cw-LINAC were performed followed by investigations on emittance transfer. In addition further charge states of Ar ($^{40}Ar^{8+}$,$^{40}Ar^{9+}$) were requested from the experiments for comparative measurements.

Several short periods of biophysics experiments in 2015 were provided with ion beams of $^{12}C^{2+}$, and of $^{3}He^{1+}$, respectively.

Two-thirds of the complete beam time were covered by $^{48}Ca^{10+}$ beam and were dedicated to various experiments on Super Heavy Element (SHE) research mainly performing experiments on the chemistry of element 114 at TASCA and on laser spectroscopy of Nobelium at SHIPTRAP, respectively. Two corresponding long $^{48}Ca^{10+}$ runs were characterized by good beam stability and the typical low material consumption of ^{48}Ca sample material.

After the implementation of new TWTA-based microwave transmitters as upgrade measure in the last year [6] this equipment was utilized during a part of the $^{48}Ca^{10+}$ beam time and during the $^{84}Kr^{13+}$ beam time, which had been requested as further ion beam for the experiments on emittance transfer at the local experimental area at the HLI.

This operation opened the opportunity to perform further investigations on microwave frequency tuning at the CAPRICE ECRIS under operating conditions using the ^{84}Kr ion beam with its broad charge state distribution. In fact by tuning the microwave frequency to 14.464 GHz up to 40% more current of $^{84}Kr^{13+}$ was provided at the entrance of the RFQ with respect to 14.5 GHz, the normal operating frequency. The charge state distributions shown in figure 1 confirm that the frequency tuning can be used for operating conditions with the aim to increase the intensity of higher charge states (i.e. $^{84}Kr^{n+}$ with n>11). At the operating frequency of 14.444 GHz the highest intensity of the highest detected charge state, $^{84}Kr^{19+}$, was measured and a current gain of 16 times was obtained with respect to the normal operating frequency.

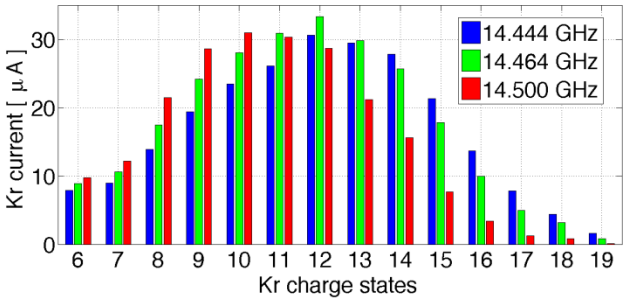

Figure 1: Charge spectra of ^{84}Kr with frequency tuning.

References

[1] A. Adonin, R. Hollinger, this report.
[2] W. Barth et al., Heavy ion linac as a high current proton beam injector, Phys.Rev.STAB, **18**, 050102 (2015).
[3] M. Heilmann et al., this report.
[4] W. Barth et al., U^{28+}-intensity record applying a H_2-gas stripper cell, Phys.Rev.STAB, **18**, 040101 (2015).
[5] W. Barth et al., this report.
[6] K. Tinschert et al., GSI Scientific Report 2013, GSI Report 2014-1 (2014) 302

DOI:10.15120/GR-2016-1

Further development of H-rich molecular beam operation from high current ion sources for production of intense proton and carbon beams

A. Adonin and R. Hollinger
GSI, Darmstadt, Germany

As it was shown previously [1] for light ion beams (especially for protons) the performance of UNILAC high current injector (HSI) including the ion source and LEBT is strongly limited mainly due to the injection requirements of the RFQ. As a promising solution for protons, the concept of production and acceleration of singly charged H-rich molecular ion beams from high current ion sources with next following cracking and conversion it to intense proton beam at the gas stripper has been developed. First experiments have been successfully performed in 2014 with methane (CH_4) and ethane (C_2H_6) gases using the MUCIS-1990 ion source [1].

Further investigations have been carried out with heavier alkanes: propane (C_3H_8) and isobutane (C_4H_{10}). In Fig.1 mass-spectra of the first four elements from alkane group (C_nH_{2n+2}) are presented. The spectra correspond to the case of the best performance of the ion source with certain gas and maximum ion beam current in front of the RFQ. It is obvious that the heavier the working gas the more complex is the mass-spectrum. Also one could note that for propane and isobutane the distribution maximum is shifted to lighter molecules. This is due to the complex dissociation/recombination processes in the plasma. The molecular ion species provided maximum proton yield behind the gas stripper for each working gas are marked with red colour on the spectra (Fig.1).

The best results have been achieved with methane (CH_4) and isobutane (C_4H_{10}) gases, providing molecular ion species CH_3^+ and $C_3H_7^+$ respectively. The beam intensity in front of the RFQ reached 2.5 mA for CH_3^+ and 0.8 mA for $C_3H_7^+$. The measured beam emittance for $C_3H_7^+$ ion beam was about 20-25% smaller than for CH_3^+ beam resulting in improved transmission through HSI [2] and higher proton yield behind the gas stripper. As the result, the new record intensities of up to 4.3 mA for protons as well as of up to 10 mA for $^{12}C^{6+}$ ions in the post-stripper section have been achieved [3].

During the experiments with alkanes different volume type ion sources (MUCIS-1990, CHORDIS and MUCIS-2010) have been tested with various extraction systems (1-hole, 7-holes and 13-holes) and various plasma electrode potentials. Along with the gases a volatile liquid iodoethane (C_2H_5I) was tested as a working substance for ion source, but the performance was notably worse than for alkanes. Further performance improvement could be achieved by reducing the distance between the extraction system of the ion source and the post-acceleration (PA) system as well as between PA and the first focusing element in the LEBT. This will be realized with installation of a new PA-system at terminal North, which is planned for the near future.

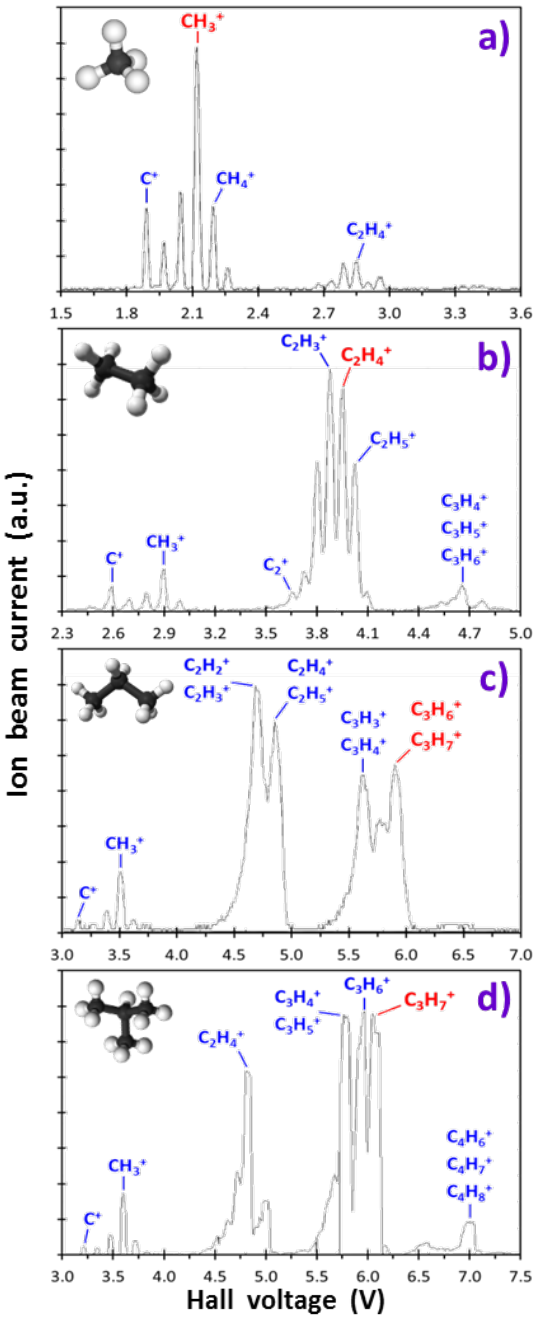

Figure 1: Mass-spectra of alkane gases: a) methane; b) ethane; c) propane; d) isobutane.

References

[1] A. Adonin, R. Hollinger, GSI Scientific Report 2014, GSI Report 2015-1 (2015) 399.
[2] A.Adonin et al., Rev.Sci.Instrum. 87, 02B709 (2016).
[3] M. Heilmann et al., this report.

DOI:10.15120/GR-2016-1

Progress on the 1.4 MeV/u pulsed gas stripper for the GSI UNILAC

P. Scharrer[1,2,3], E. Jäger[2], W. Barth[1,2], M. Bevcic[2], Ch. E. Düllmann[1,2,3], L. Groening[2], K. P. Horn[2], J. Khuyagbaatar[1,2], J. Krier[2], and A. Yakushev[1,2]

[1]Helmholtz Institut Mainz, 55099 Mainz, Germany; [2]GSI Helmholtzzentrum für Schwerionenforschung GmbH, 64291 Darmstadt, Germany; [3]Johannes Gutenberg-Universität Mainz, 55099 Mainz, Germany

The GSI Universal Linear Accelerator (UNILAC) will serve as part of the injector system for the Facility for Antiproton and Ion Research (FAIR) [1]. An UNILAC upgrade program has already started dedicated to meet the high demands of FAIR [2]. As part of this program a pulsed gas stripper has been developed, to replace the 1.4 MeV/u N_2 gas-jet stripper.

The gas stripper device is equiped with a pulsed gas injection, synchronized with the beam pulse timing, to increase the effective gas density during a beam pulse transit [3]. The aim is to enhance the beam intensity behind the stripper by increasing the fraction of ions with the desired charge state. In past measurement series, H_2 was identified as most promising stripper gas to achieve this goal [4]. Initial measurements using U-beams on the pulsed H_2-target showed an increased stripping efficiency into the desired 28^+ charge state of about 60 %. At back-pressures up to 12 MPa, increasing charge states were observed [5]. The behavior of the charge state distribution suggested even higher charge states at further increased gas densities. This is depicted in Fig. 1 by the charge state distributions of U-ions after passing the H_2-target at increasing target thicknesses. The target thickness is estimated from energy loss measurements using SRIM2013 [6].

In 2015, the whole setup was improved enabling for higher gas densities. A new generation of pulsed gas valves was used, which can tolerate an increased back-pressure up to 30 MPa. This improvement allows for target thicknesses of the H_2-target of about $\leq 70\,\mu g/cm^2$. Additionally, a new specialized power supply was commissioned, improving the reliability and control of the gas valves. The required opening time to reach a maximum gas density is about $\leq 250\,\mu s$, depending on back-pressure and gas type. The gas supply for the valves was modified to deliver H_2 with the desired back-pressure.

The flange, equiped with the new injection system, is mounted on top of the main stripper chamber. A four-stage differential pumping system provides for the required vacuum pressures ($\leq 10^{-3}$ Pa) in the adjacent beam line towards the High Current Injector (HSI) and the Alvarez section. A roots vacuum pump, installed on the bottom of the main stripper chamber, as well as several turbo pumps are used (see [4]).

Systematic measurements of charge fractions, beam emittance and energy-loss were conducted using ^{238}U-, ^{209}Bi-, ^{50}Ti- and ^{40}Ar-beams on H_2- and He-targets, as well as N_2 as a reference stripper gas. The experimental data are still under evaluation.

Additionally, measurements of the gas flow through the stripper cell and the gas pressure near the interaction zone were conducted. The gas flow was measured to 1.0 ± 0.5 L/min using the H_2-target at 8 MPa back-pressure for operation with U^{28+}-beams (100 μs, 1 Hz repetition rate). This is a significantly reduced gas consumption compared to the N_2 gas-jet stripper operation (22 L/min).

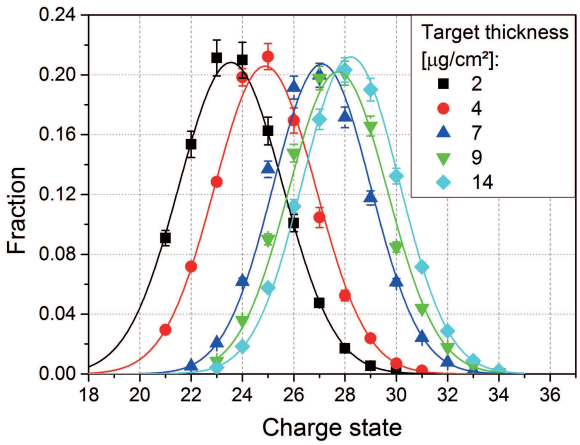

Figure 1: Charge state distributions of U-ions passing through the H_2-target at increasing target thicknesses.

First measurements in mixed beam operation as well as in long-pulsed beam operation were performed. Mixed beam operation was succesfully tested by stripping U- and Ti-beams in H_2- and N_2-targets, respectively. In long-pulsed beam operation with high repetition rates (up to 5 ms, 50 Hz), the use of H_2 and He at increased back-pressures is limited by the pumping system. However for this operation mode, the performance of the pulsed gas cell with N_2 remains the same as with the N_2-jet stripper.

References

[1] FAIR Baseline Technical Report, GSI Darmstadt, Germany, Vol. 2, p. 335 (2006).

[2] L. Groening et al., in Proceedings of HIAT2015, September 7-11, Yokohama, Japan (2015).

[3] P. Scharrer et al., J. Radioanal. Nucl. Chem. 305, p. 837-842 (2015).

[4] P. Scharrer et. al., in Proceedings of IPAC2015, May 3-8, Richmond, VA, USA (2015).

[5] W. Barth et al., Phys. Rev. ST Acc. Beams 18, 040101 (2015).

[6] J.F. Ziegler et al., The Stopping and Range of Ions in Solids, Vol. 1, Pergamon Press, New York, 1985.

DOI:10.15120/GR-2016-1

Development of a new digital LLRF system for the UNILAC based on MTCA.4

J. Zappai, B. Schlitt, A. Schnase and G. Schreiber
GSI, Darmstadt, Germany

The substitution of the existing low level RF (LLRF) system is part of the RF system modernisation programme of the UNILAC Post-Stripper Linac [1,2]. In this context the control of the cavity field amplitude and phase ($\lesssim 0.1$ % and $\lesssim 0.1^\circ$ respectively), pulse shaping and a fast interlock mechanism have to be elaborated. Challenges are the huge dynamic amplitude range corresponding to an ion mass-to-charge ratio between typically 1.0 for protons and 8.5 for U^{28+}, non-linear RF amplifier characteristics and beam loading. For an U^{28+} ion beam with a beam current of 15 mA the beam loading is about 300 kW for Alvarez tanks compared to $\leq$ 1100 kW cavity losses.

Design of a new d-LLRF system

Due to long operation time of the existing LLRF system and limited availability of spare parts, long-term reliability in view of the operation as injector for FAIR cannot be ensured. The use of GSI synchrotron LLRF components was evaluated and finally overruled by the intrinsic disparity of pulsed linac operation. Tests of a commercially available system [2] revealed the need to develop a precise, flexible LLRF system with state-of-the-art technology. MTCA.4 is an open hardware standard originating from the telecom market. The development of a MTCA.4 based LLRF system for XFEL by DESY offers synergy effects and long-term availability of components. A new test system was setup at GSI comprising primarily the SIS8300-L2 digitizer (10 x 16 bit, 125 MS/s ADC, 2 x 16 bit, 250 MS/s DAC, Xilinx Virtex 6 FPGA) and the DS8VM1 vector modulator board (Fig. 1).

The new design (Fig. 2) includes direct undersampling of the 108.4 MHz probe signal with a sampling rate of 86.7 MHz, digital down conversion to base band and translation in amplitude and phase by CORDIC algorithm. The control loop includes separate PI feedback and feed forward controls. Simulations showed good results in reducing the impact of beam loading by applying an adaptive feed forward. Additionally a beam current based feed forward is envisaged. The control signals are re-translated in I and Q base band via CORDIC and converted to two analog signals for the vector modulator.

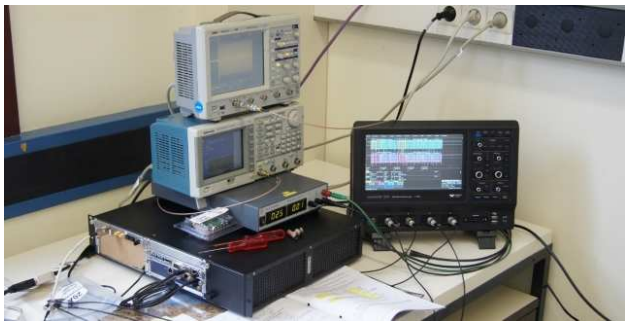

Figure 1: MTCA.4 d-LLRF test system

As next steps our firmware will be integrated and first RF tests with a test cavity and a frequency mixer for beam loading simulation are going to be conducted.

Control system integration & further features

The integration of the new LLRF system will be possible as 1:1 exchange of the existing system due to use of an interface adapter board. In the long-run the use of the FAIR standards FESA and White Rabbit is considered. Additional features like a resonance frequency control, a faster cold start process and VNA functionalities for maintenance support are under discussion.

References

[1] B. Schlitt et al., this report.

[2] B. Schlitt, G. Eichler, S. Hermann, M. Hörr, A. Schnase, G. Schreiber, W. Vinzenz, GSI Sci. Rep. 2014 (2015) 413.

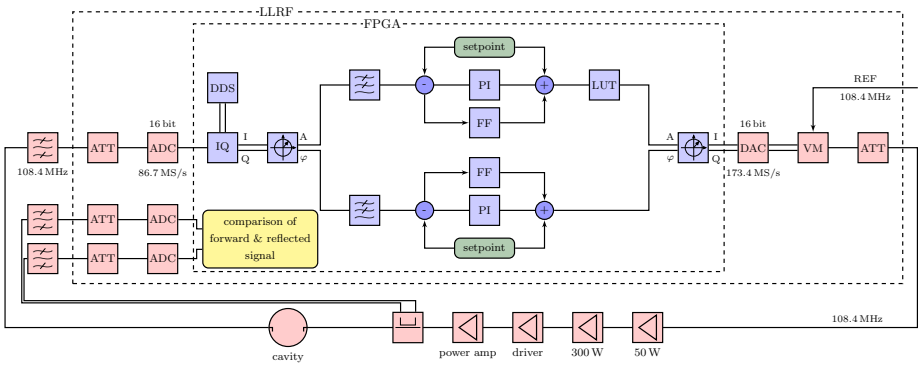

Figure 2: Block diagram of the new d-LLRF prototype

DOI:10.15120/GR-2016-1

RF system modernisation at the UNILAC 108 MHz post stripper linac

B. Schlitt, J. Catta, G. Eichler, S. Hermann, M. Hörr, M. Müh, S. Petit, M. Pilz, A. Schnase, G. Schreiber, W. Vinzenz, A. Windolf, and J. Zappai

GSI, Darmstadt, Germany

Modernisation of the existing RF systems & new developments

A substantial modernisation of the 108 MHz RF systems of the Alvarez post-stripper linac at the UNILAC was launched in 2014 to prepare the existing facility for the future FAIR operation [1,2]. As a first step, the old 1.6 MW high power RF amplifier (HPA) stages are modernised in a way that the central cavity amplifiers can be replaced by new stages later. Therefore, the outdated control and monitoring equipment of the HPA stage of the Alvarez tank A3 was substituted by recent developments installed in a new separate control rack. The old control grid power supply was replaced by a new commercial device. First RF tests of the rebuilt A3 amplifier were successfully performed in summer 2015.

Since the powerful 1 MVA, 24 kV anode power supplies will be reused in future, the old relay based local control of the A3 power supply was substituted by a new PLC system (Fig. 1) and first tests succeeded. Further tests of the complete A3 system comprising the rebuilt HPA stage and the updated anode power supply are planned for 2016. The same modernisation is planned for the remaining Alvarez RF systems for 2016 – 2017.

For long-term substitution of the old driver amplifiers, a call for tenders for a modern 150 kW solid state RF amplifier prototype was launched. Delivery and tests of the prototype are planned for 2017/18.

Finally, the development of a new digital low-level RF (d-LLRF) system for RF amplitude and phase control started. A test system based on the MTCA.4 standard comprising commercial vector modulator and FPGA boards developed at DESY in cooperation with industrial partners was set up [3].

A new microcontroller based prototype system for resonance frequency control of the accelerating structures was developed in 2015 and is currently being tested.

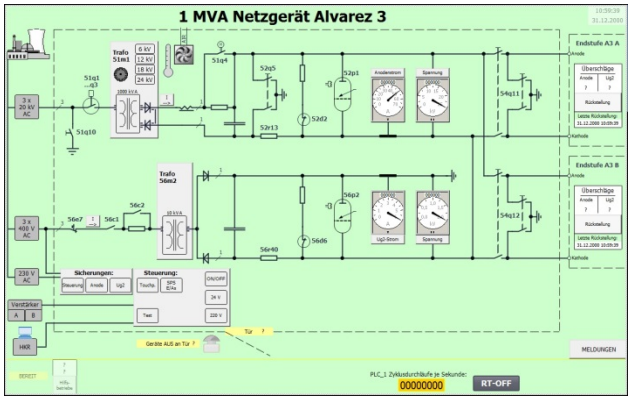

Figure 1: Graphical user interface (main page) of the PLC system for the existing 1 MVA anode power supplies.

New 1.8 MW cavity amplifier prototype

The design of a new 1.8 MW cavity amplifier prototype for short pulse operation (≤ 2 ms pulse length at ≤ 10 Hz rep. rate) was completed by Thales, including dedicated peripherals (filament power supply, cavity tuning motorisation, air and water cooling distribution and monitoring, etc.). All components were manufactured and the amplifier was fully assembled in 2015. Commissioning started in January 2016 (Fig. 2) and the specified 1.8 MW RF peak output power was reached on dummy load at the factory. Factory acceptance tests are scheduled for Q2/2016 and site acceptance tests at GSI for Q4/2016.

At GSI, a test bench for the Thales amplifier is in preparation. To clear space for the test stand, the old RF amplifiers of the single gap resonators E6 to E9 and the related power supplies were dismantled. Integration of the new amplifier into the existing equipment (anode power supply, driver amplifier, RF transmission lines, etc.) is in preparation, as well as control racks similar to those built for the A3 amplifier. After tests on dummy load, operation of the new amplifier on Alvarez tank 4 is planned during routine operation from 2018 on.

In addition, electromagnetic field simulations and equivalent circuit model investigations of the new cavity amplifier were performed at GSI, in particular, to investigate higher order mode effects [4].

Figure 2: New 1.8 MW high power cavity amplifier prototype during preparation for commissioning at Thales.

References

[1] B. Schlitt, M. Hoerr, A. Schnase, G. Schreiber, and W. Vinzenz, LINAC2014, TUPP058 (2014).
[2] B. Schlitt et al., GSI Scientific Report 2014, p. 413.
[3] J. Zappai et al., this report.
[4] M. Müh et al., this report.

DOI:10.15120/GR-2016-1

QA parameter distributions of Si-APDs in large-scale production

A. Wilms[1], *J. Bailey*[1], *T. Bel*[1], *A. El Mosleh*[1], *F. Himburg*[1], *A.-K. Kopp*[1], *L. Ngappi*[1], *F. Roether*[1], *D. Scharnberg*[1], *P. Schüßler*[1], *T. Tchamfa*[1], *C. Warneke*[1], *and P. Wicke*[1]

[1]GSI, Darmstadt, Germany

Introduction

The large area APDs used for the readout of the PANDA-EMC (build out of $PbWO_4$-II crystals) have to be quality assured due to their required technical specifications at $T = 20°C$ for an envisaged internal gain of $M = 100$. According to the envisaged operating temperature of $T = -25°C$ all QA parameters are measured temperature dependently in addition. The results for the QA measurements at $T = 20°C$ of a sample of 3420 APDs (1/4 of screened APDs so far) are being reported and discussed.

Main QA parameters: Results & Discussion

The main parameters determined at $T = 20°C$ for QA purposes are: Breakdown Voltage $U_{Br}\,[V]$, Bias Voltage $U_{Bias}\,[V]$ at $M = 100$, dark current, Gainvariance with Voltage $1/M \cdot dM/dV\,[\%]$ at $M = 100$ and $\Delta U = (U_{Br} - U_{Bias}(M = 100))\,[V]$. Their frequency distributions are shown in figures 1-4.
The shown data are based on 3420 validated APDs delivered from different LOTs including different amounts of wafers. The Breakdown Voltage distribution as well as the distribution of the Bias Voltages shown in fig.1 and fig.2 show a superposition of two main distributions originated in either differences in the doping profile of different LOTs, or/and variances in the corresponding internal layer thicknesses. This observed LOT dependence of those two APD

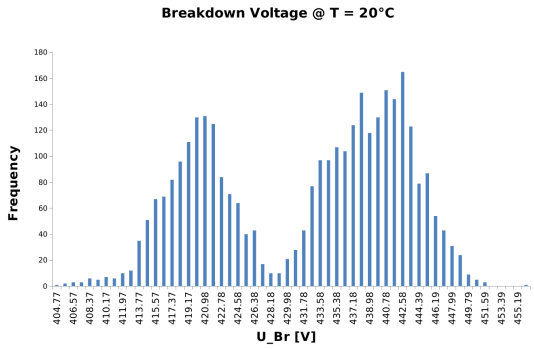

Figure 1: Frequency distribution of measured Breakdown Voltages

parameters could neither be observed in the corresponding Gainvariance distribution shown in fig.3 nor in the distribution of the dark current for $M = 100$, which is not shown here. During the preceded extensive R&D phase it turned out that the parameter ΔU could be used as an indicator for radiation hardness of these photosensors. The corresponding frequency distribution is shown in fig. 4 and shows two overlapping gaussian distributions, originated in the same LOT dependence mentioned above, shown in the sub-figure ($\Delta U(U_{Br})$) of fig.4. Up to now over 98% of the delivered APDs sucessfully passed the first internal validation cycle and could directly been declared as ”inside techn. specs.” without further validation/analysis cycles necessary.

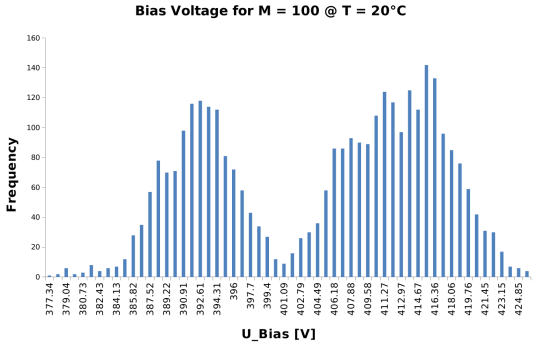

Figure 2: Frequency distribution of measured Bias Voltages for $M = 100$

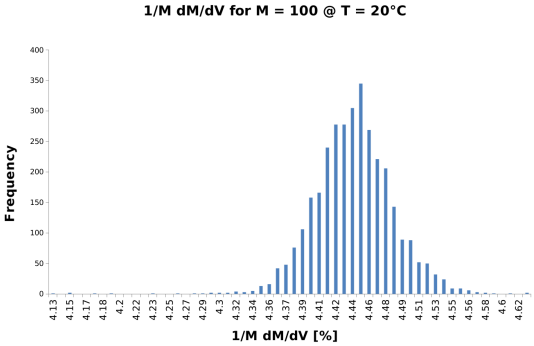

Figure 3: Frequency distribution of measured Gainvariance with Voltage at $M = 100$

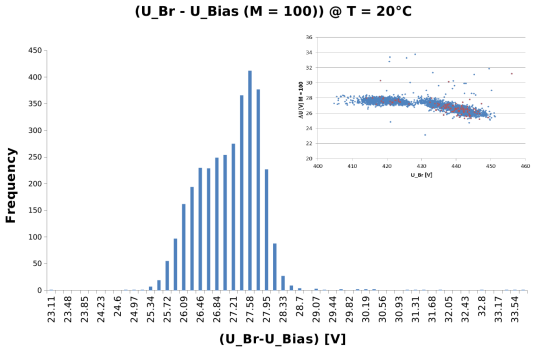

Figure 4: Measured Voltage gap between Breakdown Voltage and Bias Voltage for $M = 100$

DOI:10.15120/GR-2016-1

DOI:10.15120/GR-2016-1

Waferdependence of quantum efficiency of LAAPDs in large-scale production

A. Wilms[1], *J. Bailey*[1], *T. Bel*[1], *A. El Mosleh*[1], *F. Himburg*[1], *A.-K. Kopp*[1], *A. Leszczyńska*[2], *L. Ngappi*[1], *F. Roether*[1], *D. Scharnberg*[1], *P. Schüßler*[1], *T. Tchamfa*[1], *C. Warneke*[1], *and P. Wicke*[1]

[1]GSI, Darmstadt, Germany; [2]Gda'nsk University of Technology, Poland

Introduction

The QE (quantum efficiency) of photosensors is one of the most important optical parameters to be evaluated among the electrical parameters e.g. dark current or noise. Therefore the QE of Large Area Avalanche Photodiodes (LAAPDs) developed for photodetection of light emitted by low light yield scintillator materials (e.g. PWO used in CMS, PANDA, etc.) has to be investigated in terms of variations/stability in large-scale production processes. During evaluation of the LAAPD quality assurence procedure, special care has been taken in investigating the QE distribution at $\lambda = 420\,nm$ among single wafers produced from different LOTs.

Measured quantities

The QE of six wafers from three different LOTs have been investigated. The QE value distribution of those ~ 400 APDs is shown in fig.1 and the wafer dependent quantities are listed in table 1.

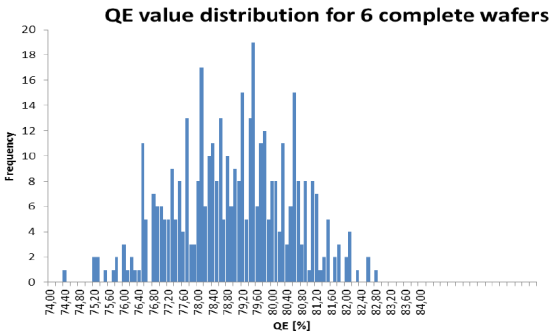

Figure 1: QE value distribution at $\lambda = 420\,nm$ of 417 APDs from 6 different wafers (3 different LOTs).

LOT No.	Wafer No.	APD amount/wafer	APD amount/LOT	QE [%] (420 nm)
14	16	71	1216	77.2
15	01	76	213	77.9
16	02	64	1280	78.5
16	06	67	1280	79.8
16	07	64	1280	78.5
16	10	73	1280	80.2

Table 1: Measured APDs: Quantities and wafer-dependent QE mean values

The QE value profile for $\lambda = 420\,nm$ for each wafer investigated is shown in fig.2. For every y-x position of the single wafers (with an APD present) the QE values are shown in fig.3 next to each other.

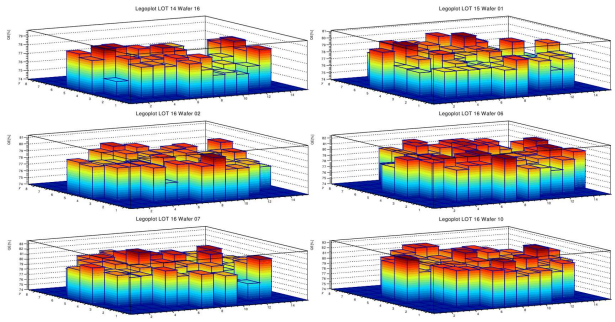

Figure 2: QE: wafer profile of 6 different wafers

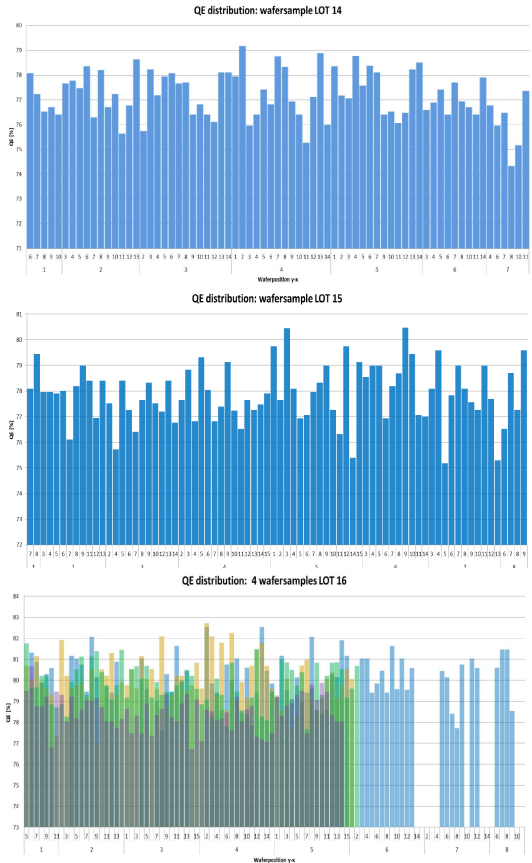

Figure 3: QE (y-x) distributions: Top: Wafer 16, LOT 14; middle: Wafer 01, LOT 15; bottom: 4 wafers of LOT 16 (empty wafer positions included)

Conclusions

The spread of the mean QE values of the measured wafers is in the order of a few percent (cf. table 1). Based on these investigated wafers no apparent QE dependence (at $\lambda = 420\,nm$) on the wafer position could be observed.

DOI:10.15120/GR-2016-1

Developments for the CR stochastic cooling system

C. Dimopoulou[1], *D. Barker*[1], *R. Böhm*[1], *M. Bräscher*[1], *R. Hettrich*[1], *J. Krieg*[1], *W. Maier*[1], *C. Peschke*[1], *A. Stuhl*[1], *L. Thorndahl*[2], *and S. Wunderlich*[1]

[1]GSI, Darmstadt, Germany; [2]CERN, Geneva, Switzerland

Further progress was made in 2015 on in-house developing, engineering and testing activities for the demanding CR stochastic cooling system [1] in the frequency bandwidth 1-2 GHz.

Cryogenic pickup tank with plunging electrodes

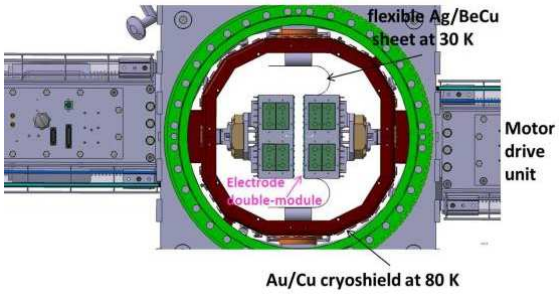

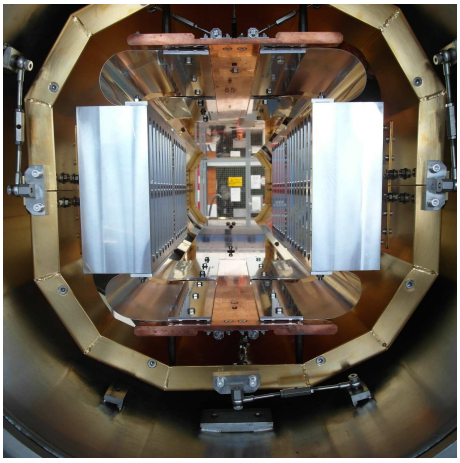

Figure 1: Section of the prototype pickup tank. The cryoshield, the Ag/BeCu sheets and the motor drive units driving synchronously the slotline electrode modules are shown. Final assembly in the tank before pumping down and performing the cryogenic test.

The assembly inside the prototype pickup tank (Fig. 1) comprising 2 motor drive units (instead of 8 in the full version) bearing dummy modules (i.e. without slotline electrodes), the flexible Ag/BeCu sheets mounted on the long Cu bars, the cryoshield and the two cryoheads (up, down on the tank) has been completed and first UHV and cryogenic tests have been performed (Fig. 2). The 2nd stage of the cryoheads and the module reached 10-12 K and 20 K, respectively , the Cu bar temperature lied in between (i.e. in the worst case 10 K above the cryoheads 2nd stage). These first results confirmed that the thermal concept with the 2 cryoheads and the cryoshield is appropriate (i.e. not underspecified) for the full version. Further systematic measurements are underway.

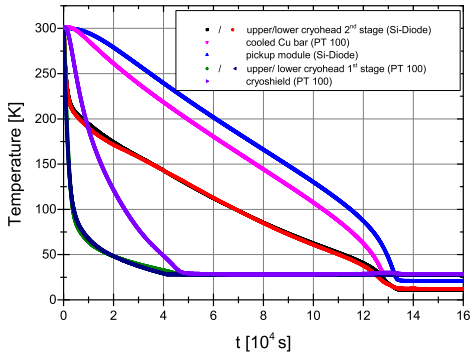

Figure 2: Cooling down in the prototype pickup tank. The PT100 temperature sensor does not measure below 28 K, the Si-diode covers the full range.

In the special chamber for testing motor drive units under pre-vacuum conditions, at room temperature, one motor drive unit with electrode module can be mounted so as to slide along the Ag/BeCu sheets. In the tests, the Ag/BeCu sheets (the ones shown in Fig. 1) were found unreliable because they break after typically 10^5 cycles (aim is 10 million cycles). An improved concept for these sheets (geometry, manufacturing process) is in preparation.

Palmer pickup

A pickup without moving eelctrodes but with very large horizontal ($\pm$ 200 mm) and vertical ($\pm$ 66 mm) apertures with respect to the beam axis is specified, so as not to intercept the injected beams (before the bunch rotation). The former implies that many unwanted RF modes lie inside the cooling band 1-2 GHz, these must be damped by filling the structure with ferrite. The latter limits the sensitivity of the pickup, so that a long structure (2 m pickup length) is needed to reach sufficient impedance, but implies high phase non-linearity in the output signal with respect to the particle pulse. After dedicated electromagnetic simulations with the HFSS code the RF design for the Faltin structures including ferrite has been optimized in the band 1-2 GHz [2]. This solution (Fig. 3) is the best compromise for (i) maximum pickup impedance coupled to the beam, (ii) linear output signal phase with respect to the

DOI:10.15120/GR-2016-1

particle pulse (iii) flat frequency response (transmission coefficient $S_{21}(f)$), avoiding resonances, (iv) suppression of unwanted rf modes. Consequently, the engineering of the pickup tank has started (Fig. 3).

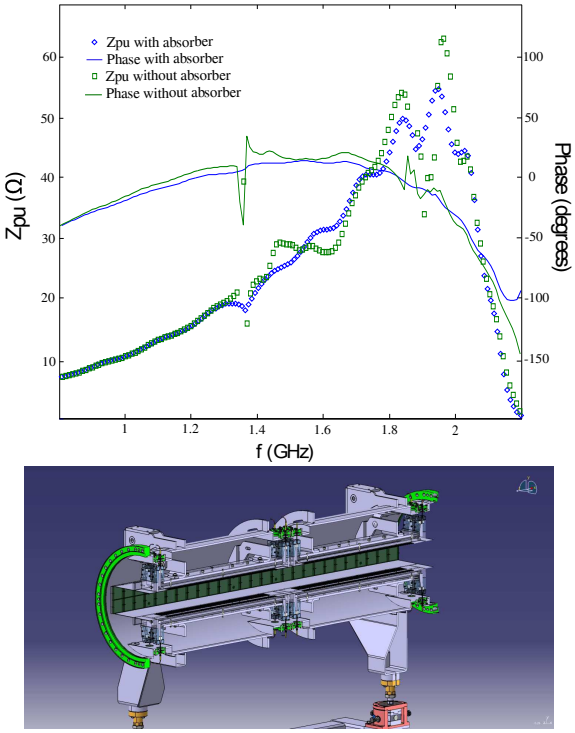

Figure 3: Top: Pickup impedance and nonlinear phase deviation for Faltin rail structure consisting of two rails of 49 slots each whose signals have been combined. The performance both with and without the presence of ferrite damping material is shown. HFSS simulations with a beam centered vertically and with horizontal offset of 40 mm. Bottom: Palmer pickup with its Faltin electrode rails, ferrites and RF feedthroughs. One half of the tank is shown.

RF signal processing components 1-2 GHz

The RF block diagram of the stochastic cooling system [3] as integrated into the building has been refined so as to save electrical length, since the flight time of the quasi-relativistic particles from pickup to kicker is very short. The time delay budgets from pickup to kicker have been checked including realistic electrical lengths of the designed slotline/Faltin electrodes as well as conservative assumptions for the electrical length of the kicker electrodes and all intermediate signal processing components and cables. There is almost no margin, especially for the Palmer cooling branch.

The preseries unit (mw power 250 W in the 1-2 GHz band, water cooled) of the ordered power amplifiers at the kickers is under development. It will be ready for acceptance tests early 2016.

In-house design of demanding RF components [4]: The pickup module controller and the variable phase shifters are under development. A functioning prototype of the embedded powermeter is now available (Fig. 4). The measured data show that the critical values: insertion loss, amplitude response, phase distortion and group delay are within acceptable limits. Therefore, the device is only a small imperfection to the signal path, which was a critical design aspect. At the same time, the dynamic range is quite high which enables versatile applications for the power meter, e.g. also in the ESR stochasting cooling system.

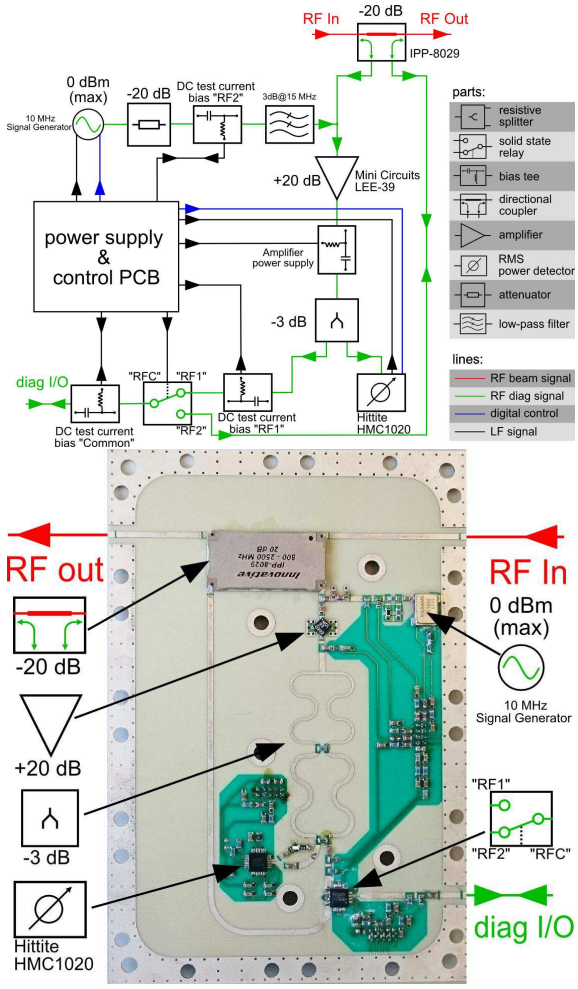

Figure 4: Block diagram of the embedded power meter. Prototype of the RF PCB of the power meter.

References

[1] CR Technical Design Reports 2016, 2014 and C. Dimopoulou, ICFA Beam Dynamics Newsletter No. 64, p.108 (2014).

[2] D. Barker et al., JACoW Proc. COOL'15, Newport News, FRWAUD03 (2015).

[3] C. Peschke et al., JACoW Proc. COOL'13, Mürren, WEPPO20 (2013).

[4] S. Wunderlich et al., JACoW Proc. COOL'15, Newport News, TUPF07 (2015).

Installation of the electron cooling system at CRYRING

J.Roßbach[1], *C.Dimopoulou*[1], *R.Heß*[1], *M.Bräscher*[1], *M.Kelnhofer*[1], *J.Krieg*[1], *and M. Lestinsky*[1]
[1]GSI, Darmstadt, Germany

Initially, CRYRING was the designated storage ring for FLAIR [1]. It was moved into a cave behind the ESR [2] to benefit from an earlier realisation of a working machine for low energy ions. Activities concentrate around this CRYRING@ESR project as it also serves as a test bench for FAIR developments (control system, beam diagnostics, vacuum etc.).

CRYING@ESR is dedicated to low-energy experiments with highly-charged heavy ions like collision spectroscopy at the electron cooler, a transverse electron target and a laser spectroscopy setup [3]. The electron cooler is the most important device for preparation of (decelerated) stored beams and most experiments. In particular, for electron-ion recombination studies: (i) The adiabatic magnetic expansion by a factor 100 offers a transversally very cold electron beam with $k_B T_\perp = 1.5-3.5$ meV (compared to $k_B T_\perp \approx 200$ meV in the ESR). The expected longitudinal electron beam temperature $k_B T_\parallel = 0.05 - 0.20$ meV is as usual determined by the longitudinal-longitudinal relaxation [4] (ii) The electron beam energy has to be ramped in a small range around the nominal electron energy which is matched to the ion velocity. Fast and precise ramping of the cooler voltage will be realised by a special HV amplifier in the range $\pm$ 2 kV installed on the HV platform [3].

In 2015 considerable efforts were made to rebuild the CRYRING machine and provide the associated infrastructure (Fig. 1). In parallel, the cooler had to undergo repairs because of damage to the gun toroid vacuum chamber, which occurred after the transport from Sweden (complete dismantling of the cooler gun side was necessary for welding purposes). Refurbishments were also made to wiring, cooling water circuits and to the vacuum system by adding gauges and some new heating jackets. After successful leak test the cooler was moved to its final position inside the cave (Fig. 2).

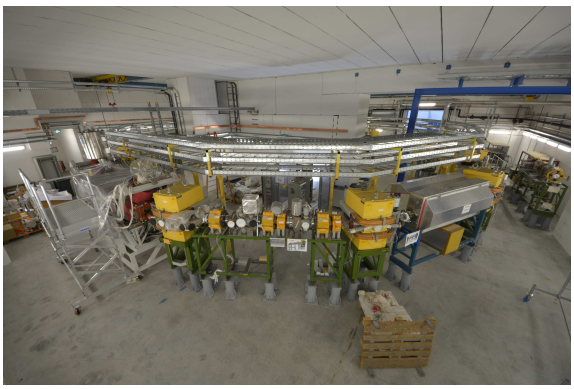

Figure 1: CRYRING in the cave behind the ESR.

Furthermore a high voltage cage was installed for housing of the components which are on a high potential during operation. An isolation transformer powering the components on the high potential side was also installed. The high voltage power supplies inside the high voltage cage are now remote-controllable. The magnets of the cooler were connected to their power supply and to the water cooling system. High voltage power supplies were tested for function and stability. Safety was improved at the collector and gun side of the cooler (protection against contact with high voltage).

Refurbishment of the cryopumps and cyrocompressors for the cooler itself as well as for the coldhead and compressor of the superconducting solenoid is ongoing. A cryogenic liquid helium transfer line was ordered for easy handling and fast refilling of the superconducting gun solenoid. Its delivery is scheduled for May 2016.

Figure 2: CRYRING cooler in the cave. Beam direction from left to right.

Commissioning of the cooler is scheduled for the second half of 2016.

References

[1] C. P. Welsch et al., Hypefine Interactions 172, Issue 1-3, p.71 (2007).

[2] M. Lestinsky et al., Proc. of STORI'14, Phys. Scr. T166 (2015) 014075.

[3] M. Lestinsky et al., Technical Design Report: Experimental Instrumentation of CRYRING@ESR, internal report (2015).

[4] H. Danared et al., Nucl. Instr. and Math. A 441, p.123 (2000).

DOI:10.15120/GR-2016-1

Accelerator operation report

S.Reimann[1], *P.Schütt*[1], *M.Sapinski*[1], *M.Vossberg*[1]
[1]GSI, Darmstadt, Germany

This report describes the operation statistics of the GSI accelerator facility of the year 2015. The information is based on the data of the GSI electronic logbook OLOG [1], which allows a detailed evaluation of operation statistics especially for the time-sharing operation mode of the GSI accelerators.

General overview

Due to the long term maintenance works on SIS18 cavities and the time consuming exchange of all water cooled power cables of the SIS18 magnets, no SIS18 operation and therefore also no ESR operation was possible in 2015. Caused by upgrading the RF-systems of Alvarez sections 3 and 4, the maximum available UNLIAC energy was limited to 5.9 MeV/u.

Considering this and with respect to the reduced availability of operations personnel, it was decided to limit the UNILAC operation mode: most of the time, single-beam-operation was scheduled and parallel tuning for different user experiments was avoided.

So after the 8 months shutdown and maintenance period, the re-commissioning of the UNILAC started in July. In total, the UNILAC was operated 3120 hours (including 504 hours of commissioning).

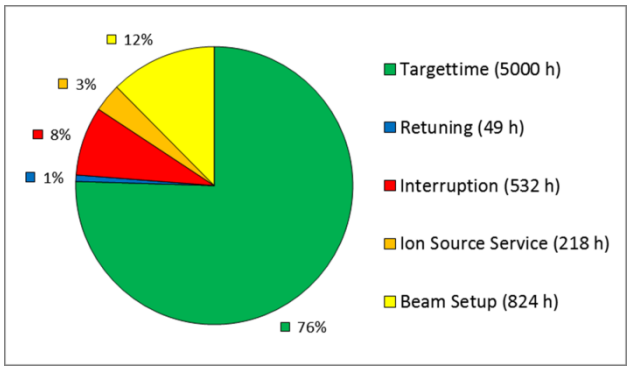

Figure 1: Distribution of overall beam time for all beam modes

Figure 1 shows the overall beam time of the UNILAC in 2015. In total 5000 hours of beam-on-target-time (parallel operation) were successfully delivered to the different experiments, which is 76% of total beam time (75% in 2014). Since the SIS18 was not operated in 2015, here we only compare the UNILAC statistics of both beam times.

The percentage of interruption time, beam setup and target time was quite similar to 2014, as shown in Table 1.

In general, 2015 was a physics experiment dominated beam time. At the UNILAC 614 hours (10%) of beam time have been used for machine experiments which is only half of the share, we reserved in 2014.

UNILAC only	2014	2015
Integral target time	6976 h	**5000 h**
Beam setup	1024 h	**824 h**
Time for retuning	58 h	**49 h**
Time for interruption	791 h	**751 h**
Total beam time	8849 h	**6624 h**

Table 1: Overall beam time of the GSI accelerator facility

Experiments

13 different experiments received beam from the UNILAC, Figure 2 gives an overview of target time for different experimental areas. The main recipients were again TASCA in X8, SHIPTRAP in Y7 and the material research at M1 and M3. Details concerning the experimental programs are given in [2].

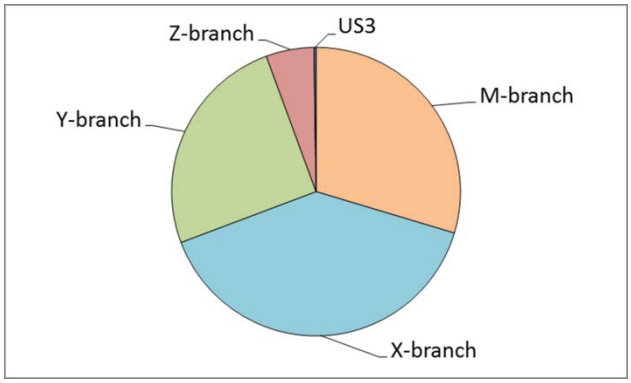

Figure 2: Distribution of target time to the different experimental areas

Except the Z-branch, the major experimental branches at the UNLIAC received roughly the same share of beam time. Although plasma physics (Z) shows up in this statistics, in fact there was almost no beam delivered to the Z-branch. For the LIGHT-experiment at Z6, in general only a 5 Hz virtual machine with no beam was requested to synchronise the LASER with the 108 MHz RF-signal. The intermediate target US3 at the 1.4 MeV charge separator was used for machine experiments only.

Breakdown statistics

Table 2 shows all unscheduled down time events in more detail. In comparison to 2014 there was no major change in relative down time at the UNILAC but it should be noted at this point, that 2014 was a year with a quite low performance.

DOI:10.15120/GR-2016-1

Even though we provided an extensive machine commissioning and a restricted operation mode, the reliability was not improved.

	Down time	Share (h)
Power supplies	82 h	26%
Beam diagnostics	10 h	3%
Operation	1 h	0%
Safety-/ Interlock system	1 h	0%
Ion Sources	23 h	7%
RF-systems & structures	140 h	48%
Controls	17 h	5%
Infrastructure	8 h	2%
Others/ ambiguous	27 h	8%
Total of unscheduled down time	**309 h**	**100%**

Table 2: Statistics of all unscheduled down time events

With 48%, the total downtime associated with RF-systems and RF- structures is strongly dominating the breakdown statistics. 134 breakdown events related to RF were registered, but not all of them are caused by the RF-system itself, the longest breaks were caused by leakages of vacuum tanks, drift-tubes or quadrupole magnets, e.g. the water leakage in Alvarez quadrupoles, or the necessary flushing of the cooling pipes of the re-buncher BB6.

It could be stated, that the old age of the RF-resonators has become the main risk for breakdowns at the UNILAC. It is strongly recommended to hold a reasonable amount of spare parts and get back to preventive maintenance strategy.

Isotope statistics

During 2015, 10 different isotopes have been accelerated. Figure 3 shows the operation time for each isotope.

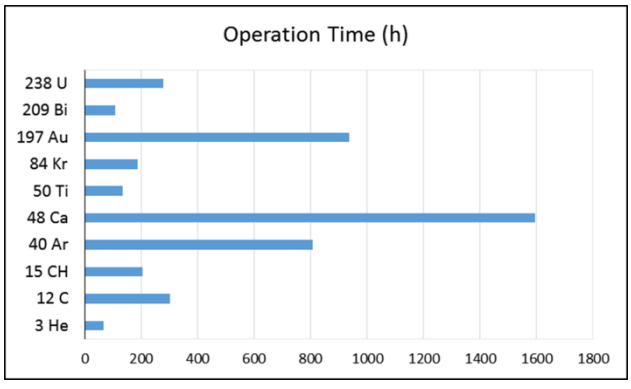

Figure 3: Total beam time for different ion species

With 1598 hours and a percentage of 35%, Calcium from the ECR ion source was the most requested element during this beam time.

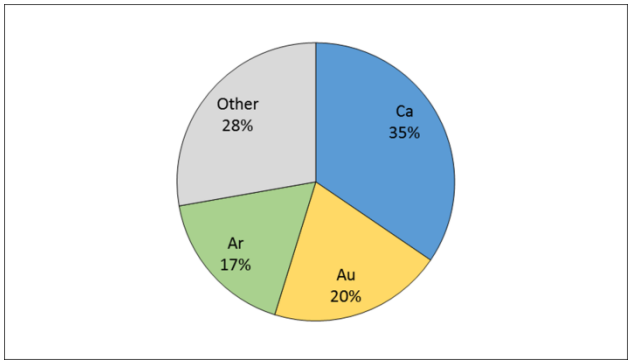

Figure 4: Distribution of main elements

Calcium, Gold and Argon were dominating these statistics. Together they accounted for 72% of all delivered beams in 2015.

Summary

Despite of the technical problems, all physics and machine experiments could be successfully supplied with the requested beam. The preliminary RF commissioning period and the restricted operation mode, which was perfectly implemented into the beam time schedule, ensured the necessary operation stability.

References

[1] P.Schuett, the GSI Operation Logbook OLog, WAO2010 (http://wao10.komac.re.kr/PDF/O-17.pdf)
[2] Report of beam time coordinator, this report

DOI:10.15120/GR-2016-1

Resolution of local topological ambiguity within the “roseN” framework

B. R. Schlei[*]
GSI, Darmstadt, Germany

Abstract

The “roseN” (i.e., RObust (hyper)Surface Extraction in n dimensions) framework provides us with the means of generating – with respect to a given iso-value – continuous manifolds of co-dimension 1 for discrete n-dimensional spaces that are made up of n-cubical cells. Here, we revisit the application of its connectivity diagram within two, three, and four dimensions, respectively. Our considerations of canonical bases of the exterior algebras $\bigwedge(\mathbb{R}^n)$ of the vector spaces $\mathbb{R}^n$, with $n = 2, 3, 4$, enable us to resolve local topological ambiguity in any given integral dimension n directly.

Introduction

Note that the following presentation is subject to a pending patent application (*cf.*, Ref. [1]). In two dimensions (2D), “rose2” is implemented through the DICONEX algorithm [2]. In three dimensions (3D), “rose3” is implemented through VESTA [3]. Last but not least, in four dimensions (4D) “rose4” is implemented through the STEVE algorithm [4]. roseN is protomesh-based [4]. Furthermore, note that $n \geq 2$.

First, both all final manifold support points and all auxiliary connectivity points are indexed within a n-dimensional (nD) space under consideration. Next, properly designed building blocks, which contain specific vector pairs (*cf.*, Ref.s [3, 4]) aid the construction of one-dimensional (1D) oriented polygonal paths within nD. The 1D polygonal paths are always closed (as opposed to strings), and they are represented by a finite list of successive vectors.

In order to determine the unique successor of a given vector, a local topological ambiguity may be encountered. In case that one of the auxiliary connectivity points offers more than one choice for the continuation, it represents a so-called “point of ambiguity” (POA, *cf.*, Ref.s [2, 3, 4]). In 2D, 3D, and 4D, the connectivity diagram as shown in Fig. 1 is applied in order to resolve the potential local topological ambiguity (*cf.*, Ref.s [2, 3, 4], respectively).

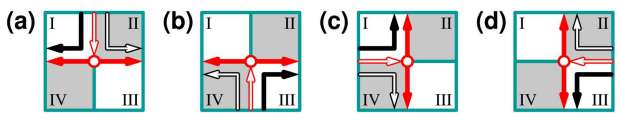

Figure 1: Connectivity diagram (see text).

[*] b.schlei@gsi.de

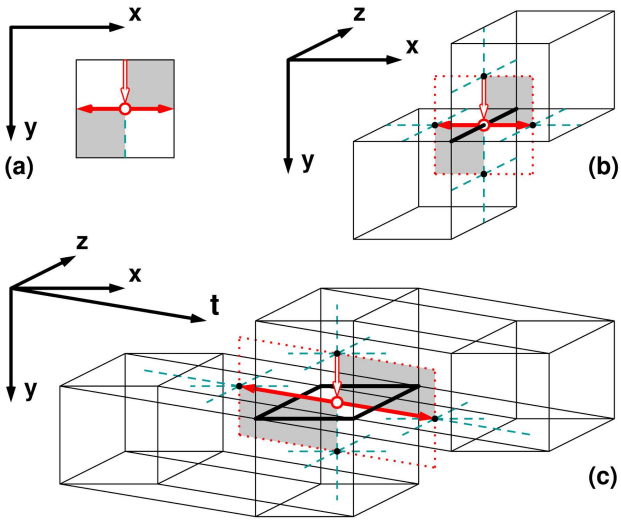

Figure 2: Instances of local topological ambiguity in (a) 2D while using DICONEX [2], (b) 3D while using VESTA [3], and (c) 4D while using STEVE [4] (see text). The dashed lines (azure) represent further vectors, black dots represent final manifold support points, and white dots represent points of ambiguity.

Contour Extraction in Two Dimensions

In 2D, DICONEX [2] processes, e.g., digital image data. In the process of enclosing selected pixels with a set of (1D) contours, a POA may be encountered as pictured in Fig. 2.a. The two selected (gray) pixels are in contact through a single point only. For the incoming (white) vector, there are two choices to continue its path. Here, the connectivity diagram (*cf.*, Fig.s 1.a and 1.b) aids the resolution of the local topological ambiguity. If one continues for this POA always along black (white) bent vectors (i.e., bivectors), one eventually connects (disconnects) the areas of both pixels.

Let us consider the canonical basis of the exterior algebra $\bigwedge(\mathbb{R}^2)$ of the vector space $\mathbb{R}^2$ (*cf.*, e.g., Ref. [5])

$$\{\mathbf{E}_i^{2D}\} = \{\, 1,\ \mathbf{e}_x,\ \mathbf{e}_y,\ \mathbf{e}_x \wedge \mathbf{e}_y \,\},\ i = 1, ..., 4. \quad (1)$$

The connectivity diagram in Fig. 1 can be viewed as bivectors, which in 2D are proportional to $\mathbf{E}_4^{2D}$. Local topological ambiguities are encountered in 2D if, and only if, two pixels are *in contact through a single point*, which is proportional to $\mathbf{E}_1^{2D}$. As a result, we have $\mathbf{E}_1^{2D} \longrightarrow \mathbf{E}_4^{2D}$.

DOI:10.15120/GR-2016-1

Surface Extraction in Three Dimensions

In 3D, VESTA [3] processes, e.g., voxel data. In the process of enclosing selected voxels with a set of (2D) surfaces, a POA may be encountered if, and only if, two voxels are *in contact through a single edge* as pictured in Fig. 2.b.

Let us consider the canonical basis of the exterior algebra $\bigwedge(\mathbb{R}^3)$ of the vector space $\mathbb{R}^3$ (*cf.*, Ref. [5])

$$\begin{aligned}\{\mathbf{E}_i^{3D}\} \;=\; \{\, 1,\;\; \mathbf{e}_x,\;\; \mathbf{e}_y,\;\; \mathbf{e}_z,\;\; \mathbf{e}_x \wedge \mathbf{e}_y,\;\; \mathbf{e}_x \wedge \mathbf{e}_z,\\ \mathbf{e}_y \wedge \mathbf{e}_z,\;\; \mathbf{e}_x \wedge \mathbf{e}_y \wedge \mathbf{e}_z \,\},\;\; i = 1, ..., 8.\end{aligned} \tag{2}$$

The connectivity diagram in Fig. 1.a – 1.d can be viewed (again) as bivectors, which in 3D are proportional to either $\mathbf{E}_5^{3D}$, $\mathbf{E}_6^{3D}$, and/or $\mathbf{E}_7^{3D}$. Local topological ambiguities are encountered in 3D if, and only if, two voxels are *in contact through a single edge*, which is proportional to either one of the vectors $\mathbf{E}_2^{3D}$, $\mathbf{E}_3^{3D}$, and/or $\mathbf{E}_4^{3D}$. As a result, we have $\mathbf{E}_2^{3D} \longrightarrow \mathbf{E}_7^{3D}$, $\mathbf{E}_3^{3D} \longrightarrow \mathbf{E}_6^{3D}$, and $\mathbf{E}_4^{3D} \longrightarrow \mathbf{E}_5^{3D}$. The latter relation is pictured in Fig. 2.b.

Volume Extraction in Four Dimensions

In 4D, STEVE [4] processes so-called toxel data. In the process of enclosing selected toxels with a set of (3D) volumes, a POA may be encountered if, and only if, two toxels (i.e., tesseract shaped picture elements) are *in contact through a single face* as pictured in Fig. 2.c.

Let us consider the canonical basis of the exterior algebra $\bigwedge(\mathbb{R}^4)$ of the vector space $\mathbb{R}^4$ (*cf.*, – once again – Ref. [5])

$$\begin{aligned}\{\mathbf{E}_i^{4D}\} \;=\; \{\, 1,\;\; \mathbf{e}_x,\;\; \mathbf{e}_y,\;\; \mathbf{e}_z,\;\; \mathbf{e}_t,\;\; \mathbf{e}_x \wedge \mathbf{e}_y,\\ \mathbf{e}_x \wedge \mathbf{e}_z,\;\; \mathbf{e}_x \wedge \mathbf{e}_t,\;\; \mathbf{e}_y \wedge \mathbf{e}_z,\;\; \mathbf{e}_y \wedge \mathbf{e}_t,\\ \mathbf{e}_z \wedge \mathbf{e}_t,\;\; \mathbf{e}_x \wedge \mathbf{e}_y \wedge \mathbf{e}_z,\;\; \mathbf{e}_x \wedge \mathbf{e}_y \wedge \mathbf{e}_t,\\ \mathbf{e}_x \wedge \mathbf{e}_z \wedge \mathbf{e}_t,\;\; \mathbf{e}_y \wedge \mathbf{e}_z \wedge \mathbf{e}_t,\\ \mathbf{e}_x \wedge \mathbf{e}_y \wedge \mathbf{e}_z \wedge \mathbf{e}_t \,\},\;\; i = 1, ..., 16.\end{aligned} \tag{3}$$

The connectivity diagram in Fig. 1.a – 1.d can be viewed as bivectors, which in 4D are proportional to either $\mathbf{E}_6^{4D}$, $\mathbf{E}_7^{4D}$, $\mathbf{E}_8^{4D}$, $\mathbf{E}_9^{4D}$, $\mathbf{E}_{10}^{4D}$, and/or $\mathbf{E}_{11}^{4D}$. Local topological ambiguities are encountered in 4D if, and only if, two toxels are *in contact through a single face*, which is proportional to either one of the same bivectors. As a result, we have $\mathbf{E}_6^{4D} \longrightarrow \mathbf{E}_{11}^{4D}$, $\mathbf{E}_7^{4D} \longrightarrow \mathbf{E}_{10}^{4D}$, $\mathbf{E}_8^{4D} \longrightarrow \mathbf{E}_9^{4D}$, $\mathbf{E}_9^{4D} \longrightarrow \mathbf{E}_8^{4D}$, $\mathbf{E}_{10}^{4D} \longrightarrow \mathbf{E}_7^{4D}$, and $\mathbf{E}_{11}^{4D} \longrightarrow \mathbf{E}_6^{4D}$. In Fig. 2.c, the relation $\mathbf{E}_7^{4D} \longrightarrow \mathbf{E}_{10}^{4D}$ is shown.

Hypersurface Extraction in n Dimensions

To generalize the above made observations, in nD a POA may be encountered if, and only if, two n-cubes are *in contact through a single* $(n-2)$*-cube*. Note that a $(n-2)$-cube has co-dimension 2.

If we consider the canonical basis of the exterior algebra $\bigwedge(\mathbb{R}^n)$ of the vector space $\mathbb{R}^n$, we obtain

$$\bigwedge^{n-2}(\mathbb{R}^n) \;\ni\; \mathbf{E}_j^{nD} \;\longrightarrow\; \mathbf{E}_k^{nD} \;\in\; \bigwedge^{2}(\mathbb{R}^n), \tag{4}$$

with $j = \sum_{i=0}^{n-3} \binom{n}{i} + 1, ..., \sum_{i=0}^{n-2} \binom{n}{i}$, and $k = 2^n - j + 1$, while recalling that $\bigwedge(\mathbb{R}^n) = \bigwedge^0(\mathbb{R}^n) \oplus \bigwedge^1(\mathbb{R}^n) \oplus \bigwedge^2(\mathbb{R}^n) \oplus ... \oplus \bigwedge^{n-2}(\mathbb{R}^n) \oplus \bigwedge^{n-1}(\mathbb{R}^n) \oplus \bigwedge^n(\mathbb{R}^n)$, and $\dim(\bigwedge^i(\mathbb{R}^n)) = \binom{n}{i}$, i = 0, ..., n (*cf.*, e.g., Ref. [6]).

Hence, the attitude of the connectivity diagram (*cf.*, Fig. 1) is uniquely defined through the attitude of the $(n-2)$-cubic contact space within the considered nD space.

Summary

To summarize, the connectivity diagram as shown in Fig. 1 *is valid for all integral dimensions*, $n \geq 2$, within the roseN framework. This observation is new (*cf.*, Eq. 4, in particular).

To be specific, these further insights will allow for computationally very efficient implementations of roseN (*cf.*, Ref.s [7, 8]) in any integral dimension, n, since the decomposition of n-cubical spaces into lower dimensional, e.g., 3D, subspaces may be avoided from now on.

I.e., local topological ambiguity, which is in general present in the data, both measured and simulated, can be resolved – henceforward – *directly* within the nD space under consideration.

References

[1] B. R. Schlei, "Verfahren zur Hyperflächenkonstruktion in n Dimensionen," German Patent Applications No. 10 2011 050 721.3 and No. 10 2011 051 203.9; submitted by GSI Helmholtzzentrum für Schwerionenforschung GmbH, Planckstr. 1, 64291 Darmstadt, Germany, on May 30, 2011, and June 20, 2011, respectively; also published as "Method for Hypersurface Construction in n Dimensions," WO 2012163657 A1 (2012), EP 2715673 A1 (2014), and US 20140104270 A1 (2014).

[2] B. R. Schlei, "A New Computational Framework for 2D Shape-Enclosing Contours," Image and Vision Computing 27 (2009) 637, doi: 10.1016/j.imavis.2008.06.014.

[3] B. R. Schlei, "Volume-Enclosing Surface Extraction", Computers & Graphics 36 (2012) p. 111, doi: 10.1016/j.cag.2011.12.008.

[4] B. R. Schlei, "STEVE - Space-Time-Enclosing Volume Extraction", (2013) arXiv:1302.5683 [cs.CG].

[5] C. Perwass, *Geometric Algebra with Applications in Engineering*, Geometry and Computing, Springer, 2009.

[6] G. Scheja, U. Storch, *Lehrbuch der Algebra, Tl. 2 (Mathematische Leitfäden)*, Teubner, 1988.

[7] B. R. Schlei, "GPU Programming - Speeding Up the 3D Surface Generator VESTA", GSI Scientific Report 2014 (2015) p. 460, doi: 10.15120/GR-2015-1-FG-GENERAL-42.

[8] B. R. Schlei, "Visualization of the 4D Transversal Phase Space of Charged Particle Beams", GSI Report No.: GSI-2016-00420, - (2016), doi: 10.15120/2016-R02011.

DOI:10.15120/GR-2016-1

Status of the Barrier-Bucket system for the ESR

M. Frey[1], P. Hülsmann[1], F. Michler[1], H. Klingbeil[1,2], D. Domont-Yankulova[2], K. Groß[2], J. Harzheim[2]
[1]GSI, Darmstadt, Germany; [2]TU Darmstadt, Germany

Introduction

In combination with beam cooling, Barrier-Bucket operation allows an intensity increase of particle beams by concentrating particles in one bucket, while creating an empty bucket for the next injection ("longitudinal stacking"). This can be achieved by generation of two RF voltage single-sine waves as barrier pulses, of which one is shifted in time to compress the beam (Fig. 1).

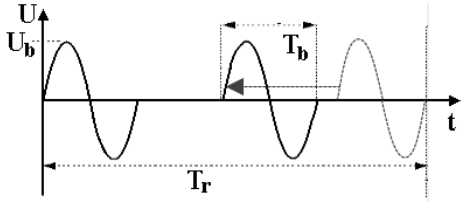

Fig. 1: barrier pulses of duration T_b and amplitude U_b are shifted to compress the beam revolving with period T_r

The generation of Barrier-Buckets in the ESR has been successfully demonstrated with existing ferrite cavities [1], but beam-dynamics requirements regarding barrier-voltage and –frequency made the design of a new cavity based on magnetic alloy (MA) ring cores necessary.

Design of the cavity

Since the power amplifier for the cavity is a solid-state device with 50 Ω output, the cavity as its load should have a similar impedance to enable matching. Impedance measurements of a ring core (FT-3M, 290x660x25 mm³) were used to find a frequency-dependent ring core model in PSpice. A design including four ring cores with four coupling loops connected in parallel (Fig. 2) and parasitic capacitances was then evaluated in PSpice and later compared to measurements from a prototype cavity [2].

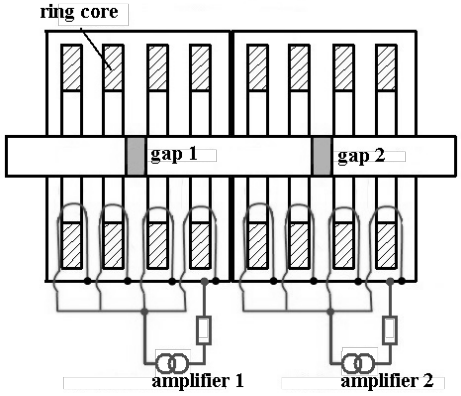

Fig. 2: at each gap, one barrier pulse is generated

Pre-distortion of signals

In order to enable a precise termination of the single sine wave, pre-distortion of the signal is necessary. For linear, time-invariant systems this can be achieved by Fourier-analysis of the system under consideration.

Periodic signals can be expressed as a Fourier series:

$$U(t) = \sum_{n=-\infty}^{\infty} \underline{c_n} e^{in\omega_r t} \quad (1)$$

The desired single-sine signal has Fourier coefficients:

$$\underline{c_n} = \frac{1}{2iT_r}\left(\int_{-\frac{T_b}{2}}^{\frac{T_b}{2}} e^{i\omega_b t} e^{-in\omega_r t} dt - \int_{-\frac{T_b}{2}}^{\frac{T_b}{2}} e^{-i\omega_b t} e^{-in\omega_r t} dt \right) \quad (2)$$

When the transfer function $\underline{H}$ of the system under consideration is measured, its inverse $\underline{H}^{-1}$ can be calculated and the Fourier coefficients of the pre-distorted signal are:

$$\tilde{\underline{c}}_n = \underline{H}^{-1} \underline{c}_n \quad (3)$$

Transformation to time-domain delivers the pre-distorted signal $\tilde{U}(t)$, which is applied to the system´s input in order to produce the single-sine signal at the gap.

Experimental results

The procedure described above has been applied to a prototype system consisting of two ring cores (VitroVAC, 355x700x30 mm³), one amplifier AR 1000A225 and a 1:800 gap voltage divider. It yields a barrier amplitude of U_b=454 V with about 1% ringing after the pulse. The high signal quality measured at the prototype (Fig. 3) is a proof of principle for the planned system.

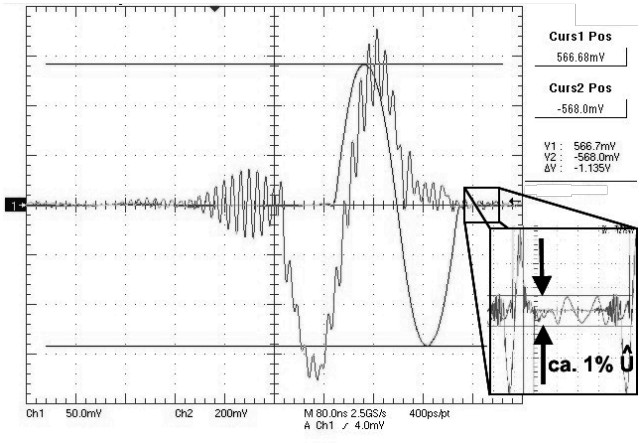

Fig. 3: pre-distorted input (jagged) and gap signal (smooth)

References

1. **Schreiber, G.** *Barrier-Buckets am Experimentierspeicherring der Gesellschaft für Schwerionenforschung.* 2006. Dissertation.
2. **J. Harzheim, D. Domont-Yankulova, H. Klingbeil, R. Königstein.** *Modeling of broadband cavities with P-Spice.* GSI scientific report 2015 (this publication).

DOI:10.15120/GR-2016-1

Investigation of the CERN Ionization Chamber detectors for beam loss monitoring at GSI-HEST*

V. S. Lavrik[1,2], *P. Boutachkov*[1], *O. Kester*[1,2], *and A. Reiter*[1]
[1]GSI, Darmstadt, Germany; [2]Goethe University Frankfurt am Main, Frankfurt, Germany

Beam losses occur at different locations in an accelerator facility. At GSI the beam transport is optimized with the aid of a variety of detectors. The CERN Ionization Chamber [1] (BLMI), is one of the detectors considered for use in the beam loss monitoring system at the future GSI-FAIR facility. The main advantages of these detectors are robustness to radiation damage, variation in the measured charge of order of 10% between different detectors [2] and sensitivity over 10^5 decades, when combined with charge to frequency readout electronics [3].

Controlled beam loss experiments were performed with N, Ni, Kr, Xe and U beams at energies in the range of 300 to 900 MeV/u. The data were compared to simulations with FLUKA transport code [4, 5]. Part of this data sets is discussed in this report. The inset of Figure 1 illustrates the layout of an experiment where three BLMI detectors were attached to the beam tube at various distances from a thin interaction target. The target was Chromox with effective thickness of 1.2 mm, positioned upstream relative to the detectors. The experimental data shown with black squares in Figure 1 were obtained with ^{58}Ni ions at 300 MeV/u beam. The beam intensity was determined by correcting the SIS18-DC transformer [6] reading with the measured extraction and transmission efficiency from SIS18 to the experimental station with a systematic error within 10% [7]. The simulation shown with red squares in Figure 1 agrees within a factor of two with the experimental data. The other experimental data sets agreed with simulations within the same factor. For more details see [7].

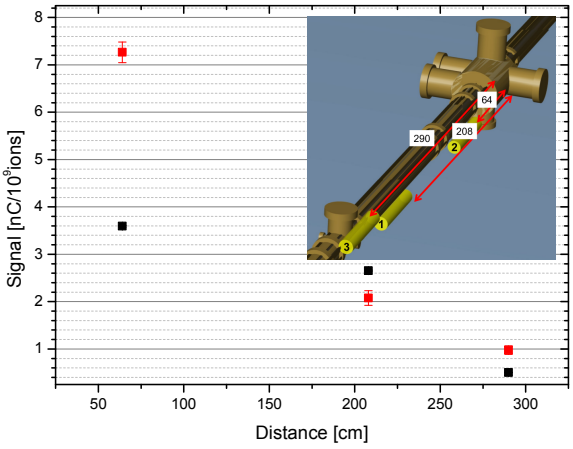

Figure 1: Comparison of FLUKA simulation (red squares) to experimental data (black squares) obtained with ^{58}Ni ions at 300 MeV/u. The experiment layout is shown in the inset.

Figure 2 represents the calculated charge per 10^9 lost ions from a detector position 64 cm downstream from the target for variety of beams and beam energies. This result can be scaled to a specific beam loss scenario in order to estimate the expected BLMI signal in a particular application.

In conclusion FLUKA simulations performed with the recipe described in [7] reproduce the experimental data obtained with N, Ni, Kr, Xe and U in the energy range of 300 to 900 MeV/u within factor of two. The results support the predictions of FLUKA simulations for BLMI detector response to loss scenarios at FAIR.

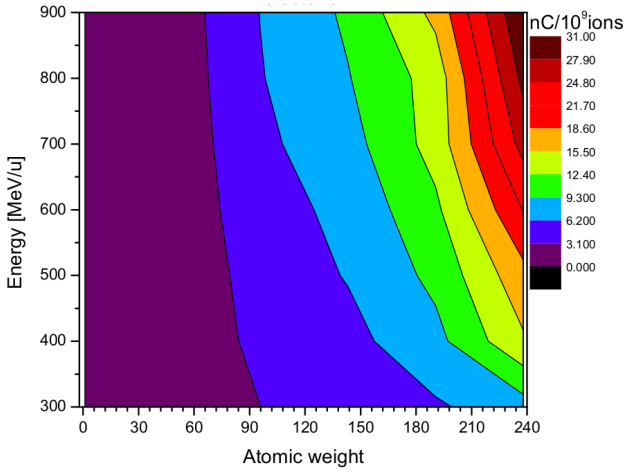

Figure 2: Calculated detector response for BLMI positioned 64 cm downstream from the target as a function of mass number and energy. For more details see [7].

References

[1] M. Stockner *et al.*, "Classification of the LHC BLM Ionization Chamber", DIPAC'07, May 2007

[2] V.S. Lavrik, P. Boutachkov, S. Damjanovic and B. Voss, GSI Scientific report, p. 486 (2014)

[3] H. Reeg, DIPAC01 Conf. Proc., p. 120 (2001).

[4] T.T. Böhlen *et al.*, Nuclear Data Sheets 120, 211-214 (2014)

[5] M. Stockner *et al.*, CERN-AB-2006-086 BI

[6] H. Reeg, N. Schneider, DIPAC99 Conf. Proc., p.147 (1999)

[7] V.S. Lavrik, PhD. thesis, Goethe University, to be submitted in 2016

* Work supported by FIAS

DOI:10.15120/GR-2016-1

New development of lead tungstate crystals for the PANDA-EMC*

V. Dormenev[1], K.-T. Brinkmann[1], J. Houzvicka[2], M. Korzhik[3], R. W. Novotny[1], H.-G. Zaunick[1], and for the PANDA collaboration

[1]2nd Physics Institute, Justus-Liebig-University, Giessen, Germany; [2]CRYTUR, spol. s.r.o., Turnov, Czech Republic; [3]Institute for Nuclear Problems, Minsk, Belarus.

Presently, there is still a strong interest to consider high-quality lead tungstate ($PbWO_4$, PWO) scintillation crystals for electromagnetic calorimetry (EMC). In close cooperation with the company CRYTUR (Turnov, Czech Republic) a new development has been initiated in 2014 to produce high-quality crystals using the Czochralski technique. The so far obtained results confirm already that the chosen technological approach will allow to produce PWO crystals with properties reaching the PWO-II specifications of the PANDA experiment at FAIR (Darmstadt, Germany).

Introduction

Lead tungstate crystal is one of the most widely used scintillation materials in electromagnetic calorimetry in modern accelerator experiments [1]. It has an unique set of physical and scintillation properties [2], which allow the construction of an affordable and compact electromagnetic calorimeter (EMC).

The first generation of mass-production lead tungstate crystals, characterized as PWO-I, was developed for the CMS-ECAL detector at CERN. The technology of CMS type crystals was optimized for radiation hardness to reduce the degradation of the light collection caused by radiation induced optical transmittance losses. In the frame of the PANDA project the new generation of PWO-II crystals was developed. The light yield at room temperature was doubled without degrading the remaining scintillation properties. An additional increase of the light yield by a factor of 3.5-4 could be obtained by operating the detectors at a temperature of t –25º C.

The majority of PWO crystals for CMS and for the PANDA calorimeters was produced by Czochralski method by the Bogoroditsk Technicall Chemical Plant (BTCP, Bogoroditsk, Russia) until its shut down some years ago. As a remaining producer for mass production of PWO crystals the Shanghai Institute of Ceramics, Chinese Academy of Science (SICCAS, Shanghai, China) was considered. It produces lead tungstate crystals using the modified Bridgman method. However, up to now the provided samples could not reach the required quality limits.

As an alternative, the company CRYTUR (Turnov, Czech Republic) with good experience in the development and production of different types of inorganic oxide crystals has joined a research program to develop the technology for mass production of lead tungstate crystals.

* Work supported by EU, GSI and BMBF.

The aim of the investigations was to obtain full size (up to 20 cm) lead tungstate crystals produced by Czochralski method according to the PANDA EMC specifications as listed in Table I.

TABLE I
SPECIFICATION LIMITS FOR PWO CRYSTALS OF THE PANDA EMC

Parameter	Limit
longitudinal optical transmittance at 360 nm	≥35 %
longitudinal optical transmittance at 420 nm	≥ 60 %
longitudinal optical transmittance at 620 nm	≥ 70 %
dk (420 nm)	< 1.1 m^{-1}
LY at T= +18° C within 100 ns integration time	≥ 16 phe/MeV
LY (100 ns)/LY(1000 ns) at T= +18° C	> 90 %

dk is the radiation induced absorption coefficients and is calculated as $dk = [ln(T_b/T_a]/d$, where T_b, T_a are the optical transmittances before and after irradiation, correspondently, and d is the thickness of the PWO sample. LY is the abbreviation for light yield, which is measured in units of photoelectrons per MeV, phe/MeV, deposited energy. The light yield is measured with a standard two inch photomultiplier (PMT) with bialkali photocathode. A thin layer of optical glue is placed between PMT and the PWO sample.

The achieved performance

In the first stage some series of lead tungstate ingots with a volume of a few cubic centimetres were grown under different conditions to select the optimal growing technology and the necessary level of doping. It was established that the growth of un-doped PWO in air leads to a stronger absorption within the whole spectral region of scintillation emission (350-550 nm) caused by damage due to ionizing radiation. The growth of un-doped PWO in a completely oxygen-free atmosphere delivers a crystal of strongly reduced quality.

The growth of un-doped PWO in a N_2 + O_2 atmosphere provides better transmission characteristics and a grade of radiation hardness comparable to the samples grown in air. The doping with a sufficient amount of La and Y ions improves significantly the transmission characteristics in particular below 420 nm (suppression of 350 nm absorption centres [3]) and the improvement of the transmittance at 420 nm is significantly larger, which is mandatory. In general, the combination of La and Y doping and a N_2+O_2 atmosphere provided the best set of characteristics. On the other hand, La and Y doping reduces slightly the overall scintillation efficiency, but most primarily slower components which is in fact positive for maintaining the fast response.

At the next stage tests of full size samples with a length up to 20 cm were performed. The very first ingot showed a yellow colouring due to over-doping but the next one was clear and visually transparent. The optimization of

DOI:10.15120/GR-2016-1

the crystal production at CRYTUR is based on identical raw material as it was used by BTCP.

All samples were optically polished. The rectangular shape was chosen to allow a reliable investigation of the homogeneity by measuring the optical transmittance in transversal direction at different positions along the length of the crystal as well.

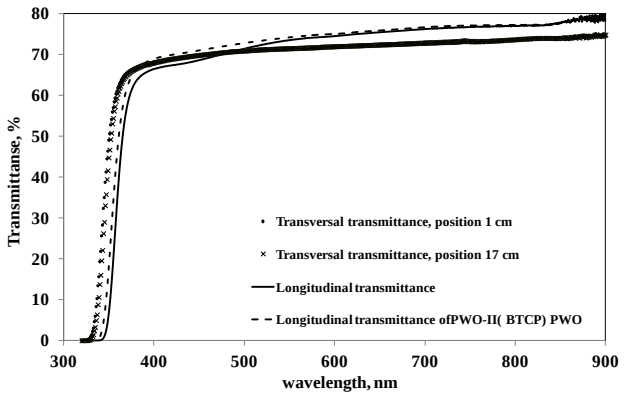

Figure 1: Spectra of the transversal and longitudinal optical transmittance of the 185 mm long sample. The longitudinal transmittance of a 200 mm PWO-II crystal produced by BTCP is included for comparison.

Typical test results of a sample produced at the end of 2015 are presented on figures 1-3. The crystal was grown in a new crucible in nitrogen atmosphere doped with La and Y with dimensions of 20x20x185 mm^3. The longitudinal optical transmittance before and after irradiation with an integral dose of 30 Gy at a dose rate of ~ 2 Gy per minute were measured using a Varian Cary 4000 spectrophotometer. The dose of 30 Gy corresponds to the value, which will be reached in the most forward part of the PANDA EMC after half year of the operation. The transversal optical transmittance was measured with a Hitachi 3200 spectrophotometer. The light yield was measured using a calibrated Hamamatsu R2059 photomultiplier at temperatures of +18°C and -25°C, respectively. TYVEK® paper was used as reflector material.

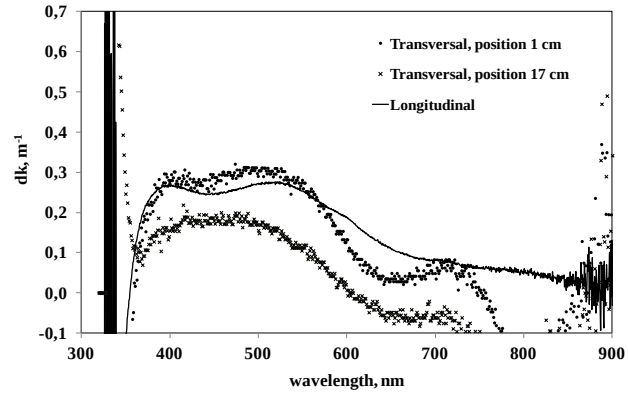

Figure 2: Spectra of the radiation induced coefficient of the 185 mm long sample measured in transversal and longitudinal directions. The sample has been irradiated with γ-rays up to an integral dose of 30 Gy.

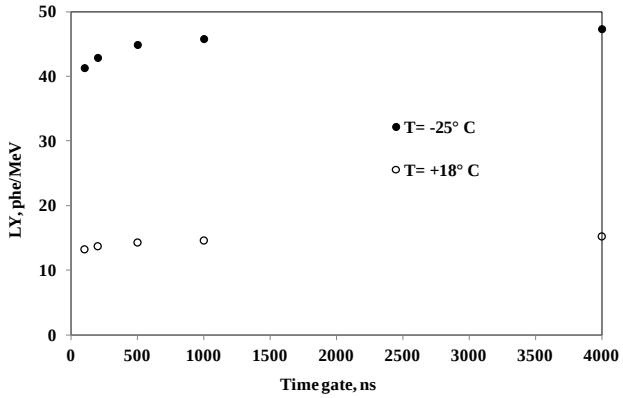

Figure 3: Dependence of the recorded light yield on the integration time for the 185 mm long crystal sample measured at two different temperatures.

The values of transversal and longitudinal transmittances and the radiation induced coefficients satisfy the PANDA specification limits. However, the absolute value of the longitudinal transmission is significantly below the typical distribution of a former BTCP crystal. Since the crystal has rectangular shape the measured values of the light yield are not enhanced due to optical focusing. Nevertheless, the mean absolute light yield comes close to the specification limit of 16 phe/MeV. Based on the obtained results one can conclude that the last samples of lead tungstate crystals produced by CRYTUR obviously contain a slightly too high doping concentration of La and Y which might explain the slightly too low light yield.

Conclusion

The development of PWO crystals was restarted by the CRYTUR Company. The obtained results confirm already now that the technological approach of the company will allow to produce lead tungstate crystals with properties very close to the PWO-II specifications of the PANDA experiment at FAIR (Darmstadt, Germany). Further investigations will be done to obtain the optimal doping level. As a next step, crystals in PANDA geometry will be produced and characterized using a set of additional technically improved furnaces.

References

[1] F. Pauss (Editor-in Chief), "CMS. The Electromagnetic Calorimeter. Technical Design Report," CERN, Geneve, Switzerland, CERN/LHCC 97-33 CMS TDR 4, Dec. 15, 1997.

[2] E. Auffray et al., "Status of PWO crystal production for the electromagnetic calorimeter of CMS and of its construction," Nucl. Instr. and Meth. in Phys. Res. A, vol. 537, Issues 1-2, pp. 373-378, Jan. 21, 2005.

[3] A. A. Annenkov, M.V. Korzhik, P. Lecoq, "Lead tungstate scintillation material," Nucl. Instr. and Meth. in Phys. Res. A, vol. 490, Issues 1-2, pp. 30-50, Sept. 1, 2002.

DOI:10.15120/GR-2016-1

Modeling of broadband cavities in PSpice

J. Harzheim[2], D. Domont-Yankulova[2], R. Königstein[2], H. Klingbeil[1,2], M. Frey[1], and P. Hülsmann[1]
[1]GSI, Darmstadt, Germany; [2]TU Darmstadt, Germany

PSpice models for the SIS100 barrier bucket cavity and the ESR barrier bucket cavity have been created and compared with measurements.

Introduction

At GSI, barrier bucket systems are planned for the SIS100 synchrotron and the ESR storage ring. In order to achieve a single-sine gap signal of the desired amplitude and quality, effects in the linear and nonlinear region of the system have to be investigated. Therefore, the cavities and the amplifier stages are to be modeled in PSpice.

PSpice model of the cavity

As the frequency-dependent properties of the ring cores highly dominate the properties of the cavity, the cores have to be modeled in a first step. In a second step, these models are used to build up the whole cavity.

Modeling of MA ring-cores

In a first step the admittance of the ring core is measured in the frequency range 100 kHz - 30 MHz in a measurement setup shown in figure 1. After influences from the measurement environment are subtracted from the data, the measured admittance is fitted by a rational function of the form using a vector-fitting algorithm [1].

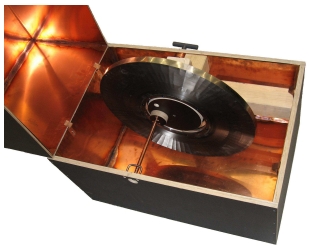

Figure 1: Measurement setup for ring cores

$$f(s) = \sum_{i=1}^{N} \frac{r_i}{s - p_i} + d + se. \qquad (1)$$

From this fit function an equivalent circuit can be derived as shown in figure 2. Each branch of the circuit represents one summand of (1).

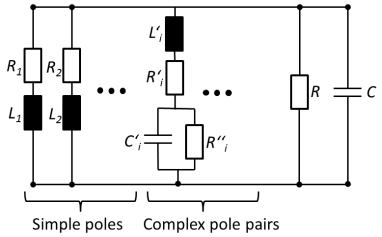

Figure 2: Equivalent circuit for one ring core

Model for the ESR cavity

The final cavity will consist of two halves of one gap and four ring cores each. Via these cores connected in parallel, the desired voltage will be induced to the gap. In the PSpice model, the windings are realised by a parallel circuit of ring cores and couplers. The gaps are modeled by a capacitance. In additiont, stray capacitances have been included to the coupling loop based on measurement results. The PSpice model of the cavity is shown in figure 3.

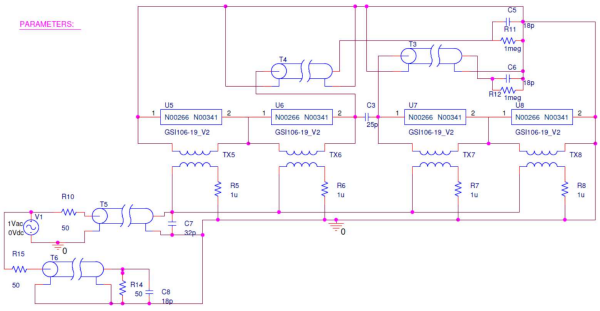

Figure 3: PSpice model for one cavity half including measurement devices

Simulation results

For small signal barrier-bucket generation, the transfer function of the system is measured. Using this transfer function, the signal will be predistorted to generate a single-sine gap voltage. Transfer functions and the predistorted signals from measurement and simulation are shown in figure 4 and 5.

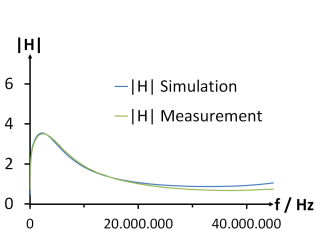

Figure 4: Transfer function

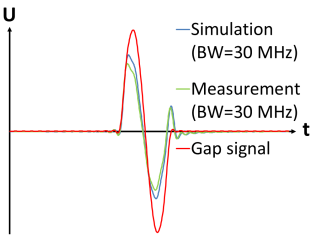

Figure 5: Predistorted signals and gap signal

References

[1] B.Gustavsen and A. Semylen, “Rational approximation of frequency domain responses by vector fitting”, EPAC’96, Sitges, June 1996, p. 798IEEE Trans. Power Delivery, vol. 14 no. 3, 1999

DOI:10.15120/GR-2016-1

Ion extraction simulations for the proton injector for FAIR*

C. Ullmann[1,2], *A. Adonin*[1], *R. Berezov*[1], *R. Hollinger*[1], *and O. Kester*[1,2]
[1]GSI, Darmstadt, Germany; [2]Goethe Universität, Frankfurt am Main, Germany

Introduction

IBSIMU (IonBeamSIMUlations) is a 3D simulation code developed to simulate H^- Beams [1]. The code is further used to analyze the behavior of positive ion beams. For the proton injector it is necessary to analyze the emittance, brilliance and perveance of the ion beam to find optimized working parameters for experiments during commissioning of the proton injector. The commissioning will take place at the end of 2016 at CEA/Saclay.

IBSIMU simulations

The proton injector front end for FAIR consists of an ECR-type ion source and a pentode extraction system consisting of a plasma electrode, a puller electrode, two ground electrodes and a encapsulated screening electrode [2]. A short LEBT (Low Energy Beam Transport) including two solenoid-steerer systems and a diagnostics chamber behind the extraction and provides for transport of the ion beam to the RFQ. For the simulations shown in this report, the following plasma parameters are defined: temperature of the ions $T_i = 0.5\,eV$, temperature of the electrons $T_e = 5\,eV$. 1x10^6 particles are used for the simulation with a fraction of $95.5\%\,H^+$, $2.5\%\,H_2^+$ and $2\%\,H_3^+$ and the related masses and charge state. The potential of the plasma electrode is set to $U_{Pl} = 95kV$. A distribution of the electric field could be reached with the following voltages in the system: Puller electrode $U_{Pu} = 52$ kV, screening electrode $U_{SE} = 2.5$ kV. A space charge compensation of 98% is assumed at the reach-through of the screening electrode. The proton beam current is set to 100 mA as needed for FAIR operation. Figure 1 shows the so called matched case extraction for the ion beam. Only the ion extraction picture section is shown. The maximum divergence angle of the ion beam is $\omega_{max} = 94\,mrad$ at the entrance to the LEBT at $0.124\,m$. Figure 2 shows the adjustment of the divergence angle (ω_{max}, $\omega_{90\%particles}$, $\omega_{90\%angle}$) to the ion beam current density at the entrance of the LEBT at 0.124 m. In all cases the simulated divergence angle for the system is not lower then $\omega_{90\%particles}$=44 mrad and $\omega_{90\%angle}$=60 mrad for $I_{ionbeam} = 100\,mA$, taking only 90% of the particles into account. Beam losses in the extraction system occur due to the loss of secondary ions and recombination processes. All simulated data has to be verified during the commissioning.

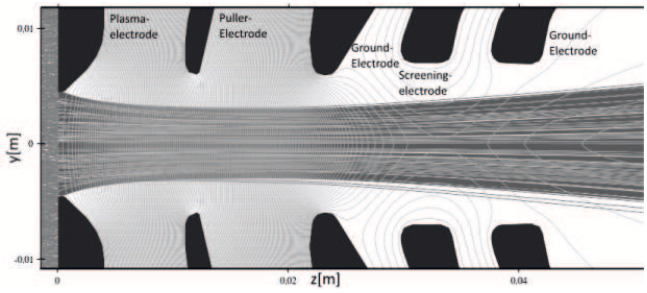

Figure 1: Pentode Extraction in matched case with $I_{ionbeam} = 100\,mA$, $U_{Pl} = 95\,kV$, $U_{Pu} = 52\,kV$, $U_{SE} = -2.5\,kV$ and $\omega_{max} = 75\,mrad$ (1) Plasma electrode (2) Puller Electrode (3) Ground electrode (4) Screening electrode

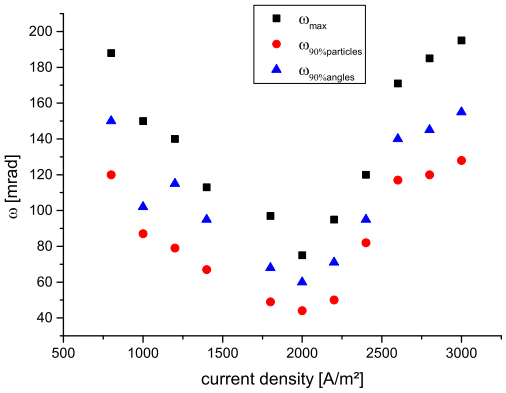

Figure 2: Divergence angle of the ion beam ω_{max}, $\omega_{90\%particles}$, $\omega_{90\%angle}$ as a function of the ion beam current density J.

References

[1] T. Kalvas, "Development and use of computational tools for modelling negative hydrogen ion source extraction systems", Department of Physics, University of Jyväskylä, Research Report No. 10/2013.

[2] R.Berezov, et al. "Status of the proton injector for FAIR", GSI scientific report 2012, PHN-FAIR-01

* Work supported by HIC4FAIR/HGShire

DOI:10.15120/GR-2016-1

Phase calibration strategies for synchrotron RF signals

A. Andreev[†1], *D. Lens*[2], *H. Klingbeil*[1,2]
[1]TEMF, TU Darmstadt, Germany; [2]GSI, Darmstadt, Germany

Introduction

The reference RF signals for the low level RF (LLRF) systems of the FAIR synchrotrons are generated by digital synthesis modules (DDS) mounted in one so-called Group-DDS crate which allows to perform various multi-harmonic operations [1]. According to the high accuracy requirements the phase difference of the reference RF signals must be better than 1°. The DDS modules themselves show a frequency-dependent phase response that must be compensated to keep the DDS modules in phase during the whole acceleration cycle.

Group-DDS phase calibration

Each DDS unit operates at a certain frequency defined by the harmonic number *h* that is generally independent of the module and can be changed during the operation. Since the harmonic numbers of the DDS modules are different, the frequency-dependent phase response is not the same for all the modules, and a phase shift between different DDS RF signals occurs during the acceleration ramp.

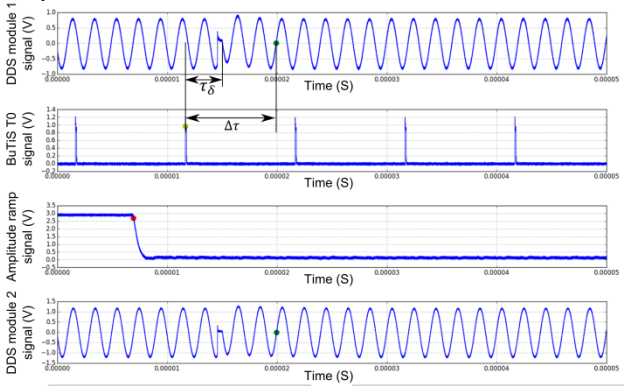

Figure 1: DDS modules and BuTiS T_0 signals during calibration

In the currently used Group-DDS calibration procedure [2] the DDS module configured to the highest harmonic number is used as a reference and harmonic numbers of the modules are fixed. If the harmonic number of the DDS module is changed, then the calibration data stored in calibration electronics modules (CEL) are no longer valid and one has to repeat the process for the new *h* value. Therefore, a new calibration method with respect to the absolute phases of DDS modules is being verified. By means of the proposed method one can use the same calibration data for all the DDS modules, independent of the harmonic number they are realizing.

The BuTiS 10 µs T_0 pulse is a common reference for the DDS signal start events, and can be used as a reference to determine the phase of the DDS output RF signal. The time difference between both signals is the time between the rising edge of the T_0 pulse τ_0 and the zero crossing of DDS signal τ_{DDS}: $\Delta\tau = \tau_{DDS} - \tau_0$ (Figure 1). The corresponding phase of the DDS module is $\Delta\phi_f = 2\pi f(\Delta\tau - \tau_\delta)$, where f is the frequency of the DDS module i.e. frequency under calibration, which is precisely estimated with the four-parameter sine wave fit algorithm [3].

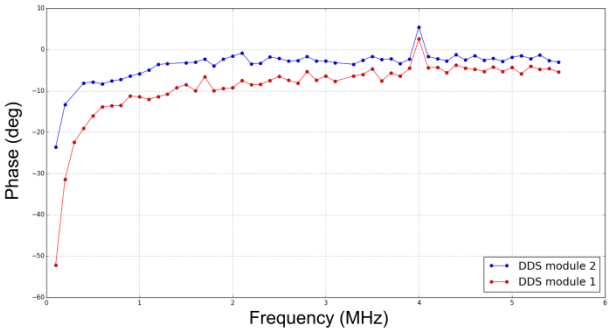

Figure 2: DDS modules phases with respect to BuTiS T_0 pulse.

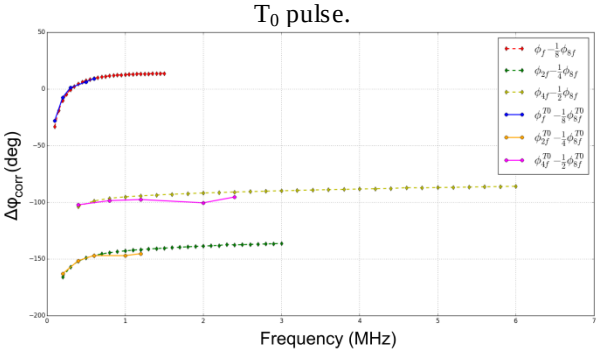

Figure 3: Comparison with the currently used procedure.

The resulting phase curves (Figure 2) show a good agreement with the results of the currently used procedure (Figure 3) after applying to the phase correction values additional phase offsets corresponding to the harmonic ratio of the frequencies under comparison.

Future work

The next step will be an automation of the proposed calibration procedure, long-term tests and evaluation of the temperature influence on the calibration results.

References

[1] H. Klingbeil et al., Phys. Rev. ST Accel. Beams 14, 102802, (2011).
[2] D. Lens, B. Zipfel, "Group-DDS Calibration".
[3] P. Händel, IEEE Trans. on Instr. and Meas., Vol. 49, No. 6, December 2000.

[†]andreev@temf.tu-darmstadt.de

DOI:10.15120/GR-2016-1

Status of a high gradient CH – cavity*

Ali Almomani[1] *and Ulrich Ratzinger*[1]
[1]IAP, Frankfurt University, Frankfurt am Main, Germany

The activities in room temperature pulsed linac development aim on compact designs and on an increase of the voltage gain per meter. A high gradient CH – cavity operated at 325 MHz was developed and successfully built at IAP – Frankfurt. The mean effective accelerating field for this cavity is about 13.3 MV/m at a beam energy of 12.5 AMeV, corresponding to β=0.164. The results might influence the rebuilt and a later energy upgrade of the UNILAC – Alvarez section. Another motivation is the development of an efficient pulsed ion accelerator for significantly higher energies like 60 AMeV. The new GSI 3 MW Thales klystron test stand will be used for the cavity RF power tests. Detailed investigations for two different types of copper plating (high lustre and lustre less) with respect to the high spark limit can be performed on this cavity. The first measurement results of the frequency and the on axis electric field for this cavity will be presented.

Cavity Layout

The development of CH – cavities towards a high field gradient [1-3] is the main design aspect of this cavity. Therefore, the drift tube shape and the stems were optimized to keep the peak electric surface fields at modest levels.

At the same time the effective shunt impedance of 52 MΩ/m and the gap voltage distribution as shown by Fig. 3 are kept in an attractive level. A 7 gap CH – cavity has been developed and successfully mounted and tuned at IAP Frankfurt after being fabricated at NTG, Germany [1-3].

First Measurement on CH-Cavity

The CH-cavity was successfully built, copper – plated and delivered to IAP – Frankfurt. It was checked and prepared for the first measurements in order to check the resonance frequency, quality Factor and the on axis electric field.

In order to reach the resonance frequency of the cavity, two static tuners and one movable tuner will be used. The range of the movable tuner is shown in Figure 1.

The resonance frequency of 325.2 MHz has been reached at 41 mm tuner position inside the cavity. The expected quality factor (Q_0 - value), from CST simulations, at this frequency is reached 12500, against Q_{meas} = 12200±200 (see Figure 2). Figure 3 shows the measured on axis electric field.

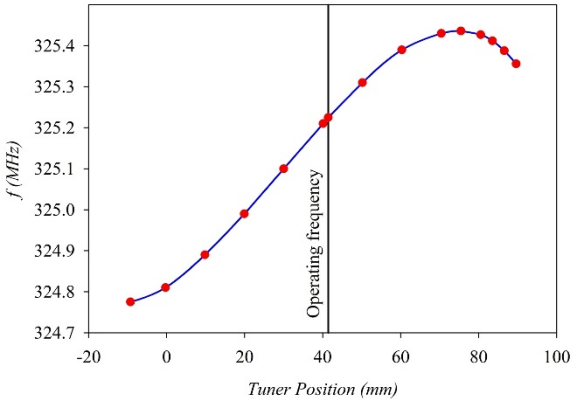

Figure 1: Frequency range for the movable tuner.

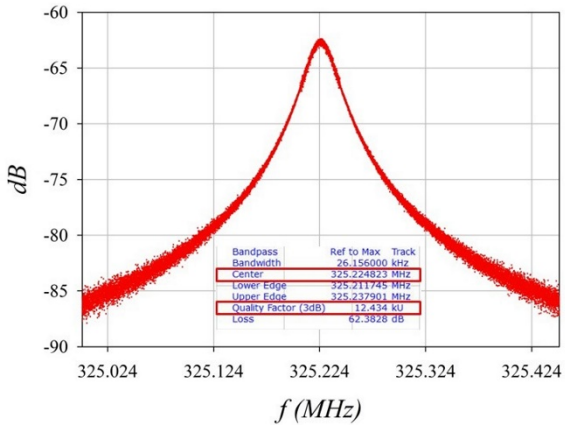

Figure 2: Frequency and Q – value measurements.

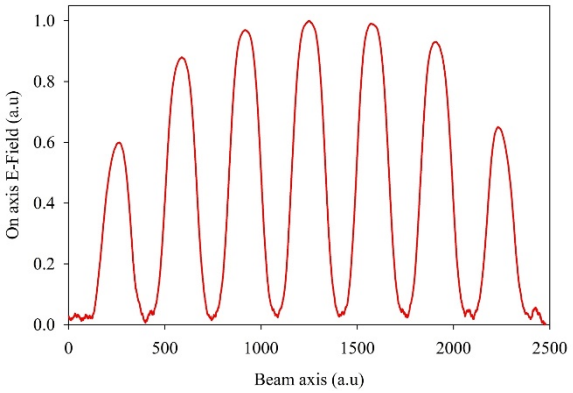

Figure 3: On axis electric field.

References

[1] A. Almomani et al., Phys. Rev. ST-AB 15, 051302 (2012).

[2] A. Almomani and U. Ratzinger, Proc. LINAC 14, Geneva, Switzerland, p. 208 (2014).

[3] A. Almomani and U. Ratzinger, Proc. IPAC 15, Richmond, VA, USA, p. 3724 (2015).

* Work supported by BMBF, contract No. 05P12RFRB9.
#a.almomani@iap.uni-frankfurt.de

DOI:10.15120/GR-2016-1

Intensity-sensitive and position-resolving cavity for the CR: proof of principle*

X. Chen[1,2], *M. S. Sanjari*[1], *Yu. A. Litvinov*[1,3], *F. Nolden*[1], *M. Steck*[1], *and Th. Stöhlker*[1,4]
[1]GSI, Darmstadt; [2]Uni-HD, Heidelberg; [3]MPI-K, Heidelberg; [4]HI Jena, Jena

In the future FAIR facility, the Collector Ring (CR) will be the foremost one in the sequence of storage rings. The main usage of the CR is to collect and stochastically cool anti-protons and rare isotope beams from the SuperFRS for the physics experiments to be carried out downstream. In addition, the CR can be employed as a direct experimental site for, e.g., the nuclear mass measurements after the ring is set to the isochronous ion-optical mode. Despite the traditional TOF detector, a Schottky resonator is also capable of precisely determining masses from the revolution frequencies of stored ions, given that they fulfill the isochronous condition very well. To correct for the frequency spread introduced by the anisochronism effect [1], we thus propose to develop an innovative Schottky resonator with transverse sensitivity [2].

The novel design of the intensity-sensitive and position-resolving cavity is optimized for the machine parameters and ion optics of the CR. The critical feature of the design is horizontally offsetting the cavity from the central orbit of the beam to one side and utilizing the resonant monopole mode of the EM fields inside the cavity. Only by this means can we achieve a fairly large magnitude and gradient of shunt impedance $R_{\rm sh}/Q_0$—a parameter characterizing the coupling strength between the cavity and the beam—in the aperture region. In order to minimize the crosstalk between two mutually orthogonal directions in the transverse plane, the cavity is deliberately stretched vertically such that the $R_{\rm sh}/Q_0$ map evenly increases from left to right with almost no variations in the perpendicular direction.

The feasibility of two shapes, namely rectangle and ellipse, has intensively been investigated for the cavity design by analytic and numerical means. Afterwards, a scaled cavity has been constructed based on each of those geometries (Fig. 1). Since every part of the cavity is scaled down by the same factor of four, the shunt impedance is unchanged, ensuring that the measurement results can directly be compared to the simulation outcomes. Moreover, to empirically determine the dielectric constant of a ceramic bead, we have constructed a pillbox cavity to be used as a calibrator in the benchtop measurements.

Having measured the dielectric constant of the bead, we then profiled the electric fields inside the cavities using a so-called bead-pull method, from which the shunt impedance can be deduced. The entire benchtop measurements were carried out on an automated test platform [3]. Once the control program is tweaked properly, the 2D profiling process can proceed automatically with great precision. The final result of the measured $R_{\rm sh}/Q_0$ in the aperture region for the elliptic cavity is shown in Fig. 2. In general, $R_{\rm sh}/Q_0$ manifests an ascending trend from left to right, while the apparent excess near edges is due to the measurement artifact with a spherical bead [4].

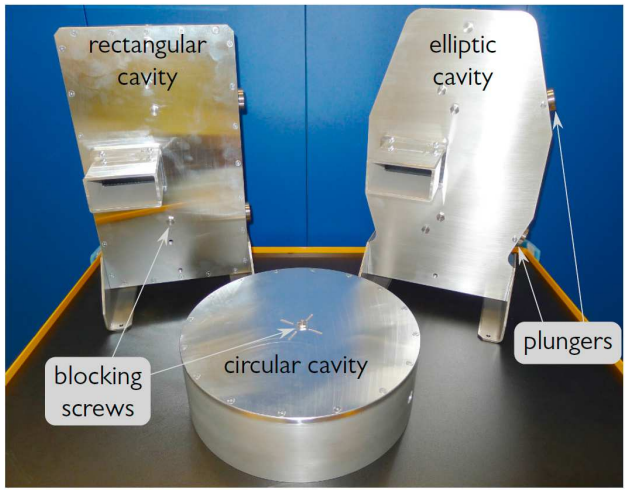

Figure 1: Photo of two model cavities (left and right) and the calibration cavity (middle).

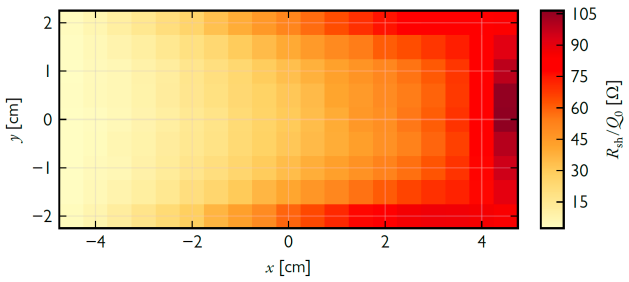

Figure 2: Measured shunt impedance in the aperture region of the elliptic cavity. A quite similar result is also observed for the rectangular cavity.

References

[1] X. Chen *et al.*, *Hyperfine Interact.*, **235** (2015) 51
[2] M. S. Sanjari *et al.*, *Phys. Scr.*, **T166** (2015) 014060
[3] X. Chen *et al.*, *Phys. Scr.*, **T166** (2015) 014061
[4] X. Chen *et al.*, "Intensity-sensitive and position-resolving cavity for heavy-ion storage rings", submitted to *Nucl. Instrum. Meth. A*

*Work supported by EU Marie Curie ITN "oPAC" (PITN-GA-2011-289485), Helmholtz-CAS Joint Research Group (HCJRG-108).

First plasma produced for the FAIR proton linac

R. Berezov[1], N. Chauvin[2], O. Delferriere[2], J. Fils[1], R. Hollinger[1], O. Tuske[2], C. Ullmann[3], and W. Vinzenz[1]

[1]GSI, Darmstadt, Germany; [2]CEA, Saclay, France; [3]IAP, Frankfurt am Main, Germany

The future compact proton linac will produce proton beams with energy of 70 MeV that will be injected into upgraded Heavy Ion Synchrotron (SIS 18), accelerated to 4 GeV, and further accelerated to 30 GeV in SIS 100 for the production of anti-protons. The first part of the linac includes the high current ion source and Low Energy Beam Transport section (LEBT) designed and built at CEA/Saclay. The proton injector will deliver a pulsed proton beam in the energy range of 95 keV and up to 100 mA ion beam current [1]. The expected emittance at the entrance of the RFQ (Radio Frequency Quadrupole) is lower than 0.3 π mm mrad (normalized, rms).

The microwave ion source with a five electrode extraction system operates at a frequency of 2.45 GHz. The RF power is produced by a magnetron microwave generator and is injected into a plasma chamber through rectangular waveguide. The duty cycle of the ion source is 4 Hz with a flat top pulse length of 0.2 ms. Pulsed mode operation of the ion source leads to a longer life time and reduces the requirements for the cooling system [2].

The LEBT focusing system (shown in the Figure 1) consists of two solenoids with two horizontal and vertical integrated magnetic steerers. A diagnostic chamber with different diagnostic tools is mounted between the solenoids. The current is measured with a current transformer behind the extraction system and the second solenoid. An electrostatic chopper is placed between the second solenoid and the RFQ to cut the beam pulse to 36 µs.

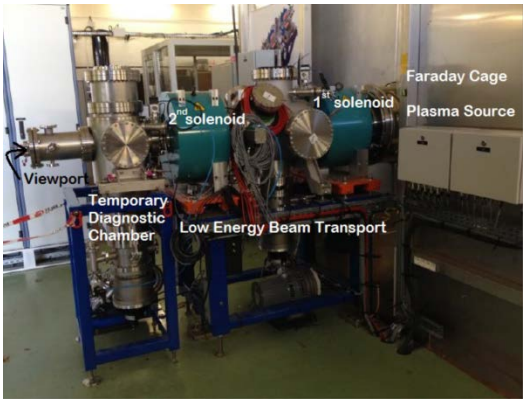

Figure 1: Proton injector at CEA/Saclay.

The proton injector is almost ready for commissioning at CEA/Saclay. The ion source is mounted on the high voltage platform inside the Faraday cage. The LEBT is installed outside the Faraday cage at ground potential and is connected to the ion source through accelerating column. The mini-control system fabricated at GSI to operate the proton injector remotely is transported and installed at CEA. The first part of control system to operate ion source including magnetron, impedance adapter, gas inlet connection etc. successfully tested. The second part mainly includes connection of the power supplies. The operation will be performed after delivering all necessary power supplies to CEA.

In November 2015 the first plasma was produced at the ion source for the proton linac for FAIR at CEA (Figure 2). The photo of the plasma was taken through the LEBT. A glass window from fused silica has been installed behind a temporally diagnostic chamber after the second solenoid.

Figure 2: First plasma production for proton linac.

As a first step of the commissioning an emittance measurement with an Alison scanner just after the extraction system will be done. A Wien filter will be also used for the detection of different ion species (H^+, H_2^+, H_3^+). These measurements will be carried out between the solenoids inside the diagnostic chamber, and before RFQ entrance to feature the beam parameters produced from the proton injector.

It is also planned to measure the space charge compensation in the LEBT with a 4-grid analyzer designed at CEA and modernized at GSI. First tests with this analyzer have been successfully performed at the high current test bench at GSI with high current argon beam. The stability of the ion source including beam fluctuation and pulse-to-pulse repetition will be tested during the long time operation. After delivering all power supplies, cabling connections and operation of the mini control system at CEA/Saclay it is planned to start commissioning of the proton injector in Q4 2016.

References

[1] R. Berezov et. al., “High intensity proton injector for facility of antiproton and ion research”, Rev. Sci. Instrum. 87, 02A705, (2016).

[2] C. Ullmann, R. Berezov et. al., “Status and computer simulations for the front end of the proton injector for FAIR”, in Procceding of IPAC 2014 (Dresden, Germany, 2014).

DOI:10.15120/GR-2016-1

Status of the short superconducting 217 MHz CH-cavity*

M. Basten[#,1], M. Amberg[1,3], K. Aulenbacher[3,4], W. Barth[2,3], M. Busch[1], F. Dziuba[1], V. Gettmann[3], M. Heilmann[2], S. Mickat[2,3], M. Miski-Oglu[3], H. Podlech[1], M. Schwarz[1], S. Yaramyshev[2]

[1]Frankfurt Universtiy, 60438 Frankfurt, Germany; [2]GSI Helmholtzzentrum, 64291 Darmstadt, Germany; [3]Helmholtz-Institut Mainz (HIM), 55099 Mainz, Germany; [4]KPH Mainz University, 55128 Mainz, Germany

Presently cavity 2 and 3 of the advanced cw linac demonstrator at GSI is under construction at Research Instruments (RI). It is the next milestone realizing an new sc heavy ion cw-LINAC at GSI. The first milestone will be the successful beam test of the entire demonstrator. The demonstrator cavity has been successfully rf tested at cryo conditions the University of Frankfurt [1]. The recent design of the sc cw-LINAC comprises the advanced demonstrator as the first cryomodule and several additional cryomodules each with 2 short CH-cavities and 1 solenoid [2,3]. The general design of the advanced demonstrator will be reused for all following cavities. The short cavity consisting of 8 accelerating cells is designed for high power applications. The design gradient is 5 MV/m. Its resonant frequency is the second harmonic of that of the High Charge Injector (HLI) at GSI, Darmstadt. Table 1 shows the main parameters of the short sc 217 MHz CH-cavity. In Figure 1 the layout of this cavity is depicted.

Design of the short CH-Cavity

The design of the cavity is based on 8 equidistant gaps without girders and with stiffening brackets at the front and end cap to reduce pressure sensitivity. Avoiding high fabrication costs and extended fabrication duration the short cavity design is without girders. In a final step the design had to be changed to provide for constant welding depths at the stems. As a consequence the cavity is flattened around the stems. Due to these changes the pressure sensitivity went up from 5 Hz/mbar to 12 Hz/mbar which is still better than the demonstrator cavity.

Parameter	Unit	
β		0.069
Frequency	MHz	215
Accelerating cells		8
Length (βλ-definition)	mm	381.6
Cavity diameter (outer)	mm	408
Cell length	mm	47.7
Aperture diameter	mm	30
Static tuner		3
Dynamic bellow tuner		2
Wall thickness	mm	3-4
Accelerating gradient	MV/m	5
E_p/E_a		5.2
B_p/E_a	mT/(MV/m)	<10
G	Ω	50
R_a/Q_0		1070

Table 1: Specifications of the 217 MHz short CH-cavity

* Work supported by HIM, GSI

#Basten@iap.uni-frankfurt.de

Figure 1: Final design of the sc 217 MHz CH-cavity.

Status

The final design of the 217 MHz short CH-cavity was finished at the beginning of 2015, the construction started end of 2015. Several simulations with CST-Microwave-Studio have been performed to determine parameters as the optimum drift tube length, stem width and cavity diameter [4]. The dynamic tuner design has been revised to reduce the number of gaps and the risk of multipacting. A new design of the dynamic tuners was investigated using CST-Microwave-Studio as well as Ansys Workbench [5]. From this RI started to prepare the technical drawings and necessary informations. The niobium was delivered to RI at Bergisch Gladbach at the end of 2015. The construction phase is scheduled till the end of 2016.

References

[1] F. Dziuba et al., Measurements on the Superconducting 217 MHz CH Cavity during the Manufacturing Phase, SRF 2015, Whistler, Kanada, TUPB075

[2] W. Barth, K. Aulenbacher, F. Dziuba, M. Amberg, V. Gettmann, S. Mickat, H. Podlech, U. Ratzinger, Further R&D for a New Superconducting cw Heavy Ion Linac@GSI, in Proc. of IPAC'14, Dresden, Germany, p. 3211-3213 (2014)

[3] H. Podlech, Proposal for a Superconducting 217 MHz CH-Cavity, institute report: IAP-ACCC-01122013 (2013)

[4] CST Microwave Studio, http://www.cst.com

[5] ANSYS is a registered trademark of SAS IP Inc., www.ansys.com

DOI:10.15120/GR-2016-1

The status of the CRYRING@ESR project*

F. Herfurth[†1], *M. Lestinsky*[1], *Z. Andelkovic*[1], *R. Bär*[1], *A. Bräuning-Demian*[1], *S. Litvinov*[1], *O. Dolinskii*[1], *W. Enders*[1], *M. Engström*[1], *S. Fedotova*[1], *B. Franzke*[1], *W. Geithner*[1], *O. Gorda*[1], *A. Källberg*[2], *N. Kotovskiy*[1], *A. Reiter*[1], *A. Simonsson*[2], *T. Sieber*[1], *J. Sjöholm*[2], *M. Steck*[1], *Th. Stöhlker*[1], *and G. Vorobjev*[1]

[1]GSI, Darmstadt, Germany; [2]MSL, Stockholm University, Stockholm, Sweden

The low energy storage ring LSR [1] will provide highly charged ions and antiprotons at low energy for two collaborations at FAIR, SPARC and FLAIR. Those collaborations intend to perform precision experiments pursuing atomic and nuclear physics questions [3]. The LSR is a Swedish in-kind contribution to the FAIR facility in Darmstadt.

The LSR is the low energy storage ring CRYRING modernized and adapted to the additional needs for injection and ejection of antiprotons and highly charged ions at about 10 MeV/nucleon. CRYRING has been operated at the Manne Siegbahn Laboratory in Stockholm until 2010, was dismantled in 2012 and transported to GSI in the first months of 2013. At GSI it is being installed behind the ESR, as proposed and described in detail in 2012 by a swedish-german working group [2].

CRYRING can decelerate, cool and store heavy, highly charged ions and anti protons injected at about 10 MeV/nucleon down to a few 100 keV/nucleon. It provides a high performance electron cooler and a straight section for flexible experiment installations as for instance a gas jet target. It is equipped with it's own injector and ion source, to allow for standalone commissioning.

After finally completing the planning of all cable routes, the installation of all cables went on over the year and is near completion. All magnets are now connected to their power supplies and the cooling water is connected and running. The infrastructure for the high voltage operation of ion source and electron cooler has been installed and is ready for commissioning. The mechanical installation of vacuum chambers and supports was ongoing. The secure and controlled access to the cave has been installed and all necessary documents, including the online course and test, have been prepared.

One of the major activities in 2015 was to commission the local injector, an ion source for singly charged ions in combination with an RFQ accelerator. The ion source has been characterized extensively and is running with different ion species, as for instance D_2^+, H_2^+, and Ar^+. Most interesting for commissioning is H_2^+, several μA of which have been produced steadily over weeks. Optimal settings for transport towards the RFQ and further have been identified. All beam line elements are now integrated using the FAIR control system. The FAIR General Machine Timing (GMT) is used to chop the continuous beam from the source into 500 μs long portions, well suited for injection into the ring.

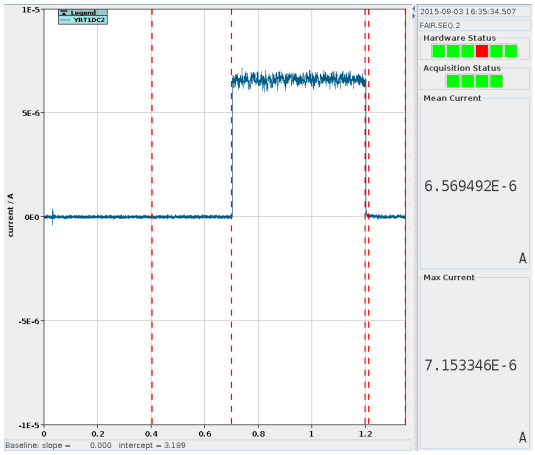

Figure 1: Signal on a Faraday cup - Ion current in amperes versus time in milliseconds. This is a partial screenshot from the application CUPID running to display the Faraday cup signals within the new FAIR control system.

An example result of this implementation is shown in fig. 1. The ion source was running at 20 kV with Argongas. After magnetic analysis it produces 6.5 μA of Ar^+ on average, which are chopped into one 500 μs bunch every second.

The such produced beam was transported and accelerated. The RFQ accelerator was commissioned with H_2^+ ions. About 3 μA have been accelerated and detected with a Faraday cup for intensity measurements and capacitive pickups for bunch analysis. Furthermore, the set of capacitive pickups was used to determine the beam energy measuring the time of flight to about 300 keV/nucleon. The local injector is hence prepared to produce beam for the ring commissioning.

References

[1] H. Danared, et al. (2011) "LSR - Low-energy Storage Ring, Technical design report", MSL, Stockholm University, v 1.3.

[2] M. Lestinsky, et al. (2012) "CRYRING@ESR: A study group report", GSI, Darmstadt,

[3] M. Lestinsky, et al. (2014), "CRYRING@ESR: Present Status and Future Research", Proceedings of the 9th International Conference on Nuclear Physics at Storage Rings (STORI 2014), Sankt Goar, Germany.

* Work supported by GSI/HI Jena/FAIR@GSI PSP code:1.3.4.2./The SPARC collaboration/Uni Krakov/KVI Groningen

† F.Herfurth@gsi.de

DOI:10.15120/GR-2016-1

Development of a topology for the bunch-to-bucket transfer for FAIR *

T. Ferrand[1,3,#], *H. Klingbeil*[1,3], *J. Bai*[1,2], *O. Bachmann*[3]
[1]GSI, Darmstadt, Germany; [2]IAP, Goethe Universität, Frankfurt, Germany;
[3]TEMF, Technische Universität Darmstadt, Darmstadt, Germany.

Introduction

One of the key features of the FAIR project is its so-called bunch-to-bucket beam transfer technology, currently under development.

A bunch-to-bucket transfer between a source and a target synchrotron consists of extracting a bunched beam from the source synchrotron within one revolution and of capturing it at the injection within the target synchrotron. bunch-to-bucket transfers require to synchronize the two synchrotrons' RF systems in order to make the bunches hit precisely the center of their corresponding buckets [1].

Topology for the Bunch-to-Bucket Transfer

In the framework of a bunch-to-bucket transfer, the target synchrotron is set to its injection energy. The beam is accelerated in the source synchrotron until it reaches this target energy (see Fig. 1).

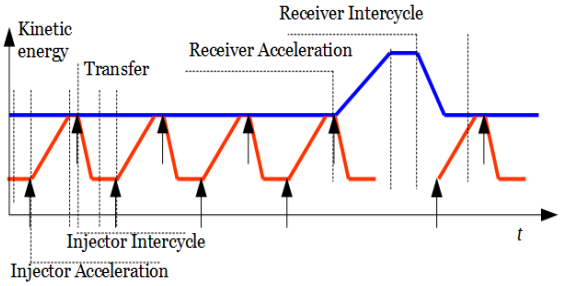

Figure 1: A supercycle (example of the expected bunch-to-bucket transfer strategy between SIS18 and SIS100)

Once the acceleration is complete, the relative phase advance between the reference RF signals of both synchrotrons is evaluated and corrected before the beam is kicked out.

The LLRF topology for FAIR is based on modular and local signal generation using the DDS principle [2]. The campus-wide distributed BuTiS time base enables to synchronize these locally generated signals with a jitter in the picosecond range. Phase advance measurement for RF feedback and control is handled by a DSP system.

Data transfer between the different locations is handled by the General Machine Timing (GMT) system by means of the White Rabbit network [3].

Phase advance measurements between the two RF systems can be performed locally according to a common synchronization reference (SYNC) signal.

In order to synchronize the two RF systems, three additional LLRF functions are required. To perform these specific functions, a new Multi-purpose Hardware Unit (MHU) is being developed at GSI in cooperation with the IES institute at TU Darmstadt [4].

- Phase Advance Prediction (PAP).

The DSP-based phase measurement (see mark 1 in Fig. 2) is performed independently of the BuTiS time base for technological reasons [5]. The phase advance prediction function aims at determining a reference phase advance value at a precise BuTiS time and at forwarding this value to the GMT (see mark 2 in Fig. 2).

- Phase Correction Module (PCM).

This function aims at resynchronizing distributed copies of the target synchrotron reference RF signal of harmonic number 1 (SR, see mark 3 in Fig. 2).

- Phase Shift Module (PSM).

According to the synchronization scenario, the phase advance between the two RF systems may require active control. This function aims at modulating DDS output RF signals adiabatically according to the phase advance measurement (see mark 4 in Fig. 2).

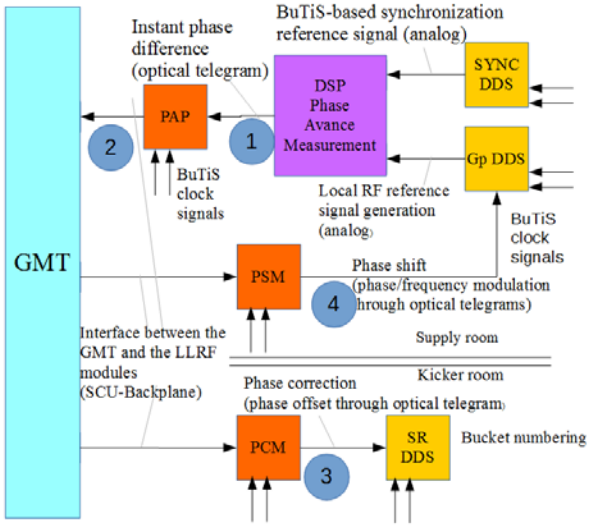

Figure 1: Simplified overview of the bunch-to-bucket transfer system for one synchrotron.

References

[1] T. Ferrand, H. Klingbeil, H Damerau, CERN-ACC-NOTE-2015-0025, 2015.
[2] H. Klingbeil, "Common Specification on LLRF for Ring RF Systems", GSI, 2011.
[3] J. Serrano et al., proceeding ICALEPCS, Kobe, Japan, 2009.
[4] O. Bachmann, D. Lens, T. Ferrand, "Multipurpose Hardware Unit for Deterministic Bunch-to-Bucket Transfer Between Synchrotrons", 2016.
[5] H. Klingbeil, "A Fast DSP-Based Phase-Detector for Closed-Loop RF Control in Synchrotrons", Trans. Instrum. Meas. IEEE 54(3), 2005.

* Work supported GSI

Python code for Schottky analysis in storage ring experiments

M. S. Sanjari[1], *C. Kleffner*[1], *and Yu. A. Litvinov*[1]
[1]GSI Darmstadt

Schottky analysis plays a central role in storage ring physics. Apart from the indespensible role in the diagnosis of beam characteristics, Schottky signals allow a wide range of experiments for nuclear astrophysics ranging from mass to lifetime measurements [1]. In this work we introduce two separate codes developed in 2015 for Schottky data analysis, which can also be used together to provide an even more powerful tool.

iq_suite

iq_suite is a library for accessing recorded offline data which have been obtained using different data acquisition systems. The inphase-quadrature (IQ) data samples is seamlessly provided to the user, regardless of its original file format as a complex array of desired length. While several file formats (such as IQT, TIQ, TCAP, TDMS, WAV and raw) are already covered, the library allows for easy addition of emerging ones. The file interface reads only the portion of needed data into the memory.

The library consists of several helper functions, plotters, frequency analysis methods including multi-taper spectral estimation method and peak finders. These together with the huge body of scientific libraries available for the Python language, provide a powerful means for manual and automatic analysis of Schottky data in storage ring experiments.

A command line interface (CLI) and a multi-platform graphical user interface (GUI) enhance the working experience for quick visual inspections. This code which is available under the terms of GPL v3 license, is regularly updated [2].

barion

barion is a relativistic calculator for the physics of particles in storage rings. It is based on a modular object oriented library for interfacing with the atomic mass evaluation data. The current version of the program uses the AME2012 [3] which is downloaded on user demand. Future versions of AME are automatically considered.

The library consists of several helper functions allowing for calculations such as ionic mass to charge ratio[1] and particle identification in different storage rings. For particle identification, **barion** can be used in conjunction with **iq_suite**.

The platform independent GUI is a convenient tool for the experimental physicist with several handy functions. This code is also available under GPL v3 [4].

[1]References for electron binding energies are available in the source.

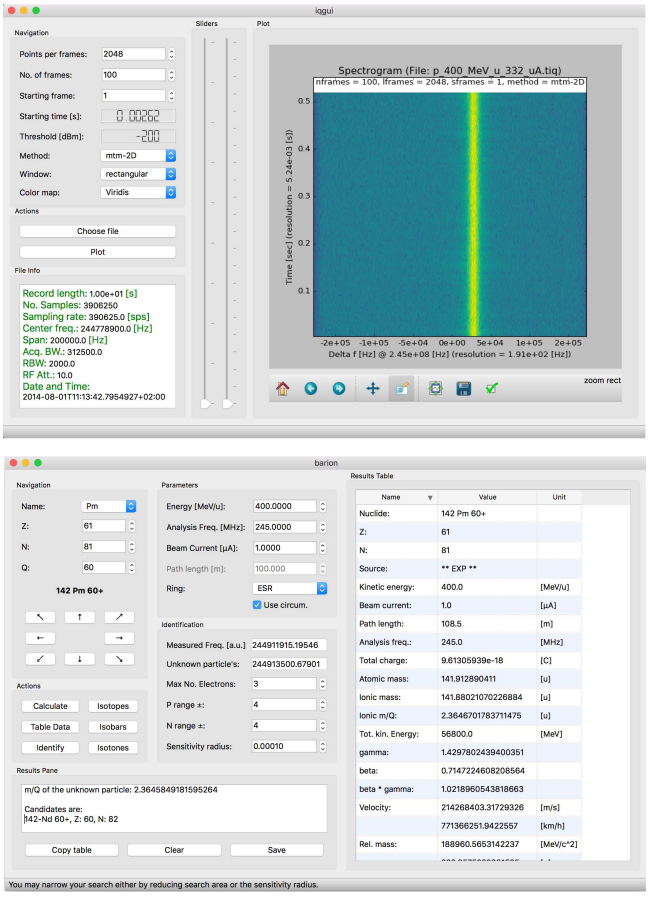

Figure 1: GUIs of iq_suite (top) and barion (bottom)

Acknowledgments

The authors thank C. Brandau, C. Trageser and Ch. Kozhuharov for providing information on the TDMS and TCAP file formats respectively.

References

[1] Yu. A. Litvinov et. al. *Nucl. Instrum. Meth. B* **317** (2013) pp 603–616

[2] **iq_sutie**, https://github.com/xaratustrah/iq_suite

[3] G. Audi et. al. *Chinese Phys C* **36** (2012) pp 1287-1602

[4] **barion**, https://github.com/xaratustrah/barion

DOI:10.15120/GR-2016-1

Analysis of the revolution frequency stability in the ESR during the E82 experiment using resonant the Schottky pickup

M. S. Sanjari[1], *Yu. A. Litvinov*[1], *M. Steck*[1], *and the Two-Body-Weak-Decay collaboration*[1]
[1]GSI Darmstadt

During the experiment E82 in autumn 2014, the two body decay of 142-Pm has been studied. While the main analysis of the data is still in progress, as a secondary analysis, the same data is used to analyze the stability of ESR during this experiment. This works contains a report about this analysis performed in 2015. It is shown that a revolution frequency stability of $\pm 2 \times 10^{-6}$ is achievable.

Experimental setup

A detailed description of the experimental setup can be found in the published account of a previously conducted experiment [1]. Samarium ions are accelerated and fragmented. Among these fragments, hydrogen-like 142 promethium is separated in GSI's in-flight fragment separator FRS. These are then injected every 64 seconds into the ESR with an energy of 400 MeV/u, cooled using stochastic and electron cooling, and finally monitored for their orbital electron capture decay using ESR's resonant Schottky pickup [2, 3], while the data is recorded for offline analysis.

Data analysis

For the analysis a code has been written that uses the **iq_sutie** library [4]. Over 9000 injections where analyzed in the period of October 2 until October 12, 2014. The promethium mother ions were detected automatically. To make sure all cooling effects are taken into account, 15 s into the record, 120 frames of each 1024 samples corresponding to a time interval of about 5 s are taken. A 142-Pm mother ion peak is searched within a neighborhood above a power threshold around a seed frequency which was obtained by manual analysis at the 124^{th} harmonic, where the resonant Schottky is tuned. Then the frequency of the peak is determined, recorded and consequently used as a seed for the next search. The results are depicted in figure 1 (top). Some manually analyzed samples are also shown for comparison.

This figure confirms an entry in the experiment log book, that a small change in the ESR settings have been conducted on the third day after a breakdown. From then on, for the rest of the 10 experiment days the stability of the revolution frequency of the ions circulating in the ESR was about $\pm 2 \times 10^{-6}$ as shown in figure 1 (middle). A spectrum analysis of this portion of data (see figure 1 bottom) shows no significant effects of daily load cycles of the power grid on magnet power supply units and other devices in the ESR.

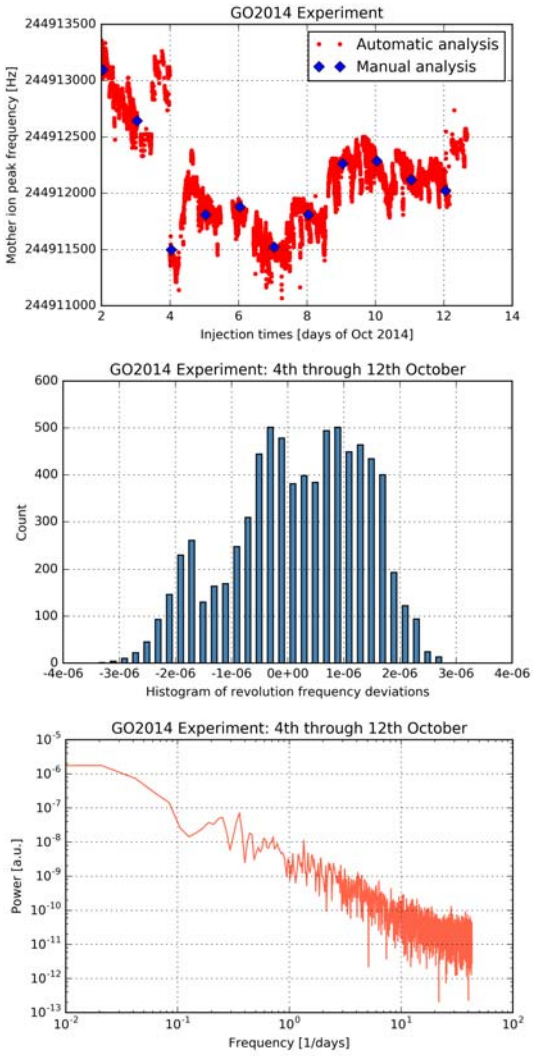

Figure 1: Peak frequencies vs time for all days (top). Revolution frequency deviations over last 8 days (middle). Spectrum of rev. freq. deviations over last 8 days (bottom)

References

[1] P. Kienle et. al. *Phys. Lett. B.* v 726 **4–5** (2013) pp 638–645

[2] F. Nolden et. al. *Nucl. Instrum. Meth. A* **659** (2011) pp 69–77.

[3] M. S. Sanjari *PhD Thesis*, Goethe University, Frankfurt am Main, Germany (2013).

[4] M. S. Sanjari et. al., GSI Scientific report 2015.

DOI:10.15120/GR-2016-1

Proposal for a conceptual design of the HEBT Beam Stoppers ('Diffusors') based on FLUKA/ANSYS studies

S. Damjanovic[1], L. Bozyk[1], F. Hagenbuck[1], B. Merk[1], T. Radon[1],
[1]GSI, Darmstadt, Germany

This report summarizes the conceptual design study for the beam stoppers, which are planned to be installed along the High Energy Beam Transport (HEBT) line system. They will provide redundancy to interlock magnets to ensure safe operation. These mobile blocks will be moved in inactive beamlines. In case of a malfunction, they will intercept unwanted beam, thereby the radiation level in the downstream areas with personnel access remains acceptably low. In order to find the optimal configuration in terms of the absorbed energy, FLUKA simulations have been performed for accidental scenarios for the most critical HEBT diffusors D12, D13 (see Figure 1), D14, D20, D22 and D23 (close to the pbar-target area, the APPA cave, and a number of NE areas). The conclusions on personal safety based on the FLUKA studies can be summarized as follows. An unique size of the diffusors with a minimum length of 40 cm stainless steel would be required to guarantee personal safety in all zones with open access (for details see [1]).

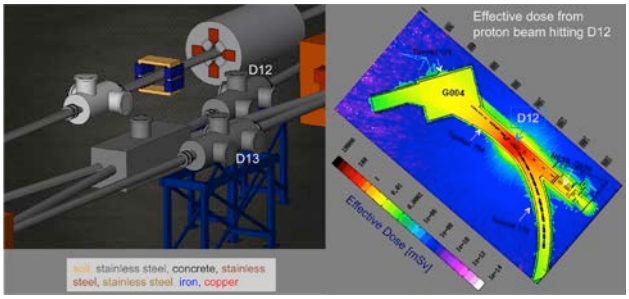

Figure 1: FLUKA geometry of the diffusors D12 and D13; effective dose for a p-beam pulse hitting D12 (right)

Accidental scenarios involving diffusors entail rapid energy deposition which could cause material damage, melting or stress. To ensure mechanical integrity of the beam stoppers, the selected material should work below its maximum service temperature, while general stress should remain within the elastic limit. The risk of material damage due to rapid heating by the beam was investigated

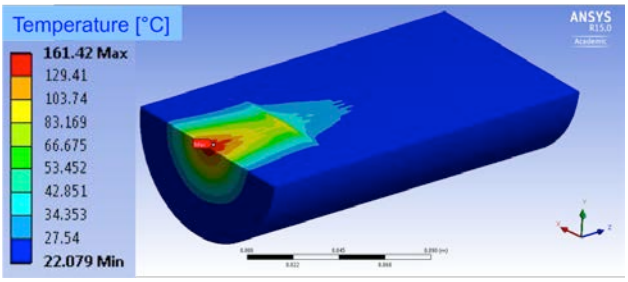

Figure 2: Single pulse T distribution within the diffusor from one pulse (5×10^{11}) of U ions at E_k=2.7 GeV/n.

performing coupled FLUKA/ANSYS simulations. First the thermal load from the beam impact is calculated by FLUKA in terms of energy deposition. This is then used as an input into a thermo-mechanical analysis with ANSYS to calculate single pulse temperatures and thermal stresses. While the proton beam is the worst case scenario when calculating the radiation level in surrounding areas, the material damage risk is larger for ion beams. The resulting single-pulse temperature distribution inside the diffusor for the worst case is shown in Figure 2. The peak temperature of ~160 °C is reached during a 100 ns pulse, which is significantly below the stainless steel melting point. To finalize the material risk analysis, two further quantities, von-Mises stress and equivalent strain had to be analysed in order to evaluate possible material failure due to stress (rapture, yielding and plasticity). Thus a non-linear structural analysis was performed.

A summary of the results for single-pulse temperatures and von-Mises stresses in direct comparison to the corresponding material limits is illustrated in Figure 3. Stainless steel with the standard grades, 316 L (EN 1.4404), is

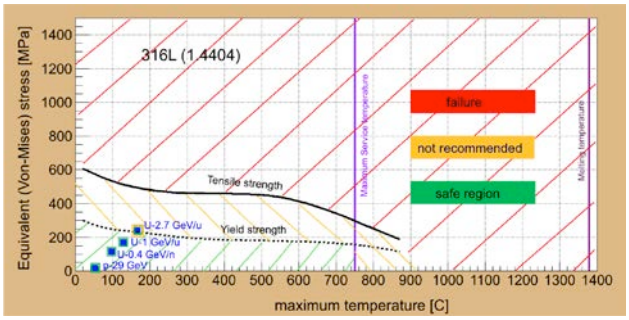

Figure 3: Summary of the single-pulse temperature and thermal stress analysis for proton and U-ion beams.

selected. As visible from this figure, all points are well below the tensile strength limit, thus no rapture will happen. For the worst case, U beam at maximum energy, the border of yielding is reached (the maximum equivalent plastic strain is <0.01%), while for all other beams the values are well below the elastic limit. However, given that diffusors will see at most a few pulses per year, the operation with diffusors made of 316L stainless steel can be considered safe also from the structural point of view. Given a low-cost and a low content of Co, 316L should be a good material choice for the HEBT diffusors.

References

[1] S. Damjanovic et al. EDMS Note: 1541910, FAIR-FTSIX-SR-001

DOI:10.15120/GR-2016-1

Performance of the CALIFA DAQ in the R^{3}B pilot experiment s438b*

M. Winkel†[1] *and the R3B Collaboration*[2]

[1]Technische Universität München (TUM), Germany; [2]GSI, Darmstadt, Germany

In the s438b R^{3}B pilot experiment, the performance of the CALIFA readout was investigated using the quasi-free ^{48}Ca(p,2p)^{47}K reaction in inverse kinematics.

The experimental setup, shown in figure 1, consisted of a series of prototypes of the various R^{3}B detector systems arranged around the ALADIN magnet in cave C. For the CALIFA demonstrator, two so called petals, covering polar angles $25.9° \leq \Theta \leq 66.0°$, were mounted around the target with azimuthal angles $\Delta\varphi = 180°$. Each petal was composed of 64 CsI(Tl) scintillation crystals, read out by large area avalanche photo diodes, arranged in 4 rows (φ) and 8 columns (Θ). For the test case of a (p,2p) reaction, a ^{48}Ca beam with kinetic energy $E = 550$ AMeV and a CH_2 target were used.

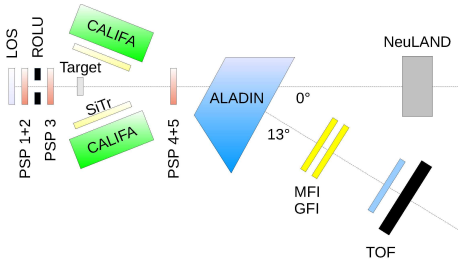

Figure 1: Setup of the s438b experiment.

Substantially, the DAQ as described in [1, 2] was used for the CALIFA demonstrator. A fully digital, real time signal processing was applied to the preamplified signals, using the FEBEX 3B digitizers [3] and a dedicated firmware, developed for CALIFA [4]. One of the firmwares major features is the built in Quick Particle Identification (QPID), allowing to discriminate not only between γ-rays and charged particles down to energies well below $E \lesssim 1$ MeV, but also between protons being stopped in the scintillator material, and high energetic protons punching through the crystals ($E \gtrsim 300$ MeV). This discrimination enables the full energy reconstruction of those protons using the *iPhos* technique [5].

For the common operation of all subsystems, the approach as planned for the NUSTAR DAQ was used for the first time, where all detectors are operated independently, synchronized by White Rabbit time stamps.

The tracking detectors behind the target were used to identify the charge of the ^{47}K residual nucleus, resulting from the one proton removal. With the QPID information events with one proton in each petal were selected. Applying both restrictions, the characteristic polar angle anti correlation gets clearly visible with an opening angle of $\langle\Theta_1 + \Theta_2\rangle = 78.1°$ (see fig. 2).

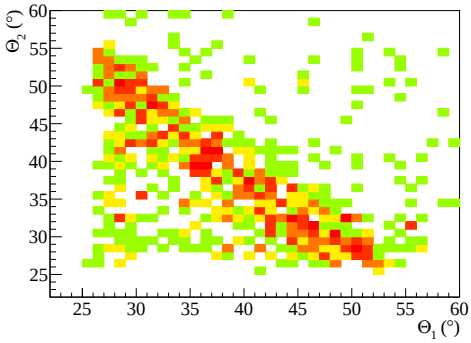

Figure 2: Only using the polar angles of hit crystals in CALIFA, the two emitted protons already show the characteristic anti correlation of the (p,2p) reaction.

Utilizing the 4 momentum conservation, the momentum distribution of the protons inside the ^{48}Ca nucleus can be obtained from the energies and detection angles of the two scattered protons. The distributions correspond to a Fermi momentum of $p_F = (268 \pm 47)\ \frac{\text{MeV}}{c}$, which is in good agreement with the previously published value of $p_F = (248 \pm 5)\ \frac{\text{MeV}}{c}$ [6]. Using the full R^{3}B tracking system, the momentum resolution will improve significantly, but even without, CALIFA can already determine such momentum distributions which can be analyzed in coincidence with the corresponding gamma radiation.

The experiment confirmed the concept for the NUSTAR DAQ and the excellent performance of the CALIFA signal processing under realistic conditions.

References

[1] R3B, TDR of the CALIFA Barrel, 2011

[2] R3B, TDR of the CALIFA Endcap, 2015

[3] J. Hoffmann, “FEBEX3/16, preliminary specification”, 2011

[4] M. Winkel, PhD thesis, Technische Universität München, 2016

[5] M. Bendel *et al*, J. Phys.: Conf. Ser. **587** 12049, 2015. doi:10.1088/1742-6596/587/1/012049

[6] P. Zimmerman, M. Yearian, Z. Physik **A278** 291-293, 1976. doi:10.1007/BF01409181

*Work supported by GSI (TMLFRG1316), BMBF (05P12WOFNF, 05P15WOFNA), Ministerio de Economía y Competitividad (FPA2013-47831-C2) and Xunta de Galicia (GRC 2013-11)

† On behalf of the CALIFA working group - max.winkel@ph.tum.de

TCT characterization of the newest generation of DoI *

E. Berdermann[1], *S. Gsell*[2], *M. Fischer*[2], *M. Kiš*[†1], *M. Mayr*[2], *C.J. Schmidt*[1], *M. Schreck*[2], *and M. Träger*[1]

[1]GSI, Darmstadt, Germany; [2]University of Augsburg, Germany

The ongoing development of the heteroepitaxially grown diamond material at University of Augsburg, also referred to as Diamond on Iridium (DoI), has reached a stage in which the electronic characteristics of samples characterized at GSI are very similar to those of commercial single-crystal diamonds and far superior to polycrystalline diamonds. Within past few years the growth process was optimized so that the charge collection efficiency and the energy resolution of the samples were improved in comparison to last generation of the material reported in previous annual reports [1-2].

The characterization by the transient current technique (TCT) was used consistently to previous measurements, reported in [2], using a low activity Am-241 α-source. The obtained average signals for the sample MFAIX-334 are shown in Fig. 1. In this case the drift of holes is producing

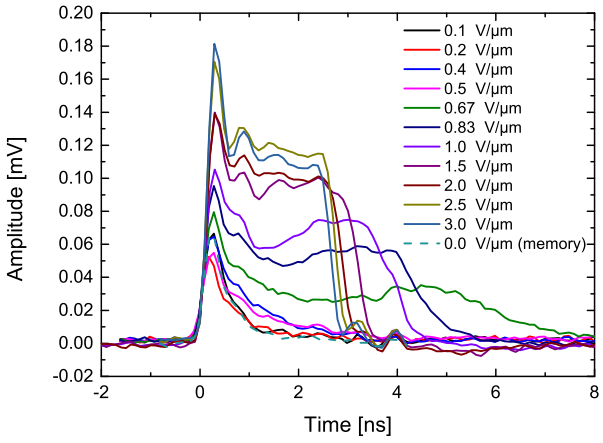

Figure 1: Averaged TCT waveforms for drift of the holes across the 300 μm thick DoI sample for different applied field strengths. The signals are showing great homogeneity of the internal field at higher bias.

almost trapezoidal signals for higher applied drift fields. This encouraging result was obtained only after strong priming of the sample by exposure to an ionizing radiation source. By priming the charge carrier traps/recombination centers are rendered inactive at the price of space-charge buildup that reflects it self in a double-peak structure in the regime of lower drift fields.

Over the years we have seen a continuous improvement in charge collection efficiency (CCE) with current values for the holes above 80%. We attribute this to advancements in material synthesis specifically the reduction in dislocation density. On the other hand electron collection is still typically around 50% which indicates that the dislocations may preferentially cause electron traps.

TCT characterization is a primary tool for accessing basic information on the electronic properties of solid-state sensors, in particular, the charge-transport parameters and the internal electric field profile. However, the ultimate characterization of the homogeneity of the crystal structure is given by the samples energy resolution measured with monoenergetic charged particles using high-resolution charge-sensitive electronics. Fig. 2 shows the α-energy spectrum of a mixed-nuclid source. The CCE for holes

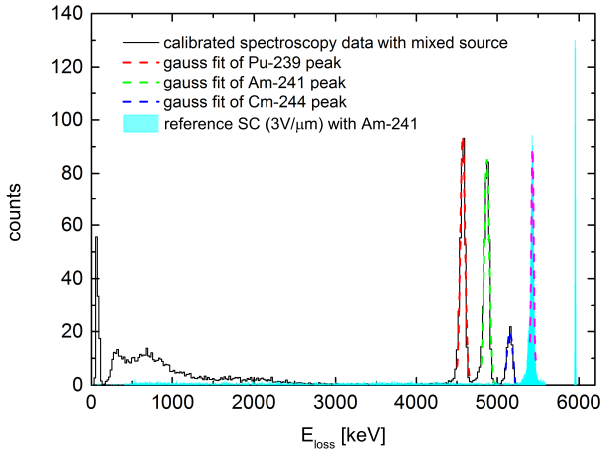

Figure 2: The calibrated spectra for holes extraction obtained by a 3-line mixed alpha-source and charge-sensitive electronics for MFAIX-334. A commercial single crystal diamond detector is shown for reference.

is at the level of 90%, and for electrons (spectrum not show) at 75%. An energy resolution better than 1% for holes and 6.4% for electrons have been obtained, whereas for both charge carriers in homoepitaxial single crystal diamond CCE $>$ 95% and energy resolution dE/E of 0.27% can be achieved. The good energy resolution obtained with holes reflects the good quality and bulk uniformity of the sample. Also the best up to date results obtained with electrons are strongly suggesting that the material development should focus on a further reduction in dislocation density.

References

[1] E. Berdermann et al., GSI Scientific Report 2011, 245, (2012)

[2] E. Berdermann et al., GSI Scientific Report 2013, 342, (2014)

* Work supported in part by EC under the HadronPhysics3 Grant No. 283286

† m.kis@gsi.de

DOI:10.15120/GR-2016-1

Beam-loss criteria for heavy-ion accelerators*

P. Katrík[1 #], D. H. H. Hoffmann[2], E. Mustafin[1], I. Strašík[1], M. Pavlovič[3]
[1]GSI, Darmstadt, Germany; [2]TU Darmstadt, Darmstadt, Germany, [3]FEI STU, Bratislava, Slovakia.

Activation of high-energy heavy-ion accelerators due to beam losses is a serious issue for some accelerator components. Knowledge about accumulated nuclides inside the activated accelerator components is important for their handling, treatment, storage, transportation and final disposal [1].

The beam losses below 1 W/m are considered as tolerable for "hands-on" maintenance on proton machines [2]. In our previous studies, a scaling law has been established to expand the existing proton beam-loss tolerance to heavy-ion beams using the FLUKA 2008 code [3]. Cross-checking of two Monte Carlo code versions was triggered by the release of the FLUKA 2011 with the new feature for nucleus-nucleus interactions calculated below 100 MeV/u [4].

Simulations

A bulky target has been chosen to represent compact structures like magnet yokes or coils. The cylindrical bulky target was 60 cm long and had a diameter of 20 cm. The target material was high-purity (better than 99.9%) copper (density of 8.92 g/cm^3). Irradiation was simulated using a continuous ^{238}U ion beam normalized to the beam power of 1 W during 100 days, and 20 years, respectively. Different beam energies ranging between 25 MeV/u and 1 GeV/u have been chosen. The produced nuclides, their activities and effective dose-rates were scored at several defined time-points: immediately at the end of irradiation, 1 day, 100 days, 1 year and 20 years after the end of irradiation. This paper presents a selection of the obtained data.

Results and Discussion

The new feature in the FLUKA 2011 does show an impact on the induced activity resulting in stricter beam-loss criteria compared to older versions (see Table 1, the 1st and the 2nd column). The simulation shows that there is an accumulation of the long-living nuclides at irradiation lasting 20 years. That is why the beam-loss criteria are even decreasing compared to the ones for 100 days of irradiation (see Table 1, the 3rd column). The scaling law based on proton losses cannot be applied for heavy-ion beams at energies below 150 MeV/u, because one of the main assumptions – the same population of produced nuclides – is not valid anymore below this energy [3]. For the same reason, the effective dose-rate becomes the keystone instead of induced activity (see Table 2).

Table 1: The beam-loss criteria for ^{238}U beams with different energies calculated by previous and recent FLUKA versions at the end of irradiation.

		Beam-loss criteria [W/m]		
	Irradiation time:	100 days	100 days	20 years
Beam energy:	1 GeV/u	5	5	4
	500 MeV/u	12	12	9
	200 MeV/u	60	40	30
	150 MeV/u		52	39
		FLUKA 2008.3.6	FLUKA 2011.2b.5	

The list of the nuclides with dominant contribution to the effective dose-rate from proton and uranium accelerators after 20 years of operation and 20 years of cooling is shown in Table 2. The production of the nuclides depends on the ion species and the beam energy. Comparison within the same beam species shows that pole positions for 1 GeV/u and 200 MeV/u is engaged by target fragments and projectile fragments, respectively.

References

[1] International Atomic Energy Agency, "Classification of Radioactive Waste", Safety Series No. 111-G-1.1(1994).
[2] N. V. Mokhov et al., "Proceedings of the 7th ICFA Mini-workshop on High Intensity High Brightness Hadron Beams", Wisconsin, September 1999, p 51-61
[3] I. Strašík et al., Phys. Rev. ST Accel. Beams 13, (2010) 071004.
[4] P. Katrík et al., "New results on the beam-loss criteria for heavy-ion accelerators", SATIF 12, Batavia, Illinois, USA, June 2015, p. 124

Table 2: Effective dose-rates (EDR) of nuclides produced by proton and uranium beams with different energies after 20 years of irradiation of Cu target followed by 20 years of cooling simulated by FLUKA 2011.2b.5.

Beam:	Effective dose-rates [mSv/h] ^{1}H with E = 1 GeV/u		Effective dose-rates [mSv/h] ^{238}U with E = 1 GeV/u		Effective dose-rates [mSv/h] ^{238}U with E = 200 MeV/u
Sc-44	$1.0\times10^{-10}\pm8\times10^{-13}$	Sc-44	$1.2\times10^{-11}\pm3\times10^{-14}$	Bi-207	$2.0\times10^{-12}\pm5\times10^{-14}$
Ti-44	$5.7\times10^{-11}\pm4\times10^{-13}$	Ti-44	$7.1\times10^{-12}\pm2\times10^{-14}$	Tl-208	$6.1\times10^{-13}\pm2\times10^{-14}$
Co-60	$1.7\times10^{-11}\pm3\times10^{-14}$	Co-60	$3.7\times10^{-12}\pm3\times10^{-15}$	Co-60	$4.9\times10^{-13}\pm1\times10^{-15}$
K-42	$6.6\times10^{-12}\pm3\times10^{-13}$	Bi-207	$3.1\times10^{-12}\pm2\times10^{-14}$	Bi-210	$3.3\times10^{-13}\pm8\times10^{-15}$
Na-22	$5.4\times10^{-12}\pm1\times10^{-13}$	K-42	$1.2\times10^{-12}\pm8\times10^{-15}$	Sc-44	$2.2\times10^{-13}\pm7\times10^{-15}$
Ar-39	$2.3\times10^{-13}\pm1\times10^{-15}$	Tl-208	$7.5\times10^{-13}\pm9\times10^{-15}$	Pm-145	$1.5\times10^{-13}\pm3\times10^{-15}$
Fe-55	$2.6\times10^{-14}\pm4\times10^{-17}$	Na-22	$7.5\times10^{-13}\pm3\times10^{-15}$	K-42	$1.4\times10^{-13}\pm6\times10^{-15}$
Al-26	$1.7\times10^{-14}\pm3\times10^{-16}$	Bi-210	$4.7\times10^{-13}\pm4\times10^{-15}$	Ba-133	$1.4\times10^{-13}\pm3\times10^{-15}$
Ni-59	$4.8\times10^{-15}\pm6\times10^{-18}$	Bi-212	$1.4\times10^{-13}\pm2\times10^{-15}$	Ti-44	$1.3\times10^{-13}\pm4\times10^{-15}$
Mn-54	$3.5\times10^{-15}\pm7\times10^{-18}$	Pb-212	$1.3\times10^{-13}\pm2\times10^{-15}$	Bi-212	$1.1\times10^{-13}\pm3\times10^{-15}$
SUM:	$1.9\times10^{-10}\pm9\times10^{-13}$		$3.0\times10^{-11}\pm4\times10^{-14}$		$4.3\times10^{-12}\pm6\times10^{-14}$

* Work supported by HGS-HIRe.
# p.katrik@gsi.de

DOI:10.15120/GR-2016-1

Progress of the 325 MHz Test Stand at GSI in 2015

A. Schnase, E. Plechov, S. Pütz, J. Salvatore, B. Schlitt, G. Schreiber, W. Vinzenz
GSI, Darmstadt, Germany

In 2015 we continued with the schedule outlined in [1] to prepare the test stand for cavity operation with a 3 MW Thales TH2181 klystron at 325.224 MHz. A key element is a high voltage modulator from CERN Linac 4, which was received as a loan. The modulator was integrated into the existing infrastructure as shown in fig. 1.

Figure 1: CERN modulator in test area

First operation of the klystron was without applying RF; testing the interaction with the HV modulator. As next step, 2.5 MW RF power with 0.2 ms pulses at 2 Hz repetition rate was send to a water-cooled dummy load [2]. The circulator, which was adjusted to operate with 25°C cooling water, was tested with low-level signals, where the effect of cavity sparks was simulated with waveguide parts of specified length terminated with a short circuit plate. The test was carried out in 125 mm steps, which is one 1/12 of the λ=1.5 m wavelength in the waveguide. The circulator passed the low-level tests. Then the klystron was connected to the circulator as for standard operation. The circulator tests with short circuits in 8 specified distances were repeated with forward power up to 2.5 MW. Figure 2 shows an example, where a short circuit plate is placed in 375 mm + 2·125 mm distance.

Figure 2: Circulator output with 375 mm and 2x125 mm distance elements to the short circuit plate

The waveguide directional couplers gave reasonable results for the forward power measurements. Although the cavity can reflect the whole RF power, due to the circulator the reflected power to the klystron should be small. For this purpose the directivity of the directional couplers was not sufficient. Therefore we established a procedure to improve the directivity of the directional couplers [3].

CH cavity tests

During preparation of the RF power source, the infrastructure, e.g. vacuum, water-cooling and tuning elements for the prototype CH cavity in the shielded area was completed in parallel. A critical path is the 6 1/8 inch coaxial line from WR 2300 waveguide to cavity input coupler, which is marked with an orange arrow in fig. 3. Figure 4 shows signals from the CH cavity at 937 kW pulsed forward power behind the circulator.

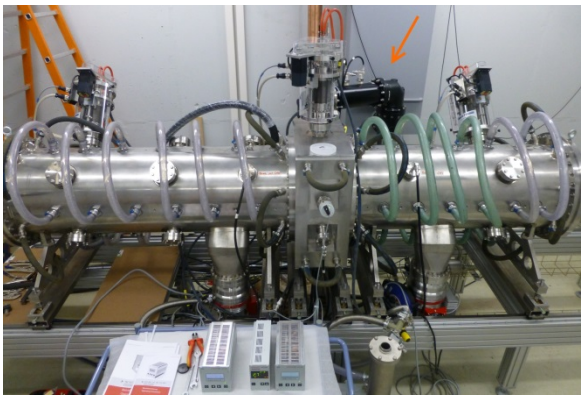

Figure 3: CH cavity connected to RF line (orange arrow)

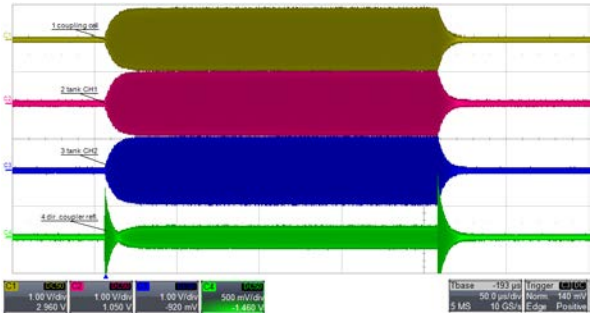

Figure 4: CH cavity signals. Yellow: coupling cell, red: tank CH1, blue: tank CH2, green: reflected power

Acknowledgements

We like to thank M. Vossberg and M. Kaiser for their help in preparing the CH cavity for RF operation.

References

[1] A. Schnase, et. al. “Progress of the klystron and cavity test stand for the FAIR proton linac”, GSI scientific report 2014, p. 441

[2] A. Schnase, et. al. “Progress of the Klystron and Cavity Test Stand for the FAIR Proton Linac”, IPAC2015, Richmond, VA, WEPMA022, pp. 2802

[3] A. Schnase, et. al. “Development of a procedure for directional coupler calibration at the 325 MHz test stand”, this annual report.

DOI:10.15120/GR-2016-1

Development of a procedure for directional coupler calibration at the 325 MHz test stand

A. Schnase, E. Plechov, G. Schreiber
GSI, Darmstadt, Germany

At the 325 MHz test stand, the main task is to send RF pulses from a power source [1] to a cavity while measuring the relation of forward and reflected power. For measurements waveguides WR2300 with directional couplers are used. The figure of merit of a directional coupler is the directivity [2], which is the ratio of isolation and coupling. The company, who provided the directional couplers, adjusted the coupling to the specified -60 dB value, but the isolation was questionable. Thus we had to develop a feasible method to obtain reliable results.

Coupler testing standard method

The standard coupler characterization method is shown in fig. 1. One coupler "FWD" measures the forward wave and a second coupler "REF" measures the reflected wave. Port P_1 of the network analyzer provides a stimulus wave a_1. For an ideal matched load, port P_3 measures the FWD coupling and Port P_2 the REF isolation. In reality, there is some reflection b_1, which is measured as S_{11}. When the roles of matched load and port P_1 are changed, FWD isolation and REF coupling are obtained.

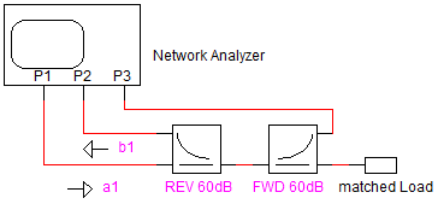

Figure 1: Coupler characterization (FWD coupling, REF isolation)

When this measurement method is applied to waveguide directional couplers, a matched waveguide load is needed. The available water-cooled loads show reflections $|S_{11}| \approx$ -30 dB. This is sufficient as circulator termination to protect the klystron power source, but does not allow measuring a directivity of better than -30 dB. To connect the directional coupler to the network analyzer, a transition from coaxial to waveguide is necessary. Consequently one can use a second transition with a high quality coaxial matched load as substitute for the waveguide load. Such transition can be characterized by a set of S-parameters (S_{11}, S_{12}, S_{21}, S_{22}). Unfortunately the manufacturer only provided S_{11} at the coaxial port. We tried to measure the transfer functions of the 3 available transitions using short circuit plates set in defined distances of 0, 125, 250, ... 750 mm, and noticed that the S-parameters change substantially as function of mechanical balance.

Coupler testing with moveable short

Combining a transition with a movable short, (fig. 2), the measured S_{11} allows calculating the S-parameters of the transition with a simulation model of the setup.

Figure 2: Moveable short (left) combined with transition

A directional coupler together with a λ/4 waveguide is inserted as shown in fig. 3 (left). On the right, an external mounted circuit finally improves the directivity.

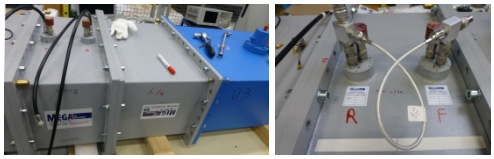

Figure 3: directional coupler + λ/4 waveguide inserted. Right: external circuit improves isolation.

Mechanical forces on the transition influence the S-parameters shown in fig. 4: the results for the transition Ü3 differ, when the directional coupler is reversed.

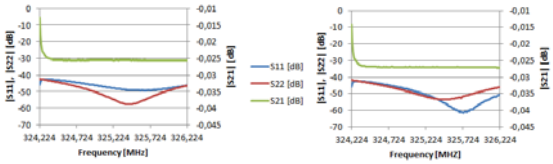

Figure 4: Transition S-Parameters depend on orientation (left: coupler 644 normal position, right: reverse position)

The measured transfer functions S_{21} und S_{31} for different positions of the short at the REF and FWD coupler are fed into a model to obtain the coupling and isolation vectors. The directivity of the REF coupler is improved by an external compensation circuit from -28.8 dB to better than -50 dB (fig. 5), while the FWD directivity is kept near -28.5 dB, which is good enough for its application.

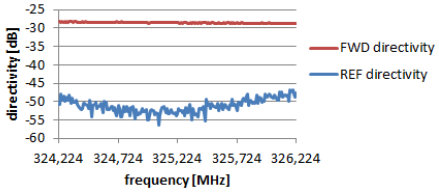

Figure 5: Improved directivity of the REF coupler 644

References

[1] A. Schnase, et. al. "Progress of the Klystron and Cavity Test Stand for the FAIR Proton Linac", IPAC2015, Richmond, VA, WEPMA022, pp. 2802
[2] Bird Technologies "Straight talk about directivity."

DOI:10.15120/GR-2016-1

Recent results on radiation hardness of three-dimensional diamond detectors*

S. Sciortino[†1,2], *S. Lagomarsino*[1,2], *M. Bellini*[3], *V. Cindro*[4], *C. Corsi*[5], *K. Kanxheri*[6,7], *A. Morozzi*[6,7], *D. Passeri*[6,7], *L. Servoli*[7], *E. Berdermann*[8], *M. Kiš*[8], *C. J. Schmidt*[8], *M. Träger*[8], *R. Visinka*[8], *M. Fischer*[9], *S. Gsell*[9], *M. Mayr*[9], *and M. Schreck*[9]

[1]INFN, Florence, Italy; [2]Department of Physics and Astronomy, Florence, Italy; [3]INO-CNR, Florence, Italy; [4]Jožef Stefan Institut, Ljubljana, Slovenia; [5]LENS, Florence, Italy; [6]University of Perugia, Perugia, Italy; [7]INFN, Perugia, Italy; [8]GSI, Darmstadt, Germany; [9]University of Augsburg, Augsburg, Germany

Three-dimensional (3D) diamond detectors are intensively investigated at present as particle sensors and radiation dosimeters due to the appealing properties of the material itself (radiation tolerance, very low leakage currents, tissue-equivalence) combined with the advantages of the 3D architecture (smaller distance between electrodes, low operating voltage bias, well defined active volume). At the same time, recent progress on heteroepitaxial chemical vapour deposition (CVD) of diamond on iridium substrates (DOI) makes interesting a comparison of this new material with the polycrystalline (pCVD) and the homoepitaxially grown, single-crystal material (scCVD) investigated so far. We have previously carried out a research on the performances of 3D diamond sensors fabricated on pCVD and scCVD material purchased from Element Six, together with a study of radiation tolerance of pCVD 3D sensors. More recently we extended our investigation on DOI material synthesized at the Augsburg University. In this report we present preliminary results on radiation hardness of DOI 3D-sensors and compare them to that of the sensors obtained with the standard material.

Materials and methods

We have fabricated 3D diamond sensors on three scCVD[1] and four pCVD square plates [2] from Element Six. The scCVD plates have a 4.5 mm side and a thickness in the range 500-540 μm, the pCVD samples are sized 5×5×0.5 mm^3. 3D sensors were also implemented on a 5×5×0.5 mm^3 DOI sample. Conductive electrodes were grown along the diamond thickness by laser irradiation with an 800 nm Ti:Sa femtosecond laser. The pulse width ranged from 25 to 65 fs. The energy per pulse was of the order of 1 μJ. The beam was focused in the diamond bulk with a 10 × objective. Assuming a gaussian beam, the waist radius was about 2.5 μm and the depth of focus (Rayleigh range) of about 35 μm. The phase transition was initiated by focusing the laser beam at one of the surface and then continued along the bulk by moving the sample parallel to the laser beam at a speed of 20 μm/s. No self-focusing effect was observed. The range of energies employed were not sufficient to start the phase transition in the bulk of scCVD diamond although we suceeded to do so in the pCVD bulk, as a consequence we conclude that the phase transition is assisted by surface defects or grain boundaries. The outcome of the irradiation is strongly dependent on the laser energy and pulse width. Experiments and simulation aimed to get a deeper insight into the physics of laser graphitization are in progress[3]. We also remark that the used beam is only approximatively gaussian. Spherical aberration results into irregular aspect ratio of the column electrodes and resistivity of the modified material as high as 1 Ωcm [4]. By correcting the laser wavefront with adaptive optics, as the laser beam is moved along the diamond bulk, a minimum resistivity of 22 mΩcm has been achieved [5]. This issue seems critical for timing application of 3D detectors, for this reason we are going to implement a controlled optics with a deformable mirror to correct for aberration during the process.

We fabricated 3D sensors of different unit cell (i.e. column density) in each samples. These sensors (about 1.6 × 1.8 mm^2) are formed by two groups of columnar electrodes, the columns of each group starting from one of the surface and ending at about 50 μm from the opposite one, to avoid any possible parasitic surface discharge. The columns were electrically connected at each side by graphitic paths engraved on the diamond surface by irradiation with a ns Nd YAG laser. More details are given in the cited references[1, 2]. The unit cell sizes used are 100 × 160 μm^2 (125 columns/mm^2), 70 × 114 μm^2 (250 columns/mm^2), 50 × 80 μm^2 (500 columns/mm^2). A reference planar (2D) detector was also fabricated in each sample, with the surface structure only. We have planned the neutron irradiations shown in the Table (1-MeV neutron equivalent fluences), and already performed some of them at the Reactor Centre of the Jozef Stefan Institute in Ljubljana. The irradiation still to be carried out are colored in red in the Table.

Charge collection measurements

The charge collection efficiencies (CCE) of the sensors has been simulated and measured before and after irradiation by means of a standard setup with a 1.6 μs shaping time. To attain the maximum charge collection we have to apply a voltage bias such that the velocity of the charge carriers is close to saturation and the charge collected is

*Work supported by INFN GV national experiment 3D_SOD/Collaboration between GSI and University of Florence in the framework of the Detektor Platform of the Helmoltz Centres/AIDA-2020 Project: 3D_Diamond.

† silvio.sciortino@unifi.it

DOI:10.15120/GR-2016-1

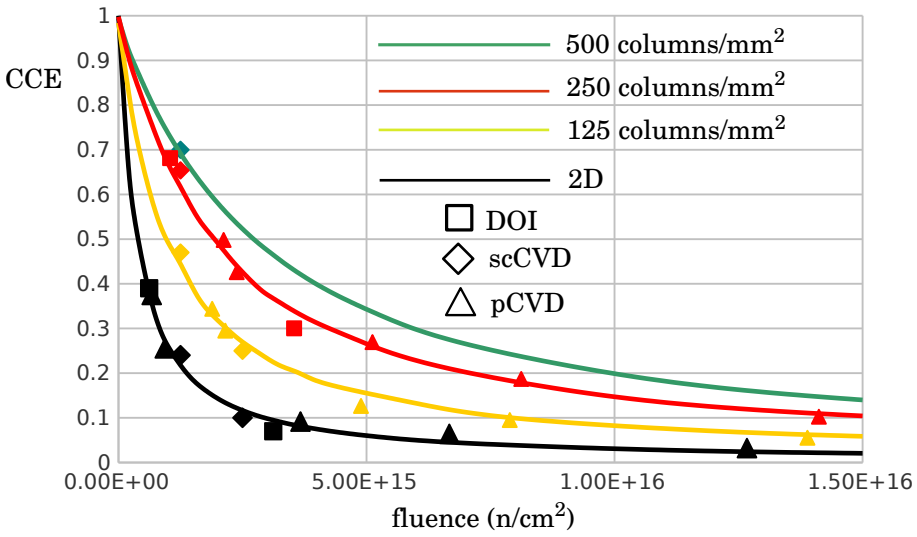

Figure 1:

pCVD	scCVD	DOI
2.64×10^{14}		
	1.25×10^{15}	
3×10^{15}	2.5×10^{15}	2.5×10^{15}
	5×10^{15}	5×10^{15}
6×10^{15}	7.5×10^{15}	7.5×10^{15}
1.2×10^{16}	1.0×10^{16}	1.0×10^{16}

Table 1: Plan of irradiations of the sensors implemented on samples of different CVD material. Fluences are in unit of 1 MeV-equivalent neutrons/cm^2. The irradiation not yet performed are indicated in red.

limited by the lifetime of the generated holes and electrons. The applied bias voltage for the 3D sensors were in the range 10-140 V for the scCVD and DOI samples and 10-80 V in the pCVD case, depending on the irradiation level. At higher voltages, leakage currents as high as tens of nanoampers, quite anomalous for diamond, prevented a reliable measurement. These currents are more pronounced for higher column density, and can be ascribed to grain boundaries (in the pCVD samples) and possible local damage of the lattice surrounding the electrodes. Damage related to the electrodes fabrication is evidenced by the fact that the CCE is less than one (about 0.9) in the unirradiated 3D sensors fabricated in the scCVD samples at 250 and 500 columns/mm^2. This is a defect of the fabrication technology to be addressed in the future and we suggest that it is due to a formation of a defective layer of nanocrystalline diamond surrounding the electrodes, as observed by Raman spectroscopy[4]. In fact a micrometric defective layer in a region where the applied field has the highest value can account for the observed inefficiency. Hence, when discussing the bulk radiation damage, in the next section, we will neglect this surface effect by normalizing the initial CCE of the scCVD samples to 100 %.

3D diamond radiation tolerance

The simulation of the CCE as a function of the irradiation fluence ϕ relies on the basic hypothesis expressed by the following Eq 1

$$\frac{1}{\tau} = \frac{1}{\tau_0} + k\phi \qquad (1)$$

τ is the average lifetime of the carriers and τ_0 is the value before irradiation. In Fig. 1 the simulated CCE curves, for the different column densities, is fitted to the experimental points of the 3D sensors together with the 2D reference sensors. For each sensor, at ϕ=0, a different value of τ_0 is determined, characteristic of the material (pCVD, scCVD, DOI) and dependent on the sample. Then, with a suitable choice of a unique constant k all the other experimental points lies on the correspondent curve

We note that the 3D / 2D gain reaches a factor 5.5 for the 250 columns/mm^2 sensors. With a 500 colums/mm^2 sensor, it could reach a factor 7.

Conclusion and perspectives

We have demonstrated a major improvement of the radiation tolerance of diamond sensors with the implementation of the 3D concept. Moreover we have assessed that the DOI material is well fitted in the same general framework describing the standard material. Further improvements on radiation resistance are expectable with higher column densities, but several factors limits the convenience of the higher densities. First, each column has a cross-section of about 100 μm^2, which limits the detector volume. Moreover, capacity per unit-surface increases with column density, which increases the noise level. Third, run-away currents tend to appear at high voltages, more pronounced with shorter inter-electrode distances. Nevertheless, we can conclude that the performances of diamond sensors, in term of collected charge after strong radiation damage, could

DOI:10.15120/GR-2016-1

be improved by implementation of the 3D concept of at least a factor 3 (our lowest electrodes' density), compared with conventional planar detectors, with limited (< 2 %) loss of active volume and tolerable increase of capacity (2 pf/mm^2).

References

[1] S. Lagomarsino, M. Bellini, C. Corsi, F. Gorelli, G. Parrini, M. Santoro, and S. Sciortino, "Three-dimensional Diamond Detectors: Charge Collection Efficiency of Graphitic Electrodes", Appl. Phys. Lett. 103, (2013) 233507; doi: 10.1063/1.4839555

[2] Stefano Lagomarsino, Marco Bellini, Chiara Corsi, Vladimir Cindro, Keida Kanxheri, Arianna Morozzi, Daniele Passeri, Leonello Servoli, Christian J. Schmidt, and Silvio Sciortino, "Radiation Hardness of Three-dimensional Polycrystalline Diamond Detectors", Appl. Phys. Lett. 106 (2015) 193509; doi: 10.1063/1.4921116GSI

[3] Stefano Lagomarsino and Silvio Sciortino, Boyan Obreshkov, Tzveta Apostolova, Chiara Corsi, Marco Bellini, Eleni Berdermann and Christian J. Schmidt, "Photoionization of Monocrystalline CVD Diamond Irradiated with Ultrashort Intense Laser Pulse", Phys. Rev. B 93 (2016) 085128

[4] S. Lagomarsino, M. Bellini, C. Corsi, S. Fanetti, F. Gorelli, I. Liontos, G. Parrini, M. Santoro, S. Sciortino, "Electrical and Raman-imaging Characterization of Laser-made Electrodes for 3D Diamond Detectors", Diamond Relat. Mater. 43 (2014) 23–28.

[5] Bangshan Sun, Patrick S. Salter, and Martin J. Booth, "High Conductivity Micro-wires in Diamond Following Arbitrary Paths", Appl. Phys. Lett. 105 (2014) 231105

DOI:10.15120/GR-2016-1

Status of the CW-LINAC demonstrator project

M.Miski-Oglu[2], V.Gettmann[2], W.Barth[1, 2], S.Mickat[1, 2], S. Yaramyshev[1], M.Amberg[2], H.Podlech[3], U.Ratzinger[3], F.Dziuba[3], and K. Aulenbacher[2, 4]

[1]GSI, Darmstadt, Germany; [2]HIM, Institute Mainz, Germany; [3]IAP, Frankfurt, Germany; [4]IKP, Mainz, Germany.

CH-cavity

The Demonstrator is the first section of the proposed cw-LINAC [1]. The fabrication of the Demonstrator is still in progress. The complete system is expected to be tested at GSI with beam in 2016.

Meanwhile the CH-cavity[2] is fabricated by Research Instruments (RI) and delivered to "Institut für Angewandte Physik /Goethe Universität Frankfurt am Main. The cavity was tested at operational (liquid Helium) temperature of 4.2K. The test shows that design resonance frequency of 216.816 MHz has been achieved. Figure 1 shows the measured unloaded quality factor Q_0 as function of the accelerating field E_a. The design value of E_a =5.1 MV/m is achieved at a quality factor $Q_0=5\cdot10^8$. After testing the cavity was sent back to RI for the final step in fabrication: the helium jacked has been welded to the cavity and the cavity. The delivery to GSI is expected in June 2016. The unloaded quality factor of the cavity can be further improved by additional high pressure rinsing to be performed at Helmholz Institut in Mainz (HIM). The beam test of full equipped demonstrator at GSI is scheduled for July 2016.

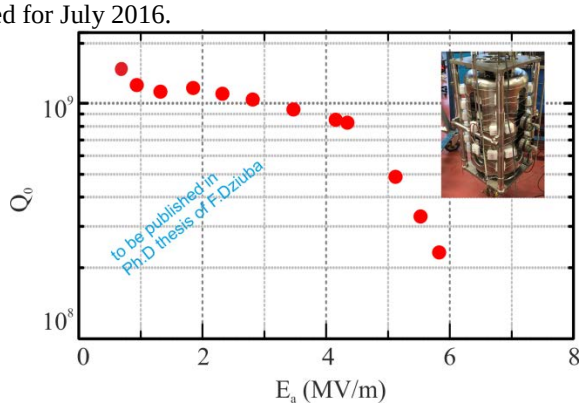

Figure 1: The unloaded quality factor as function of the accelerating field.

Cryostat and setup at GSI-HLI

The liquid helium supply infrastructure at GSI is tested and ready for operation. The cryostat for the demonstrator cavity was fabricated by Cryogenic Ltd. and is alredy delivered to GSI. Figure 2 shows the cryostat in the cw-LINAC bunker during the cold test at GSI (December 2015). The cryostat is loaded with two superconducting (sc) solenoids and a dummy cavity. The sc-solenoids achieved the design magnetic field of 9.3T at 110A excitation current. An additional cw re-buncher cavity is in fabrication and expected to be delivered in April 2016. The control room is arranged and equipped with the 5kW-RF-Amplifier for the CH-cavity and the 12kW-RF-Amplifier for the cw Buncher.

Figure 2: Cryostat inside cw-LINAC bunker at GSI during the cold test

Measurement of transverse emittance at cw-Bunker

During commissioning of the matching line to the cw-Demonstrator (in 2015) the transverse emittance of the Ar^{7+} and $Ar1^{0+}$ beams from the HLI injector was measured. As an example fig.3 shows the beam emittance measured with a slit grid device.

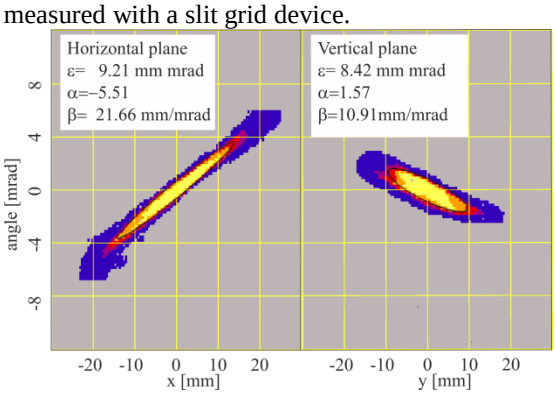

Figure 3: Measured transverse beam emittance of Ar^{10+} ion beam at position of the CH-cavity.

This experimental data are used to simulating beam dynamics of the advanced demonstrator cw-LINAC, containing up to six further CH-cavities. Two of those are already ordered and expected to be delivered in second quarter of 2017. The tendering for the new cryostat, hosting these two cavities, is scheduled for second quarter of 2016

References

[1] V. Gettmann et al. Status of the sc cw-LINAC demonstrator installation, Annual report GSI, Darmstadt, Germany (2014).

[2] F. Dziuba et al. Measurements on the superconducting 217MHz CH cavity during the manufacturing phase, Proceedings of SRF 2015 in Whistler, Canada (2015).

DOI:10.15120/GR-2016-1

FAIR HEBT system - Status report

F. Hagenbuck, L. Bozyk, A. Krämer, B. Merk, C. Mühle, S. Ratschow, B.R. Schlei, P. Spiller, B. Walasek-Höhne, H. Welker, and C. Will

GSI, Darmstadt, Germany

In 2011/2012 almost all HEBT magnets (331/365) needed in the MSV were assigned by FAIR Council resolutions to the Efremov Institute (NIIEFA, St. Petersburg, Russia; batch1-3). Whereas a first contract on the production of 51 dipole magnets (batch1) was closed between FAIR and NIIEFA in July 2013, contract negotiations of batch2 (17 dipole magnets, 95 quadrupole magnets, 80 steering magnets) did fail in April 2015 and NIIEFA announced its decision to withdraw from their offer to provide the magnets of batch2 and batch3 (5 dipole magnets, 71 quadrupole magnets, 12 steering magnets). At short notice the Budker Institute (BINP, Novosibirsk, Russia) declared its readiness to take over the magnets of batch2 and batch3 and after the release of the detailed specifications of batch3 in September 2015, the contract between FAIR and BINP on the magnets of batch2 and batch3 was closed in October 2015.

In December 2015 the factory acceptance test (FAT) of the first pre-series dipole magnet (type dip1s_0, used in 18 Tm beam lines) of batch1 and its corresponding vacuum chamber (vacuum chambers batch1 are built by BINP) were successfully concluded together at NIIEFA (except integration of vacuum chamber into the magnet all tests of the vacuum chamber were performed at BINP). Magnet and vacuum chamber, see Fig. 1 and Fig. 2, were delivered to GSI/FAIR at the end of 2015, where both components have to undergo in the beginning of 2016 the site acceptance test to get finally accepted. The production of the second pre-series dipole magnet of batch1 (magnet type used in 100 Tm beam lines) and of its corresponding vacuum chamber started in 2015. Their FAT shall be concluded together at NIIEFA in June 2016. Furthermore the production of yoke halfs for the series dipole magnets

Figure 1: First pre-series dipole magnet dip1s_0.

Figure 2: First pre-series vacuum chamber for dip1s_0.

for the 18 Tm beam lines and of a third pre-series vacuum chamber (for dipole magnet used in 13 Tm beam line) was started in 2015. The delivery of the last magnet of batch1 to GSI/FAIR is scheduled for September 2018.

In July 2015 the detailed specifications of five power converter types for quadrupole magnets used in the 100 Tm beam lines and the power converter type for the 18 Tm steering magnets were released. Based on these specifications a second contract between FAIR, the indian shareholder Bose Institute (Kolkata) and the provider ECIL (Electronics Corporation of India Limited) comprising in total 118 power converters (74 for quadrupole and 44 for steering magnets) was prepared. In September 2015 the final design review of the power converter type HB.Q2 for the standard 18 Tm quadrupole magnets and in December 2015 of HB.Q10 for 100 Tm quadrupole magnets were concluded successfully. The FAT of the pre-series power converter of both types shall take place in summer 2016. All power converters of type HB.Q2 and the pre-series power converter of type HB.Q10 are part of the first contract with the Bose Institute and ECIL.

In October 2015 the company I-DESIGN (Pune, India) was nominated by the indian shareholder to supply the HEBT beam diagnostics vacuum chambers. The delivery of a prototype chamber is planned for autumn 2016.

For the safety beam plugs in the HEBT system FLUKA as well as coupled FLUKA/ANSYS studies were performed to identify the required dimensions and the best material respectively [1].

References

[1] S. Damjanovic et al., “Proposal for a conceptual design of the HEBT Beam Stoppers (Diffusors) based on FLUKA/ANSYS studies”, GSI Scient. Report 2015

DOI:10.15120/GR-2016-1

Numeric simulations of the GSI bunch shape monitor *†

B. Zwicker[1,2], *P. Forck*[1,2], *O. Kester*[1,2], *and T. Sieber*[1]
[1]GSI, Darmstadt, Germany; [2]IAP, University Frankfurt, Germany

Introduction

Within the FAIR Project a proton LINAC [1] is scheduled as a new injector for SIS18. A non-invasive Bunch Shape Monitor (BSM) is foreseen to determine the longitudinal bunch structure with a phase resolution of 1.0° with respect to the 325 MHz RF. It is intended to ensure proper longitudinal matching of the accelerating structures. The current GSI BSM prototype [2] is based on the creation of secondary electrons from residual gas by the ion beam passage. The secondary electrons are accelerated by an external driving potential towards a time-resolved imaging system [3]. While propagating through the BSM the electrons show a time spread which contributes to the time resolution. Numerical simulations will investigate this contribution.

The Utilization of Secondary Electrons

The GSI BSM prototype is utilizing secondary electrons which are created by beam gas interaction within the Field-Box. By applying a homogenous driving potential up to -31 kV, an electron beam is formed which carries the time structure. The sophisticated electron optical system consists of several adjustable apertures, an Energy Analyzer and an Einzel lens to achieve a high image quality. The electron beam is imaged on a micro channel plate and phosphor screen based assembly which is logged by a low noise CCD Camera for further processing. Hereby, the electron beam is deflected by an RF Deflector working in resonance at 36 MHz in order to transform the time information (relative time of arrival), into a spatial distribution on the detector which finally yields the longitudinal bunch structure.

Due to different electron trajectories and due to the limited energy resolution (electron velocity) the time of arrival at the RF Deflector shows a time spread which will deteriorate the time resolution. The geometric properties of the electron beam and the energy sensitivity of the spectrometer are determined by the apertures, therefore the numerical simulation considers only different aperture settings.

The Electron Time Structure

The AMaze 3D [4] finite-elements software is a modular script based program with an optional user interface to solve static field distributions and track particles in three dimensions. A simplified available 3D model was used as a template for the mesh model, consisting of extensive 57.492.384 cells. For high throughput and efficient calculation a trivial electron distribution is used with $E_{\mathrm{kin}} = 0$ and $\vec{p}_{\mathrm{i}} = 0$.

The time structure of the traveling electrons is read out at the center of the RF Deflector which transforms the time information into a spatial distribution. Hereafter any time structure does not contribute to the time resolution of the BSM. This investigation was executed for three aperture setups to compare the results which are listed in table 1.

Table 1: Results of the particle tracking to the RF Deflector

Aperture [mm]	N	x_{i} [mm]	z_{i} [mm]	Δt_σ [ps]
1.0	18499	± 0.22	± 0.67	± 27.0
0.6	6720	± 0.14	± 0.39	± 16.4
0.2	667	± 0.04	± 0.13	± 5.2

For each aperture setup the amount N of evaluated particles, the maximum initial range x_{i} of the evaluated particles in the aperture x-axis, the maximum initial range z_{i} of the particles in the vertical (also potential) plane, the RMS value of the time of arrival Δt_σ are shown. The average run time of the electrons is about $t_{\mathrm{run}} \approx 5.5$ ns.

For a given, experimentally achieved highest time resolution of 37 ps for the 0.2 mm aperture setting the calculated time deviation of the electrons is $\Delta t_\sigma = 5.2$ ps, therefore it does not significantly contribute to the time resolution.

The results show that the utilization of electrons for high time resolution beam diagnostics is only restricted by the atomic process of the creation of free electrons with $t_\sigma < 6$ ps [5]. This highlights the suitability of the BSM as a non-intercepting device even for extremely high time resolutions of 10 ps as demanded for the FAIR proton LINAC. Also the area of origin of the analyzed electrons with $x_{\mathrm{i}} = \pm 40$ µm (0.2 mm aperture) is comparable to the 100 µm wire diameter of a commercial invasive BSM.

References

[1] L. Groening et al., LINAC'12, Tel-Aviv, THPB034, p. 927
[2] B. Zwicker, doctoral thesis, Frankfurt, 2016
[3] P. Forck et al., DIPAC'05, Lyon, p. 48
[4] Field Precision LLC, Albuquerque, USA, http://www.fieldp.com/
[5] H. Foerster et. al., Journal of Applied Physics, 1955

* Supported by EU-Project CRISP, WP3 T1 Non-intercepting Bunch Shape Monitors
† Supported by Frankfurt Institute for Advanced Science

Optical beam profile measurements using light emission from nitrogen at various pressures *

Y. Shutko[†1], *D. H. H. Hoffmann*[1], *P. Forck*[2,3], *F. Becker*[2], *C. Dorn*[2], *R. Haseitl*[2], *B. Walasek-Höhne*[2], *S. Udrea*[‡3], *T. Dandl*[4], *J. Wieser*[4], *and A. Ulrich*[4]

[1]TU Darmstadt; [2]GSI, Darmstadt; [3]Goethe Universität Frankfurt am Main; [4]TU München

A Beam Induced Fluorescence (BIF) monitor is a diagnostic tool, based on the detection of photons emitted from residual gas excited by the ion beam [1]. To apply this method to the FAIR facilities, the influence of different parameters such as gas pressure, beam energies, etc. has to be investigated. Imaging spectroscopy was performed in a gas cell with a titanium entrance foil at the Munich Tandem van de Graaff accelerator with a continuous 200 nA S^{8+} beam at 3.75 MeV/u. Experiments were performed for nitrogen in a gas pressure range from 0.001 to 30 mbar. A detailed description of the experimental set-up can be found in [2].

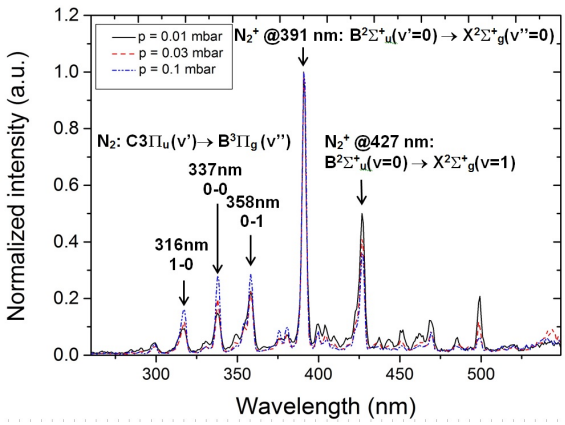

Figure 1: Nitrogen spectra obtained at different gas pressures with labeled dominant molecular transitions.

Nitrogen spectra obtained at different pressures are presented in Fig. 1. Two emission bands were investigated in detail: the 337 nm band corresponding to neutral nitrogen ($C^3\Pi_u(v' = 0) \rightarrow B^3\Pi_g(v'' = 0)$), and the 391 nm band corresponding to ionized nitrogen ($B^2\Sigma_u^+(v' = 0) \rightarrow X^2\Sigma_g^+(v'' = 0)$) [3]. Profiles of the imaged beam based on these transitions are shown in Fig. 2. The imaged beam profile width of the neutral N_2 $C \rightarrow B(0-0)$ transition shows a strong dependence on pressure, while the width of N_2^+ $B \rightarrow X(0-0)$ transition remains almost constant [2]. This behavior can be interpreted by different excitation mechanisms of these two molecular transitions. The 391 nm band, which represents the correct transverse profile of the imaged beam in the entire measurement range, is caused only by collisions of the beam projectiles and gas molecules which lead to ionization of nitrogen and secondary electron emission. These electrons excite N_2 molecules to the electronic state $C^3\Pi_u$ and transition to $B^3\Pi_g$ levels are observed at the 337 nm band. The mean free path of the secondary electrons emitted from the beam path depends on the gas pressure. This fact in combination with larger excitation cross section of secondary electrons for neutral molecules disturbs the measured beam profile, see Fig. 3. A detailed discussion is given in [4].

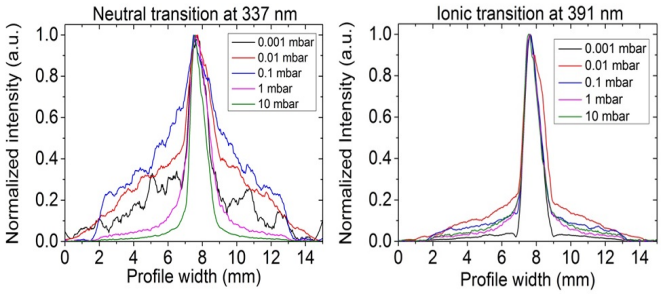

Figure 2: Profiles of the imaged beam measured for different pressures using the neutral (337 nm) and ionic (391 nm) nitrogen emission bands.

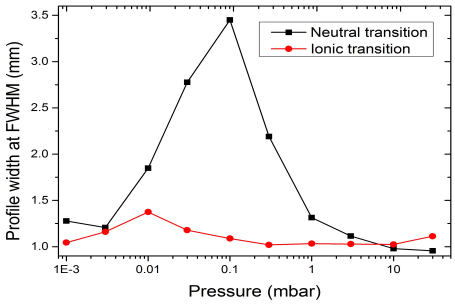

Figure 3: Profile width of the imaged beam, characterized by FWHM, of the neutral (337 nm) and ionic (391 nm) nitrogen emission bands.

References

[1] C. A. Andre, et al.,Proc. of DIPAC2011, p.185.

[2] F. Becker, et al., Proc. of IPAC2012, p. 798.

[3] A. Lofthus and H. Krupenie. J. Phys. Chem. Ref. Data, Vol. 6, No. 1, 1977. p.113.

[4] Y. Shutko, PhD thesis, TU Darmstadt, in preparation.

* Work supported by BMBF project No. 05P12RDRBN and Graduate School of Excellence ESE TU- Darmstadt.

† y.shutko@gsi.de

‡ Work supported by LOEWE-HIC for FAIR

DOI:10.15120/GR-2016-1

Development of an advanced CCC system for FAIR*

F. Kurian[1#,2,3], T. Sieber[1], M. Schwickert[1]
[1]GSI, Darmstadt, Germany; [2]Helmholtz Institute, Jena, Germany; [3]Goethe University Frankfurt, Germany

To satisfy the requirements of online, non-intercepting intensity measurement down to nA range, several units of Cryogenic Current Comparators (CCC) are planned to be installed at various locations in the FAIR facility. After detailed investigations and test measurements on the refurbished CCC system at GSI [1, 2], an advanced CCC unit (FAIR-CCC) is under construction at GSI in collaboration with Friedrich-Schiller University, Jena, Helmholtz Institute, Jena and CERN, Geneva [3]. Details of various components of the cryostat for FAIR-CCC system are reported in this contribution.

Simulations on optimization of the magnetic shield geometry

Given by the extremely low azimuthal magnetic field strength of the beam current to be measured, non-azimuthal magnetic stray fields need to be attenuated. This is realized using a superconducting magnetic shield folded into a meander shaped cavity around the pickup coil. As the geometrical parameters such as the inner and outer diameters and number of meanders define the field attenuation, detailed simulations were performed using the FEM simulation package COMSOL multiphysics™ to determine the influence of these parameters on the field attenuation.

Field attenuation of an external transverse magnetic field was simulated for shields with different dimensions. Major conclusions from the simulations were: 1) the gap width (g, as shown in the figure 1a) between the superconducting meander plates does not influence the attenuation factor; 2) field attenuation reduces as the diameter of the shield is increased as required by the larger beam tube diameter at FAIR as shown in figure 1b.

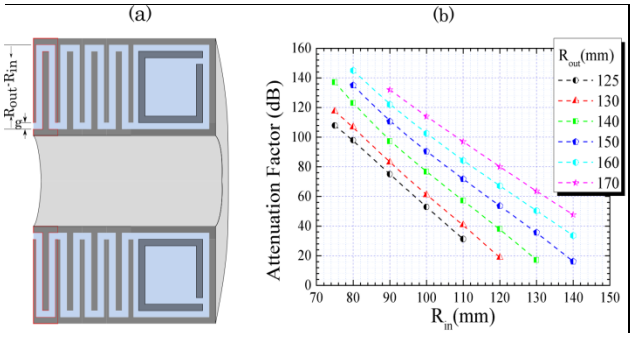

Figure 1: (a) Cross-sectional view of the magnetic shield geometry model. (b) Attenuation factor plotted for various inner and outer diameters of the magnetic shield.

Design criteria of the CCC cryostat for FAIR

The cryostat for FAIR has to fulfill two basic requirements. 1) It has to accommodate a warm UHV beam tube 2) the beam tube must have a diameter of 150 mm. Additionally the cryostat has to provide excellent vibration damping and good access to the CCC components without disassembling the whole structure is required. A design which has been worked out to match these requirements is shown in Figure 2. The isolation vacuum chamber consists of a rectangular stainless steel frame covered with O-ring sealed aluminum windows, which allows direct access to the inner components.

The lower half of the front- and backside is made from steel and has a DN 250-CF contour for mounting of a big connection flange. On this flange the UHV beam tube is fixed from both sides. The beam tube itself is equipped with a ceramic gap and bellows to suppress mirror currents and vibrations.

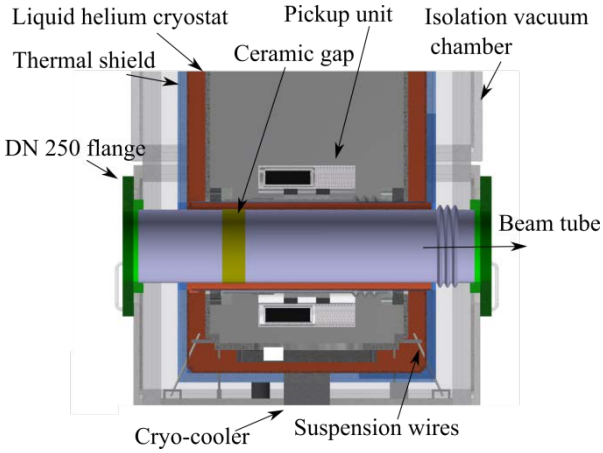

Figure 2: Inner part of the FAIR CCC cryostat.

The stainless steel/aluminum tank houses a thermal shield (copper) covered by MLI, which is at the bottom of the tank connected to a refrigerator. The refrigerator shall provide the cooling down to <50 K to the shield. It is fixed with suspension wires (which also carry the thermal shield) to the top and bottom plates. The basic idea of this design is that shield and container can be lifted upwards from the vacuum tank if the UHV beam tube is removed to the side and suspensions at the bottom are released.
It is foreseen that the FAIR-CCC including the new cryostat will be installed in Cryring for test operation. In this stage helium will be filled manually. Tests with a He reliquefier will take place in a second stage.

References

[1] F. Kurian *et. al.*, "Beam Test with the Cryogenic Current Comparator", GSI Scientific Report 2014
[2] F. Kurian *et. al.*, "Pressure and Temperature Dependence of Cryogenic Current Comparator Measurements", GSI Scientific Report 2014
[3] R. Geithner *et.al.*, Cryogenic current comparator for storage rings and accelerators, Proceedings of IBIC, 2015

* Work supported by Helmholtz Institute, Jena
#f.kurian@gsi.de

Raman investigations of swift heavy ion irradiated alumina*

S. Lederer[†1,2], *P. Forck*[1], *A. Lieberwirth*[1,2], *and W. Ensinger*[2]
[1]GSI, Darmstadt, Germany; [2]Technische Universität Darmstadt, Germany

Polycrystalline α-alumina samples (purity: 99.8 %) were irradiated with ^{63}Cu ions @ 0.5 MeV/u and ^{132}Xe ions @ 4.8 MeV/u with similar particle fluences up to $3 \cdot 10^{12}$ ions/cm^2. After irradiation, Raman measurements were performed with both, the irradiated and pristine material. Analysis of the Raman spectra indicates the amorphization of the alumina samples.

Introduction and Experiments

Scintillating screens are used at accelerator facilities for ion beam diagnostics with very high ion fluxes [1]. However, during irradiation the increasing radiation damage leads to massive degradation of the materials' mechanical performance. Due to its radiation hardness, alumina is an interesting material for scintillation applications [2].
Polycrystalline α-Al_2O_3 samples were irradiated at Helmholtz-Zentrum Dresden-Rossendorf with a beam of 0.5 MeV/u ^{63}Cu ions and at GSI Helmholtzzentrum für Schwerionenforschung with ^{132}Xe ions @ 4.8 MeV/u. Irradiations were performed with similar particle fluences up to $3 \cdot 10^{12}$ ions/cm^2. To evaluate the radiation damage, Raman measurements were performed using a *Horiba LabRAM HR 800* spectrometer at an exciting LASER wavelength of 488 nm.

Results and Discussion

α-alumina crystallizes in space group R$\bar{3}$c and exhibits 18 optical modes. Among these 7 are Raman active ($2A_{1g}$+$5E_g$), 6 are IR active ($2A_{2u}$+$4E_u$) and 5 are neither Raman nor IR active modes ($2A_{1u}$+$3A_{2g}$) [3]. For the pristine material, several Raman modes with peaks at $\sim 380, 418, 432, 450, 578, 648, 752$ cm^{-1} are assigned and compared to Ref. [3].
In the upper part of Figure 1 the Raman spectra of irradiated and pristine material is shown from 300 cm^{-1} to 800 cm^{-1}. The fluorescence background increases with the accumulated particle fluence and is due to the recombination of LASER-excited states.
The lower part of the figure shows an inset of the Raman spectra from 350 cm^{-1} to 450 cm^{-1}. For increasing particle fluence the width of the peaks increases whereas the peak intensity decreases. This behavior can be assigned to amorphization of the material, determined by the break of Al–O bonds. The increasing density of defects leads to a reduced phonon lifetime, giving rise to an increasing peak width [4]. Furthermore the disorder contributes to residual stresses and the Raman peak intensity decreases. The increasing residual stresses also introduce a blue shift of the A_{1g} and E_g modes to higher frequencies. According to Ref. [5] a shift of the Raman modes is due to irradiation induced tensile strain. When the material is damaged the Raman selection rule of $q = 0$ relaxes and the Raman modes are shifted towards higher wavenumbers.

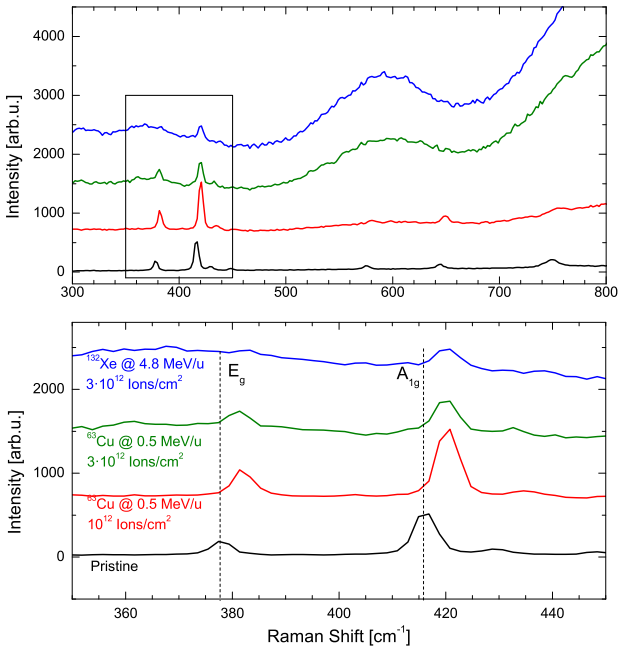

Figure 1: Evolution of Raman spectra of α-Al_2O_3 for different ion species and particle fluences.

The results show, that swift heavy ion irradiation leads to massive creation of radiation damage and influences the screens' mechanical behavior.

Acknowledgements

The authors would like to thank J. von Borany and S. Akhmadaliev from Helmholtz-Zentrum Dresden-Rossendorf for valuable help during beam time.

References

[1] E. Gütlich, P. Forck, B. Walasek-Höhne, and W. Ensinger, IEEE Trans. Nucl. Sci. 59 (2012), 2354-2359.

[2] N. Khalfaoui, J.P. Stoquert, F. Haas, C. Trautmann, A. Meftah, and M. Toulemonde, Nucl. Instrum. Methods B 146 (2012), 247-253.

[3] R. Krishnan, R. Kesavamoorthy, S. Dash, A.K. Tyagi, and B. Raj, Scripta Mater. 48 (2003), 1099-1104.

[4] T. Jawhari, Analusis 28 (2000), 15-21.

[5] X. Wang, Y. Zhang, S. Liu, and Z. Zhao, Nucl. Instrum. Methods B 319 (2014), 55-61.

* Work supported by BMBF, grant no. 05P12RDRBJ.
† S.Lederer@gsi.de

DOI:10.15120/GR-2016-1

Preparation for a profile monitor for an electron lens to be installed at high current synchrotrons

S. Udrea[1,2], *P. Forck*[1,2]
[1]Goethe Universität, Frankfurt, Germany; [2]GSI, Darmstadt, Germany.

Electron lenses (e-lens) [1] have been proposed and used to mitigate several issues related to the beam dynamics in high current synchrotrons. The e-lens systems at the Fermi National Accelerator Laboratory's (FNAL) Tevatron and Brookhaven National Laboratory's (BNL) RHIC accelerator facilities have been successfully applied to reduce bunch-to-bunch differences caused by long range beam-beam interactions and to suppress the tune spread resulting from head-on beam-beam collisions [2,3]. An electron lens system is presently under development with the goal to act as primary collimator for the future high luminosity LHC (HL-LHC). Moreover, at GSI an electron lens system also is proposed and should be applied for space charge compensation in the SIS-18 synchrotron to mitigate beam losses and allow for the high intensities at the future FAIR facility.

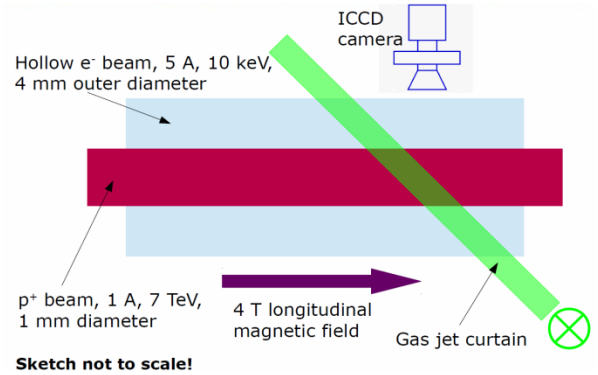

Figure 1: A schematic of the e-lens system planned at CERN for the collimation of the HL-LHC proton beam and the associated transverse beam diagnostics.

For an effective functionality, a very good alignment is necessary between the primary ion beam and the low energy electron beam. This cannot be achieved without suitable beam diagnostics, which can distinguish between the electron and ion beams. For the e-lens at CERN a beam diagnostics setup based on beam induced fluorescence (BIF) [4] has been proposed. For the realisation of this setup a collaboration between CERN, GSI and the Cockroft Institute has been started.

BIF setup for transverse diagnostics

The e-lens system at CERN will be comparable to those used at FNAL and BNL. The main difference will be the use of a hollow electron beam which is supposed for beam halo reduction of the proton beam. The parameters are summarized in Fig. 1: the 1 A, 7 TeV, 1 mm diameter proton beam of the HL-LHC will be embedded in a 5 A, 10 keV hollow electron beam with an outer diameter of about 4 mm. The interaction between the two beams takes place within a 4 T longitudinal magnetic field, which stabilizes the electron beam. The proposed BIF setup is composed of a supersonic gas jet curtain [5] perpendicular to the vertical plane containing the two particle beams and inclined such as to allow for the observation of the fluorescence radiation resulting from the interaction of the electron and proton beams with the gas molecules. To obtain an image of the transverse profiles of the beams an ICCD camera system with suitable optics is intended. The system consists of an image intensifier made of micro channel plates (MCP) in chevron configuration and a CCD camera with appropriate relay optics. The optical system which creates the profile's image is planned to be composed of a focussing achromatic lens and a telephoto lens, to allow for proper magnification and good resolution.

Relevant fluorescence processes

Presently the most appropriate gas to be employed in the supersonic gas jet curtain is nitrogen. The main reasons for this are that it has very good fluorescence efficiency and based on present knowledge it may allow distinguishing between the electron and the proton beam.

Most of the electromagnetic radiation of N_2 molecules excited by protons or electrons results from two excitation processes:

$$N_2 + p/e^- \rightarrow (N_2^+)^* + e^- + p/e^- \rightarrow N_2^+ + \gamma + e^- + p/e^- \quad (1)$$

$$N_2 + e^- \rightarrow (N_2)^* + e^- \rightarrow N_2 + \gamma + e^- \quad (2)$$

The first one leads to emission in a band around 391 nm while the second one in a band around 337 nm. Moreover, the second process cannot be initiated directly by protons because it implies a spin flip mechanism which requires the interaction of identical particles. Thus one expects different photon intensities in the two bands in the regions excited by the proton and ion beams respectively.

Preliminary experiments with an electron beam and a nitrogen supersonic gas jet will be performed at the Cockroft Institute during 2016. The main goal of these investigations is to determine the fluorescence yield and the spectral distribution of the emitted photons.

References

[1] V. Shiltsev et al., Phys. Rev. STAB, **2**, 071001, 1999
[2] A. Valishev et al., Proc. IPAC 2010
[3] W. Fischer et al., Proc. IPAC 2010
[4] C. Andre et al., Proc. DIPAC 2011
[5] V. Tzoganis, and C.P. Welsch, Appl. Phys. Lett., **104**, 204104, 2014

DOI:10.15120/GR-2016-1

Construction, characterization and optimization of a plasma window based on a cascade arc design for FAIR*

B. Bohlender[1], J. Wiechula[1#], Marcus Iberler[1], O. Kester[1,2] and J. Jacoby[1]
[1]Goethe University, Frankfurt, Germany; [2]GSI , Darmstadt, Germany

For many different applications at GSI and for the new FAIR project, it is important and necessary to extract the ion beam from the high vacuum of the accelerator into a gas filled target chamber. In order to prevent the gas inside the chamber from flooding the accelerator section, usually thin metal membranes or differential pumping systems are used. In order to improve these systems, concerning the lifetime and the length respectively, a plasma window, similar to A. Hershcovitch's [1] design, is being built and investigated for the requirements at FAIR. Especially for the transition to the gas stripper system, where the pressure is significantly higher than inside the accelerator section the plasma window would be a benefit as a sealed off system between vacuum and high pressure. In regard to the adaption of a plasma stripper system [2] the plasma window is also thought as an improvement and alternative concept to conventional differential pumping systems. Moreover a plasma window is requested at FAIR because of the high ion beam intensities where a metal membrane as vacuum-atmosphere interface bears the risk of being destroyed.

Experimental setup and working principle

The plasma window mainly consists of a certain number of cathode tips, an anode plate and several free floating electrode plates. Similar systems are well known since the mid-50s as wall-stabilized cascade arc discharges [3]. The plasma arc is initialized between the negative cathode tips and the grounded anode plate. For first investigations, the diameter of the channel between the cathode and the anode is d=2.5 mm, the effective discharge length is about l=63 mm. Stepwise the diameter will be adapted to the requirements of FAIR. The high dissipation of heat is encountered with a water cooling system (fig.1).

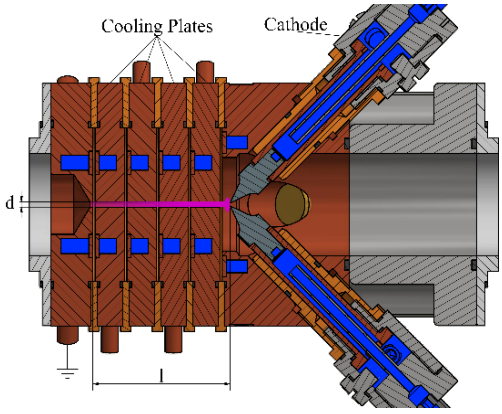

Figure 1: Schematic view of the plasma window.

According to Hershkovitch two main effects are dominant as working principle for a plasma window as a vacuum-atmosphere interface. The main effect is due to pressure equalization between arc discharge and atmosphere. In pressure equilibrium the density is reduced when the temperature is enhanced. To match atmospheric pressure at room temperature, the arc plasma and gas density needs to be a certain factor of the room temperature gas density. This factor is given by the ratio between room temperature in the low pressure part and arc discharge temperature. Therefore, a reduction in the vacuum chamber pressure by this factor is expected. The second effect is due to the fact that the viscosity in a plasma is increased at higher temperatures. Thus, a backflow of the gas from the high pressure cell into the low pressure cell is reduced. In addition the plasma window may act as a plasma lens due the Lorentz force [1].

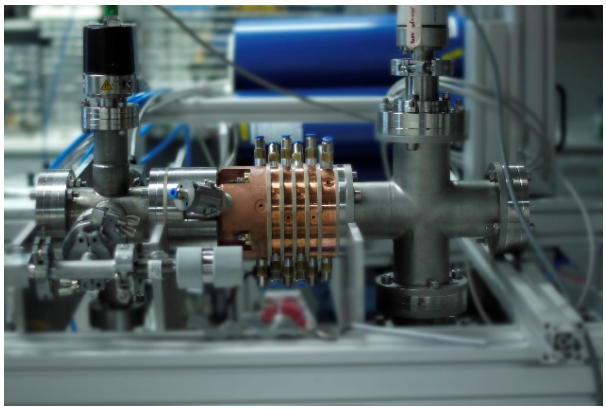

Figure 2: Present status of the plasma window.

Status and outlook

The present setup is shown in fig. 2. First investigations are directed to estimate the breakdown voltage as well as a stable burning voltage as function of the gas pressure. Next tests will include an estimation of the U-I-characteristic, the determination of the pressure gradient as well as an optical analysis for the plasma parameters density and temperature. In addition the influence of the number of cathode tips will be studied. The long term goal is the implementation of the plasma window into an accelerator section at GSI and FAIR.

References

[1] A. Hershcovitch, Journal of Applied Physics 78 (9), 1995.
[2] G. Xu et al., GSI Report 2014-1, p. 290.
[3] H. Maecker, Z. Naturforschg. 11a, 457—459, 1956

* Work supported by BMBF contract No. 05P2015.
# wiechula@physik.uni-frankfurt.de
* This report is also submitted to 'News and Reports from High Energy Density generated by Heavy Ion and Laser Beams 2015'

DOI:10.15120/GR-2016-1

The SIS100 laser cooling facility*

D. Winters[†1], *T. Beck*[2], *G. Birkl*[‡2], *O. Boine-Frankenheim*[‡1,2], *M. Bussmann*[3], *C. Egelkamp*[4], *L. Eidam*[2], *V. Hannen*[4], *D. Kiefer*[2], *Th. Kühl*[1,5], *M. Löser*[3,7], *X. Ma*[§6], *U. Schramm*[‡3,7], *M. Siebold*[3], *Th. Stöhlker*[1,5,8], *Th. Walther*[‡2], *W. Wen*[6], *D. Winzen*[4], *and P. Spiller*[1]

[1]GSI Helmholtzzentrum, Darmstadt, Germany; [2]Technical University Darmstadt, Germany; [3]Helmholtz-Zentrum Dresden-Rossendorf, Germany; [4]Münster University, Germany; [5]Helmholtz Institute Jena, Germany; [6]Institute of Modern Physics-CAS, Lanzhou, China; [7]Technical University Dresden, Germany; [8]Jena University, Germany

The FAIR heavy-ion synchrotron SIS100 will accelerate intense beams of relativistic highly charged ions [1]. However, at these extreme velocities ($\gamma \approx 12$), established ion beam cooling techniques, such as electron and/or stochastic cooling, are difficult and expensive to implement. Laser cooling of bunched ion beams was then considered to be a valid, interesting, and effordable alternative for the SIS100 [2, 3]. Therefore, within POFIII ARD 'Matter and Technologies', the project group 'SIS100 laser cooling' was formed to specifiy, design, order, construct, set up, and test the *SIS100 laser cooling facility* for FAIR. The project group consists of scientists from GSI and the collaborating partner universities and research centers in Dresden-Rossendorf, Darmstadt, Jena, Münster, and Lanzhou (China).

The laser systems will be developed by the Helmholtz-Zentrum Dresden-Rossendorf (HZDR) / TU-Dresden, and by the TU-Darmstadt, with strong support from the BMBF. These laser systems can be operated at 257 nm or 514 nm, and produce about 100 mW of coherent radiation. The TU-Darmstadt has already built a fast scanning cw-laser system [4]. Within the new BMBF funding period, a pulsed laser system for long (up to 1 ns) pulses and with a very high repetition rate (up to 1,5 MHz) will be developed [5]. The HZDR has also developed a pulsed laser system with a repetition rate up to 1 MHz, but for short pulses ($\sim$ps) [6]. Within the new BMBF funding period, they will try to improve the pulses and increase the power. By combining these laser systems, strong cooling power over a broad spectral range can be obtained. Also, the spectral shape of the combined laser light can be tailored for optimal cooling rate or range. The group in Münster will conduct a study for xuv/x-ray detectors for the SIS100, again supported by BMBF. Due to the high velocities in the SIS100, relativistic effects strongly influence the fluorescence and dedicated *in vacuo* detection, surrounding the ion beam, is required.

From the 2015 ARD money, we (GSI) were able to purchase important infrastructure for the laser lab at the SIS100, *i.e.* two sophisticated damped optical tables for the laser systems (Newport), two portable digital oscilloscopes (Tektronix), a fast (15 GHz, 100 GS/s) 4-channel oscilloscope (Tektronix), a laser beam profile camera (Ophir Spiricon), laser power and intensity detectors with readout instruments (Gentec), and a complete laser beam stabilization system (TEM Messtechnik). See figure 1.

Figure 1: Collage showing a selection of the required infrastructure we could purchase in 2015. Top left, damped optical table. Top right, fast (15 GHz, 100 GS/s) 4-channel oscilloscope. Bottom, laser beam stabilization system.

In 2016, two test beamtimes for laser cooling are planned: one at the CSRe of the IMP in Lanzhou, China, and one at the ESR in Darmstadt. At the CSRe, the pulsed laser system from HZDR will be used. At the ESR, this system will also be used but in combination with the cw-laser system from the TU-Darmstadt. In addition, the new xuv-detector system from Münster University will be employed for the first time [7]. The project group will finish the designs for the scrapers and the laser/fluorescence sections in the SIS100.

References

[1] P. Spiller *et al.*, Proceedings of IPAC 2015, Richmond, USA, **THPF015** (2015) 3715.

[2] M. Bussmann *et al.*, ICFA Beam Dynamics Newsletter **65** (2014) 8.

[3] D. Winters *et al.*, GSI scientific report 2014, **FG-SIS100-04** (2015) 473.

[4] T. Beck *et al.*, GSI scientific report 2012, **PNI-IONS-EXP-06** (2012) 314.

[5] D. Kiefer *et al.*, GSI scientific report 2015.

[6] M. Siebold *et al.*, Opt. Expr. **20** (2012) 21992.

[7] C. Egelkamp *et al.*, GSI scientific report 2015.

* Work supported by HGF POFIII ARD-ST2.

† d.winters@gsi.de

‡ Work supported by BMBF.

§ Work supported by BMBF-WTZ.

Gas dynamics simulations for heavy ion induced desorption measurements with the single shot method *

Ch. Maurer[†1,2], *L. Bozyk*[1], *P. Spiller*[1], *and D.H.H. Hoffmann*[2]
[1]GSI, Darmstadt, Germany; [2]TU Darmstadt, Institut für Kernphysik, Germany

Introduction

Beam induced gas desorption is a key process that drives beam intensity limiting ionization losses in heavy ion synchrotrons in general and in the upcoming SIS100 in particular. Measuring the beam impact induced desorption yield of (cryogenic) collimator materials behind from a synchrotron presents a challenge in itself, since the well established continuous bombardment method [1] cannot be used. Instead, a technique suitable for repetition rates in the mHz-regime is needed. The key task is to find a way to compute the number of desorbed particles from the measured pressure pulse. The gas dynamics simulations presented here are used to gain a better understanding of the influence of adsorption/redesorption processes, the experiment's geometry and temperature on the shape of the pressure pulse and to improve the accuracy of the data analysis.

Current Method

An important component of a typical single shot desorption experiment is its diagnostic volume V, which also contains the target. Gas desorbed from the target after beam impact disperses in this region, giving rise to a characteristic pressure pulse, called "desorption peak". Using the ideal gas law, the number ob desorbed particles ΔN is then calculated as

$$\Delta N = \frac{\Delta p V}{k_B T}, \qquad (1)$$

where Δp is the desorption peak's height and T is the gas temperature. This method assumes a uniform gas temperature and the coincidence of the desorption peak's maximum with a homogenous distribution of all desorbed gas in the diagnostic volume. Furthermore, this spreading is supposed to take place on a faster timescale than pumping, so that gas escaping from V before a homogenuous distribution is reached can be neglected. Comparing measurements with different geometries [2, 3] shows significant deviations in the time structure of the desorption peak. Therefore, a deeper understanding of the dynamics involved is needed to facilitate a more accurate analysis.

Gas Dynamic Simulations

A gas dynamic simulation code, such as Molflow+, provides a means to model the desorption peak's formation [4]. It tracks gas particles in a given geometry and can compute pressure profiles from the results. The latest version is capable to simulate time dependent pressure evolutions with regard to adjustable sojourn times t between adsorption on and redesorption from the chamber walls. First simulations show the influence of sojourn times on the peak height (Fig. 1), pointing out the need for an improved analysis.

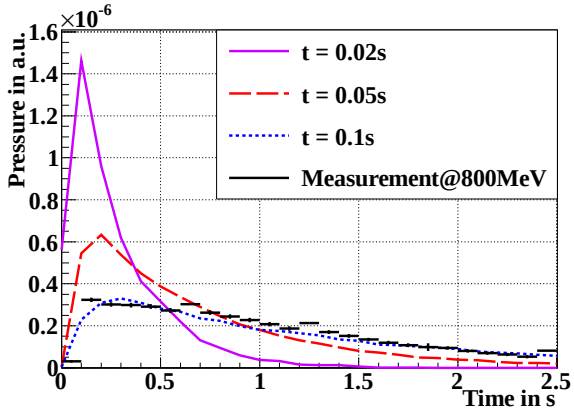

Figure 1: A Measurement and simulated desorption peaks with different sojourn times t for the geometry in [2].

Outlook

Gas dynamics simulation with Molflow+ promise a significant gain in accuracy for high energy desorption measurements. Improving future desorption experiments as well as reevaluation of already existing data will boost our understanding of the desorption process, improve the prediction by simulations, and might to better solutions regarding beam loss due to dynamic vacuum effects.

References

[1] D. P. Holzer et al., "Heavy-ion-induced desorption yields of cryogenic surfaces bombarded with 1.4 MeV/u xenon ions", in PhysRefSTAB **16**, p. 083201 (2013)

[2] L. Bozyk, H. Kollmus, P.J. Spiller, "Development of a Cryocatcher-System for SIS100", in Proc. of IPAC 2012, p. 3239

[3] Ch. Maurer et al., "Heavy Ion Induced Desorption Measurements on Cryogenic Targets," in Proc. of IPAC 2014, p. 867

[4] M. Ady, R. Kersevan "Introduction to the Latest Version of the Test-particle Monte Carlo Code Molflow+" in Proc. of IPAC 2014, p.2348

* This report is also submitted to "News and Reports from High Energy Density generated by Heavy Ion and Laser Beams 2015"

† C.Maurer@gsi.de

DOI:10.15120/GR-2016-1

Status and design of the normal conducting magnets for SIS100

P. Rottländer[*1], *U. Kopf*[2], *H. Leibrock*[1], *J. Macavei*[1], *C. Mühle*[1], *and A. Kalimov*[3]
[1]GSI, Darmstadt, Germany; [2]PROCAD GmbH, Kleinheubach, Germany; [3]St.Petersburg State Polytechnic University, St. Petersburg, Russia

Most of the SIS100 magnets are superconducting; however, there are some magnets which had to be constructed with normal conducting coils. Six Resonance Sextupoles will be installed in close vicinity to other components that are operated at room temperature. A suitable manufacturer has been found for the same during 2015 and the mechanical design has been finished (Fig. 1). The first magnet is expected to be delivered in May 2016.

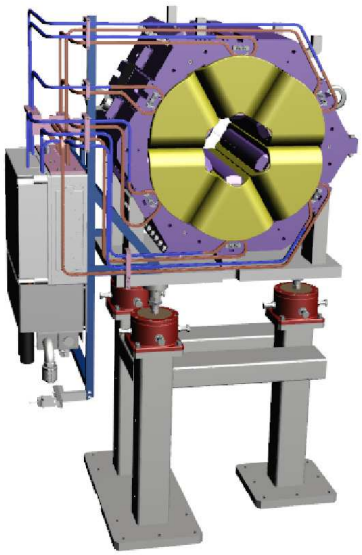

Figure 1: Final 3D design of the Resonance Sextupole.

The rapidly ramped γ_t Jump Quadrupole is mounted to superconducting main quadrupoles and is therefore the only normal conducting magnet which will be operated at cryogenic temperatures. The magnetic and mechanical design has been completed and the Detailed Specification has been finished. Details can be found in [1].

Simulations indicate that the radiation level in the extraction line will be too high for safe operation of the superconducting magnets. Therefore, it was decided to build normal conducting quadrupoles matching the main superconducting ones. Originally, it was planned to devise an opening mechanism, allowing to mount heating jackets for baking the vacuum chamber. It was found that the mechanism would collide with the enlarged bypass line. Thus, the aperture has been enlarged to allow for a permanently installed heating jacket. Now the design is at its physical limit: Any further enlargement would result in a decrease of quadrupole strength and/or field homogeneity. Mechanical pre-design will start soon.

Magnetic septa are placed close to branching points of beam lines when it is necessary to operate both beam lines simultaneously. Therefore, they have to provide a homogeneous field for one beam and an almost field-free region for the other in close vicinity. There were some old magnetic designs for the septa, but during a visit at CERN it became clear that some fundamental design limits were not met, thus reducing safety and lifetime of the septa.

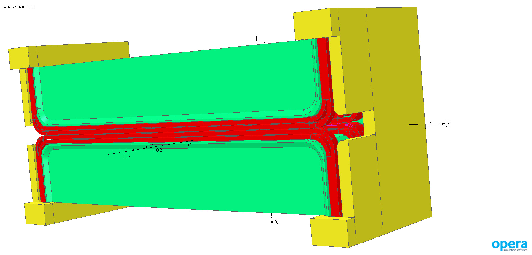

Figure 2: Injection septum 1 seen from the orbit. The screen has been hidden.

For both septa, solutions have been found which are great improvements over the first studies. The pole faces as mirrors and spacers between the coil turns virtually create a long coil. This results in an acceptable field homogeneity. Fringe field effects were corrected with suitable bending radii at the coil ends. (Fig. 2)

A screen plate between coil and orbit as well as shielding boxes around the magnet ends suppress stray field in the orbit region. In order to suppress sextupole effects, the first injection septum will be curved. Instead of two parallel hollow conductors in the backleg of the coil, there will be only one with a hard-soldered, solid wire in parallel. In this way, several soldered joints can be avoided which otherwise would pose risks of water leaks.

Pre-construction has been finished and a call for competition has been carried out. It is expected that a manufacturer will be found in the second quarter of 2016.

References

[1] H. Leibrock et al. “Fast ramped Quadrupoles for the Transition Jump Scheme of the SIS100 Synchrotron of the FAIR Project”,*IEEE Trans. on Appl. Superconduct.*, Volume: 26 Issue: 4, June 2016.

* p.rottlaender@gsi.de

DOI:10.15120/GR-2016-1

Photogrammetric deformation analysis during welding test on the SIS100 dipole yoke mock-up

A. Junge[1], I. Pschorn[1], V. Velonas[1],T. Miertsch[1], K. Knappmeier[1], J. Holluba[2], M. Rosan[3]
GSI, Darmstadt, Germany.

A special welding process developed by the Technology Laboratory (ENTL) department and performed at GSI has been tested on the SIS100 dipole yoke mock-up. The aim of the welding process was to keep the deformations and movements of the yoke, which were caused by the process itself, as small as possible. Each different step of the yoke welding sequence should be monitored by high precision geometric measurements. All measurements were carried out by the department NC Magnets & Alignment (ENMA) with contactless optical measurement methods of photogrammetry. During the process week, it was of big importance to monitor and lead the whole welding process by a series of intermediate measurements.

Figure 1: Photogrammetric measurement system AICON-DPA Pro [1]

A photogrammetric measurement system (Figure 1), which includes hardware (reflex camera [SLR] with a purpose-built high precision lens) as well as special software for photogrammetric processing, can support a highly precise detection of a wide variety of signalized measurement points in a very short time. Thereby, the measurement system is predestined for metrological support of scientific studies (e.g. welding experiments / material tests) and their analysis at different time periods.

The typical accuracy of this kind of photogrammetric measurement system, in a measurement volume of 1m², is about 20µm.

It has to be pointed out that, as a starting reference measurement 600 marks were attached on the component (Figure 2). Afterwards, the positions of these marks were detected and calculated in the three dimensional space by a photogrammetric system. These measurement marks constitute the reference for the whole welding test and were not modified during that time. Thus, it was possible to determined and analyze the components deformation and movements in different epochs. After each change of state, about 160 images were taken. The measurement time was approximately 15 minutes.

For the deformation analysis during the welding process all further measurements were compared to the first (reference) measurement.

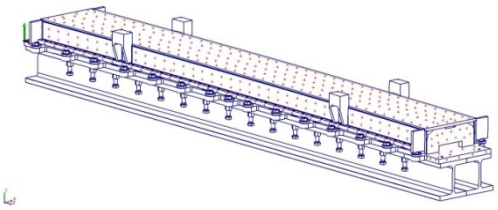

Figure 2: SIS100 dipole yoke mock-up with added marks on the welding apparatus

In order to have a closer look of the error vectors, they can be magnified in the software. The directions of the vectors represent the differences between the nominal and the actual points. The vectors direction gives us the opportunity to check whether the component has been deformed or not (Figure 3). Consider the length and color of the vector, the magnitude of the amount of the error can be estimated.

The maximum 3D deformation after the welding process is compared to the reference measurement, which is in our case 0.93mm. The measurement uncertainty was about 50µm in the whole measurement volume of 3.3m x 1.2m x 1.0m.

Supported by the Survey & Alignment Group the welding process has been optimized in order to minimize the welding distortion. The test showed, that in compliance with a dedicated welding procedure it is possible to weld a dipole yoke with final deformation of less than 1mm.[2]

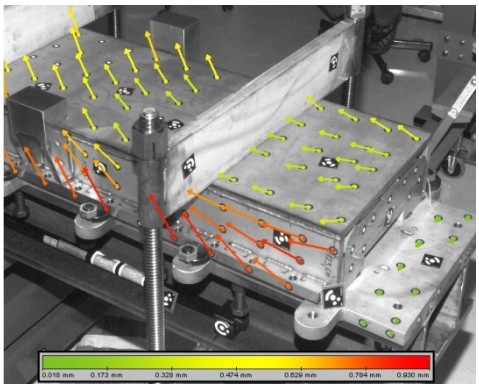

Figure 3: Deformations - error vectors (range from 0.018 mm (green) to 0.930 mm (red))

References

[1] AICON 3D Systems, http://www.aicon3d.de
[2] A. Junge „Schweißversuch MockUp Dipol SIS100“

[1] alignment@gsi.de
[2] j.holluba@gsi.de; [3] m.rosan@gsi.de

DOI:10.15120/GR-2016-1

First steps of the development of a simplified FEM model for an arc section of SIS100 synchrotron: justification and first approaches*

J. Ceballos Velasco† [1,2], *M.C. Serna Moreno*[2], *V. Datskov*[1], *E. Fischer*[1], *and PBMT department*[1]
[1]GSI, Darmstadt, Germany; [2]University of Castilla-La Mancha, Ciudad Real, Spain

Introduction and Motivation

The hitherto FEM calculations performed for the superconducting (SC) modules, the Dipole Module (DPM) and the Quadrupole Doublet Modules (QDM), to be installed in SIS100 have been done taking into account only individual modules. The interaction between adjacent modules via various interfaces has not been considered yet in the simulations carried out for the design of the modules.

By the assembly of the different modules, the individual structural conditions such as the length and position of the cryogenic piping, the diameter of the vacuum vessels, or the weight of the cold masses in combination with their positioning given by the separation distance and interconnection angles leads to additional forces (see Fig. 1) to be taken into account in a full study.

These interplay reactions must be studied in order to guarantee the functionality of the synchrotron in terms of the displacement of the cold masses and the vacuum vessels, where the positioning precision is defined in Table 1 [1, 2].

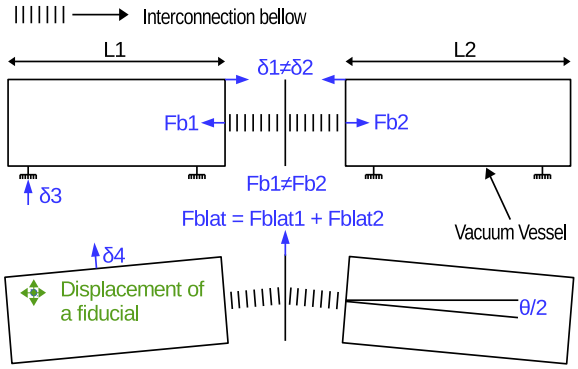

Figure 1: Scheme of the interaction between two consecutive SC modules during operation. Additional forces may appear in reality. The displacement of a fiducials due to the external forces on the components is described; it must guarantee the criteria established in Table 1 .

FEM Models: State of the art and new proposal

With the full definition of the geometry, mechanical contacts, and non-linear material response, current FEM models are able to describe the behavior of SC modules in detail. However, the more the complexity of these models increases the more the time consumption for evaluation grows. Moreover, the control of the calculation process by the user might be restricted due to the non-linearity. Thus, by the development of a simplified FEM model to describe the physical properties of all modules under investigation the time consumption of the analysis of the SIS100 structure can be reduced, and a high control of the all features of the simulation can be ensured. Some proposed simplifications are listed below.

Table 1: Specified stability criteria for SC modules' components: vacuum vessel, Dipole (DP), main Quadrupoles (QP) and Corrector Magnets (CM).

DPM	Vacuum Vessel		$\pm 50\ \mu m$
	DP vertex point	Linear pos.	$\pm 50\ \mu m$
		X-rotation (lat.)	$\pm 50\ \mu rad$
		Y-rotation (long.)	$\pm 50\ \mu rad$
QDM	Vacuum Vessel		$\pm 50\ \mu m$
	Main QPs		$\pm 125\ \mu m$
	CM		$\pm 175\ \mu m$

- Selection of the proper elements for each case and physical phenomenon.
- Simplification of the geometry taking advantage of the elements formulation.
- Linear analysis.

Outlook

Future applications can be developed with the aforementioned simplified FEM model as the study of the mechanical stability in terms of displacements in case of earthquake or quench failure. It also could be adapted to new upcoming machines to be installed in FAIR.

References

[1] J. P. Meier, "Specification for the preparation of production-ready engineering design and documentation for SIS100 cryo-magnetic quadrupole modules and missing dipole modules", GSI detailed specification,2013, p. 13.

[2] E. Fischer et al, "Detailed specification SIS100 Dipole Magnet", GSI detailed specification, 2013, p. 36-37.

* Work supported by FAIR@GSI PSP code: G2.08.02.10 and the University of Castilla-La Mancha

† j.ceballosvelasco@gsi.de

Mitigation of particle-in-cell induced numerical noise for space charge simulation of SIS100

F. Kesting[1,2] *and G. Franchetti*[1,2]

[1]IAP, Goethe University, Frankfurt am Main, Germany; [2]GSI, Darmstadt, Germany

Numerical noise emerges unavoidably in particle-in-cell space charge simulations, and causes artificial diffusion of macro-particles eventually leading to beam loss. In SIS100 the collimation system accepts a maximum beam loss of $\sim 10\%$ of nominal intensity [1], therefore noise induced beam loss should be much smaller than 10% not to alter the prediction of beam loss on collimators. Tentatively, we require the artificial beam loss not to exceed 1% corresponding to a maximum emittance growth of 1% for a KV beam. In this report, we find simulation parameters for such requirement in order to assess the computational load.

Recent studies on the propagation of numerical noise [2] allow an estimate on artificial emittance growth $\Delta\epsilon$ for particle-in-cell (PIC) tracking. In such simulations, the particle beam is represented by N_M macro-particles, and the space charge is calculated on a mesh of $N_G \times N_G$ grid points. For an integration length Δs, a beam size σ_x and an initial emittance ϵ_x, we find the average slope of emittance growth for a coasting beam as

$$\frac{\Delta\varepsilon_x}{\Delta s} \simeq \frac{\sqrt{N_G}}{N_M}\frac{\sigma_x^2}{4\varepsilon_x}\delta F_x^2 \Delta s, \qquad (1)$$

where δF_x is the standard deviation of fluctuation of the space charge force in the center of the beam [2]. This scaling law is valid as long as the fluctuations δF_x are not correlated, which is the preferred and most common case. An integration of Eq. 1 allows to estimate optimal simulation parameters, as demonstrated in Ref. [2] for round coasting beams. We next infer the consequences of Eq. 1 for bunched beams in a 2.5 dimensional (2D5) model.

For bunched Gaussian beams, we distinguish two different types of 2D5 slicing: a) equidistant slicing [3], where the spatial resolution is constant in the longitudinal plane, and b) adaptive slicing, where the number of macro-particles per longitudinal slice is constant. The relative field fluctuations are constant for adaptive slicing, but vary along the bunch for constant slicing. This is confirmed by numerical investigations on both slicing models using the MICROMAP tracking library, as shown in Fig. 1.

To find optimal simulation parameters in the 2D5 model, we apply Eq. 1 on each of the N_z slices, and use a weighting depending on the number of particles per slice. For both slicing models, the dependence of the force fluctuations on the number of slices can be approximated by a linear scaling. A complete derivation is part of future publications.

In the following, we consider a typical scenario with space charge tune-shifts $\Delta Q_x \approx \Delta Q_y \approx 0.2$, at the working point $Q_x = 18.87$ and $Q_y = 18.72$ in the constant focusing approximation. We apply 42 space charge kicks per betatron-wavelength, while the spectral Poisson solver uses a grid of $N_G \times N_G = 64 \times 64$ points within $6\sigma_x \times 6\sigma_y$. The number of longitudinal slices is varied from $N_z = 4$ to $N_z = 30$, while the field fluctuations δF_x were found for each setting using MICROMAP. In the following table, we give estimates on the number of macro-particles necessary in order to limit the artificial emittance growth to a maximum of 1 percent.

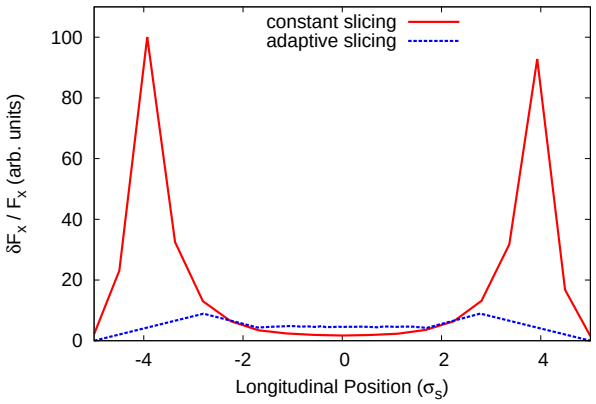

Figure 1: Comparison of relative force fluctuations $\delta F_X / F_x$ for bunched beams along s with constant slicing (red line) and adaptive slicing (blue line).

# slices	macro-particles - constant slicing	macro-particles - adaptive slicing
4	$1.3 \cdot 10^6$	$6.5 \cdot 10^6$
10	$3.8 \cdot 10^6$	$1.2 \cdot 10^7$
20	$8.0 \cdot 10^6$	$2.2 \cdot 10^7$
30	$1.2 \cdot 10^7$	$3.2 \cdot 10^7$

The mitigation of numerical noise in self-consistent simulations for the SIS100 thus requires a high computational demand. The number of macro-particles has to be further increased in case of stronger space charge, higher beam resolution, longer storage time, or stronger restrictions on artificial emittance growth.

References

[1] P. Spiller, and G. Franchetti. NIM-A 561.2 (2006): 305-309.

[2] F. Kesting, and G. Franchetti PRSTAB 18, 114201 (2015)

[3] F. Kesting, G. Franchetti, and U. Ratzinger, in Proceedings International Particle Accelerator Conference IPAC2014,Dresden, Germany, June 15-20, 2014 (EPS-AG, Dresden,2014), p. 3005.

DOI:10.15120/GR-2016-1

A magneto-resistance sensor based DC beam current transformer for FAIR*

E. Soliman[1,2], K. Hofmann[1], H. Reeg[3] and M. Schwickert[3]
[1]Technische Universität Darmstadt, Germany; [2]German University in Cairo, Egypt; [3]GSI, Darmstadt, Germany

A Novel DC Current Transformer (N-DCCT) is currently under development for the SIS100 synchrotron. The proposed system is based on magneto-resistance (MR) sensors detecting the magnetic field of the ion-beam. The N-DCCT prototype consists of a high permeability slotted ring core, equipped with two commercially available tunneling MR sensors inside the core's air gaps. The sensor's output voltage sum is directly proportional to the ion-beam current.

Detection principle

Conventional DC current transformers use the magnetic-modulator method to precisely determine the magnetic field, and thus the current, of the passing ion beam. However, interference of the modulation harmonics leads to false current readings at certain revolution frequencies and lead to the development of a novel instrument.

The N-DCCT is based on the clamp-on ammeter design featuring a split toroid to allow e.g. easy dismounting of the sensor before vacuum bake-out, see Fig. 1. Two magnetic field sensors are placed inside the gaps of the slotted ring core made from high-permeability alloy VITROVAC 6025F ®.

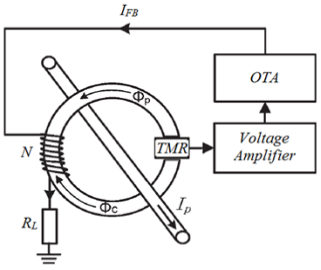

Figure 1: Schematic of an N-DCCT with feedback-loop.

Noise analysis

A wide variety of giant-magneto resistance (GMR) and tunneling magneto resistance (TMR) sensors is available in IC technology. To select the optimum sensor type a detailed analysis of the sensitivity and noise figure of various MR sensors was carried out. To compare the sensor performance their 'detectivity' D, defined as

$$D := \frac{\sqrt{S_V}}{R_{BV}} \qquad (1)$$

was experimentally determined, where $\sqrt{S_V}$ [mT/√Hz] is the output noise power spectral density and R_{BV} [V/mT] is the slope of the sensor's transfer function. Both sensor types suffer from electronic as well as magnetic noise contributions. The electronic noise for both sensors has contributions from thermal and 1/f-noise, but especially for TMR sensors the shot noise, caused by the random flow of charge carriers across the tunnel junction, is more dominant [1]. For the four different sensors studied, TMR sensors showed the best (lowest) D value, cf. Table 1.

Sensor	$\sqrt{S_V}$ [µT/√Hz]	R_{BV} [V/mT]	D [nT/√Hz]
GMR AA002	80	3	25
TMR 45F	200	12	16
TMR 57F (DFN)	65	4	16
TMR 57F (SOP)	359	6	57

Table 1: Measured GMR and TMR parameters, cf. [2].

Feedback-loop design

In order to further improve the linearity and sensitivity of the N-DCCT a feedback-loop was designed. As depicted in Fig. 1 the idea is to create a feedback current I_{FB} that is applied to a feedback winding with N turns on the ring core, to cancel out the magnetic field generated by the ion beam ('zero flux measurement'). A PCB was designed to convert the voltage output of the sensor's Wheatstone-bridge into a feedback current, using operational transconductor amplifiers (OTA). A set of multiple parallel OTAs is used to supply the required, relatively high feedback current, thus enhancing the overall dynamic range of the N-DCCT. The feedback winding is terminated by a precision resistor. The voltage across this resistive load is a direct measure for the beam current I_P. Since typical beam currents are in the range of few milli-Amperes to Amperes, considerably more than 1 turn is needed.

As a first step, the signal-to-noise ratio and the system stability were investigated for two different commercial OTAs (OPA860 and OPA861). Four parallel OTAs of each type were tested. The output noise power spectral density at DC yielded 91 dB (OPA860) and 74 dB (OPA861), respectively. Both, the MATLAB simulations of the feedback circuit, as well as the measurement of the system's step response show good stability of the feedback loop. For the two setups the minimum detectable beam current at DC was calculated as 15 µA/√Hz for OPA860, and 8 µA/√Hz for OPA861. Further developments are planned to increase the analogue bandwidth of the N-DCCT and to enhance the EMC-safety.

References

[1] Z. Q. Lei, G. J. Li, W. F. Egelhoff, P. T. Lai, and P. W. T. Pong, IEEE Trans. on Mag., vol. 47, pp. 602, 2011.

[2] E. Soliman, K. Hofmann, H. Reeg and M. Schwickert, Conf. Proc. Sensors Applications Symposium 2016, Catania, Italy, to be published.

* Work supported by BMBF, contract no. 05P12RDRBG

DOI:10.15120/GR-2016-1

Local cryogenics of SIS100 – cryogenic by-pass line*

B. Streicher[1], *T. Eisel*[1], *C.H. Schroeder*[1], *and H. Kollmus*[1]
[1]CSCY, GSI, Darmstadt, Germany

Introduction

The complex local cryogenic system of SIS100 will distribute more than 10 kW cooling power @ 4.5 K and up to 13 kA electrical current to 300 superconducting magnets and other physics equipment. By-pass lines, having a total length of 300 m, circumvent warm equipment, e.g. normal conducting cavities and magnets. Between the warm equipment, superconducting magnets are located, which also need to be supplied from the by-pass lines with helium @ 4.5K and cold electrical connections. The by-pass lines are part of the Polish in-kind contribution to FAIR. The work is coordinated by the Jagiellonian University of Krakow and the components will be designed, manufactured and commissioned by the Wroclaw University of Technology (WrUT).

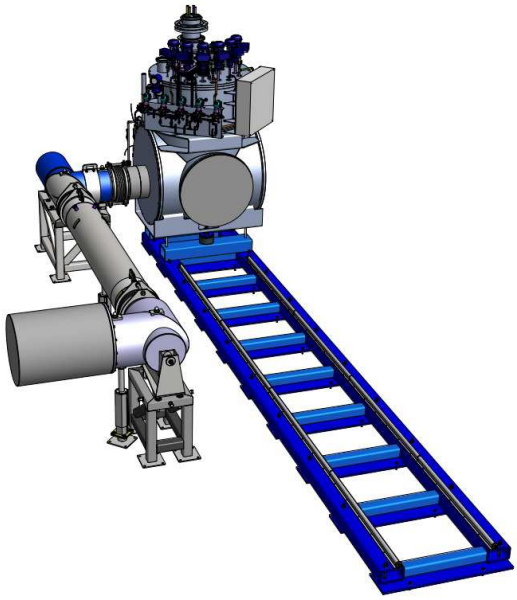

Figure 1: 3D model of the BPL instaled at the STF connected to the side-flange of the Feed-Box.

Cryogenic by-pass line

1S50YP

The first by-pass line module, which will interconnect the feed box with the arc termination magnet module, is currently been built by the company KrioSystem under supervision from GSI. The work is at the time of writing approaching the final state of completion (see Figure 2). During the production phase an intense contact was established between GSI, WrUT and KrioSystem including several visits to the production facilities in Poland to assure high production quality. A practical course for soldering superconducting joints was organized and performed at GSI to train the polish technicians. Furthermore, several unknown issues were investigated by measurements at the serial (STF) and prototype (PTF) test facilities at GSI. These included evaluation of heat load to superconducting joints and measurement of electrical parameters of bus bar supports like parasitic capacities. There are still ongoing measurements at the STF, namely of helium mass flow through the combination of electric heater and capillary tube. These measurements will evaluate the possibility to adapt the flow through the magnet and/or vacuum chamber to different machine operating cycles. After delivery of the first by-pass line module 1S50YP in May 2016 it will be temporarily installed at the STF facility (see Figure 1). Here it will undergo a full scale site-acceptance test (SAT) including cool down and electrical test of 13kA of current. Having successfully passed the envisaged SAT, the series production of standard straight by-pass line modules will begin.

Figure 2: Foto of the first BPL-piece close to completion at KrioSystem.

1S52YP

The furter development of the SIS100 local cryogenic components continued with the design of a complete ”long” straight module of the BPL system. WrUT designed the 1S52YP segment in the second half of 2015. The new concept of supporting the shielding inside the vacuum vessel was integrated as well as sliding and strong supports of the cold mass inside the shield was developed. The mechanical reliability of this design is currently being reviewed by GSI personnel and the final design review is taking place at the end of May 2016.

* FAIR@GSI PSP code: 2.8.12 and 2.14.8.1.6

DOI:10.15120/GR-2016-1

Benchmarking of DAQ system for FAIR beam position monitors

R. Singh, A. Reiter, O. Chorniy, K. Lang, W. Kaufmann, P. Kowina, M. Schwickert, and B. Walasek-Hoehne

GSI, Darmstadt, Germany

Introduction

A common data acquisition system is planned for FAIR synchrotrons such as SIS-100, CR and HESR as well as the high energy beam transport lines (HEBT) for beam position monitors (BPM). A first prototype of the new Libera platform B was supplied by the Slovenian in-kind contributors [1] for tests at the GSI site. The acquisition system is based on a 16 bit 250 MSa/s ADC system, and each acquisition unit consists of up to 16 ADC channels which can serve four BPMs. The tests for benchmarking the system were broadly divided into two parts; the first part dealt with the testing of individual ADC characteristics and long term stability of the acquisition unit, while the second part investigated the robustness and accuracy of the FPGA signal processing algorithms under expected beam signals scenarios at the FAIR facility.

Benchmarking

Important ADC characteristics such as effective number of bits (ENOB) and differential non-linearity (DNL) were validated by single tone/double tone tests [2] and were found in accordance with the specifications, i.e. ENOB = 11.5 ± 0.5 bits and DNL < 0.5 units. The stability issues found are already resolved with the in-kind partners.

Since the hardware will be used to serve very different machines, several modes of operation are implemented in the FPGA to satisfy the use-cases. The modes of operation can be coarsely classified as:

1. Raw-data mode: It is the "oscilloscope mode" and this functionality is required for all BPM systems.
2. Single-pass mode: For the HEBT BPMs.
3. Multiple-pass orbit mode: Mean beam positions over several turns. For low current and large aperture machines such as CR, a narrow band analysis (NBA) will be implemented to achieve the resolution requirements of this mode.
4. Multiple-pass bunch-by-bunch mode: Required primarily for optics measurements of the synchrotron.

First tests were performed for the most demanding multiple-pass orbit and bunch-by-bunch modes. Expected beam signals are simulated for potential SIS-100 and CR scenarios and position is calculated with the algorithms implemented in the FPGA. Figure 1 compares the measured position resolution for a simulated beam at two off-center positions with a statistical model which only requires knowledge on the rms noise voltage and the bunch shapes [3]. A relatively high noise $\sigma_v = 30$ mV rms was added to the 600 ns bunch (4σ). For the applied root-sum-square (RSS) estimator the agreement between data and model calculation is very good.

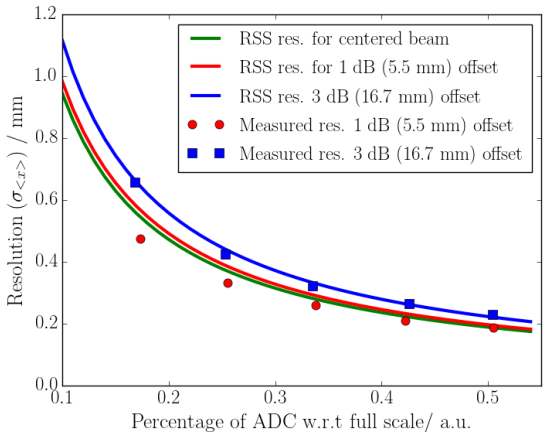

Figure 1: Comparison of the measured resolution to prediction by the statistical model.

The shortest bunches for FAIR facility are expected to be $\approx$ 50 ns (4σ) and the noise level of the FAIR BPM amplifier [4] is about 10 times smaller compared to the test, roughly 3.5 mV rms. With these input parameters the model estimate is below the specified system resolution of 0.1 mm. These numbers will be verified when the first prototype of the HPA amplifier is delivered by mid 2016.

Conclusion

The new DAQ system for FAIR BPMs has passed a first series of tests. More detailed tests will follow and be completed with SIS18 beam tests in 2016. Together with the new BPM amplifier prototype benchmarking of the full acquisition system can be carried out at an early stage.

References

[1] Instrumentation Technologies, "Libera Hadron", www.i-tech.si/accelerators-instrumentation/libera-hadron/benefits_7

[2] W. Kester (Ed.), "The Data Conversion Handbook", Analog Devices (2005)

[3] A. Reiter et al., "Statistical Treatment of BPM Data", Internal report GSI-LOBI-TN-08-BPM_StatisticalAnalysis (2016)

[4] LOBI Tech. Note, f-tn-bd-009_BPM_Preamplifiers_v2.0.pdf

DOI:10.15120/GR-2016-1

DOI:10.15120/GR-2016-1

Design and tuning of digital filters for RF feedback loops in heavy-ion synchrotrons*

B. Reichardt[†1], *D. Mihailescu-Stoica*[‡1], *J. Adamy*[1], *D. Domont-Yankulova*[1,2,3], *H. Klingbeil*[2,3], *and D. Lens*[3]

[1]TU Darmstadt RMR, Darmstadt, Germany; [2]TU Darmstadt TEMF, Darmstadt, Germany; [3]GSI, Darmstadt, Germany

Damping of longitudinal coherent bunched-beam oscillations are needed in SIS18 and SIS100 to stabilize the beam, prevent emittance growth and keep beam loss low during acceleration. In last year's work several approaches of digital filters for beam-phase control have been examined. An FIR (finite impulse response) filter with 3 taps, cf. [1], has been successfully used at GSI in several machine experiments for a beam- phase control system and a longitudinal feedback system. In principle, much more taps can be used, but it is still an open topic, whether more complex filters will lead to better results. Therefore, a detailed control-theoretic study has been started and the progress is reported in the following.

Requirements and filter properties

A numerical differentiator approach based on a least squares algorithm [2] has been chosen as an alternative to the established 3-tap filter. Both filters make use of the inner product between two vectors in an FIR filter design. The non-zero coefficients of the 3-tap filter, together with a certain amount of zero taps, form a bias-free bandpass filter. The length of the derivative-estimator filter has to be adapted during the acceleration ramp. Currently, it is assumed that the optimal length depends on the incoherent linear synchrotron frequency, but alternatives will be studied in detail.

The future hardware platform for the filter implementation will allow filters with up to 64 non-zero taps. A filter bank will be used to select different filters based on available parameters such as the synchrotron frequency. Alternatively, a continuous tuning of the coefficients will be possible [3].

Simulation and outlook

Nonlinear tracking simulations were performed for Ar 18+ as ion species at an energy of 11.4 MeV/u for a stationary operation with a linear synchrotron frequency of 740 Hz.

In this case the derivative-estimator has a length of L = 52 non-zero taps without additional zero-taps and is tuned to a high damping rate.

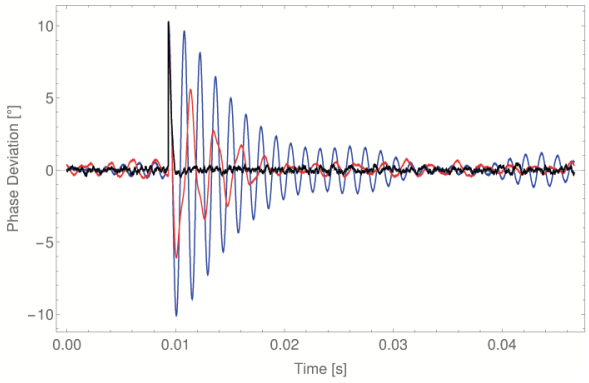

Figure 1: Beam-phase with respect to uncorrected Group-DDS: Open-loop (blue), controller with derivative-estimator (black), controller with 3-tap filter (red), with a 10° distortion at 0.01s

A typical simulation result is shown in Fig.1. A disturbance of 10° on the beam phase is applied at 0.01s to intentionally excite a feedback reaction. The results indicate that the 3-tap- filter has smaller emittance growth, whereas the derivative-estimator damps the oscillation much faster. The emittance growth using the 3-tap filter is over 3 times smaller compared to using the derivative-estimator filter, although the beam-phase is stabilized much faster by the derivative estimator.

Currently under investigation is the influence of the filter length and gain on emittance growth for the derivative estimator, as well as tuning rules for the acceleration process, with respect to ion species, bunch lengths, etc.

In future both controller designs will be studied on slow and fast acceleration ramps, as they occur in the FAIR project. Another important subject to be studied is the influence of the cavity dynamics on the stability and efficiency.

References

[1] H. Klingbeil et al., "A Digital Beam-Phase Control System for Heavy-Ion-Synchrotrons", IEEE Transactions on nuclear science Vol. 54, No. 6, December 2007

[2] P. Mai and C. Hillermeier, "Least Squares based Derivative Estimation: Theory and Tuning Rules for the Practical Application", at-Automatisierungstechnik, October 2008

[3] K. Möller et al., "FPGA Based Tunable Digital Filtering for Closed Loop RF Control in Synchrotrons", GSI Scientific Report, 2013

* Supported by the Helmholtz Graduate School for Hadron and Ion Research

† benjamin.reichardt@rmr.tu-darmstadt.de

‡ dinu.mihailescu-stoica@rmr.tu-darmstadt.de

DOI:10.15120/GR-2016-1

Characterization of scintillation screen materials for HEBT diagnostics*

A. Lieberwirth[1,2,#], W. Ensinger[2], P. Forck[1,3], O. Kester[1,3], S. Lederer[2] and T. Sieber[1]
[1]GSI Darmstadt, Germany; [2]Technische Universität Darmstadt, Germany; [3]IAP, Universität Frankfurt/Main, Germany

Seven different scintillation screens were tested at the diagnostics test setup (HTP) behind SIS18, including phosphor screens (P43 and P46 phosphor), single crystals (Cerium-doped $Y_2Al_5O_{12}$:Ce) and polycrystalline pure Aluminum oxides Al_2O_3 (so called A999) and Chromium-doped Al_2O_3:Cr. The screens were irradiated with five different projectiles (protons, nitrogen, nickel, xenon and uranium), extracted from SIS18 in fast (1 µs) and slow (300-400 ms) extraction mode at 300 MeV/u. The number of particles per pulse was varied between $3 \cdot 10^6$ and $2 \cdot 10^{10}$ ppp. The scintillation response was recorded with an optical system, to investigate in detail the light output L, the light yield Y (which is the light output divided by the energy loss $\Delta E_{ion} = dE/dx \cdot \Delta x$ within the relevant thickness Δx), and the beam profile projections in horizontal and vertical direction [1].

Figure 1 shows the light output of all investigated target screens as function of number of irradiated particles per pulse. The scintillation was induced by a fast extracted uranium beam. The error bars for the light output L are in the range of 5-20 %. For the beam intensities the error bars correspond to 15 %. The figure shows that in the given intensity range all targets have linear light output i.e. no saturation effects were observed for the given intensites. This was verified also for the other ion species [1,2,3].

The lowest light output was observed for un-doped Aluminum Oxide (A999 #6). A Chromium doping of 0.04 percent (Al_2O_3:Cr #7) leads to a five times higher light output. Due to the large amount of deposited energy (caused by increased target thickness), the highest light output was measured at a YAG:Ce single crystal #5. In the group of phosphor targets, the highest light output is observed for P43 phosphor #1.

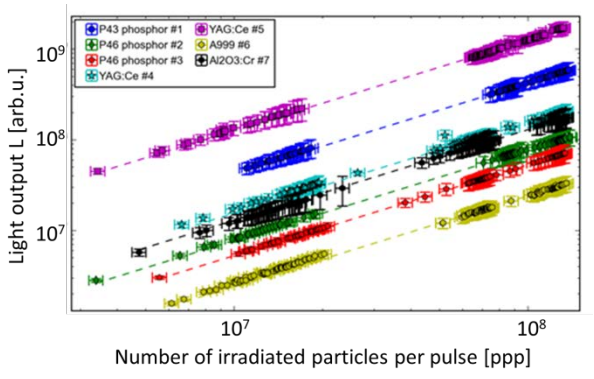

Figure 1: Light output L induced by a fast extracted Uranium beam.

Differences in light output were observed between irradiation in fast and slow extraction mode, but the factor is small, compared to the differences in extraction times. This observation is confirmed by the light yield Y, which is plotted (normalized to $Y_{nitrogen}$) as a function of atomic number Z of the projectiles in figure 2. The light yield was calculated using the slopes m of the light output curves as $Y = m / \Delta E_{ion}$, where ΔE_{ion} is the energy deposited in the scintillator material by a single ion. The data in figure 2 are normalized for each material individually.

The plot shows that the variations in the light yield for different projectiles are comparatively small, considering the large differences in atomic mass (and the corresponding energy deposition). This is an important result, because independence of the light yield from the ion species is an essential requirement for the application in beam diagnostics at FAIR.

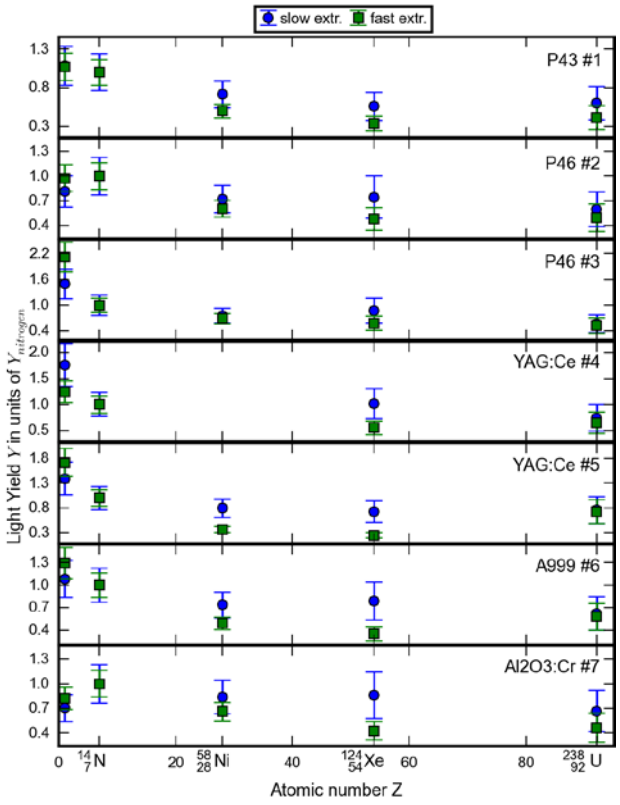

Figure 2: Normalized light yield from all targets in dependence of the atomic number of the projectiles.

References

[1] A. Lieberwirth, "Investigations on Imaging Properties of Inorganic Scintillation Screens under Irradiation with High Energetic Heavy Ions", PhD Thesis, TU Darmstadt, in preparation.
[2] A. Lieberwirth et al., GSI Annual Report 2014.
[3] A. Lieberwirth et al., Nucl. Instrum. Meth. **B 365**, 533 (2015).

* Work supported by the BMBF, contract No. 05P12RDRBJ and FIAS
#A.Lieberwirth@gsi.de

Status of the Series Test Facility and the HeSu

C.H. Schroeder[1], A. Breidert[1], A. Beusch[1], M. Kauschke[1], M. Martínez-López[1], B. Streicher[1], F. Walter[1], F. Wamers[1], H. Kollmus[1]
[1]GSI, Darmstadt, Germany

The Series Test Facility (STF)

All 108 dipole magnets for the SIS100 have to be tested at GSI in a reasonable time of 2.5 to 3 years. Since the existing test environment, the so called prototype test facility (PTF) has only two benches for magnet testing it was necessary to build a dedicated cryogenic infrastructure for the series testing. The specification was ready in August 2012 and the contract was signed with Linde KT in spring 2013. In summer 2014 all parts for the cold box, the distribution system and the test benches have been delivered and successively installed in the buildings SH2/3 and SH5. After intensive commissioning the site acceptance test (SAT) was successfully completed in spring 2015. In table 1 the specified cooling capacity and liquefaction rate is shown in comparison to the performance reached during SAT.

Table 1: Performance achieved during SAT

	Specified	*Achieved*	*Ratio*
Cooling capacity at 4K	700 W	778 W	+11%
Cooling capacity at 50 K	2000 W	2030 W	+1.5%
Liquefaction	6.0 g/s	6.0 g/s	0%
4 K equivalent	1500 W	1580 W	+5.3%

Since there was a high request for FAIR prototype testing, and a limited testing capacity at the universal cryostat of the PTF, a second universal cryostat for the STF was ordered in 2015. This universal cryostat was extensively used, e.g., for the testing of vacuum chamber cooling schemes, for hydraulic measurements on restrictors or for the SAT of SIS100 man current leads. Already in 2015 an uptime of the cryo plant of 5000 h was reached.
Figure 1 shows a picture of the assembly in building SH2/3 with the main distribution system and the four test benches allowing the testing of one magnet per week.

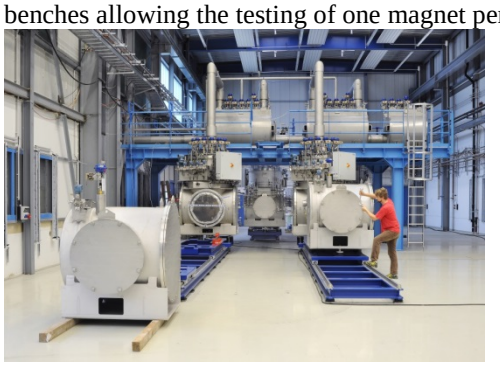

Figure 1: Picture of the STF

In addition to the testing of SIS100 dipole magnets the facility is suitable for testing of SIS100 quadrupole magnets, a SIS100 string configuration and even SuperFRS magnets.

The Helium Supply Unit (HeSu)

In order to provide easy access to liquid helium for experimental purposes, the GSI helium liquefier (HeSu) was purchased. After the commissioning in 2014 [1] HeSu has been intensively serving research groups like LINAC, SHE physics and atomic physics throughout 2015. The total liquid helium delivered up to now accounts for 7000 liters.
The respective groups provided the helium for the liquefaction in the form of helium gas bundles of pure or impure gas. The price for impure helium is significantly lower than the price for pure helium or helium in liquid form, therefore, the purification capacities and liquefaction of the HeSu could be effectively used to save money.
For improving the flexibility of the supply, new mobile helium dewars were ordered. Overall, the HeSu has now four mobile dewars with a capacity of 250 liters each. Efficiency and operation of the liquefier are being improved continuously. A new connection from the HeSu to the STF has been installed to use the STF buffer tank as an additional helium gas storage unit. A second connection was added to improve and simplify the supply of impure helium from the gas bundles into the recovery system. In addition, a camera was positioned near the gas balloon to control the proper functioning of the recovery system. It allows the HeSu operators and the liquid helium users to control the gas flow into the recovery and balloon preventing it from overfilling. Future plans for improving the helium liquefier system include:

* The purchase of a new gas balloon, as well as other storage systems, to reduce the helium losses and increase the storage capacity.
* To increase the number of GSI and FAIR helium users connected to the helium recovery system in order to decrease the helium loss.

References

[1] A. Breidert et al.: “Status and commissioning of the Helium Supply Plant (HeSu) and the Series Test Facility (STF)”, GSI Scientific Report 2014.

DOI:10.15120/GR-2016-1

Calculations for the shielding flask of the Super-FRS

M. Helmecke, E. Kozlova, K. Knie, T. Radon, A. Sokolov, H. Weick
GSI, Darmstadt, Germany;

All components which are hit by the primary beam will be highly activated. Therefore, a dedicated safety concept for the handling of these components (maintenance, repair or disposal) is necessary. The components will be transferred into a hot cell next to the beamline for further processing, e.g. dismounting, by using a shielding flask. Dedicated shielding calculations for this shielding flask have been performed by using the Monte Carlo code FLUKA [1, 2].

The largest and most activated parts that have to be handled with the shielding flask are the six beam catchers [3]. Beryllium and graphite beam absorbers are used to stop the heavy-ion beam or to convert it to lighter fragments and to absorb most of the beam energy. They are coupled to a copper heat sink and mounted to an iron shielding plug of a size of 60 cm x 80 cm x 174 cm with drives, vacuum seals and feedthroughs on top. The total weight of it that has to be handled by the crane is about 7.5 t. The internal crane has a capacity of 10t and the flask with load is transported with a crane of 80t. At maximum FAIR Uranium beam intensity the activation comes up to 10 TBq two weeks after beam stop and a large variety of isotopes with different decay energies are created.

To obtain a realistic scenario for the estimation of the required wall thickness of the shielding flask, the residual dose of one beam catcher is calculated by using two different methods.

In the first method, called “two step method”, the simulation of production of radioactive nuclides in the beam catcher and plug, their build-up and decay for a certain irradiation pattern and cooling time are performed as the first step. All information on the produced radio-nuclides is written to external files via a user-routine. In this calculation, the shielding environment in the Super-FRS beam-catcher area is included. In the second step the simulation of radioactive decay and decay radiation is done with the flask geometry. The information on radio nuclides are read from files created in the first step. The result is presented in Fig. 1. As a realistic scenario, 3 days after four periods of irradiation with an ^{238}U beam of 1.5 GeV/u with an intensity of $3x10^{11}$/s over 90 days with a subsequent cooling time of 120 days between blocks are assumed.

In addition, the decay of the residual dose of the flask is calculated directly with the “one step method”: In this case the activation of the beam catcher and the flask are calculated only from one simulation without reading from external files. Fig.1 shows the distribution of the residual dose rate. Fig. 2 shows a projection of the residual dose rate in the iron of the shielding flask at its maximum (directly behind the beam catcher); Fig.2 can be used for detailed adjustment of the wall thickness. The total weight of the shielding flask is indicated for three different wall thicknesses (weight without net load).

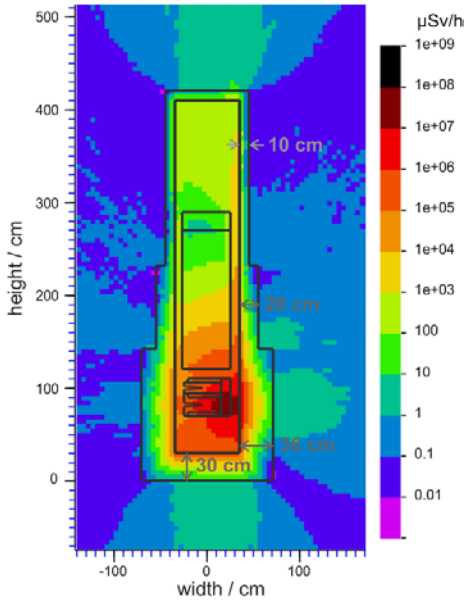

Fig.1. Residual dose rates of the beam catcher und plug in the shielding flask.

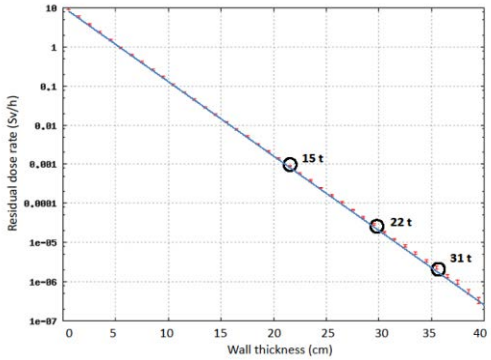

Fig.2 Residual doses rate reduction by the wall of the shielding flask.

References

[1] T.T. Böhlen et al., Nuclear Data Sheets 120, 211-214 (2014).
[2] A. Ferrari et al., CERN-2005-10 (2005), INFN/TC_05/11, SLAC-R-773.
[3] E. Kozlova et al., Nucl. Instr. and Meth. B 266 (2008) 4275.

DOI:10.15120/GR-2016-1

Proof-of-principal operation of the time-of-flight Cherenkov detector for the SFRS at FAIR

N. Kuzminchuk-Feuerstein[*1], *B. Voss*[1], *E. Fiks*[2], *I. Kaufeld*[3], *V. Kleipa*[1], *and the SFRS collaboration*[1]

[1]GSI, Darmstadt, Germany; [2]National Research Tomsk Polytechnic University, Tomsk, Russia; [3]Hochschule RheinMain University of Applied Sciences, Rüsselsheim, Germany

A prototype of a Cherenkov detector, employing Iodine Naphthalene ($C_{10}H_7I$) fluid radiator and equipped with two photomultiplier tubes (PMTs) was designed, constructed and approved in principal operation with nickel ions at CaveC [1]. A Cherenkov detector is proposed for the future time-of-flight (TOF) measurements and hence, in conjunction with momentum or energy of the particles, for their identification at SFRS at FAIR.

In particular timing accuracy and detection efficiency was measured with low/high energies as well as low/high intensities of the ions. The measurements were done with respect to two plastic scintillators, which were placed in front and behind the Cherenkov detector. In the measurements the time difference ΔT between the events detected by left PMT1 and right PMT2 was measured. The waveforms from both PMTs were stored with a digital oscilloscope. The event time of each waveform were determined with a software constant-discrimination method. The distribution of ΔT= $t_1(PMT1)$-$t_2(PMT2)$ is taken as a coincidence time-of-flight distribution. The sigma of this distribution σ_{coin} defines the time spread between the left and right and is used to characterize the timing accuracy of the detector. Fig. 1 shows results of the timing accuracy (σ_{coin}) measurements (left) with the ion energies of 320 MeV/u and 1.5 GeV/u. The beam intensities were 10^3 and $0.6{\cdot}10^6$ ions/spill correspondingly. Right ordinate indicates improvements in the measured relative detection efficiency from 10% to 70% [2]. Additionally in the measurements with 1.5 GeV/u ion energy the intensity of the beam were varied in steps up to $4.6{\cdot}10^6$ ions/spill. Pulse-height distributions were accumulated with a digital oscilloscope and analyzed for each energy-intensity combination. Fig. 2 indicates obvious increase by two times in detected signal amplitudes. Higher number of detected events and improved signal-to-noise ratio lead to better event time determination of each acquired signal and hence to better timing accuracy. Consequently the timing accuracy (σ_{coin}) improves from 478 ps to 267 ps.

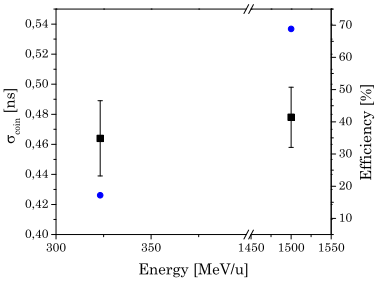

Figure 1: Left: timing accuracy of Cherenkov detector at different ion energies. Right: measured detection efficiency. The particle rate is 10^3 and $0.8{\cdot}10^6$ ions/spill.

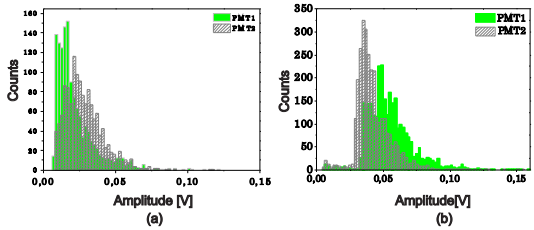

Figure 2: Pulse-hight distribution for the ion intensities of $0.8{\cdot}10^6$ ions/spill (a) and $3.4{\cdot}10^6$ ions/spill (b) measured by both photomultiplier tubes assembled to Cherenkov detector.

Construction is in progress of a new glass cuvette to achieve higher number of Cherenkov photons creation as well as optimum in photon transmission to the PMTs. New cuvette has 85 mm height compared to previously used with 50 mm. The thickness of the cuvette is enhanced to 5.2 mm. With a new cuvette construction and support system the coupling between cuvette and PMTs will be enlarged from 100 mm^2 to 425 mm^2. Particularly measurements with an ion beam is planned for next year.

In addition, measurements with cosmic muons of the photon emission in the wavelength range of 400 - 1050 nm, using Si-APD-receiver was performed in the laboratory. Prepared cuvette filled with $C_{10}H_7I$ and assembled with the Si-APD receiver was mounted between two plastic scintillators and number of detected photons was counted. This receiver contains an amplifier with differential output and a photo diode. The photo diode is biased with an external and adjustable HV-Voltage. The APD-Receiver is placed in a socket, mounted on the circuit board, to simplify the exchange and test of different wavelength sensitivity of the fluid radiator.

References

[1] N. Kuzminchuk-Feuerstein et. al., GSI Scientific Report 2014, 141

[2] N. Ferber, "Konzipierung und Charakterisierung eines DIRC-Detektors zur hochauflösenden Teilchenidentifikation mittels TOF-Methode", Master Thesis (2014). Rüsselsheim, Germany

* n.kuzminchuk@gsi.de

DOI:10.15120/GR-2016-1

Calibration of an ionization chamber with diamond detector*

S. Schlemme[1,2], C. Nociforo[2], M. Kis[2], A. Kratz[2], F. Schirru[2], J. Enders[1] and the FAIR@GSI division
[1]TU Darmstadt, Germany, [2]GSI, Darmstadt, Germany.

We have verified the linearity of the ionization chamber IC current as a function of the beam counts detected by a single-crystal CVD diamond detector.

A self-calibrating ionisation chamber is often required for precise intensity calibration of high-energy heavy-ion beam monitors like the SEETRAM [1]. Ionization chambers operated in current mode provide precise beam intensity values if calibrated with detectors capable of measuring individual ion pulses. Diamond detectors have been selected as beam intensity monitors of the slow-extracted SIS ion beams to be delivered to the Super-FRS target with intensity of up to several MHz. In addition, they will be used to perform absolute calibrations of the Super-FRS IC and SEETRAM.

To reduce uncertainties in the beam current calibrations the ratio between the number of monitor particles and the IC current has to be measured at several different ion rates, below the saturation point of the particle monitor and above the minimum rate measured by the ionization chamber. Under these conditions, a linear dependence between the measured particle counts and the IC charge can be observed. We have checked it performing the calibration of a two-gap IC at LNS-INFN (Catania) with 62 AMeV ^{12}C cyclotron beam by using a scCVDD detector [2]. Despite the particle count efficiency of the 0.09 mm thick diamond can be assumed to be 100 %, its active area did not cover the whole area of the beam spot. Thus measurements with and without a collimator (Ø 2.6 mm) mounted in front of the setup were needed. Hence the counts measured by the scCVDD have been corrected by the ratio - defining the geometrical losses - of the total beam transmission divided by the beam transmission through the active area of the diamond detector. Hence the counts measured by the scCVDD have been corrected by the ratio - defining the geometrical losses - of the total beam transmission divided by the beam transmission through the active area of the diamond detector. These values have been obtained by simulating the ^{12}C transmission through the setup, reproducing the position/angular ion distribution measured by additional detectors and the diamond count rate. The beam properties of 30 mrad angular divergence and diameter of 11 ± 1 mm were found to match these boundary conditions, delivering a transmission value through the scCVDD of 54.58 ± 0.03 % and consequently a geometrical correction factor of 1.832 ± 0.001. Simulations showed also a negligible intensity dependence of the number of ions transmitted through the collimator.

The diamond was connected to a broadband DBA amplifier. Its counts were measured via VME scaler, after discrimination. Before the calibration process the IC charge was measured for different high voltages between 200 V and 825 V to find a suitable working voltage (for P10 gas at 1 atm). The IC showed a stable charge output in the range 500-600 V.

In Figure 1 the scCVDD count rates is plotted against the measured IC current. The fit of the data points shows a linear dependence in the range of 0.1-2.5 MHz ion rates. Further data points measured at higher rates, included in Figure 1, showed a parabolic dependence due to pile-up effects in the scCVDD signals. The first order coefficient of the fitted second-order polynomial corresponds to a value of 7645 ± 452 counts per charge unit.

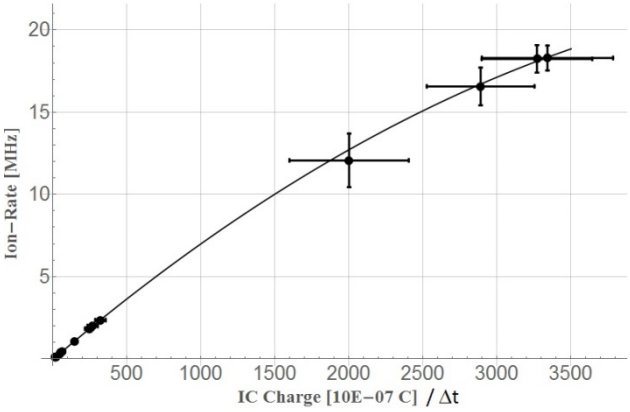

Figure 1: scCVDD ion rates vs IC current. The time unit is Δt = 1 s. The solid line represents a second-order polynomial fit.

This calibration factor is obtained for a certain sensitivity of the current digitizer. The above calibration could be carried out while maintaining the same sensitivity of 10^{-7} C without observing any saturation effects of the IC digitizer (mod. CD1012). Changes in the current magnitudes may require different calibration factors. At other experiments, especially at FAIR where large rate differences are expected, this effect has to be taken into account. Further the calibration depends on different factors like the gas type and flow as well as the bias of the monitors. For this reason calibrations must be foreseen to be repeated. In addition, a large source of systematics error may be caused by unstable time-distributed beams. The presence of additional diamond monitors at the Super-FRS has been foreseen in order to test the time dependence of the SIS spill structure.

References

[1] B. Jurado et al., Nucl. Instr. Meth. A 483 (2002) 312.
[2] C. Nociforo et al., ´Detector developments for the Super-FRS´, NN2015 proceedings, in press.

*PSP 2.4.6.1.1

DOI:10.15120/GR-2016-1

Status of the Super-FRS Local Cryogenics

F. Wamers[1], Y. Xiang[1], M. Kauschke[1], H.Kollmus[1], A.Täschner[1], M.Winkler[1]
[1]GSI, Darmstadt, Germany

Super-FRS Local Cryogenics Overview

The operation of the Super-FRS superconducting magnets at about 4.5 K requires a "Local Cryogenics" infrastructure that supplies and returns liquid and/or gaseous helium to and from the magnet cryostats, so that they can be cooled down (warmed up) and during beam operation be kept cold (~ 4.5 K) in a liquid-helium (LHe) bath, while being screened by a 50 to 80 K thermal shield. Via the interfacing "Distribution System", the Super-FRS Local Cryogenics will be connected to the FAIR central refrigeration plant "Cryo2" and the Cooldown-Warmup-Unit "CWU", a LN2-based pre-cooler needed for cool-down and warm-up. For the cooling of the Super-FRS magnets, four main helium process levels will be used: 4 K supply (@ 4 bar), 5 K return (@ 1.3 bar), thermal-shield supply (50 K @ 18 bar), and thermal-shield return (80 K @ 17 bar). In addition to that, auxiliary lines for warm-gas supply, warm-gas return and cold/warm-gas return are foreseen. These levels will be distributed through (vacuum-insulated) steel pipes interconnecting a chain of cryogenic feedboxes next to the cryostats in the Super-FRS tunnel. Each of those feedboxes services groups of cryostats (typically three dipoles or two multiplets) via their own cryo "Jumper" connection. In total, the Super-FRS Local Cryogenics has been organised into nine substructures, namely cryo-branches, and a "Branch-Box" for the flow distribution between the main and the parallel experiment branches. A scheme is shown in Figure 1.

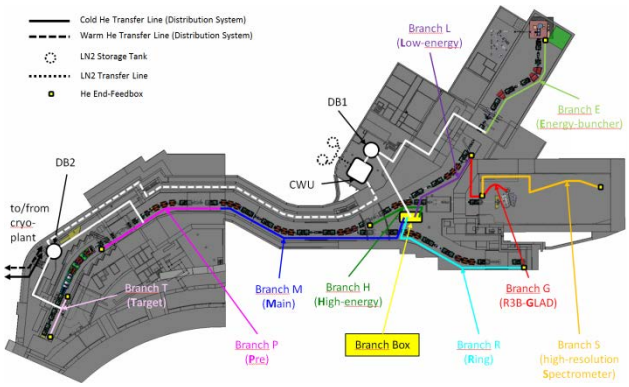

Figure 1: Scheme of the Super-FRS Local Cryogenics.

Super-FRS Cryogenic Heat Loads

In order to provide specification parameters for the design of the Super-FRS local-cryogenics, the FAIR cryo distribution system, and most importantly to the FAIR central cryogenic plant, the cryogenic properties and heat loads of the Super-FRS have been summarised in an official document [1]; that includes the estimated contributions of both the magnets/cryostats and the local cryogenics.

Table 2 summarises the Super-FRS heat loads, in terms of 5 K load, 50 to 80 K load, and necessary liquefaction rate due to the current leads.

Static heat loads	5 K / W	50-80 K / W	Liq. / (g/s)
Magnet cryostats	765	8716	8.4
Local cryogenics	864	5722	0.0
Total	**1628**	**14438**	**8.4**

Table 2: Heat Loads of the Super-FRS.

Based on these heat loads, Table 3 presents the resulting cool-down and filling times, taking into account total Super-FRS cold mass, the LHe inventory, and exemplary parameters of the future FAIR cryo plant.

Total cold mass / tons	1432
Cool-down time 300 to 80 K / days	16.9
Cool-down time from 80 to 5 K / days	14.6
LHe volume to be filled / litres	47710
Time for LHe filling / days	1.5
Total cool-down and filling time / days	**33**

Table 3: Cooldown & LHe filling time of the Super-FRS.

Cryo-Branch T and Jumper Connections

With our In-Kind partners from the University of Wroclaw (Poland), we have agreed to propel the procurement of the Local Cryogenics 'along the beam': We'll start with branch "T" at TFF1 (Figure 3), for which a conceptual design has been made, including a design study for the cryo jumpers with "Cryotherm" GmbH.

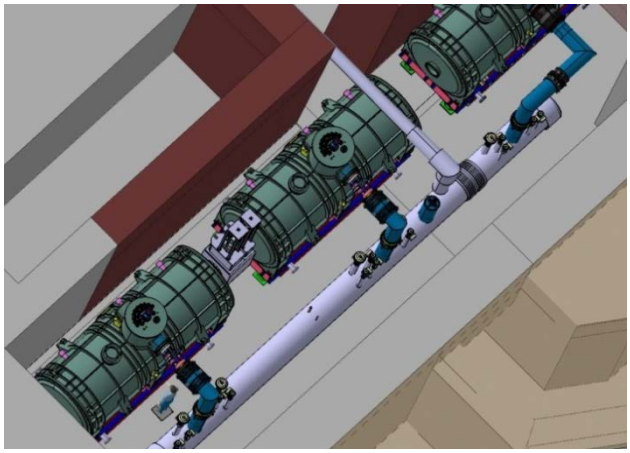

Figure 3: Conceptual design of cryo branch T.

References

[1] Y. Xiang and F. Wamers, "Static Heat Loads and Cool-Down of the Super-FRS", November 2015, https://edms.cern.ch/document/1552771/6

DOI:10.15120/GR-2016-1

Super-FRS design status report*

M. Winkler† [1], *S. Althoff*[1], *F. Amjad*[1], *K.-H. Behr*[1], *A. Bergmann*[1], *T. Blatz*[1], *A. Brünle*[1], *E.J. Cho*[1], *W. Freisleben*[1], *H. Geissel*[1,2], *M. Gleim*[1], *E. Kozlova*[1], *A. Krämer*[1], *A. Kratz*[1], *J. Kurdal*[1], *H. Leibrock*[1], *H. Müller*[1], *G. Münzenberg*[1], *C. Mühle*[1], *I. Mukha*[1], *C. Nociforo*[1], *S. Pietri*[1], *A. Prochazka*[1], *S. Purushothaman*[1], *M.V. Ricciardi*[1], *C. Scheidenberger*[1,2], *F. Schirru*[1], *C. Schlör*[1], *P. Schnizer*[1], *H. Simon*[1], *C. Schlör*[1], *P. Szwangruber*[1,3], *F. Wamers*[1], *H. Weick*[1], *A. Wiest*[1], *J.S. Winfield*[1], *and Y. Xiang*[1]

[1]GSI, Darmstadt, Germany; [2]JLU Giessen, Germany

System design

During 2015 the ion-optics for the Super-FRS, including the focusing system before the production target, has been slightly modified and improved. In particular, the focal plane at the exit of the LEB (FLF2) has been extended in order to house additional detectors from HISPEC/DESPEC and extra space has been allowed for the magnet cryostats of the Energy Buncher after first magnet designs had been completed by the Indian colleagues from VECC.

Based on the revised lattice of the Energy Buncher Spectrometer [1] the layout of the LEB cave has been worked out (see Fig. 1). The building includes various experimental stations of the HISPEC/DESPEC collaboration as well as the cryogenic stopping cell [2] which is located at the final focus of the Energy Buncher (FLF6) and which is then coupled to the MATS/LASPEC experimental area.

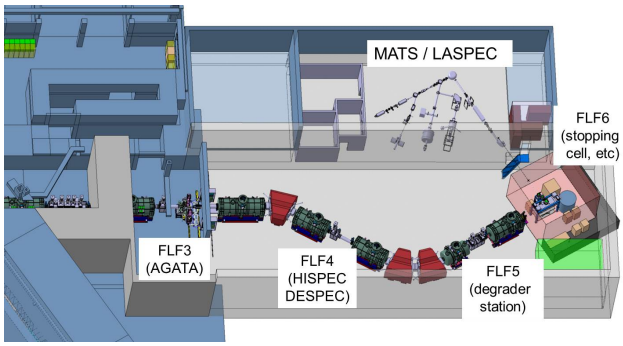

Figure 1: Layout of the LEB cave which houses the Energy Buncher, the HISPEC/DESPEC experimental areas, the stopping-cell, as well as the MATS/LASPEC. experiment

Magnets

On July 1^{st}, 2015 GSI awarded ASG Superconductors SpA in Genoa (Italy) a contract to design and manufacture the superconducting multiplets of the Super-FRS, which are one of its most important components. ASG has a long-standing experience in developing superconducting magnets. They provided, for example, one-third of the LHC dipole magnets at CERN and they participated in the development of the GLAD magnet system for the R3B experiment at FAIR. The contract amount is about 50 million Euros, which will be the largest purchase within the FAIR accelerator.

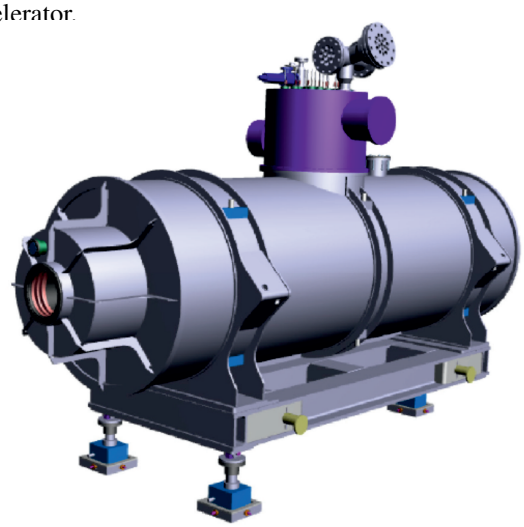

Figure 2: Preliminary model of the long Super-FRS SC multiplet. The overall length is approximately 7 m; beam axis is at 2 m and overall hight is about 4m. The system will weight 70 ton.

In the following two years it is foreseen to develop two types of first-of-series multiplets which then will be tested extensively at CERN prior to the series production of the remaining 31 multiplets. Fig. 2 shows the preliminary ASG model of the so-called long multiplet version.

CEA Saclay (France) could finalize the design of the superconducting dipole magnets for Super-FRS. A Concepual Design Report as well as the Detailed Specification for this magnet were established. These documents are the base for the tendering which is in preparation right now.

The redesign of the alignment support [3] for the radiation resistent magnet was finished and the construction of the new system is under way. Also all remote connectors for this magnet were revised in order to guarantee later a reliable operation of this magnet which is located in the heavily shielded target area. It is foreseen to test all new components intensively in 2016 prior to finalize the specification. After that the tendering of the remaining radiation resistent magnets can be started.

* Work supported by EU, CRISP contract No. 283745
† m.winkler@gsi.de

Local cryogenics

The activities of Super-FRS local cryogenics concentrated on the design of the so-called jumper-connection which is the main interface between the feedbox and the SC magnet. This activity was mainly driven by the advanced planning of the test benches for magnet testing at CERN. Moreover the coupling of the cryogenic line to the LEB cave was initiated and we could establish a complete cryogenic heat load table for Super-FRS (including associated SC components from NUSTAR experiments). An important step was also the agreement on the strategy for procurement of local cryogenic components with the Polish in-kind partner. A dedicated report can be found at [4].

Target area / handling system

In 2015 we could detail the planning of the target area shielding [5] due to a) an advanced design of the overhead crane in the target building, b) an advanced planning of the mainetenance-tunnel (located directly above the beam tunnel), and c) last but not least the final fixing of the primary beam parameters. Consequently the iron shielding could be reduced significantly, a large amount of mobile shielding could be transformed into site concrete, and the slab shielding planning of the tunnel ceiling in the target area could be simlified considerably.

The Indian in-kind partner from CMERI presented a first complete design of the beam-catcher system which consists of a large volume vacuum chamber and the beam catchers itself (BC1 and BC2 fixed, BC3 movable) which are mounted on shielded plugs (see Fig. 3). The chamber includes the pillow seal interface (guidance frame) and also a special designed pumping port which weakens the radiation shielding as less as possible.

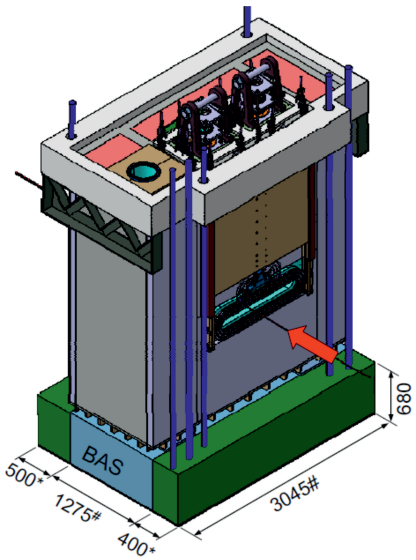

Figure 3: Preliminary design of the BC3 chamber

The specification for the target chamber and its plug inserts could be finalized. A collaboration contract with our colleagues from KVI-CART (the Netherlands) was set-up and is ready to sign. In a first step a fully design of the complete system is planned which includes e.g. also integrated optical diagnostics for the high-power production target. A challanging part is the guidence sytem of plugs inside the chamber and the ineterface to the transport flask which actually is an Finnish in-kind contribution. It was agreed to build a dedicated mock-up for this part within the collaboration contract.

Beam instrumentation

The first-of-seriesx- slit system was built by the colleagues from KVI-CART (see Fig. 4). The slits themself consist of two Densimet blocks having dimensions of 195x180x250 mm^3.The opening of the slits is +/-195 mm whith a precision of +/-0.1 mm. Long-term test are ongoing and the FAT is expected to be finalized in mid 2016.

Figure 4: Test set-up of the FoS x-slit system

R&D and establishing of specification for various types of detectors could be pushed such as for the PDC, the SEM grids (beam profiler), and diamond and silicon detectors (ToF). In particular the prototype development of the GEM-TPC (tracking detector) was further advanced together with the colleagues from HIP, Finland. It will be tested for the first time with the new developed GEMEX read-out electronics at GSI during this year's beam time.

References

[1] H. Geissel et al., "Dispersion-matched spectrometer in the low-energy branch of Super-FRS", NIM B 317 (2013) 227

[2] T. Dickel et al., 'Rate Capability of the Prototype Cryogenic Stopping Cell for the Super-FRS", this report

[3] M. Winkler et al., "Super-FRS Design Status Report", GSI Scientific Report 2014 (2015) 496

[4] F. Wamers et al., "Status of the Super-FRS Local Cryogenics", this report

[5] I. Conrad et al., "Adaption of the Super-FRS Shielding Layout", this report

DOI:10.15120/GR-2016-1

Publications and dissertations in 2015

Matter and universe – 610

174 publications listed in Web of Science or SCOPUS

M. Ablikim et al.
Amplitude analysis of the $\pi^0\pi^0$ system produced in radiative J/ψ decays.
Physical review / D, 92(5):052003.
doi: 10.1103/PhysRevD.92.052003.

M. Ablikim et al.
Confirmation of a charged charmoniumlike state $Z_c(3885)^{\mp}$ in $e^+e^- \to \pi^{\pm}(D\bar{D}^*)^{\mp}$ with double D tag.
Physical review / D, 92(9):092006.
doi: 10.1103/PhysRevD.92.092006.

M. Ablikim et al.
Evidence for $e^+e^- \to \gamma\chi_{c1,2}$ at center-of-mass energies from 4.009 to 4.360 GeV.
Chinese physics / C, 39(4):041001.
doi: 10.1088/1674-1137/39/4/041001.

M. Ablikim et al.
Measurement of $\mathcal{B}(\psi(3770) \to \gamma\chi_{c1})$ and search for $\psi(3770) \to \gamma\chi_{c2}$.
Physical review / D, 91(9):092009.
doi: 10.1103/PhysRevD.91.092009.

M. Ablikim et al.
Measurement of the Absolute Branching Fraction for $\Lambda_c^+ \to \Lambda e^+\nu_e$.
Physical review letters, 115(22):221805.
doi: 10.1103/PhysRevLett.115.221805.

M. Ablikim et al.
Measurement of the $e^+e^- \to \eta J/\psi$ cross section and search for $e^+e^- \to \pi^0 J/\psi$ at center-of-mass energies between 3.810 and 4.600 GeV.
Physical review / D, 91(11):112005.
doi: 10.1103/PhysRevD.91.112005.

M. Ablikim et al.
Measurement of the form factors in the decay $D^+ \to \omega e^+\nu_e$ and search for the decay $D^+ \to \phi e^+\nu_e$.
Physical review / D, 92(7):071101.
doi: 10.1103/PhysRevD.92.071101.

M. Ablikim et al.
Measurement of the matrix elements for the decays $\eta \to \pi^+\pi^-\pi^0$ and $\eta/\eta' \to \pi^0\pi^0\pi^0$.
Physical review / D, 92(1):012014.
doi: 10.1103/PhysRevD.92.012014.

M. Ablikim et al.
Measurement of the proton form factor by studying $e^+e^- \to p\bar{p}$.
Physical review / D, 91(11):112004.
doi: 10.1103/PhysRevD.91.112004.

M. Ablikim et al.
Measurements of $\psi(3686) \to K^-\Lambda\bar{\Xi}^+ + c.c.$ and $\psi(3686) \to \gamma K^-\Lambda\bar{\Xi}^+ + c.c.$.
Physical review / D, 91(9):092006.
doi: 10.1103/PhysRevD.91.092006.

M. Ablikim et al.
Observation and Spin-Parity Determination of the $X(1835)$ in $J/\psi \to \gamma K_S^0 K_S^0 \eta$.
Physical review letters, 115(9):091803.
doi: 10.1103/PhysRevLett.115.091803.

M. Ablikim et al.
Observation of a Neutral Charmoniumlike State $Z_c(4025)^0$ in $e^+e^- \to (D^*\bar{D}^*)^0\pi^0$.
Physical review letters, 115(18):182002.
doi: 10.1103/PhysRevLett.115.182002.

M. Ablikim et al.
Observation of a Neutral Structure near the $D\bar{D}^*$ Mass Threshold in $e^+e^- \to (D\bar{D}^*)^0\pi^0$ at $\sqrt{s} = 4.226$ and 4.257 GeV.
Physical review letters, 115(22):222002.
doi: 10.1103/PhysRevLett.115.222002.

M. Ablikim et al.
Observation of $\eta' \to \omega e^+e^-$.
Physical review / D, 92(5):051101.
doi: 10.1103/PhysRevD.92.051101.

M. Ablikim et al.
Observation of the $\psi(1^3D_2)$ State in $e^+e^- \to \pi^+\pi^-\gamma\chi_{c1}$ at BESIII.
Physical review letters, 115(1):011803.
doi: 10.1103/PhysRevLett.115.011803.

M. Ablikim et al.
Observation of the Dalitz decay $\eta' \to \gamma e^+e^-$.
Physical review / D, 92(1):012001.
doi: 10.1103/PhysRevD.92.012001.

M. Ablikim et al.
Observation of the electromagnetic doubly OZI-suppressed decay $J/\psi \to \phi\pi^0$.
Physical review / D, 91(11):112001.
doi: 10.1103/PhysRevD.91.112001.

M. Ablikim et al.
Observation of the isospin-violating decay $J/\psi \to \phi\pi^0 f^0(980)$.
Physical review / D, 92(1):012007.
doi: 10.1103/PhysRevD.92.012007.

M. Ablikim et al.
Observation of $Z_c(3900)^0$ in $e^+e^- \to \pi^0\pi^0 J/\psi$.
Physical review letters, 115(11):112003.
doi: 10.1103/PhysRevLett.115.112003.

M. Ablikim et al.
Precision measurement of the integrated luminosity of the data taken by BESIII at center-of-mass energies between 3.810 GeV and 4.600 GeV.
Chinese physics / C, 39(9):093001.
doi: 10.1088/1674-1137/39/9/093001.

M. Ablikim et al.
Search for $D^0 \to \gamma\gamma$ and improved measurement of the branching fraction for $D^0 \to \pi^0\pi^0$.
Physical review / D, 91(11):112015.
doi: 10.1103/PhysRevD.91.112015.

M. Ablikim et al.
Search for the isospin violating decay $Y(4260) \to J/\psi\eta\pi^0$.
Physical review / D, 92(1):012008.
doi: 10.1103/PhysRevD.92.012008.

M. Ablikim et al.
Search for the Y(4140) via $e^+e^- \to \gamma\phi J/\psi$ at $\sqrt{s}$ = 4.23 , 4.26 and 4.36 GeV.
Physical review / D, 91(3):032002.
doi: 10.1103/PhysRevD.91.032002.

M. Ablikim et al.
Search for $Z_c(3900)^\pm \to \omega\pi^\pm$.
Physical review / D, 92(3):032009.
doi: 10.1103/PhysRevD.92.032009.

M. Ablikim et al.
Searches for isospin-violating transitions $\chi_{c0,2} \to \pi^0\eta_c$.
Physical review / D, 91(11):112018.
doi: 10.1103/PhysRevD.91.112018.

M. Ablikim et al.
Study of χ_{cJ} decaying into $\phi K^*(892)\bar{K}$.
Physical review / D, 91(11):112008.
doi: 10.1103/PhysRevD.91.112008.

M. Ablikim et al.
Study of decay dynamics and C P asymmetry in $D^+ \to K_L^0 e^+ \nu_e$ decay.
Physical review / D, 92(11):112008.
doi: 10.1103/PhysRevD.92.112008.

M. Ablikim et al.
Study of dynamics of $D^0 \to K^- e^+ \nu_e$ and $D^0 \to \pi^- e^+ \nu_e$ decays.
Physical review / D, 92(7):072012.
doi: 10.1103/PhysRevD.92.072012.

M. Ablikim et al.
Study of $e^+e^- \to \omega\chi_{cJ}$ at Center of Mass Energies from 4.21 to 4.42 GeV.
Physical review letters, 114(9):092003.
doi: 10.1103/PhysRevLett.114.092003.

M. Ablikim et al.
Study of $J/\psi \to \eta\phi\pi^+\pi^-$ at BESIII.
Physical review / D, 91(5):052017.
doi: 10.1103/PhysRevD.91.052017.

D. Ackermann*.
Nuclear spectroscopy in nuclei with Z≥110.
Nuclear physics / A, 944:376.
doi: 10.1016/j.nuclphysa.2015.09.002.

J. Adam et al.
Coherent ρ^0 photoproduction in ultra-peripheral Pb-Pb collisions at $\sqrt{s_{\rm NN}} = 2.76$ TeV.
Journal of high energy physics, 2015(9):95.
doi: 10.1007/JHEP09(2015)095.

G. Agakishiev et al.
K*(892)$^+$ production in proton-proton collisions at $E_{beam} = 3.5$ GeV.
Physical review / C, 92(2):024903.
doi: 10.1103/PhysRevC.92.024903.

G. Agakishiev et al.
Study of the quasi-free $np \to np\pi^+\pi^-$ reaction with a deuterium beam at 1.25 GeV/nucleon.
Physics letters / B, 750:184.
doi: 10.1016/j.physletb.2015.09.016.

G. Agakishiev et al.
Subthreshold Ξ- Production in Collisions of p(3.5 GeV)+Nb.
Physical review letters, 114(21):212301.
doi: 10.1103/PhysRevLett.114.212301.

M. E. E. Aguado et al.
Shapes of ^{192,190}Pb ground states from β -decay studies using the total-absorption technique.
Physical review / C, 92(4):044321.
doi: 10.1103/PhysRevC.92.044321.

J. Aichelin et al.
K^+ mesons, a robust probe to measure the hadronic equation of state?
Physics of particles and nuclei, 46(5):737.
doi: 10.1134/S1063779615050020.

A. Akber et al.
Increased isomeric lifetime of hydrogen-like ^{192m}Os.
Physical review / C, 91(3):031301.
doi: 10.1103/PhysRevC.91.031301.

J. Alcántara-Núñez et al.
Isotopic yields of spallation residues produced in ^{136}Xe-induced reactions on deuterium at 500 A MeV.
Physical review / C, 92(2):024607.
doi: 10.1103/PhysRevC.92.024607.

T. Alexander et al.
Isomeric Ratios in ^{206}Hg.
Acta physica Polonica / B, 46(3):601.
doi: 10.5506/APhysPolB.46.601.

ALICE Collaboration*.
Centrality dependence of high-p$_T$ D meson suppression in Pb-Pb collisions at $\sqrt{s_{\rm NN}} = 2.76$ TeV.
Journal of high energy physics, 2015(11):205.
doi: 10.1007/JHEP11(2015)205.

DOI:10.15120/GR-2016-1

ALICE Collaboration*.
Centrality dependence of inclusive J/ψ production in p-Pb collisions at $\sqrt{s_{\rm NN}} = 5.02$ TeV.
Journal of high energy physics, 2015(11):127.
doi: 10.1007/JHEP11(2015)127.

ALICE Collaboration*.
Centrality dependence of particle production in p − Pb collisions at s NN = 5.02 TeV.
Physical review / C, 91(6):064905.
doi: 10.1103/PhysRevC.91.064905.

ALICE Collaboration*.
Charged jet cross sections and properties in proton-proton collisions at $\sqrt{s}$ = 7 TeV.
Physical review / D, 91(11):112012.
doi: 10.1103/PhysRevD.91.112012.

ALICE Collaboration*.
Coherent ψ(2S) photo-production in ultra-peripheral Pb-Pb collisions at $\sqrt{s_{\rm NN}} = 2.76$ TeV.
Physics letters / B, 751:358.
doi: 10.1016/j.physletb.2015.10.040.

ALICE Collaboration*.
Elliptic flow of identified hadrons in Pb-Pb collisions at $\sqrt{s_{\rm NN}} =$ 2.76 TeV.
Journal of high energy physics, 2015(6):190.
doi: 10.1007/JHEP06(2015)190.

ALICE Collaboration*.
Forward-backward multiplicity correlations in pp collisions at s $\sqrt{s}$ = 0.9, 2.76 and 7 TeV.
Journal of high energy physics, 2015(5):97.
doi: 10.1007/JHEP05(2015)097.

ALICE Collaboration*.
Inclusive photon production at forward rapidities in proton–proton collisions at $\sqrt{\rm s}$ = 0.9, 2.76 and 7 TeV.
The European physical journal / C, 75(4):146.
doi: 10.1140/epjc/s10052-015-3356-2.

ALICE Collaboration*.
Inclusive, prompt and non-prompt J/ψ production at midrapidity in Pb-Pb collisions at $\sqrt{s_{\rm NN}} = 2.76$ TeV.
Journal of high energy physics, 2015(7):51.
doi: 10.1007/JHEP07(2015)051.

ALICE Collaboration*.
K*(892)^0 and (1020) production in Pb-Pb collisions at $\sqrt{s_{NN}}$ = 2.76 TeV.
Physical review / C, 91(2):024609.
doi: 10.1103/PhysRevC.91.024609.

ALICE Collaboration*.
Measurement of charged jet production cross sections and nuclear modification in p–Pb collisions at $\sqrt{s_{\rm NN}} = 5.02$ TeV.
Physics letters / B, 749:68.
doi: 10.1016/j.physletb.2015.07.054.

ALICE Collaboration.
Measurement of charm and beauty production at central rapidity versus charged-particle multiplicity in proton-proton collisions at $\sqrt{s} = 7$ TeV.
Journal of high energy physics, 1509(9):148.
doi: 10.1007/JHEP09(2015)148.

ALICE Collaboration.
Measurement of dijet $k_{\rm T}$ in p-Pb collisions at $\sqrt{s_{\rm NN}} = 5.02$ TeV.
Physics letters / B, 746:385.
doi: 10.1016/j.physletb.2015.05.033.

ALICE Collaboration*.
Measurement of jet quenching with semi-inclusive hadron-jet distributions in central Pb-Pb collisions at $\sqrt{s_{\rm NN}} = 2.76$ TeV.
Journal of high energy physics, 2015(9):170.
doi: 10.1007/JHEP09(2015)170.

ALICE Collaboration*.
Measurement of jet suppression in central Pb–Pb collisions at $\sqrt{s_{\rm NN}} = 2.76$ TeV.
Physics letters / B, 746:1.
doi: 10.1016/j.physletb.2015.04.039.

ALICE Collaboration*.
Measurement of pion, kaon and proton production in proton–proton collisions at $\sqrt{s} = 7$ TeV.
The European physical journal / C, 75(5):226.
doi: 10.1140/epjc/s10052-015-3422-9.

ALICE Collaboration*.
One-dimensional pion, kaon, and proton femtoscopy in Pb-Pb collisions at $\sqrt{s_{\rm NN}}$ = 2.76 TeV.
Physical review / C, 92(5):054908.
doi: 10.1103/PhysRevC.92.054908.

ALICE Collaboration*.
Precision measurement of the mass difference between light nuclei and anti-nuclei.
Nature physics, 11(10):811.
doi: 10.1038/nphys3432.

ALICE Collaboration*.
Production of $(1385)^{\pm}$ and $(1530)^{0}$ in proton–proton collisions at $\sqrt{\rm s} = 7$ TeV.
The European physical journal / C, 75(1):1.
doi: 10.1140/epjc/s10052-014-3191-x.

ALICE Collaboration*.
Production of inclusive (1S) and (2S) in p–Pb collisions at $\sqrt{s_{\rm NN}} = 5.02$ TeV.
Physics letters / B, 740:105.
doi: 10.1016/j.physletb.2014.11.041.

ALICE Collaboration*.
Rapidity and transverse-momentum dependence of the inclusive J/ψ nuclear modification factor in p-Pb collisions at $\sqrt{s_{\rm NN}}$ = 5.02 TeV.
Journal of high energy physics, 2015(6):55.
doi: 10.1007/JHEP06(2015)055.

ALICE Collaboration*.
Two-pion femtoscopy in p -Pb collisions at s N N = 5.02 TeV.
Physical review / C, 91(3):034906.
doi: 10.1103/PhysRevC.91.034906.

G. A. Almási* and G. Wolf.
Thermal, chemical and spectral equilibration in heavy-ion collisions.
Nuclear physics / A, 943:117.
doi: 10.1016/j.nuclphysa.2015.09.003.

C. Amsler et al.
Spin density matrix of the ω in the reaction $\bar{p}p \to \omega\pi^0$.
The European physical journal / C, 75(3):124.
doi: 10.1140/epjc/s10052-015-3341-9.

S. Antalic et al.
Nuclear Isomers in ^{259}Sg and ^{255}Rf.
The European physical journal / A, 51(4):41.
doi: 10.1140/epja/i2015-15041-0.

S. Antić and S. Typel*.
Neutron star equations of state with optical potential constraint.
Nuclear physics / A, 938:92.
doi: 10.1016/j.nuclphysa.2015.03.004.

M. Asai, F.-P. Hessberger* and A. Lopez-Martens.
Nuclear structure of elements with 100≤Z≤109 from alpha spectroscopy.
Nuclear physics / A, 944:308.
doi: 10.1016/j.nuclphysa.2015.06.011.

H. Backe et al.
Prospects for laser spectroscopy, ion chemistry and mobility measurements of superheavy elements in buffer-gas traps.
Nuclear physics / A, 944:492.
doi: 10.1016/j.nuclphysa.2015.07.002.

K. G. Balasi, K. Langanke* and G. M. Pinedo*.
Neutrino–nucleus reactions and their role for supernova dynamics and nucleosynthesis.
Progress in particle and nuclear physics, 85:33.
doi: 10.1016/j.ppnp.2015.08.001.

S. Benić et al.
A new quark-hadron hybrid equation of state for astrophysics.
Astronomy and astrophysics, 577:A40.
doi: 10.1051/0004-6361/201425318.

BESIII Collaboration.
Measurement of the branching fractions of $D_s^+ \to \eta' X$ and $D_s^+ \to \eta'\rho^+$ in $e^+e^- \to D_s^+ D_s^-$.
Physics letters / B, 750:466.
doi: 10.1016/j.physletb.2015.09.059.

BESIII Collaboration.
Measurement of y_{CP} in D^0–$\bar{D}^0$ oscillation using quantum correlations in $e^+e^- \to D^0\bar{D}^0$ at $\sqrt{s}$=3.773 GeV.
Physics letters / B, 744:339.
doi: 10.1016/j.physletb.2015.04.008.

BESIII collaboration.
An Improved Limit for Γ_{ee} of X(3872) and Γ_{ee} Measurement of $\psi(3686)$.
Physics letters / B, 749:414.
doi: 10.1016/j.physletb.2015.08.013.

R. S. Bhalerao, A. Jaiswal* and S. Pal.
Collective flow in event-by-event partonic transport plus hydrodynamics hybrid approach.
Physical review / C, 92(1):014903.
doi: 10.1103/PhysRevC.92.014903.

J. W. Blanchard* et al.
Measurement of untruncated nuclear spin interactions via zero- to ultralow-field nuclear magnetic resonance.
Physical review / B, 92(22):220202.
doi: 10.1103/PhysRevB.92.220202.

A. Blanco et al.
Performance of timing resistive plate chambers with relativistic neutrons from 300 to 1500 MeV.
Journal of Instrumentation, 10(02):C02034.
doi: 10.1088/1748-0221/10/02/C02034.

M. Block*.
Direct mass measurements of the heaviest elements with Penning traps.
Nuclear physics / A, 944:471.
doi: 10.1016/j.nuclphysa.2015.09.009.

A. Borschevsky* et al.
Ionization potentials and electron affinities of the superheavy elements 115–117 and their sixth-row homologues Bi, Po, and At.
Physical review / A, 91(2):020501.
doi: 10.1103/PhysRevA.91.020501.

B. B. Brandt et al.
Pion quasiparticle in the low-temperature phase of QCD.
Physical review / D, 92(9):094510.
doi: 10.1103/PhysRevD.92.094510.

P. Braun-Munzinger* et al.
Confronting fluctuations of conserved charges in central nuclear collisions at the LHC with predictions from Lattice QCD.
Physics letters / B, 747:292.
doi: 10.1016/j.physletb.2015.05.077.

F. Browne et al.
Gamma-ray Spectroscopy in the Vicinity of ^{108}Zr.
Acta physica Polonica / B, 46(3):721.
doi: 10.5506/APhysPolB.46.721.

F. Browne et al.
Lifetime measurements of the first 2^+ states in ^{104,106}Zr: Evolution of ground-state deformations.
Physics letters / B, 750:448.
doi: 10.1016/j.physletb.2015.09.043.

S. Capitani* et al.
Nucleon electromagnetic form factors in two-flavor QCD.
Physical review / D, 92(5):054511.
doi: 10.1103/PhysRevD.92.054511.

J. M. Cornejo et al.
Extending the applicability of an open-ring trap to perform experiments with a single laser-cooled ion.
Review of scientific instruments, 86(10):103104.
doi: 10.1063/1.4932310.

DOI:10.15120/GR-2016-1

U. Datta et al.
Response of multi-strip multi-gap resistive plate chamber.
Journal of Instrumentation, 10(07):P07005.
doi: 10.1088/1748-0221/10/07/P07005.

H. M. Deveraja* et al.
Observation of new Neutron-deficient isotopes with Z≥92 in multinucleon Transfer reactions.
Physics letters / B, 748:199.
doi: 10.1016/j.physletb.2015.07.006.

T. Dickel* et al.
A high-performance multiple-reflection time-of-flight mass spectrometer and isobar separator for the research with exotic nuclei.
Nuclear instruments & methods in physics research / A, 777:172.
doi: 10.1016/j.nima.2014.12.094.

T. Dickel* et al.
First spatial separation of a heavy ion isomeric beam with a multiple-reflection time-of-flight mass spectrometer.
Physics letters / B, 744:137.
doi: 10.1016/j.physletb.2015.03.047.

D. Djukanovic et al.
Complex-mass renormalization in hadronic EFT: Applicability at two-loop order.
The European physical journal / A, 51(8):101.
doi: 10.1140/epja/i2015-15101-5.

C. E. Düllmann*.
Seaborgium's complex studies.
Nature chemistry, 7(9):760.
doi: 10.1038/nchem.2328.

C. E. Düllmann* et al.
Nuclear Physics A - Special Issue on Superheavy Elements - Foreword.
Nuclear physics / A, 944:1.
doi: 10.1016/j.nuclphysa.2015.11.004.

A. A. Dzhioev, A. I. Vdovin and J. Wambach*.
Neutrino absorption by hot nuclei in supernova environments.
Physical review / C, 92(4):045804.
doi: 10.1103/PhysRevC.92.045804.

P. Egelhof*, Y. Litvinov* and M. Steck*.
[Preface] Proceedings of the 9th International Conference on Nuclear Physics at Storage Rings STORI'14.
Physica scripta, T166:010301.
doi: 10.1088/0031-8949/2015/T166/010301.

M. Eichler et al.
The role of fission in neutron star mergers and its impact on the r-process peaks.
The astrophysical journal / 1, 808(1):30.
doi: 10.1088/0004-637X/808/1/30.

S. Eliseev et al.
Direct Measurement of the Mass Difference of ^{163}Ho and ^{163}Dy Solves the Q-Value Puzzle for the Neutrino Mass Determination.
Physical review letters, 115(6):062501.
doi: 10.1103/PhysRevLett.115.062501.

A. Esser et al.
Observation of H Λ 4 Hyperhydrogen by Decay-Pion Spectroscopy in Electron Scattering.
Physical review letters, 114(23):232501.
doi: 10.1103/PhysRevLett.114.232501.

J. Even* et al.
In situ synthesis of volatile carbonyl complexes with short-lived nuclides.
Journal of radioanalytical and nuclear chemistry, 303(3):2457.
doi: 10.1007/s10967-014-3793-7.

D. Farfurnik et al.
Optimizing a dynamical decoupling protocol for solid-state electronic spin ensembles in diamond.
Physical review / B, 92(6):060301.
doi: 10.1103/PhysRevB.92.060301.

T. Feldker et al.
Rydberg Excitation of a Single Trapped Ion.
Physical review letters, 115(17):173001.
doi: 10.1103/PhysRevLett.115.173001.

J. P. Fernández-García et al.
Simultaneous analysis of the elastic scattering and breakup channel for the reaction $^{11}Li + ^{208}Pb$ at energies near the Coulomb barrier.
Physical review / C, 92(4):044608.
doi: 10.1103/PhysRevC.92.044608.

L. Fister and J. M. Pawlowski.
Functional renormalization group in a finite volume.
Physical review / D, 92(7):076009.
doi: 10.1103/PhysRevD.92.076009.

B. Friman* et al.
Strangeness fluctuations from K − π interactions.
Physical review / D, 92(7):074003.
doi: 10.1103/PhysRevD.92.074003.

H. Fujioka et al.
Search for η'(958)–nucleus Bound States by (p,d) Reaction at GSI and FAIR.
Acta physica Polonica / B, 46(1):127.
doi: 10.5506/APhysPolB.46.127.

J. M. Gates et al.
Decay spectroscopy of element 115 daughters: ^{280}Rg → ^{276}Mt and ^{276}Mt → ^{272}Bh.
Physical review / C, 92(2):021301.
doi: 10.1103/PhysRevC.92.021301.

S. Goriely and G. M. Pinedo*.
The production of transuranium elements by the r-process nucleosynthesis.
Nuclear physics / A, 944:158.
doi: 10.1016/j.nuclphysa.2015.07.020.

J. Green et al.
Lattice QCD Calculation of Hadronic Light-by-Light Scattering.
Physical review letters, 115(22):222003.
doi: 10.1103/PhysRevLett.115.222003.

V. Gülpers, G. von Hippel and H. Wittig*.
The scalar radius of the pion from lattice QCD in the continuum limit.
The European physical journal / A, 51(12):158.
doi: 10.1140/epja/i2015-15158-0.

T. Harris* and H. B. Meyer*.
Nonperturbative improvement of the vector current in Wilson lattice QCD.
Physical review / D, 92(11):114503.
doi: 10.1103/PhysRevD.92.114503.

M. Heil* et al.
Erratum: Stellar neutron capture cross sections of ^{20,21,22}Ne [Phys. Rev. C 90 , 045804 (2014)].
Physical review / C, 92(1):019902.
doi: 10.1103/PhysRevC.92.019902.

S. Heinz* et al.
Nuclear molecule Formation and time delay in collisions of nuclei with $Z_1 + Z_2 \geq 110$.
The European physical journal / A, 51(11):140.
doi: 10.1140/epja/i2015-15140-x.

M. Hempel et al.
Constraining supernova equations of state with equilibrium constants from heavy-ion collisions.
Physical review / C, 91(4):045805.
doi: 10.1103/PhysRevC.91.045805.

J. d. J. Mendoza-Temis et al.
Nuclear robustness of the r process in neutron-star mergers.
Physical review / C, 92(5):055805.
doi: 10.1103/PhysRevC.92.055805.

K. Jadambaa* et al.
Experimental study of the quasifission, fusion-fission, and deexcitation of Cf compound nuclei.
Physical review / C, 91(5):054608.
doi: 10.1103/PhysRevC.91.054608.

K. Jadambaa* et al.
New Short-Lived Isotope ^{221}U and the Mass Surface Near N = 126.
Physical review letters, 115(24):242502.
doi: 10.1103/PhysRevLett.115.242502.

A. Jaiswal, B. Friman and K. Redlich*.
Relativistic second-order dissipative hydrodynamics at finite chemical potential.
Physics letters / B, 751:548.
doi: 10.1016/j.physletb.2015.11.018.

A. Jarmola et al.
Longitudinal spin-relaxation in nitrogen-vacancy centers in electron irradiated diamond.
Applied physics letters, 107(24):242403.
doi: 10.1063/1.4937489.

Z. Kalaninová et al.
Levels in ^{223}Th populated by Alpha decay of ^{227}U.
Physical review / C, 92(1):014321.
doi: 10.1103/PhysRevC.92.014321.

O. Kiselev*.
The EXL project, recent results and future perspectives.
Physica scripta, T166:014004.
doi: 10.1088/0031-8949/2015/T166/014004.

S. Kraft-Bermuth et al.
Precise determination of the 1s Lamb Shift in hydrogen-like heavy ions at the ESR storage ring using microcalorimeters.
Physica scripta, T166:014028.
doi: 10.1088/0031-8949/2015/T166/014028.

K. Langanke* and G. M. Pinedo*.
Recent progress and some open questions in nuclear astrophysics.
Physica scripta, T166:014001.
doi: 10.1088/0031-8949/2015/T166/014001.

C. Lederer et al.
Erratum: $^{62}Ni(n,\gamma)$ and $^{63}Ni(n,\gamma)$ cross sections measured at the n_TOF facility at CERN [Phys. Rev. C 89 , 025810 (2014)].
Physical review / C, 92(1):019903.
doi: 10.1103/PhysRevC.92.019903.

T.-G. Lee et al.
Landau-Peierls instability in a Fulde-Ferrell type inhomogeneous chiral condensed phase.
Physical review / D, 92(3):034024.
doi: 10.1103/PhysRevD.92.034024.

A. A. Lis et al.
β-delayed three-proton decay of ^{31}Ar.
Physical review / C, 91(6):064309.
doi: 10.1103/PhysRevC.91.064309.

A. S. Lorente* et al.
Antihyperon potentials in nuclei via exclusive antiproton–nucleus reactions.
Physics letters / B, 749:421.
doi: 10.1016/j.physletb.2015.08.025.

G. Lorusso et al.
β -Decay Half-Lives of 110 Neutron-Rich Nuclei across the N = 82 Shell Gap: Implications for the Mechanism and Universality of the Astrophysical r Process.
Physical review letters, 114(19):192501.
doi: 10.1103/PhysRevLett.114.192501.

R. Lozeva et al.
New decay scheme of the $^{136}_{51}Sb_{85}$ 6^- isomer.
Physical review / C, 92(2):024304.
doi: 10.1103/PhysRevC.92.024304.

M. Lutz*, E. E. Kolomeitsev and C. L. Korpa.
Spectral representation for u - and t -channel exchange processes in a partial-wave decomposition.
Physical review / D, 92(1):016003.
doi: 10.1103/PhysRevD.92.016003.

J. Machado et al.
Performance of timing Resistive Plate Chambers with protons from 200 to 800 MeV.
Journal of Instrumentation, 10(01):C01043.
doi: 10.1088/1748-0221/10/01/C01043.

DOI:10.15120/GR-2016-1

J. Marganiec* et al.
Studies of continuum states in ^{16}Ne using three-body correlation techniques.
The European physical journal / A, 51(1):9.
doi: 10.1140/epja/i2015-15009-0.

J.-F. Martin et al.
Studies on fission with ALADIN.
The European physical journal / A, 51(12):174.
doi: 10.1140/epja/i2015-15174-0.

B. Mei* et al.
First measurement of the Ru $^{96}(p,\gamma)$Rh^{97} cross section for the p process with a storage ring.
Physical review / C, 92(3):035803.
doi: 10.1103/PhysRevC.92.035803.

F. Molina et al.
T_z = − 1 → 0 β decays of ^{54}Ni, ^{50}Fe, ^{46}Cr , and ^{42}Ti and comparison with mirror (^{3}He, t) measurements.
Physical review / C, 91(1):014301.
doi: 10.1103/PhysRevC.91.014301.

A. I. Morales et al.
First measurement of the β -decay half-life of ^{206}Au.
epl, 111(5):52001.
doi: 10.1209/0295-5075/111/52001.

I. Mukha* et al.
Observation and Spectroscopy of New Proton-Unbound Isotopes ^{30}Ar and ^{29}Cl : An Interplay of Prompt Two-Proton and Sequential Decay.
Physical review letters, 115(20):202501.
doi: 10.1103/PhysRevLett.115.202501.

G. Münzenberg*.
From bohrium to copernicium and beyond SHE research at SHIP.
Nuclear physics / A, 944:5.
doi: 10.1016/j.nuclphysa.2015.06.008.

M. Mutterer et al.
Experimental techniques for in-ring reaction experiments.
Physica scripta, T166:014053.
doi: 10.1088/0031-8949/2015/T166/014053.

T. Neff*, H. Feldmeier* and W. Horiuchi.
Short-range correlations in nuclei with similarity renormalization group transformations.
Physical review / C, 92(2):024003.
doi: 10.1103/PhysRevC.92.024003.

K. Nishio et al.
Excitation energy dependence of fragment-mass distributions from fission of ^{180,190}Hg formed in fusion reactions of ^{36}Ar + ^{144,154}Sm.
Physics letters / B, 748:89.
doi: 10.1016/j.physletb.2015.06.068.

K. Ooe et al.
Development of a new continuous dissolution apparatus with a hydrophobic membrane for superheavy element chemistry.
Journal of radioanalytical and nuclear chemistry, 303(2):1317.
doi: 10.1007/s10967-014-3469-3.

V. Perschina-Nägele*.
Electronic structure and properties of superheavy elements.
Nuclear physics / A, 944:578.
doi: 10.1016/j.nuclphysa.2015.04.007.

K. Piasecki et al.
Influence of mesons on negative kaons in Ni + Ni collisions at 1.91 A GeV beam energy.
Physical review / C, 91(5):054904.
doi: 10.1103/PhysRevC.91.054904.

E. Prasad et al.
Observation of mass-asymmetric fission of mercury nuclei in heavy ion fusion.
Physical review / C, 91(6):064605.
doi: 10.1103/PhysRevC.91.064605.

V. Prassa et al.
High- K isomers in transactinide nuclei close to N = 162.
Physical review / C, 91(3):034324.
doi: 10.1103/PhysRevC.91.034324.

S. Pustelny et al.
Nonlinear magneto-optical rotation in rubidium vapor excited with blue light.
Physical review / A, 92(5):053410.
doi: 10.1103/PhysRevA.92.053410.

D. Ralet* et al.
Data-flow coupling and data-acquisition triggers for the PreSPEC-AGATA campaign at GSI.
Nuclear instruments & methods in physics research / A, 786:32.
doi: 10.1016/j.nima.2015.03.025.

M. Ranjan et al.
Design, construction and cooling system performance of a prototype cryogenic stopping cell for the Super-FRS at FAIR.
Nuclear instruments & methods in physics research / A, 770:87.
doi: 10.1016/j.nima.2014.09.075.

C. Rappold* et al.
Hypernuclear production cross section in the reaction of ^{6}Li + ^{12}C at 2AGeV.
Physics letters / B, 747:129.
doi: 10.1016/j.physletb.2015.05.059.

T. Rodriguez, A. Arzhanov and G. M. Pinedo*.
Toward global beyond-mean-field calculations of nuclear masses and low-energy spectra.
Physical review / C, 91(4):044315.
doi: 10.1103/PhysRevC.91.044315.

J. L. Rodríguez-Sánchez et al.
Complete characterization of the fission fragments produced in reactions induced by ^{208}Pb projectiles on proton at 500A MeV.
Physical review / C, 91(6):064616.
doi: 10.1103/PhysRevC.91.064616.

J. L. Rodríguez-Sánchez et al.
Constraining the level density using fission of lead projectiles.
Physical review / C, 92(4):044612.
doi: 10.1103/PhysRevC.92.044612.

T. K. Sato et al.
Measurement of the first ionization potential of lawrencium, element 103.
Nature, 520(7546):209.
doi: 10.1038/nature14342.

M. Schädel*.
Chemistry of the superheavy elements.
Philosophical transactions of the Royal Society of London / A, 373(2037):20140191.
doi: 10.1098/rsta.2014.0191.

M. v. Schmid et al.
Investigation of the nuclear matter distribution of ^{56}Ni by elastic proton scattering in inverse kinematics.
Physica scripta, T166:014005.
doi: 10.1088/0031-8949/2015/T166/014005.

F. Schneider et al.
Preparatory studies for a high-precision Penning-trap measurement of the ^{163}Ho electron capture Q-value.
The European physical journal / A, 51(7):89.
doi: 10.1140/epja/i2015-15089-8.

A. Sharma et al.
Optical control of resonant light transmission for an atom-cavity system.
Physical review / A, 91(4):043824.
doi: 10.1103/PhysRevA.91.043824.

Y. Shimizu et al.
Zero-field nuclear magnetic resonance spectroscopy of viscous liquids.
Journal of magnetic resonance, 250:1.
doi: 10.1016/j.jmr.2014.10.012.

H. Simon*.
The ELISe experiment, potential paths towards its realization.
Physica scripta, T166:014072.
doi: 10.1088/0031-8949/2015/T166/014072.

B. P. Singh et al.
Experimental access to Transition Distribution Amplitudes with the PANDA experiment at FAIR.
The European physical journal / A, 51(8):107.
doi: 10.1140/epja/i2015-15107-y.

P.-A. Söderström et al.
Two-hole structure outside ^{78}Ni: Existence of a μs isomer of ^{76}Co and β decay into ^{76}Ni.
Physical review / C, 92(5):051305.
doi: 10.1103/PhysRevC.92.051305.

H. Stöcker* et al.
Under-saturation of quarks at early stages of relativistic nuclear collisions: The hot glue initial scenario and its observable signatures.
Astronomische Nachrichten, 336(8-9):744.
doi: 10.1002/asna.201512252.

J. Struckmeier*, D. Vasak and H. Stoecker*.
Extended canonical field theory of matter and space-time.
Astronomische Nachrichten, 336(8-9):731.
doi: 10.1002/asna.201512247.

J. Taprogge et al.
β decay of ^{129}Cd and excited states in ^{129}In.
Physical review / C, 91(5):054324.
doi: 10.1103/PhysRevC.91.054324.

K. V. Tilburg et al.
Search for Ultralight Scalar Dark Matter with Atomic Spectroscopy.
Physical review letters, 115(1):011802.
doi: 10.1103/PhysRevLett.115.011802.

A. Toyoshima et al.
Chemical studies of Mo and W in preparation of a seaborgium (Sg) reduction experiment using MDG, FEC, and SISAK.
Journal of radioanalytical and nuclear chemistry, 303(2):1169.
doi: 10.1007/s10967-014-3438-x.

A. Türler, R. Eichler and A. Yakushev*.
Chemical studies of elements with Z104 in gas phase.
Nuclear physics / A, 944:640.
doi: 10.1016/j.nuclphysa.2015.09.012.

S. Typel*.
Cluster correlations in dense matter and equation of state.
Physics of particles and nuclei, 46(5):777.
doi: 10.1134/S1063779615050299.

S. Typel*, M. Oertel and T. Klähn.
CompOSE CompStar online supernova equations of state harmonising the concert of nuclear physics and astrophysics compose.obspm.fr.
Physics of particles and nuclei, 46(4):633.
doi: 10.1134/S1063779615040061.

F. Uhlig et al.
Breakthrough in the lifetime of microchannel plate photomultipliers.
Nuclear instruments & methods in physics research / A, 787:105.
doi: 10.1016/j.nima.2014.11.046.

A. Vascon et al.
Improving material properties and performance of nuclear targets for transmutation-relevant experiments.
Journal of radioanalytical and nuclear chemistry, 305(3):913.
doi: 10.1007/s10967-014-3916-1.

A. Vascon et al.
Quantitative molecular plating of large-area ^{242}Pu targets with improved layer properties.
Applied radiation and isotopes, 95:36.
doi: 10.1016/j.apradiso.2014.10.002.

L. v. d. Wense et al.
Determination of the extraction efficiency for ^{233}U source α-recoil ions from the MLL buffer-gas stopping cell.
The European physical journal / A, 51(3):29.
doi: 10.1140/epja/i2015-15029-8.

M.-R. Wu et al.
Effects of neutrino oscillations on nucleosynthesis and neutrino signals for an 18 M supernova model.
Physical review / D, 91(6):065016.
doi: 10.1103/PhysRevD.91.065016.

DOI:10.15120/GR-2016-1

M. I. Yavor* et al.
Ion-optical design of a high-performance multiple-reflection time-of-flight mass spectrometer and isobar separator.
International journal of mass spectrometry, 381-382:1.
doi: 10.1016/j.ijms.2015.01.002.

J. C. Zamora et al.
Isoscalar giant resonance studies in a stored-beam experiment within EXL.
Physica scripta, T166:014006.
doi: 10.1088/0031-8949/2015/T166/014006.

26 dissertations

L. Atar.
Investigation of the Single-Particle Structure of Oxygen Isotopes in Quasi-free Knockout Reactions at the R^{3}B/LAND Setup.
Technische Universität Darmstadt, 2015.

M. Bach*.
Energy- and cost-efficient Lattice-QCD computations using graphics processing units.
Johann Wolfgang Goethe-Universität Frankfurt, 2015.

G. Caspar*.
Semiklassische Beschreibung gebundener Zustände und der Vakuumfluktuationen in sphärisch symmetrischen Metriken.
Johann Wolfgang Goethe-Universität Frankfurt, 2015.

M. Diwisch.
Present and Future Isochronous Mass Spectrometry at GSI-FAIR: 25 New Masses of Fission Fragments, Novel Analysis Method, Design of a New Time-of-Flight Detector System.
Justus-Liebig-Universität Gießen, 2015.

D. Doering*.
Studies to improve the radiation hardness of CMOS-sensors in the application for vertex detectors of heavy-ion experiments.
Johann Wolfgang Goethe-Universität Frankfurt, 2015.

K. Göbel*.
Measurement of the ^{94}Mo(γ,n) reaction by Coulomb dissociation and related post-processing nucleosynthesis simulations for the p-process.
Johann Wolfgang Goethe-Universität Frankfurt, 2015.

R. Haake*.
Measurement of charged jets in p-Pb collisions at $\sqrt{s_{NN}}$ = 5.02 TeV with the ALICE detector.
Westfälische Wilhelms-Universität Münster, 2015.

W. Heupel*.
Light tetraquarks and mesons in a DSE/BSE approach.
Justus-Liebig-Universität Gießen, 2015.

S. Janowski*.
Phänomenologie des Dilatons in einem chiralen Modell mit (Axial-) Vektormesonen.
Johann Wolfgang Goethe-Universität FrankfurtWGU Frankfurt, 2015.

G. Kalicy*.
Development and test of a prototype for the PANDA Barrel DIRC detector at FAIR.
Johann Wolfgang Goethe-Universität Frankfurt, 2015.

A. Koloczek*.
Systematic s-process sensitivity studies.
Johann Wolfgang Goethe-Universität Frankfurt, 2015.

K. Koop.
Nachweis von vorwärtsgestreuten Protonen in photoninduzierten Reaktionen am Nukleon.
RFWU Bonn, 2015.

A. Lohs*.
Neutrino Reactions in Hot and Dense Matter.
Technische Universität Darmstadt, 2015.

B. Mei*.
Nuclear reactions for astrophysics with storage rings.
Johann Wolfgang Goethe-Universität Frankfurt, 2015.

B. Milanovic*.
Development of the readout controller for the CBM Micro-Vertex Detector.
Johann Wolfgang Goethe-Universität Frankfurt, 2015.

M. Patsyuk*.
Simulation, reconstruction, and design optimization for the PANDA barrel DIRC.
Johann Wolfgang Goethe-Universität Frankfurt, 2015.

A. Pitka*.
D^0- $\overline{D^0}$-Mischung im Zerfall D^0 - K_s π^+ π^- am PANDA-Experiment.
Justus-Liebig-Universität GießenJustus-Liebig-Universität Gießen, 2015.

T. Quagli*.
Hardware developments for the strip detector of the PANDA MVD.
Justus-Liebig-Universität Gießen, 2015.

D. Ralet*.
Lifetime measurement in the mass region $A \approx 100$ with the Pre-SPEC - AGATA setup.
Technische Universität Darmstadt, 2015.

P. Schrock*.
The electric dipole response of ^{132}Sn.
Technische Universität Darmstadt, 2015.

S. Schuchmann*.
Modification of K0s and Λ(Λ) transverse momentum spectra in Pb-Pb collisions at √sNN=2.76 TeV with ALICE.
Johann Wolfgang Goethe-Universität Frankfurt, 2015.

C. Stahl*.
New methods for the γ-ray spectroscopy with position-sensitive detector systems.
Technische Universität Darmstadt, 2015.

T. Tischler*.
Mechanical integration of the Micro Vertex Detector for the CBM experiment.
Johann Wolfgang Goethe-Universität Frankfurt, 2015.

R. Tripolt*.
Spectral Functions and Transport Coefficients from the Functional Renormalization Group.
Technische Universität Darmstadt, 2015.

F. R. Uhlig.
Charakterisierung und Anwendung von schnellen Photosensoren im Hinblick auf ihren Einsatz im PANDA-Experiment.
Friedrich-Alexander-Universität Erlangen-Nürnberg, 2015.

C. Wesp*.
Dynamical simulation of a linear sigma model near the chiral phase transition.
Johann Wolfgang Goethe-Universität Frankfurt, 2015.

From matter to materials and life – 620

135 publications listed in Web of Science or SCOPUS

[Editorial] Swift Heavy Ions in Matter.
Nuclear instruments & methods in physics research / B, 365:435.
doi: 10.1016/j.nimb.2015.11.013.

I. Alencar et al.
In situ Resonant Ultrasound Spectroscopy during irradiation of solids with relativistic heavy ions.
Acta materialia, 89:60.
doi: 10.1016/j.actamat.2015.01.031.

M. Ali*, S. Nasir* and W. Ensinger.
Bioconjugation-induced ionic current rectification in aptamer-modified single cylindrical nanopores.
Chemical communications, 51(16):3454.
doi: 10.1039/C5CC00257E.

M. Ali* et al.
Ionic Transport through Chemically Functionalized Hydrogen Peroxide-Sensitive Asymmetric Nanopores.
ACS applied materials & interfaces, 7(35):19541.
doi: 10.1021/acsami.5b06015.

N. E. Andreev et al.
Interaction of annular-focused laser beams with solid targets.
Laser and particle beams, 33(03):541.
doi: 10.1017/S0263034615000580.

D. Atanasov* et al.
Between atomic and nuclear physics: radioactive decays of highly-charged ions.
Journal of physics / B, 48(14):144024.
doi: 10.1088/0953-4075/48/14/144024.

D. Atanasov* et al.
Precision Mass Measurements of $^{129-131}$Cd and Their Impact on Stellar Nucleosynthesis via the Rapid Neutron Capture Process.
Physical review letters, 115(23):232501.
doi: 10.1103/PhysRevLett.115.232501.

B. Aurand* et al.
Reduction of X-ray generation in high-intensity laser ion acceleration.
Applied physics / B, 118(2):247.
doi: 10.1007/s00340-014-5979-7.

D. Banaś et al.
Subshell-selective x-ray studies of radiative recombination of U^{92+} ions with electrons for very low relative energies.
Physical review / A, 92(3):032710.
doi: 10.1103/PhysRevA.92.032710.

R. S. Belikov et al.
Negative pressure and spallation in graphite targets under nano- and picosecond laser irradiation.
Quantum electronics, 45(5):421.
doi: 10.1070/QE2015v045n05ABEH015759.

D. Bernhardt* et al.
Electron-ion collision spectroscopy: Lithium-like xenon ions.
Physical review / A, 91(1):012710.
doi: 10.1103/PhysRevA.91.012710.

D. Bernhardt* et al.
Spectroscopy of berylliumlike xenon ions using dielectronic recombination.
Journal of physics / B, 48(14):144008.
doi: 10.1088/0953-4075/48/14/144008.

H. Beyer* et al.
Crystal optics for precision x-ray spectroscopy on highly charged ions—conception and proof.
Journal of physics / B, 48(14):144010.
doi: 10.1088/0953-4075/48/14/144010.

K.-H. Blumenhagen* et al.
Identification and reduction of unwanted stray radiation using an energy- and position-sensitive Compton polarimeter.
Physica scripta, T166:014032.
doi: 10.1088/0031-8949/2015/T166/014032.

B. Botermann et al.
Erratum: Test of Time Dilation Using Stored Li^+ Ions as Clocks at Relativistic Speed [Phys. Rev. Lett. 113 , 120405 (2014)].
Physical review letters, 114(23):239902.
doi: 10.1103/PhysRevLett.114.239902.

C. Brabetz* et al.
Laser-driven ion acceleration with hollow laser beams.
Physics of plasmas, 22(1):013105.
doi: 10.1063/1.4905638.

C. Brandau* et al.
Storage-ring experiments on dielectronic recombination at the interface of atomic and nuclear physics.
Physica scripta, T166:014022.
doi: 10.1088/0031-8949/2015/T166/014022.

L. Breuer et al.
Time-of-flight secondary neutral & ion mass spectrometry using swift heavy ions.
Nuclear instruments & methods in physics research / B, 365:482.
doi: 10.1016/j.nimb.2015.07.117.

F. Burkart et al.
Analysis of 440GeV proton beam–matter interaction experiments at the High Radiation Materials test facility at CERN.
Journal of applied physics, 118(5):055902.
doi: 10.1063/1.4927721.

DOI:10.15120/GR-2016-1

L. Burr* et al.
Surface Enrichment in Au–Ag Alloy Nanowires and Investigation of the Dealloying Process.
The journal of physical chemistry / C, 119(36):20949.
doi: 10.1021/acs.jpcc.5b05596.

S. Busold* et al.
Towards highest peak intensities for ultra-short MeV-range ion bunches.
Scientific reports, 5:12459.
doi: 10.1038/srep12459.

M. Cassinelli* et al.
Structural and compositional characterization of $Bi_{1-x}Sb_x$ nanowire arrays grown by pulsed deposition to improve growth uniformity.
Nuclear instruments & methods in physics research / B, 365:668.
doi: 10.1016/j.nimb.2015.07.107.

W. Cayzac et al.
Predictions for the energy loss of light ions in laser-generated plasmas at low and medium velocities.
Physical review / E, 92(5):053109.
doi: 10.1103/PhysRevE.92.053109.

R. J. Chen et al.
Simulations of the isochronous mass spectrometry at the HIRFL-CSR.
Physica scripta, T166:014044.
doi: 10.1088/0031-8949/2015/T166/014044.

X. Chen* et al.
Report on a computer-controlled automatic test platform for precision RF cavity characterizations.
Physica scripta, T166:014061.
doi: 10.1088/0031-8949/2015/T166/014061.

S. Dedera et al.
On-line Raman spectroscopy of calcite and malachite during irradiation with swift heavy ions.
Nuclear instruments & methods in physics research / B, 365:564.
doi: 10.1016/j.nimb.2015.09.079.

D. T. Doherty et al.
Nuclear transfer reaction measurements at the ESR—for the investigation of the astrophysical $^{15}O(\alpha,\gamma)^{19}Ne$ reaction.
Physica scripta, T166:014007.
doi: 10.1088/0031-8949/2015/T166/014007.

B. Ecker* et al.
Double-stage soft x-ray laser pumped by multiple pulses applied in grazing incidence.
Journal of physics / B, 48(14):144009.
doi: 10.1088/0953-4075/48/14/144009.

S. Fritzsche*, A. Surzhykov* and A. Volotka.
Relativistically prolonged lifetime of the 2s2p $^3P_0$ level of zeronuclear-spin beryllium-like ions.
New journal of physics, 17(10):103009.
doi: 10.1088/1367-2630/17/10/103009.

T. Gaßner* and H. Beyer*.
Spatial characterization of the internal gas target at the ESR for the FOCAL experiment.
Physica scripta, T166:014052.
doi: 10.1088/0031-8949/2015/T166/014052.

R. Geithner* et al.
A squid-based beam current monitor for FAIR/CRYRING.
Physica scripta, T166:014057.
doi: 10.1088/0031-8949/2015/T166/014057.

J. Glorius*, Y. Litvinov* and R. Reifarth.
Neutron-induced reaction studies using stored ions.
Physica scripta, T166:014008.
doi: 10.1088/0031-8949/2015/T166/014008.

V. Gomez et al.
Charging a Capacitor from an External Fluctuating Potential using a Single Conical Nanopore.
Scientific reports, 5:9501.
doi: 10.1038/srep09501.

V. Gomez et al.
Converting external potential fluctuations into nonzero time-average electric currents using a single nanopore.
Applied physics letters, 106(7):073701.
doi: 10.1063/1.4909532.

O. Gorda* et al.
Ion-optical design of CRYRING@ESR.
Physica scripta, T166:014043.
doi: 10.1088/0031-8949/2015/T166/014043.

C. Gorges et al.
Isotope shift of ^{40,42,44,48}Ca in the 4s $^2S_{1/2}$ → 4p $^2P_{3/2}$ transition.
Journal of physics / B, 48(24):245008.
doi: 10.1088/0953-4075/48/24/245008.

M. Guerra et al.
Electron impact ionization cross-sections for few-electron uranium ions.
Journal of physics / B, 48(14):144027.
doi: 10.1088/0953-4075/48/14/144027.

A. Gumberidze*, T. Stöhlker* and Y. Litvinov*.
Atomic physics at the future facility for antiproton and ion research: status report 2014.
Physica scripta, T166:014076.
doi: 10.1088/0031-8949/2015/T166/014076.

A. Gumberidze* et al.
Ground-state excitation of heavy highly-charged ions.
Journal of physics / B, 48(14):144006.
doi: 10.1088/0953-4075/48/14/144006.

M. Hahn et al.
Storage ring cross section measurements for electron impact ionization of Fe^{7+}.
The astrophysical journal / 1, 813(1):16.
doi: 10.1088/0004-637X/813/1/16.

T. Hahn et al.
Broadband XUV polarimetry of high harmonics from plasma surfaces using multiple Fresnel reflections.
Applied physics / B, 118(2):241.
doi: 10.1007/s00340-014-5977-9.

K. P. Heeg et al.
Tunable Subluminal Propagation of Narrow-band X-Ray Pulses.
Physical review letters, 114(20):203601.
doi: 10.1103/PhysRevLett.114.203601.

D. Hengstler et al.
Towards FAIR: first measurements of metallic magnetic calorimeters for high-resolution x-ray spectroscopy at GSI.
Physica scripta, T166:014054.
doi: 10.1088/0031-8949/2015/T166/014054.

F. Herfurth* et al.
The HITRAP facility for slow highly charged ions.
Physica scripta, T166:014065.
doi: 10.1088/0031-8949/2015/T166/014065.

P.-M. Hillenbrand* et al.
Electron-capture-to-continuum cusp in U^{88+}+N_2 collisions.
Physical review / A, 91(2):022705.
doi: 10.1103/PhysRevA.91.022705.

P.-M. Hillenbrand* et al.
Experimental concepts of positron spectroscopy at HESR.
Physica scripta, T166:014026.
doi: 10.1088/0031-8949/2015/T166/014026.

F. Horst* et al.
A TLD-based ten channel system for the spectrometry of bremsstrahlung generated by laser-matter interaction.
Nuclear instruments & methods in physics research / A, 782:69.
doi: 10.1016/j.nima.2015.02.010.

C. Hubert* et al.
Swift heavy ion-induced radiation damage in isotropic graphite studied by micro-indentation and in-situ electrical resistivity.
Nuclear instruments & methods in physics research / B, 365:509.
doi: 10.1016/j.nimb.2015.08.056.

A. Hübner* et al.
Deposition of metals and metal oxides on plastic foils.
Journal of radioanalytical and nuclear chemistry, 305(3):703.
doi: 10.1007/s10967-015-3998-4.

C. P. João et al.
A 10-mJ-level compact CPA system based on Yb:KGW for ultrafast optical parametric amplifier pumping.
Applied physics / B, 118(3):401.
doi: 10.1007/s00340-015-6003-6.

T. Katayama et al.
Antiproton chain of the FAIR storage rings.
Physica scripta, T166:014073.
doi: 10.1088/0031-8949/2015/T166/014073.

B. Kindler* et al.
Coating of diamonds for detector application.
Journal of radioanalytical and nuclear chemistry, 305(3):963.
doi: 10.1007/s10967-014-3912-5.

F. Köhler* et al.
The electron mass from g -factor measurements on hydrogen-like carbon $^{12}C^{5+}$.
Journal of physics / B, 48(14):144032.
doi: 10.1088/0953-4075/48/14/144032.

O. Kovalenko* et al.
Investigation of the heavy-ion mode in the FAIR High Energy Storage Ring.
Physica scripta, T166:014042.
doi: 10.1088/0031-8949/2015/T166/014042.

O. Kovtun et al.
Spin-orbit interaction in bremsstrahlung and its effect on the electron motion in a strong Coulomb field.
Physical review / A, 92(6):062707.
doi: 10.1103/PhysRevA.92.062707.

D. Kraus et al.
The complex ion structure of warm dense carbon measured by spectrally resolved x-ray scattering.
Physics of plasmas, 22(5):056307.
doi: 10.1063/1.4920943.

J. Krauser et al.
Electrical conduction of ion tracks in tetrahedral amorphous carbon: temperature, field and doping dependence and comparison with matrix data.
New journal of physics, 17(12):123009.
doi: 10.1088/1367-2630/17/12/123009.

T. Krings et al.
Multi-element readout of structured HPGe-detectors for high-resolution x-ray spectroscopy using CUBE-preamplifiers.
Journal of Instrumentation, 10(02):C02043.
doi: 10.1088/1748-0221/10/02/C02043.

M. Kunitski et al.
Observation of the Efimov state of the helium trimer.
Science, 348(6234):551.
doi: 10.1126/science.aaa5601.

K. Kupka* et al.
Intense heavy ion beam-induced temperature effects in carbon-based stripper foils.
Journal of radioanalytical and nuclear chemistry, 305(3):875.
doi: 10.1007/s10967-015-4057-x.

B. Landgraf* et al.
Generation of multi-millijoule red-shifted pulses for seeding stimulated Raman backscattering amplifiers.
Optics express, 23(6):7400.
doi: 10.1364/OE.23.007400.

M. Lang et al.
Advances in understanding of swift heavy-ion tracks in complex ceramics.
Current opinion in solid state & materials science, 19(1):39.
doi: 10.1016/j.cossms.2014.10.002.

M. Lang et al.
Characterization of ion-induced radiation effects in nuclear materials using synchrotron x-ray techniques.
Journal of materials research, 30(09):1366.
doi: 10.1557/jmr.2015.6.

DOI:10.15120/GR-2016-1

M. Lestinsky* et al.
CRYRING@ESR: present status and future research.
Physica scripta, T166:014075.
doi: 10.1088/0031-8949/2015/T166/014075.

G. Loisch et al.
Hydrogen plasma dynamics in the spherical theta pinch plasma target for heavy ion stripping.
Physics of plasmas, 22(5):053502.
doi: 10.1063/1.4919851.

I. A. Maltsev et al.
Electron-positron pair creation in low-energy collisions of heavy bare nuclei.
Physical review / A, 91(3):032708.
doi: 10.1103/PhysRevA.91.032708.

J. Marganiec* et al.
Coulomb Dissociation Experiment of ^{27}P.
Acta physica Polonica / B, 46(3):473.
doi: 10.5506/APhysPolB.46.473.

B. Marx-Glowna et al.
Influence of higher harmonics of the undulator in X-ray polarimetry and crystal monochromator design.
Journal of synchrotron radiation, 22(5):1151.
doi: 10.1107/S1600577515011510.

E. Matei et al.
Electrical properties of single CdTe nanowires.
Beilstein journal of nanotechnology, 6:444.
doi: 10.3762/bjnano.6.45.

C. Mejía et al.
Radiolysis and sputtering of carbon dioxide ice induced by swift Ti, Ni, and Xe ions.
Nuclear instruments & methods in physics research / B, 365:477.
doi: 10.1016/j.nimb.2015.09.039.

F. Muench et al.
Self-Supporting Metal Nanotube Networks Obtained by Highly Conformal Electroless Plating.
ChemPlusChem, 80(9):1448.
doi: 10.1002/cplu.201500073.

R. A. Müller et al.
Effect of bound-state dressing in laser-assisted radiative recombination.
Physical review / A, 92(5):053426.
doi: 10.1103/PhysRevA.92.053426.

Q. H. Nguyen* et al.
Transport properties of track-etched membranes having variable effective pore-lengths.
Nanotechnology, 26(48):485502.
doi: 10.1088/0957-4484/26/48/485502.

W. Nörtershäuser and R. Sánchez*.
Laser spectroscopy at storage rings.
Physica scripta, T166:014020.
doi: 10.1088/0031-8949/2015/T166/014020.

A. Ortner et al.
Role of charge transfer in heavy-ion-beam–plasma interactions at intermediate energies.
Physical review / E, 91(2):023104.
doi: 10.1103/PhysRevE.91.023104.

R. I. Palomares et al.
In situ defect annealing of swift heavy ion irradiated CeO_2 and ThO_2 using synchrotron X-ray diffraction and a hydrothermal diamond anvil cell.
Journal of applied crystallography, 48(3):711.
doi: 10.1107/S160057671500477X.

R. M. Papaléo et al.
Confinement Effects of Ion Tracks in Ultrathin Polymer Films.
Physical review letters, 114(11):118302.
doi: 10.1103/PhysRevLett.114.118302.

S. Park et al.
Response of $Gd_2Ti_2O_7$ and $La_2Ti_2O_7$ to swift-heavy ion irradiation and annealing.
Acta materialia, 93:1.
doi: 10.1016/j.actamat.2015.04.010.

F. Pellemoine et al.
Study on structural recovery of graphite irradiated with swift heavy ions at high temperature.
Nuclear instruments & methods in physics research / B, 365:522.
doi: 10.1016/j.nimb.2015.09.007.

G. Pérez-Mitta et al.
Host–guest supramolecular chemistry in solid-state nanopores: potassium-driven modulation of ionic transport in nanofluidic diodes.
Nanoscale, 7(38):15594.
doi: 10.1039/C5NR04645A.

G. Pérez-Mitta et al.
Nanofluidic Diodes with Dynamic Rectification Properties Stemming from Reversible Electrochemical Conversions in Conducting Polymers.
Journal of the American Chemical Society, 137(49):15382.
doi: 10.1021/jacs.5b10692.

G. Pérez-Mitta et al.
Polydopamine Meets Solid-State Nanopores: A Bioinspired Integrative Surface Chemistry Approach To Tailor the Functional Properties of Nanofluidic Diodes.
Journal of the American Chemical Society, 137(18):6011.
doi: 10.1021/jacs.5b01638.

A. A. Peshkov*, S. Fritzsche* and A. Surzhykov*.
Ionization of H_2^+ molecular ions by twisted Bessel light.
Physical review / A, 92(4):043415.
doi: 10.1103/PhysRevA.92.043415.

N. Petridis* et al.
Prototype internal target design for storage ring experiments.
Physica scripta, T166:014051.
doi: 10.1088/0031-8949/2015/T166/014051.

A. R. Piriz, Y. B. Sun and N. A. Tahir*.
Analytic model for the dynamic Z-pinch.
Physics of plasmas, 22(6):062704.
doi: 10.1063/1.4922078.

A. R. Piriz, Y. B. Sun and N. A. Tahir*.
Hydrodynamic instability of elastic-plastic solid plates at the early stage of acceleration.
Physical review / E, 91(3):033007.
doi: 10.1103/PhysRevE.91.033007.

Y. Qiu et al.
Pores with Longitudinal Irregularities Distinguish Objects by Shape.
ACS nano, 9(4):4390.
doi: 10.1021/acsnano.5b00877.

P. Ramirez et al.
Energy conversion from external fluctuating signals based on asymmetric nanopores.
Nano energy, 16:375.
doi: 10.1016/j.nanoen.2015.07.013.

S. Ringleb et al.
HILITE—ions in intense photon fields.
Physica scripta, T166:014067.
doi: 10.1088/0031-8949/2015/T166/014067.

O. Rosmej* et al.
The hydrodynamic and radiative properties of low-density foams heated by x-rays.
Plasma physics and controlled fusion, 57(9):094001.
doi: 10.1088/0741-3335/57/9/094001.

J. Rothhardt* et al.
Prospects for laser spectroscopy of highly charged ions with high-harmonic XUV and soft x-ray sources.
Physica scripta, T166:014030.
doi: 10.1088/0031-8949/2015/T166/014030.

D. R. Rusby et al.
Measurement of the angle, temperature and flux of fast electrons emitted from intense laser–solid interactions.
Journal of plasma physics, 81(05):475810505.
doi: 10.1017/S0022377815000835.

R. Sánchez* et al.
Hyperfine transition in $^{209}Bi^{80+}$ — one step forward.
Physica scripta, T166:014021.
doi: 10.1088/0031-8949/2015/T166/014021.

D. Schauries et al.
Ion track annealing in quartz investigated by small angle X-ray scattering.
19th International Conference on Ion Beam Modification of Materials, Leuven (Belgium), 14 Sep 2015 - 19 Sep 2015.
Elsevier, Amsterdam [u.a.], 14th Sept. 2015.
doi: 10.1016/j.nimb.2015.07.081.

D. Schauries et al.
Orientation dependent annealing kinetics of ion tracks in c-SiO_2.
Journal of applied physics, 118(22):224305.
doi: 10.1063/1.4936601.

D. Schauries et al.
Size characterization of ion tracks in PET and PTFE using SAXS.
Nuclear instruments & methods in physics research / B, 365:573.
doi: 10.1016/j.nimb.2015.08.071.

A. Schlüter et al.
Phase field modelling of dynamic thermal fracture in the context of irradiation damage.
Continuum mechanics and thermodynamics, 1:1.
doi: 10.1007/s00161-015-0456-z.

S. Schmidt et al.
Non-destructive single-pass low-noise detection of ions in a beamline.
Review of scientific instruments, 86(11):113302.
doi: 10.1063/1.4935551.

I. Schubert* et al.
Growth and morphological analysis of segmented AuAg alloy nanowires created by pulsed electrodeposition in ion-track etched membranes.
Beilstein journal of nanotechnology, 6:1272.
doi: 10.3762/bjnano.6.131.

I. Schubert* et al.
STEM-EELS analysis of multipole surface plasmon modes in symmetry-broken AuAg nanowire dimers.
Nanoscale, 7(11):4935.
doi: 10.1039/C4NR06578F.

G. G. Scott et al.
Optimization of plasma mirror reflectivity and optical quality using double laser pulses.
New journal of physics, 17(3):033027.
doi: 10.1088/1367-2630/17/3/033027.

C. Shah et al.
Polarization measurement of dielectronic recombination transitions in highly charged krypton ions.
Physical review / A, 92(4):042702.
doi: 10.1103/PhysRevA.92.042702.

N. Sobel et al.
Conformal SiO2 coating of sub-100 nm diameter channels of polycarbonate etched ion-track channels by atomic layer deposition.
Beilstein journal of nanotechnology, 6:472.
doi: 10.3762/bjnano.6.48.

A. Spende et al.
TiO_2, SiO_2, and Al_2O_3 coated nanopores and nanotubes produced by ALD in etched ion-track membranes for transport measurements.
Nanotechnology, 26(33):335301.
doi: 10.1088/0957-4484/26/33/335301.

T. Stöhlker* and Y. A. Litvinov*.
Atomic physics experiments at the high energy storage ring.
Physica scripta, T166:014025.
doi: 10.1088/0031-8949/2015/T166/014025.

T. Stöhlker* et al.
APPA at FAIR: From fundamental to applied research.
Nuclear instruments & methods in physics research / B, 365(Part B):S0168583X15006552.
doi: 10.1016/j.nimb.2015.07.077.

DOI:10.15120/GR-2016-1

B. H. Sun et al.
Toward precision mass measurements of neutron-rich nuclei relevant to r-process nucleosynthesis.
Frontiers of physics, 10(4):1.
doi: 10.1007/s11467-015-0503-z.

A. Surzhykov* et al.
Corrigendum: Rayleigh x-ray scattering from many-electron atoms and ions.
Journal of physics / B, 4(18):189501.
doi: 10.1088/0953-4075/48/18/189501.

A. Surzhykov* et al.
Interaction of twisted light with many-electron atoms and ions.
Physical review / A, 91(1):013403.
doi: 10.1103/PhysRevA.91.013403.

A. Surzhykov et al.
Rayleigh x-ray scattering from many-electron atoms and ions.
Journal of physics / B, 48(14):144015.
doi: 10.1088/0953-4075/48/14/144015.

S. Tashenov et al.
Coherent population of magnetic sublevels of $2p_{3/2}$ state in hydrogenlike uranium by radiative recombination.
Physica scripta, T166:014027.
doi: 10.1088/0031-8949/2015/T166/014027.

R. Thomaz et al.
Oxygen loss induced by swift heavy ions of low and high dE/dx in PMMA thin films.
Nuclear instruments & methods in physics research / B, 365:578.
doi: 10.1016/j.nimb.2015.09.019.

C. L. Tracy et al.
Phase transformations in Ln_2O_3 materials irradiated with swift heavy ions.
Physical review / B, 92(17):174101.
doi: 10.1103/PhysRevB.92.174101.

C. L. Tracy et al.
Redox response of actinide materials to highly ionizing radiation.
Nature Communications, 6:6133.
doi: 10.1038/ncomms7133.

S. Trotsenko* et al.
Experimental study of the dielectronic recombination into Li-like uranium.
Physica scripta, T166:014024.
doi: 10.1088/0031-8949/2015/T166/014024.

X. L. Tu* et al.
Study of projectile fragmentation reaction with isochronous mass spectrometry.
Physica scripta, T166:014009.
doi: 10.1088/0031-8949/2015/T166/014009.

J. Ullmann* et al.
An improved value for the hyperfine splitting of hydrogen-like $^{209}Bi^{82+}$.
Journal of physics / B, 48(14):144022.
doi: 10.1088/0953-4075/48/14/144022.

M. Vogel* et al.
Penning-trap experiments for spectroscopy of highly-charged ions at HITRAP.
Physica scripta, T166:014066.
doi: 10.1088/0031-8949/2015/T166/014066.

F. Wagner et al.
Simultaneous observation of angularly separated laser-driven proton beams accelerated via two different mechanisms.
Physics of plasmas, 22(6):063110.
doi: 10.1063/1.4922661.

G. Weber* et al.
Combined linear polarization and angular distribution measurements of x-rays for precise determination of multipole-mixing in characteristic transitions of high- Z systems.
Journal of physics / B, 48(14):144031.
doi: 10.1088/0953-4075/48/14/144031.

D. Winters* et al.
Laser cooling of relativistic heavy-ion beams for FAIR.
Physica scripta, T166:014048.
doi: 10.1088/0031-8949/2015/T166/014048.

P. Woods et al.
Nuclear astrophysics experiments at storage rings: midterm perspectives at GSI.
Physica scripta, T166:014002.
doi: 10.1088/0031-8949/2015/T166/014002.

Z. W. Wu, S. Fritzsche* and A. Surzhykov*.
Nuclear magnetic dipole moment effect on the angular distribution of the Kα lines.
Physica scripta, T166:014029.
doi: 10.1088/0031-8949/2015/T166/014029.

Z. W. Wu*, A. Surzhykov* and S. Fritzsche*.
Reply to "Comment on 'Hyperfine-induced modifications to the angular distribution of the $K_{\alpha 1}$ x-ray emission' ".
Physical review / A, 91(5):056502.
doi: 10.1103/PhysRevA.91.056502.

P. Wustelt et al.
Momentum-resolved study of the saturation intensity in multiple ionization.
Physical review / A, 91(3):031401.
doi: 10.1103/PhysRevA.91.031401.

Y. M. Xing et al.
First isochronous mass measurements with two time-of-flight detectors at CSRe.
Physica scripta, T166:014010.
doi: 10.1088/0031-8949/2015/T166/014010.

G. Xu et al.
New model of calculating the energy transfer efficiency for the spherical theta-pinch device.
Physics of plasmas, 22(5):052703.
doi: 10.1063/1.4919938.

X. Xu et al.
A data analysis method for isochronous mass spectrometry using two time-of-flight detectors at CSRe.
Chinese physics / C, 39(10):106201.
doi: 10.1088/1674-1137/39/10/106201.

X. Xu et al.
Direct mass measurements of neutron-rich ^{86}Kr projectile fragments and the persistence of neutron magic number N =32 in Sc isotopes.
Chinese physics / C, 39(10):104001.
doi: 10.1088/1674-1137/39/10/104001.

C. A. Yablinsky et al.
Characterization of swift heavy ion irradiation damage in ceria.
Journal of materials research, 30(9):1473.
doi: 10.1557/jmr.2015.43.

V. Yahia et al.
Reduction of stimulated Brillouin backscattering with plasma beam smoothing.
Physics of plasmas, 22(4):042707.
doi: 10.1063/1.4918942.

X. Yan* et al.
Investigation of the momentum compaction factor of the ESR thorough Schottky mass measurements.
Physica scripta, T166:014045.
doi: 10.1088/0031-8949/2015/T166/014045.

V. A. Yerokhin* et al.
Target effects in negative-continuum-assisted dielectronic recombination.
Physical review / A, 92(4):042708.
doi: 10.1103/PhysRevA.92.042708.

R. Zabels et al.
Depth profiles of indentation hardness and dislocation mobility in MgO single crystals irradiated with swift ^{84}Kr and ^{14}N ions.
Applied physics / A, 120(1):167.
doi: 10.1007/s00339-015-9145-9.

V. A. Zaytsev et al.
Parity nonconservation effect in the resonance elastic electron scattering on heavy He-like ions.
Journal of physics / B, 48(16):165003.
doi: 10.1088/0953-4075/48/16/165003.

12 dissertations

A. Ananyeva*.
Double Resonant Coherent Excitation of Highly-Charged Ions in Crystals.
Johann Wolfgang Goethe-Universität Frankfurt, 2015.

X. Chen.
Non-Interceptive Position Detection for Short-Lived Radioactive Nuclei in Heavy-Ion Storage Rings.
Universität Heidelberg, 2015.

B. Gao.
Bound-state beta decay of ^{205}Tl.
Lanzhou (China), 2015.

J. Holmberg.
QED corrections to atomic wavefunctions in highly charged ions.
Universität Heidelberg, 2015.

T. Jahrsetz.
Two-photon processes in highly charged ions.
Universität Heidelberg, 2015.

F. Köhler.
Bound-Electron g-Factor Measurements for the Determination of the Electron Mass and Isotope Shifts in Highly Charged Ions.
Universität Heidelberg, 2015.

O. Kovalenko.
Ion optics and beam dynamics optimization at the HESR storage ring for the SPARC experiments with highly charged heavy ions.
Universität Heidelberg, 2015.

D. von Lindenfels*.
Experimental Studies of Highly Charged Ions in a Penning Trap for the Measurement of Electron Magnetic Moments by Double-Resonance Spectroscopy.
Universität Heidelberg, 2015.

A. Ortner*.
Energieverlust und Ladungsverteilung von Calciumionen in dichtem, schwach gekoppeltem Kohlenstoffplasma.
Technische Universität Darmstadt, 2015.

A. Schönlein.
Erzeugung von intensiver Röntgenstrahlung und Materie hoher Energiedichte durch laserbeschleunigte Elektronen.
Johann Wolfgang Goethe-Universität Frankfurt, 2015.

K. S. Schulze.
Methoden und Möglichkeiten der hochpräzisen Röntgenpolarimetrie.
Friedrich-Schiller-Universität Jena, 2015.

J. Wiechula.
UV/VUV-Spektroskopie an dichten Plasmen.
Johann Wolfgang Goethe-Universität Frankfurt, 2015.

Matter and technologies – 630

20 publications listed in Web of Science or SCOPUS

W. Barth* et al.
Heavy ion linac as a high current proton beam injector.
Physical review / Special topics / Accelerators and beams, 18(5):050102.
doi: 10.1103/PhysRevSTAB.18.050102.

W. Barth* et al.
U^{28+}-intensity record applying a H_2-gas stripper cell.
Physical review / Special topics / Accelerators and beams, 18(4):040101.
doi: 10.1103/PhysRevSTAB.18.040101.

S. Biswas et al.
Measurement of the spark probability of a GEM detector for the CBM muon chamber (MuCh).
Nuclear instruments & methods in physics research / A, 800:93.
doi: 10.1016/j.nima.2015.08.022.

DOI:10.15120/GR-2016-1

E. Fischer* et al.
Fast-Ramped Superconducting Magnets for FAIR Production Status and First Test Results.
IEEE transactions on applied superconductivity, 25(3):1.
doi: 10.1109/TASC.2015.2392157.

I. Hofmann and O. Boine-Frankenheim*.
Space-Charge Structural Instabilities and Resonances in High-Intensity BeamsHY.
Physical review letters, 115(20):204802.
doi: 10.1103/PhysRevLett.115.204802.

A. Kalimov et al.
Optimization of the Sextupole Magnets With Trim Coils for the Collector Ring of the FAIR Project.
IEEE transactions on magnetics, 51(3):1.
doi: 10.1109/TMAG.2014.2362680.

Z. Lecz, O. Boine-Frankenheim* and V. Kornilov*.
Transverse divergence in target normal sheath acceleration of a thick contamination layer.
Nuclear instruments & methods in physics research / A, 774:42.
doi: 10.1016/j.nima.2014.11.062.

D. Lens*, T. Faulwasser and C. M. Kellett.
Ansätze zur modellprädiktiven Regelung der longitudinalen Strahldynamik in Synchrotronen.
Automatisierungstechnik, 63(8):621.
doi: 10.1515/auto-2015-0020.

S. R. Mirfayzi et al.
Calibration of time of flight detectors using laser-driven neutron source.
Review of scientific instruments, 86(7):073308.
doi: 10.1063/1.4923088.

U. Niedermayer*, O. Boine-Frankenheim* and H. D. Gersem.
Space charge and resistive wall impedance computation in the frequency domain using the finite element method.
Physical review / Special topics / Accelerators and beams, 18(3):032001.
doi: 10.1103/PhysRevSTAB.18.032001.

U. Niedermayer*, L. Eidam* and O. Boine-Frankenheim*.
Analytic modeling, simulation and interpretation of broadband beam coupling impedance bench measurements.
Nuclear instruments & methods in physics research / A, 776:129.
doi: 10.1016/j.nima.2014.12.053.

M. Reese* et al.
Automatic intrinsic calibration of double-sided silicon strip detectors.
Nuclear instruments & methods in physics research / A, 779:63.
doi: 10.1016/j.nima.2015.01.032.

M. S. Sanjari* et al.
Conceptual design of elliptical cavities for intensity and position sensitive beam measurements in storage rings.
Physica scripta, T166:014060.
doi: 10.1088/0031-8949/2015/T166/014060.

P. Scharrer et al.
Electron stripping of Bi ions using a modified 1.4 MeV/u gas stripper with pulsed gas injection.
Journal of radioanalytical and nuclear chemistry, 305(3):837.
doi: 10.1007/s10967-015-4036-2.

P. Schmidt*, O. Boine-Frankenheim and P. Mulser.
Laser induced focusing for over-dense plasma beams.
Physics of plasmas, 22(9):093120.
doi: 10.1063/1.4931739.

P. Schnizer* et al.
Low-Temperature Test Capabilities for the Superconducting Magnets of FAIR.
IEEE transactions on applied superconductivity, 25(3):1.
doi: 10.1109/TASC.2014.2376704.

I. Strašík, I. Prokhorov and O. Boine-Frankenheim*.
Beam halo collimation in heavy ion synchrotrons.
Physical review / Special topics / Accelerators and beams, 18(8):081001.
doi: 10.1103/PhysRevSTAB.18.081001.

C. Trageser* et al.
A new data acquisition system for Schottky signals in atomic physics experiments at GSI's and FAIR's storage rings.
Physica scripta, T166:014062.
doi: 10.1088/0031-8949/2015/T166/014062.

C. Xiao* et al.
Straight low energy beam transport for intense uranium beams.
Nuclear instruments & methods in physics research / A, 788:173.
doi: 10.1016/j.nima.2015.03.055.

S. Yaramyshev* et al.
Virtual charge state separator as an advanced tool coupling measurements and simulations.
Physical review / Special topics / Accelerators and beams, 18(5):050103.
doi: 10.1103/PhysRevSTAB.18.050103.

3 dissertations

J. Grieser*.
Beam Phase Feedback in a Heavy-Ion Synchrotron with Dual-Harmonic Cavity System.
Technische Universität Darmstadt, 2015.

U. Niermayer*.
Determination of Beam Coupling Impedance in the Frequency Domain.
Technische Universität Darmstadt, 2015.

C. Tenholt*.
Entwicklung eines hochstromgepulsten Luftspulen-Quadrupols.
Johann Wolfgang Goethe-Universität Frankfurt, 2015.

Cancer Research – 310

34 publications listed in Web of Science or SCOPUS

E. Abdollahi* et al.
Upgrading the GSI beamline microscope with a confocal fluorescence lifetime scanner to monitor charged particle induced chromatin decondensation in living cells.
Nuclear instruments & methods in physics research / B, 365:626.
doi: 10.1016/j.nimb.2015.07.005.

D. Boscolo et al.
TLD efficiency calculations for heavy ions: an analytical approach.
The European physical journal / D, 69(12):286.
doi: 10.1140/epjd/e2015-60208-3.

T. Dettmering* et al.
Increased effectiveness of carbon ions in the production of reactive oxygen species in normal human fibroblasts.
Journal of radiation research, 56(1):67.
doi: 10.1093/jrr/rru083.

A. Eichhorn* et al.
SU-C-303-06: Treatment Planning Study for Non-Invasive Cardiac Arrhythmia Ablation with Scanned Carbon Ions in An Animal Model.
Medical physics, 42(6):3198.
doi: 10.1118/1.4923823.

T. Friedrich*, M. Durante* and M. Scholz*.
Comments to the paper "Modelling of cell killing due to sparsely ionizing radiation in normoxic and hypoxic conditions and an extension to high LET radiation" by A. Mairani et al., Int. J. Radiat. Biol. 89(10), 2013, 782–793.
International journal of radiation biology, 91(1):127.
doi: 10.3109/09553002.2014.952459.

T. Friedrich*, M. Durante* and M. Scholz*.
Simulation of DSB yield for high LET radiation.
Radiation protection dosimetry, 166(1-4):61.
doi: 10.1093/rpd/ncv147.

J. L. Frieß et al.
Electrophysiologic and cellular characteristics of cardiomyocytes after X-ray irradiation.
Mutation research / Fundamental and molecular mechanisms of mutagenesis, 777:1.
doi: 10.1016/j.mrfmmm.2015.03.012.

C. S. Gibhardt et al.
X-ray irradiation activates K^+ channels via H_2O_2 signaling.
Scientific reports, 5:13861.
doi: 10.1038/srep13861.

C. Graeff* et al.
Administration of romosozumab improves vertebral trabecular and cortical bone as assessed with quantitative computed tomography and finite element analysis.
Bone, 81:364.
doi: 10.1016/j.bone.2015.07.036.

R. Grün* et al.
Assessment of potential advantages of relevant ions for particle therapy: A model based study.
Medical physics, 42(2):1037.
doi: 10.1118/1.4905374.

L. Herr* et al.
A Comparison of Kinetic Photon Cell Survival Models.
Radiation research, 184(5):494.
doi: 10.1667/RR13862.1.

L. Herr* et al.
New Insight into Quantitative Modeling of DNA Double-Strand Break Rejoining.
Radiation research, 184(3):280.
doi: 10.1667/RR14060.1.

L. Herr* et al.
Sensitivity of the Giant LOop Binary LEsion (GLOBLE) cell survival model on parameters characterising dose rate effects.
Radiation protection dosimetry, 166(1-4):56.
doi: 10.1093/rpd/ncv150.

A. Hufnagl* et al.
The link between cell-cycle dependent radiosensitivity and repair pathways: A model based on the local, sister-chromatid conformation dependent switch between NHEJ and HR.
DNA repair, 27:28.
doi: 10.1016/j.dnarep.2015.01.002.

T. Kamada et al.
Carbon ion radiotherapy in Japan: an assessment of 20 years of clinical experience.
The lancet / Oncology, 16(2):e93.
doi: 10.1016/S1470-2045(14)70412-7.

A. W. Kijas et al.
ATM-dependent phosphorylation of MRE11 controls extent of resection during homology directed repair by signalling through Exonuclease 1.
Nucleic acids symposium series, 43(17):8352.
doi: 10.1093/nar/gkv754.

D. Kraft* et al.
NF-κB-dependent DNA damage-signaling differentially regulates DNA double-strand break repair mechanisms in immature and mature human hematopoietic cells.
Leukemia, 29(7):1543.
doi: 10.1038/leu.2015.28.

D. Kraft* et al.
Transmission of clonal chromosomal abnormalities in human hematopoietic stem and progenitor cells surviving radiation exposure.
Mutation research / Fundamental and molecular mechanisms of mutagenesis, 777:43.
doi: 10.1016/j.mrfmmm.2015.04.007.

J. Krimmer et al.
Collimated prompt gamma TOF measurements with multi-slit multi-detector configurations.
Journal of Instrumentation, 10(01):P01011.
doi: 10.1088/1748-0221/10/01/P01011.

DOI:10.15120/GR-2016-1

M. Large et al.
Study of the anti-inflammatory effects of low-dose radiationUntersuchung der antientzündlichen Effekte von niedrigdosierter Röntgenbestrahlung.
Strahlentherapie und Onkologie, 191(9):742.
doi: 10.1007/s00066-015-0848-9.

H. I. Lehmann et al.
Atrioventricular node ablation in Langendorff-perfused porcine hearts using carbon ion particle therapy: methods and an in vivo feasibility investigation for catheter-free ablation of cardiac arrhythmias.
Circulation / Arrhythmia and electrophysiology, 8(2):429.
doi: 10.1161/CIRCEP.114.002436.

Y. Lorat et al.
Nanoscale analysis of clustered DNA damage after high-LET irradiation by quantitative electron microscopy–the heavy burden to repair.
DNA repair, 28:93.
doi: 10.1016/j.dnarep.2015.01.007.

A. Maier* et al.
Experimental setup for radon exposure and first diffusion studies using gamma spectroscopy.
Nuclear instruments & methods in physics research / B, 362:187.
doi: 10.1016/j.nimb.2015.09.042.

I. Mattei et al.
Prompt-γ production of 220 MeV/u ^{12}C ions interacting with a PMMA target.
Journal of Instrumentation, 10(10):P10034.
doi: 10.1088/1748-0221/10/10/P10034.

J. Mirsch et al.
Direct measurement of the 3-dimensional DNA lesion distribution induced by energetic charged particles in a mouse model tissue.
Proceedings of the National Academy of Sciences of the United States of America, 112(40):12396.
doi: 10.1073/pnas.1508702112.

M. Prall* et al.
Treatment of arrhythmias by external charged particle beams: a Langendorff feasibility study.
Biomedizinische Technik, 60(2):146.
doi: 10.1515/bmt-2014-0101.

B. Roth et al.
Low-dose photon irradiation alters cell differentiation via activation of hIK channels.
Pflügers Archiv, 467(8):1835.
doi: 10.1007/s00424-014-1601-4.

M. Saager et al.
Split dose carbon ion irradiation of the rat spinal cord: Dependence of the relative biological effectiveness on dose and linear energy transfer.
Radiotherapy and oncology, 117(2):358.
doi: 10.1016/j.radonc.2015.07.006.

E. Scifoni*.
Radiation biophysical aspects of charged particles: From the nanoscale to therapy.
Modern physics letters / A, 30(17):1540019.
doi: 10.1142/S0217732315400192.

O. Steinsträter* et al.
Integration of a model-independent interface for RBE predictions in a treatment planning system for active particle beam scanning.
Physics in medicine and biology, 60(17):6811.
doi: 10.1088/0031-9155/60/17/6811.

W. Tinganelli* et al.
Kill-painting of hypoxic tumours in charged particle therapy.
Scientific reports, 5:17016.
doi: 10.1038/srep17016.

F. Tommasino* et al.
Application of the local effect model to predict DNA double-strand break rejoining after photon and high-LET irradiation.
Radiation protection dosimetry, 166(1-4):66.
doi: 10.1093/rpd/ncv164.

F. Tommasino* et al.
Induction and Processing of the Radiation-Induced Gamma-H2AX Signal and Its Link to the Underlying Pattern of DSB: A Combined Experimental and Modelling Study.
PLoS one, 10(6):e0129416.
doi: 10.1371/journal.pone.0129416.

I. Yohannes et al.
SU-E-T-663: Radiation Properties of a Water-Equivalent Material Formulated Using the Stoichiometric Analysis Method in Heavy Charged Particle Therapy.
Medical physics, 42(6):3489.
doi: 10.1118/1.4925026.

5 dissertations

R. Brevet*.
Optimized treatment parameters to account for interfractional variability in scanned ion beam therapy of lung cancer.
Technische Universität Darmstadt, 2015.

L. Herr*.
Modeling of time-dose-LET effects in the cellular response to radiation.
Technische Universität Darmstadt, Darmstadt, 2015.

S. Hild*.
Adaptive Treatment of prostate carcinoma in scanned ion beam therapy [cumulative PhD].
Friedrich-Alexander-Universität Erlangen-Nürnberg, 2015.

S. Luft*.
Impact of ionizing radiation on human embryonic stem cells.
Technische Universität Darmstadt, 2015.

A. Maier*.
Entwicklung einer Radonkammer und Messung der Radonlöslichkeit in Gewebe.
Technische Universität Darmstadt, 2015.

Experiments performed at the GSI accelerators in 2015

Compiled by Daniel Severin[1], beam time coordinator 2015

[1]GSI, Darmstadt, Germany

In all tables 1 shift represents 8 hours of beam delivered to an experiment including necessary accelerator tuning time.

Exp	Short title	Spokesperson	Area	Ion	Shifts
U284	Study of nuclear structure of 265-Sg with ALBEGA	Düllmann	X8	^{48}Ca	97
U288	Study of chemical properties of element 114	Yakushev/ Herzberg			
U285	Ion energy loss in plasma at the maximum of the stopping power	Cayzac	Z6	C	2
U287	LIGHT: Laser acceleration and transport of ions (p,C,O,F)	Roth	Z6	C	3
U290	Laser spectroscopy of Nobelium	Backe/ Block	Y7	^{48}Ca	57
U292	On-line commissioning of the cryogenic SHIPTRAP gas cell	Block	Y7	^{48}Ca	7
UBIO	Biology Experiments at UNILAC	Friedrich	X0, X6	He, C, Au	24
UMAT	Material Science Experiments at the UNILAC	Trautmann	X0, M1, M2, M3	C. Ca, Au, U	92

DOI:10.15120/GR-2016-1

Statutory organs and scientific advisory committees of GSI (2015)

Compiled by K. Füssel

Supervisory Board / Aufsichtsrat (AR):

Staatssekretär Dr. G. Schütte [chair],
Bundesministerium für Bildung und Forschung, Bonn/Berlin (Germany),
as representative of the Federal Republic of Germany

Dr. B. Vierkorn-Rudolf,
Bundesministerium für Bildung und Forschung, Bonn/Berlin (Germany),
as representative of the Federal Republic of Germany

Ministerialdirigent Dr. R. Bernhardt [vice-chair],
Hessisches Ministerium für Wissenschaft und Kunst, Wiesbaden (Germany),
as representative of the State of Hesse in Germany

Ministerialdirigentin I. Schäfer,
Ministerium für Bildung, Wissenschaft, Weiterbildung und Kultur, Mainz (Germany),
as representative of the State of Rhineland-Palatinate in Germany

Ministerialrat D. Klein (first half of 2015),
Thüringer Ministerium für Bildung, Wissenschaft und Kultur, Erfurt (Germany),
as representative of the State of Thuringia in Germany

Dr. B. Ebersold (second half of 2015)
Thüringer Ministerium für Bildung, Wissenschaft und Kultur, Erfurt (Germany),
as representative of the State of Thuringia in Germany

Prof. Dr. K.-H. Kampert,
Bergische Universität Wuppertal (Germany),
as representative of the Scientific Council of GSI

Prof. Dr. U. Steigenberger,
ISIS Rutherford Appleton Laboratory, Oxfordshire (United Kingdom),
as representatives from the fields of science and economy

Prof. Dr. R. Heuer,
European Organization for Nuclear Research CERN, Geneva (Switzerland),
as representatives from the fields of science and economy

Dr. B. Lommel,
GSI Helmholtzzentrum für Schwerionenforschung,
as spokesperson of the Scientific-Technical Council of GSI

Directors' Board / Geschäftsführung (GF):

U. Weyrich, Prof. Dr. K. Langanke
Prof. Dr. O. Kester (assoc.), Dr.-Ing. J. Henschel (assoc.), Prof. Dr. T. Stöhlker (assoc.),

Scientific Council / Wissenschaftlicher Beirat (WBR):

K.-H. Kampert [chair], Bergische Universität Wuppertal (Germany);
A. Bracco, University of Milano (Italy); *P. Chomaz*, CEA/Saclay, Gif-sur-Yvette (France); *R. Hayano*, University of Tokyo (Japan); *B. Jacak*, Stony Brook University, Stony Brook, New York (USA); *S. Jacquemot*, LULI, Palaiseau (France); *T. Roser*, BNL, Upton (USA); *E. Tomasi-Gustafsson*, CEA/Saclay, IRFU/SPhN, IN2P3/IPN Orsay (France); *A. Warczak*, Jagiellonian University, Warsaw (Poland);

DOI:10.15120/GR-2016-1

Secretary: K.-D. Groß

Scientific and Technical Council / Wissenschaftlich-Technischer Rat (WTR):

https://www.gsi.de/work/organisation/wissenschaftliche_gremien/wtr.htm

B. Lommel (Spokesperson); *D. Ackermann; R. Bär; W. Barth; W. Bayer; P. Braun-Munzinger; A. Bräuning-Demian; M. Durante; R. Fuchs; M. Gorska; F. Herfurth; Y. Leifels* (Vice-Spokesperson)*; V. Lindenstruth; Y. Litvinov; P. Malzacher; F. Maas; D. Ondreka; K. Peters; H. Reich-Sprenger; C. Scheidenberger; L. Schmitt; M. Schwickert; P. Senger; H. Simon; P. Spiller; J. Stadlmann; M. Steck; T. Stöhlker; C. Trautmann; G. Walter; U. Weinrich;*

Scientific Programme Advisory Committees of GSI

https://www.gsi.de/work/organisation/wissenschaftliche_gremien.htm

General Program Advisory Committee G-PAC:

P. Giubellino[chair], INFN Turin, Turin (Italy);
acting referees in 2015:
P. Apel, JINR (Russia); *N. Bassler*, Aarhus University (Denmark); *G. Battistoni*, INFN (Italy); *W. Catford*, University of Physics (UK); *Th. Cornelius*, IM2NP UMR CNRS (France); *D. Gericke*, University Warwick (UK); *M. Harakeh*, KVI (The Netherlands); *S. Klaumünzer*, HZB (Germany); *R. Krücken*, TRIUMF (Canada); *M. Lewitowicz*, GANIL (France); *N. Pietralla*, Technical University Darmstadt (Germany); *G. Reitz*, DLR (Germany); *H. Rothard*, GANIL (France); *D. Schneider*, LLNL-NIF (USA); *A. Türler*, PSI (Switzerland); *M. Wada*, RIKEN (Japan); *W. J. Weber*, University of Tennessee (USA);

PHELIX Committee:

https://www.gsi.de/work/organisation/wissenschaftliche_gremien/pac/ppac.htm

V. Fortov [chair], JIHT, RAS, Moscow (Russia);
D. Gericke, University of Warwick, Coventry (UK); *A. Golubev*, ITEP, Moscow (Russia); *D. Schneider [vice-chair]*, LLNL-NIF, Livermore, California (USA); V. *Tikhonchuk*, University of Bordeaux 1, Talence (France); *P. Thierolf*, LMU, München (Germany).

GSI Users' Group Executive Committee (UEC):

https://www.gsi.de/work/organisation/wissenschaftliche_gremien/user/gsi_users_group.htm

Nuclear Structure:
T. Faestermann (Germany); M. Pfutzner (Poland); D. Cortina (Spain); A. Jungclaus (Spain); P. Regan [past chair], (UK)
Nuclear Collision:
P. Salabura (Poland); T. Matulewicz (Poland); Nicole Bastid (France)
Atomic Physics:
D. Dauvergne (France); A. Müller (Germany)
Plasma Physics:
J. Jacoby (Germany); T. Kühl (Germany)
Heavy Elements:
J. Kratz (Germany); A. Türler (Germany)
Theory:
W. Cassing (Germany)
Biophysics:
M. Löbrich (Germany)
Materials Research:
W. Ensinger [chair], (Germany)
Students:
B. Schuster (Germany)

DOI:10.15120/GR-2016-1

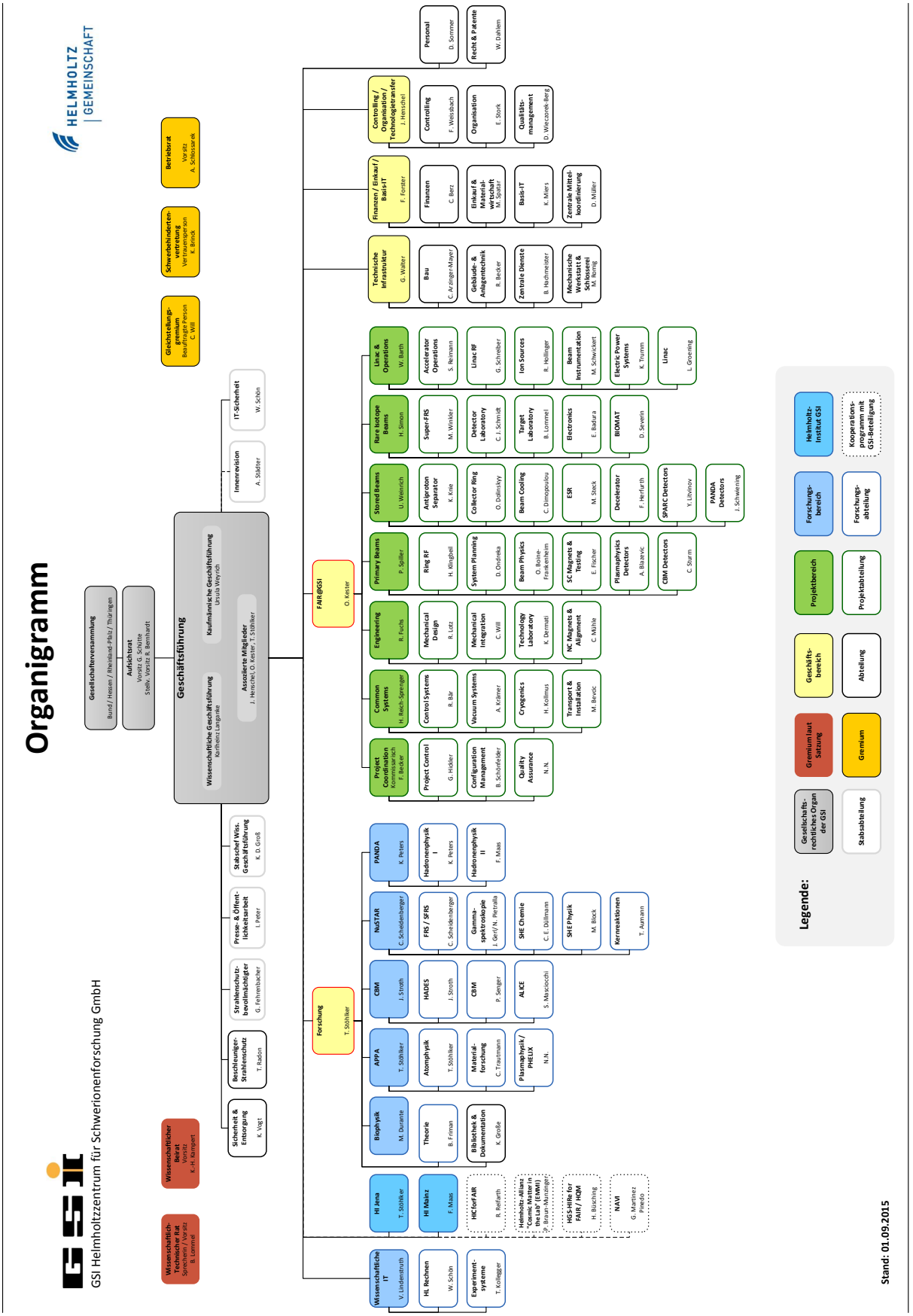
Organigramm
GSI Helmholtzzentrum für Schwerionenforschung GmbH
HELMHOLTZ GEMEINSCHAFT
Gesellschafterversammlung
Bund / Hessen / Rheinland-Pfalz / Thüringen
Aufsichtsrat
Vorsitz G. Schütte
Stellv. Vorsitz K. Beimdiek
Geschäftsführung
Wissenschaftliche Geschäftsführung
Karlheinz Langanke
Kaufmännische Geschäftsführung
Ursula Weyrich
Assoziierte Mitglieder
J. Henschel, O. Kester, T. Stöhlker
Betriebsrat
Vorsitz
A. Schlosarek
Schwerbehinderten-vertretung
Vertrauensperson
K. Brinck
Gleichstellungs-gremium
Beauftragte Person
C. Will
Innenrevision
A. Stidster
IT-Sicherheit
W. Schön
Stabsbereich Wiss. Geschäftsführung
K. D. Groß
Presse- & Öffent-lichkeitsarbeit
I. Peter
Strahlenschutz-beauftragter
G. Fehrenbacher
Beschleuniger-Strahlenschutz
T. Radon
Sicherheit & Entsorgung
K. Vogt
Wissenschaftlich-Technischer Rat
Sprecherin / Vorsitz
B. Lommel
Wissenschaftlicher Beirat
Vorsitz
K.-H. Kampert
FAIR@GSI
O. Kester
Forschung
T. Stöhlker
Wissenschaftliche IT
V. Lindenstruth
HI Jena
T. Stöhlker
HI Mainz
F. Maas
HIC for FAIR
R. Reifarth
Helmholtz-Allianz "Cosmic Matter in the Lab" (EMMI)
P. Reiter, H. Weick
HGS-Hire for FAIR / HQM
H. Büsching
NAVI
G. Martinez
P. Reiter
Experiment-systeme
T. Kollegger
HL Rechnen
W. Schön
Bibliothek & Dokumentation
K. Große
Theorie
B. Friman
Atomphysik
T. Stöhlker
Material-forschung
C. Trautmann
Plasmaphysik / PHELIX
N.N.
Biophysik
M. Durante
APPA
T. Stöhlker
CBM
J. Stroth
HADES
J. Stroth
CBM
P. Senger
ALICE
S. Masciocchi
NuSTAR
C. Scheidenberger
FRS / SFRS
C. Scheidenberger
Gamma-spektroskopie
J. Gerl / N. Pietralla
SHE Chemie
C. E. Düllmann
SHE Physik
M. Block
Kernreaktionen
T. Aumann
PANDA
K. Peters
Hadronenphysik I
K. Peters
Hadronenphysik II
F. Maas
Project Coordination
Kommissarisch
F. Becker
Project Control
G. Hickler
Configuration Management
B. Schönfelder
Quality Assurance
N.N.
Common Systems
H. Reich-Sprenger
Control Systems
R. Bär
Vacuum Systems
A. Krämer
Cryogenics
H. Kollmus
Transport & Installation
M. Bevcic
Engineering
R. Fuchs
Mechanical Design
R. Lotz
Mechanical Integration
C. Will
Technology Laboratory
K. Dermati
NC Magnets & Alignment
C. Mühle
Primary Beams
P. Spiller
Ring RF
H. Klingbeil
System Planning
D. Ondreka
Beam Physics
O. Boine-Frankenheim
SC Magnets & Testing
E. Fischer
Plasmaphysics Detectors
A. Blazevic
CBM Detectors
C. Sturm
Stored Beams
U. Weinrich
Antiproton Separator
K. Knie
Collector Ring
O. Dolinskyy
Beam Cooling
C. Dimopoulou
ESR
M. Steck
Decelerator
F. Herfurth
SPARC Detectors
Y. Litvinov
PANDA Detectors
J. Schweining
Rare Isotope Beams
H. Simon
Super-FRS
M. Winkler
Detector Laboratory
C. J. Schmidt
Target Laboratory
B. Lommel
Electronics
E. Badura
BIOMAT
D. Severin
Linac & Operations
W. Barth
Accelerator Operations
S. Reimann
Linac RF
G. Schreiber
Ion Sources
R. Hollinger
Beam Instrumentation
M. Schwickert
Electric Power Systems
K. Thumm
Linac
L. Groening
Technische Infrastruktur
G. Walter
Bau
C. Arzinger-Mayer
Gebäude- & Anlagentechnik
R. Becker
Zentrale Dienste
B. Hachmeister
Mechanische Werkstatt & Schlosserei
M. Romig
Finanzen / Einkauf / Basis-IT
F. Forster
Finanzen
C. Berz
Einkauf & Materialwirtschaft
M. Spatar
Basis-IT
K. Miers
Zentrale Mittelkoordinierung
D. Müller
Controlling / Organisation / Technologietransfer
J. Henschel
Controlling
F. Weissbach
Organisation
E. Stork
Qualitäts-management
D. Wieczorek-Berg
Personal
D. Sommer
Recht & Patente
W. Dahlem
Legende:
Gesellschafts-rechtliches Organ der GSI
Gremium laut Satzung
Geschäfts-bereich
Projektbereich
Forschungs-bereich
Helmholtz-Institut GSI
Stabsabteilung
Gremium
Abteilung
Projektabteilung
Forschungs-abteilung
Kooperations-programm mit GSI-Beteiligung
Stand: 01.09.2015

DOI:10.15120/GR-2016-1